9th International Conference on

Fundamental and applied MHD, Thermo acoustic and Space technologies

SEVENTH FRAMEWORK PROGRAMME

Theme 9: SPACE

Riga – Latvia
June 16-20 , 2 0 1 4

Chairmen A. Alemany France, J. Freibergs, Latvia

Co-chairmen :

J.P. Chopart, France – C. Latge, France – M. Francois, France - E. Gaia, Italy

Secretaries : B. Collovati, France - M. Broka, Latvia
pamir@simap.grenoble-inp.fr

Supporting Organisation

CNRS :	Centre National de la Recherche Scientifique
INP :	Institut Polytechnique de Grenoble
UJF :	Université Joseph Fourier Grenoble
CEA :	Commissariat à l'Energie Atomique

Ministère de l'Enseignement Supérieur et de la Recherche
Ambassade de France à Alger
Ambassade de France à Riga

Organising committee

A. Alemany, M. Broka, J.P. Chopart, B. Collovati , A.L. Daltin, J. Freibergs. M. Francois E. Gaia, C. Latge, S. Shchanitsina

Scientific committee

Alemany A., France

Alradi M., Syria

Aogaki R., Japan

Balbaud F., CEA France

Blums E., Latvia

Bouabdallah A., Algeria

Buligins L., Latvia

Cebers A., Latvia

Chopart J.P., France

Cuevas S., Mexico

Ellappan R.K., India

Etay J., France

Francois M., France

Freibergs J., Latvia

Frick P., Russia

Gailitis A., Latvia

Gaia E., Italy

Gerbeth G., Germany

Jakovics A., Latvia

Latgé C., France

Li Puma A., France

Mogi I., Japan

Molokov S., UK

Mond M., Israel

Odenbach S.,Germany

Proctor M.R.E., UK

Skorvanek I., Slovakia

Thess A., Germany

Uhlemann M., Germany

Zabinski P., Poland

Montici A., Italy

Poli G., France

Roux J.P., France

Sellier A., France

Preface

The Pamir conference is organised for the 9^{th} time and for the second time in Latvia. As in the past, Pamir is a generalist conference on magneto hydro dynamics (MHD) and more generally in magneto sciences. It is focussed on basic MHD problems as for example turbulence and dynamo effect but considering also energetic and electro processing of material as well as the technology of liquid metal which is of a first importance in the concept of large power plant as I.T.E.R and the new recent development of the fast breeder reactors represented by generation 4.

The main relevant fluids considered by the topics of the conference are liquid metals which have high electrical conductivity but an important aspect of the magneto science is devoted to poorly conducting fluids as electrolytes submitted to the influence of magnetic fields offering large possibilities to control and improve the mass transfer in such media. In this field of research a new project in course of elaboration, **MACE** as **MA**gnetic **C**ontrol of **E**lectro chemistry, will be proposed in the frame of the **COST** program of the EU, under the leading of Professor **Piotr Zabinski** from the University of Krakov, Poland. A MACE meeting will be organised during the Pamir Conference.

Thus the conference is focussed on fundamental and applied researches combining several disciplines as hydrodynamics, mass and heat transfers, electromagnetism... Both theoretical and experimental aspects are considered as well as analytical and numerical methods. The participation of engineers from industrial companies and researchers from universities are particularly important in the objective of Research and Development activities.

As in the last Pamir 2011, the present edition is coupled with a summer school centred on the activity of the European project "Space Thermo acoustic Radio-Isotopic Power System".

"**Space TRIPS**".

Space TRIPS aims to demonstrate the feasibility of a highly efficient and reliable electrical generator for space, using radio isotopic heat source. The project is based on the modelling, design, construction and experimentation of a prototype of MHD electrical generator driven by a thermo acoustic engine. A design implementing this technology will be completed to asses the performance of a space system.

The project takes advantages of the complementary competences of 6 partners from 4 European countries.

They are

- HEKYOM start up company, French, develops Thermo acoustics applications
- CNRS (Centre National de la Recherche Scientifique) French research organisation
- IPUL Institute of Physics of the University of Latvia
- AREVA TA French company about nuclear activity
- Thales Alenia Space Italy specialised in Space Technology
- HZDR Germany , Research specialized in MHD activities

As it is usual in the EU project the dissemination of knowledge is an important aspect of space TRIPS especially in direction of young scientists and engineers. This is the reason why a summer school is organised in parallel with the conference and why two specific sessions of the conference are devoted for one at the thermo acoustic process and for the other to the space technology.

Space TRIPS is largely represented in the board of the two events, as chairmen

A. Alemany, France. J. Freibergs, Latvia

and co chairmen:

J.P. Chopart, France – C. Latge, France – M. François, France - E. Gaia, Italy

Foreword

These two volumes are the proceedings of the communication of the 9th Pamir International Conference held in Riga, Latvia, June 16 – 20, 2014.

The present edition of Pamir benefits of the support of the EU by the way of the project Space Trips (Space Thermo acoustic Radio-Isotopic Power System) at the origin of the summer school that welcomes students of many European countries. The organizers of these two events express their gratitude to the University of Latvia which host the sessions of the conference, The French embassy in Latvia and the “Institut Francais en Lettonie” to host the Space Trips summer school. The papers are indexed according to the topics and the numerotation accorded to each of them.

Volume 1 contains the papers of:

A - Basic MHD
B - Thermo acoustic
C - Space: stress on technologies

Volume 2 contains the papers of:

D - Liquid metal technologies for coolant applications
E - Applied MHD for material application
F - Ferrofluid

For further information, please contact the secretaries of the conference:

Beatrice Collovati
Pamir e-mail: pamir@simap.grenoble-inp.fr

Maja Broka
IPUL e-mail: mbroka@sal.lv

Svetlana Shchanitsina
Magnetohydrodynamics, IPUL: e-mail: sveta@sal.lv

CONTENTS

VOLUME 1

A. BASIC MHD
A.1. Convection and heat transfer in MHD

A.2. Dynamo

A.3. Instability and transition to turbulence

A.5. Modelling of MHD turbulence

A.6. Numerical and experimental methods

A.7. Strong magnetic field

A.8. Novel MHD problems and applications

B. THERMO ACOUSTIC
B.1. Linear and nonlinear theory

B.2. Modelling and numerical simulation 2D and 3D

B.5. Engines for refrigeration, air conditioning electrical power

B.7. Thermo acoustics for space missions

C. SPACE: STRESS ON TECHNOLOGIES

C.1. MHD: possible uses and problems

C.7. Nuclear sources: testing, integration, launch and decommissioning

MIXED CONVECTION IN HORIZONTAL DUCTS WITH STRONG TRANSVERSE MAGNETIC FIELDS

ZHANG X., LV X., ZIKANOV* O.
University of Michigan – Dearborn, Dearborn, USA
*Corresponding author email: zikanov@umich.edu

Abstract: Mixed convection in liquid metal flows in horizontal ducts with strong transverse magnetic fields is analyzed numerically. Our goal is to understand the nature of the convection instabilities that may occur in liquid metal blankets for fusion reactors. High Hartmann ($Ha \leq 800$) and Grashof ($Gr \leq 10^9$) numbers are considered. In the case of bottom heating, roll-like structures aligned with the magnetic field and producing strong low-frequency temperature fluctuations at walls arise at high Ha and Gr. In the duct with sidewall heating, streamwise-uniform, laminar, steady-state flows are found at moderate and high Ha.

1. Introduction

In this paper, we consider the influence of very strong (high Hartmann numbers) magnetic fields on mixed (combined natural and forced) thermal convection in flows within horizontal ducts. The case of low magnetic Reynolds and Prandtl numbers is considered. The main motivation is the role of such flows in several possible designs of liquid metal (Li or PbLi) blankets for future nuclear fusion reactors (see, e.g. [1]). It is known that a strong magnetic field can dramatically change the flow's behavior. The effect is due to the Lorentz force and the conversion of the flow's kinetic energy into heat by the Joule dissipation of induced electric currents. An extensive discussion of the effect can be found, for example, in [2]. Since conventional turbulence is most likely fully suppressed by such a strong magnetic field, the flow structure and distribution of temperature are largely determined by the buoyancy force in its interaction with the Lorentz force, viscosity, and imposed pressure gradients. The immediate precursor of our work is the paper [3], where the linear stability and DNS analyses were conducted for the flow through a round horizontal pipe with transverse horizontal magnetic field and uniform constant-rate heating applied to the bottom half of the wall. The computational work was performed to explain the results of the experiments [4], where temperature fluctuations disappeared at moderately strong magnetic fields indicating suppression of turbulence, but reappeared at stronger magnetic fields in the form of high-amplitude low-frequency oscillations. The results of the numerical analysis of [3] were in a remarkably good quantitative agreement with the experimental data and produced the explanation that the oscillations are caused by the convection instability in the form of rolls aligned with the magnetic field. Our analysis is conducted in a manner similar to that of [3] but for the square duct geometry, two orientations of the magnetic field, and in a much broader range of Gr and Ha.

2. Theoretical and numerical model

As shown in fig. 1, we consider flows in horizontal ducts with imposed horizontal transverse magnetic field **B** and uniform constant-rate heating applied to either bottom or vertical wall. The other three walls are thermally insulated. All walls are electrically insulated. The liquid metal is modeled as an incompressible, electrically conducting Newtonian viscous fluid with constant physical properties. The Boussinesq approximation is applied for the temperature-related buoyancy force. Following the assumption of small magnetic Reynolds and Prandtl

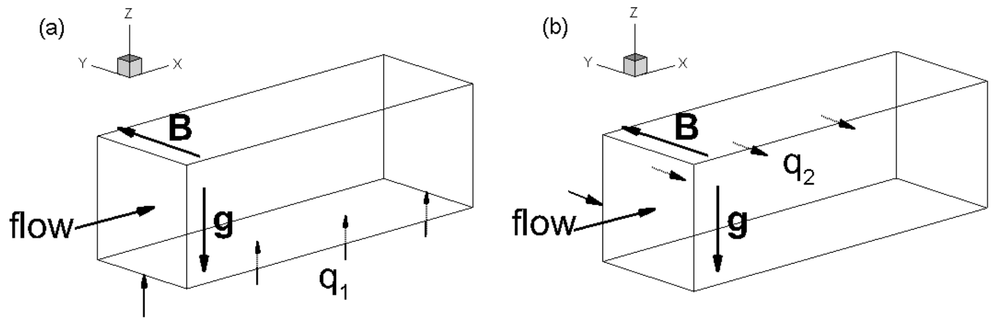

Figure 1: Flow geometry and coordinate system for bottom heating duct (a), sidewall heating duct (b).

numbers typically valid in the fusion reactor blankets, we use the quasi-static approximation (see, e.g. [2]). The governing equations are non-dimensionalized using the duct half-width d as the length scale, mean streamwise velocity U as the velocity scale, wall heating-based group qd/κ ,where κ is the thermal conductivity, as the temperature scale, B as the scale of the magnetic field strength, and dUB as the scale of electric potential. The non-dimensional governing equations are:

$$\partial_t \mathbf{u} + (\mathbf{u}\cdot\nabla)\mathbf{u} = -\nabla p - \nabla\hat{p} - \nabla\tilde{p} + \mathrm{Re}^{-1}\nabla^2\mathbf{u} + \mathbf{F}_b + \mathbf{F}_L,$$
$$\nabla\cdot\mathbf{u} = 0,$$
$$\partial_t\theta + \mathbf{u}\cdot\nabla\theta = \mathrm{Pe}^{-1}\nabla^2\theta - u_x \, {dT_m}/{dx}.$$

Temperature field is a sum of fluctuations θ and the mean-mixed temperature $T_m(x)$. Pressure is decomposed into the component $\hat{p}$(x) corresponding to spatially uniform streamwise gradient $d\hat{p}/dx$ adjusted at every time step to maintain constant mean velocity, component $\tilde{p}$ that balances the buoyancy force due to the x-dependent mean-mixed temperature $T_m(x)$ (see [3]), and perturbations p. The buoyancy and Lorentz forces are: $\mathbf{F}_b = -\mathrm{Gr}\mathrm{Re}^{-2}\mathbf{e}_z\theta$ and $\mathbf{F}_L = -\mathrm{Ha}^2\mathrm{Re}^{-1}\mathbf{j}\times\mathbf{e}_y$. The electric current is determined by the Ohm's law $\mathbf{j} = -\nabla\phi + \mathbf{u}\times\mathbf{e}_y$, where electric potential ϕ is a solution of the Poisson equation $\nabla^2\phi = \nabla\cdot(\mathbf{u}\times\mathbf{e}_y)$. The non-dimensional parameters of the problem are the Reynolds number $\mathrm{Re} = Ud/\nu$, Hartmann number $\mathrm{Ha} = Bd(\sigma/\rho\nu)^{1/2}$, Peclet number $\mathrm{Pe} = Ud/\chi$, and Grashof number $\mathrm{Gr} = g\beta q d^4/\nu^2\kappa$. The boundary conditions at the duct walls are the no-slip conditions **u**=0 for velocity, perfect electric insulation $\partial\phi/\partial n = 0$, conditions of constant-rate heating at the lower wall or side wall $\partial\theta/\partial n = -1$ and thermal insulation at the other walls $\partial\theta/\partial n = 0$. The inlet-exit conditions are those of periodicity of the velocity **u**, temperature fluctuations θ and pressure fluctuations p.

The numerical method is a version of the finite difference model first introduced in [5] and later used for various flows at strong magnetic fields (e.g. in [3]). The spatial discretization is of the second order and performed on a non-uniform collocated grid. The grid is clustered towards the walls according to the coordinate transformations: $y = \tanh(A_y\eta)/\tanh(A_y)$, $z = \tanh(A_z\xi)/\tanh(A_z)$. The spatial discretization is conservative with spatial derivatives evaluated using the velocity and current fluxes obtained by special interpolations to half-integer grid points (see [6], [7]). The time discretization uses the standard projection algorithm (see, e.g. [8]). The body forces and nonlinear convection terms are treated explicitly using the backward difference Adams-Bashforth scheme as described in [5]. The conduction and viscosity terms are treated implicitly in order to avoid the stringent stability limitations on the time step that arise at strong near-wall clustering. The elliptic equations for potential, pressure, three velocity components, and temperature are solved using the Fourier decomposition in the streamwise coordinate and the direct reduction solution of the two-dimensional equations for the Fourier components conducted on the transformed grid ($\eta - \xi$) (see [5]). The algorithm is parallelized using the hybrid MPI-OpenMP approach. The MPI memory distribution is along the y-coordinate in the physical space and along the streamwise wavenumber in the Fourier space.

The equations always have a solution in the form of a streamwise-uniform steady flow, which we take as the base flow. For every combination of Ha and Gr, we first compute the base flow by imposing streamwise-uniformity. The linear stability analysis of this flow is conducted next. We follow the evolution of small-amplitude perturbations added to the flow. For such perturbations, we can analyze instability to individual Fourier harmonics in the framework of a linearized problem. For this purpose, the DNS code is modified by applying Fourier filtering, which separates the zero mode and the mode, stability to which is studied from the rest (see [3] for a discussion). The computations are conducted in the domain of a desired wavelength. Finally, fully 3D DNS of the flow is conducted.

3. Results

We consider fully developed flows in long ducts (fig 1). Single values Pr = 0.0321 and Re = 5000 are used in the analysis. The first of them corresponds to the LiPb eutectic alloy at temperature around 570 K [9], while the second is selected arbitrarily. The Grashof number Gr varies in the range between 10^5 and 10^9. For the Hartmann number we select the range $50 \leq \mathrm{Ha} \leq 800$. The computational domain is a duct with cross-section 2×2 and periodic inlet-exit conditions. The streamwise size of the domain is 4π for DNS and equal to the wavelength of the tested Fourier mode for stability analysis. The computational grids are determined as functions of Ha and Gr in the grid sensitivity tests. We keep at least 6 points in each Hartmann layer and at least 12 points in each Shercliff layer. The DNS requires streamwise grid step not larger than 0.1. The maximum time step providing a numerically stable solution is used. Its value varies with Ha and Gr, but never exceeds 10^{-2}.

3.1 Duct with bottom heating [12]. The summary of transverse circulation structures is shown in fig. 2. At each value of Ha, the Gr has to increase above a certain limit to overcome the suppression by the magnetic field and to cause development of secondary circulations in transverse plane. The heating also creates a profile of mean temperature linearly growing along the duct and the associated buoyancy force leads to significant top-bottom asymmetry of mean velocity [6]. The linear stability analysis shows the formation of convection rolls aligned with the magnetic field as a common feature of the flow invariably observed at Ha > 200 and sufficiently high Gr. The rolls are localized in the lower half of the duct. At high Ha, the rolls approach Q2D form, while increase of Gr, via the modification of mean flow, localizes the rolls near the heated wall (see fig. 3). Transport of the rolls by the mean flow causes high-amplitude low-frequency temperature fluctuations at walls.

The DNS results agree with the stability analysis and confirm that the secondary flow regimes can be of one of the two types depending on whether Gr is smaller or larger than a certain threshold Gr*(Ha). The low-Gr type observed at Gr < Gr* is characterized by complete domination of the instability-generated spanwise rolls and quasi-two-dimensional distributions of velocity and temperature fields. In the high-Gr flows at Gr > Gr*, the spanwise rolls are combined with a streamwise roll similar to the circulation roll in the streamwise-uniform base flow. Significant flow and variations of temperature along the magnetic field lines are present. This classification is important when we consider that 3D computations are unfeasible at the parameter values typical for a fusion reactor. It is commonly assumed that the Q2D modeling [10] can be utilized at high Ha (see [11]). Our results, however, demonstrate that even at high Ha the applicability of the model is not a-priori certain. The model is applicable to the low-Gr regimes, but would be based on incorrect assumptions and produce erroneous results at the values of Gr, at which high-Gr regimes are realized.

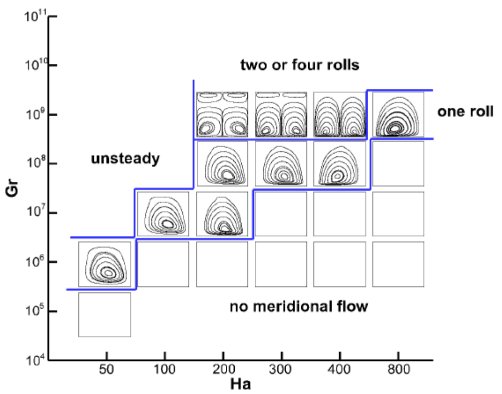

Figure 2. Bottom heating. Transverse plane circulation patterns found in computed base flows. Blank squares indicate flow regimes, in which the kinetic energy of transverse velocity components is less than 10^{-6}.

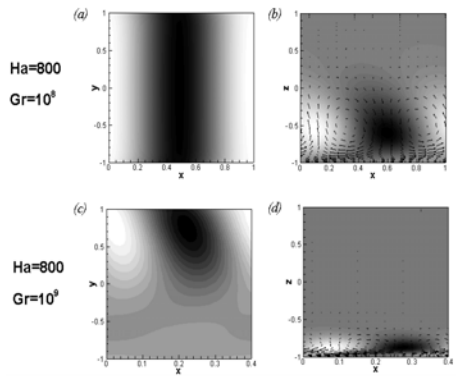

Figure 3. Bottom heating. Convection modes in the horizontal plane (left), vertical streamwise mid-plane (right), at Ha = 800 and Gr = 10^8 (upper) and Gr = 10^9 (lower). Vectors and contours show velocity and temperature perturbations, respectively.

3.1 Duct with sidewall heating [13]. Fig 4 summarizes the observed structures of the transverse circulation in the streamwise-uniform flows with sidewall heating duct. Circulations with the average kinetic energy of transverse velocity components below 10^{-6} are not shown. In the DNS analysis, only the flows at Ha = 50 and 100 with Gr = 10^9 demonstrate three-dimensionality. All the other flows are found to be laminar, steady-state, and 2D (uniform in the streamwise direction). This is fully confirmed by the stability analysis that finds no growth of perturbations at the wavelengths between 0.05π and 20π. An illustration of a 2D flow is presented in fig. 5.

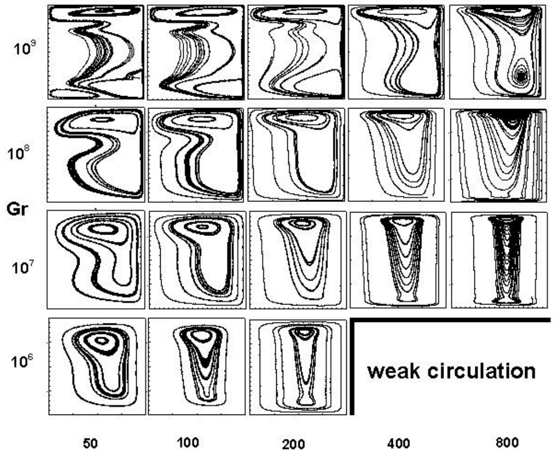

Figure 4: Sidewall heating. Transverse plane circulation patterns found in computed base flows. The flow regimes, in which the kinetic energy of transverse velocity components is less than 10^{-6} are not shown.

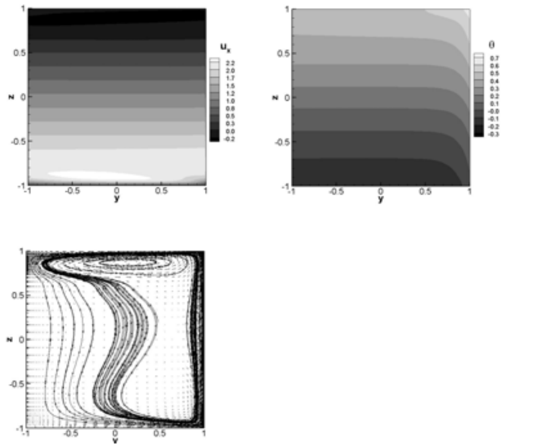

Figure 5: Sidewall heating. 2D flow at Ha = 400, Gr = 10^9. Streamwise velocity u_x, temperature θ, and vector field and streamlines of the transverse circulation u_y, (u_y, u_z) are shown.

Acknowledgments: Authors thank Dmitry Krasnov for continuing assistance with the numerical model. Financial support was provided by the US NSF (Grant CBET 1232851).

4. References

[1] Smolentsev, S., Moreau, R., Bühler, L. & Mistrangelo, C. MHD thermofluid issues of liquid-metal blankets: Phenomena and advances. Fusion Eng. Design **85** (7-9), 1196 -1205 (2010).
[2] Davidson, P. A., An Introduction to Magnetohydrodynamics, (2001).
[3] Zikanov, O., Listratov, Ya. & Sviridov, V. G. Natural convection in horizontal pipe flow with strong transverse magnetic field, J. Fluid Mech. **720**, 486–516 (2013).
[4] Genin, L. G., Zhilin, V. G., Ivochkin, Y. P., Razuvanov, N. G., Belyaev, I. A., Listratov, Y. I. & Sviridov, V. G. Temperature fluctuations in a heated horizontal tube affected by transverse magnetic field. Fundamental and Applied MHD, Proc. the 8th PAMIR Conference, pp. 37–41. Borgo, Corsica, France (2011).
[5] Krasnov, D., Zikanov, O. & Boeck, T. Comparative study of finite difference approaches to simulation of magnetohydrodynamic turbulence at low magnetic Reynolds number, Comp. Fluids. **50**, 46–59 (2011).
[6] Morinishi, Y., Lund, T. S., Vasilyev, O. V. & Moin, P. Fully conservative higher order finite difference schemes for incompressible flow, J. Comp. Phys. **143**, 90–124 (1998).
[7] Ni, M. J., Munipalli, R., Huang, P., Morley, N. B., Abdou, M. A. A current density conservative scheme for incompressible MHD flows at low magnetic Reynolds number. Part I: On a rectangular collocated grid system, J. Comp. Phys. **227,** 174204 (2007).
[8] Zikanov, O. Essential computational fluid dynamics. Wiley (2010).
[9] Mas de les Valls, E., Sedano, L.a., Batet, L., Ricapito, I., Aiello, a., Gastaldi, O. &Gabriel, F. Lead-lithium eutectic material database for nuclear fusion technology, J. Nucl. Mater. 376 (3), 353–357 (2008).
[10] Sommeria, J. & Moreau, R. Why, how and when MHD-turbulence becomes two-dimensional, J. Fluid Mech. **118**, 507–518 (1982).
[11] Vetcha, N., Smolentsev, S., Abdou, M. & Moreau, R. Study of instabilities and quasi-two-dimensional turbulence in volumetrically heated magnetohydrodynamic flows in a vertical rectangular duct, Phys. Fluids **25** (2), 024102 (2013).
[12] Zhang, X., Zikanov, O. Mixed convection in a horizontal duct with bottom heating and strong transverse magnetic field (submitted to J. Fluid Mech. (2014).
[13] Lv, X., Zikanov, O. Mixed convection in horizontal duct flow with transverse magnetic field and heating of side wall (submitted to Phys. Fluids (2014).

MAGNETO CONVECTIVE INSTABILITIES DRIVEN BY INTERNAL UNIFORM VOLUMETRIC HEATING

MISTRANGELO C., BÜHLER L.
Karlsruhe Institute of Technology (KIT), Postfach 3640, 76021 Karlsruhe, Germany
E-mail: chiara.mistrangelo@kit.edu

Abstract: A linear stability analysis is performed to investigate the onset of convective motions in a flat cavity filled with liquid metal in which a volumetric heat source is distributed uniformly and a horizontal magnetic field is imposed. A quasi-2D mathematical model is derived by integrating the 3D governing equations along magnetic field direction, which yields a dissipation term in the 2D equations that accounts for 3D viscous effects in thin boundary layers at walls perpendicular to the field. This type of buoyant flow without magnetic field has been investigated by Roberts [1] and the present study extends those results to magnetohydrodynamic conditions. Numerical simulations are performed to support the analytical results and to describe the main convective flow patterns.

1. Introduction

Thermal convective motion produced by uniform internal heat sources in a liquid metal layer, as analyzed in the present study, is a fundamental heat transfer problem of interest for engineering applications such as e.g. nuclear fusion reactors. Here a plasma is confined in a torus by means of a strong magnetic field. Neutron heat is removed by a liquid metal circulating in the so called blanket. Most of the nuclear power is deposited in the liquid metal leading to significantly non-uniform thermal conditions that result in complex convective flow patterns affected by the magnetic field [2] [3].

The problem of natural convection driven by a temperature difference across a fluid layer, the so called Rayleigh-Bénard convection, has been extensively analyzed for applications in crystal growth technology. When the fluid is heated from below it remains motionless until the temperature difference, quantified by the non-dimensional Rayleigh number Ra, exceeds a critical value Ra_{cr} and then thermal convection sets in. Chandrasekhar [4] shows that by applying a magnetic field instabilities occur at higher values of Ra compared to hydrodynamic conditions. At marginal stability convection appears in the form of rolls aligned with the horizontal component of the magnetic field. Analytical and experimental investigations of MHD Bénard-convection can be found in [5]. When a strong magnetic field is applied electromagnetic Lorentz forces elongate vortices along magnetic field lines and force the fluid to move in planes perpendicular to the field, while motion along field lines is damped [6]. This leads to a quasi-two dimensional (Q2D) MHD flow where dissipation losses, due to Joule and viscous effects, are localized in thin Hartmann layers along walls perpendicular to the magnetic field. An explanation of dissipative effects in Hartmann layers is given in [7] [8]. Q2D models reduce the basic governing equations to a 2D problem by analytical integration along magnetic field lines. In the 2D equations 3D MHD effects are modeled by a term that accounts for viscous and Joule's dissipation in Hartmann layers. Those approaches are used to investigate problems related to fusion blankets where intense magnetic fields are present [9].

In the problem studied in this paper convective motions are driven by heat sources distributed in a fluid. The steady laminar hydrodynamic convection in an infinite horizontal fluid layer confined between an isothermal upper plate and a lower one that is thermally insulating has been studied by different authors. This configuration differs from Bénard-convection since temperature boundary conditions are asymmetric and the vertical temperature profile in the motionless state is parabolic rather than linear.

Experimental studies of instabilities in a horizontal fluid layer heated uniformly are described in [10]. Roberts [1] carried out a stability analysis that shows that convective motions occur at $Ra_{\rm cr} \simeq 2772$ in the form of marginally stable rolls. Thirlby [11] performed a numerical analysis and determined the parameters at which polygonal cells and rolls occur in hydrodynamic flows.

The aim of the present study is investigating the influence of a horizontal magnetic field on the onset of instabilities in liquid metal flows with volumetric thermal sources and identifying the main convective patterns. The geometrical configuration chosen for this study is the one used in [1]. Model equations describing the Q2D MHD convective flow are derived (§) and a linear stability analysis is performed (§) to determine the onset of convection depending on intensity of applied heat source and strength of magnetic field. A better understanding of the features of convective flow patterns is obtained by means of numerical simulations.

2. Formulation of the problem and governing equations

Let us consider an electrically conducting liquid metal, filling a horizontal shallow cavity, where a volumetric heat source q is uniformly distributed in the fluid (Figure 1). The top wall at $y = H$ is isothermal, the bottom at $y = 0$ adiabatic, $\partial T/\partial y = 0$, and the Hartmann walls at $z = \pm A$, perpendicular to the magnetic field, are adiabatic, $\partial T/\partial z = 0$.

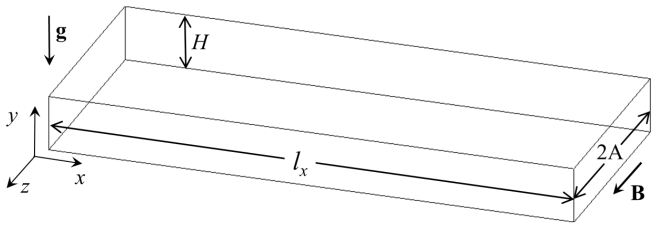

Figure 1. Sketch of geometry and reference system. Walls perpendicular to the magnetic field are thermally insulating, the top wall of the cavity is kept at constant temperature, the bottom is adiabatic. Periodic conditions are assumed in x- direction. A constant magnetic field is applied in horizontal z- direction.

Density changes due to temperature variation are restricted to the buoyancy term, $\rho\beta(T\text{-}T_{ref})\mathbf{g}$, according to the Boussinesq approximation. Here ρ is the density at the reference temperature T_{ref}, β the volumetric thermal expansion coefficient and $\mathbf{g} = -g\mathbf{y}$ the gravitational acceleration. The non-dimensional equations governing the problem account for balance of momentum, conservation of mass and charge and current density is determined by Ohm's law:

$$\frac{1}{Pr}\left(\frac{\partial \mathbf{v}}{\partial t} + (\mathbf{v}\cdot\nabla)\mathbf{v}\right) = -\nabla p + \nabla^2\mathbf{v} + RaT\hat{\mathbf{y}} + Ha^2(\mathbf{j}\times \tag{1}$$

$$\nabla\cdot\mathbf{v} = 0 \qquad \nabla\cdot\mathbf{j} = 0 \qquad \mathbf{j} = -\nabla\phi + \mathbf{v}\times\mathbf{B}. \qquad (2)\ (3)\ (4)$$

The temperature distribution is given by the energy balance equation

$$\frac{\partial T}{\partial t} + (\mathbf{v}\cdot\nabla)T = \nabla^2 T + 1 \tag{5}$$

The dimensional volumetric heat source q has been scaled by $\lambda\Delta T/H^2$ and normalized to 1 by defining the characteristic temperature difference as $\Delta T = qH^2/\lambda$. The dimensionless variables $\mathbf{v}$, t, $\mathbf{j}$, ϕ and $\mathbf{B}$ are obtained by scaling velocity, time, electric current density, electric potential and magnetic field by the reference quantities $v_0 = \alpha/H$, H^2/α, $\sigma v_0 B_0$, $v_0 B_0 H$ and B_0, respectively. The typical length scale H is the distance between horizontal walls. Thermal diffusivity $\alpha = \lambda/(\rho c_{\rm p})$, thermal conductivity λ, specific heat c_p, kinematic viscosity ν and electric conductivity σ are assumed to be constant in the temperature range considered. The non-dimensional temperature T is given by $(T^* - T_{ref})/\Delta T$, where T^* is the local dimensional temperature. The dimensionless parameters that control the flow are Prandtl number Pr, Rayleigh number Ra and Hartmann number Ha:

$$Pr = \frac{\nu}{\alpha}, \qquad Ra = \frac{g\beta q H^5 \rho c_p}{\nu \lambda^2}, \qquad Ha = B_0 H \sqrt{\frac{\sigma}{\rho \nu}}. \tag{6}$$

The Prandtl number represents the rate of momentum diffusion to the one of heat diffusion. The Rayleigh number describes the intensity of the applied heating. The Hartmann number gives a non-dimensional measure for the strength of the magnetic field. In order to quantify the magnitude of convection we introduce a quantity defined as the ratio between mean temperature differences across the fluid layer without motion and with convection [1] [11]:

$$M = \frac{\int_V T_{cond}\, dV}{\int_V T_{conv}\, dV} = \frac{1}{3\overline{\overline{T}}}. \tag{7}$$

3. 2D model equations

The procedure followed for the analysis is analogous to the one used in [5] [7] [8]. Starting from the 3D equations (§) an equation for vorticity $\boldsymbol{\omega} = \nabla \times \mathbf{v}$ is obtained. For the given boundary conditions and an applied magnetic field in z-direction the flow is characterized by a Q2D velocity $\mathbf{v} = (u,v,0)$ and vorticity $\boldsymbol{\omega} = (0,0,\omega)$, where u, v, ω may depend on (x,y,z):

$$\frac{1}{Pr}\left(\partial_t \omega + u\partial_x \omega + v\partial_y \omega\right) = \nabla^2 \omega + Ha^2 \partial_z j_z + Ra\partial_x T. \tag{8}$$

In a quasi 2D flow velocity and vorticity can be expressed by a separation ansatz, e.g. $u = \hat{u}(t,x,y)\, f(z)$. By integrating the vorticity equation along field lines, with no slip at Hartmann walls, $f(z = \pm a) = 0$, and thin wall condition [12] we obtain

$$\frac{1}{Pr}\left(\partial_t \hat{\omega} + \hat{u}\partial_x \hat{\omega} + \hat{v}\partial_y \hat{\omega}\right) = \nabla_{xy}{}^2 \hat{\omega} - \frac{1}{\tau}\hat{\omega} + Ra\partial_x T \quad \text{with} \quad \frac{1}{\tau} = \frac{Ha}{a} + \frac{cHa^2}{a+c}, \tag{9}$$

where $c = \sigma_w t_w/(\sigma H)$ is the conductance parameter. In (9) terms on the left hand side represent convective transport of vorticity and its time variation, on the right hand side there are two dissipation terms. The first one describes viscous losses due to gradients of vorticity in a plane perpendicular to **B**. The term $-\hat{\omega}/\tau$ represents viscous and Joule dissipation in the Hartmann layer and in the wall and τ is related to a typical decay time of vorticity [7]. For electrically insulating Hartmann walls ($c = 0$) $1/\tau \rightarrow Ha/a$ and for perfectly conducting walls ($c = \infty$) $1/\tau \rightarrow Ha^2$, namely in ducts with highly electrically conducting walls a rapid damping occurs.

4. Linear stability analysis

The basic steady state in the problem studied is motionless and with a parabolic temperature distribution along the vertical coordinate y. When the internal heat source, i.e. Ra, is large enough the base state loses its stability due to increased buoyancy forces that are not balanced anymore by viscous effects and thermal conductivity. Convective motions occur whose intensity depends on the internal heat source (Ra) and the magnetic field (Ha). A linear stability analysis is performed that consists in following the evolution of small perturbations applied to the equilibrium state by linearizing equation (9). The stability is determined by solving the resulting eigenvalue problem. In order to derive disturbance equations, temperature, velocity and vorticity are decomposed as the sum of a basic state denoted by the subscript 0 and a perturbation indicated by prime and multiplied by a small parameter ε, e.g. $T = T_0 + \varepsilon T'$. Those expressions are introduced in (5) and (9) and terms of $O(\varepsilon^2)$ are neglected in the small perturbation limit. We expand perturbations in normal modes as e.g. $T' = i\Theta(y)e^{st+ikx}$ where k is a real horizontal wavenumber, s the temporal rate of growth of the perturbation. In order to satisfy mass conservation (2) we introduce a streamfunction $\psi'(x,y)$, such that $\mathbf{u}' = \nabla \times (\psi' \cdot \hat{\mathbf{z}})$ and $\omega' = -\nabla^2 \psi'$. After some mathematical work and at the stability limit the equations describing the stability of the problem become:

$$\left[\left(D^2-k^2\right)-\frac{1}{\tau}\right]\Omega-kRa\Theta=0, \qquad \left(D^2-k^2\right)\Theta-ky\Psi=0, \qquad \left(D^2-k^2\right)\Psi+\Omega=0, \tag{10}$$

where $D^2 = \partial^2/\partial y^2$ and Ω, Θ, Ψ are the amplitude functions of vorticity, temperature and streamfunction perturbations, respectively. A numerical procedure has been implemented in Matlab where finite difference techniques are used for the solution of the eigenvalue problem.

5. Results

For $1/\tau \rightarrow 0$ the problem is equivalent to the hydrodynamic flow (Ha = 0) considered in [1], for which Ra_{cr} = 2772 and k_{cr} = 2.63 are predicted. This case is first investigated to validate the used numerical model. In a second step a uniform horizontal magnetic field is imposed and its influence on the stability of the considered magneto-convective flow is studied. Numerical simulations are also performed both to confirm the linear stability analysis and to complement the results by means of 3D and Q2D nonlinear solutions for $Ra > Ra_{cr}$.

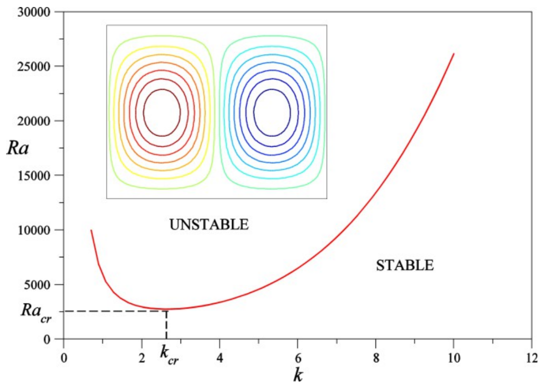

Figure 2. Neutral stability curve for the hydrodynamic flow (Ha = 0) showing marginal Rayleigh number as a function of the wavenumber.

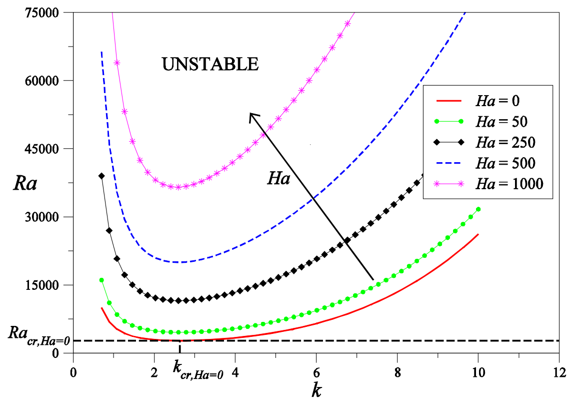

Figure 3. Neutral stability curves for the case of electrically insulating walls, c = 0, and various Hartmann numbers Ha.

Figure 2 shows the neutral stability curve for Ha = 0. As the control parameter Ra increases, the base state first becomes linearly unstable at $Ra = Ra_{cr}$ with respect to perturbations with horizontal wavenumber $k = k_{cr}$. Results agree very well with those presented in [1]. In the region below the curve perturbations of any wavelength decrease, namely the flow is stable, no convective motion occurs and the temperature has a parabolic profile between the plates. Above the curve the flow is unstable and convection occurs with a certain range of unstable wave numbers. In Figure 2 contours of the streamfunction are depicted showing two counter rotating convective cells that appear at the instability threshold.

Let us consider now magneto-convective flows in an electrically insulating cavity (c = 0) with A/H = 2. We analyze the influence of the magnetic field strength (Ha). In Figure 3 neutral stability curves are depicted for various Ha. The curve for the hydrodynamic case (Ha = 0) is shown for comparison. It can be seen that, as expected [4], the magnetic field stabilizes the flow, i.e. by increasing Ha the onset of convection occurs at higher values of Ra.

We fix now the Hartmann number Ha = 200 ($1/\tau$ = 100). The axial length l_x (see Figure 1) is chosen such that 8 convective cells fit in the computational domain at Ra_{cr}. Numerical simulations are performed by using the Q2D model described in §3 that have been implemented in the finite volume code OpenFOAM.

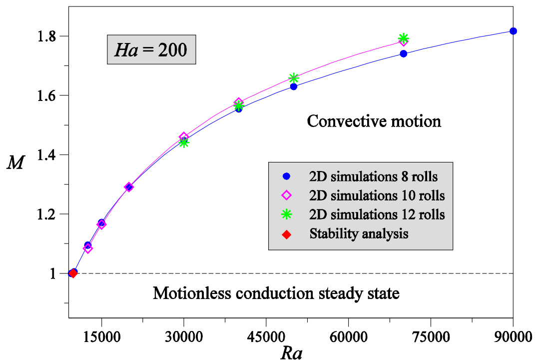

Figure 4. Factor M that quantifies the strength of the convective motion as a function of the Rayleigh number.

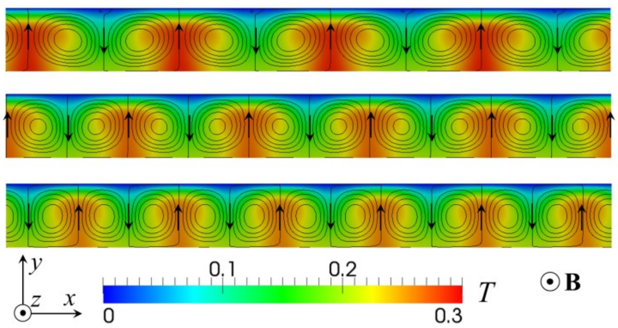

Figure 5. Contours of scaled temperature and electric potential isolines (non-dimensional distance 0.9) for Q2D MHD flow at Ha = 200 and Ra = 70000.

In order to quantify the intensity of the convective motion the quantity M (7) is calculated and plotted as a function of Ra in Figure 4. The numerically predicted critical Rayleigh number, $Ra_{cr} = Ra(M = 1)$, agrees very well with the one obtained by the stability analysis, Ra_{cr} = 9821.3. By increasing the Rayleigh number M becomes larger, i.e. the convective heat transfer intensifies. For sufficiently large Ra various solutions coexist characterized by 8, 10 and 12 rolls. An example is shown in Figure 5 for the flow at Ra = 70000. Here contours of temperature T and isolines of electric potential, which serve as approximate streamlines, are depicted on the cross-section of the cavity.

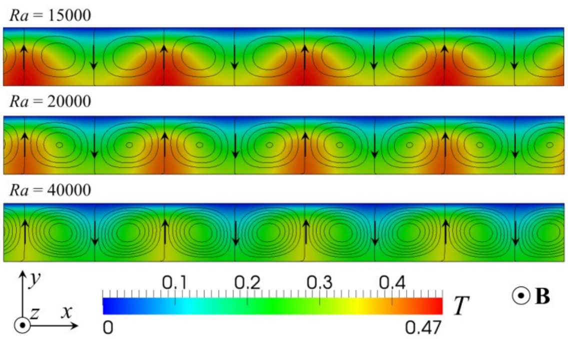

Figure 6. Contours of scaled temperature and electric potential isolines (non-dimensional distance 0.56) for Q2D MHD flows at Ha = 200 and different Ra.

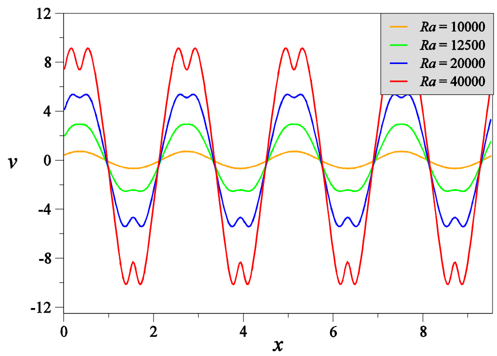

Figure 7. Vertical velocity as a function of the coordinate x for various Ra.

In Figure 6 contours of temperature and isolines of potential are compared for three Ra. In the selected scale for the temperature (see §2) ΔT is proportional to the volumetric heat source and therefore it increases with Ra and the normalized temperature reduces. When the heating is stronger the motion intensifies as indicated by a larger number of potential isolines. In Figure 7 the vertical component of the velocity is plotted for various Ra along the axial coordinate on a line at y = 0.5. When approaching the stability limit (Ra_{cr} = 9821.3) the velocity profile resembles a harmonic function. By rising Ra additional modes appear due to nonlinear interactions leading to more complex velocity profiles.

6. Conclusions

The influence of a magnetic field on the stability of convective flows caused by a uniform volumetric heat source distributed in a liquid metal layer has been studied. A linear stability analysis is performed based on a Q2D model and the critical Rayleigh number for the onset of convection has been calculated for increasing Ha. The occurrence of convection is delayed when Ha becomes larger. For supercritical conditions solutions with different wavenumbers coexist. The velocity distribution shows that when convective motion sets in only harmonic functions contribute and by increasing *Ra* higher modes appear due to nonlinear interactions.

Acknowledgement: This work, supported by the European Communities under the contract of Association between EURATOM/KIT, was carried out within the framework of the European Fusion Development Agreement. The views and opinions expressed herein do not necessarily reflect those of the European Commission.

References

[1] P. H. Roberts, "Convection in horizontal layers with internal heat generation. Theory," *Jounal of Fluid Mechanics,* vol. 30, pp. 33-49, 1967.

[2] A. Kharicha, S. Molokov, S. Aleksandrova and L. Bühler, "Buoyant convection in the HCLL blanket in a strong uniform magnetic field," 2004.

[3] C. Mistrangelo, B. L. and G. Aiello, "Buoyant-MHD flows in HCLL blankets caused by spatially varying thermal loads," *IEEE Transactions on Plasma Science,* p. in print, 2014.

[4] S. Chandrasekhar, Hydrodynamic and hydromagnetic stability, New York: Dover Publications, Inc., 1961.

[5] U. Burr and U. Müller, "Rayleigh-Bénard convection in liquid metal layers under the influence of a horizontal magnetic field," *Journal of Fluid Mechanics,* vol. 453, pp. 345-369, 2002.

[6] P. A. Davidson, "Magnetic Damping of Jets and Vortices," *Journal of Fluid Mechanics,* vol. 299, pp. 153-186, 1995.

[7] L. Bühler, "Instabilities in quasi-two-dimensional magnetohydrodynamic flows," *Journal of Fluid Mechanics,* vol. 326, pp. 125-150, 1996.

[8] J. Sommeria and R. Moreau, "Why, how, and when MHD turbulence becomes two-dimensional," *Journal of Fluid Mechanics,* vol. 118, pp. 507-518, 1982.

[9] S. Smolentsev, N. Vetcha and M. Abdou, "Effect of a magnetic field on stability and transitions in liquid breeder flows in a blanket," *Fusion Engineering and Design,* vol. 88, no. 6-8, pp. 607-610, 2013.

[10] D. J. Tritton and M. N. Zarraga, "Convection in horizontal layers with internal heat generation. Experiments," *Journal of Fluid Mechanics,* vol. 30, pp. 21-31, 1967.

[11] R. Thirlby, "Convection in an internally heated layer," *Journal of Fluid Mechanics,* vol. 44, no. 4, pp. 673-693, 1970.

[12] J. S. Walker, "Magnetohydrodynamic flows in rectangular ducts with thin conducting walls," *Journal de Mecanique,* vol. 20, no. 1, pp. 79-112, 1981.

[13] J. Sommeria, "Experimental study of the two-dimensional inverse energy cascade in a square box," *Journal of Fluid Mechanics,* vol. 170, pp. 139-168, 1986.

MIXED CONVECTION IN VERTICAL DUCTS WITH STRONG TRANSVERSE MAGNETIC FIELDS

LIU L., SCHIGELONE A., ZHANG X., ZIKANOV* O.
University of Michigan – Dearborn, Dearborn, MI 48128, USA
*Corresponding author email: zikanov@umich.edu

Abstract: Fundamental features of mixed convection are investigated for upward and downward flows in long vertical ducts with one heated wall and strong imposed transverse magnetic field. It is found that the Q2D model accurate for the upward flow, but not always accurate for the downward one. Another feature of the downward flow is the exponentially growing streamwise-uniform elevator modes. Finally, the flows are prone to Kelvin-Helmholtz instabilities associated with inflection points of streamwise velocity profiles.

1. Introduction

This paper presents the first results of our computational study of mixed (combined natural and forced) convection in MHD flows of liquid metals in vertical ducts. Ducts of square cross-section with electrically insulated walls are considered. Three of the walls are thermally insulated, while the fourth wall is subject to constant-rate heating. A uniform steady-state magnetic field is imposed in the direction perpendicular to the flow and to the direction of the temperature gradient established by the wall heating. The focus of the study is on situations with strong heating and magnetic field (large values of Grashof and Hartmann numbers). The cases of upward and downward flows are considered. The study is relevant to the liquid metal blankets of fusion reactors, more specifically, to the blankets with long poloidal channels, in which electrical and thermal insulation of the walls is applied [1]. The system is simplified by assuming a fully developed flow, perfect electrical and thermal insulation of the walls, and constant physical properties of the liquid, as well as by replacing the volumetric heating near the first wall by the wall heating. At the same time, no a-priori assumptions about the flow's dimensionality and time-dependency are made. The computational model permits development of 3D and time-dependent structures. The study can be characterized as a theoretical analysis of basic features of convection in vertical ducts with strong transverse magnetic field.

Despite their evident importance for the operation of liquid metal blankets, the effects of natural and mixed convection in the presence of strong magnetic fields are still poorly understood. The only earlier computational work directly addressing the configuration of this paper is [2], where quasi-2D modeling was employed to study convection instabilities in upward flows in long vertical ducts. Instabilities of two types (the Kelvin-Helmholtz type associated with inflection points in the streamwise velocity profile and the boundary layer type) were found, both leading to oscillations of velocity and temperature fields. These results are consistent with the measurements [3] that showed high-amplitude oscillations of temperature in mercury flows in vertical pipes. We note that the effect of convection-generated oscillations is not limited to flows in vertical tubes. It is a general phenomenon likely to occur in tubes of almost all orientations. For example, the computational and experimental analysis of flows in horizontal pipes [4,5] and ducts [6] with bottom heating show that a sufficiently strong transverse horizontal magnetic field results in the convection instability in the form of growing rolls aligned with the field and transported by the main flow.

2. Theoretical and numerical model

We consider a flow of an incompressible, Newtonian, electrically conducting fluid (a liquid metal) in a vertical duct of square cross-section. Heating of constant uniform rate q is applied to one of the walls. Constant magnetic field **B** oriented perpendicularly to the duct and to the direction of the heating-induced temperature gradient is imposed in the entire flow domain. The flow with the mean velocity U directed either upwards or downwards is driven by an applied pressure gradient $\nabla\hat{p}$. Using U as the velocity scale, the duct's half-width d as the length scale, qd/κ, where κ is the thermal conductivity, as the temperature scale, and the B-derived scales for the electromagnetic fields, we can write the non-dimensional equations as

$$\partial_t \mathbf{u} + (\mathbf{u}\cdot\nabla)\mathbf{u} = -\nabla p - \nabla\hat{p} + \mathrm{Re}^{-1}\nabla^2\mathbf{u} + \mathbf{F}_b + \mathbf{F}_L, \quad (1)$$

$$\nabla\cdot\mathbf{u} = 0, \quad \partial_t\theta + \mathbf{u}\cdot\nabla\theta = \mathrm{Pe}^{-1}\nabla^2\theta - u_x\, dT_m/dx. \quad (2)$$

In the equations and the following discussion, the coordinates x,y,z are, respectively, in the streamwise direction, direction of the magnetic field, and direction orthogonal to the heated wall. The pressure field is the sum of $\hat{p}$(x) with spatially uniform gradient $d\hat{p}/dx$ adjusted at every time step to maintain constant mean velocity and fluctuation $p(\mathbf{x},t)$. The temperature field T is the sum of the mean-mixed temperature $T_m(x) = A^{-1}\int u_x T\, dA = 2Pe^{-1}x$ and fluctuations $\theta(\mathbf{x},t)$. The buoyancy force is computed using the Boussinesq approximation as $\mathbf{F}_b = \mathrm{Gr}\mathrm{Re}^{-2}\alpha\mathbf{e}_x\theta$. Here, we assume that the buoyancy due to the mean-mixed temperature is fully balanced by a vertical pressure gradient and use the coefficient α to account for the two possible flow directions: α=1 in upward flow (x facing upwards) and α=-1 in downward flow (x facing downwards). The Lorentz force is $\mathbf{F}_L = \mathrm{Ha}^2\mathrm{Re}^{-1}\mathbf{j}\times\mathbf{e}_y$, where the current density is determined by the Ohm's law $\mathbf{j} = -\nabla\phi + \mathbf{u}\times\mathbf{e}_y$ and the electric potential is a solution of the Poisson equation $\nabla^2\phi = \nabla\cdot(\mathbf{u}\times\mathbf{e}_y)$. The non-dimensional parameters are the Reynolds number $\mathrm{Re} = Ud/\nu$, Hartmann number $\mathrm{Ha} = Bd(\sigma/\rho\nu)^{1/2}$, Peclet number $\mathrm{Pe} = Ud/\chi$, and Grashof number $\mathrm{Gr} = g\beta q d^4/\nu^2\kappa$. The boundary conditions at the walls are: **u**=0, $\partial\phi/\partial n = 0$, $\partial\theta/\partial n = 0$ at the thermally insulated walls, and $\partial\theta/\partial n = -1$ at the heated wall. Inlet-exit periodicity of ϑ, p, **u** and ϕ is assumed.

We use a version of the finite difference model introduced in [7] and later adapted to flows with mixed convection in [4,6]. The method uses the second-order time discretization, in which viscous and conductive terms are treated implicitly and the incompressibility is satisfied by the standard projection algorithm (see, e.g. [8]). The spatial discretization is of the second order on a structured collocated grid with points clustered near the walls via the tanh coordinate transformation (see [6,7] and the discussion of various clustering schemes applied to the MHD convection in [9]). The discretization uses fluxes of velocity and electric current interpolated to half-integer points. In the non-viscous, non-conductive limit, it exactly conserves mass, momentum, electric charge, and internal energy, while kinetic energy is conserved with the dissipative error of the 3rd order.

In the computations, we keep constant Re=5000 and Pr=0.0321, while Ha and Gr vary in broad ranges. The computational domain is a duct of 2x2 cross-section and sufficient streamwise length. The computational grids are tested in a thorough sensitivity analysis so that the smallest grids providing accurate solutions are determined (see [6,9] for details). Such grids typically have about 7 points within each Hartmann boundary layer and 10-12 points within each Shercliff (sidewall) boundary layer.

3. Results

3.1 Analytical Q2D solutions in comparison with computations. In high-Ha flows of certain geometries, one can apply the Q2D model [10], in which the flow fields are averaged wall-to-wall in the magnetic field direction and the electromagnetic effects are reduced to linear friction at the Hartmann walls. The model can be applied in our case, where the averaging is in the y-direction. We do that for the streamwise-uniform steady-state flows:

$$\mathbf{u} = u(y,z)\mathbf{e}_x, \qquad \theta = \theta(y,z), \qquad p = 0 \; . \tag{3}$$

Such solutions always exist in our system. As discussed below, they can be stable or unstable depending on the values of Ha and Gr.

Applying the Q2D approximation and the just assumed state of the flow, we derive:

$$C + \mathrm{GrRe}^{-2}\alpha\bar{\theta} + \mathrm{Re}^{-1}\,\bar{u}'' - \mathrm{HaRe}^{-1}\bar{u} = 0, \quad \bar{u} = \mathrm{Re}^{-1}\bar{\theta}, \tag{4}$$

$$\bar{u}(\pm 1) = 0, \qquad \bar{\theta}(-1) = -1, \qquad \bar{\theta}(1) = 0 \; , \tag{5}$$

where $\bar{u}(z)$ and $\bar{\theta}(z)$ are the y-averaged fields, and $C = -\dfrac{d\bar{p}}{dx}$. The system can be reduced to a boundary-value problem for a 4th-order ordinary differential equation with constant coefficients and solved analytically (a similar solution for the case of internal heating is available in [2]).

00The results are presented in Fig. 1, where the analytically found profiles $\bar{u}(z)$ are compared with the computed solutions of the full problem. In order to obtain the streamwise-uniform numerical solutions, we apply x-averaging at every time step and compute the evolution of the flow until convergence to a steady state is achieved. After that, the computed profiles $u(y,z)$, $\theta(y,z)$ are averaged in y. We see in Fig. 1a that in the case of the upward flow the agreement between the Q2D and full solutions is very good. This has been found in all our computations conducted at Ha=50, 100, 200, 400, 800 and Gr=10^6, 10^7, 10^8, 10^9. Quite different results are obtained for the downward flows. Here, the Q2D model allows us to accurately calculate u and θ only at low Gr. At high Gr, as illustrated in Figs. 1c,d, the Q2D solutions are inaccurate or even unphysical. The upper boundary of the interval of acceptable accuracy increases with Ha, but even at Ha=400 and 800, high values of Gr render the Q2D model inaccurate.

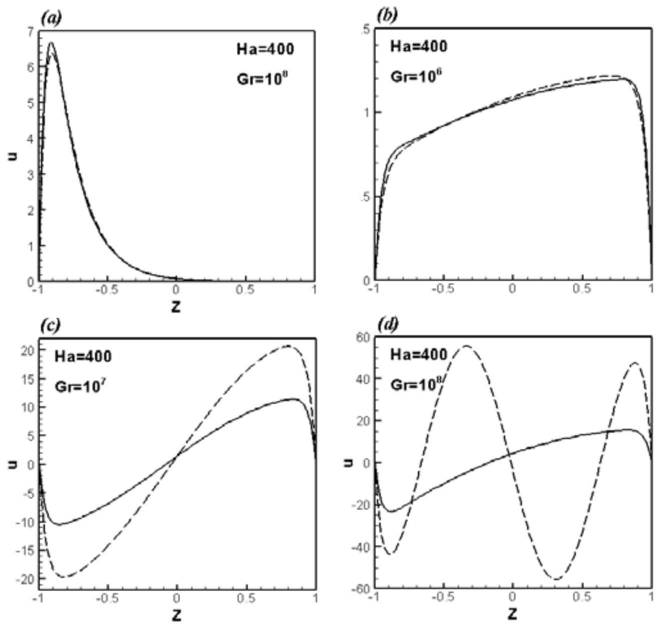

Figure 1: Comparison between analytical Q2D (dashed lines) and computed (solid lines) solutions for streamwise-uniform steady-state flows. *(a)* – upward flow, *(b)-(d)* – downward flow. Heated wall is at z =-1.

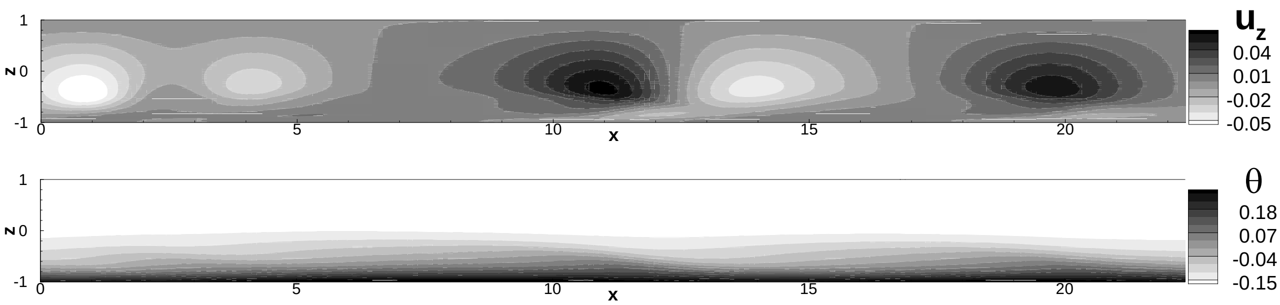

Figure 2: 3D DNS of upward flow at Ha=200, Gr=10. Instantaneous distributions of transverse velocity component u_z and temperature θ in fully developed flow are shown for the mid-plane normal to the magnetic field.

00

3.2 Elevator modes in downward flows. In the case of downward flow, solutions of type (3) could not be computed at high values of Gr. Instead of converging to steady states, the calculated fields demonstrated exponential growth as in:

$$u = e^{\gamma t} u_0(y,z) e_x, \qquad \theta = e^{\gamma t} \theta_0(y,z), \qquad p = 0, \qquad C = e^{\gamma t} C_0, \qquad \gamma > 0 \;. \quad (6)$$

Substituting (6) into the governing equations, we obtain the eigenvalue problem, the mathematical solution of which is yet to be found. From the physical viewpoint, existence of (6) is not surprising. In the downward flow, the balance between wall heating and streamwise convective transport results in the mean-mixed temperature $T_m(x)$ increasing downwards, i.e. unstable stratification. In the absence of top and bottom boundaries, unstably stratified systems are known to have exponentially growing vertically uniform solutions called the 'elevator modes' (see, e.g. [11]). Under normal circumstances, such solutions are not observed, since the growing upward and downward jets typically present in them quickly become unstable and succumb to turbulence. In MHD flows, however, a sufficiently strong magnetic field stabilizes the jets and make the elevator modes actually realized numerical solutions. This was demonstrated in the periodic box computations [12], where, to our knowledge, the elevator modes were first identified and described.

It is hard to say how relevant the solutions (6) to the processes in channels of liquid metal blankets. The top and bottom boundaries of a channel would make the clear-cut elevator modes impossible. At the same time, we may hypothesize that in a long channel the unstable stratification cause strong upward and downward jets. The jets, possibly, grow to large amplitudes and break down to inflection point instabilities creating sporadic turbulence-like bursts of velocity and temperature fluctuations. This scenario and its role as an explanation of strong temperature fluctuations observed in [4] will be explored in our future work.

3.3 Stability analysis and DNS. For the cases, where the steady-state streamwise-uniform solutions (3) could be obtained we conducted their stability analysis. This was done using a modification of the 3D DNS method, in which we followed the evolution of small-amplitude perturbations added to (3) and restricted to a given streamwise wavelength λ using FFT filtering (see [4,6] for details of the method). We have found that, with exception of flows at Gr=10^6, the solutions (3) are unstable in wide ranges of λ for both upward and downward flows. The instability modes are the typical Kelvin-Helmholtz rolls oriented along the magnetic field lines and associated with inflection points in the base flow profiles. Similar modes are found in the Q2D analysis of the upward flow [2].

The flow regimes arising from the instabilities were investigated in DNS. The computational domains sufficiently long to include all or nearly all the unstable modes were used. Typical results are illustrated in Fig. 2.

Acknowledgments: Authors thank Dmitry Krasnov for continuing assistance with the numerical model. Financial support was provided by the US NSF (Grant CBET 1232851).

4. References

[1] Smolentsev, S., Moreau, R., Bühler, L. & Mistrangelo, C. "MHD thermofluid issues of liquid-metal blankets: Phenomena and advances." *Fusion Eng. Design* **85** (7-9), 1196 -1205 (2010).
[2] Vetcha, N., Smolentsev, S., Abdou, M. & Moreau, R. "Study of instabilities and quasi-two-dimensional turbulence in volumetrically heated magnetohydrodynamic flows in a vertical rectangular duct," *Phys. Fluids* **25** (2), 024102 (2013).
[3] Genin, L. G., Zhilin, V. G., Ivochkin, Y. P., Razuvanov, N. G., Sviridov, V. G. Shestakov, A. A. & Sviridov, E. V. "Liquid metal heat transfer in a vertical tube affected by transverse magnetic field." *Fundamental and Applied MHD*, Proc. of 8th PAMIR Conference, pp. 31–35. Borgo, Corsica, France (2011).
[4] Zikanov, O., Listratov, Ya. & Sviridov, V. G. "Natural convection in horizontal pipe flow with strong transverse magnetic field," *J. Fluid Mech.* **720**, 486–516 (2013).
[5] Genin, L. G., Zhilin, V. G., Ivochkin, Y. P., Razuvanov, N. G., Belyaev, I. A., Listratov, Y. I. & Sviridov, V. G. "Temperature fluctuations in a heated horizontal tube affected by transverse magnetic field." *Fundamental and Applied MHD*, Proc. of 8th PAMIR Conference, pp. 37–41. Borgo, Corsica, France (2011).
[6] Zhang, X. & Zikanov, O. "Mixed convection in a horizontal duct with bottom heating and strong transverse magnetic field," submitted to *J. Fluid Mech.* (2014), see also the paper by Zhang, Lv & Zikanov in this volume.
[7] Krasnov, D., Zikanov, O. & Boeck, T. "Comparative study of finite difference approaches to simulation of magnetohydrodynamic turbulence at low magnetic Reynolds number," Comp. Fluids. **50**, 46–59 (2011).
[8] Zikanov, O. "Essential computational fluid dynamics." New York: *Wiley Higher Education* (2010).
[9] Lv, X. & Zikanov, O. "Mixed convection in a horizontal duct with transverse magnetic field and heating of side wall," submitted to *Phys. Fluids* (2014).
[10] Sommeria, J. & Moreau, R. "Why, how and when MHD-turbulence becomes two-dimensional," *J. Fluid Mech*. **118**, 507–518 (1982).
[11] Calvazarini, E., Doering, C. R., Gibbon, J. D., Lohse, D., Tanabe, A. & Toschi, F. Exponentially growing solutions of homogeneous Rayleigh–Benard flow," *Phys. Rev. E* **73**, R035301 (2006).
[12] Zikanov, O., Thess, A., Sommeria, J. "Turbulent convection driven by an imposed temperature gradient in the presence of a constant vertical magnetic field," *Notes on Num. Fluid Mech.*, **66**, 187-199 (1998).

LIQUID METAL DOWNFLOW IN AN INCLINED HEATED TUBE AFFECTED BY LONGITUDINAL MAGNETIC FIELD

BELYAEV I.A., SVIRIDOV V.G., ZAGORSKY V.S.
[1] Moscow Power Engineering Institute, 14 Krasnokazarmennaya str., Moscow, Russia
[2] Joint Institute of High Temperatures of the Russian Academy of Science
13/19 Igorskaya str., Moscow, Russia
E-mail: iabelyaev@gmail.com

Abstract: Experimental study of heat transfer liquid metal downflow in inclined heated tube (inclination 11º; 30º; 45º to the horizon) under the influence of a longitudinal magnetic field has been done. Mercury was used as a model liquid. The test section is a steel tube with inner diameter 19 mm and approximately 100 calibers length, last 40 calibers are heated. MF is homogenous at calibers. Modes of the parameters: Stuart number $N = Ha^2/Re = 0 \div 23$, Richardson number $Ri = Gr/Re^2 = 0 \div 0.8$ in the case of uniform heating were investigated. The studies were conducted using a probe method with the use of microthermocouples. Fields of averaged longitudinal velocity, average temperature and temperature fluctuations have been measured; local and average Nusselt number on the tube perimeter than have been calculated.

1. Introduction

Liquid metals (LM) are considered as a coolant or working media in advanced fission and fusion devices. In the latter case, considering tokamak concept, the LM flow will be affected by strong magnetic field (MF), which can lead to a catastrophic increase of hydraulic resistance. However, reasonable arrangement of heat exchange channels can minimize the negative effects that are presenting themselves in the MF. Direction of the flow along the lines of magnetic induction is capable to remove a significant portion of the MHD interaction complexities. However, the impact of MF on a flow with presence of high heat fluxes, that give rise to buoyancy forces, is ambiguous and cannot be reduced only to the suppression of secondary flows and turbulence [1] In any tokamak reactor MF is a result of toroidal and poloidal components. So MF is directed at some angle to the horizon. In ITER TBM projects [2] this angle is about 11º. In more compact devices (such as fusion neutron sources (FSN) [3]) it can be up to 45º. Straight inclined tube configuration (Fig 1) is considered as a first approximation to design with LM flow directed along with MF.

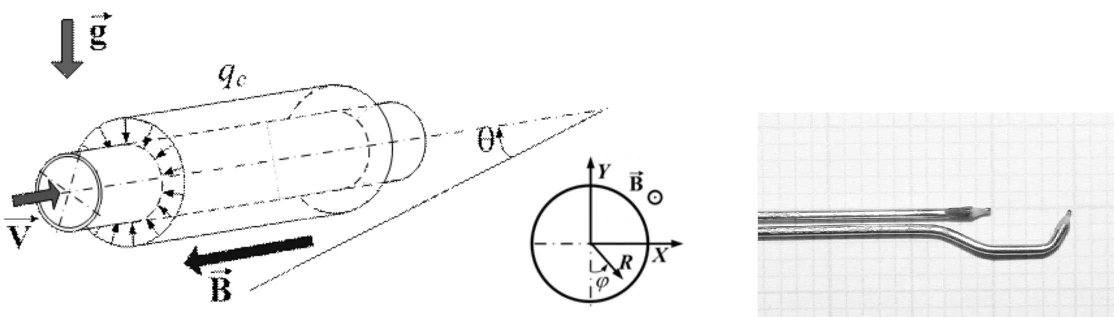

Figure 1: Flow configuration, coordinate system
and the correlation thermocouple probe construction.

Experimental study of this configuration have been made using MPEI mercury loop [1]. Criteria ranges that have been investigated during research are shown in Table 1.

Table 1. Criteria ranges

Criterion	Range
$Re=U\ d/\nu$	$5\cdot10^3\div55\cdot10^3$
$Ha=B\ d(\sigma/\mu)^{0.5}$	$0\div480$
$Gr_q=g\ \beta\ q\ d^4/(\lambda\ \nu^2)$	$0\div1.2\cdot10^8$
$C=\sigma_w L_w/(\sigma d)$	0.04
$Nu=(q_c d/\lambda)/(T_w-T_{bulk})$	–

Table 1 legend: Re - Reynolds number, ν - the kinematic viscosity coefficient, Ha - Hartmann number, σ - conductivity of the medium, μ - dynamic viscosity, Gr_q - Grashof number, g – gravity acceleration, C - relative conductivity of the wall, σ_w – wall conductivity, L_w - wall thickness.

2. Experimental results

Fields of temperature and dimensionless longitudinal velocity obtained in section z/d=37 for tube with 45 degrees inclination in one of investigated regimes are shown on fig. 2 and fig. 3. Section z/d=37 is chosen as a last point of homogeneous MF. Construction of correlation thermocouple probe (Fig.1) which is capable to measure temperature and time averaged longitudinal velocity produces area where measurements cannot be made. Fields are constructed from the experimental points by polynomial triangulation.

In regimes without MF, one can see that temperature isolines are curved by secondary TGC vortices. Traditional for horizontal tubes these TGC vortices with axes along the tube are quite significant in inclined tubes too. In addition, we observe velocity suppression near the upper wall and amplification near the lower wall due to counter thermo gravitation. Both of these thermo gravitational effects lead to temperature inhomogeneity along the wall.

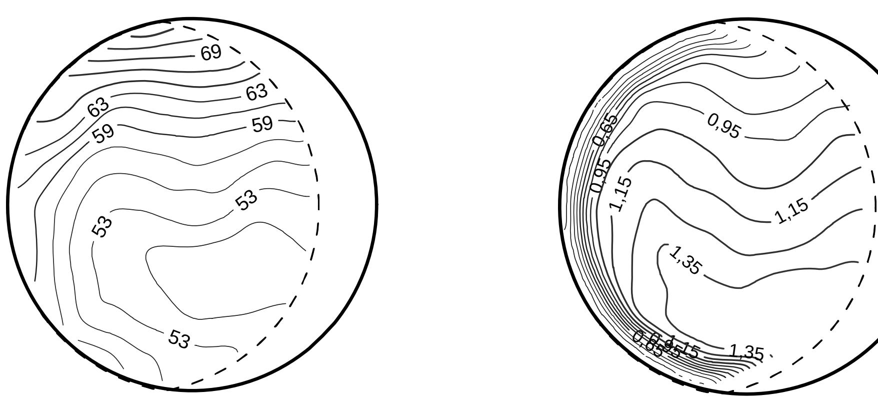

a) Temperature ˚ C b) The dimensionless longitudinal velocity

Figure 2: Fields in section z/d = 37, θ = 45 ˚, Re = $10\bullet10^3$, $Gr_q = 0.8\bullet10^8$, Ha = 0.

In regime with MF strong enough to fully suppress isothermal turbulence one can see area of stable reverse flow near the top of the tube (Fig.3 (b)).

Correlation method, in principle, is a direct method of measuring speed, so it can be applied for the straight and reverse flow, but in the transition region from straight to reverse flow method is not applicable. Also in case of reverse flow probe produces additional disturbance to measurements, which are difficult to compensate. Thus, we assume that the fact of the return flow presence is clear but the region and negative velocity values themselves are defined not precisely enough.

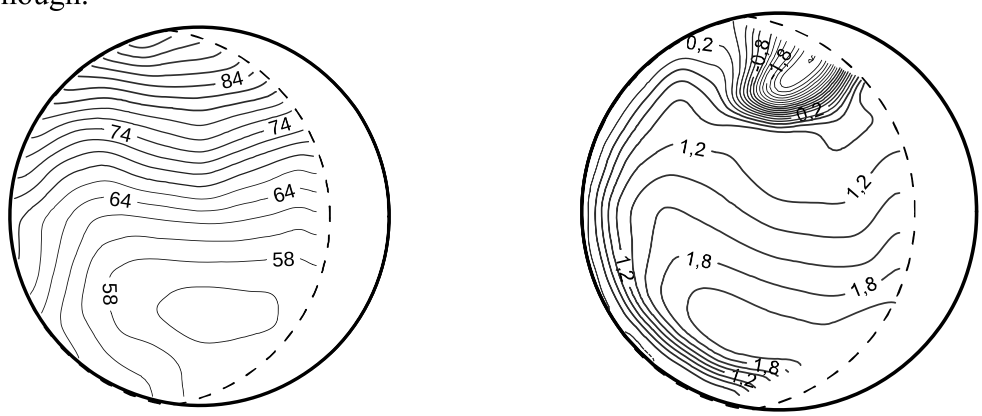

a) Temperature ˚ C   b) The dimensionless longitudinal velocity

Figure 3: Fields in section z/d = 37, θ = 45 ˚, Re = 10•10^3, Gr$_q$ = 0.8•10^8, Ha = 480.

The emergence of the reverse flow in MF is not accompanied by any growth of temperature fluctuations amplitude (Fig. 4(a)). In some regimes where flow have been affected by MF but development of reverse flow have not happened, we observed growth of temperature fluctuation amplitude (Fig. 4(b)).

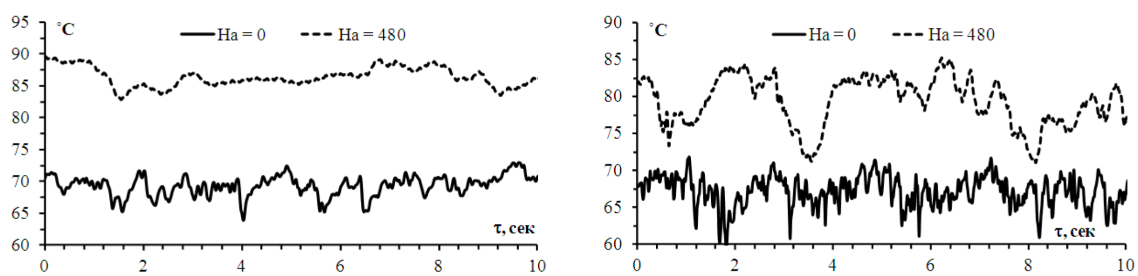

a) $Gr_q = 0.8\cdot10^8$, $Re = 10\cdot10^3$ b) $Gr_q = 1.2\cdot10^8$, $Re = 20\cdot10^3$

Figure 4: Temperature waveforms near the upper generatrix (R = 0.8, φ = 180˚), *z/d* = 37, θ =45˚.

In case of reverse flow presence temperature fields are quite similar qualitatively (Fig 2(a), Fig.3(a)), but overheating near the top generatrix (φ=180) is significantly increased quantitatively. This is shown in the form of distributions of local dimensionless temperature (□(φ) = 1/Nu(φ)) along the perimeter for different inclinations (Fig. 6).

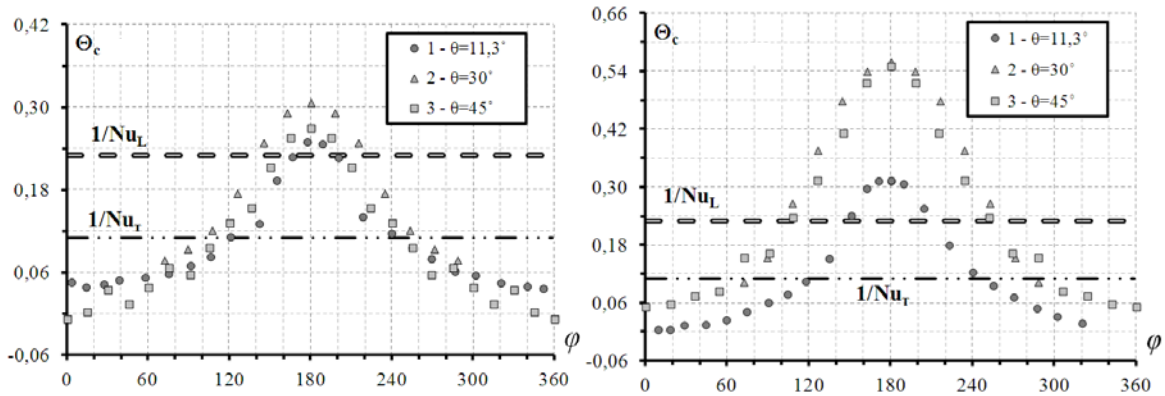

a) Ha = 0 b) Ha = 480

Figure 5: Θ distribution along tube perimeter z/d = 37, Re = $10 \cdot 10^3$, Gr = $0.8 \cdot 10^8$, for various inclinations.

Without MF experimental points with different inclinations lie close enough to each other. Natural convection causes a significant temperature difference between upper (φ = 180˚) and lower (φ = 0˚, 360˚) generatrix. Imposition of the longitudinal magnetic field MF (Fig. 5(b)) at an inclination of 11 ˚ changes picture slightly [4]. A different result is observed at inclination angles of 30˚, 45 ˚ as there development of reverse flow is happening. In this case, local temperature increases throughout the cross section, especially near the upper generatrix where significant overheating occur. What is more, "bell-shaped" form of temperature distribution along the perimeter is saved. As we can see from fig.5, lowest temperature is at lower generatrix and highest at upper in regimes with reverse flow and without. As for the horizontal tube configuration, we found degraded heat transfer zone in case of uniform heating even without MF. This is important, because of the additional thermal stress risk for heat exchanger design [1].

The results of heat transfer studies at different inclination angles are generalized in the form of distributions of local dimensionless wall temperature Θ at upper and lower generatrix from various Peclet numbers (Pe = Re•Pr) (Fig. 6). This difference for such a configuration means total difference of temperatures at tube perimeter. In horizontal and inclined tubes (up to 45 ˚) without magnetic field, (Fig. 6(a)) we observe a similar pattern: difference between Θ in cross section decreases with Pe growth, and values of Θ tend to characteristics of purely turbulent heat transfer without influence of TGC (Θ_T).

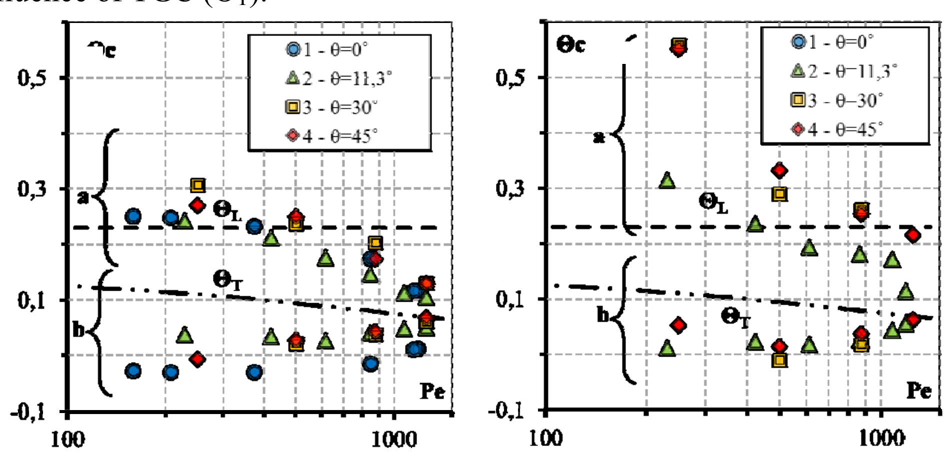

a) Ha = 0 b) Ha = 480

Figure 6: Local Θ at upper φ = 180° (a) and lower φ = 0° generatrix (b), $Gr_q = 0.8 \cdot 10^8$.

When applying the MF (Ha = 480) (Fig. 6(b)) in inclined tubes difference in the values of Θ in a cross section increases as the angle grows despite the fact that configuration is changing to vertical one. It is known, that in vertical configuration with uniform heating we have uniform temperature distribution. Significant heterogeneity in the temperature distribution over the cross section is observed up to the maximum available number Pe. This happens due to counter TGC forces, which slow down flow near the upper generatrix and even provide development of stable reverse flow at low Pe numbers.

3. Conclusion

In summary for downflow in tubes with inclination up to θ=45º to the horizon characteristics of heat transfer are much closer to a horizontal tube than to a vertical one. As in horizontal tubes, heterogeneity of wall temperature along the section perimeter is significant. The temperature difference at the top and bottom of the tube exceeds the values obtained in the equivalent modes for horizontal tubes, especially in the presence of a longitudinal MF.

The role of thermogravitational convection in the entire range of regime parameters is essential. Specificity of inclined tubes is inhibited region near the upper generatrix. It was observed that in the presence of a strong longitudinal MF reverse flow may develop from these inhibited regions. This phenomenon was first discovered and investigated experimentally by direct measurement of the longitudinal velocity component using thermocouple correlation technic. In the region near the upper generatrix a reverse flow was observed while lower part of the flow was accelerated by performing the contrary law of continuity. Reverse flow lead to extremely high heterogeneity in the distribution of the wall temperature over the tube section and extremely low Nusselt number: Nu<1 for local values on top of the tube. Transition to regimes with reverse flow were obtained smoothly, without crisis. Observed in regimes with longitudinal magnetic field reverse flow is quite stable, as increase of temperature gradient across the section were not accompanied with any growth of temperature fluctuations amplitude.

Work is supported by RF president award СП-2363.2012.2 and RF president grant MK-4882.2012.8.

4. References

[1] Belyaev, I.A., Genin, L.G., Listratov, Ya.I., Melnikov, I.A., Sviridov, V.G., Sviridov, E.V., Ivochkin, Yu.P., Razuvanov, N.G., Shpanskiy, Yu.S.: Liquid metal heat transfer specific in a tokamak reactor. Magnetohydrodynamics vol. 49 (2013),, no. 1-2, pp. 177-190.
[2] ITER Design Description Document. Part 1.6. Blanket. Part 1.7. Divertor. ITER Joint Central Team – San-Diego, USA – 1994.
[3] Kuteev, B.V., Lukash, Y., Petrov, V.S., Shpanskiy, Yu.S.: Magnetic system of a compact spherical tokamak FNS-ST. VANT 2010(4): p. 40-47, (in Russ.).
[4] Belyaev, I.A., Listratov, Ya. I., Razuvanov, G.N., .Sviridov, V.G.: Liquid metal heat transfer in an inclined tube affected by a longitudinal magnetic field. Proc. the 8th International PAMIR Conference on Fundamental and Applied MHD, France, 2011, p.43-49.

DNS OF MIXED CONVECTION IN A LIQUID METAL FLOW WITH IMPOSED TRANSVERSE MAGNETIC FIELD

LISTRATOV Ya.[1], OGNERUBOV D.[1], SVIRIDOV V.[1], ZIKANOV O.[2]
Affilation: [1]National Research University “Moscow Power Engineering Institute”– 111250, Russia, Moscow, Krasnokazarmennaya st, 14, [2]Department of Mechanical Engineering, University of Michigan, State of Michigan, USA
e-mail address of corresponding author: yaroslav.listratov@gmail.com

Abstract : We present the results of direct numerical simulation (DNS) of magnetohydrodynamic flow in circular horizontal pipe under strong transverse magnetic field with influence of natural convection. Under consideration flow modes which possible in liquid metal circuits of fusion reactor blanket cooling systems [1]. Sufficient amount of experimental data with MHD-flows of liquid mercury in long vertical and horizontal pipes under strong transverse and longitudinal magnetic fields [2-3] show that at high Hartmann numbers (Ha~300) appears strong temperature fluctuations. More of that thermal stresses that appears in pipe wall could be comparable with breaking point stresses of channel wall material.

1. Introduction

The main objective of this research is to find explanation and validation of the experimental data in case of the slow high-amplitude fluctuations of temperature that arise at strong magnetic fields. These data obtained at the Moscow Power Engineering Institute (MPEI) and the Joint Institute of High Temperatures (JIHT) of the Russian Academy of Science on the mercury facility. The configuration chosen for the analysis is that of a long horizontal pipe liquid metal flow with the lower half of the wall heated at a constant heat transfer rate *q* and a uniform magnetic field *B* imposed in the transverse horizontal direction (fig 1).

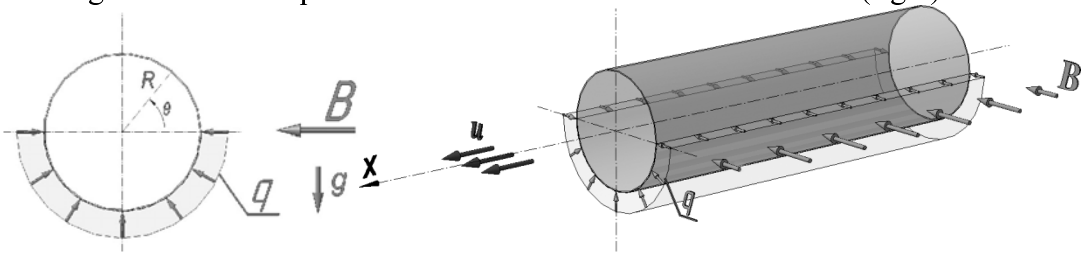

Figure 1: Flow configuration

The most interesting results of the experiment have been recently announced [4] are shown on the figure 2. Without the magnetic field (fig. 2a) fluctuations are irregular and typical for the turbulent flow as confirmed by the spectrum. A sufficiently strong magnetic field (Ha=100) should suppress the turbulence and lead to a flow without temperature fluctuations (fig. 2b). Stronger magnetic field (Ha=300), however, reappears fluctuations with significantly higher amplitude and low dominating frequency (fig. 2c). The fluctuations do not disappear up to highest value Ha = 500 reached in the experiments. The distributions of the temperature fluctuation intensity along the pipe are shown on the figure 3. After the flow enters the zone of uniform magnetic field, which starts at x/d=6, the intensity decreases, as result of turbulence suppression. The decrease continues until the end of the magnet at Ha=100. However at Ha=300 and 500 the decrease is replaced by growth at some distance. This growth is associated with fluctuations illustrated on the figure 2c. It is very important to analyze this phenomenon because similar fluctuations appeared in a liquid metal blanket of a fusion reactor can cause thermal stresses on the blanket wall.

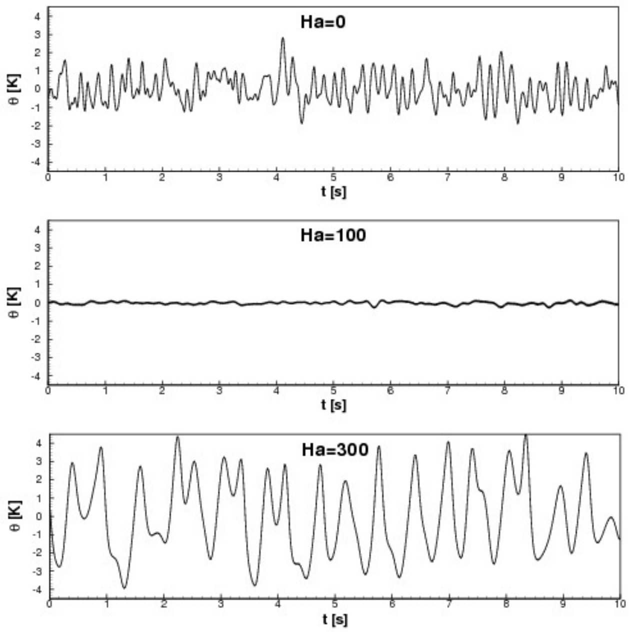

Figure 2: Time signals of temperature fluctuations measured at the point with coordinates r/d=0.35, θ=3π/2 (bottom of the pipe), x/d=37 after beginning of the heating.
Flow parameters: $Re=ud/\nu=10^4$, $Gr=gbqd^4/\nu^2\lambda=8.5\cdot10^7$, $Ha=Bd(\sigma/\rho\nu)^{1/2}$.

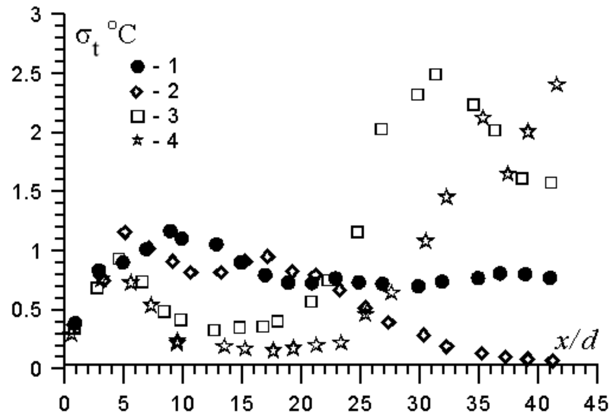

1 – Ha=0, 2 – Ha=100, 3 – Ha=300, 4 – Ha=500

Figure 3: The temperature fluctuation intensity distributions (time averaged) measured along the pipe at the point with coordinates r/d=0.35, θ=3π/2 (bottom of the pipe).
$Re=10^4$, $Gr=8.5\cdot10^7$.

For the start the linear stability analysis and direct numerical simulations are conducted to analyse this case [5]. It is found at the magnetic field strength far exceeding the laminarization threshold, the natural convection develops in the form of coherent quasi-two-dimensional rolls aligned with the magnetic field. Transport of the rolls by the mean flow causes high-amplitude, low-frequency fluctuations of temperature. Given work is an extension of the research of this phenomenon. Direct numerical simulations are performed to determine flow patterns in the range of the non-dimensional flow parameters achievable in the experiments: Re=5000-11000, $Gr=0-1.3\cdot10^8$, Ha=0-300, Pr=0.022.

2. Presentation of the problem

The numerical model is designed to be possibly close to the conditions of the experiment [5]. In particular, as illustrated in figure 4, the computational domain includes the entire experimental test section. The segment with wall heating and the segment with nearly uniform magnetic field have the same lengths as in the experiment.

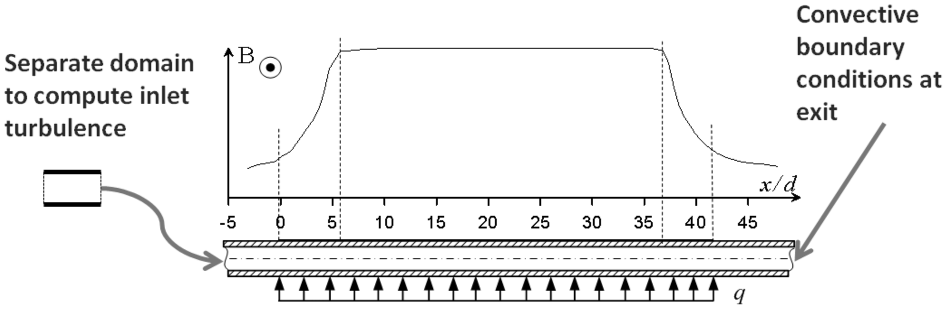

Figure 4: The computational domain. Distribution of magnetic field obtained in experiment.

The numerical model included the procedure used to generate the isothermal turbulent flow at the inlet. The computational grid has Nr=90 (clustered) and N_{θ}=96. In the axial direction, the grid has 1696 uniform distributed points, which corresponds to 32 points per unit length.
The entire computed flow in its fully developed state for various Ha is illustrated in figure 5.

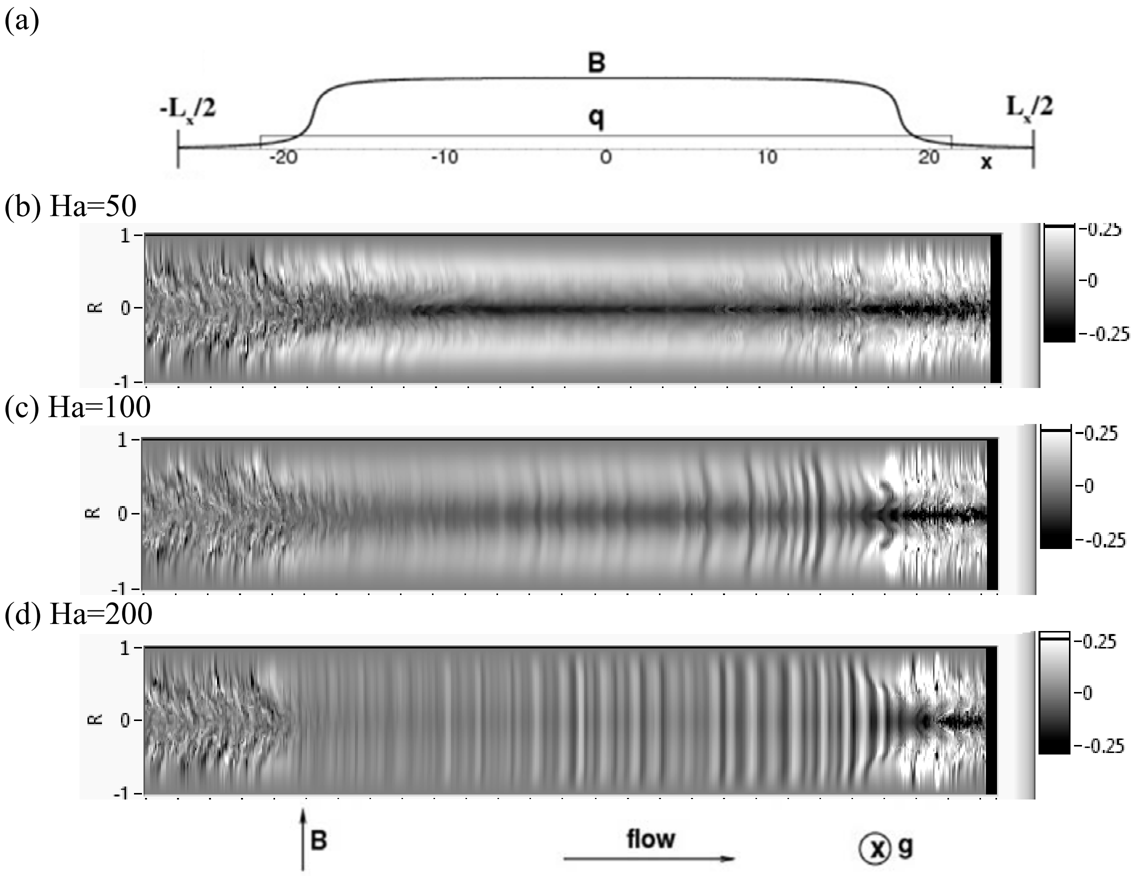

Figure 5: DNS results. (a) distributions of the transverse magnetic field *B* and wall heating *q* along the computational domain; (b-d) fully developed flow shown using snapshots vertical velocity u_z in the horizontal cross-section through the pipe axis. Re = 9000, Gr = $6 \cdot 10^7$.

The flow visibly changes about midway through the magnet zone. A pattern of upward and downward motions and associated variations of temperature appear and increases in amplitude as we move downstream. In the absence of turbulence, the natural thermogravitational convection becomes a dominant mechanism that determines the temperature and velocity field. At Ha=50 or less the geometrically preferable form of the laminar convection is that of streamwise rolls with upward flow along the walls and downward flow in the middle (fig. 6a). However, at Ha = 200 and higher the convection structures developing in the flow change their type and become aligned with the magnetic field (fig. 6b). At Ha = 100, an intermediate mode of convection rolls with unstable states moving downstream is observed.

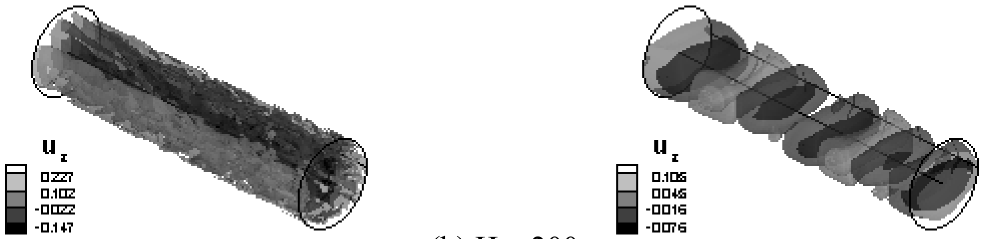

(a) Ha=50 (b) Ha=200

Figure 6: Structure of convection rolls at moderate (a) and strong (b) magnetic field. Isosurfaces of three-dimensional vertical velocity u_z in the pipe segment 35 < x/d < 38. Re =9000, Gr =$6{\cdot}10^7$.

The DNS results will now be compared with the experiment. The distributions of the temperature fluctuation intensity along the pipe at Ha=300 are shown on the figure 7.

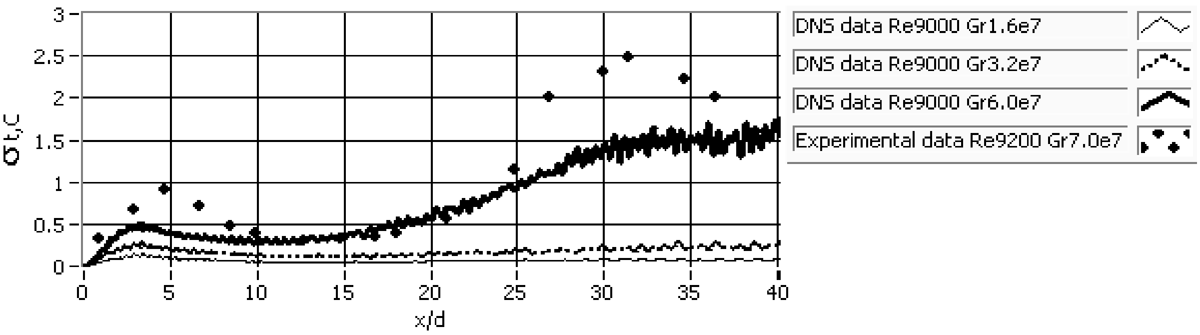

Figure 7: The temperature fluctuation intensity distributions (time averaged) computed along the pipe at the point with coordinates r/d=0.35, θ=3π/2 (bottom of the pipe). Ha=300

As in the experiment intensity decreases after the entering uniform magnetic field. At some distance we observe a growth due to re-oriented rolls aligned with the magnetic field. However, if we reduce the heating that is the Grashof number, it lead to return the mode of streamwise rolls with low level of temperature fluctuations.

Figure 8 show the distribution of time-averaged dimensionless wall temperature along the pipe perimeter in middle section.

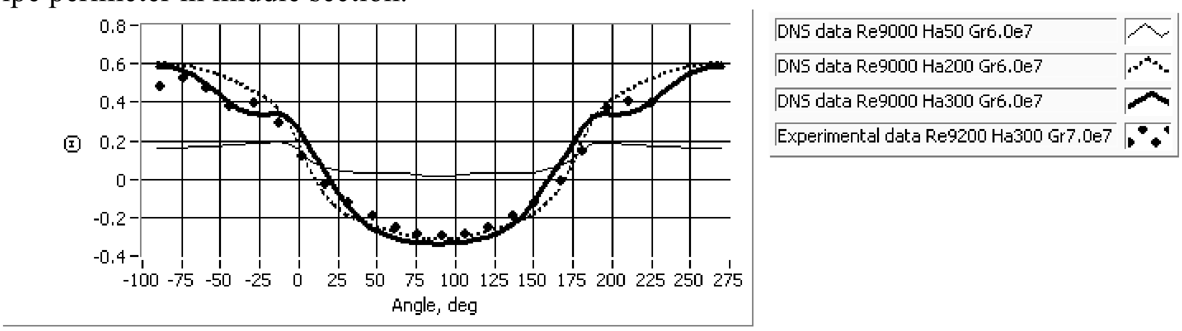

Figure 8: Comparison between DNS and experiment. Lines correspond to the time-averaged dimensionless wall temperature distribution in the pipe section x/d=30 after beginning for various Ha in DNS, while symbols show the data measured in the experiment.

We see that the DNS results have a good agreements with the experimental data. Moreover, figure 8 show overly inhomogeneous distribution of the wall temperature in case of strong magnetic field (Ha = 200 and higher) unlike at Ha = 50. This is confirmed if we consider the temperature perturbations at the topmost and bottommost wall points (figure 9). Such inhomogeneity can lead to the dangerous thermal stresses on the wall.

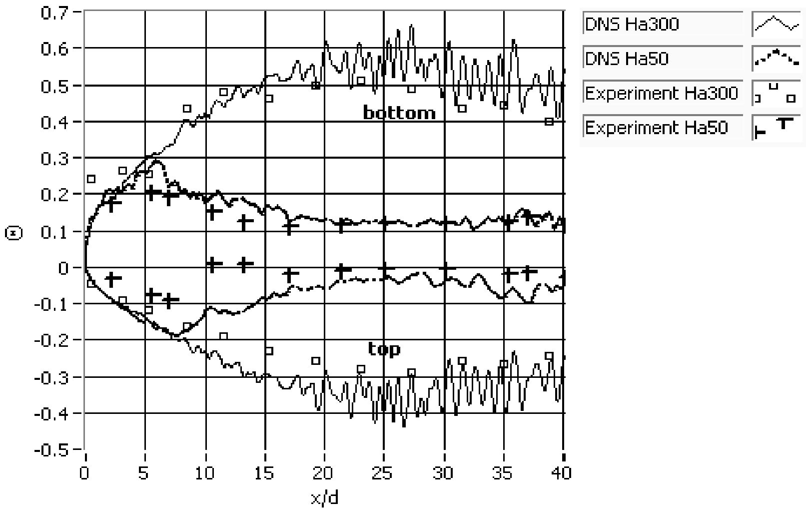

Figure 9: Comparison between the DNS and the experiment. Lines correspond to the instantaneous temperature distribution, while symbols show the time-averaged data measured in the experiment. (a) Temperature perturbations at the topmost (∇ = π/2) and bottommost (∇ = 3π/2) wall points. Re = 9000, Gr = $6 \cdot 10^7$.

3. Conclusion

We have conducted the DNS analysis of the flow in a horizontal pipe with the lower half of the wall heated and an imposed transverse magnetic field. The main results are the detection and detailed study of the convection structures having the form of rolls aligned with the field. Existence of such structures was suspected on the basis of the experimental results, but could not be proven because of the limitations of flow visualization in liquid metals. Our computations leave no reasonable doubt that such convection structures appear at high Hartmann numbers and are responsible for the anomalous temperature fluctuations detected in the experiments.

Financial support of this research was provided by the Ministry of Education and Science of the Russian Federation, Russian Fund for Basic Research.

4. References

[1] Smoletsev, S.; Moreau, R. & Abdou, M.: Characterization of key magnetohydrodynamic phenomena for PbLi flows for the US DCLL blanket. Fusion Eng. Design, 83 771-783 (2008).

[2] Sviridov, V. G.; Razuvanov, N. G.; Ivochkin, Yu. P.; Listratov, Ya. I.; Sviridov, E. V.; Genin, L.G.; V.G.; Belyaev, I. A.: Liquid Metal Heat Transfer Investigations Applied to Tokamak Reactor. Proc. the International Heat Transfer Conference IHTC14, USA, pp.1-8 (2010).

[3] Sviridov, V. G.; Razuvanov, N. G.; Ivochkin, Yu. P.; Listratov, Ya. I.; Sviridov, E. V.: The experimental liquid metal heat transfer investigations applied to fusion reactors. Fundamental and Applied MHD, Proc. 7th PAMIR Conf., Giens, France, pp. 885-890 (2008).

[4] Genin, L. G., Zhilin, V. G., Ivochkin, Y. P., Razuvanov, N. G., Belyaev, I. A., Listratov, Y. I., Sviridov, V. G. Temperature fluctuations in a heated horizontal tube affected by transverse magnetic field. Fundamental and Applied MHD, Proc.the 8th International Pamir Conference, Borgo, Corsica, pp. 37–41 (2011).

[5] O. Zikanov, Ya.I.Listratov, and V.G.Sviridov. Natural convection in horizontal pipe flow with strong transverse magnetic field. J. Fluid Mech., vol. 720, pp. 486–516 (2013).

THE IMPACT OF EM FIELD ON COMBUSTION

VALDMANIS J., BARMINA I., ZAKE M., VALDMANIS R., CIPIJS A.
Institute of Physics, University of Latvia, 32 Miera str., Salaspils, LV-2169, Latvia
E-mail: jvaldman@sal.lv

Abstract: The results of an experimental study of the biomass pellets combustion processes using a 20 kW model are presented. In the experimental model, the maximum stationarity of the combustion process is achieved by varying the parameters (geometry, primary and secondary airflow). The effects of electric current at 50 Hz and 13.56 MHz frequencies were studied. Theoretical problems and further investigations aspects are discussed.

1. Introduction

There are many experimental investigations of electromagnetic (EM) field influence on the combustion processes in gases. It is found that it is possible to control the gas combustion flame form applying an EM field at the flame starting region [1]. The optimal value of electric field voltage is 80-100 kV. The effect is positive when the central electrode is positive, which drives away the negative charges from the flame. Actually, the flame is electrically polarized and the EM forces can control the flame form [1]. However, the high voltage is connected with technical and safety problems. In the present study, we tried to find methods to reduce EM voltage but maintain the positive electromagnetic field influence on the combustion process.

2. Presentation of the problem

There is an essential difference between the combustion processes in gas and in the case of pellets. In gases, there is good mixing of the burning mass at the flame starting point and the combustion process is stable in time that makes easier the investigation of EM field effects. In the pellet case, it is hard to achieve a stable combustion in time because there is a non stationarity of feeding, ash problem, and others. In order to have a stable combustion process, a 20 kW experimental setup (Fig.1) was produced. A result was achieved by using uniform pellet feeding and optimizing the primary and secondary air supply. Fig 2 illustrates the temperature, O_2, CO_2, CO and H_2 mass fraction variations in time. The measurements were made by Testo-350 at the top part of the burner (Fig.1) and the combustion process was stable. In order to choose an optimal EM method, the electrical resistance in the flame and in the pellet zone was measured. The resistance in the flame zone was hundreds of MΩ, but in the pellets' carbonized zone it decreased to hundreds Ω. So, if compared with the gas combustion, where there is only the flame zone with large resistance, high voltage is necessary to have EM effect. In our case, there is possibility to realize an EM interaction through the low resistance zone (carbonized pellets). Another argument is the specific electron transition effects in structured carbon like graphene that has been intensively investigated lately [2]. Electrons in such structures become massless and their motion, which in fact is a current, is ultrafast. As in the carbonized pellet zone there also are carbon structures, some analogy could be found there.

Figure 1: Experimental setup:
1 - gasifier with pellets
2 - quartz cylinder
3 - ceramic grate
4 - primary hot air feed
5 - infeed of pellets
6 - secondary hot air feed;
7 – combustion chamber
8 - diagnostic sensor for to measure gas composition and temperature.
9 - generator
10 - central axial electrode;
11 - circular ground electrode.

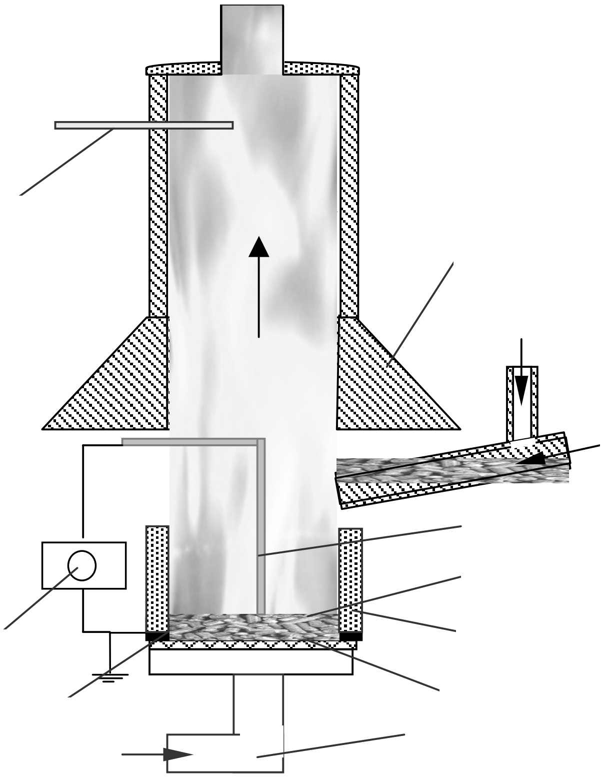

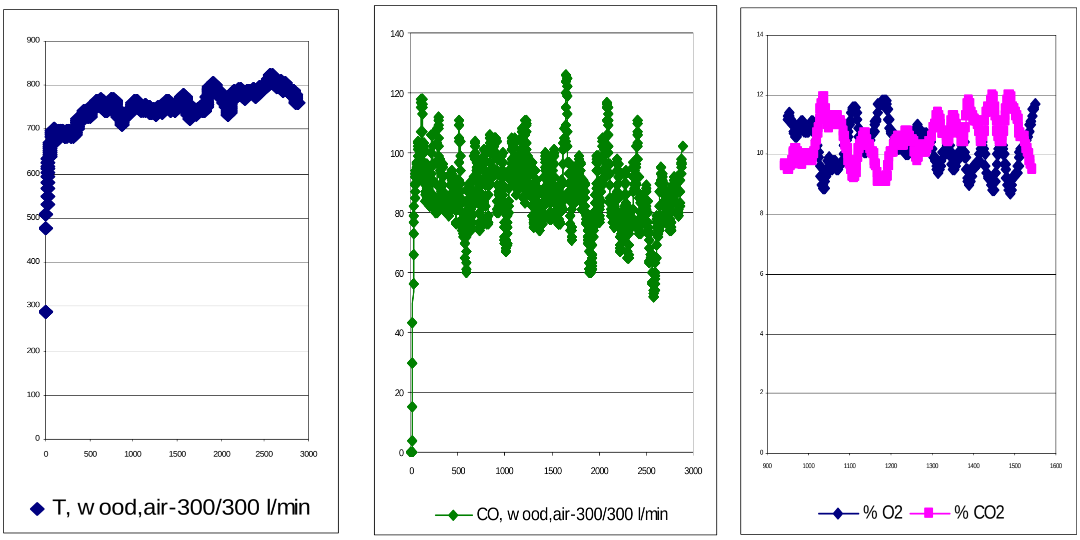

Figure 2: Time-dependent variations of temperature, mass fractions of CO and O_2 CO_2.

So, in experiments, the current was generated just in the pellets' carbonized zone. There 50 Hz, DC and also 13.56 MHz EM fields were used. In the 50 Hz case, the maximum voltage was 220 V, the maximum current 20-25 A. In the 13.56 MHz case, the EM processes were limited by the generator power (600 W). The common characteristics in the all cases are the electrical current distribution non-stationarity and the existence of discrete bright spot formations. There is some analogy with known plasmons or **spasers** (surface plasmon application by stimulated emission radiations) [3]. In the 50 Hz case, when the current mean value increases, instead of stationary character, near the central electrode the spots start to explode, and the discharging process extends from the pellets to the flame zone. The flame becomes much brighter and corona discharging appears. Qualitatively, the EM process can be characterized by a theoretical model [4]. The central electrode has a definite voltage and the earth potential is near the cylinder surface (Fig.1).

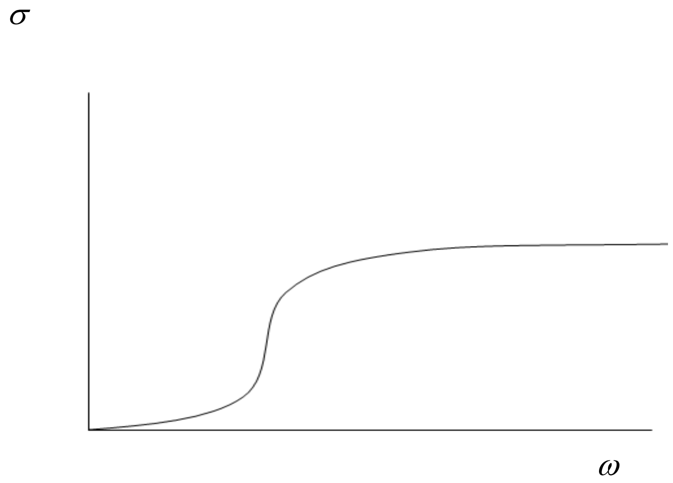

Figure 3: The electrical conductivity as a function of ω.

The electric field in the combustion zone is

$$E = \frac{\varphi}{r \ln \frac{r_a}{r_i}}, \qquad (1)$$

where φ is the potential difference, r is the distance from the central electrode, r_a and r_i are the radii of the cylinder and electrode, respectively. The electrical field (1) in the pellets' carbonized zone induces an electric current

$$j = \sigma E\,,\ \sigma = \varepsilon_0 \omega \frac{\omega / \upsilon}{1 + (\omega / \upsilon)^2}\,,\ \omega = e\sqrt{\frac{n_e}{\varepsilon_0} m}\,, \qquad (2)$$

where σ is the conductivity , e is an electron charge, n_e denotes the charged particles density, m is the mass, υ is the collisions frequency, ω is the Langmuir frequency. When ω is small, $\sigma \sim \omega^2$, and σ = const when ω is large (Fig.3).

The processes in the combustion zone can be described by the system of equations:

$$\begin{aligned} &\frac{dn_e}{dt} = n_1 n_e \beta - n_e^3 \alpha \\ &\frac{3}{2} \frac{n_e dT_e}{dt} = \sigma E^2 - Q_{el} - Q_R - W_1 \frac{dn_e}{dt} \\ &\frac{3}{2} \frac{(n_1 + n_e) dT}{dt} = Q_{el} \end{aligned} \qquad (3)$$

where W_1 is the energy of ionization, n_1 is the neutral particles' density, n_e is the electron density, β is the coefficient of ionization, α is the recombination coefficient , Q_{el}, Q_R are energy losses due to elastic collisions and radiations, T_e, T are the temperatures of electrons and other particles. In our experiments, with the smallest current, the electric resistance values were of 1-2 kΩ. When the current increases to 15-20 A, the resistance decreases to tenths of Ω.

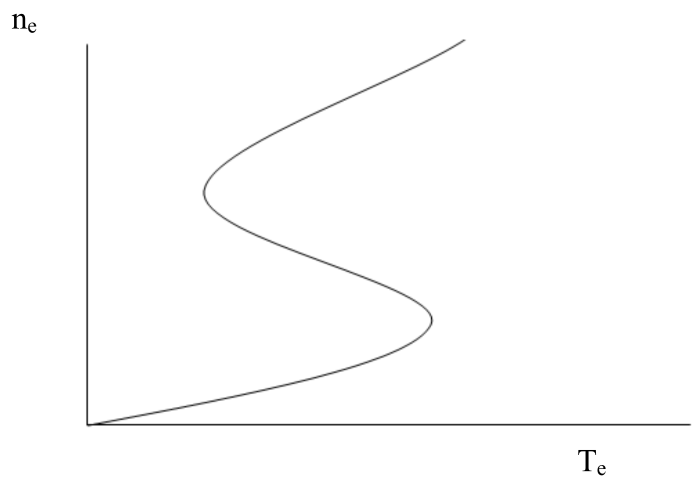

Figure 4: S- type electron density as a function of the temperature T_e.

The current distribution in the pellets zone is non-homogeneous, as shows the picture with bright hot spots. The quasi-stationarity of the hot spots' character changes when the current increases (15-20 A) and there are observed some spots exploding near the central electrode. In fact, the electric current process from the carbonized pellets' zone extends to the flame, and there is a transition from the small branch of n_e concentrations to the higher one (Fig.4).

The characteristic distributions of hot spots in the burner are illustrated in Fig. 5.

a **b**

Figure 5: Distribution of hot spots in the burner (a: 50 Hz, 5 A; b: 50 Hz with rectifier, 8 A).

Visual observation shows that the characteristic life-time of the hot spots is some seconds and dimensions (1-10) mm. In order to estimate the current distribution, stability experiments with an external magnetic field (B_z) were performed. In that case, we had a force field $f_\varphi \sim j_r B_z$. The experimental results show that the number of hot spots decreases as well as the total current mean value. It means that the resistance of the pellet zone increases. It looks as if the current paths are disturbed by the force field. Some experiments were performed under a radial magnetic field when $j \parallel B$. In that case, both the stability of the current distribution picture and the total current value increase.

3. Discussion and conclusions.

In the case under discussion, there are some analogies with the known effects in good conducting graphene when it attracts H or O to the free bonds and becomes graphane with high resistance [5-7]. In our case, the situation is opposite. At the starting point, the pellets' bounds are saturated and there is large resistance. When the volatiles (these are H and O) go out (carbonizing process), the resistance decreases.

The question about the physical mechanisms of hot spots and their influence on the combustion process arises. This also can be regarded as an opposite situation of the known effect when a concentrated laser beam enhances the thermo-current processes in graphene. In our case, the external current generates bright hot spots.

One of the results is that in the 20 kW model the stable combustion regime was achieved.

The electric current through the pellet zone stimulates a gradual evolution of the volatiles. The electric resistance changes in the pellet zone correlate with the rate of volatiles pick on.

The specific pattern of currents' distribution and their influence on the combustion processes need further investigations.

4. References

[1] Guimond D. et al. Insertion of electrostatically charged fuel atomization technology into a U.S. Navy shipboard gas turbine engine, ASME Proceedings, (2004), paper No. GT2004-54298, 1883-1890.

[2] Srinivasan, C; Saraswathi: From graphite to graphene and now to graphane. Current Science,vol. 97(2009) 302-

[3] Stokman, M, J: Nanoplasmonics: The physics behind the applications. Physics Today, (2011) 39-44.

[4] Biberman, L.M. et al. Kinetics of Nonequilibrium Low-Temperature Plasmas. Paperback. (2012) 498.

[5] Kauranen, M; Zayats A,V.: Nonlinear plasmonics. Nature Photonics 6 (2012) 737-748.

[6] Shi, S.F et al.: Controlling graphene ultrafast hot carrier response from metal-like to semiconductor-like by electrostatic gating. Nano Lett.14(3) (2014) 1578-1582.

[7] Liu, Z.K. et al. Discovery of a three-dimensional topological Dirac-semimetal. Science, January (2014) 864-867.

EXPERIMENTAL INVESTIGATION OF RAYLEIGH-BENARD CONVECTION IN A LIQUID METAL LAYER EXPOSED TO A HORIZONTAL MAGNETIC FIELD

TASAKA[1] Y., IGAKI[1] K., YANAGISAWA[2] T., ECKERT[3] S., VOGT[3] T.
[1]Laboratory for Flow Control, Hokkaido University, Sapporo, Japan
[2]IFREE, JAMSTEC, Yokosuka, Japan
[3]HZDR, Dresden, Germany
E-mail: s.eckert@hzdr.de

Rayleigh-Benard convection has been investigated inside a liquid metal layer under the influence of a DC magnetic field. Similar configurations can be found in geophysical or steel production. Our group reported recently that spontaneous flow reversals of quasi two-dimensional rolls randomly occur in Rayleigh-Benard convection of liquid metal exposed to a horizontal magnetic field (Yanagisawa, *et al.*, *PRE*, 2011). In fluid layers with relatively large aspect ratios the flow pattern consisting of several convection rolls appears to be almost isotropic. However, the rolls are aligned with the magnetic field direction if the Lorentz force becomes either comparable to the buoyancy or larger. In our experiment, where the fluid layer has a dimension of 200x200x40 mm (corresponding to an aspect ratio of 5), the convection pattern can show 3, 4 or 5 rolls regimes depending on the Rayleigh number *Ra* and the Chandrasekhar number *Q*. Flow reversals occur spontaneously between these steady states in the *Ra*-*Q* parameter space.

A new regime has been found in experiments conducted at high Chandrasekhar numbers in a magnetic system at HZDR. In this regime the flow reversals occur regularly as shown in Fig. 1 which displays a spatio-temporal velocity map measured by ultrasonic velocity profiling in the GaInSn fluid layer. The coloration in the map indicates the sign and intensity of the horizontal velocity whereas the vertical axis stands for the distance from the side wall along a measuring line perpendicular to the magnetic field (ch2). Thus, the stripes represent the existence of 5 quasi two-dimensional rolls in the fluid layer at $Ra \sim 4.9 * 10^4$ and $Q \sim 3.8 * 10^3$, respectively. 15 reversals can be observed during the measurement time of more than 14000 sec (~ 4 hours). The non-dimensional characteristic time of the reversal normalized by circulation time of the roll is around 100, being similar to the characteristic time of the 'random' flow reversals reported by Yanagisawa, *et al.* (2011). Detailed observations reveal that unlike the case of spontaneous flow reversals a deformation of each cell start just after completion of the last reversal occurs. The ends of the cells show lateral movements against each other. These perturbations grow exponentially with time resulting in a reversal of the flow direction.

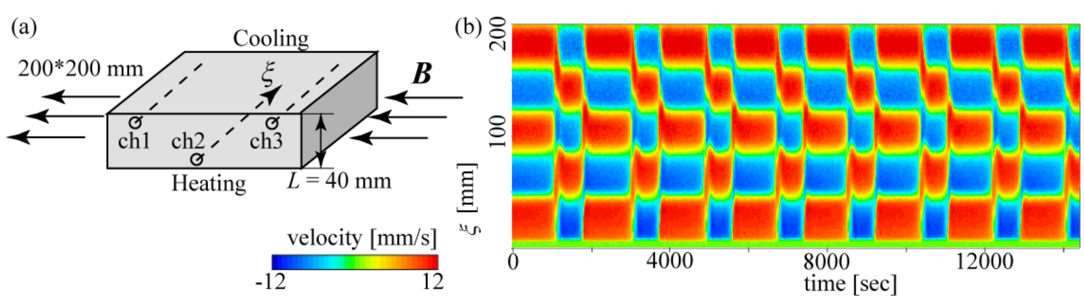

Figure 1: (a) Experimental configuration, (b) Spatio-temporal velocity map showing an example for periodic reversals of the direction of convection rolls

THE ELECTRIC FIELD EFFECT ON COMBUSTION DYNAMICS

BARMINA I., VALDMANIS R., ZAKE M.
Institute of Physics, University of Latvia, 32 Miera str., Salaspils, LV-2169
E-mail: mzfi@sal.lv

Abstract: The DC electric field effect on the development of combustion dynamics downstream the swirling flame flow is studied experimentally with the aim to provide the complex electric field control of the swirling flame dynamics, flame structure, temperature, composition, processes of heat/mass transfer and heat energy production at thermo-chemical conversion of biomass pellets. The mechanism of field effect on the combustion characteristics is discussed with account of field-induced ion drift motion in the field direction providing electric control of the flame structure, composition and main combustion characteristics at thermo-chemical conversion of biomass pellets.

1. Introduction

The DC and AC electric field effects on different types of fuel combustion in the engines, turbines, boilers and furnaces have been investigated to provide combustion control to improve combustion conditions and flame stability [1-9]. Various experimental and numerical studies confirm that the electric field-induced "ionic wind" phenomenon [1, 6, 8] strongly affects the flame shape, dynamics, the formation of polluting NO_x emission, soot formation and processes of interrelated heat/mass transfer. In typical furnaces and boilers, this means electrodynamic control of heat/mass transfer at a relatively low applied power that is less than 0.1% of the thermal power produced by fuel combustion [7]. Since the electric field provides the enhanced heat/mass transfer in the field direction, one may use electric field control technology to enhance the heat transfer to the boiler tubes or protect the critical engine parts from heat fluxes. In addition to field-enhanced control of the processes of heat/mass transfer, the field-enhanced variation of flow dynamics allows to control the residence time of reactions by promoting or by limiting the reactions that lead to the NO_x and CO formation. Motivated by the field-induced variations of flame dynamics and processes of heat/mass transfer, the main objective of the present work is to provide a complex experimental study of the field-induced processes of the thermal decomposition of biomass pellets and thermo-chemical conversion of produced volatiles (CO, H_2). The previous study of the electric field effect on the combustion of volatiles has been carried out with high swirl intensity ($S > 0.6$) determining the formation of a toroidal recirculation zone close to the flame base [4, 5], with field-induced variations of heat/mass transfer and flame structure. The present study is focused on the electric control of the formation of lean partially premixed swirling flame of the volatiles at low swirl intensity ($S < 0.6$) by operating below the vortex breakdown threshold [10]. The DC electric field effect on the thermal decomposition of biomass and formation of main combustion characteristics is analyzed by varying the applied voltage and polarity of the axially inserted electrode.

2. Experimental

The electric field effect on the combustion dynamics at thermo-chemical conversion of biomass pellets was studied experimentally using a compact pilot setup that includes a biomass gasifier charged with biomass pellets and a sectioned water-cooled combustor, downstream of which the dominant burnout of the volatiles develops [11, 12]. The propane flame is used as an external heat energy source for additional heat energy supply (1.2 kJ/s) into the upper part of biomass with the aim to initiate thermal decomposition of pelletized biomass. To provide the air excess ratio $\alpha \approx 0.4$-0.6, the primary air is supplied at an average rate of 28-30 l/min under the biomass layer to support the process of biomass gasification and initiate the formation of axial flow of the volatile compounds (CO, H_2). The volatiles' combustion is supported by the secondary swirling air supply at an average rate of 34-35 l/min through the tangential inlets at the combustor bottom. The secondary air supply provides the lean combustion conditions in the flame reaction zone, with the air excess ratio $\alpha \approx 1.5$-1.8. The electric field effect on the combustion dynamics was studied using an electrode of 150 mm total length axially arranged through the biomass layer, with the electrode top close to the flame base promoting complex field-enhanced variations of the biomass thermal decomposition, flame dynamics and swirl flow structure. The bias voltage and polarity of the electrode relative to the grounded water-cooled walls of the device can be varied in the -2.7 - +2.7 kV range, while the ion current in this study is limited to 1-1.5 mA to minimize the effects of Joule dissipation and corona discharge on the processes of biomass thermo-chemical conversion.

The diagnostic tools used in this study are Pt/Pt-Rh thermocouples for local time-dependent measurements of the flame temperature, a portable air flowmeter Testo 453 with a Pitot tube for measuring the formation of flame velocity profiles, Testo 350-XL for local measurements of the combustion efficiency, flame temperature (T) and flame composition, i.e. mass fraction of the main volatiles CO, H_2, NO_x, fragments of unburned hydrocarbons and volume fraction of the main product CO_2. To estimate the total amount of heat energy produced at thermo-chemical conversion of biomass pellets, calorimetric measurements of the cooling water flow were made providing measurements of time-dependent variations of the flame temperature and of the cooling water flow temperature that were recorded using a computer data acquisition system PC-20TR. All measurements of the DC electric field effects on the gasification and combustion characteristics were made at constant average axial and tangential airflow rates, determining the swirl number of the undisturbed inlet flow $S < 0.6$.

3. Results and discussion

With the given field configuration, the primary DC field effect on thermo-chemical conversion of biomass pellets can be related to the field-enhanced thermal decomposition of biomass pellets. The DC field-enhanced thermal decomposition results in an increase of the biomass mass loss rate (dm/dt), which can be approximated by a linear dependence on the applied bias voltage at high R-squared values ($R^2 \approx 0.96$). By increasing the bias voltage up to ±2.7 kV, the average mass loss rate of biomass pellets can be increased by 12-16% determining the field-enhanced formation of axial flow of the volatiles injected into the combustor at the average axial flow rate 1.2 m/s close to the flame base, with the low swirl number ($S \approx 0.3$). For the fuel-lean conditions with the high level of air excess (150-170%) in the undisturbed flame reaction zone (U = 0), the field-enhanced formation of the volatiles resulted in a decrease of the air excess by ~25%, improving the volatiles' combustion conditions. As a consequence of the field-enhanced thermal decomposition of biomass, a faster ignition of the volatiles with a faster rise of the flame temperature, volume fraction of CO_2 and produced heat power up to their peak values was observed (fig.1). Moreover, the measurements of the total amount of the produced heat energy revealed a linear correlation between the field-enhanced variations of the biomass weight loss and the produced heat energy at thermo-chemical conversion of the volatiles.

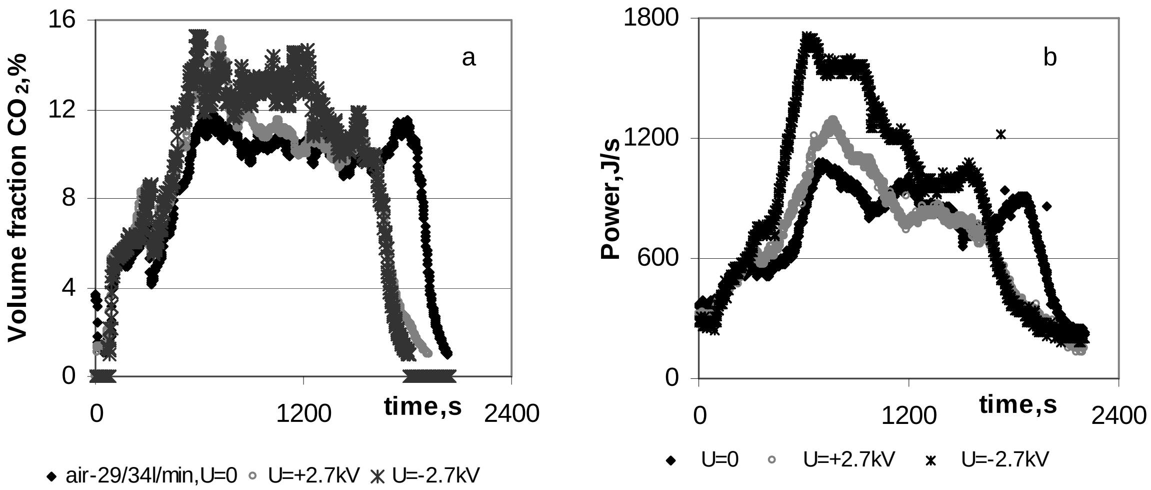

Figure 1: DC electric field effect on the kinetics of CO_2 formation (a) and heat power production (b) at thermo-chemical conversion of biomass pellets.

In addition to the DC field-enhanced thermal decomposition of biomass pellets, the field-enhanced variations of the flame structure were observed. Increasing the negative bias voltage of the axially inserted electrode promoted the radial expansion of the flame reaction zone with the correlating increase of the axial flow velocity average values (u) from 0.7 m/s to 0.84 m/s, while the tangential flow velocity average values (w) decreased from 0.62 to 0.35 m/s, so decreasing the swirl intensity. The field-enhanced radial expansion of the flame reaction zone resulted in the correlating increase of the flame temperature and volume fraction of CO_2 along the outside part of the flame reaction zone at $r/R > 0.5$ (fig. 2a, c, e). The field-enhanced radial expansion of the flame reaction zone towards the positively biased channel walls allows to suggest that the field-enhanced thermal decomposition of biomass pellets would promote the formation of negatively charged fragments of unburned hydrocarbons (CHO_2^-, CHO_3^-) as well as of negative ions of O_2^-, OH^-, and O^-), with the field-enhanced heat/mass transfer (ionic wind) towards the channel walls. The reverse DC field effect on the heat/mass transfer and flow dynamics was observed for positive bias voltage of the axially inserted electrode. In this case, the dominant feature of the field effect on the flame formation was a field-enhanced decrease of the axial flow velocity average value from 0.96 m/s to 0.81 m/s, with the correlating increase of the tangential flow velocity average value from 0.3 m/s to 0.43 m/s, so enhancing the swirl intensity and field-enhanced mixing of the flame compounds. With the low swirl number, the field-enhanced mixing of the flame compounds predominately occurred along the outside part of the flame reaction zone (at $r/R \approx 0.6$) and supported the enhanced thermo-chemical conversion of the volatiles, determining local decrease of free oxygen below 6%, increase of the flame temperature, the volume fraction of CO_2 up to their peak values and the field-enhanced formation of the annular reaction zone at $r/R \approx 0.4$-0.7 (fig. 2b, d, f). In fact, the field-enhanced temperature local increase correlates with the local increase of the rate of temperature-sensitive NO_x formation, so increasing the average mass fraction of NO_x emission in the products by ~7-8%.

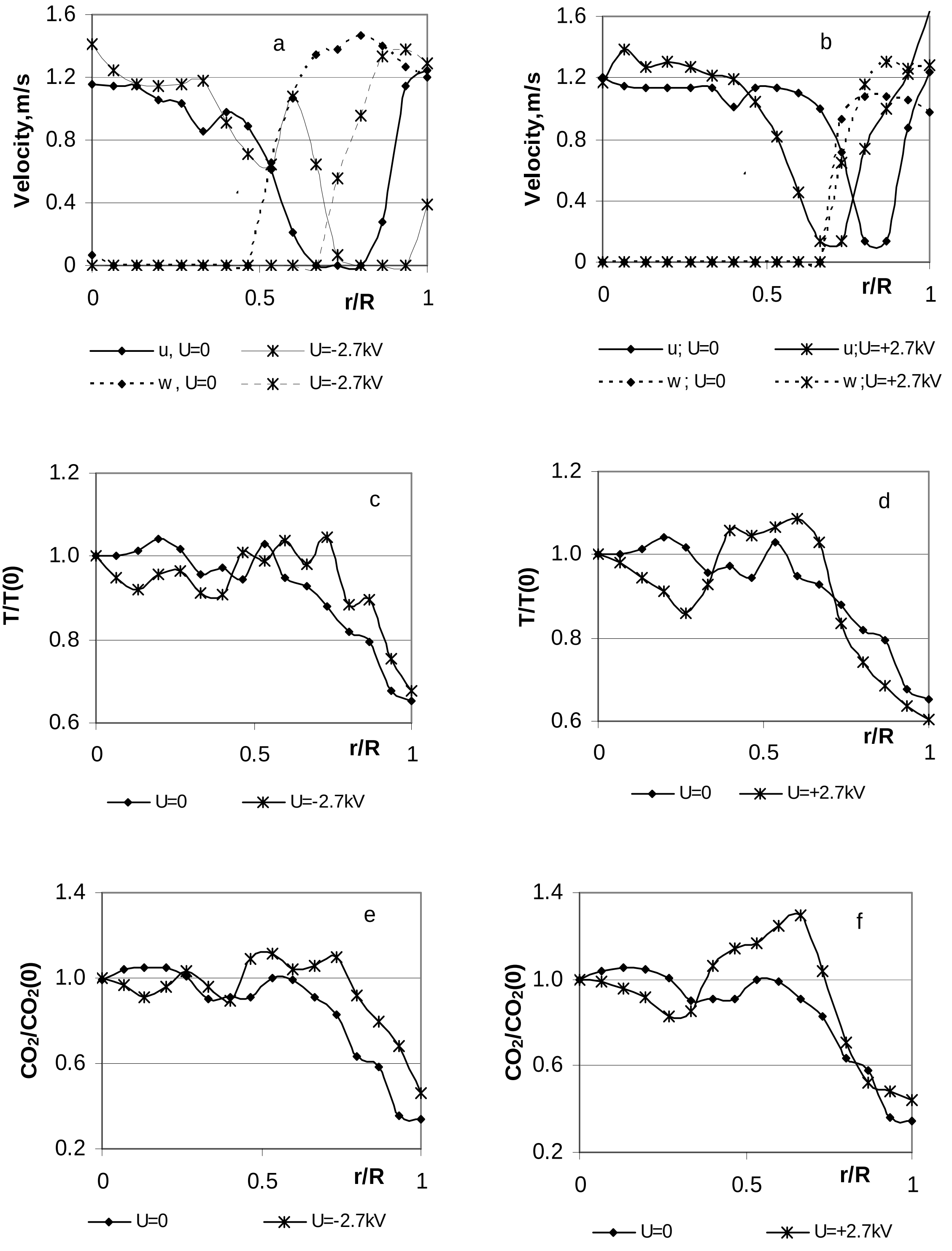

Figure 2: DC electric field effect on the formation of flame velocity (a, b), temperature (c, d) and composition (e, f) profiles at constant bias voltage (U = ±2.7 kV) and variations of DC field polarity.

Conclusion

Based on the results obtained, the following conclusions on the DC electric field effect on the thermo-chemical conversion of biomass pellets at the low swirl number of the swirling flame flow (S < 0.6) can be drawn.

The DC field effect on the thermo-chemical conversion of biomass pellets develops as a multistage process, determining the primary effect of biomass field-enhanced thermal decomposition with field-enhanced formation and thermo-chemical conversion of volatiles, promoting a faster ignition with a more complete combustion of the volatiles and a higher amount of the produced heat energy in the flame reaction zone.

The process of thermo-chemical conversion of the volatiles is influenced by the field-induced variations of the flame dynamics, with field-enhanced variations of the processes of heat heat/mass transfer determining the formation of flame velocity and composition profiles, flame shape and structure. The field-enhanced radial mass transfer to the channel walls, with radial expansion of the flame reaction zone and homogenization of the flow structure, dominates at negative bias voltage of the axially inserted electrode, whereas positive bias voltage with field-enhanced mass transfer of the flame species towards the flame axis reduces the width of the reaction zone the field-enhanced mixing of the flame compounds and local variations of the flame composition along the outside part of the reaction zone with field-enhanced formation of the annular reaction zone.

Acknowledgments. The authors would like to acknowledge the financial support from Latvian research grant N623/1.

4. References

[1] Lawton, J.; Weinber, F.J.: Electric Aspects of Combustion. Clarendon Oress, Oxford, 1969.

[2] Place, E.R.; Weinberg, F.J.: Electrical control of flame carbon, Proc. Royal Society, vol. 289A (1965), pp. 192-205.

[3] Won, S.H.; Cha, M.S.; Park, C.S.; Chung, S.H.: Effect of electric fields on reattachment and propagation speed of tribrachial flames in laminar coflow jets, Proc. the Combustion Institute, vol. 31 (2007), 963-970.

[4] Zake, M.; Barmina, I.; Turlajs, D.: The electric field control of the polluting emissions from the flame, Global Nest, 2001, vol.3, N2, pp.95-108.

[5] Zake, M.; Barmina, I.; Turlajs, D.; Lubane, M.; Krumina, A.: Swirling flame: Part 2. Electric field effect on the soot formation and greenhouse emission, Magnetohydrodynamics, vol.40 (2004), 182-2002.

[6] Zhang,Y; Wu, Y.; Yang, H.; Zhang, H.; Zhu, M.: Effect of high-frequency alternating electric fields on the behavior and nitric oxide emission of laminar non-premixed flames, Fuel, vol.109 (1013), 350-355.

[7] Colannino J., 2012. Electrodynamics Combustion Control TM Technology, In: A Clear Sign White Paper, 1-8.

[8] Vatazhin, A.B.; Likhter, V.A.; Sepp, V.A.; Shulgin, V.I. Effect of an electric field on the nitrogen oxide emission and structure of a laminar propane diffusion flame, Fluid Dynamics, vol. 30 (1995), 166-174.

[9] Bates S.C., 1993, Energy Fields Effects in Internal Combustion Engines, Final Report of Consulting Research for ORNL, Subcontract 80X-SN737V, 1-13. In: http://www.tvu.com/PEFinEng.html

[10] Cheng, R. K., Yegian , D. T., Miyasato , M. M., Samuelsen , G. S., Pellizzari , R., Loftus, P. and Benson, C. (2000).Scaling and Development of Low-Swirl Burners for Low-Emission Furnaces and Boilers. Proc. Comb. Inst. 28: 1305 -1313.

[11] Barmina, I., Lickrastina, A., Purmalis, M., Zake, M., Valdmanis, R., Valdmanis, J., Arshanitsa, A., Solodovnik, V., & Telysheva, G. (2012). Effect of biomass high-frequency pre-treatment on combustion characteristics. Chemical Engineering Transactions, 26, 895-900.

[12]] Barmina, I., Lickrastina, A., Zake, M., Arshanitsa, A., Solodovnik, V., & Telysheva, G. (2013) Experimental study of the thermal decomposition and combustion of lignocellulosic biomass pellets, Latvian Journal of Physics and Technical Sciences, vol. 50, no. 3, pp.35-49.

A SPECTRAL SOLENOIDAL-GALERKIN METHOD FOR THERMAL CONVECTION UNDER THE INFLUENCE OF ROTATION AND OBLIQUE MAGNETIC FIELD

D. YARIMPABUC[1], H.I. TARMAN[2] and C. YILDIRIM[3]

[1]Department of Mathematics, Osmaniye Korkut Ata University, Osmaniye, TURKEY,
[2]Department of Engineering Science,Middle East Technical University, Ankara, TURKEY,
[3]Department of Mechanical Engineering, Akdeniz University, Antalya, TURKEY.

E-mail address of corresponding author: durmusyarimpabuc@osmaniye.edu.tr

Abstract: The effects of a uniform rotation in the vertical direction and a uniform oblique magnetic field on thermal convection between rigid plates are simulated numerically. Solenoidal-Galerkin method is based on solenoidal basis functions that satisfy the boundary conditons and divergence-free conditons for both the velocity and the inclined magnetic field, exactly. The bases for thermal field are also constructed to satisfy the boundary conditions. The governing partial differential equations are reduced to a system of ordinary differential equations under Galerkin projection and subsequently integrated in time, numerically.

1 Introduction

In many astrophysical and geophysical phenomena, hydromagnetic convection in a rotating fluid layer plays an important role. In particular, the effects of rotation and magnetic field along a vertical axis on thermal convection in a horizontal fluid layer is one of the most studied problem in the convective flows due to its ease in studying the onset of instability and geometric simplicity.

The onset of thermal instability in the Bénard layers under the effects of uniform magnetic field and rotation was first studied by Chandrasekhar [1]. It was shown that the magnetic field and rotation together delayed the onset of convection. Nakagawa performed some experimental studies on the action of magnetic field and rotation to understand the instability in a layer when the numerical and theoretical approaches are limited [3]. Although both rotation and magnetic field have inhibition effects on onset of convection, it is also found that acting together both rotation and magnetic field oppose each other such that critical Rayleigh number for the onset of convection for rotation or magnetic field acting separately is larger than that when both present,[2, 4, 5].

In this work, solenoidal bases are used to expand the velocity field in a Galerkin projection onto dual solenoidal bases so that the pressure which comes without boundary condition is eliminated. Solenoidal bases for the magnetic field are generated from the solenoidal bases for velocity by utilizing a quasi-steady relationship between the velocity and the induced magnetic field. All these processes reduce the burden on the numerical technique and increases the accuracy with which the divergence-free conditions are satisfied. The technique is validated in the linear case for rotating hydromagnetic convection by reproducing the marginal stability curves for varying Chandrasekhar and Coriolis numbers. Some numerical simulations are performed in the nonlinear regime and satisfactorily compared with the literature.

2 Governing Equations

Thermal convective motion of a perfectly conducting fluid under Boussinesq approximations is considered in a periodic horizontal layer of thickness d between conducting plates that are heated from below and cooled from above under the influence of rotation about the vertical axis and a uniform magnetic field B_0, which is applied externally in the yz plane with angle χ from y axis (Figure 1).

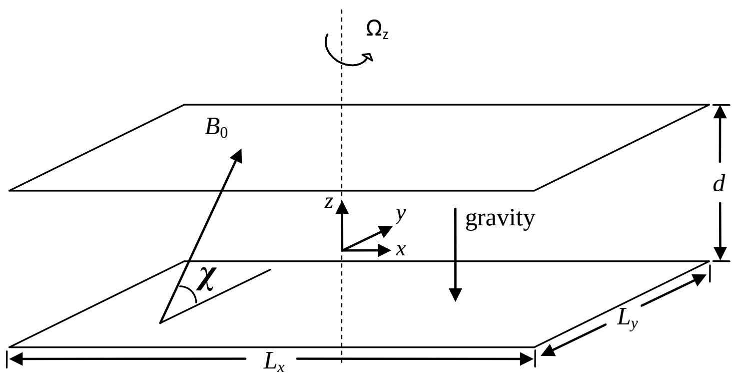

RotMagdoma

Figure 1: The geometry of the periodic convective domain

The nondimensionalization is performed in accordance with [2] except for the length scale which is based on the half depth $d_h = \frac{1}{2}d$ for computational convenience. Therefore, the dimensionless form of the governing equations are:

$$\nabla \cdot \mathbf{u} = 0, \tag{1}$$

$$\frac{\partial \mathbf{u}}{\partial t} = -\left(\mathbf{u} \cdot \nabla\right)\mathbf{u} - \nabla\Pi + PrRa_h\Theta\mathbf{e_z} + Pr\nabla^2\mathbf{u} + Q_hPr\left(\mathbf{e_B}.\nabla\right)\mathbf{b} - 2Pr\Omega_h\mathbf{e_z} \times u, \tag{2}$$

$$\frac{\partial \Theta}{\partial t} + \left(\mathbf{u} \cdot \nabla\right)\Theta = \frac{u \cdot \mathbf{e_z}}{2} + \nabla^2\Theta, \tag{3}$$

$$\nabla^2\mathbf{b} = -\left(\mathbf{e_B}.\nabla\right)\mathbf{u}, \tag{4}$$

$$\nabla \cdot \mathbf{b} = 0, \tag{5}$$

with

$$\mathbf{e_B} = Cos\chi\mathbf{e}_y + Sin\chi\mathbf{e}_z \tag{6}$$

where Π denotes the pressure, $\mathbf{u} = (u, v, w)$ the velocity vector, $\mathbf{b} = (b_x, b_y, b_z)$ the induced magnetic field and Θ is the deviation from the linear conductive temperature profile. Here,

$\mathbf{e_y}$ and $\mathbf{e_z}$ are unit vectors in horizontal $y-$direction and vertical $z-$direction, respectively. The resulting dimensionless numbers are:

$$Ra = \frac{g\alpha \triangle T d^3}{\kappa\nu}, \qquad Q = \frac{B_0^2 d^2}{\rho\mu\nu\lambda}, \qquad \Omega = \frac{\Omega_z d^2}{\nu}, \qquad Pr = \frac{\nu}{\kappa}, \tag{7}$$

Rayleigh ($Ra = 8Ra_h$), Chandrasekhar ($Q = 4Q_h$), the Coriolis parameter ($\Omega = 4\Omega_h$) and Prandtl (Pr), respectively. The appearance of Ra_h, Q_h and Ω_h in equation (2) is due to the use of half-depth as the length scale. Here, g denotes acceleration of gravity, α the thermal expansion coefficient, κ the thermal diffusivity, ν the kinematic viscosity, ρ the density, μ the magnetic permeability, λ the magnetic diffusivity and Ω_z the rotation rate about the vertical axis. Magnetic field in the dimensionless form becomes

$$\mathbf{B} = Cos\chi\mathbf{e}_y + Sin\chi\mathbf{e}_z + \frac{\kappa}{\lambda}\mathbf{b} \tag{8}$$

which indicates that the induced magnetic field $\mathbf{b}$ is weak compared to the externally imposed uniform magnetic field B_0 under the limit $\kappa \ll \lambda$. Thus $\mathbf{b}$ can be viewed as a slaved variable prescribed by the velocity field as stated by the quasi-steady relationship (4). Liquid metals or melts are characterized by this limit.

We assume that the flow takes place in a doubly periodic three-dimensional rectangular region Ω in Fig. 1 with aspect ratio $s_x \times s_y \times 2$ or $\Gamma\left[\frac{1}{2}s_x : \frac{1}{2}s_y\right]$ such that

$$0 \leq x \leq s_x, \quad 0 \leq y \leq s_y, \quad -1 \leq z \leq 1, \tag{9}$$

where $s_x = L_x/d_h$ and $s_y = L_y/d_h$ are the dimensionless periods in the horizontal x and y directions, respectively. While periodic boundary conditions are used for all the dependent variables in the horizontal directions, the boundary conditions at the perfectly conducting plates in the vertical that are maintained at constant temperatures take the form

$$\mathbf{u} = 0 \;\; and \;\; \frac{\partial b_x}{\partial z} = \frac{\partial b_y}{\partial z} = b_z = \Theta = 0 \;\; at \;\; z = \pm 1. \tag{10}$$

3 Solenoidal Basis

Solenoidal (divergence-free) basis functions $\mathbf{V}_p(\mathbf{x})$

$$\nabla \cdot \mathbf{V}_p = 0, \qquad \mathbf{V}_p(\mathbf{x})\,|_{z=\pm 1} = \mathbf{0}. \tag{11}$$

and for the subsequent Galerkin projection procedure, dual bases $\overline{\mathbf{V}}_p^{(j)}(\mathbf{x})$

$$\nabla \cdot \overline{\mathbf{V}}_p^{(j)} = 0, \qquad \overline{\mathbf{V}}_p^{(j)} \cdot \mathbf{e}_z\,|_{z=\pm 1} = 0. \tag{12}$$

are constructed so that both divergence-free criteria are exactly satisfied and the pressure variable is completely eliminated in the projection. Thus, the number of equations and the number of flow variables are reduced.

The quasi-steady relationship (4) between the velocity and the magnetic field variables is used to generate the corresponding magnetic solenoidal basis functions, [7]. This is a crucial step in this approach. In order to facilitate the numerical evaluation of the Galerkin projection integrals, the solenoidal basis functions are based on the Legendre polynomials in the vertical z-direction which are so constructed to satisfy the boundary conditions.

4 Numerical Procedure:

The flow is assumed periodic in the horizontal directions that allows the use of Fourier series expansions of the dependent flow variables,

$$\begin{bmatrix} \mathbf{u} \\ \Theta \\ \mathbf{b} \end{bmatrix}(x,y,z,t) = \sum_{m,n} \begin{bmatrix} \hat{\mathbf{u}} \\ \hat{\Theta} \\ \hat{\mathbf{b}} \end{bmatrix}(m,n,z,t)e^{(i\xi_m x + i\eta_n y)} \tag{13}$$

where $\xi_m = \frac{2\pi m}{s_x}$ and $\eta_n = \frac{2\pi n}{s_y}$ are the wave numbers with the ranges $1-\frac{1}{2}N_x \leq m \leq \frac{1}{2}N_x$ and $1-\frac{1}{2}N_y \leq n \leq \frac{1}{2}N_y$ for the indices m and n. The vertical profiles for velocity and the magnetic fields are further expanded in terms of the solenoidal bases

$$\hat{\mathbf{u}}(m,n,z,t) = \sum_{p=0}^{M} a_p^{(1)}(t)\mathbf{V}_p^{(1)}(z) + a_p^{(2)}(t)\mathbf{V}_p^{(2)}(z), \tag{14}$$

$$\hat{\mathbf{b}}(m,n,z,t) = \sum_{p=0}^{M} a_p^{(1)}(t)\mathbf{B}_p^{(1)}(z) + a_p^{(2)}(t)\mathbf{B}_p^{(2)}(z). \tag{15}$$

The velocity and magnetic fields share the same time evolution as dictated by the quasi-steady link stated in (4). The expansion for the thermal field is

$$\hat{\Theta}(m,n,z,t) = \sum_{p=0}^{M} b_p(t)T_p(z), \tag{16}$$

where $T_p(z) = (1-z^2)L_p(z)$ with its dual $\overline{T}_p(z) = L_p(z)$. The evolution of the time dependent expansion coefficients $a_p^{(j)}(t)$ and $b_p(t)$ is determined by numerically integrating the projected equations in time. For the numerical evaluation of the inner product integrals arising in the projection procedure, Gauss-Legendre-Lobatto (GLL) quadrature is used.

5 Linear Stability

Numerical experiments are performed first to determine the linear stability of the conductive (no-motion) state leading to the critical values when the convective motion just sets in for testing the solenoidal bases and the projection procedure. For this purpose, The linearized governing equations

$$\frac{\partial \mathbf{u}}{\partial t} = -\nabla\Pi + PrRa_h\Theta\mathbf{e}_z + Pr\nabla^2\mathbf{u} + Q_hPr(\mathbf{e}_z\cdot\nabla)\mathbf{b} - 2Pr\Omega_h\mathbf{e_z}\times u, \tag{17}$$

$$\frac{\partial\Theta}{\partial t} = \frac{1}{2}\mathbf{e}_z\cdot\mathbf{u} + \nabla^2\Theta \tag{18}$$

are projected onto the dual space after the substitution of the expansions in terms of the solenoidal bases. Then, they are transformed into the system of ordinary differential equations

$$[M]_{(3\times 3)} \begin{bmatrix} \dot{a}_p^{(1)} \\ \dot{a}_p^{(2)} \\ \dot{b}_p \end{bmatrix} = [S]_{(3\times 3)} \begin{bmatrix} a_p^{(1)} \\ a_p^{(2)} \\ b_p \end{bmatrix} \tag{19}$$

where $[M]$, $[S]$ are mass and stiffness matrices, respectviely [7]. The assumption of a time dependence in the form

$$[a^{(1)}; a^{(2)}; b] \propto exp(\varsigma t) \tag{20}$$

reduces the system to a generalized eigenvalue problem for the eigenvalues ς.

Table 1: The critical Rayleigh number Ra_c at $Q = 1210$ for various Taylor Number ($Ta = 4\Omega^2$) values.

	Aurnou and Olson [5]	Present Work
Taylor number	$Ra_c(Nu)$	$Ra_c(Nu)$
0	27100	27101.6
11000	28300	28311.2
95000	29800	29810.5

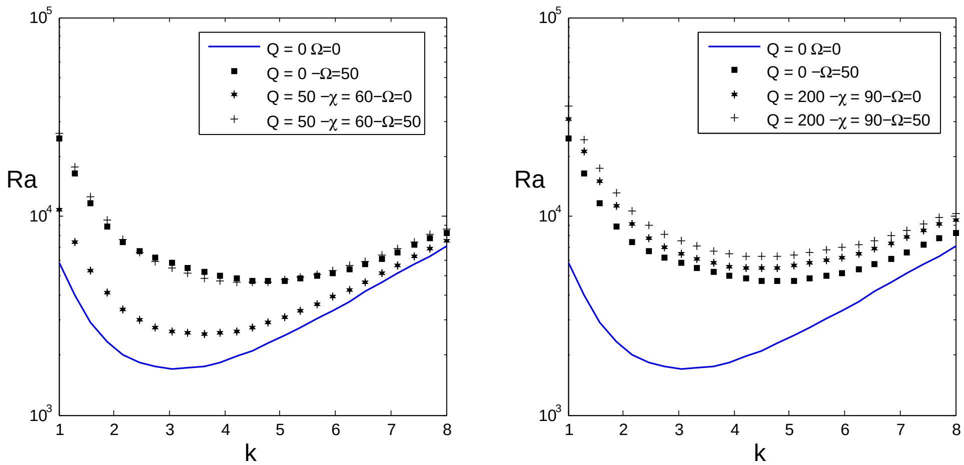

Figure 2: Marginal stability curves for different magnetic field Q and Coriolis Force Ω values.

The critical Rayleigh number Ra_c at $Q = 1210$ for various Taylor Number ($Ta = 4\Omega^2$) values, are listed in Table 1 for the rightmost eigenvalue just crossing the imaginary axis. These are obtained at the selection of $n = 1$ and $m = 0$ in (13). They are in agreement with the experimental study of Aurnou and Olson [5]. The corresponding marginal stability curves for two different cases are plotted in Figure 2. Since, only the vertical component of the magnetic field has an effect on the stability in this regime, Coriolis force dominates over the Lorentz force on the left in Figure 2, which means that the results are similar to the absence of the magnetic field. The figure on the right arises when the Lorentz force dominates over the Coriolis forces in which case the results are similar to the absence of rotation, [2, 4].

6 Nonlinear Analysis

Nonlinear governing equations are discretized in time using a semi-implicit scheme in which the non-linear advection, magnetic and rotation terms are treated explicitly using the third-order Adams Bashforth (AB3) method, and diffusion terms are discretized implicitly by third order Adams-Moulton (AM3).

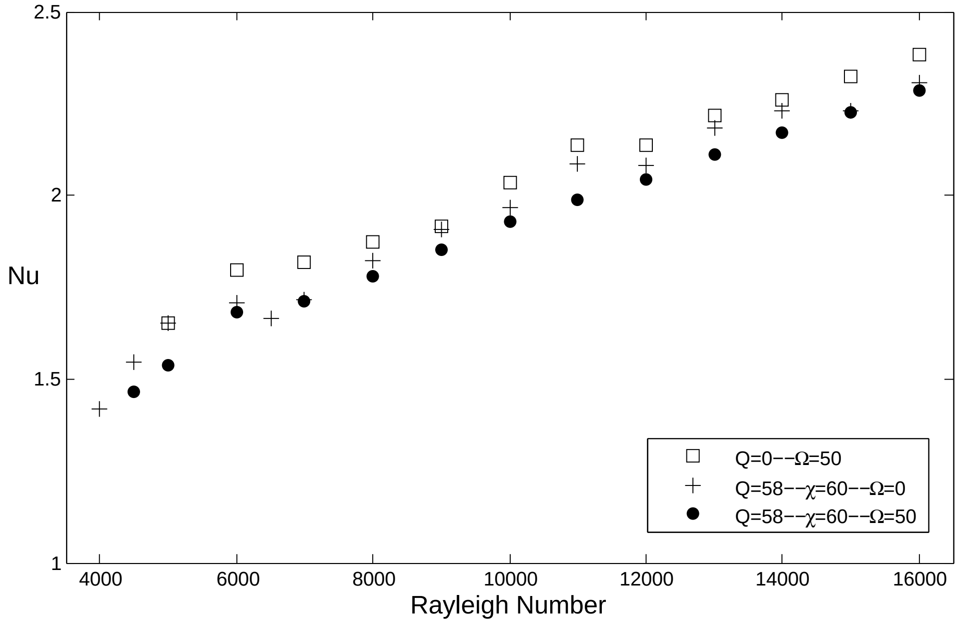

Figure 3: Nusselt versus Rayleigh number at $Pr = 0.1$, $\Gamma\,[3.1 : 3.0]$, $Q = 58$ with an angle $\chi = 60$ and $\Omega = 50$.

The numerical experiments are performed to study the effects of the magnetic field with an angle $\chi = 60$ and the rotation, separately and together, with varying Rayleigh number on the convective heat transport efficiency indicated by Nusselt number (Nu) which is the ratio of the heat transport with and without convection. The flow is chosen to take place in a convective box with the aspect ratio $\Gamma\,[3.1 : 3.0]$ for Prandtl number, $Pr = 0.1$, Chandrasekhar number $Q = 58$ with an angle $\chi = 60$ and Coriolis numbers $\Omega = 50$. Since only the vertical component of the magnetic field has an inhibition effect on the steady flow, in order to make the magnetic field and rotational effects comparable ($Q \sim Ta^{1/2}$, [5]), Chandrasekhar number $Q = 58$ is chosen. Figure 3 shows the Nusselt number versus Rayleigh number for three different cases. In the case where the Coriolis and Lorentz forces are comparable, the minimum temperature gradient for required instability is reduced when compared with the other cases where rotation and magnetic field are acting separately. This is also obtained in [2, 4, 5].

References

[1] Subrahmanyan C.: The Instability of a Layer of Fluid Heated below and Subject to the Simultaneous Action of a Magnetic Field and Rotation. Proc. Roy. Soc. A. 225(1954) 173–184

[2] Subrahmanyan C.: Hydrodynamics and Hydromagnetic Instability. Oxford: Clarendon Press 1961.

[3] Y. Nakagawa.: Experiments on the instability of a layer mercury heated from below and subjected to the simultaneous action of a magnetic field and rotation. Proc. R. Soc. Lond. A. 242(1957) 81–88.

[4] I.A. Eltayeb.: Oberstabile hydromagnetic convection in rotating fluid layer. J. Fluid Mech. 71-1(1975) 161–179.

[5] J. M. Aurnou and P. L. Olson.: Experiments on Rayleigh Benard convection, magneto convection and rotating magneto convection in liquid gallium. J. Fluid Mech. 430(2001) 283–307.

[6] C. Yıldırım, D. Yarımpabuç and H.I. Tarman.: A Spectral Solenoidal-Galerkin Method for Rotating Thermal Convection between Rigid Plates. Mathematical Problems in Engineering. (2013) 8 pages.

[7] D. Yarımpabuç, H.I. Tarman and C. Yıldırım.: Numerical Simulations of Thermal Convection under the Influence of an Inclined Magnetic Field by Using Solenoidal Bases. .Mathematical Methods in the Applied Sciences. Accepted.

The Onset of Rotating Magnetoconvection at Low Ekman

AUJOGUE K.[1], SREENIVASAN B.[1], POTHERAT A.[1]

[1]Applied Mathematic Research Center, Coventry University
aujoguek@uni.coventry.ac.uk

Abstract

A linear stability investigation of rotating magnetoconvection between two differentially heated horizontal planes in a transverse uniform magnetic field at low Ekman number is presented. This study was conducted for Elsasser number Λ (ratio of the Lorentz force to the Coriolis force) from 10^{-3} to 1 and Ekman number E from 10^{-9} to 10^{-2}. Scalings for the critical Rayleigh number and wavenumber at the onset of magnetoconvection were found.

1 Introduction

This work is motivated by applications to the flow in the region of the Earth liquid core magnetoconvection (known as the tangent cylinder). This region seems to play a great role in the structure of the magnetic field and its north pole drift. The main part of the magnetic field is generated by the Earth core liquid flow. To gain better insight on this problem the studies of this flow have relied mostly on DNS [2, 11, 12]. These studies are very expensive and difficult due to the low Ekman and Rayleigh numbers of the order 10^{-14} and 10^{-12} respectively in the Earth core [7]. In order to get closer to more Earthlike regimes, we implemented a linear stability approach. Linear stability is a well known fluids mechanic tool for this kind of problem. Similar problems were envisaged in the past with different basic state on the profil temperature or the magnetic field, and negelecting the inertial and viscous terms in the resolution [3, 4, 10, 6]. These works were conducted for electrically conductive flow rotating in between planes with temperature gradient and horizontal magnetic field. Therefore these configurations are more likely to correspond to the convection outside the tangent cylinder than inside it. We propose here a different kind of basic state closer to tangent cylinder conditions following B. Sreenivasan & C. A. Jones. [11] and Chandrasekhar [5] before them. We found scalings for the different modes of convection. We implemented a new model taking into account the variation of conductivity and thermal diffusivity along the vertical axis. This new linear stablity model was compared with the Chandrasekhar's one [5] for Ekman number $E = 10^{-9}$ and following the phenomenological laws for the Earth core put forward by Pozzo *et al.* [9].

2 Implemented models and results

2.1 Governing equations and geometry

We consider an incompressible fluid (viscosity ν, thermal diffusivity κ, magnetic diffusivity η, density ρ, expansion coefficient α) confined by two differentialy heated infinite horizontal plane boundaries, separated by a distance d. The temperature difference between them is ΔT. The flow rotates at a speed Ω around the vertical axis $\mathbf{z}$ and is subject to a transverse uniform magnetic field $\mathbf{B} = B_0\mathbf{e_z}$. Figure 1 illustrates our geometry.

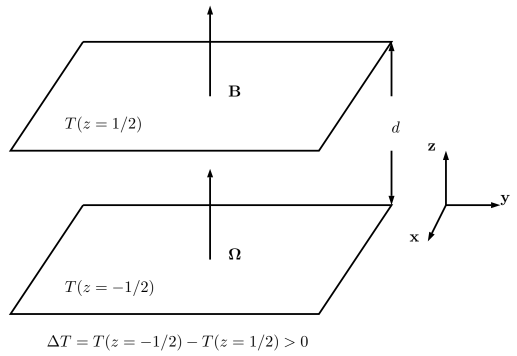

Figure 1: Schematic illustration of the geometry

The flow is governed by the full incompressible MHD equations under the Boussinesq approximation, coupled with energy equation [11, 8]. We normalized lengths by d, the velocity by $\frac{\eta}{d}$, the pressure by $\rho\eta\Omega$, the magnetic field by B_0, the time by $\frac{d^2}{\eta}$, the temperature by ΔT, the rotation speed by Ω. The system becomes controlled by 5 non dimensional parameters: the Ekman number $E = \frac{\nu}{\Omega d^2}$, the Rayleigh number $Ra = \frac{g\alpha\Delta T d}{\eta\Omega}$, the Elsasser number $\Lambda = \frac{B^2}{\mu_0\eta\Omega}$, the Prandtl number $Pr = \frac{\nu}{\kappa}$ and the magnetic Prandtl number $Pm = \frac{\nu}{\eta}$. We applied the two sets of boundary conditions defined by Chandrasekhar [5]: stress free magnetic (SFM) and no-slip magnetic (NSM). For both sets of boundary conditions, the system has a simple solution with $\mathbf{u}_0 = 0$, $\mathbf{B}_0 = 0$, and $T = T_0 + z\Delta T$. We are interested in the linear stability of this basic state. Physical quantities of the problem are decomposed as $g(z) = g_0 + \hat{g}(z)e^{i\mathbf{a}.\mathbf{r}_\perp}$, where $\mathbf{r}_\perp = (x, y)$ and $\mathbf{a}$ is the wave number because of invariance in the $\mathbf{x}$ and $\mathbf{y}$ direction. Following B. Sreenivasan and C. A. Jones [11], we shall only seek the shape of the unstable modes, not their growth rate. The linear stability problem is then solved in the steady state. Furthermore, we shall only consider cases where $Pm = Pr = 1$, under these asumptions, the linearized system is the same described in [11].

$$E(D^2 - a^2)\hat{\omega_z} + 2D\hat{u_z} + \Lambda D\hat{j_z} = 0, \tag{1}$$

$$E(D^2 - a^2)^2\hat{u_z} - 2D\hat{\omega_z} + \Lambda(D^2 - a^2)D\hat{b_z} - 2Ra\hat{T}' = 0, \tag{2}$$

$$(D^2 - a^2)\hat{b_z} + D\hat{u_z} = 0, \tag{3}$$

$$(D^2 - a^2)\hat{j_z} + D\hat{\omega_z} = 0, \tag{4}$$

$$(D^2 - a^2)\hat{T}' + \hat{u_z} = 0, \tag{5}$$

D symbolizes the derivative along $\mathbf{z}$. $\hat{\omega_z} = \boldsymbol{\nabla} \times (\mathbf{u}).\mathbf{e_z}$, $\hat{u_z}$, $\hat{j_z}$, $\hat{b_z}$ and $\hat{T}'$ are the z component complex amplitude of the vorticity, velocity, current, magnetic field, and temperature perturbations respectively and $a =\| \mathbf{a} \|$ is a non dimensional wave number. Following Chandrasekhar [5] and using mass conservation, boundary conditions are expressed as (6, 7).

$$D^2\hat{u_z} = \hat{u_z} = D\hat{\omega_z} = \hat{j_z} = \hat{T}' = 0 \quad \text{for} \quad z = \pm 1/2, \tag{6}$$

$$D\hat{u_z} = \hat{u_z} = \hat{\omega_z} = \hat{j_z} = \hat{T'} = 0 \quad \text{for} \quad z = \pm 1/2\,. \tag{7}$$

The problem becomes a generalized eigenvalue problem of the form $AX = RaBX$. The critical Rayleigh number for the onset of convection Ra_c is found as an eigenvalue of the problem for any given a and minimized over a as in Chandrasekhar [5].

2.2 Resolution

We solved the problem numerically using a spectral collocation method based on Tchebychev Polynomials. In the no-slip case, a boundary layer of the thickness $\delta = 2\sqrt{E\pi}$ develops along the wall, we have ensured that at least 3 collocation points were in it [1]. The validity of the results was guaranteed by convergence tests. We observe a quick convergence to the relative error ϵ over Ra_c at $N = 3000$, the number of collocation points. We made sure that the relative error ϵ was of the same order than the numerical precision.

2.3 Results

In figure 2, we illustrate the typical behaviour of the critical Ra_c with respect to a. For each case, we note three specific values for Ra_c. The first is a minimum occurring at low a, its position and value depends hardly on E but is mostly controlled by Λ. As such, it is referred to as the magnetic mode that we shall denote (Ra_c^m, a_c^m) with Ra_c^m the magnetic critical Rayleigh number and a_c^m the magnetic critical wave number. The second is a local minimum for relatively high a, its position and values depend mostly on E. We shall thus refer to it as the viscous mode (Ra_c^v, a_c^v) where Ra_c^v is the viscous critical Rayleigh number and a_c^v the viscous critical wave number. The third is a local maximum located between the two previous modes. We call this maximum the intermediate mode (Ra_c^{int}, a_c^{int}). For low E, the value of Ra_c^{int} is several orders of magnitude higher than Ra_c^v and Ra_c^m so a clear separation exists between magnetically controlled modes and those controlled by viscosity.

During the simulations, Λ has been restricted to values below 1 which are relevant to geophysical problems (regime of the Earth core). For higher values of the Elsasser number, B. Sreenivasan and C. A. Jones [11] have shown that the Lorentz force has a stabilizing effect on the flow so that $Ra_c^m(\Lambda)$ increases instead of decreasing as it does for $\Lambda < 1$. For both types of boundary conditions we observed the same results. The system can be characterised by two limits, L_1 when the intermediate and the magnetic mode overlap, $Ra_c^m = Ra_c^{int}$, and L_2 when the most unstable mode switches from magnetic to viscous control, $Ra_c^m = Ra_c^v$. In the limit of $E \to 0$ and $\Lambda \to 0$, we found that L_1 behaves as $\Lambda \propto E^{-1}$ and L_2 as $\Lambda \propto E^{-1/3}$. The behaviour of L_1 is a new result highlighting the transition from a viscous only control system to a magnetic and viscous control system. The scaling for L_2 shows when the magnetic mode becomes more unstable than the viscous mode. This second result respects the scaling found by Chandrasekhar [5] about the viscous mode.

Using the same notation, boundary conditions, and logic, we obtained a linear stability model with variable electrical conductivity and thermal diffusivity along $\mathbf{z}$. This model appears as:

$$E(D^2 - a^2)\hat{\omega_z} + 2D\hat{u_z} + \sigma(z)\Lambda_0 D\hat{j_z} = 0, \tag{8}$$

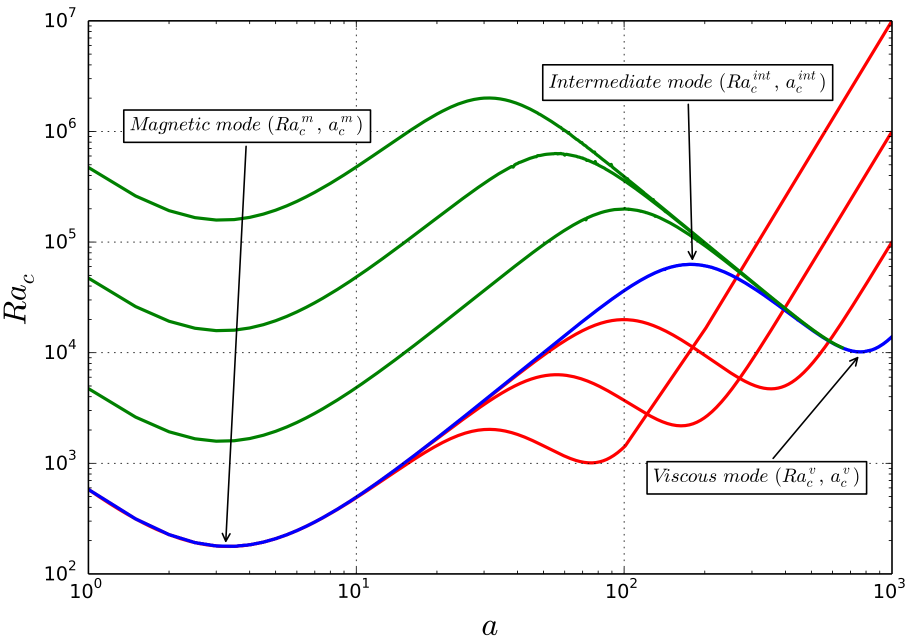

Figure 2: Variation of Ra_c with a. The blue curve's input parameters are $E = 10^{-8}$ and $\Lambda = 1$. The red curves' input parameters are $E = 10^{-8}$ and $\Lambda = 10^{-1}$ to 10^{-3}. The green curves' input parameters are $E = 10^{-5}$ to 10^{-7} at $\Lambda = 1$.

$$E(D^2-a^2)^2\hat{u_z}-2D\hat{\omega_z}+\Lambda(\sigma'(z)-B_0\sigma(z)D)(D^2-a^2)\hat{b_z}-Raa^2(\sigma(z)+T_{eq}(z)\sigma'(z))\hat{T'}=0, \tag{9}$$

$$\frac{1}{\sigma(z)}(D^2-a^2)\hat{b_z}+B_0D\hat{u_z}=0, \tag{10}$$

$$\frac{1}{\sigma(z)}(D^2-a^2)\hat{j_z}+B_0D\hat{\omega_z}+(\frac{1}{\sigma(z)})'D\hat{j_z}=0, \tag{11}$$

$$\sigma(z)\kappa(z)(D^2-a^2)\hat{T'}+\hat{u_z}=0, \tag{12}$$

where $\sigma(z)$, $\kappa(z)$ and $T_{eq}(z)$ are linear functions along $\mathbf{z}$ based on the values given by Pozzo *et al.* [9] at the basic state. We solve this new set of equations as we did for the previous one.

Figure 3 presents the difference in between the new model (with variable κ and ν) and the classic model (uniform basic state). In both cases, the results were obtained with SFM boundary conditions, $E = 10^{-9}$, $\Lambda = 1$, and $a = [1, 2200]$ as input parameters. The new system appears to be generally more unstable. The three modes of interest are pushed to lower values of Ra_c.

3 Discussion

In this paper, the scalings on the different modes for convections were found in the case of the classic model. Asymptotic regimes were reached in the limit of $E \to 0$. For both boundary conditions the behaviour is similar, we only observed a faster convergence to asymptotic regime for SFM in the limit of $E \to 0$. This result is of importance because it suggests that DNS pursued at E of order 10^{-7} with

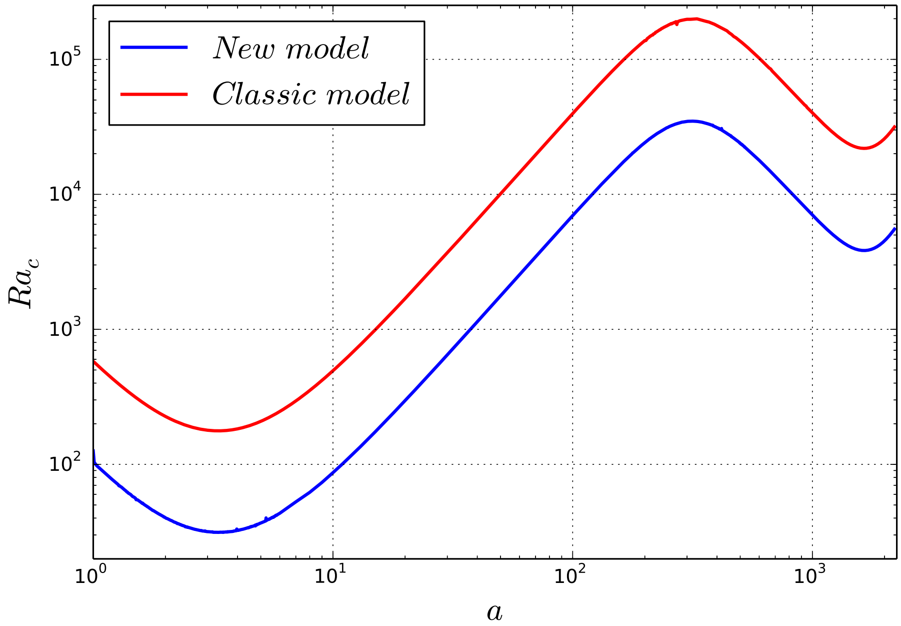

Figure 3: Comparaison in between the two models

SFM provide very accurate insight on the flow inside the tangent cylinder. A new model was implemented showing that variable thermal diffusivity and electrical conductivity generated a more unstable system.

References

[1] D. J. Acheson and R. Hide. Hydromagnetics of rotating fluids. *Reports on Progress in Physics*, 36:159–221, February 1973.

[2] Julien Aubert. Steady zonal flows in spherical shell dynamos. *Journal of Fluid Mechanics*, 542:53–67, 2005.

[3] J Boda. Thermal and magnetically driven instabilities in a non-constantly stratified fluid layer. *Geophysical & Astrophysical Fluid Dynamics*, 44(1-4):77–90, 1988.

[4] Ján Boďa, Gustáv Siráň, and Reviewer P Hejda. Linear stability of a non-constantly stratified horizontal layer penetrated by an azimuthal magnetic field. *Studia geophysica et geodaetica*, 32(3):272–286, 1988.

[5] Subrahmanyan Chandrasekhar. Hydrodynamic and hydromagnetic stability. *International Series of Monographs on Physics, Oxford: Clarendon, 1961*, 1, 1961.

[6] Chen Chuxin and Guo Xiaocheng. Convective instability in a rapidly rotating fluid layer in the presence of a non-uniform magnetic field. *Acta Mechanica Sinica*, 19(6):527–534, 2003.

[7] David Gubbins. The rayleigh number for convection in the earthÕs core. *Physics of the Earth and Planetary Interiors*, 128(1):3–12, 2001.

[8] Peter Olson and Gary A Glatzmaier. Magnetoconvection in a rotating spherical shell: structure of flow in the outer core. *Physics of the Earth and Planetary Interiors*, 92(1):109–118, 1995.

[9] Monica Pozzo, Chris Davies, David Gubbins, and Dario Alfè. Thermal and electrical conductivity of iron at earth/'s core conditions. *Nature*, 485(7398):355–358, 2012.

[10] AM Soward. Thermal and magnetically driven convection in a rapidly rotating fluid layer. *Journal of Fluid Mechanics*, 90(04):669–684, 1979.

[11] Binod Sreenivasan and Chris A Jones. Azimuthal winds, convection and dynamo action in the polar regions of planetary cores. *Geophysical and Astrophysical Fluid Dynamics*, 100(4-5):319–339, 2006.

[12] Binod Sreenivasan and Chris A Jones. The role of inertia in the evolution of spherical dynamos. *Geophysical Journal International*, 164(2):467–476, 2006.

EFFECT OF ASPECT RATIO ON STEADY LIQUID METAL THROUGH THE GRAËTZ FLOW SYSTEM IN MHD

LECHEHEB[1] S., YAHI[2] F., TIGRINE[1] Z., MOKHTARI[1] F., BOUBDALLAH[1] A.
[1] Thermodynamics and Energetic Systems Lab, Faculty of Physics, USTHB, BP 32 El alia, Babezzouar Algiers, Algeria
[2]UniversityM'Hamed Bougara –Boumerdes, Algeria
E-mail: lecheheb.sabrina@gmail.com

This work dealt with the geometrical effect on the Graëtz flow system following the influence of the duct length to width ratio, aspect ratio Γ, on heat-transfer rates, pressure distribution and thermal performances as local and mean Nusselt numbers of molten metal flow through horizontal rectangular channel in the Poiseuille flow conditions subjected to uniform transversal magnetic field.

We modeled the process to establish the properties related to heat transfer involving the both thermal regions of Graëtz system in MHD. Thus, using a computational fluid dynamics procedure based on finite volume method (Fluent Code), we studied numerically the problem in order to characterize and control the viscous MHD flow according to an imposed axial temperature gradient.

As a result of the effect of aspect ratio on the liquid metal for the considered geometry. This one is connected with the sensitive parameters, namely, the Brinkman number Br, the Hartmann number Ha and the Peclet number Pe.

The advantage of such modifications will directly affect the probability distribution of the temperature field, with or without a magnetic field effect. Under these conditions, we note that an early transition regime [1] from the laminar flow to turbulence and therefore by decreasing Γ to enhance both heat transfer rates and flow mixing by pressure drop as Γ deceases.

Keywords: Graetz flow system, Thermal performance, Poiseuille flow, Aspect ratio, Nusselt number

Reference

[1] Mondal, R.N.: Effect of Aspect ratio on unsteady solutions through curved duct flow, Appl. Math. Mech. Engl, Ed., 34 (9), 1107-1122 (2013).

125 MM SODIUM LOOP FOR SCALED DOWN 4-TH GENERATION NUCLEAR REACTOR THERMO-HYDRAULIC EQUIPMENT TESTING

GOLDSTEINS[2,3,4] L., FAUTRELLE[2] Y., BISCARRAT[3] C., MIKANOVSKIS[1] O., PLATACIS[1] E., POZNAKS[1] A., ROMANCUKS[1] A., SOBOLEVS[1] A., ZIKS[1] A., BULIGINS[4] L.

[1] Institute of Physics University of Latvia, 32 Miera str., LV-2169, Salaspils, Latvia
[2] Grenoble INP, SIMAP/EPM Laboratory, Domaine Universitaire, BP 38402, Saint Martin d'Hères, Cedex France
[3] CEA, CADARACHE, DTN/STPA/LCIT, Bat.204, 13108 St Paul lès Durance, Cedex France
[4] Faculty of Physics and Mathematics, University of Latvia, 8 Zellu str., LV-1002, Riga, Latvia

E-mail address of corresponding author: Leonids.Buligins@lu.lv

Abstract: In the context of the 4th generation nuclear reactors development a considerable interest exists on the stability of the sodium Electro-Magnetic Induction Pumps (EMIP). The MHD instability, which is known already since 70ies may occur in EMIPs with highly conductive materials, like sodium. This instability leads to formation of contra verse flow, pressure losses and limited usage of EMIP. Experimental investigations of this instability are planned in newly installed 125 mm sodium loop.

1. Introduction

Large scale induction electromagnetic pumps are foreseen to be used in ASTRID (Advanced Sodium Technological Reactor for Industrial Demonstration) protoype [1]. A model facility is being built in CEA Cadarache, called PEMDYN to support theoretical developments in EMIP design.

There are many investigations devoted to the development of large scale annular linear induction pumps (ALIP). The instability criterion has been theoretically derived in [2], the boundary between flow stability and instability has been determined experimentally in [3], experimental and numerical results are compared in [4, 5]. While qualitative agreement between theoretical predictions and experiment can be observed, a more detailed analytical study [6] and experiment with controlled velocity/magnetic field perturbation implementation is necessary to deepen the understanding of the instability mechanisms in EMIP.

2. Description of the experiment

To investigate the stability of the EMIP a 125 mm sodium loop has been built at the Institute of Physics of the University of Latvia (IPUL). The principal scheme of the measuring and control system of the loop DN – 125 is shown in fig 1.

The loop is equipped with two electromagnetic switchable induction pumps providing a liquid metal flow rate up to 150 l/s^{-1} at discharge pressure of 4.4 bars. Two flow meters - of the induction types and a Venturi tube are installed on the loop. The working temperature of the loop is 200° C - 500° C. To control the temperature of the loop, it is equipped with three component (LM-Oil-H_2O) heat exchanger with maximum cooling power 120 kW. The cooling power is controlled by the oil level in the ring-like channel. The control range is 2-120 kW at sodium temperature of 300° C.

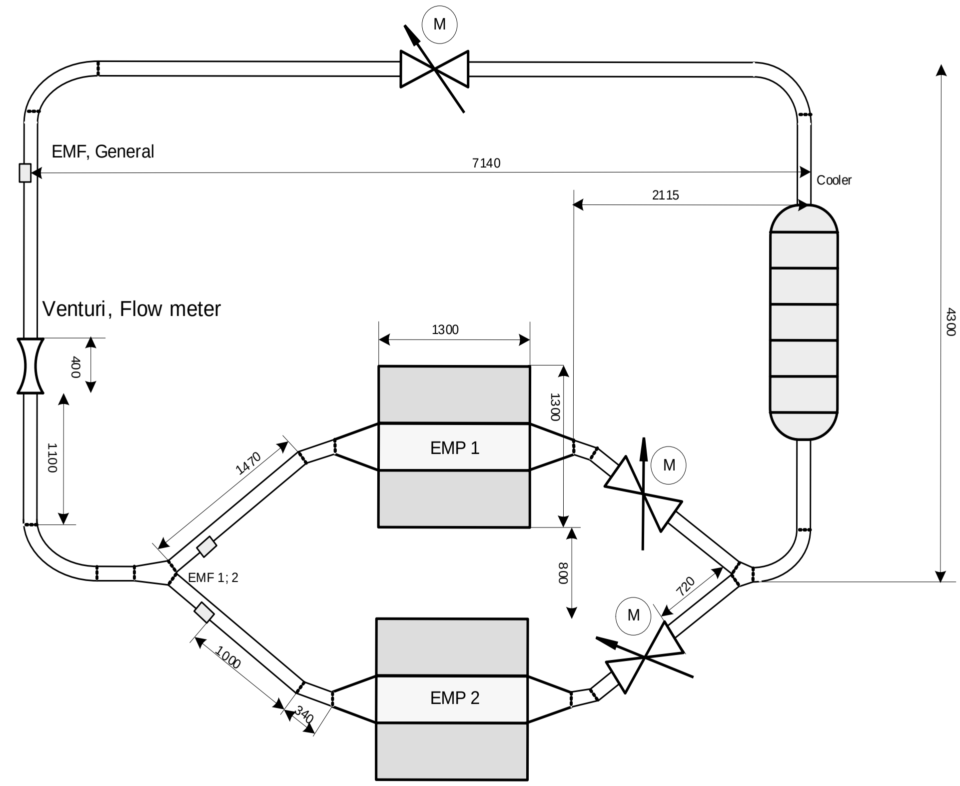

Figure 1: Principal scheme of the measuring and control system of the loop DN – 125.

The overall view of the sodium loop DN – 125 with one installed electromagnetic pump is shown in fig 2.

Figure 2: View of the sodium loop DN – 125.

The channel of the EMIP is equipped with magnetic field, potential and temperature sensors for determination of the distributions of these fields (fig 3.). Up to 144 magnetic coils are foreseen to determine the distribution of the magnetic field. These distributions are to be compared with analytical and numerical results of the stability analysis of EMIP [6].
The inlet zone of the channel serves as a perturbation forming region for controlled velocity distribution. This will allow more detailed comparison of experimental data with predictions of theoretical models.

Three experimental measurement sessions are planned in 2014.-2015.

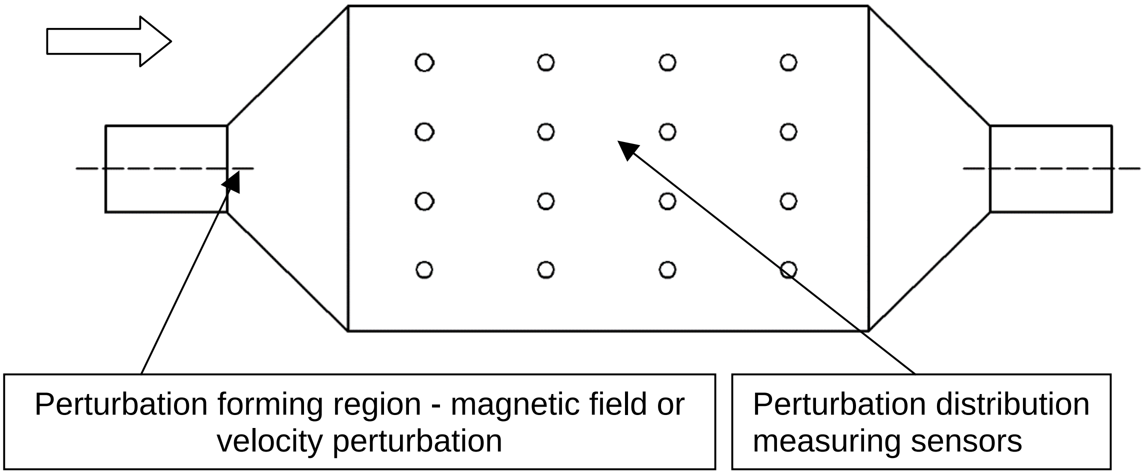

Figure 3: Channel inlet zone and sensor location.

3. Conclusion

A 125 mm sodium loop has been built at the Institute of Physics of the University of Latvia (IPUL) with controlled velocity/magnetic field perturbation implementation in the channel inlet zone and a large number of sensors in the channel zone for detailed comparison of analytical [6] and experiment results to deepen the understanding of the instability mechanisms in EMIP.

4. References

[1] VITRY S., MORCILLO A., REY F., DUMONT M., ETAY J., FAUTRELLE Y.: Development of large flow ALIP EMP for application in ASTRID sodium cooled fast reactor and future power plant reactors. Proc. the 8th PAMIR International Conference September 5-9, 2011, Borgo, Corsica, France, vol2. p.551-556.

[2] GAILITIS A.; LIELAUSIS O.: Instability of homogeneous velocity distribution in an induction-type MHD machine. Magnetohydrodynamics, (1975), No. 1, pp. 87 – 101.

[3] OTA H., KATSUKI K., FUNATO M., TAGUCHI J., FANNING A.W., DOI Y., NIBE N., UETA M. and INAGAKI T.: Development of 160m^3/min Large Capacity Sodium-Immersed Self-Cooled Electromagnetic Pump. Journal of NUCLEAR SCIENCE and TECHNOLOGY, vol. 41, No. 4, p. 511–523 (April 2004).

[4] H. ARASEKI, I. R. KIRILLOV, G. V. PRESLITSKY, A. P. OGORODNIKOV. Magnetohydrodynamic instability in annular linear induction pump. Part I. Experiment and numerical analysis. Nuclear Engineering and Design 227 (2004), pp. 29 – 50.

[5] KIRILLOV I.R., OBUKHOV D.M., PRESLITSKY G.V.: LOW-FREQUENCY PRESSURE PULSATIONS IN ANNULAR LINEAR INDUCTION PUMPS. Proc. the 8th PAMIR International Conference September 5-9, 2011, Borgo, Corsica, France, Vol2. p.483-487.

[6] GOLDSTEINS L., GAILITIS A., BULIGINS L., FAUTRELLE Y., BISCARRAT C. ANALYTICAL INVESTIGATION OF MHD INSTABILITY IN ANNULAR LINEAR ELECTROMAGNETIC INDUCTION PUMP. Proc. the 9th PAMIR International Conference June 16 – 20, 2014, Riga, Latvia, 5p.

Turbulent Magnetic Prandtl Number and Spatial Parity Violation

[1]JURČIŠINOVÁ E., [1]JURČIŠIN M., [1,2]REMECKÝ R., and [1]ZALOM P.

[1]Institute of Experimental Physics, Slovak Academy of Sciences, Košice, Slovakia
[2]Bogoliubov Laboratory of Theoretical Physics, JINR, Dubna, Russian Federation

e-mail address for corresponding author: remecky@saske.sk

Abstact: Using the field theoretic RG approach in the two-loop approximation the influence of helicity (spatial parity violation) on the turbulent magnetic Prandtl number is studied in the model of the kinematic MHD turbulence, where the magnetic field behaves as a passive vector quantity advected by the helical turbulent environment given by the stochastic Navier-Stokes equation. It is shown that the presence of helicity decreases the value of the turbulent magnetic Prandtl number and that the two-loop helical contribution to the turbulent magnetic Prandtl number is up to 4.2% of its nonhelical value.

1 Introduction

One of the most important characteristics of the behavior of the magnetic field in a conductive medium is the magnetic Prandtl number, a dimensionless parameter defined as the ratio of the kinematic viscosity to the coefficient of the magnetic diffusivity. The ratio of the turbulent viscosity to the turbulent magnetic diffusivity is the so-called turbulent magnetic Prandtl number $Pr_{m,t}$ [1, 2], which is an analogy to the turbulent Prandtl number of the thermal diffusion [3, 4] and which obtains a universal value in the limit of fully developed turbulence.

Theoretical investigations of the phenomena connected with fully developed turbulence are often based on the renormalization group (RG) methods [4, 5, 6] in the framework of the field theoretic RG technique which is based on the standard formalism of quantum field theory. Due to the fact that the field theoretical models of fully developed turbulent systems belong among the models with strong coupling constants [6, 7], it is also important to calculate the higher-loop corrections at least to estimate the stability and the relevance of the one-loop results with respect to the perturbation corrections.

The complete field theoretic two-loop RG analysis of the genuine MHD turbulence described by the coupled stochastic MHD equations is still missing due to its complexity. Nevertheless, even in this situation the two-loop value of the turbulent magnetic Prandtl number can be studied and estimated by using the so-called kinematic MHD turbulence. In the framework of the kinematic MHD turbulence the Lorentz force term in the corresponding stochastic Navier-Stokes equation is considered negligibly small and the magnetic field behaves as a kind of passively advected vector field (see, e.g., Ref. [8]).

2 Kinematic MHD turbulence

To describe the passive solenoidal magnetic field in a helical turbulent environment we use the model of the kinematic MHD turbulence which is given by the following system of stochastic equations:

$$\partial_t \mathbf{b} = \nu_0 u_0 \Delta \mathbf{b} - (\mathbf{v}\cdot\partial)\mathbf{b} + (\mathbf{b}\cdot\partial)\mathbf{v} + \mathbf{f}^{\mathbf{b}}, \quad (1)$$

$$\partial_t \mathbf{v} = \nu_0 \Delta \mathbf{v} - (\mathbf{v}\cdot\partial)\mathbf{v} - \partial\mathcal{P} + \mathbf{f}^{\mathbf{v}}, \quad (2)$$

where ν_0 is the viscosity coefficient, u_0 is the reciprocal magnetic Prandtl number, $\mathbf{v} \equiv \mathbf{v}(x)$ is an incompressible velocity field, and $\mathcal{P} \equiv \mathcal{P}(x)$ is the pressure. Both $\mathbf{v}$ and $\mathbf{b}$ are divergence-free vector fields, i.e., $\partial \cdot \mathbf{v} = \partial \cdot \mathbf{b} = 0$.

The quantities $\mathbf{f^v}$ and $\mathbf{f^b}$ in Eqs. (1) and (2) are random noises which simulate the corresponding energy pumping into the system to maintain the steady state of the dissipative turbulent environment. In what follows, we suppose that the magnetic energy pumping is given by a transverse Gaussian random noise $\mathbf{f^b} = \mathbf{f^b}(x)$ with zero mean and the correlation function in the form

$$D^b_{ij}(x;0) \equiv \langle f^b_i(x) f^b_j(0)\rangle = \delta(t) C_{ij}(|\mathbf{x}|/L), \tag{3}$$

which represents the source of the fluctuations of the magnetic field. The explicit form of the function C_{ij} in (3) is not essential in what follows, the only condition which must be satisfied is that C_{ij} decreases rapidly for $|\mathbf{x}| \gg L$.

The transverse random force per unit mass $\mathbf{f^v} = \mathbf{f^v}(x)$ simulates the kinetic energy pumping into the system on large scales. It has to be chosen in a form suitable for the description of real infrared energy pumping. In addition, we require the powerlike form of the energy pumping which enables us to apply the RG technique for investigation of the problem [5, 6]. Both conditions are satisfied by the following Gaussian statistics of the random force $\mathbf{f^v}$ with zero mean and pair correlation function:

$$D^v_{ij}(x;0) \equiv \langle f^v_i(x) f^v_j(0)\rangle = \delta(t) \int \frac{d^d\mathbf{k}}{(2\pi)^d} D_0 k^{4-d-2\epsilon} R_{ij}(\mathbf{k}) e^{i\mathbf{k}\cdot\mathbf{x}}. \tag{4}$$

Geometrical properties of the energy pumping are completely controlled by the form of the transverse projector $R_{ij}(\mathbf{k})$ in (4). In the case of fully symmetric and isotropic energy pumping it is given by the standard transverse projector

$$R_{ij} \equiv P_{ij} = \delta_{ij} - k_i k_j/k^2. \tag{5}$$

On the other hand, in the isotropic but helical case the transverse projector $R_{ij}(\mathbf{k})$ has the following form

$$R_{ij}(\mathbf{k}) = P_{ij}(\mathbf{k}) + H_{ij}(\mathbf{k}) = \delta_{ij} - k_i k_j/k^2 + i\rho\varepsilon_{ijl} k_l/k. \tag{6}$$

Here, ε_{ijl} is the Levi-Civita completely antisymmetric tensor of rank 3 and the real parameter, ρ, characterizes the amount of helicity in the system. Due to the requirement of positive definiteness of the correlation function the absolute value of ρ must be in the interval $|\rho| \in [0, 1]$.

3 Field Theoretic Formulation of the Model

The stochastic problem (1)–(4) can be reformulated into a field theoretic model of the double set of fields $\Phi = \{\mathbf{v}, \mathbf{b}, \mathbf{v}', \mathbf{b}'\}$ with the action functional in the following form:

$$S(\Phi) = \frac{1}{2}\int dt_1\, d^d\mathbf{x}_1\, dt_2\, d^d\mathbf{x}_2 \Big[v'_i(x_1) D^v_{ij}(x_1;x_2) v'_j(x_2) + b'_i(x_1) D^b_{ij}(x_1;x_2) b'_j(x_2)\Big]$$
$$+ \int dt\, d^d\mathbf{x} \{\mathbf{v}'[-\partial_t + \nu_0\triangle - (\mathbf{v}\cdot\partial)]\mathbf{v} + \mathbf{b}'[-\partial_t\mathbf{b} + \nu_0 u_0 \triangle\mathbf{b} - (\mathbf{v}\cdot\partial)\mathbf{b} + (\mathbf{b}\cdot\partial)\mathbf{v}]\}, \tag{7}$$

where $x_l = (t_l, \mathbf{x}_l)$, $l = 1, 2$, $\mathbf{v}'(x)$ and $\mathbf{b}'(x)$ are auxiliary transverse fields which have the same tensor properties as fields $\mathbf{v}(x)$ and $\mathbf{b}(x)$ and required integrations and summations over dummy indices are assumed.

The field theoretic model (7) corresponds to standard Feynman diagrammatic perturbation theory with a set of bare propagators and vertices. In the present model propagators have the following form

$$\langle b'_i b_j \rangle_0 = \langle b_i b'_j \rangle_0^* = \frac{P_{ij}(\mathbf{k})}{i\omega + \nu_0 u_0 k^2}, \tag{8}$$

$$\langle v'_i v_j \rangle_0 = \langle v_i v'_j \rangle_0^* = \frac{P_{ij}(\mathbf{k})}{i\omega + \nu_0 k^2}, \tag{9}$$

$$\langle b_i b_j \rangle_0 = \frac{C_{ij}(\mathbf{k})}{|-i\omega + \nu_0 u_0 k^2|^2}, \tag{10}$$

$$\langle v_i v_j \rangle_0 = \frac{g_0 \nu_0^3 k^{4-d-2\varepsilon} R_{ij}(\mathbf{k})}{|-i\omega + \nu_0 k^2|^2}. \tag{11}$$

where $C_{ij}(\mathbf{k})$ is the Fourier transform of function $C_{ij}(\mathbf{r}/L)$ in Eq. (3). On the other hand, the triple (interaction) vertices are $b'_i(-v_j\partial_j b_i + b_j \partial_j v_i)$ and $-v'_i v_j \partial_j v_i$.

Let us briefly remind that the formulation of the stochastic problem given by Eqs. (1)–(4) through the field theoretic model with the action functional (7) allows one to use the well-defined field theoretic means, e.g., the RG technique, to analyze the problem. At the same time, the statistical averages of random quantities in the stochastic problem are replaced with the corresponding functional averages with weight $\exp S(\Phi)$ (see, e.g., Ref. [6] for details).

4 The helical magnetic turbulent Prandtl number

The final formulas for the determination of the two-loop inverse turbulent Prandtl number of passively advected scalar field and for the corresponding inverse turbulent magnetic Prandtl number in the framework of the kinematic MHD turbulence have completely the same form [9, 10, 11] and in the language of the kinematic MHD turbulence it reads

$$\begin{aligned} u_{eff} &= u_*^{(1)}\left(1+\varepsilon\left\{\frac{1+u_*^{(1)}}{1+2u_*^{(1)}}\left[\lambda-\frac{128(d+2)^2}{3(d-1)^2}\mathcal{B}(u_*^{(1)})\right]\right.\right. \\ &+ \left.\left.\frac{(2\pi)^d}{S_d}\frac{8(d+2)}{3(d-1)}[a_v - a_b(u_*^{(1)})]\right\}\right), \end{aligned} \tag{12}$$

where λ and $\mathcal{B}(u_*^{(1)})$ are given by the calculation of the corresponding two-loop Feynman diagrams in our helical and isotropic problem and quantities a_v and $a_b(u_*^{(1)})$ are given by the corresponding expansions to the leading order in ε of the scaling functions of the response functions $\langle vv' \rangle$ and $\langle bb' \rangle$ of the velocity field and the magnetic field, respectively (see Ref. [11] for details). Their numerical values for physically the most important three-dimensional case ($d = 3$) are

$$u_*^{(1)} = 1.39297, \tag{13}$$

$$\lambda = -1.0994, \tag{14}$$

$$a_v = -0.047718/(2\pi^2), \tag{15}$$

$$a_b = -0.041389/(2\pi^2), \tag{16}$$

$$\mathcal{B}(u_*^{(1)}, \rho) = -4.4320 \times 10^{-3} - 0.1326 \times 10^{-3}\rho^2, \tag{17}$$

and the two-loop value of the turbulent magnetic Prandtl number obtains the following final explicit dependence on the helicity parameter ρ (for the physical value $\varepsilon = 2$)

$$Pr_{m,t}(\rho) \equiv u_{eff}^{-1} = \frac{1}{1.42046 + 0.06229\rho^2}. \tag{18}$$

In the limit $\rho \to 0$ one comes to the nonhelical value $Pr_{m,t} = 0.7040$. On the other hand, in the fully helical case, i.e., when $|\rho| = 1$, one has $Pr_{m,t} = 0.6744$. In addition, looking at Eq. (18), one can conclude that the turbulent magnetic Prandtl number decreases in a helical turbulent environment, i.e., when the absolute value of the parameter ρ increases. In (Fig. 1) the dependence of the turbulent magnetic Prandtl number on the helicity parameter ρ is compared with the analogous dependence of the turbulent Prandtl number of passively advected scalar quantity.

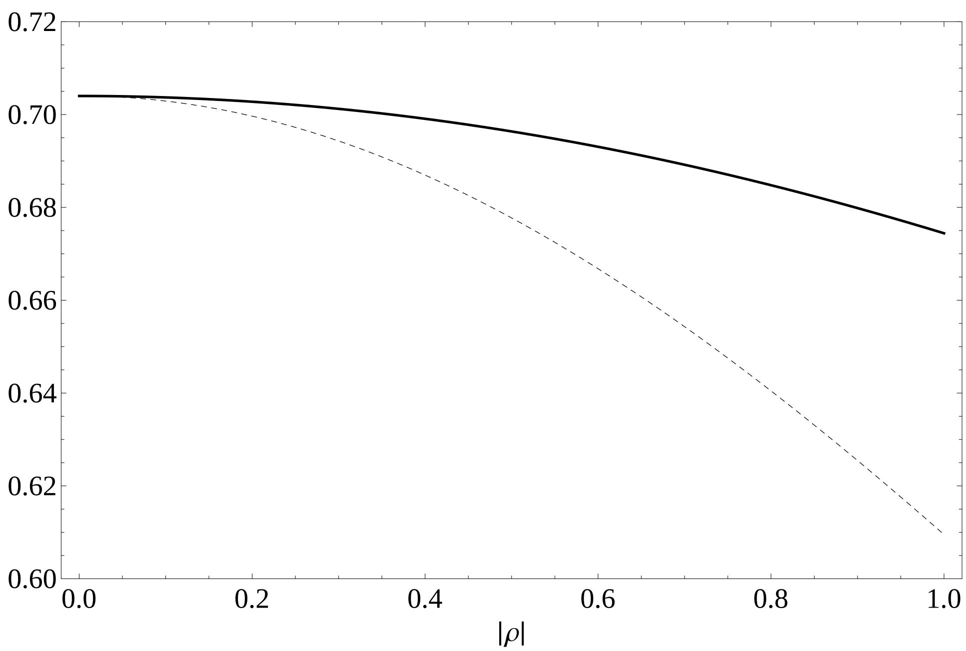

Figure 1: The dependence of the turbulent magnetic Prandtl number $Pr_{m,t}$ (thick line) in the model of the kinematic MHD turbulence and of the turbulent Prandtl number Pr_t (dashed line) of passively advected scalar field on the helicity parameter ρ.

5 Conclusion

In the present paper we have investigated the turbulent magnetic Prandtl number in the framework of the kinematic MHD turbulence under the presence of helicity by using the field theoretic RG technique within the second-order approximation. The explicit dependence ot the $Pr_{m,t}$ on the helicity parameter ρ is found (18).

It was shown that the presence of helicity decreases the value of the turbulent magnetic Prandtl number up to 4.2%, $Pr_{m,t} = 0.6744$ for $|\rho| = 1$, in comparison to its value in the nonhelical system, $Pr_{m,t} = 0.7040$ for $|\rho| = 0$. The fact that the $Pr_{m,t}$ decreases as a function of the absolute value of the helicity parameter also means that the coefficient of turbulent magnetic diffusivity increases as a function of the helicity parameter.

Furthermore we have compared the turbulent magnetic Prandtl number in the helical MHD turbulence to the corresponding turbulent Prandtl number in the model of the passively advected scalar field. In (Fig. 1) one can see that Pr_t and $Pr_{m,t}$ have the same values in the fully symmetric isotropic turbulent environments but are different in the helical systems, i.e., in the systems with spatial parity violation (helicity). It means that the helical turbulent environment distinguishes the internal tensor properties of the advected fields.

The fact that both Prandtl numbers, namely, the turbulent Prandtl number and the turbulent magnetic Prandtl number, decrease as functions of the helicity parameter also means that the corresponding diffusion coefficients increase in helical environments. At the same time, the turbulent diffusion coefficients of scalar fields (temperature field or impurity concentration field) are much more sensitive to the presence of helicity in the system; i.e., their values are essentially more strongly influenced by the helicity than the coefficient of turbulent magnetic diffusivity of the magnetic field in the kinematic MHD turbulence. Therefore, we can conclude that the properties of diffusion processes in the helical turbulent environments can considerably depend on the internal (tensor) properties of the advected fields.

The work was supported by the VEGA grant No. 2/0093/13 of Slovak Academy of Sciences and by the realization of the project ITMS No. 26220120009, based on the supporting operational Research and development program financed from the European Regional Development Fund.

References

[1] Yoshizawa, A.; Itoh, S. I.; Itoh, K: (2003); Plasma and Fluid Turbulence: Theory and Modelling; Bristol; IoP;

[2] Biskamp, D.: (2003); Magnetohydrodynamic Turbulence; Cambridge, Cambridge University Press;

[3] Monin, A. S.; Yaglom, A. M.: (1975); Statistical Fluid Mechanics, Vol. 2; Cambridge, MA; MIT Press;

[4] McComb, W. D.: (1990): The Physics of Fluid Turbulence; Oxford; Clarendon;

[5] Adzhemyan, L. Ts.; Antonov, N. V.; Vasil'ev, A. N.: (1996); 166; 1257; Usp. Fiz. Nauk;

[6] Vasil'ev, A. N.: 2004, The Field Theoretic Renormalization Group in Critical Behavior Theory and Stochastic Dynamics; Chapman & Hall/CRC, CRC Press;

[7] Adzhemyan, L. Ts.; Antonov, N. V.; Vasil'ev, A. N.: (1999); The Field Theoretic Renormalization Group in Fully Developed Turbulence; London; Gordon and Breach;

[8] O. G. Chkhetiani, O. G.; Hnatich, M.; Jurčišinová, E.; Jurčišin, M.; Mazzino, A.; Repašan, M.: (2006); 39; 7913; J. Phys. A: Math. Gen.;

[9] Adzhemyan, L. Ts.,; Honkonen, J.; Kim, T. L.; Sladkoff, L.: (2005); 71; 056311; Phys. Rev. E;

[10] Jurčišinová, E.; Jurčišin, M.; Remecky, R.: (2011); 84; 046311; Phys. Rev. E;

[11] Jurčišinová, E.; Jurčišin, M.; Remecky, R.: (2013); 87; 043010; Phys. Rev. E.

ELECTRO VORTEX FLOWS IN HEMISPHERE VOLUME WITH DIFFERENT BOTTOM ELECTRODE POSITIONS

SEMKO[1] O., IVOCHKIN[2] YU., TEPLYAKOV[2] I., KAZAK[1] O.
[1] Department of Physics and Technology, Donetsk National University, University str. 24, Donetsk, Ukraine
[2] Institution of the Russian Academy of Sciences Joint Institute for High Temperatures RAS, 13/19, Izhorskaya str., Moscow, Russian
E-mail address of corresponding author: olegkazak@yandex.ru

Abstract: This paper devoted to the theoretical and experimental investigation of isothermal electrovortex flows of liquid metal in hemisphere volume with top and bottom electrodes. It is shown that changing bottom electrode position significantly change velocity and structure of electrovortex flows through the liquid metal volume. This results can be used in numerous industrial applications, especially in metallurgical applications such as DC arc furnace with bottom electrode.

1. Introduction

The theoretical and experimental investigation of electro vortex flows (EVF) in hemisphere volume with different geometrical parameters has both theoretical and applied value, especially for numerous metallurgical application such as DC arc furnaces with bottom electrode, electro-welding, etc [1-3]. This work devoted to the numerical and experimental modelling of EVF in hemisphere volume with two electrodes: top and bottom. The bottom electrode in this work set up in different positions.

2. Presentation of the problem

The generalize installation with hemispherical volume of liquid metal presented in Fig. 1. The main parts of the installation are insulator, liquid metal, top and bottom electrodes, air above the installation.

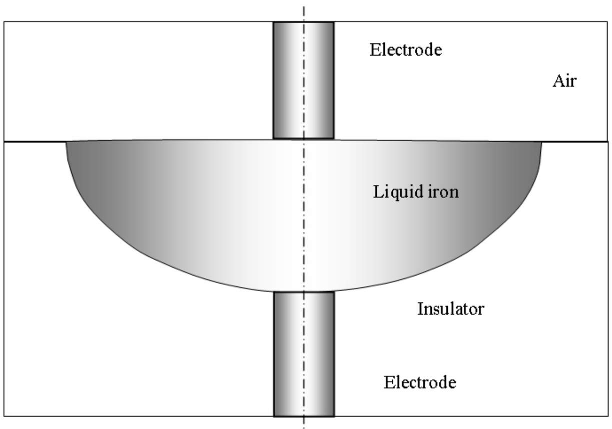

Figure 1: The arrangement of hemisphere installation with two electrodes.

To build a mathematical model of the processes in this installation let us take the following assumptions: the medium is considered non-magnetic; the medium is a good conductor and its permittivity can be neglected; convective current, caused by the medium movements compared to the current of conductance, can be neglected; physical characteristics of the medium (conductance, viscosity and heat-conduction indexes, etc.) are assumed to be homogeneous and isotropic and do not depend on temperature and pressure; medium heating caused by viscosity (viscous dissipation of energy) can be ignored.

The processes are rather slow and can be described in quasi-steady or just steady formulation. For steady processes the system of equations of magnetic hydrodynamics, describing the molten metal flows in this installation is as follows:

momentum equation

$$(\vec{u}\nabla)\vec{u} = -\frac{1}{\rho}\nabla p + \nu\Delta\vec{u} + \vec{g} + \frac{1}{\rho}\vec{j}\times\vec{B} \quad (1)$$

equation of continuity

$$\nabla\cdot\vec{u} = 0 \quad (2)$$

Maxwell's equations

$$\nabla\cdot\vec{B} = 0;\nabla\times\vec{H} = \vec{j}; \quad (3)$$

$$\nabla\times\vec{E} = 0;\nabla\cdot\vec{D} = \rho_e; \quad (4)$$

Ohm's law for fluid in motion

$$\vec{j} = \sigma(\vec{E} + \vec{u}\times\vec{B}); \quad (5)$$

charge conservation law

$$\nabla\cdot\vec{j} = 0; \quad (6)$$

where: $\vec{u}$ - liquid velocity, ρ - density, p - pressure, $\vec{g}$ - gravitation, ν - coefficient of kinematics viscosity, $\vec{j}$ - current density, $\vec{B}$ - magnetic induction intensity vector $\vec{B} = \mu\mu_0\vec{H}$, $\vec{H}$ - magnetic field vector, σ - specific conductance, ε_0 и μ_0 - electrical and magnetic constant, $\vec{E}$ - electrical field intensity, $\vec{D}$ - electric induction, $\vec{D} = \varepsilon\varepsilon_0\vec{E}$, ρ_e - volume density of electric charge. The following forces are considered in the equation (1): $-\rho^{-1}\nabla p$ - pressure force, $\nu\Delta\vec{u}$ - force of viscous drag, $\rho^{-1}\vec{j}\times\vec{B}$ - Lorentz electromagnetic force.

The problem was solved with the following boundary conditions:

– for electric field

$$\vec{E}_1\times\vec{n} = \vec{E}_2\times\vec{n},\ \vec{D}_1\times\vec{n} = \vec{D}_2\times\vec{n}; \quad (7)$$

– for magnetic field

$$\vec{B}_1\times\vec{n} = \vec{B}_2\times\vec{n},\ \vec{H}_1\times\vec{\tau} = \vec{H}_2\times\vec{\tau}; \quad (8)$$

– for current density on boundary with insulated and normal cross-section of electrode

$$\vec{j}\times\vec{n} = 0,\ j = j_0. \quad (9)$$

where: $\vec{n}$ - normal vector, $\vec{\tau}$ - tangential vector, j_0 - initial current density.

– for hydrodynamic parameters no-slip boundary condition was used for hydrodynamic processes at boundaries with solid walls and slip boundary condition on free surface. Mathematically it means that velocity and turbulent components for no-slip boundary condition were all set to zero

$$u=0, v=0, w=0, k=0, \varepsilon=0.$$

For the simulation of flow in wall region the universal logarithmic law was applied

$$\frac{\rho u_p k_{const}^{1/2} C_\mu^{1/4}}{\tau_w} = \frac{1}{k_{const}}\ln(Ey^+),$$

where $y^+ = \frac{y_p k_{const}^{1/2} C_\mu^{1/4}}{\upsilon}$, $E_{const} = 9.79$ - empirical constant, $k_{const} = 0.42$ - Von Karman's constant, τ_w - shear stress on the wall, y_p– resultant velocity of the fluid near the wall, y^+ - dimensionless normal distance from the resultant velocity, y_p - distance of the first node point p from the wall. For slip boundary condition normal component of velocity will be set to zero $u_n = 0$.

For all types of analysis on the axis of symmetry of the calculation domain the following condition were used:

$$\frac{\partial u}{\partial y} = 0, \frac{\partial w}{\partial y} = 0, \frac{\partial k}{\partial y} = 0, \frac{\partial \varepsilon}{\partial y} = 0.$$

The problem in question has no analytical solution and, therefore, it was solved numerically. As a result of the numerical solving methods analysis the ANSYS system were chosen. The problem belongs to the class of multiphysics and the strategy of solution consists of the following stages:

1st stage – solving electromagnetic fields;

2nd stage – solving EVF.

This consecutive order of solving this problem is due to the specialty of solving multiphysics problems in ANSYS. The result of electromagnetic field modelling is the value of electromagnetic force and other electromagnetic parameters, obtained for every nodal point in terms of liquid metal volume. To determine velocity of liquid metal produced by electromagnetic effect the distribution of electromagnetic force as the initial condition can be used at the next 2nd stage. At this stage it is necessary to check how motion of metal changes all electromagnetic parameters. Taking into account all these factors and repeating this algorithm to achieve the precision of the results, we obtain the velocity distribution with the closest correspondence to the experimental data.

The turbulent EVF was simulated with taken into account $k-\varepsilon$ turbulence model, that tested for the same vortex flow in laboratory installation. The obtained results in $k-\varepsilon$ turbulence model for this installation correlate with the experimental data within 15% limits [1-2]. That is why the further calculations are carry out with taking into account $k-\varepsilon$ turbulence model. The comparisons of the experimental and numerical results are given in Fig. 2.

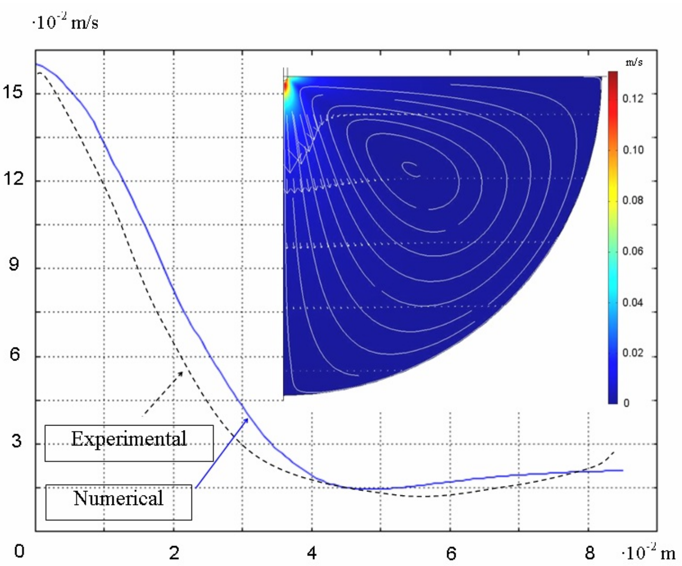

Figure 2: Numerical and experimental results for the laboratory unit.

Some results of simulation the processes proceeding in liquid metal are given below. Fig. 3 demonstrates the fields of the rotor Lorentz force near the bottom electrode (anode), where 1 – insulator, 2 – liquid metal, 3 – bottom electrode. The value of Lorentz force ranged and comprised about 30% of volumetric gravity force. The results of the calculations prove the fact that the Lorentz force in such furnaces is essential for the appearance of EVF.

At the next stage, according to the solution strategy, the hydrodynamic processes in liquid metal were simulated taking into account the electromagnetic parameters in axial symmetry formulation. In Fig. 4 the hydrodynamic fields of velocity vector, contour and streamlines are given. The figure demonstrates that the higher intensity of vortex flows appears in liquid metal volume. The vortex arises near the bottom electrode, as Fig. 4 shows. The vortex flow of liquid metal on axis of symmetry is directed upwards. When the flow achieves the upper boundary of liquid metal, it comes along the boundary and comes down. The maximum value of the vortex flow velocity was located on the axis of symmetry and reaches 0.3 m/s. The vortex flow velocity value in close proximity to the bottom electrode comprises about 0.1 m/s. According to the figure, at the top electrode area the inverse vortex flow appears. This vortex is produced by the uneven distribution of current density near the top electrode.

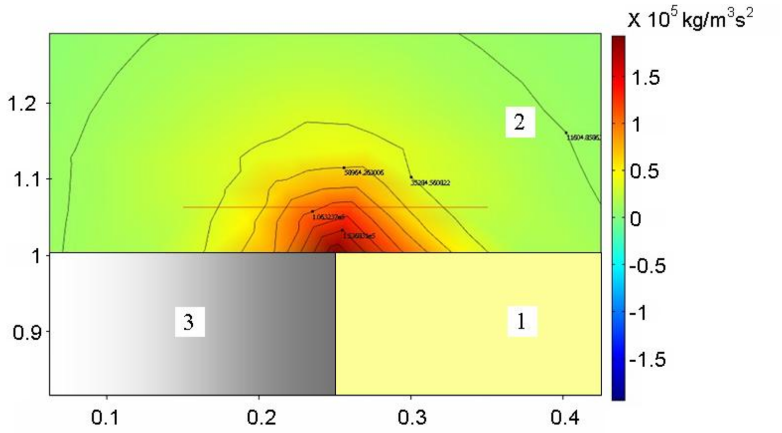

Figure 3: Rotor Lorentz force near the bottom electrode (1 – insulator, 2 – liquid metal, 3 – bottom electrode).

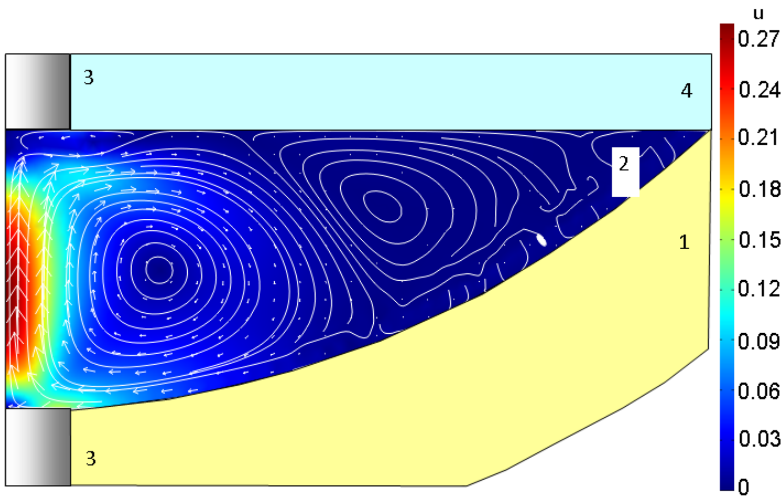

Figure 4: The vector, contour field and streamlines of vortex flow velocity (1 – insulator, 2 – liquid metal, 3 – electrodes, 4 – air).

It is shown that lifting the bottom electrode above the surface by the electrode radius value leads to the decrease of shear stress on the fettle area by 30%, while bottom electrode lower than the insulator surface by the electrode radius value and expanding it by the same value reduce the stress – by 10%.

The verification of the obtained results has shown a good correlation with the general theoretical data concerning EVF, the results obtained by other authors, as well as a good correlation with the experimental data for laboratory installations. All of that has proved the reliability of the methods and approaches, as well as the accuracy of the obtained results.

3. Conclusion

The physical and mathematical model of processes proceeding in hemisphere volume with different bottom electrode positions has been build. To describe the processes in the hemisphere volume the model of the magnetohydrodynamics is adopted. The strategy of solving the stated conjugate problem in commercial software packages is worked out. Numerical modelling of proceeding processes in liquid metal for hemisphere volume with different bottom electrode positions is carried out. It is established that the volumetric Lorentz force makes up governing contribution to the vortex flow appearance. It is shown that bottom electrode positions changes lead to essential changes of structure and intensive of the EVF velocity. The results of the calculations in ANSYS are compared with the experimental data, calculations in COMSOL, general theoretical conceptions. Similarity of the calculations done by different methods and experimental data proves the reliability of the methods and significance of the results.

4. References

[1] Ivochkin Yu., Oksman A., Kazak O., Teplyakov I., Zhilin V.: Numerical and experimental investigation of the electrovortex flow in hemispherical container under action of external magnetic field, Proc. the 8th International PAMIR Conference on fundamental and applied MHD. Borgo, Corsica, France September 5-9 (2011) 85-88.

[2] Kazak O., Semko O.: Numerical modelling of electrically vortical flows, Proc. the 8th International PAMIR Conference on fundamental and applied MHD. Borgo, Corsica, France September 5-9 (2011) 605-609.

[3] Kazak O. Modelling of vortex flows in DC electric arc furnace with different bottom electrode positions Metallurgical and Materials Transactions B, Volume 44B Number 3 (2013) 1243-1250.

HEAT TRANSFER OF MHD FLOW: EXPERIMENTAL AND NUMERICAL RESEARCH

MELNIKOV[1] I.A., SVIRIDOV[2] E.V., SVIRIDOV[1] V.G., RASUVANOV[2] N.G.
[1] Moscow Power Engineering Institute, 14 Krasnokazarmennaya str., Moscow, Russia
[2] Joint Institute of High Temperatures, RAS, 13/19 Izhorskaya str., Moscow, Russia
E-mail address of corresponding author: corpuskula@gmail.com

Abstract: This article is devoted to experimental and numerical investigation of heat transfer in a MHD flow configuration: downflow of mercury in a vertical tube with nonuniform heating in the transverse magnetic field. Investigations were carried out with help of the unique experimental liquid metal MHD complex, which has no analogues in Russia and abroad. The MHD complex is a part of the MPEI - JIHT RAS laboratory. Numerical simulation by means of CFD code ANES20XE was carried out as well. The paper also includes a brief description of the experimental facility, methodology, main results of the experiments, mathematical description and some results of numerical simulation.

1. Introduction

Liquid metals have specific features and are attractive coolants for power industry. Especially promising is usage of liquid metals in fusion power plants such as TOKAMAK, where liquid metal flows in a strong magnetic field (divertor and blanket cooling system). By designing the elements of a TOKAMAK it`s necessary to take into consideration hydrodynamics- and heat transfer laws of MHD flow. This question is not researched thoroughly.

Described in abstract MHD-configuration (fig. 1) is the most probable while cooling thermonuclear reactor blanket. Experimental researches of this configuration were carried out using JIHT RAS facility. Available criteria ranges are presented in table 1.

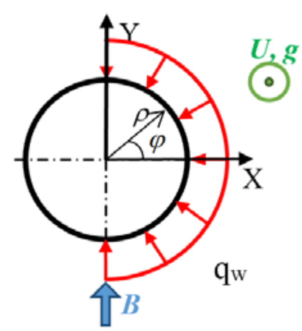

Figure 1: MHD configuration,

Table 1. Criteria ranges

Criterion	Calculation	Range
Reynolds number	$Re = \frac{U_{AVG} \cdot D_0}{\nu}$	$10^4 - 10^5$
Hartmann number	$Ha = B_0 D_0 \sqrt{\frac{\sigma_E}{\mu}}$	$0 - 600$
Grasshof number	$Gr_q = \frac{g \beta D_0^4 q_W}{\lambda \nu^2}$	$0 - 0.8 \cdot 10^8$

Table 1 legend: D_0 – tube diameter; U_{AVG} – section averaged velocity; ν - the kinematic viscosity coefficient, μ - the dynamic viscosity coefficient; B_0 – magnetic induction value; σ_E - electrical conductivity; q_W – heat flux density on the wall; λ – thermal conductivity; β - thermal expansion coefficient.

2. Experimental investigation

During experimental investigations two unexpected features were found. The first one: magnetic field leads to extremely nonuniform distribution of local wall temperature (1) along the perimeter of tube cross section. This is shown on Fig.2.

$$\Theta_W = \frac{\lambda}{(q_W D_0)(T_W - T_{BULK})} \tag{1}$$

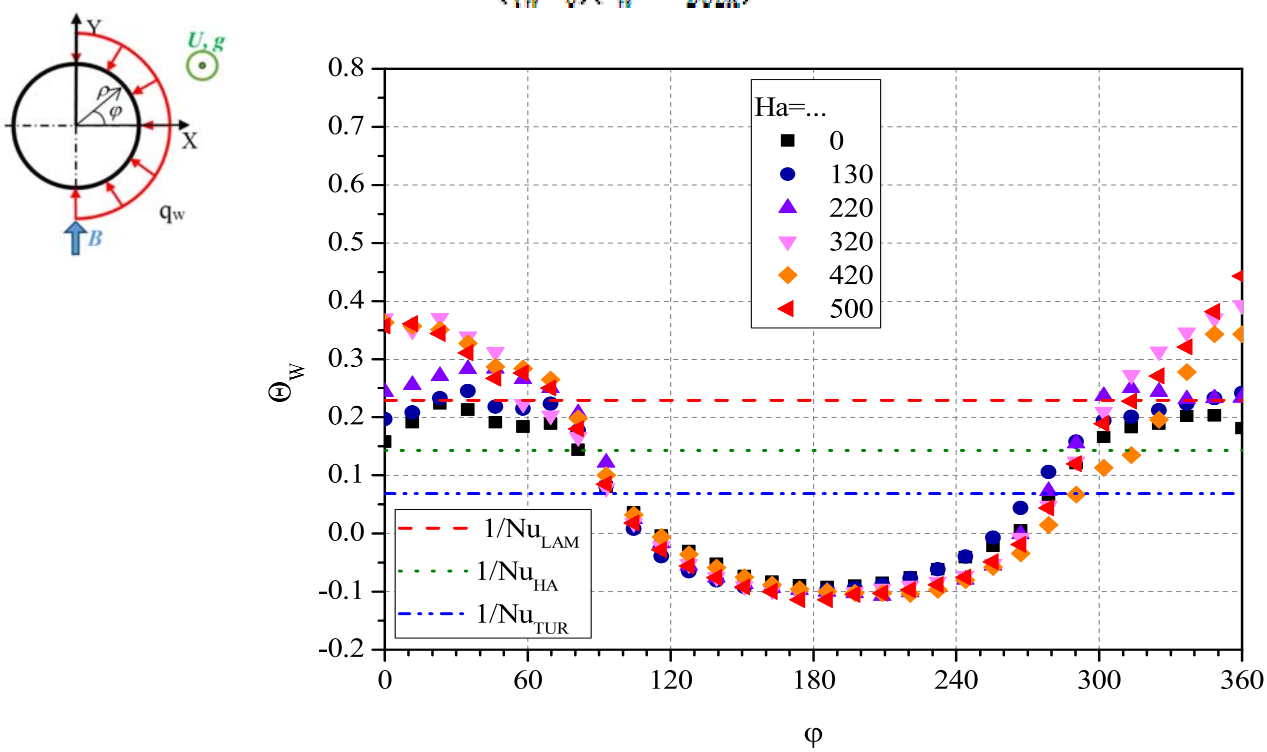

Figure 2: Temperature field Re = 35000, $Gr_q = 0.6 \cdot 10^8$.

The second feature is related to TGC evolution under conditions of transverse magnetic field. In some regimes, TGC causes extremely low frequency temperature fluctuation with high amplitude in the whole tube section (Fig. 3).

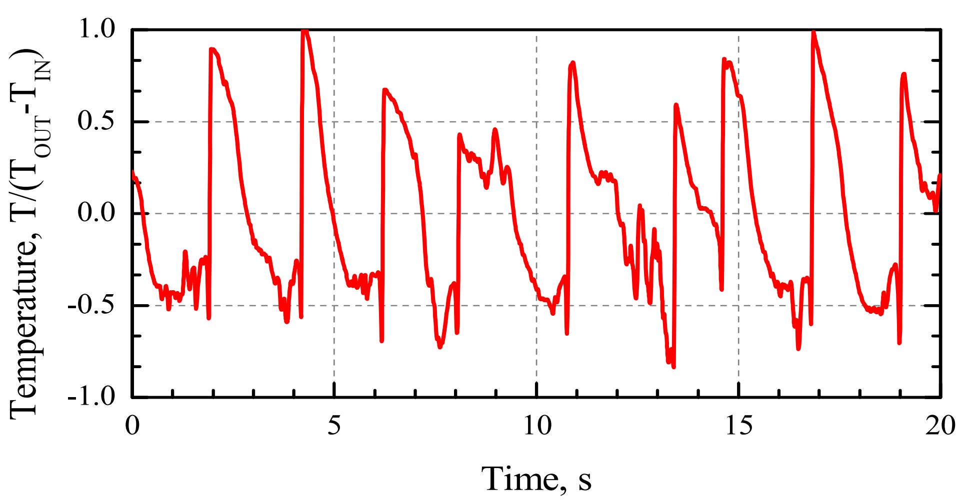

Figure 3: Temperature fluctuations.

The two effects cause additional thermal loads in the wall and it is very dangerous for wall material. More information about these features you can find in work [1].

Relative temperature fluctuation intensity $\tilde{\sigma} = \frac{\sigma}{\sigma_0}$ (σ_0 - temperature fluctuation intensity without MF) is a very important value. It can be used for TGC profound effect boundary detection. Experimental data of relative temperature fluctuation intensity for various Hartmann and Reynolds numbers are presented in Fig.4.

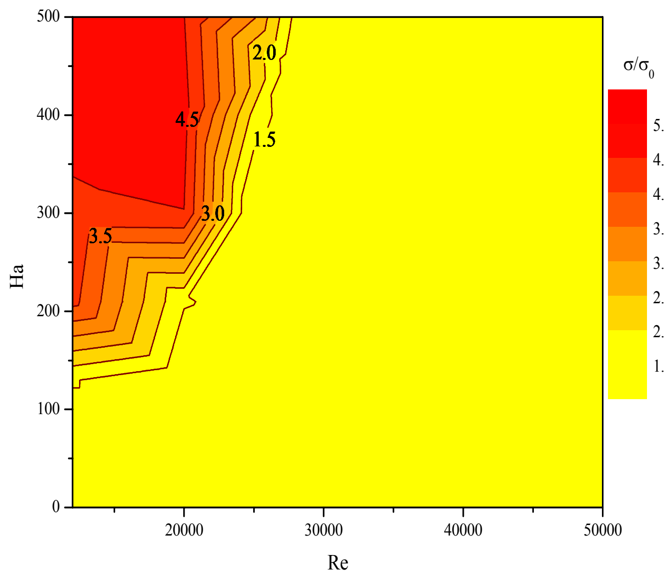

Figure 4: Temperature fluctuations.

Fig.4 describes zone of TGC profound effect. Abnormally temperature fluctuations caused by TGC evolution are observed in domain where relative temperature fluctuation intensity is more then 1 (red-zone on Fig. 4.) Reproducing these regimes on real heat exchanger leads to its extraordinary work and may damage the wall. Two curves families are observed in experiments (Fig. 5):

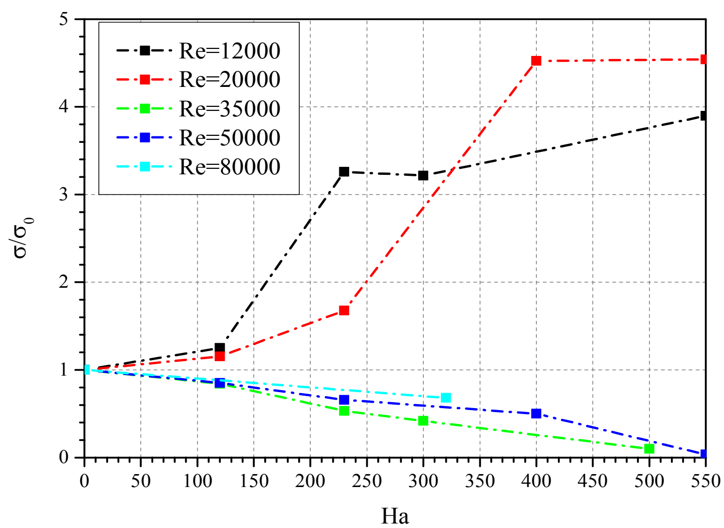

Figure 5: Relative temperature fluctuation intensity.

First case: magnetic field leads to TGC evolution $\left(\frac{Gr_q}{Re^2} \geq 0.1\right)$. Second case: magnetic field kills turbulent transfer $\left(\frac{Gr_q}{Re^2} < 0.1\right)$. In this case, relative temperature fluctuation intensity decreases and can be correlated with turbulent velocity fluctuations. Based on these curves, a model of turbulence transfer in conditions of transverse MF in a circular tube was constructed.

3. Numerical simulations

The system of MHD equation for LM flow in a circular tube is below (2)-(7):

$$div(\rho u) = 0 \tag{2}$$

$$div(\rho u u_x) = -\frac{\partial P}{\partial x} + div\left((\mu + \mu_T)\nabla u_x\right) + \sum f_x \tag{3}$$

$$div\left(\rho u u_y\right) = -\frac{\partial P}{\partial y} + div\left((\mu + \mu_T)\nabla u_y\right) + \sum f_y \tag{4}$$

$$div(\rho u u_z) = -\frac{\partial P}{\partial z} + div\left((\mu + \mu_T)\nabla u_z\right) + \sum f_z \tag{5}$$

$$div(\rho u C_p T) = div\left((\lambda + \lambda_T)\nabla T\right) \tag{6}$$

$$0 = div(\nabla \Phi) - div(u \times B) \tag{7}$$

Where $\sum f_i = fe_i + fg_i$;

$fe = j \times B$ - electromagnetic force; $fg = -\beta\rho(T - T_{ARH})g$ - buoyancy force; μ_T – turbulent viscosity; λ_T – turbulent thermal conductivity; Φ – electrical potential

Model of turbulent transfer in circular tube under conditions of transverse magnetic field

$$\left(\frac{\varepsilon_T}{\nu}\right)_{Ha} = \gamma\left(\frac{\varepsilon_T}{\nu}\right)_{Ha=0} \tag{8}$$

Two different functions $\gamma(Ha, Re)$ were tested:

$$\gamma = 0 \tag{9}$$

$$\gamma = \gamma_{EXP}(Ha, Re) \tag{10}$$

The model $\gamma = 0$ is based on current knowledge and experimental data on hydraulic resistance in transverse MF in a circular tube. The model $\gamma_{EXP}(Ha, Re)$ is a function based on experimental data presented in this work (relative temperature fluctuation intensity). The function considers turbulent transfer kill by magnetic field.

Simulations were carried out on decart (Fig. 6) and cylindrical meshes. Results do not depend on the mesh type and are presented in this work for a decart mesh.

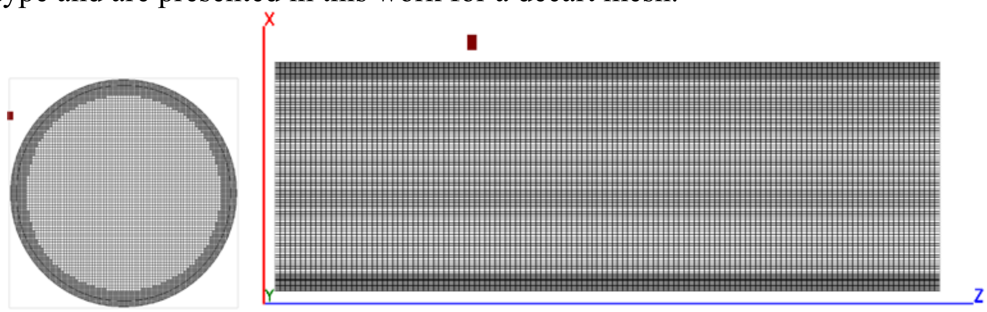

Figure 6: Decart mesh.

Numerical simulation of described task with help of CFD-code ANES20XE was carried out. Calculated values were compared with experimental data. Local temperature distribution of some regimes are presented on Fig. 7 – Fig. 8. As shown, results, obtained with $\gamma_{EXP}(Ha, Re)$, match with experimental ones well.

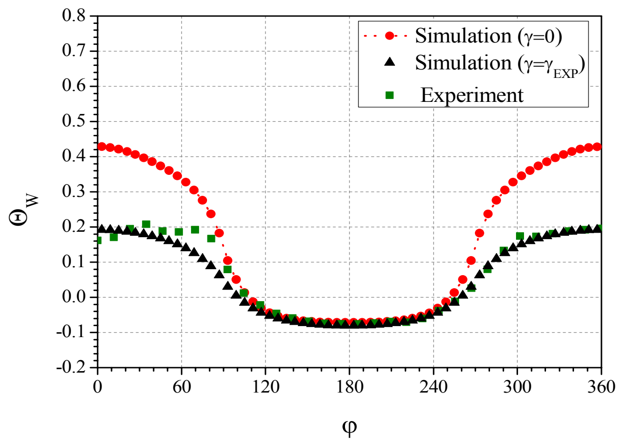

Fig. 7. $Re = 65000;\ Ha = 130; Gr = 0.6 \cdot 10^8$

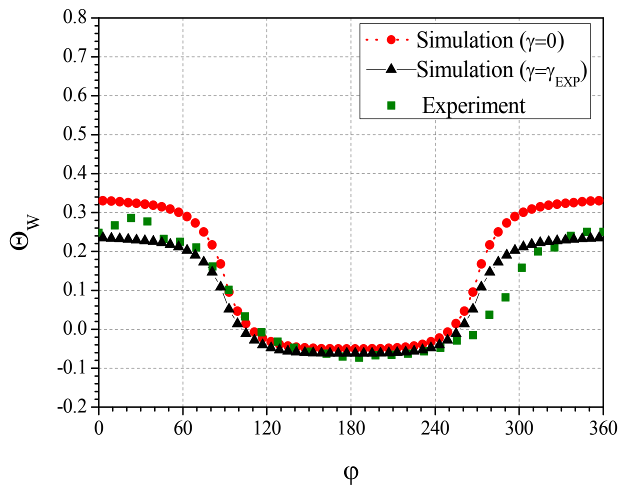

Figure 8: Re = 80000, Ha = 400, Gr = 0.6 10^8.

3. Conclusion

MHD flow in a vertical tube under conditions of transverse MF was investigated. Two unexpected features were found. One of them is caused by TGC evolution in MF. Border of this effect was properly explored. A turbulent transfer model in transverse MF in circular tube, based on relative temperature fluctuations, was constructed. Numerical simulation of described task was carried out. Results, obtained with constructed model, correlate with experimental data well.

4. References

[1] Melnikov, I.A., Rasuvanov, N.G., Sviridov, V.G., Sviridov, E.V., Shestakov, A.A.: An investigation of heat exchange of liquid metal during flow in a vertical tube with non-uniform heating in the transverse magnetic field. Thermal Engineering, vol. 60 (2013), no. 5, pp. 355-362.

VALIDITY OF QUASI-2D MODELS FOR MAGNETO-CONVECTION

BÜHLER[1] L., MISTRANGELO[1] C., MOLOKOV[2] S.

[1] *Karlsruhe Institute of Technology (KIT)*, Postfach 3640, 76021 Karlsruhe, Germany

[2] *Coventry University,* Priory Street, Coventry CV1 5FB, UK

leo.buehler@kit.edu

Abstract: For applications in nuclear fusion reactors where magnetic fields are very strong, liquid metal flow in the core of ducts can often be regarded as inertialess and practically inviscid, while viscous effects are localized in thin boundary layers. The intense electromagnetic Lorentz forces, resulting from the interaction of induced electric currents and imposed magnetic field, tend to remove flow variations along magnetic field lines and they force the fluid to circulate mainly in planes perpendicular to the field. The established quasi-two dimensional (Q2D) magnetohydrodynamic (MHD) flow can be predicted by means of an approximate model by reducing the basic governing equations to a 2D problem by analytical integration along magnetic field lines. Such models have been applied in the past by numerous authors to investigate duct flow problems and magneto-convection. However, limitations of those Q2D approaches have never been systematically studied.

1. Introduction

Liquid metal flows in strong magnetic fields are dominated by Lorentz forces, and viscous effects are confined to very thin boundary layers. The flow in the inviscid core is highly correlated along magnetic field lines and changes of variables in this direction are often negligible. This fact has been exploited in the past to derive Q2D model equations following the ideas proposed by Sommeria & Moreau (1982) [1]. Q2D models enable an efficient solution of 3D MHD problems, e.g. for shear flow instabilities [2] [3], DNS simulations of Q2D turbulent flows [4], including heat transfer and buoyant flows [5] [6] [7], interpretation of experimental data [8] [9], or simulations for fusion blanket applications [10] etc. It has been shown that results for inertial isothermal flows obtained by the Q2D model can be further improved by a proper modeling of inertia terms, which leads to "barrel" or "cigar" shape flow patterns aligned along the magnetic field [11] [12] instead of pure 2D structures.

The purpose of the present work is showing that Q2D models may have significant deficits for particular classes of buoyant flows, a fact that is not at all obvious from a first point of view. As an example we consider buoyant MHD flows in a horizontal liquid metal layer of height H, length lH and width $2aH$ (see Figure 1). We apply the Q2D model equations and compare results with 3D numerical simulations of full governing equations. Such geometries are typical in horizontal Bridgman crystal growth or for liquid metal blankets of fusion reactors.

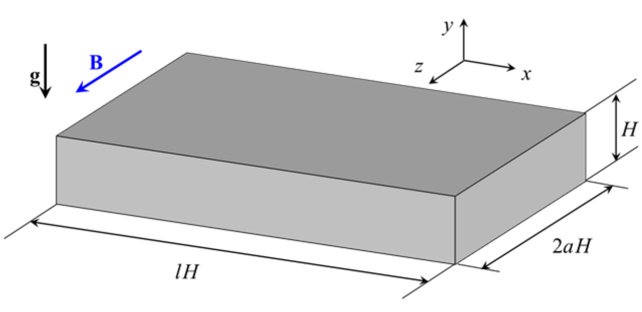

Figure 1 Sketch of geometry and coordinates. The flat cavity, filled with liquid metal, is differentially heated at $x/H=\pm\frac{1}{2}l$, such that a mean axial temperature gradient $G\hat{\mathbf{x}}$ establishes. Top and bottom walls at $y/H=\pm\frac{1}{2}$ have temperature profiles that vary linearly between the values of the differentially heated walls. The other walls are adiabatic. The convective motion is damped by a horizontal magnetic field.

2. Model equations

Buoyant flows of viscous, electrically conducting fluids in a uniform horizontal magnetic field are described by nondimensional equations for balance of energy, momentum and mass, by Ohm's law and by an electric potential equation to ensure charge conservation $\nabla\cdot\mathbf{j} = 0$:

$$Pr\,\mathrm{D}_t T = \nabla^2 T\,, \tag{1}$$

$$D_t\mathbf{u} + \nabla p - \nabla^2\mathbf{u} = GrT\hat{\mathbf{y}} + Ha^2(\mathbf{j}\times\mathbf{B}),\ \nabla\cdot\mathbf{u} = 0, \qquad (2)\ (3)$$

$$\mathbf{j} = -\nabla\phi + \mathbf{u}\times\mathbf{B}\ \text{ and } \nabla^2\phi = \nabla\cdot(\mathbf{u}\times\mathbf{B}) = \mathbf{B}\cdot\boldsymbol{\omega}\,. \qquad (4)\ (5)$$

Here T, $\mathbf{u}$, $\mathbf{B} = \hat{\mathbf{z}}$, $\mathbf{j}$, p and ϕ stand for the temperature difference with respect to a reference value, velocity, magnetic field, current density, pressure and electric potential, scaled by characteristic values ΔT, u_0, B_0, $\sigma u_0 B_0$, $\sigma u_0 B_0^2 H$ and $u_0 B_0 H$, respectively. Dimensionless parameters are the Prandtl number, Grashof number and Hartmann number:

$$Pr = \frac{\nu}{\kappa}, \qquad Gr = \frac{g\beta H^3\Delta T}{\nu^2}, \qquad Ha = B_0 H\sqrt{\frac{\sigma}{\rho\nu}}. \tag{6}$$

Kinematic viscosity ν, thermal diffusivity κ and electric conductivity σ are assumed to be constant, ρ is the density at the reference temperature and β is the volumetric thermal expansion. B_0 is a typical magnitude of the magnetic field, $u_0 = \nu/H$ and ΔT is derived from the mean horizontal temperature gradient $G\hat{\mathbf{x}}$ as $\Delta T = GH$. At walls we have no-slip $\mathbf{u} = 0$. Currents may continue their path inside walls and create there a distribution of wall potential according to the thin-wall condition [13], $\mathbf{j}\cdot\mathbf{n} = c\nabla_w^2\phi_w$, where $c = \sigma_w t_w/(\sigma H)$ stands for the conductance ratio of walls with conductivity σ_w and thickness t_w, ∇_w is the gradient in the plane of the wall and the unit normal $\mathbf{n}$ points into the fluid.

It is well known that for strong magnetic fields, $Ha \gg 1$, the flow takes place preferentially in planes perpendicular to $\mathbf{B}$, i.e. $\mathbf{u} \approx \mathbf{u}_\perp$, and it is described by an equation for the field aligned component ω_z of vorticity $\boldsymbol{\omega} = \nabla\times\mathbf{u}$ that is obtained by taking the curl of (2)

$$(\nabla\times\mathrm{D}_t\mathbf{u}_\perp)_z - \nabla^2\omega_z = Gr\,\partial_x T + Ha^2\partial_z j_z\,. \tag{7}$$

Following the ideas usually referred to as Q2D approach (see [1] and others), the vorticity equation (7) and potential equation (5) are integrated along magnetic field lines (overbar above variables denotes average along field lines);

$$\overline{(\nabla\times\mathrm{D}_t\mathbf{u}_\perp)}_z - \nabla_\perp^2\overline{\omega}_z - \frac{1}{a}\partial_z\omega_z(z=a) = Gr\,\partial_x\overline{T} + Ha^2\frac{1}{a}j_z(z=a), \tag{8}$$

$$\nabla_\perp^2\overline{\phi} + \frac{1}{a}\partial_z\phi(z=a) = \nabla_\perp^2\overline{\phi} - \frac{1}{a}j_z(z=a) = \overline{\omega}_z\,. \tag{9}$$

When Q2D models are applied, it is usually assumed that the potential does not change along magnetic field lines, $\overline{\phi} = \phi(z=a) = \phi_H$. With the thin-wall condition $j_z(z=a) = -c\nabla_\perp^2\phi_H$ [13] and viscous friction $\partial_z\omega_z(z=a) = -Ha\overline{\omega}_z$ applied at the Hartmann wall, j_z and $\overline{\phi} = \phi_H$ can be eliminated from (8) and (9) and the Q2D equation vorticity becomes

$$\overline{(\nabla\times\mathrm{D}_t\mathbf{u}_\perp)}_z - \nabla_\perp^2\overline{\omega}_z = Gr\,\partial_x\overline{T} - \underbrace{\left(\frac{cHa^2}{a+c} + \frac{Ha}{a}\right)}_{1/\tau}\overline{\omega}_z\,. \tag{10}$$

Instead of solving (10) we may solve the following equation, the curl of which yields (10):

$$\overline{\mathrm{D}_t \mathbf{u}_\perp} - \nabla_\perp{}^2 \overline{\mathbf{u}}_\perp + \nabla_\perp \overline{p} = Gr\overline{T}\hat{\mathbf{y}} - \frac{1}{\tau}\overline{\mathbf{u}}_\perp \text{ with } \nabla \cdot \overline{\mathbf{u}}_\perp = 0. \tag{11}$$

The model derived above is valid only for a *uniform* horizontal temperature gradient as shown in the following. For liquid metals with $Pr \ll 1$ conduction heat governs (1) which supports the ansatz $T=x+Pr\,\theta$, where θ describes deviations from pure heat conduction. Flows with $Gr \gg 1$ and $Ha \gg 1$ are dominated by the right-hand side of (7), through a balance between Lorentz forces and buoyancy, and for $Pr \ll 1$ current density and potential become approximately

$$-\partial_z j_z = \partial_{zz}\phi = Gr / Ha^2 \partial_x T \approx Gr / Ha^2 . \tag{12}$$

By integration along z the potential ϕ and its mean value $\overline{\phi}$ along z are determined as

$$\phi = \phi_H + \frac{Gr}{2Ha^2}\left(z^2 - a^2\right) \text{ and } \overline{\phi} = \phi_H - \frac{a^2 Gr}{3Ha^2}, \tag{13}$$

where the potential ϕ_H at the Hartmann wall at $z = a$ has been introduced as integration function. Already at leading order the potential ϕ is not at all uniform in the core along field lines. For flows where $\partial_x \overline{T} \neq const$ the last term in equation (13) depends also on (x,y) and finally an additional contribution will appear in (11). Moreover, the electric properties of field aligned walls never enter into the Q2D model, although their conductance may have an essential impact on the global closure of current paths with severe consequences for the flow. This will be shown in the following by some selected examples.

3. Results

Let us first consider flows in a perfectly electrically conducting cavity with $c=\infty$. Results from numerical simulations using Q2D and full 3D equations are compared (the latter ones with up to $8\cdot10^6$ grid points, all layers well resolved, grid-independent results achieved). Figure 2 shows contours of velocity magnitude in the vertical symmetry plane $z=0$ for $a=1$, $Gr=10^8$, $Pr=0.015$, $Ha=1000$. Results deviate by more than one order of magnitude and they are qualitatively quite different. While Q2D solutions show a more or less smooth velocity field, 3D simulations predict a low velocity core and thin boundary layers with very high velocity along the walls at $y=\pm½$ and $x=\pm½l$. However, there is significant disagreement only in layers along those walls. This can be seen by a quantitative comparison of axial velocity profiles as shown in Figure 3. At some distance from the walls Q2D and 3D results in the core agree quite well. Nevertheless, since the layers carry the major mass flux a 3D simulation is mandatory and Q2D results are practically useless as can be seen also by a comparison of temperature profiles in the middle of the cavity (Figure 3). The flow rate in field aligned layers that is missing in the Q2D model can be estimated according to [14] e.g. at the upper wall for a cross-section $x=constant$ as

$$Q_\delta = \int_{-a}^{a}\int_\delta u\,dy\,dz = -\int_{-a}^{a}\int_\delta \partial_y \phi\, dy\,dz = -2a\int_\delta \partial_y \overline{\phi}\, dy = -2a\left(\overline{\phi}_w - \overline{\phi}_\delta\right) = -2a\frac{a^2 Gr}{3Ha^2}. \tag{14}$$

Here $\int_\delta dy$ indicates integration across the layer. For perfectly conducting walls $\phi_w = 0$ while the potential $\overline{\phi}_\delta$ at the edge of the layer is given by (13). The vorticity in the core at leading order may be estimated from (10) as $\overline{\omega}_z = \partial_x \overline{v} - \partial_y \overline{u} = \tau\, Gr$, from which the axial core flow rate in the upper half of the cavity results by integration as

$$Q_c = \int_{-a}^{a}\int_0^{1/2} u\,dy\,dz = -\frac{1}{4}a\frac{Gr}{Ha^2}. \tag{15}$$

This simple estimate shows clearly that the error in not-considering the parallel layers in Q2D models can be significant. Further 3D simulations with perfectly conducting Hartmann walls and insulating field-aligned walls show an additional increase in side layer velocity by another order of magnitude so that a comparison with corresponding Q2D results becomes even worse.

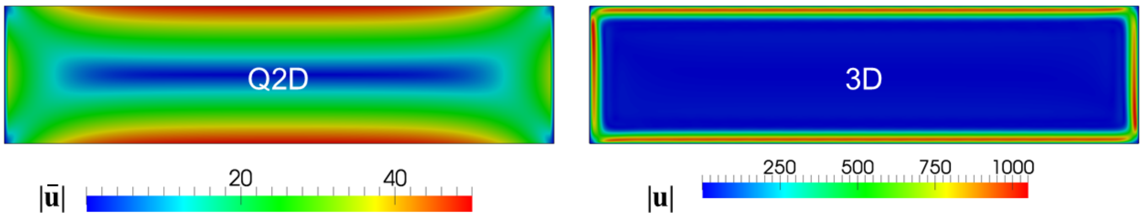

Figure 2 Colored contours of velocity magnitude in the vertical symmetry plane z=0 obtained by Q2D and 3D simulations for a=1, Gr=10^8, Pr=0.015, Ha=1000, c=∞.

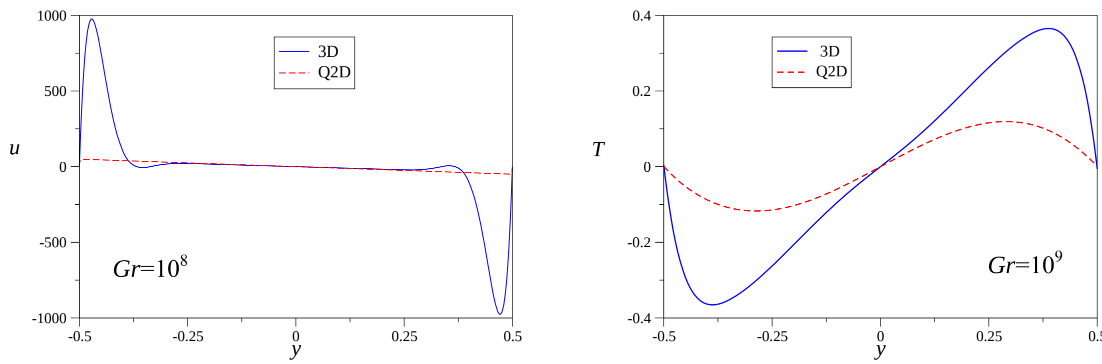

Figure 3 Comparison of axial velocity and temperature along y at (x,z)=(0,0) obtained by Q2D and 3D simulations for a=1, Pr=0.015, Ha=1000, c=∞.

For walls that are poorly conducting or insulating as in [7] the agreement between Q2D and 3D improves because the layer flow rate decreases while simultaneously the core flow rate increases. Results for a=1, Pr=0.015, Gr=10^6, Ha=1000, c=0 are shown in Figure 4. For such parameters the Q2D model is able to predict the velocity magnitude, i.e. results are not as bad as for conducting Hartmann walls. Nevertheless, one can observe still minor differences between the O2D model and 3D simulations.

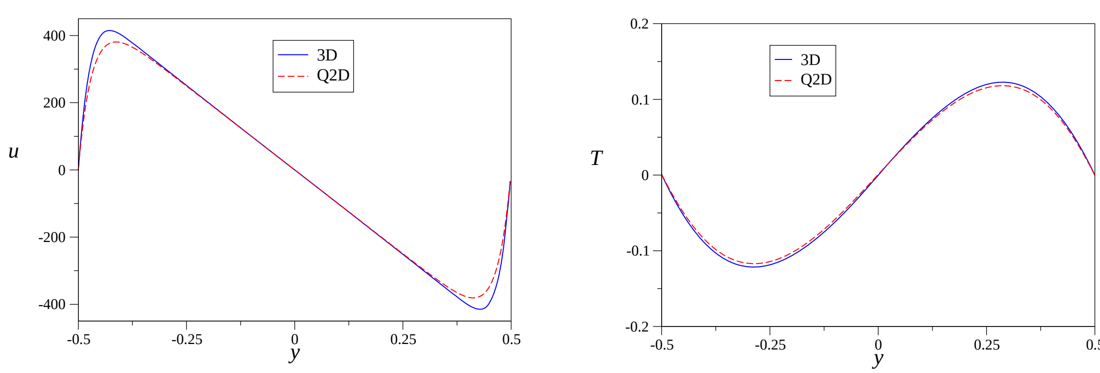

Figure 4 Comparison of axial velocity and temperature along y at (x,z)=(0,0) obtained by Q2D and 3D simulations for a=1, Gr=10^6, Pr=0.015, Ha=1000, c=0.

4. Conclusions

Q2D models have been often applied in the past as efficient tools for numerical simulations of various MHD phenomena for $Ha \gg 1$. It has been shown in the present work that those models may have severe deficits for instance because the electric conductivity of field-aligned walls is not considered. Moreover, for the derivation of Q2D models it is usually assumed that the electric potential is uniform along magnetic field lines, an assumption that is not justified for convection problems. A comparison of results with 3D numerical simulations suggests that for electrically insulating walls Q2D models give reasonable estimates for velocity and heat transfer. For electrically conducting walls, however, Q2D results become useless so that 3D simulations are mandatory.

5. References

[1] J. Sommeria and R. Moreau, "Why, how, and when MHD turbulence becomes two-dimensional," *Journal of Fluid Mechanics,* vol. 118, pp. 507-518, 1982.

[2] L. Bühler, "Instabilities in quasi-two-dimensional magnetohydrodynamic flows," *Journal of Fluid Mechanics,* vol. 326, pp. 125-150, 1996.

[3] N. Vetcha, S. Smolentsev and M. Abdou, "Linear stability analysis for the Hartmann flow with interfacial slip," *Magnetohydrodynamics,* vol. 48, pp. 147-155, 2012.

[4] S. Smolentsev and R. Moreau, "Modeling quasi-two-dimensional turbulence in MHD duct flows," in *Proceedings of the Summer Program 2006, CTR, Stanford University*, 2006, pp. 419-430.

[5] W. K. Hussam and G. J. Sheard, "Heat transfer in a high Hartmann number MHD duct flow with a circular cylinder placed near the heated side-wall," *International Journal of Heat and Mass Transfer,* vol. 67, pp. 944-954, 2013.

[6] S. Smolentsev, N. Vetcha and M. Abdou, "Effect of a magnetic field on stability and transitions in liquid breeder flows in a blanket," *Fusion Engineering and Design,* vol. 88, no. 6-8, pp. 607-610, 2013.

[7] A. Y. Gelfgat and S. Molokov, "Quasi-two-dimensional convection in a three-dimensional laterally heated box in a strong magnetic field normal to main circulation," *Physics of Fluids,* vol. 23, no. 3, pp. 034101-1-13, 2011.

[8] L. Barleon, P. Jochmann, K. J. Mack, U. Burr and R. Stieglitz, "Experimental Investigations on the Magneto-Convective Flow in a Vertical Gap," in *4th International Conference on Energy Transfer in Magnetohydrodynamic Flows*, Giens, France, 2000.

[9] U. Burr and U. Müller, "Rayleigh-Bénard Convection in Liquid Metal Layers under the Influence of a Horizontal Magnetic Field," *Journal of Fluid Mechanics,* vol. 453, pp. 345-369, 2002.

[10] E. Mas de les Valls, L. Batet, V. de Medina, J. Fradera, M. Sanmartí and L. Sedano, "Influence of thermal performance on design parameters of a He/LiPb dual coolant DEMO concept blanket design," *Fusion Engineering and Design,* vol. 87, pp. 969-973, 2012.

[11] A. Pothérat, J. Sommeria and R. Moreau, "An Effective Two-Dimensional Model for MHD Flows with Transverse Magnetic Field," *Journal of Fluid Mechanics,* vol. 424, pp. 75-100, 2000.

[12] B. Mück, C. Günther, U. Müller and L. Bühler, "Three-dimensional MHD flows in rectangular ducts with internal obstacles," *Journal of Fluid Mechanics,* vol. 418, pp. 265-295, 2000.

[13] J. S. Walker, "Magnetohydrodynamic flows in rectangular ducts with thin conducting walls," *Journal de Mécanique,* vol. 20, no. 1, pp. 79-112, 1981.

[14] M. S. Tillack and K. McCarthy, "Flow quantity in side layers for MHD flow in conducting rectangular ducts," Techn. Rep. UCLA-IFNT-89-01, 1989.

Acknowledgement: This work, supported by the European Communities under the contract of Association between EURATOM - KIT, was carried out within the framework of the European Fusion Development Agreement. The views and opinions expressed herein do not necessarily reflect those of the European Commission.

Linear stability of convective flow in an infinite horizontal layer with horizontal temperature gradient and vertical magnetic field

HUDOBA, A., MOLOKOV, S.,
Department of Mathematics and Physics, Coventry University,
Priory Street, Coventry, CV1 5FB, United Kingdom
E-mail: hudobaa@uni.coventry.ac.uk

The problem of instabilities in the buoyant convective flows subject to high magnetic fields is of particular importance in such industrial applications as fusion reactor blankets, semiconductor crystal growth and electromagnetic processing of materials. In the present study we investigate linear stability of buoyancy-driven convection in a laterally heated layer between two infinite plates subject to a uniform, vertical magnetic field and in the presence of gravity. The mechanisms for different wall conductivities and different values of Hartmann, Ha, and magnetic Prandtl, Pr_m, numbers are investigated. We compare the problem for small, but non-zero Pr_m, with the inductionless approximation in order to determine the validity of that approximation. Linear stability results show that the instability critically depends on the electrical and thermal boundary conditions, and on the Prandtl number, Pr, and on Ha and Pr_m. The instability is driven by different mechanisms depending on these parameters.

1 Problem formulation

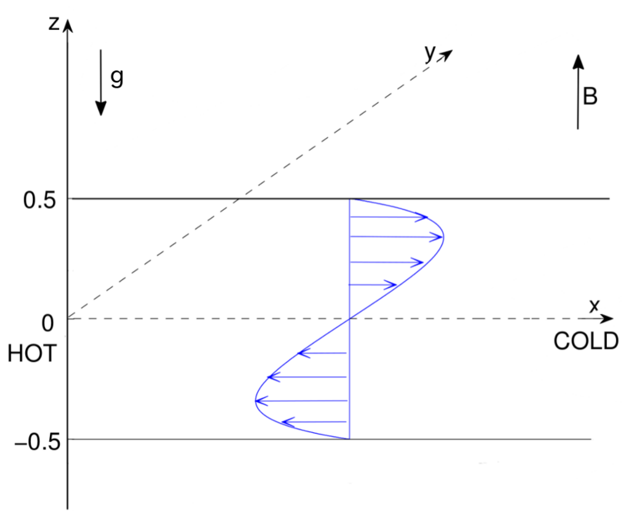

Figure 1. Schematic diagram of the buoyant convective flow with horizontal temperature gradient and a vertical magnetic field

Consider the problem of linear stability of buoyancy-driven convection resulted from axial heating of a fluid layer bounded by infinite horizontal rigid plates, as shown in Fig. 1. The flow, subject to a uniform, vertical magnetic field $\mathbf{B}_0 = B_0\mathbf{e_z}$ is studied in the presence of gravity $\mathbf{g}$. Here (x, y, z) are Cartesian co-ordinates. In a laboratory implementation, two opposite vertical boundaries are set at different temperatures and the horizontal gradient drives the fluid upward near the hot and downward near the cold wall.
The flow is time-dependent, viscous, electrically conducting and incompressible. Material parameters of the fluid are defined by the density ρ, kinematic viscosity ν, thermal conductivity κ, thermal expansion coefficient β and electric conductivity σ. Constant horizontal temperature gradient, which induces a steady circulation, is applied. The top and bottom rigid boundaries of the layer can be either perfectly insulating or perfectly conducting, both thermally and electrically.

2 Governing equations and boundary conditions

The behaviour of the flow is governed by the set of magnetohydrodynamic equations combining Navier-Stokes equations of motion of fluid substances, the energy equation and Maxwell electrodynamics equations. Detailed derivation of these equations has been presented in [1].

The nondimensional form of governing equations results from scaling the length by a reference distance d (the distance between walls), time by d^2/ν, velocity by ν/d, pressure by $\rho\nu^2/d^2$, temperature by ΔT and magnetic field by B_0. Nondimentional Hartmann, Ha, Grashof, Gr, and Prandtl, Pr, numbers are used as control parameters: $Ha = B_0 d\sqrt{\sigma/(\rho\nu)}$, $Gr = g\beta\Delta T(d^4/\nu^2)$, $Pr = \nu/\kappa$, $Pr_m = \mu\sigma\nu$.

The resulting set of nondimensional equations governing the motion of the fluid is:

$$\partial_t \mathbf{v} + (\mathbf{v}\cdot\nabla)\mathbf{v} = -\nabla p + \nabla^2\mathbf{v} + \frac{Ha^2}{Pr_m}(\nabla\times\mathbf{B})\times\mathbf{B} + GrT\hat{e}_z \ , \tag{1}$$

$$\partial_t \mathbf{B} + (\mathbf{v}\cdot\nabla)\mathbf{B} = \frac{1}{Pr_m}\nabla^2\mathbf{B} + (\mathbf{B}\cdot\nabla)\mathbf{v} \ , \qquad \partial_t T + (\mathbf{v}\cdot\nabla)T = \frac{1}{Pr}\nabla^2 T \ , \qquad (2),(3)$$

where $\mathbf{v}$, p, $\mathbf{B}$, T are the fluid velocity, pressure, magnetic field and temperature, respectively.

2.1 Basic flow

The problem of buoyant convective flow subject to a vertical magnetic field has a steady mean flow solution [2] with velocity $\mathbf{u}_0 = [u_0(z), 0, 0]$, magnetic field $\mathbf{B} = [b_0(z), 0, 1]$ and temperature $T_0(x,z)$ profiles:

$$u_0 = \frac{Gr}{Ha^2}\left\{ z - \frac{\sinh(Haz)}{\sinh(Ha)} \right\} \ , \tag{4}$$

$$b_0 = \frac{Pr_m Gr}{Ha^2}\left\{ \frac{\cosh(Haz)}{Ha\sinh(Ha)} - \frac{1}{2}z^2 + \frac{1}{2} - \frac{\cosh(Ha)}{Ha\sinh(Ha)} \right\} \ , \tag{5}$$

$$T_0 = -x + \frac{PrGr}{Ha^2}\left\{ \frac{\sinh(Haz)}{Ha^2\sinh(Ha)} - \frac{1}{6}z^3 + Dz \right\} \ , \tag{6}$$

with $D = \frac{1}{6} - \frac{1}{Ha^2}$ for thermally conducting and $D = \frac{1}{2} - \frac{\cosh(Ha)}{Ha\sinh(Ha)}$ for thermally insulating walls.

2.2 Disturbance equations and boundary conditions

In order to test whether the equilibrium state is stable, reaction of the system to small perturbations is examined. The stability is investigated here by the linear analysis. Assuming that disturbances to the flow are fully 3D, the flow can be decomposed into the base flow and the fluctuating component $F = F_0 + \tilde{f}(x,y,z,t)$. Additionally the perturbations can be expressed with Fourier expansions in the $x-$ and $y-$ directions $\tilde{f}(x,y,z,t) = \hat{f}(z)\exp\{ixk_x + iyk_y + \lambda t\}$, where k_x and k_y are the wavenumbers in the $x-$ and $y-$ directions, respectively, and $\lambda = \lambda_r + i\lambda_i$ with real part λ_r representing the growth rate and λ_i an angular oscillation frequency.

Assuming that the introduced perturbation is infinitisemally small, the problem is linearised. Additionally in order to reduce the number of variables the vorticity vector is introduced $\underline{\omega} = \nabla \times \mathbf{v}$. This leads to the following set of equations for the disturbed vorticity, velocity, magnetic field, electric current components, and the disturbed temperature:

$$\{\mathbf{D}^2 - u_0 ik_x\}\hat{\omega}_z + (\partial_z u_0) ik_y \hat{w} + Ha^2\{\partial_z + b_0 ik_x\}\hat{j}_z - \frac{Ha^2}{Pr_m}(\partial_z b_0) ik_y \hat{b}_z = \lambda \hat{\omega}_z \ , \tag{7}$$

$$\{\mathbf{D}^4 - u_0 ik_x \mathbf{D}^2 + (\partial_z^2 u_0) ik_x\}\hat{w} + \frac{Ha^2}{Pr_m}\{+\mathbf{D}^2\partial_z + b_0 ik_x \mathbf{D}^2 - (\partial_z^2 b_0) ik_x\}\hat{b}_z - Grk^2\hat{\theta} = \lambda \mathbf{D}^2 \hat{w} \ , \tag{8}$$

$$\{\frac{1}{Pr_m}\mathbf{D}^2 - u_0 ik_x\}\hat{b}_z + \{b_0 ik_x + \partial_z\}\hat{w} = \lambda \hat{b}_z \ , \tag{9}$$

$$\{\mathbf{D}^2 - Pr_m u_0 ik_x\}\hat{j}_z + \{b_0 ik_x + \partial_z\}\hat{\omega}_z + (\partial_z b_0) ik_y \hat{w} - (\partial_z u_0) ik_y \hat{b}_z = \lambda Pr_m \hat{j}_z \ , \tag{10}$$

$$\{Pr^{-1}\mathbf{D}^2 - u_0 ik_x\}\hat{\theta} - \{\partial_z T_0 + i(\partial_x T_0)\frac{k_x}{k^2}\partial_z\}\hat{w} - i(\partial_x T_0)\frac{k_y}{k^2}\hat{\omega}_z = \lambda \hat{\theta} \ . \tag{11}$$

Here the operator $\mathbf{D} = i\mathbf{k} + [0, 0, \partial z]$ has been introduced.

The appropriate boundary conditions have been applied at the top and bottom rigid boundaries. In the case of thermal and electromagnetic boundary conditions, limit cases are considered here: perfectly conducting or perfectly insulating. These conditions are:

$\hat{\omega}_z = 0$ and $\hat{w} = \partial_z \hat{w} = 0$ at $z = \pm 0.5$,
$\hat{\theta} = 0$ for thermally conducting and $\partial_z \hat{\theta} = 0$ for thermally insulating walls at $z = \pm 0.5$,
$\partial_z \hat{j}_z = 0$ and $\hat{b}_z = 0$ for electrically conducting walls at $z = \pm 0.5$,
$\hat{j}_z = 0$ and $\{\partial_z \pm k\}\hat{b}_z = 0$ for electrically insulating walls at $z = \pm 0.5$.

3 Linear stability results

The problem has been solved numerically by the Chebyshev spectral collocation method and the numerical linear stability results have been obtained. Characteristic lows are given by the critical Grashof number, Gr, (giving the strength of buoyancy forces) as a function of parameters. Beyond those critical values, the basic flow loses its stability. Such neutral stability results have been calculated for fixed values of Pr and Ha, defining $(Gr)_{crit}$ for which an eigenvalue has a real part equal to zero, by minimisation along k_x and k_y.

Here we present the results for the transverse modes ($k_y = 0$) having their axes perpendicular to the main flow. For $Pr_m \to 0$ the electrical boundary conditions show no effect on the transverse instabilities. The magnetic field stabilises these modes very efficiently shifting the onset of instabilities to higher Grashof numbers. The stationary instabilities reach the limiting values at $Ha \simeq 14.5$ for the thermally conducting case and $Ha \simeq 11.5$ for the thermally insulating case, before their disappearance (Figs. 2 and 3). The wavenumbers are slowly decreasing with Ha until reaching the minima just before the disappearance of these modes. At the higher values of Ha, instabilities appear mainly as a result of potentially unstable thermal stratification zones near the horizontal boundaries and exist only for thermally conducting cases.

The inductionless approximation is confirmed to be valid for Pr_m up to $Pr_m = 10^{-4}$ for the range of Ha considered here. An increase of the value of Pr_m results in a divergence between the two cases of electromagnetic boundary conditions.

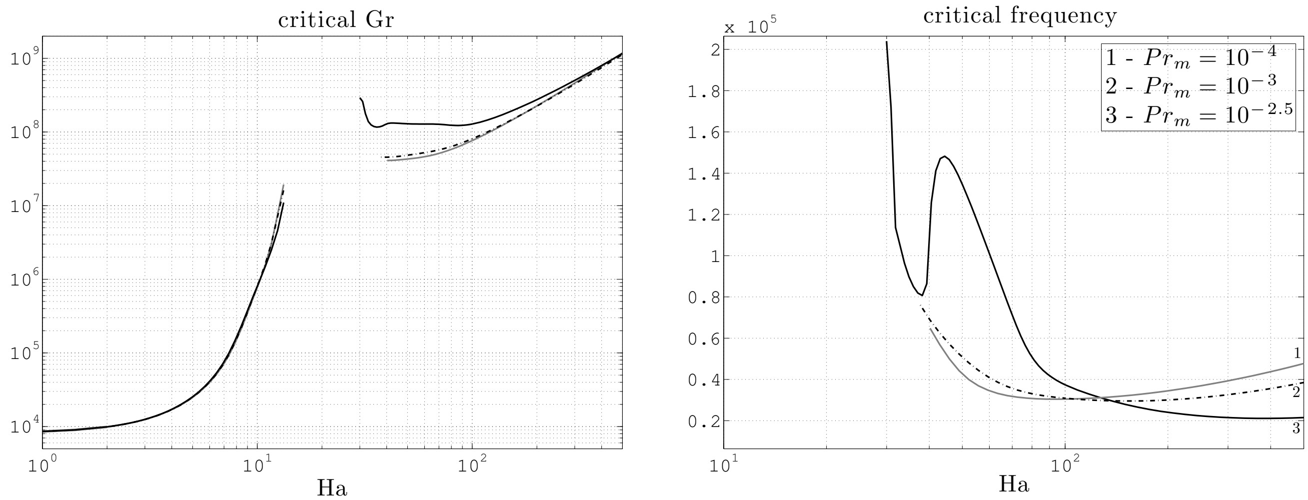

Figure 2. Critical values of parameters, thermally & electrically conducting walls

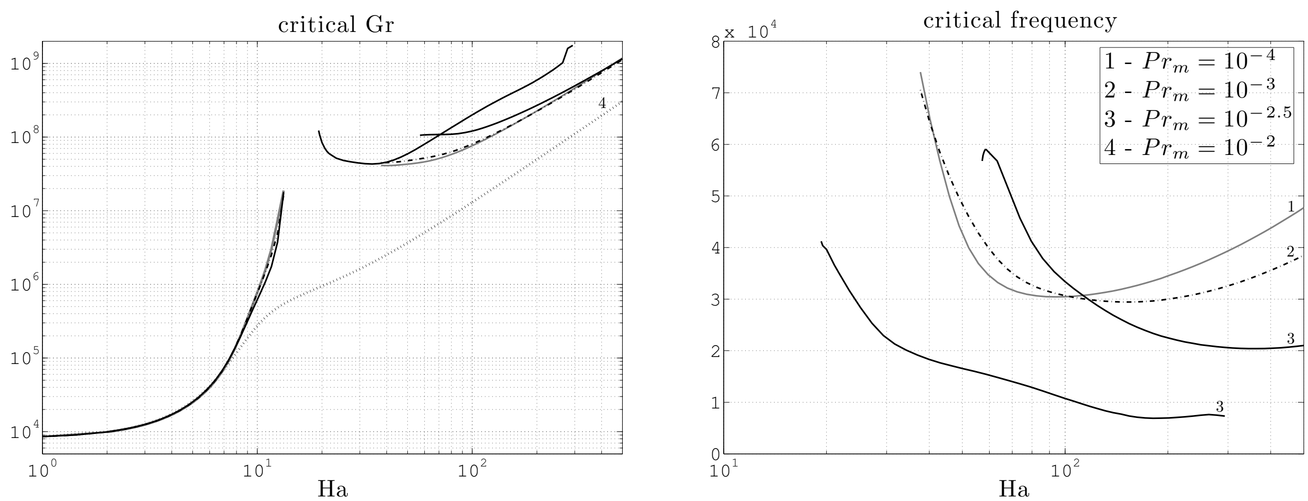

Figure 3. Critical values of parameters, thermally conducting & electrically insulating walls.

The stationary branches, for all the boundary conditions, lie very closely to one another for different magnetic Prandtl numbers, with the lower Pr_m modes disappearing at slightly lower Ha values. The wavenumber decreases with the increasing Pr_m, which is apparent for the thermally insulating cases (Figs. 4 and 5; notice that all the modes in these figures are stationary). The increase of Pr_m number has a stabilising effect on thermal oscillatory branches for both cases of electromagnetic boundary conditions (Figs. 2 and 3). The osciallatory instabilities appear at higher frequencies for the higher Pr_m, while the wavenumbers decrease causing the increase of the marginal cells.

We observed new branches of instabilities for the cases of electrically insulating walls (Figs. 3 and 5). The new modes appearing at higher Ha in the case of thermally conducting boundaries are more stable (Fig.3), with low wavenumbers and relatively low frequencies. The new stationary instabilities, appearing for both thermally conducting and insulating boundaries, become the most dangerous modes (Figs. 3 and 5).

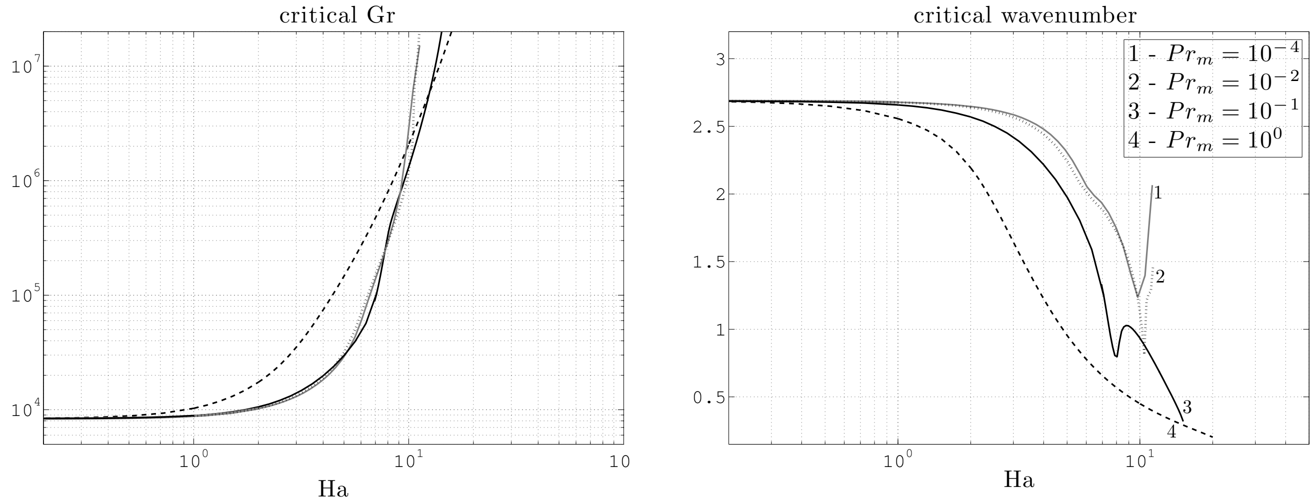

Figure 4. Critical values of parameters, thermally insulating & electrically conducting walls.

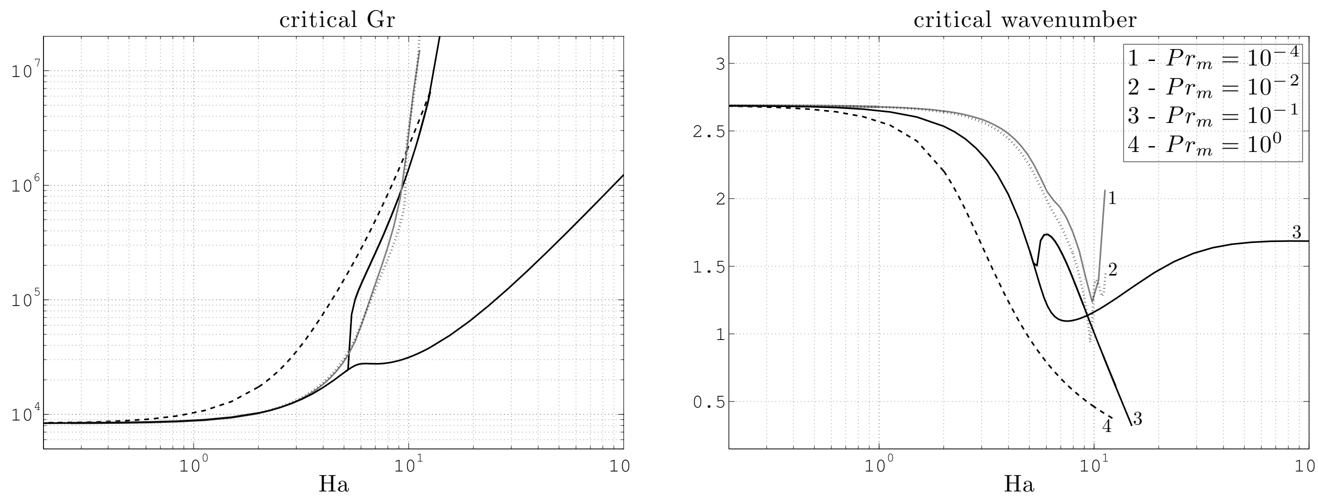

Figure 5. Critical values of parameters, thermally insulating & electrically insulating walls

4 Conclusions

The results show that the inductionless approximation is valid for the values of Pr_m up to $Pr_m = 10^{-4}$ for the range of Ha considered here. Further increase of Pr_m will cause a divergence between different modes, depending on the boundary conditions, and on the values of critical parameters. For the case of electrically insulating boundaries there are new most dangerous instabilities appearing for the whole range of Ha. The detailed results of this investigation, together with the results for the longitudinal modes will be discussed in a full journal paper.

References

[1] Muller, U.; Buhler, L.: Magnetofluiddynamics in channels and containers. Springer, 2001.
[2] Priede, J.; Aleksandrova, S.; Molokov, S.: Stability of buoyant convection in laterally heated liquid metal layer subject to transverse magnetic field. Proc. of the 7th PAMIR Conference, France, 2008
[3] Lappa, M.: Thermal convection. Patterns, evolution and stability. John Wiley & Sons, 2010.
[4] Kaddeche, S.; Henry,D.; BenHadid, H.: J. Fluid Mech. 480 (2003) 185-216

Time- and space-resolved temperature measurements on a periodically magnetized Gadolinium plate

Zhe Lei, Xuegeng Yang, Barbara Pulko, Stefan Odenbach, Kerstin Eckert
Institute of Fluid Mechanics, Chair of Magnetofluiddynamics, Measuring and Automation Technology, TU Dresden, D-01069 Dresden, Germany
E-mail: Zhe.Lei@tu-dresden.de; Kerstin.Eckert@tu-dresden.de

Abstract: The present work provides space- and time-resolved measurements of the temperature field inside a simplified flat-plate heat exchanger made of Gadolinium which serves as the magneto-caloric material (MCM). To measure the temperature field during periodic magnetization and demagnetization cycles of the MCM, both thermocouples and a Mach-Zehnder interferometer were used. Particular attention is paid to the analysis of the thermal boundary layer close the MCM, from which the heat flux into the fluid can be calculated.

1. Introduction

Magnetic cooling, based on the adiabatic temperature change of magneto-caloric materials (MCM) in a changing magnetic field, is an emerging new cooling technology [1]. Due to important advantages compared to conventional cooling based on gas compression, this technology has drawn an increasing concern. It has the potential of operating more silently and uses both non-toxic solid cooling material and environment-friendly heat transfer fluids. Besides, zero ozone depletion potential and less energy consumption makes it a promising alternative of next generation cooling technology. Furthermore and most importantly, the magneto-caloric cooling machines potentially possess a high efficiency, which is theoretically close to the Carnot cycle [1].

Despite increasing research on the thermodynamic principles and measurements [2,3] of magneto-caloric effect (MCE), corrosion and anticorrosion substitute solution studies [4] numerous issues have to be resolved before a widespread commercial use of the technique is achieved. The significant heat resistances in the active magneto-caloric regenerator, i.e. the suboptimal heat transfer from the MCM into the heat transfer fluid belong to these issues.

In this work, we provide for the first time space- and time- resolved temperature measurement in a simplified prototype of an active magnetic regenerator. For this purpose, both a Mach-Zehnder (M-Z) interferometer and direct measurement with thermocouples were applied to map the temperature field of the heat transfer fluid. Additionally, numerical simulation of the one-dimensional heat conduction was performed to facilitate the selection of heat transfer fluids suitable for interferometry.

2. Experimental setup and numerical simulation

Gadolinium (99.5% pure) was used as MCM. The Gd plates have an area of 9.6 mm x 9.6 mm and a thickness of 0.8 mm and were polished to a roughness of less than 0.01 mm. Two Gd plates were glued at the side walls of an optical cuvette (Hellma) with an inner geometry of 10 x 10 x 10 mm^3. The resulting space between the Gadolinium plates is 8.4 mm. This cuvette was filled either with deionized water or synthesis grade n-decane. Two NdFeB magnets (50 x

30 x 12 mm^3) were used to generate a magnetic field of 350 mT inside a gap of 15 mm. The inhomogeneity at height of the Gd plates is less than 3 mT. The pair of magnets is mounted on a 1-D motorized translation stage to generate a periodic magnetic field by means of which the Gd plates are exposed to periodic magnetization and demagnetization cycles. The experimental setup is schematically illustrated in Fig. 1.

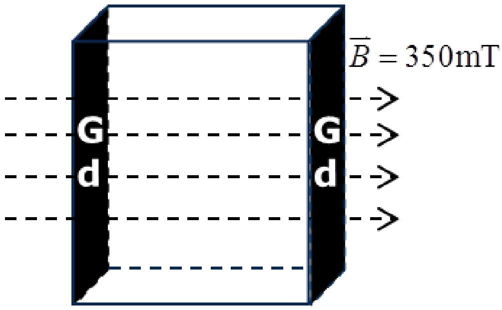

Figure 1: MCE measurement under a homogeneous magnetic field

Initially, the direct temperature measurements of the temperature change of Gd were performed with 0.25 mm thick ungrounded Type E thermocouples. For these measurements, four thermocouples were inserted into the gap of two parallel Gd plates, i.e. they are directly sandwiched by the plates. The thermocouples were adhered to the Gd plate and connected to a digital multimeter (Keithley 2700 including switching model 7708). The temperature data, gained by the thermocouples, served as calibration data for interferometric measurement to increase the accuracy and extend the measurement area of temperature field specifically near the surface of the Gd plates.

In the next step a Mach-Zehnder (M-Z) interferometer, employing a He-Ne laser (632.8 nm), was used to monitor the time and space- resolved temperature field *T(x,y,t)* during periodic magnetization and demagnetization of Gd. The interferograms were recorded with a frame rate of 30 Hz. Each experiment set was repeated for at least 3 times.

To support the selection of a heat transfer fluid which is suitable for temperature measurements in the interferometer, the one-dimensional unsteady heat conduction equation in the form

$$\frac{\partial T}{\partial x} = \frac{k}{\rho c_p}\frac{\partial^2 T}{\partial x^2} \qquad (1)$$

is solved by means of the finite volume method. In eq. (1), T is temperature; x is space distance normal to the Gd plate; k is the heat conductivity; ρ the density and c_p is the specific heat capacity. The harmonic mean heat conductivity k at the boundary of Gd and fluid is defined as

$$k = \frac{1}{\frac{1}{k_{Gd}} + \frac{1}{k_{fluid}}}. \qquad (2)$$

In accordance with our application, natural convection during heat transfer from Gd to fluid or vice versa can be neglected due to the small temperature differences.

3. Result and discussion

Fig. 2 shows the temperature changes at the surface of the Gadolinium plate during one complete cycle of magnetization (120 s) and demagnetization (120 s), measured by four thermocouples at room temperature by T_0=(295.2±0.2) K. Immediately after magnetization, the temperature rises by ΔT = (0.35 ± 0.05) K to exponentially decrease later on to T_0. Here, the temperature histories of the four thermocouples agree well since the temperature differences between the four thermocouples are less than 0.1 K. After removing the magnet, the temperature rapidly drops down by ΔT.

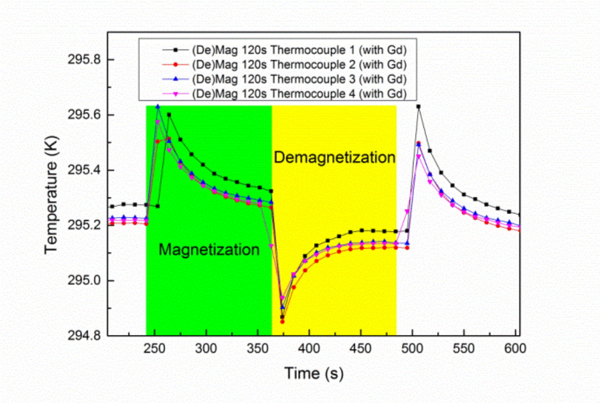

Figure 2: Temperature measurement with thermocouples during a full cycle of magnetization and demagnetization over 120 s.

In the next step we have investigated, by means of Mach-Zehnder interferometry, how the measured temperature change of the Gadolinium plate translates into the temperature field of the fluid surrounding the Gd plate. First, water was taken for that purpose because it is naturally the first choice of an environment friendly heat transfer fluid. However, Fig. 3a shows the disillusioning result that the temperature rise in water is smaller than the noise in the measurement, hence not reliably resolvable by the instrument.

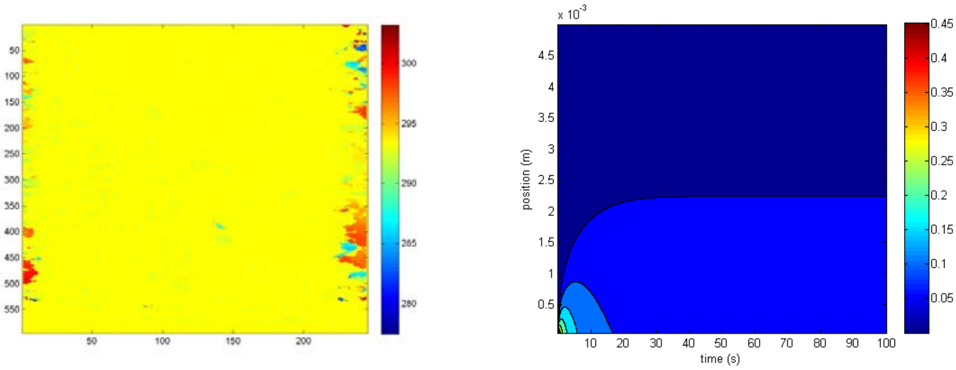

(a) (b)

Figure 3: (a) M-Z Interferometer temperature measurement of heat transfer from 2 magneto-caloric plates into water; (b) 1-D unsteady thermo-diffusion simulation of heat transfer into water between two parallel magneto-caloric Gd plates.

The simulation in Fig. 3b reveals the reason why. It shows the 1-D temperature profile normal to the Gd plate with progressing time. Only in the very beginning, a measurable ΔT of about 0.3 K appears. However, by virtue of the comparatively high thermal diffusivity $\kappa = k / (\rho\ c_p)$, of water this temperature rise is diminished to less than 0.1 K within about 5 sec.

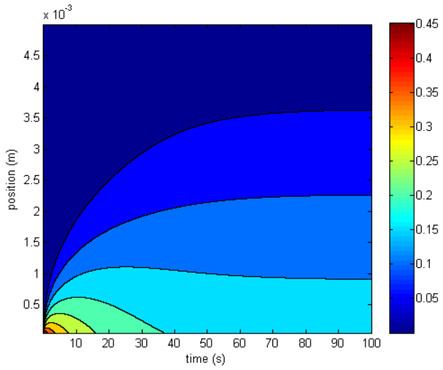

Figure 4: 1-D temperature profile versus time at the center of the Gd plate as obtained from 1-D simulation of the unsteady heat conduction equation (1) of the MCE with n-decane.

After simulation of several other organic liquids of smaller heat capacity, n-decane turned out to be the best compromise. Fig. 4 shows the corresponding 1-D temperature profile $T(x)$ after an adiabatic temperature increase of Gadolinium of 0.5 K. On comparing the simulation of the MCE when using either water (Fig. 3b) or n-decane (Fig. 4) as heat transfer fluid, it is obvious that a clearer and measurable temperature profile with n-decane is theoretically achievable.

The results of the M-Z interferometer experiments using n-decane in the setup of Fig. 1 are shown in Fig. 5. Here, the temperature field is plotted both after 5 s of magnetization (Fig. 5a) and after 5 s of demagnetization (Fig. 5b) with 350 mT. The two Gadolinium plates are located at both vertical boundaries perpendicular to the measurement arm of M-Z interferometer and appear in Fig. 5 as vertical boundary at the left and right side of each picture. The figure shows nicely the formation of the thermal boundary layers at the Gd plates. Heat losses in the upper and lower part of the optical cell as well as a minor variation of the thickness of Gd plates contribute to a slight imperfection of the isotherms. As a result, the isotherms are a bit convex instead of exactly one-dimensional.

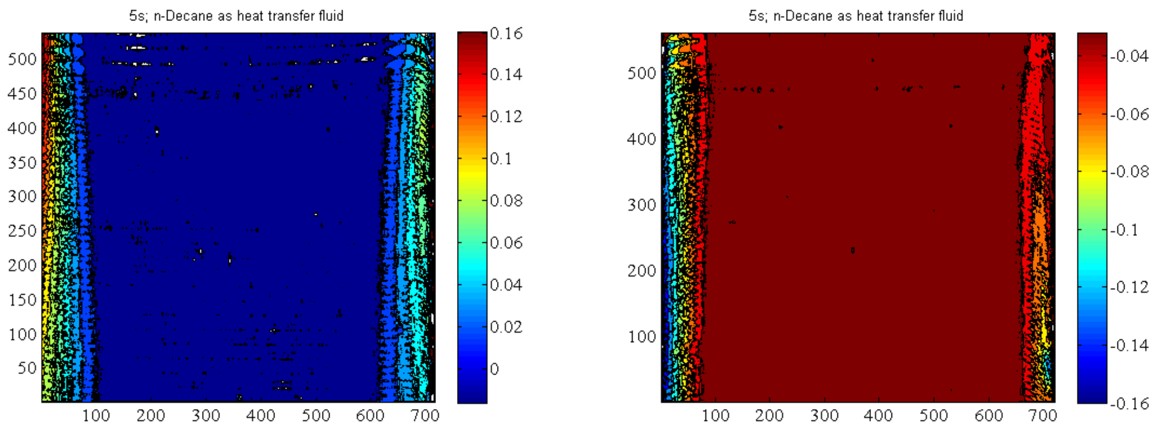

(a) (b)

Figure 5: M-Z Interferometer measurement of temperature field in n-decane: (a) 5 s after magnetisation and (b) 5 s after demagnetisation.

The temperature profiles normal to the Gd plates in the cell center, derived from the temperature field in Fig. 5a are plotted with progressing time during the magnetization phase in Fig. 6. The horizontal coordinate is the distance normal to the surface of the Gd plate. The vertical coordinate is the temperature of the n-decane at the specified position. The developments of the T(x) profiles with time is clearly visible. The reason why the measured temperature maximum of 0.15 K after 5 s stays below the maximum temperature rise detected by the thermocouples (0.35 K) is related to the fact that region very close to the Gd plates is currently not visible for the interferometer.

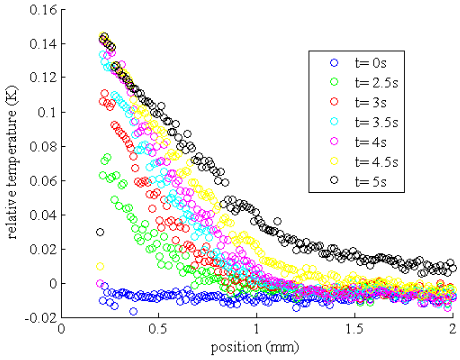

Figure 6: Temperature profile T(x) with progressing time during the magnetization phase, measured by the M-Z interferometer.

This problem is related to the difficulties in the adjustment of the Gd plates parallel to the measurement arm of M-Z interferometer. This leads to a reduction of the accessible field of view in the cell as illustrated in Fig. 7. However, the tilt angles α and β are small and considerably less than 1°. As a result, the temperature data near the Gd plate, i.e. over an interval of $\Delta x \approx 0.2$ mm are missing.

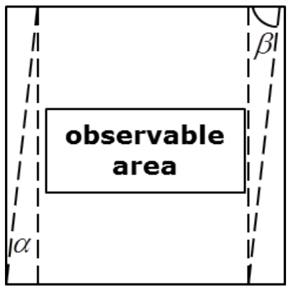

Figure 7: Sketch of the observable area of the M-Z interferometer caused by a small tilt of the Gd plates in the optical cell.

Current work is devoted to two issues: (i) to combine the temperature data acquired by both methods (M-Z interferometer and thermocouples) to obtain the complete time- and space-resolved temperature profiles. (ii) By implementing a magnetohydrodynamic convection we seek to enhance the heat transfer from the Gd plates into the heat transfer fluid.

4. References

[1] K. A. Gschneidner, Jr.; Pecharsky, V. K.: Thirty years of near room temperature magnetic cooling: Where we are today and future prospects. Int. J. Refrigeration. 31(2008) 945-961.
[2] Pecharsky, V.K.; Gschneidner, Jr.; Pecharsky, A.O.; Tishin, A.M.: Thermodynamics of the magnetocaloric effect. Phys. Rev. B. 64 (2001) 144406-144406-13.
[3] Kuz'min, M.D.; Skokov, K.P.; Karpenkov, D.Yu.; Moore, J.D.; Richter, M.; Gutfleisch, O.: Magnetic field dependence of the maximum adiabatic temperature change. Appl. Phys. Lett. 99 (2011) 012501-012501-3.
[4] Zhang, M.; Ye, R.; Long, Y.; Chang, Y.: Inhibition of La-Fe-Co-Si compound corrosion in distilled water by sodium molybdate and disodium hydrogen phosphate. J. Rare Earths. 29 (2011) 138-142.

LIQUID METAL HEAT TRANSFER IN A TOKAMAK REACTOR

BELYAEV[1] I.A., GENIN[1] L.G., LISTRATOV[1] YA.I., SVIRIDOV[1] V.G., SVIRIDOV[1] E.V., IVOCHKIN[2] YU.P., RAZUVANOV[2] I.G.
[1]Moscow Power Engineering Institute (MPEI), Moscow, Russia
[2]Joint Institute of High Temperatures Russian Academy of Science (JIHT RAS), Moscow, Russia

Complex experimental study and numerical simulation of liquid metal (LM) flow and heat transfer in various MHD configurations affected by longitudinal or transverse magnetic field (MF) have been performed [1]. The experimental studies are conducted in MHD facility by a joint team of MPEI-JIHT RAS. The MHD facility combines two mercury loops, where investigations in a longitudinal and in a transverse MF are available (Fig.1). It is well known that mercury is not considered as a possible coolant in energetics. However, mercury is, undoubtedly, the best of the working media for experiments on the MHD heat transfer.


Figure 1: MPEI and JIHT RAS loop for investigations of mercury flow and heat transfer in the longitudinal and transverse magnetic field.

Flow in horizontal, vertical and inclined tubes have been considered. Examined configurations are shown in Fig. 2, where outlined vectors: V - the velocity of the flow, g - the free fall acceleration, B – the MF induction. Heating is uniform in length, and, in general case, heterogeneous on the perimeter of the cross-section of the tube or channel (Fig. 3). The geometry of the flow and MHD convective heat exchange correspond to the various situations of the cooling channels in blanket and divertor of a tokamak- reactor.

The length of the heating zone and the uniform MF area are, respectively, 42d and 29d, where the tube diameter d=19mm.Channel section is 16x56. mm. Measurements in the mercury flow have been provided by probe methods using various sensors: thermocouples, correlation and electromagnetic velocity sensors. With the help of micro thermocouples, three-dimensional (3D) fields of average temperature and temperature fluctuations were measured, then local (along the perimeter and the length of the tube) and average heat transfer coefficients were defined. The probe technique for wall temperature measurements made in possible to eliminate the error associated with the thermal contact resistance at the liquid metal-solid wall boundary. Correlation and electromagnetic sensors were used to measure longitudinal and transverse components of local velocity. Experiments were fully automated.

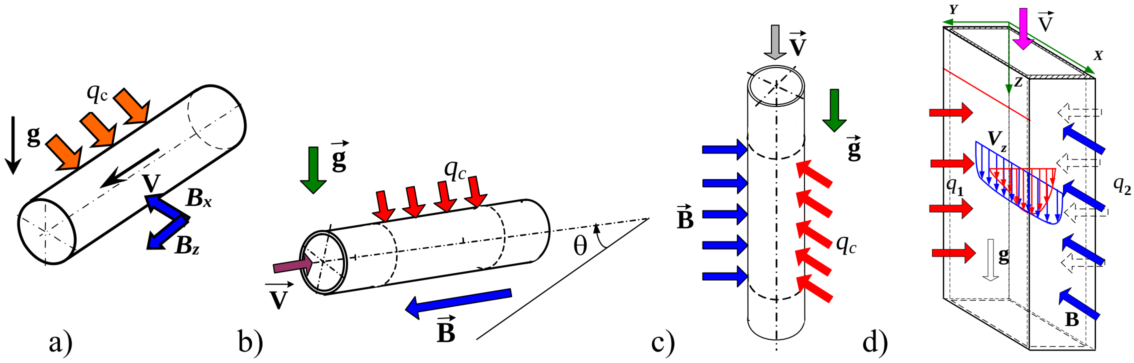

Figure 2: Flow configuration: a) horizontal heated tube in the longitudinal or transverse MF, b) down flow in an inclined to the horizon tube in the longitudinal MF, c) down flow in the vertical tube in transverse MF, d) down flow in the vertical rectangular channel in transverse MF.

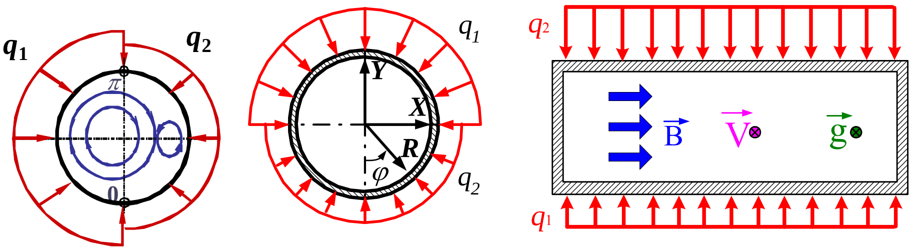

Figure 3: Heating configurations.

Table 1.Criteria in experiments.

Criterion	JIHT Loop	MPEI Loop
$\mathrm{Re} = \dfrac{wd}{\nu}$	$5 \cdot 10^3 \div 1.2 \cdot 10^5$	$5 \cdot 10^3 \div 7 \cdot 10^4$
$\mathrm{Ha} = Bd\sqrt{\dfrac{\sigma}{\mu}}$	Transverse MF $0 \div 500$	Longitudinal MF 0-480
$\mathrm{Gr_q} = \dfrac{g\beta q d^4}{\lambda \nu^2}$	$0 \div 10^8$	

Along with the experiments, numerical simulation of MHD heat transfer has been developed. The basic of the estimated model is a system of Reynolds averaged Navier-Stocks(RANS) equations. The Boussinesq approximation and the authors model of MF affect on the turbulent transfer of momentum and heat were used.

Analysis of all the experimental data taken together allows us to make two general conclusions about the nature of the joint effect of the MF and thermo gravitational convection (TGC) on the flow and heat transfer of the LM in the tube.

The first one is the existence, in some modes, the areas of “degraded” local heat transfer and, as a result, the extremely nonuniform distribution of mean wall temperature along the perimeter of tube cross section.

For example, in horizontal tube affected by longitudinal MF TGC manifests itself in the form of large longitudinal vortices (Fig. 3) with axes parallel to the vector of the MF induction. MF stabilizes these vortices. As a result, flow loses axial symmetry, heat distribution becomes inhomogeneous in the tube cross-section, with the formation of zones of «degraded» and «enhanced» heat transfer. We call heat transfer «degraded » when local Nusselt criteria are below laminar values $\mathrm{Nu_L} = 4.36$ [2].

It is an frequent situation when the designers of heat exchangers, in case of lack preliminary information on heat transfer, use the laminar value Nu_L = 4.36 as «the lowest possible». As it can be seen for example in Fig. 3, this cannot be done, because the local Nusselt criteria can be significantly lower.

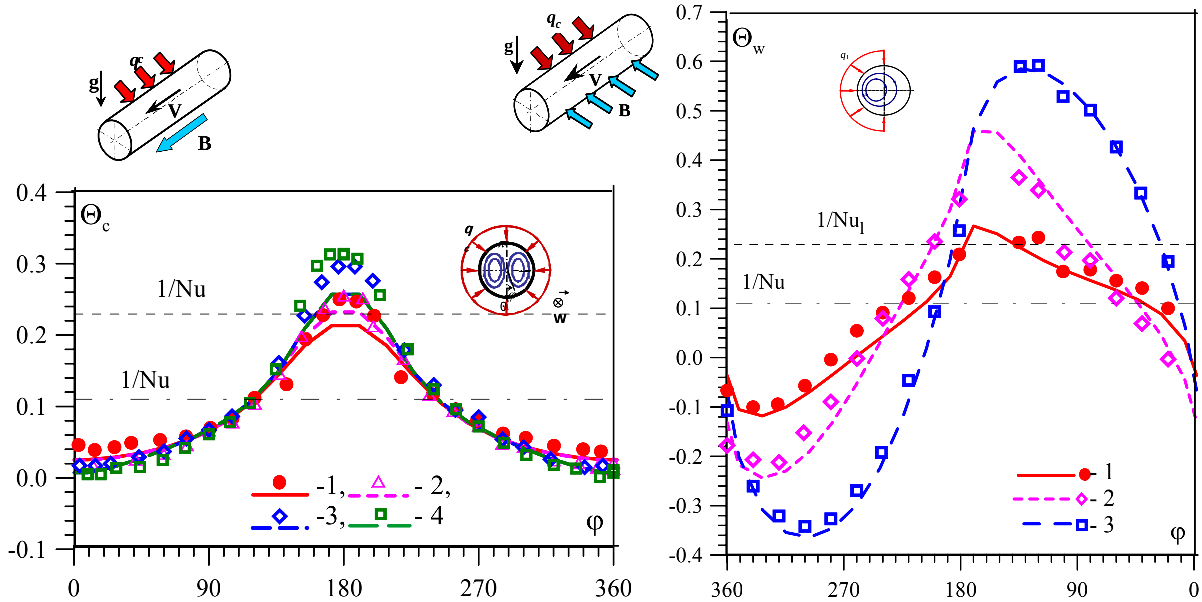

a) longitudinal MF, homogeneous heating b) transverse MF, inhomogeneous heating

Figure 3: Dimensionless wall temperature Θ along the perimeter of the horizontal tube cross section *z/d*=37, points – experiment, lines – calculation Re = 10000, q = 35 kW/m^2($Gr_q = 0.8{\cdot}10^8$): 1) Ha = 0; 2) 150; 3) 300; 4) 450;

In the vertical tube affected by transverse MF there is also heterogeneity of the wall temperature along the perimeter of the tube section (Fig. 4) [3]. However, physical reason in this case is different. The matter is in the presence of Hartman effect in the transverse MF. This effect leads to a flattening of velocity profile in the direction of the magnetic induction vector, while in the perpendicular direction speed profiles have an elongated shape, typical for laminar flow. Strong axial asymmetry of the velocity profile and reinforced counter TGC leads to the heterogeneity of local heat transfer coefficients and wall temperature along the perimeter of the tube cross section.

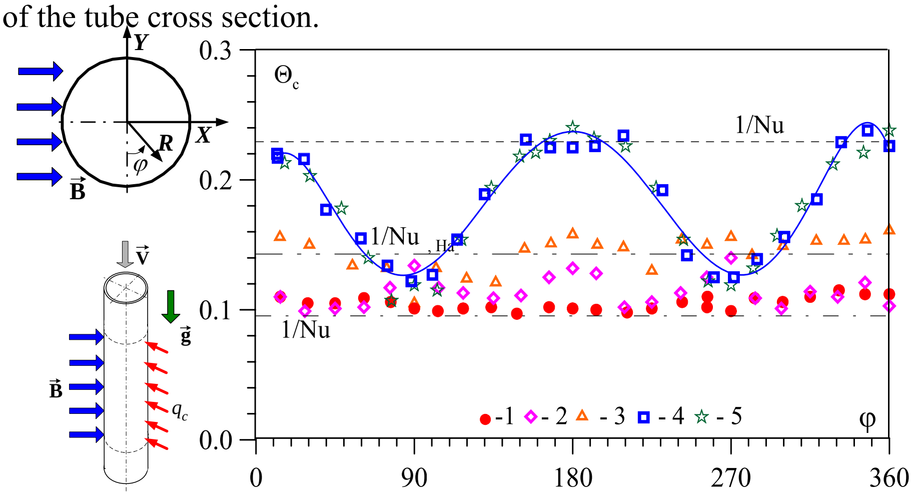

Figure 4: Dimensionless wall temperature Θ along the perimeter of the vertical tube cross section z/d = 37 affected by the transverse MF with the homogeneous heating Re = 20000, q = 55 kW/m^2: 1) Ha = 0; 2) 100; 3) 220; 4) 320; 5) 500. Points – experiment, lines – experiment data approximation.

The second effect is the presence of extremely high temperature fluctuation of low frequency in the core of MHD flow and near the wall. Example of such fluctuations observed in one of examined configurations is shown on Fig.5. This effect present itself when TGC forces compete with MF forces. Such a situations develops in heated vertical tubes with downflow affected by transverse [4] or longitudinal [1] MF and in horizontal tubes affected by transverse MF when heating configuration produces unstable density stratification due to thermo gravitation [5]. The physical cause of both effects is the same: the joint affect of MF and TGC upon the nonisothermal MHD LM flow, which results in generation of stable large-scale quasi-2D vortices with the axes parallel to MF vector. The affect of MF upon the LM mean velocity profile is also essential. Both of these effects are dangerous for wall material.

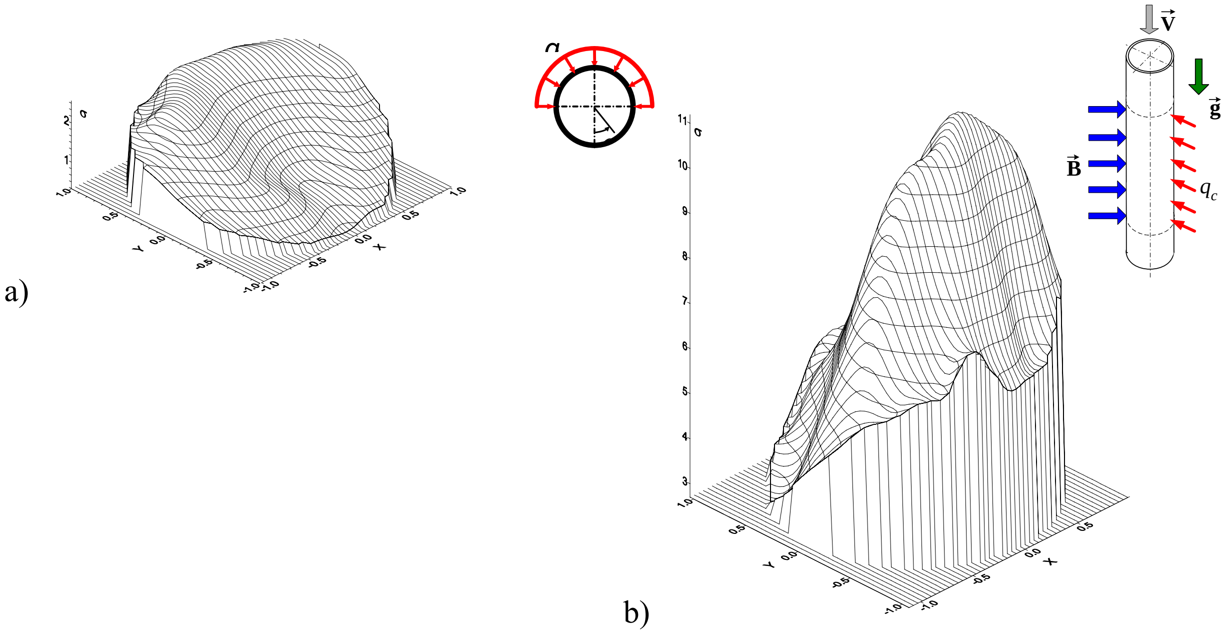

Figure 5: Temperature fluctuation intensity field in the vertical tube cross-section z/d = 37, q_1/q_2= 55/0 W/m^2 ($Gr_q = 1.25 \cdot 10^8$), Re = 20000: a) Ha = 0; b) 300.

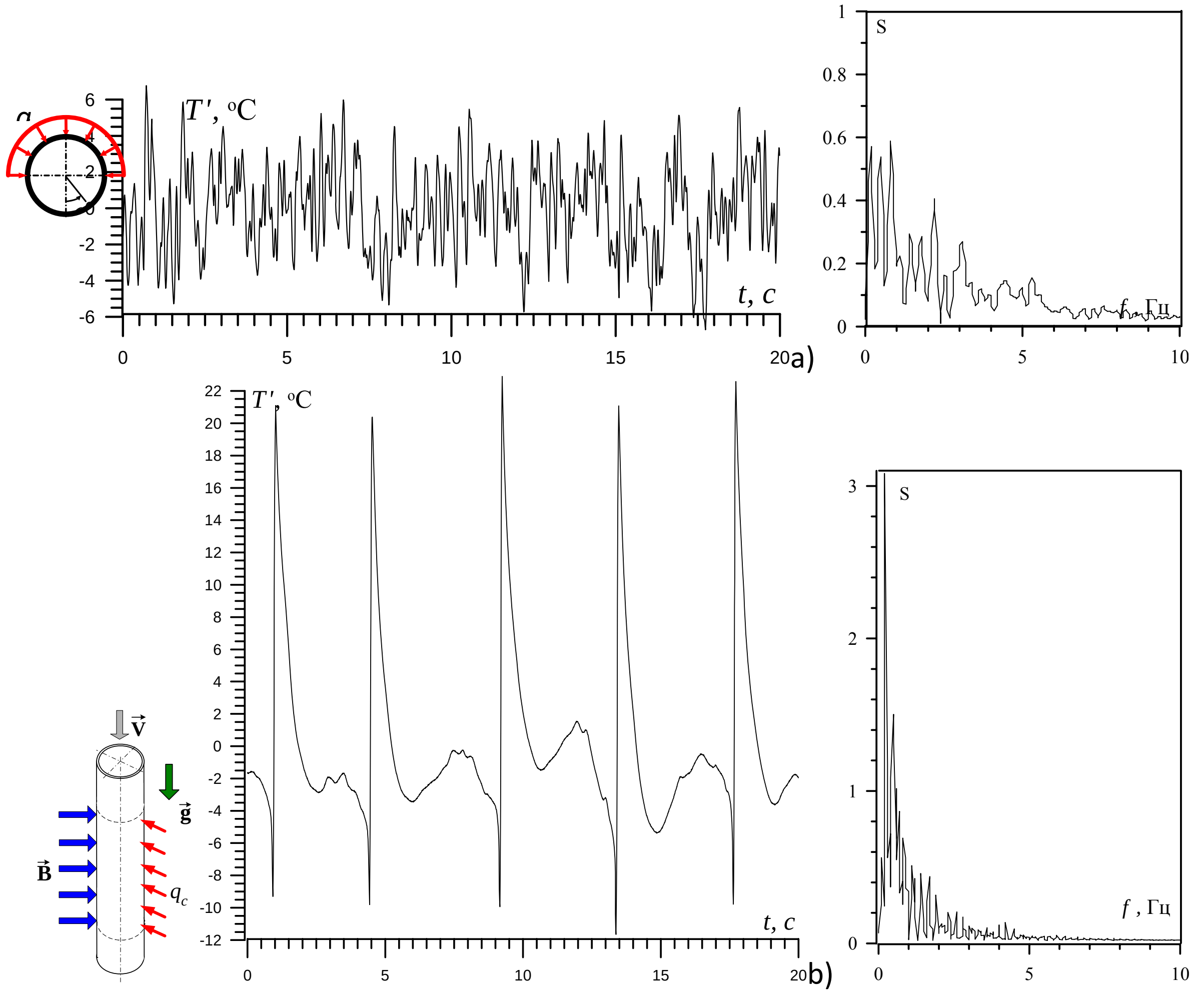

Figure 6: Characteristic temperature fluctuations and its power spectrum in vertical tube with inhomogeneous heating: z/d =37, q1/q2 = 55/0 кW/m2, Re =20000, transverse MF, at intensity maximum) Ha = 0; b) 330.

The work is supported by the Russian Fund for Basic Research, the RF Ministry of Education and JSC "NIIEFA".

References

[1]. Belyaev, I.A., Genin, L.G., Listratov, Ya.I., Melnikov, I.A., Sviridov, V.G., Sviridov, E.V., Ivochkin, Yu.P., Razuvanov, N.G., Shpanskiy, Yu.S.: Liquid metal heat transfer specific in a tokamak reactor. Magnetohydrodynamics, vol. 49 (2013), no. 1-2, 177-190.

[2] Sviridov, V.G., Razuvanov, N.G., Ivotchkin, Yu.P., Listratov, Ya.I., Sviridov, E.V., Genin, L.G., Zhilin, V.G., Belyaev, I.A.:. Liquid metal heat transfer investigations applied to tokamak reactor. Proc. the International Heat Transfer Conference IHTC14 p.1-8, Washington, DC, USA, August 8-13, 2010.

[3] Genin, L.G., Zhilin, V.G., Ivochkin, Yu.P., Razuvanov, N.G.,Sviridov, V.G., Shestakov, A.A., Sviridov, E.V. Liquid metal heat transfer in a vertical tube affected by transverse magnetic field. Proc. the 8th International PAMIR Conference on Fundamental and Applied MHD, France, 2011.

[4] Melnikov, I.A., Razuvanov, N.G.,Sviridov, V.G., Shestakov, A.A., Sviridov, E.V.; An investigation of heat exchange of liquid metal during flow in a vertical tube with non-uniform heating in transverse magnetic field. Thermal Engineering, vol.60 (2013), no.5, pp 355-362.

[5] Genin, L.G., Zhilin, V.G., Ivochkin, YUu.P., Razuvanov, N.G., Belyaev, I.A., Listratov, Ya.I., Sviridov, V.G.:.Temperature fluctuations in a heated horizontal tube affected by transverse magnetic field. Proc. the 8th International PAMIR Conference on Fundamental and Applied MHD, France, 2011, p.37-43.

TURBULENT CONVECTIVE HEAT TRANSFER IN A LONG CYLINDER WITH LIQUID SODIUM

MAMYKIN[1] A., FRICK[1] P., KHALILOV[1] R., KOLESNICHENKO[1] I., PAKHOLKOV[2] V., PAVLINOV[1] A., ROGOZHKIN[2] S.
[1]Institute of Continuous Media Mechanics, Perm, Russia
[2]JSC "Afrikantov OKBM", Nizhny Novgorod, Russia
E-mail address of corresponding author: mad@icmm.ru

Abstract: Turbulent convection at low Prandtl numbers is studied experimentally. The experiments are performed in a cylindrical cell of large aspect ratio (H/D = 5) at different angles of inclination from vertical. The cell is filled with liquid sodium. The range of Rayleigh number is $3 \times 10^4 < Ra < 1.5 \times 10^8$. The averaged and spectral characteristics of temperature fluctuations are measured by thermocouple sensors and mean velocities are calculated using the cross-correlation analysis of these fluctuations.

1. Introduction

Experimental studies of sodium convection in cylindrical vessels are necessary to providing project calculations and verification of CFD codes on the example of a cylindrical cell (pipe section) and to better understanding turbulent convective processes occurring in the cooling circuits pipes of reactor facilities with sodium coolant. Currently available investigations devoted to the study of convection in fluids with small Prandtl number are performed on cells with aspect ratio of not greater than one [1-2]. In this paper we present results of an experimental study of convective flow of sodium in a relatively long cylindrical vessel in various positions (horizontal, inclined by 45°, vertical channel).

2. Experimental set-up

The experiments are carried out in a cylindrical container made of stainless still with an inside diameter of D = 0.168 m and a height of H = 0.850 m. Heating and cooling are produced by end heat exchangers. Hot heat exchanger consists of four closely adjacent to each other copper plates 15 mm in thickness. In directly adjacent to sodium cooper plate are drilled holes and turned channels for 5 thermocouples installation. Two of them are immersed in sodium at 5 and 1 mm for the boundary conditions measurements. Other 3 thermocouples are used for monitoring the radial uniformity of heating. The rest 3 copper plates have a cavity for placement of electric heating elements. The heater produces a maximum power of 6 kW. Cold heat exchanger is made of two copper plates of 15 mm thick. One of them, which directly adjacent to sodium, is identical to above-mentioned measuring plate and contains 5 thermocouples. In the second copper plate is turned channel for circulating cooling fluid. As the cooling fluid we use the mineral oil. A sketch of the experimental device is shown in Fig. 1 left. Additionally, the experimental setup includes the sodium storage system, the cell filling system, the frame to install the cylinder and lock it at predetermined angles, a set of sensors, the system for remote monitoring, the system for parameters of heating and cooling control, the system for measurements and acquisition of experimental data.

3. Measurement techniques. Cross-correlation method.

Measurements in sodium are performed using thermocouples made of the chromel-alumel thermocouple cable placed in a tube with an outer diameter of 1 mm. The space between the thermocouple and the tube wall is filled with mineral insulation, withstands temperatures up to 800 °C. Installation of thermocouples into the vessel is performed using an additional tube diameter of 3 mm and a length of 100 mm. It is welded to the channel, and then it is soldered thermocouple (Fig. 1 right). Data acquisition from each thermocouple is produced with a frequency up to 75 Hz.

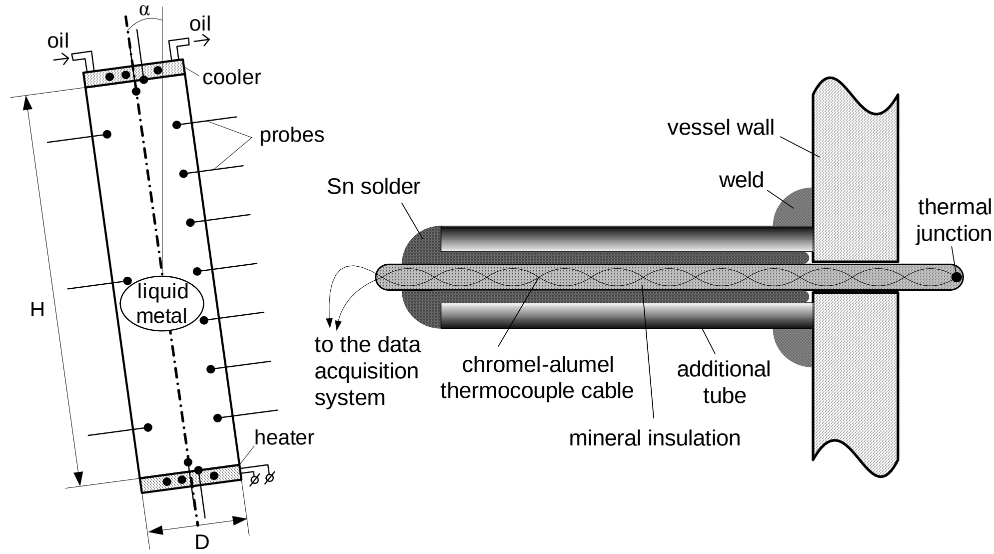

Figure 1: A sketch of the experimental cell (left); a scheme of thermocouple sensor (right).

Velocity measurements in liquid sodium are generally difficult to perform due to the opacity and aggressiveness of the melt at high temperature. However, it is possible to receive mean velocity values by calculating the cross-correlation of temperature fluctuations on the neighboring thermocouples. In case of a turbulent convection of the liquid medium there are overheated areas, which move together with the flow. Passing successively through two temperature sensors, such areas cause the bursts of temperature on these sensors with a certain time delay. Knowing the value of this delay and the distance between the sensors, the mean flow velocity in the space between these sensors can be defined. The maximum of cross-correlation function determines the mean time delay between the bursts on the neighboring sensors. In case of our experimental set-up, cross-correlation function is drawn for each pair of sensors in a line of thermocouples that allows us to get the velocity distribution along the cylinder (Fig. 2).

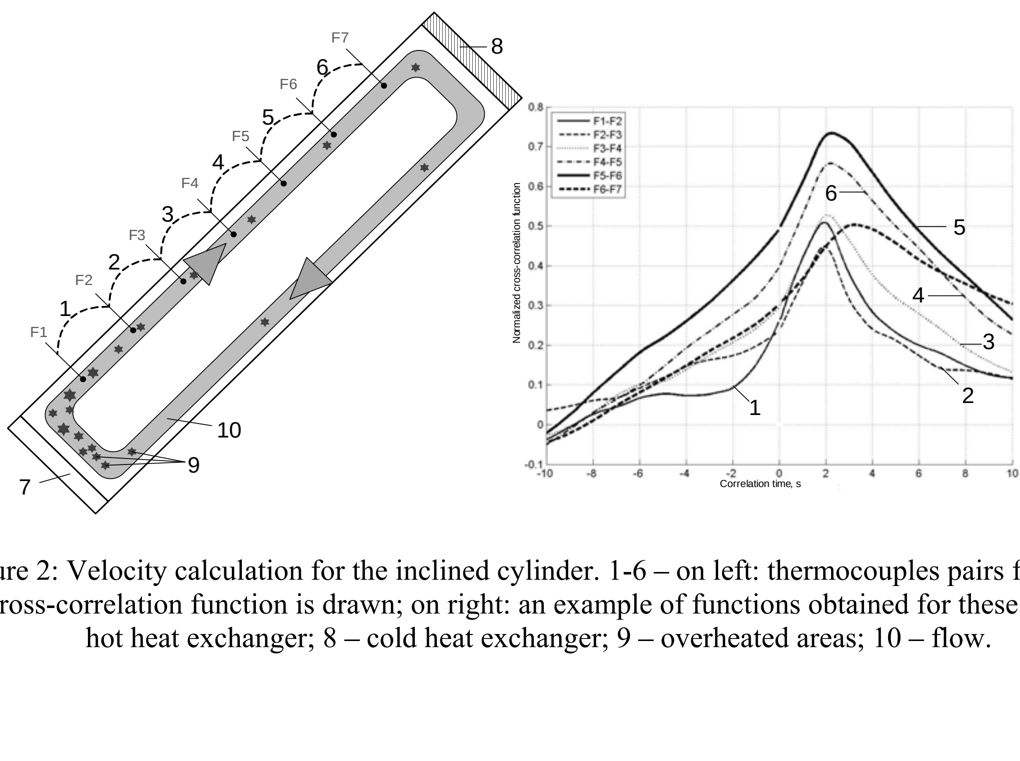

Figure 2: Velocity calculation for the inclined cylinder. 1-6 – on left: thermocouples pairs for which the cross-correlation function is drawn; on right: an example of functions obtained for these pairs; 7 – hot heat exchanger; 8 – cold heat exchanger; 9 – overheated areas; 10 – flow.

4. Results and discussions

Measurements are carried out in a stationary mode with a preset temperature of hot heat exchanger T_h. For each cylinder position from 5 to 7 experiments with different power of heating are conducted. Fig. 3 shows a scheme of a horizontal vessel applied with a time-averaged value of temperature minus the average temperature in the channel and the average velocity for T_h = 225°C.

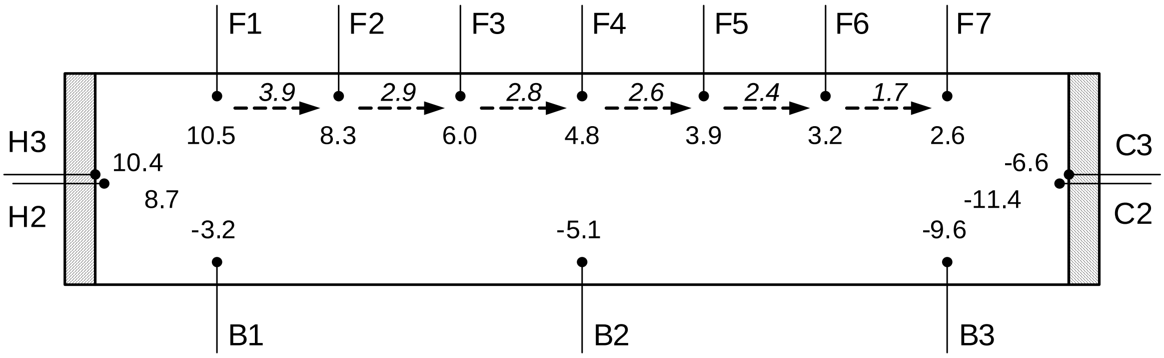

Figure 3: Horizontal vessel with applied experimental data. A dashed arrow with italic numbers shows direction and values of the average velocity.

At horizontal position of the cylinder experiments are carried out for Th = 175; 200; 225; 250; 275; 300; 325 °C which correspond to the Rayleigh number Ra = 0.49; 0.57; 0.67; 0.80; 0.93; 1.09; 1.27 * 10^5 calculated according to the formula:

$$Ra = \frac{g\beta\nabla T}{\nu\chi} r^4,$$

where r - radius of the cylinder, β - expansion coefficient, ν - kinematic viscosity, χ - thermal diffusivity, g - acceleration of gravity.
Velocity and temperature distribution along the cylinder are shown in Fig. 4.

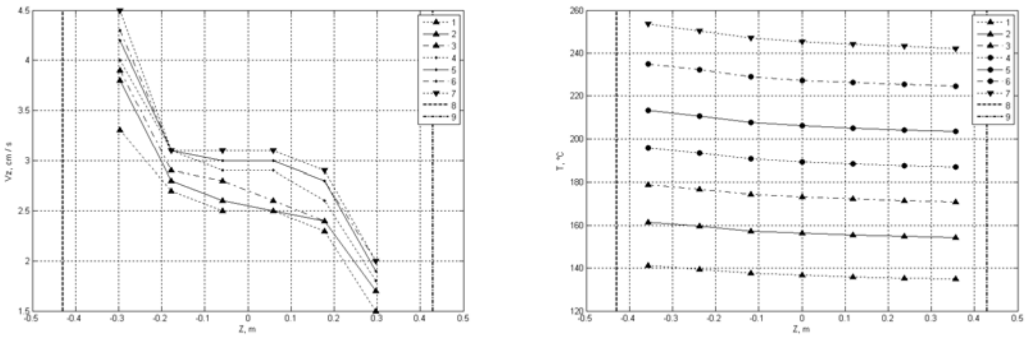

Figure 4: Velocity and temperature distribution along the horizontal cylinder. 1-7 correspond to different values of T_h.;8-9 correspond to Na-(heat exchanger) boundaries.

Fig. 5 shows a scheme of an inclined channel applied with the experimental data for T_h = 275°C. At such position of the cylinder experiments are carried out for Th = 175; 200; 225; 250; 275 °C which correspond to the Rayleigh number Ra = 0.34; 0.4; 0.45; 0.52; 0.63 * 10^5. Velocity and temperature distribution along the cylinder are shown in Fig. 5, right.
Fig. 6 left shows a scheme of a vertical channel applied with the experimental data for T_h = 175°C. Fig. 6 top right shows plots of cross-correlation functions. It can be seen that the maxima of the curves are poorly expressed and near zero in the time axis. This indicates that the amount of overheated areas that have passed through a pair of thermocouples in one and in the opposite direction is about the same. Thus, large-scale flow in the vertical cylinder cannot be registered.

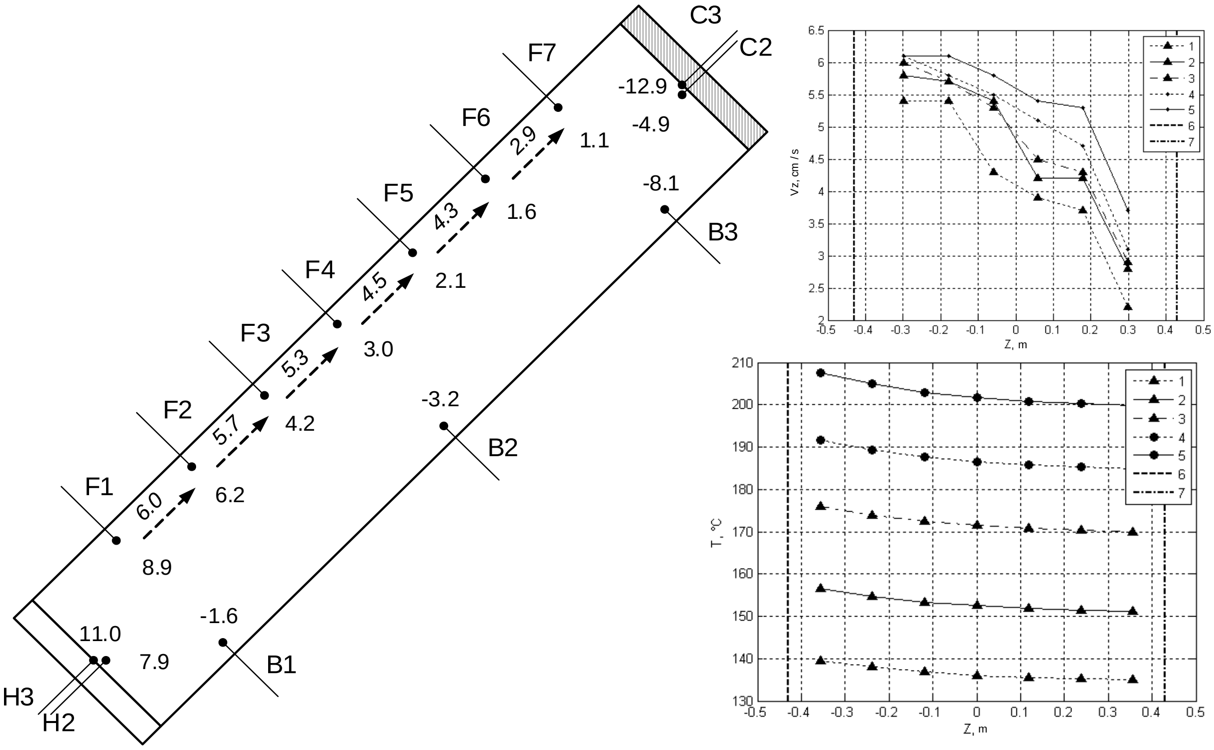

Figure 5: Inclined vessel with applied experimental data (left). Velocity and temperature distribution along the cylinder (right). 1-5 correspond to different values of T_h. 6-7 correspond to Na-(heat exchanger) boundaries.

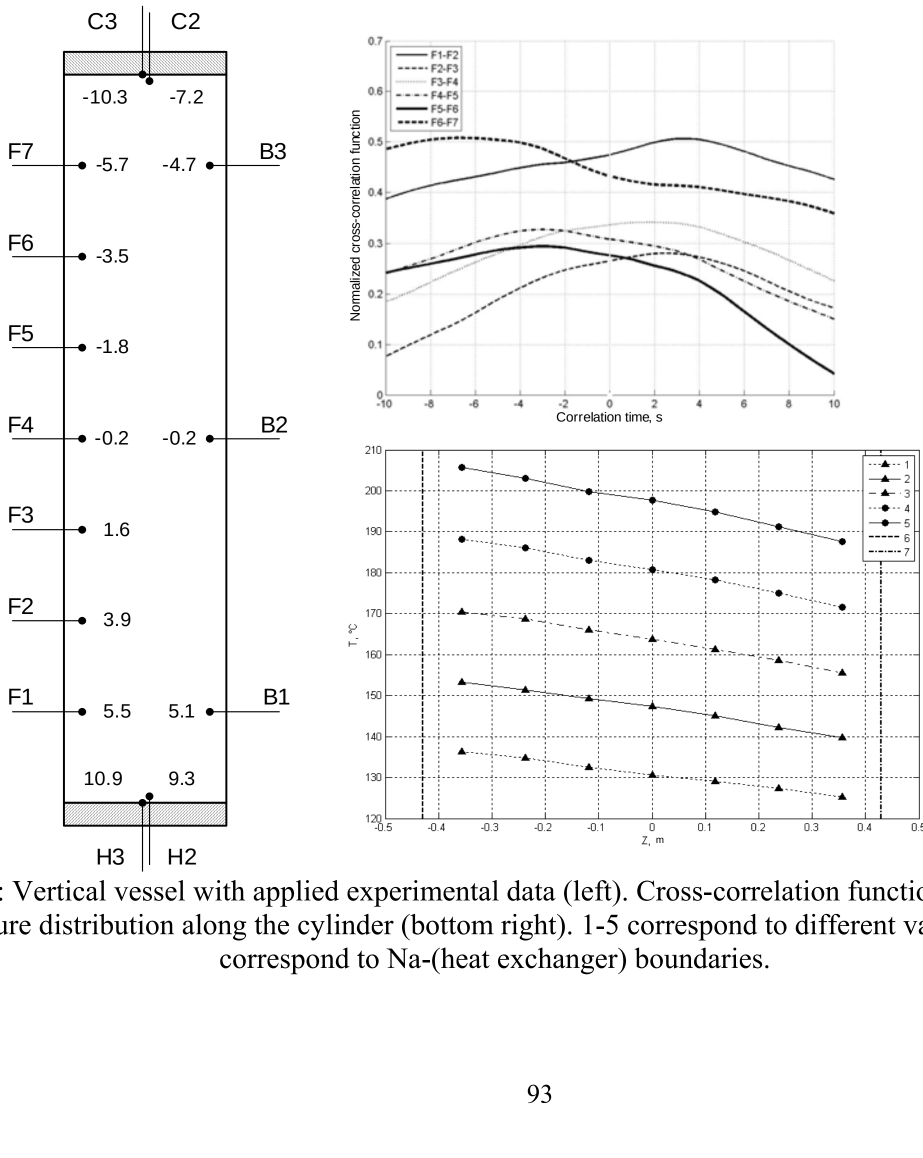

Figure 6: Vertical vessel with applied experimental data (left). Cross-correlation functions (top right); temperature distribution along the cylinder (bottom right). 1-5 correspond to different values of T_h. 6-7 correspond to Na-(heat exchanger) boundaries.

At vertical position of the cylinder experiments are carried out for Th = 175; 200; 225; 250; 275°C which correspond to the Rayleigh number Ra = 0.63; 0.77; 0.91; 1.05; 1.23 * 10^5.
Fig. 7 shows typical spectra of temperature fluctuations for thermocouples F1-F4 for all positions of the cylinder.

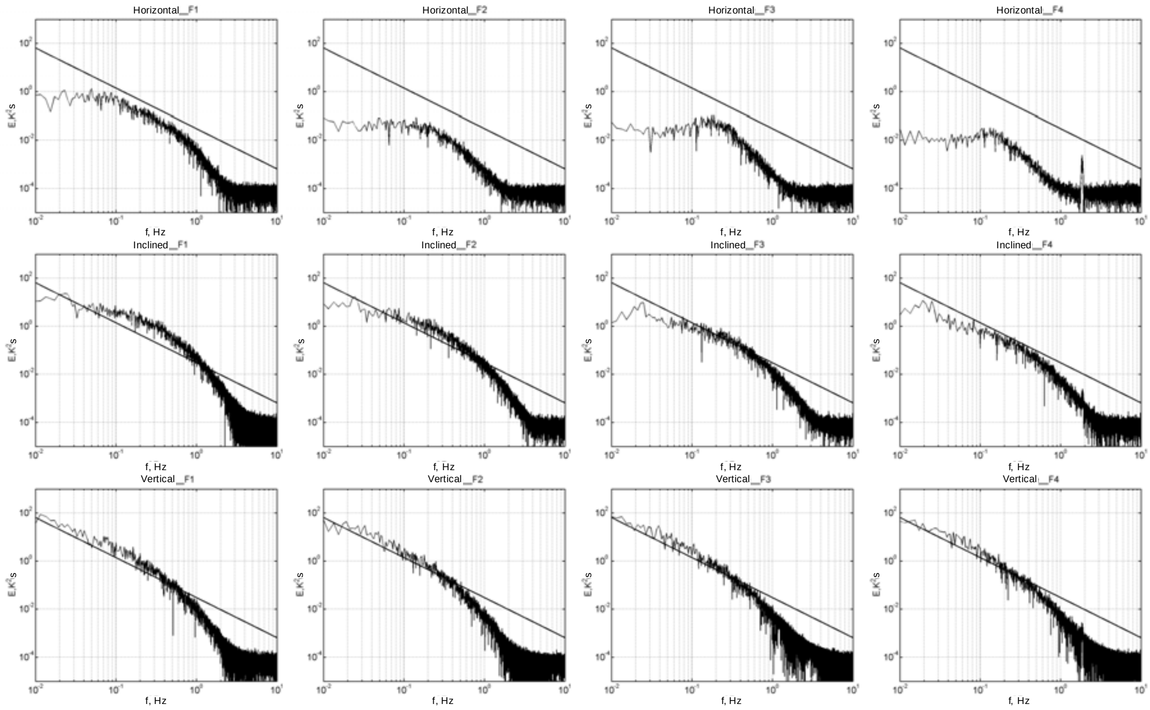

Figure 7: Typical spectra of temperature fluctuations for thermocouples F1-F4. From top to bottom - horizontal, inclined at 45° and vertical positions of the cylinder. Straight line – shows the Kolmogorov slope (-5/3).

For the case of a horizontal cylinder (top row in Fig. 7), it is obvious that form of the spectra changes along the cylinder from hot to cold heat exchanger - spectrum noticeably "sags", indicating a decrease in energy of turbulent fluctuations when approaching the cold heat exchanger. Moreover, there are obvious peaks at a frequency of about 0.15 Hz on the spectra of thermocouples F3 ÷ F5. Also, an inertial interval on the spectra of thermocouples F1 ÷ F3 exists.
In the case of cylinder inclined by 45° (middle row in Fig. 7), with removal from the hot heat exchanger spectra also "sags", but not so fast as in the case of the horizontal cylinder. At the same time on the spectra of all thermocouples inertial intervals are allocated.
In the case of a cylinder, vertically mounted, form of the spectra along the cylinder does not substantially changes. Thus on the spectra of all thermocouples inertial intervals are allocated.
Above-presented spectra indicate a turbulent nature of the convective flow in the cylinder at all considered conditions. The Reynolds number takes, however, a moderate value in the range varying from 3290 (minimum heat in horizontal cylinder) to 8050 (maximum heat in the inclined cylinder). Indeed, the spectra of the temperature fluctuations in the horizontal cylinder indicate that the inertial interval appear only in the area of average speed maximum values (in the floating up area near the hot heat exchanger and, apparently, floating down area near the cold heat exchanger.)

5. References

[1] Ahlers G., Grossmann S., Lohse D. Heat transfer and large scale dynamics in turbulent Rayleigh-Benard convection. Review of Modern Physics, 2009, vol. 81, p.503-537.

[2] Horanyi S., Krebs L., Müller U. Turbulent Rayleigh-Bénard convection in low Prandtl-number fluids. Int. J. Heat Mass Transfer, vol. 42, p. 3983-4003, 1999.

META:LIC CONCEPT THERMO-HYDRODYNAMICS TESTING FACILITY AT THE INSTITUTE OF PHYSICS OF THE UNIVERSITY OF LATVIA (IPUL)

PLATACIS[1] E., POZNAKS[1] A., ROMANCHUKS[1] A., NIKOLUSKINS[1] R., BULIGINS[2] L.

[1] Institute of Physics University of Latvia, 32 Miera str., LV-2169, Salaspils, Latvia
[2] Faculty of Physics and Mathematics, University of Latvia, 8 Zellu str., LV-1002, Riga, Latvia
E-mail address of corresponding author: leonids.buligins@lu.lv

Abstract : Heat transfer in the Pb-Bi loop with inductive heat source as a model for proton beam caused heat deposition is considered. The experimental setup for inductive heating does not allow an easy estimation of the deposited total power and its spatial distribution, therefore the total power has been determined indirectly using temperature measurements upstream and downstream of the heated region and flowrate data. The heat source spatial distribution has been determined by axis-symmetric finite element model describing time harmonic magnetic field created by the inductor coil. The calculated temperatures agree well with time averaged thermocouple measurements.

1. Introduction

The aim of the MEgawatt TArget: Lead bIsmuth Cooled (META:LIC) development has been to provide of a comparative target solution to the reference target for ESS [1]. To validate the META:LIC design, experiment focused on thermo-hydrodynamics of the liquid metal flow and was conducted on a mock-up of the META:LIC target at the LBE loop at the Institute of Physics of the University of Latvia (IPUL). The LBE loop has a total length of 10 m and 1100 kg of LBE. The loop is equipped with a cylindrical electromagnetic induction pump with permanent magnets, which is able to provide a liquid metal flow rate up to 12.0 l/s^{-1} at discharge pressure of 4.0 bars. Two flow meters of the induction and conduction types, as well as a Venturi tube are installed on the loop. Pressure is monitored with high temperature pressure transmitter 35 XHTC from KELLER AG.
The heat deposition by proton beam is modelled with inductive heat source. The heating is realized with the aid of a coil (inductor) connected to the high frequency 15 kHz generator. The core of the inductor has been made from the epoxy resin with ferromagnetic particles distributed in the resin, the experimentally determined relative permeability 100. The experimental setup for inductive heating does not allow an easy estimation of the deposited total power and its spatial distribution, therefore the total power has been determined indirectly using temperature measurements upstream and downstream of the heated region and flowrate data. The heat source spatial distribution has been determined by axis-symmetric finite element model describing time harmonic magnetic field created by the inductor coil. Software FEMM [2] is used for electromagnetic problem and ANSYS Fluent [3] for hydrodynamic and heat transfer.

2. Experimental setup

The test section geometry is shown in fig 1. Thermocouples are located at different depth in the melt 2, 4, 6 and 10 mm from the wall. The numbering of thermocouples is shown in fig 2. The thermocouples Tc.t.1-10 are located in close vicinity to the heated zone and, due to the specific character of the heat deposition in the experimental setup, can be used for determination of the temperature distribution. The thermocouples Tc.t.12-14 are located upstream the heated zone and measure the inflowing metal temperature, whereas Tc.t.0 and Tc.t.11 are located downstream the heated zone and are used for the outflowing metal temperature regarding to the heated zone. The measured temperatures by these thermocouples (Tc.t.12-14, Tc.t.0 and Tc.t.11) should be regarded as volume averaged ones due to the turbulent mixing and relatively high distance from the heated zone.

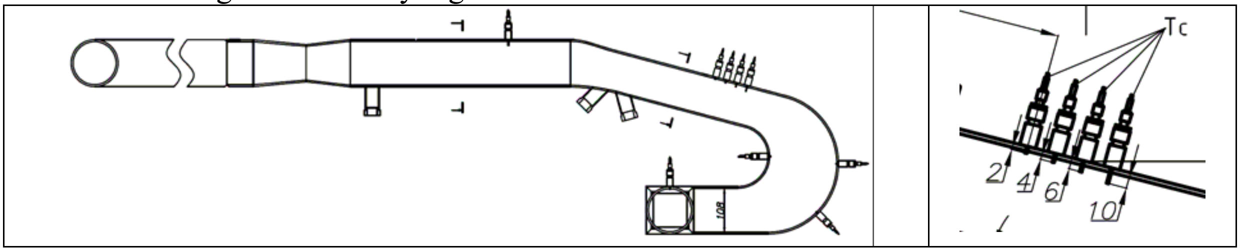

Figure 1: Test section geometry and thermocouple location.

The heat transfer in the loop has been modelled with the inductive heating. The heating is realized with the aid of a coil (inductor) connected to the high frequency (15 kHz) generator, see fig 2. At the chosen frequency the skin depth for stainless steel is about 3,5 mm, therefore the heat source for the melt can be considered as a heat flux at the surface. Temperature measurements with three locations of the inductor have been carried out. They are denoted as left, center and right according to the shown in fig 2 inductor location relative to the thermocouples Tc.t.1-10. The experimental setup for inductive heating did not allow an easy estimation of the deposited total power and its spatial distribution, therefore the total power had to be determined indirectly using temperature measurements upstream and downstream of the heated region and flowrate data.

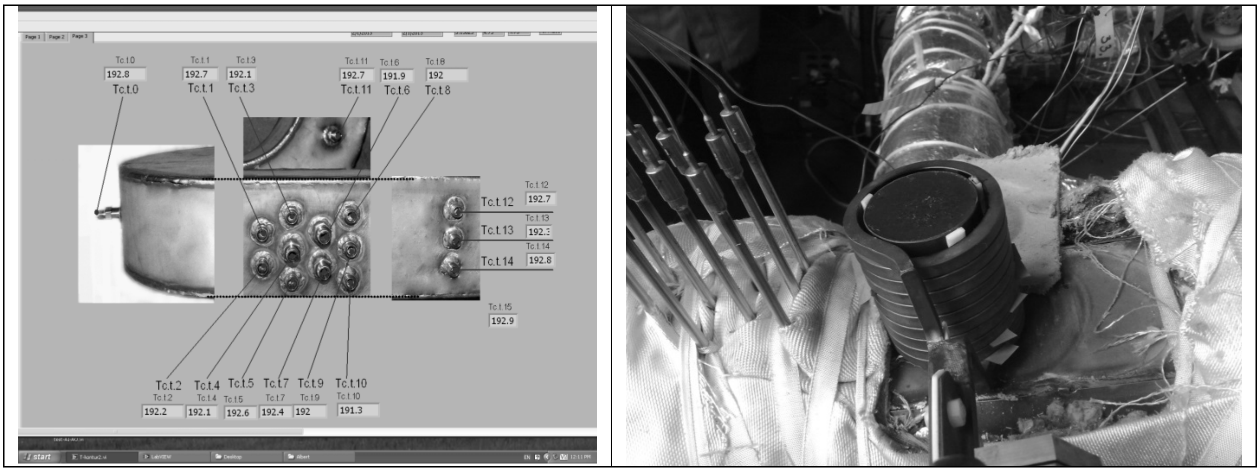

Figure 2: Thermocouple location and numbering and the inductor for heating.

The deposited power has been determined from the integral flow parameters. We use as a characteristic temperature T_{in} for the entrance of heated region and T_{out} for the exit of heated region. The power then is determined as $P = Q\rho c(T_{out} - T_{in})$. The determined values of power for three heater locations (left, center and right - P_l, P_c, P_r and average P_{av}) are presented in table 1. One has to take into account, however, that the measurements are made at specific moments of time and the unsteady character of the flow leads to the temperature fluctuations, decreasing the accuracy of steady state predictions from small number of measurements in time. Nevertheless, this method allows the determination of the total deposited power in the melt even if the accuracy is not very high.

Table 1: Deposited power determined from integral flow parameters

Q(l/s)	P_l (kW)	P_c (kW)	P_r (kW)	P_{av} (kW)
2	6.52	5.63	5.65	5.93
4	9.04	7.23	6.80	7.69
8	7.50	7.68	7.05	7.41

3. Inductive heating model

Another problem is connected with the heat source density distribution over the surface of the channel. The heat source spatial distribution has been determined by axis-symmetric finite element model describing time harmonic magnetic field created by the inductor coil with software FEMM [2]. The parameters used in calculations are presented in table 2.

Table 2: Electrical parameters of the materials

Material	Electrical conductivity (Ms/m)	Relative permeability
316 stainless steel	1.334	1
Pb-Bi	0.9	1
core	0	100

The axis-symmetrical model consisting of core, coil, stainless steel channel wall and lead-bismuth melt with used finite element mesh is shown in fig 3. Due to the high inductor frequency the mesh in channel wall is very fine and the depth of lead-bismuth in the model is limited.

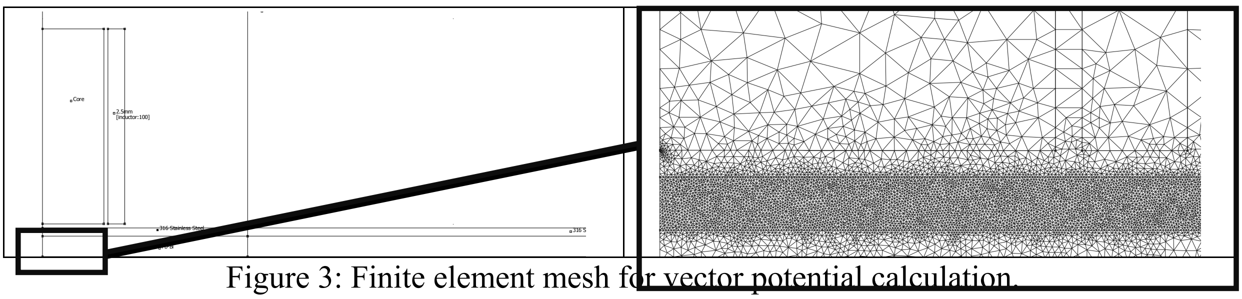

Figure 3: Finite element mesh for vector potential calculation.

The calculated current density and Joule sources are presented in fig 4. As expected, due to the small skin depth, the most of the heat is deposited in channel wall and only small part directly in the liquid metal.

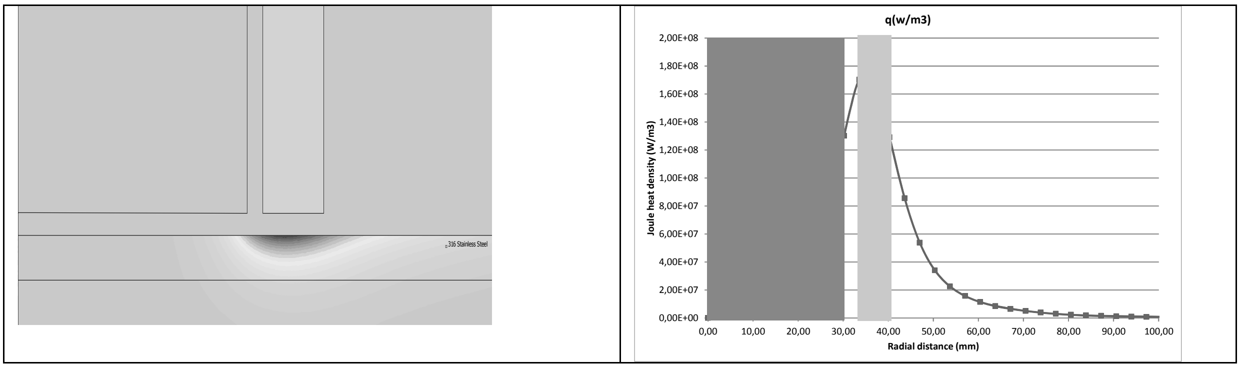

Figure 4: Magnitude of current density (left) and Joule heat source density on the wall surface (right).

This is confirmed by the integral values of the dissipated heat power presented in the table 3. These results indicate, that heat flux boundary condition can be applied to describe the heat source in the considered experimental setup. By decreasing the supply frequency, the skin depth will increase and a volumetric heat source model would be more appropriate.

Table 3: Total dissipated power in stainless steel wall and Pb-Bi

Zone	Power (%)
stainless steel	90.4
Pb-Bi	9.6

As can be seen the heat source density is not homogeneous, the maximum is located under the coil and the minimum is located in the middle of the core. This certainly raises the question on how appropriate is the considered heat source for the modelling proton beam heat deposition, because in the beam the maximum is located in the center. Apparently the proposed method can be used for integral heat transfer model experiments without aiming at precise temperature distributions. At present stage it is assumed that the power is located in the outer half of the radius of the circular surface with diameter 80 mm.

4. Heat transfer model

The heat transfer has been calculated with Ansys Fluent 12. k- ω SST model of turbulence. Pb-Bi properties are taken from [4]. The comparison of measured and calculated values of the temperature at the thermocouple Tc.t8-10. locations (table 4) shows good agreement. Despite symmetrical inductor and thermocouple arrangement, the measured temperature distribution is not symmetrical to the channel middle plane. The downstream geometry has impact on the flow distribution in the heat transfer zone, therefore the results are limited to the specific geometry in the considered experimental setup. The present study has been focusing on the channel part downstream the heated zone, but certain influence is also expected from the upstream geometry.

Table 4: Calculated and measured temperatures

Thermocouple location	Calculated velocity (m/s)	Calculated temperature (°C)	Measured temperature (°C)
Tc.t8	0.85	205.5	201.9
Tc.t9	0.91	197.7	198.4
Tc.t10	0.90	199.9	199.9

3. Conclusion

- The inductive heating can successfully be used for the modeling of the integral heat deposition in the spallation target. The local heat and temperature distributions are different.
- By adjusting the frequency it is possible to achieve different depth of heat deposition.
- Reliable determination of the total power might require some additional measurements of the temperature upstream and downstream the heated zone.
- Heat source density distribution over the surface has to be determined separately experimentally or by solution of corresponding eddy current problem.
- The unsteady character of the flow leads to the temperature fluctuations, decreasing the accuracy of steady state predictions from the measurements.
- The results are limited to the specific geometry in the considered experimental setup. The loop geometry influences the flow conditions in the heat transfer zone, investigated case shows the downstream geometry influence, upstream geometry also might have influence on the flow and, consequently, heat transfer conditions in the heat deposit zone.

4. Acknowledgements.

The financial support of the project No 2DP/260/2.1.1.1.0/10/APIA/VIAA/166 is gratefully acknowledged.

5. References

[1] ESS Technical Design Report. ESS, Lund, 2013.
[2] D. Meeker, “Finite Element Method Magnetics.” dmeeker@ieee.org, p. 158, 2010.
[3] ANSYS, “ANSYS FLUENT 12.0 User’s Guide.” p. 2070, 2009.
[4] “Handbook on Lead-bismuth Eutectic Alloy and Lead Properties, Materials Compatibility, Thermal-hydraulics and Technologies,” OECD/NEA Nuclear Science Committee Working Party on Scientific Issues of the Fuel Cycle Working Group on Lead-bismuth Eutectic, 2007.

EFFECTIVENESS OF THE USE OF TRAVELING MAGNETIC FIELD REVERSALS IN ALLOY STIRRING

OBORIN[1] P., KHRIPCHENKO[1] S., GOLBRAIKH[2] E.
[1]Institute of Continuous Media Mechanics UB RAS, 1 Akad. Korolyov str., Perm, 614013 Russia,
[2]Physics Department, Ben-Gurion University of the Negev, POB 653, Beer-Sheva 84105, Israel
E-mail address of corresponding author: pao@icmm.ru

Abstract : We have used stirring of liquid metal impacted by the travelling magnetic field. As the travelling magnetic field direction changes, the flow is restructured in the bath filled with metal. The flow restructuring is of interest in terms of stirring process intensification. The paper presents the experimental and numeric research into the influence of the flow restructuring on passive impurity stirring process.

1. Introduction

Usually, stirring means a process during which the degree of homogenization increases. Stirring is widely used in industry to intensify preparation of mixtures (alloys in metallurgy). The process intensification enables saving time, energy, resources, and improving the finished product quality and reducing the reject rate.

The impurity stirring research can not be wholly reduced to the velocity field study problem. However, if there is some convection, it is evident that degeneracy of spatial inhomogeneity of scalar field is mainly determine by the velocity field. Herewith the flow structure impacts stirring as much as the velocity amplitude. The paper is concerned with the study of the effect of passive impurity stirring intensity increase during the flow restructuring. The flow restructuring means the change of the flow structure occurring in several seconds.

Application of the external rotating magnetic field reversal mode for impact on liquid metal was suggested in [1]. We used this method as applied to the travelling magnetic field to enable the flow restructuring. In [2] we have already generally studied the formation of stirring flow in molten metal by means of the travelling magnetic field. It was noticed that the impurity homogenization rate is slowed upon formation of “stationary” flow. Herewith, as the numerical study showed, the process can be intensified using the travelling magnetic field direction change (reversing).

The electromagnetic forces in the melt in the mixer furnace bath are determined by amplitude and frequency of the electromagnetic field at the bath wall which is generated by the TMF induction coil current. So, the medium properties, cavity shape, amplitude and frequency of the current wholly determine the stirring process. It can be demonstrated how any change of these parameters influences the flow on qualitative estimate level. However, any estimate of the influence of the travelling magnetic field reversal (TMFR) on the flow structure is a more complicated problem.

To estimate any influence of TMFR on the impurity stirring it is necessary to understand the processes occurring during reversing, especially those in the time interval from the travelling magnetic field direction change till achievement of a quasistationary mode by the flow. To that end some experimental measurements of the reversal mode velocity were performed, as well as numerical simulation of the passive impurity transfer.

2. Experimental details

The experiment was designed with the goal to study the molten metal flow in the reversal mode. The experimental setup consisted of: a bath, a travelling magnetic field induction coil, a power supply, a three-phase transformer. The velocity was measured using an ultrasonic Doppler velocimeter (UDV, model DOP 2000, Signal Processing SA, Lausanne). The bath capacity was 8 L. The bath was manufactured of textolite, the front wall being made of organic glass. The working metal was gallium alloy (Ga 87,5%, Sn 10,5%, Zn 2%), in liquid phase at 170C or higher temperature. The liquid layer height was 9.5 cm. The vertical section of the bath is rectangular trapezoid with 9.5 cm height and 18 and 24 cm bases.

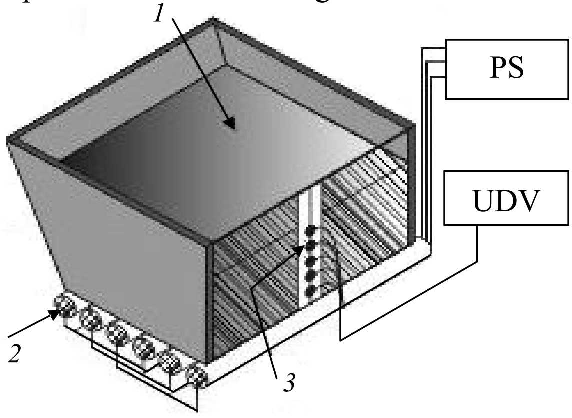

Figure 1: Schematic of the experimental setup. 1. – liquid metal; 2 – magnetic field inductor; 3 – UDV probes; UDV – ultrasonic Doppler velocimeter; PS – power supply.

A travelling magnetic field induction coil located under the bath bottom was used for formation of the flow in the melt. The induction coil created the volume force in the liquid metal directed along the bath bottom parallel to its side walls. The main forces were focused in the skin layer of the electromagnetic field near the bath bottom.

The metal movement velocity was measured using ultrasonic Doppler anemometer (UDV, model DOP 2000, Signal Processing SA, Lausanne) equipped with 4 MHz sensors (TR0410RS diameter 10 mm, Signal Processing SA, Lausanne), operating in multiplexer mode. Five sensors UDV (1-5 channel, sensor numbering is from below upwards, see Fig. 1.) were located on the front ultrasonic-transparent plexiglass wall of the setup on a special, horizontally sliding rail. The center-to-center distance between the neighbouring sensors is 1.5 cm.

3. Numerical simulation

Despite physical simulation is widely used in studying of multiphase media, it is often difficult to observe the conditions of similarity and to conduct experimental measurements which makes it necessary to prefer the numerical simulation when studying the impurity transfer.

There are many approaches and models for the numerical study of multiphase flow behaviour which were embodied in several computation techniques which can generally be classified as one of two Euler or Lagrange methods. For purely Eurlerian methods, a common approach is to make the "one-fluid" assumption in which a number of different fluids are modeled as a single fluid with rapidly varying material properties[3]

As a result, the system to be solved actually looks as follows:

$$\frac{\partial \mathbf{V}}{\partial t} + (\mathbf{V}\nabla)\mathbf{V} = -\frac{1}{\rho}\nabla p + \nu\Delta\mathbf{V} + \mathbf{g} + \frac{\mathbf{f}}{\rho},$$

$$\mathrm{div}\mathbf{V} = 0,$$

$$\frac{\partial C}{\partial t} + (\mathbf{V}\nabla)\mathrm{C} = \nabla \cdot (D\nabla C),$$

We consider the electrically conducting fluid, so the right hand side of the equation includes the electrodynamic body force induced by the travelling magnetic field. The approximate solution for the force in a flat layer of a conducting material induced under the influence of the travelling magnetic field in Fourier space was obtained in [4]:

$$f_x = \frac{9 I_0^{\,2} \mu_0}{\pi^2 R_0^{\,3} e^2 \rho} \frac{ch(2ky)}{ch(2kh)} e^{2i(\omega t - \frac{x}{\lambda})}$$

This system was solved using library interFoam CFD model (included into OpenFOAM). The common property of the computation techniques used in OpenFOAM is the use of a 3D non-structured finite-volume grid, in addition, all models enable vectorizing the computation process.

To estimate the stirring efficiency, we have introduced the stirring efficiency parameter which is just the mean square deviation of concentration in the whole volume. This parameter was normed for a unit to make it convenient.

There are several approaches to stirring estimate. However, the researches use mainly some methods for their particular problem and conditions, for example: achievement of 95% homogenization of scalar field in the volume being mixed [5]. We use the efficient stirring time parameter in out approach. It is the time in which the initial stirring efficiency coefficient decreases by factor of 10.

4. Results

At a first approximation, the hydrodynamics of the process being studied without any use of reversal can be assumed as follows: At first, liquid is resting, once the inductor is switched on, the electromagnetic force accelerates the liquid and in some time the quasistationary flow is set in the liquid. In the experimentally measured mode the flow is one big stable whirl with small unstable whirls near the walls and corners of the bath. The maximum intensity of the flow is near the bottom and surface. The electromagnetic energy is used for the formation of a big whirl, its spin-up and dissipation of the energy on the walls.

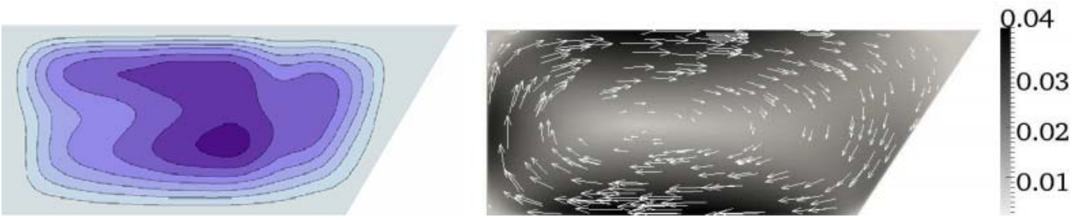

Figure 2:The flow pattern reconstructed using the experimental measurements (left) and the numerical computation results (right).

The results of computations and experimental measurements of the velocity profiles along x axis for 15 Hz frequency values in 200 A induction coil are shown in Fig 3.

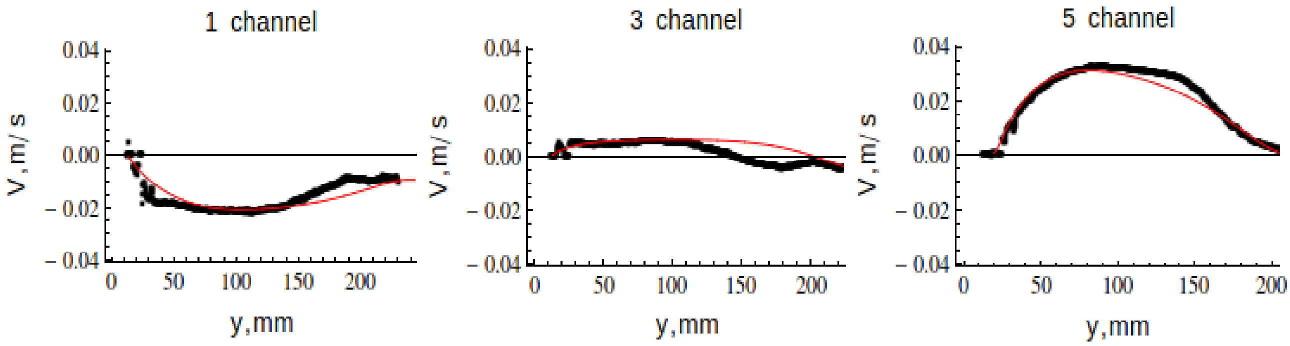

Figure 3: Average velocity profiles (red line) obtained from computations vs experimentally measured profiles (black line).

Fig. 3 illustrates that the numerical simulation results match with the experimental data well.

As the numerical simulation results show, the impurity transfer dynamics in its turn can be illustrated as follows. At first (several seconds after the beginning) the intense dissolution of the impurity occurs. Some temporary whirls stirring the impurity occur. At the same time, the stable flow (a large-scale whirl) is formed. Once the stable whirl is formed and absorbs the impurity, the impurity in the center of the whirl is transferred as a whole due to possible suppression of any turbulent fluctuations, and its rearrangement slows down resulting in the decrease of the rate of the impurity "dissolution". At the same time any turbulence facilitates the impurity breakaway and carrying away to the hydrodynamic swirl due to which stirring continues "slowly and surely".

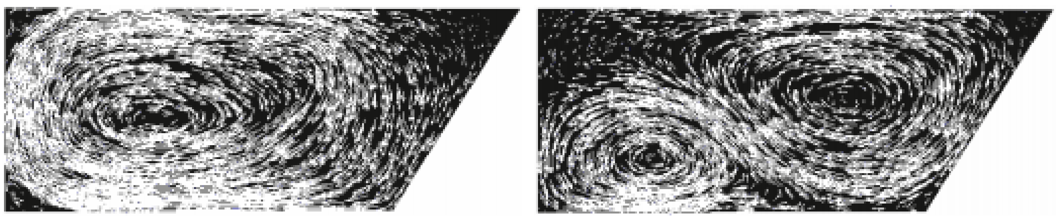

Figure 4: An example of the numeric calculation for 0.01 Hz reversal frequency.

When the reversal is used, the electromagnetic force is controlled in such a way that during the first half of the time interval the electromagnetic force acts in one direction, and during the second half of the time interval it acts in the opposite direction.

Some experiments were conducted to study the reversal at different frequencies. The general conclusion of them was: the flow structure is only determined by the reversal frequency in a particular frequency range. At low frequencies, when the force action in a respective direction is dozens of seconds, the liquid is highly responsive to the force action, and the structure of the flow itself is one or two interacting whirls.

At higher frequencies, when the reversal halfcycle is about on second, the liquid behavior is less predictable. Due to inertia of the liquid, when the low layers are decelerated and turn in the opposite direction, the upper layers still continue to move in the previous direction. So, as the reversal frequency increases, the whole flow is decelerated, becomes more complicated and unstable. The high-frequency reversal prevents the flow from the full development, and the velocity intensity is lower in this case than in the case where it is absent. Thus, the low-frequency reversal, when the stationary mode and transfer mode co-exist, is of interest.

The experimental research into this mode revealed an interesting peculiarity. During the transitional flow some zones are formed in the liquid where the velocity exceeds one under the permanent stirring. Once the main flow is formed, the flow velocity is slowed down. It can be explained by the fact that less energy is consumed for the stationary structure maintenance than for the flow restructuring. During the restructuring a boosted turbulization occurs locally causing the increase of the kinetic energy dissipation and intensifying of the diffusion processes.

The velocity profile formation process during reversal can be divided into several stages:

1. There is a developed flow.
2. After the reversal "the feeding" of this flow is suspended but still functions. At the same time the energy for formation of the other flow is exhausted.
3. At the third stage a new structure is formed, the areas from the new and old structures existing simultaneously. The lack of energy for maintenance of the existing mode results in unstabilities which cause destabilization of the system and its destruction. Because the new flow embraces only some part of the whole volume, the velocity in such a flow exceeds the stationary flow velocity locally.
4. The new structure becomes prevailing, and any rudiments of the old structure disappear.
5. Spin-up of the new structure.

5. Conclusion

This paper investigated any influence of the flow restructuring using the travelling magnetic field reversal on the impurity stirring in the molten metal experimentally and numerically. The impurity homogenization in the flow under investigation proceeds influenced by three inter-related flows: A large-scale transfer of the impurity by big whirls, stirring by means of the full-scale medium movement up to turbulence scale, and stirring by means of the molecular diffusion.

The research showed that the flow restructuring by reversing makes the flow more complex and divides the big and stable whirls into several ones. Thus the use of the reversal makes the energy distribution more uniform over the space. In addition, the reversal enables to locally achieve the short-term velocities exceeding those in a single-direction flow, thus making regions with the increased turbulization in a volume which also facilitate the stirring intensification.

The work is supported by the RFBR (Grant 14-08-96002) and by the project of the International Research Group "Magnetohydrodynamic Stirring of Liquid Metal and Its Influence on the Solidified Alloy Structure".

4. References

[1] Eckert, S. et al.: Efficient melt stirring using pulse sequences of a rotating magnetic field: Part 1. Flow field in a liquid metal column. Metallurgical and Materials Transactions B, 6 (2007) 977–988.

[2] Oborin, P.A.; Khripchenko S.Y. Study of liquid metal flow and passive impurity transport driven by a traveling magnetic field in a rectangular cavity Computational continuum mechanics. 2 (2013) 207-213.

[3] Morgan, G: Application of the interFoam VoF code to coastal wave/structure interaction. PhD Thesis (2012).

[4] Ostroumov, G.: Physical and mathematical foundations of the magnetic stirring melts. Metallurgizdat, Moscow, 1960 (in Russ.).

[5] Roy; S.; Acharya, S; Scalar mixing in a turbulent stirred tank with pitched blade turbine: Role of impeller speed perturbation. J Chemical Engineering Research and Design. 7 (2012) 884-898.

INFLUENCE OF THE SWIRLED ELECTROVORTEX FLOW ON THE MELTING OF THE EUTECTIC ALLOY IN-GA-SN

IVOCHKIN[1] Y., TEPLYAKOV[1] I., GUSEVA[1] A., VINOGRADOV[1] D., PROTOKOVILOV[2] I., TOKAREV[3] Y.
[1]Joint Institute for High Temperatures Russian Academy of Sciences, 125412 Moscow, Izhorskaya 13-2, Russia; vortex@iht.mpei.ac.ru
[2]The E.O. Paton electric welding institute of the National Academy of Sciences of Ukraine 03680 Kiev, Bozhenko 11, Ukraine
[3]The Nuclear Safety Institute Russian Academy of Sciences, 115191 Moscow, 52 B. Tulskaya, Russia

Abstract
It was shown with experimental and computational methods that the process of metal melting essentially depends on the intensity and hydrodynamic structure of electrovortex flows (EVF) developing in smelting furnace. It was found that by controlling the EVF with an external longitudinal magnetic field one can reduce the melting time.

1. Introduction

The so-called electrovortex flow (EVF) is formed by the interaction of an electric current, spreding into the current-carrying fluid volume, with its own magnetic field [1]. It is assumed that in natural conditions electrovortex flow, as well as free convection [2], may be the cause of hydrodynamic structures similar to a tornado. In technology intensive EVF is observed in various high-current technological processes, for example, in the electroarc or electroslag remelting of metal [3]. Hydrodynamic structure of EVF was most fully investigated by numerical methods for working models of melting baths with axisymmetric geometry, in which the electrodes of different diameters were located at the butt-ends of the cylindrical shape container [3 - 5]. In [6] the pioneering measurements of the velocity fields of electrovortex flows were carried out in a cylindrical working section, the results of which indicate their complex multivortex structure. In subsequent studies [7 - 9], devoted to the study of the electrovortex flows formed at the axisymmetric spreading of the electric current from a point source in a hemispherical volume filled with liquid metal, it has been experimentally shown that the hydrodynamic structure of EVT is substantially determined by the intensity and orientation of the external, even relatively weak magnetic fields acting on the experimental setup. In particular, it has been proven by experimental and computational methods that the paradoxical spontaneous horizontal swirl of the axisymmetric electrovortex flow in the hemispherical bath is caused by interaction between spreading electric current in a liquid metal with the magnetic field of the Earth.

Furthermore it has been found that intensive swirling flow around the horizontal axis of the bath, due to the influence of the external longitudinal magnetic field leads to the formation of secondary vortices in the vertical plane and suppression the downward flow in the volume of current-carrying fluid, except a small region near the small electrode. Based on the results of earlier studies, one can assume that the presence of EVF and change of their hydrodynamic structure under the influence of the external magnetic fields affect the metal melting process. However, the analysis of literature revealed no studies on the quantitative characteristics of this effect.

Therefore, we have carried out additional experimental and computational studies on the influence of EVF on electrosmelting of metals, methods and the results are shown below.

2. Experimental setup, measurement and calculation methods

Experimental studies simulating EVF applied to electroarc remelting process were carried out at the setup shown in Fig. 1. An eutectic indium-gallium-tin alloy (weight content: Ga – 67%, In – 20.55, Sn – 12.5%, melting point +10.5 0C) was used as the working liquid in the experiments. Alloy filled copper hemispherical container with a diameter 188 mm which also served as a large electrode. Small electrode - copper cylinder with diameter 5mm with hemispherical end was immersed into the alloy in the middle of the working bath. Physical properties of the alloy are given in [10]. Power source developed on the basis of three-phase AC rectifier ($I \le 1500A$) was used to supply an experimental setup. To create an external longitudinal magnetic field the coil consisting of 15 turns of hollow copper tube (cooled with pumped water) was used. Coil power was supplied from a stabilized power source, providing smooth control of DC in the range from 0 to 100A. This system allowed to get the magnetic field with induction B = 5 × 10-3 T in the middle of the working area at a current of 100A.

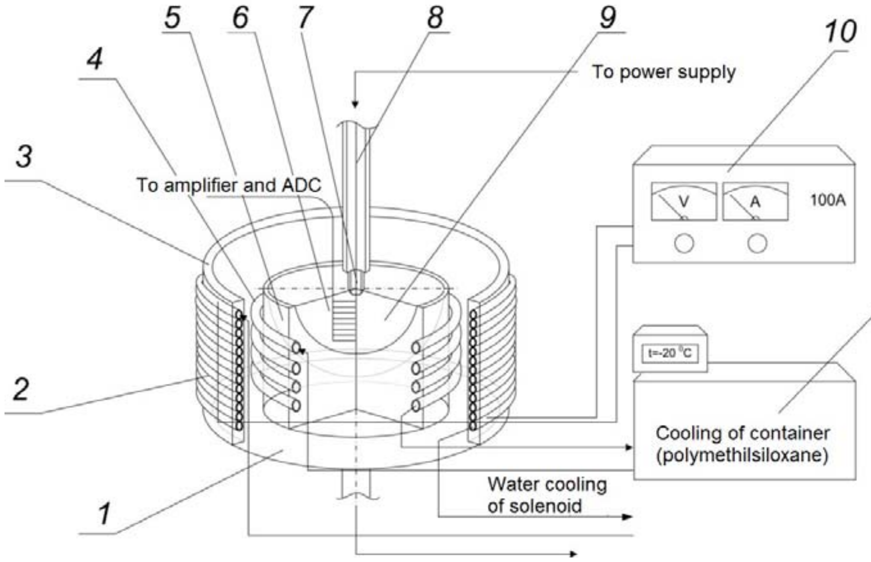

Fig. 1. Experimental setup. *1* — cooling vessel, *2* — water-cooled solenoid, *3* — heat insulation, *4* — heat exchanger, *5* — copper container, *6* — thermocouple probe, *7* — small electrode, *8* — current lead, *9* — eutectic alloy In-Ga-Sn, *10* — power supply of solenoid, *11* — refrigerator.

Before the experiments special coolant - polymethylsiloxane (PMS-5) at a temperature of 250C was poured into a cylindrical cooling tank, located in the gap between the working section and a solenoid. In addition, polymethylsi-loxane was pumped through the heat exchanger - tube wrapped around the copper container filled with alloy. These preliminary procedures allowed to cool alloy In-Ga-Sn up to 0^0C (at the air temperature 25^0C), i.e. substantially below its freezing temperature of ~ 10^0C. After liquid solidification in the whole volume of the hemispherical container, polymethylsiloxane was poured from the bath cooling system. Then an electric current was passed through the working area and heating and melting of liquid metal happened The probe-comb consisting of 8 chromel - alumel thermocouples with diameter of junction 0.5 mm was used to get thermograms in the volume of the alloy. The width and depth of the molten zone were measured with a special probe.

In a numerical study of the influence of EVF on the metal melting process, so-called enthalpy-porous model built-in software package ANSYS Fluent was used [11]. In this model two-phase zone liquid - solid is considered as a porous medium with a porosity equal to the propor-tion of the liquid phase, and the pressure loss caused by the presence of not molten material was taken into account by introducing of an additional dissipative term into the motion equation. The conservation equations system of momentum, enthalpy and continuity was solved in inductionless approximation, i.e., consideration of the influence of magnetic field on the velocity field and the temperature was taken into account by addition of the Ampere force **F** = **j** × **B** in the motion equation.

To determine the current density **j** in all elements of the working area, including both electrodes, the equation for the electric potential Φ (div(σgradΦ) = 0) was solved with boundary conditions at the upper and lower end of the current leads $\Phi=\Phi_0$ and Φ=0 corresponding to a complete electrical current flowing through the setup. Current density **j** was calculated from the equation **j** =-gradΦ. More complete description of the calculation of the magnetic fields and forces acting on the electroconductive liquid is presented in [12]. At solving the motion equation, no-slip conditions were set on all surfaces, including open surface of metal because solid oxide film has been formed on it. For the energy equation on the borders with the air free convection conditions were set, and the temperature of the environment was considered 25^0C.

3. Results

Typical results of experimental studies on the spreading of the melting front deep down into the bath and the metal surface are shown in Fig. 2. Shapes of the melting curve boundary at different times in the whole volume of the metal shown in Fig. 3. Experiments were carried out at a current I = 400 A at the presence of the Earth's natural magnetic field (EMF), and adding there an artificially created longitudinal (relative to axis of the setup) magnetic field of solenoid with induction B = 5 × 10^{-3} T. The table below shows some data on rate and time of melting.

As seen from these graphs, there is a significant difference in the shape of the melting front with the presence of artificially generated external magnetic fields, and its absence.

In the first case, the shape of this curve follows the shape of the melting pool, and under the influence of EMF melting front has a typical shape elongated along the axis of the bath. Also the time of complete melting of the metal in the bath under the influence of an external magnetic field was 12% lower than in its absence.

Analyzing presented results one can assume that the process of melting in the processing bath is as follows. At the start of heating of the metal with the electric current, a small portion of metal near small electrode melts.

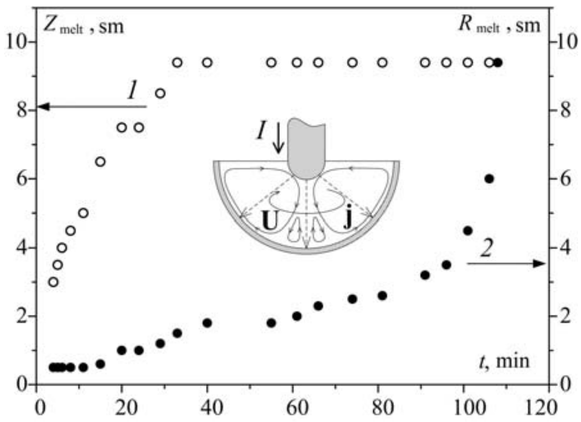

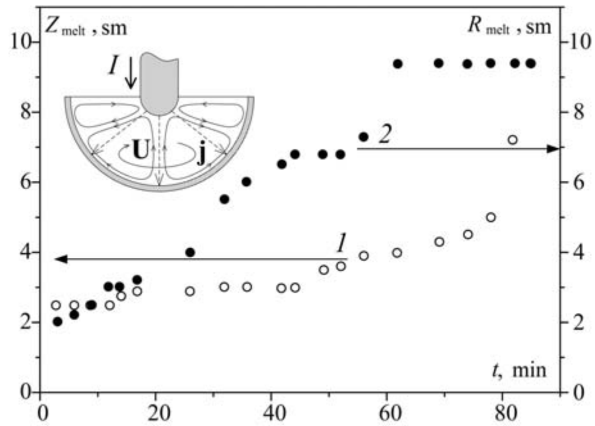

Fig 2. Moving the melting front in the direction of the axis of the metal bath and radially on its surface. I = 400A. Influence of (a) – Earth's magnetic field (EMF) (B~5×10^{-5}Тл); (b) – EMF and solenoid B= 5×10^{-3} Тл. *1* и *2* – coordinates of melting point on axis and radius of the bath.

EVF occurs in the molten liquid volume, and in the ideal case, the absence of an external magnetic field EVF is a single axisymmetric toroidal curl, creating a jet axial flow under a small electrode [1]. Influence of EMF leads [8] to the azimuthal rotation developing in the current-carrying liquid. This movement of the melt in the horizontal plane leads to the generation of secondary vertical vortex near the bottom area which, although directed opposite EVT, but because of its relatively low intensity has no significant effect on the original structure of EVF (see Fig. 2a). Hot melt flow causes intense melting of the metal in the direction of axis Z, and melting in axis R direction became appreciable only when the liquid phase of the metal reaches bath bottom. Under influence of external longitudinal magnetic field of the solenoid, azimuthal swirl of the liquid also occurs in the horizontal plane in the working bath, but this swirl is more intense than under the influence of EMF. This rotation leads to generation of the strong secondary vortex in the vertical plane moving the melt upward along the axis of working area, and to weakening of primary EVF (Fig. 2b). Moreover intense azimuthal motion of the fluid enhances heat and mass transfer processes in the horizontal plane, thereby increasing metal melting rate in a radial (in the cylindrical coordinates) direction.

The results of numerical calculations (see Fig. 3) are qualitatively consistent with the results of experiments and confirm the melting flow processes described above. The observed quantitative differences can be explained, in particular by to some uncertain parameters (e.g., the value of effective porosity in the mushy zone). Also it should be noted the considerable complexity of calculations because the duration of calculation of one melting mode on the PC with 4-cores processor was more than one month.

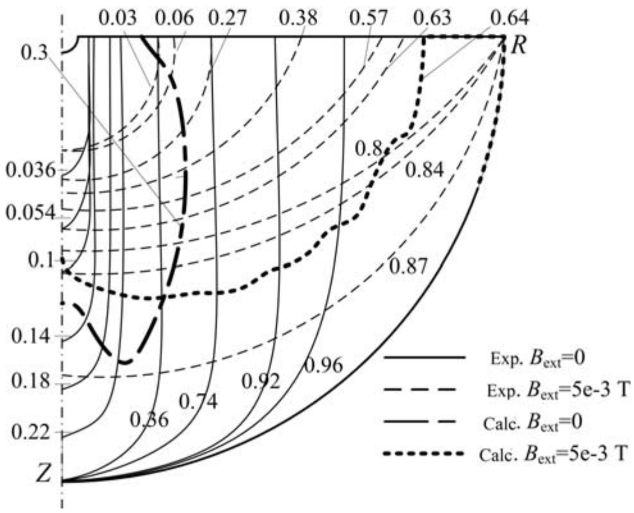

Fig.3. Melting front spreading with an external magnetic field and without. I = 400 A. The numbers on the lines - time from the beginning of the experiment, divided by the time of full molten of metal.

	Total melting time	Average melting rate along Z-axis	Average melting rate along R-axis
With magnetic field B=5×10^{-3} T	1 h 38 min	0.10 sm/min	0.14 sm/min
Without magnetic field	1 h 50 min	0.24 sm/min	0.09 sm/min

4. Conclusions

As a result of experimental and numerical studies there was found that the impact of constant axial (longitudinal) magnetic field leads to an intensification of the processes of melting and reduction of melting time. The mechanism of this phenomenon is connected with the occurrence of the azimuthal swirl of melt metal in these conditions and the radical transformation of the flow in a hemispherical bath with a central electrode. Hydrodynamic structure of flows formed in the working bath leads to more intensive (due to the formation of additional reverse flows) removal of heat from the hot region near the small electrode deep into melt. Furthermore, due to occurrence and interaction of additional large eddy formations, the direction of the prevailing EVF changes. For this reason the melting front loses axial and gets a radial direction.

Let note two important practical circumstances. First, the way to create external magnetic fields near the melting units with a solenoid is the most simple method. Second, many baths of industrial arc furnaces has a horizontal orientation (ratio of diameter to depth ~ 5:1) Therefore, it can be assumed that the effect described above can be used in these devices to intensify the melting process in the radial direction and increasing its energy efficiency.

This work was supported by RFBR/SFBR of Ukraine, grant No.13-08-90444 and 53.7/027.

LIST OF SYMBOLS

B — magnetic field induction, T;
F — Ampere's force, N/m^3;
j — electric current density, A/m^2;
I – electric current, A;
t – time, min;
σ – conductivity, S/m;
Φ – electric potential, V.

References

[1]. Bojarevich V., Frejbergs Ja., Shilova E.I., Shcherbinin E.V., 1989. Electrically induced vortical flows. Khuwer Acad. Publ., Dordrecht, Boston, London.

[2]. A.Y. Varaksin, M.E. Romash, V.N. Kopeitsev. Effect of net structures on wall-free non-stationary air heat vortices. International Journal of Heat and Mass Transfer. 2013. V.64. P. 817 – 828.

[3]. Kompan Ya.Yu., Shcherbinin E.V., 1989. MHD controlled electroslag welding and smelting. Mashinostroenie, Moscow.

[4]. Vlasyuk V.Kh., 1988. Turbulent electrovortex flows in a cylindrical space. Magnitnaya Gidrodinamika 24, 328 333.

[5]. V. Kh. Vlasyuk and E. V. Shcherbinin. Electrically induced vortical flows in a two-layer fluid, Magnetohydrodynamics, Vol. 35, No. 1, 13-20, 1999. P. 17 — 27.

[6]. V. G. Zhilin, Yu. P. Ivochkin, A. A. Oksman, G. R. Lurin'sh, A. I. Chaikovskii, A. Yu. Chudnovskii and E. V. Shcherbinin, An experimental investigation of the velocity field in an axisymmetric electrovortical flow in a cylindrical container, Vol. 22, No. 3, 323-328, 1986.

[7]. Zhilin V., Ivochkin Yu., Igumnov V., Oksman A. Experimental investigation of the electrovortex flows in hemispherical volume. High Temperature. Vol. 33, № 1, 1995, p. 3 – 6.

[8]. Ivochkin Yu, Teplyakov I., Guseva A., Tokarev Yu.. Numerical and experimental investigation of the swirled electrovortex flow structure. Thermal Processes in Engineering, 2012. №8. p.345-352.

[9]. V. G. Zhilin, Yu. P. Ivochkin, I. O. Teplyakov. The problem of swirling of axisymmetric electrovortex flows, vol. 49, № 6, 2011, p. 927-929.

[10]. V. Ya. Prokhorenko, E. A. Ratushnyak, B. I. Stadnyk, V. I. Lakh, and A. M. Koval. Physical properties of thermometric alloy In-Ga-Sn. High Temperature vol.8. №2, 1970. p.374.

[11]. V. R. Voller and C. Prakash. A Fixed-Grid Numerical Modeling Methodology for Convection-Diffusion Mushy Region Phase-Change Problems. Int. J. Heat Mass Transfer. 30. 1709–1720. 1987.

[12]. Ivochkin Yu, Teplyakov I., Guseva A., Lozina E., Klemetyeva I., Tokarev Yu. Investigation of the free surface deformation and its influence to intensity of electrovortex flow of liquid metal. Thermal Processes in Engineering, 2012. №11. p.487-495.

[13]. Nazarchuk A., Protokovilov I., Porokhonko V., Ivochkin Yu., Teplyakov I. Features of inducing pulsed magnetic fields for magnetically-controlled electroslag melting. Advances in electrometallurgy. №4б 2013., p.21-13.

[14]. Protokovilov I., Nazarchuk A., Porokhonko V., Ivochkin Yu., Vinogradov D. Methods of generation of external magnetic fields for control of electroslag welding process . The Paton Welding Journal 2013, №12 (727). p. 45.

[15]. Yachikov I. Mathematical simulation of the electrovortex flow and heat and mass transfer in current-carrying melt of the metallurgical units. Magnitogorsk. 2009, p,363.

MODEL EXPERIMENTS FOR INVESTIGATIONS OF HEAT TRANSFER PHENOMENA IN THE CZOCHRALSKI CRYSTAL GROWTH

PAL J, CRAMER A, ECKERT S, GERBETH G, GRANTS I
Helmholtz-Zentrum Dresden-Rossendorf (HZDR), Institute of Fluid Dynamics, Magnetohydrodynamics, P.O. Box 510119, 01314 Dresden, Germany
e-mail address of corresponding author: j.pal@hzdr.de

Abstract: A low temperature liquid metal model of the Czochralski crystal growth process is considered experimentally under conditions of high aspect ratio. We focus on the influence of a rotating magnetic field (RMF) and/or crystal rotation on temperature fluctuation near the crystal edge. The radial flow structure is observed by ultrasound Doppler velocimetry (UDV). It is concluded that the effect of RMF on the temperature fluctuation is less expressed than in a Rayleigh-Bénard cell.

1. Introduction

About 95% of the mono-crystalline silicon is produced by the Czochralski (Cz) method. In the process, a single seed crystal is attached to the free surface of molten high purity silicon in a cylindrical quartz crucible. Under rotation and simultaneous pulling of the seed the melt crystallizes and a mono-crystalline rod develops as the final product. The fluid flow inside the crucible serves as a carrier for mass and temperature and affects crucially the quality of the growing crystal.

The RMF is known to efficiently suppress the Rayleigh-Bénard (RB) instability in a liquid metal cylinder of a size that is relevant for industrial Cz growth [1]. It has been speculated that this RMF property may better stabilize the melt than the Cz crucible rotation allowing, thus, to increase the initial filling height. The current study aims to test this hypothesis in a low temperature model of the Cz process. This is why we use a melt aspect ratio a=H/D=0.59 that is much higher than usual in industry. Besides, this value marks the transition between axisymmetric and mono-cellular convection in the RB cell [2].

The existence of a triple point in the Cz system is one of the most important differences to the RB cell. This is the point where the free surface of melt meets the growing crystal. Flow and temperature conditions at this point have a particularly profound effect on the quality of the end product. Therefore, our study is focused on measurements in the vicinity of this point. For details concerning the relevant theoretical background and the experimental setup we refer to [2,3].

2. Experimental setup

The central part of the setup comprises the double-walled glass crucible (diameter D) filled up to a height H with liquid GaInSn, where H is equal to the melt volume divided by the top surface area. A photograph of the crucible is shown on the left side of Fig. 1. Heating was controlled by passing thermostated silicone oil through the wall gap. The growing crystal is simulated by a co-axially mounted copper cylinder cooled by thermostated water (so-called cold finger). The cold finger is immersed about 3 mm into the liquid GaInSn.

Two versions of temperature boundary conditions are realized at the free melt surface: (1) air-cooled surface with practically negligible heat loss, and (2) water cooled surface as shown in Fig. 1. The second version is meant to better model radiative heat loss in the Cz process. For purpose of surface protection from oxidation a weak aqueous solution of KOH is added to the surface of GaInSn. This layer is cooled by thermostated copper coils.

As the experiment was demounted in the interval between the measuring campaigns conducted for both versions of surface cooling, additional measurements were carried out to check the reproducibility of the results (see next section). For applying an RMF for electromagnetic flow control in the crucible, the experiment was mounted inside the coil system MULTIMAG, whose features are described in [4].

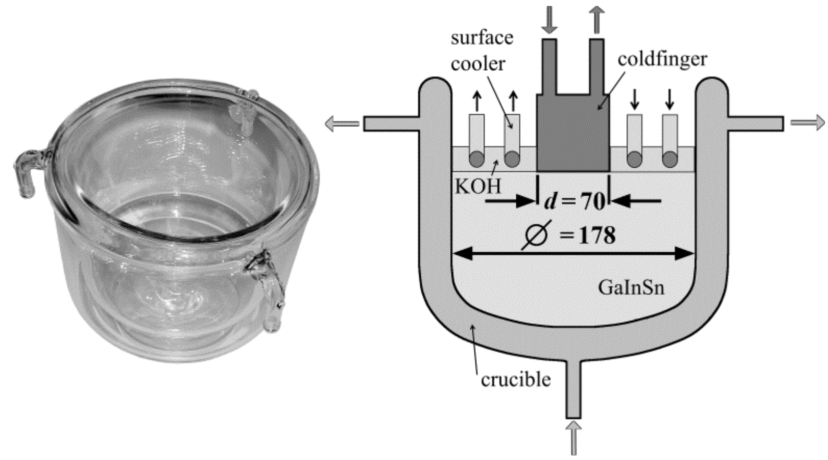

Figure 1: The left photo depicts the double-walled glass crucible. The right part shows a sketch of the experimental setup with the cold finger modelling the growing crystal and the additional surface cooler.

3. Results

The UDV technique was used to measure the radial component of the fluid velocity slightly below the free surface. The ultrasonic sensor was immersed into the melt at several azimuthal positions close to the inner rim of the crucible. The first series of experiments was performed in a setup version with the air-cooled free surface. The flow measurements were repeated several times in order to check the reproducibility of the results. Fig. 2 displays the radial component of the fluid velocity measured beneath the free surface. The grey circle marks the area which is covered by the cold finger. The measurements reveal a complex flow structure which may occur similarly in a Cz crucible. A converging flow can be observed at the surface indicated by the arrows at the inner rim of the crucible. However, the flow pattern is not axisymmetric. The thick black lines illustrate a dominating flow direction which extends beyond the axis whereas the thick grey lines show an inwards flow which does not reach the axis of the crucible. The ellipses highlight the zones where a conversion of the flow direction was observed.

Fig. 2 compares two different flow regimes measured before and after rebuilding the experimental facility, respectively. A stable flow structure, Fig. 2a, was observed during the first measuring campaign [2]. The flow measurements shown in Fig. 2b were performed after the reconstruction. The additional surface cooling was not yet installed in this case, so that identical thermal boundary conditions can be assumed. On the contrary, the flow regime shown in Fig. 2b developed occasionally, remained for several hours and changed then again to the first one. The reason for such random changes between these two regimes is not yet clear. Although big efforts were made to reproduce identically the first setup, remaining uncertainties such as axis tilting or slightly different filling levels of the GaInSn may cause these effects. However, both flow regimes show a comparable behaviour, the major difference is a rotation of about 160° around the centre axis.

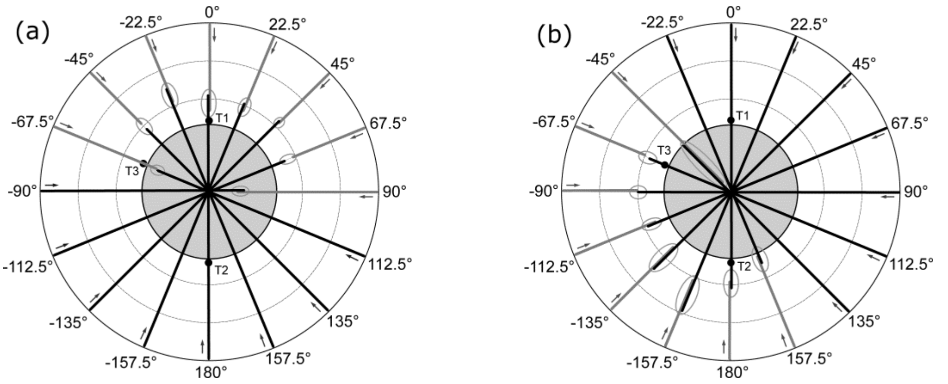

Figure 2: Top-view visualization of two flow regimes just below the surface. (a) as measured in the first setup (cf. Fig. 7 in [3]); (b) second setup but still without the surface cooler. T1 to T3 indicate the places where thermocouples were positioned.

The following temperature measurements reported here were carried out with the activated surface cooler. Motivated by the UDV measurements, three distinct azimuthal positions (cf. positions T1-T3 in Fig. 2.) were chosen to monitor the temperature near the triple point. Temperature time series recorded in the pure buoyant case (without RMF or rotation of the cold finger) are shown in Fig. 3. The differences with respect to the absolute value of the temperature and the amplitude of the temperature fluctuations demonstrate the non-axisymmetric character of the flow.

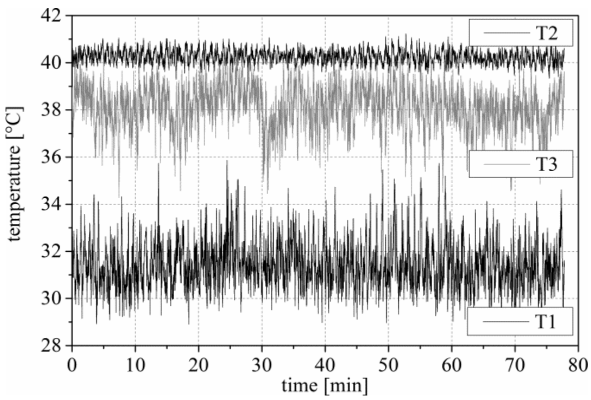

Figure 3: Temperature time series in the pure buoyant case showing the non-axisymmetric character of the flow. T1, T2 and T3 indicate at which positions the signals were recorded.

The temperature fluctuations detected at the positions T1 and T3 are much more pronounced compared to the signal recorded at position T2 and indicate, thus, the flow regime shown in Fig. 2a may be present in this case. The measuring positions T1 and T3 are located close to the zone where opposite streams of the radially inward flow collide. This zone is characterized by a highly turbulent flow. In contrast, the ascending fluid at the azimuthal position 180° flows towards the centre, reaches position T2 and passes the cold finger without distinct perturbation. Therefore, the fluctuations in the temperature are there less compared to the other positions. Under the cold finger the fluid cools down and meets, after passing T1, the fluid coming from the opposite side at the azimuthal position 0°.

From the knowledge about such a flow structure it becomes comprehensible why the crucible and/or the crystal in a growth facility need to be rotated. It would be difficult to grow a circular, high quality single crystal under such asymmetric flow conditions. In order to approach a more axisymmetric temperature distribution, the rotation of the crystal is applied as a method to modify the temperature field. An alternative method in comparison to mechanical rotation can be the generation of a melt rotation by applying an RMF. The impact of an RMF is described by the dimensionless Taylor number Ta [2, 3].

Whatever kind of rotation is applied to the system, the thermal structures will be transported by the fluid flow. Fig. 4 shows temperature measurements for both cases of cold finger and RMF rotation. The time series were recorded at the position T2. Furthermore, the rotational parameters applied were varied in a wide range: Ta between 2.0×10^5 and 2.0×10^8; the revolution rate of the cold finger from 5 up to 55 rpm. In both cases a characteristic oscillation frequency of the temperature signal was observed which indicate the advection of the thermal structures. The diagram on the left side in Fig. 5 summarizes these results.

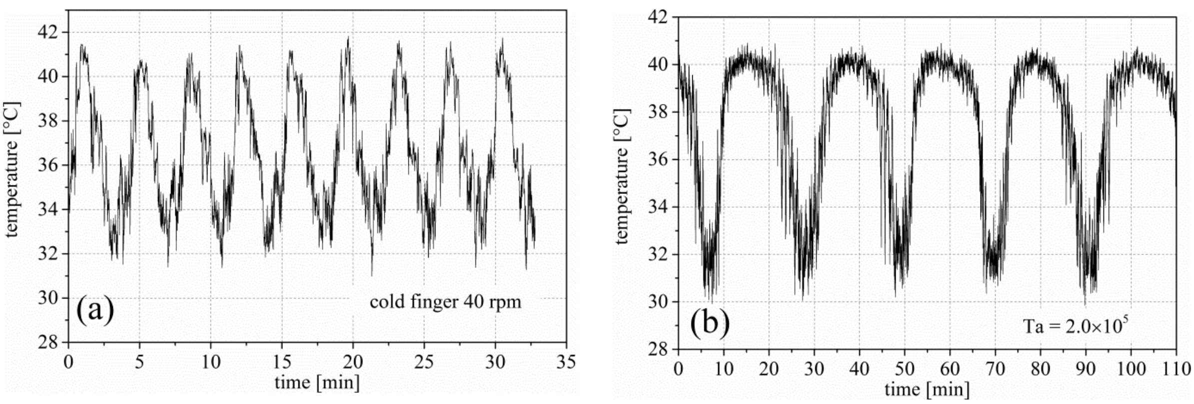

Figure 4: Measured temperature time series at T2 under the influence of (a) cold finger rotation, and (b) of the RMF. Similar large oscillating temperature structures occur at T1 and T3 too, but with a certain phase difference caused by the rotation of the fluid.

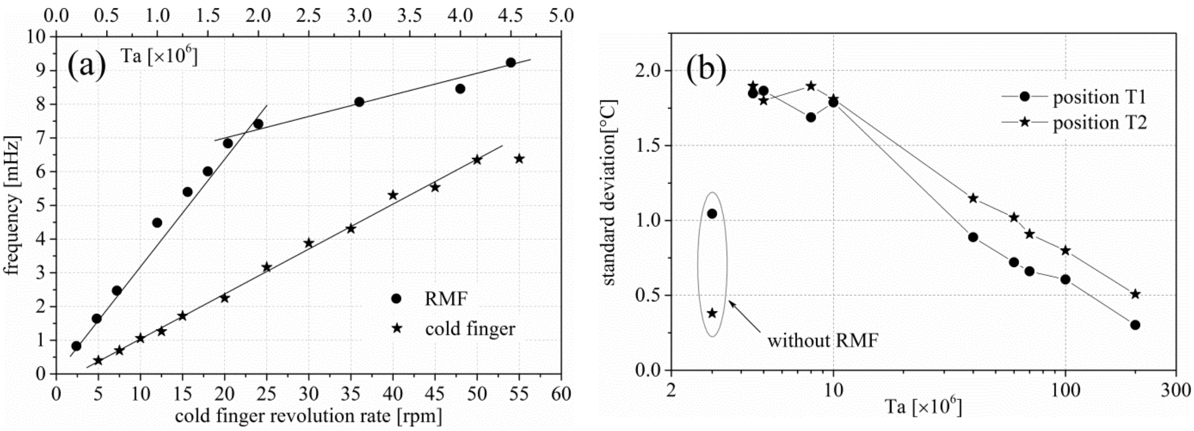

Figure 5: (a) Rotation rate of the thermal structures as function of the cold finger revolution rate (lower abscissa) and of the Ta number (upper abscissa). (b) Standard deviation of the temperature fluctuations in the higher Ta number range after break down of the regular thermal structures.

The oscillation of the thermal structures was observed up to the maximal possible cold finger revolution rate. In contrast, for application of an RMF at Ta numbers up to approximately 4.5×10^6 two "scaling" ranges were detected. Going to higher Ta numbers beyond 4.5×10^6 the previously observed regular thermal structures break down. With increasing Ta, cf. diagram in Fig. 5b, the standard deviation of the temperature fluctuations decrease and reach typical values found in the mere buoyancy case for relatively high Ta numbers.

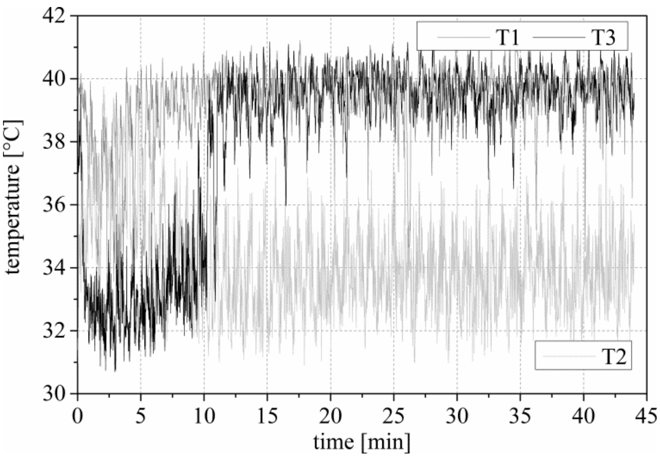

Figure 6: Temperature time diagram for a combination between an RMF and an oppositely rotating cold finger.

It is clear that thermal structures such as shown in Fig. 4 may not be very beneficial for the growth of high quality single crystals. However, a combination of the RMF forced rotation and an oppositely rotating cold finger appears to be a promising approach to achieve a symmetric flow without distinct large-scale temperature fluctuations. Such a measurement is shown in Fig. 6. In this situation, an RMF with Ta = 6.0×10^5 (equivalent to a thermal structure rotation rate of 2.5 mHz as seen in Fig. 5a) was first applied to the melt. Then, the corresponding revolution rate of the cold finger with 21 rpm was switched on (t = 0min). Fig. 6 demonstrates that the large thermal structures disappear after approximately 10 to 15 minutes.

4. Summary and outlook

Flow velocities and temperatures are measured in a Cz model with a high aspect ratio. Influence of crystal and/or RMF driven melt rotation on temperature fluctuation is investigated in vicinity of the triple point. Separately applied RMF stirring or crystal rotation causes large scale rotating structure that is an inferior condition in crystal growth. An appropriate combination of the RMF and crystal rotation brings this structure to standstill. It is concluded that the stabilizing RMF effect in the present Cz model is much less expressed than in an RB cell.

Acknowledgements: The research is supported by the German Helmholtz Association in frame of the Helmholtz-Alliance “LIMTECH”.

5. References

[1] I. Grants, G. Gerbeth, Transition between turbulent magnetically driven flow states in a Rayleigh-Bénard cell, Physics of Fluids 24,2 (2012) 024103.

[2] A. Cramer, J. Pal, G. Gerbeth, Ultrasonic flow measurements in a model of a Czochralski puller, Flow. Meas. Instrum. 37 (2014) 99-106.

[3] A. Cramer, J. Pal, G. Gerbeth, Model experiments for the Czochralski crystal growth technique, European Physical Journal - Special Topics 220 (2013) 259-273.

[4] J. Pal, A. Cramer, Th. Gundrum, G. Gerbeth, MULTIMAG - A MULTIpurpose MAGnetic system for physical modelling in magnetohydrodynamics, Flow. Meas. Instrum. 20 (2009) 241-251.

FLUCTUATIONS IN MEAN-FIELD DYNAMOS

SOKOLOFF D.
Moscow State University, Moscow, 119991, Russia
sokoloff.dd@gmail.com

Abstract: Conventional astrophysical dynamo models are usually formulated in terms of mean-field dynamos. This approach do not include in an explicit form magnetic field fluctuations as well as fluctuations of the dynamo governing parameters. Both types of fluctuations surely are presented in dynamos. We discuss how to include them in the mean-field description and what is the role of fluctuations in the astrophysical phenomenology.

1. Introduction

A traditional approach in treatment of various physical problems in random media is based on a consideration of mean-field equation for the physical field under investigation. This approach in dynamo theory was developed about 50 years ago and is known as mean-field dynamo. Of course, it is possible now to avoid mean-field approach and addresses a dynamo problem in the framework of direct numerical simulations only. The point however is that the mean-field description of a dynamo problem remains important for interpretation of results of direct numerical simulations. Particularly important roles plays mean-field dynamos in astrophysical problems because our knowledge concerning internal structure of remote celestial bodies is usually very limited and gives some mean quantities only. A specific feature of mean-field dynamos is that the number of the random turbulent or convective shells which are involved in the averaging in development of mean-field dynamo models is usually rather large (say, $N=10^4$) however is much lower than, say, Avogardo number which controls averaging in molecular physics. Correspondingly, fluctuations in mean-field dynamos play a much more important role in mean-field dynamos rather in other domains of statistical physics.

Here we present a review of a sequence of recent papers, which consider the role of fluctuations in mean-field dynamos. We argue that the most important kind of fluctuations is fluctuations of the α-coefficient, which plays a crucial role in many mean-field dynamos. The point is that the α-effect is usually quite weak (a naive estimate is $\alpha \approx 0.1\, v$ where v is the rms velocity) and one can expect 10% - 20% fluctuations of α for $N = 10^4$. We argue that this level of α-fluctuations in solar dynamos is sufficient to explain such phenomena as the famous Maunder minimum and other transient phenomena in solar cyclic activity. A possible role of the α-fluctuations in geodynamo is discussed.

We discuss a possible role of large-scale fluctuations of the mean-field velocities and their possible importance for advective dynamos as well as the large-scale manifestations of small-scale magnetic fluctuations in solar mean-field dynamos.

2. Mathematical implementation

Introducing fluctuations in a mean-field description we face some mathematical problems. The point is that the mean-field equations contain mean values of various microscopic quantities, i.e. non-random quantities only. In order to overcome this problem we have to include in the theory two kind of random quantities and two kind of averaging. The first averaging gives conventional mean-field equations while the second type of randomness remains to describe fluctuations of the dynamo governing parameters (mainly α) and fluctuations of the mean magnetic field. In practice these fluctuations are modeled by a proper random number generator and then are governed by the standard mean-field equations.

We consider solutions for individual realizations of the fluctuations and play with the random number generator to mimic the whole variety of the models. In principle, one could try to perform an additional averaging of the conventional mean-field equations taken over the ensemble of the fluctuations under discussion. We performed an exploratory investigation for this supplementary approach to recognize various mathematical difficulties arising. At least for the instant, we prefer to stay on the safe side and avoid any averaging of, say, α-fluctuations.

The format of mathematical description of the problem chosen follows conventional traditions of, say, molecular physics. In our opinion however mathematical foundation of this choice deserves a further discussion.

3. An example: Magnetic cycles in M-dwarfs.

Below we present an example [1] of the options which open the approach under discussion to explain astronomical phenomenology. The example deals with a particular type of stellar magnetic activity known for so-called M-dwarfs which are fully convective stars slightly smaller than the Sun.

M-dwarfs demonstrate two types of activity: 1) strong (kilogauss) almost axisymmetric poloidal magnetic fields; and 2) considerably weaker non-axisymmetric fields, sometimes including a substantial toroidal component.

Dynamo bistability has been proposed as an explanation. However it is not straightforward to obtain such a bistability in dynamo models. On the other hand, the solar magnetic dipole at times of magnetic field inversion becomes transverse to the rotation axis, while the magnetic field becomes weaker at times far from that of inversion. Thus the Sun resembles a star with the second type of activity. Paper [1] suggests that M-dwarfs can have magnetic cycles, and that M-dwarfs with the second type of activity can just be stars observed at times of magnetic field inversion. Then the relative number of M-dwarfs with the second type of activity can be used in the framework of this model to determine parameters of stellar convection near the surface.

Many solar observers have reported that the solar magnetic dipole does not vanish during the reversal while mean-field solar dynamo models predict an oscillating mean solar magnetic field whose magnetic dipole moment have to vanish at each activity cycle (11 years).

This apparent contradiction between expectations from dynamo modelling and observation can be resolved as follows [2]. The point is that a mean-field dynamo model deals with *mean* magnetic field and the averaging is performed over an ensemble of convective velocity cells, while the observational magnetic dipole data refer to *large-scale* magnetic field. Both quantities coincide for an infinitely large ensemble of convective cells, but in practice the number of cells is only moderately large. Because the convective cell ensemble contains a not extremely large number of cells, large-scale fluctuations of magnetic field arise which yield a fluctuating component $\delta\mathbf{d} = (b/B)\, N^{-1/2}(B_P/B_T)$ of the solar magnetic dipole $\mathbf{d}$. Here b is the rms value of small-scale magnetic field, i.e. the magnetic fluctuations, B is the typical value of the mean magnetic field which is determined mainly by the toroidal magnetic field B_T and the factor B_T/B_P takes into account that the magnetic dipole moment is determined by the poloidal magnetic field B_P.

The fluctuating part of the magnetic dipole is larger than the part determined by the mean magnetic field is about 4 months, i.e. about 3% of the solar magnetic cycle [3]. Assuming that the magnetic activity of M-dwarfs is more-or-less similar to that of the Sun, we can convert the relative time $\delta t/T$ during the magnetic activity cycle during which the magnetic dipole is determined by magnetic fluctuations and is strongly inclined to the rotation axis and expect that 3% of M-dwarfs should exhibit the second type of activity.

We can say also what physical parameters are required, e.g. N, to get a satisfactory correspondence with the observational data. In particular, if we want to explain that about 30% of M-dwarfs demonstrate the second type of activity, we have to assume that the number of convective cells at the surface of M-dwarfs is about two order of magnitudes lower than near the surface of the Sun, i.e. 10^2 instead of 10^4. Given the much greater relative depth of the convection zone in M-dwarfs compared to the Sun, an increase in the size of convection cells and corresponding decrease of N is not implausible.

4. Conclusion

The idea to include the dynamo governing parameters as well as magnetic field fluctuations in the mean-field dynamo models opens new perspectives to explain various features of magnetic activity known for various celestial bodies. Possibly, the idea can be useful as well for interpretation of laboratory dynamo experiments for which the dynamo generated magnetic field also can demonstrated a random behaviour (e.g. [4]).

Acknowledgements. Financial support from RFBR under grant 12-02-00170a is acknowledged.

5. References

[1] Kitchatinov, L.L.; Moss, D.; Sokoloff, D.: Magnetic fields in fully convective M-dwarfs: oscillatory dynamos vs bistability, arXiv:1401.1764, accepter to the MNRAS.

[2] Kitchatinov, L.L.; Moss, D.; Sokoloff, D.: Reversals of the solar dipole, Astronomy and Astrophysics, 550 (2013), L9, 4 pp., 2013

[3] Moss, D.; Pipin, V. V.; Sokoloff, D. D.; Hoeksema, J. T.: Reversals of the solar magnetic dipole in the light of observation\-al data and simple dynamo models, arXiv:1312.6379 (2013).

[4] Berhanu, M.; Monchaux, R.; Fauve, S.; Mordant, N.; Petrelis, F.; Chiffaudel, A.;Daviaud, F.; Dubrulle, B.; Marie, L.; Ravelet, F.; Bourgoin, M.; Odier, Ph.; Pinton, J.-F.; Volk, R.,:Magnetic field reversals in an experimental turbulent dynamo Europhys. Lett. 77 (2007), 59001, 5.

Mean-field coefficients for helical flow fields

GIESECKE A., STEFANI F., GERBETH G.
Helmholtz-Zentrum Dresden-Rossendorf, P.O. Box 510119, D-01314 Dresden – Germany
e-mail: a.giesecke@hzdr.de

Abstract: We perform simulations of the kinematic induction equation in order to examine a helical flow of a conducting liquid interacting with magnetic material with permeability $\mu > 1$. We examine two paradigmatic systems that reflect the flow conditions in the core of a sodium fast reactor, and we show that in the limit of large μ the critical magnetic Reynolds number required for the onset of dynamo action is reduced by 25%.

1. Introduction

The experimental confirmation of the magnetohydrodynamic dynamo effect has been of great importance for the understanding of geo- and astrophysical magnetic fields. Besides of this fundamental relevance, a complementary argument for the development of dynamo experiments originated from considerations on the safe operation of sodium fast reactors [1] because the helical structure of the flow in the core (figure 1), combined with the large flow rate, provides appropriate prerequisites for the occurrence of dynamo action. However, this effect is undesired, because the backreaction of a self-excited magnetic field may cause an inhomogeneous flow braking or a pressure drop in the cooling system, so that an efficient removement of heat from the reactor core can be hampered with unknown consequences for the safety of the reactor.

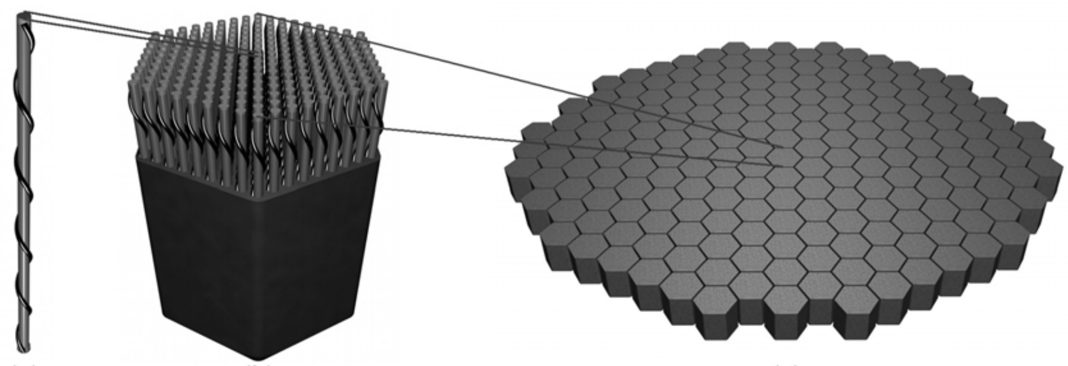

Figure 1: Idealized composition of the core of a sodium fast reactor. (a) Nuclear fuel rod surrounded by a screw-like spacer that forces the flow on a helical path. (b) A few hundreds of fuel rods are bundled into so-called assemblies. (c) The whole reactor core is composed of a few hundreds of assemblies.

Previous studies have shown no conclusive evidences for the occurrence of dynamo action in the core of a fast reactor [2,3,4,5], but it is hypothesized that the parameter regime reached by the French fast breeder reactor *Superphenix* is well within the range that allows for dynamo action if some magnetic material is introduced into the core [6]. In the present study we revisite the arguments from [6], and in order to develop global models for electromagnetic induction in the core of fast reactors we resort to the mean-field dynamo theory [7] which allows a consideration of tens of thousands of helical flow cells in terms of an α- and β-effect including the impact of magnetic material. We develop and validate the necessary methodology required for the computation of the mean-field coefficients which may be used for future estimates of dynamo action in systems that are characterized by different size and different magnetic materials. The examination of the impact of magnetic material is motivated by the key role of soft iron impellers for the VKS dynamo and by the repeatedly manifested idea to make use of *Oxide Dispersion Strengthened* (ODS) ferritic/martensitic alloys in the core of a fast reactor. These alloys have a lower sensitivity for nuclear radiation, but exhibit a permeability much larger than one. We start with the analysis of the induction action of the fully resolved velocity field and compute the mean-field coefficients required for a consistent mean-field model using the testfield method [8]. In a second step we use the α- and β-coefficients as an input for mean-field dynamo simulations in order to proof that mean-field models are capable to reproduce the growth-rate and principle field structure of the fully resolved model by requiring much less computational efforts.

2. Mean-field dynamo theory and testfield method

We splitt the magnetic field and the velocity field into a mean, large scale part and a small scale part: $\mathbf{B} = \overline{\mathbf{B}} + \mathbf{b}$ and $\mathbf{U} = \overline{\mathbf{U}} + \mathbf{u}$. Then the mean magnetic field is governed by the mean field induction eqaution:

$$\partial \overline{\mathbf{B}} / \partial t = \nabla \times \left(\overline{\mathbf{U}} \times \overline{\mathbf{B}} + \overline{\mathbf{u} \times \mathbf{b}} - \eta \nabla \times \overline{\mathbf{B}} \right) \tag{1}$$

which includes a term called the mean electromotive force $\mathbf{F} = \overline{\mathbf{u} \times \mathbf{b}}$, which only depends on the statistical properties of small scale flow and small scale field. Under the assumptions that the variations of $\overline{\mathbf{B}}$ around a given point are small, $\mathbf{F}$ can be represented by the first terms of a Taylor expansion

$$F_i = \alpha_{ij} \overline{B}_j + \beta_{ijk} \partial \overline{B}_j / \partial x_k . \tag{2}$$

In order to compute the mean-field coefficients we utilize the testfield method developped by Schrinner et al [8]. In that method α_{ij} and β_{ijk} are computed from different realizations of the electromotive force that are obtained from externally applied, linearly independent mean fields. Defining the small scale velocity as the deviation from the horizontal average, the small scale magnetic field is computed numerically by solving

$$\partial \mathbf{b} / \partial t = \nabla \times \left(\overline{\mathbf{U}} \times \mathbf{b} + \mathbf{u} \times \overline{\mathbf{B}} + \left(\mathbf{u} \times \mathbf{b} - \overline{\mathbf{u} \times \mathbf{b}} \right) - \eta \nabla \times \mathbf{b} \right). \tag{3}$$

Then the electromotive force is computed directly by correlating small scale flow with the small scale field and subsequently performing a horizontal averaging. The combination of different realizations of $\mathbf{F}$ obtained from different, linearly independent testfields yields a linear system of equations, whose solution gives the desired mean-field coefficients. In order to compute mean-field coefficients that are consistent with the structure of the large scale field from the fully resolved model, it is necessary to consider the scale dependence of the mean-field coefficients by choosing appropriate testfields. We define the testfields as follows:

$$\overline{\mathbf{B}}_1 = \cos(\pi z) \hat{\mathbf{y}} \text{ and } \overline{\mathbf{B}}_2 = \sin(\pi z) \hat{\mathbf{y}} \tag{4}$$

which is in agreement with the definitions used by [10].

3. Flow model and permeability distribution

In the present study we examine two paradigmatic flow models: In model A we assume a flow consisting of various helical eddies that are separated by walls (left panel in figure 3). Following the idea of [3], the helical flow within one cell represents the mean flow within one assembly of nuclear fuel rods ignoring the even smaller scale flow around individual rods. The second approach (model B, see right panel in figure 4) uses a more detailed picture of the

flow conditions within a single assembly. The model is based on the so called spin generator flow that has been utilized for the simulation of the Karlsruhe Dynamo [9] and assumes a circular flow around a central rod superimposed with a constant vertical flow.
In order to characterize the amplitude of the flow we define a local magnetic Reynolds number that is based on the flow amplitude u_0, the "normal" magnetic diffusivity $\eta = (\mu_0 \sigma)^{-1}$ and the size D of a single eddy (model A) or the distance between two adjacent rods (model B): $Rm = u_0 D / \eta$.

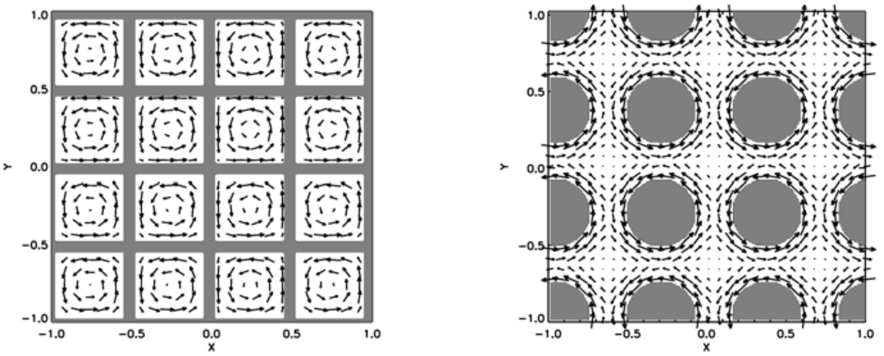

Figure 2: Flow pattern for model A (left) and model B (right). The gray shaded regions represent walls or rods and may have a permea-bility $\mu_r > 1$. The vertical flow is constant in each cell and vanishes in the wall/rod regions. The horizontal flow is denoted by the arrows.

In order to incorporate the effects of a non-uniform permeability distribution in terms of mean-field coefficients we rewrite the induction equation in the form

$$\partial \mathbf{B} / \partial t = \nabla \times \left(\mathbf{U} \times \mathbf{B} + \eta \nabla \ln \mu_r \times \mathbf{B} - \eta \nabla \times \mathbf{B} \right) \qquad (6)$$

with $\eta = \eta / \mu_r(r)$. This modified induction equation contains an additional velocity-like term $u(r) = \eta \nabla \ln(\mu_r)$ which contributes to the mean flow as well as to the small scale flow when applied in the testfield method.

4. Results

The results for a uniform permeability distribution with $\mu_r = 1$ are shown in figure 3. The α-effect is in accordance with the results reported by [9] in case of the ideal Roberts flow. In the same way we write $\alpha = K\eta / D Rm^2 \Phi(Rm)$ with a non-analytic function Φ that only depends on Rm and a normalisation factor K that is universal for each model and does not depend on the cell size D. Regarding the coefficient β we find significant differences between both models. In model A we see a transition to negative values (but in a way that the sum of η and β remains positive), whereas the β-effect remains allways positive in model B. The right column in figure 3 shows a comparison of the growth-rates from the fully resolved models (FRM) with the corresponding mean field models (MFM) that made use of the coefficients determined from the FRM. The mean field induction equation that is solved numerically reads

$$\partial \overline{\mathbf{B}} / \partial t = \nabla \times \left(\overline{\mathbf{U}} \times \overline{\mathbf{B}} - \alpha \left(\overline{\mathbf{B}} - \gamma \hat{\mathbf{z}} \times \overline{\mathbf{B}} - \left(\hat{\mathbf{z}} \cdot \overline{\mathbf{B}} \right) \hat{\mathbf{z}} \right) - \bar{\eta} \nabla \times \overline{\mathbf{B}} - \beta \hat{\mathbf{z}} \times d\overline{\mathbf{B}} / dz - \delta_2 \left(\hat{\mathbf{z}} \cdot \nabla \right) \overline{\mathbf{B}} \right) \qquad (7)$$

where the coefficients α, β, γ and δ_2 are related to the tensor elements from Eq. (2) by $-\alpha = \alpha_{xx} = \alpha_{yy}$, $\beta = \beta_{xyz} = -\beta_{yxz}$, $-\gamma = \alpha_{xy} = -\alpha_{yx}$ and $\delta_2 = \beta_{xxz} = \beta_{yyz}$.
We obtain a good agreement between FRM and MFM if the system is not strongly over-critical. The agreement improves for an increasing number of helical eddies. However, the

results become more complex when $\mu_r > 1$ (figure 4). For a fixed μ_r we always find that α grows

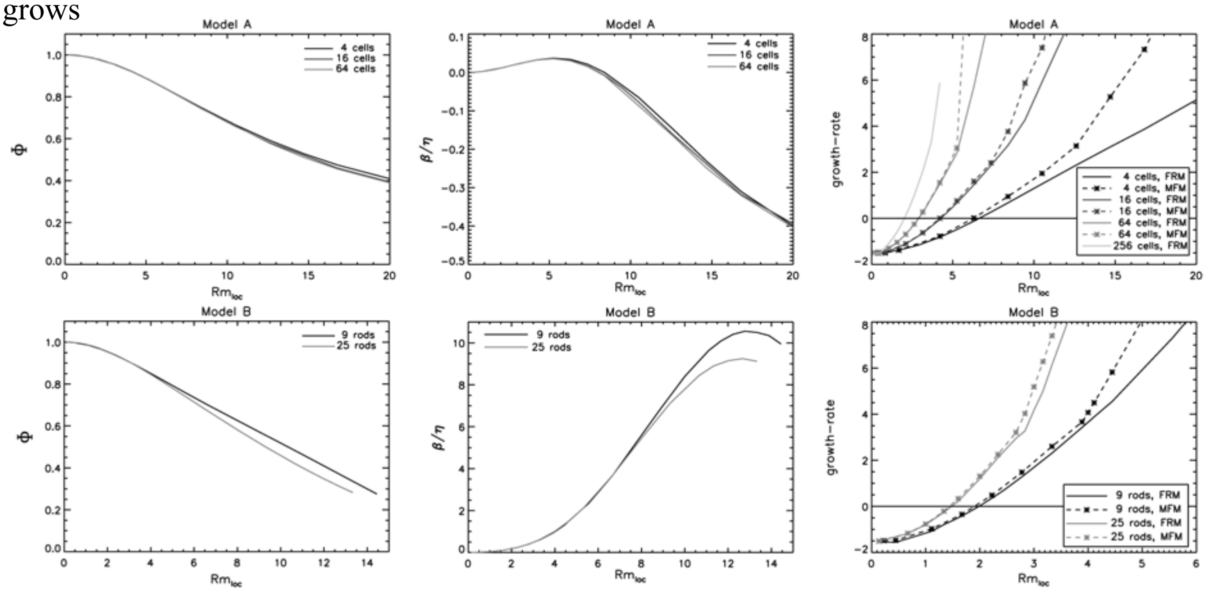

Figure 3: Mean field coefficients and growth-rates versus Rm for μ_r=1. From left to right: Φ, β, and growth-rates. Solid curves denote the growth-rates from the fully resolved model (FRM) and dashed curves denote the growth-rates from the mean-field models (MFM). Top row: model A, bottom row: model B.

with increasing *Rm*. Both models show a different behavior concerning the dependence on μ_r. For model A, we observe a significant supression of α for small μ_r, followed by a slow recovery for larger μ_r. In contrast, we see a moderate increase of α for small μ_r in model B followed by a saturation regime for μ_r>1.

Regarding the coefficient β, we find an abrupt transition to negative values around $\mu_r \approx 3$ in model A, whereas β increases linearly with increasing μ_r in model B, which, furthermore, does not show any indications for a transition to negative values.

Again, we find a good agreement between the FRM growth-rates and the MFM growth-rates but with some increasing deviations for large *Rm* and large μ_r. Considering the whole range of achievable μ_r in model A we find a reduction of the critical magnetic Reynolds number from Rm^{crit} = 4.2 at μ_r = 1 to Rm^{crit} = 3.2 at μ_r = 20. The relative reduction is roughly the same for

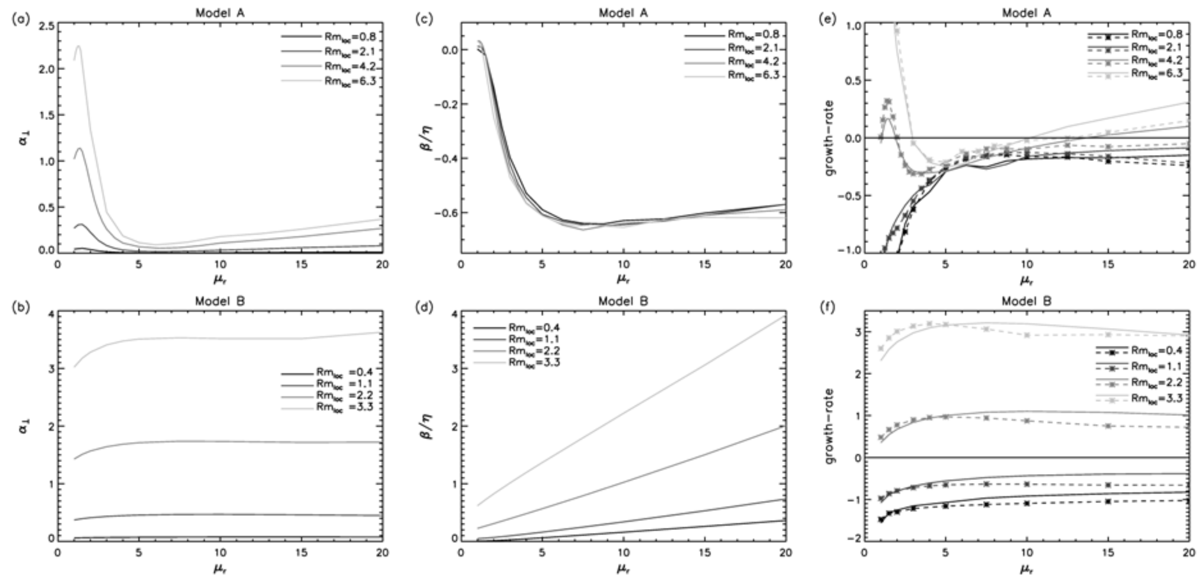

Figure 4: Mean field coefficients and growth-rates versus μ_r. From left to right: α, β, growth-rate. The solid curves on the right panel show the FRM growth-rates, the dashed curves show the MFM growth-rates. Top row: model A, bottom row: model B.

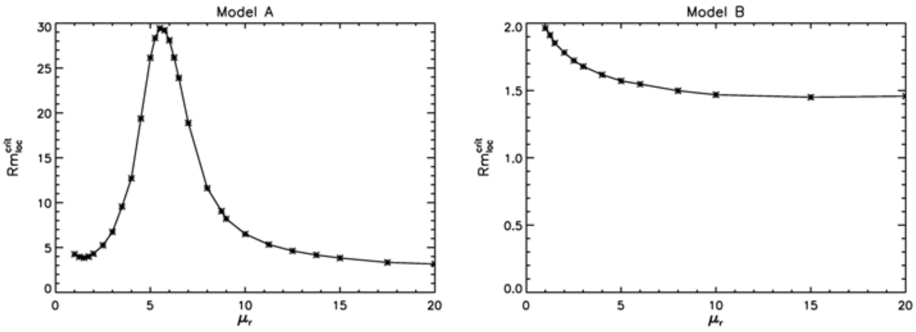

Figure 5: Critical magnetic Reynolds number for the onset of dynamo action versus permeability. Left: model A, right: model B.

model B, where $Rm^{crit} = 2.0$ at μ_r=1 is reduced to $Rm^{crit} = 1.5$ at $\mu_r = 20$ (figure 5). Regarding the asymptotic behavior for large μ_r in figure 5 it seems unlikely that a further increase of μ_r will provide for a further significant reduction of Rm^{crit}.

5. Conclusion

We have performed numerical simulations of the kinematic induction equation for two different helical flow types including internal walls or rods that may have magnetic properties. In the limit of large permeability, we found a moderate impact of μ_r on dynamo action in terms of a reduction of Rm^{crit} of roughly 25% compared to the non-magnetic case.
Comparing the growth-rates obtained from fully resolved models with the corresponding mean-field models we found a good agreement between both approaches, at least for $\mu_r < 20$.
For non-magnetic internals we show that the α-effect can be expressed in terms of a function Φ that allows a conclusion on α for larger systems when flow scale and flow amplitude are known. In combination with the β-effect, which is roughly independent of the flow scale, this allows a modelling of systems that may consist of tens of thousands of individual helical cells embedded into some large scale flow structure.
The possible application to specific reactor cores will need much more information on geometric details and material properties, such as the size of the core, the number of fuel rods contained therein, and the total flow rate as well as the consideration of the hexagonal geometry of the assemblies, which will be left for future work. Nevertheless, we believe that a consideration of these details will only result in minor modifications to our findings and are therefore of secondary importance.

Acknowledgements. The authors kindly acknowledge support by the Helmholtz Allianz LIMTECH.

References

[1] Rädler, K. H. in 'Magnetohydrodynamics - Historical Evolution and Trends', Springer (2007), 55-72.
[2] Bevir, M. K.: J. Brit. Nucl. Eng. Soc. 12 (1973), 455-458.
[3] Pierson, E. J.: Nucl. Sci. Eng. 57 (1975), 155-163.
[4] Plunian, F., Marty, P., Alemanny, A.: J. Fluid Mech. 382 (1999), 137-154.
[5] Alemany, A., Marty, P., Plunian, F. & Soto, J.: J. Fluid Mech. 403 (2000), 263-276.
[6] Soto, J.: PhD thesis, L'Institut National Polytechniques De Grenoble (1999).
[7] Krause, F. & Rädler, K. H.: Mean-field magnetohydrodynamics and dynamo theory, Pergamon Press 1980.
[8] Schrinner, M. et al.: Astron. Nachr. 326 (2005), 245-249.
[9] Rädler, K. H. et al.: Nonlin. Processes Geophys. 9 (2002), 171-187.
[10] Rädler, K. H. & Brandenburg, A.: Phys. Rev. E 67 (2003), 026401.

Numerical simulations for the DRESDYN precession dynamo

GIESECKE A., ALBRECHT T., GERBETH G., GUNDRUM T., STEFANI F.
Affiliation: Helmholtz-Zentrum Dresden-Rossendorf, P.O. Box 510119, D-01314 Dresden – Germany
e-mail: a.giesecke@hzdr.de

Abstract: The next generation dynamo experiment currently under development at the Helmholz-Zentrum Dresden-Rossendorf (HZDR) will consist of a precessing cylindrical container filled with liquid sodium. We perform numerical simulations of kinematic dynamo action applying a velocity field that is obtained from hydrodynamic models of a precession driven flow. So far, the resulting magnetic field growth-rates remain below the dynamo threshold for magnetic Reynolds numbers up to Rm = 2000.

1. Introduction

Planetary magnetic fields are generated by the dynamo effect, the process that provides for a transfer of kinetic energy from a flow of a conducting fluid into magnetic energy. Usually, it is assumed that these flows are driven by thermal and/or chemical convection but other mechanisms are possible as well. In particular, precessional forcing has long been discussed as an at least additional power source for the geodynamo [1,2]. A fluid flow of liquid sodium in a cylindrical container, solely driven by precession, is considered as the source for magnetic field generation in the next gener-ation dynamo experiment currently under development in the framework of the project DRESDYN at the Helmholtz-Zentrum Dresden-Rossendorf (HZDR). In contrast to previous dynamo experiments no internal blades, propellers or complex systems of guiding tubes will be used for the optimization of the flow properties. However, rather large dimensions of the container are necessary in order to reach sufficiently large magnetic Reynolds numbers required for the onset of dynamo action, making the construction of the experiment a challenge (figure 1). At present a small scale water experiment is running in order to estimate the hydrodynamic flow properties in dependence of Reynolds number Re, precession angle α, and precession ratio $\Gamma = \Omega/\omega$ (figure 2). Flow measurements of axial velocity profiles at different radial posi-tions are done using Ultrasonic Doppler Velocimetry. First experimental results confirm that precession provides an efficient flow forcing mechanism which in the final realisation of the liquid metal experiment will allow magnetic Reynolds numbers up to $Rm \sim 700$. This value is rather close to the critical Rm reported by [3] for the onset of dynamo action in a precessing cylinder.

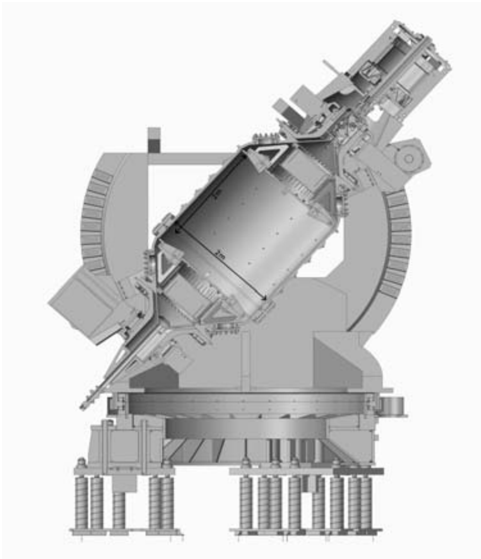

Figure 1: Sketch of the planned experiment. Diameter and height of the cylindrical container will be approximately 2 m.

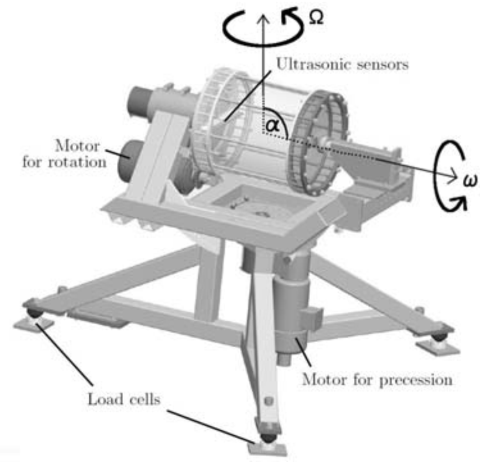

Figure 2: Sketch of the water mock-up. The dimensions of the cylinder are roughly 6 times smaller than the future liquid metal experiment.

2. Hydrodynamic simulations of precession in a cylindrical container

Hydrodynamic simulations of a precession driven flow are performed using SEMTEX [4]. The code applies a spectral element method on the meridional planes and Fourier decomposition in the azimuthal direction for the numerical solution of the Navier-Stokes equation which in the precessing frame reads:

$$\partial \mathbf{u} / \partial t + (\mathbf{u} \cdot \nabla)\mathbf{u} + 2(\boldsymbol{\omega} + \boldsymbol{\Omega}) \times \mathbf{u} = \nu \nabla^2 \mathbf{u} + \nabla \Phi \,. \tag{1}$$

Here $\mathbf{u}$ denotes the velocity field, $\boldsymbol{\omega}$ the rotation around the symmetry axis of the container, $\boldsymbol{\Omega}$ the rotation around the precession axis, ν the viscosity and Φ the modified pressure that includes the centrifugal contributions. In the precessing frame the boundary conditions are given by $\mathbf{u} = \boldsymbol{\omega} \times \mathbf{r}$. For small precession ratios and Reynolds numbers, $Re=\omega R^2/\nu$, we obtain a good agreement between simulations and measurements with the flow being dominated by the fundamental Kelvin mode with an azimuthal wavenumber m=1 (figure 3). The agreement is less convincing for larger precession ratios (right column in figure 3). A slight tilt of the fundamental mode with respect to the rotation axis is apparent in the simulations (top row) as well as in the experimental data (bottom row).

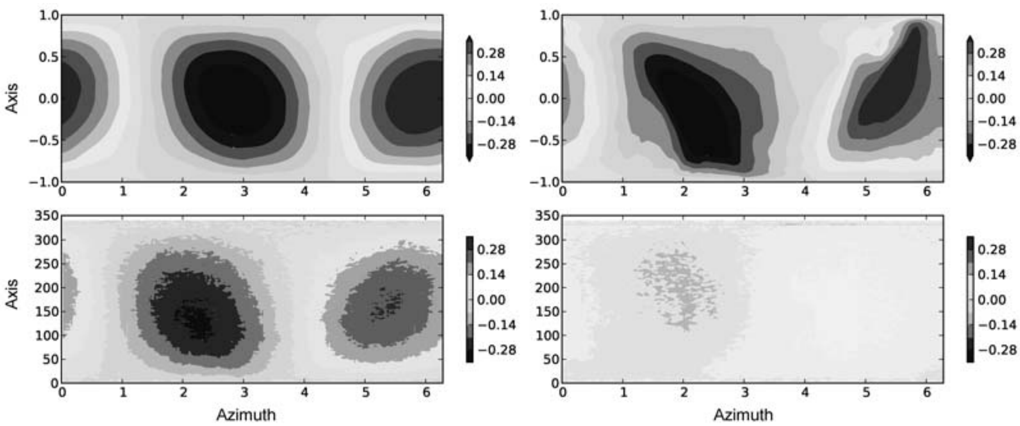

Figure 3: Comparison of the axial velocity at r=0.74 from hydrodynamic simulations (top) and experimental measurements (bottom). Left: Γ = 0.06, right: Γ = 0.10.

The most striking feature found in the water experiment is an abrupt transition from a laminar state to a disordered chaotic behavior at a critical precession ratio. This transition is less pronounced in the numerical simulations, which, however, are carried out at a much smaller Reynolds number. An indication of the change of state in the flow simulations is reflected in the re-orientation of the main fluid rotation axis which in the disordered state is aligned parallel to the precession axis (right side figure 4).

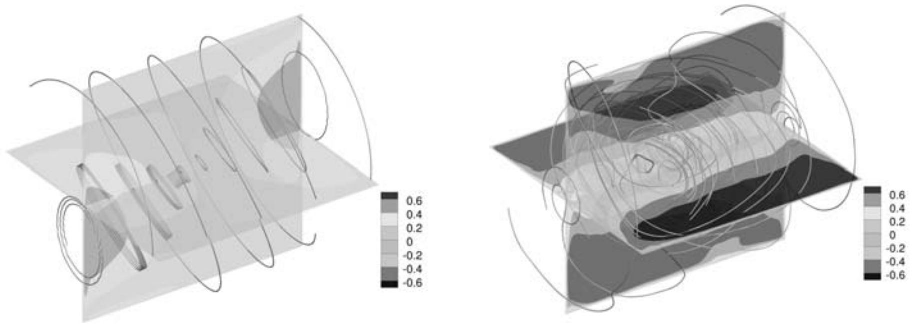

Figure 4: Streamlines from simulations with weak precession (Γ =0.03, left) and strong precession (Γ = 0.15, right). Note the bulk fluid rotating around the precession axis in the latter case.

3. Kinematic dynamo action from a simulated precessional flow

In the following the velocity field obtained from the hydrodynamic simulations is used as an input in a kinematic solver for the magnetic induction equation which reads

$$\partial \mathbf{B} / \partial t = \nabla \times (\mathbf{u} \times \mathbf{B} - \eta \nabla \times \mathbf{B}), \tag{2}$$

with the magnetic flux density **B** and the magnetic diffusivity η. The resulting growth-rates and the corresponding critical magnetic Reynolds numbers will provide a restriction of the useful parameter regime and will allow an optimization of the experimental configuration. We start with a flow obtained at a low Reynolds number of Re=1500 and a precession ratio Γ=0.1. At these parameters the flow in the precessing frame is (more or less) stationary with a rather simple pattern that is very close to the fundamental m=1 Kelvin mode (left column in figure 3). The temporal behavior of the magnetic energy is shown in the left panel of figure 5. We do not find growing solutions up to a magnetic Reynolds number of $Rm=\omega R^2/\eta$=2000, and from the behavior of the corresponding growth-rates (right panel in figure 4) it seems unlikely that a crossing of the dynamo threshold occurs within reasonable Rm.

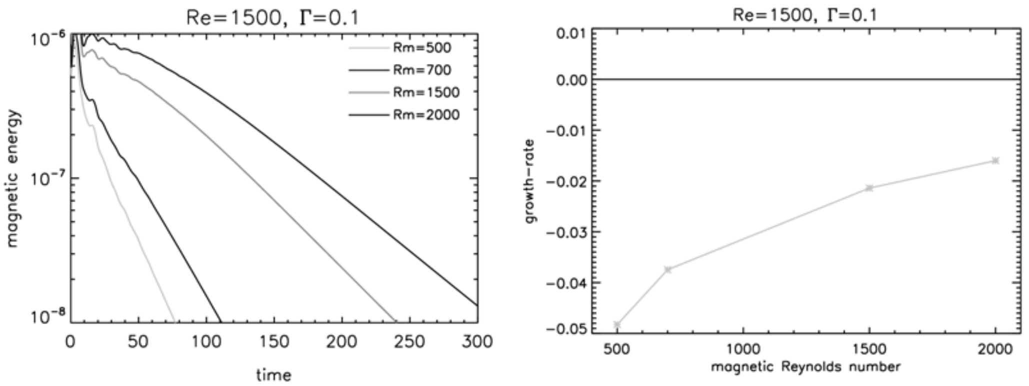

Figure 5: Left: temporal behavior of the magnetic energy for a velocity field obtained at Re = 1500 and Γ = 0.10. Right: Corresponding growth-rates of the fundamental dynamo eigenmode versus Rm.

Next, we take a velocity field from the more turbulent regime at Re = 6500. At this value, the flow is time-dependent but still dominated by the m=1 mode (figure 6). Again, we do not find any growing solutions for the magnetic field, however, the behavior of the growth-rates indicates a critical magnetic Reynolds number in the range of Rm =3000...4000 (figure 7), which unfortunately would be far out of reach in the forthcoming dynamo experiment.

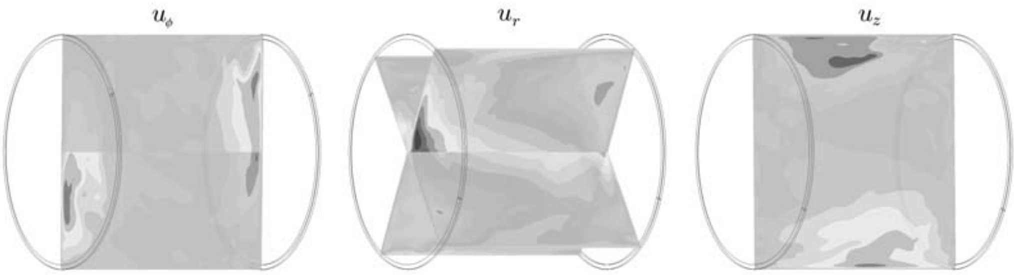

Figure 6: Snapshot of the time-dependent velocity field at Re = 6500 and Γ = 0.08.

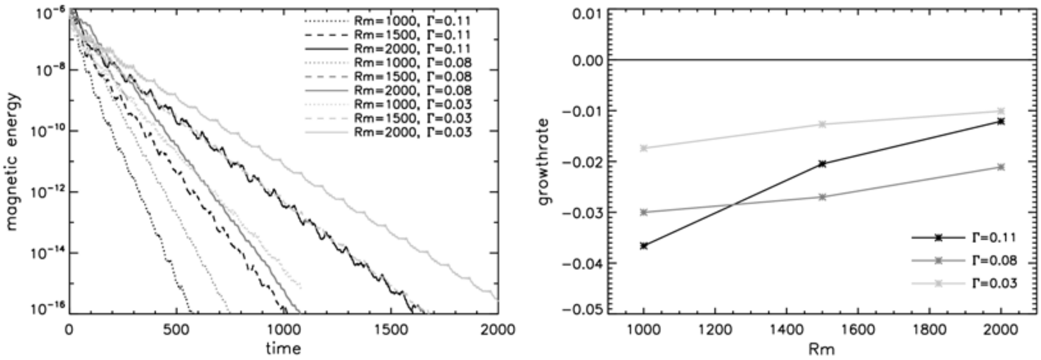

Figure 7: Left: temporal behavior of the magnetic field amplitude for a velocity field obtained at Re = 6500. Right: Corresponding growth-rates of the fundamental dynamo eigenmode versus Rm.

4. Conclusion

Using velocity fields obtained from simulations at *Re*=1500 and *Re*=6500, our kinematic simulations do not show growing magnetic fields. Hence, for the slow rotation rates examined so far, the flow structure most probably is too simplistic to provide for dynamo action. However, for larger Reynolds numbers, we expect more complex structures to emerge. There are two promising candidates from which we expect better properties regarding their ability to drive a dynamo. So- called triadic resonances, that consist of the forced fundamental (*m*=1) mode and two free inertial modes with larger azimuthal wavenumber, have repeatedly been observed in experiments and simulations of precessing flows [5,6]. A subclass of these modes have a close similarity to the columnar convection rolls that are responsible for dynamo action in geodynamo models and there is little reason to believe that this should not be the case with a precession driven flow field. The second possibility relies on observations of cyclones in the French precession experiment ATER [7]. In that experiment large scale vortex-like structures emerge for intermediate precession ratios.

Figure 8: Idealized model for cyclones observed in the ATER experiment [7].

These vortices are oriented along the rotation axis of the cylindrical container, and, depending on the parameter regime, their number varies between one and four (figure 8). The vortices are cyclonic, i.e., their sense of rotation is determined by the rotation orientation of the cylindrical container. We suspect that these vortices provide a significant amount of helicity, but so far, the axial dependence of their contribution and their interaction with the fundamental m=1 mode is unknown. Furthermore, cyclones were neither observed in the HZDR experiment (so far, no appropriate velocity measurements in a horizontal plane are available) nor in any simulations which probably must run at much higher Reynolds number in order to reveal these modes.

Acknowledgements. The authors kindly acknowledge support by the Helmholtz Allianz LIMTECH.

References

[1] Malkus, W.V.R.: Science 160 (1968), 259-264.
[2] Tilgner, A.: Phys. Fluids 3 (2005), 034104.
[3] Nore, C. et al.: Phys. Rev. E. 84 (2011), 016317.
[4] Blackburn, H.M. & Sherwin, S.J.: J Comp. Phys. 197 (2004), 759-778.
[5] Meunier, P. et al.: J. Fluid Mech. 599 (2008), 405-440.
[6] Lorenzani, S. & Tilgner, A.: J. Fluid Mech. 492 (2003), 363-379.
[7] Mouhali, W. et al.: Exp. Fluids, 53 (2012), 1693-1700.

GENERATION OF HELICITIES IN THE ROTATING LAYER

RESHETNYAK M.
Institute of the Physics of the Earth, Russian Academy of Sciences
123995, Moscow, Russia
E-mail: m.reshetnyak@gmail.com

Magnetic fields are widely distributed in the Universe. Generation of the magnetic fields accompanied by the transformation of the kinetic energy of the conductive liquid to the energy of the magnetic field is a subject of the dynamo theory [1]. In general, dynamo equations include equations of thermal or (and) compositional convection as it is in planetary dynamo as well as the induction equation for the magnetic field **B**. These equations have a set of quantities (integrals of motion), which can conserve, provided diffusion effects as well as the external forces are absent. Thus in 3D the Navier-Stokes equation conserves the mean over the volume kinetic energy $E_K = \mathbf{V}^2/2$ and kinetic helicity $\chi = \langle \mathbf{V}\cdot\mathrm{rot}\mathbf{V}\rangle$, where $\langle\ldots\rangle$ denotes averaging over the domain and **V** is the velocity field. The Navier-Stokes equation with the induction equation conserves the magnetic helicity $\chi^M = \langle \mathbf{A}\cdot\mathbf{B}\rangle$ and the so-called cross-helicity $\chi^C = \langle \mathbf{V}\cdot\mathbf{B}\rangle$. Here **A** is the vector potential of the magnetic field $\mathbf{B} = \mathrm{rot}\mathbf{A}$.

For each of these quantities one can derive from the original dynamo system its own evolution equation. However, these new equations already are the simplified forms of the original equations; its study can be instructive and sometimes tell us something new without solving more sophisticated full dynamo equations. So as helicities by definition can change the sign, its conservation in the full volume of generation can be trivial. Moreover, some of these quantities can change its sign with transition from large-scales to small ones. That is why understanding of the structure of these quantities in the physical and wave spaces is important.

Here we consider this problem on an example of a rapidly rotating flat layer heated from below, where thermal convection of the conductive fluid takes place. The axis of rotation and the gravity direction coincide. The mathematical model is close to that in [2]. We used the Boussinesq approximation with the fixed temperatures at the boundaries $z = 0, 1$, the stress-free and non-penetrating boundary conditions for the velocity field **V**. The parameters of convection are chosen in such a way that to mimic the geostrophic state with the cyclonic cell forms typical to the planetary convection in the cores of the planets [3]: the Ekman number $E = 2\mathrm{x}10^{-5}$, the Prandtl number $Pr = 1$, the Roberts number $q = 2$, and the modified Rayleigh number $Ra = 300$.

The magnetic equation is written for the vector potential of the magnetic field, accompanied with the pseudo-vacuum boundary conditions. For all the considered physical fields the periodical boundary conditions in the both horizontal directions are applied. To solve these equation we used the control-volume method (SIMPLE algorithm by Patankar [4]) adopted to the cluster parallel computers using MPI. To solve equations we used the mesh grids 128^3 in all directions.

We started simulation for the pure convective regime, see evolution of the mean over the volume temperature fluctuations from the non-convective temperature profile and mean kinetic energy in Fig.1ab. The developed turbulent convection is anisotropic with cells elongated along the axis of rotation and with perpendicular scale $\sim E^{1/3}$. After the one diffusion time (based on the thermal diffusion) at the moment $T = T_B$ the seed of the magnetic field was introduced. The kinematic dynamo stage continued also about one diffusion time before the full dynamo state has developed, Fig.1c.

To follow evolution of the physical fields and its derivatives in the wave space we used the wavelet transform based on the complex Morlet wavelet for the space coordinates. Normalization of wavelets is chosen in such a way that to the periodic signals with different periods and equal amplitudes correspond the equal spectral amplitudes. Application of the wavelets for the non-periodical fields, like turbulence, seems more natural rather using the fast Fourier transform. Due to the rapid rotation it is important to distinguish two directions: along and perpendicular to the axis of rotation, so that one has two spectra on the wavenumbers $k_{\perp}$, and $k_{\parallel}$, correspondingly. Latter we consider only the transversal spectra, which are more effected by rotation.

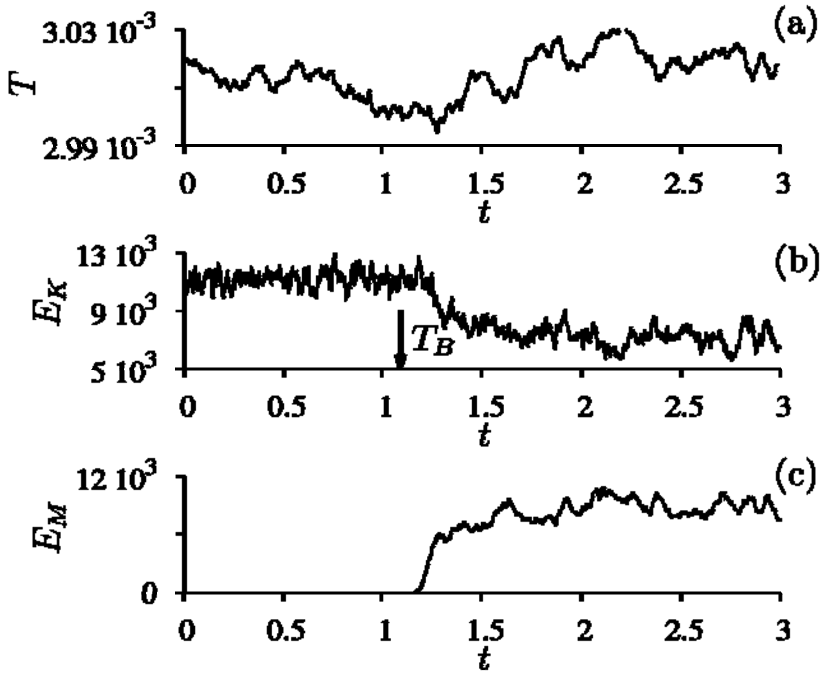

Figure 1: Evolution of the temperature fluctuations (a), kinetic (b) and magnetic (c) energies in the rotating layer. In the moment T_B magnetic field is switched on.

So as helicities can change its sign in the middle horizontal plane, for all the quantities we consider spectra at some point with the fixed horizontal coordinates (x_0, y_0) and integrate all the values in the vertical coordinate in the range z=[0, 0.5].

Evolution of the wavelet spectra is presented in Fig.2. The increase of the magnetic energy E_M to the nonlinear level is accompanied with the decrease of the kinetic energy E_K about 30%.

The cyclonic convection, developed due to the geostrophic state, is a source of the mean kinetic helicity in the system, which is believed to be a source of the large-scale magnetic fields in the planets. Equation for the kinetic helicity generation due to the Coriolis force can be derived from the following relation: $\frac{\partial \mathbf{V}}{\partial t} \sim -\mathbf{1_z} \times \mathbf{V}$. That leads to $\frac{\partial \chi}{\partial t} \sim \frac{\partial}{\partial x_i}(V_i V_z)$, where summation over the repeated indexes is assumed. Finally, due to the periodical boundary conditions in the horizontal directions, evolution of the mean kinetic helicity over the lower half-volume can be estimated as: $\frac{\partial}{\partial t}\int \chi dr^3 = \frac{1}{2}\left[\int\int V_z^2 dxdy\right]_{z=0}^{z=0.5}$. So as the normal velocity V_z is zero at z = 0, helicity is positive in the lower half-volume, where flow converges. In the upper half-volume z = [0.5, 1], where flow diverges, the sign of helicity is opposite. Note that these arguments can be used also for the certain wavenumebr $k_{\perp}^{f}$ provided the Rossby number for

$k_\perp^f$ is small. This estimate is supported by our simulations where χ is positive in the lower half-volume at all $k_\perp$.

The next one is the current helicity χ^J = <**J**·**B**>, where **J** is the electric current (Fig.2d). In contrast to the kinetic helicity, χ^J has different signs at the small and large scales. This phenomenon calls the separation in scales [5]. As well as the kinetic helicity, the current helicity is anti-symmetric in respect to the middle plane *z*=0.5. It is known that χ^J is closely connected to the magnetic helicity χ^M, see [5]. In the same time, it is based on the physical quantities **J** and **B**, which can be derived from observations. Information on the signs of χ^J at the different scales can be used for extrapolation of the observable fields to the invisible part of the spectra. This situation is common for the solar physics, e.g., for the solar active regions [6].

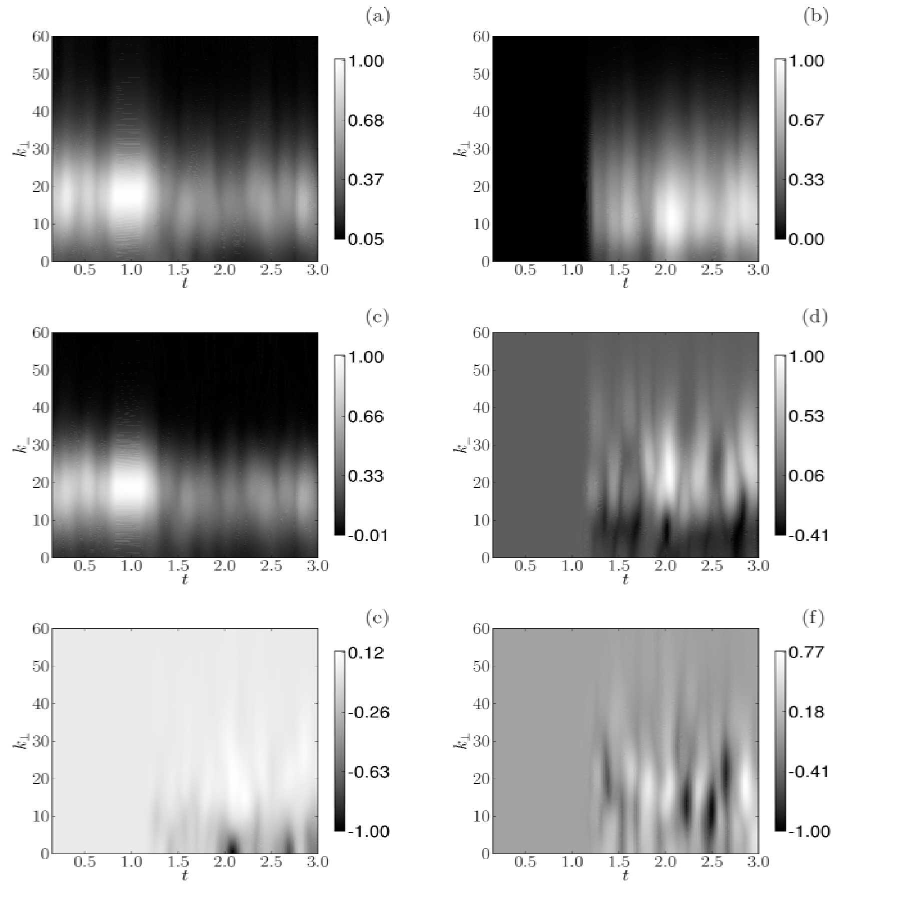

Figure 2: Evolution in time of the transversal wavelet spectra of the kinetic (a) and magnetic (b) energies, kinetic (c), current (d), magnetic (e), and cross- (f) helicities.

Magnetic helicity χ^M is the integral of the induction equation, based only on the magnetic quantities **A** and **B.** Note, the vector potential **A** is defined up to the gradient of some arbitrary function. This fact requires careful treatment of the magnetic helicity, see [5]. Spectrum of χ^M, presented in Fig.2.e also demonstrates the effect of the scales separation. The rough estimate leads to a simple relation between χ^J and χ^M: $\chi^J \sim k_\perp^2 \chi^M$.

The last kind of helicity is the cross-helicity χ^C, which is also the invariant of the dynamo equation in the limit of zero dissipation and absence of the external forces. Its evolution and structure of the spectra (Fig. 2f) differ from the previous kinds of helicities. It has no separation in scales but the sign of χ^C, which is the same at all the scales, changes in time. The additional integration in *x*-*y* plane leads to the very negligible estimate of χ^C over the half-volume. Note that due to the quadratic dependence of the Lorentz force on the magnetic field **B**, the hydromagnetic states with **B** and –**B** are equivalent. It means that existence of the non-zero χ^C with the rapidly alternating magnetic field in time, like it happens in the turbulent flow, would contradict this statement.

References

[1] Rudiger, G., Kitchatinov, L.L., Hollerbach, R.: Magnetic processes in astrophysics. Theory, simulations, experiments. Verlag GmbH: Wiley-VCHr, 2013, 346 p.

[2] Hejda, P., Reshetnyak, M.: Nonlinearity in dynamo. Geophys. Astrophys. Fluid Dynam. 104 (2010) 6 25–34.

[3] Roberts, P.H., King, E.M.: On the genesis of the Earth's magnetism. Rep. Prog. Phys. 76 (2013) 096801.

[4] Patankar, S.V.: Numerical Heat Transfer and Fluid Flow. NY: Taylor & Francis, 1980, 198 p.

[5] Brandenburg, A., Subramanian, K..: Astrophysical magnetic fields and nonlinear dynamo theory Phys. Rep. 417 (2005) 1–209. arXiv:astro-ph/.

[6] Zhang, H., Brandenburg, A., Sokoloff, D.D.: Magnetic helicity and energy spectra of a solar active region. Astrophys. J. Lett. 784 (2014) L45.

EXPERIMENTAL STUDY OF TURBULENT DIAMAGNETISM IN LIQUID SODIUM FLOW

FRICK P., DENISOV S., NOSKOV V., STEPANOV R., PAVLINOV A.
Institute of Continuous Media Mechanics, 1 Korolyov str., Perm, Russia
E-mail: frick@icmm.ru

Abstract : The magnetic field suppression by strong turbulent flow of liquid sodium is studied experimentally in a nonstationary turbulent flow under moderate magnetic Reynolds number Rm > 10. The applied magnetic field is collinear to the streamline of the large-scale mean flow, what excludes the induction effects by the mean flow and the contribution of the turbulent diffusion. We show that during the highly turbulent stage of flow evolution the *mean* magnetic field is reduced by a factor of 0.6. The observed effect can be explained as the result of turbulent diamagnetism described by the term curl **(g×B)** in the mean-field induction equation (here **g** is the gradient of the energy of turbulent fluctuations and **B** is the mean magnetic field).

1. Introduction

The intensive small-scale turbulence in electroconducting fluids provides a variety of induction effects, described by about 20 terms in the general form of mean electromotive force [1]. Very few among them have been isolated and studied in detail. For laboratory study it is a hard problem to provide a MHD configuration which permits to separate the contribution of different effects. In our talk, we present results of laboratory study of the magnetic field suppression in the domain of strong turbulent fluctuations. We perform series of experiments with a nonstationary turbulent flow of liquid sodium, generated in a fast rotating toroidal channel after its abrupt braking. We applied the stationary curl-free magnetic field which is collinear to the streamline of the large-scale mean flow. This excludes an induction effects by the mean flow and the contribution of effective diffusion (the so-called beta-effect).

2. Experimental setup

We study spin-down flows of liquid sodium in a toroidal channel made of titanium alloy [2]. The torus has the radius R = 0.18m and the radius of the channel cross-section r_0 = 0.08 m. The rotation frequency of the channel is up to 50 rps, and the flow in the channel is generated by abrupt braking. The braking time does not exceed 0.3 s. The flow velocity reaches a maximum after the channel stops, and in the case of the free channel its toroidal component constitutes almost 70% of the linear velocity of the channel before braking. This means that the Reynolds number $Re = V\cdot r_0/\upsilon$ increases to $Re \approx 3\cdot 10^6$ at the most, which corresponds to the magnetic Reynolds number $Rm \approx 30$.

For velocity measurements, we use a 2-axis local probe [3]. One of probe axis is oriented in azimuthal direction of clockwise channel rotation (toroidal) and its other axis oriented in radial direction (poloidal). At the first stage of braking the toroidal velocity of the fluid with respect to the halting vessel increases (as the probe is attached to the vessel, the measurement is performed in this initially moving frame of reference, and the initial zero value of the fluid velocity corresponds to solid body rotation). The maximum of the toroidal fluid velocity is reached as the vessel stops, and the subsequent dynamics is measured in the frame at rest. In this process, a transverse (poloidal) velocity has been developed. The corresponding variations of the toroidal and poloidal velocities, averaged over 20 runs are shown in Fig.2. The generation of poloidal velocity is provided by the curved channel and becomes more effective with increasing "thickness" of the torus [4]. For the maximal rotation rate, $\Omega = 50$ rps, at the end of braking the ratio of poloidal to toroidal mean velocities reaches $U^{pol} / U^{tor} = 0.18$. The maximal toroidal velocity $U^{tor} = 0.69\ V_0 = 39$ m/s, where V_0 is the velocity of the sodium on the channel axis before the brake. For details, refer to [3].

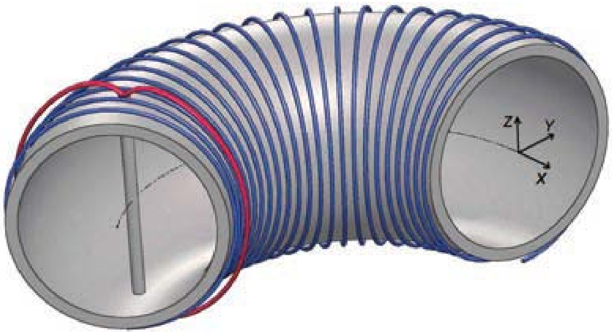

a)

b)

Figure 1: a) schematic of the toroidal channel; b) 3-component magnetic field probe.

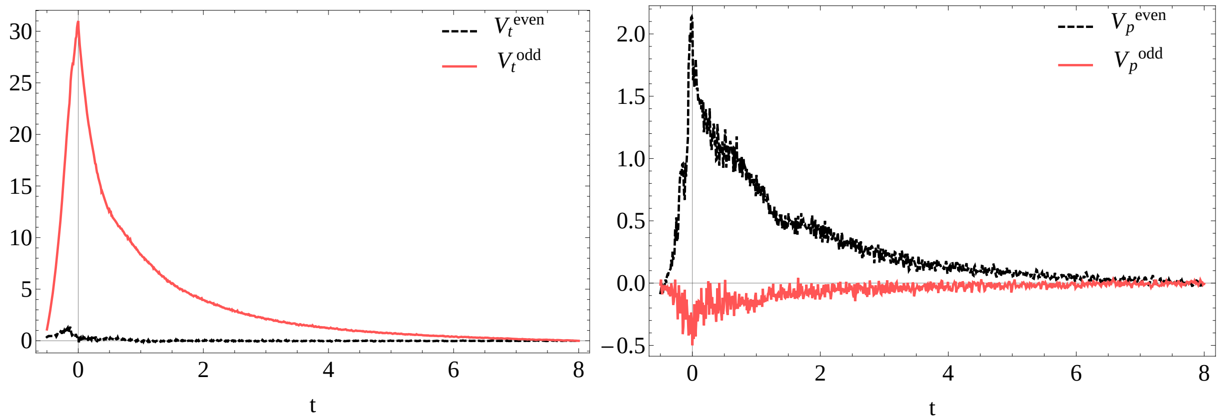

Figure 2: Evolution of mean toroidal (left) and poloidal (right) velocity for $\Omega = 40??$ rps
Red line corresponds to a half the sum and black one is a half the difference of measurements, obtained by clockwise and counterclockwise rotation of torus.

A coil, wound around the channel, is supplied by stabilized direct current and produces the toroidal field $B_T \approx 4G$ (at the channel centerline). A tube of diameter 10 mm, crosses the channel parallel to the axis of rotation (Fig.1a) and located at the channel cross-section opposite to the position of the velocity probe. This tube can be used separately for local and integral magnetic field measurements. We measure three components of the local induced magnetic field **b** by a 3D Hall probe (see Fig.1b), constructed on Sentron's CSA-1V chips with 300 V/T magnetic sensitivity. The probe can move in the tube and can be fixed at the desired coordinate z.

To obtain integral magnetic field properties the same tube can be used to wound additional measuring coils, embracing two halves of channel's cross-section (shown by red in

Fig.1). Coil's signal describes the change of internal magnetic flux as U= –dΦ/dt. This signal is being amplified using low noise voltage preamplifier SR560 (Stanford Research Systems, Inc., Sunnyvale, USA).

3. Characteristics of magnetic field

To obtain mean and statistical properties of local magnetic field 11 experiments for each magnetic probe position and rotation direction are made. To recoup external magnetic field influence one more series was performed with $B_T = 0$. Evolution of b_X and b_Z for several probe's coordinates is shown on Fig.3. t=0 corresponds to the beginning of braking. Coordinate z shows the position of the probe in the tube: z=0 corresponds to central position in the torus' cross-section, z=±80 are left- and right most possible positions in the tube.

Upper panels in Fig.3 show the even part of the magnetic field (the half-sum of signals, obtained for opposite direction of channel rotation) and lower panels show the odd component with respect to the direction of rotation. The main effect of magnetic field suppression is clearly seen in the B_X component. This can be explained as displacement of magnetic field from the turbulent core to the outer part of the channel cross-section. Some nonuniformities of magnetic field can be seen on B_Z graph.

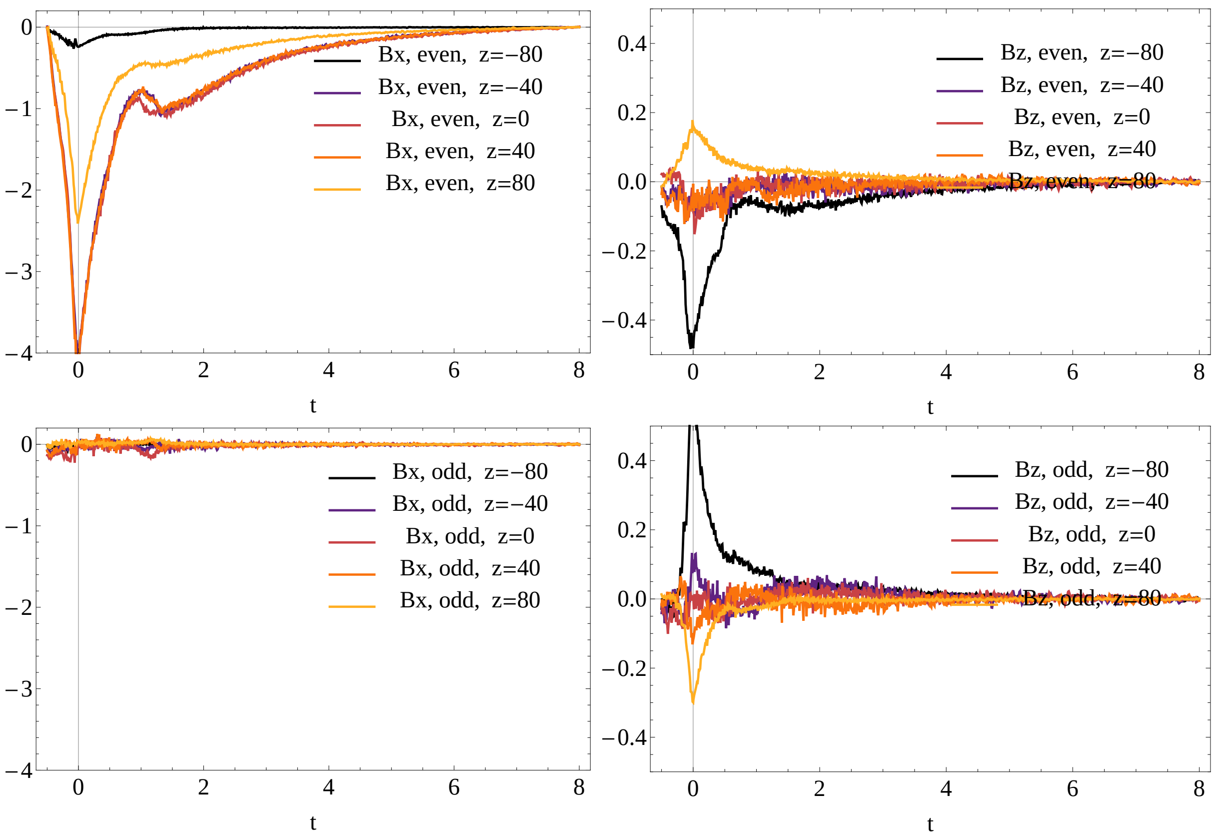

Figure 3: Local magnetic field evolution in several points along z-axis. Upper graphs correspond to a half-sum and lower ones show the half-difference of measurements, obtained by clockwise and counterclockwise rotation of torus.

Putting maximal values of longitudinal magnetic field component suppression for each probe's position allows us to restore the distribution of magnetic field along the z axis in the cross-section of the torus (see Fig.4). From integral measurements we can see the conservation of total magnetic flux in the cross-section of the coil. It means that the magnetic field is partially displaced to the channel periphery, where the B_z field should increase. We do not observe any increase, thus the fields should be shifted into the walls.

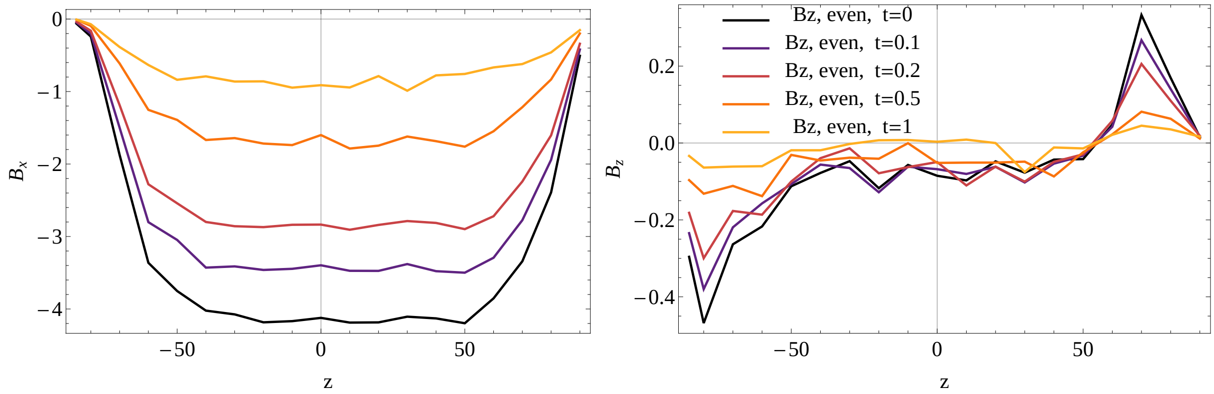

Figure 4: Profiles of local magnetic field components for several time intervals from the beginning of breaking with constant component subtracted.

Comparison of graphs from Fig.5 gives information about the origin of magnetic field displacement. Evolutions of magnetic field fluctuations follows the evolution of energy of velocity pulsations, which are caused by the turbulence.

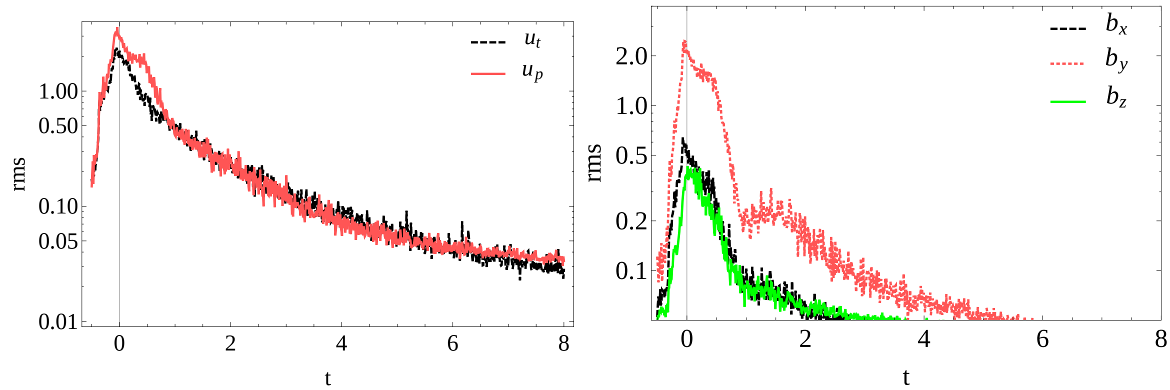

Figure 5: Fluctuating part of the torodal and poloidal velocity (left) and of local magnetic field components (right).

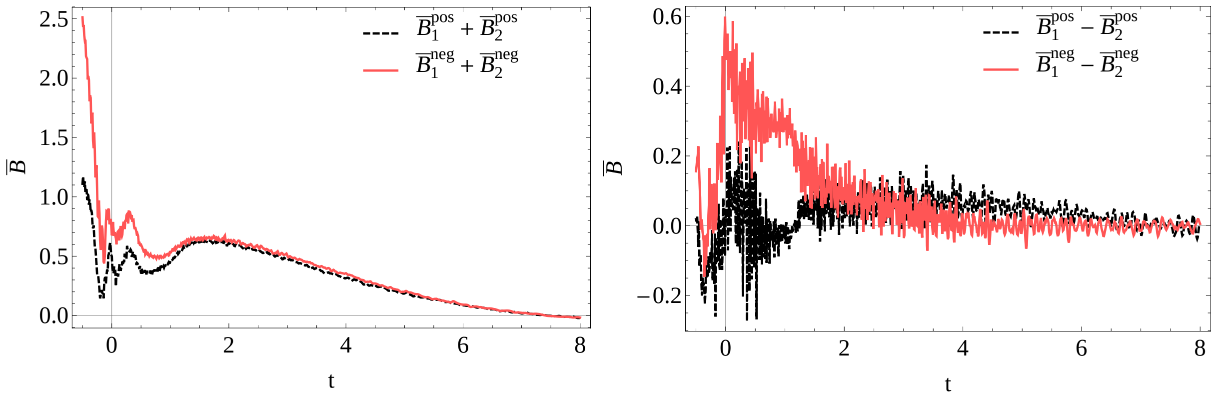

Figure 6: Sum (left) and difference (right) of measurements obtained by measuring coils. Dashed line and solid line correspond to clockwise and counterclockwise rotation of torus, respectively.

Local measurements do not provide the whole information about distribution of the magnetic field for clear interpretation. Integral measurements of magnetic flux can support our guess about the turbulent diamagnetic effect responsible for magnetic field dump in the turbulent flow. Mean field theory suggest that magnetic field must be pushed from intensive turbulence to more quiet regions. In our case it means that the magnetic fields can be transported to the border of the channel or even in the walls, therefore so that we do not observe an increase of magnetic field by local probes. Independent measurements of EMF in two coils allow us to estimate the averaged magnetic field over the channel half cross-sections (see fig. 6). First of all we do not observe significant change of the total magnetic flux along the channel. We explain an increase of 1 Gauss order as result of advection of inhomogeneous magnetic field near the wall caused by rough step of induction coil wings. This value is in agreement with measurements of B_z component due to same effect. The second interesting result we found in residual flux between two coils (right panel in Fig.6). We explain strong fluctuation as an effect of the Karman vortices generated by the stream flows around the tube installed in the channel. These vortices produced specific oscillations with frequency decaying as the ratio of the mean flow to radius of the tube.

4. Conclusion

Our measurements show that during the highly turbulent stage of flow evolution the *mean* magnetic field is reduced by a factor of 0.6. The observed effect can be explained as the result of turbulent diamagnetism described by the term curl ($\mathbf{g}\times\mathbf{B}$) in the mean-field induction equation (here **g** is the gradient of the energy of turbulent fluctuations and **B** is the mean magnetic field).

Acknowledgements. Financial support from RFBR project 14-01-96010_r_ural_a is gratefully acknowledged.

5. References

[1] Raedler K.-H., Stepanov R. Phys. Rev. E, 2006, V.73. 056311.

[2] Frick, P., Noskov, V., Denisov, S., Stepanov, R. Direct measurement of effective magnetic diffusivity in turbulent flow of liquid sodium. Phys. Rev. Lett., vol. 105 (2010), no. 18, pp. 184502.

[3] Noskov, V. et al. Dynamics of a turbulent spin-down flow inside a torus. Phys. Fluids, vol. 21 (2009), no. 4, pp. 045108

[4] Frick, P., Noskov, V., Denisov, S., Stepanov, R. Turbulent viscosity and turbulent magnetic diffusivity in a decaying spin-down flow of liquid sodium. Phys. Rev. E, vol. 85 (2012), no. 1, p. 016303.

DYNAMO ACTION IN PRECESSING CYLINDERS

NORE[1] C., LEORAT[2] J., GUERMOND[3] J.-L., CAPPANERA[1] L., LUDDENS[1,4] F.
[1]*LIMSI-CNRS/*Bâtiment 508, BP 133, 91403 Orsay cedex, France et Université Paris-Sud, 91405 Orsay cedex, France, [2]*Luth*, Observatoire de Paris-Meudon, place Janssen, F-92195-Meudon, France, [3]Department of Mathematics, Texas A&M University, 3368 TAMU, College Station, Texas 77843-3368, USA,
[4]*IMB* Université Bordeaux I, 351 cours de la Libération, 33405 Talence cedex, France.
E-mail address of corresponding author: caroline.nore@limsi.fr

Abstract : It is numerically demonstrated by means of a magnetohydrodynamic (MHD) code that precession can trigger dynamo action in a cylindrical container. Fixing the angle between the spin and the precession axis to be $\pi/2$, two configurations of the spinning axis can be explored: either the symmetry axis of the cylinder is parallel to the spin axis (this configuration is henceforth referred to as the *axial spin* case), or it is perpendicular to the spin axis (this configuration is referred to as the *equatorial spin* case). In both cases, when the Reynolds number, based on the radius of the cylinder and its spin angular velocity, increases, the flow, which is initially centro-symmetric, loses its stability and bifurcates to a quasi-periodic motion. This unsteady and asymmetric flow is shown to be capable of sustaining dynamo action in the linear and nonlinear regimes. The magnetic field thus generated is mainly quadrupolar in the *axial spin* case while it is mainly dipolar in the *equatorial spin* case. These numerical evidences of dynamo action in a precessing cylindrical container may be useful for the design of new dynamo experiments, such as the one planned at the DRESDYN facility in Germany [1].

1. Introduction

The idea that precession can be a potent mechanism to drive dynamo action has long been debated (see for example [2]). Modern astrophysical observations of some planetary dynamos can contribute to resolving this issue, although definite evidence is still lacking. Because of the large computing resources required, it is only recently that numerical computations have demonstrated that dynamo action occurs in different precessing containers: spherical [3] and spheroidal [4] ones. Since neither spheres nor spheroids are convenient for large-scale experiments, it is instructive to investigate whether similar results can be obtained in cylindrical containers. The purpose of the present paper is to report results from our investigating this issue by using a nonlinear magnetohydrodynamic (MHD) code called SFEMaNS (for Spectral / Finite Elements for Maxwell and Navier-Stokes equations, [5]). This code solves the nonlinear MHD equations for incompressible fluids in heterogenous domains (with spatial distributions of electrical conductivity or magnetic permeability) composed on conducting and non-conducting parts. SFEMaNS is spectral in the azimuthal direction and uses finite elements in meridional section (see [6] for more details). Six parameters govern the flow: the aspect ratio of the container, the precession angle (angle between the spin axis OS and the precession axis OP), the spin angle (angle between the symmetry axis OZ and the spin axis OS), the precession rate ε (ratio of the precession and spin angular velocity), the Reynolds number Re and the magnetic Reynolds number Rm (see fig. 1). Choosing the container height equal to its diameter, the precession axis orthogonal to the spin axis (precession angle is $\pi/2$) and the precession rate ε=0.15, we are left with two limit configurations: one called *axial spin* for which the spin angle is 0 and the symmetry axis of the cylinder remains fixed in the precession frame (see fig. 1 right) and another one called *equatorial spin* for which the spin angle is π/2 and the symmetry axis rotates in the precession frame (see fig. 1 left). We focus our attention on these two configurations because, in the *axial spin* case, the wall speed is tangent to the wall and only the viscous stress on the wall drives the flow while, in the *equatorial spin* case, the flow is driven by the pressure on the wall and is therefore inertially driven. The MHD equations solved by SFEMaNS are written:

$$\partial_t \mathbf{u} + (\mathbf{u} \cdot \nabla)\mathbf{u} + 2\varepsilon \mathbf{e}_p \times \mathbf{u} + \nabla p = \frac{1}{R_e}\Delta \mathbf{u} + \mathbf{f},$$
$$\nabla \cdot \mathbf{u} = 0,$$
$$\partial_t \mathbf{h} - \nabla \times (\mathbf{u} \times \mathbf{h}) = \frac{1}{R_m}\Delta \mathbf{h},$$
$$\nabla \cdot \mathbf{h} = 0,$$

where **u**, p and **h** are the velocity field, the pressure and the magnetic field, respectively. **f** is the Lorentz force.

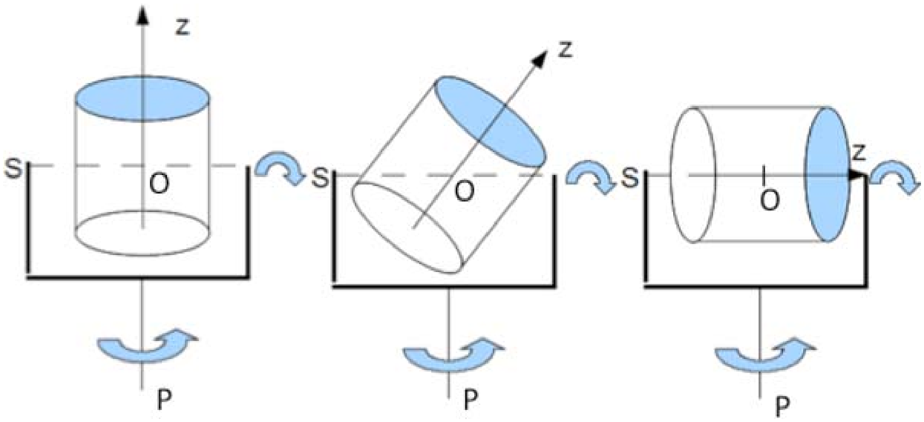

Figure 1: Different configurations for precession driving: (left) equatorial spin (the spin angle is π/2); (middle) oblique spin; (right) axial spin (the spin angle is 0). OS is the spin axis, OP the precession axis and OZ the symmetry axis.

2. Hydrodynamic study

In this section we examine the two configurations in the hydrodynamic regime, where Re is the control parameter. At low Reynolds number, the flow is steady and centro-symmetric, meaning that **u**(**r**)=-**u**(-**r**). At larger Reynolds numbers, the loss of centro-symmetry can be monitored by inspecting the symmetric and antisymmetric components of the velocity field: $\mathbf{u_s}$(**r**,t)= (**u**(**r**,t)-**u**(-**r**,t))/2 and $\mathbf{u_a}$(**r**,t)= (**u**(**r**,t)+**u**(-**r**,t))/2. In the Navier-Stokes simulations reported here, we monitor the time evolution of the total kinetic energy K(t)= 0.5 ∫ $\mathbf{u}^2$ dV and that of the asymmetric kinetic energy Ka(t)= 0.5 ∫ $\mathbf{u_a}^2$ dV. The time evolution of these two quantities are reported in Figure 2 in the two cases configurations. For the *axial spin* case, the efficiency of the viscous forcing decreases when Re increases; for the *equatorial spin* case, saturation is not achieved yet at Re = 2000, (see left panel). The asymmetry ratio is larger in the *equatorial spin* case than in the *axial spin* case (see right panel). Based on the phenomenological argument that dynamo action is favored by symmetry breaking, it could be anticipated that the *equatorial spin* case would generate dynamo action at a lower threshold than the *axial spin* case. However, it is shown below that this intuitive argument is incorrect.

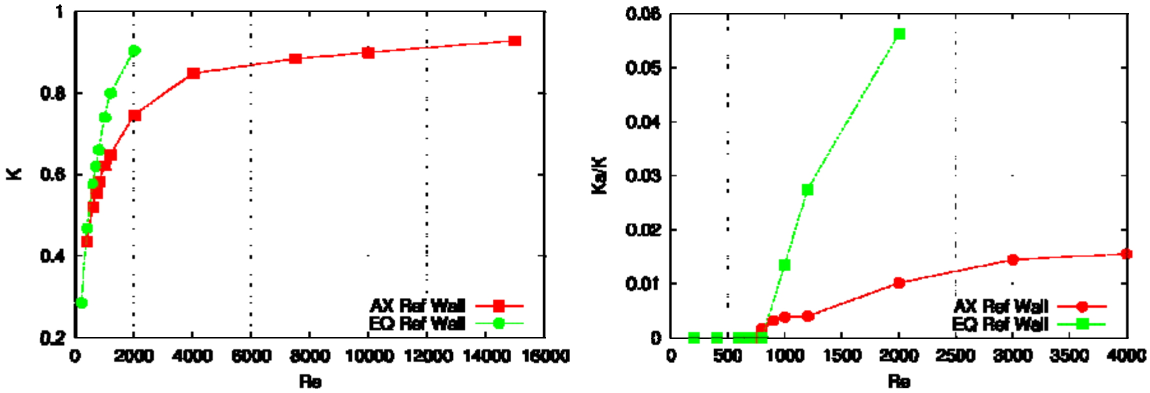

Figure 2: Comparisons between the axial and equatorial spin cases in the reference frame of the wall (also called the *mantle frame*) for a fixed precession rate 0.15: (left) total kinetic energy as a function of Re; (right) asymmetry ratio Ka(t)/K(t) as a function of Re.

3. Dynamo action

We now investigate the MHD regime, where Re and Rm are the two control parameters. The nonlinear MHD simulations use a small magnetic seed field as initial data or restart from a state computed at neighboring parameters. As already observed for spherical and spheroidal dynamos, dynamo action occurs after symmetry breaking of the flow when the magnetic dissipation is small enough, i.e. for magnetic Reynolds numbers Rm above a critical value $Rm_c(Re)$.

In the *axial spin* case, we have found [7] that $Rm_c \approx 750$ at Re = 1200. The generated magnetic field is unsteady and mainly quadrupolar. The computed critical curve $Rm_c(Re)$ is shown in Figure 3. The critical magnetic Reynolds number is not a monotonic function of Re; there is a minimum value at Re = 1200. It seems that increasing Re leads to an efficiency reduction of the dynamo.

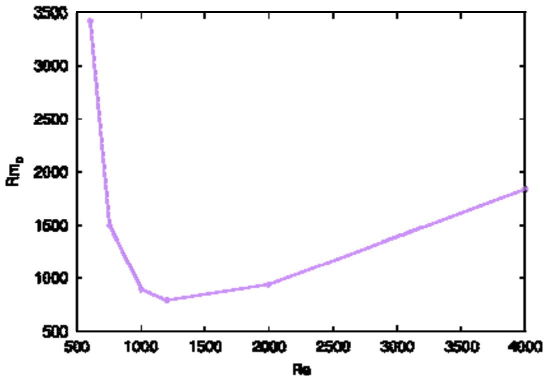

Figure 3: Critical curve $Rm_c(Re)$ in the *axial spin* case.

In the *equatorial spin* case, various MHD runs are performed at Re=1200 for different values of the magnetic Reynolds numbers Rm. The onset of dynamo action is monitored by recording the time evolution of the magnetic energy in the conducting fluid $M(t)= 0.5 \int \mathbf{h}^2\, dV$. Two types of simulations are done: linear dynamo runs are first performed by imposing $\mathbf{f} = 0$ in the Navier-Stokes equations, i.e. the retroaction of the Lorentz force on the velocity field is disabled, then the Lorentz force **f** is restored in the Navier-Stokes equations to observe the nonlinear saturation.

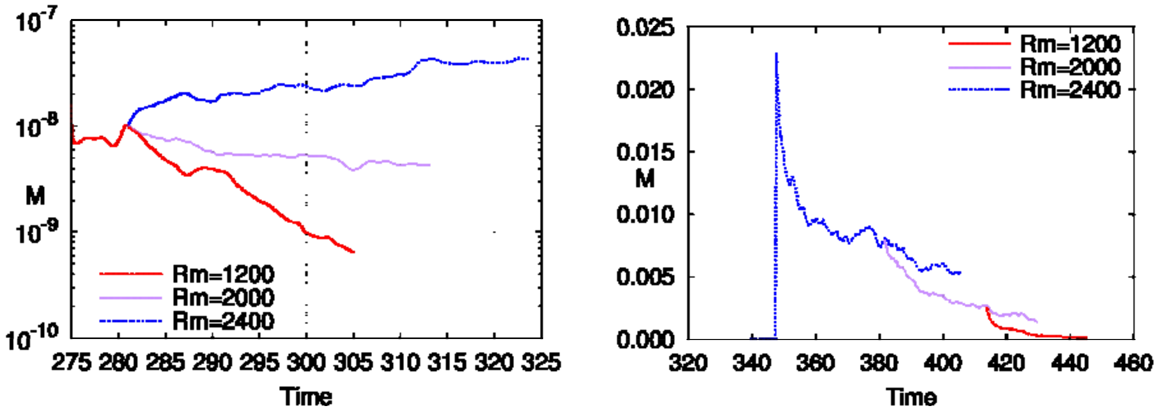

Figure 4: Time evolution of the magnetic energy M in the conducting fluid (left) in the linear regime from t = 275 at Re = 1200 and various Rm as indicated (in lin-log scale) and (right) in the nonlinear regime for Re = 1200 and various Rm as indicated. *Equatorial spin* case.

(1) A first series of linear dynamo simulations is done with Rm=1200, 2000 and 2400. The time evolution of M is shown in Figure 4 (left). The initial velocity and magnetic field for the runs at Rm=2000 and 2400 are the velocity and the magnetic fields obtained from the run at Rm=1200 at t=282. Dynamo action occurs when M(t) is an increasing function of time for large times with a positive growthrate (as is the case for Rm=2400). Linear interpolation of the growthrates gives the critical magnetic Reynolds number $Rm_c \approx 2130$ at Re=1200, i.e. the critical magnetic Reynolds number is almost three times larger than that in the *axial spin* case.

(2) To observe the nonlinear saturation (the Lorentz force **f** is restored in the Navier-Stokes equations), we use as initial data the velocity and magnetic fields from the linear MHD run at t=346 for Rm=2400. The amplitude of the initial magnetic field is multiplied by 400 to reach saturation faster; the initial velocity field is kept unchanged. Figure 4 (right) shows that M decreases rapidly over a time period corresponding to one turnover time, i.e. until t=352, and begins to oscillate thereafter. After restarting the MHD run at t=382 with Rm=2000 and running it until t=428, we observe that M decreases. After restarting the MHD run at t=412 with Rm=1200 and running it until t=446, we observe that the dynamo dies in a short time lapse. A snapshot of the vorticity and the magnetic field lines at Re=1200 and Rm=2400 is shown on fig. 5. We observe a central S-shaped vortex deformed by the precession and connected to the walls through viscous boundary layers. The magnetic energy is dominated by the azimuthal modes m=1, 2, 3 and the magnetic field lines exhibit a dominant dipolar shape.

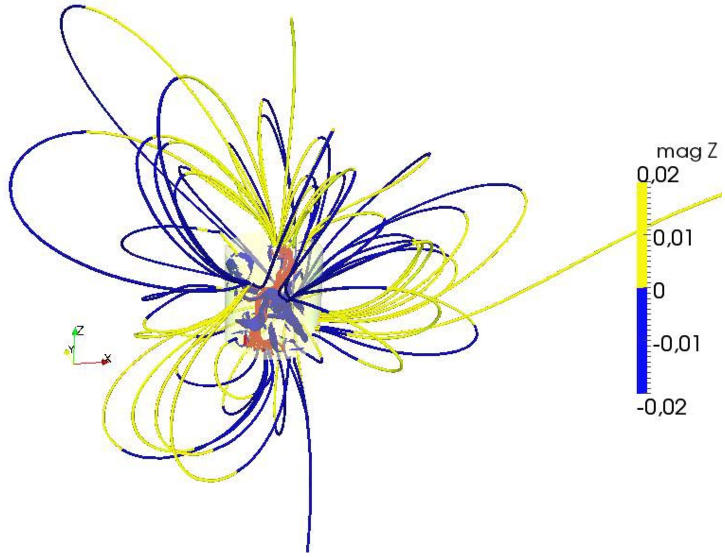

Figure 5: Snapshot at Re=1200 and Rm = 2400 of the vorticity field lines (grey/red) and the magnetic field lines colored by the axial component (light grey/yellow for positive vertical magnetic field component and black/blue for negative vertical magnetic field component). The view is seen from the side (Ox is the spin axis, Oz the precession axis). *Equatorial spin* case.

4. Conclusion

We have studied the dynamo capabilities of a precessing cylinder in two limit configurations. The dynamo threshold found in the *equatorial spin* configuration is larger than that found in the *axial spin* configuration at the same Reynolds number Re=1200. This result contradicts the intuition that wall-normal stress would enhance symmetry breaking and would favor dynamo action. The challenge is now to increase the Reynolds numbers in the MHD simulations to more realistic values.

5. References

[1] Stefani, F., Eckert, S., Gerbeth, G., Giesecke, A., Gundrum, Th., Steglich, C., Weier, T., Wustmann, B. DRESDYN - A new facility for MHD experiments with liquid sodium. Magnetohydrodynamics 48, 103-113, 2012 .
[2] W. V. R. Malkus. Precession of the Earth as the cause of geomagnetism: Experiments lend support to the proposal that precessional torques drive the Earth's dynamo. Science, 160(3825): 259–264, 1968.
[3] A. Tilgner. Precession driven dynamos. Physics of Fluids, 17(3):034104, 2005.
[4] C.-C. Wu and P. Roberts. On a dynamo driven by topographic precession. Geophysical & Astrophysical Fluid Dynamics, 103(6):467–501, 2009.
[5] J.-L. Guermond, R. Laguerre, J. Léorat, and C. Nore. Nonlinear magnetohydrodynamics in axisymmetric heterogeneous domains using a Fourier/finite element technique and an interior penalty method. J. Comput. Phys., 228:2739–2757, 2009.
[6] J. L. Guermond, J. Léorat, F. Luddens, C. Nore and A. Ribeiro, Effects of discontinuous magnetic permeability on magnetodynamic problems, J. Comp. Physics 230, 6299–6319, 2011.
[7] C. Nore, J. Léorat, J. L. Guermond and F. Luddens, Nonlinear dynamo action in a precessing cylindrical container, Physical Review E 84, 016317, 2011.

ORIENTATION, KINETIC AND MAGNETIC ENERGY OF PLANETARY DYNAMOS, THEIR INVERSIONS AND ASYMMETRIES

Starchenko S. V.

IZMIRAN, Kaluga highway 4, Troitsk, Moscow, 142190.

E-mail: sstarchenko@mail.ru

Abstract: I derive, simplify and analyze integral evolutional laws of the kinetic, magnetic, and orientation energies in the liquid core of the Earth's type planets. These laws are reduced to the system of three ordinary differential equations for a given convection power. Estimates are obtained for the characteristic velocities, magnetic fields, periods and scales depending on the convection power at the stable states and near the inversion/excursion. That allows estimating how diffusion can determine the average period between geomagnetic reversals due to turbulent, thermal, electromagnetic and critical viscosity-compositional processes.

1. Introduction

I derive, simplify and analyze integral evolutional laws of the kinetic, magnetic, and original orientation energies in the liquid core of the Earth's type planets. These integral laws are reduced to the simplest system of three ordinary differential equations for a given convection power.

Estimates are obtained for the characteristic velocities, magnetic fields, periods and scales depending on the convection power at the stable states and near the inversion/excursion. It was shown that for the implementation of this short-time inversion/excursion the convection power should achieve some rare value, while a normal deviation from this value results in longer-time stable period. Here the inversion is a global process when the volume integral of the scalar product of convective velocity on the magnetic field changes sign.

So, the inversions and asymmetries are due to two types of stable states. Named as "lined" is a state with the magnetic field predominantly directed along velocity, while "contra lined" state is with their opposite direction. The lined state is characterized by smaller convection power and magnetic field in contrast to the contra lined state. The duration of the lined state is likely smaller than the duration of opposite state when the geodynamo power gradually increases with time, while for decreasing power it is vice versa.

Basing on the obtained results I estimate how diffusion can determine the average period between geomagnetic reversals due to turbulent, thermal, electromagnetic and critical viscosity-compositional processes. Predominant in this process, in many cases, can be identified from the dependence of the reversal frequency on the magnetic field intensity from paleomagnetic data. The data available to me suggest domination of the thermal processes.

2. Initial equations and hydromagnetic integrals

Initial equations with buoyancy acceleration **A**, velocity **V** and electromagnetic fields are from [1, 2] for the Earth's type planets:

$$\frac{\partial \mathbf{V}}{\partial t} - \mathbf{V}\times\nabla\times\mathbf{V} + 2\Omega\mathbf{1}_z\times\mathbf{V} + \nabla p + \nu\nabla\times(\nabla\times\mathbf{V}) = \mathbf{A} - \frac{\mathbf{B}\times\nabla\times\mathbf{B}}{\mu_0\rho},\ \nabla\cdot\mathbf{V} = 0. \qquad (1, 2)$$

$$\frac{\partial \mathbf{B}}{\partial t} = -\nabla\times\mathbf{E}, \nabla\cdot\mathbf{B} = 0, \mathbf{E} + \mathbf{V}\times\mathbf{B} = \frac{\nabla\times\mathbf{B}}{\mu_0\sigma}. \qquad (3, 4, 5)$$

Notations are standard hereafter. Magnetic **B**, electric **E** and velocity **V** fields in (1-5) should satisfy jump (6, 7) and no-sleep (8) conditions on outside insulating $r = r_*$ and inside conducting $r = r_i$ co-rotating boundaries:

[B]=0, **[E]=0**, **V=0**. (6, 7, 8)

Integrating the scalar product of $\rho\mathbf{V}$ by (1) over the conducting planetary core one obtain the well-known equation for the kinetic energy:

$$\rho\frac{d}{dt}\left(\int_0^{r_*}\frac{V^2}{2}d^3r\right)=\int_0^{r_*}\left(\rho\mathbf{A}\cdot\mathbf{V}-\frac{\mathbf{V}\times\mathbf{B}\cdot\nabla\times\mathbf{B}}{\mu_0}-\rho\nu|\nabla\times\mathbf{V}|^2\right)d^3r. \tag{9}$$

Similarly $\mathbf{B}/\mu_0$ times (3) with making use of (4-8) and **E=0** on the insulating boundary give us known magnetic energy equation (10) together with Lorentz force power representation (11) that will be useful for further simplification:

$$\frac{d}{dt}\left(\int_0^{r_*}\frac{B^2}{2\mu_0}d^3r\right)=\int_0^{r_*}\left(\frac{\mathbf{V}\times\mathbf{B}\cdot\nabla\times\mathbf{B}}{\mu_0}-\frac{|\nabla\times\mathbf{B}|^2}{\mu_0^2\sigma}\right)d^3r,\ \frac{\mathbf{V}\times\mathbf{B}\cdot\nabla\times\mathbf{B}}{\mu_0}=\sigma|\mathbf{V}\times\mathbf{B}|^2-\sigma\mathbf{V}\times\mathbf{B}\cdot\mathbf{E}. \tag{10, 11}$$

To obtain the equation for cross-helicity $\mathbf{V}\cdot\mathbf{B}$, I multiply (1) with **B**, (3) with **V**, add the results, integrate, simplify and denoting $\eta=\nu+1/\mu_0\sigma$, obtain:

$$\frac{d}{dt}\left(\int_0^{r_*}\mathbf{V}\cdot\mathbf{B}d^3r\right)=\int_0^{r_*}\left(\mathbf{A}\cdot\mathbf{B}-2\Omega\mathbf{1}_z\cdot\mathbf{V}\times\mathbf{B}-\eta\nabla\times\mathbf{V}\cdot\nabla\times\mathbf{B}\right)d^3r$$
$$+\int_{r=r_*}(\nu\mathbf{1}_r\times\mathbf{B}\cdot\nabla\times\mathbf{V}-pB_r)d^2r\ . \tag{12}$$

Multiplying the first integral in (12) by $\sqrt{\rho/\mu_0}$, I define orientation energy:

$$\mathrm{O}\equiv\sqrt{\frac{\rho}{\mu_0}}\int_0^{r_*}\mathbf{V}\cdot\mathbf{B}d^3r. \tag{13}$$

Let's as well universally define a given convection power as

$$W\equiv\int_0^{r_*}\mathbf{A}\cdot\mathbf{V}d^3r. \tag{14}$$

3. Simplified system

I define time-dependent kinetic Y, magnetic X and orientation Z values as

$$Y=\sqrt{\int_0^{r_*}V^2d^3r}\approx V_*,\ X=\sqrt{\int_0^{r_*}B^2d^3r}\approx B_*,\ Z=\int_0^{r_*}\mathbf{V}\cdot\mathbf{B}d^3r, \tag{15}$$

while stars are marking slowly varying with time typical values.

Using given $W(t)$ from (14), simply approximating vectors production and derivatives and neglecting by small terms I obtain from (9-12) the simplest system:

$$Y\frac{dY}{dt}=W-\frac{c}{\rho}(X^2Y^2-Z^2),\ X\frac{dX}{dt}=\mu_0c(X^2Y^2-Z^2)-\frac{X^2}{\tau},\ \frac{dZ}{dt}=CW-\omega(XY-Z). \tag{16}$$

Here c, τ, C and ω cold slowly change with time and will be estimated below.

All the derivatives of the system (16) are zero in stationary point that is denoted by s:

$$Y_s=\frac{1}{2}\frac{W_0+W}{\sqrt{\tau\mu_0cW_0W}},\ X_s=\sqrt{\tau\mu_0\rho W},\ \frac{Z_s}{Y_sX_s}=\frac{W_0-W}{W_0+W}\approx\cos o,\ W_0\equiv\frac{\rho}{c}\left(\frac{\omega}{C}\right)^2. \tag{17}$$

Here o is an average between velocity and magnetic field. This angle $o\approx\pi$ in the stable state, while $o\approx\pm\pi/2$ during inversion/excursion when $W=W_0$. Supposing $C=B_0/V_0$, $X_s=B_0$, $Y_s=V_0$ for this moment I obtain typical inversion/excursion values:

$$V_0=\sqrt{\frac{W_0}{\omega}}\approx 0.7\text{mm/s},B_0=\sqrt{\frac{\omega\rho}{c}}\approx 1\text{mT},\tau_0=\frac{\omega}{\mu_0cW_0}\approx\ 2\cdot 10^8\text{s}\Rightarrow d_0\approx 10\,\text{km}. \tag{18}$$

Those estimates are for $W_0 = 3{\cdot}10^{-13}$ Вт/кг from [Braginsky, Roberts, 1995; Starchenko, Jones, 2002; Starchenko, Pushkarev, 2013; Olson et al., 2013], well-known $\rho = 10^4$ kg/m^3, while $\omega = 10^{-6}$/s and $c = 10^4$ Sm/m are from the chapter 5 below.

4. Inversion frequencies due to diffusion

Well-known value of the average time between inversions is about half million years [3, 4, 5]. Here I consider different diffusion processes matching this value.

Turbulent diffusion coefficient I estimate as $V_* d/3$ giving the average time $T = 3(r_*)^2/V_* d$. For that using (17) and ($C=B_*/V_*$, $X_s=B_*$, $Y_s=V_*$) I obtain as required:

$$T \approx 3r_*^2 \frac{\mu_0}{B_*}\sqrt{\frac{2W\omega\rho c}{W_0+W}} \approx 1.5{\cdot}10^{13}\text{s}. \tag{19}$$

for different realistic parameters from [6, 2, 1]. Obviously this time T is diminishing with a growing of magnetic field that could be tested with paleomagnetic data.

Using up to date determination of conductivity σ from [6] one immediately obtain desired half-million years as a typical magnetic diffusion time $(r_*)^2\mu_0\sigma$ that depends on relatively well-known material properties only.

Thermal diffusion time on magnetic size d could be represented from (16-17) using $X_s = B_*$ as

$$T \approx B_*^2/(\mu_0^2 c\rho W k)\,. \tag{20}$$

This again gives half-million years with thermal diffusion $k=2{\cdot}10^{-5}$ m^2/s from [6]. That (20) contrary to (19) is growing with a growing of magnetic field and that is indeed rudely confirmed with paleomagnetic data of [4].

5. Scaling of the energy equations

Here using (15) and planetary dynamo numerical [7] and analytic [8] scaling laws I estimate coefficient of the energy system (16) as functions of the given convection power $W(t)$.

Using well-known after Prof. Christensen magnetic scaling law for B_* and (17) I obtain an excellent representation for the first coefficient from (16) τ that has a meaning (and real value!) of the secular variation

$$B_* = (\mu_0\rho)^{1/2}(WH)^{1/3} = X_s \Rightarrow \tau = (H^2/W)^{1/3}\,. \tag{21}$$

Here $H = (r_* - r_i)$ and τ, as it is directly observed for centuries, is of order decades for geodynamo typical W~10^{-13} W/kg [7, 2, 1].

Scaling law for velocity V_*, (17) and (21) gives quadratic equation for $\sqrt{W_0}$:

$$V_* = \left(W^2 H/\Omega\right)^{1/5} = Y_s \Rightarrow W_0 - 2\Omega^{-1/5}W^{11/15}H^{8/15}\sqrt{\mu_0 c W_0} + W = 0\,. \tag{22}$$

That gives W_0 via given W as

$$W_0 = \left(\Omega^{-1/5}W^{11/15}H^{8/15}\sqrt{\mu_0 c} \pm \sqrt{(\Omega^{-1/5}W^{11/15}H^{8/15})^2\mu_0 c - W}\right)^2. \tag{23}$$

Here « + » for $W_0 > W$ and « - » for $W_0 < W$, while $W = W_0$ during inversion or excursion and

$$W = W_0 = \Omega^{-3/2}H^4(\mu_0 c_0)^{15/4},\ c = c_0 = (\Omega^6 W_0^{-7}H^{-16})^{1/15}/\mu_0 \tag{24}$$

that had been already used in (18) above.

Sinus of the average angle between magnetic and velocity field from [Starchenko, Pushkarev, 2013] s could be presented from cosines from (17) as

$$\frac{W_0 - W}{W_0 + W} = \cos o = \pm\sqrt{1-s^2} = \pm\sqrt{1-\left(\frac{W}{H^2\Omega^3}\right)^{4/15}}\,. \tag{25}$$

From (25) one can obtain W_0 via W. That in (23) determines $c(t)$ from (16). Two remained coefficients of (16) are determined by (17) as

$$C\sqrt{cW_0/\rho} = \omega, \tag{26}$$

that with (23) determine all the coefficients with up to only one fitting parameter.

Acknowledgements

Author is grateful for the supports by Russian RFBR grant No 13-05-00893.

References

[1] Braginsky S. I., Roberts P. H. Equations governing convection in the Earth's core and the geodynamo // Geophys. Astro. Fluid. 1995. V. 79. P. 1–97.
[2] Starchenko S.V., Jones C.A. Typical velocities and magnetic field strengths in planetary interiors // Icarus. 2002. V. 157. P. 426-435.
[3] Ogg J.G., Ogg G., Gradstein F.M. The Concise Geologic Time scale // Cambridge University Press. 2008. 150 pp.
[4] Shcherbakov V., Fabian K. The geodynamo as a random walker: A view on reversal statistics // J. Geophys. Res. 2012. V. 117. B03101. doi:10.1029/2011JB008931.
[5] Olson P., Deguen R., Hinnov L.A., Zhong S., Controls on geomagnetic reversals and core evolution by mantle convection in the Phanerozoic // Phys. Earth Planet. Int. 2013. V.214. P. 87-103.
[6] Gomia H., Ohtaa K., Hirosea K., Labrossed S., Caracasd R., Verstraetef M.J., Hernlundb J.W. The high conductivity of iron and thermal evolution of the Earth's core // Phys. Earth Planet. Inter. 2013. V. 224. P. 88-103.
[7] Christensen U. R. Dynamo Scaling Laws and Applications to the Planets // Space Sci. Rev. 2010. V. 152. P. 565–590.
[8] Starchenko S.V., Pushkarev Y.D. Magnetohydrodynamic scaling of geodynamo and a planetary protocore concept // Magnetohydrodynamics. 2013. V. 49. No 1. P. 35-42.

TURBULENT DYNAMO PROBLEM IN ANISOTROPIC HELICAL MAGNETOHYDRODYNAMIC TURBULENCE

JURCISIN M., STEHLIK M., JURCISINOVA E.
Institute of Experimental Physics, Slovak Academy of Sciences
Email: jurcisin@saske.sk

One fundamental theoretical problem in the magnetohydrodynamics is the turbulent dynamo problem, i.e., the problem of the generation of a large-scale homogeneous magnetic field by the energy of the turbulent motion, which attracts large attention due to many applications in both the astrophysical and laboratory plasmas. It is known that the dynamo problem can be investigated on the fundamental level of a microscopic model by using the field theoretic formulation of the stochastic problem based on the stochastic magnetohydrodynamics equations with the presence of helicity (spatial parity violation) [1, 2]. In Refs. [1, 2], it was shown by using the field theoretic renormalization group technique that the presence of the helicity in the system leads to instabilities which are stabilized by the spontaneous occurrence of a non-vanishing homogeneous mean magnetic field which, at the same time, breaks the symmetry of the system. Namely, the generation of the large-scale magnetic field is the necessary condition for damping all perturbations to obtain stable system. However, because the instabilities are not manifested at the level of the action function itself but are found only starting from one-loop approximation, therefore the symmetry is broken dynamically (dynamical symmetry breaking mechanism). In this respect, in Refs. [1, 2] this mechanism was used for investigation of the stochastic magnetohydrodynamics with helical isotropic energy pumping and the absolute value of the generated magnetic field was found. However, the direction of the generated magnetic field remains arbitrary here. On the other hand, as we shall show in the present work the direction of the generated magnetic field is determined uniquely when the presence of anisotropy is supposed in the system. In this respect, we consider the stochastic magnetohydrodynamics with helical and, at the same time, uniaxial anisotropic energy pumping. By using the field theoretic renormalization group approach in the one-loop approximation it is shown that the presence of the uniaxial anisotropy causes that the spontaneously generated large-scale magnetic field has to be oriented in parallel to the axis that defines the direction of the uniaxial anisotropy. Besides, the explicit dependence of the absolute value of the generated magnetic field as function of the anisotropy parameters is found.

References

[1] Adzhemyan, L., Vasil'ev, A.N., Gnatich, M.: Theor. Math. Phys. 72 (1987) 940.
[2] Hnatich, M., Jurcisin, M., Stehlik, M.: Magnetohydrodynamics 37 (2001) 80.

TOWARDS A PRECESSION DRIVEN DYNAMO EXPERIMENT

STEFANI, F.[1], ALBRECHT, T.[1], GERBETH, G.[1], GIESECKE, A.[1], GUNDRUM, T. [1] , STEGLICH, C. [1], NORE, C. [2]
Affiliation: [1]Helmholtz-Zentrum Dresden-Rossendorf, P.O. Box 510119, D-01314 Dresden, Germany, [2]LIMSI-CNRS/Bâtiment 508, BP 133, 91403 Orsay cedex, France et Université Paris-Sud, 91405 Orsay cedex, France
e-mail: F.Stefani@hzdr.de

Abstract : The most ambitious project within the DREsden Sodium facility for DYNamo and thermohydraulic studies (DRESDYN) is the construction of a precession-driven dynamo experiment. After discussing the scientific background and some results of water pre-experiments and numerical predictions, we focus on the numerous structural and design problems of the machine. We also delineate the progress of the building construction, and the status of some other experiments that are planned in the framework of DRESDYN.

1. Introduction

Pioneered by the Riga [1] and Karlsruhe [2] liquid sodium experiments, the last fifteen years have seen significant progress in the experimental study of the dynamo effect and of related magnetic instabilities, such as the magnetorotational instability (MRI) [3,4] and the kink-type Tayler instability (TI) [5]. A milestone on this way was the observation of magnetic field reversals in the VKS experiment [6] which has spurred renewed interest in simple models to explain the corresponding geomagnetic phenomenon [7]. This is but one example for the fact that liquid metal experiments, though never representing perfect models of specific cosmic bodies, can indeed stimulate geophysical research.
One of the pressing questions of geo- and astrophysical magnetohydrodynamics concerns the energy source of different cosmic dynamos. While thermal and/or compositional buoyancy is considered the favourite candidate, precession has long been discussed as a complementary energy source of the geodynamo [8,9], in particular at an early evolutionary stage of the Earth, prior to the formation of the solid core. Some influence of orbital parameter variations can also be guessed from paleomagnetic measurements that show an impact of the 100 kyr Milankovic cycle of the Earth's orbit eccentricity on the reversal statistics of the geomagnetic field [10]. Recently, precession driving has also been discussed in connection with the generation of the lunar magnetic field [11], and with dynamos in asteroids [12].
Therefore, an experimental validation of precession driven dynamo action appears very attractive, yet the constructional effort and safety requirements for its realization are tremendous. In this paper, we delineate the present state of the preparations of such an experiment, along with giving an overview about the further liquid sodium experiments that are planned within the DRESDYN project at Helmholtz-Zentrum Dresden-Rossendorf.

2. To B or not to B

Compared to the flow structures underlying the Riga, Karlsruhe and VKS experiment, the dynamo action of precession driven flows is not well understood. Recent dynamo simulations in spheres [9], cubes [13], and cylinders [14] were typically carried out at Reynolds numbers Re of a few thousand, and with magnetic Prandtl numbers Pm not far from 1. Under these conditions, dynamo action in cubes and cylinders was obtained at magnetic Reynolds numbers Rm:=$\mu\sigma R^2\Omega_{rot}$ of around 700 (R is the radius, Ω is the cylinder rotation rate), which is indeed the value our experiment is aiming at. Yet, there are uncertainties about this value, which have much to do with the inaccessibility of realistic Reynolds numbers in numerical simulations. What has been achieved in this respect is some qualitative, though not quantitative, agreement of the dominant flow structures between experiment and numerics for precessing cylindrical flows. Basically, at low precession ratios $\eta := \Omega_{prec}/\Omega_{rot}$ the flow is dominated by one or a few Kelvin modes. This more or less laminar regime breaks down suddenly at $\eta \sim 0.1$ (details depend on the aspect ratio of the cylinder and the angle between rotation and precession axis). There are two global features by which this laminar-turbulent transition can be easily characterized. The first one is the energy dissipation, measurable by the motor power of the rotating cylinder. The second one is the maximum pressure difference between opposite points on the side wall of the cylinder. Figure 1a shows the maximum pressure p (numerically determined at Re=6680) and the maximum pressure difference Δp (numerically determined at Re=6680 and experimentally at Re=1.6×10^6), with all values up-scaled to the dimensions of the large machine. The right end-point, at $\eta \sim 0.07$, of the parabola-like experimental Δp curve marks the sudden transition between the laminar and turbulent regime. The corresponding numerical Δp curve is qualitatively similar, but shows significant quantitative deviations.

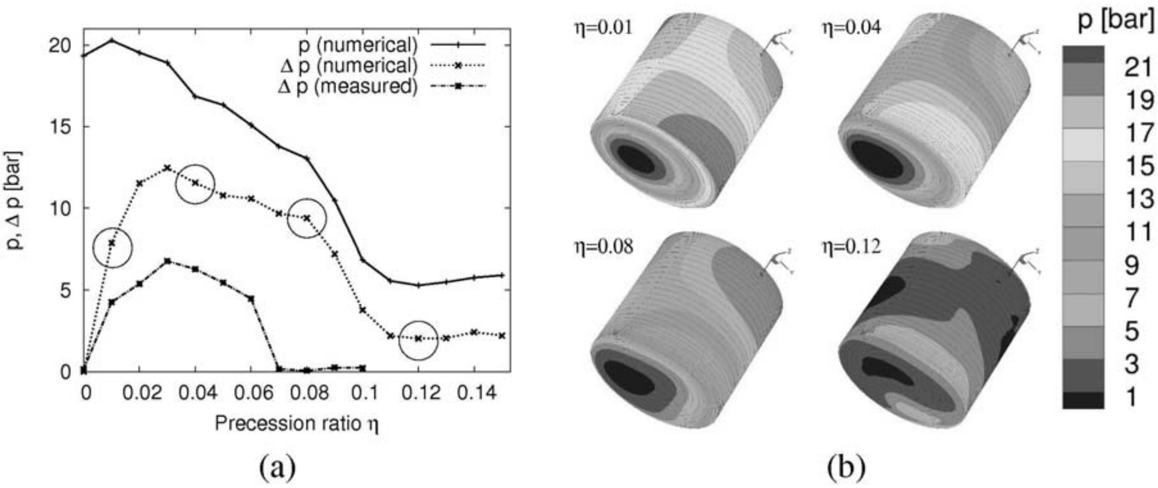

Figure 1: Pressure values for a precessing cylinder with 90° angle between rotation and precession axes, when scaled to the large device. (a) Maximum pressure p (numerically determined at Re=6680) and maximum pressure difference Δp (numerical and experimental). (b) Pressure distribution (numerical) for 4 specific precession ratios.

Up to present, dynamo action for precessing cylindrical flows has been confirmed numerically for the case Pm~1 and $\eta=0.15$ [14]. The critical Rm depends on the specific electrical boundary conditions, with a surprisingly low optimum value of 550 for the case of electrically conducting side layers and insulating lid layers (actually, this finding has led us to consider an inner copper layer attached to the outer stainless steel shell).

Encouraging as this low critical Rm may look, the question of self-excitation in a real precession experiment is far from being settled. Further simulations at lower Pm have led to an increase of the critical Rm, and for lower values of η dynamo action has not been shown yet.

Interestingly, an intermediate regime characterized by the occurrence of a few medium-sized cyclones has been observed at the ATER experiment in Paris-Meudon [15]. So far, these vortex-like structures could not be identified at our water experiment. Here, work is going on to utilize 3D particle image velocimetry to gather simultaneous information on the axial components of velocity and vorticity. The helicity distribution that can be computed from them could then serve as an input for dynamo simulations. In general, we expect more conclusive dynamo predictions, in particular for the cyclonic and the turbulent regime, from a close interplay of water test measurements and advanced numerical simulations.

3. Status of preparations

In comparison with previous dynamo experiments, the precession experiment has a higher degree of homogeneity since it contains neither impellers nor guiding blades. Its central module encases a sodium filled cylindrical volume of 2 m diameter and the same height (Figure 2). For this volume, we aim at reaching a rotation rate of 10 Hz (to obtain Rm~700), and a precession rate of 1 Hz (to cover the laminar, the cyclonic, and the turbulent flow regimes). With total gyroscopic torques of up to 8×10^6 Nm, we operate at the edge of technical feasibility, so that much optimization work is needed to make the machine safely operable.

The complicated simultaneous rotation around two axes poses several challenges: filling and emptying procedures, heating and cooling methods, and handling of thermal expansion. A decision was made in favor of a slightly enlarged vessel, comprising two conical end-pieces that serve, first, for a well-defined filling and emptying procedure at 43° vessel tilting, and, second, for hosting two bellows which compensate the thermal expansion of the liquid sodium.

Having defined this basic structure of the central vessel, much effort was, and is still, devoted to the optimization of the shell. A shell thickness of around 3 cm is needed anyway to withstand the centrifugal pressure of 20 bar in case of pure rotation. For increasing precession ratio, this total pressure decreases, but is complemented by a pressure pulsation due to the gyroscopic forces (Figure 1). In addition to those mechanical stresses, we have also to consider the thermal stresses that arise from the temperature difference over the shell when the dynamo is cooled by a strong flow of air.

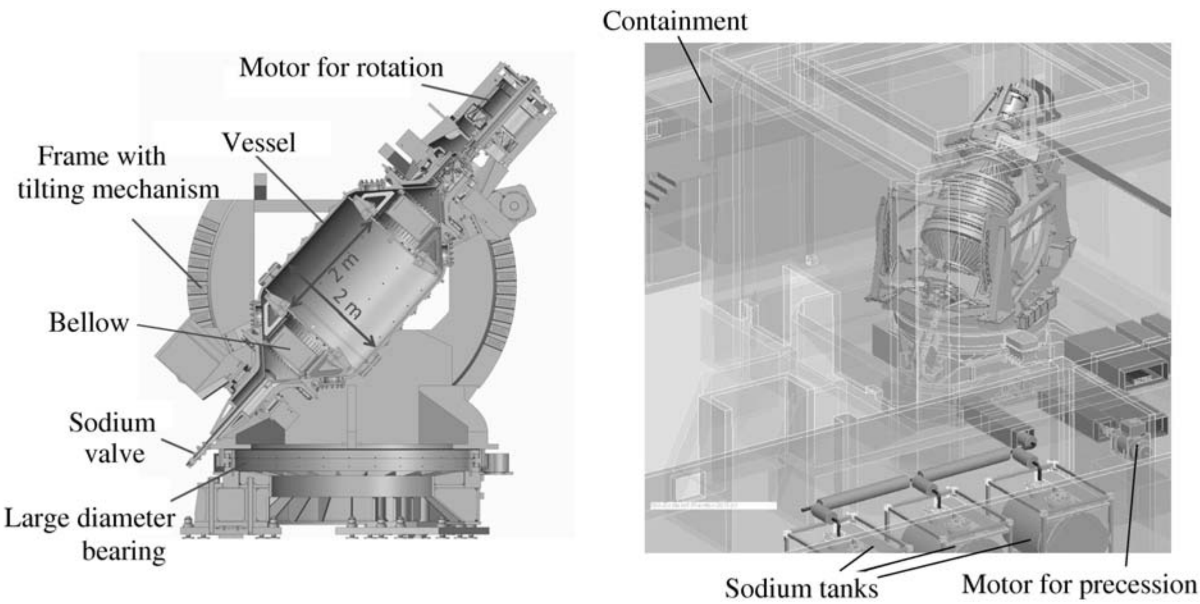

Figure 2: Present status of the design of the precession experiment

The next step is the design of the bearings and of a frame that allows to choose different angles between rotation and precession axis. Finding appropriate roller bearings for the vessel turned out to be extremely challenging, mainly because of the huge gyroscopic torque. It is the same gyroscopic torque that also requires a very stable basement (Figure 3a), standing on seven pillars, each reaching 22 m deep into the bedrock. The dynamo experiment itself is embedded in a containment (Figure 2, right), preventing the rest of the building from the consequences of possible sodium leaks. Since the double rotation cannot be stopped quickly in case of an accident, this containment is the only chance of preventing jets that would spill out of a potential leak from perfectly covering all surrounding areas with burning sodium. For such accidents, the containment can be flooded with argon, which is stored in liquid form.

(a) (b)

Figure 3: The DRESDYN building: (a) Construction of the three feet of the precession experiment. (b) Present status of the shell construction (as of April 7, 2014).

4. DRESDYN – What else is it good for?

Given the significant investment that is needed for the very precession experiment and the infrastructure to support it, we have combined this specific installation with creating a general platform for a variety of further liquid metal experiments. Another experiment with geo- and astrophysical relevance is devoted to the investigation of different combinations of the MRI and the current-driven TI. Basically, the set-up is a Taylor-Couette experiment with 2 m height and 20 cm gap width. With rotation rates of the inner cylinder of up to 20 Hz we plan to reach an Rm of around 40, while the axial magnetic field will lead to a Lundquist number of 8. Both values are about twice the respective critical values [16] for the standard version of MRI (with only an axial magnetic field applied). Still below those critical values we plan to investigate how the helical version of MRI approaches the limit of standard MRI. For this purpose, we will use a strong central current, as it was already done in the PROMISE experiment [3,4]. This insulated central current can be supplemented by another axial current, guided through the (rotating) liquid sodium, which will then allow to investigate arbitrary combinations of MRI and TI. A recent theoretical study [17] has shown that even a slight addition of current through the liquid would extend the range of application of the helical and azimuthal MRI to Keplerian flow profiles.
The TI will also play a central role in a third experiment in which different flow instabilities in liquid metal batteries (LMB) will be studied. LMB’s consist of three self-assembling liquid layers [18], an alkali or earth-alkali metal (Na, Mg), an electrolyte, and a metal or half-metal

(Bi,Sb). In order to be competitive, LMB's have to be constructed quite large, so that charging and discharging currents in the order of some kA are to be expected. Under those conditions, the occurrence of the TI and of interface instabilities must be carefully avoided [19,20].
The next installation is an In-Service-Inspection (ISI) experiment for various studies related to safety aspects of sodium fast reactors (SFR). Related to this, we also intend to investigate the impact of magnetic materials on the conditions of magnetic-field self-excitation in the helical core flows of SFR's.
The construction of the DRESDYN building is well advanced. Figure 3b illustrates the status of the shell construction as of April 2014. The interior construction is expected to be finalized in 2015. Thereafter, the installation of the various experiments can start. It goes without saying that both the precession and the MRI/TI experiment will first be tested with water, before we can dare to run them with liquid sodium.

Acknowledgment

We acknowledge support from the Helmholtz Alliance LIMTECH.

References

[1] Gailitis, A. et al.: Phys. Rev. Lett. 84 (2000) 4365-4368
[2] Stieglitz, R.; Müller, U.: Phys. Fluids 13 (2001) 561-564
[3] Stefani, F. et al.: Phys. Rev. Lett. 97 (2006) 184502
[4] Seilmayer, M. et al.: Phys. Rev. Lett. (2013), subm.; arXiv:1311.7223
[5] Seilmayer, M. et al.: Phys. Rev. Lett. 108 (2012) 244501
[6] Berhanu, M. et al.: Europhys. Lett. 77 (2007) 59001
[7] Petrelis, F. et al.: Phys. Rev. Lett. 102 (2009) 144503
[8] Malkus, W.V.R.: Science 160 (1968) 259-264.
[9] Tilgner, A.: Phys. Fluids 17 (2005) 034104
[10] Consolini, G.; De Michelis, P.: Phys. Rev. Lett. 90 (2003) 05850
[11] Dwyer, C.A. et al.: Nature 479 (2011) 212-214
[12] Fu, R.R. et al.: Science 338 (2012) 238-241
[13] Krauze, A.: Magnetohydrodynamics 46 (2010) 271-280
[14] Nore, C. et al.: Phys. Rev. E 84 (2011) 016317
[15] Mouhali, W. et al.: Exp Fluids 53 (2012) 1693-1700
[16] Rüdiger, G. et al.: Phys. Rev. E. 67 (2003) 046312
[17] Kirillov, O., Stefani, F.: Phys. Rev. Lett. 111 (2013) 061103
[18] Kim, H. et al.: Chem. Rev. 113 (2013) 2075-2099
[19] Stefani, F. et al: Energ. Convers. Manage. 52 (2011) 2982-2986
[20] Weber , N. et al: New J. Phys. 15 (2013) 043034

MEASUREMENTS IN A DOWNSCALED WATER MOCKUP AND NUMERICAL SIMULATION FOR THE DRESDYN LARGE SCALE PRECESSION EXPERIMENT

GUNDRUM. Th., STEGLICH, C., STEFANI, F., GERBETH, G. ALBRECHT, T., GIESECKE, A.
Helmholtz-Zentrum Dresden-Rossendorf, P.O. Box 510119, D-01314 Dresden, Germany,
e-mail: Th.Gundrum@hzdr.de

Abstract: Precession has long been discussed as a complementary energy source of homogeneous dynamo action. In the framework of DRESDYN (DREsden Sodium facility for DYNamo and thermohydraulic studies) a precession driven dynamo experiment is under construction. For proper dimensioning of the sodium experiment, measurements at the 1:6 down scaled water mockup are compared to numerical simulations. We present pressure, velocity, and motor power measurements for the water mockup. Furthermore, we provide an insight into mechanical engineering aspects of the real sodium experiment.

1. Introduction

Although most theories of the geodynamo rely on a flow driven by thermal and/or compositional buoyancy [1], precession has long been discussed as a complementary energy source [2,3,4]. This idea seems to be supported by paleomagnetic measurements showing a modulation of the geomagnetic field intensity by the 100 kyr Milankovic cycle of the Earth's orbit eccentricity and by the corresponding 41 kyr cycle of the Earth's axis obliquity [5]. Most interesting in this respect is the correlation of geomagnetic field variations with climate changes, as hypothesized for the sequence of ice ages [6]. Recently, precession driving has also been discussed in connection with the generation of the ancient lunar magnetic field [7], and with dynamos in asteroids [8].
Aside from geophysical questions, precession driven dynamo action is also interesting from the viewpoint of fundamental MHD. This applies, in particular, to the experimental study of dynamo action which has made great progress during the last 15 years [9]. In a sequence with the previous liquid metal experiments in Riga [10], Karlsruhe [11] and Cadarache [12], a precession driven dynamo experiment would represent a logical next step towards a real homogeneous dynamo. With just a fluid rotating around two axes, it would neither contain any propeller, as in Riga, nor any assembly of guiding tubes, as in Karlsruhe, nor any soft-iron material (which is crucial for the low critical magnetic Reynolds number and the nearly axisymmetric eigenmode) as in the Cadarache experiment [13]. The precession driven dynamo experiment that is planned to be set-up in the framework of the DREsden Sodium facility for DYNamo and thermohydraulic studies (DRESDYN) will be a cylindrical stainless-steel vessel of approximately 2 m diameter and length, rotating with up to 10 Hz around its symmetry axis, and with up to 1 Hz around the precession axis whose angle to the symmetry axis can be varied between 90° and 45°. With the indicated rotation and precession rates, this precessing vessel would exert a huge gyroscopic moment of around 8×10^6 Nm on the ground which requires the construction of a very solid basement.
Despite some numerical evidence for the possibility of dynamo action in precessing cylinders [14] and cubes [15], many aspects are still in need of further investigation. In order to figure out optimal design and process parameters for the later large-scale liquid sodium experiment, we have started a series of experiments at a smaller, 1:6 down-scaled, water precession experiment that is shown in Figure 1.

2. The water mock-up and the ultrasonic Doppler system

The 1:6 scaled water experiment is quite similar to the ATER experiment guided by J. Léorat [16], but allows additionally for choosing different angles between the rotation and the precession axes. The installed measurement equipment enables the determination of the torques and motor powers needed to drive the rotation of the cylinder and the turntable, and of the gyroscopic torques acting on the basement.

Concerning the flow field determination, we have installed a number of ultrasonic sensors for the determination of the axial velocity component. While the facility can run with rotation rates of 10 Hz and precession rates of 1 Hz, the well-known relation d $v_{max}=c^2/(8\ f)$ between signal depth d and maximal velocity v_{max}, for given sound velocity c and frequency f, restricts the UDV measurements to rather low rotation rates.

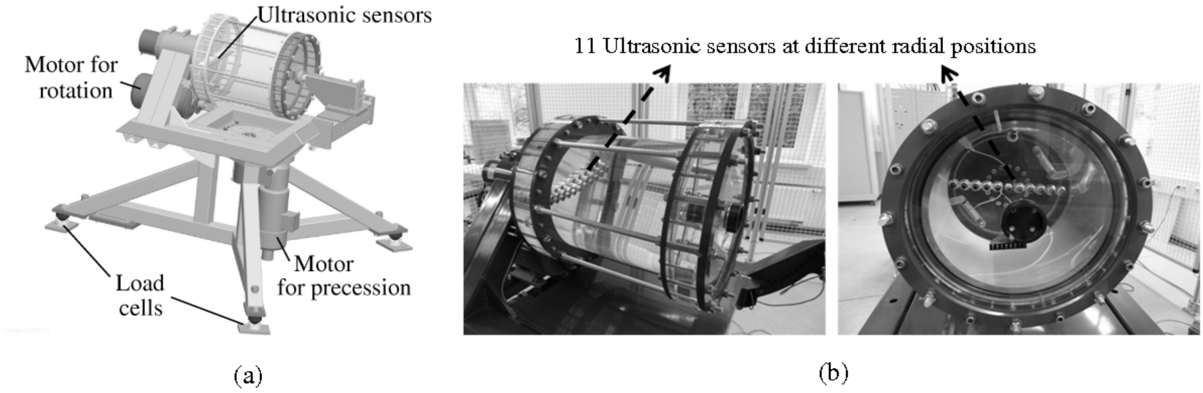

Figure 1: Drawing (a) and photography (b) of the 1:6 downscaled water precession experiment for the determination of velocity fields, motor powers, and torques on the basement for various driving conditions.

3. Results

For a rather low rotation rate of 0.2 Hz and two different precession ratios ε, Figure 2 shows the averaged results of the axial velocity measured by UDV for an angle between the two axes of 90°. The left-right asymmetry in Figure 2a (ε=0.053) is a typical indication for the dominant non-axisymmetric Kelvin mode with an azimuthal wave number m=1. When scaled to the planned 10 Hz rotation rate, and to the 6 times larger sodium facility, the observed velocity of 40 mm/s would correspond to a value of around 12 m/s. For a higher precession ratio, ε=0.107, this clear structure disappears and gives way to a turbulent flow regime.

The difference between these two precession ratios illustrates a typical feature of precessing flows in cylinders. With the details depending slightly on the aspect ratio of height to diameter of the cylinder, we first observe a laminar flow with only a few non-axisymmetric modes which changes suddenly, at some critical value, to a turbulent flow. At this point the torque that is necessary for driving the rotation, and hence the motor power, jumps significantly.

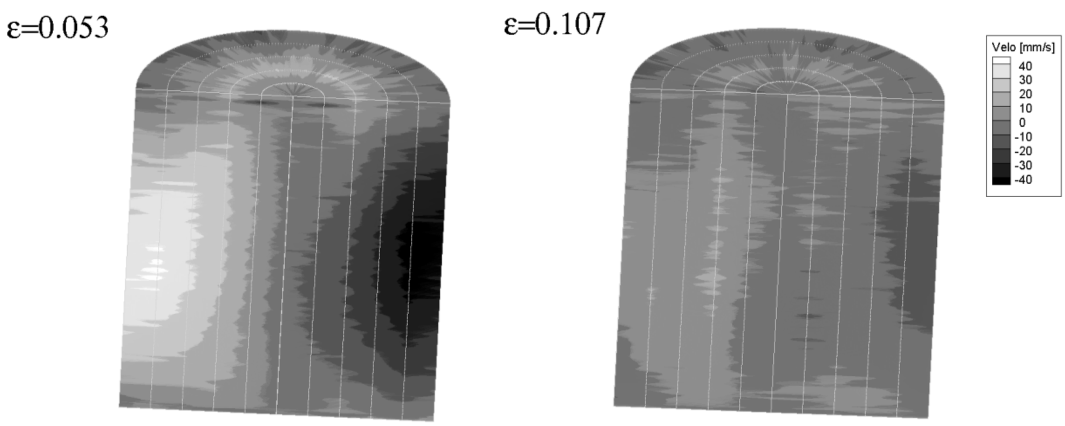

(a) (b)

Figure 2: Averaged axial velocity component measured by the 6 UDV sensors for two different precession ratios in the laminar case (a) at ε=0.053, and in the turbulent case (b) at ε=0.107. The cylinder rotation rate was 0.2 Hz.

This behaviour is illustrated in Figure 3 which shows, now for a cylinder rotation rate of 10 Hz, sudden jumps of the electrical motor power with increasing ε. Figure 3 shows the comparison between 3 different cylinder rotation rates, which all exhibit a typical hysteresis of the transition between laminar and turbulent regime. It is interesting to note that the critical precession ratios for this transition depend only slightly on the rotation rate.

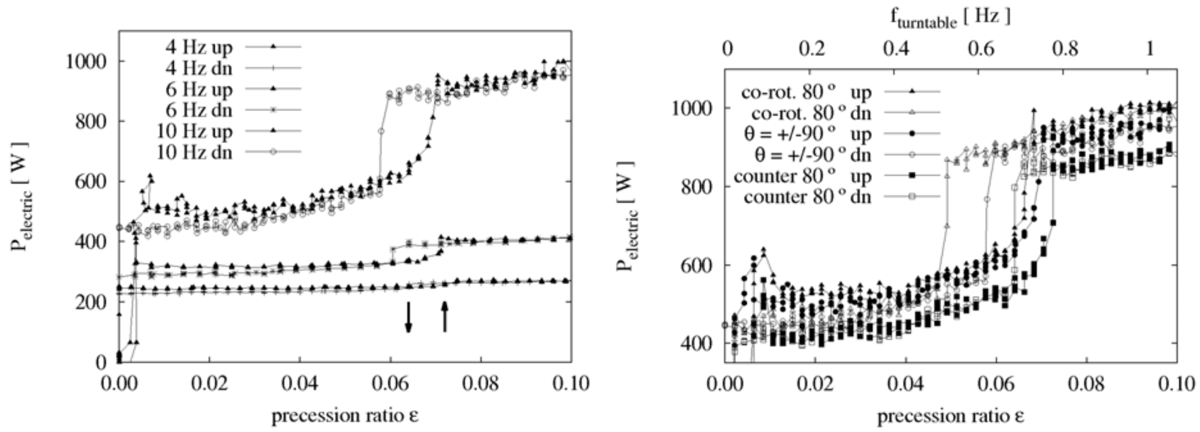

(a) (b)

Figure 3: Electrical power measured at the motor for the cylinder rotation. (a) Comparison between 3 different cylinder rotation rates, which all show a typical hysteresis of the transition between the laminar and the turbulent regime. Note that the critical precession ratios for this transition depend only slightly on the rotation rate. (b) Comparison between 3 different angles of the axes between rotation and precession and rotation axes.

In Figure 3b, we compare this transition behavior for 3 different angles between rotation and precession axes. For 90°, the upward jump occurs approximately at ε~0.065, while for decreasing precession ratio the downward jump occurs at ε~0.055. The critical precession ratio changes slightly when we modify the angle between the axes to 80°. Then we have to distinguish between the co-rotating case and the counter-rotating case. It seems that the hysteresis becomes broader for the co-rotating case, and narrower for the counter-rotating case, although this needs further confirmation.

4. Conclusions

This paper was motivated by the ongoing construction of a precession driven dynamo experiment. For the detailed characterization of the fluid flow in a precessing cylinder at different precession ratios and angles, we have carried out a variety of experiments at an 1:6 downscaled water mock-up. The power measurements have confirmed the existence of a critical value of the precession ratio at which a transition between a laminar and a turbulent flow regime occurs which seems to depend only weakly on the Reynolds number. Up to present, the UDV flow measurements were restricted to a rather small rotation rate of 0.2 Hz, due to the limitation of the maximum product of depth and velocity. An important goal for future measurements is the detailed characterization of the few large-scale helical eddies in the cyclonic regime, as they were identified by Particle Image Velocimetry (PIV) at the ATER experiment in Meudon [17]. For this purpose, we presently implement and test a 3D-PIV system for the simultaneous determination of all three velocity components in some finite volume of the cylinder.
The next step will then be to assemble the acquired information about the stationary and fluctuating parts of the velocity field into an appropriate form that can then be utilized in dynamo codes to determine in detail the conditions and optimal parameters for magnetic field self-excitations in the precession driven dynamo.

Acknowledgments.

We acknowledge financial support from the Helmholtz Alliance LIMTECH.

References

[1] Wicht, J.; Tilgner, A.: Space Sci. Rev. 152 (2010), 501-542
[2] Malkus, W.V.R.: Science 160 (1968) 259-264.
[3] Gans, R.F.: J. Fluid Mech. 45 (1970) 111-130.
[4] Tilgner, A.: Phys. Fluids 17 (2005) 034104.
[5] Consolini, G.; De Michelis, P.: Phys. Rev. Lett. 90 (2003) 058501.
[6] Courtillot V et al.: Earth Planet. Sci. Lett. 253 (2007), 328–339.
[7] Dwyer, C.A. et al.: Nature 479 (2011) 212-214
[8] Fu, R.R. et al.: Science 338 (2012) 238-241
[9] Stefani, F. et al.: Z. Angew. Math. Mech. 88 (2008) 930-954.
[10] Gailitis A et al.: Phys. Rev. Lett. 84 (2000) 4365-4368.
[11] Stieglitz, R.: Müller, U.: Phys. Fluids13 (2001),561–564.
[12] Monchaux, R. et al.: Phys. Rev. Lett. 98 (2007) 044502.
[13] Giesecke, A. et al.: Phys. Rev. Lett. 104 (2010) 044503.
[14] Nore, C. et al.: Phys. Rev. E 84 (2011), 016317.
[15] Krauze, A.: Magnetohydrodynamics 46 (2010) 271-280
[16] Léorat, J.: Magnetohydrodynamics 42 (2006), 143-151.
[17] Mouhali, W. et al.: Exp Fluids 53 (2012) 1693-1700

DYNAMO EQUATIONS WITH RANDOM COEFFICIENTS

MIKHAILOV[1] E.A., MODYAEV[2] I.I., SOKOLOFF[1], D.D.
Affiliation: [1]*Moscow State University, Faculty of Physics*, 119991, Moscow, Russia [2]*Moscow State University, Faculty of Mechanics and Mathematics*, 119991, Moscow, Russia
e-mail address of corresponding author: ea.mikhajlov@ physics.msu.ru

Abstract : We study the galactic dynamo equations with random alpha-coefficient which takes two different values corresponding to warm gas and hot gas. Probability that alpha-coefficient takes the value which corresponds to the hot gas is p. We obtain a critical value of the probability *p*, for which the dynamo cannot support the magnetic field growth and calculate the growth rates for various statistical moments of magnetic field.

1. Introduction

It is believed that generation of galactic magnetic fields is a result of dynamo based on a joint action of differential rotation and alpha-effect. Intensity of the effects are usually described by dimensionless parameters R_α and R_ω [1].

Alpha-effect depends on the temperature of the interstellar medium. If there are some intensive processes in the galaxy, such as star formation or supernovae explosions which create regions of ionized hydrogen then the turbulent motions including alpha-effect can be changed. In order to include that in galactic dynamo we consider the alpha-effect parameter as a random process such as alpha takes two different values. The first value is connected with warmed atomic hydrogen, and the second one describes the turbulent motions in regions with highly ionized hot gas. The second option occurs with probability *p* which is connected with ratio between hot and warm gas components.

2. The model

We exploit the so-called no-z model which replaces *z*-derivatives (*z*-axis is perpendicular to the disc plane) by some algebraic expressions and obtain the magnetic field component perpendicular to the disc plane from the solenoidality condition [2, 3]:

$$\frac{\partial B_r}{\partial t} = -R_\alpha B_\varphi - \frac{\pi^2}{4} B_r + \lambda^2 \left\{ \frac{\partial}{\partial r}\left(\frac{\partial}{r\partial r}(rB_r) \right) + \frac{1}{r^2}\frac{\partial^2 B_r}{\partial \varphi^2} - \frac{2}{r^2}\frac{\partial B_\varphi}{\partial \varphi} \right\}; \tag{1}$$

$$\frac{\partial B_\varphi}{\partial t} = -R_\omega B_r - \frac{\pi^2}{4} B_\varphi + \lambda^2 \left\{ \frac{\partial}{\partial r}\left(\frac{\partial}{r\partial r}(rB_\varphi) \right) + \frac{1}{r^2}\frac{\partial^2 B_\varphi}{\partial \varphi^2} - \frac{2}{r^2}\frac{\partial B_r}{\partial \varphi} \right\}. \tag{2}$$

where B_r and B_φ are the magnetic field components in the disc plane, R_α is the dimensionless amplitude of alpha-effect, R_ω is the dimensionless amplitude of differential rotation, $\lambda = h/R$ is the disc aspect ratio, where h is the half-thickness of the galaxy disc, R

is its radius. The distances are measured in galactic radii ($0 < r < 1$), and time is measured in $\frac{h^2}{\eta}$ where η is the turbulent diffusivity. A conventional estimate is $R_\alpha \sim 1$, $R_\omega \sim 10$.

We assume that $R_\omega = 10$ and R_α are described by a random law:

$$R_\alpha = \begin{cases} 0.1 \quad with \quad probability \quad p; \\ 1 \quad with \quad probability \quad (1-p). \end{cases} \tag{3}$$

The memory time for R_α is 0.01 or (in some cases) 0.1.

3. Local approach

Here we present the results for the simplest case of an infinitely thin disc and neglect the losses due to diffusion in the disc plane. Then $\lambda = 0$ and the dynamo equations read

$$\frac{dB_r}{dt} = -R_\alpha B_\varphi - \frac{\pi^2}{4} B_r; \tag{4}$$

$$\frac{dB_\varphi}{dt} = -R_\omega B_r - \frac{\pi^2}{4} B_\varphi. \tag{5}$$

We introduce the so-called dynamo number $D = R_\alpha R_\omega$. If generation is weak, i.e. dynamo number is small, magnetic field decays, if however dynamo number exceeds a critical value $D_{cr} \approx 7$, magnetic field grows.

The dynamo equations (3) – (4) can be rewritten in the matrix form:

$$\frac{d}{dt}\left(B_r, B_\varphi\right) = \left(B_r, B_\varphi\right)\begin{pmatrix} -\frac{\pi^2}{4} & -R_\omega \\ -R_\alpha & -\frac{\pi^2}{4} \end{pmatrix}. \tag{6}$$

which can be solved as follows:

$$\vec{B}(n\Delta t) = \vec{B}((n-1)\Delta t)\exp\left(-\frac{\pi^2}{4}\Delta t\right)C_n, \tag{7}$$

where C_n is the transition matrix:

$$C_n = \begin{pmatrix} \cosh\left(\sqrt{R_\alpha R_\omega}\Delta t\right) & -\sqrt{\frac{R_\omega}{R_\alpha}}\sinh\left(\sqrt{R_\alpha R_\omega}\Delta t\right) \\ -\sqrt{\frac{R_\alpha}{R_\omega}}\sinh\left(\sqrt{R_\alpha R_\omega}\Delta t\right) & \cosh\left(\sqrt{R_\alpha R_\omega}\Delta t\right) \end{pmatrix}. \tag{8}$$

and:

$$\vec{B}(n\Delta t) = \vec{B}(0)C_1 ... C_n . \tag{9}$$

Let

$$\tan\theta = \frac{B_\varphi}{B_r}. \tag{10}$$

The angle θ at every time $t_n = n\Delta t$ has some distribution $\pi_n(\theta)$, which can be described by so-called transition probability density:

$$\pi_{n+1}(\theta) = \int_{-\pi/2}^{+\pi/2} p(\theta,\chi)\pi_n(\chi)d\chi. \tag{11}$$

For $n \to \infty$ the distribution function has a limit: $\pi_n(\theta) \to \pi_\infty(\theta)$. Then, the magnetic field grows rate is

$$\gamma = \frac{1}{\Delta t}\left\langle \ln\left\| \vec{w}A_n \right\| \right\rangle - \frac{\pi^2}{4}, \tag{12}$$

where $\vec{w} = (\cos\alpha, \sin\alpha)$ and α has the limit distribution $\pi_\infty(\alpha)$ [4].

4. Results

First of all, we investigate the dynamo equations numerically for various values of p (Fig.1). The magnetic field grows for $p < 0.43$, and decays for higher p.

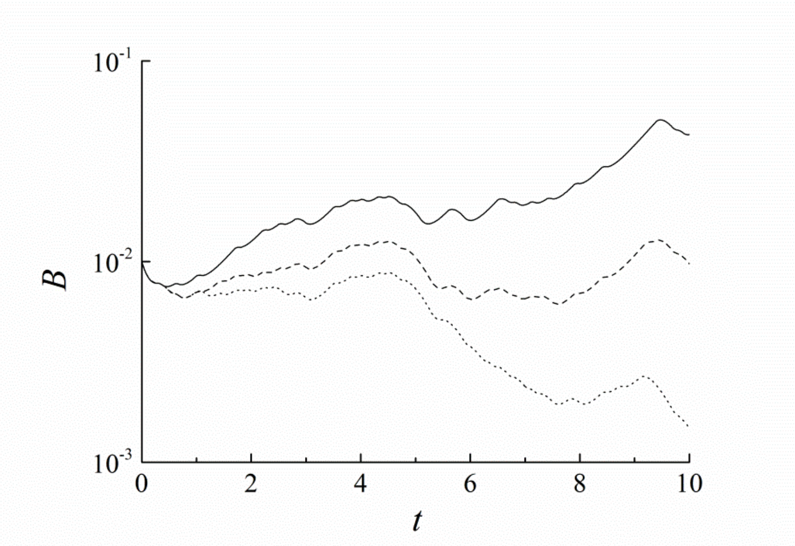

Figure 1: The magnetic field growth for various p. The solid line shows $p = 0.30$, the long-dashed one - $p = 0.40$, the short-dashed one - $p = 0.50$.

The typical growth rates of various statistical momentums of B are given in Table 1. The higher momentums grow faster than lower ones. We found analytically the limiting probability density π (Fig. 2) and calculate the magnetic field growth rate analytically using this density. Numerical and analytical estimates are compared in the Table 1.

We note that the theoretical estimates for the magnetic field growth rate are systematically larger than the numerical ones. Presumably, it means that the theoretical growth rate is determined by very rare random events. Another manifestation of intermittency [5] is the fact that the growth rates of statistical moments grows with the order of the moment.

Table 1: Velocities of different magnetic field momentums growth

	γ_{B}	$\gamma_{\langle \mathrm{B} \rangle}$	$\gamma_{\sqrt{\langle B^2 \rangle}}$	γ_{theor}
$p = 0.30$	0.219	0.224	0.227	0.250
$p = 0.40$	0.040	0.052	0.056	0.065
$p = 0.50$	-0.133	-0.132	-0.128	-0.116

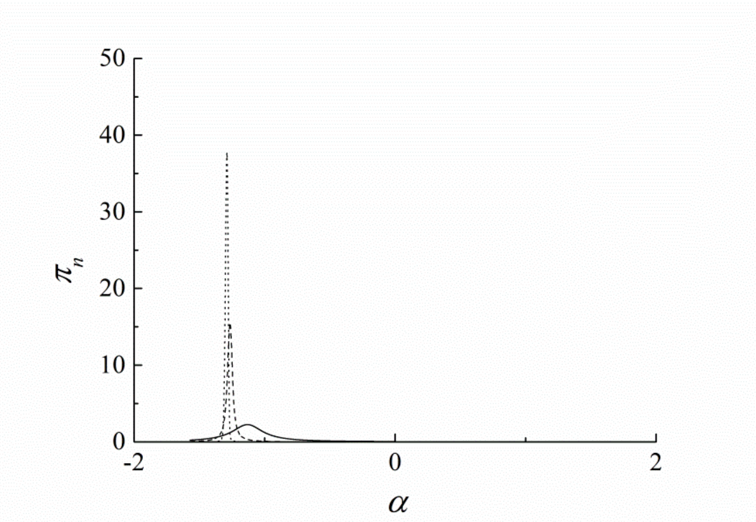

Figure 2: The probability density for different n: the solid line shows $n = 20$, the long-dashed line - $n = 50$, the short-dashed one - $n = 100$.

6. References

[1] Beck, R.; Brandenburg, A.; Moss. D.; Shukurov, A.; Sokoloff, D.: Galactic Magnetism: Recent Developments and Perspectives. Ann. Rev. Astron. Astrophys., 34 (1996), 155 - 206.

[2] Moss, D.: On the generation of bisymmetric magnetic field structures in spiral galaxies by tidal interactions. MNRAS, 275 (1995), 191 - 194.

[3] Phillips, A.: A comparison of the asymptotic and no-z approximations for galactic dynamos. Geophys. Astrophys. Fluid Dynam., 94 (2001), 135 - 151.

[4] Illarionov, E.A.; Sokoloff, D.D.; Tutubalin, V.N.: Stationary distribution of product of matrices with random coefficients. Numerical Methods and Programming, 13 (2012), 218 – 225.

[5] Zel'dovich, Ya.B.; Molchanov, S.A.; Ruzmaikin, A.A.; Sokolov. D.D. Intermittency in random media. Sov. Phys. Usp. 30 (1987), 353–369.

MHD TURBULENCE AND MAGNETIC DYNAMOS

SHEBALIN JOHN V.
Astromaterials Research Office/NASA Johnson Space Center, Houston, TX 77058, USA
E-mail: john.v.shebalin@nasa.gov

Abstract : An inherent dynamo process exists in magnetohydrodynamic turbulence and is statistical in nature. Turbulent planetary and stellar magnetofluids exhibit large-scale magnetic fields and this statistical process may be involved in the origin of these fields.

1. Introduction

Turbulent magnetohydrodynamic (MHD) flows are expected to exist inside astrophysical [1] and geophysical [2] objects, and have also been seen in laboratory dynamo experiments [3]. In these physical systems, coherent large-scale magnetic fields are observed and appear to arise from an internal dynamo process. In turn, numerical experiments have shown that coherent, large-scale magnetic fields arise spontaneously in incompressible, homogeneous MHD turbulence, an effect that is especially clear in the ideal case, when viscosity and resistivity are zero [4,5], but is also evident in the dissipative case [6]. The inherent dynamo in MHD turbulence is statistical and involves broken ergodicity manifesting itself as a broken symmetry. The theory of this inherent dynamo has been elucidated relatively recently [7,8] and the aim here is to give a qualitative overview of the connection between MHD turbulence and magnetic dynamos; further mathematical details can be found in the references cited.

2. Ideal MHD turbulence

The Earth, due to its proximity, is our best-studied planetary body with regard to MHD dynamos and much has been written about it, e.g., [9]. The essential facts are that the Earth has a solid inner core and a large fluid outer core, both composed mostly of iron, as well as a mantle and then a crust overlying the core. Although density varies from top to bottom in the outer core by about 20 percent, the magnetofluid is usually treated as incompressible, allowing for a simplified mathematical model of its MHD flows. In addition, it is expected that kinetic and magnetic Reynolds numbers are large enough, and that there is enough convective stirring occurring, so that the outer core is filled with turbulent magnetofluid. In taking the limit of infinitely large Reynolds numbers, we arrive at ideal, incompressible MHD turbulence. The primary dynamical variables are the turbulent velocity field $\mathbf{u}$ and the turbulent magnetic field $\mathbf{b}$; these are functions of time and position and satisfy $\nabla\cdot\mathbf{u} = \nabla\cdot\mathbf{b} = 0$. The basic equations of incompressible MHD turbulence are well known and are discussed in detail elsewhere, e.g., [10]. (Here we discuss only three-dimensional MHD turbulence.)

To theoretically study and numerically simulate MHD turbulence, we use so-called Galerkin expansions, summations over a complete set of orthogonal basis functions, each with its own coefficient, to represent either $\mathbf{u}$ or $\mathbf{b}$. Each term in the series satisfies given boundary conditions (b.c.s) and any other requirements that are imposed, so that a truncated expansion can approximate $\mathbf{u}$ or $\mathbf{b}$ to the desired accuracy. For example, if periodic b.c.s are used, then a Fourier (trigonometric) series is appropriate, while for a spherical shell with homogeneous b.c.s (to be defined below), then expansion in terms of spherical Bessel function-spherical harmonics can be employed. Galerkin basis functions are smooth and continuous, so that exact spatial partial derivatives can be found, while time dependence is completely contained in the expansion coefficients. In essence, a Galerkin method transforms the partial differential MHD equations into a finite set of nonlinear, coupled, ordinary differential equations.

The simplest geometry for analysis and simulation of a confined magnetofluid is that of a box with periodic b.c.s. The spherical case is more pertinent for the geodynamo, but b.c.s suitable for theory and computation must be determined. First, we assume that the outer core has concentric, spherical boundaries. The confined magnetofluid is ideal and the magnetic field is said to be 'locked into the flow field,' which moves it about, stretching and bending it. The magnetic field reacts back on the flow field and attempts to move it around, in turn. In this case, we assume that near solid physical boundaries, except in a thin boundary layer, both velocity and magnetic fields are essentially parallel to the boundary and that only inside the boundary layer does the magnetic field grow a nonzero component normal to the solid boundary. Then, for our mathematical boundaries, we use virtual spherical surfaces, sitting on top of the boundary layers, where we impose 'homogeneous b.c.s.' These homogeneous b.c.s are such that all primary (velocity and magnetic) fields and all derived fields (vorticity, electric current, magnetic vector potential) have zero normal components, but unconstrained parallel components, on the homogeneous boundaries [11]. (Homogeneous b.c.s appear justified when we look at numerical solutions from non-ideal MHD simulations with non-homogeneous b.c.s [12].) It turns out that the statistical mechanics of ideal MHD turbulence takes essentially the same form in either a periodic box [8] or in a spherical shell with homogeneous b.c.s [11], so that Fourier analysis and simulation serve as a viable surrogate for the seemingly more realistic spherical Bessel function-spherical harmonic approach.

3. Statistical mechanics

The set of expansion coefficients representing ideal MHD turbulence forms a conservative dynamical system that generally has not just one, but three constants of the motion: the energy $E = ½\int(u^2+b^2)dV$, cross helicity $H_C = ½\int\mathbf{u}\cdot\mathbf{b}dV$ and magnetic helicity $H_M = ½\int\mathbf{a}\cdot\mathbf{b}dV$; the magnetic vector potential $\mathbf{a}$ is defined by $\nabla\times\mathbf{a} = \mathbf{b}$ and $\nabla\cdot\mathbf{a} = 0$, and integration is over the bounded volume V. When V rotates as a whole, H_C is no longer constant, but $\to 0$ with time. Let $\tilde{\mathbf{u}}(\mathbf{k},t)$ and $\tilde{\mathbf{b}}(\mathbf{k},t)$ represent expansion coefficients for the velocity and magnetic field, respectively. The wave vectors $\mathbf{k}$ have components such that $|\mathbf{k}| \leq K < \infty$; the lowest values of $k = |\mathbf{k}|$ correspond to the longest length-scale in the physical volume. The set of all independent velocity and magnetic field coefficients defines the phase space Γ of the dynamical system, whose dimension is proportional to K^3. Statistically, the system is described by a canonical ensemble with partition function $Z = \int\exp(-\alpha E - \beta H_C - \gamma H_M)d\Gamma$; integration is over all of phase space Γ and the cofactors α, β and γ are called 'inverse temperatures' or 'undetermined multipliers' as their values are initially unknown. The probability density function is given by $D = Z^{-1}\exp(-\alpha E - \beta H_C - \gamma H_M)$ and may be used to determine expectation values for the two independent, complex components of $\tilde{\mathbf{u}}(\mathbf{k})$ or $\tilde{\mathbf{b}}(\mathbf{k})$.

Historical and theoretical details of ideal MHD statistics may be found elsewhere [8]. Here, only those details needed for a brief, qualitative discussion will be mentioned. To begin, the three inverse temperatures α, β and γ may be expressed as functions of only one unknown variable φ, which we have chosen to be the expectation value of the magnetic energy. Thus, the entropy functional of the system, $\sigma(\varphi) = -\int D\log D d\Gamma$ is also a function of φ. As is well known [13], entropy is the minimum of the entropy functional. The value of φ appropriate for the finite dynamical system with given E, H_C and H_M is then found by determining the value $\varphi = \varphi_o$ that minimizes $\sigma(\varphi)$. Requiring $d\sigma(\varphi)/d\varphi = 0$ yields $2\varphi_o \approx E + \kappa|H_M|[1 - (H_C/\varphi_o)^2]$, after much work [8,11], where and $\kappa|H_M| < E$, and where $\kappa = 1$ for the periodic box Fourier case [8], while $\kappa \approx 1.8638$ for a spherical shell geodynamo [11]. When the volume V is rotating as a whole, $H_C \to 0$ and $\varphi_o \approx \frac{1}{2}(E + \kappa|H_M|)$. In addition, analysis reveals that the energy in the longest wavelength mode is $O(N)$ times greater than in any shorter wavelength mode in the system, where N is the number of modes (i.e., independent values of $\mathbf{k}$ in the Galerkin expansion). This is in contradistinction to ideal fluid turbulence, where the smallest length-scale modes have the most energy [14]. Dissipation depletes smallest length-scale modes quickly of their energy, while leaving the largest-scale modes relatively untouched. Thus, ideal results have much less relevance to real fluid turbulence, which has a direct cascade to smaller length scales in its energy spectrum [14], than for real MHD turbulence, which has an inverse cascade to larger length scales [15].

An advance in the statistical mechanics of ideal MHD turbulence was the discovery of ideal eigenmodes [7]. The phase space probability density D is a product of modal densities of the form $D_{\mathbf{k}} \sim \exp[-\tilde{\mathsf{y}}^\dagger(\mathbf{k})\,\mathsf{M}_k\,\tilde{\mathsf{y}}(\mathbf{k})]$; $\tilde{\mathsf{y}}$ is a 4 component, complex column vector whose Hermitean adjoint is $\tilde{\mathsf{y}}^\dagger = [\,\tilde{u}_1^*(\mathbf{k})\ \tilde{u}_2^*(\mathbf{k})\ \tilde{b}_1^*(\mathbf{k})\ \tilde{b}_2^*(\mathbf{k})]$; here, ‘*’ denotes complex conjugate, $\tilde{u}_i(\mathbf{k})$ and $\tilde{b}_i(\mathbf{k})$, i = 1, 2, are the independent components of $\tilde{\mathbf{u}}(\mathbf{k})$ and $\tilde{\mathbf{b}}(\mathbf{k})$, and M_k is the modal Hermitean covariance matrix. We solve the matrix equation $\mathsf{M}_k\tilde{\mathsf{e}} = \lambda\tilde{\mathsf{e}}$ to find eigenvalues λ and eigenvectors $\tilde{\mathsf{e}}$; the matrix M_k, and its eigenvalues $\lambda_k^{(i)}$, i = 1,2,3,4, are

$$\mathsf{M}_k = \begin{bmatrix} \alpha & 0 & \beta/2 & 0 \\ 0 & \alpha & 0 & \beta/2 \\ \beta/2 & 0 & \alpha & -i\gamma/k \\ 0 & \beta/2 & i\gamma/k & \alpha \end{bmatrix}, \quad \begin{aligned} \lambda_k^{(1)} &= \alpha - \tfrac{1}{2}(\eta_k + \gamma/k) \\ \lambda_k^{(2)} &= \alpha + \tfrac{1}{2}(\eta_k + \gamma/k) \\ \lambda_k^{(3)} &= \alpha + \tfrac{1}{2}(\eta_k - \gamma/k) \\ \lambda_k^{(4)} &= \alpha - \tfrac{1}{2}(\eta_k - \gamma/k) \end{aligned}, \quad \eta_k = \sqrt{\beta^2 + \frac{\gamma^2}{k^2}}. \tag{1}$$

The explicit form of eigenvectors $\tilde{\mathsf{e}}_i(\mathbf{k})$ and transformation matrix U_k are given elsewhere [8]. Corresponding to the eigenvalues $\lambda_k^{(i)}$, i = 1,2,3,4, the transformed vector $\tilde{\mathsf{v}}(\mathbf{k}) = \mathsf{U}_k^\dagger\tilde{\mathsf{y}}(\mathbf{k})$ has components $\tilde{v}_i(\mathbf{k})$:

$$\begin{aligned} \tilde{v}_1(\mathbf{k}) &= \bar{\beta}\zeta_k^-\left[\tilde{u}_1(\mathbf{k}) + i\tilde{u}_2(\mathbf{k})\right] - \zeta_k^+\left[\tilde{b}_1(\mathbf{k}) + i\tilde{b}_2(\mathbf{k})\right] \\ \tilde{v}_2(\mathbf{k}) &= \bar{\beta}\zeta_k^-\left[\tilde{u}_1(\mathbf{k}) - i\tilde{u}_2(\mathbf{k})\right] + \zeta_k^+\left[\tilde{b}_1(\mathbf{k}) - i\tilde{b}_2(\mathbf{k})\right] \\ \tilde{v}_3(\mathbf{k}) &= \bar{\beta}\zeta_k^+\left[\tilde{u}_1(\mathbf{k}) + i\tilde{u}_2(\mathbf{k})\right] + \zeta_k^-\left[\tilde{b}_1(\mathbf{k}) + i\tilde{b}_2(\mathbf{k})\right] \\ \tilde{v}_4(\mathbf{k}) &= \bar{\beta}\zeta_k^+\left[\tilde{u}_1(\mathbf{k}) - i\tilde{u}_2(\mathbf{k})\right] - \zeta_k^-\left[\tilde{b}_1(\mathbf{k}) - i\tilde{b}_2(\mathbf{k})\right] \end{aligned}, \quad \begin{aligned} \zeta_k^\pm &\equiv \frac{1}{2}\sqrt{1 \pm \frac{\gamma}{k\eta_k}}, \\ \bar{\beta} &= \mathrm{sgn}(\beta). \end{aligned} \tag{2}$$

These equations give the transformed variables or ‘eigenvariables’ $\tilde{v}_i(\mathbf{k})$ for each mode and, implicitly, also give U_k and $\tilde{\mathsf{e}}_i(\mathbf{k})$. Note that the equations for $\tilde{v}_1(\mathbf{k})$ and $\tilde{v}_3(\mathbf{k})$ are decoupled from the equations for $\tilde{v}_2(\mathbf{k})$ and $\tilde{v}_4(\mathbf{k})$. The eigenanalysis results given here will help in the discussion of broken ergodicity in the next section.

4. Broken ergodicity

Each $\tilde{v}_i(\mathbf{k})$ is has its own $\lambda_k^{(i)}$, which are given in (1). The matrix $\mathsf{U}_k \in$ SU(4) so that $|\tilde{\mathbf{u}}(\mathbf{k})|^2 + |\tilde{\mathbf{b}}(\mathbf{k})|^2 = \Sigma_{i=1}^4 |\tilde{v}_i(\mathbf{k})|^2$, i.e., each side expresses the energy in mode $\mathbf{k}$. However, we have seen that the largest-scale mode $\boldsymbol{\kappa}$ contains $O(N)$ more energy than any of the other $N-1$

modes. If we assume that $H_M > 0$, it can be shown [8,11] that $\gamma < 0$. Then, looking at (1), we see that $\lambda_\kappa^{(4)} = \alpha - \frac{1}{2}(\eta_\kappa + |\gamma|/k)$ must be much smaller than any other $\lambda_\kappa^{(i)}$, i = 1,2,3, or any other $\lambda_k^{(i)}$, $k > \kappa$, i = 1,2,3,4. Analysis [8,11] reveals that the fraction of energy in statistical equilibrium that is expected to reside in $\tilde{v}_4(\boldsymbol{\kappa})$ is $\sim 1/\lambda_\kappa^{(4)} \sim 1$, while all other $\tilde{v}_i(\mathbf{k})$ are $\sim 1/\lambda_k^{(i)} \sim N^{-1}$; here, we have assumed $E = 1$, and that $H_M \neq 0$. Then, eigenvariable $\tilde{v}_4(\boldsymbol{\kappa})$ is O(1) as $N \to \infty$, while $\tilde{v}_i(\boldsymbol{\kappa}) \sim \varepsilon \approx 0$, for i = 1,2,3, and the equations for $\tilde{v}_1(\boldsymbol{\kappa})$ and $\tilde{v}_3(\boldsymbol{\kappa})$ in (2) will have left-sides that are O(ε); this is only achieved if $\tilde{u}_1(\boldsymbol{\kappa}) + i\tilde{u}_2(\boldsymbol{\kappa}) \approx \tilde{b}_1(\boldsymbol{\kappa}) + i\tilde{b}_2(\boldsymbol{\kappa}) \approx 0$, i.e., the negative helicity part of mode $\boldsymbol{\kappa}$ is zero. Thus, the positive helicity parts of the largest-scale mode $\boldsymbol{\kappa}$, $\tilde{u}_1(\boldsymbol{\kappa}) - i\tilde{u}_2(\boldsymbol{\kappa})$ and $\tilde{b}_1(\boldsymbol{\kappa}) - i\tilde{b}_2(\boldsymbol{\kappa})$, are maximal. Since $\tilde{u}_2(\boldsymbol{\kappa}) \approx i\tilde{u}_1(\boldsymbol{\kappa})$ and $\tilde{b}_2(\boldsymbol{\kappa}) \approx i\tilde{b}_1(\boldsymbol{\kappa})$, we have $\tilde{\mathbf{u}}(\boldsymbol{\kappa}) \approx i\boldsymbol{\kappa} \times \tilde{\mathbf{u}}(\boldsymbol{\kappa})$, $\tilde{\mathbf{b}}(\boldsymbol{\kappa}) \approx i\boldsymbol{\kappa} \times \tilde{\mathbf{b}}(\boldsymbol{\kappa})$ and $\tilde{\mathbf{u}}(\boldsymbol{\kappa}) \sim \tilde{\mathbf{b}}(\boldsymbol{\kappa})$, i.e., 'dynamic alignment' [10; pp. 78-79]. (These are Fourier case results [8], where $\kappa = 1$, but analogous results exist in the spherical geodynamo case [11], where $\kappa = 1.8638$.)

In terms of the ideal MHD equations [10], these results imply that $d\log|\tilde{v}_4(\boldsymbol{\kappa})|/dt \sim \varepsilon \approx 0$, while for all other eigenvariables, $d\log|\tilde{v}_i(\mathbf{k})|/dt \sim 1$. Although statistical theory [15] ostensibly predicted that all $\tilde{v}_i(\mathbf{k})$ have mean values of zero, this requires that all $\tilde{v}_i(\mathbf{k})$ have sufficiently strongly stochastic forcing. Here, we have seen that when ideal MHD turbulence is in statistical equilibrium, it has generally entered into a single helicity state at the largest scale and that this state is quantified by the eigenvariable $\tilde{v}_4(\boldsymbol{\kappa})$, which has far more energy than any other eigenvariable. This leads to a situation in which there is very little driving the eigenvariable $\tilde{v}_4(\boldsymbol{\kappa})$ to change its value and it becomes almost static, while all other other eigenvariables continue to be driven relatively strongly and appear to have zero mean values. Thus, in MHD turbulence, we have *broken ergodicity*, defined [16] as occurring when, 'In a system that is non-ergodic on physical timescales the phase point is effectively confined in one subregion or component of phase space.' Broken ergodicity manifests itself in MHD turbulence as a stationary structure at the largest scales of the volume containing a turbulent magnetofluid. It produces an effectively coherent structure out of seeming chaos. We will see a numerical example of this in the next section.

5. Numerical simulation

As an example of broken ergodicity, drawn from Fourier method MHD run 1a [6,8], consider fig. 1, showing $\mathrm{Re}\,\tilde{v}_i(\boldsymbol{\kappa})$ vs $\mathrm{Im}\,\tilde{v}_i(\boldsymbol{\kappa})$ from simulation time t = 0 to 200; + indicates the origin and • the initial point. Run 1a had $E = 1$, $H_C = 0.348$, $H_M = 0.092$, 64^3 grid points and 2×10^5 time steps ($\Delta t = 10^{-3}$). We have seen the same sort of behaviour in all of our ideal MHD runs ($0 \le |H_C| < E/2$; $0 < |H_M| < E$), as long as they have enough time steps and enough grid points. When dissipation is added for the same initial conditions, the $\tilde{v}_4(\boldsymbol{\kappa})$ begin to follow their ideal trajectories [6,8], but eventually turn back towards the origin as $E \to 0$. The majority of the energy in $\tilde{v}_4(\boldsymbol{\kappa})$ is magnetic; as $\kappa|H_M|/E \to 1$, energy becomes purely magnetic and concentrates at $\mathbf{k} = \boldsymbol{\kappa}$. However, if a mean field (i.e., constant in space and time) $\mathbf{B}_o$ is added to $\mathbf{b}$, $H_M \to 0$ with time, and the spectral peak at $\mathbf{k} = \boldsymbol{\kappa}$ disappears, while if the volume rotates with angular velocity $\boldsymbol{\Omega}_o$, the peak persists, but the energy in $\tilde{v}_4(\boldsymbol{\kappa})$ is essentially all magnetic. Furthermore, as $|\boldsymbol{\Omega}_o|$ increases, the dipole moment vector $\boldsymbol{\mu}$ begins to align with $\boldsymbol{\Omega}_o$, but the angle between them saturates relatively quickly as $|\boldsymbol{\Omega}_o|$ increases, at around 20° for simulations on a 32^3 grid [17] (an effect which remains to be explained theoretically).

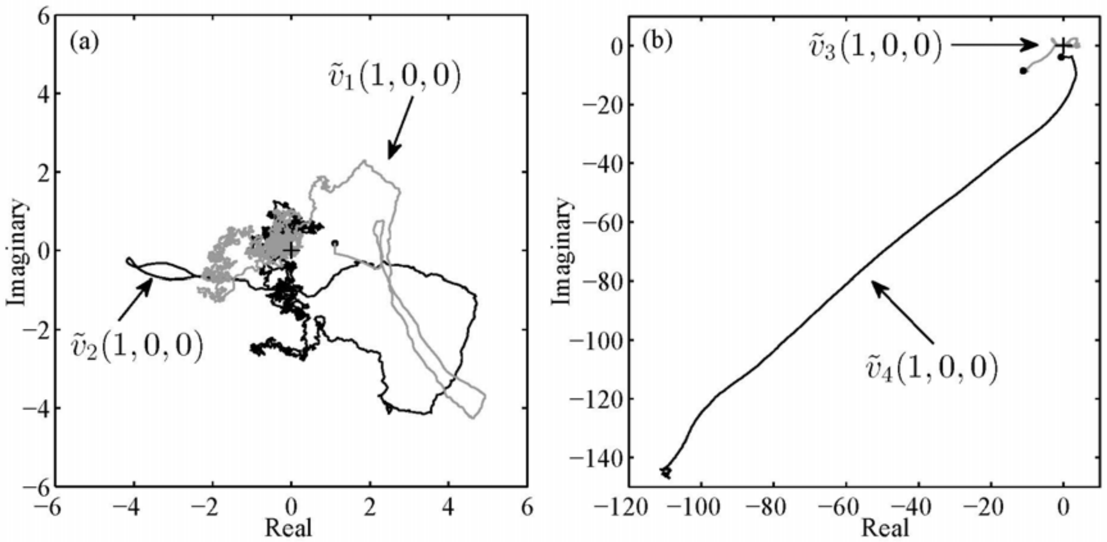

Figure 1: Evolution of (unnormalized) eigenvariables for $\boldsymbol{\kappa}$ = (1,0,0) from 64^3 run 1a [6].

6. Conclusion

Here, we have presented theoretical and numerical results concerning MHD turbulence and magnetic dynamos. The principle conclusion is that a statistical process involving broken ergodicity and magnetic helicity creates inherent dynamo action in MHD turbulence, causing the emergence of a large-scale, coherent magnetic field. This result may be relevant to understanding the oigin of planetary and stellar magnetic fields.

7. References

[1] Falgarone, E.; Passot, T.: Turbulence and Magnetic Fields in Astrophysics. Springer-Verlag, Berlin (2003).

[2] Jones, C.A.: Planetary Magnetic Fields and Fluid Dynamos. Annual Reviews of Fluid Mechanics 43 (2011) 583-614.

[3] Gailitis, A.; Lielausis, O.; Platacis, E.; Gerbeth, G.; Stefani, F.: Riga dynamo experiment and its theoretical background. Physics of Plasmas 11 (2004) 2838-2843.

[4] Shebalin, J.V.: Broken ergodicity and coherent structure in homogeneous turbulence. Physica D 37 (1989) 173-191.

[5] Shebalin, J.V.: Broken symmetry in ideal magnetohydrodynamic turbulence. Physics of Plasmas 1 (1994) 541-547.

[6] Shebalin, J.V.: Broken symmetries and magnetic dynamos. Physics of Plasmas 14 (2007) 102301.

[7] Shebalin, J.V.: Plasma relaxation and the turbulent dynamo. Physics of Plasmas 16 (2009) 072301.

[8] Shebalin, J.V.: Broken Ergodicity in Magnetohydrodynamic Turbulence. Geophysical and Astrophysical Fluid Dynamics 107 (2013) 411-466.

[9] Schubert, G. and Olson, P., Editors: Core Dynamics. Elsevier B.V., Amsterdam, NL (2009).

[10] Biskamp, D.: Magnetohydrodynamic Turbulence. Cambridge U.P., Cambridge, UK (2003) pp. 11-16.

[11] Shebalin, J.V.: Broken ergodicity, magnetic helicity and the MHD dynamo. Geophysical and Astrophysical Fluid Dynamics 107 (2013) 353-375.

[12] Glatzmaier, G.A. and Roberts, P.H.: A three-dimensional self-consistent computer simulation of a geomagnetic field reversal. Nature 377 (1995) 203-209.

[13] Khinchin, A.I.: Mathematical Foundations of Statistical Mechanics. Dover Books, NY (1949) 137-145.

[14] Kraichnan, R.H.: Helical turbulence and absolute equilibrium. Journal of Fluid Mechanics 59 (1973) 745-752.

[15] Frisch, U.; Pouquet, A.; Leorat, J.; Mazure, A.: Possibility of an inverse cascade of magnetic helicity in magnetohydrodynamic turbulence. Journal of Fluid Mechanics 68 (1975) 769-778.

[16] Palmer, R.G.: Broken ergodicity. Advances in Physics 31 (1982) 669-735.

[17] Shebalin, J. V.: Global invariants in ideal magnetohydrodynamic turbulence, Physics of Plasmas 20 (2013) 102305.

Feasible homopolar dynamo with sliding liquid-metal contacts

AVALOS-ZÚÑIGA, R.,[1] PRIEDE, J.[2]

[1] *CICATA-Qro, Instituto Politécnico Nacional, Cerro Blanco 141, Colinas del Cimatario, Querétaro, Mexico*; ravalosz@ipn.mx

[2] *Applied Mathematics Research Centre, Coventry University, Coventry, CV1 5FB, UK*; j.priede@coventry.ac.uk

Abstract: We present a feasible homopolar dynamo design consisting of a flat, multi-arm spiral coil, which is placed above a fast-spinning metal ring and connected to the latter by sliding liquid-metal electrical contacts. Using a simple, analytically solvable axisymmetric model, we determine the optimal design of such a setup. For small contact resistance, the lowest magnetic Reynolds number, $Rm \approx 34.6$, at which the dynamo can work, is attained at the optimal ratio of the outer and inner radii of the rings $R_i/R_o \approx 0.36$ and the spiral pitch angle 54.7°. In a setup of two copper rings with the thickness of $3\,\mathrm{cm}$, $R_i = 10\,\mathrm{cm}$ and $R_o = 30\,\mathrm{cm}$, self-excitation of the magnetic field is expected at a critical rotation frequency around $10\,\mathrm{Hz}$.

1 Introduction

The homopolar dynamo is one of the simplest models of the self-excitation of magnetic field by moving conductors which is often used to illustrate the dynamo action that is thought to be behind the magnetic fields of the Earth, the Sun and other cosmic bodies [1, 2]. In its simplest form originally considered by Bullard [3], the dynamo consists of a solid metal disc which rotates about its axis, and a wire twisted around it and connected through sliding contacts to the rim and the axis of the disc. At a sufficiently high rotation rate, the voltage induced by the rotation of the disc in the magnetic field generated by an initial current perturbation can exceed the voltage drop due to the ohmic resistance. At this point, initial perturbation starts to grow exponentially leading to the self-excitation of current and its associated magnetic.

Despite its simplicity no successful implementation of the disc dynamo is known so far. The problem appears to be the sliding electrical contacts which are required to convey the current between the rim and the axis of the rotating disc. Electrical resistance of the sliding contacts, usually made of solid graphite brushes, is typically by several orders of magnitude higher than that of the rest of the setup. This results in unrealistically high rotation rates which are required for dynamo to operate [4]. To overcome this problem we propose to use liquid-metal sliding electrical contacts similar to those employed in homopolar motors and generators [5]. The aim of this paper is to develop a feasible design of the disc dynamo which could achieve self-excitation at realistic rotation rates.

2 Physical and mathematical models

The principal setup of the proposed disc dynamo shown in Fig. 1(a) consists of a stationary coil (1) made of a copper disc sectioned by spiral slits and a fast-spinning disc (2) placed beneath it, which

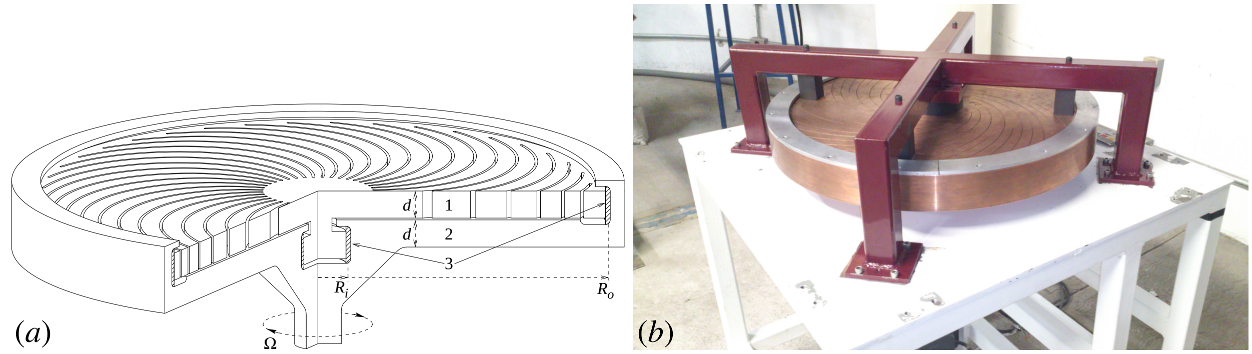

Figure 1: Schematic view of the disc dynamo setup consisting of a stationary coil (1) made of a copper disc sectioned by spiral slits and a fast-spinning disc (2), which is electrically connected to the former by sliding liquid-metal contacts (hatched) (3) (*a*) and the experimental device (*b*).

is electrically connected to the former by sliding liquid electrical contacts (3). The coil is supported by the holders which are not shown in this basic view. The liquid metal is hold in vertical state by the centrifugal force. Such a compact and symmetric design not only minimizes the electrical resistance in the system but also makes it amendable to simple analysis which is carried out in the following.

To simplify the analysis both discs are subsequently assumed to be thin coaxial rings of thickness d, the outer radius $R_o \gg d$, and the inner radius $R_i = \lambda R_o$, where $0 < \lambda < 1$ the ratio of the inner and outer radii. The rings are separated by a small axial distance and connected to each other at their rims through the sliding liquid-metal electrical contacts. The design of the stationary top ring, which forms a compact coil consisting of spiral sections is described in detail below. The bottom ring is mounted on an axle which is driven by an electric motor with the angular velocity Ω. The electric current I_0 is induced by the rotation of the bottom ring in the magnetic field generated by the same current returning through the coil formed by the top ring. In the solid rotating ring, the current is assumed to flow radially with the linear density $J_r = \frac{I_0}{2\pi r}$, which decreases due to the charge conservation inversely with the cylindrical radius r. Current returns through the top ring where it is deflected by the spiral slits that produce an azimuthal component proportional to the radial one:

$$J_\phi = -J_r\beta = \frac{I_0\beta}{2\pi r}, \tag{1}$$

where $\arctan\beta$ the pitch angle of the current lines relative to the radial direction. The shape of slits following the current lines is governed by $\frac{J_\phi}{J_r} = \frac{r d\phi}{dr} = -\beta$ and given by the logarithmic spirals

$$\phi(r) = \phi_0 - \beta \ln r, \tag{2}$$

where ϕ is the azimuthal angle. The electric potential distribution in the coil ring follows from Ohm's law

$$\vec{J} = \frac{I_0}{2\pi r}\left(-\vec{e}_r + \beta\vec{e}_\phi\right) = -\sigma d \vec{\nabla}\varphi_c, \tag{3}$$

as $\varphi_c(r,\phi) = \frac{I_0}{2\pi\sigma d}\left(\ln r - \beta\phi\right)$. Thus, the potential difference along the current line between the rims of the ring is

$$\Delta\varphi_c = \left[\varphi_c(r,\phi(r))\right]_{R_i}^{R_o} = -\frac{I_0}{2\pi\sigma d}(1+\beta^2)\ln\lambda. \tag{4}$$

The potential difference across the bottom ring, which rotates as a solid body with the azimuthal velocity $v_\phi = r\Omega$, is defined by the radial component of Ohm's law for a moving medium

$$J_r = \frac{I_0}{2\pi r} = \sigma d(-\partial_r \varphi_d + v_\phi B_z),$$

where B_z is the axial component of the magnetic field. Integrating the expression above over the ring radius we obtain

$$-\frac{I_0}{2\pi}\ln\lambda = \sigma d\left(-\Delta\varphi_d + \Omega\Phi_d\right), \tag{5}$$

where $\Delta\varphi_d = [\varphi_d(r)]_{R_i}^{R_o}$ is the potential difference across the rotating ring and $\Phi_d = \int_{R_i}^{R_o} B_z r\,dr$ is the magnetic flux through it. Using the relation $B_z = r^{-1}\partial_r(rA_\phi)$, the latter can be expressed in terms of the azimuthal component of the magnetic vector potential A_ϕ as

$$\Phi_d = \left[rA_\phi\right]_{r=R_i}^{R_o}. \tag{6}$$

In the stationary state, which is assumed here, the potential difference induced by the rotating ring in Eq. (5) is supposed to balance that over the coil defined by Eq. (4) as well as the potential drop over the liquid-metal contacts with the effective resistance $\mathscr{R} : \Delta\varphi_d = \Delta\varphi_c + \mathscr{R}I_0$. This equation implicitly defines the marginal rotation rate at which a steady current can sustain itself.

To complete the solution we need to evaluate the magnetic flux (6) through the rotating disc. The azimuthal component of the vector potential appearing in Eq. (6) is generated by the respective component of the electric current which is present only in the coil. Thus, we have

$$A_\phi(r,z) = \frac{\mu_0}{4\pi}\int_0^{2\pi}\int_{R_i}^{R_0} \frac{J_\phi(r')\cos\phi\, r'\,dr'\,d\phi}{\sqrt{r'^2 - 2r'r\cos\phi + r^2 + z^2}},$$

where z is the axial distance from the coil ring carrying the azimuthal current J_ϕ defined by Eq. (1). Note that the poloidal currents with radial and axial components circulating through the rings and liquid-metal contacts produce purely toroidal magnetic field, which is parallel to the velocity of the rotating ring and, thus, do not interact with the latter. In the plane of the ring $(z=0)$, the double integral above can be evaluated analytically as $A_\phi(r,0) = \frac{\mu_0\beta I_0}{8\pi^2}\left[F(R_i/r) - F(R_o/r)\right]$, where the function $F(x) = (1-x)K(m_+) + (1+x)E(m_+), + \mathrm{sgn}(1-x)\left[(1+x)K(m_-) + (1-x)E(m_-)\right]$, which is produced by the computer algebra system Mathematica in terms of the complete elliptic integrals of the first and second kind, $K(m_\pm)$ and $E(m_\pm)$, of the *parameter* $m_\pm = \frac{\pm 4x}{(1\pm x)^2}$ [6]. Taking into account that $F(1) = 4$, the magnetic flux (6) can be written as

$$\Phi_c = \frac{\mu_0\beta I_0 R_o}{8\pi^2}\bar{\Phi}(\lambda), \tag{7}$$

where $\bar{\Phi}(\lambda) = F(\lambda) + \lambda F(\lambda^{-1}) - 4(1+\lambda)$ is a dimensionless magnetic flux and $\lambda = R_i/R_o$ is the radii ratio.

In the following, we assume the axial separation between the rings to be so small that the magnetic flux through the rotating ring is effectively the same as that through the coil, i. e., $\Phi_d \approx \Phi_c$. Substituting the relevant parameters into the equation defining the marginal rotation rate we eventually obtain

$$Rm = \mu_0\sigma d R_o\Omega = \frac{4\pi(\bar{\mathscr{R}} - (2+\kappa\beta^2)\ln\lambda)}{\kappa\beta\bar{\Phi}(\lambda)}, \tag{8}$$

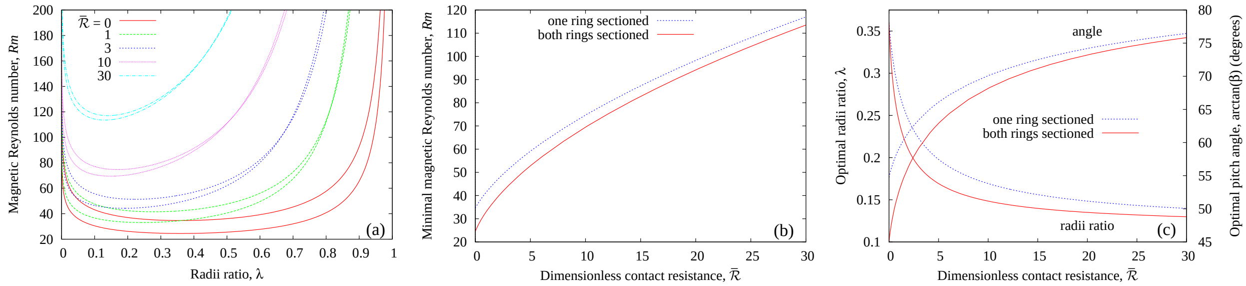

Figure 2: Marginal Rm versus λ for only one ring sectioned $(\kappa = 1)$ at various dimensionless contact resistances $\bar{\mathcal{R}}$ and the optimal β, (a). Minimal magnetic Reynolds number Rm (b), optimal radii ratio λ, and the coil pitch angle $\arctan\beta$ (c) versus the dimensionless contact resistance$\bar{\mathcal{R}}$.

which is the marginal magnetic Reynolds number defining the dynamo threshold depending on the spiral pitch angle $\arctan\beta$, the radii ratio λ, and the dimensionless contact resistance $\bar{\mathcal{R}} = 2\pi\sigma d\mathcal{R}$.

The case of solid rotating ring considered above corresponds to $\kappa = 1$, whereas $\kappa = 2$ corresponds to the rotating ring sectioned similarly to the stationary one except for the opposite direction of the spiral slits. As seen from the expression above, the latter case is equivalent to the former with both Rm and β reduced by a factor of $\sqrt{2}$.

Now, let us determine the optimal β and λ that yield the lowest Rm for a given $\bar{\mathcal{R}}$. In the simplest case of a negligible contact resistance, which corresponds to $\bar{\mathcal{R}} = 0$, Eq. (8) yields $Rm \sim 2/(\kappa\beta) + \beta$. It means that Rm attains a minimum at $\beta_c = \sqrt{2/\kappa}$, which corresponds to the optimal pitch angles of 54.74° and 45° for only one and both rings sectioned. The respective lowest values of Rm, 34.63 and 24.49, are attained at the same optimal radii ratio of $\lambda = 0.3602$. (see Fig. 2(a) for the case of only one ring sectioned). The minimal Rm increases with $\bar{\mathcal{R}}$, which also causes a steep reduction of the optimal radii ratio and a comparably fast rise of the pitch angle (see Fig. 2(b,c)).

3 Feasible setup

Finally, let us evaluate the rotation rate required for self-excitation in a setup with the outer radius of $R_o = 30\,\mathrm{cm}$ and the ring thickness of $d = 3\,\mathrm{cm}$. First, we need to estimate electrical resistance of sliding liquid-metal contacts. A suitable metal for such contacts may be the eutectic alloy of GaInSn [5], which is liquid at room temperature with the kinematic viscosity $\nu = 3.5\times10^{-7}\,\mathrm{m/s^2}$, electrical conductivity $\sigma_{\mathrm{GaInSn}} = 3.3\times10^{6}\,\mathrm{S/m}$. Assuming the contact gap width of $\delta = 0.5\,\mathrm{cm}$ and the inner radius $R_i \approx 10\,\mathrm{cm}$, we have $\mathcal{R}_i \approx \frac{\delta\sigma_{\mathrm{GaInSn}}^{-1}}{2\pi dR_i} \approx 0.02\,\mu\Omega$. The resistance of the outer contact is by a factor of $\lambda = R_i/R_0 = 0.33$ lower than $\mathcal{R}_i$. Then the dimensionless contact resistance can be estimated as $\bar{\mathcal{R}} = 2\pi\sigma_{\mathrm{Cu}}d\mathcal{R}_i(1+\lambda) \approx \frac{\sigma_{\mathrm{Cu}}}{\sigma_{\mathrm{GaInSn}}}\frac{\delta}{R_i}(1+\lambda) \approx 0.2$. If only one disc is sectioned, which is easier to manufacture, the respective magnetic Reynolds number is $Rm \approx 40$. This corresponds to the rotation frequency $f = \frac{\Omega}{2\pi} = \frac{Rm}{2\pi\mu_0\sigma_{\mathrm{Cu}}dR_o} \approx 10\,\mathrm{Hz}$, which is well within the operation range of standard AC electric motors. The respective linear velocity of the outer edge of the ring is around $v \approx 20\,\mathrm{m/s}$. At this velocity the tensile stress at the rim of the ring, $\rho_{\mathrm{Cu}}v^2 \approx 4\,\mathrm{MPa}$, is more than by an order of magnitude below the yield strength of annealed Copper [7]. The optimal inner radius $R_i \approx 0.3R_0 \approx 9\,\mathrm{cm}$ following from Fig. 2(c) is not far from the value assumed above. The respective pitch angle for $\beta \approx 1.6$ is about 58°.

The number of spiral arms is determined by the following arguments. The current distribution defined by Eq. (1) can hold only in the inner parts of the ring which are radially confined between the spiral slits. This ideal distribution is expected to break down at the rims, which are radially exposed to the edges of the ring located at the nearly equipotential metal liquid contacts. In order to confine this perturbation to the outer rim with $r/R_o \gtrsim 0.9$, Eq. (2) suggests that $\frac{-2\pi}{\beta \ln 0.9} \approx 40$ equally distributed spiral slits are required.

The last critical issue is the viscous power losses associated with the turbulent drag acting on the outer sliding contacts at high shear rates. These losses can be estimated as $Q = S\tau v \approx 7\,\mathrm{kW}$, where $S \approx 2\pi dR_o$ the area of the outer sliding contact, $\tau = \frac{c}{4}\frac{\rho v^2}{2}$ is the turbulent shear stress, and $c \approx 0.02$ is the Darcy friction factor for turbulent pipe flow with the Reynolds number $Re \sim 10^5$[8]. Note that the relatively large setup size is due to the turbulent energy dissipation which scales as $Q \sim (dR_o)^{-2} \sim \Omega^2$. Namely, reducing the system size by one third would require about five times higher power input to achieve self-exitation of the magnetic field.

In conclusion, the proposed disc dynamo design appears feasible in terms of both the disc spinning rate and the power required to drive it. A corresponding device, which is shown in Fig. 1(b), has been built and is to undergo first tests in May 2014.

References

[1] Moffatt, H.K.: *Magnetic field generation in electrically conducting fluids*. Cambridge, 1978.

[2] Beck, R.; Brandenburg, A.; Moss, D.; Shukurov, A.; Sokolov, D.: Galactic magnetism: recent developments and perspectives, Annu. Rev. Astron. Astrophys. 34 (1996) 155–206.

[3] Bullard, E.C.: The stability of a homopolar dynamo, Proc. Camb., Phil. Soc. 51 (1955) 744–760.

[4] Rädler, K.-H.; Rheinhardt, M.: Can a disc dynamo work in the laboratory? Magnetohydrodynamics 38 (2002) 211–217.

[5] Maribo, D.; Gavrilash, M.; Reilly, P. J.; Lynch, W.A.; Sondergaard, N.A.: Comparison of Several Liquid Metal Sliding Electric Contacts, Proceedings of the 56th IEEE Holm Conference on Electrical Contacts (HOLM) (2010) 1–7.

[6] Abramowitz, M.; Stegun, I.A.: *Handbook of mathematical functions,* Dover, New York, 1972.

[7] Li, M.; Zinkle, S.J.: Physical and Mechanical Properties of Copper and Copper Alloys, In: R.J.M. Konings (ed.), Comprehensive Nuclear Materials, vol 4, Elsevier, Amsterdam, 2012, pp. 667–690.

[8] Maribo, D.; Sondergaard, N.A.: Further studies of a low-melting point alloy used in a liquid metal current collector, IEEE Transactions on Components, Hybrids, and Manufacturing Technology 10 (1987) 452–455

The effect of axial electric current on the helical magneterotational instability

PRIEDE, J.
Applied Mathematics Research Centre, Coventry University, UK
j.priede@coventry.ac.uk

Abstract: We present the results of numerical stability analysis of a cylindrical Taylor-Couette flow of liquid metal carrying an axial electric current in the presence of a generally helical external magnetic field. Two purely electromagnetic instabilities are found in the presence of the electric current. The first is a pinch-type instability driven by the interaction of electric current with its own magnetic field, which is known as the Tayler instability. The axisymmetric mode of this instability requires a free-space component of the azimuthal magnetic field which is possible in annular but in solid cylindrical geometry. The second appears to be a new type of electromagnetic instability driven by the interaction of electric current with a weak collinear external magnetic field.

1 Introduction

The present paper is concerned with the effect of the axial current passing through liquid metal in the Taylor-Couette set-up on the so-called helical magnetorotational instability (HMRI). However the HMRI is able to destabilize centrifugally stable velocity distributions [1, 2], it does not reach up to the astrophysically relevant Keplerian rotation profile [3, 4]. Recently, it has been suggested that this limitation of HMRI can be overcome when the azimuthal magnetic field component is allowed to have a non-zero rotation, which means an electric current passing through the fluid [5]. From the physical point of view, current provides an additional energy source. Thus, instability no longer requires background flow and so can extend over an unlimited range of velocity profiles. In this paper, we show that there are two such instabilities which appear in the presence of a background electric current. The first is the so-called Tayler instability which is a pinch-type instability driven by the interaction of electric current with its own magnetic field [6]. The second is a new type of instability driven by the interaction of electric current with a weak collinear external magnetic field.

2 Formulation of the problem

Consider an incompressible fluid of kinematic viscosity ν and electrical conductivity σ filling the gap between two infinite concentric cylinders with inner radius R_i and outer radius R_o rotating respectively with angular velocities Ω_i and Ω_o in the presence of helical magnetic field $\vec{B}_0 = \vec{e}_z B_z + \vec{e}_\phi B_\phi$ with the axial component $B_z = \alpha B_0$ and the azimuthal component

$$B_\phi = B_0\left[(\beta-\gamma)R_i/r + \gamma r/R_i\right] \tag{1}$$

in cylindrical coordinates (r,ϕ,z). The dimensionless coefficient α defines the magnitude of the axial component of the magnetic field relative to that of the azimuthal component. The latter has a free-space part defined by the coefficient β and a rotational part defined by the coefficientγ which is associated with the axial current density in the fluid $\vec{j}_0 = \frac{1}{\mu_0}\vec{\nabla}\times\vec{B}_0 = \vec{e}_z\frac{2\gamma B_0}{\mu_0 R_i}$, where μ_0

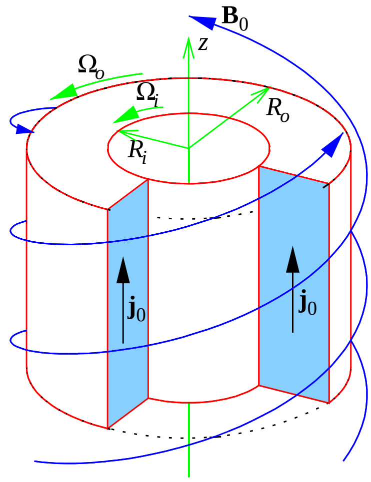

Figure 1: Sketch of the problem.

is the magnetic permeability of vacuum. Note that in annular geometry with $R_i \neq 0$, the latter produces also a free-space component with the effective helicity $-\gamma$.

Following the inductionless approximation, which holds for most of liquid-metal magnetohydrodynamics characterized by small magnetic Reynolds numbers $Re_m = \mu_0 \sigma v_0 L \ll 1$, where v_0 and L are the characteristic velocity and length scales, the magnetic field of the currents induced by the fluid flow is assumed to be negligible relative to the imposed field $\vec{B}_0$ everywhere except the Navier-Stokes equation

$$\partial_t \vec{v} + (\vec{v} \cdot \vec{\nabla})\vec{v} = \rho^{-1}\left(-\vec{\nabla} p + \vec{j} \times \vec{B}\right) + \nu \vec{\nabla}^2 \vec{v}, \tag{2}$$

where, as shown below, its interaction with the background electric current $\vec{j}_0$ results in a non-negligible perturbation of the electromagnetic body force. The electric current is governed by Ohm's law for a moving medium $\vec{j} = \sigma\left(\vec{E} + \vec{v} \times \vec{B}_0\right)$ and related to the magnetic field by Ampère's law $\vec{j} = \mu_0^{-1} \vec{\nabla} \times \vec{B}$. In addition, we assume that the characteristic time of velocity variation is much longer than the magnetic diffusion time $\tau_0 \gg \tau_m = \mu_0 \sigma L^2$. This leads to the quasi-stationary approximation, according to which $\vec{\nabla} \times \vec{E} = 0$ and $\vec{E} = -\vec{\nabla}\Phi$, where Φ is the electrostatic potential. Mass and charge conservation imply $\vec{\nabla} \cdot \vec{v} = \vec{\nabla} \cdot \vec{j} = 0$.

The problem admits base state with a purely azimuthal velocity distribution $\vec{v}_0(r) = \vec{e}_\phi v_0(r)$, where $v_0(r) = r\frac{\Omega_o R_o^2 - \Omega_i R_i^2}{R_o^2 - R_i^2} + \frac{1}{r}\frac{\Omega_o - \Omega_i}{R_o^{-2} - R_i^{-2}}$. Note that the magnetic field does not affect the base flow because it gives rise only to the electrostatic potential $\Phi_0(r) = B_0 \int v_0(r)\,dr$ whose gradient compensates the induced electric field so that there is no current in the base state ($\vec{j}_0 = 0$). However, a current may appear in a perturbed state

$$\left\{\begin{array}{c} \vec{v}, p \\ \vec{B}, \Phi \end{array}\right\}(\vec{r}, t) = \left\{\begin{array}{c} \vec{v}_0, p_0 \\ \vec{B}_0, \Phi_0 \end{array}\right\}(r) + \left\{\begin{array}{c} \vec{v}_1, p_1 \\ \vec{B}_1, \Phi_1 \end{array}\right\}(\vec{r}, t),$$

where $\vec{v}_1$, p_1, $\vec{B}_1$, and Φ_1 present small-amplitude perturbations.

In the following, we focus on axisymmetric perturbations for which the solenoidity constraints are satisfied by meridional stream functions for fluid flow and electric current as $\vec{v} = v\vec{e}_\phi + \vec{\nabla} \times (\psi \vec{e}_\phi)$, $\vec{j} = j\vec{e}_\phi + \vec{\nabla} \times (h\vec{e}_\phi)$. Note that h is the azimuthal component of the induced magnetic field which is used subsequently instead of Φ for the description of the induced current. For numerical purposes, we introduce also the vorticity $\vec{\omega} = \omega\vec{e}_\phi + \vec{\nabla} \times (v\vec{e}_\phi) = \vec{\nabla} \times \vec{v}$ as an auxiliary variable. The perturbation is sought in the normal mode form $\left\{v_1, \omega_1, \psi_1, h_1, g_1\right\}(\vec{r}, t) =$

$\{\hat{v},\hat{\omega},\hat{\psi},\hat{h},\hat{g}\}(r)\times e^{\gamma t+ikz}$, where γ is, in general, a complex growth rate and k is the axial wave number which is real for the conventional stability analysis and complex for absolute instability. Henceforth, we proceed to dimensionless variables by using R_i, R_i^2/ν, $R_i\Omega_i$, B_0, and $\sigma\mu_0 B_0 R_i^2\Omega_i$ as the length, time, velocity, and the induced magnetic field scales, respectively. Non-dimensionalised governing equations then read as

$$\gamma\hat{v} = D_k\hat{v} + Re\, ikr^{-1}(r^2\Omega)'\hat{\psi} + Ha^2(ik\alpha\hat{h} + 2\gamma\hat{g}), \tag{3}$$
$$\gamma\hat{\omega} = D_k\hat{\omega} + 2Re\, ik\Omega\hat{v} + Ha^2 ik[ik\alpha\hat{\psi} - 2((\beta-\gamma)r^{-2}+\gamma)\hat{h}], \tag{4}$$
$$0 = D_k\hat{\psi} + \hat{\omega}, \tag{5}$$
$$0 = D_k\hat{h} + ik[\alpha\hat{v} - 2(\beta-\gamma)r^{-2}\hat{\psi}], \tag{6}$$
$$0 = D_k\hat{g} + k^2\alpha\hat{\psi}, \tag{7}$$

where $D_k f \equiv r^{-1}(rf')' - (r^{-2}+k^2)f$ and the prime stands for $\frac{\mathrm{d}}{\mathrm{d}r}$; $Re = R_i^2\Omega_i/\nu$ and $Ha = R_i B_0\sqrt{\frac{\sigma}{\rho\nu}}$ are Reynolds and Hartmann numbers, respectively; $\Omega(r) = \frac{\lambda^{-2}-\mu+r^{-2}(\mu-1)}{\lambda^{-2}-1}$ is the dimensionless angular velocity of the base flow defined by $\lambda = R_o/R_i$ and $\mu = \Omega_o/\Omega_i$.

The boundary conditions for the flow perturbation on the inner and outer cylinders at $r=1$ and $r=\lambda$, respectively, are $\hat{v}=\hat{\psi}=\hat{\psi}'=0$. The boundary conditions for $\hat{h}$ for insulating and perfectly conducting cylinders, respectively, are $\hat{h}=0$ and $(r\hat{h})'=0$ at $r=1;\lambda$. The boundary conditions for the radial component of the induced magnetic field $\hat{g}$ follow from the solution of Eq. (7) in the free space, where $\hat{\psi}\equiv 0$. Thus, we have $\hat{g}(r)=G_iI_1(kr)$ and $\hat{g}(r)=G_oK_1(kr)$ for $0\le r\le 1$ and $r\ge\lambda$, respectively, where I_n and K_n are the modified Bessel functions of the first and second types of index n. Taking the ratio $(r\hat{g})'/\hat{g}$ to eliminate the unknown constants G_i and G_o leads to the following boundary conditions for $\hat{g}$ $(r\hat{g})'=c_i(kr)\hat{g}$ at $r=1$ and $(r\hat{g})'=c_o(kr)\hat{g}$ at $r=\lambda$, where $c_i(kr)=krI_0(kr)/I_1(kr)$ and $c_o(kr)=-krK_0(kr)/K_1(kr)$.

3 Results

In the following, the ratio of radii of inner and outer cylinders is fixed to $\lambda=2$ and the cylinders are assumed to be insulating. We start with a hydrodynamically unstable flow corresponding to the ratio of rotation rates $\mu=0.2$, which is below the Rayleigh limit $\mu_c=\lambda^{-2}=0.25$. The magnetic field is helical with the axial component fixed by $\alpha=1$ and the azimuthal component generated only by the current passing through the fluid which corresponds $\beta=0$. In purely axial magnetic field corresponding to $\gamma=0$, the flow becomes centrifugally unstable to stationary Taylor vortices when Reynolds number exceeds the marginal value which is plotted in Fig. 2 against the wave number. Addition of a weak azimuthal component of the magnetic field

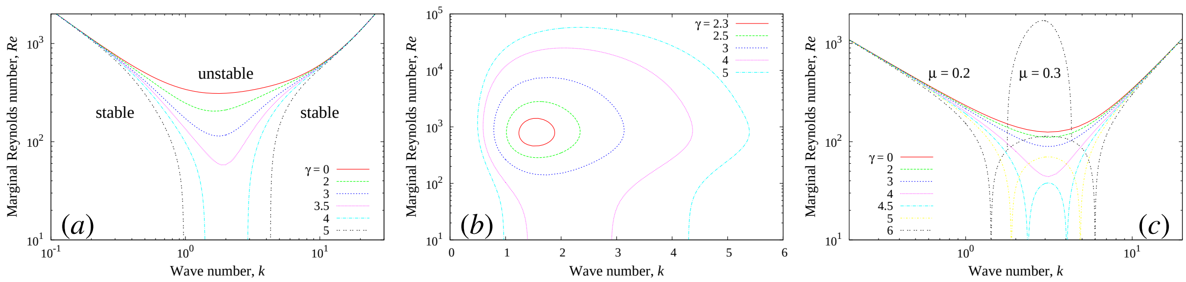

Figure 2: Marginal Reynolds number versus the wave number for a hydrodynamically unstable flow with $\mu=0.2$ (a) and for a hydrodynamically stable flow with $\mu=0.3$ (b) at various helicities γ of rotational helical magnetic field with $\alpha=1$, $\beta=0$ and $\alpha=\beta=0$ (c) for $Ha=10$.

reduces the instability threshold and makes the instability oscillatory ($\omega \neq 0$). However, the main result seen in Fig. 2(a) is the drop of the marginal Reynolds number to zero in a range of intermediate wave numbers when $\gamma \gtrsim 3.7$. Zero Reynolds number means that this instability is entirely electromagnetic and independent of the base flow. We will see later that there are two different electromagnetic mechanisms driving this instability.

Next, let us turn to the hydrodynamically stable flow with the ratio of rotation rates set to $\mu = 0.3 > \mu_c$ which is above the Rayleigh limit. As seen in Fig. 2(b), a moderately helical rotational magnetic field can destabilize this flow similarly to helical free-space magnetic field. In both cases, neutral stability curves from closed contours which means that the instability is constrained to certain ranges of the wave numbers and Reynolds numbers. Namely, in contrast to the hydrodynamically unstable case considered above, there are now two marginal Reynolds numbers – the lower one by exceeding which the flow destabilizes, and the upper one by exceeding which the flow restabilizes. This picture changes when the helicity of the rotational field exceeds$\gamma \approx 3.7$. As for the hydrodynamically unstable case considered above, marginal Reynolds number again drops to zero in a certain range of intermediate wave numbers when γ exceeds this critical value.

Let us consider what happens when the axial component of the magnetic field is switched off by setting $\alpha = 0$. It means that the magnetic field is purely azimuthal and it is generated only by the axial current passing in the liquid annulus. Marginal Reynolds number and the frequency for both hidrodynamically unstable ($\mu = 0.2$) and stable ($\mu = 0.3$) flows in the magnetic fields of various strength defined by γ and $Ha = 10$ is plotted in Fig. 2(c) against the wave number. In the hydrodynamically unstable case, the effect of purely azimuthal field is very similar to that of the helical field considered above. Namely, the increase of the axial electric current defined by γ results in the decrease of marginal Reynolds number, which again drops to zero in a certain range of wave numbers when $\gamma \gtrsim 4.5$. In contrast to helical magnetic field, now the instability is basically stationary ($\omega = 0$), although some oscillatory modes appear in the hydrodynamically stable case at high sufficiently high γ and Reynolds numbers. Also the hydrodynamically stable flow is affected by this purely azimuthal magnetic field in a slightly different way. Namely, all neutral stability curves in this case end at zero Reynolds number. Thus, the lower critical Reynolds number, if any, is always zero in the hydrodynamically case.

Obviously, here we have a z-pinch-type instability which occurs due to a weak compression of the azimuthal magnetic field lines by a radially inward meridional flow perturbation. This enhances the electromagnetic pinch force generated by the interaction of the axial electric current with its own magnetic field and, thus, amplifies the initial perturbation. It is important to notice that axisymmetric meridional flow affects only the free-space ($\sim r^{-1}$) but not the rotational ($\sim r$) component of the azimuthal magnetic field. The respective induction term is absent in Eq. (6) because axisymmetric meridional flow conserves the flux of the rotational azimuthal magnetic field. Thus, besides the rotational component this instability requires also a free-space component of the azimuthal magnetic field. The latter, however, is possible only in annular but not in cylindrical geometry. As seen from Eq. (1), the free-space component of the azimuthal magnetic field associated the axial electric current in annular geometry ($R_i \neq 0$) can be compensated by additional free-space magnetic field with $\beta = \gamma$ which leaves only the rotational component $\sim r$ as in a solid cylinder.

Now let us check what happens when the axisymmetric pinch instability is eliminated by applying a compensating free-space magnetic field with $\beta = \gamma$. In this case, to have any electromagnetic effect on the axisymmetric disturbances considered here, we need to switch on the axial magnetic field by setting $\alpha = 1$. The elimination of the pinch instability turns out to have a surprisingly little effect. Both the critical Reynolds number and frequency, which are shown in Fig. **??**(b) versus the ratio of rotation rates of outer and inner cylinders for $Ha = 10$, look very

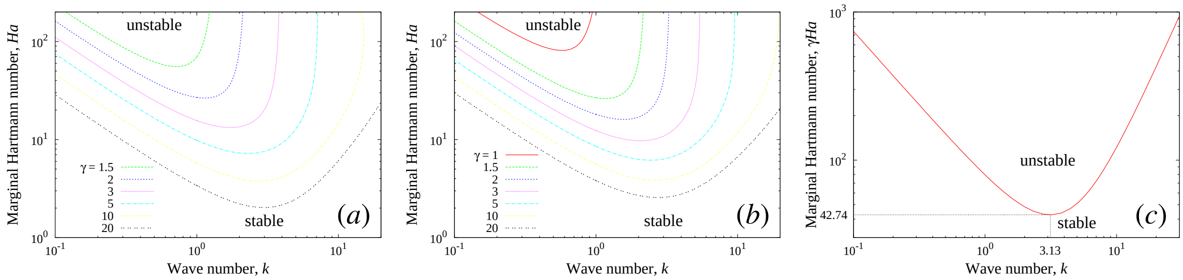

Figure 3: Marginal Hartmann number versus the wave number for purely electromagnetic ($Re = 0$) stationary ($\omega = 0$) instabilities in a rotational magnetic field with $\alpha = 1, \beta = 0$ (a), $\alpha = 1, \beta = \gamma$ (b) and $\alpha = \beta = 0$ (c) at various axial currents defined by γ.

similar to the respective characteristics shown in Fig. **??**(a) for the rotational helical magnetic field with an uncompensated free-space component. As before, the increase of the axial current reduces the critical Reynolds number, which in this case drops to zero at the critical value $\beta = \gamma \approx 2.9$ leading to an unlimited extension of the instability beyond the Rayleigh limit.

Zero marginal Reynolds number means that the instability does not depend on the background flow and is driven entirely by electromagnetic force which is defined by the Hartmann number. The marginal Ha at which neutrally stable purely electromagnetically sustained disturbances of given wave number appear is plotted in Fig. 3 for various axial current parameters γ in helical magnetic field with uncompensated $(\alpha = 1, \beta = 0)$ (a) and compensated $\beta = \gamma$ (b) free-space azimuthal components, and in a purely azimuthal field generated only by the axial current in the liquid annulus $(\alpha = \beta = 0)$ (c). For the first two helical field configurations, marginal Ha is seen to vary with γ in a similar way. For purely azimuthal field configuration, when the axial field component is absent, it is important to note that the instability is determined by the effective Hartmann number γHa which is independent of γ. As seen in Fig. 3(c), the lowest value $\gamma Ha_c \approx 42.74$ is attained at the critical wave number $k_c \approx 3.13$.

References

[1] Hollerbach; R.; Rüdiger, G.: New type of magnetorotational instability in cylindrical Taylor-Couette flow, Phys. Rev. Lett. **95** (2005) 124501.

[2] Stefani, F.; Gerbeth, G.; Gundrum, Th.; Hollerbach, R.; Priede, J.; Rüdiger, G.; Szklarski, J.: Helical magnetorotational instability in a Taylor-Couette flow with strongly reduced Ekman pumping Phys. Rev. E **80** (2009) 066303.

[3] Liu, W.; Goodman, J.; Herron, I.; Ji, H.: Helical magnetorotational instability in magnetized Taylor-Couette flow, Phys. Rev. E **74** (2006) 056302.

[4] Priede, J.: Inviscid helical magnetorotational instability in cylindrical Taylor-Couette flow, Phys. Rev. E **84** (2011) 066314.

[5] Kirillov, O. N.; Stefani, F.: Extending the range of the inductionless magnetorotational instability, Phys. Rev. Lett. **111** (2013) 061103.

[6] Seilmayer, M.; Stefani, F.; Gundrum, Th.; Weier, T.; Gerbeth, G.; Gellert, M.; Rüdiger, G.: Experimental evidence for a transient tayler instability in a cylindrical liquid-metal column, Phys. Rev. Lett. **108** (2012) 244501.

Stability investigation of Hartmann flow with the convective approximation

I.Yu. Kalashnikov

National Research Nuclear University MEPhI, department 32,
Kashira highway, 31.

kalasxel@gmail.com

Abstract

The report focuses on the linear analysis of a plane-parallel flow stability in transverse magnetic field (Hartmann flow) with the convective approximation. Obtained and solved equations that describes the perturbation growth. Founded perturbation modes and non-excitation conditions of ones. Obtained the equation for the instability increment and shown to have an instable root of the equation. Also shown that founded instabilities is qualitatively agrees with the experimental data.

Introduction

Hartmann flow is steady stream between two fixed infinite parallel planes arising for due to the pressure drop that occurs in a magnetic field directed perperpendicular planes. We choose the z axis co-directional with the external magnetic field B_0, and the x axis direct along the stream. For such flow there is an exact solution:

$$V_x(z) = \frac{k_2\delta}{k_1\sinh(k_1\delta)}(\cosh(k_1\delta) - \cosh(k_2 z)), \tag{1}$$

$$\sqrt{\frac{\nu_m}{4\pi\rho\nu}}B_x = -\frac{k_2}{k_1}z + \frac{k_2\delta}{k_1\sinh(k_1\delta)}\sinh(k_1 z), \tag{2}$$

where $k_1 = B_0/\sqrt{4\pi\rho\nu\nu_m}$, $k_2 = -(1/\rho\nu)(\partial p/\partial x)$. Constants ν and ν_m are kinematic and magnetic viscosity, ρ is density of the fluid.

From (1), (2) we can show that with increasing transverse magnetic fields velocity profile becomes flatter. This flatness is characterized by the Hartmann number: $Ha = B_0/\sqrt{4\pi\rho\nu\nu_m}$.

Stability of the Hartmann flow was first considered in [1] where the influence of the magnetic field is taken into account only by changing the velocity field, and obtained (quite expected) result that with increasing magnetic field stability increases too.

Also worth noting the work of [2], which has been studied experimentally the transition to turbulence due to the instability Hartmann layer and conditions of turbulence suppression. Found that when the parameter $R = Re/Ha > 380$ the flow becomes turbulent. Numerical simulations [3] gives approximately the same result. Because R is inversely proportional to the magnetic field, then again, it can be concluded that a weak magnetic field destabilizes the current.

Two-dimensional perturbations

Assume that instabilities are convective, ie perturbations that arise at any point does not have time to develop, and are carried over beyond the real pipe. But because the magnetic field has (because embeddedness) inhibitory effect, then feasibility of such an assumption, it should be small.

We can leave this value from the dimensional parameters of the liquid in three ways: ν_m/δ, ν/δ and $\sqrt{\nu\nu_m}/\delta$. Since on embeddedness affects only magnetic viscosity, it is logical to choose the first variant. Thus we obtain:

$$\frac{B_0\delta}{\sqrt{4\pi\rho\nu_m}} \ll 1. \tag{3}$$

In this approximation, we consider that the perturbation does not evolve, moving along the main flow, ie $\partial/\partial x = 0$. Then investigate the stability of the system of equations:

$$\frac{\partial \mathbf{V}}{\partial t} + (\mathbf{V},\nabla)\mathbf{V} + \frac{1}{\rho}(P + \frac{\mathbf{B}^2}{8\pi}) - \frac{1}{4\pi\rho}(\mathbf{B},\nabla)\mathbf{B} - \nu\nabla^2\mathbf{V} = 0, \tag{4}$$

$$\frac{\partial \mathbf{B}}{\partial t} - (\mathbf{B},\nabla)\mathbf{V} + (\mathbf{V},\nabla)\mathbf{B} - \nu_m\nabla^2\mathbf{V} = 0, \tag{5}$$

$$\nabla\cdot\mathbf{V} = 0, \tag{6}$$

$$\nabla\cdot\mathbf{B} = 0, \tag{7}$$

assuming that the main flow is obeys (1), (2), and all the convective instability.

Making the transformation $\mathbf{B}\to\mathbf{B}+\mathbf{b}$, $\mathbf{V}\to\mathbf{V}+\mathbf{v}$, $P\to P+\varphi$, where $\mathbf{V}=(V(z),0,0)$, $\mathbf{B}=(B(z),0,B_0)$ - known. We leave only linear members of perturbations. Further, since on the time t and the coordinate y movement is infinite, then assume that on these variables perturbation is periodic : $f(y,z,t)\to f(z)exp(i\gamma t - iky)$. Ie in each layer dz extends plane wave. Denoting then $b_x = b$ and $v_x = v$ write:

$$\mathbf{b} = (b, \frac{\partial a}{\partial z}, -\frac{\partial a}{\partial y}) = (b, \frac{\partial a}{\partial z}, ika), \tag{8}$$

$$\mathbf{v} = (v, \frac{\partial q}{\partial z}, -\frac{\partial q}{\partial y}) = (v, \frac{\partial q}{\partial z}, ikq), \tag{9}$$

where a and q - x components of the vector potential.

Through this transformation of equation (6) and (7) disappears, and y and z components of the equation (5) are identical. Then the system equations describing the amplitude of a plane wave perturbation has the form:

$$i\gamma v + ikV'q - \frac{B_0}{4\pi\rho}\frac{db}{dz} - ik\frac{B'}{4\pi\rho}a + \nu k^2 v - \nu\frac{d^2 b}{dz^2} = 0, \tag{10}$$

$$i\gamma b - ikV'a - B_0\frac{dv}{dz} + ikB'q + \nu_m k^2 b - \nu_m\frac{d^2 b}{dz^2} = 0, \tag{11}$$

$$\frac{dM}{dz} - ikN = \frac{B_0}{4\pi\rho}\nabla^2 a, \tag{12}$$

$$\frac{dN}{dz} + ikM = 0, \tag{13}$$

where stood the two quantities:

$$M = i\gamma q + \nu k^2 q - \nu \frac{d^2 q}{dz^2}, \tag{14}$$

$$N = \frac{\varphi}{\rho} + \frac{Bb}{4\pi\rho}. \tag{15}$$

For N values the boundary conditions are obviously zero: $N(\pm\delta) = 0$. However, you need another condition to determine the possible wave numbers k. Note that if in the expression for M make replacement $z \to -z$ (or $k \to -k$) it does not change. So we can say that $M(\delta) = M(-\delta)$.

Then from (14), (15) and substituted the boundary conditions we obtain the eigenvalues of the wave number:

$$k = -i\frac{\pi}{\delta}n, \quad n \in \mathbb{Z}. \tag{16}$$

Ie for $k = 0$, there is instability, being increased either the right or left relative to the flow. Nonzero modes will not be excited, if δ is sufficiently large. We can compare δ with the parameters of liquid three ways, but since this instability is due to hydrodynamic and electrodynamic forces then choose the variant for δ, where ν and ν_m includes equally. Therefore, considering convection assumptions we have range for δ:

$$\frac{\sqrt{4\pi\rho\nu\nu_m}}{B_0} \ll \delta \ll \frac{\sqrt{4\pi\rho}\nu_m}{B_0}, \tag{17}$$

which implies that $\nu \ll \nu_m$ or magnetic Prandtl number $Pr_m \ll 1$. And as $Ha \gg 1$.

One-dimensional perturbations

It should be noted that for $k \neq 0$ system obtained can be solved exactly, but we restrict our investigation is one-dimensional flow in the y-stable region. Then the vector perturbations are two-dimensional (no z component). We obtain two independent systems for the potentials (18), (19) and for the components of the perturbation (20), (21):

$$i\gamma a - B_0\frac{dq}{dz} - \nu_m \frac{d^2 a}{dz^2} = 0, \tag{18}$$

$$i\gamma q - \frac{B_0}{4\pi\rho}\frac{da}{dz} - \nu \frac{d^2 q}{dz^2} = 0, \tag{19}$$

$$i\gamma b - B_0\frac{dv}{dz} - \nu_m \frac{d^2 b}{dz^2} = 0, \tag{20}$$

$$i\gamma v - \frac{B_0}{4\pi\rho}\frac{db}{dz} - \nu \frac{d^2 v}{dz^2} = 0, \tag{21}$$

the pressure disturbance Is expressed through disturbance of the magnetic field as follows:

$$\varphi = -\frac{Bb}{4\pi}. \tag{22}$$

Boundary conditions are as follows:

$$b(\pm\delta) = v(\pm\delta) = \frac{da}{dz}(\pm\delta) = \frac{dq}{dz}(\pm\delta) = 0. \tag{23}$$

Note that when $\nu = \nu_m$ in both systems is the symmetry: when replacing $b \to v\sqrt{4\pi\rho}$ (or $a \to q\sqrt{4\pi\rho}$) form of the equations is not changed. Therefore, the spectrum obtained is a degenerate, so that the eigenfunctions can be found in the form $b = \sigma v\sqrt{4\pi\rho}$, where $\sigma = \pm 1$. We have eigenvalues corresponding to stable flow:

$$i\gamma = -\frac{\nu}{(2\delta)^2}(\pi^2 n^2 + Ha^2) \leq 0, \;\; n \in \mathbb{Z}. \tag{24}$$

This means that for close values of kinematic and magnetic viscosity low and one-dimensional perturbations are damped and the flow is stable. However, as follows from (17), there already been undamped perturbation mode.

System (18), (19) and (20), (21) in the solution will give the same eigenvalues λ and lead to the same equation for the eigenvalues of the increment γ. We solve (20), (21). We seek a solution in the form $b = b_0 e^{\lambda z}$, $v = v_0 e^{\lambda z}$. Obtain the eigenvalues:

$$\lambda^2 = \frac{1}{2}\left[i\gamma\left(\frac{1}{\nu} + \frac{1}{\nu_m}\right) + \frac{{B_0}^2}{4\pi\rho\nu\nu_m} \pm \sqrt{\left[i\gamma\left(\frac{1}{\nu} + \frac{1}{\nu_m}\right) + \frac{{B_0}^2}{4\pi\rho\nu\nu_m}\right]^2 - \frac{4\gamma^2}{\nu\nu_m}} \right]. \tag{25}$$

In view of the boundary conditions we obtain the equation for increment γ:

$$b_1 v_2 \cosh(\lambda_1\delta)\sinh(\lambda_2\delta) = v_1 b_2 \sinh(\lambda_1\delta)\cosh(\lambda_2\delta), \tag{26}$$

where: $b_1 = B_0\lambda_1\delta$, $b_2 = B_0\lambda_2\delta$, $v_1 = \delta(i\gamma - \nu_m{\lambda_1}^2)$, $v_2 = \delta(i\gamma - \nu_m{\lambda_2}^2)$ (λ_1 taken with plus before the square root).

Dimensionless $\gamma\delta^2/\nu \to \gamma$. In the first approximation we set $Pr_m = 0$. Then we obtain the following for the eigenvalues: $\lambda_1\delta \simeq \sqrt{i\gamma + Ha^2}$, $\lambda_2 \simeq 0$. Equation (26) can be factored and written in the form:

$$i\gamma\sqrt{i\gamma + Ha^2} = \tanh\sqrt{i\gamma + Ha^2}. \tag{27}$$

Roots of equation (27) must satisfy equation (26) in the approximation $Pr_m = 0$.

One of the roots (stable) is immediately visible: $i\gamma = -Ha^2 < 0$. Another root corresponding a pure imaginary increment indicates flow instability: $i\gamma > 0$.

Discussion and conclusions

On Fig. 1 shows a summary of the experimental results on the study of the stability of the Hartmann flow [4]. In these experiments, the measured resistance coefficient: $\lambda = -2p'\delta/\rho V^2$. For Hartmann flow it has the form: $\lambda_H \simeq 2Ha/Re$. At the graph the deviation of bisector from the coordinate angle means that flow for the given parameters already turbulent.

From (3) follow that in the convective approximation $\lambda \ll Ha^{-1}{Re_m}^{-1}$. Since the experiments were carried out at $Ha \sim 10^2$ and $Re_m \sim 10^{-3}$ (mercury) it is possible to say that

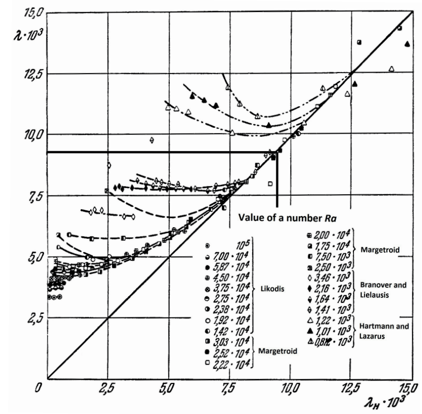

Figure 1: Experimental data on the resistance coefficient in comparison with the theory for the flow of Hartmann. Highlighted the range of applicability of the convective approximation.

$\lambda_H \ll 10$. And as can be seen from Fig. 1 in this field flow is not laminar. Thus found instability really take place.

Fulfillment of the condition (17) provides only the absence of perturbations aimed parallel to the planes (ie absence component of the perturbation).As seen from (27) with increasing Ha instability is suppressed. This can be explained by the fact that with increasing magnetic field (and as a consequence an increase in the Hartmann number) embeddedness effect will dominate, making it difficult to form instabilities in the initially laminar flow instabilities.But the equation (27) obtained in the limit $Pr_m \to 0$. To determine more precise conditions under which the flow could be sustained needs detailed analysis of (26).

It should also be noted that in the limit $Ha \to 0$ instability is still present, although it itself becomes for Poiseuille. Absence of such a limit transition observed in [5], and explained that a non-zero magnetic field already generates instability, which then can develop without using a magnetic field.

References

1. R. Lock. The Stability of the Flow of an Electrically Conducting Fluid between Parallel Planes under a Transverse Magnetic Field. Proc. R. Soc. Lond. A. 233 (1955) 105 - 125.

2. P. Moresco, T. Alboussière. Experimental study of the instability of the Hartmann layer. J. Fluid Mech. 504 (2004) 167 - 181.

3. D.S. Krasnov, E. Zienicke, O. Zikanov, T. Boeck, A. Thess. Numerical study of the instability of the Hartmann layer. J. Fluid Mech. 504 (2004) 183 - 211.

4. H. Branover, A. Chinober. Magnetohydrodynamics of incompressible fluids. The main editorial physical and mathematical literature publishing house "Science". Moscow, 1970. pp 88–96 (in Russian).

5. E. Velikhov. Stability of an ideally conducting fluid between rotating cylinders in a magnetic field. Soviet Physics JETP. 36 (1959) 1398 - 1404.

INSTABILITY OF ELECTROLYTIC FLOW DRIVEN BY AN AZIMUTHAL LORENTZ FORCE IN A CYLINDRICAL CONTAINER

PEREZ-BARRERA[1,2] J., PEREZ-ESPINOZA[1], J. ENRIQUE, ORTIZ[1], A., NUÑEZ[2], J., RAMOS[1] E., CUEVAS[1] S.
[1]Instituto de Energías Renovables, Universidad Nacional Autónoma de México, Temixco, Morelos, 62580 MEXICO
[2]Universidad de la Ciénega del Estado de Michoacan, Saguayo, Mich., 59103 MEXICO.
E-mail address of corresponding author: scg@ier.unam.mx

Abstract: We study experimentally and theoretically the free surface flow produced by an azimuthal Lorentz force in a layer of either a liquid metal or an electrolyte contained in an open electromagnetic stirrer with cylindrical geometry. The force is created by the interaction of an electric current applied in radial direction and an approximately constant magnetic field (0.04 T) parallel to the cylinder's axis. For the liquid metal flow, we found a pure azimuthal motion at the free surface with applied currents from 1 to 2 A. However, for the electrolytic flow we observed the appearance of an instability that leads to the formation of anticyclonic vortices in the horizontal plane normal to the magnetic field with applied currents in the range 25-400 mA. We found 4 to 11 traveling vortices that form a polygon and remain for long times once they appear.

1. Introduction

Magnetohydrodynamic flows in annular ducts have been widely explored both experimentally and theoretically. From the experimental point of view, annular ducts avoid the difficulty of considering the entrance region that is present in rectilinear ducts under a strong uniform magnetic field. In the most common configuration, the annular duct is formed in the gap between two coaxial electrically conducting cylinders, limited by insulating top and bottom walls. By placing the duct in the center of a magnetic solenoid, we get an approximately uniform magnetic field parallel to the cylinder's axis. If an electric potential difference is applied between the lateral walls of the cylinders, a radial electric current density will arise in the conducting fluid. The interaction of the radial current with the axial magnetic field produces an azimuthal Lorentz force that drives the flow. Since the pioneering work of Baylis [1] and Baylis and Hunt [2], attention has been mainly focused on liquid metal flows at high Hartmann numbers, motivated by important applications related with metallurgical and fusion blanket technologies. Moresco and Alboussière [3] used the annular duct configuration to investigate experimentally the stability properties of the Hartmann layer and the transition to turbulence in a liquid metal flow. More recently, disregarding the Hartmann walls with the aim at understanding better the role of the sidewall layers, Zhao et al. [4] explored numerically the centrifugal instability between coaxial infinite conducting cylinders at large Hartmann numbers. They found a system of several axially elongated counter-rotating vortices arranged in the radial direction. In a subsequent numerical study, Zhao and Zikanov [5] considered the existence of insulating top and bottom Hartmann walls in an annular (toroidal) duct of square cross-section with the same geometry and parameter range used in the experiment by Moresco and Alboussière. The purpose was to analyze the flow features at Reynolds numbers below the threshold of transition to turbulence in Hartmann layers. Among many interesting things, they found that the first instability leads to an axisymmetric unsteady flow characterized by quasi-periodic transformations of meridional circulation vortices.

In contrast with the substantial number of studies of MHD flows in annular ducts using liquid metals, it appears that just a few works have been published for the case of electrolytes. Unlike liquid metal MHD flows, the Hartmann number in electrolytic flows is usually very small. Digilov [6] analyzed the flow of an electrolyte driven by an azimuthal Lorentz force in an annular channel. The author obtained an analytic solution for the case of infinite cylinders although he assumed that the electric field established between the cylinders (electrodes) is decoupled from the fluid flow, which in general is not the case. He performed very simple demonstrative experiments finding a pure azimuthal stable flow that showed reasonable agreement with the theory. Digilov, however, called the attention about the existence of flow regions where, according to the theory of Marcus [7], anticyclonic vortices could appear. In a recent paper, Qin and Bau [8] performed a theoretical analysis of the electromagnetically driven flow of a binary electrolyte in a concentric annulus under a uniform, axial magnetic field. They studied the linear stability of the azimuthal flow when the cylinders are infinitely long and found that when the current is directed outwardly, electrochemical effects destabilize the flow, originating convective flows in the transverse plane. In turn, when the current is directed inwardly, electrochemical reactions have a stabilizing effect and the azimuthal flow is linearly stable for all Dean numbers. When the annular duct is finite, pure azimuthal flows are not possible and the flow is always three-dimensional independently of the direction of the current. To the best of our knowledge, this is the only stability analysis performed in electrolytic MHD flows in annular channels.

In the present study, we investigate experimentally the free surface flow driven by an azimuthal Lorentz force in a layer of either a liquid metal or an electrolyte contained in two different open cylindrical configurations. When the fluid is an electrolyte, experiments have shown the appearance of a flow instability consisting of a varying number of anticyclonic traveling vortices for given flow conditions, that is, electric potential difference between the electrodes and height of the fluid layer. In spite of the rather simple experimental configurations, the studied flow offers a rich dynamic behavior.

2. Experimental setup

The experimental setup consists of a cylindrical open cavity of 76 mm diameter and 12 mm depth with one electrode made of a thin sheet of copper wrapped around the inner wall of the cavity. A second electrode is introduced in two different configurations (see Fig. 1). In the first one, an inner concentric copper cylinder of 25.4 mm diameter is inserted so that the fluid is contained in the gap between the cylinders. In the second configuration a circular coin-shaped copper electrode (of the same diameter as the inner cylinder of configuration I) is placed concentrically and embedded in the bottom of the container so that the fluid occupies the whole extension of the cylindrical container. In both configurations the container is filled with either a liquid metal layer of 5 mm thick (eutectic alloy GaInSn) or a weak electrolytic solution of sodium bicarbonate (NaHCO3) at 8.6% by weight that forms a layer whose thickness was varied from 2.5 to 10 mm. The container is placed on top of a rectangular permanent magnet (150 mm X 100 mm X 25.4 mm) so that an approximately uniform magnetic field in the axial direction exists within the layer thickness. The magnetic field strength on the bottom of the container is 0.04 T. When an electric potential difference is set between the electrodes, a DC radial electric current passes (either outwardly or inwardly, depending on the polarity of the electrodes) through the conducting fluid whose intensity varied from 1 to 2 A for liquid metal and form 25 to 400 mA for the electrolyte. The interaction of the radial current and the axial magnetic field produces a Lorentz force that generates fluid motion mainly in the azimuthal direction. Note that electric current in configuration II is not strictly radial in the electrode region but presents an axial component that decreases the strength of the driving Lorentz force in that region.

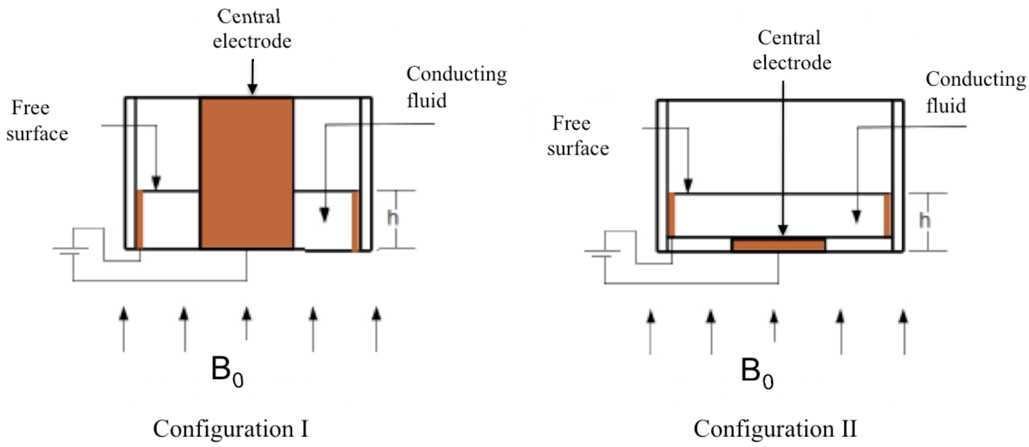

Figure 1: Sketch (lateral view) of the experimental setup in the two explored configurations.

3. Results

Let us first present some experimental results for the liquid metal flow. By taking the 5 mm thickness of the liquid metal layer as the characteristic length, the Hartmann number in this case is approximately 8. In order to avoid oxidation, a thin layer of hydrochloric acid of 1 mm thick was poured on top of the liquid metal, producing small bubbles. Using these bubbles as flow tracers, Particle Image Velocimetry (PIV) was implemented to discern approximately the free surface flow of the liquid metal. Within the range of explored electric current intensities (1 to 2 A), the PIV analysis revealed a pure azimuthal flow on the free surface, as shown in Fig 2. Due to the restricted experimental conditions results are not conclusive and a more complete characterization of the flow is necessary.

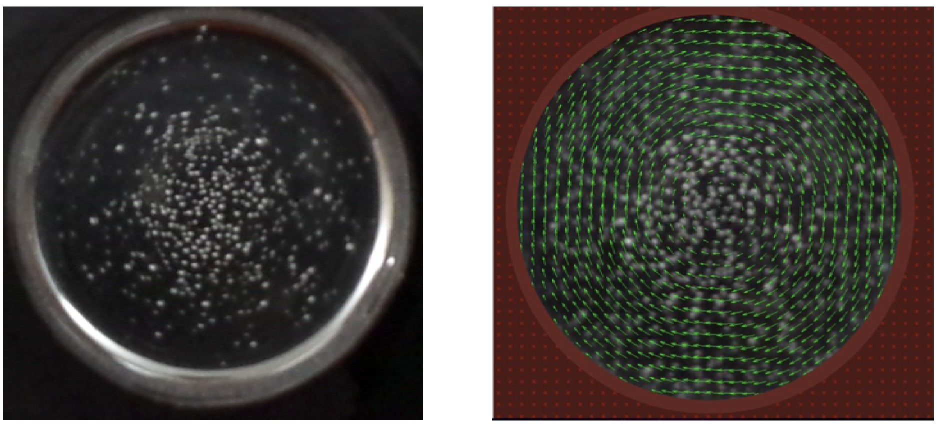

Figure 2: Top view of the liquid metal driven flow with configuration II for an electric current of 2 A. The left panel shows the bubbles created once the acid is poured on top of the liquid metal. The right panel shows the purely azimuthal velocity field obtained from the PIV analysis using the bubbles as tracers. Notice the almost stagnant region where the central embedded electrode is located.

For the electrolytic flow, experiments in both configurations showed the appearance of an instability that leads to the formation of anticyclonic vortices (i.e vortices that rotate in opposite sense to the global azimuthatl flow) independently of the direction of the current. Due to the small electrical conductivity of the electrolyte ($\sigma \approx 6.36$ S m^{-1}) and the weak magnetic field, the Hartmann number is very low (Ha $\approx$ 0.03). Traveling anticyclonic vortices, visualized using dye, are observed to appear close to the wall of the exterior cylinder, their number varying from 4 to 11 according to the flow conditions. Vortices form a polygon and once they appear, they remain for long times. Figure 3 shows a sample of the vortex visualization in both configurations. By changing the layer depth and potential difference, it is possible to find the critical layer thickness and electric current for the appearance of the instability. All the experiments correspond to small aspect ratios, $0.01 < h/L < 0.4$, where h is the layer thickness and L is the space between the outer and inner electrodes. For the smallest aspect ratio bottom friction inhibits the appearance of anticyclonic vortices. As the aspect ratio increases, the current intensity necessary for the emergence of vortices diminishes. The flow very close to the surface was explored using PIV. This analysis revealed that in some cases vortices also appear close to the inner electrode although these structures were not detected with dye visualization.

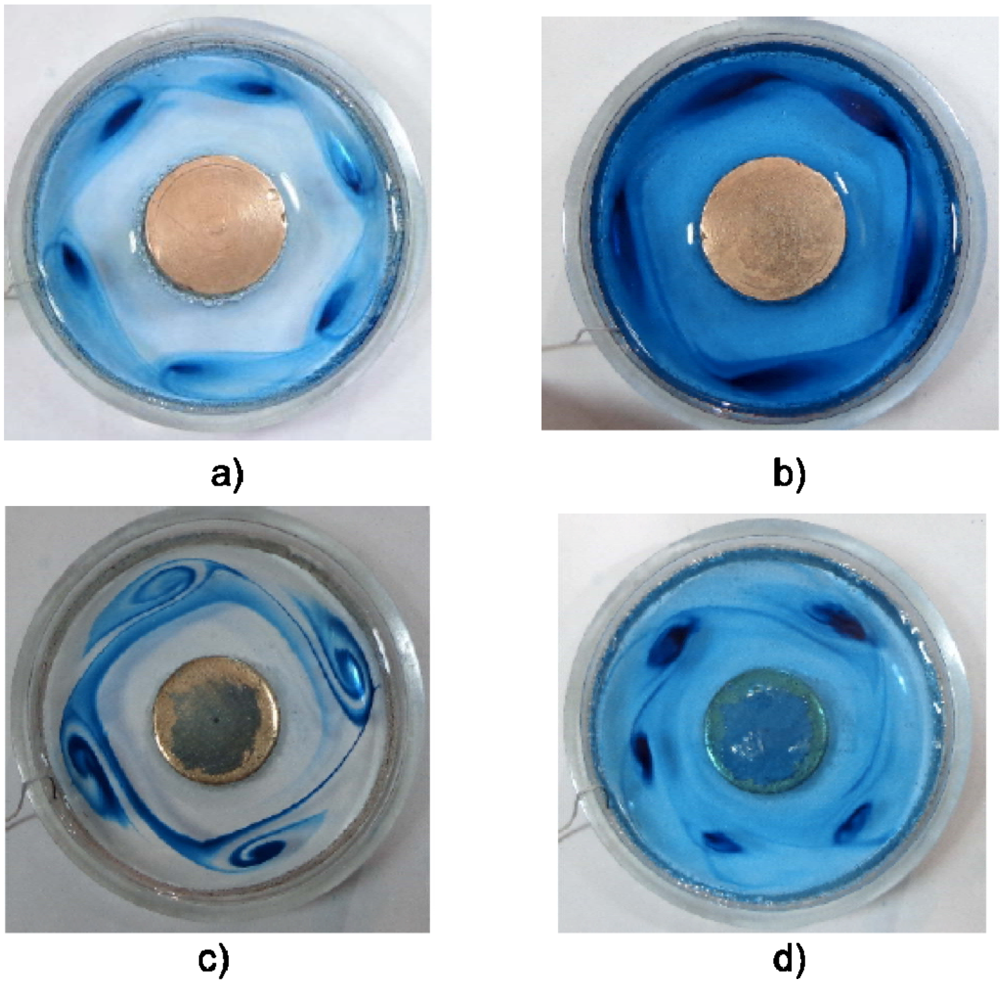

Figure 3: Dye visualization of the instability observed for a layer thickness of 10 mm. a) and b) correspond to configuration I. c) and d) correspond to configuration II. Current intensity for a) and c) is 100 mA. while for b) and d) is 300 mA.

According to Marcus [7] vortices embedded in a shearing zonal flow where shear stress and vorticity have opposite sign, tend to be fragmented and destroyed in a turn-around time. In those regions where the signs are the same, vortices redistribute their vorticity so that its maximum value is at the center. This appears to be consistent with the shear stress and vorticity calculated from the analytical solution [9] corresponding to the flow between infinite cylinders. This solution (see Fig. 4) shows that shear stress and vorticity have the same sign close to the inner and outer cylinders and, according to Marcus, these are the zones where vortices could exist. These zones can be modified by varying the gap between the cylinders.

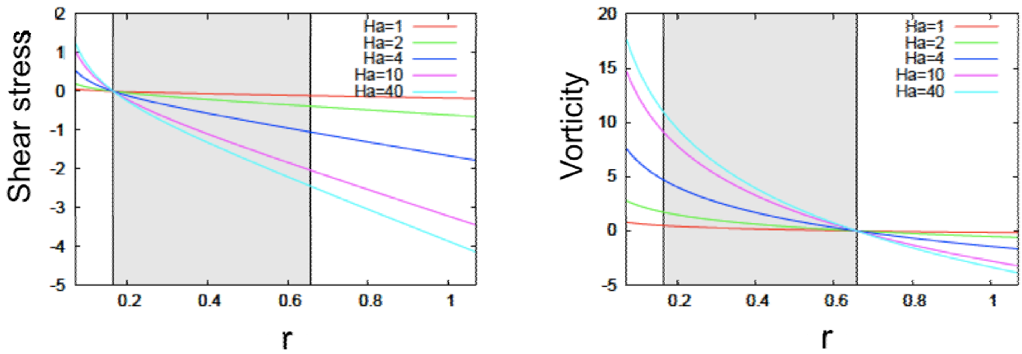

Figure 4: Shear stress and vorticity as function of the radial coordinate at different Ha, calculated from the exact analytical solution for infinite coaxial conducting cylinders [9]. Shaded region denotes the zone where, according to Marcus [7], vortices cannot persist.

4. Conclusion

We reported the existence of an instability in the electrolytic flow driven by an azimutal Lorentz force in a cylindrical electromagnetic stirrer. The instability is characterized by the emergence of stable anticyclonic traveling vortices that form a polygon in the plane normal to the axial magnetic field. We observed a varying number of vortices mainly located near the outer cylinder although PIV analysis revealed the existence of vortices close to the inner electrode. This behavior seems to be supported by the theoretical analysis of Marcus [7] for a shearing zonal flow.

Financial support from CONACYT, Mexico, through Project 131399 is acknowledged.

5. References

[1] Baylis, J. A.: Experiments on laminar flows in curved ducts of square cross-section. J. Fluid Mech. 48 (1971) 417-422.

[2] Baylis, J. A.; Hunt, J. C. R.: MHD flow in an annular channel: theory and experiment. J. Fluid Mech. 48 (1971) 423-428.

[3] Moresco, P.; Alboussière, T.: Experimental study of the instability of the Hartmann layer. J. Fluid Mech. 504 (2004) 167.

[4] Zhao, Y.; Zikanov, O.; Kraznov, D.: Instability of magnetohydrodynamics flow in an annular channel at high Hartmann number. Phys. Fluids, 23 (2011) 084103.

[5] Zhao, Y.; Zikanov, O.: Instabilities and turbulence in magnetohydrodynamics flow in a toroidal duct prior to transition in Hartmann layers. J. Fluid Mech., 692 (2012) 288-316.

[6] Digilov, .: Making a fluid rotate: Circular flow of a weakly conducting fluid induced by a Lorentz body force. Am. J. Phys., 75 (2007) 361-367.

[7] Marcus, P. S.: Vortex dynamics in a shearing zonal flow. J. Fluid Mech., 215 (1990) 393-430.

[8] Qin, M.; Bau, H. H.: Magnetohydrodynamics flow of a binary electrolyte in a concentric annulus. Phys. Fluids, 23 (2012) 037101.

[9] Pérez-Barrera, J.: Theoretical study of the flow driven by an azimuthal Lorentz force in an electromagnetic stirrer. MSc Thesis, National Autonomous University of Mexico (2013) (in Spanish).

Experimental study of forced and freely decaying wall bounded MHD turbulence, at low Rm

BAKER[1,2] Nathaniel, POTHĒRAT[2] Alban, DAVOUST[3] Laurent, DEBRAY[4] François.
Affiliation: [1] CNRS CRETA – 38042 Grenoble – France
[2] AMRC, Faculty of Eng. and Comp., Coventry University – Coventry CV1 5FB - UK
[3] SIMAP, EPM Group – 38402 Saint Martin d'Hères – France
[4] LNCMI, CNRS-UPS-INSA-UJF – 38042 Grenoble – France
e-mail address of corresponding author: nathaniel.baker@creta.cnrs.fr

Abstract: We investigate experimentally the properties of low-Rm MHD turbulence, which takes place in a wall bounded domain. First, we look at forced turbulence and show that it is possible to observe turbulent velocity fluctuations featuring 2D behaviour (in the sense that they do not depend on a spatial coordinate), even though a strongly 3D mean flow exists. Second, we analyse the free decay of the turbulence, during which we can distinguish several distinctive regimes.

Introduction

One of the main features of MHD flows is the action of the Lorentz force, which tends to damp momentum along the magnetic field. This process can be interpreted as a diffusion of momentum along the magnetic field [1], eventually bringing the flow towards a two-dimensional state. Until now, most studies - whether experimental ([2], [3]), theoretical [4], or numerical [5] - have focused on cases where turbulence evolves in a space featuring either a free surface, infinitely distant boundaries, or periodic boundary conditions. However, the presence of obstacles is an intrinsic feature of real flows, and any attempt to fully explain their dynamics must account for them. The purpose of this study is to understand the effects of walls on the dynamics of electrically-driven low-Rm MHD turbulence. This paper breaks down into three parts: we will start by presenting our experimental setup, before analyzing the statistical properties of the fully developed turbulent flow, and finally looking at the dynamics of its free decay.

1. Experimental methods

Our work was conducted using the Flowcube, an experimental rig designed to generate and investigate electrically driven turbulence in a closed cubic domain [6]. It consists of a frame of inner length L = 100 mm closed by electrically insulating side plates. Instruments are embedded flush within each one of these plates in order to either drive the flow (current injection electrodes) or analyze its properties (potential probes and ultrasound transducers). The cube is placed inside the 450 mm bore of a superconducting magnet, which applies a vertical magnetic field $B_0\,\mathbf{e_z}$ of up to 4T. The cube is filled with Gallinstan, an eutectic alloy of gallium, indium and tin, which is liquid at room temperature, and characterized by a density ρ = 6400 kg/m3, a kinematic viscosity $\nu = 4 \times 10^{-7}$ m²/s and an electrical conductivity $\sigma = 3.4 \times 10^{6}$ S/m. Electrical current is injected by means of a 10 x 10 square array of electrodes, alternately connected to the positive and negative poles of a DC power supply. The injection electrodes are located on the bottom plate, and are uniformly separated by a distance l^i = 10 mm from each other. 100 uniformly spaced potential probes mesh a 30 mm x 30 mm square area located on the bottom plate with a spatial resolution Δx = 2.5 mm. These probes give access to the electric potential field at the plate's surface, from which can be deduced the velocity field perpendicular to the magnetic field in the plane right above the bottom Hartmann layer [7]. Finally, a vertical row of ultrasound transducers give horizontal velocity profiles at different heights along the magnetic field. The spatial domain explored by the transducers spans from x = 10 mm to x = 90 mm (the immediate vicinity of the side walls must be ignored as the signals are corrupted by strong echoes), with a spatial resolution Δx = 0.22 mm.

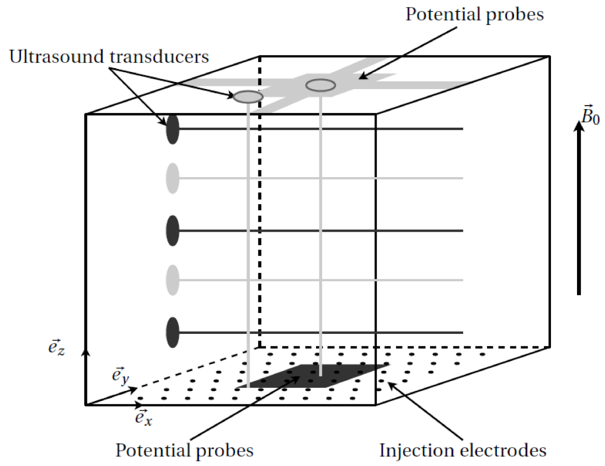

Figure 1: *Sketch of the Flowcube. Electrical current is injected through the injection electrodes at the bottom. The data acquired in sections 2 and 3 come from the probes colored in dark gray (left ultrasound transducers and bottom potential probes respectively). Probes colored in light gray are present in the experiment but not exploited in this paper.*

The operating conditions used for the experiments are characterized by a Hartmann number Ha ~ 7300 and a Reynolds number based on the turbulent fluctuations Re ~ 30000. A total electrical current I = 300 Amps was injected. These parameters were selected for two reasons: first, they yield a strongly three-dimensional forced flow, where inertia and the Lorentz force are in strong competition. Second, they lead to a reasonably long decay (around 15 seconds), which is easy to capture. The forcing was even and carefully monitored during the measurements. During a typical experimental run, the forced state was recorded for 3 minutes after the transient regime vanished (almost instantly). The decay was then triggered by suddenly switching off the power supply. The recording was kept running during 30 seconds after the decay had been triggered.

2. Forced Turbulence

In this section, we analyze the statistical properties of forced turbulence. The data presented below result from averaging 35000 velocity profiles (50 experimental runs, during which 700 forced profiles were recorded).

Figure 2 shows the normalized mean flow and turbulent fluctuations horizontal profiles, at different locations away from the forcing. Figure 2.a's bottom signal features a quasi periodic profile, whose half wavelength is l^i = 10 mm. This length corresponds to the spacing between injection electrodes and can be interpreted as the characteristic length of the forcing. The peaks and troughs are therefore evidence of counter rotating structures generated by the forcing. As we move up in the box, one can see that the amplitude of the mean flow, relative to the bottom flow decreases dramatically with height. In fact, there appears to be a factor 10 between the bottom flow where the forcing takes place and the top flow. This behavior can be put on account of the Lorrentz force not being strong enough to compete with inertia throughout the box, therefore leading to strong three-dimensionality [8]. Figure 2.b, shows that the intensity of the fluctuations at the bottom features strong spatial variations. Those variations are quickly damped along z, giving a rather even and uniform fluctuation distribution far from the forcing area. Contrary to the mean flow, the amplitude of the fluctuations is not damped with height, and seems to be affected by side walls only.

Figure 3 gives a synthesized view of the previous argument. In particular, figure 3.a shows how quickly the mean flow is damped along z, resulting in a very weak residual flow for z > 50 mm. In the same spirit, 3.b shows how the intensity of fluctuations is smoothed out and become constant for z > 50 mm. In other words, horizontal turbulent fluctuations seem to feature a 2D behavior (in the sense that they do not depend on the spatial coordinate z), although the mean flow is strongly three-dimensional. It is also worth noting that the fluctuations are much more intense than the mean flow at any given height. Indeed, they happen to be twice as important at the bottom, but become more than twenty times larger at the top.

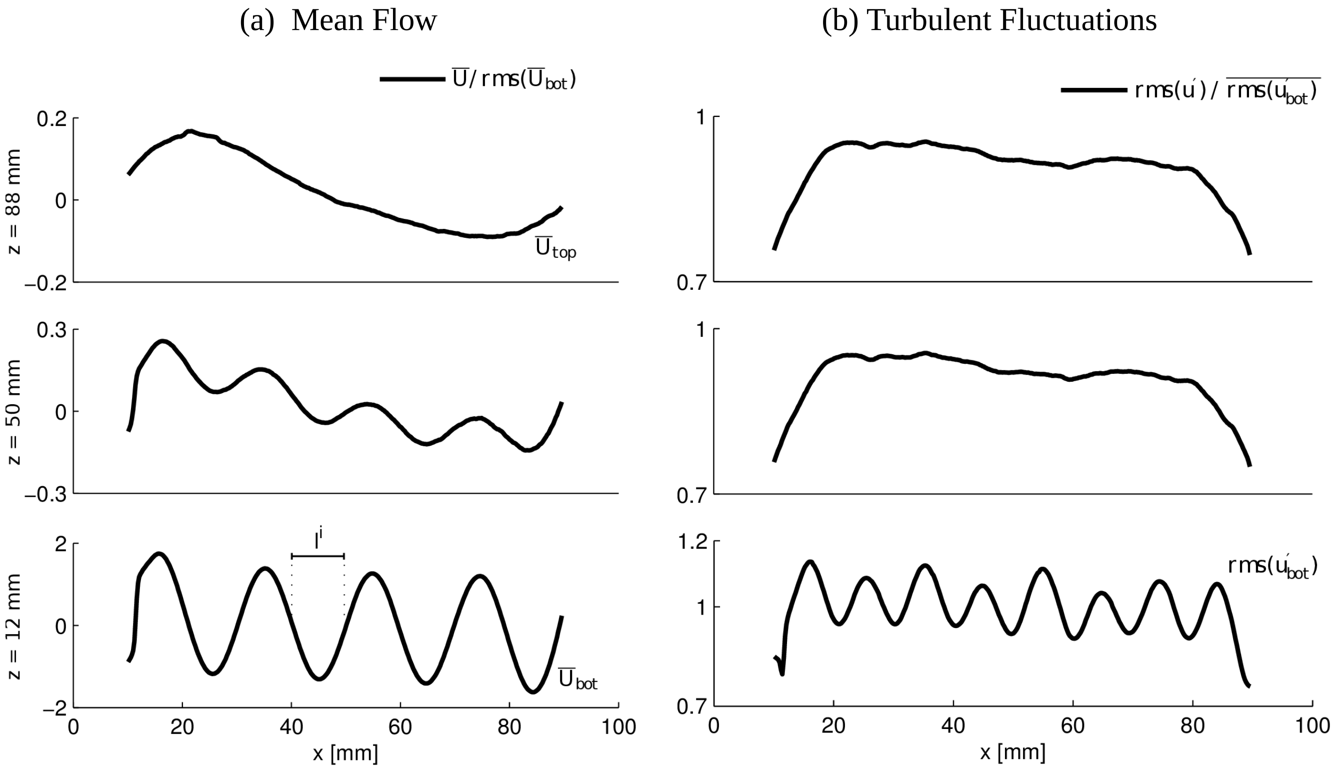

Figure 2: *horizontal mean flow (left) and turbulent fluctuations (right) perpendicular to the magnetic field. Both graphs are normalized by the rms (resp. mean) of the bottom signal. Notice the damping of smaller structures by the Lorentz force along z.*

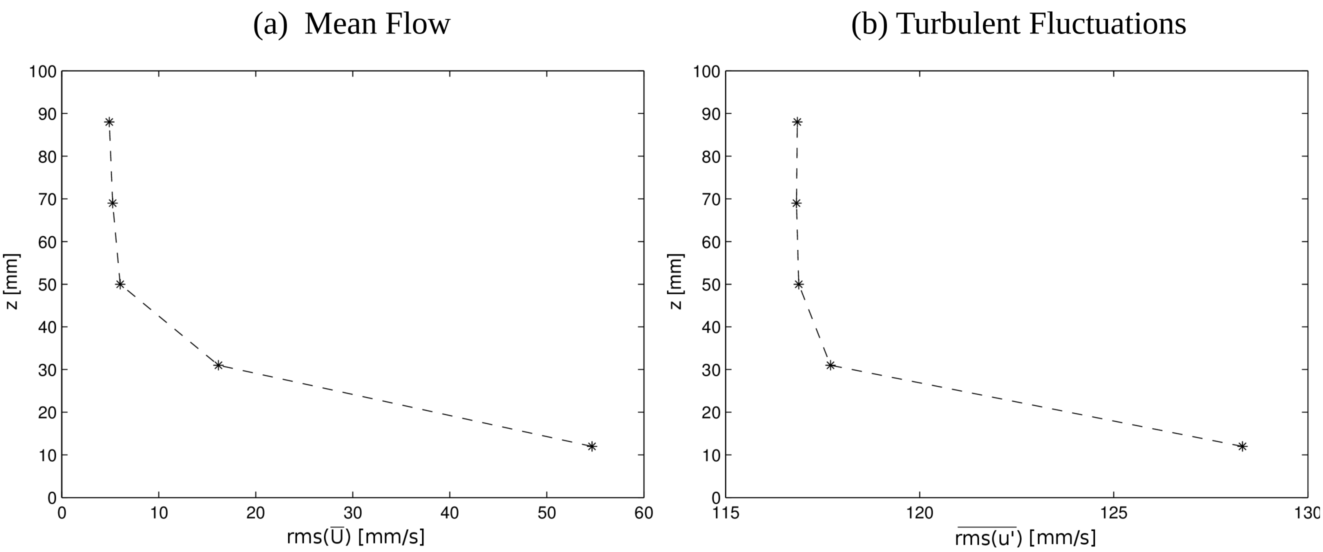

Figure 3: *Statistical properties against height. Mean flow (left), turbulent fluctuations (right).*

Figure 4 gives an alternate representation in Fourier space of the signals displayed earlier. The spectral examination of the velocity signals indicates how energy is distributed amongst the different scales along x. The bottom spectrum shows a peak (marked by the dotted line) corresponding to the scale $l^p = 19$ mm, which happens to be twice the spacing between electrodes, or in other words the size of a pair of counter rotating vortices. The energy therefore seems to be concentrated in this elementary pattern: the pair of counter-rotating vortices act as the energy injection scale in the experiment. Furthermore, the peak visible at the bottom (i.e. close to where the forcing takes place) does not appear elsewhere, meaning that the energy has been redistributed amongst scales with height. It is also worth noting the various breaks in slopes that occur in these spectra, even though the underlying physical mechanisms remain to be determined. Nonetheless, the steep slopes at the right end of the spectra indicate that smaller scales receive very little energy.

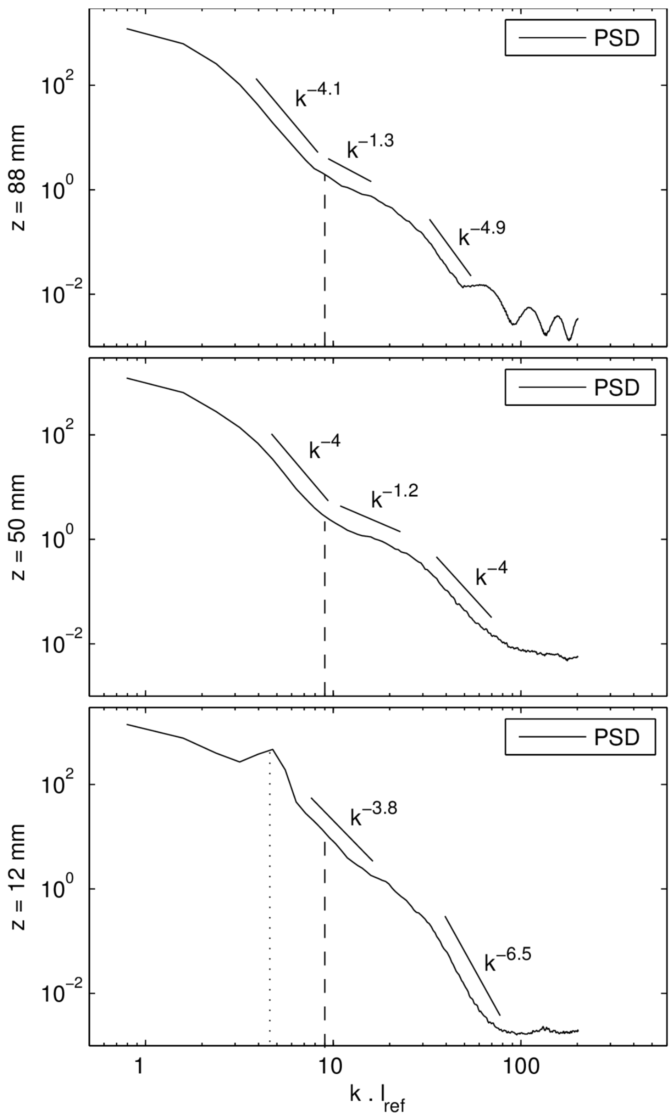

Figure 4: *Power spectral density at three different heights. The x-axis is normalized by the length explored by the ultrasound transducers. In this case, l_{ref} = 90 mm. The spacing between injection electrodes is marked by the dashed lines, the energy containing scale is marked by the dotted line.*

3. Decaying turbulence

Next, we turn our attention to freely decaying turbulence. The results shown in this section come from averaging over 50 different decays.

Figure 5.a displays the decay of the kinetic energy per unit volume contained in the bottom square E(t), which is defined by :

$$E(t)=\sum_i \frac{u_i(t)^2}{2} \quad .$$

In the previous formula, $u_i(t)$ refers to the i^{th} velocity value deduced from the bottom electric potential measurements at the given time t. The signal is normalized by E(0), which refers to the same quantity, but evaluated during the forced state (i.e. right before the decay was triggered). Time is normalized by the Joule time $\tau_J = \rho / \sigma B_0^2$. Figure 5.b shows the time decay of particular Fourier coefficients contained within the investigation area. In other words, we look at the decay of the energy for a given set of structures. Note however that since we are restricted to a 30 mm x 30 mm square sampled at 2.5 mm, we actually have access to a very limited range of scales contained within 5 mm < l < 15 mm. These scales happen to be very close to the injection scale, which limits the extent of our study. Nonetheless, one can clearly identify three distinct regimes on both graphs: region (a) for $0 < t/\tau_J < 1500$, region (b) for $1500 < t/\tau_J < 5000$ and region (c) for $t/\tau_J < 5000$. As the decay goes on, the slopes of figure 5.a become steeper, meaning that energy gets damped more quickly. Looking at figure 5.b, region (a) is a region where energy dissipation very clearly depends on the scale. More specifically, the bigger structures seem to loose their energy faster than the smaller ones. In region (b), one can observe a very distinctive regime change, where the decay rate becomes scale independent. This regime exhibits a steady $t^{-1.5}$ decay law in agreement with figure 5.a. Region (c) can be referred to as the final stage of the decay. In this region the decay appears to become scale specific again, however unlike in the early decay, the structures whose energy is dissipated faster are now the smaller ones.

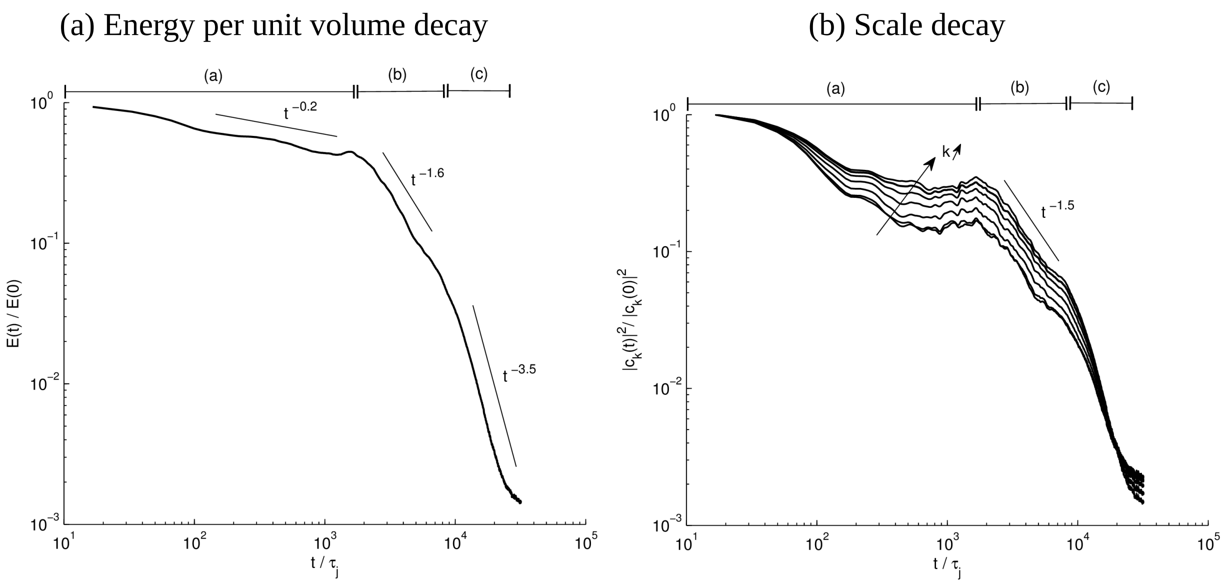

Figure 5: *Decay of the kinetic energy per unit volume inside the middle square of the bottom plate. The time axis is normalized by the Joule time τ_J = 0.47 ms, which is the shortest phenomenon occurring in the experiment. Time decay of Fourier coefficients, normalized by their respective value before the decay is triggered. The scales considered here are contained within the 30 mm x 30 mm central square. The time axis is normalized by the Joule time. k ~ 1/l is the wave number associated to the structure of size l.*

4. Conclusion

We have presented different aspects of wall-bounded low-Rm MHD turbulence under Ha ~ 7300 and Re ~ 30000. In these conditions, we observed a forced mean flow presenting very strong three-dimensionality, characterized by a weak residual flow featuring large structures at the top of the box, despite strong forcing took place at small scales at the bottom. This behavior can be explained by the Lorentz force diffusing vorticity along the magnetic field, damping velocity gradients - thus smaller structures - along the magnetic field. This phenomenon translates into spectral space by various slopes whose physical meaning is still to be tackled. In addition, we obtained unprecedented results regarding the decay of wall-bounded MHD turbulence. Even though they are still very qualitative, we were able to clearly identify different phases where radically different physical phenomena are likely to occur.

The work presented here is still very much in progress, and many issues need to be addressed before we can give a definitive answer to what is happening during the decay. First, more decays must be measured until the results have fully converged. Second, it is necessary to analyze a broader range of structures, as those we were limited to are too close to each other. Last, we need to explore other operating settings, especially higher magnetic fields.

5. References

[1] J. Sommeria and R. Moreau. Journal of Fluid Mechanics, 118:507–518, 1982.
[2] J. Sommeria. Journal of Fluid Mechanics, 189:553–569, 1988.
[3] B. Sreenivasan and T. Alboussière. Journal of Fluid Mechanics, 464:287–309, 2002.
[4] H. K.Moffatt. Journal of Fluid Mechanics, 28(03):571–592, 1967.
[5] O. Zikanov and A. Thess. Journal of Fluid Mechanics, 358:299–333, 1998.
[6] R. Klein and A. Pothérat. Physical review letters, 104(3), 2010.
[7] A. Kljukin and A. Thess. Experiments in Fluids, 25(4):298–304, 1998.
[8] A. Pothérat and R. Klein. http://arxiv.org/pdf/1305.7105v1.pdf.

ON THE FLOW INSTABILITY
IN A HELICAL CHANNEL OF THE INDUCTION PUMP

KAPUSTA[1] A., MIKHAILOVICH[1] B., REIMAL[2] L.
[1]Center for MHD Studies, Department of Mechanical Engineering
Ben-Gurion University of the Negev, P.O.B. 653, Beer-Sheva 8410502, Israel
[2] MAHYD & CY, Ed.Vilde 52-142, Tallinn 13421, Estonia
E-mail: borismic@bgu.ac.il

Abstract: A soft instability of helical flows of various structures arising under the impact of helically traveling magnetic field of the form $B_\rho = B_0 \cos(\omega t - k_\theta \theta)$ is examined. We consider inductionless approximation using the "external" friction model in the helical coordinate system ρ, θ, ζ. Neutral stability curves are calculated in logarithmic Hartmann-Reynolds plane for the pitch angle of helical channel $\alpha = 5^0$.

1. Introduction

The structure of flows arising in helical channels of induction pumps under the action of a rotating magnetic field (RMF) depends both on such characteristics of helical channels as curvature and torsion and on MHD flow parameters. A joint impact of these characteristics determines the channels drag and, to a certain extent, the efficiency of the pump operation.

2. Mathematical model

We examine soft instability of laminar and turbulent flows with respect to the appearance of stationary or non-stationary spatially periodic secondary structures or waves in the induction-free approximation and using the "external" friction model.

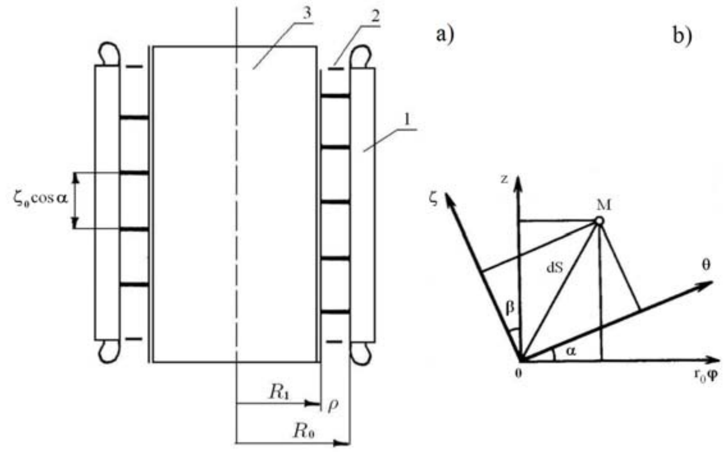

Figure1: Schematic diagram for estimations (a):1- RMF inductor; 2 - helical channel; 3 - ferromagnetic core; (b) – relations between helical and cylindrical coordinates.

MHD processes in helical channels are described by the following dimensionless vector equations:

$$\mathrm{Re}_\omega \left[\frac{\partial \vec{v}}{\partial t} + (\vec{v}\nabla)\vec{v} \right] = -\mathrm{Re}_\omega \nabla P + L\vec{v} - \lambda\vec{v} + \langle \vec{f} \rangle_{em}, \quad (1)$$

$$div\, \vec{v} = 0, \quad (2)$$

and boundary conditions $\vec{v}\big|_r = 0,$ (3)

where $\mathrm{Re}_\omega = \omega(R_0 - R_1)^2 / \nu,\ Ha = B_0(R_0 - R_1)\sqrt{\sigma/\eta},\ L = -rot\,rot,\ \ \vec{e}_i$ are the unit vectors of the helical coordinate system (HCS) ρ_0, θ, ζ (fig. 1) , $<\vec{f}>_{em} = \sum_{i=1}^{3} \vec{e}_i f_i$,

$<f_0> = Ha^2 Sk_{att}\varphi(\rho_0)\cos^2\alpha;\ S = 1 - \dfrac{v_\theta(r_1 + 0.5)\cos^2\alpha}{\rho_0};\ \varphi(\rho_0) = \left(G_1\rho_0^{\frac{\mu-2}{2}} + G_2\rho_0^{-\frac{\mu+2}{2}}\right)^2$;

$\rho_0 = r_1 + \rho;\ \ \mu = \sqrt{1 + 4\cos^4\alpha}; G_1, G_2$ are functions of μ, r_1 [1], k_{att} is an attenuation factor [2], $\lambda = \dfrac{C_\varepsilon(\mathrm{Re}_\omega < V_0 >)^{1-\varepsilon}}{\delta_\zeta}$ is the "external" friction factor [3], $C_\varepsilon = 0.219\,\mathrm{e}^{10.895\varepsilon};\ \ <V_f> = 0.5\omega(R_1 + R_0)$ mean velocity of magnetic field. Factor C_ε and structural parameter ε are determined using *P*-*Q* characteristic of the helical induction pump ACH-3 [2], $\delta_\zeta = \zeta_0 / (R_0 - R_1)$. In case of the laminar flow $\lambda = 0$.

The system (1) - (3) components in HCS have the following form:

$$\mathrm{Re}_\omega\left[\frac{\partial v_\rho}{\partial t} + (v_i\cdot\nabla)v_j - \frac{v_\theta^2 + v_\zeta^2}{\rho_0}\right] = -\mathrm{Re}_\omega\frac{\partial P}{\partial\rho} + (\Delta - \lambda)v_\rho + f_\rho -$$
$$-\frac{2}{\rho_0^2}\left(\frac{\cos^2\alpha}{\delta_\theta}\frac{\partial v_\theta}{\partial\theta} + \frac{\sin^2\alpha}{\delta_\zeta}\frac{\partial v_\zeta}{\partial\zeta}\right),$$
$$\mathrm{Re}_\omega\left[\frac{\partial v_\theta}{\partial t} + (v_i\nabla)v_j + \frac{v_\rho v_\vartheta}{\rho_0}\right] = -\mathrm{Re}_\omega\frac{\cos^2\alpha}{\rho_0\delta_\theta}\frac{\partial P}{\partial\theta} + (\Delta - \lambda)v_\theta + f_\theta + \frac{2\cos^2\alpha}{\delta_\theta\rho_0^2}\frac{\partial v_\rho}{\partial\theta}, \qquad (4)$$
$$\mathrm{Re}_\omega\left[\frac{\partial v_\zeta}{\partial t} + (v_i\nabla)v_j + \frac{v_\rho v_\zeta}{\rho_0}\right] = -\mathrm{Re}_\omega\frac{\sin^2\alpha}{\rho_0\delta_\zeta}\frac{\partial P}{\partial\zeta} + (\Delta - \lambda)v_\zeta + \frac{2\sin^2\alpha}{\rho_0^2\delta_\zeta}\frac{\partial v_\rho}{\partial\zeta} + f_\zeta,$$

where $(v_i\cdot\nabla)v_j = v_\rho\cdot\dfrac{\partial v_j}{\partial\rho} + \dfrac{v_\theta\cos^2\alpha}{\delta_\theta\rho_0}\dfrac{\partial v_j}{\partial\theta} + \dfrac{v_\zeta\sin^2\alpha}{\delta_\zeta\rho_0}\dfrac{\partial v_j}{\partial\zeta}$,

$f_\zeta = -2Ha^2 v_\zeta, < f_\theta > \ = f_0 - 2Ha^2 v_\theta$

$$\Delta v_i = \frac{\partial^2 v_i}{\partial\rho^2} + \frac{2}{\rho_0}\frac{\partial v_i}{\partial\rho} + \frac{\cos^4\alpha}{\delta_\theta^2\rho_0^2}\frac{\partial^2 v_i}{\partial\theta^2} + \frac{\sin^4\alpha}{\delta_\zeta^2\rho_0^2}\frac{\partial^2 v_i}{\partial\zeta^2},\quad i, j = \rho, \theta, \zeta, \qquad (5)$$
$$div\,\vec{v} = \frac{\partial v_\rho}{\partial\rho} + \frac{2}{\rho_0}v_\rho + \frac{\cos^2\alpha}{\delta_\theta\rho_0}\frac{\partial v_\theta}{\partial\theta} + \frac{\sin^2\alpha}{\delta_\zeta\rho_0}\frac{\partial v_\zeta}{\partial\zeta}.$$

3. Problem solution

The velocity of a unidirectional laminar or mean turbulent flow in a helical channel arising under the action of the force f_0 is determined from the solution of the following equation:

$$V_0'' + \frac{2}{\rho_0}V_0' - \lambda V_0 - Ha^2\cos^4\alpha\cdot\varphi(\rho_0)\frac{k_{att}(r_1 + 0.5)}{\rho_0}V_0 = -Ha^2\cos^4\alpha\cdot\varphi(\rho_0)k_{att} \quad (6)$$

with boundary conditions $V_0\big|_{\rho_0 = r_1} = V_0\big|_{\rho_0 = r_1 + 1} = 0.$

Following the Galerkin method, we obtain: $\quad V_0 = \sum_{k=1}^{\infty} H_k\xi(\alpha_k\rho_0), \qquad (7)$

where H_k is determined from the solution of k equations $\left\| H_k O_{kl} = P_l \right\|$,

$P_l = Ha^2 \cos^2 \alpha \cdot k_{att} In_{04l}$, $Q_{kl} = \alpha_k^2 In_{0kl} + \lambda In_{01kl} - 2\alpha_k In_{02kl} + Ha^2 \cos^4 \alpha \cdot k_{att}(r_1 + 0.5) In_{03kl}$,

$$\xi(\alpha_k \rho_0) = \sin \alpha_k \rho_0 + A_k sh \alpha_k \rho_0, \quad A_k = -\sin \alpha_k r_1 / sh \alpha_k r_1,;$$

α_k are the roots of the equation $\sin \alpha_k (r_1 + 1) sh \alpha_k r_1 - \sin \alpha_k r_1 sh \alpha_k (r_1 + 1) = 0.$

We specify small velocity and pressure disturbances in the form of waves travelling along the θ and ζ axes, whose amplitude depends on the coordinate ρ, i.e.

$$\begin{vmatrix} v_\rho \\ v_\theta \\ v_\zeta \\ P \end{vmatrix} = \begin{matrix} \\ V_0 + \\ \\ P_0 + \end{matrix} \begin{vmatrix} u(\rho) \\ v(\rho) \\ w(\rho) \\ q(\rho) \end{vmatrix} \times \exp[\sigma\tau + i(a_\theta \theta + a_\zeta \zeta)], \tag{8}$$

where $\sigma = \sigma_R + i\sigma_I$.

Substituting (8) into (4), (5) and neglecting the squares of minor disturbances, we obtain the following system of equations connecting velocity and pressure disturbances:

$$gu - \frac{2\,\mathrm{Re}_\omega V_0}{\rho_0} v = -\mathrm{Re}_\omega Dq + \Delta u - \frac{2i}{\rho_0^2}(h_\theta v + h_\zeta w), \tag{9}$$

$$gv + \mathrm{Re}_\omega (D_* V_0) u = -\frac{i\,\mathrm{Re}_\omega h_\theta}{\rho_0} q + \Delta v + \frac{2ih_\theta}{\rho_0^2} u, \tag{10}$$

$$(g + Ha^2) w = -\frac{i\,\mathrm{Re}_\omega h_\zeta}{\rho_0} q + \Delta w + \frac{2ih_\zeta}{\rho_0^2} u, \tag{11}$$

$$Du + \frac{2_0}{\rho_0} u + \frac{i}{\rho_0}(h_\theta v + h_\zeta w) = 0, \tag{12}$$

where $g = \mathrm{Re}_\omega \sigma + \lambda + Ha^2$, $g_H = g + Ha^2$, $D + \frac{\partial}{\partial \rho}$, $D_* = \frac{\partial}{\partial \rho} + \frac{1}{\rho_0}$, $\sigma = \sigma_R + i\sigma_I$,

$\Delta = D^2 + \frac{2}{\rho_0} D - \frac{h^2}{\rho_0^2}$, $h^2 = h_\theta^2 + h_\zeta^2$, a_θ, a_ζ are components of the wave vector, $\delta_\theta = \theta_0 / (R_0 - R_1)$, $\delta_\zeta = \zeta_0 / (R_0 - R_1)$, $\theta_0 = \frac{\pi(R_0 + R_1)}{\cos \alpha}$ is the length of the channel turn, ζ_0 is the channel height, $h_\theta = \frac{a_\theta \cos^2 \alpha}{\delta_\theta}$, $h_\zeta = \frac{a_\zeta \sin^2 \alpha}{\delta_\zeta}$.

Expressing *w* through *u* and *v* using (12), determining *q* and *Dq* using (11) and excluding *q* from (9), (10), we obtain:

$$D(A_1 u) - h_\zeta^2(\Delta_1 - g) u + ih_\theta D(A_2 v) - \frac{2\,\mathrm{Re}_\omega h_\zeta^2 V_0}{\rho_0} v = 0, \tag{13}$$

$$\left[\frac{h_\theta^2}{\rho_0}\left(A_1 - 2ih_\zeta^2\right) + \mathrm{Re}_\omega h_\zeta^2 (D_* V_0) \right] u + \left[\frac{ih_\theta^2}{\rho_0} A_2 - h_\zeta^2(\Delta + g) \right] v = 0, \tag{14}$$

where A_1, A_2, Δ_1 are linear differential operators:

$$A_1 = \rho_0^2 D^3 + 6\rho_0 D^2 + (6 - h^2 - g_H \rho_0^2) D - 2(h^2 / \rho_0^2 + g_H \rho_0),$$

$$A_2 = \rho_0 D^2 + 2D - (h^2 / \rho_0 + g_H \rho_0^2), \quad \Delta_1 = D^2 + \frac{4}{\rho_0} D + \frac{4 - h^2}{\rho_0^2}.$$

Further, the problem of the stability of laminar or mean turbulent flow profile is considered within the sub-region $0 \le \rho \le 1$ of the range of values ρ_0. In this case, boundary conditions for the system (13), (14) are

$$u\big|_{\rho=0} = u\big|_{\rho=1} = Du\big|_{\rho=1} = 0, \tag{15}$$

$$v\big|_{\rho=0} = v\big|_{\rho=1} = 0. \tag{16}$$

We seek the solution to Eqs. (13)-(14) by the Galerkin method in the form

$$u = \sum_{k=1}^{\infty} C_k \zeta(\gamma_k \rho), \tag{17}$$

$$v = \sum_{k=1}^{\infty} B_k k\pi\rho, \tag{18}$$

where C_k, B_k are complex coefficients of the expansions (17), (18),

$$\zeta(\gamma_k \rho) = \sin\gamma_k \rho + A_k^* sh\gamma_k \rho, \tag{19}$$

$A_k^* = -\sin\gamma_k / sh\gamma_k$, γ_k are roots of the equation $\sin\gamma_k ch\gamma_k - sh\gamma_k \cos\gamma_k = 0$.

Substituting the series (17), (18) into Eqs. (13), (14) and accomplishing the procedure of Galerkin's method, we obtain a system of $2l$ homogeneous algebraic equations binding the coefficients C_k and B_k. Using the solvability condition for this system, singling out the real and imaginary parts of the obtained expression, using, to the first approximation, the stability change principle $\sigma = 0$ and assuming that $h_\theta = 0, k = l = 1,$ we obtain an equation connecting critical values of MHD parameters Ha, Re_ω and a_ζ:

$$\begin{aligned}&\{\gamma_k^4 In_{1kl} - 8\gamma_k^3 In_{2kl} - \gamma_k^2[(12-h_\zeta^2)In_{3kl} - g_H In_{4kl}] - 4\gamma_k(g_H In_{5kl} + h_\zeta^2 In_{6kl}) - \\ &-2(g_H In_{7kl} - h_\zeta^2 In_{8kl}) + h_\zeta^2[\gamma_k^2 In_{9kl} + 4\gamma_k In_{10kl} + (4-h_\zeta^2)In_{11kl} + g_R In_{12kl}]\}\times \\ &\times(k^2\pi^2 In_{13kl} - 2k\pi In_{14kl} + h_\zeta^2 In_{15kl} + g_R In_{16kl}) - 2\,\mathrm{Re}_\omega^2 h_\zeta^2 In_{17kl} In_{18kl} = 0,\end{aligned} \tag{20}$$

where the integrals In_{kl} are given in the Appendix.

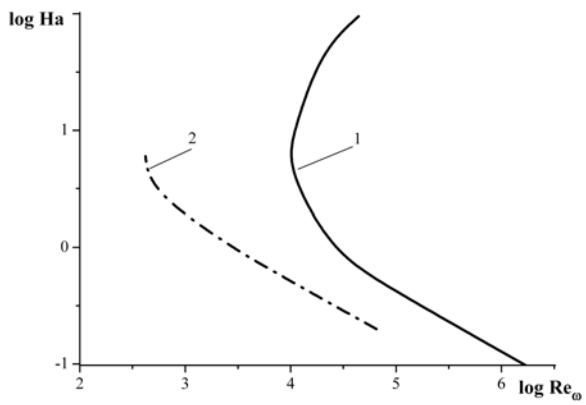

Figure 2: Estimations of neutral stability parameters for MHD flows: 1 – in helical channel, 2 – in cylindrical cavity [4].

Our estimations by (20) show (fig.2) that helical MHD flows under study possess of higher stability level relatively to disturbances of Taylor vortices type in comparison with rotational MHD flows in cylindrical cavities under RMF effect [4].

4. Conclusion

A complete solution of the instability problem of MHD flows in helical channels using the "external" friction model was derived. Neutral stability conditions were analyzed in the first approximation at $\sigma = 0,\ \ k = l = 1$. Obtained estimations were compared with known ones for rotating MHD flows in cylindrical channels under the impact of RMF.

5. References

[1] Kapusta, A.; Mikhailovich, B.; Reimal, L.; Tilman B.: 2D-Theory of turbulent flow of melts in helical channels of MHD-pumps. Magnetohydrodynamics. 47 (4) (2011) 359-367.

[2] Keskula, V.F.; Reima,l L.R.: Peculiarities of electromagnetic calculations of induction helical pump without inner core. Articles Collection of NIPTI, Moscow, Energy. 13 (1971) 108-119.

[3] Golbraikh, E.; Kapusta, A.; Mikhailovich, B.: Rotating Turbulent MHD Flows. I. Semi-empirical model validation. Magnetohydrodynamics. 43 (1) (2007) 35-44.

[4] Kapusta,A., Zibold, A.: Stationary instability of axisymmetric flow of a liquid in a RMF. Magnetohydrodynamics. 13 (3) (1977) 312-319.

Appendix

The following are the integrals used in the problem (*k, l* integral indices are not shown for simplicity):

$$In_0 = \int_{r_1}^{r_1+1} \xi^*(\alpha_k\rho_0)\xi(\alpha_l\rho_0)d\rho,\ \ In_{01} = \int_{r_1}^{r_1+1} \xi(\alpha_k\rho_0)\xi(\alpha_l\rho_0)d\rho,$$

$$In_{02} = \int_{r_1}^{r_1+1} \rho_0^{-1}(\cos\alpha_k\rho_0 + A_k\ ch\alpha_k\rho_0)\zeta(\gamma_l\rho_0)d\rho,\ In_{03} = \int_{r_1}^{r_1+1} \rho_0^{-1}\varphi(\rho_0)\xi(\alpha_k\rho_0)\xi(\alpha_l\rho_0)d\rho,$$

$$In_{04} = \int_{r_1}^{r_1+1} \varphi(\rho_0)\xi(\alpha_l\rho_0)d\rho;$$

$$In_1 = \int_0^1 \rho_0^2\zeta(\gamma_k\rho)\zeta(\gamma_l\rho)d\rho,\qquad In_2 = \int_0^1 \rho_0(\cos\gamma_k\rho - A_k^* ch\,\gamma_k\rho)\zeta(\gamma_l\rho)d\rho,$$

$$In_3 = \int_0^1 (\sin\gamma_k\rho - A_k^* sh\,\gamma_k\rho)\zeta(\gamma_l\rho)d\rho,\qquad In_4 = \int_0^1 \rho_0^2(\sin\gamma_k\rho - A_k^* sh\,\gamma_k\rho)\zeta(\gamma_l\rho)d\rho,$$

$$In_5 = \int_0^1 \rho_0(\cos\gamma_k\rho + A_k^* ch\,\gamma_k\rho)\zeta(\gamma_l\rho)d\rho,\ \ In_6 = \int_0^1 \rho_0^{-1}(\cos\gamma_k\rho + A_k^* ch\,\gamma_k\rho)\zeta(\gamma_l\rho)d\rho,$$

$$In_7 = \int_0^1 (\cos\gamma_k\rho + A_k^* ch\,\gamma_k\rho)\zeta(\gamma_l\rho)d\rho,\qquad In_8 = \int_0^1 \rho_0^{-2}\zeta(\gamma_k\rho)\zeta(\gamma_l\rho)d\rho,\qquad In_9 = In_3,$$

$$In_{10} = In_6,\quad In_{11} = In_8,\quad In_{12} = \int_0^1 \zeta(\gamma_k\rho)\zeta(\gamma_l\rho)d\rho,\qquad In_{13} = \int_0^1 \sin k\pi\rho\sin l\pi\rho d\rho,$$

$$In_{14} = \int_0^1 (\cos\gamma_k\rho + A_k^* ch\,\gamma_k\rho)\sin l\pi\rho d\rho,\quad In_{15} = \int_0^1 \rho_0^{-2}\sin k\pi\rho\sin l\pi\rho d\rho,$$

$$In_{16} = \int_0^1 (\sin\gamma_k\rho - A_k^* sh\,\gamma_k\rho)\sin l\pi\rho d\rho,\quad In_{17} = \int_0^1 \rho_0^{-1}V_0\sin k\pi\rho\zeta(\gamma_l\rho)d\rho,$$

$$In_{18} = \int_0^1 (D_*V_0)\zeta(\gamma_k\rho)\sin l\pi\rho d\rho.$$

EXPERIMENTAL OBSERVATIONS OF THE DYNAMICS OF WAKES OF MAGNETIC OBSTACLES

DOMÍNGUEZ[1] D.R., ROMÁN[1] J.J., BELTRÁN[2] A., CUEVAS[1] S. and RAMOS[1] E.
[1] Renewable Energy Institute, Universidad Nacional Autónoma de México, 62580, Temixco Mor. Mexico,
[2] Materials Research Institute, Universidad Nacional Autónoma de México, 04510, México D.F., Mexico.
E-mail address of corresponding author: erm@ier.unam.mx

Abstract: Experimental recordings of the flow generated by magnetic obstacles have been made using a liquid metal flowing through a localized magnetic field. The relative motion of the fluid and the magnetic field generate electric currents that in turn produce a Lorentz force that opposes the motion of the fluid at the position where the magnetic field is located. This effect is known as a magnetic obstacle. Previous theoretical studies predict that for a given Hartmann number, the flow transits from a steady state to a time-dependent state as the Reynolds number grows. If the Reynolds number is increased further, the flow becomes steady again. Our experimental observations suggest that this prediction is correct.

1. Introduction

A magnetic obstacle is defined as the force that opposes the flow of an electricity conducting fluid due to the presence of a localized magnetic field. The relative motion between the fluid and the applied magnetic field induces electric currents that in turn generate a magnetic field and a Lorentz force that tends to disturb the original flow. This phenomenon was identified in the 70's [1], [2] and has been analyzed more recently in references [3] - [8]. The flow topology and stability has been described in terms of the Reynolds (Re) and Hartmann (Ha) numbers both from the experimental and numerical view points. An important feature of the wakes generated by magnetic obstacles, detected with the ultrasonic velocity profile method, is that the length of the recirculation region behind the magnetic obstacle increases with the Reynolds number to reach a maximum and then decreases [7]. Theoretical studies indicate that the for large enough Hartmann numbers, increasing the Reynolds number results in the formation of a wake behind the magnetic obstacle with characteristics similar to a von Kármán vortex street that occurs behind a rigid obstacle, but in sharp contrast to this last case, a further increase of the Reynolds number leads to a reduction of vortex shedding behind the magnetic obstacle [8]. In the present contribution, we describe the experimental recordings that were made to detect the axial velocity of the flow of a liquid metal in presence of a magnetic obstacle with the objective of determining representative properties of the wake that allow us to infer the dynamics of the whole structure of the wake.

2. Experimental setup

The experimental device used in the observations described in this report is a rectangular loop made of acrylic (Polymethyl methacrylate) walls with a rectangular effective cross section of 1 cm x 8 cm. The lengths of the large and short legs of the duct are 85.8 cm and 40 cm respectively. The loop is built in sections joined with flanges and the whole system is fixed with mounts that separate it from the floor of the table, making it easier to detect possible leaks. Straddling at the central region of one of the long legs a rotatory MHD pump is located. The pump consists of a motor that spins two disks where 24 permanent magnets are mounted radially. This device sets the liquid metal in motion around the loop. A photograph of the liquid metal loop is shown in Figure 1.

Figure 1: The experimental liquid metal loop. The MHD pump is in the far long leg. The disk and the liquid metal rotate in the counterclockwise direction. The magnet is near the middle of the near long leg, 30 cm away from the upstream corner and 4 cm over the lower wall of the duct. The ultrasonic gauge is in the far right of the picture.

The working fluid is a Ga(68%) In(20%)Sn(12%) eutectic mixture which has a melting temperature of 10.5 oC. The magnetic obstacle is created with two 2.54 x 2.54 x 1.25 cm Neodynium magnets placed on the outer side of opposite vertical walls of the central part of one of the long legs. The magnets are located at 30 cm from the upstream corner and 4 cm from the lower horizontal wall of the duct. With this magnet arrangement, the maximum magnetic field that can be obtained at the center of the duct is 0.23 T. The position of the magnets is illustrated in Figure 1. The velocity of the liquid metal is measured with a Signal Processing ultrasonic Doppler velocimeter (UDV) using a probe 0.8 cm in diameter and a wave frequency of 4 Hz. With this equipment it is possible to determine one component of the velocity along the propagation line of acoustic wave emerging from the emitter. The ultrasonic gauge was fixed at the downstream end of the region of analysis to detect the axial velocity along the axial coordinate. An appropriate mount was used to place the gauge different vertical positions. In steady-state flows, axial measurements at different vertical positions allow the reconstruction of the axial velocity distribution in the vertical plane. Given that the geometry of the duct and the physical properties of the fluid are fixed, the range of Reynolds numbers available in the experimental equipment depends on the power delivered by the pump (or equivalently the pressure difference) and the resistance of the duct. The most accurate way to estimate the Reynolds number is through direct calibration. This is done by detecting the distribution of the average axial velocity in absence of magnetic field for a range of MHD pump rotation rates. Once this variable is measured the Reynolds based on the hydraulic diameter of the cross section can be calculated and for our experimental conditions it is $869 < Re < 4960$. The range of Hartmann numbers available depends on the intensity of the permanent magnets used and their relative position with respect to the liquid metal. Increasing the distance of the magnets to the vertical walls reduces the effective magnitude of the magnetic field inside the duct and a range of Hartmann numbers can be obtained. Under the geometry of our experiment, and for the liquid metal used, we have $57 < Ha < 96$.

3. Theoretical remarks

A theoretical model for a quasi two-dimensional MHD flow in presence of a magnetic obstacle reported previously has been used in the interpretation of the experimental recordings; here we describe only the salient features. More details are given in reference [8].

The model consists on the mass and momentum conservation equations including the Lorentz force as a source of momentum of the form

$$\mathbf{S} = \frac{Ha^2}{Re}\mathbf{j} \times \mathbf{B_o}, \tag{1}$$

where **j** is the electric current, and **Bo** is the externally imposed magnetic field which has a localized spatial distribution corresponding to a pair of permanent magnets of small dimensions compared with the test section of the duct. The electric current is calculated using the equation for the induced magnetic field in the direction perpendicular to the vertical planes and Ampere's law. The non-dimensional parameters are the Reynolds and the Hartmann numbers defined by

$$Re = \frac{UL}{\nu} \quad \text{and} \quad Ha = B_o D\sqrt{\frac{\sigma}{\rho\nu}} \tag{2}$$

In the previous equations, *L* is the hydraulic diameter of the duct and *D* is the gap between the vertical walls of the duct. The symbol *U* is the vertical average axial velocity and ν, ρ, and σ stand for the kinematic viscosity, the density and the electric conductivity respectively.
The boundary conditions considered are uniform flow at the channel entrance and outflow at the downstream end of the integration volume. At the lateral walls, periodic boundary conditions are considered.
Theoretical results found in reference [8] indicate that for a given Hartmann number, and small Reynolds numbers, no vortices are shed. For a Reynolds number larger than a threshold which depends on the Hartmann number, vortices are shed but only for a Reynolds number interval, ie., for a given Hartmann number, vortex shedding is suppressed for large enough Reynolds numbers. As is described below, this feature is consistent with the observed in the experimental records reported.

4. Experimental results

In all results reported, the axis of coordinates is defined at the center of the magnet with the axial and transversal coordinates increasing in the downstream and upward directions respectively. The axial velocity u_x in the (x, t) space as obtained with the UDV is plotted according to the color code bar for Ha = 96 and Re =2965 and for the vertical position y = -12.7 mm. The left panel displays the velocity u_x(x; t) for 0< t< 100 s. and the right panel is a zoom to show the detail. The most salient feature of the records is that the axial velocity just upstream of the magnet is reduced and then it grows in the region 0< x < 100 mm. as compared with its upstream value. The inclined, parallel strips recorded in the region x > 200 mm indicate the transit of a periodic perturbation in time for a fixed point in space, or in space for a snapshot.

In order to a make a quantitative analysis, we show in Figure 3 a sample of velocity at the fixed point (x = 250 mm, y = -12.7 mm) as a function of time for Ha = 60 and Re = 869, 2965, 4520 and 4960. The original traces have been smoothed with a moving average filter of 15 points.
The intensity of the flow can be quantified in terms of the parameter $\mathcal{A}$ related to the amplitude of the oscillation as

$$\mathcal{A} = u_x - \langle u_x \rangle \tag{3}$$

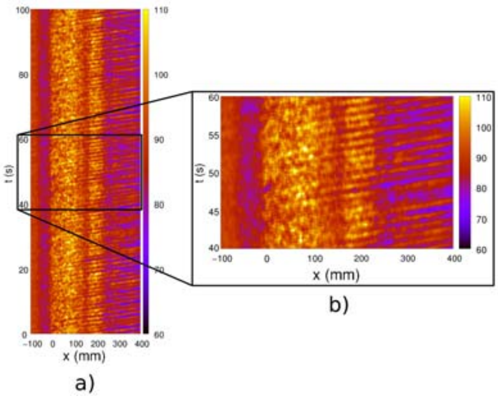

Figure 2: Map of axial velocity u_x in the (x,t) space, y = -12.7 mm. The panel on the right hand side is a zoom. The color indicates the magnitude of the axial velocity. Re = 2965, Ha = 96.

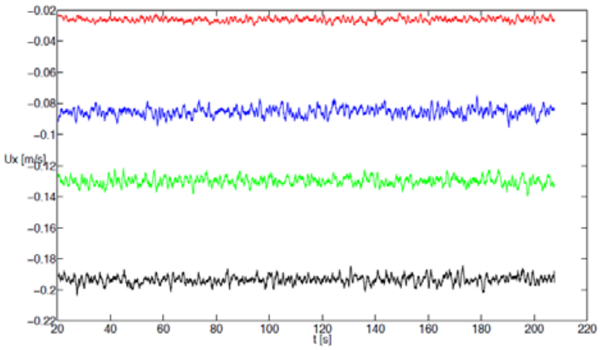

Figure 3: Axial velocity u_x as a function of time at the point x = 250 mm, y = -12.7 mm for Ha = 60. Starting from the top, traces were obtained for Re= 869, 2965, 4520 and 4960.

where $< u_x >$ is the average axial velocity over a time interval I. In Fig. 4 we show an example of the parameter $\mathcal{A}$ as a function of time for three Reynolds numbers, Re=869, 2965 and 4960. Although the dynamic behavior of the traces is complex, inspection indicates that the amplitude of the traces is not a monotonous function of the Reynolds number. In order to make a more quantitative assertion, we also define the parameter $\mathcal{L}2$ as:

$$\mathcal{L}^2 = \frac{1}{I}\int_o^I \mathcal{A}^2 dt \tag{4}$$

Notice that $\mathcal{L}2$ is a function of the Hartmann and Reynolds numbers only and indicates the average of the square of the amplitude of the axial velocity oscillation with respect to its average value in the interval I.

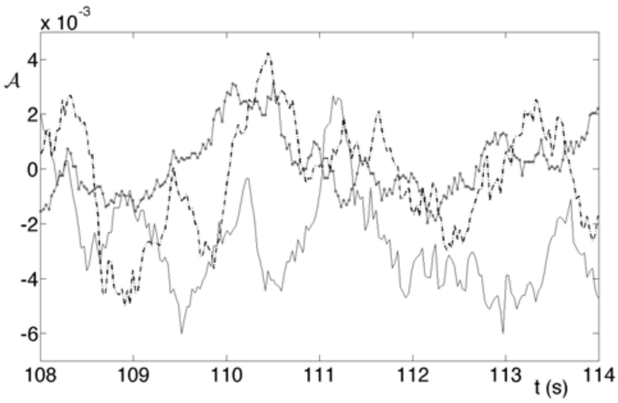

Figure 4: The parameter $\mathcal{A}$ as a function of time for three Reynolds numbers: Re = 869 (line-circles), 2965 (line) and 4960(line-dot).

In figure 5, $\mathcal{L}2$ is shown as a function of Re for Hartmann = 60. As it can be appreciated, for Re < Re_M= 4033 the trace is an increasing function of Reynolds number, but then, it reaches a maximum to decrease for larger Reynolds numbers. This experimental record is consistent with the theoretical result which indicates that after a critical Reynolds number, the vortices in the wake of the magnetic obstacle reduce their intensity as the Reynolds number increases.

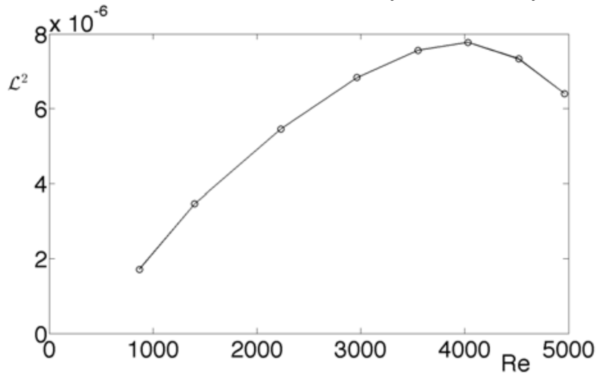

Figure 5: The parameter $\mathcal{L}2$ as a function of the Reynolds number for Ha = 60. The trace of $\mathcal{L}2$ attains a maximum at ReM = 4033.

5. Conclusion

Experimental records of the wake formed by a magnetic obstacle in a liquid metal made with an ultrasonic velocimeter have been presented. The velocity records show the presence of intermittent perturbations that indicate the presence of vortex shedding. In the magnetic obstacle, where a local body force opposes the flow, for flows with a Reynolds number larger that a critical value (Re ~ 4000), we observe that increasing the Reynolds number reduces the oscillatory motion in the wake, reducing in turn the influence of the presence of the obstacle in the downstream flow. This observation is in agreement with a Q2D theory reported previously.

6. References

[1] Gelfgat, Y. M. and Olshanskii, S. V. Velocity structure of flows in non-uniform constant magnetic fields. ii. experimental results. Magnetohydrodynamics **14**, 151–154 (1978)

[2] Gelfgat, Y. M., Peterson, D. E. and Shcherbinin, E. V. Velocity structure of flows in nonuniform constant magnetic fields 1. Numerical calculations. Magnetohydrodynamics **14**, 55–61 (1978)

[3] Cuevas, S.; Smolentsev, S. and Abdou, M. A.: On the flow past a magnetic obstacle. J. Fluid. Mech. **553**, 227-252 (2006)

[4] Cuevas, S.; Smolentsev, S. and Abdou, M. A.: Vorticity generation in the creeping flow past a magnetic obstacle. Phys. Rev E **74** 056301 (2006)

[5] Votyakov E. V., Kolesnikov Y. Andreev O., Zienicke E. and Thess A.: Structure of the wake of a magnetic obstacle. Phys. Rev. Lett. **98**, 144504 (2007)

[6] Votyakov E. V., Zienicke E. and Kolesnikov Y. B. Constrained flow around a magnetic obstacle. J. Fluid Mech. **610**, 131- 156 (2008)

[7] Andreev O., Kolesnikov Y. and Thess A. Application of the ultrasonic velocity profile method to the mapping of liquid metal flows under the influence of a non-uniform magnetic field. Exp. Fluids **49,** 77-83, (2009)

[8] Ramos E., Beltrán A. Cuevas S. and Smolentsev S.: Dynamic properties of a magnetic obstacle. Fundamental and Applied MHD, Book of abstracts, 7th International PAMIR conference, Volume 2, pp 891-895. Presqu'Ile de Giens, France (2008)

NUMERICAL SIMULATION OF THE NON-AXISYMMETRIC MAGNETOROTATIONAL INSTABILITY IN A DOMINANTLY AZIMUTHAL MAGNETIC FIELD

GALINDO, Vladimir, STEFANI, Frank and SEILMAYER, Martin
Helmholtz-Zentrum Dresden-Rossendorf
P.O. Box 510119, D-01314 Dresden, Germany
email: v.galindo@hzdr.de

Abstract: In a Taylor-Couette experiment on the non-axisymmetric version of the magnetorotational instability, performed by Seilmayer et al. [1], a dominantly azimuthal magnetic field was created by a central vertical copper rod connected to the power source by two horizontal rods at a height of approximately 0.8 m below and above the cylindrical volume. The liquid metal flow in the cylindrical gap between the cylinders was simulated using the OpenFoam library including a Poisson equation for the determination of the induced electric potential. The slight deviation from a purely axisymmetric azimuthal imposed magnetic field turns out to have a surprisingly strong effect on both the critical Hartmann number and the flow structure of the instability.

1. Introduction

Rotating flows with a radially increasing angular momentum are hydrodynamically stable but can be destabilized by magnetic fields via the magnetorotational instability (MRI) [2, 3]. If the magnetic field is purely azimuthal, we obtain a non-axisymmetric version of MRI [4, 5], called the azimuthal magnetorotational instability (AMRI), which plays a central role in the concept of the MRI dynamo in accretion disks [6].

In a recent liquid metal experiment [1], AMRI was shown to set in approximately at the predicted value of the magnetic field strength. Yet, there were some significant differences between the observed and numerically predicted rms values of the velocity. In this paper, these discrepancies are explained by the strong sensitivity of the AMRI with respect to slight deviations of the applied magnetic field from axisymmetry. For this purpose, we simulate the experiment using the OpenFoam library including a Poisson equation for the determination of the induced electric potential.

2. Problem formulation

Figure 1 shows a sketch of the considered problem which comprises the main features of the magnetized Taylor-Couette experiment as reported by Seilmayer et al. [1]. A strong axial electric current I_a flows in a vertical copper rod creating in the melt a dominantly azimuthal magnetic field.

Due to the contributions of the connections to the power supply, the applied magnetic field is not anymore purely azimuthal and axisymmetric, but has also radial and axial components (see Fig 2). In the case of an axisymmetric azimuthal magnetic field we would have $\boldsymbol{B} = B\ \boldsymbol{e}_\varphi$ with a maximal value at the inner cylinder $B_{max} = B(R_i) = \mu_0 I_a/(2\pi R_i) \approx 80\ mT$ (for $I_a = 16\ kA$). Whereas the axial component B_z is three orders of magnitude smaller than the azimuthal component B_φ, the B_r component can not be neglected and should be taken into account.

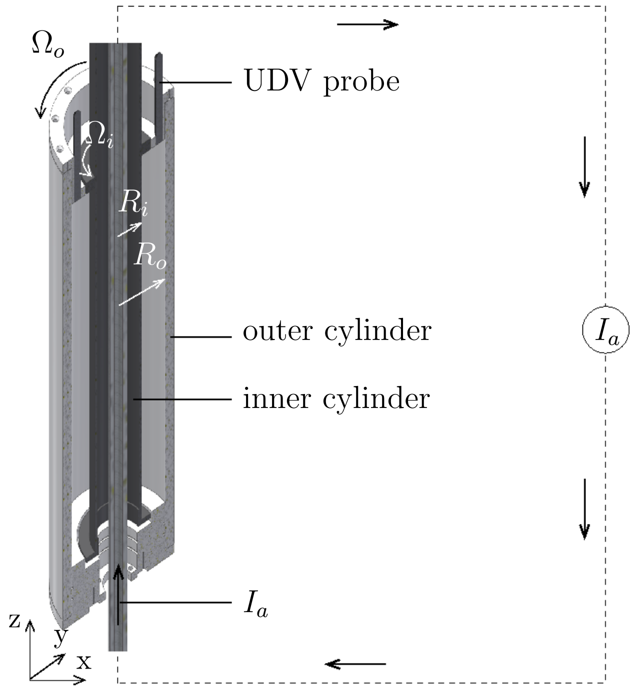

Figure 1: Sketch of the geometry of the experiment.

2.1. Governing equations

The interaction between the induced electric current density $\boldsymbol{j}$ and the magnetic field $\boldsymbol{B}$ yields the induced electromagnetic force density $\boldsymbol{j} \times \boldsymbol{B}$ (Lorentz-force) in the melt. Using the radius of the inner cylinder R_i as the length scale, the azimuthal velocity of the inner cylinder $\Omega_i R_i$ as the velocity scale, defining $B_i = B(R_i)$, taking into account Ohm's law $\boldsymbol{j} = \sigma(-\nabla\Phi + \boldsymbol{u} \times \boldsymbol{B})$ and the electric charge conservation $\nabla \cdot \boldsymbol{j} = 0$, we obtain the dimensionless equation for the momentum conservation

$$\dot{\boldsymbol{u}} + (\boldsymbol{u} \cdot \nabla)\boldsymbol{u} = -\nabla p + \frac{1}{Re}\Delta\boldsymbol{u} + \frac{Ha^2}{Re}\big(-\nabla\Phi + \boldsymbol{u} \times \boldsymbol{B}\big) \times \boldsymbol{B}\,. \tag{1}$$

Here we use the definitions $Re = \Omega_i R_i^2/\nu$ and $Ha = \sqrt{\dfrac{\sigma}{\rho\,\nu}} B_i R_i$ for the Reynolds and Hartmann numbers, respectively. The electric potential Φ can be determined by the Poisson equation:

$$\Delta\Phi = \nabla \cdot (\boldsymbol{u} \times \boldsymbol{B})\,. \tag{2}$$

We solve equations (1) and (2) simultaneously in the low induction approximation, i.e. the magnetic induction B is considered to be independent of the flow velocity and is computed only once using the Biot-Savart law. For more details about the numerical method see [7].

We use no-slip boundary conditions for the velocity at the rigid walls, and slip boundary conditions at the narrow open slits between the outer and inner end-caps. At the external wall, i.e. the outer copper cylinder, we chose for the electric potential $\Phi = 0$, and for the rest of the boundaries we apply insulating boundary conditions ($j_n = 0$).

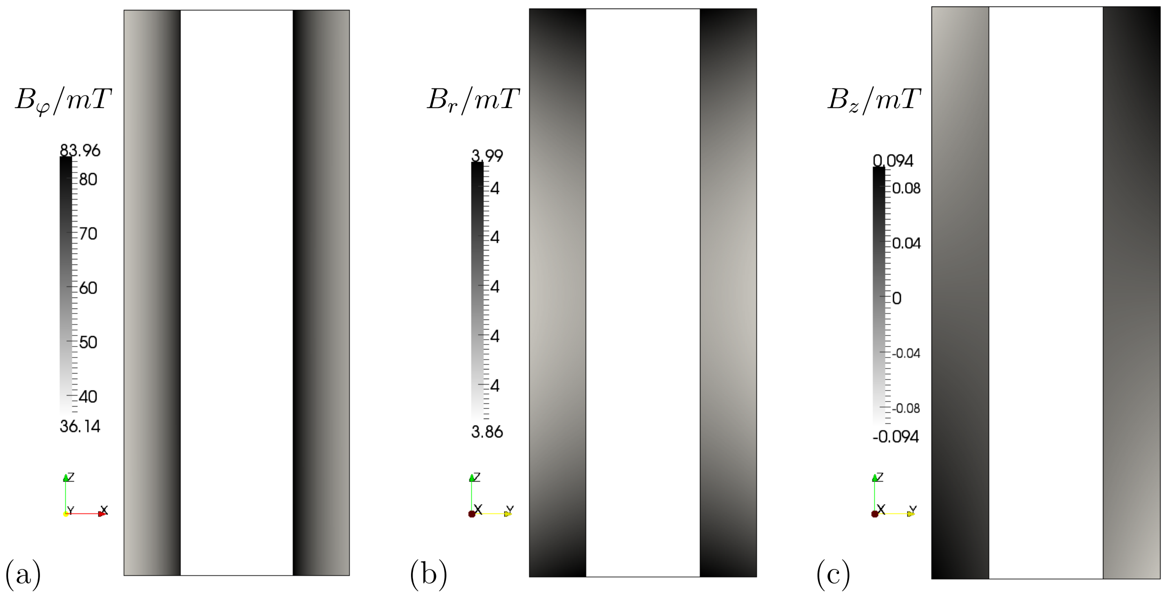

Figure 2: Magnetic field components B_φ (a) in the "xz"-plane parallel to the current loop, and B_r (b) and B_z (c) in the "yz" plane.

3. Results

Figure 3 shows the numerically obtained drift frequency of the AMRI mode with $m = 1$ for the particular case $Re = 1480$ and $\mu = \Omega_o/\Omega_i = 0.26$, in comparison with the 1-d linear stability analysis for an infinitely long cylinder [5] and with the experimental results from [1].

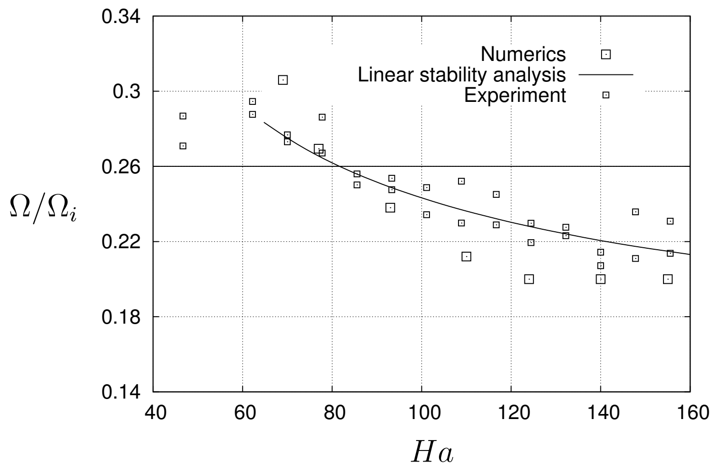

Figure 3: Drift frequency of the azimuthal mode $m = 1$ for $Re = 1480$ and $\mu = \Omega_o/\Omega_i = 0.26$.

Figure 4 shows the computed velocity profiles $u_z(r = 0.07\ m, z)$ of the azimuthal mode $m = 1$ as a function of time for different values of the rotation ratio $\mu = \Omega_o/\Omega_i$ in the hypothetical case of a purely axisymmetric azimuthal magnetic field. Evidently, the AMRI disappears with increasing μ.

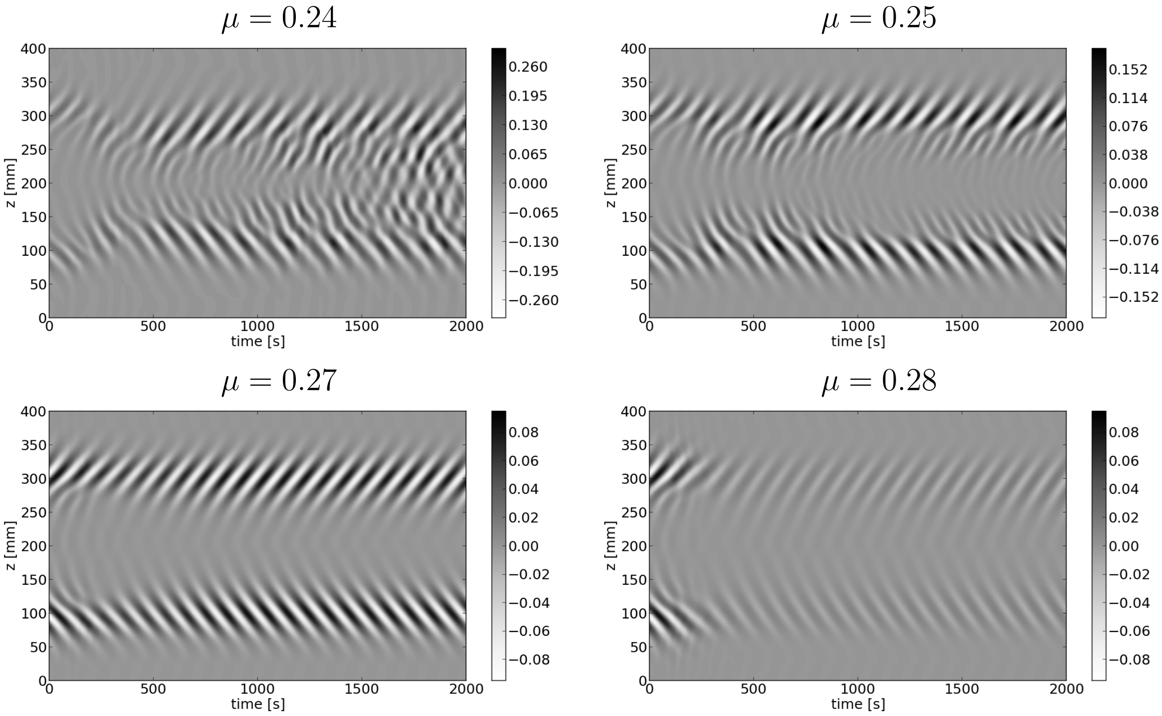

Figure 4: Velocity profiles $u_z(r = 0.07\ m, z)$ of the azimuthal mode $m = 1$ over time for different values of the rotation ratio $\mu = \Omega_o/\Omega_i$ for the case of an axisymmetric imposed azimuthal magnetic field.

Figure 5 shows the isosurface of the axial velocity component u_z for the case of axisymmetric (left) and non-axisymmetric applied magnetic field (right). For axisymmetry, the resulting pattern represents a spiral, rotating slightly slower than the outer cylinder. This spiral is concentrated approximately in the middle of the upper and lower halves of the cylinder, where we observe a preference for either the upward moving or the downward moving spiral. Since such a symmetry breaking would not appear in an infinite length system, it must be attributed to the (minor) flow modifications due to the end walls. The corresponding simulation for the case that the deviation of the applied magnetic field from axisymmetry is correctly taken into account is shown on the r.h.s. of Figure 5. The effect is remarkable: the formerly clearly separated spiral structures now also fill the middle part of the cylinder and penetrate into the other halves. It is interesting to note that a similar picture of interpenetrating spirals had been observed in simulations of a corotating spiral Poiseuille flow [8].

4. Conclusions

We have shown that a careful 3-d simulation is needed to understand the experimental results of a recent experiment on AMRI. The observed, and numerically confirmed, strong sensitivity of AMRI with respect to a slight symmetry breaking deserves further attention. Present work is devoted to the question whether the AMRI shifts also to higher values of the rotation ratio of outer to inner cylinder when the symmetry breaking of the applied field is taken into account. It would be of significant astrophysical importance if slight modifications of an azimuthal field would allow the inductionless AMRI to apply also to rotation profiles as shallow as the Keplerian one.

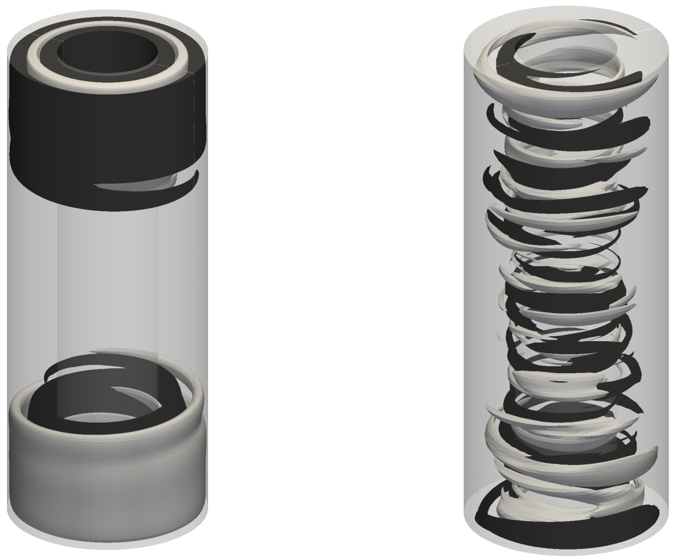

Figure 5: Isosurface of the axial velocity component u_z for the cases axisymmetric (left) and non-axisymmetric (right) applied magnetic field ($Ha = 124$) showing different flow structures.

5. Acknowledgment

We acknowledge support from Deutsche Forschungsgemeinschaft under Grant No. STE 991/1-2, and from the Helmholtz Alliance LIMTECH.

References

[1] Seilmayer, M. et al.: Phys. Rev. Lett., submitted (2013); arXiv:1311.7223

[2] Velikhov, E. P.: Sov. Phys. JETP 36 (1959) 995

[3] Balbus, S. A.; Hawley, J.F.: Astrophys. J. 376 (1991) 214

[4] Hollerbach, R. et al.: Phys. Rev. Lett. 104 (2010) 044502

[5] Rüdiger, G. et al.: Mon. Not. R. Astr. Soc. 438 (2014) 271

[6] Herault, J. et al.: Phys. Rev. E 84 (2011) 036321

[7] Weber, N. et al.: New J. Phys. 15 043034 (2013) 043034

[8] Avila, M. et al.: Phys. Fluids 18 043034 (2006) 064101

MAGNETIC FIELD EFFECT ON THE ONSET OF HELICOIDAL INSTABILITY IN UP AND DOWN CONICAL FLOW SYSTEM

YAHI[1,2] F., BOUABDALLAH[2] A., HAMNOUNE[2] Y., LECHEHEB[2] S., MOKHTARI[2,3] F.

[1]UniversityM'Hamed Bougara –Boumerdes-Algeria
[2]Thermodynamics and Energetic Systems Laboratory, Faculty of Physics University of Science and TechnologyHouariBoumediene, Algiers, Algeria
[3]University Mouloud Mammeri de Tizi-Ouzou, Algeria
E-mail: yahi.fatma@gmail.com, abouab2002@yahoo.fr

Abstract: This work is concerned with the axial magnetic field effect on the onset of the helicoidal wave (spiral mode) in a rotating conical system flow defined by two truncated concentric conical cylinders, the inner cone is rotating and the external one is fixed. Two configurations are considered, down flow system and up flow system (figure.1.a and .1.b). Therefore, we introduce a new coordinates system to analyze the perturbed velocity field in each configurations. Firstly, we determine the mean velocity distribution corresponding to the steady laminar regime. Secondly, assuming the linear theory, we establish the equations system of stability with the associated boundary conditions. By means of the Galerkin method, we get the dispersion relation leading to determine the variation of Taylor number versus wavenumber. Then we interpret the stability diagram according to the onset of spiral mode in hydromagnetic stability in both cases (up and down conical flow system) compared with those obtained in the classical Taylor-Couette flow system (cylindrical case).

Introduction

The hydrodynamics of rotating systems aims to study the mechanisms and properties prediction related to natural phenomena. Mainly in meteorology for understanding atmospheric phenomena and its application to weather prediction. In astrophysics, to investigate the atmospheric dynamics of the planets and to analyze the rotating stars heart as sun which is subjected to both hydrodynamic and hydromagnetic effects which is studied by Chandrasekhar problem [1].

As well as in industrial processes including liquid metal, this flow system is also of great importance, not only in the design of rotating machinery such as multiple concentric drives, turbine rotor, but also for the application to chemical equipment such as compact rotating heat exchangers and mixers. However, in this flow system the hydrodynamic equations associated to the electromagnetism equations presents a specific behavior that is difficult to predict theoretically and numerically.

To our best knowledge there has been no attempt on the theoretical and experimental approach to the effect of magnetic field on the nature and structure of the laminar-turbulent transition regime in conical Taylor-Couette flow system. However, in the cylindrical configuration it is well know that the magnetic field stabilized the stationary axial wave (Taylor vortex) by delaying it onset at the critical Taylor number Ta = Tc_1.

In this context, we propose an analytical approach to predict the helicoidal instability or spiral mode in conical Taylor-Couette flow system. We investigated the magnetohydrodynamic stability which is considered for the evaluation of the influence of an axial magnetic field, it is supposed to stabilize and delaying the onset of spiral mode as predicted by S.Chandrasekhar in the case of Taylor-Couette flow system.

1. Problem formulation

We consider a flow between two coaxial cones so as to the inner cone ($r = R_{1max}$) is rotating with angular velocity Ω_1 and the outer cone ($r = R_{2max}$) is maintained at rest ($\Omega_2 = 0$). The cones have the same apex angle $\varphi = 12°$.

1.1. Coordinates system. The coordinate system used in the study of the flow confined between two coaxial cylinders or two spheres does not apply here because the cone radius varies with the height which is related to the fluid confinement (Fig.1). Furthermore, the boundary conditions associated with the cone system is not constant along the generatrix. For this purpose the chosen orthogonal curvilinear coordinates system consists of three axes z, x and θ such as z is supported by the generatrix of the inner cone. Thus, x is the coordinate axis perpendicular to the surface (S) and θ is the third coordinate perpendicular to z and x which corresponds to the azimuthal coordinate [3, 4]. Therefore, the new coordinates are $X = (x\cos\varphi + z\sin\varphi)\cos\theta, \quad Y = (x\cos\varphi + z\sin\varphi)\sin\theta$ *and* $Z = z\cos\varphi$

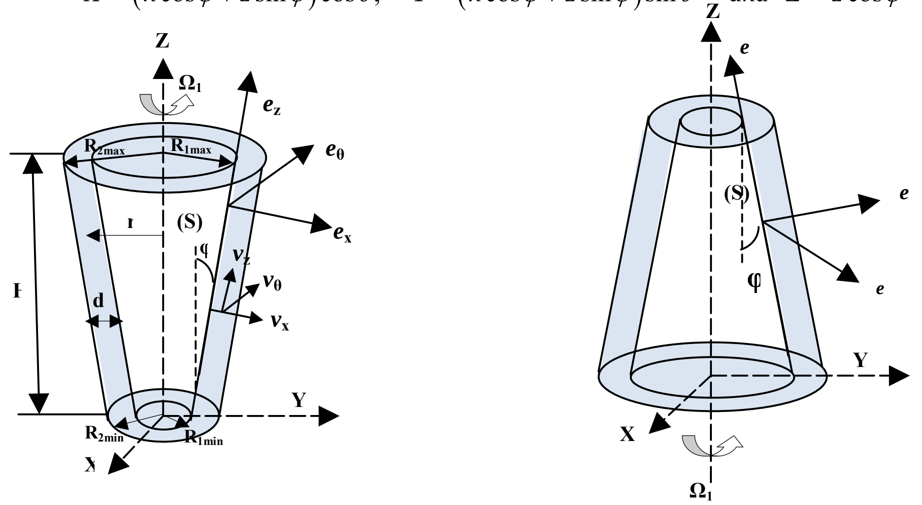

Figure 1: a**:** Up flow system configuration, b: down flow system configuration.

1.2. Governing equations. In order to predict the onset of the spiral mode of a fluid flow characterized by a density ρ, a kinematic viscosity ν, a magnetic permeability μ and an electrical conductivity σ, we consider the Navier Stokes and Maxwell equations as follows

$$\begin{cases} \dfrac{\partial V}{\partial t} + V.\nabla V = -\dfrac{1}{\rho}\nabla p + \nu\Delta V + \dfrac{1}{\rho} J\times B \qquad with \quad J = \sigma(E + V\times B) & (1) \\ \nabla\cdot V = 0 & (2) \\ \dfrac{\partial B}{\partial t} = \nabla\times(V\times B) + \dfrac{1}{\mu\sigma}\Delta B & (3) \\ \nabla\cdot B = 0 & (4) \end{cases}$$

In view to simplify the system of equations (1-4) we suppose the following assumptions as the physical properties (ρ, ν, μ and σ) of the fluid are constants, the problem is axisymmetric $\partial/\partial\theta = 0$, the magnetic field is steady in the axial direction $B = B_0 e_z$ and we assume insulating walls.

Boundary conditions: The boundary conditions associated to the problem are given as

$x = 0: \quad V_x = V_z = 0, \quad V_\theta = \Omega z\sin\phi, \; B_x = B_\theta = 0 \quad \text{and} \quad B_z = B_0$

$x = d: \quad V_x = V_z = V_\theta = 0$

1. 3 Flow control parameters. For simplicity, the governing equations are writing in dimensionless form using the following reduced variables and functions given by:

$$t^* = \frac{\upsilon}{d^2}t, \eta = x/d, \zeta = z/d, r^* = r/d = \zeta\sin\phi + \eta\cos\phi, V_x^* = V_x / V_\theta^0, V_\theta^* = V_\theta / V_\theta^0, V_z^* = V_z / V_\theta^0 \text{ and } p^* = p/(\rho V_\theta^{0\,2})$$

The flow is characterised by several control parameters, the annular gap **δ = d/R_{1max} = 0.12,** the Reynolds number $\mathbf{Re = R_{1max}\Omega d/\nu}$ which is the ratio between the viscose force and inertial forces, the Taylor number $\mathbf{Ta = (R_{1max}\Omega d/\nu)\delta^{1/2}}$ the magnetic Reynolds number $R_m = 4\pi\mu\sigma d V_\theta^0$ It shows the relationship between the terms of convection and diffusion in a magnetic fluid and the Hartmann number $\mathbf{Ha = R_m B_0 / V_\theta^0 \sqrt{1/2\pi\rho\mu}}$ which is the ratio of the Lorentz force and viscous forces.

2. Solving problem.

2.1. Mean hydromagnetic field. By expending the equations system (5-8), we notice that the previous system is independent of the imposed magnetic field. For this, we note that the axial magnetic field doesn't affect the mean velocity component in both configurations up and dawn. The same result is obtained by Chandrasekhar in the classical Taylor-Couette flow [1].

22. Perturbed hydrodynamic field. In order to solving the previous equations system (1-4), by means of the Galerkin method which led to establish an eigenvalues problem. For that, we propose the solutions that showing the axial periodicity depending on the ζ component and satisfying the spiral wave nature given by

$$v_x^* = v_x^*(\eta)e^{j(\lambda\zeta-\beta\tau)} \qquad v_z^* = v_z^*(\eta)e^{j(\lambda\zeta-\beta\tau)} \qquad v_\theta^* = v_\theta^*(\eta)e^{j(\lambda\zeta-\beta\tau)} \qquad p^* = p^*(\eta)e^{j(\lambda\zeta-\beta\tau)}$$

$$b_x^* = b_x^*(\eta)e^{j(\lambda\zeta-\beta\tau)} \qquad b_z^* = b_z^*(\eta)e^{j(\lambda\zeta-\beta\tau)} \qquad b_\theta^* = b_\theta^*(\eta)e^{j(\lambda\zeta-\beta\tau)}$$

With injecting those solutions in the previous system and we used the operator D defined by $D = d/d\eta$ in order to simplify the partial differential equations where we must eliminate the pressure term in order to obtaining the stability equations versus the magnetic field component b_x^* and b_θ^* .

$$L_1 b_x^*(\eta) + L_2 b_\theta^*(\eta) = 0 \qquad \text{(I)}$$

$$L_1' b_x^*(\eta) + L_2' b_\theta^*(\eta) = 0 \qquad \text{(II)}$$

2.3. Implementation of the Galerkin method. One must choose a basic approximation of the solution as follows

- Radial component: $b_x^* = \sum_{n=1}^{N} \alpha_n b_{xn}^*$ with $b_{xn}^* = \eta^2 (1-\eta)^2 \eta^{n-1}$
- Tangential component: $b_\theta^* = \sum_{n=1}^{N} \beta_n b_{\theta n}^*$ with $b_{\theta n}^* = \eta (1-\eta) \eta^{n-1}$

The magnetic field must satisfy the boundary conditions of problem. This will then imposes

$$b_{xn}^* = b_{\theta n}^* = Db_{xn}^* = 0 \quad at \quad \eta = 0 \;\; and \;\; \eta = 1$$

By injecting expressions in equation (I) and (II), we establish the evaluation of the error associated with two velocity components as Follows

$$L_1 \sum_{n=1}^{N} \alpha_n b_{xn}^* + L_2 b_{\theta n}^* = \varepsilon_{n\alpha}^{(1)} \;,\quad L_1 b_{xn}^* + L_2 \sum_{n=1}^{N} \beta_n b_{\theta n}^* = \varepsilon_{n\beta}^{(1)} \qquad (I')$$

The total error committed in the equation (19) is the sum of previous errors

$$\varepsilon_n^{(1)} = \varepsilon_{n\alpha}^{(1)} + \varepsilon_{n\beta}^{(1)} \quad , \qquad \varepsilon_n^{(1)} = L_1 \sum_{n=1}^{N} \alpha_n b_{xn}^* + L_2 \sum_{n=1}^{N} \beta_n b_{\theta n}^*$$

It is now optimized values to minimize errors in each of the previous system of equations. To do this, it is necessary to make a point based on the property which follows from the properties related to the integral inner product, namely:

$$\langle f \,|\, g \rangle = 0 \quad if \quad f = 0, \qquad \int_0^1 f.g\,dx = 0 \quad if \quad f = 0 \quad x \in [\;0,\;1\;]$$

The application of this property to the result of the error $f = \varepsilon_n^{(1)}$ of order n committed in the first equation gives the following relation

$$\left\langle \varepsilon_n^{(1)} \,\middle|\, b_{xm}^* \right\rangle = \int_0^1 \varepsilon_n^{(1)} b_{xm}^* d\eta = 0$$

This is reflected by the fact that the corresponding error $\varepsilon_n^{(1)}$ becomes perpendicular to the base of decomposition chosen b_{xm}^* . Under these conditions, we $\int_0^1 \left(\int_0^{2\pi/\lambda} \sum_{n=1}^{N} \left(L_1 \alpha_n b_{xn}^* + L_2 \beta_n b_{\theta n}^* \right) d\zeta \right) b_{xm}^* d\eta$

$$a_{nm}=\int_0^1\left(\int_0^{2\pi/\lambda}L_1 b^*_{xn}d\zeta\right)b^*_{xm}d\eta,\ b_{nm}=\int_0^1\left(\int_0^{2\pi/\lambda}L_2 b^*_{\theta n}d\zeta\right)b^*_{xm}d\eta,\ c_{11}=\int_0^1\left(\int_0^{2\pi/\lambda}L'_1 b^*_{xn}d\zeta\right)b^*_{\theta m}d\eta,\ d_{11}=\int_0^1\left(\int_0^{2\pi/\lambda}L'_2 b^*_{\theta n}d\zeta\right)b^*_{\theta m}d\eta$$

A necessary condition for the existence of a solution (nontrivial solution) is to impose that the determinant of the Cramer previous system is zero. This condition leads us to solve the associated eigenvalue problem. In other words, it is set according to λ*, σ, α, ω, Ha and R_m on physical point of view this corresponds to a dispersion relation.

Is performed solving the eigenvalue problem by performing a first order approximation by setting n = m = 1. Under these conditions, the Galerkin matrix G of order 2 has the form:
To the solution is not trivial is imposed: det G = 0 is: $a_{11}d_{11}-c_{11}b_{11}=0$

3. Results and discussion

3.1. Theoretical results. By imposing a null determinant associated with the eigenvalues problem, it is established a relationship which leads to the following solutions. The Taylor number evolution according to the wave number λ* and the magnetic Reynolds number Rm = 10^{-3} follows a parabolic behavior law characterized by a maximum in the set (Ta=24.5, λ* = 0.01) in the cas of up conical system but in the down configuration Taylor number increases and reaches a maximum value (35000-100000) . The magnetic Reynolds number Rm = 10^{-3} corresponding to the industrial applications such as the MHD generator-gaz and the diffuse discharge.
By varying the Hartmann number Ha and keeping the magnetic Reynolds number constant, we notice that the critical Taylor number decreases when the magnetic Reynolds number increases about 10 %. The previous curves indicate us that the variation of the Hartmann number produces any visible change on this type of flow in the both cases of Rm = 10^{-3} and Rm = 10^{-2}.

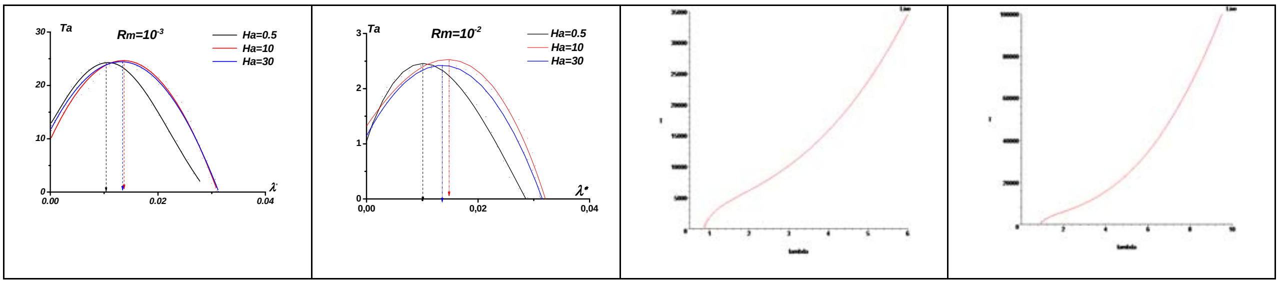

Figure 2: Taylor number evolution versus the wave number λ*.

From Rm = 10, we observe a change of the previous behavior laws which is characterized by a maximum for (Ta=35, λ* = 0.4 and Ta=3.06, λ* = 0.4) the Hartman number has an important effect in this case for the Down configuration.

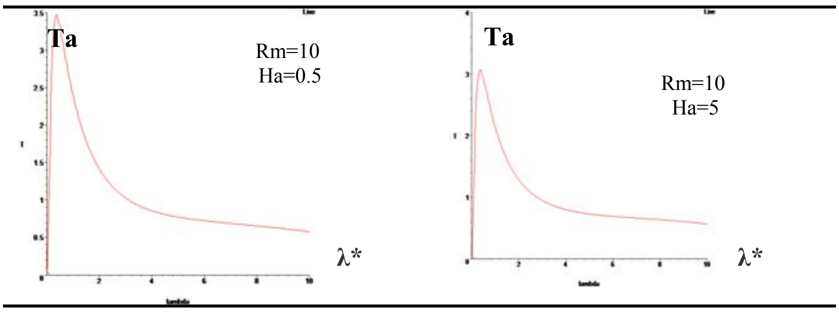

Figure3: Taylor number evolution versus the wave number λ* in the case of Rm = 10.

In the case of the controlled thermonuclear reactions (Rm=100), the variation of the Taylor number versus the wave number evolves according to two different laws. In the range 0 < λ^*<2, the law is parabolic characterized by a maximum at λ^*m = 0.99, Ta = Tm =14.9. For 2 < λ^* <4 the behavior law crosses an inflection point of coordinate λ^*_c = 2.7, Ta = Tc1 = 38.1 whose position is invariant in the interval $0.5 \leq Ha \leq 30$, followed by a maximum $\lambda^*_M = 3.18$, $Ta = T_M = 50.4$ for the Hartmann number $Ha = 0.5$ and $Ha = 10$.

In the case $Ha = 5$, it is observed a significant change of the behavior law except in $0 < \lambda^* < 2$. Beyond $\lambda^* = 2$, the behavior law, the inflection point position and the maximum point remain invariables for any Hartmann number.

The analysis of these results led us to note that the magnetic field advances the onset of the spiral mode (helicoidal wave).

For higher Reynolds magnetic number $Rm = 10^3$ it is noticed that the Taylor number evolution according to the wave number λ^* changes its behavior in the range $2 < \lambda^* < 4$.

By varying the Hartmann number between $Ha = 0.5$ and 30, it is noted that the critical Taylor number conversely increases with the wavelength λ^*_c.

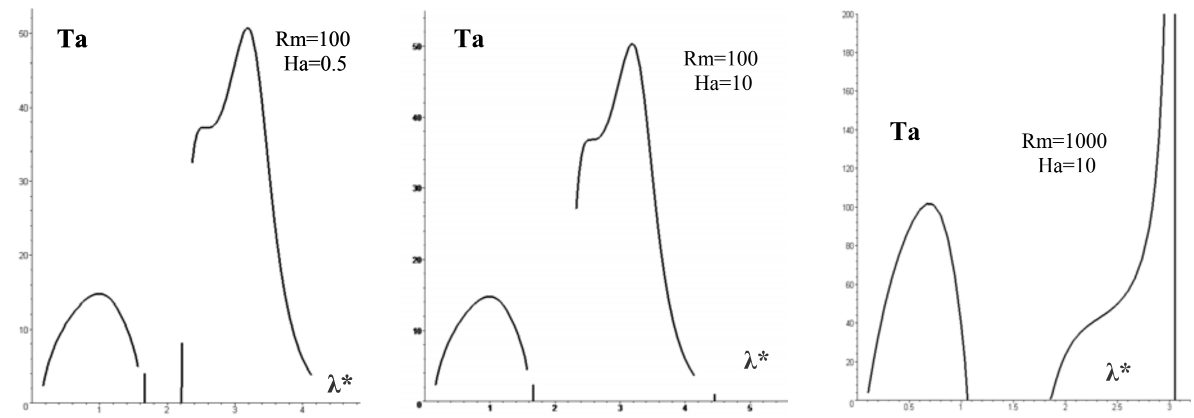

Figure 4: Evolution of Taylor number versus the wave number λ^* in the case of $Rm=10^2$, $Rm=10^3$ in the Up conical flow system.

Conclusion

Following a new coordinates system it was possible to solve the equations of motion in the approximation of the small annular gap configuration in the rotating conical flow system. It was found that the imposed magnetic field does not affect the mean hydrodynamic field. Therefore, there is a change in the behavior laws by varying the magnetic Reynolds number and is placed in different areas such as gas-generator-MHD, controlled thermonuclear reactions, plasmas and astrophysics. The study of the stability problem of the effective magnetic field shows the existence of a delay in the onset of spiral mode which becomes more important when the Hartman number increases. Conversely, the spiral mode wavenumber decreases when the Hartman number increases this is consistent with the result of Chandrasekhar established in classical Taylor-Couette flow system.

References

[1] Chandrasekhar, S. :Hydrodynamic and Hydromagnetic Stability, Oxford University Press, London, 1961.
[2] Wimmer, M.: Experimental investigation of Taylor vortex between conical cylinders. JFM 292.205-227 (1995).
[3] Noui-Mehidi, M.N., Bouabdallah, A.: A laminar-turbulent transition in the flow between rotating coaxial cones (1993).
[4] Noui-Mehidi, M.N., Wimmer, M.: Free surface effects on the flow between conical cylinders. Acta Mechanica 135, 13-25 (1999).
[5] Boubdallah, A.: Instabilités et Turbulence dans l'écoulement de Taylor-Couette. Thèse de Doctorat ès Sciences, Nancy, (1980).

EXPERIMENTAL INVESTIGATION OF INERTIAL WAVES INSIDE A CYLINDRICAL LIQUID METAL COLUMN

VOGT Tobias, RÄBIGER Dirk and ECKERT Sven
Helmholtz-Zentrum Dresden-Rossendorf, PO Box 510119, 01314 Dresden, Germany
E-Mail address of the corresponding author: t.vogt@hzdr.de

Abstract: The dynamics of free inertial waves inside a cylindrical volume was investigated experimentally in this study. The liquid metal GaInSn was chosen as fluid in order to enable a contactless stimulation of the flow inside the cylinder by means of a rotating magnetic field which generates a supercritical rotating motion of the liquid. The experiment demonstrates that inertial waves may be excited spontaneously by turbulent structures in the rotating flow. The ultrasound Doppler velocimetry was used to record the flow structure and to identify the inertial waves occurring in the setup.

1. Introduction

Inertial waves appear to be a ubiquitous feature in rotating fluids. Consequently, this type of waves can be found almost everywhere in nature as well as in technical facilities where a fluid is in rotating motion. In nature, very large-scale inertial waves occur due to earth's rotation for example in the atmosphere [1] in oceans [2] and also deep inside the liquid earth's core [3]. Beside this, inertial waves can also be detected in a variety of technical applications. In all cases, the source for an inertial wave is a disorder in the centrifugal force balance of the rotating fluid. Such an imbalance leads inevitably to a radial motion of fluid and thus to a Coriolis force which acts in azimuthal direction on radially shifted fluid. Depending on the radial distribution of the angular momentum of the basic rotating flow, the radial motion of fluid can lead to two scenarios. If viscous damping is neglected, the border between the two possible scenarios is given by the Rayleigh (1917) stability criterion.

$$\frac{\partial}{\partial_r}\left(u_\varphi * r\right) \geq 0$$

If the azimuthal velocity decreases faster than this limit, the centrifugal force and the radial pressure gradient are out of balance and even small disturbances of the flow field will lead to turbulence. Otherwise, the flow is stable, but can oscillate via inertial waves when disturbed appropriately.

The aim of the present experimental work is to investigate the occurrence and properties of inertial waves in a magnetically driven swirling liquid metal flow. Flow measurements inside the closed cylindrical liquid metal column were carried out by means of the ultrasound Doppler technique.

2. Experimental Description

The flow measurements were conducted in the eutectic alloy $Ga^{68}In^{20}Sn^{12}$, which was filled into closed cylindrical vessels made of Perspex. The fluid vessels were placed concentrically inside the bore hole (diameter 350 mm, height 400 mm) of the MULTIpurpose MAGnetic field system (MULTIMAG) at HZDR. MULTIMAG is a compact magnetic coil system for the generation of rotating (RMF), vertically travelling (TMF) and pulsating magnetic fields and superposition thereof with a high accuracy [4]. Measurements of the fluid velocities were obtained by means of the ultrasound Doppler velocimetry (UDV), which is suitable to deliver

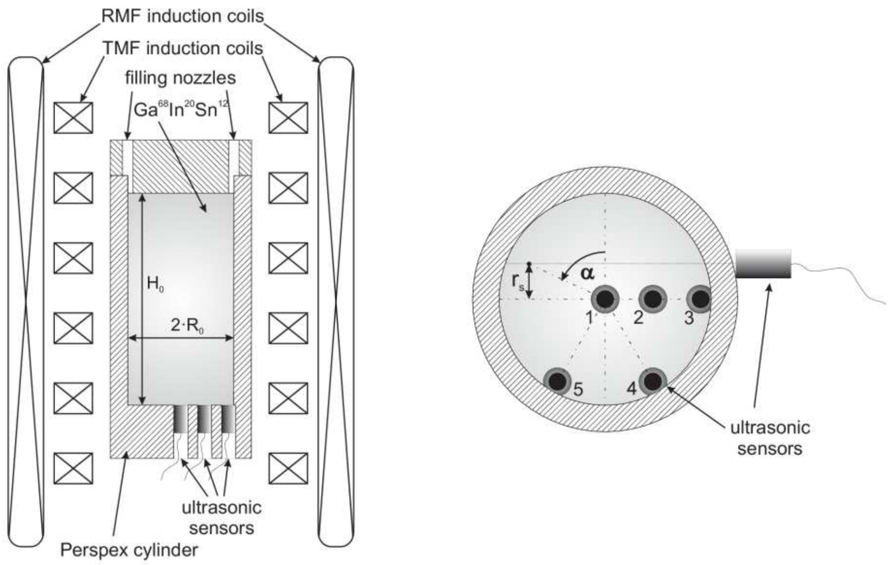

Figure 1**:** Schematic drawing of the experimental setup and applied sensor positions

instantaneous velocity profiles in opaque fluids such as liquid metals. A schematically drawing of the experimental setup is shown in figure 1.

The RMF induces a Lorentz force in the liquid metal which is time-independent and has only one azimuthal component in the cylindrical configuration [5]:

$$F_{\emptyset} = \frac{1}{2}\sigma\omega B_r^2 r f(r,z)$$

here, $\sigma = 3.2 \times 10^6$ S/m is the electrical conductivity of GaInSn, $\omega/2\pi = 50$ Hz is the frequency of the RMF and r stands for the vessel radius. The shape function $f(r, z)$ reflects the influence of the finite cylinder length. The Lorentz force has its maximum near the sidewall of the vessel at the half-height and reduces to zero at the axis and the horizontal end walls. The magnetic Taylor number gives the dimensionless force magnitude that is used to characterize the RMF-driven flow:

$$Ta = \frac{\sigma\omega B_r^2 R_0^4}{\rho\vartheta^2}$$

The magnetic flux density (B_r) in both equations is given in terms of the root mean square value.

The classification of the different inertial wave modes is done in this work with the waveform vector (γ_i, n), where γ_i is the wavenumber of the i^{th} radial mode and n is the axial mode number.

3. Spontaneous occurrence of inertial waves

Inertial waves can straightforwardly be excited in a liquid metal column by distinct variations of the electromagnetic driving force. For instance, pronounced inertial waves were found during an RMF-driven spin-up, after the magnetic field has been suddenly switched on [6, 7]. These inertial waves are completely damped by viscous effects before the flow reaches the

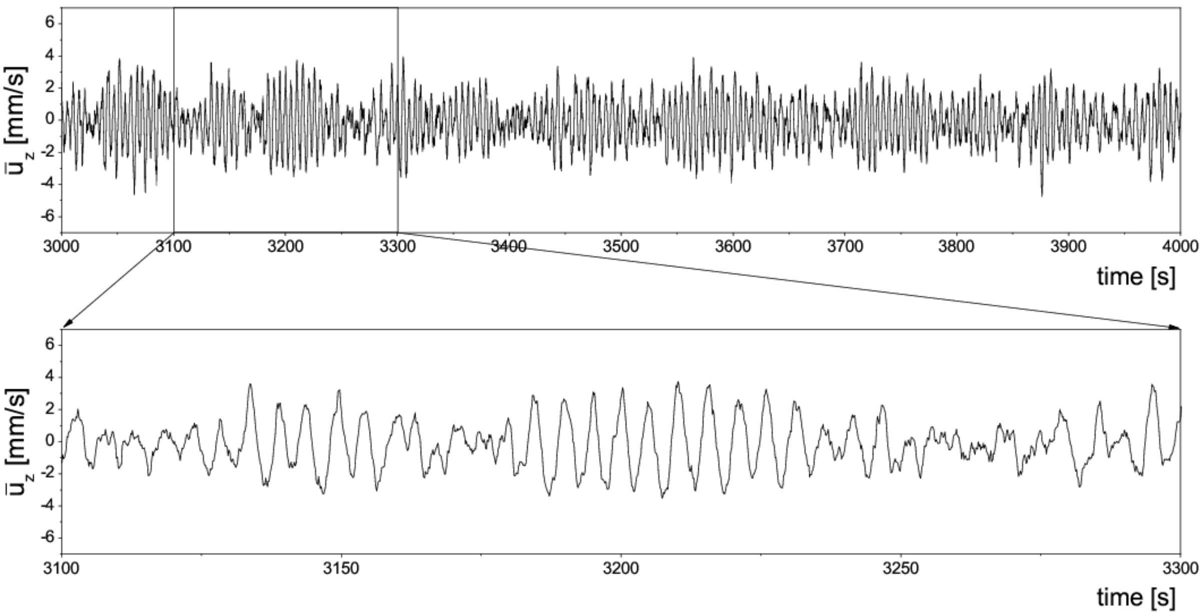

Figure 2: Mean axial velocity averaged along the cylinder height [$0 \leq z \leq H_0$]; recorded during a long-term measurement without magnetic disturbance B_R = 1.3 mT; $r/R_0 = 0$

steady state at the end of the spin-up. Having this in mind, one would hardly expect that inertial waves occur during a stationary rotation without any external perturbation. In a recent work [8], Sauret et al. analyzed the flow in a librating cylinder by means of numerical simulations. The authors reported a new mechanism of spontaneous excitation of inertial waves in the center of a librating cylinder ensuing from turbulent sidewall boundary layers. To check whether turbulent fluctuations may act as source of such inertial waves, an experiment was performed under stationary flow conditions with a continuously rotating liquid. Any geometrical or electromagnetic perturbation was avoided. The measurements were performed inside a cylinder of the aspect ratio $A = H_0/2R_0 = 3$ (H_0 = 180 mm and R_0 = 30 mm). The rotating flow inside the cylindrical vessel was driven by an RMF at a constant field strength of B_R = 1.3 mT which corresponds to a value of the magnetic Taylor-number of $Ta = 1.79 \times 10^6 \gg Ta^{cr}$. The nature of RMF-driven flows at about $100 \times Ta^{cr}$ can be considered as supercritical to certain instabilities. Figure 2 displays a section of a long-term measurement lasting over a period of about one hour. In this figure, the evolution of the vertical velocity (u_z) averaged along the axis of the liquid metal column is shown. An almost periodic oscillation of the mean axial velocity becomes visible collapsing from time to time. Because any external forcing was avoided here, the inertial wave must be triggered by the flow itself. A frequency and wave-mode analysis of this inertial wave was done in terms of a 2D-FFT, which is shown in figure 3. In this figure, the vertical axis is determined by the axial mode-number which is defined as $n = 2H_0/\lambda$, whereby λ is the wavelength. The abscissa in this figure represents the frequency. The normalized amplitude of the respective wave modes is represented by the gray scale. This 2D-FFT was performed within the measuring time interval of t = 3000...4000 s. The diagram clearly reveals the dominating (γ_1, 1) mode with a frequency of $f \approx 0.2$ Hz. Due to the fact that the wave-length of the n = 1 inertial wave is twice the cylinder height and thus, the FFT does not identify a complete wave, the mode-number information of the FFT is projected to n = 0 (representing a uniform component) and to various positive and negative integer wave length (a likewise decomposition occurs for all odd modes). The n = 2 signature at f = 0 Hz is a signature of the Bödewadt recirculation. Several other inertial wave modes can be identified in this FFT plot in addition to the dominant (γ_1, 1) mode. One example therefor is the n = 2 mode at $f \approx 0.4$ Hz. The interesting question is how these inertial wave modes are excited. A typical feature of an RMF-driven

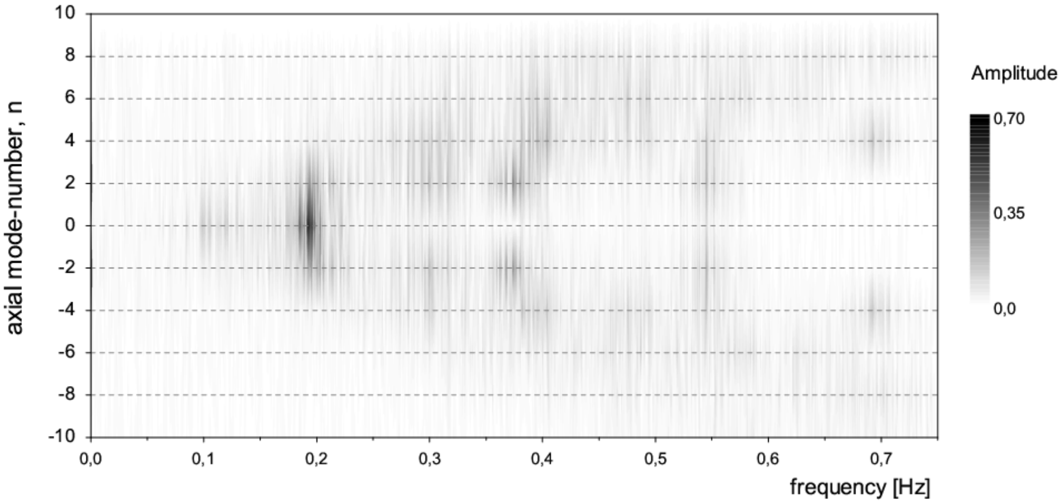

Figure 3: 2D-FFT of the spatio-temporal flow structure recorded during a long-term measurement without magnetic disturbance (corresponds to the measurement shown in fig. 2, top) B_R = 1.3 mT; $r/R_0 = 0$

flow at supercritical Ta numbers is the formation of Taylor-Görtler (TG) vortices, which is a result of the instability of the side wall layers. These TG-vortices develop typically in the boundary layer at the side wall of the cylindrical vessel. After formation, the TG-vortices are conveyed by the secondary flow towards the horizontal end walls of the vessel, where they dissipate in the Bödewadt layers [9]. The impingement of the TG-vortex on the Bödewadt layer provokes a temporary disturbance of the boundary layer. Velocity measurements made during an RMF-driven spin-up [10] showed how such a disturbance propagates inside the boundary layer and excites an inertial wave appearing in the center of the vessel, as observed in figure 2. These findings suggest the assumption that the phenomenon of the spontaneous generation of inertial waves might be caused by the dissipation of TG-vortices in the Bödewadt-layers. With the exception of the (γ_1, 1) mode all inertial waves detected in the velocity measurements do not become prevalent with respect to the turbulent motion. Thus, we want to focus now a bit more in detail on the dominant (γ_1, 1) mode. Figure 2 demonstrates that the amplitude of the (γ_1, 1) mode remains more or less stable for many periods, although it suddenly decays intermittently. Thus, there must be a mechanism sustaining the (γ_1, 1) wave. We suppose that this interesting phenomenon can be ascribed to an interaction between the (γ_1, 1) mode and the pronounced Bödewadt layers at the top and bottom wall of the vessel. According to the velocity recordings in figure 2, the inertial wave implicates an alternatingly up- or downwards directed flow along the vessel axis. This alternating flow leads to periodic variations of the Bödewadt layer thickness and thus to a periodic modulation of the Ekman-transport. Let us consider a moment, when the inertial wave in the center of the vessel is directed upwards. At that instant the Ekman-transport beneath the lid of the fluid cylinder is repressed, while the liquid metal is still pumped inwards in the bottom Bödewadt layer. As a result an upwards directed jet is formed in the core of the fluid vessel. A half cycle later, the situation becomes inverted. This alternating Ekman-transport is necessarily in phase with the inertial wave. In this way, a continuous energy transfer may be enabled from the primary swirling flow over the Ekman-transport toward the inertial wave. Such a mechanism, which is speculative at present, could be responsible for the enduring persistence of the (γ_1, 1) inertial mode. This mechanism would also explain the observations reported by Zhang et al. [11] for the situation of an RMF-driven flow in a liquid metal column, where the free surface of a liquid metal was covered by a distinct oxide layer. In that case, an intense distortion of the bulk flow occurred without external stimulation. The authors suggest the friction forces between the rigid oxide layer and the side wall to be responsible for the development of pronounced flow oscillations in the bulk of the melt. However, they did not associate their findings with the occurrence of inertial waves. A closer analysis of the flow pattern found in the reported experiment and a comparison with the results of the present study reveals the existence of the (γ_1, 1) mode in that experiment. The strong interaction between this inertial wave and the oxide layer, which causes strong and persistent flow oscillations, appears to be similar to the mechanism described here.

4. Conclusion

In this work, the occurrence of spontaneously excited inertial waves was studied inside a cylindrical vessel. A rotating magnetic field (RMF) generates a swirling motion inside the liquid metal filled in the cylinder. A prominent feature of our experimental configuration is the interaction between the inertial modes and the secondary flow arising from the Ekman transport. We observed the formation of an (γ_1, 1) inertial wave mode even without any external triggering in form of deliberate disturbances of the rotating flow field. The reason for such a spontaneous excitation of (γ_1, 1) inertial waves can be explained by the existence of Taylor-Görtler vortices at the sidewall of the vessel. These TG-vortices are conveyed by the secondary flow towards the top and bottom of the vessel where they dissipate in the Bödewadt layer. Such a vortex dissipation in the Bödewadt layer leads to a perturbation of the Ekman pumping resulting in the excitation of an inertial wave.

5. References

[1] Thompson, R. 1978, Observation of inertial waves in the stratosphere. Quarterly Journal of the Royal Meteorological Society 104 (441), 691–698.

[2] Fu, L.L. 1980, Observations and models of inertial waves in the deep ocean. PhD thesis, Massachusetts Institute of Technology and Woods Hole Oceanographic Institution.

[3] Aldridge, K.D. & Lumb, LI 1987 Inertial waves identified in the earth's fluid outer core. Nature 325, 421–423.

[4] Pal, J., Cramer, A., Gundrum, T. & Gerbeth, G. 2009 MULTIMAG, a multipurpose magnetic system for physical modelling in magnetohydrodynamics. Flow Measurement and Instrumentation 20 (6), 241–251.

[5] Gorbachev, L.P. Nikitin, N.V. & Ustinov, A.L. 1974 Magnetohydrodynamic rotation of electrically conducting liquid in a cylindrical vessel of finite dimensions. Magn. Gidrodin.,no. 4, pp. 32-42 (4).

[6] Nikrityuk, P.A., Ungarish, M., Eckert, K. & Grundmann, R. 2005 Spin-up of a liquid metal flow driven by a rotating magnetic field in a finite cylinder: A numerical and an analytical study. Physics of Fluids 17, 067101.

[7] Räbiger, D., Eckert, S. & Gerbeth, G. 2010 Measurements of an unsteady liquid metal flow during spin-up driven by a rotating magnetic field. Exp. Fluids 48 (2), 233–244.

[8] Sauret, A., Cebron, D., Le Bars, M. & Le Dizes, S. 2005 Fluid flows in a liberating cylinder. Physics of Fluids 24, 026603.

[9] Stiller, J., Frana, K. & Cramer, A. 2006 Transitional and weakly turbulent flow in a rotating magnetic field. Physics of Fluids 18, 074105.

[10] Vogt, T. Grants, I. Räbiger, D. Eckert, S. & Gerbeth, G. 2012 On the formation of Taylor–Görtler vortices in RMF-driven spin-up flows. Exp. Fluids 52 (1), 1–10.

[11] Zhang, C. Shatrov, V. Priede, J. Eckert, S. & Gerbeth, G. 2011 Intermittent behavior caused by surface oxidation in a liquid metal flow driven by a rotating magnetic field. Metallurgical and Materials Transactions B 42 (6), 1188–1200.

A SPHERICAL COUETTE EXPERIMENT TO OBSERVE INDUCTIONLESS MHD INSTABILITIES AT MEDIUM REYNOLDS NUMBERS

Elliot Kaplan[1,*], Benjamin Gohl[1], Martin Seilmayer[1], and Frank Stefani[1]

[1]Helmholtz-Zentrum Dresden-Rossendorf—Bautzner Landstraße 400—01328 Dresden—Germany
[*]e.kaplan@hzdr.de

Abstract: A liquid metal (GaInSn) spherical Couette flow is being carried out at the Helmholtz-Zentrum in Dresden-Rossendorf to explore a region of Reynolds-Hartmann space in which numerical simulations [1, 2] show hydrodynamically unstable and magnetohydrodynamically unstable regions separated by an isthmus of stability. The region is of further interest because these (inductionless) instabilities have similar signatures to the instabilities found in a larger scale, less thoroughly diagnosed experiment, that were reported as the (induction dependent) Magnetorotational instabiliity (MRI) [3].

1. Introduction

Two spheres, one inside the other, in differential rotation with a layer of fluid between will generate a broad array of possible dynamics in the enclosed fluid, depending on the aspect ratio, the rotation rates of the spheres, and the viscosity of the fluid. If the fluid is electrically conducting and permeated by a magnetic field, applied and/or self-excited, the array of possible dynamics broadens further. The configuration, known as magnetized spherical Couette flow, was first studied numerically by Hollerbach [4] as an extension of the nonmagnetic spherical Couette problem [5, 6]. Since then the flow has been investigated, numerically [1, 7–9] and experimentally [3, 10], under a variety of imposed fields and magnetic boundary conditions. A compendium of magnetized spherical Couette results can be found in [11].

A long, albeit contentiously, discussed result of magnetized spherical Couette flow was the observation of an angular momentum transporting, magnetically induced instability in a turbulent (Reynolds number (Re) $\approx 10^7$, where $\mathrm{Re} = r_1^2\Omega/\nu$, with r_1 inner radius, Ω inner sphere rotation rate, and ν bulk viscosity of the fluid) liquid metal flow, which was described in [3] as the long sought-after Magnetorotational Instability (MRI). In contrast to the MRI as usually described [12], this instability was non-axisymmetric and demonstrated an equatorial symmetry whose parity depended on the strength of the applied magnetic field. Subsequent numerical investigations [1, 7] turned up a collection of induction-free instabilities—related to the hydrodynamic jet instability, the Kelvin-Helmholtz-like Shercliff instability, and a return flow instability—that replicated the parity properties, as well as the torque on the outer sphere (the proxy measurement of angular momentum transport). A more modestly scaled (Re $< 10^5$), but more comprehensively diagnosed (Ultrasonic Doppler Velocimetry (UDV), electric potential measurements), spherical Couette experiment is being carried out at the Helmholtz-Zentrum Dresden-Rossendorf in order to better characterize these instabilities, their criteria, and their saturation. Presented here are initial data from the experiment, as well as some phenomenology of the saturation and bifurcation of the instabilities via nonlinear transfer of energy between azimuthal modes as revealed by the numerical simulations.

2. Simulation

Preliminary simulation of the experiment was carried out using a code, described in [13], that solves for a flow, driven by the rotating inner sphere, according to the incompressible Navier-Stokes Equation:

$$\nabla \cdot \mathbf{U} = 0, \qquad \nabla \times \mathbf{U} = \boldsymbol{\omega}, \qquad \partial\boldsymbol{\omega}/\partial t = \nabla \times \mathbf{F} + \nabla^2 \boldsymbol{\omega}. \tag{1}$$

The body force $\mathbf{F}$ is given by

$$\mathbf{F} = \mathrm{Re}\,(\nabla \times \mathbf{U}) \times \mathbf{U} + \mathrm{Ha}^2\,(\nabla \times \mathbf{B}) \times \mathbf{B}, \tag{2}$$

with $\mathbf{U}$ and $\mathbf{B}$ vector fields of the velocity and magnetic fields respectively, and Ha the Hartmann number ($B_0 r_1 \sqrt{\sigma/\rho\nu}$, B_0 applied field strength, σ electrical conductivity, ρ mass density).

The magnetic field is split into an applied ($\mathbf{B}_0$) and an induced ($\mathbf{b}$) component, where the applied field is curl free within the flow domain. The Lorentz force is then given by

$$(\nabla \times \mathbf{B}) \times \mathbf{B} = (\nabla \times \mathbf{b}) \times \mathbf{B}_0 + (\nabla \times \mathbf{b}) \times \mathbf{b}, \tag{3}$$

where $\mathbf{b}$ is given by the magnetic induction equation in the (so-called inductionless) limit where diffusion ($\nabla^2\mathbf{b}$) exactly balances advection ($\nabla \times (\mathbf{U} \times \mathbf{B}_0)$):

$$0 = \nabla^2 \mathbf{b} + \nabla \times (\mathbf{U} \times \mathbf{B}_0)\,. \tag{4}$$

The $((\nabla \times \mathbf{b}) \times \mathbf{b})$ term in Eqn. 3 is taken to be small. In all of the simulations performed in preparation for this experiment, the applied field was taken to be axial.

The simulations are run according to the following proceedure. First a flow including only the axisymmetric modes is evolved to a steady state solution for given values of (Re, Ha). The linear stability of the m $\neq$ 0 harmonics are then tested through a linearized Navier-Stokes calculation. The unstable flows are then seeded with three-dimensional, nonaxisymmetric noise and evolved until the instability saturates. Figure 1a shows the stability boundaries for a flow with aspect ration 0.5. Figure 1b-d show energy densities of the instabilities associated flow of Re 1000 and Ha 10, 30 and 70 respectively, with streamlines of the axisymmetric meridional flow overlaid. Figure 1e-f shows the same with isocontours of the angular momentum. The values of Re and Ha are chosen because the actual instability takes on a different character in each. At low Ha, the instability arises in the jet (1b). At medium Ha, it arises in the stagnation point of the meridional flow (1c). At high Ha, it arises along the Shercliff Layer (1g).

The steady states of the full three-dimensional calculation have the practical use of guiding diagnostic design and expectations for the low Re cases (discussed further in Section 3. below). They also demonstrate a saturation mechanism for the instabilities [14].

3. Apparatus

The physical experiment consists of one of two possible inner spheres (r_1 = 3 cm or 4.5cm) held in the center of an outer sphere (r_2 = 9 cm). The outer sphere is a Polymethyl Methacetate (PMMA) acrylic with cylindrical holders for ultrasonic doppler velocimetry (UDV), and perforations to admit copper electrodes for potential measurement. Figure 2a shows a Solidworks® model of the experiment including the diagnostics, Figure 2b shows the actual manufactured vessel. The space between the spheres is filled with a GaInSn eutectic alloy. Because of the high density of the medium (roughly 6 times that of water), each inner sphere holds a lead weight to counter the buoyancy force. The axial magnetic field is provided by a pair of copper

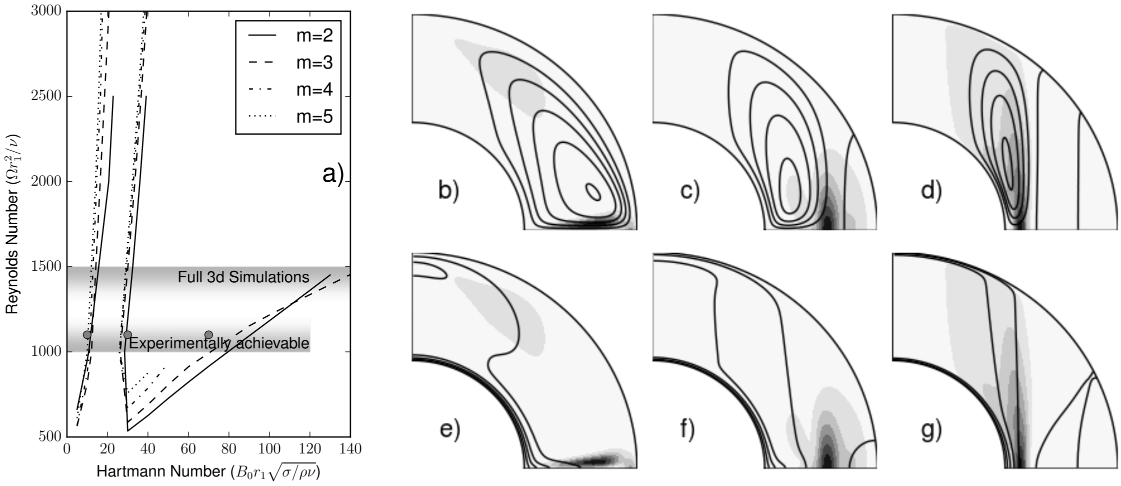

Figure 1: a) Critical Reynolds numbers as a function of Hartmann number for symmetric and antisymmetric instabilities calculated from a linearized Navier-Stokes equation analysis of the axisymmetric base flows. The boundaries of the region which can be reasonably simulated, and the region which can be reached in the experiment are indicated by the shaded bands. The (Ha, Re) values of the flows Figures b-g are indicated by circles. b-g). Profiles of the energy density of the most unstable eigenmode from at three different Hartmann numbers at Re 1100. b-d show streamlines of the meridional flow over the energy density of the m=2 harmonic. e-g show contours of the angular momentum over the same. b and e show the equatorially antisymmetric jet instability (Re 1100, Ha 10). c and f show the equatorially symmetric return flow instability (Re 1100, Ha 30). d and g show the equatorially symmetric Shercliff layer instability (Re 1100, Ha 70).

electromagnets (not pictured) with central radii of 30 cm, with a vertical gap of 31 cm between them (a near Helmholtz configuration). The inner and outer spheres are driven with a minimum rotation frequency of $\sim$0.02 hz by a pair of 90 W electromotors connected to 100 x 1 gears. The electromagnets provide 1 mT of axial magnetic field (or 1.17 Ha) per 4.2 Amps through the coils.

The simulations of Section 2. provide estimates of the potential differences between electrodes and the velocities measured along the UDV chords. Table 1 shows a summary of these predictions, as well as engineering data, for the lowest Re runs of interest. At such low rotation rates, the peak velocity signals are on the order of a half mm/s for all three classes of instability, which can be reasonably measured using standard UDV probes. The potential differences are drastically different between the instabilities—the potential is a product of the background magnetic field and the flow—but even the lowest voltages are measurable when appropriately preamplified. The initial run campaigns of the experiment will seek to confirm the most interesting features of Fig. 1: the stability isthmus in the vicinity of Ha 20, the Reynolds line around Ha 30 where an increase in Re stabilizes the flow (in contradiction to typical intuition), and the transition between the three types on instability.

4. Summary

As of the writing of this proceedings paper, the vessel, the test stand and the electromagnetic coils have all been manufactured. It remains to affix the diagnostics to the sphere and to attach

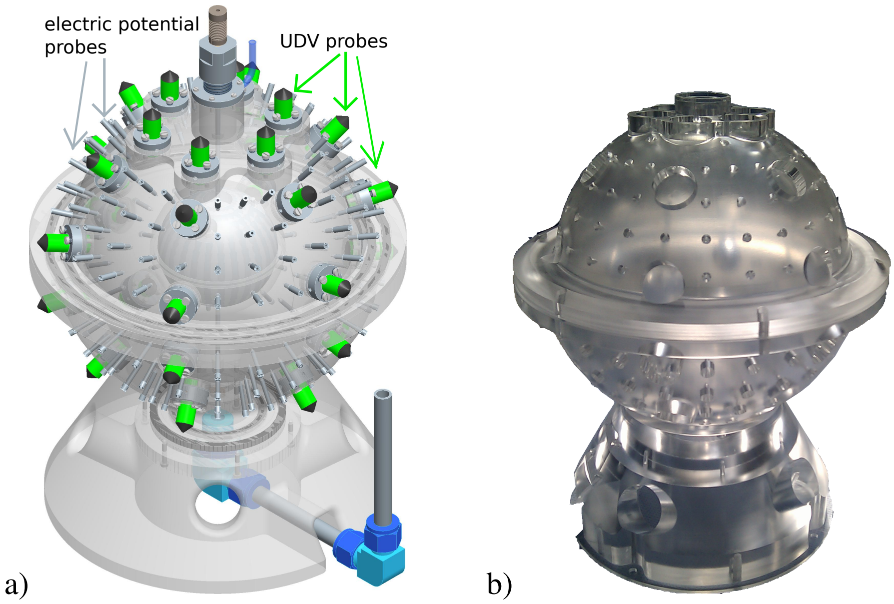

Figure 2: (A) Solidworks® model the spherical Couette experiment. Some UDV and potential probes are indicated in the figure. The elbowed tube is for the gallium fill. (B) real spherical vessel. Pits hold the real diagnostics.

the power and cooling supplies to the electromagnets.

Acknowledgements

This work is supported by the Deutsche Forschungsgemeinschaft under grant STE 991/1-2.

5. References

[1] Hollerbach, R. (2009). Non-axisymmetric instabilities in magnetic spherical Couette flow. *Proc. R. Soc. London A*, 465:2003–2013.

[2] Travnikov, V.; Eckert, K.; and Odenbach, S.: (2011). Influence of an axial magnetic field on the stability of spherical Couette flows with different gap widths. *Acta Mech*, 219:255–268.

[3] Sisan, D. R.; Mujica, N.; Tillotson, W. A.; Huang, Y.-M.; Dorland, W.; Hassam, A. B.; Antonsen, T. M.; and Lathrop, D. P.: (2004). Experimental Observation and Characterization of the Magnetorotational Instability. *Phys. Rev. Lett.*, 93(11):114502.

[4] Hollerbach, R. (1994). Magnetohydrodynamic Ekman and Stewartson Layers in a Rotating Spherical Shell. *R. Soc. London Proc. Ser. A*, 444:333–346.

Reynolds	Hartmann	Ω_{in}	$\boldsymbol{B}_0$	$\overline{\phi}_{max}$	$\widetilde{\phi}_{max}$	$\overline{v}_{max}$	$\widetilde{v}_{max}$
1000	10	0.0235 Hz.	9 mT	10 μV	367 nV	0.412 mm/s	0.305 mm/s
1000	30	0.0235 Hz.	26 mT	32 μV	1.1 μV	0.340 mm/s	0.331 mm/s
1000	70	0.0235 Hz.	60 mT	70 μV	8.6 mV	0.067 mm/s	0.438 mm/s

Table 1: Predictions for diagnostic outputs for three typical run conditions. The mean potential ($\overline{\phi}$) represents the time averaged potential difference between the pole and the equator. The fluctuating potential ($\widetilde{\phi}$) represents the largest amplitude potential difference between two points at a single latitude. The mean and fluctuating velocities are taken by projecting the simulated flow along a UDV chord. The max values over any probe is shown.

[5] Stewartson, K. (1966). On almost rigid rotations. *J. Fluid Mech.*, 1:131–144.

[6] Proudman, I. (1956). The almost-rigid rotation of viscous fluid between concentric spheres. *J. Fluid Mech.*, 1:505–516.

[7] Gissinger, C.; Ji, H.; and Goodman, J.: (2011). Instabilities in magnetized spherical Couette flow. *Phys. Rev. E*, 84(2):026308.

[8] Hollerbach, R. and Skinner, S.: (2001). Instabilities of magnetically induced schear layers and jets. *Proc. R. Soc. London A*, 457:785–802.

[9] Dormy, E.; Jault, D.; and Soward, A. M.: (2002). A super-rotating shear layer in magnetohydrodynamic spherical Couette flow. *J. Fluid Mech.*, 452:263–291.

[10] Nataf, H.-C.; Alboussière, T.; Brito, D.; Cardin, P.; Gagnière, N.; Jault, D.; and Schmitt, D.: (2008). Rapidly rotating spherical Couette flow in a dipolar magnetic field: An experimental study of the mean axisymmetric flow. *Physics of the Earth and Planetary Interiors*, 170:60–72.

[11] Rüdiger, G.; Kitchatinov, L. L.; and Hollerbach, R.: (2013). *Magnetic Processes in Astrophysics*, pages 287–326. Wiley-VCH Verlag GmbH & Co. KGaA.

[12] Balbus, S. A. and Hawley, J. F.: (1991). A powerful local shear instability in weakly magnetized disks. *Astrophys. J.*, 376:214–233.

[13] Hollerbach, R. (2000). A spectral solution of the magneto-convection equations in spherical geometry. *Int. J. Numer. Meth. Fluids*, 32:773–797.

[14] Kaplan, E. (2014). On the saturation of non-axisymmetric instabilites of magnetized spherical Couette flow. *ArXiv e-prints*: 1402.5064.

FORCES EXPERIENCED BY AN ISOLATING SPHERE MOVING CLOSE TO A WALL

HEITKAM[1] S., SELLIER[2] A., SCHWARZ[1] S., FRÖHLICH[1] J.
[1]Institute of Fluid Mechanics, TU Dresden, 01062 Dresden, Germany
[2]LadHyX, Ecole Polytechnique, 91128 Palaiseau cedex, France
E-mail: sascha.heitkam@tu-dresden.de

Abstract
The paper presents phase-resolving numerical simulations to compute the force acting on an insulating sphere moving in a conducting liquid along an insulating wall. The superposition of a magnetic field and a perpendicular electric field, both parallel to the wall, results in Lorentz forces that create rotating flows in the vicinity of the sphere. Complex interactions of viscous and inertial fluid forces, electric induction, and Lorentz forces take place. By carefully changing the parameters of the problem the influence of these mechanisms on the force acting on the sphere is investigated. The configuration is proposed as a suitable test case to assess numerical methods for MHD multiphase flows.

1. Introduction

The behaviour of an insulating particle exposed to electric and magnetic fields is highly relevant for electrolysis processes, electrostatic separation of particles, and metallurgy. Here, we suppose the insulating sphere to represent a gas bubble in liquid aluminium, a situation relevant when generating metal foam, for example [1,2]. Leenov and Kolin [3] derived the force F_S acting on a spherical, insulating particle exposed to a magnetic field B and a perpendicular electric current $j = \sigma E$ to be

$$F_S = \sigma E B \pi R^3 \quad . \tag{1}$$

Sellier [4-6] extended this approach, deriving force and momentum acting on spheres and arbitrarily shaped particles close to a plane wall. He also derived the resulting velocity and rotation of a sphere under the assumption of vanishing Reynolds number. Also, the induction term in the Ohm's law

$$j = \sigma(-\nabla\Phi + u \times B) \quad . \tag{2}$$

was neglected, corresponding to a high ratio of applied electric field gradient $\nabla\Phi$ and electric induction $u \times B$. Additionally, the magnetic field was supposed to be constant in space and time, which means firstly, that it is not influenced by the different material properties inside the sphere and secondly, that magnetic induction and, therefore, the magnetic Reynolds number is small.
In this work, numerical simulations of the fluid dynamics and the MHD effects are presented, to find the limits of these assumptions and to investigate the behaviour beyond.

2. CFD code

The coupled fluid dynamic and MHD problem is solved with the in-house code PRIME [7-9]. It solves the unsteady, incompressible Navier-Stokes equations on a staggered Cartesian grid. For time advancement a low-storage three-step Runge-Kutta scheme is used, combined with an implicit treatment of the viscous terms. Turbulence modelling is not applied. Instead, very fine spatial and temporal resolution is employed to resolve even the smallest turbulent structures. The particle surface is modelled with the Immersed-Boundary method [7] with the surface being represented by Lagrangian marker points. At these points additional forces are

introduced into the Navier-Stokes equations to impose a no-slip boundary condition. The sum of these forces equals the action of the fluid on the particle which hence is directly available in the method.
The magnetic field is assumed to be constant in space and time, because gas bubbles and liquid aluminium both have a magnetic susceptibility close to zero. By definition, the electric conductivity σ_s of an insulating sphere is much smaller than the conductivity of the fluid $\sigma_s \ll \sigma$. Therefore, an additional Laplace equation for the correction Φ_{cor} of the electric potential has to be solved to ensure, that the electric current

$$j = \alpha \, \sigma \left(-\nabla(\Phi + \Phi_{cor}) + u \times B\right) \qquad (3)$$

is divergence-free [9]. For the different electric conductivity of sphere and fluid is accounted by the parameter α which equals one outside the sphere, zero inside and is computed with a second order cut-cell approach around the particle surface described in [7]. The applied numerical scheme can handle non-vanishing inertial effects of the fluid and electric induction in the fluid. Therefore, it can be used to extend the earlier results of Sellier [4-6].

3. Setup

In order to limit the set of variables while still including the interactions of MHD mechanisms, the setup shown in fig. 1 is proposed. An insulating sphere with radius R is moving with imposed, constant velocity u_s parallel to an insulating plane wall without rotation. The distance between particle surface and wall remains constant and is chosen to be $0.5\,R$. An electric field is oriented parallel to the direction of movement, a constant magnetic field is oriented parallel to the wall and perpendicular to the electric field.

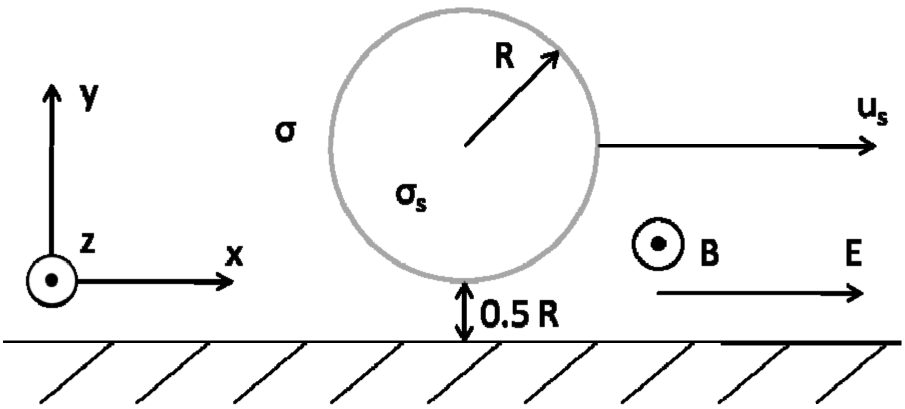

Figure 1: Geometrical setup of the simulation.

At the wall and at the surface of the particle, a no-slip condition for the fluid is applied.
The force on the bubble is computed in the way described above. The force in x-direction, F_x, results primarily from the fluid drag and is therefore normalized by the Stokesian drag to yield the non-dimensional force

$$f_x = \frac{F_x}{\square} 6\pi\mu R u_s \,. \qquad (4)$$

The force in y-direction results primarily from the Lorentz force, with (1) describing the homogeneous case, and hence is normalized by the corresponding value [3]

$$f_y = \frac{F_y}{\square} \sigma \, E \, B \pi \, R^3 \,. \qquad (5)$$

The problem has three independent parameters: the velocity of the sphere, resulting in the Reynolds number $Re_s = 2\, u_s R \frac{\square}{\nu}$, the magnetic field strength B , and the product of the

electric and the magnetic field strength $\sigma E B$, in the following referred to as electromagnetic field strength. The reason for discussing the magnetic field strength separately here is that it acts by electric induction on the moving conducting liquid, independently of the applied electric field.
Table I provides the considered material properties which are those of a small gas bubble in liquid aluminium, while Table II gives an overview of the different simulations carried out.

Table I: Physical parameters of the setup.

Bubble diameter	$D\,[m]$	$2x10^{-3}$		Fluid density	$\rho\,[kg\,m^{-3}]$	2400
Fluid viscosity	$\nu\,[m^2 s^{-1}]$	$5x10^{-7}$		Electric conductivity	$\sigma\,[S\,m^{-1}]$	$5x10^{6}$

Table II: Combination of parameters defining Cases A..E. Bold numbers indicate the parameters which are modified to investigate their influence.

Case		A	B	C	D	E
Reynolds number	Re_s	0	0	$10..10^3$	3	$3..30$
Electromagnetic field strength	$0.75\frac{\sigma EB}{\rho}[m$	$\pm 10^{-3}..10$	± 10	0	0	-10^{-1}
Magnetic field strength	$B\,[T]$	10^{-5}	$10^{-3}..10$	0	$10^{-3}..10^{-1}$	10^{-5}

4. Results for an immobile sphere

In a first step, forces on a fixed sphere are addressed. Figure 2a shows the force f_y for small magnetic field strength as a function of the electromagnetic field strength (Case A).

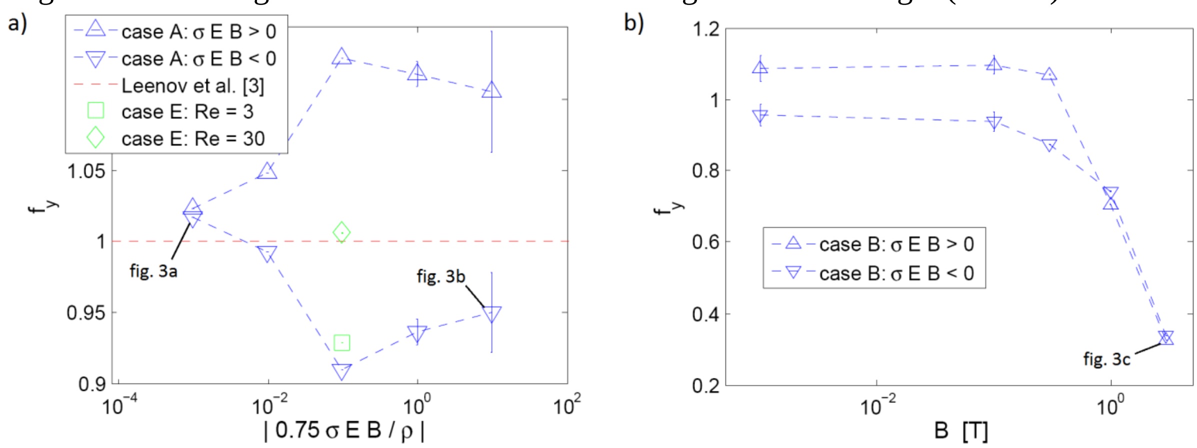

Figure 2: Wall-normal force on a sphere close to a wall. (a) Force as a function of electromagnetic field strength at constant, small magnetic field strength for a fixed sphere (Case A) and slowly moving sphere (Case E). (b) Force as a function of magnetic field strength at a constant, high electromagnetic field strength (Case B). Labeled simulations are visualized in fig. 3.

For $0.75\frac{\sigma EB}{\rho} = 10^{-3}$, the velocity of the fluid is small and its inertia negligible. Thus, f_y is independent of the sign of σEB . The difference to Leenov and Kolin [3] (fig. 2a) stems from

the interaction with the wall which is not present in their work. The electric current is concentrated in the gap between sphere and wall (fig. 3a), resulting in higher Lorentz forces in this region and hence, in a larger force on the sphere than in the absence of a wall. With increasing electromagnetic field strength, nonlinear inertia terms in the Navier-Stokes equation come into play with the sign of the force modification depending on the sign of the electromagnetic field (fig. 2a). At even higher field strengths, the flow becomes turbulent, resulting in fluctuating forces on the sphere.
In the second step, the magnetic field strength is varied (Case B). At constant, high electromagnetic field strength the magnetic field is increased while the electric field is decreased correspondingly. As shown in fig. 3, the stronger magnetic field damps the fluid motion, so that the inertia effects become less prominent. Fluctuations and dependency on the sign of the electromagnetic field disappear (fig. 2b). At the same time, the total force on the sphere is significantly reduced, even though the product of applied electric and magnetic field strength remains constant in this investigation.

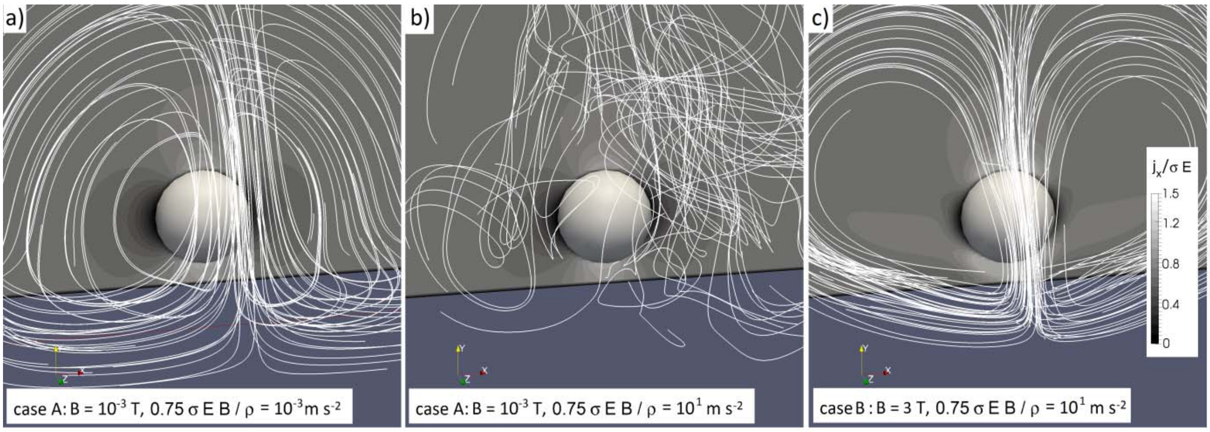

Figure 3: The plots show a contour of the horizontal component of the electric current j_x and arbitrarily chosen instantaneous fluid stream lines for the cases specified in the insets. The colour scale is the same for all plots.

5. Results for a moving sphere

Now the sphere is moved parallel to the wall. For absence of electric and magnetic fields (Case C) the force experienced by the sphere is parallel to the wall and depends nonlinearly on the velocity (fig. 4a). A purely magnetic field (Case D) can increase the force due to induced currents which create Lorentz forces that in turn damp the velocity. This is in agreement with Lenz’s law.

The electromagnetic field, mentioned above, creates a stationary vortex structure around the sphere (fig. 3a), resulting in nonlinear inertia effects. Increasing the velocity of the sphere (Case E), the flow more and more tends towards a dipole-type flow structure as shown in fig. 4b. This results in a reduction of the nonlinear effects on the force normal to the wall. With increasing velocity of the sphere the force normal to the wall tends towards the results for negligible induction and inertia. At the same time, the force in tangential direction is increased slightly by adding an electromagnetic field (Case E). This is shown in fig. 4 a.

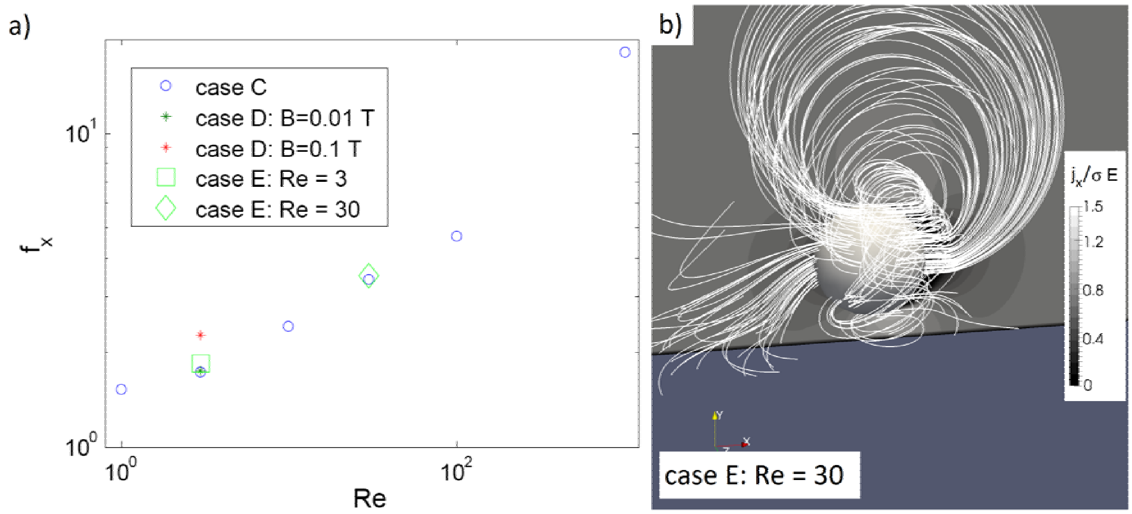

Figure 4: Force on a sphere moving tangentially to a wall. (a) Force without electric and magnetic fields (Case C), with a magnetic field only (Case D) and with an electromagnetic field (Case E). (b) Flow structure around the moving sphere in an electromagnetic field for Case E (Re = 30).

6. Concluding remarks

The magnetohydrodynamic flow around a fixed and a moving sphere in the vicinity of a wall has been simulated. The results agree very well with values from the literature, in cases where these are available. Due to the electrical insulation of a sphere, a curling vortex system is induced in its vicinity. With increasing field strength, nonlinear effects resulting from inertia and induction come into play. A magnetic field can damp the fluid motion and reduce turbulence, as it is well known from Hartmann flow and other configurations. Increasing the magnitude of the magnetic field at constant external electromagnetic field strength (i.e. simultaneously reducing the electric field), the force on the sphere is reduced.

7. References

[1] Heitkam,S.; Schwarz, S.; Fröhlich, J.: Simulation of the influence of electromagnetic fields on the drainage in wet metal foam. Magnetohydrodyn. 48 (2012) 313-320.
[2] Heitkam,S.; Schwarz, S.; Santarelli, C.; Fröhlich, J.: Influence of an electromagnetic field on the formation of wet metal foam. Eur. Phys. J. Special Topics 220 (2013) 207-214.
[3] Leenov, D.; Kolin, A.: Theory of electromagnetophoresis. 1. Magnetohydrodynamic forces experienced by spherical and symmetrically oriented cylindrical particles. J. Chem. Phys. 22 (1954) 683-688.
[4] Moffatt H. K.; Sellier, A.: Migration of an insulating particle under the action of uniform ambient electric and magnetic fields. Part 1. General theory. J. Fluid Mech. 464 (2002) 287-296.
[5] Sellier, A.: Migration of an insulating particle under the action of uniform ambient electric and magnetic fields. Part 2. Boundary formulation and ellipsoidal particles. J. Fluid Mech. 488 (2003) 335-353.
[6] Sellier, A.: Migration of a solid conducting sphere immersed in a liquid metal near a plane boundary under the action of uniform ambient electric and magnetic fields. 6th PAMIR Conference on Fundamental and Applied MHD (2005) 311-314.
[7] Kempe, T.: A numerical method for interface-resolving simulations of particle laden flows with collisions, TUDpress Verlag der Wissenschaften GmbH, 2013.
[8] Kempe, T.: Fröhlich, J.: An improved immersed boundary method with direct forcing for the simulation of particle laden flows. J. Comput. Phys. 231 (2012) 3663-3684.
[9] Schwarz, S.: Fröhlich, J.: Numerical study of single bubble motion in liquid metal exposed to a longitudinal magnetic field. Int. J. Multiphase Flow. 62 (2014) 134-151.

Two-dimensional nonlinear travelling waves in MHD channel flow

HAGAN, J. and PRIEDE, J.
Applied Mathematics Research Centre, Coventry University, United Kingdom
haganj@coventry.ac.uk; j.priede@coventry.ac.uk

Abstract: The present study is concerned with the stability of a flow of viscous conducting liquid driven by pressure gradient in the channel between two parallel walls subject to a transverse magnetic field. Although the magnetic field has a strong stabilizing effect, this flow, similarly to its hydrodynamic counterpart – plane Poiseuille flow, is known to become turbulent significantly below the threshold predicted by linear stability theory. We investigate the effect of the magnetic field on 2D nonlinear travelling-wave states which are found at substantially subcritical Reynolds numbers starting from $Re_n = 2939$ without the magnetic field and from $Re_n \sim 6.50 \times 10^3 Ha$ in a sufficiently strong magnetic field defined by the Hartmann number Ha. Although the latter value is by a factor of seven lower than the linear stability threshold $Re_l \sim 4.83 \times 10^4 Ha$, it is still more by an order of magnitude higher than the experimentally observed value for the onset of turbulence in this flow.

1 Introduction

The flow of viscous incompressible liquid driven by a constant pressure gradient in the channel between two parallel walls, which is generally known as plane Poiseuille or simply channel flow, is one of the simplest and most extensively studied models of hydrodynamic instabilities and transition to turbulence in shear flows. The development of turbulence in the magnetohydrodynamic (MHD) counterpart of this flow, which is known as Hartmann flow and arises when a conducting liquid flows in the presence of a transverse magnetic field, is currently not so well understood. The MHD channel flow, which was first described theoretically by Hartmann [1] is still an active subject of research [2, 3].

The present study is concerned with finding such 2D travelling-wave states in Hartmann flow. Starting from plane Poiseuille flow, we trace such subcritical equilibrium states by gradually increasing the magnetic field. Using an accurate numerical method based on Chebyshev collocation approximation and a sufficiently large number of harmonics we find such states extend to subcritical Reynolds number $R_n \approx 6500$ which is almost by a factor of two smaller than that predicted by the mean-field approximation [5].

2 Formulation of problem

Consider the flow of an incompressible viscous electrically conducting liquid with density ρ, kinematic viscosity ν and electrical conductivity σ driven by a constant gradient of pressure p in the channel of the width $2h$ between two parallel walls in the presence of a transverse homogeneous magnetic field $\vec{B}$. The velocity distribution of the flow $\vec{v}(\vec{r},t)$ is governed by the Navier-Stokes equation $\partial_t \vec{v} + (\vec{v}\cdot\vec{\nabla})\vec{v} = -\rho^{-1}\vec{\nabla}p + \nu\vec{\nabla}^2\vec{v} + \rho^{-1}\vec{f}$, where $\vec{f} = \vec{j}\times\vec{B}$ is the electromagnetic body force containing the induced electric current $\vec{j}$, which is governed by Ohm's law for a moving medium $\vec{j} = \sigma(\vec{E} + \vec{v}\times\vec{B})$, where $\vec{E}$ is the electric field in the stationary frame of reference. The flow is assumed to be sufficiently slow that the induced magnetic field is negligible relative to the imposed one. This supposes a small magnetic Reynolds number

$Re_m = \mu_0 \sigma v_0 h \ll 1$, where μ_0 is the permeability of vacuum and v_0 is the characteristic velocity of the flow. In addition, we assume that the characteristic time of velocity variation is much longer than the magnetic diffusion time $\tau_m = \mu_0 \sigma h^2$. This allows us to use the quasi-stationary approximation leading to $\vec{E} = -\vec{\nabla}\phi$, where ϕ is the electrostatic potential. The velocity and current satisfy mass and charge conservation $\vec{\nabla} \cdot \vec{v} = \vec{\nabla} \cdot \vec{j} = 0$. Applying the latter to the Ohm's law yields $\vec{\nabla}^2 \phi = \vec{B} \cdot \vec{\omega}$, where $\vec{\omega} = \vec{\nabla} \times \vec{v}$ is vorticity. At the channel walls S, the normal (n) and tangential (τ) velocity components satisfy the impermeability and no-slip boundary conditions $v_n|_s = 0$ and $v_\tau|_s = 0$. Electrical conductivity of the walls is irrelevant for the type of flow considered in this study.

We employ right-handed Cartesian coordinates with the origin set at the mid-height of the channel, the x- and the z-axes directed, respectively, against the applied pressure gradient $\vec{\nabla} p_0 = P\vec{e}_x$ and along the magnetic field $\vec{B} = B\vec{e}_z$ so that the channel walls are located at $z = \pm h$, and the velocity is defined as $\vec{v} = (u, v, w)$. Subsequently, all variables are non-dimensionalised by using h, h^2/ν and $Bh\nu$ as the length, time and electric potential scales, respectively. The velocity is scaled by the viscous diffusion speed ν/h, which we employ as the characteristic velocity instead of the commonly used centreline velocity.

The problem admits a rectilinear base flow $\vec{v}_0(z) = \bar{u}_0(z)\vec{e}_x = Re\,\bar{u}(z)\vec{e}_x$ for which the Navier-Stokes equation reduces to $\bar{u}'' - Ha^2\bar{u} = \bar{P}$, where $Re = Uh/\nu$ is the Reynolds number based on the centreline velocity U, $Ha = dB\sqrt{\sigma/\rho\nu}$ is the Hartmann number, and $\bar{P}$ is a dimensionless pressure gradient satisfying the normalization condition $\bar{u}(0) = 1$. This equation defines the well-known Hartmann flow profile $\bar{u}(z) = \frac{\cosh(Ha) - \cosh(zHa)}{\cosh(Ha) - 1}$ with $\bar{P} = -\frac{Ha^2 \cosh(Ha)}{\cosh(Ha) - 1}$, which relates the centreline velocity with the applied pressure gradient $P = \bar{P}U\nu\rho/h^2$. In the weak magnetic field $(Ha \ll 1)$, the Hartman flow reduces to the classic plane Poiseuille flow $\bar{u}(z) = 1 - z^2$.

3 Theoretical background

3.1 Linear stability of the base flow

The two-dimensional travelling waves considered this study are expected to emerge in the result of linear instability of the Hartmann flow with respect to infinitesimal perturbations $\vec{v}_1(\vec{x}, t)$. Owing to the invariance of the base flow in both t and $\vec{x} = (x, y)$, perturbations are sought as Fourier modes $\vec{v}_1(\vec{r}, t) = \hat{\vec{v}}(z)e^{\lambda t + i\vec{k}\cdot\vec{x}} + \text{c.c.}$ defined by complex amplitude distribution $\hat{\vec{v}}(z)$, temporal growth rate λ and the wave vector $\vec{k} = (\alpha, \beta)$. The incompressibility constraint, which takes the form $\vec{D}_k \cdot \hat{\vec{v}} = 0$, where $\vec{D}_k \equiv \vec{e}_z \frac{\mathrm{d}}{\mathrm{d}z} + i\vec{k}$ is a spectral counterpart of the nabla operator, is satisfied by expressing the component of the velocity perturbation in the direction of the wave vector as $\hat{u}_{\shortparallel} = \vec{e}_{\shortparallel} \cdot \hat{\vec{v}} = ik^{-1}\hat{w}'$, where $\vec{e}_{\shortparallel} = \vec{k}/k$ and $k = |\vec{k}|$. Taking the *curl* of the linearised Navier-Stokes equation to eliminate the pressure gradient and then projecting it onto $\vec{e}_z \times \vec{e}_{\shortparallel}$, after some transformations we obtain a modified Orr-Sommerfeld type equation which includes a magnetic term

$$\lambda \vec{D}_k^2 \hat{w} = \left[\vec{D}_k^4 - Ha^2(\vec{e}_z \cdot \vec{D}_k)^2 + ikRe(\bar{u}'' - \bar{u}\vec{D}_k^2)\right]\hat{w}. \tag{1}$$

The no-slip and impermeability boundary conditions require $\hat{w} = \hat{w}' = 0$ at $z = \pm 1$. The equation above is written in a non-standard form corresponding to our choice of the characteristic velocity. Note that the Reynolds number appears in this equation as a factor at the convective term rather than its reciprocal at the viscous term as in the standard form. As a result, the growth rate λ differs by a factor Re from its standard definition.

Since the equation above as its non-magnetic counterpart admits Squire's transformation, in the following we consider only two-dimensional perturbations ($k = \alpha$), which are the most unstable. The problem is solved numerically using the Chebyshev collocation method which is described in detail in Ref. [4].

3.2 Nonlinear 2D travelling waves

Two-dimensional travelling waves emerge as follows. First, the neutrally stable mode with a purely real frequency $\omega = -\mathrm{i}\lambda$ interacting with itself through the quadratically nonlinear term in the Navier-Stokes equation produces a steady streamwise invariant perturbation of the mean flow as well as a second harmonic $\sim \mathrm{e}^{2\mathrm{i}(\omega t+\alpha x)}$. Further nonlinear interactions produce higher harmonics, which similarly to the fundamental and second harmonic travel with the same phase speed $c = -\omega/\alpha$. Thus, the solution can be sought in the form$\vec{v}(\vec{r},t) = \sum_{n=-\infty}^{\infty} E^n \vec{\hat{v}}_n(z)$,where $E = \mathrm{e}^{\mathrm{i}(\omega t+\alpha x)}$ contains ω, which needs to determined together $\vec{\hat{v}}_n$ by solving a non-linear eigenvalue problem. The reality of solution requires $\vec{\hat{v}}_{-n} = \vec{\hat{v}}_n^*$, where the asterisk stands for the complex conjugate. The incompressibility constraint applied to the nth velocity harmonic results in $\vec{D}_{\alpha_n} \cdot \vec{\hat{v}}_n = 0$, where $\vec{D}_{\alpha_n} \equiv \vec{e}_z \frac{\mathrm{d}}{\mathrm{d}z} + \mathrm{i}\vec{e}_x \alpha_n$ with $\alpha_n = \alpha n$ stands for the spectral counterpart of the nabla operator. This constraint can be satisfied by expressing the streamwise velocity component $\hat{u}_n = \vec{e}_x \cdot \vec{\hat{v}}_n = \mathrm{i}\alpha_n^{-1} \hat{w}_n'$ in terms of the transverse component $\hat{w}_n = \vec{e}_z \cdot \vec{\hat{v}}_n$, which we employ instead of the commonly used stream function. Henceforth, the prime is used as a shorthand for d/dz. Note that the previous expression is not applicable to the zeroth harmonic, for which it yields $\hat{w}_0 \equiv 0$. Thus, $\hat{u}_0$ needs to be considered separately in this velocity-based formulation.

Taking the *curl* of the Navier-Stokes equation to eliminate the pressure gradient and then projecting it onto $\vec{e}_y$, we obtain

$$[\vec{D}_{\alpha_n}^2 - \mathrm{i}\omega n]\hat{\zeta}_n - Ha^2 \hat{u}_n' = \hat{h}_n, \tag{2}$$

where

$$\hat{\zeta}_n = \vec{e}_y \cdot \vec{D}_{\alpha_n} \times \vec{\hat{v}}_n = \begin{cases} \mathrm{i}\alpha_n^{-1} \vec{D}_{\alpha_n}^2 \hat{w}_n, & n \neq 0; \\ \hat{u}_0', & n = 0. \end{cases} \tag{3}$$

and $\hat{h}_n = \sum\limits_m \vec{\hat{v}}_{n-m} \cdot \vec{D}_{\alpha_m} \hat{\zeta}_m$ are the y-components of the nth harmonic of the vorticity $\vec{\zeta} = \vec{\nabla} \times \vec{v}$ and that of the *curl* of the nonlinear term $\vec{h} = \vec{\nabla} \times (\vec{v} \cdot \vec{\nabla})\vec{v}$. Henceforth, the omitted summation limits are assumed to be infinite. Separating the terms involving $\hat{u}_0$, the previous expression for h can be rewritten as $\hat{h}_n = \mathrm{i}\alpha_n^{-1}(\hat{h}_n^w + \hat{h}_n^u)$, where

$$\hat{h}_n^w = n \sum_{m \neq 0} m^{-1} (\hat{w}_{n-m} \vec{D}_{\alpha_m}^2 \hat{w}_m' - \hat{w}_m' \vec{D}_{\alpha_{n-m}}^2 \hat{w}_{n-m}), \tag{4}$$

$$\hat{h}_n^u = \mathrm{i}\alpha_n [\hat{u}_0 - \hat{u}_0'' \vec{D}_{\alpha_n}^2] \hat{w}_n \equiv \mathscr{N}_n(\hat{u}_0)\hat{w}_n. \tag{5}$$

Eventually, using the expressions above, (2) can be written as $\mathscr{L}_n(\mathrm{i}\omega, \hat{u}_0)\hat{w}_n = \hat{h}_n^w$ with the operator

$$\mathscr{L}_n(\mathrm{i}\omega, \hat{u}_0) = [\vec{D}_{\alpha_n}^2 - \mathrm{i}\omega n]\vec{D}_{\alpha_n}^2 - Ha^2(\vec{e}_z \cdot \vec{D}_{\alpha_n})^2 - \mathscr{N}_n(\hat{u}_0). \tag{6}$$

This equation governs all harmonics except the zeroth one, for which, in accordance with the incompressibility constraint it implies $\hat{w}_0 \equiv 0$. Zeroth velocity harmonic, which has only the streamwise component $\hat{u}_0$, is governed directly the x-component of the Navier-Stokes equation: $\hat{u}_0'' - Ha^2 \hat{u}_0 = \hat{P}_0 + \hat{g}_0$,where $\hat{P}_0 = \bar{P}Re$ is a dimensionless mean pressure gradient and $\hat{g}_0 =$

$\mathrm{i}\sum_{m\neq 0}\alpha_m^{-1}\hat{w}_m^*\hat{w}_m''$ is the x-component of the zeroth harmonic of the nonlinear term $\vec{g}=(\vec{v}\cdot\vec{\nabla})\vec{v}$. Velocity harmonics are subject to the usual no-slip and impermeability boundary conditions $\hat{w}_n=\hat{w}_n'=\hat{u}_0=0$ at $z=\pm 1$.

4 Results

Weakly nonlinear analysis shows that the instability of the Hartmann flow is invariably subcritical regardless of the magnetic field strength [3]. In the present study, we determine how far the subcritical equilibrium states, which bifurcate from the Hartmann flow, extend below the linear stability threshold. Let us first validate our method described in Sec. 3.2 by computing critical Reynolds number for 2D travelling waves in plane Poiseuille flow, which corresponds to $Ha=0$. To characterize the deviation of the velocity distribution from the base state, besides the transverse velocity amplitude A, we use also the amplitude associated with the energy of perturbation scaled by the energy of the basic flow $A_E^2=\int_0^1\langle|\vec{v}(x,z)-\vec{v}_0(z)|^2\rangle dz/\int_0^1|\vec{v}_0(z)|^2dz$, where the angular brackets denote for the streamwise average.

We start with a relatively low Hartmann number $Ha=1$ for which the flow becomes linearly unstable at $Re_l=10016.3$ with $\alpha_l=0.971827$ [3]. The energy amplitude of equilibrium states versus the wavenumber is plotted in figure 1 for various subcritical values of Re. As for the non-magnetic plane Poiseuille flow, equilibrium states form closed contours, which shrink as Re is reduced, and collapse to a point at the critical $Re_n=3961.36$ below which 2D travelling waves vanish. It means that subcritical perturbations have both a lower and an upper equilibrium amplitude. Both these amplitudes are plotted in figure 1 together with the respective value of $\hat{w}_1''(1)$, which is the quantity predicted by the weakly nonlinear analysis [3]. As seen, the the lower branch of $\hat{w}_1''(1)$ is predicted well by weakly nonlinear solution for subcritical Reynolds numbers down to $Re\approx 7000$.

A similar structure of subcritical equilibrium states is found also for $Ha=5$ and $Re_n=43\,8302$. At this large Re it becomes difficult to compute accurately the upper equilibrium states which require the numerical resolution of at least 48×32. The strongly subcritical states, which in this case extend down to $Re_n\approx 32860$, can reliably be computed with a substantially lower resolution of 48×10. In the following, we focus on such strongly subcritical Reynolds numbers at which 2D travelling waves emerge. The respective Reynolds number defines what is subsequently referred to as the 2D nonlinear stability threshold.

The critical Reynolds number and wavenumber for 2D nonlinear stability threshold are

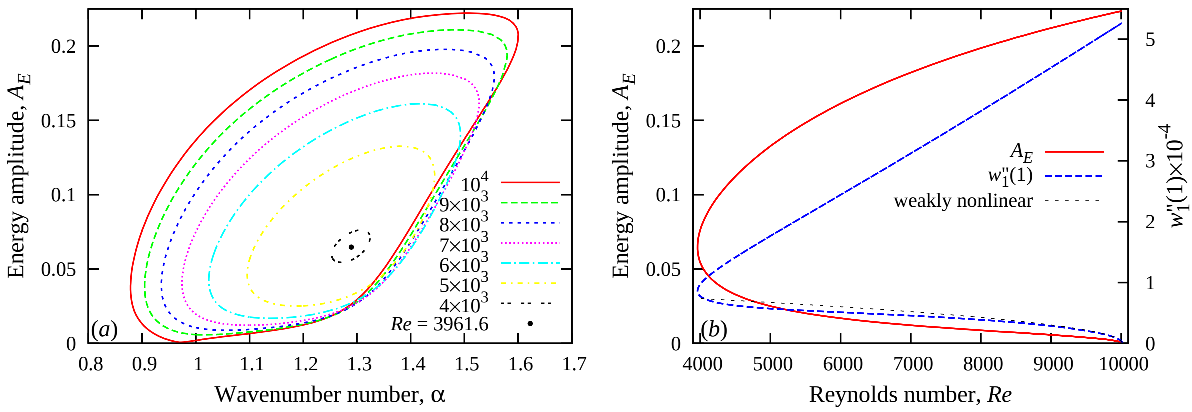

Figure 1: The energy amplitude of equilibrium states versus the wavenumber α for $Ha=1$ and various Re computed with the resolution $M\times N=32\times 8$.

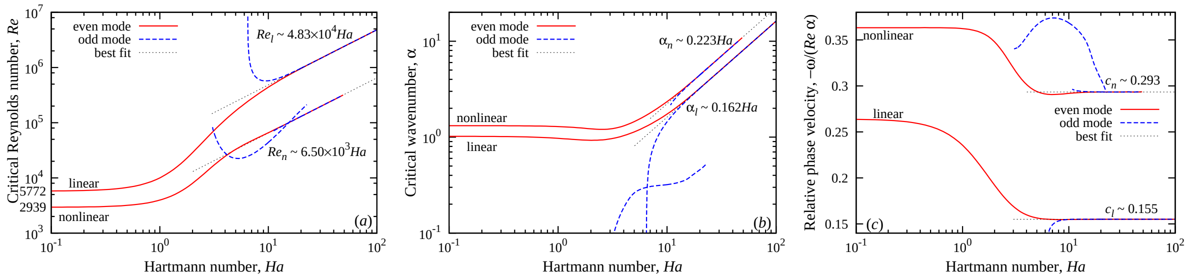

Figure 2: Critical Reynolds number (a), wavenumber (b) and phase speed (c) for even and odd modes of linear and nonlinear instabilities against the Hartmann number.

shown in figure 2 together with critical parameters for linear stability versus the Hartmann number [3]. At small Hartmann numbers, instability is associated with the even mode for which 2D travelling waves appear at $Re_n = 2939$. As the Hartmann number exceeds $Ha \approx 2.8$, which is about half of the respective value for the linear instability, an odd equilibrium mode appears with a large Reynolds number and a small wavenumber. This long-wave odd mode exists only within a limited range of Hartmann numbers up to $Ha \approx 20$. At $Ha \approx 10$ another odd mode appears with a slightly higher Reynolds number but much shorter wavelength. At $Ha \approx 15$ Reynolds number of the latter mode becomes smaller than that for the long-wave mode. The characteristics of this short-wave odd mode are seen closely approaching those of the original even mode. In a sufficiently strong magnetic field, the critical Reynolds number and wavenumber for both nonlinear modes increase with the Hartmann number similarly to the respective threshold parameters of the linear instability [3]. Namely, for $Ha \gtrsim 20$ the best fit yields $Re_n \sim 6.50 \times 10^3 Ha, \alpha_n \sim 0.223Ha, c_n \sim 0.293$. It is important to notice that the critical Reynolds number above is almost by an order of magnitude lower than that for the linear instability $Re_l \sim 48\,300Ha$. In the mean-field approximation using only one harmonic, we find $Re_n \sim 12\,300Ha$, which is almost by a factor of two higher than the accurate result above and coincides with the result reported by [5].

References

[1] Hartmann, J.: Hg–dynamics I. Theory of the laminar flow of an electrically conductive liquid in a homogeneous magnetic field. *K. Dan. Vidensk. Selsk. Mat. Fys. Medd.* **15**(6) (1937) 1–28.

[2] Krasnov, D., Thess, A., Boeck, T., Zhao, Y. & Zikanov, O. (2013) Patterned turbulence in liquid metal flow: Computational reconstruction of the Hartmann experiment. *Phys. Rev. Lett.* **110**, 084501–5.

[3] Hagan, J.; Priede, J.: Weakly nonlinear stability analysis of MHD channel flow using an efficient numerical approach, *Phys. Fluids* 25 (2013) 124108

[4] Hagan, J.; Priede, J.: Capacitance matrix technique for avoiding spurious eigenmodes in the solution of hydrodynamic stability problems by Chebyshev collocation method, *J. Comp. Phys.* **238** (2013) 210–216.

[5] Lifshits, A. M.; Shtern, V. N.: Monoharmonic analysis of the nonlinear stability of Hartmann flow. *Magnetohydrodynamics* **15** (1980) 243–258.

Stability boundaries of axisymmetric and two-dimensional perturbations in MHD Dean flow

Yang Yu[1,2], Thomas Boeck[2]
[1]Northeastern University, P. O. Box 314, 110004 Shenyang, China
[2]Institute of Thermodynamics and Fluid Mechanics,
TU Ilmenau, P.O. Box 100565, 98684 Ilmenau, Germany

Abstract. We study the linear stability of annular MHD channel flow with a uniform axial magnetic field in order to determine when two-dimensional instabilities of Orr type can appear. They are a prerequisite for intermittent turbulent behavior known from plane MHD channel flow with a spanwise field. The annular flow is driven by Lorentz forces caused by a radial electric current and the imposed axial field. Stability of this MHD Dean flow is investigated for axially uniform Orr modes and axisymmetric Dean modes. Orr mode instability dominates only for small gap width and in strong magnetic fields.

Introduction. The interaction of flows of liquid metals and other conducting liquids with magnetic fields can be used for flow control or measurement purposes in metallurgy and other materials processing applications. Typically, the magnetic field has a damping effect in such MHD flows. The flow structures in wall-bounded MHD flows are also modified due to electromagnetic boundary layers. Transition to turbulence and the properties of turbulent MHD flows can therefore differ significantly from non-MHD flows. Such questions have been explored by computational studies in recent years since experiments are difficult and typically provide only very limited information on such flows.

The selective damping of gradients in the flow along the direction of the magnetic field can also favor flow instabilities that are otherwise superseded by other processes. An example is the so-called large-scale intermittency (LSI) in plane MHD channel flow with a homogeneous spanwise field found in a number of computational studies [1, 2]. In this problem, the viscous instability of Orr modes (also called Tollmien-Schlichting modes) is unaffected by the magnetic damping but the growth of non-modal perturbations normally causing bypass transition is suppressed. One therefore finds a cyclic evolution between the unstable laminar state and turbulent flow that is quickly suppressed by Joule dissipation. Experimental verification of this phenomenon is missing so far and may be difficult to achieve due to the additional friction at Hartmann walls that are not taken into account in channel flow simulations of LSI. Another problem is the generation of a sufficiently strong and homogeneous field over a sufficient length of a straight channel. Experimentally it is preferable to use an annular channel that can be placed in the bore of a solenoid magnet, which generates an axial field. The flow can then be driven by an azimuthal Lorentz force that results from applying a radial current between the cylindrical walls of the annular channel [3]. The problem in this setup is the presence of centrifugal instabilities that may supersede the Orr mode instability. In the present paper we therefore consider the magnetic damping of such centrifugal instabilities. The goal is to identify parameters where Orr mode instability prevails so that the LSI could be observed at least in principle.

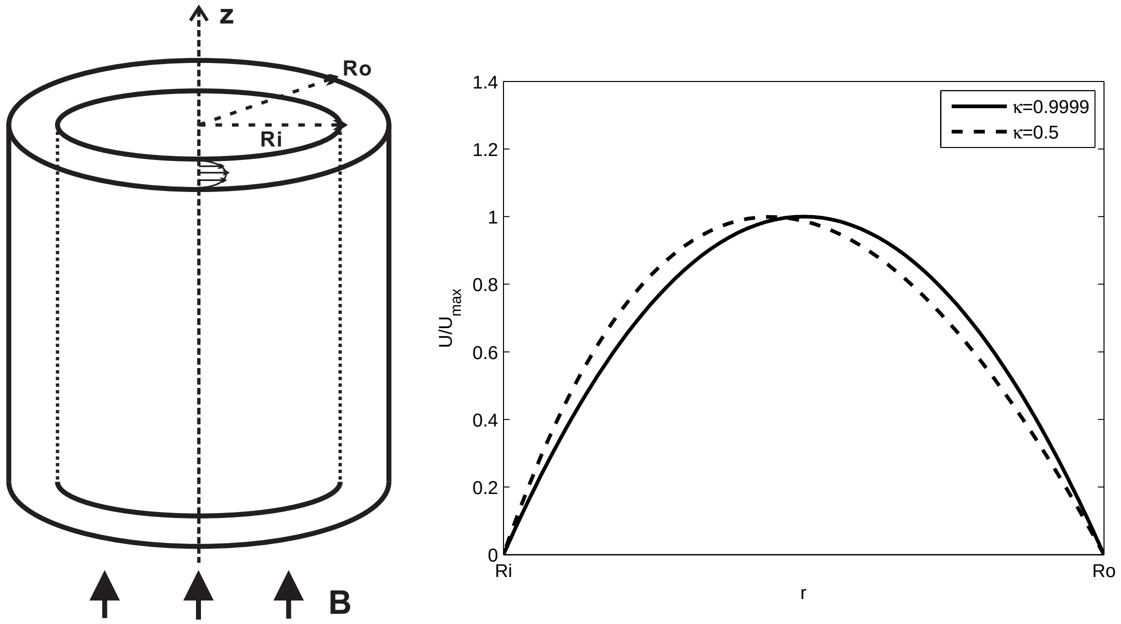

Figure 1: Sketch of the geometry (left) and basic flow structure (right)

Previous studies have focused on the narrow gap approximation [4]. We consider the problem without making this assumption. End walls have to be neglected in order to obtain one-dimensional stability problems that can be solved with modest computational expense.

Governing equations and parameters. We consider the flow of an incompressible electrically conducting fluid with conductivity σ, density ρ and kinematic viscosity ν in the gap between two concentric cylinders. A potential difference is imposed between the cylinders, which are assumed to be perfectly conducting. The driving Lorentz force results from the interaction between the imposed uniform axial magnetic field $\boldsymbol{B}_0 = B_0\boldsymbol{e}_z$ and the radial electric current. The base flow has only an azimuthal velocity component, which depends on the radial coordinate. End walls in the axial direction are not taken into account. Fig. 1 shows the basic geometry schematically.

The governing equations for velocity $\boldsymbol{u}$ and electric potential ϕ in the quasistatic approximation are the Navier-Stokes equations together with Ohm's law for the current density $\boldsymbol{j}$ and charge conservation, i.e.

$$\frac{\partial \boldsymbol{u}}{\partial t} + (\boldsymbol{u}\cdot\nabla)\boldsymbol{u} = -\frac{1}{\rho}\nabla p + \nu\nabla^2\boldsymbol{u} + \frac{1}{\rho}\boldsymbol{j}\times\boldsymbol{B}_0, \tag{1}$$

$$\nabla\cdot\boldsymbol{u} = 0, \tag{2}$$

$$\boldsymbol{j} = \sigma(-\nabla\phi + \boldsymbol{u}\times\boldsymbol{B}_0), \tag{3}$$

$$\nabla\cdot\boldsymbol{j} = 0 \leftrightarrow \nabla^2\phi = \nabla\cdot(\boldsymbol{u}\times\boldsymbol{B}_0)\,. \tag{4}$$

In the following we use cylindrical coordinates r, θ and z and corresponding vector components. Boundary conditions are zero velocity and fixed electric potentials ϕ_i and ϕ_o at the inner and outer walls located at $r = R_i$ and $r = R_o$. For the presentation of results we introduce the ratio

$$\kappa = R_i/R_o \tag{5}$$

to characterize the influence of curvature with $\kappa = 1$ corresponding to plane channel flow.

The Reynolds number

$$Re = \bar{U}d/\nu \tag{6}$$

is defined with the average azimuthal velocity $\bar{U}$ and the gap width $d = R_o - R_i$ Finally, the Hartmann number is defined by

$$Ha = dB_0\sqrt{\sigma/\rho\nu}. \tag{7}$$

The basic velocity distribution of this so-called Dean flow has only the azimuthal component $u_\theta = V$ that depends on r and κ. It is given by

$$V(\eta) = \bar{U}C(\kappa)\left\{\eta\log\eta + \frac{\kappa^2\log\kappa}{1-\kappa^2}\left[\eta - \eta^{-1}\right]\right\}, \tag{8}$$

where $\eta = r/R_o$ and C is determined by the imposed volume flux. Fig. 1 shows that $V(\eta)$ is asymmetric and that it approaches the parabolic profile for $\kappa \to 1$.

The linear stability analysis using normal modes requires linearization of eq. (1-4) about $V(\eta)$. Normal modes are periodic in both θ and z, i.e. they are exponentials

$$\exp(i\omega t)\exp(im\theta)\exp(i\alpha z) \tag{9}$$

in θ, z and time t with complex frequency ω, an integer azimuthal wave number m and a real axial wavenumber α.

We are not interested in general perturbations with both m and α non-zero. For the non-magnetic case the flow typically becomes first unstable to axisymmetric perturbations ($m = 0$) called Dean modes. Intermittency in plane MHD channel flow requires a linear instability to Orr modes unaffected by the magnetic field, i.e. with $\alpha = 0$. We want to find conditions where similar behavior may be obtained in direct numerical simulations (DNS) of the Dean flow, i.e. parameter combinations of κ, Re, and Ha where the basic flow is only unstable with respect to the Orr mode. We therefore determine the neutral stability limits of Orr modes with $\alpha = 0$ and Dean modes with $m = 0$.

Two-dimensional Orr modes ($\alpha = 0$) have radial and azimuthal components that can be represented by a stream function $\psi = f(r)\exp(im\theta + i\omega t)$. Dean modes have all three velocity components. Each of them takes the form $g(r)\exp(i\alpha z + i\omega t)$. In either case, we use an expansion in Chebyshev polynomials for discretization in the radial coordinate. A linear algebraic eigenvalue problem for ω is then obtained by means of a Chebyshev collocation method and solved in MATLAB using the QZ algorithm. Neutral conditions are then determined by varying either Re or Ha until $\omega_i = 0$ is achieved.

An alternative approach is possible by DNS, which have also been used for stability studies in the same geometry [5].

Results and discussion. We first consider the Orr modes, which depend on κ and Re. In plane channel (Poiseuille) flow Orr modes become unstable at $Re_P^c \approx 5772$ with a nondimensional wavenumber $\alpha_P^c = 1.02$ based on $d/2$, i.e. a dimensional wavelength of $d\pi/\alpha_P^c$ [6]. These values should be recovered in the limit $\kappa \to 1$. We have therefore started our computations near $\kappa = 1$. In contrast to plane channel flow the wavenumber m has to be integer. This leads to significant changes when κ becomes small since the values of m are then fairly low. The results are shown in Fig. 2. We see that Re_c increases as κ is reduced until it reaches a maximum near $\kappa = 0.55$. The subsequent decrease is due to a switch from $m = 3$ to $m = 2$. Below $\kappa \approx 0.45$ the $m = 2$ branch does not exist. Fig. 2 also shows Re_c and the wavenumber m for plane Poiseuille flow for comparison with the Dean

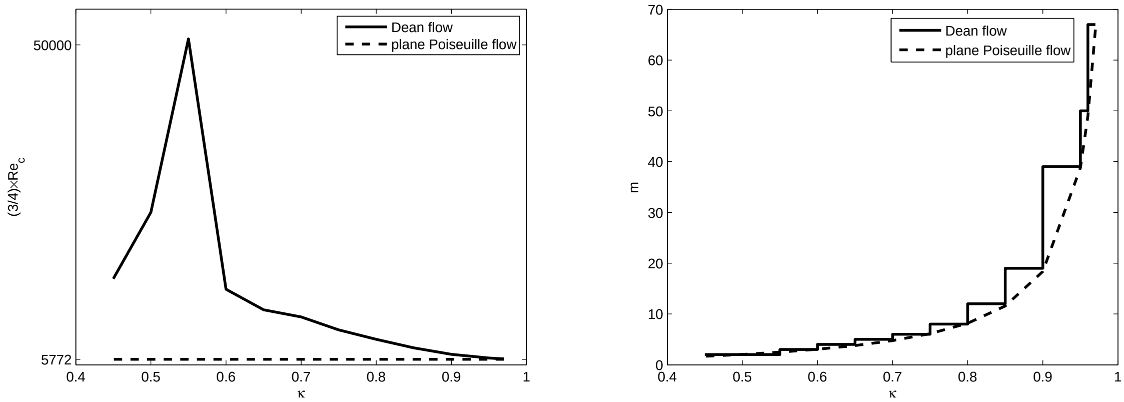

Figure 2: Stability limits of Orr modes (left) and corresponding azimuthal wavenumbers m (right) as function of the radius ratio κ. In plane channel flow the Reynolds number is based on the maximum velocity and the channel half-width, hence the prefactor 3/4.

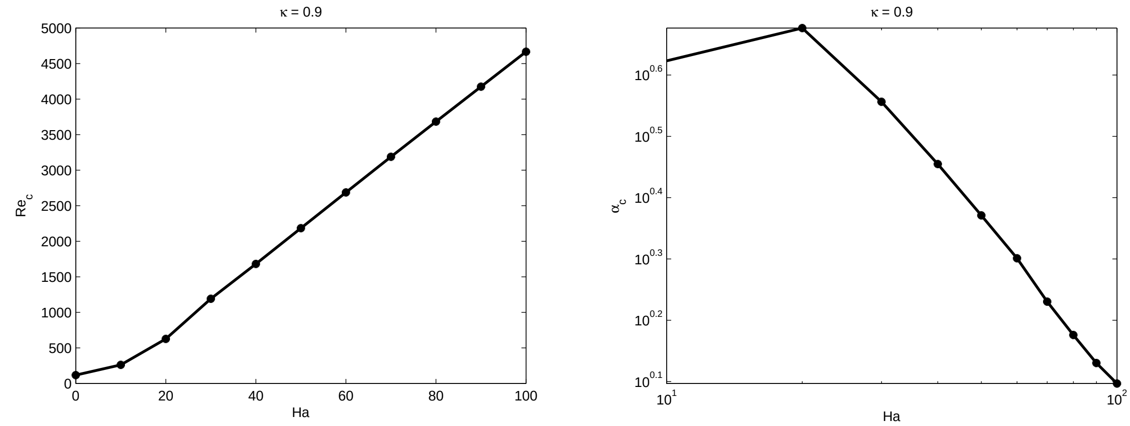

Figure 3: Critical Reynolds number of Dean mode for $\kappa = 0.9$ (left) and corresponding axial wavenumber (right).

flow. The wavenumber m for Poiseuille flow has been computed as $m = 2\alpha_c^P \kappa/(1-\kappa)$, i.e. as the ratio of the the circumference of the inner cylinder to the critical wavelength $d\pi/\alpha_P^c$. We see that this provides a fairly good estimation of m except for low $\kappa < 0.6$. The discontinuous changes in m for the Dean flow should normally proceed in increments $\Delta m = 1$. The larger jumps in Fig. 2 are due to the finite number of κ values explored in our computations.

For Dean modes the non-magnetic stability limit Re_c has been computed in the narrow-gap approximation. It is given by [4]

$$Re_c \approx 35.94\sqrt{\kappa/(1-\kappa)}, \qquad \alpha_c \approx 3.96, \tag{10}$$

where the nondimensional wavenumber α_c is based on the length d. We have first verified these results for κ close to unity. Finite values of Ha lead to a monotonous increase in Re_c due to the magnetic damping. It becomes linear in Ha when Ha is sufficiently large, i.e. the slope dRe_c/dHa is constant. The corresponding axial wave numbers α_c decrease as $1/Ha$. Both effects are illustrated in Fig. 3. In contrast to Re_c, α_c hardly change with κ. However, at fixed Ha Re_c increases strongly with κ.

Based on our results, we have determined regions in the Re-Ha plane where Dean

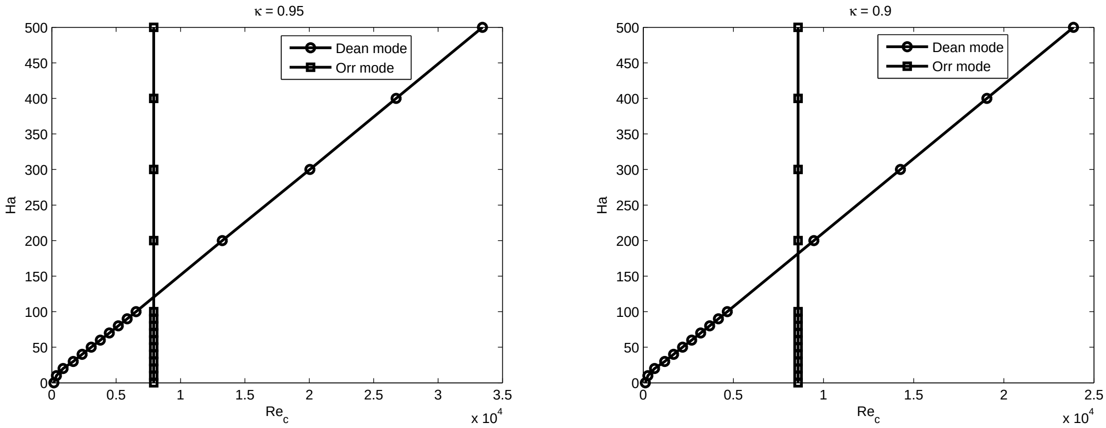

Figure 4: Stability limits in the Re-Ha-plane for Orr modes and Dean modes for $\kappa = 0.9$ (left) and $\kappa = 0.95$ (right).

modes are sufficiently suppressed by the magnetic damping so that the Orr modes become unstable first. Fig. 4 shows two different values of κ. Orr modes are unstable for $Re > Re_c^O$ irrespective of Ha. The Dean modes are unstable for $Re > Re_c^D(Ha)$, i.e. below the corresponding limiting curve in the Re-Ha-plane. The region of Orr mode instability lies therefore in the upper triangular section of the plane. The minimum values of Ha are substantial and increase strongly when κ is reduced.

Conclusions. The Dean mode instability can only be suppressed in favor of Orr modes when the gap width is small and the Hartmann number is substantial. For this reason, experiments in a parameter range where LSI could potentially exist would require a substantial diameter of the annular channel as well as fairly strong fields. Investigation of the effects due to end walls requires DNS at large values of κ and high aspect ratios of axial size to gap width.

Acknowledgments. We are grateful to O. Zikanov and D. Krasnov for interesting discussions. YY's work is supported by the China Scholarship Council. TB acknowledges financial support from the Deutsche Forschungsgemeinschaft.

References

[1] Boeck, T., Krasnov, D., Thess, A. and Zikanov, O.: Large-scale intermittency of liquid-metal channel flow in a magnetic field. Phys. Rev. Lett. 101 (2008) 244501.

[2] Dey, P. and Zikanov, O.: Scalar transport and perturbation dynamics in intermittent magnetohydrodynamic flow. Phys. Fluids 24 (2012) 084104.

[3] Moresco, P. and Alboussière, T.: Experimental study of the instability of the Hartmann layer. J. Fluid Mech. 504 (2004) 167-181.

[4] Chandrasekhar, S.: *Hydrodynamic and Hydomagnetic Stability.* Oxford University Press (1961).

[5] Zhao, Y., Zikanov, O., and Krasnov, D.: Instability of magnetohydrodynamic flow in an annular channel at high Hartmann number. Phys. Fluids 23 (2011) 084103.

[6] Orszag, S. A.: Accurate solution of the Orr-Sommerfeld stability equation. J. Fluid Mech. 50 (1971) 689-703.

Secondary Instability of Hartmann Layers in Plane MHD Channel Flow

Shuai Dong[1], Dmitry Krasnov[2], Thomas Boeck[2]
[1]Dept. of Power Eng., North China Electric Power University, 071003 Baoding, China
[2]Dept. of Mech. Eng., TU Ilmenau, 98684 Ilmenau, Germany

Abstract. We consider the transient amplification of primary and secondary linear perturbations in a Hartmann channel flow at low and moderate Hartmann numbers. We explore primary perturbations of different vertical symmetry in order to examine influences due to the finite distance between the channel walls. Secondary perturbations at opposite walls can be shown to interact at larger Hartmann numbers than primary perturbations. Strong amplification of secondary perturbations due to inflectional instability mechanisms is found when the primary perturbations have a sufficiently large amplitude.

Introduction. When an incompressible and electrically conducting liquid flows between two unbounded parallel plates under the presence of an uniform and constant magnetic field perpendicular to the walls, the profile of the mean flow becomes flat in the core due to the interaction of the induced electric current with the imposed magnetic field. Meanwhile, two thin boundary layers develop at the walls. They are named after Julius Hartmann [1], who first investigated MHD channel flow in 1937. The thickness δ_{Ha} of these layers is inversely proportional to the magnetic field B, which is characterized by a non-dimensional parameter called the Hartmann number Ha. When Ha is sufficiently large, the Hartmann layers at the top and the bottom walls do not overlap and can be considered as independent from each other. An isolated Hartmann layer could become unstable when the local Reynolds number R, which is defined with δ_{Ha} as length scale, exceeds some threshold.

The stability of Hartmann layers has been explored experimentally in laminarization studies to determine at which values of R_c turbulent flow becomes laminar. Early works showed that re-laminarization may occur in the range $150 < R_c < 250$. A recent experiment [2] found $R_c \sim 380$ from measurements of the friction coefficient as function for R. The same R_c was observed for the inverse process of transition from laminar flow to turbulence.

The stability of Hartmann layers was first studied by normal mode analysis. It turned out that exponential growth of infinitesimal perturbations appears at values of R two orders of magnitude higher than R_c in the experiments [3]. This is similar to other shear flows, e.g. pipe flow, where classical normal mode stability analysis fails to predict transition. Recent developments in linear stability theory revealed that the transient amplification of non-modal perturbations may play a significant role in the so-called subcritical transition of shear flows [4]. For plane channel flow, streamwise vortices provide the strongest amplification. Such streamwise vortices interact with the mean flow and evolve into streamwise streaks, which are viewed a key element in the transition scenario and the dynamic processes sustaining turbulence. Based on these ideas, Krasnov et al.

[5] explored a reasonable two-step transition scenario for the Hartmann layer by direct numerical simulations (DNS). It consists of (i) large transient growth of initially small, streamwise-independent disturbances that leads to a modulation of the laminar Hartmann flow, and (ii) the linear instability of the modulated flow with respect to some three-dimensional secondary perturbations. Transition could be triggered when both R and the amplitude of primary and secondary perturbations was sufficiently large. In this way, R_c was found to be between 350 and 400, which is already very close to the experimental results. However, in this work the secondary perturbations were simply strong random noise.

The purpose of the present paper is to analyze the two-step transition scenario in more detail. Guided by similar works on secondary perturbations in hydrodynamic channel flows, we focus on optimal perturbations evolving on Hartmann layer streaks and examine the residual interaction between opposite Hartmann layers at low and moderate Hartmann numbers.

Governing equations, numerical method, parameters. The flow of an incompressible electrically conducting fluid between two unbounded plates is considered in the inductionless approximation. The flow is driven by a constant mass flux and subjected to a constant and uniform magnetic field imposed perpendicularly to the walls. The nondimensional governing equations and boundary conditions are

$$\frac{\partial \boldsymbol{v}}{\partial t} + (\boldsymbol{v} \cdot \nabla)\boldsymbol{v} = -\nabla p + \frac{1}{Re}\nabla^2 \boldsymbol{v} + \frac{Ha^2}{Re}\left(-\nabla\phi \times \boldsymbol{e} + (\boldsymbol{v} \times \boldsymbol{e}) \times \boldsymbol{e}\right), \tag{1}$$

$$\nabla \cdot \boldsymbol{v} = 0, \tag{2}$$

$$\nabla^2 \phi = \nabla \cdot (\boldsymbol{v} \times \boldsymbol{e}), \tag{3}$$

$$u = v = w = \frac{\partial \phi}{\partial z} = 0 \text{ at } z = \pm 1, \quad \text{periodicity in } x \text{ and } y \text{ directions}, \tag{4}$$

where $\boldsymbol{e} \equiv (0, 0, 1)$ and x, y, z denotes streamwise, spanwise and wall normal directions, respectively. The center line velocity U of the laminar Hartmann flow, the half width of the channel L, and the imposed magnetic field strength B have been taken for non-dimensionlization. The nondimensional parameters in the equations above are the Reynolds number $Re \equiv UL/\nu$, and the Hartmann number $Ha \equiv BL\,(\sigma/\rho\nu)^{1/2}$. The local Reynolds number R is $R \equiv Re/Ha$.

For the analysis of secondary perturbations, the governing equations (1–3) are linearized about the modulated MHD Hartmann flow $\mathbf{U}(y, z, t)$. The secondary linear perturbations take the form $\mathbf{u}_p(x, y, z, t) = \mathbf{u}(y, z, t)\exp(i\alpha x)$, where α denotes the streamwise wavenumber. The growth of the perturbations is evaluated by the kinetic perturbation energy. An energy norm is defined as $E(t) = (1/2)\int |\mathbf{u}_p|^2 dV$, thus the ratio of $E(t)$ and the initial perturbation energy $E(0)$ is the perturbation energy amplification factor, $G(t) = E(t)/E(0)$.

Using a Lagrangian formalism, the maximum value $G_{max}(Re, Ha, \tau, \alpha)$ for given parameters is determined via an optimization with two constraints: (i) the perturbation energy $E(0) = 1$; (ii) the perturbation satisfies the linearized governing equations as well as the boundary conditions in the time interval $0 < t < \tau$. The Lagrangian multipliers, so-called adjoint fields, are introduced to enforce these constraints [4]. The optimal perturbation and amplification at the final time τ can be obtained by an iterative scheme, in which forward integration of the linearized governing equation is followed by backward integration of the adjoint equations. Details can be found in Ref. [6].

Results and discussion. Interaction between top and bottom Hartmann layers is first considered for primary optimal perturbations. They are calculated by the same iterative procedure using direct and adjoint equations but with the laminar Hartmann flow profile as basic flow. Since the laminar flow depends only on z, primary perturbations have stream- and spanwise periodicity with wavenumbers α and β. Large transient amplification factors $G(Re, Ha, \tau, \alpha, \beta)$ of such perturbations occur for $\alpha = 0$, i.e. streamwise vortices at initial time $t = 0$ with $\beta > 0$, which evolve into streaks by the lift-up mechanism. The largest amplification $G^I_{max}(Re, Ha)$ occurs for a certain optimal time $\tau = T^I_{opt}$ and wavenumber β_{opt}.

The vertical perturbation structure can be assumed to be antisymmetric or symmetric in z for the initial wall-normal velocity component, which results in an *symmetric* or *antisymmetric* perturbation (with respect to streamwise perturbation velocity). Fig. 1 illustrates such perturbations for $Ha = 10$. They appear to have very similar shape, and show almost identical values G^I_{max} at essentially the same optimal time T^I_{opt} and wavenumber β_{opt}. For this reason, the two opposite Hartmann layers can be considered as isolated at $Ha = 10$ with respect to primary perturbations.

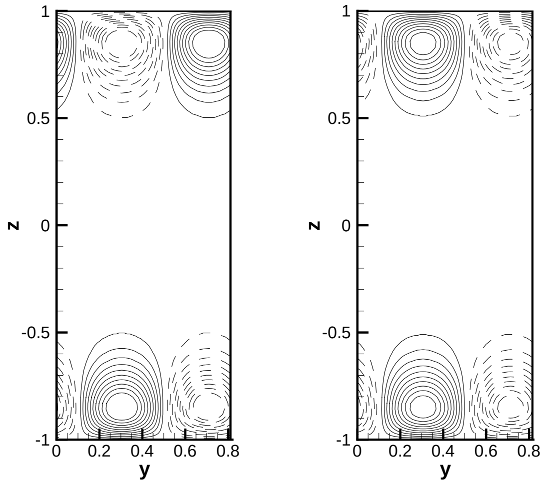

Figure 1: The streamwise velocity distribution at $t = T^I_{opt}$ for antisymmetric (left) and symmetric (right) primary perturbations at $Re = 5000$ and $Ha = 10$.

At lower Ha this is no longer the case. Fig. 2 shows that antisymmetric and symmetric primary optimal perturbations differ in maximum amplification and corresponding β. Only for $Ha > 7$, β_{opt} is found to be proportional to Ha and in good numerical agreement with Ref. [7], where optimal linear growth for an isolated Hartmann layer is investigated. At small Ha the antisymmetric perturbations have higher amplification, which is in agreement with non-MHD channel flow [4]. For an isolated Hartmann layer, the amplification $G^I_{max}(Re, Ha) \sim R^2$ [7].

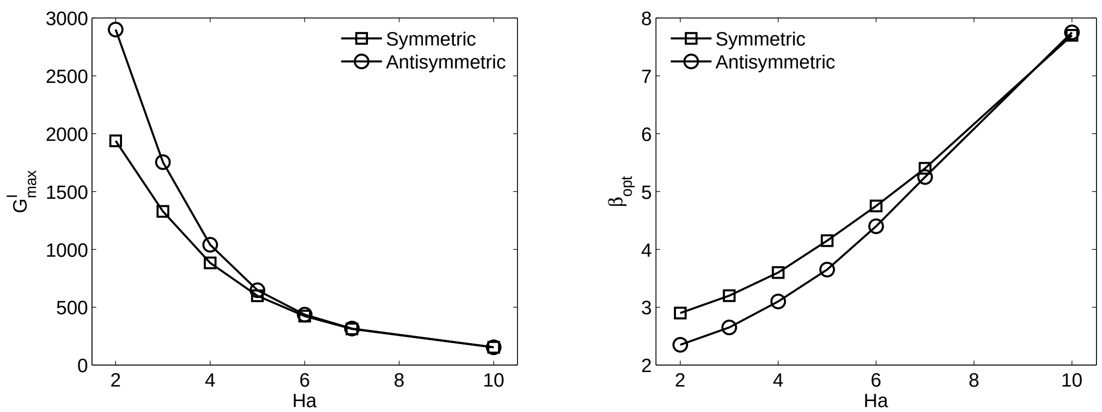

Figure 2: Maximum of primary perturbation energy amplification G^I_{max} (left) and the corresponding optimal spanwise wavenumber β_{opt} (right) for different Ha at $Re = 5000$.

For the secondary perturbation analysis, the basic modulated Hartmann flow is generated from antisymmetric primary perturbations and computed using the DNS code from Ref. [5]. The secondary optimal perturbations are computed with the method and code from Ref. [6]. The spanwise direction is periodic with a periodicity length $L_y = 2\pi/\beta_{opt}$.

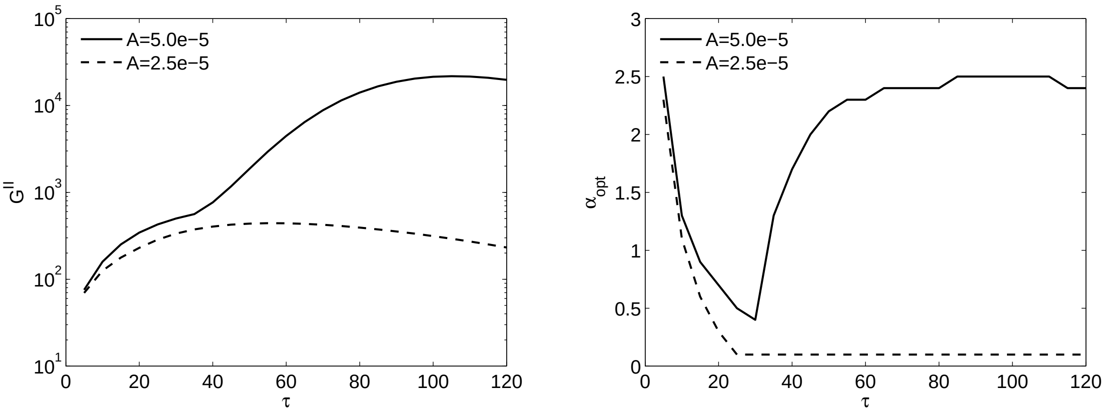

Figure 3: Maximum of secondary perturbation energy amplification (left) and corresponding optimal wavenumber α_{opt} (right) at $Re = 5000$ for streaks of two different amplitudes.

The maximum energy amplification $G^{II}_{max}(Re, Ha, \tau)$ and the corresponding optimal α_{opt} depend on the amplitude $A = E(0)/E_B$ of the streaks, where E_B is the energy of the basic Hartmann flow and $E(0)$ the kinetic energy of the initial primary perturbation, i.e. the streamwise vortices. As is shown in Fig. 3, for low amplitude A the optimal α is very close to zero, i.e., the secondary perturbations resemble the primary perturbations and are amplified by the same lift-up mechanism. Their energy amplification is also close to the one of the primary perturbation. For the higher amplitude streaks α becomes non-zero, and the amplification is significantly higher. This can be attributed to inflectional instability supported by the deformed basic velocity distribution.

When the Hartmann layers are isolated, the secondary perturbations should scale with δ_{Ha}, i.e. the amplification should be independent of Ha at fixed R. For this similarity to hold the deformed velocity profile should have the same shape. The proper choice to seed the initial perturbation is to keep ARe^2/Ha fixed as Ha is changed.

Fig. 4 shows a comparison at $R = 300$. The amplification changes from $Ha = 10$ to $Ha = 20$ but remains about the same at $Ha = 30$. Secondary perturbations at opposite walls are therefore still interacting at $Ha = 10$. The wavenumber α increases approximately in proportion with Ha. Since the time scale also changes, time is multiplied with $Ha/10$ in Fig. 4.

The global maximum value of amplification factor G^{II}_{max} as function of R is shown in Fig. 5 for several Ha and two sets of streak amplitudes that satisfy $ARe^2/Ha = const.$ as Re and Ha are changed. At the lower amplitude, the relation $G^{II}_{max} \sim R^2$ is satisfied to a good approximation, which indicates that the amplification is largely due to the lift-up mechanism. For the stronger streaks, the maximum amplification changes exponentially with R, and only the curves for $Ha = 20$ and $Ha = 30$ are in good agreement. The exponential growth with R can be interpreted as the result of inviscid inflectional instability of the streaky base flow and the increasing life time of the streaks due to slower decay at higher R. This allows secondary perturbations to grow over times $\sim R$.

Further work will be concerned with the detailed structure of secondary perturbations. It would also be interesting to explore possible links with the changes in transition values R with Ha noted in the DNS work by Zienicke and Krasnov [8].

Acknowledgments. TB, DK acknowledge financial support from the Deutsche Forschungsgemeinschaft. SD's work is supported by National Natural Science Foundation of China (No.11302076) and Natural Science Foundation of Hebei Province(No.A2014502047).

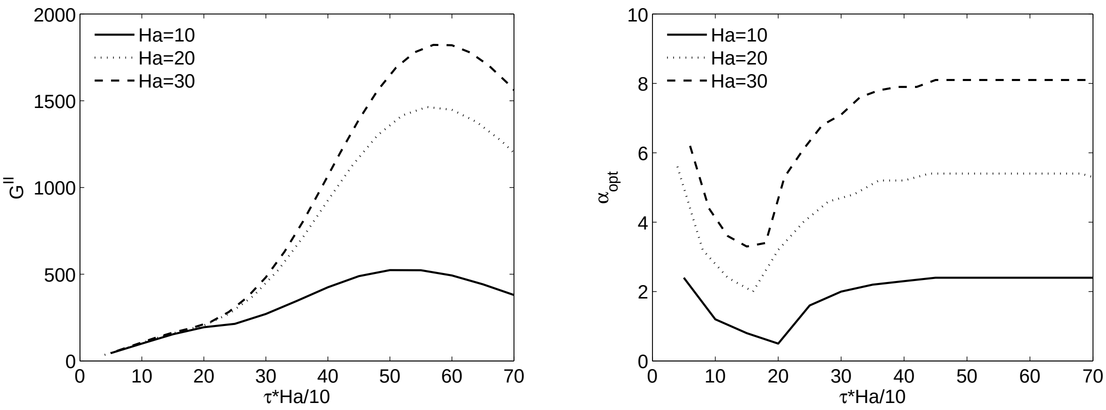

Figure 4: Maximum of secondary perturbation energy amplification (left) and the corresponding optimal wavenumber α_{opt} (right) for higher amplitude streaks at $R = 300$ and different Ha. $A = 1.39 \times 10^{-4}$ for $Ha = 10$. It varies with Ha according to $AHa = const$.

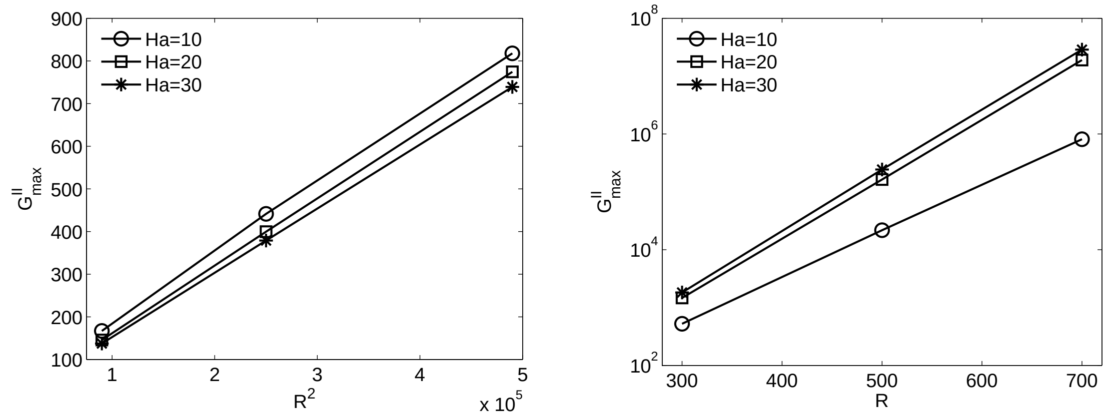

Figure 5: Maximum of secondary perturbation energy amplification $G^{II}_{\max}$ as function of R for small amplitude streaks (left) and large amplitude streaks (right). At $Ha = 10$ the small amplitude is $A = 6.95 \times 10^{-5}$ and the large amplitude is twice as large.

References

[1] Hartmann, J. and Lazarus F.: Experimental investigations on the flow of mercury in a homogeneous magnetic field. K. Dan. Vidensk. Selsk. Mat. Fys. Medd. 15 (1937) 1-45.

[2] Moresco, P. and Alboussière, T.: Experimental study of the instability of the Hartmann layer. J. Fluid Mech. 504 (2004) 167-181.

[3] Lingwood, R. J. and Alboussière, T.: On the stability of the Hartmann layer. Phys. Fluids 11 (1999) 2058-2068.

[4] Schmid, P. J. and Henningson, D. S.: *Stability and Transition in Shear Flows.* Springer (2001).

[5] Krasnov, D., Zienicke, E., Zikanov, O., Boeck, T. and Thess, A.: Numerical study of the instability of the Hartmann layer. J. Fluid Mech. 504 (2004) 183-211.

[6] Dong, S., Krasnov, D. and Boeck, T.: Secondary energy growth and turbulence suppression in conducting channel flow with streamwise magnetic field. Phys. Fluids 24 (2012) 074101.

[7] Gerard-Varet, D.: Amplification of small perturbations in a Hartmann layer. Phys. Fluids 14 (2002) 1458-1467.

[8] Zienicke, E. A. and Krasnov, D.: Parametric study of streak breakdown mechanism in Hartmann flow. Phys. Fluids 17 (2005) 114101.

EXPERIMENTAL RESULTS ON THE AZIMUTHAL MAGNETOROTATIONAL INSTABILITY

SEILMAYER, M.[1], GALINDO, V.[1], GERBETH, G.[1], GUNDRUM, T.[1], STEFANI, F.[1], GELLERT, M.[2], RÜDIGER, G.[2], SCHULTZ, M.[2], HOLLERBACH, R.[3]
[1]Helmholtz-Zentrum Dresden-Rossendorf, P.O. Box 510119, D-01314 Dresden, Germany
[2]Leibniz-Institut für Astrophysik Potsdam, An der Sternwarte 16, D-14482 Potsdam, Germany
[3]Department of Applied Mathematics, University of Leeds, Leeds LS2 9JT, UK
E-mail: M.Seilmayer@hzdr.de

Abstract: Hydrodynamically stable rotating flows can be destabilized by an azimuthal magnetic field. The arising non-axisymmetric, or azimuthal magnetorotational instability (AMRI) is important for explaining the angular momentum transport in accretion disks, and plays a central role in the concept of the MRI dynamo. We report the observation of AMRI in a magnetized liquid metal Taylor-Couette experiment, and discuss the surprisingly strong effects of a slight symmetry breaking of the applied magnetic field.

1. Introduction

Angular momentum transport in accretion disks around protostars and black holes relies on the action of the magnetorotational instability (MRI). The working principle of this instability was explained by Velikhov [1] as early as 1959. However, it took more than 30 years before Balbus and Hawley recognized its relevance for the evolution of stellar systems, X-ray binaries, and active galactic nuclei [2].
The topology of the underlying magnetic field determines the azimuthal dependence of the arising instability. While a uniform axial magnetic field threading the flow (non-zero net-flux) leads to an axisymmetric perturbation ($m = 0$), a purely azimuthal fields (zero net-flux) leads to a non-axisymmetric ($m = 1$) mode. The latter case is particularly interesting for subcritical MRI dynamos, in which the MRI-triggering field is partly sustained by the MRI-driven turbulence itself [3,4,5].
In 2005, it was shown by Hollerbach and Rüdiger [6] that the combination of an axial and an azimuthal magnetic field, giving a helical magnetic field, has a significant effect on the scaling behaviour of the MRI. This helical version of MRI (HMRI) requires only a Reynolds number $\mathrm{Re}\sim 1000$, and a Hartmann number $\mathrm{Ha}\sim 10$, while the standard version (SMRI), with a purely axial field being applied, requires both the magnetic Reynolds number $\mathrm{Rm} = \mathrm{Pm}\mathrm{Re}$ and the Lundquist number $S = \mathrm{Pm}^{1/2}\mathrm{Ha}$ to be in the order of 1. This grave difference in the scaling behaviour has major consequences for the effort that is needed to study the respective effects in liquid metal experiments. Actually, the HMRI has been successfully validated at the expected moderate Re and Ha numbers [7], whereas the corresponding attempts [8,9] to obtain SMRI have not yet shown conclusive results.
As for the case of a purely azimuthal field (AMRI), it was initially believed that it operates only in the same $\mathrm{Rm}, S > O(1)$ parameter regime as the SMRI, and would thus be experimentally very hard to obtain [10, 11]. However, in 2010 it was discovered that for sufficiently steep rotation profiles the AMRI switches to the same inductionless (Re, Ha) parameter values as the HMRI [12]. The present paper is devoted to an experimental study of this inductionless version of the AMRI.

2. Experimental set-up

For our AMRI experiment, we utilize a slightly modified version of the PROMISE facility which has previously been used for investigations of the HMRI [7]. The main part of PROMISE is a cylindrical vessel (Fig. 1a) made of two concentric copper cylinders enclosing a cylindrical volume of height $h = 400\,\mathrm{mm}$, and a gap width of $d = 40\,\mathrm{mm}$ between the radii $r_{\mathrm{in}} = 40\,\mathrm{mm}$ and $r_{\mathrm{out}} = 80\,\mathrm{mm}$. This cylindrical volume is filled with the liquid eutectic alloy GaInSn whose Prandtl number is $\mathrm{Pm} = 1.4 \times 10^{-6}$. Both the upper and lower end-caps of the cylindrical volume are formed by two plastic rings, separated at $r_{\mathrm{gap}} = 56\,\mathrm{mm}$, the inner and outer ring rotating with the inner and outer cylinders, respectively.

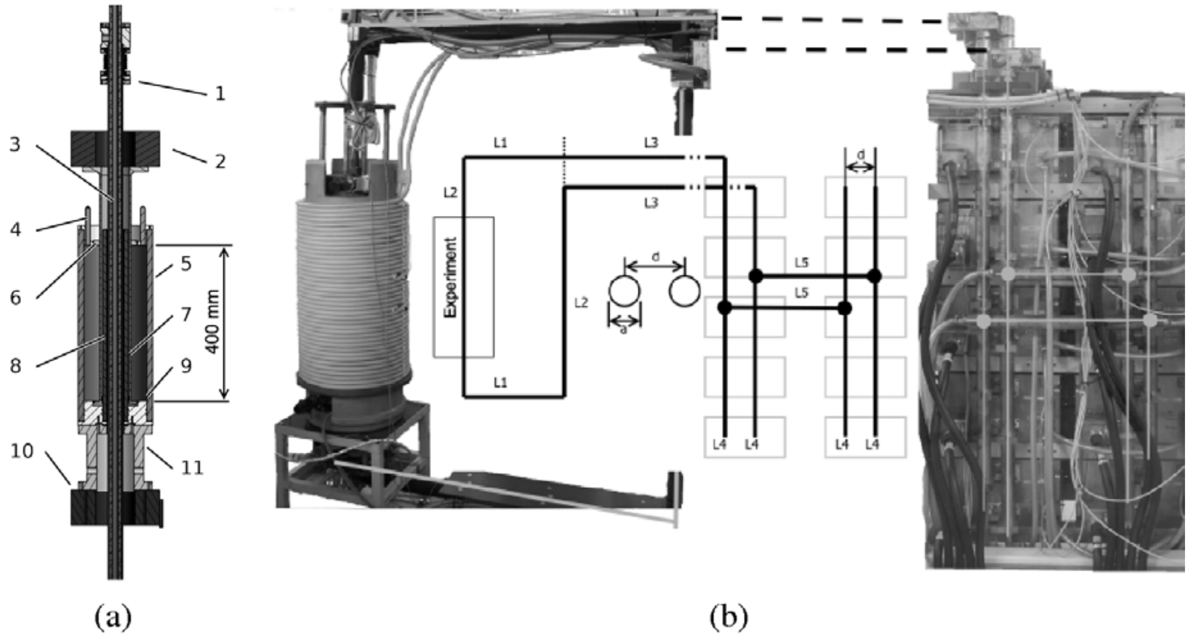

Figure 1: The present status of the PROMISE facility as used for the AMRI experiments. (a) The central Taylor-Couette module with (1) vacuum insulation for the copper rod, (2) upper motor, (3) current carrying copper rod, (4) UDV sensors, (5) outer cylinder, (6) top split rings, (7) inner cylinder, (8) center cylinder, (9) bottom split rings, (10) bottom motor, (11) spacer. (b) Modified photography of the central module, the water cooled supply rods (a = 30 mm), and the power sources.

The dominantly azimuthal magnetic field is produced by a central copper rod which carries up to $20\,\mathrm{kA}$. This value is approximately double the expected critical value for the onset of AMRI [12,13]. Since the central rod can become quite hot, it was thermally insulated by a vacuum tube to prevent any disturbing convection in the fluid. The rod is connected to the power source by two horizontal rods at a height of $0.8\,\mathrm{m}$ below the bottom and above the top of the cylindrical volume. Note that this asymmetric wiring leads to a slight deviation from a purely axisymmetric $B_\varphi(r)$, which will play an important role in the interpretation of the results. With B_z being set to zero, the AMRI is completely governed by only three non-dimensional parameters, the Reynolds number $\mathrm{Re} := d^2\Omega_{\mathrm{in}}/\nu$, the ratio of outer to inner angular frequencies $\mu := \Omega_{\mathrm{out}}/\Omega_{\mathrm{in}}$, and the Hartmann number $\mathrm{Ha} := B_\varphi(r_{\mathrm{in}})d(\sigma/\rho\nu)^{1/2}$. For converting between dimensional and non-dimensional quantities we can use the following convenient relations: $\mathrm{Re} = 4710\,\Omega_{\mathrm{in}}/\mathrm{s}^{-1}$ and $\mathrm{Ha} = 7.77\frac{I_{\mathrm{rod}}}{\mathrm{kA}}$.

For measuring the axial velocity perturbations, we use two Ultrasonic Doppler Velocimetry (UDV) transducers (from Signal Processing SA) which provide profiles of $v_z(z)$ along the beam-lines parallel to the axis of rotation. The two sensors are fixed into the outer plastic ring, $12\ \mathrm{mm}$ away from the outer copper wall, and flush mounted at the interface to the GaInSn. The signals of the sensors are transferred from the rotating frame of the outer cylinder to the laboratory frame by means of a slip ring contact. Due to the strong high-frequency noise of the power supplies, numerous shielding and grounding measures were needed to improve the signal-to-noise ratio of the measurement system.

3. Results

From theoretical predictions [12,13], AMRI was expected to set in at a critical $\mathbf{Ha}$ of about 80, which translates to a critical current of about $10\ \mathrm{kA}$. The anticipated non-axisymmetric $m = \pm 1$ spiral velocity structure, which rotates around the vertical axis with an angular frequency very close to that of the outer cylinder, can be identified by taking the difference of the signals of the two UDV transducers. In order to simulate AMRI for the real geometry of the facility and at the low $\mathbf{Pm}$ of GaInSn, we have used the OpenFoam library, enhanced by a Poisson solver for the determination of the induced electric potential (see [14] for details). The velocity structure simulated in this way can then be transformed to the co-rotating frame in order to compare the resulting velocity pattern with the experimentally observed one.

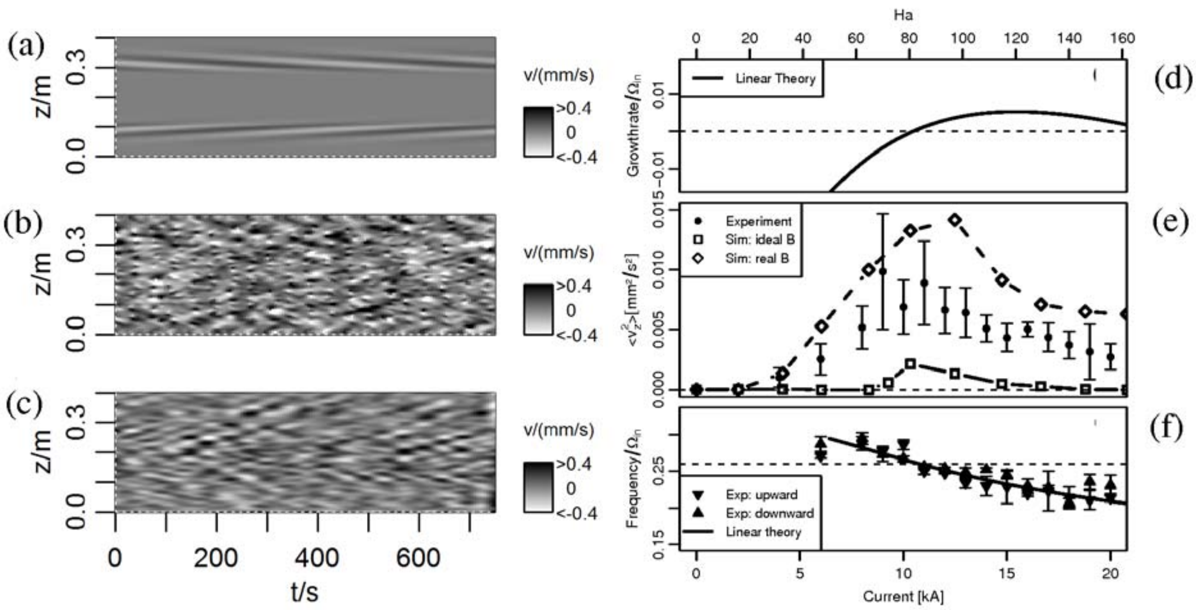

Figure 2: Results of the AMRI experiment for $\mu = 0.26$, **Re** = 1480. (a) Simulation of the velocity perturbation at **Ha** = 110 for an idealized axisymmetric field. (b) Same simulation for the realistic field. (c) Experimental results. (d) Growth rate of the AMRI as obtained from linear stability analysis, in dependence on **Ha**. (e) Simulated and measured mean squared velocity perturbation. (f) Angular drift frequency, with "upward" and "downward'" referring to the travel direction of the velocity perturbations shown on the left side.

Figure 2a shows the result of such a simulation for the particular case $\mu = 0.26$**, Re = 1480, Ha = 110**, in which, as a first guess, a perfectly axisymmetric $B_\varphi(r)$ has been assumed. The resulting "butterfly" pattern represents a spiral, rotating slightly slower than the outer cylinder. Its amplitude is concentrated approximately in the middle parts of the upper and lower halves of the cylinder, where we observe a preference for either the upward moving or the downward moving spiral. Evidently, such a symmetry breaking would not appear in an infinite length system, and must therefore be attributed to the (minor) flow modifications due to the end walls. Figure 2b shows the corresponding simulation for the case that the slight deviation of the applied magnetic field from axi-symmetry (due to the asymmetric wiring, see Figure 1b) is correctly taken into account. The effect is remarkable: the formerly clearly separated spiral structures now also fill the middle part of the cylinder and penetrate into the other halves. The corresponding velocity pattern observed in the experiment is depicted in Figure 2c and shows a great similarity with the simulation in Figure 2b. Note that a similar quasi-periodic regime of interpenetrating spirals had been observed in simulations of a co-rotating spiral Poiseuille flow [15].

A more quantitative analysis of various features of the AMRI, in dependence on Ha , is documented on the right hand side of Figure 2. Figure 2d indicates the theoretical growth rate of the AMRI as determined by a 1D-eigenvalue solver for the infinite length system [13]. In Figure 2e we show the squared rms of the UDV-measured velocity perturbation $v_z(m=1,z,t)$ and compare them with the numerically determined ones for the idealized axisymmetric field, as well as for the realistic applied magnetic field. Whereas the growth rate in Figure 2d and the numerical rms results under the axisymmetric field condition give a consistent picture, with a sharp onset of AMRI at $\mathrm{Ha}\sim 80$, the slight symmetry breaking of the field leads, first, to some smearing out of the rms for lower Ha and, second, to a significant increase of the rms velocity value, with a reasonable correspondence of numerical and experimental values.

The dependence of the numerically and experimentally determined normalized drift frequency on Ha is given in Figure 2f. AMRI represents a $m=\pm 1$ spiral pattern that rotates approximately with the rotation rate of the outer cylinder [13]. There is still some deviation from perfect co-rotation, with a slightly enhanced frequency for lower Ha and a slightly reduced frequency for higher Ha , which can be identified both in the linear theory and in the experimental data.

4. Conclusions

We have proved that AMRI occurs in a hydrodynamically stable differential rotational flow of a liquid metal when it is exposed to a dominantly azimuthal magnetic field. The dependence of the rms and the frequency of the non-axisymmetric velocity perturbations on Ha turned out to be in good agreement with numerical predictions, especially if the simulation incorporates the slight symmetry breaking of the externally applied magnetic field. In addition to the increase of the rms value, which is mainly due to the interpenetration of the two spirals, we have observed a shift of the critical Hartmann number below the numerically predicted value of approximately 80 .

Present experimental and numerical work will give an answer to the interesting question whether the AMRI shifts also to higher values of μ when the symmetry breaking of the applied field is taken into account. Actually, the general question for which steepness of the rotation profile which parameter combinations, (Rm, S) or (Re, Ha), are the relevant ones, is of astrophysical significance, since the Keplerian profile $\Omega(r)\sim r^{-3/2}$ that is of greatest interest in accretion disks is considerably shallower than the limiting Rayleigh line $\Omega(r)\sim r^{-2}$. Usually, both the HMRI as well as the AMRI switch from the (Re, Ha) scaling back to the (Rm, S) scaling for rotation profiles as shallow as Keplerian, as was first noted for the HMRI by Liu et al. [16] and generalized to higher m modes by Kirillov et al. [17]. If, however, the field profiles are taken only slightly shallower than $B_\varphi(r)\sim r^{-1}$, both the HMRI and the AMRI have recently been shown [18] to scale with (Re, Ha) even for Keplerian rotation profiles.

While this axisymmetric scenario would still require a significant induction effect, i.e. some $\mathrm{Rm} > 1$, in the rotating fluid, a possible shift of AMRI to higher values of m for slightly non-axisymmetric, yet current-free fields could have dramatic consequences for the theory of accretion disks.

In future experiments it is also planned to investigate the influence of an additionally applied B_z, which breaks the symmetry between the $m = 1$ and $m = -1$ modes [12]. Increasing B_z even further, it should also be possible to observe the transition from the $m = \pm 1$ AMRI mode back to the previous $m = 0$ HMRI mode. A large-scale liquid sodium experiment for the combined investigation of SMRI, HMRI, AMRI, and the current-driven Tayler instability [19] is planned in the framework of the DRESDYN project [20].

Acknowledgments.

We acknowledge financial support from Deutsche Forschungsgemeinschaft under Grant No. STE 991/1-2 and from the Helmholtz Alliance LIMTECH.

References

[1] Velikhov, E.P.: Sov. Phys. JETP 36 (1959) 995
[2] Balbus, S.A.; Hawley, J.F.: Astrophys. J. 376 (1991) 214
[3] Brandenburg, A. et al.: Astrophys. J. 446 (1995) 741
[4] Rincon, F. et al.: Phys. Rev. Lett. 98 (2007) 254502
[5] Herault, J. et al.: Phys. Rev. E 84 (2011) 036321
[6] Hollerbach, R.; Rüdiger, G.: Phys. Rev. Lett. 95 (2005) 124501
[7] Stefani, F. et al.: Phys. Rev. E 80 (2009) 066303
[8] Sisan, D.R. et al.: Phys. Rev. Lett. 93 (2004) 114502
[9] Nornberg, M.D. et al.: Phys. Rev. Lett. 104 (2010) 074501
[10] Ogilvie, G.I.; Pringle, J.E.: Mon. Not. R. Astr. Soc. 279 (1996) 152
[11] Rüdiger, G. et al.: Mon. Not. R. Astr. Soc. 377 (2007) 1481
[12] Hollerbach, R. et al.: Phys. Rev. Lett. 104 (2010) 044502
[13] Rüdiger, G. et al.: Mon. Not. R. Astr. Soc. 438 (2014) 271
[14] Weber, N. et al: New J. Phys. 15 (2013) 043034
[15] Avila, M. et al.: Phys. Fluids 18 (2006) 064101
[16] Liu, W. et al.: Phys. Rev. E 74 (2006) 056302
[17] Kirillov, O.N. et al: Astrophys. J. 756 (2012) 83
[18] Kirillov, O.N., Stefani, F.: Phys. Rev. Lett. 111 (2013) 061103
[19] Seilmayer, M. et al.: Phys. Rev. Lett. 108 (2012) 244501
[20] F. Stefani et al.: Magnetohydrodynamics 48 (2012) 103

FREE SURFACE DEFORMATION BY THE APPLICATION OF ELECTRICAL CURRENTS

KHARICHA [1] A., TEPLYAKOV[2] I., IVOCHKIN[2] YU., WU[3] M., LUDWIG[3] A., GUSEVA[2] A.
[1] Christian Doppler Laboratory for Advanced Process Simulation of Solidification and Melting, University of Leoben, 8700 Leoben, Austria
[2] Joint Institute for High Temperatures, RASs, Moscow, Russia
Email: abdellah.Kharicha@ unileoben.ac.at

Abstract: We report some results from an investigation on an electrically induced flow in a cylindrical container filled with an In-Ga-Sn alloy. An electric current is applied from a 4mm diameter cooper electrode and varied from 100 to 700 Amps. The deformation of the free surface just under the electrode is reported in term of depth. At some critical current an arc develops around the electrode tip. The results are interpreted with the help of a numerical model.

1.Introduction and numerical method

The present paper presents an investigation of an electrically induced flow[1,2] generated within a cylindrical container (Figure 1). Before the experiment the tip is fully immerged in the liquid metal(Galistan), once a current is applied the interface starts to deform. To understand the physical mechanisms involved in these experiments, simulations were performed with a 2D MHD-VOF numerical model. The spherically tipped electrode is dipped within the liquid metal so that the entire tip is entirely in contact with the liquid metal. The dimensions of the facilities are given in figure 1a. The current is applied from the top, and leaves from the bottom by traveling over a vertical wire strictly aligned with the electrode. The deformation of the interface (Fig. 1b, 2) is observed and measured optically with an optical camera. Before the application of the current, the electrode is carefully dipped within the liquid so that the half sphere electrode tip is fully immersed.

The numerical model assumes the system being laminar and 2D axisymmetric. The equations for electric potential, magnetic potential vectors, as well as the velocity field are solved in a fully coupled and transient way. The coupling between the flow and the electromagnetic field is done through the possible movement of the metal/air interface which can modify the electric current path. The fluid calculation domain is a hemisphere divided into 100 000 volume elements. The mesh is refined at vicinity of all wall boundaries, especially near the electrode so that the area of interest is correctly resolved. The electrode radius is 4 mm. The properties of the two phases are fixed [3] The electromagnetic domain includes the fluid domain and the electrode as well as the cooper container. The interface between the two phases is tracked with a geometric reconstruction VOF technique. A single set of momentum equations is shared by the fluids, and the volume fraction of each of the fluids in each computational cell is tracked throughout the domain. The electromagnetic field is solved by using the electric field ϕ and the magnetic potential vector $\vec{A}$. In the liquid the computed electromagnetic field is dynamically adjusted from the space distribution of the electric conductivity, which is in turn a function of the predicted phase distribution. The electric current and the induced magnetic field are fully coupled with the phase distribution. The influence of the axial component of the earth magnetic field is added to the magnetic field induced by the electric current. The motion of the metal and the air $\vec{U}$ is computed with the Navier-Stokes equations. More details about the numerical model used are given in [4]

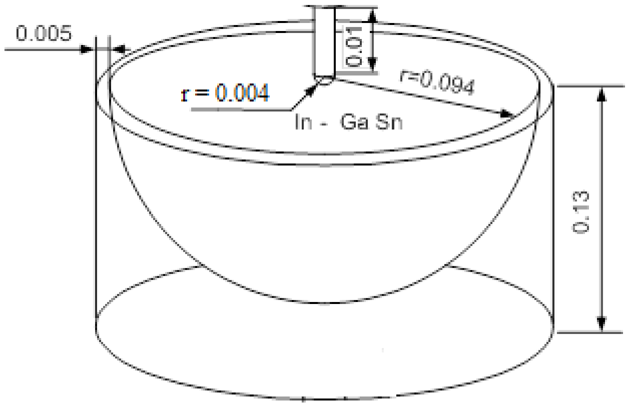

(a)

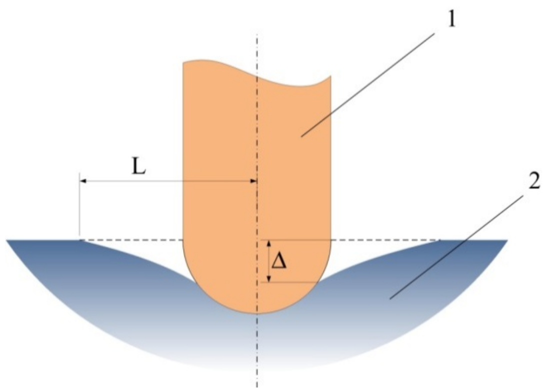

(b)

Figure 1: (a) dimension of the facility. **(b)** Scheme of surface deformation Δ – depth of cavern, L – width of cavern, 1 –electrode, 2 – liquid metal In-Ga-Sn.

Figure 2: Picture of the surface of the liquid metal. A plastic gain of pink colour surrounds the tip of the electrode. A dark area near the electrode appear when the cavern becomes deep and wide enough.

2. Results and discussion

A typical picture of the electrode region is shown in figure 2. An insulating gain of pink colour surrounds the tip of the electrode. This element is used a marker, the lower edge of tube is zero point. The distance between edge of tube and its reflection on the deformed surface of liquid metal (on photo) is measured. Notice the image reflexion produced by the clean metallic surface. Accuracy of the measurement is better than 0.05 mm. Qualitatively, the magnitude of surface deformation can be estimated by the extent of the dark region just under the electrode tip (Fig. 2). When the applied current exceeds a critical current an arc surrounding the electrode tip appears. The cavern depth increases with the applied current.

The position of the liquid metal surface at the electrode becomes invisible as soon as the arc appeared. Since the contact angle α of the free surface at the electrode is not known, simulations were performed with I_0 = 350 A for α= 120° and 90°(Fig.3). The case of α= 120° gives the deepest cavern and the best fit with the experimental data(Fig. 4), this case will be presented and discussed in detail.

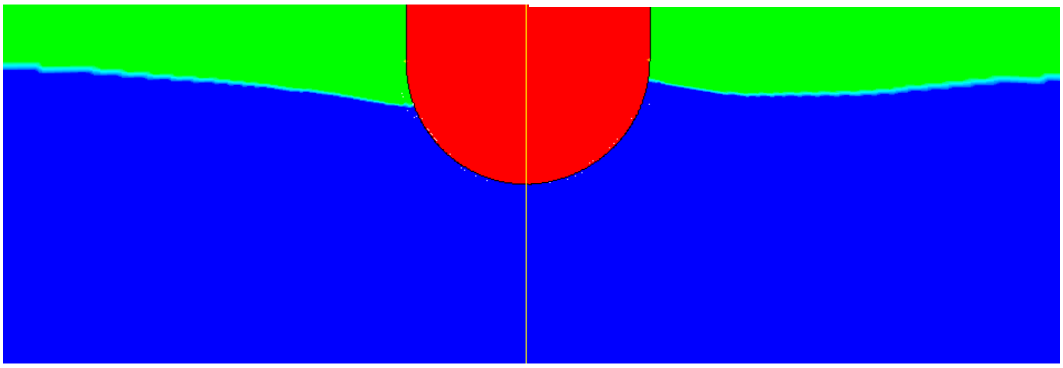

(a) 120° (b) 90°

Figure 3: Deformation of the interface predicted from simulations for electrode diameter 4 mm and for *I*=350 Amp. (Red : electrode, Green air, blue: liquid metal).

The resulting shape is determined by the balance between buoyancy, the surface tension, and the Lorenz forces. Due to the obtuse contact angle, the surface tension is oriented in the downward direction. Any further displacement of the interface must only be the result of the action of the electromagnetic forces. Assuming an equilibrium between buoyancy and the Lorentz force, we have : $\Delta \sim \alpha \dfrac{I^2}{\rho g}$, which is the main trend observed in figures 4. The factor α adds both the pinch and rotational effects of the Lorentz forces. A change in the increase rate is visible at around 100-200 Amps. This change in slope can be explained by the fact that for low applied current the pinch effect dominates, while at higher current the decrease of pressure due to the flow acceleration dominates.

The spherical shape of the electrode tip can lead to unstable configurations. As the electric current intensity is increased (I>275 A), the effective electrode radius (at the level of the interface) becomes smaller and smaller. Similarly the inclination of the electrode surface becomes less vertical and more horizontal. Equilibrium becomes difficult especially for the surface tension force which tries to keep the required contact angle. If the Lorentz force is not quickly balanced, either by buoyancy or by surface tension, the contact area will fluctuate. Amplitude of surface oscillations can be extracted by subtracting the maximum with the minimum depths reported in figure 4.

3. Conclusions

The deformation of a free surface by the application of an electric current has been experimentally and numerically studied. At low current density the interface is shifted downward by the pinch action of the Lorentz force. In the same time the rotational part of the Lorentz force drives the liquid metal flow in radial direction towards the electrode. The flow is accelerated towards the electrode and sinks in the form of a strong jet. At high current density, the velocities are strong enough to induce further displacement of the interface by a Bernoulli mechanism. The combined action of the pinch and the rotational components of the Lorentz force on the interface displacement, scales as I^2. The numerical and experimental results are in good agreements. Experimentally an arc develops around the electrode when the applied current exceeds a critical value. Just before the arc develops the electrode was still in good contact with the liquid metal. At the present stage it is not yet clear on whether the arc develops because of contact lost or because of the occurrence of an electric gas breakdown near the electrode surface.

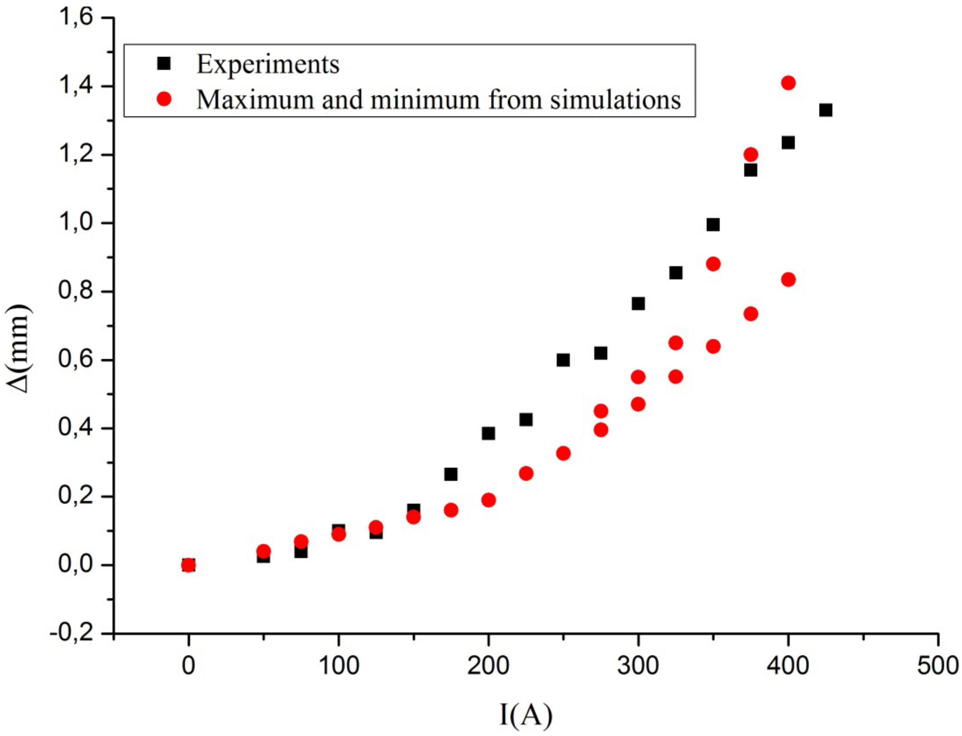

Figure 4: Predicted against experimentally observed cavern depths for the case of 4 mm electrode diameter. In the simulations the position of the interface is unstable for I>275 A.

Acknowledgements.

The financial support by the Austrian Federal Ministry of Economy, Family and Youth and the National Foundation for Research, Technology and Development is gratefully acknowledged.

References

[1] Bojarevich V., Frejbergs Ja., Shilova E.I., Shcherbinin E.V., 1989. Electrically induced vortical flows. Khuwer Acad. Publ., Dordrecht, Boston, London.

[2] Kharicha A., Wu M., Ludwig A., Karimi-Sibaki E.: J. Iron and Steel Research International, Vol.19 Supplement 1-1, (2012) 63-66. "Influence of the earth magnetic field on electrically induced flows"

[3] V.Ya. Prohorenko, E.A.Ratushnyak, B.I. Stadnik, V.I.Lah, A.M.Koval. Physical properties of thermometric alloy In-Ga-Sn. High Temperatures. vol.8, N2, 1970.

[4] Kharicha A., Ludwig A., Wu A., ISIJ International (2014) in press "On melting of electrodes during electro-slag-remelting"

MAGNETOGRAVITATIONAL STABILITY OF COMPRESSIBLE RESISTIVE ROTATING STREAMING FLUID MEDIUM

ALFAISAL A. HASAN
Basic and Applied Sciences Department, College of Engineering and Technology,
Arab Academy for Science, Technology and Maritime Transport (AASTMT)
Sadat road - P.O. Box 11 Aswan, Egypt
E-mail: alfaisal772001@yahoo.com

Abstract: Magnetohydrodynamic stability of a gravitational medium with streams of variable velocity distribution for a general wave propagation in the present of the rotation forces has been studied. The magnetic field has strong stabilizing influence but the streaming is a destabilizing. The rotating forces have a stabilizing influence under certain restrictions. It is proved that the gravitational Jean's instability criterion is not influenced by the electromagnetic force or the rotation force or even by the combined effect of them whether the fluid medium is streaming or not and whether the rotation in one or more dimension.

Key words: Magnetogravitational, Resistive, Rotating, Streaming, Compressible

1. Introduction

The self-gravitational instability of a homogeneous fluid medium at rest has been investigated since long time ago, for its practical application in astrophysics see Jeans (1902). It is founded that the model is unstable under the restriction $k^2 C_S^2 - 4\pi G\rho_o < 0$ called after Jeans by Jeans' criterion, where k is the net wave number of the propagated wave, C_S^2 is a sound speed in the fluid, of density ρ_o, and G is the self-gravitational constant. Chandrasekhar and Fermi (1953), and later on Chandrasekhar (1981) made several extensions. The Jeans' model of self-gravitational medium has been elaborated with streams of variable velocity distribution by Sengar (1981). Recently Radwan and Elazab (1988), Radwan et al. (2001), developed the magnetogravitational stability of variable streams pervaded by the constant magnetic field (H_0, 0 0). The stability of different cylindrical models under the action of self-gravitating force in addition to other forces has been elaborated by Radwan and Hasan (2008),(2009). Hasan (2011) has investigated the stability of a oscillating streaming fluid cylinder subject to the combined effect of the capillary, self-gravitating and electrodynamic forces in all axisymmetric and non-axisymmetric perturbation modes. He (2011) has investigated the stability of oscillating streaming self-gravitating dielectric incompressible fluid cylinder surrounded by tenuous medium of negligible motion pervaded by transverse varying electric field for all the axisymmetric and non-axisymmetric perturbation modes. He (2012) has studied the instability of a full fluid cylinder surrounded by self-gravitating tenuous medium pervaded by transverse varying electric field under the combined effect of the capillary, self-gravitating, and electric forces for all the modes of perturbations. He (2012) the magnetodynamic stability of a fluid jet pervaded by transverse varying magnetic field while its surrounding tenuous medium is penetrated by uniform magnetic field.

Here in the present work we study the magnetodynamic stability of a self-gravitating rotating streaming viscous fluid medium pervaded by general magnetic field. Such studies have a correlation with the formation of sunspots. Also they have relevance in describing the condensation within astronomical bodies cf. Chandrasekhar and Fermi (1953), and also Chandrasekhar (1981).

2. Basic state

We consider an infinite self-gravitating fluid medium. The fluid is assumed to be homogeneous and viscous. The model is acting upon the following forces (*i*) the pressure gradient force, (*ii*) electromagnetic force, (*iii*) self-gravitating force, (*iv*) the forces due to rotating factors and (*v*) the forces due to resistivity. We shall utilize the Cartesian coordinates (*x*, *y*, *z*) for investigating such problem. The required equations for the present problem

$$\rho\left(\frac{\partial \underline{u}}{\partial t}+(\underline{u}\cdot\nabla)\underline{u}\right)=-\nabla P+\mu(\nabla\wedge\underline{H})\wedge\underline{H}+\rho\nabla V-2\rho(\underline{u}\wedge\underline{\Omega})+\frac{1}{2}\rho(\underline{\Omega}\wedge\underline{r})^2 \qquad (1)$$

$$\frac{\partial\rho}{\partial t}+(\underline{u}\cdot\nabla)\rho=-\rho(\nabla\cdot\underline{u}) \qquad (2)$$

$$\frac{\partial\underline{H}}{\partial t}=\nabla\wedge(\underline{u}\wedge\underline{H})-\nabla(\eta\nabla\wedge\underline{H}) \qquad (3)$$

$$\nabla\cdot\underline{H}=0 \qquad (4)$$

$$\nabla^2 V=-4\pi G\rho \qquad (5)$$

$$P=K\rho^{\Gamma} \qquad (6)$$

Here ρ, $\underline{u}$, and P are the fluid density, velocity vector and kinetic pressure, μ and $\underline{H}$ are the magnetic field permeability and intensity, V and G are the self-gravitating potential and constant, η is the coefficient of resistivity, $\underline{\mathbf{\Omega}}$ is the angular velocity of rotation, K and Γ are constants where Γ is the polytropic exponent.
We assume that the medium: (i) rotates with the general uniform angular velocity

$$\underline{\Omega}=(\Omega_x,\Omega_y,\Omega_z) \qquad (7)$$

(ii) be pervaded by the two dimensions homogeneous magnetic field

$$\underline{H}_o=(0,H_{oy},H_{oz}) \qquad (8)$$

and (iii) posses streams moving in the x_direction with velocity

$$\underline{u}_o=(U(z),0,0) \qquad (9)$$

varying along the z-direction of the Cartesian coordinates (*x*, *y*, *z*).

3. Perturbation analysis

For small departures from the initial state, every variable quantity Q may be expressed as

$$Q=Q_o+Q_1 \quad , \quad |Q_1|<<Q_o \qquad (10)$$

where Q stands for each $\rho,\underline{H},P,\underline{u}$ and V. Based on the expansion (10), the perturbation equations could be obtained from (1)--(6).

4. Eigenvalue relation

Apply sinusoidal wave along the fluid interface. Consequently, from the viewpoint of the stability approaches given by Chandrasekhar, (1981), we assume that the space-time dependence of the wave propagation of the form

$$Q_1 \sim \exp\left[i\left(k_x x+k_y y+k_z z+\sigma t\right)\right] \qquad (11)$$

Here σ is gyration frequency of the assuming wave. k_x, k_y and k_z are (any real values) the wave numbers in the (*x*, *y*, *z*) directions. By an appeal to the time-space dependence (11), the relevant perturbation equations could be rewritten in the matrix form

$$\left[a_{ij}\right]\left[b_j\right]=0 \qquad (12)$$

where the elements $\left[a_{ij}\right]$ of the matrix are given in the appendix I while the elements of the column matrix $\left[b_j\right]$ are being $u, v, w, h_x, h_y, h_z, \rho_1$ and V_1.

For non-trivial solution of the equations (12), setting the determinant of the matrix $\left[a_{ij}\right]$ equal to zero (see Appendix I), we get the general eigenvalue relation of seven order in n in the form

$$A_7n^7 + A_6n^6 + A_5n^5 + A_4n^4 + A_3n^3 + A_2n^2 + A_1n + A_0 = 0 \qquad (13)$$

where the compound coefficients $A_i \ (i = 0,1,2,3,4,5,6,7)$ are calculated.

5. Discussions and results

Equation (13) is a general MHD eigenvalue relation of a rotating self-gravitating fluid medium pervaded by magnetic field of two dimensions. Some previously publishing results may be obtained as limiting cases here. That confirms the present analysis.

In absence of the rotating, electromagnetic forces and for inviscid fluid i.e. $\underline{\Omega} = 0$, $\underline{H}_o = 0$ and $\eta = 0$, equation (13) yields

$$k^2n^3 + k^2\left(k^2C_S^2 - 4\pi G\rho_o\right)n - k_xk_z\left(k^2C_S^2 - 4\pi G\rho_o\right)DU_o = 0 \qquad (14)$$

This relation coincides with the dispersion relation, of a pure self-gravitating fluid medium streams with variable streams ($U_0(z)$, 0,0) derived by Sengar (1981). For more details concerning stability of this case we may refer to Sengar (1981).

If $\underline{\Omega} = 0$, $\underline{H}_o = 0$, $\eta = 0$ and $U_o = 0$, equation (13) reduces to

$$n^2 = k^2C_S^2 - 4\pi G\rho_o \qquad (15)$$

This gives the same results given by Jean's (1902). For more details concerning the instability of this case, we may refer to the discussions of Jean's (1902). In absence of the magnetic field and we assume that the fluid medium is stationary i.e. $\underline{H}_o = 0,\ \eta = 0$ and $U_o = 0$, equation (13) gives another relation. The purpose of the present part is to determine the influence of rotation on the Jean's criterion (15) of a uniform streaming fluid. So in order to carry out and to facilitate the present situation we may choose $\Omega_x = 0$, $\underline{H}_o = 0$, $\eta = 0, k_x = 0$ and $k_y = 0$, equation (13), gives

$$n^4 + \left(4\pi G\rho_o - C_S^2k_z^2 - 4\Omega^2\right)n^2 + 4\Omega_z^2\left(C_S^2k_z^2 - 4\pi G\rho_o\right) = 0 \qquad (16)$$ with

$$\Omega^2 = \Omega_y^2 + \Omega_z^2 \qquad (17)$$

Equation (16) indicates that there must be two modes in which a wave can be propagated in the medium. If the roots of (16) are being n_1^2 and n_2^2, then we have

$$n_1^2 + n_2^2 = C_S^2k_z^2 + 4\Omega^2 - 4\pi G\rho_o \qquad (18)$$

$$n_1^2\, n_2^2 = 4\Omega_z^2\left(C_S^2k_z^2 - 4\pi G\rho_o\right) \qquad (19)$$

and so we see that both the roots n^2_1 and n^2_2 are real. The discussions of (16) indicate that if the Jean's restriction

$$C_S^2k_z^2 - 4\pi G\rho_o < 0 \qquad (20)$$

is valid, then one of the two roots n_1^2 or n_2^2 must be negative and consequently the model will be unstable. This means that under the Jean's restriction (20), the self-gravitating rotating fluid medium is unstable. This shows that the Jean's criterion for a self-gravitating medium is unaffected by the influence of the uniform rotation.

If $G = 0,\ \underline{\Omega} = 0,\ \underline{H}_o = 0$ and $\eta \neq 0,$ equation (13) degenerates to a somewhat complicated relation. The purpose of the present part is to determine the effect of the viscosity of fluid. So in order to carry out and to facilitate the present situation we may choose $k_x = 0$ and $k_y = 0$ so equation (13), at once, yields

$$\left(\sigma + k^2\eta\right)^2\left(\sigma^5k^2 + k^4\sigma C_S^2\right) = 0 \qquad (21)$$

Equation (21) indicates that resistivity has s destabilizing influence under certain restrictions.

6. Conclusion

The gravitational Jeans instability criterion is not influenced by the electromagnetic force or the rotation forces or even by the combined effect of them whether the fluid medium is streaming or not and whether the rotation in one dimension or more. The resistivity has s destabilizing influence under certain restrictions.

References

[1] Jeans, J. H., Philos. Trans. R. Soc. London, 199(1902)1.

[2] Chandrasekhar, S, Fermi, E: Problems of gravitational stability in the presence of a magnetic field. Astrophys J. 118 (1953) 116.

[3]. Chandrasekhar, S: Hydrodynamic and Hydromagnetic Stability. Dover, New York (1981).

[4] Radwan, A. E., Radwan, H. A. and Hendi, M., Chaos, Solitons and Fractals, 12 (2001) 1729.

[5] Radwan, AE, Hasan, AA, Axisymmetric electrogravitational stability of fluid cylinder ambient with transverse varying oscillating field, (IAENG). Int. J. Appl. Math. 38 (3), (2008) 113.

[6] Radwan, AE, Hasan, A.A. Magnetohydrodynamic stability of self-gravitational fluid cylinder. Appl. Math. Model 33 (4), (2009) 2121.

[7] Hasan, A.A. Electrogravitational stability of oscillating streaming fluid cylinder, Physica B. 406 (2), (2011) 234.

[8] Hasan, A.A. Electrogravitational stability of oscillating streaming dielectric compound jets ambient with a transverse varying electric field, Boundary Value Problems,2011 (31),(2011)1.

[9] Hasan, AA, Electrogravitational stability of oscillating streaming fluid cylinder. J. Appl. Mech. ASME. 79 (2), (2012) 1.

[1]. Hasan, A.A. Hydromagnetic instability of streaming jet pervaded internally by varying transverse magnetic field. Mathematical Problems in Engineering, (2012) 1.

Appendix I

The elements $a_{ij}\left(i=1,2,......,8 \text{ and } j=1,2,....,8\right)$ of the matrix $\left[a_{ij}\right]$ in equation (41) of the linear algebraic equations (30)-(38) are being

$a_{11}=\left(n\rho_o\right)$, $a_{12}=\left(2\rho_o\Omega_z\right)$, $a_{13}=\left(\rho_o DU_o-2\rho_o\Omega_y\right)$

$a_{14}=i\,\mu\left(k_yH_{oy}+k_zH_{oz}\right)$, $a_{15}=ik_x\,\mu H_{oy}$, $a_{16}=ik_x\,\mu H_{oz}$, $a_{17}=ik_xC^2$, $a_{18}=-i\,\rho_o k_x$

$a_{21}=\left(-2\rho_o\Omega_z\right)$, $a_{22}=\left(n\rho_o\right)$, $a_{23}=\left(2\rho_o\Omega_x\right)$, $a_{24}=0$

$a_{25}=i\,\mu\left(2k_yH_{oy}+k_zH_{oz}\right)$, $a_{26}=ik_y\,\mu H_{oz}$, $a_{27}=ik_yC^2$, $a_{28}=-i\,\rho_o k_y$

$a_{31}=\left(-2\rho_o\Omega_y\right)$, $a_{32}=\left(2\rho_o\Omega_x\right)$, $a_{33}=\left(n\rho_o\right)$, $a_{34}=0$

$a_{35}=ik_z\,\mu H_{oy}$, $a_{36}=i\,\mu\left(k_yH_{oy}+2k_zH_{oz}\right)$, $a_{37}=ik_zC^2$, $a_{38}=-i\,\rho_o k_z$

$a_{41}=i\left(k_yH_{oy}+k_zH_{oz}\right)$, $a_{42}=0$, $a_{43}=0$, $a_{44}=-\left(n+i\left(k_x^2+k_y^2\right)\right)$, $a_{45}=ik_xk_y$,

$a_{46}=DU_o+ik_xk_z$, $a_{47}=0$, $a_{48}=0$

$a_{51}=-ik_xH_{oy}$, $a_{52}=ik_zH_{oz}$, $a_{53}=-ik_zH_{oy}$, $a_{54}=ik_xk_y$, $a_{55}=-\left(n+i\left(k_x^2+k_z^2\right)\right)$,

$a_{56}=ik_yk_z$, $a_{57}=0$,$a_{58}=0$

$a_{61}=-ik_xH_{oz}$, $a_{62}=-ik_yH_{oz}$, $a_{63}=-ik_yH_{oy}$, $a_{64}=ik_xk_z$, $a_{65}=ik_yk_z$,

$a_{66}=-\left(n+i\left(k_x^2+k_y^2\right)\right)$, $a_{67}=0$, : $a_{68}=0$; $a_{71}=i\,\rho_o k_x$, $a_{72}=i\,\rho_o k_y$, $a_{73}=i\,\rho_o k_z$, $a_{74}=0$,

$a_{75}=0$, $a_{76}=0$, $a_{77}=n$, $a_{78}=0$; $a_{81}=0$, $a_{82}=0$, $a_{83}=0$, $a_{84}=0$, $a_{85}=0$, $a_{86}=0$,

$a_{87}=-4\pi G$, $a_{88}=k^2$

NUMERICAL STUDY OF MHD INSTABILITIES IN LIQUID METAL BATTERIES

WEBER N., GALINDO V., GRANTS I., STEFANI F., WEIER T.
Helmholtz-Zentrum Dresden-Rossendorf
Bautzner Landstr. 400, 01328 Dresden – Germany
e-mail: norbert.weber@hzdr.de

Abstract: Liquid Metal Batteries (LMB) offer a very innovative and promising concept for grid scale energy storage. Coupled with increasingly contributing – and highly fluctuating – renewable energies, they may become a key ingredient for providing energy on demand. LMBs are predicted to be economically very competitive compared to other storage devices – especially for electricity storage on the short and medium time scale. However, for safe and reliable operation, a full understanding of fluid motion in such cells is indispensable. In this paper we focus on the effects of the kink-type Tayler instability in LMBs.

1. Introduction

Liquid Metal Batteries (LMBs) represent a completely new storage concept for grid-scale energy storage. A liquid metal (e.g., Na, Mg) is floating on a second, high-density liquid electrode (e.g., Bi, Sb) – both being separated by an intermediate molten electrolyte. This self-assembling structure of the battery provides a number of distinguished advantages compared to classical batteries, as e.g., fast kinetics, potentially long life time and elevated current densities [1]. The use of abundant raw materials and a simple construction can lead to a very cheap means for stationary energy storage, as increasingly demanded by highly fluctuating renewable energies (wind, photovoltaics). Economies of scale demand for up-scaling these LMBs to a diameter of a meter, or so, in order to reach the desired price of 5-10ct/kWh/cycle. Here is the point where magnetohydrodynamics comes into play.

Reliable and safe operation requires a comprehensive understanding and control of fluid flow in LMBs to avoid interface deformations and to optimise mass transfer. Such flows may arise, e.g., due to thermal convection, electro-vortex flows, interface instabilities or the kink-type Tayler instability (TI) [2]. Arising from an interaction of the battery current with its own magnetic field, the latter one is especially relevant for large cells [3].

In the following we will present simulation results of the TI in one electrode of the battery, estimating the impact on the battery and proposing several countermeasures in order to avoid the TI.

2. Numerical Model

The numerical scheme is described in detail in [4], here we give only a short summary for sake of understandability. Solving the Navier-Stokes equation for incompressible fluids

$$\rho \frac{D\mathbf{u}}{Dt} = -\nabla p + \eta \nabla^2 \mathbf{u} + \mathbf{f}_\mathrm{L} \tag{1}$$

in a cylindrical geometry, we add the Lorentz force term $\mathbf{f}_\mathrm{L} = (\mathbf{J_0} + \mathbf{j}) \times (\mathbf{B_0} + \mathbf{b})$ as source of the instability, with ρ, $\mathbf{u}$, t, p, η denoting the fluid density, velocity, time, pressure and dynamic viscosity, respectively. We split the current density and magnetic field into a static part due to the external current ($\mathbf{J_0}$, $\mathbf{B_0}$) and an induced part ($\mathbf{j}$, $\mathbf{b}$).

The very low magnetic Prandtl numbers of liquid metals and the finite cylindrical geometry make it hard to solve the Navier-Stokes equation and induction equation simultaneously. For that reason we use an integro-differential equation approach by solving a Poisson equation for the electric potential

$$\Delta\phi = \nabla\cdot(\mathbf{u}\times\mathbf{B}) \tag{2}$$

and computing the induced current as $\mathbf{j} = \sigma(-\nabla\phi + \mathbf{u}\times\mathbf{B})$ with σ as the electric conductivity. We obtain then the induced magnetic field **b** by Biot-Savart's law.

3. Characterisation of the Tayler instability in liquid metal electrodes

Simplifying the battery electrode to an infinite long cylinder, the cell current will induce a purely azimuthal magnetic field. While the relevant criterion for onset of the TI in ideal conductors [5]

$$\partial(rB_{\phi}^{2}(r))/\partial r > 0 \tag{3}$$

depends only on the radial dependence of that field, we have to account for the stabilising role of viscosity and resistivity when working with liquid metals. That means that there is a critical cell current for the onset of the TI – which does not depend on the size of the battery.
The TI will appear first in the better conducting liquid electrode, which is typically the upper one. The scaling between different liquid metals is possible via the Hartmann number (here for a cylindrical electrode)

$$Ha = B_{\varphi}(R)R\sqrt{\frac{\sigma}{\eta}} = I\,\frac{\mu_0}{2\pi}\sqrt{\frac{\sigma}{\eta}} \tag{4}$$

with R and μ_0 meaning the electrodes radius and the vacuum permeability.

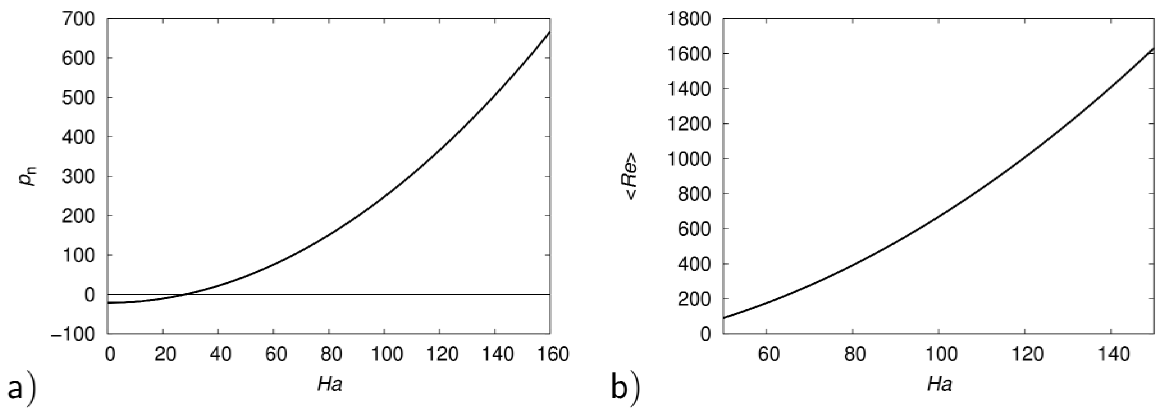

Figure 1: Growth rate normalised by $R^2\rho/\eta$ vs. Hartmann number a), and mean Reynolds number of the TI in saturation in dependence of the Hartmann number b) [6].

Figure 1a) shows the growth rate of the TI in a liquid metal column with aspect ratio height / diameter = 1.2 and a critical Hartmann number for onset of the TI of $Ha_{cr} = 29$. The Reynolds number $Re = \rho uR/\eta$ of the saturated TI is shown in figure 1b). For typical electrode materials one would expect a few millimetres to a few centimetres per second of maximum velocity in the fluid [6]. Although such flows alone may not be strong enough to shear off the electrolyte layer, their interaction with interface instabilities may indeed pose a problem for the integrity of the stratification.

4. Stabilising the Tayler Instability

In order to maintain the stable density stratification of a LMB and ensure safe operation, the TI should be avoided or at least dampened in the upper electrode.
The simplest measure for taming the TI is placing an insulating rod on the battery axis (figure 2a) [3]. Depending on the diameter, this allows for shifting the onset of the TI to much higher cell currents. Leading the cell current back through a bore in the middle of the battery (figure 2b) allows for totally suppressing the TI.

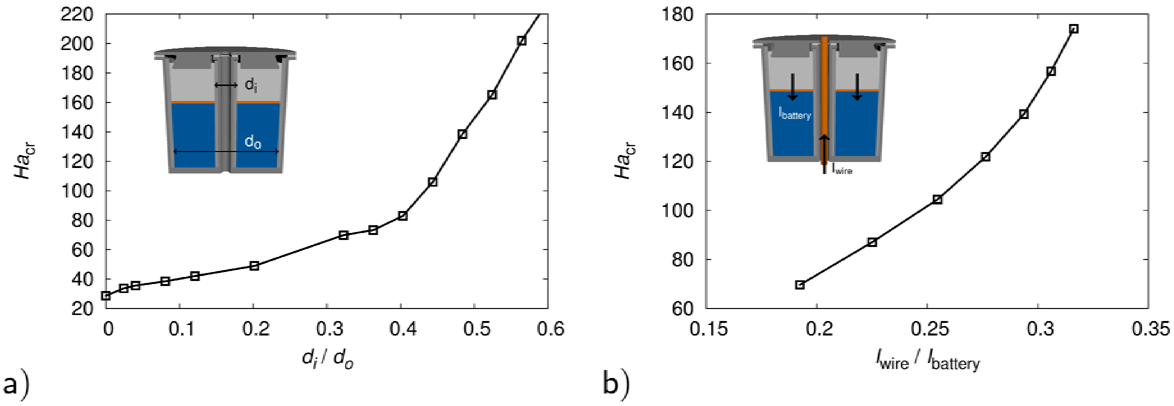

Figure 2: Critical Ha number for onset of the TI for an electrode with aspect ratio 1.2. Either the bore diameter a) or the current flowing back through the bore b) is varied [6].

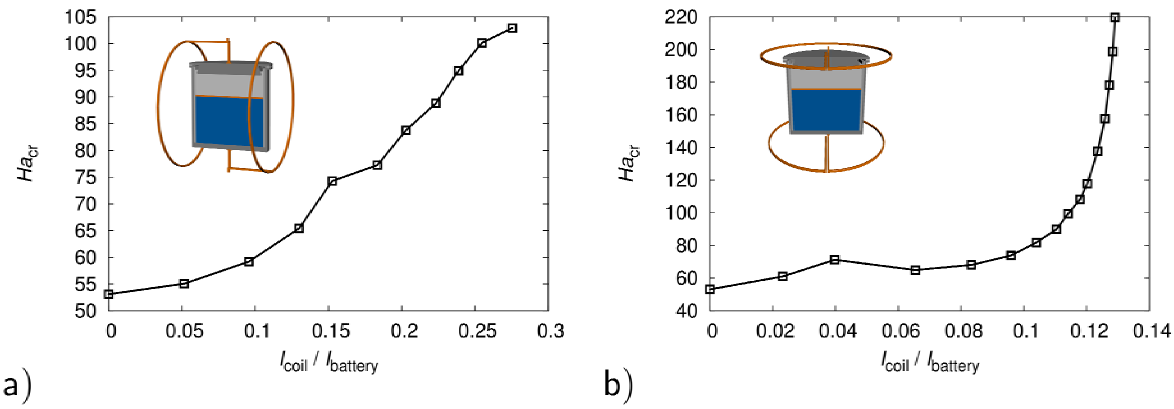

Figure 3: Critical Hartmann number for onset of the TI in a cuboid electrode of aspect ratio height / side length = 0.5 with applied horizontal a) or axial magnetic field b).

Both measures require an internal bore in the battery – which is an efficient solution for suppressing the TI, but may increase the price as the construction becomes more challenging (e.g., due to different thermal coefficients of expansion). An alternative solution is to provide an external magnetic field, generated by a Helmholtz coil [6]. Applying a purely horizontal magnetic field increases the critical current just slightly (figure 3), while an axial magnetic field suppresses the TI very effectively with guiding only 15% of the battery current through the Helmholtz coil.

Apart from the methods described above, one may also consider to guide the feeding current back on the side of the battery (figure 4). We show here results for a cylindrical electrode with aspect ratio 1 and a lateral wire at $r = 1.1R$. The current flowing through the wire is variable and may be as large as the cell current. Using this countermeasure, the cell current may be increased only by a factor of 1.7, i.e., this measure is not very effective. It should be noted that with several stacked batteries, the current through the wire may be even higher than the single cell current. In such a case, the return current may not be stabilising any more, but even trigger the TI "in opposite direction".

Providing several conductors side by side to the battery and splitting the back flowing current through all of them allows for a more homogeneous magnetic field distribution (figure 5). Especially when using two symmetric conductors, the cell current may be increased by a factor of 2.8 without triggering the TI. Using instead of this configuration three not symmetric wires, the results are similar as for a single one (figure 5b).

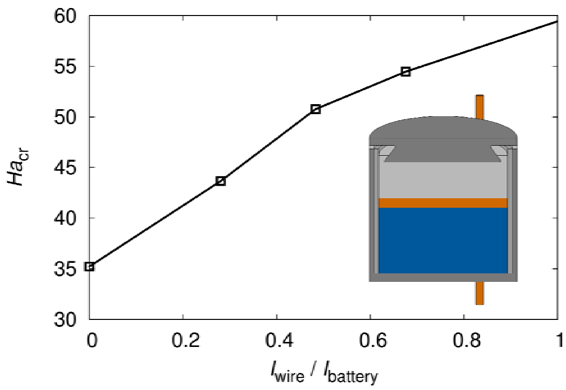

Figure 4: Simulation of the critical Hartmann number for the onset of the TI for a cylindrical electrode with aspect ratio 1. The feeding current is guided back through a wire side by side to the battery.

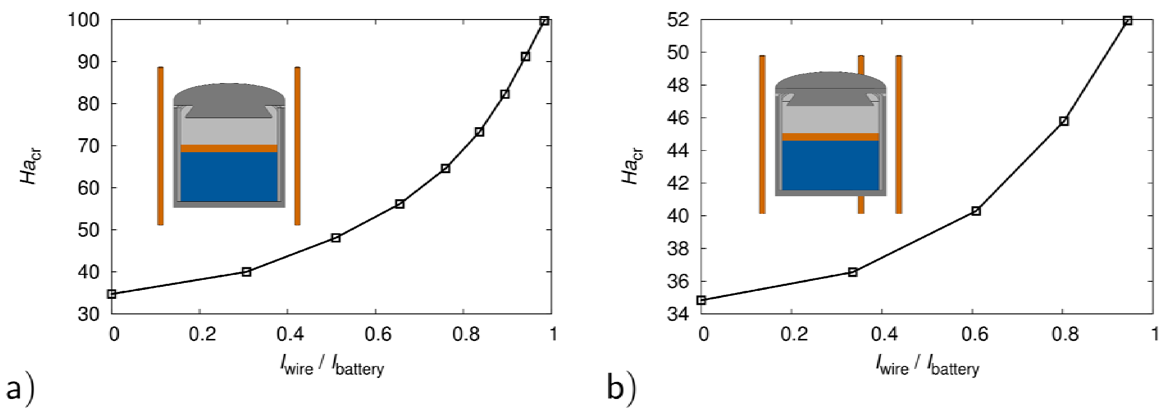

Figure 5: Simulation of the critical Hartmann number for onset of the TI for a cylindrical electrode with aspect ratio 1. The feeding current is lead back through 2 a) or 3 wires b) side by side to the battery.

5. Conclusion and outlook

We have shown that the understanding of MHD effects in LMBs is a key requirement for up scaling such batteries in order to exploit the economies of scale. We have focussed especially on the effects of the Tayler instability, which will indeed be relevant for cells with an aspect ratio larger than one with thin electrolyte layers.

The onset of the TI will take place at Hartmann numbers between 29 and 35 for an electrode aspect ratio between 0.5 and 1. While the corresponding currents may still be tolerable, Hartmann numbers in the range of 100 will induce fluid flows in the order of a few centimetres per second, which will definitely be harmful to LMBs. The consequences will be further studied with multiphase simulation.

Besides of characterising the TI in LMBs we have also proposed a number of effective countermeasures for taming the instability. In particular, providing an additional axial magnetic field generated by a Helmholtz coil is one of the most promising options for stabilising the battery. We have shown further, that an appropriate placement of the feeding lines to the battery may be used for stabilisation.

6. Acknowledgements.

This work was supported by Helmholtz-Gemeinschaft Deutscher Forschungszentren (HGF) in the frame of “Initiative für mobile und stationäre Energiespeichersysteme” as well as in the frame of the Helmholtz Alliance “Liquid metal technologies” (LIMTECH). Fruitful discussions with Marcus Gellert, Jānis Priede, Günther Rüdiger, Martin Seilmayer, Steffen Landgraf and Leopold Barry on several aspects of the TI and liquid metal batteries are gratefully acknowledged.

7. References

[1] Kim et al.: Liquid Metal Batteries: Past, Present, and Future. Chem. Rev. 113 (2013) 2075 - 2099

[2] Seilmayer, M.; Stefani, F.; Gundrum, T.; Weier, T.; Gerbeth, G.: Experimental evidence for a transient Tayler instability in a cylindrical liquid-metal column. Phys. Rev. Lett. 108 (2012) 244501.

[3] Stefani, F.; Weier, T.; Gundrum, T.; Gerbeth, G.: How to circumvent the size limitation of liquid metal batteries due to the Tayler instability. Energ. Convers. Manage. 52 (2011) 2982 – 2986.

[4] Weber, N.; Galindo, V.; Stefani, F.; Weier, T.; Wondrak, T.: Numerical simulation of the Tayler instability in liquid metals. New J. Phys. 15 (2013) 043034.

[5] Tayler, R. J.: The adiabatic stability of stars containing magnetic fields. Mon. Not. R. Astr. Soc. 161 (1973) 365 – 380

[6] Weber, N.; Galindo, V.; Stefani, F.; Weier, T.: Current-driven flow instabilities in large-scale liquid metal batteries, and how to tame them. J. Power Sources (2014), DOI: 10.1016/j.jpowsour.2014.03.055

Patterned turbulence and relaminarization in MHD pipe and duct flows

Dmitry Krasnov[1], Oleg Zikanov[2] and Thomas Boeck[1]

[1]Institute of Thermodynamics and Fluid Mechanics, Ilmenau University of Technology, 98684 Ilmenau, Germany

[2]Mechanical Engineering, University of Michigan - Dearborn, USA

Abstract

We present results of a numerical analysis of relaminarization processes in MHD duct and pipe flows. It is motivated by Julius Hartmann's classical experiments on flows of mercury in pipes and ducts under the influence of magnetic fields. The computed critical parameters for transition as well as the friction coefficients are in good agreement with Hartmann's data. The simulations provide a first detailed view of flow structures that are experimentally inaccessible. Novel flow regimes with localized turbulent spots near the side walls parallel to the magnetic field are observed.

Introduction. The processes of flow re-laminarization in tubes (i.e. pipes and ducts) were the first MHD phenomena studied experimentally by the work of Hartmann & Lazarus (1937). The experimental settings were pipes and ducts of different aspect ratios, subjected to a uniform transverse magnetic field. The flows had moderate values of the Reynolds number and magnetic fields B. Laminarization was detected by comparing the measured pressure drop with theoretical values based on laminar MHD channel flow. The transition threshold could be associated with a certain value of the Reynolds number R based on the thickness of the laminar Hartmann layer. However, theoretical works have not been able to give a satisfactory explanation of transition in the MHD tube flows so far. One reason for this is the particular structure of the laminar velocity distribution in tube flows, which is characterized by a flat core and thin electromagnetic boundary layers. The Hartmann layers form at the walls perpendicular to the magnetic field and have a thickness $\sim 1/B$. On the walls parallel to the field there are corresponding side layers called Shercliff layers (in rectangular ducts) or Roberts layers (in circular pipes). They are thicker than the Hartmann layers and have a different scaling with B. Since the shear is concentrated in Hartmann and side layers, they may both support instabilities leading to turbulence. The role of R as decisive parameter for transition points to the Hartmann layers as origin of transition. However, there are indications that instability first develops in the side layers, e.g. by an analysis of optimal linear perturbations in MHD duct flow (Krasnov *et al.* (2010)). In the present work we therefore examine relaminarization by direct numerical simulations of MHD tube flows for the parameters of the experiments by Hartmann & Lazarus experiments and extend them to higher Reynolds numbers and stronger fields. Our contribution mainly focuses on results from Krasnov *et al.* (2013) and Zikanov *et al.* (2013).

Mathematical model and numerical method. We consider flows of incompressible, Newtonian, electrically conducting fluids (e.g. liquid metals) in rectangular duct or circular pipe. The flow is subjected to a uniform magnetic field B_0. Based on the assumption of small magnetic Reynolds number Re_m, the flows are described by the quasi-static approximation of MHD equations Davidson (2001). The governing non-dimensional equations and boundary conditions are given in Krasnov *et al.* (2013). The non-dimensional parameters are the Reynolds $Re \equiv Ua/\nu$ and Hartmann $Ha \equiv Ba\,(\sigma/\rho\nu)^{1/2}$ numbers. Here U is the mean flux velocity, a is the half-diameter (pipe) or half-height (duct), σ is the electrical conductivity.

The governing equations are solved numerically by our in-house DNS solvers, implemented for rectangular (duct) and cylinder (pipe) geometries. The solvers are based on finite-difference method described in Krasnov *et al.* (2011). The spatial discretization of 2^{nd} order is on a non-uniform structured grid formed along the lines of the Cartesian (duct) or cylindrical (pipe) coordinate system. The time integration is explicit and uses projection-correction procedure to satisfy incompressibility. The computational grid can be clustered in the wall-normal (or radial) directions to provide adequate resolution of the boundary layers.

Results and discussion. The simulations have been conducted for two settings: flows periodic in the streamwise direction and flows with non-periodic inlet/exit conditions. Periodic conditions represent a fully developed flow under perfectly uniform magnetic field. The non-periodic formulation, on the other hand, is more realistic and allows us to apply non-uniform magnetic fields with sharp gradients at the entry and exit of the test sections. By that it is possible to mimic the real flow conditions in experiments, where the magnetic field is never perfectly uniform and the flow evolution is influenced by entry effects.

The specific focus of our study, apart from reproducing the classical MHD experiments Hartmann & Lazarus (1937), is on the appearence of patterned turbulence in MHD tubes. The phenomenon of patterned turbulence, i.e. coexistence of laminar and turbulent zones, is known for hydrodynamic wall-bounded shear flows, e.g. puffs and slugs in pipe flow (Reynolds, 1883; Wygnanski & Champagne, 1973) and spiral bands in Taylor-Couette flow (Andereck *et al.*, 1986). However, coexistence of stable laminar and turbulent regions has not been directly demonstrated for MHD tube flows.

Simulations of periodic duct and pipe flows. We start with the results of periodic DNS (Krasnov *et al.*, 2013), where flows in a pipe and a duct of square cross-section are analyzed at moderate (3000 to 5000) values of Re. The key feature of these simulations is the large length of the computational domain, up to 64π in terms of the hydraulic radius a. As a result of that, previously unknown patterned turbulence regimes have been observed for both pipe and duct. The regimes are realized in all DNS conducted within a certain range of Ha (e.g., at $Re = 5000$, the range was $21 < Ha < 26$ for duct and $18 < Ha < 23$ for pipe). This range of Ha is found to be the transitional one. Below and above it, all the simulations yield fully turbulent or fully laminar flows.

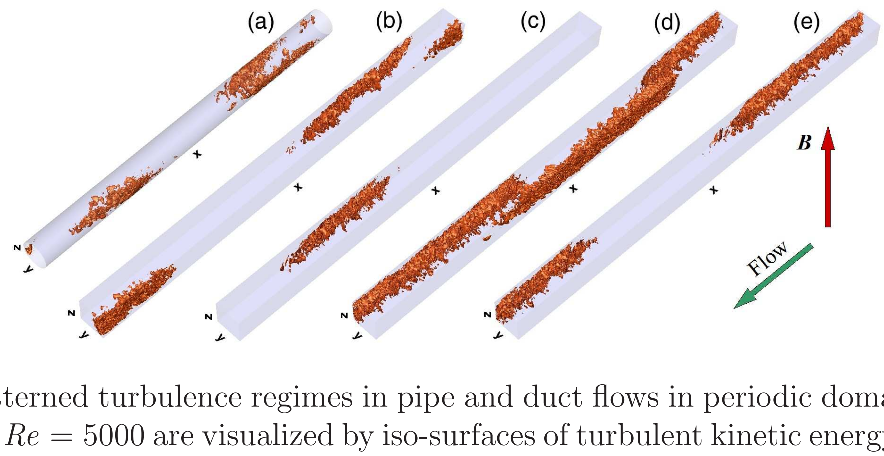

Figure 1: Patterned turbulence regimes in pipe and duct flows in periodic domains. Different flow states at $Re = 5000$ are visualized by iso-surfaces of turbulent kinetic energy of transverse velocity components: puffs in pipe at $Ha = 22$ (a), double- and single-sided puffs in duct at $Ha = 25$ (b, c), and extended turbulent zones induct at $Ha = 22$, cases of double- and single-sided patterns (d, e). The total length of the computational domain is 80 pipe radii in (a) and 32π of duct half-widths in (b)-(e).

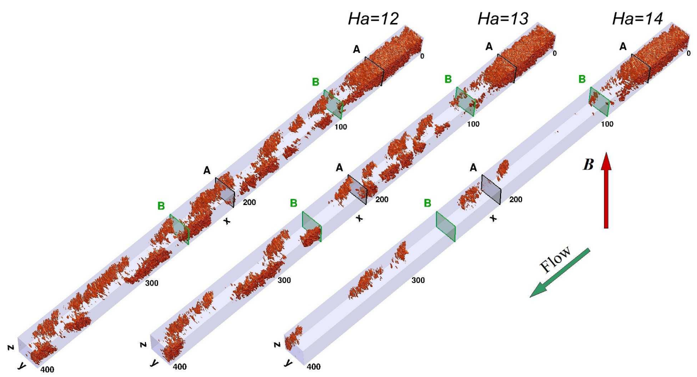

Figure 2: Patterned turbulence in spatially evolving duct flows. The isosurfaces of TKE of the transverse velocity components corresponding to 2% of the maximum are shown. Flows under stepwise magnetic field at $Re = 3000$ are visualized for $Ha = 12$, 13 and 14. (A–A) and (B–B) indicate the pressure measurement sections, the upstream location (A) also shows the point where the magnetic field begins.

The patterned turbulence regimes are illustrated in figure 1. We can see that the flow in the core and Hartmann boundary layers remains essentially laminar. The puffs localized in the sidewalls tend to form staggered patterns (fig. 1b,d) although the specific arrangement is largely influenced by initial conditions. We have also analyzed the temporal evolution of the puffs and identified multiple events as, e.g., merging and splitting of two or more neighboring puffs, two opposite-side spots forming a 'locked' state and traveling together (fig. 1a). In most cases one can identify a characteristic length of a single spot, which is about 30 radii.

Patterned turbulence in spatially evolving MHD duct and pipe flows. We have also made an attempt to reproduce the real experimental conditions of the Hartmann setup. To do so we have performed more realistic transition simulations at $Re = 3000$ with in- and outflow conditions (see Zikanov *et al.* (2013)). Turbulent conditions at the inlet are obtained from a periodic flow simulation running at the same Re and grid spacing. The streamwise domain-size was chosen as $L_x = 128\pi$ to minimize the effects of exit boundary conditions and to provide more room for the spatial evolution of turbulent spots.

The results of these runs confirm the general conclusions from the simulations with periodic boundary conditions. Fig. 2 shows a typical spatial development of the flow in this case. Here the first streamwise section marked as A indicates the position where the magnetic field begins. Downstream of this position the turbulent fluctuations are reduced by the magnetic damping and both Hartmann layers and the bulk of the duct become laminar. At $Ha = 12$ turbulence is still maintained in extended zones located near the Shercliff walls. At $Ha = 13$ we observe the appearance of relatively stable puffs of well-defined length with a tendency to arrange in a staggered pattern. At $Ha = 14$ the magnetic damping is already too strong to sustain regular pattern of turbulent puffs, however weak spots are still generated occasionally at one of the Shercliff walls. Finally, at $Ha = 15$ the flow becomes essentially laminar at the first position marked B, although sporadic events can appear, but these spots die out quickly.

The only available parameter from the Hartmann experimental study was the average pressure gradient dp/dx between two manometers, which can be recalculated in the friction coefficient $f = 2a\, dp/dx/(\rho U^2)$. We, therefore, have also measured f for both periodic and non-periodic simulations to compare with the experiments. Fig. 3 shows that the friction coefficients agree well between experiments and periodic and non-periodic simulations. Upon increasing Ha the friction is initially reduced because of the magnetic damping of turbulence. For $Ha > 15$ it increases linearly with Ha because friction in the laminar Hartmann layers becomes the dominant contribution. Relaminarization occurs close to the minimum of the friction coefficient. In experiments this has typically been found for a parameter

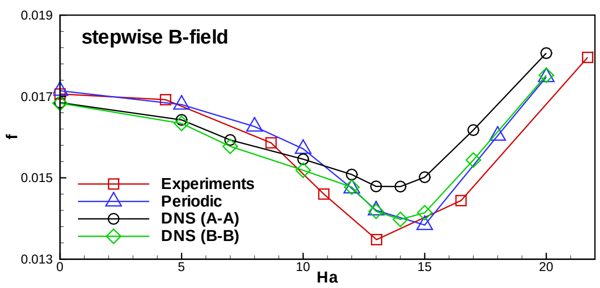

Figure 3: Friction coefficient vs. Hartmann number Ha shown for the results of simulations and experimental data (Hartmann & Lazarus, 1937).

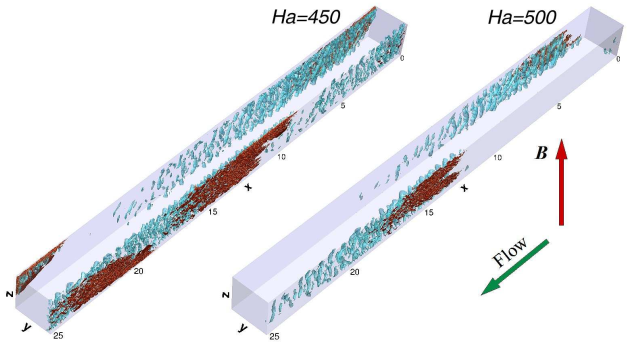

Figure 4: Patterned turbulence regimes realized in simulations of duct flow at $Re = 10^5$ and $Ha = 450,\ 500$. The isosurfaces of TKE (brown) of transverse velocity components corresponding to 2% of the maximum are shown, also shown are the isosurfaces of the second eigenvalue λ_2 (cyan) of tensor $S_{ik}S_{kj} + \Omega_{ik}\Omega_{kj}$.

$R = Re/Ha \approx 200$.

Patterned turbulence in MHD duct at high Re and Ha. The numerical simulations at low and moderate Re and Ha suggest that similar spots can also be expected in the transitional range of Ha at higher Re. So far such regimes have not been observed in our prior study of MHD duct flow at $Re = 10^5$ (Krasnov *et al.*, 2012). This can be attributed to the insufficient length of computational domain $L_x = 4\pi$. To verify this hypothesis we have conducted a series of simulations, in which the length L_x has been increased to 8π. However, the results should be viewed as preliminary because we used a coarser computational grid with $N_x \times N_y \times N_z = 2048 \times 385^2$, i.e. with steps two times larger than in Krasnov *et al.* (2012).

The results are illustrated in figure 4 for $Ha = 450$ and 500 that correspond to the transitional range of $R = Re/Ha \approx 200$. The flow is laminar in the core and the Hartmann boundary layers, but has strongly pronounced turbulent spots near the sidewalls. At $Ha = 450$ ($R = 222$, left plot) the puffs are already isolated and maintain their identity, approximate energy, and approximate length for the entire duration of the simulation. These puffs are similar to those observed earlier in MHD pipe and duct at lower Re and Ha (Krasnov *et al.*, 2013; Zikanov *et al.*, 2013). A typical puff length calculated in terms of the Shercliff layer thickness δ_{Sh}, is $L_{puff}/\delta_{Sh} \approx 130 - 150$. This is consistent with the results at lower Re and Ha, where the puff length of 30 radii amounts to $L_{puff}/\delta_{Sh} \approx 125 - 150$. At higher Ha most of our attempts have ended in fully laminar flow states. However, one simulation started with a realization at $Ha = 450$ has produced a regime with two isolated turbulent spots showing no tendency to further decay. The isolated puffs at $Ha = 500$ ($R = 200$, right plot in fig. 4) have significantly lower turbulent kinetic energy than the puffs at $Ha = 450$ and smaller length: $L_{puff} \approx 85\delta_{Sh}$.

Summary and conclusions. DNS of MHD duct and pipe flows have been performed to reproduce the classical laminarization experiments by Hartmann Hartmann & Lazarus (1937). One distinct feature is the co-existence of laminar and turbulent regions at the edge of laminarization. The peculiarity of the MHD flows is the localization of these turbulent zones in the sidewall layers. The friction coefficients measured by Hartmann are in good agreement with our DNS. It is, however, important to notice that this integral parameter provides no indication of the existence of turbulent zones as their impact on the total friction is very low. We also notice that at high $Ha \approx 450$ ... 500 the appearance of isolated puffs is accompanied by the quasi-2D columnar vortices (cyan shading in fig. 4), identified earlier in our study (Krasnov *et al.*, 2012). It seems plausible that there is an interaction between the puffs and quasi-2D vortices, such that the puffs are stretched along the magnetic field direction and resemble objects known as "turbulent bands". Further work is necessary to resolve the details of transition in the side layers and to explain why the parameter R determines the transition in a wide range of Re and Ha numbers.

Acknowledgements. TB and DK acknowledge financial support from the Helmholtz Alliance "Liquid Metal Technologies" and the Deutsche Forschungsgemeinschaft. OZ acknowledges financial support from the U.S. National Science Foundation (Grants CBET 0966557 and CBET 1232851). Computer resources were provided by the computing centers of Forschungszentrum Jülich (NIC) and TU Ilmenau.

References

Andereck, C. D., Lui, S. S. & Swinney, H. L. 1986 Flow regimes in a circular couette system with independently rotating cylinders. *J. Fluid Mech.* **164**, 155–183.

Davidson, P. A. 2001 *An Introduction to Magnetohydrodynamics*. Cambridge University Press.

Hartmann, J. & Lazarus, F. 1937 Hg-dynamics II: Experimental investigations on the flow of mercury in a homogeneous magnetic field. *K. Dan. Vidensk. Selsk. Mat. Fys. Medd.* **15** (7), 1–45.

Krasnov, D., Thess, A., Boeck, T., Zhao, Y. & Zikanov, O. 2013 Patterned turbulence in liquid metal flow: Computational reconstruction of the Hartmann experiment. *Phys. Rev. Lett.* **110**, 084501.

Krasnov, D., Zikanov, O. & Boeck, T. 2011 Comparative study of finite difference approaches to simulation of magnetohydrodynamic turbulence at low magnetic Reynolds number. *Comp. Fluids* **50**, 46–59.

Krasnov, D., Zikanov, O., Rossi, M. & Boeck, T. 2010 Optimal linear growth in magnetohydrodynamic duct flow. *J. Fluid Mech.* **653**, 273–299.

Krasnov, D. S., Zikanov, O. & Boeck, T. 2012 Numerical study of magnetohydrodynamic duct flow at high Reynolds and Hartmann numbers. *J. Fluid Mech.* **704**, 421–446.

Reynolds, O. 1883 An experimental investigation of the circumstances which determine whether the motion of water shall be direct or sinuous, and of the law of resistance in parallel channels. *Philos. T. R. Soc. A* **174**, 935–982.

Wygnanski, I. J. & Champagne, F. H. 1973 On transition in a pipe. Part 1. The origin of puffs and slugs and the flow in a turbulent slug. *J. Fluid Mech.* **59**, 281–335.

Zikanov, O., Krasnov, D., Li, Y., Boeck, T. & Thess, A. 2013 Patterned turbulence in spatially evolving magnetohydrodynamic tube flows. *Theor. Comp. Fluid Dyn.* Accepted for publication.

ULTRASOUND DOPPLER VELOCIMETRY FOR LIQUID METAL BATTERIES

STARACE M., WEBER N., SEILMAYER M., WEIER T., STEFANI F., ECKERT S.
Helmholtz-Zentrum Dresden − Rossendorf, Bautzner Landstraße 400, 01328 Dresden, Germany
E-mail address: m.starace@hzdr.de

Abstract : The Tayler instability (TI) due to current flow through a liquid GaInSn column is under consideration here. It is a consequence of electric current surpassing a critical value in the order of a few kA and manifests itself as a stack of vortices. Two ultrasound transducers encased in a copper electrode on top of the column were used to measure the vertical component of the liquid metal flow caused by the TI, which is of the order of several mm/s. UDV measurements were only possible after noise suppression mechanisms were added to the experimental setup. The results of the UDV retrievals will be discussed here.

1. Introduction

Due to the limited amount of fossil and fissile fuels on Earth, as well as the strain on the environment caused by their consumption or disposal, some societies are shifting their reliance onto renewable sources, such as solar and wind energy. This necessitates larger short-term energy storage capabilities, as the production of electrical energy cannot necessarily be adjusted to the demand. Liquid metal batteries are a proposed means of this type of large-scale energy storage. They consist of a solid container holding three phases of liquids, namely an anode metal, a cathode metal alloy and an electrolyte, such as a molten salt, separating the two. The advantages of liquid metal batteries are high current densities, reasonably low projected cost, a long cycle life, scalability, as well as their simple and self-assembling construction. Their disadvantages are low output voltages, high working temperatures required for the metals and the molten salts to remain liquid, as well as magnetohydrodynamic (MHD) instabilities.
As the electrolyte layer needs to be thin in order to have a low resistance, such instabilities could cause fluid motions that displace the electrolyte, bringing the two electrodes of the battery in contact, which would lead to battery failure.

The experiment discussed herein focuses on the pinch-type Tayler instability, which is the incompressible counterpart of the $m = 1$ kink instability of the z-pinch in compressible fluids, such as plasmas [1]. This instability is driven by an axial current flowing through a conducting fluid, which creates an azimuthal magnetic field resulting in an inward radial Lorentz force that “pinches” the fluid. A slight perturbation in a compressible system displaces the pinch locally, bunching the magnetic field together on one side and spreading it out on the other. The radial symmetry of the Lorentz force is broken as a result, causing the perturbation to grow exponentially.

In an incompressible fluid, such as a liquid metal, such small perturbations are counteracted by viscosity and resistivity as long as the current vertically flowing through the conductor remains below a critical value. Above it, the Lorentz forces become too strong for such perturbations to be damped. As a result, a stack of vortices whose axes are normal to the flow of electrical current develops. This is known as the Tayler instability (TI) [2, 3]. In a previous version of this experiment, the vertical component of the magnetic field was measured by fluxgate magnetometers. Above currents of 2.7 kA, B_z grew noticeably, indicating that to be the critical current at which the TI sets in [4]. In the newly modified version of the experiment, the vertical component of the liquid metal flow velocity is directly measured by an ultrasound Doppler velocimeter (UDV).

2. Experimental setup

A 75 cm long and 10 cm wide eutectic liquid gallium-indium-tin (GaInSn) alloy in a cylindrical polyoxymethylene container constitutes the core of this experiment. The top and bottom of the cylinder consist of copper electrodes that are connected to a switched-mode DC power supply unit (PSU) whose switching frequency is 10 kHz. The PSU, the 3 cm wide hollow copper rods delivering current to the experiment as well as the bottom electrode of the GaInSn cylinder are water cooled. The option to water-cool the top electrode exists as well, but was omitted with the aim of reducing thermal convections caused by Joule heating. Two ultrasound transducers (UST) encased within the top electrode are in direct contact with the liquid metal below (fig. 1).

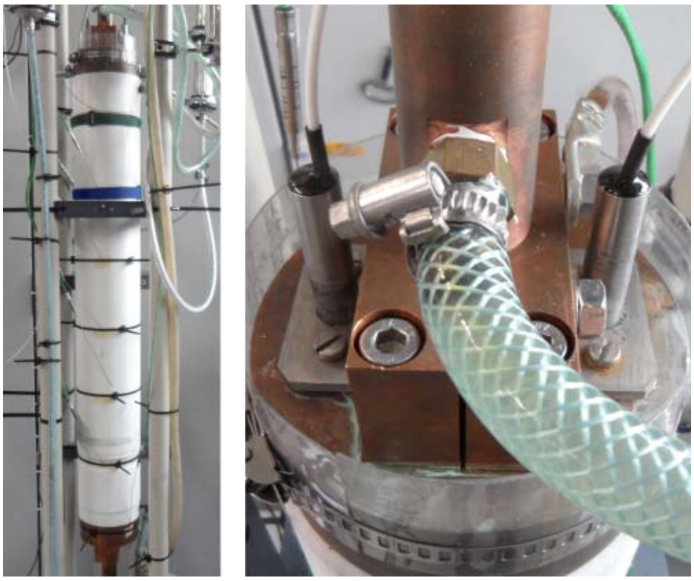

Figure 1: Left: GaInSn cylinder. Right: Top electrode with USTs.

The custom-made transducers, which can function at up to 60 °C, are 12 mm wide and their optimal operating frequency is 6 MHz. They are triggered by an UDV, which also records the echoes they measure and is controlled by a data acquisition computer.

Although the requirements for spatial and temporal resolution permit frequencies as low as 2 MHz, that regime is marred by a larger amount of noise from the PSU. This is due to the rectangular shape of the switching frequency's waveform, as a rectangular wave is equivalent to a superposition of harmonic waves with frequencies that are odd integer multiples of the switching frequency with exponentially decaying amplitudes.

Furthermore, a noise suppression assembly was constructed to ensure that meaningful UDV data can still be gathered from the sensors inside the electrode at currents in the order of several kA. It consists in part of six film capacitors manufactured by Electronicon. They have a self-inductance of 15 nH and are connected to the mains of the PSU in parallel to the TI cylinder, constituting a shunt which damps ripples in the current. Additionally, noise reduction inductors consisting of carbonyl iron and hydrogen-reduced iron powder cores were placed around the copper conductors powering the Tayler experiment. They impede the passage of alternating current through the induction of an opposing voltage. These cores have a high enough inductive reactance in the UDV frequency range to effectively suppress relevant AC ripples. Furthermore, they have a high A_L value, which is related to their inductance L and the number of turns N:

$$A_L = \frac{10^4 L}{(N)^2}. \tag{1}$$

This is because the energy that can be stored in a magnetic field of an inductor is proportional to the inductance. Here, N = 1 because a straight conductor surrounded by a ring core is equivalent to a coil around a core with a single turn.

The magnetic flux density within the cores is proportional to the applied magnetic field strength, provided it remains below 1 T, above which iron powder materials have their saturation densities. In this linear regime, the inductance is constant. As the maximum possible current that can be generated by the PSU is 8 kA, the ring cores not exclusively used for common-mode chokes (CMCs) were therefore also selected for having an estimated DC magnetic flux density (as calculated with Ampère's circuital law) below 1 T at 8 kA. 14 individual ring cores of three types manufactured by Amidon were used, namely five T225-2, eight T50-2 and a single T650-3. The latter was estimated to reach saturation, if not used as a CMC. Two of the T650-2 cores and the T650-36 core are in fact used as such. The magnetic fields within the cores caused by the opposing DC currents flowing through the conductors they surround nearly cancel each other out. As a result, the flux density within the T650-36 core is well below saturation. The magnetic fields caused by common mode currents travelling through the conductors do not cancel each other out, which is why these currents can be choked by the inductor. The noise suppression assembly is shown in figure 2.

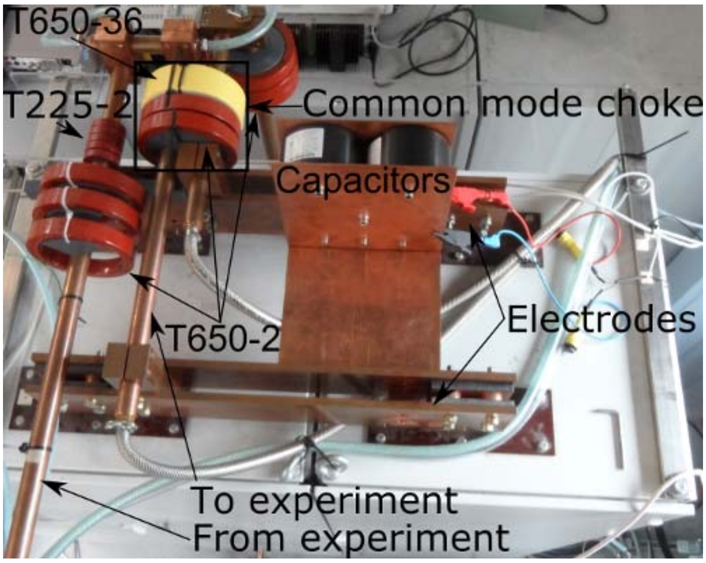

Figure 2: Noise suppression assembly on top of the PSU.

To reduce sheath currents running along the coaxial cables connecting the USTs to the UDV, the cables were wound around toroidal ferrite and split cores.

Moreover, the UDV is decoupled from the electric grid with an isolation transformer, which prevents ground loops from affecting the measurements.

2. Measurements and data analysis

The measurement results consist primarily of the relative intensities and wavelengths of echoes produced by backscattering on metal oxide particles within the fluid. Velocities are computed from the wavelength shifts in real time by the UDV.
The theoretical current threshold above which the TI appears is approximately 2.7 kA. and the wavelength of its vortices is expected to amount to 12.5 cm [3, 4]. Thermal convection caused by Joule heating, as well as electrode-driven electro-vortex flow already appear at much lower currents. The latter is however suspected to be of significance only in the vicinity of the electrodes, rather than across the entire column. The vertical velocity component measured by the two transducers as a function of time and column depth is shown in figures 3 and 4 respectively. Here, the current is switched on at t = 0 and brought to 4 kA in approximately 30 seconds. The vertical wavelength of the velocity fields is approximately twice as large as that of the theoretically predicted value for the TI, but is in agreement with results obtained from the fluxgate magnetometer measurements [4]. Although the cause of this is not well understood yet, aliasing artefacts have been ruled out. Numerical and experimental investigations into other phenomena that are at play here, i.e. the electrode-driven electro-vortex flow and thermal convection are ongoing [5].
To separate characteristic TI modes from other processes, a spectral analysis must be carried out. The Lomb-Scargle method of least squares spectral density estimation is shown in figures 5 and 6 for the velocimetry data from figs. 3 and 4 respectively. Whereas the spatial periodicity of the aforementioned flow patterns, as well as its harmonics are evident in the periodogram, the theoretically determined 8 m^{-1} inverse wavelength of the TI, is overshadowed by a wave twice as long as the predicted value, at approximately 4 m^{-1}. Further analysis will therefore be necessary, such as the isolation of individual wavelength bands and comparisons of their amplitudinal growth rates with one another as well as with the TI's growth rate as determined by fluxgate sensor measurements.

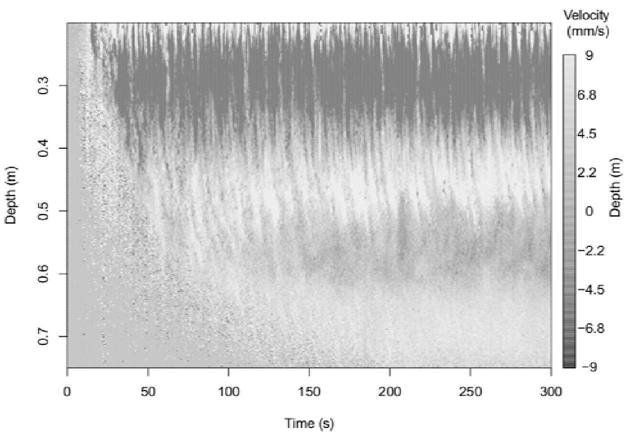

Figure 3: Vertical velocity in the GaInSn column. The current is 4 kA.

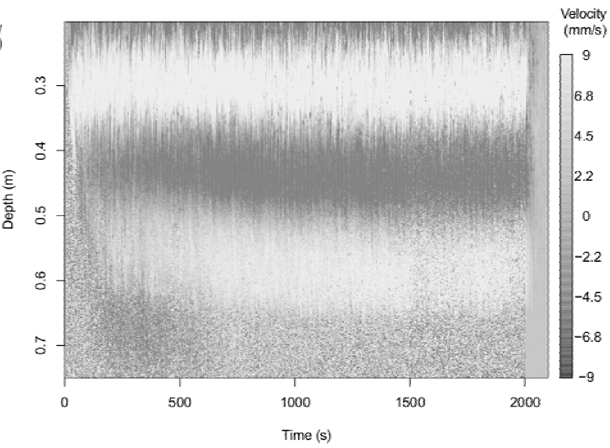

Figure 4: Vertical velocity in the GaInSn column measured by the other UST under the same conditions.

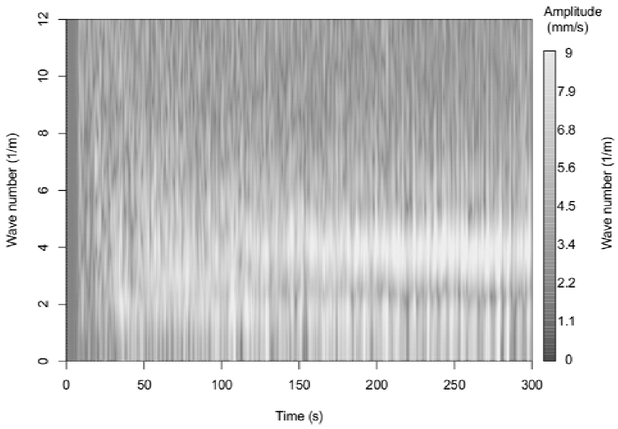

Figure 5: Lomb-Scargle periodogram of the velocity time series in fig. 3.

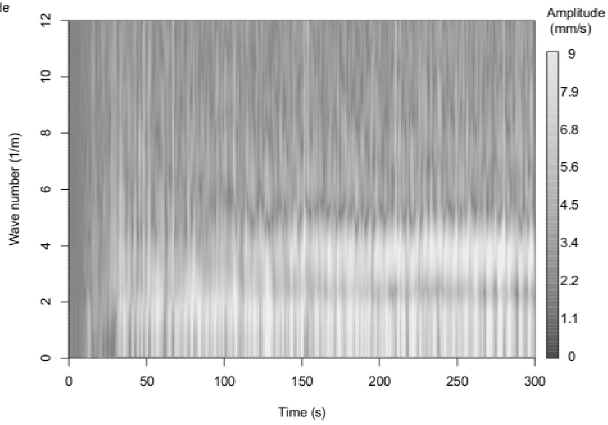

Figure 6: Lomb-Scargle periodogram of the velocity time series in fig. 4.

3. Conclusion and outlook

The basic feasibility of UDV within a high-current environment has been demonstrated and the preliminary results are in general agreement with those found with B_z-measurements [4]. However, the TI growth rate has yet to be determined and compared with the previous results. Two additional USTs will be added to measure the vertical flow 90° off the positions of the current sensors, which will allow a clearer monitoring of the flow structure. More in-depth analysis of the collected data will be performed as well, especially in the first few hundred seconds, during the growth time of the TI, before natural convection becomes more pronounced.

4. Acknowledgements

The work presented here was made possible by the Helmholtz Association of German Research Centres as part of the "Helmholtz-Initiative für mobile und stationäre Energiespeichersysteme", as well as the Helmholtz Alliance "Liquid Metal Technologies" (LIMTECH).

5. References

[1] Bergerson, W. F. et al.: Onset and Saturation of the Kink Instability in a Current-Carrying Line-Tied Plasma. Phys. Rev. Lett. 96 (2006) 015004.
[2] Spruit, H.C.: Dynamo action by differential rotation in a stably stratified stellar interior. Astron. Astrophys. 381 (2002) 923-932.
[3] Weber, N. et al.: Numerical simulation of the Tayler instability in liquid metals. New J. Phys. 15 (2013) 043034.
[4] Seilmayer, M. et al.: Experimental evidence for a transient Tayler instability in a cylindrical liquid-metal column. Phys. Rev. Lett. 108, 24 (2012) 244501.
[5]Weber, N.: unpublished, personal communication.

NON-AXISYMMETRIC RESONANT MODES UNDER OSCILLATING MAGNETIC FIELDS FOR VERY LOW INTERACTION PARAMETER VALUES

CORTÉS-DOMÍNGUEZ Iván[1], BURGUETE Javier[2]
Department of Physics and Applied Mathematics, C/ Irunlarrea 1, University of Navarra, E-31008 Pamplona, Spain
[1]icortes.1@alumni.unav.es, [2]javier@unav.es

Abstract: In this work we present results related to instabilities created into a disk shaped conducting fluid layer. No external forces are applied. Only a zero-mean time-dependent magnetic field parallel to the disk axis. The experimental setup allows very fine determination of the amplitude of possible instabilities. We show different azimuthal wavenumbers and we are studying their dynamics. The axisymmetric fluid layer destabilizes even for very small values of the interaction parameter.

1. Introduction

The action of external magnetic fields that evolve in time can produce surface waves or instabilities in conducting fluid layers [1]. There are a few experimental works related to the study of instabilities in fluids under the action of external magnetic fields [2,3,4]. This effect depends on two sets of parameters, the fluid layer characteristics (electrical conductivity, layer depth, diameter) and the magnetic field (frequency and intensity). When the magnetic field frequencies are large, the instabilities grow due to forces localized near the surface. On the other hand, for low frequency ranges, those forces may penetrate and produce bulk forces. Many experimental works have been developed for the large frequencies regime but there is a lack of results in the domain of low frequencies because of its limited potential applications. We want to study the low range of frequencies (0.1Hz to 10Hz).

Following the previous work of J.Burguete et *al.* [4] we will focus in a configuration where a thin axisymmetric conducting fluid layer with free surface is forced through a time-dependent magnetic field parallel to the axis of a circular cell. In Burguete's work, the magnetic field had always the same orientation: the magnetic field was $B_0+B_1\sin(\omega t)$, being $B_1<B_0$. In our experimental setup, we work with a zero mean magnetic field, so it oscillates between both possible orientations in a cycle. This field generates in the fluid an azimuthal current due to Lenz's law that interacts again with the magnetic field producing a radial force (Lorenz's forces). Due to the nature of the external magnetic field applied the oscillatory component of the Lorentz force's will have a frequency twice the frequency of the magnetic field [5]. Assuming that the system is axisymmetric, any perturbation that deviates the system from the axisymmetry can produce an azimuthal force that can destabilize the fluid and a flow can be created.

There are some measurements in a strongly non-linear regime [6,7] and in low frequency regime [3,4] but our system allows a much more precise study of the dynamics of the pattern close to the threshold, so we can compare with the theory that predicts an instability without threshold [2,4].

2. Presentation of the problem

We have developed an experimental setup that allows us a fine adjustment of the main control parameters (magnetic field amplitude and frecuency) to study the dynamics of these patterns and a precise observation of any deviation from axisymmetry. Our experimental setup consists of three parts, the experimental cell, magnetic field and optical system (fig1).

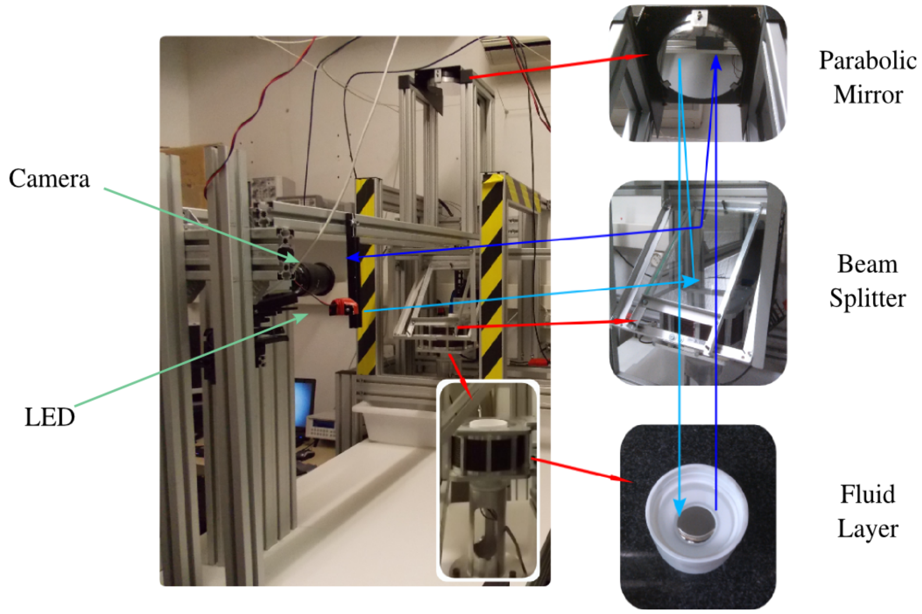

Figure 1. Experimental setup

Experimental Cell

An eutectic InGaSn alloy (liquid at room temperature) is placed on a Teflon® cylindrical cavity which a diameter of 84mm. There is a depression at the bottom part of the cell that allows to center the liquid. The alloy adopts the form of a thin circularly shaped fluid layer (a large drop of fluid) on the bottom of the container, with free surface. The drop remains centered on the cell. The InGaSn drop is up to 20mm depth. An upper layer of HCl (1%) has been placed to prevent oxidation of the eutectic alloy.

Magnetic field

No external current is applied on the fluid. The force only appears through a purely vertical time dependent magnetic field perpendicular to the free surface. This field evolves harmonically with frequencies between 0.1Hz to 10Hz. The field evolution is slow enough to avoid skin effects. The magnetic field is induced by modulating an electric current on an external coil. The power source that drives the coil can deliver up to 60A producing magnetic fields up to 70mT. This electrical current can be modulated in an extremely low frequency range. Once the experimental cell is placed inside the coil, the axis of this magnetic field is parallel to the axis of the cylinder (perpendicular to the free surface of the liquid metal layer).

Optical System

The optical system is based on the method developed by Foucault [8]. A beam of light is redirected using a mirror and a beam splitter. This configuration will allow us the direct observation of the free surface of the fluid layer (a top view). In the top view of the fluid the liquid metal remains as a mirror when the system is at rest and there are no instabilities. Any instability produces small deviations from the equilibrium position. A camera placed to record the top view allow us to study the deflections of the surface (any deflection will appear in the camera as a bright or dark region). Therefore we can record the dynamical behaviour of the system.

Our experimental setup has allowed us to observe spatial patterns (fig. 2) that appear in the phase-space between 0.4 Hz and 10Hz. An axisymmetric pattern (m=0) appears in all the phase-space. We observe very restricted windows where different patterns (m=2,3,4…) are very close and can even coexist as was noted by J. Burguete et *al.* [4].

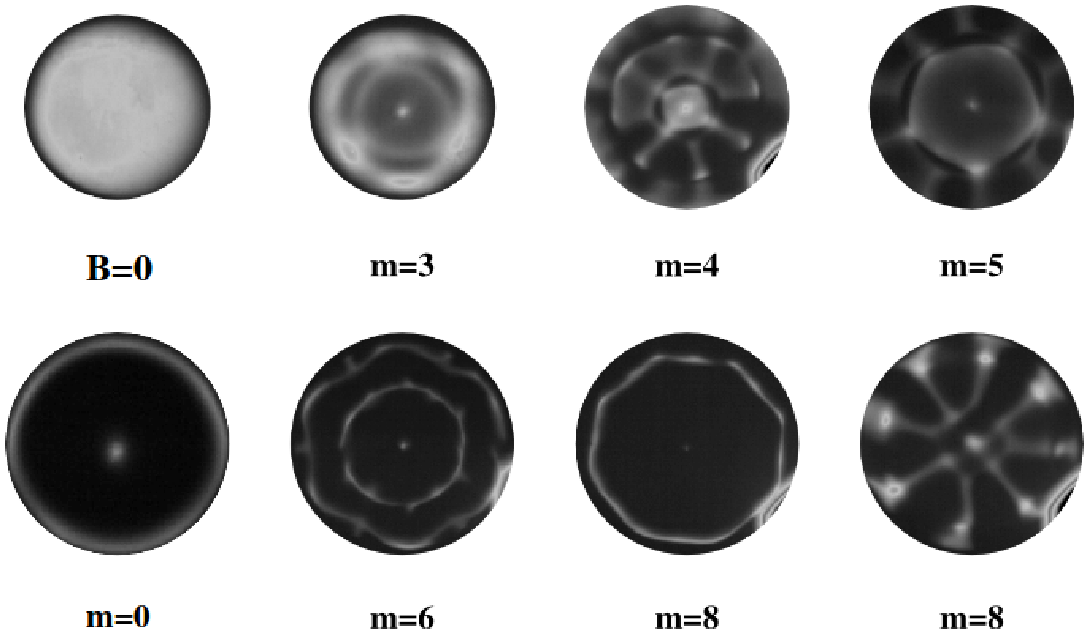

Figure 2. Different azimuthal wavenumbers (top view)

Using Fourier analysis tools it is possible to study the dynamics of the patterns. The evolution of the resonance frequencies with the intensity reveals that these patterns are not pure modes. For example, in the case of a 35ml InGaSn drop, we observe three restricted windows in wich more than azimuthal wavenumber appear simultaneously (fig. 3). If we further increase the magnetic field intensity, a cycle is established between different patterns.

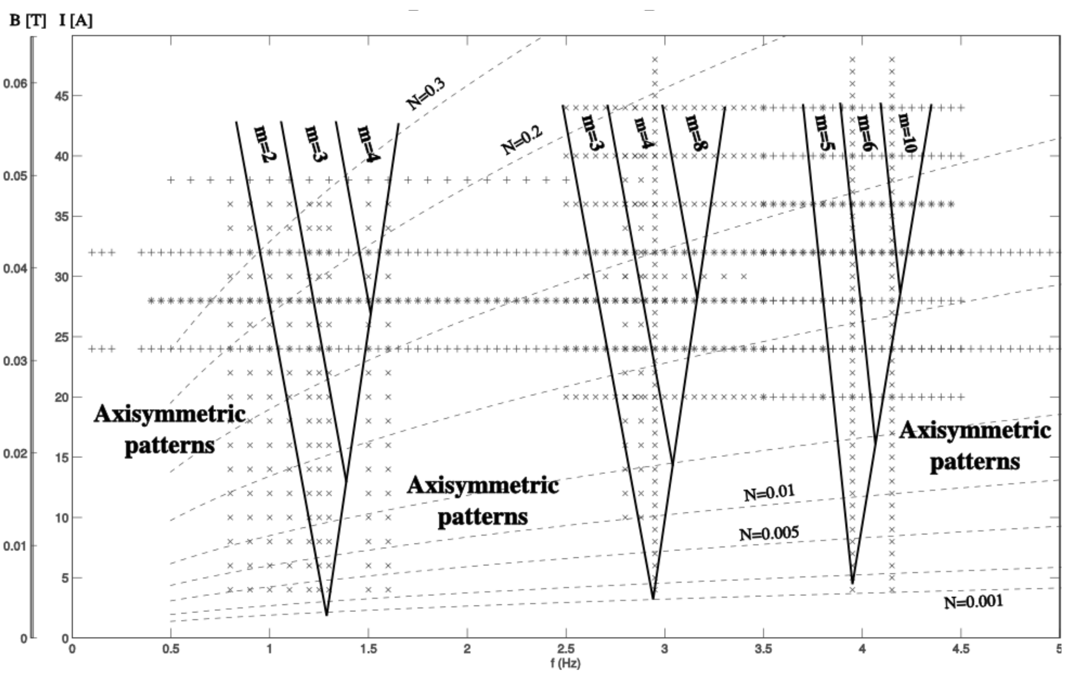

Figure 3. Phase-space of the different patterns. Dashed line : isocontours of the interaction parameter N. Each mark represents an experimetnal run.

Focusing our attention in the third restricted window of the phase-space shown in fig. 3 we can observe how in 3.95Hz frequency a dynamical behaviour alternating between modes 5, 6 and 10 has been detected. If we study the extended FFT at this frequency, we can isolate the different modes that appear simultaneously (fig. 4). We can study their growth rates and we can show how different families of harmonics grow slaved. The amplitude of this modes change with **B** for a given frequency, and different growing rates that tend to fill can be determined for different modes (fig. 5).

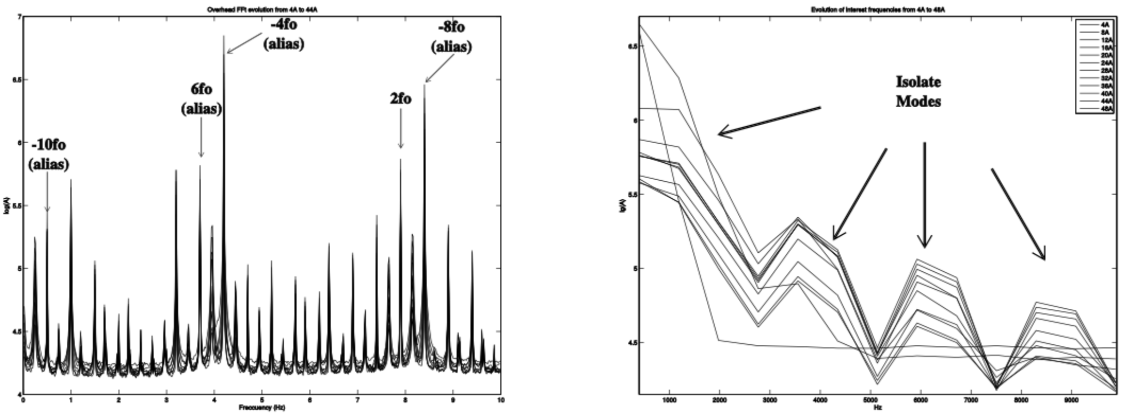

Figure 4 . Overhead and extenden FFT for increasing values of magnetic field at 3.95Hz

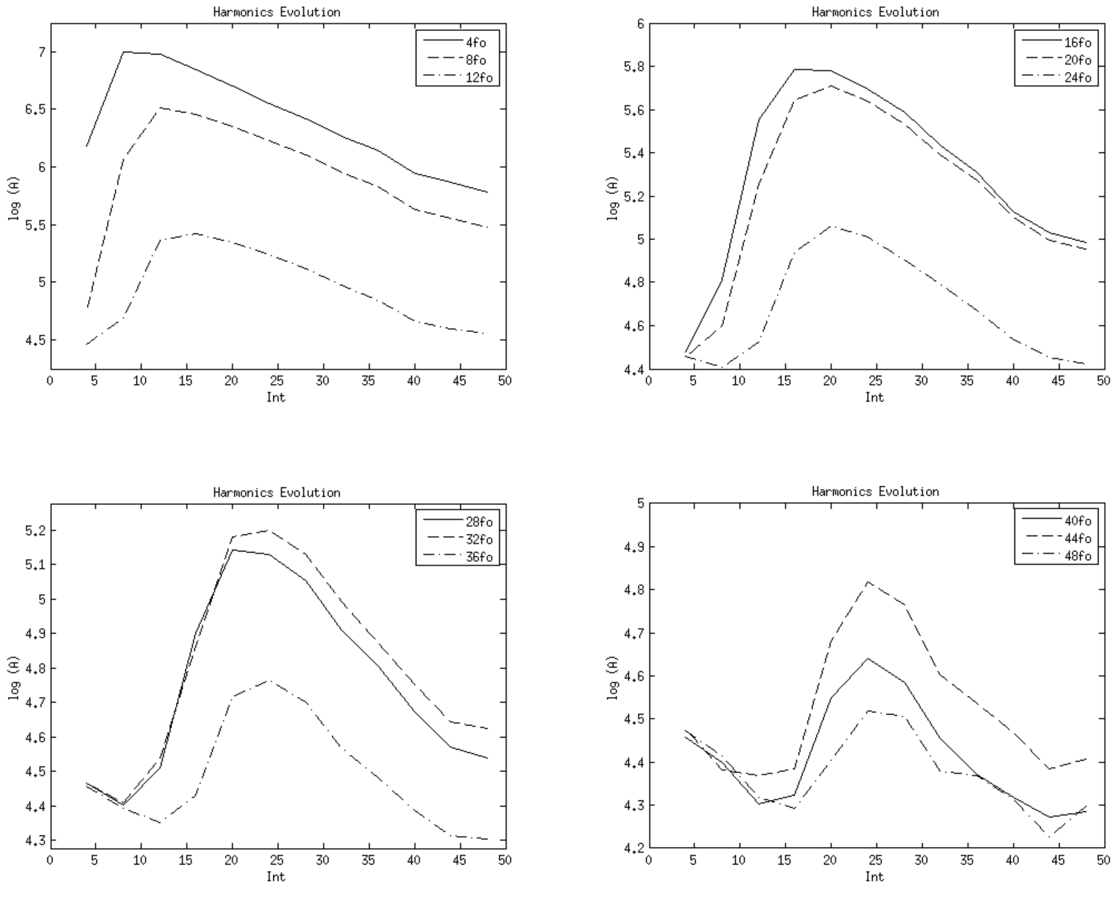

Figure 5. Grow rate of different families of harmonics that form isolated modes for increasing values of magnetic fields at 3.95Hz

3. Conclusions

Our experimental setup allows the characterization of spatial patterns very close to any potential threshold. Different symmetry breaking patterns have been found with different azimuthal wavenumbers m = 0, 2, 3, 4, 5, 6, 8, 10. For the same parameter values, the azimuthal wavenumbers can even coexist and we have identified various sets of harmonics that evolve slaved. These patterns appear for parameter values in very restricted windows and for very small interaction parameters. These instabilities have been observed for interaction parameters as low as N=0.002, and up to now we have not detected any threshold. Radial wavenumbers have been observed. So, the magnetic field can induce patterns even for very small forcings.

4. References

[1] R. Moreau, Magnetohydrodynamics, Kluwer Academic Publichers, Dordrecht, the Netherlands (1990).

[2] Fautrelle, Y.; Sneyd, A.D.; Surface waves created by low-frequency magnetic fields. European Journal of Mechanics B/Fluids. Vol.24, pp.91-112 (2005).

[3] Galpin, J.M.; Fautrelle, Y.; Liquid-metal flows induced by low frequency alternating magnetic fields. J. Fluid Mechanics, vol. 239, pp. 383-408 (1992).

[4] Burguete, J.; Miranda, M.A.; Instabilities of conducting fluid layers in cylindrical cells under the external forcing of weak magnetic fields. Magnetohydrodynamics. Vol.48, No.1. Pp.69-75 (2012).

[5] Galpin, J.M.; Fautrelle, Y.; Sneyd, A.D.; Parametric resonance in low-frequency magnetis stiring. J. Fluid Mechanics, vol. 239, pp. 409-427 (1992).

[6] F. Debray and Y. Fautrelle, Adv. in Turb. IV, in: Appl. Sci. Res., vol. 51, Kluwer (1993) p 31.

[7] F. Ingwiller, F. Bonnel, Y. Fautrelle, S. Daugan, and J. Etay Actes du 9eme FLUVISU (2001) p 18.

[8] L. Foucault, Comptes rendus de l'Academie des Sciences, Paris, vol. 47, pages 958-959 (1858).

INDUCTIONLESS MAGNETOROTATIONAL INSTABILITY BEYOND THE LIU LIMIT

KIRILLOV, O.N.[1], STEFANI, F.[1], FUKUMOTO, Y.[2]
Affiliation: [1]Helmholtz-Zentrum Dresden-Rossendorf, P.O. Box 510119, D-01314 Dresden, Germany, [2]Institute of Mathematics for Industry, 744 Motooka, Nishi-ku, Fukuoka 819-0395, Japan
e-mail: O.Kirillov@hzdr.de

Abstract: Employing the short wavelength approximation, we develop a unified framework for the investigation of the standard, the helical, and the azimuthal version of the magnetorotational instability (MRI) as well as of the current-driven Tayler instability. We show that the inductionless types of MRI that were previously thought to be restricted to comparably steep rotation profiles extend well to the Keplerian case if only the azimuthal field deviates slightly from its field-free profile.

1. Introduction

How stars and black holes are able to form from rotating matter is one of the big questions of astrophysics. Magnetic fields figure prominently into the picture via the mechanism of magnetorotational instability (MRI) [1,2]. The usual understanding is that MRI only works if matter is electrically well conductive. However, in rotating disks this is not always the case. In areas of low conductivity, like the dead zones of protoplanetary disks or the far-off regions of accretion disks that surround supermassive black holes, the MRI effect is numerically difficult to comprehend and its relevance is thus a matter of dispute. A complementary approach to this regime would be to carry out liquid metal experiments. Unfortunately, under the condition of a purely vertical field, both the rotational speed as well as the magnetic field has to be very high, so that experiments on this standard version of MRI (SMRI) are extremely involved [3,4], and a clear success has eluded them thus far.

By adding an azimuthal magnetic field to the vertical one, as proposed in [5], it became possible to observe the helical MRI (HMRI) at substantially lower rotational speeds and magnetic fields [6]. Very recently, the non-axisymmtric azimuthal MRI (AMRI) has also been observed [7]. However, one of the blemishes of these inductionless versions of MRI is the fact that they are only able to destabilize rotational profiles with a relatively steep radial decay, which for now did not include rotation profiles as shallow as the Keplerian one.

Here, we study the stability of rotational flows in the presence of a constant vertical magnetic field and an azimuthal magnetic field with an arbitrary radial dependence. Employing the short-wavelength approximation, we develop a unified framework for the investigation of SMRI, HMRI, AMRI, as well as of current-driven Tayler instability (TI) [8]. Considering the viscous and resistive case, our main focus is on the limit of small magnetic Prandtl numbers which applies, e.g., to liquid metal experiments but also to the colder parts of accretion disks. We rigorously demonstrate that the inductionless versions of MRI extend well to the Keplerian case if the azimuthal field only slightly deviates from its field-free profile [9-12].

2. Mathematical setting

The standard set of equations of viscous, resistive, incompressible magnetohydrodynamics consists of the Navier-Stokes equation and the induction equation for the time evolution of the fluid velocity **u** and the magnetic field **B,** respectively,

$$\frac{\partial \mathbf{u}}{\partial t}+\mathbf{u}\cdot\nabla\mathbf{u}=-\frac{\nabla P}{\rho}+\frac{\mathbf{B}\cdot\nabla\mathbf{B}}{\mu_0\rho}+\nu\nabla^2\mathbf{u} \quad , \qquad \frac{\partial \mathbf{B}}{\partial t}+\mathbf{u}\cdot\nabla\mathbf{B}=\mathbf{B}\cdot\nabla\mathbf{u}+\eta\nabla^2\mathbf{B},$$

where both **u** and **B** are divergence-free, and P is the total pressure. In the following, we assume a rotating flow with angular velocity $\Omega(r)$, exposed to a magnetic field with constant axial component B_z^0 and an azimuthal magnetic field with arbitrary radial dependence $B_\phi^0(r)$. Around this ground state, we consider short-wavelength perturbations of velocity and magnetic field with an, in general complex, growth rate λ and a wave vector $\mathbf{k}$ for which we use the definitions $\alpha = k_z|\mathbf{k}|^{-1}, |\mathbf{k}|^2 = k_r^2 + k_z^2$. We define the viscous, the resistive, and the two Alfvén frequencies corresponding to the vertical and the azimuthal magnetic field,

$$\omega_\nu=\nu|\mathbf{k}|^2,\quad \omega_\eta=\eta|\mathbf{k}|^2,\quad \omega_{A_z}=\frac{k_z B_z^0}{\sqrt{\rho\mu_0}},\quad \omega_{A_\phi}=\frac{B_\phi^0}{r\sqrt{\rho\mu_0}},$$

and measure the radial steepness of the angular velocity and the azimuthal Alfvén frequency by two appropriate Rossby numbers:

$$\mathrm{Ro}=\frac{r}{2\Omega}\frac{\partial\Omega}{\partial r},\quad \mathrm{Rb}=\frac{r}{2\omega_{A_\phi}}\frac{\partial\omega_{A_\phi}}{\partial r}.$$

After introducing the following dimensionless numbers,

$$\mathrm{Pm}=\frac{\omega_\nu}{\omega_\eta},\quad \beta=\alpha\frac{\omega_{A_\phi}}{\omega_{A_z}},\quad \mathrm{Re}=\alpha\frac{\Omega}{\omega_\nu},\quad \mathrm{Ha}=\frac{\omega_{A_z}}{\sqrt{\omega_\nu\omega_\eta}},\quad n=\frac{m}{\alpha},$$

we can derive the secular equation for the perturbations in the form

$$p(\lambda)=\det(\mathbf{H}-\lambda\mathbf{E})=0,$$

with the matrix

$$\mathbf{H}=\begin{pmatrix} -in\mathrm{Re}-1 & 2\alpha\,\mathrm{Re} & \dfrac{i\mathrm{Ha}(1+n\beta)}{\sqrt{\mathrm{Pm}}} & -\dfrac{2\alpha\beta\mathrm{Ha}}{\sqrt{Pm}} \\ -\dfrac{2\,\mathrm{Re}(1+\mathrm{Ro})}{\alpha} & -in\mathrm{Re}-1 & \dfrac{2\beta\mathrm{Ha}(1+\mathrm{Rb})}{\alpha\sqrt{\mathrm{Pm}}} & \dfrac{i\mathrm{Ha}(1+n\beta)}{\sqrt{\mathrm{Pm}}} \\ \dfrac{i\mathrm{Ha}(1+n\beta)}{\sqrt{\mathrm{Pm}}} & 0 & -in\mathrm{Re}-\dfrac{1}{\mathrm{Pm}} & 0 \\ \dfrac{-2\beta\mathrm{Ha}\mathrm{Rb}}{\alpha\sqrt{\mathrm{Pm}}} & \dfrac{i\mathrm{Ha}(1+n\beta)}{\sqrt{\mathrm{Pm}}} & \dfrac{2\,\mathrm{Re}\,\mathrm{Ro}}{\alpha} & -in\mathrm{Re}-\dfrac{1}{\mathrm{Pm}} \end{pmatrix}.$$

This gives a dispersion relation in form of complex fourth-order polynomial, for which Bilharz's stability criterion can be applied [10-12].

3. Some results

Soon after the discovery of the HMRI [5], and its surprising scaling with the Reynolds and Hartmann numbers (which is different from SMRI that scales with the magnetic Reynolds and Lundquist number), two limits were identified by Liu et al. [13] which we will call the Lower Liu Limit (LLL) and the Upper Liu Limit (ULL) in the following. In the inductionless limit Pm = 0, and for a current-free azimuthal field, i.e. Rb = −1, the authors had found that the flow is stable for Rossby numbers between the LLL $\mathrm{Ro}_{\mathrm{LLL}} = 2(1-2^{1/2}) = -0.8284$ and the ULL $\mathrm{Ro}_{\mathrm{ULL}} = 2(1+2^{1/2}) = +4.8284$. The existence of the LLL, in particular, is of great astrophysical relevance since it means that Keplerian rotations, characterized by Ro = −3/4, would not be affected by HMRI (and neither by AMRI, as was later shown in [9]). Despite some attempts

to extend the LLL to somewhat higher values (by considering conducting boundaries [14,15] or finite Pm [16]), it seems now that Keplerian profiles will be very hard to be destabilized.
Here, we discuss another way of extending the range of applicability of HMRI (and AMRI). We set out from the physical reasoning that the shape of the azimuthal magnetic field in a disk is not a-priori given, but is rather a product of induction effects in the disk. The ~1/r dependence would correspond to the extreme case of an axial current in the very center of the disk. Without going into the details of induction effects, which would depend strongly on the radial and vertical distributions of the conductivity, we assume here that the azimuthal field might well be flatter than 1/r, and we will test the consequences of this modification for the applicability of HMRI.

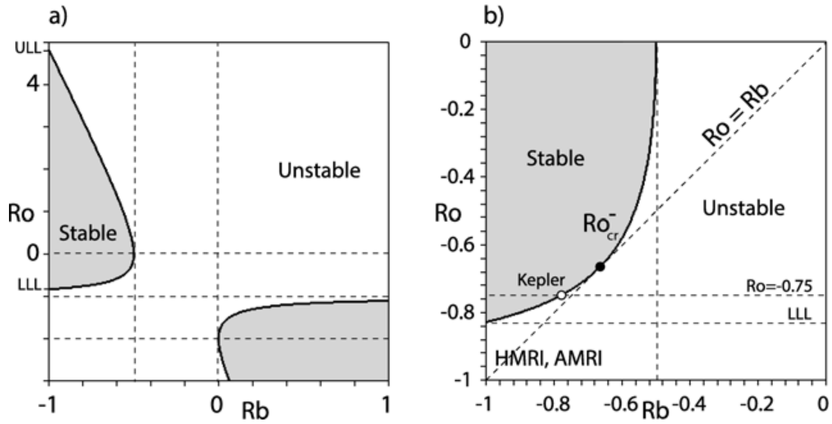

Figure 1: (a) The lower (LLL) and the upper (ULL) Liu limits existing at Rb = −1 are just the end points of a quasi-hyperbolic curve in the Ro−Rb plane. (b) A scaled fragment of the limiting curve demonstrating that the inductionless forms of the MRI can exist above the limit $Ro_{LLL} = 2(1-2^{1/2})$ in case that Rb > −1. The open circle marks the Keplerian value with Ro = −3/4 at Rb = −25/32, whereas the black circle corresponds to Ro = Rb = −2/3. The dashed diagonal represents the Chandrasekhar line Ro = Rb.

Analyzing the secular equation for arbitrary Ro and Rb, assuming Pm = 0, letting Re and Ha go to infinity, and optimizing than over β, we obtain the following curve of marginal stability in the Ro-Rb plane [10]:

$$\mathrm{Rb} = -\frac{1}{8}\frac{(\mathrm{Ro}+2)^2}{\mathrm{Ro}+1}\,.$$

This curve is visualized in Figure1. In Figure 1a we see that the two Liu limits LLL and ULL are just the endpoints of this curve. Most important for us is the fact that the Keplerian case, i.e. Ro = −0.75, is reached at Rb = −25/32 = −0.78125. Roughly speaking, a slight 20 per cent deviation from the purely current-free azimuthal field (Rb = −1), would make HMRI a viable mechanism to destabilize Keplerian flows.
A second interesting point in Figure 1b is Ro = Rb = −2/3. This is the only point where our marginal stability curve touches the so-called Chandrasekhar line, characterized by Ro = Rb which means that the angular velocity and the azimuthal Alfvén frequency have the same radial dependence. The particular Chandrasekhar equipartition solution, with Ro = Rb = −1, is known to be stable in the ideal case. What happens with the general line Ro = Rb, when viscosity and resistivity come into play? To answer this question we set the interaction parameter (or Elsasser number) $N = Ha^2/Re$ equal to the magnetic Reynolds number, N = Rm. Under this condition, the Bilharz criterion acquires the form

$$16(n^2-\mathrm{Rb}^2)(n^2-\mathrm{Rb}-2)^2\mathrm{Rm}^4+(n^6-12n^2\mathrm{Rb}^2+32n^2(\mathrm{Rb}+1)-16\mathrm{Rb}^2(\mathrm{Rb}+2))\mathrm{Rm}^2$$
$$-4Rb^2+4n^2(Rb+1)=0$$

Its solution is illustrated in Figure 2. The wide part of the instability domain in Figure 2a, existing for small Rm, represents the AMRI. Evidently, this domain shrinks with increasing Rm, degenerating to a ray for infinite Rm. In other words, when coming from infinite Rm, already an infinitesimal small electrical resistivity destabilizes the marginal stable solution. In this sense, AMRI is a typical example of a dissipation-induced instability.

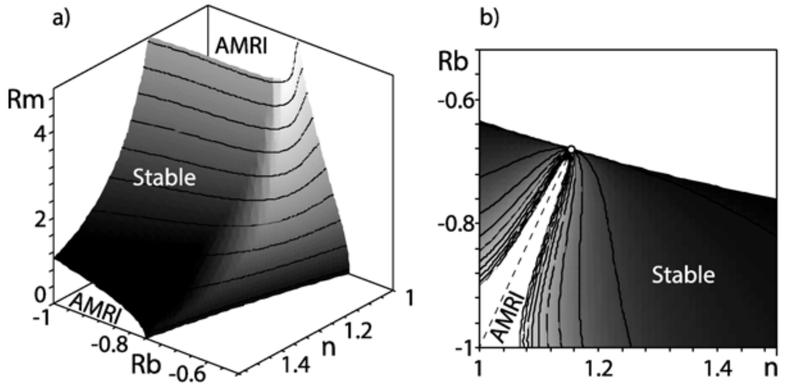

Figure 2: (a) The threshold of instability at $\mathrm{Ha}^2/\mathrm{Re} = \mathrm{Rm}$ and $\mathrm{Re} \to \infty$ in the (n, Rb, Rm) space. (b) Its projection onto the Rb−n plane. The increase in Rm makes the instability domain more narrow so that in the limit $\mathrm{Rm} \to \infty$ it degenerates into a ray (dashed) that emerges from the point (open circle) with the coordinates $n = 2/3^{1/2}$ and $\mathrm{Rb} = -2/3$ and passes through the point with n = 1 and Rb = −1.

Going over from Rb = −1 to Rb = 0 means physically a transition from an isolated central current to a homogeneous radial current distribution. The latter situation is known to be susceptible to the Tayler instability [8], which tapes into the energy of the current rather than into the rotational energy. Setting Hb: = β Ha, with Ha going to 0 and β to infinity, we obtain

$$\mathrm{Re}^2=\frac{((1+\mathrm{Hb}^2n^2)^2-4\mathrm{Hb}^2\mathrm{Rb}(1+\mathrm{Hb}^2n^2)-4\mathrm{Hb}^4n^2)(1+\mathrm{Hb}^2(n^2-2\mathrm{Rb}))^2}{4(\mathrm{Hb}^4\mathrm{Ro}^2n^2-((1+\mathrm{Hb}^2(n^2-2\mathrm{Rb}))^2-4\mathrm{Hb}^4n^2)(\mathrm{Ro}+1))}\ .$$

Figure 3 shows now the stability surface for this setting, at Pm = 0 and n = 1.278, whereby we connect Rb = −1 and Rb = 0 by a quarter of a circle according to $\mathrm{Ro(Rb)} = -(-\mathrm{Rb}^2 - 2\mathrm{Rb})^{1/2}$. Figure 3a gives a total view of this surface, while Figures 3b-d show individual slices at different values of Re. Not surprisingly, at Re = 0 we get only the current-driven TI, while for Re > 0 we see the AMRI arising as a “nose” which later connects to the TI area.

4. Conclusions

Given the dramatic differences in the parameter dependencies of SMRI on one side and HMRI/AMRI on the other side, it is of great astrophysical importance to know whether the latter forms could possibly be working for Keplerian rotation profiles. As we have seen, the answer to this question is affirmative, if the azimuthal magnetic field is only slightly shallower than ~1/r. Yet, the induction that is needed to allow this would require Rm > 1 which apparently leads us back to the realm of SMRI. However, there is still a difference here since the Lundquist number could be very small in our case. Detailed considerations for specific accretion disk problems must be left for future work.

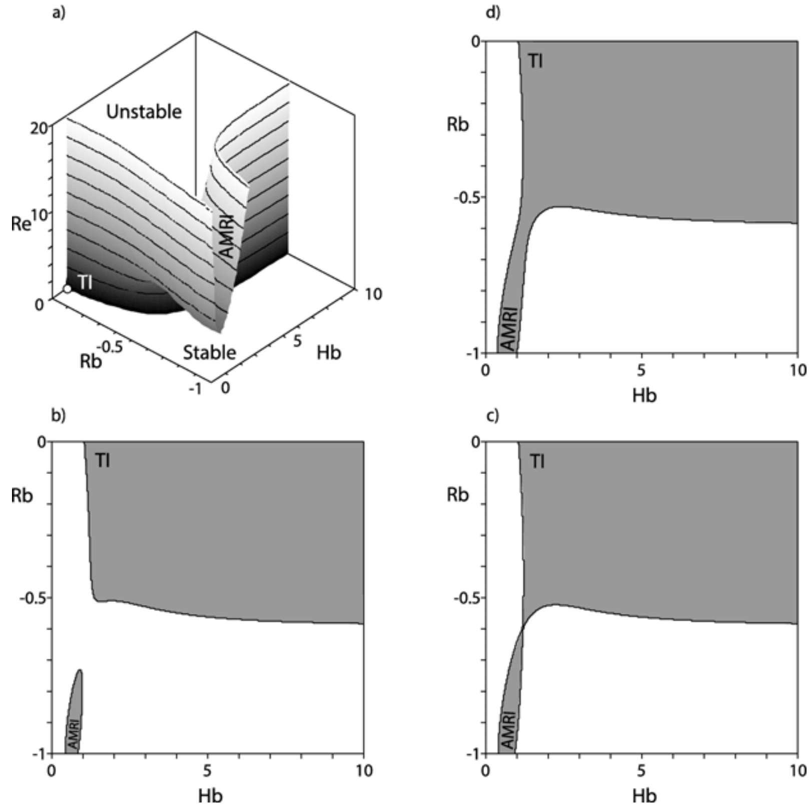

Figure 3: Instability threshold for the special case Pm = 0, and n ≈ 1.27842, when following the quarter-circle curve $Ro(Rb) = -(-Rb^2 - 2Rb)^{1/2}$. (a) The instability domain bounded in the (Hb,Rb,Re) space and its cross-sections at (b) Re = 5.4, (c) Re = 5.734, and (d) Re = 6. The domains of TI and AMRI reconnect via a saddle point at Re = 5.734.

Acknowledgments. We acknowledge support from the Helmholtz Alliance LIMTECH.

References

[1] Velikhov, E.P.: Sov. Phys. JETP 36 (1959) 995
[2] Balbus, S.A.; Hawley, J.F.: Astrophys. J. 376 (1991) 214
[3] Sisan, D.R. et al.: Phys. Rev. Lett. 93 (2004) 114502
[4] Nornberg, M.D. et al.: Phys. Rev. Lett. 104 (2010) 074501
[5] Hollerbach, R.; Rüdiger, G.: Phys. Rev. Lett. 95 (2005) 124501
[6] Stefani, F. et al.: Phys. Rev. E 80 (2009) 066303
[7] Seilmayer, M. et al.: Phys. Rev. Lett. (2003), submitted; arXiv:1311.7223
[8] Seilmayer, M. et al.: Phys. Rev. Lett. 108 (2012) 244501
[9] Kirillov, O.N. et al: Astrophys. J. 756 (2012) 83
[10] Kirillov, O.N., Stefani, F.: Phys. Rev. Lett. 111 (2013) 061103
[11] Kirillov, O.N. et al: Fluid Dyn. Res. (2014), in press; arXiv:1307.1576
[12] Kirillov, O.N. et al: J. Fluid Dyn. (2014), subm.; arXiv:1401.8276
[13] Liu, W. et al.: Phys. Rev. E 74 (2006) 056302
[14] Rüdiger, G.; Hollerbach, R.: Phys. Rev. E 76 (2007) 068301
[15] Priede, J.: Phys. Rev. E 84 (2011) 066314
[16] Kirillov, O.N.; Stefani, F.: Phys. Rev. E 84 (2011) 036304

LIQUID METAL FLOW INDUCED BY COUNTER-ROTATING PERMANENT MAGNETS IN A RECTANGULAR CRUCIBLE

ŠČEPANSKIS[1] M., NIKOLUŠKINS[2] R., BOJAREVIČS[2] A., BEINERTS[2] T., GEŽA[1,3] V., JAKOVIČS[1] A., THOMSEN[4] K.
[1] Laboratory for Mathematical Modelling of Environmental and Technological Processes, University of Lativa, Zeļļu iela 8, Rīga, LV-1002 Latvia
[2]Institute of Physics, University of Latvia, Miera iela 32, Salaspils, LV-2169, Latvia
[3]Institute of Electrotechnology, Leibniz University of Hanover, Wilhelm-Busch-Str. 4, Hannover, D-30167, Germany
[4]Paul Scherrer Institute, Spallation Neutron Source Division, 5232 Villigen, PSI, Switzerland
E-mail address of the corresponding author: mihails.scepanskis@lu.lv

Abstract: The present paper reports the first step of research project, which contains a fundamental numerical investigation of the flow of liquid gallium in the system of 4 counter-rotated cylindrical magnets and an innovative neutron radiography experiment. The design of the experimental set-up is reported. Numerical aspects of the modeling of such a system as well as preliminary results are demonstrated.

1. Introduction

The paper will consider the flow of liquid metal, which is induced by a system of four counter-rotating cylindrical Nd-Fe-B magnets (see fig 1). A liquid metal stirrer based on rotating permanent magnets has been proposed by A. Bojarevičs & Beinerts [1]. The mentioned reference contains an analytical expression for a magnetic field and an iterative solution for the flow velocity in the limits of a two-dimensional model as well as experimental measurements of the velocity.

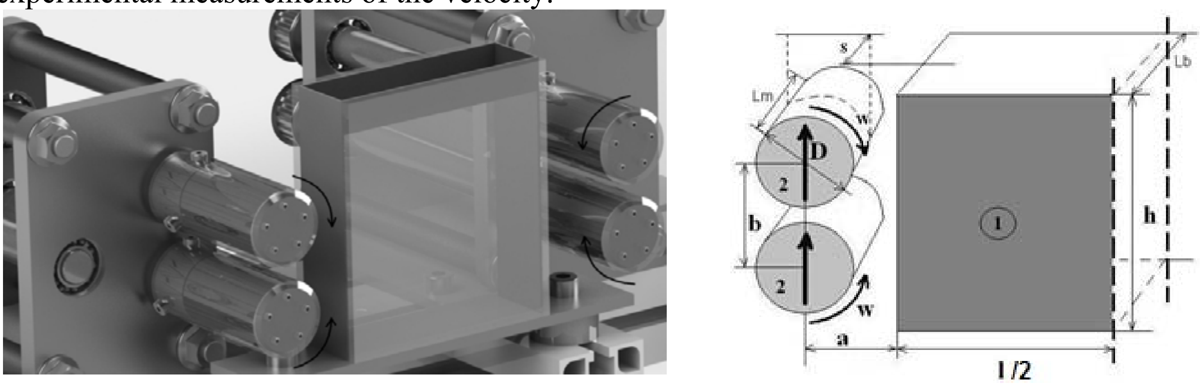

(a) (b)

Figure 1: design of the liquid metal stirrer with four counter-rotating magnets. (a) magnets and a liquid metal vessel; (b) scheme for mathematical modeling (1 – rectangular liquid metal container, 2 – cylindrical magnets).

Generally, the proposed electromagnetic (EM) system produces in a rectangular crucible the flow of a topology that is similar to that in an induction crucible furnace (ICF) that is widespread in metallurgy for melting and stirring of secondary metals. The classical approach is used in such stirrers: alternative current in a solenoidal inductor around a crucible induces current in a melt and a magnetic field that results in a Lorenz force that moves the liquid metal and forms counter-rotating vortices. Permanent magnet systems are very rare in industrial metallurgical applications due to the temperature limitation imposed by the magnets; however, recent and still unpublished A. Bojarevičs' and Beinerts' inventions found also an industrial use of such a technology for stirring of aluminum. Moreover, an application of rotating cylindrical magnets for pumping of aluminum is reported [2,3] and liquid metal pumps with magnets integrated in a single rotating cylinder or a double disk is also well-known (see, e.g., [4]).

Homogenization of solid inclusions in the ICF as an application of a stirrer is of industrial interest. Such processes were simulated using Large Eddy Simulated (LES) method by Ščepanskis et al. [5]. However, an experimental investigation of particles in turbulent flow of liquid metal is an extremely complicated challenge and only last year the first attempt to measure a particle concentration field in a small ICF has been done [6]. Nevertheless, the mentioned experiment was able to measure the concentration field only at the dynamically equilibrium stage.

Therefore, an experiment using neutron tomography technology (see, e.g., [7]) is proposed now. Unfortunately, due to technical limitations an ICF is not suitable for such an experiment. So, we decided to use the aforementioned permanent magnet system to produce the motion of liquid metal like in the ICF and to investigate the particles there. Such a permanent magnet system can also represent some other metallurgical application for stirring and pumping of liquid metal. The experiment is planned to be carried out on 25-27 of July, 2014 at Paul Scherrer Institute (Switzerland), while the present paper will demonstrate a design of the experimental set-up and numerical investigations of the flow in the rectangular vessel highlighting relevant numerical aspects.

2. Design of the stirrer

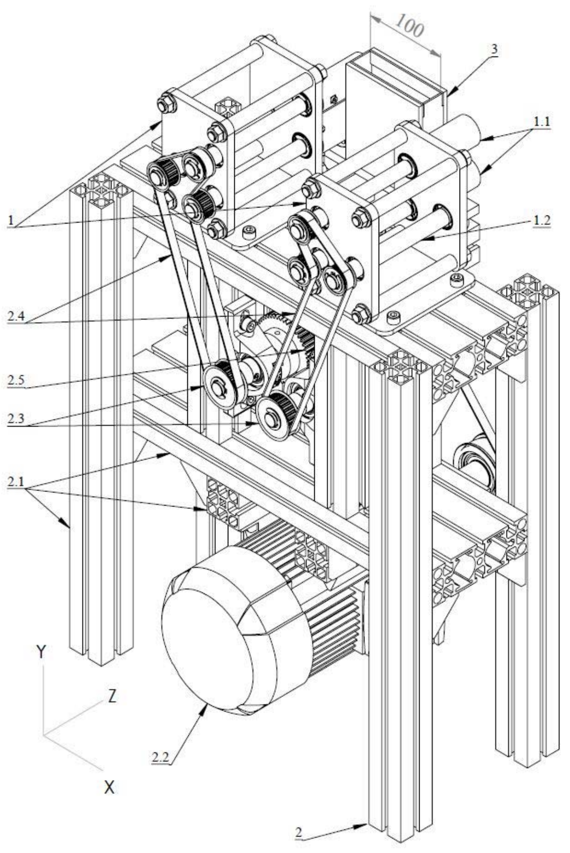

Figure 2: A sketch of the experimental set-up.

The stirrer consists of the three main units: 1) a block of shafts with rotating magnets on one side and belt pulleys on the other side; 2) a frame with a motor and driving elements, gears and pulleys; 3) a rectangular vessel with glass walls on the front and the back sides, a small heating element on the bottom. The mentioned units are marked on fig 2.

A rectangular vessel for liquid metal (marker 3 on fig 2) is made out of quartz which is a transparent material for neutrons. Inside dimensions of the vessel are 100 x 100 x 30 mm. The stirrer is constructed in such way that nothing disturbs the neutron beam, it only has to pass 2 mm thick glass.

Gallium is expected to be used for the experiment because of its relative transparency for neutrons. It is also important that no radioactive waste is expected after the limited irradiation of the gallium by neutrons. The melting temperature of this metal is 30°C, therefore, a very simple heater is integrated in the construction below the vessel of the liquid metal.

The blocks 1 (fig 2) hold shafts with the cylindrical permanent magnets (1.1) that are magnetized as it is shown on fig 1b (arrows). The magnets are covered with stainless steel cups and bolted to the common shafts. Each shaft is supported by two bearings and ends with a pulley. The third shaft (1.2), which also holds an additional pulley, is necessary for the belt connection. The whole block is moveable in the X direction (see fig 2) to carry out different experiments. Most parts of the mentioned details, including the bearings, are made of stainless steel.

The unit 2 (see fig 2) consists of aluminum and stainless steel profiles (2.1), an electric motor (2.2), shafts in the middle level of the construction (2.3) that are necessary to drive both double-sided belts (2.4). These shafts have pulleys on each side and spur gears (2.5) to change the direction of rotation of the paired shaft.

Sizes of the different element of the set-up (see marking on fig 1b) are as follows: 1) due to neutron radiography limitations the sizes of the liquid metal vessel are l = 10 cm, h = 10 cm, L_b = 3 cm; 2) the available magnets have D = 3 cm, L_m = 5 cm; 3) positions of the magnets are optimized so that b = 5 cm, a = 4 cm (subject to change in a case of necessity), s = 0.

3. Numerical simulation

A block diagram of a general algorithm, which is implemented in the present investigation, is shown on fig 3. The EM field of the system and, consequently, the Lorenz force distribution

$$\boldsymbol{f} = \boldsymbol{j} \times \boldsymbol{B} \ ,$$

in the liquid metal are calculated non-stationary and then averaged during a turnover period of the magnets. Generally, current density j is defined as follows: $\boldsymbol{j} = \sigma(\boldsymbol{E} + \boldsymbol{v} \times \boldsymbol{B})$, where σ, $\boldsymbol{v}$, $\boldsymbol{E}$ and $\boldsymbol{B}$ denote here conductivity of material, velocity of conductive liquid, an electric field and magnetic flux density. The magnetic Reynolds number $Re_m \ll 1$; therefore, an induction term ($\boldsymbol{v} \times \boldsymbol{B}$) can be neglected, while E is determined by a changing magnetic field of the rotating magnets described by the Maxwell's equations. Nevertheless, the equations of the EM field to be solved in a frame of the moving liquid and the solution should be corrected by taking into account the velocity field iteratively.

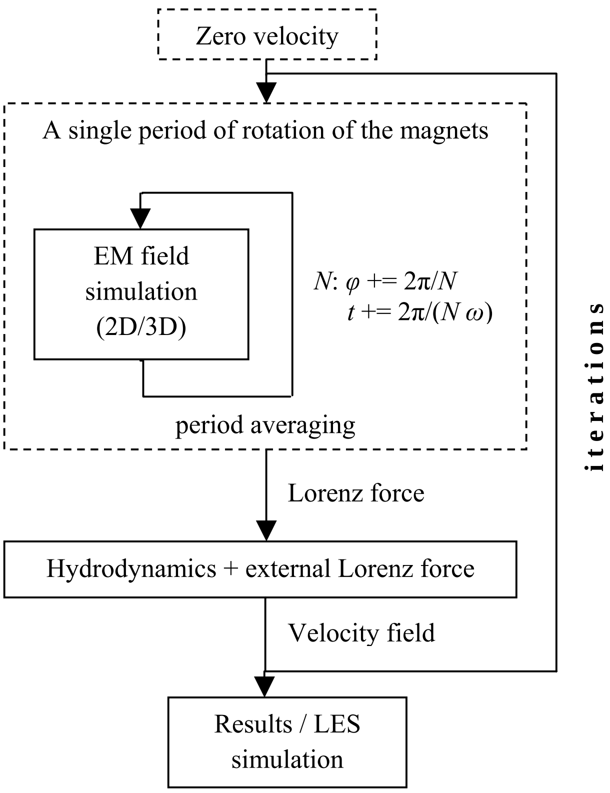

Figure 3: The block diagram of the numerical algorithm. N denotes a number of time steps within the turnover period; φ, t, ω are the rotation angle, time, angular velocity.

So, it becomes clear that the algorithm, which is illustrated on fig 3, have a couple of purely numerical degrees of freedom that have to be carefully investigated to avoid their influence on the result.

First of all, it is N – the number of time steps within the single period of rotation of the magnets, which is the most important numerical parameter. Fig 4 shows Joule heat induced in the melt as a function of N in the case of a 2D simulation (the results are shown for a case of zero velocity field – an initial step of the iterative algorithm). It is clear from fig 4a that the induced power per length unit of the restricted third direction increases monotonously with increasing N and can be described with an exponential function (see the curve on fig 4a):

$$q(N) = q_{asy} e^{-k/N}, \qquad (1)$$

where q_{asy} is the asymptotic value that is in fact the real induced heat value; k is a convergence parameter that depends on the rotation speed ω. Since the functional dependence $q(N)$ is known, the asymptotic (real) value can be reconstructed from only few points at low N using the least square method in order to avoid very long calculations in a 3D case. Fig 4b shows a quadratic dependence of the induced heat q_{asy} on ω that is theoretically expected. The influence of other numerical parameters is insignificant in the case of enough resolution.

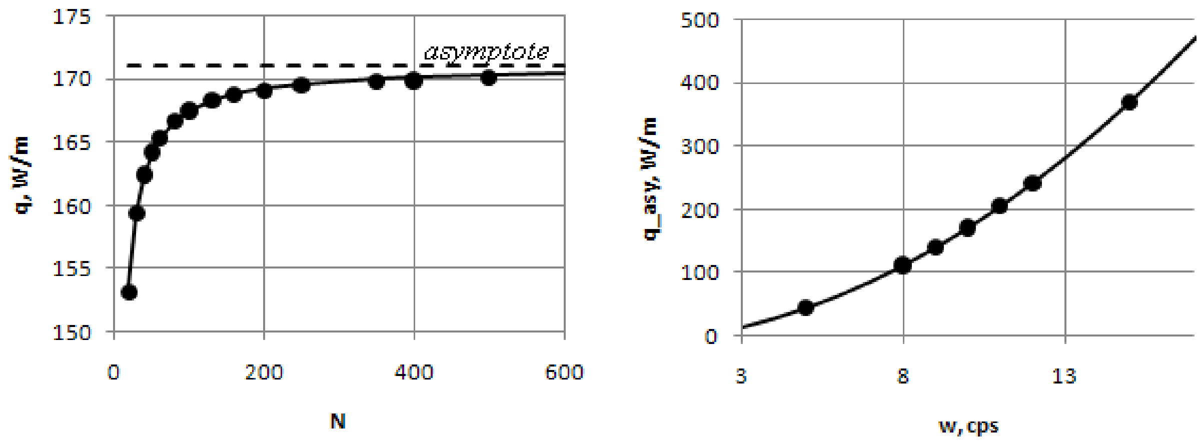

(a) (b)

Figure 4: results of the 2D modeling of the system that is shown on fig 1b; (a) induced heat power in the melt as the function of the numerical parameter N, (b) asymptotic value (see left figure) of the induced heat depending on the angular speed of the magnets.

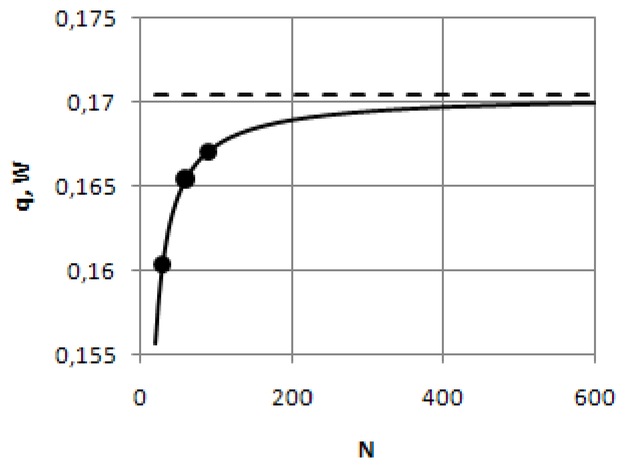

Figure 5: reconstruction of the real value of induced heat according to the function (1) in 3D case; ω = 10 cps.

Fig 5 demonstrates the results of 3D calculations (the geometric parameters of the system used in this calculation are mentioned at the end of the Section 2) for ω = 10 cps. It seems to be unrealistic at first glance that the induced heat in the 3D case is less than 4% of that in the 2D case multiplied by the length of the 3rd direction L_b = 3 cm (compare asymptotic values on fig 4a and fig 5). However, taking into account the small thickness of the vessel L_b, it becomes clear that the induced current in the thin layer of liquid metal is hard to close without significant loses. Therefore, this case dramatically differs from the 2D case that in fact means current closure at infinity. Increasing L_b and L_m 10 times we obtained the result for the 3D case to be approximately 80% of that in the 2D case. Thus the previously mentioned result for the 3D case seems to be reliable.

Another numerical parameter, which definitely influences the result, is the number of iterations that take into account the reduction of the induction effect in a movable metal (see the scheme on fig 3). This part of numerical simulation is still in progress since 3D calculation is very time consuming.

Therefore, we can demonstrate now only the velocity distribution in liquid metal in the quasi-2D case that, however, significantly overestimates the force and, consequently, the velocity of the induced flow as it was already discussed. The quasi-2D denotes here LES 3D hydrodynamics based on 2D EM calculation. Fig 6 demonstrates the topology of the time-averaged flow but the magnitude is not shown because of the discussed overestimation of the 2D case. The figure shows an interesting structure of the flow, which consists of 3 vortices instead of the expected 4 eddies. We suspect it can be a result of hydrodynamic instabilities, probably characteristic of such a system. A. Bojarevičs experimentally observed the same structure with changing direction of the central eddy along two diagonals sequentially with a period of several minutes (unpublished results). Therefore, the averaging for a 70 s long period, which is demonstrated on fig 6, cannot represent the mentioned changes.

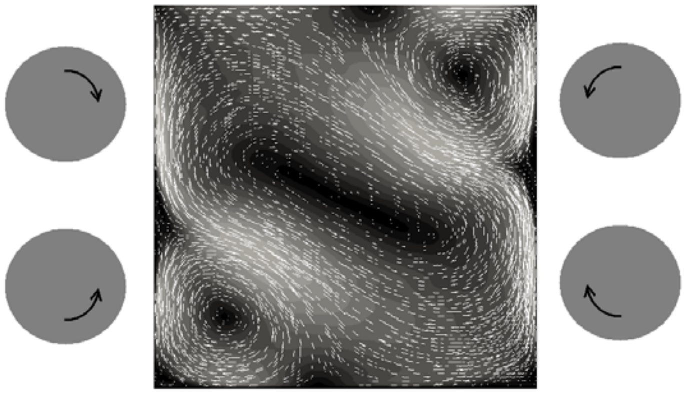

Figure 6: Topology of the time-averaged flow of liquid gallium in the system of four counter-rotated cylindrical magnets.

4. Conclusions & further plans

The experimental set-up of the four counter-rotated cylindrical magnets is designed to represent the multi-eddy structure of liquid metal flow like in wide-spread metallurgical applications.

At the beginning of the numerical investigation of such flows the significance of 3D EM calculation and the number of numerical steps of transient calculation within the single period of the magnet rotation were recognized. Fundamental numerical research of the flow including full 3D LES simulation of turbulence and the innovative neutron radiography measurements are the next steps.

5. Acknowledgements. The research, which is the contribution of Dr. M. Ščepanskis, R. Nikolu□kins and Dr. A.Bojarevičs, was financially supported by the European Social Fund (project no. 2013/0018/1DP/1.1.1.2.0/13/ APIA/VIAA/061).

6. References

[1] Bojarevics, A.; Beinerts, T.: Experiments on liquid metal flow induced by a rotating magnetic dipole. Magnetohydrodynamics. 46 (2010) no. 4 333-338.

[2] Beinerts, T.; Bojarevics, A.; Gelfgat, Yu.; Bucenieks. I.: Linear permanent-magnet pump and stirrer for molten aluminium. J. Iron Steel Res. Int.. 19 (2012) suppl. 1 528-530.

[3] Bojarevičs, A.; Gelfgats, J.; Beinerts, T.; Bucenieks, I.: Metāla sakausējuma sūknē□anas un maisī□anas peņēmiens un iekārta tā realizē□anai. Patent LV 14404 B, 20.10.2011 (in Latvian).

[4] Bucenieks, I.; Kravalis, K.: Efficiency of EM induction pumps with permanent magnets. Magnetohydrodynamics. 47 (2011), no. 1 89-96.

[5] Ščepanskis, M.; Jakovičs, A.; Nacke, B.: Homogenization of non-conductive particles in EM induced metal flow in a cylindrical vessel. Magnetohydrodynamics. 46 (2010), no. 4 413-423.

[6] Ščepanskis, M.; Jakovičs, A.; Baake, E.; Nacke, B.: Solid inclusions in an electromagnetically induced recirculated turbulent flow: simulation and experiment. Int. J. Multiphase Flow, in press (2014), doi: http://dx.doi.org/10.1016/j.ijmultiphaseflow.2014.04.004.

[7] Tremsin, A.S.; McPhate, J.B.; Vallerga, J.V.; Siegmund, O.H.W.; Bruce Feller, W.; Lehmann, E.; Kaestner, A.; Boillat, P.; Panzner, T.; Filges, U.: Neutron radiography with sub-15 μm resolution through event centroiding. Nuclear Instr. Meth. Phys. Res. A. 688 (2012) 32-40.

VISCOUS AND JOULE DISSIPATION RATIO IN ISOTROPIC MHD TURBULENCE

STEPANOV[1] R., PLUNIAN[2] F
[1]Institute of Continuous Media Mechanics, Ural Branch of RAS
1 Koroleva, , Perm, Russia
[2]ISTER, Grenoble University, France
E-mail: rodion@icmm.ru

The magnetohydrodynamics turbulence is often an object for fundamental and applied studies in electroconductive fluid mechanics. In spite of intensive researches in this field, the small-scale dynamo process at large Reynolds numbers is still difficult to investigate experimentally or numerically. This large spectrum of possible magnetic Prandtl number Pm values implies strong differences between possible generation mechanisms. The kinetic energy spectrum available for generating magnetic energy is controlled value of Pm. When $Pm \geq 1$ the resistive scale is smaller than the viscous scale implying that all velocity scales are available for generating some magnetic field. On the other hand, for $Pm < 1$, only the velocity scales larger than the resistive scale are available for the magnetic field generation. In that case, the velocity scales smaller than the resistive stay passive in the generation process. We focus on statistical property of dissipations (its scaling and ratio) as a proper diagnostic of the kinetic and magnetic field interaction in wide range of scales. MHD shell model used for simulations. We explain the difference in dissipation ratio dependences on Pm that were suggested in [1] and [2]. The effect of nonlocal interactions in scale space is discussed.

References

[1] Brandenburg, A.: 2009, Large-scale dynamos at low magnetic Prandtl numbers, Astrophys. J. 697, 1206-1213.
[2] Plunian F., Stepanov R. 2010, Cascades and dissipation ratio in rotating magnetohydrodynamic turbulence at low magnetic Prandtl number, Physical Review E, 82, P.046311.

Spectral Direct Numerical Simulations of low Rm MHD channel flows based on the least dissipative modes

KORNET Kacper and POTHERAT Alban

Applied Mathematics Research Centre, Coventry University

Abstract

We put forward a new type of spectral method for the direct numerical simulation of flows where anisotropy or very fine boundary layers are present. The mean idea is to take advantage of the fact that such structures are dissipative and that their presence should reduce the number of degrees of freedom of the flow. We applied the new method to calculate the evolution of freely decaying MHD turbulence between walls. Comparing our results with the cases calculated in a 3D periodic domain enables us to quantify the influence of the channel walls on the character of a freely decaying MHD turbulence.

1 Introduction

Simulations of liquid metal flows in channel and duct configurations under a strong magnetic field pose a difficult problem for existing numerical methods. The main obstacle is the linear increase in number of modes required to resolve thin Hartmann boundary layers with the intensity of the magnetic field B. Yet, the enormous dissipation incurred by friction and Joule dissipation in these layers decimates the degree of freedom of the flow when Ha becomes large. Their number can be estimated through the dimension d_M of the attractor of the underlying system, for which an upper bound was shown to scale as Ha^{-1} [4]. The fact that the number of modes needed to resolve the flow completely increases in numerical simulations at high Ha is therefore a property of the spectral method based on these polynomials, but does not reflect any physical constraint.

To overcome this problem we developed a new approach to the numerical calculations describing these flows. The solution of the flow is expressed in a base of eigenfunctions of the linear part of the governing equations and its adjoint. We show that in this approach the computational cost does not depend on the thickness of boundary layer and therefore it allows for performing calculations for high magnetic fields.

2 Governing equations

Flows of liquid metals in engineering applications are usually described within the frame of the Low Magnetic Reynolds number (Rm) approximation. This applies to problems where the flow is neither intense nor conductive enough to induce a magnetic field comparable to an externally applied one. The full system of the induction equation and the Navier-Stokes equations for an incompressible fluid are then approximated to the first order in Rm, which represents the ratio of these two fields. This leads to the following system [6]:

$$\begin{aligned} \frac{\partial \mathbf{u}}{\partial t} + (\mathbf{u}\cdot\nabla)\mathbf{u} &= -\frac{1}{\rho}\nabla p + \nu\Delta\mathbf{u} + \mathbf{j}\times\mathbf{B}\,, & (1)\\ \nabla\cdot\mathbf{u} &= 0\,, & (2)\\ \nabla\cdot\mathbf{j} &= 0\,, & (3)\\ \mathbf{j} &= \sigma(-\nabla\Phi + \mathbf{u}\times\mathbf{B})\,, & (4)\end{aligned}$$

where $\mathbf{u}$ denotes fluid velocity, $\mathbf{B}$ - magnetic field, $\mathbf{j}$ - electric current density, ν - kinematic viscosity, σ - electrical conductivity, Φ - electric potential. We consider a channel flow with a homogeneous transverse magnetic field $B\mathbf{e}_z$ and impermeable ($\mathbf{u}|_{wall} = \mathbf{0}$), electrically insulating ($\mathbf{j}\cdot\mathbf{n}|_{wall} = \mathbf{0}$) walls located at $z = \pm L/2$. In the xy directions we adopt the periodic boundary conditions with period L. Under this assumptions and using the reference scale L, time L^2/ν and velocity ν/L the above set of equations can be expressed in dimensionless form:

$$\frac{\partial \mathbf{u}}{\partial t} + P(\mathbf{u}\cdot\nabla)\mathbf{u} = \Delta\mathbf{u} - \frac{1}{Ha^2}\Delta^{-1}\partial_{zz}\mathbf{u}\,, \tag{5}$$

where $Ha = LB\sqrt{\sigma/\rho\nu}$ is the Hartman number and P denotes orthogonal projection onto the subspace of solenoidal fields.

3 Numerical methods

We express the solution of eq. (5) using a basis of eigenvectors of the operator $\mathcal{L}$ that represents its linear part. The features of flows at high Ha are strongly determined by the properties of this operator. Because of this, the set of modes built out of its eigenfunctions elements includes structures that are actually present in the flow. Laminar and turbulent Hartmann boundary layers that develop along the channel walls appear, in particular, as built-in features of these modes [2, 5]. They are therefore natural candidates to be used as elements of a functional basis in a numerical spectral scheme. Moreover, these modes all have negative eigenvalues, and it can be shown that to resolve the flow completely, it is only necessary to take into account all modes with eigenvalue λ with a modulus below a maximum $|\lambda_{\max}|$, such that their total number scales as Re^2/Ha [4]. Since the operator $\mathcal{L}$ represents the sum of viscous and Joule dissipation, the set of modes defined in this way is in fact the set of *least dissipative modes*. For sufficiently large values of Ha, this number becomes significantly smaller than the number of Fourier or Tchebychev modes necessary to resolve the Hartmann layers [2].

The main difficulty of solving equation (5) using the least dissipative modes lies in calculating non linear terms. We use a pseudospectral approach and calculate them in real space. Therefore we need a method to reconstruct a spectral coefficients g_n of physical vector fields known at the discrete set of points in space $\mathbf{x}_i$. This problem can be formulated as a set of linear equations for unknown spectral components:

$$\sum_n g_n \mathbf{e}_n(\mathbf{x}_i) = \mathbf{G}(\mathbf{x}_i) \quad i = 1\ldots N \tag{6}$$

where $\mathbf{e}_n$ constitutes are base of eigenvectors, and $\mathbf{G}$ represents the decomposed vector field. As the coefficients in this set of equations are constant during a single numerical run, it is worth performing LU decomposition of the corresponding matrix at the beginning of calculations and later use it to efficiently find the spectral decompositions. Moreover it enables us to save even more CPU time by omitting calculation of coefficients which wouldn't be used in further calculations. For example we are interested only in the g_n coefficients corresponding to divergence free modes. Neglecting coefficients corresponding to irrotational modes is an equivalent of performing projection representing by operator P in eq. (5). The technique described above has the advantage that the obtained spectral decomposition reproduces exactly the physical field on the given set of discretization points. Therefore momentum and energy are conserved by this procedure.

The spectral method described above was implemented by modifying the spectral code TARANG developed by [7].

To validate the present numerical scheme we compared the results it produces with those of three-dimensional, time-dependent direct numerical simulations performed with a code based on the open source framework OpenFOAM, on test cases of freely decaying MHD turbulence. OpenFOAMis based on the finite volume approach and uses a co-located grid. Our numerical domain was a cube of dimension L divided uniformly into N cells in every direction. In order to calculate correctly the electric current density in Hartman layers we always resolve each of them with at least three computational cells in the z direction as in [1]. Following the DNS of decaying MHD turbulence in a three-dimensional periodic domain by [3], the initial conditions consist of a random gaussian velocity field with $u(k) \sim \exp\left[(-k/k_p)^2\right]$ where $k_p = 8\pi/L$. This corresponds to the energy spectrum $E \sim k^4 \exp\left[-2(k/k_p)^2\right]$. For this choice of initial velocity field, the integral scales of turbulent motions is given by $l = \sqrt{2\pi}/k_p$. The velocity spectrum was normalised in such a way that cell sizes correspond to $l_K/1.4$ where $l_K = lRe^{-3/4}$ is the Kolmogorov length scale and the Reynolds number in its definition $Re = u'l/\nu$ is based on l and velocity $u' = u(k = k_p)$. With this choice, the Reynolds number and the Hartmann number are linked by $Re = 0.33Ha^{4/3}$. This strategy allows us to calculate the most intense flow possible whilst minimizing mesh-induced numerical errors at a given mesh size, since the mesh is always uniform.

For the reference case, we have chosen $Ha = 56$, a value within reach with a traditional code such as OpenFOAM. Adopting the procedure presented in previous paragraph for OpenFOAM calculations we use $N_x = N_y = N_z = 170$ number of points in every direction and initial conditions characterized by Reynolds number $Re = 28$. For the corresponding spectral calculations we use a resolution 1.5 times higher ($N_x = N_y = N_z = 256$) in order to reduce the dealiasing errors. The initial conditions were chosen in such a way that their physical expansion on grid $N_x = N_y = N_z = 170$ was identical to the initial conditions used in the calculations with OpenFOAM.

We have followed the evolution of the initial conditions up to the time corresponding to $30\,t_J$ where $t_J = \sigma B^2/\rho$ is the timescale of Joule dissipation. We have compared the evolution of global kinetic energy, the viscous and magnetic dissipation rates. All these quantities exhibit quantitatively and qualitatively the same behaviour in both codes. The spectral codes exhibits a slightly smaller values of viscous dissipation then the finite volume code and slightly larger magnetic dissipation (see fig. 3).

4 Decaying turbulence

We used the potential of the new method to study the behaviour of the MHD turbulence in two sets of calculations with higher values of the magnetic field: $Ha = 112$ and $Ha = 224$. We started both simulations from exactly the same initial conditions characterized by Reynolds number $Re = 178$ and evolved them up to $60\,t_J$. The fig. 4 shows the evolution of global kinetic energy, the viscous and magnetic dissipation rates. For both values of the magnetic field

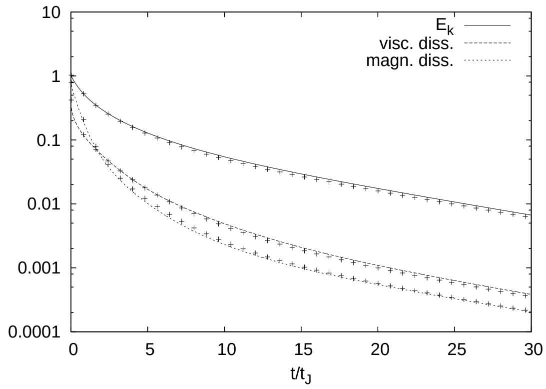

Figure 1: Total kinetic energy (normalized by its initial value) and viscous and magnetic dissipation rates (normalized by initial kinetic energy divided by t_J) in test case with $Ha = 56$ in the function of Joule times. The lines and points respectively represents the results obtained with finite volume and spectral codes.

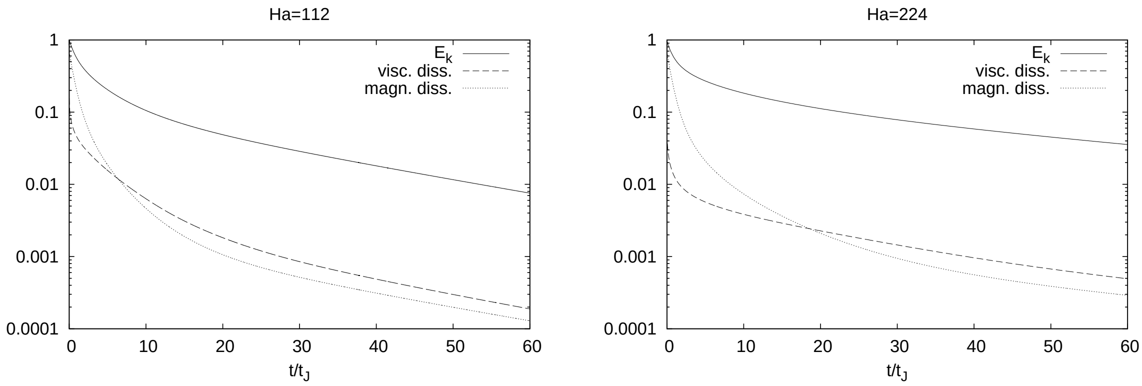

Figure 2: Total kinetic energy (normalized by its initial value) and viscous and magnetic dissipation rates (normalized by initial kinetic energy divided by t_J) in case with insulating walls for $Ha = 112$ (left panel) and $Ha = 224$ (right panel) in the function of Joule times.

the flow evolution can be split into two phases. In the first phase the energy decay is dominated by Joule dissipation. During this phase the flows changes to the state of two-dimensionality due to the diffusion of the momentum along the magnetic field. In the second phase the energy is dissipated mainly by viscosity with the ratio of viscous to magnetic dissipation reaching its maximum value of ~ 1.7 and then slightly decreasing in time. Our results indicates that in this viscously dominated phase the ratio of viscous to Joule dissipations scales as time multiplied by Ha. It is the phase when the flow is strongly two dimensional and its evolution is governed by interaction between 2D vortices and the walls.

To characterize the influence of the walls we performed two additional sets of calculations starting from exactly the same initial conditions as before but with the periodic boundary conditions imposed also in all three directions. The results are presented on fig. 4. In the beginning the dissipation rate is again dominated by Joule dissipation. This phase is very similar to the one in cases with insulating walls. In the second phase the flow is again strongly two dimensional and the energy is dissipated mainly by viscosity. However the Joule dissipation decreases much faster with time with the ratio of viscous to Joule dissipations monotonically increasing with time. Consequently at the end of the simulation the Joule dissipation is negligible, which is in strong contrast to simulations with insulating walls.

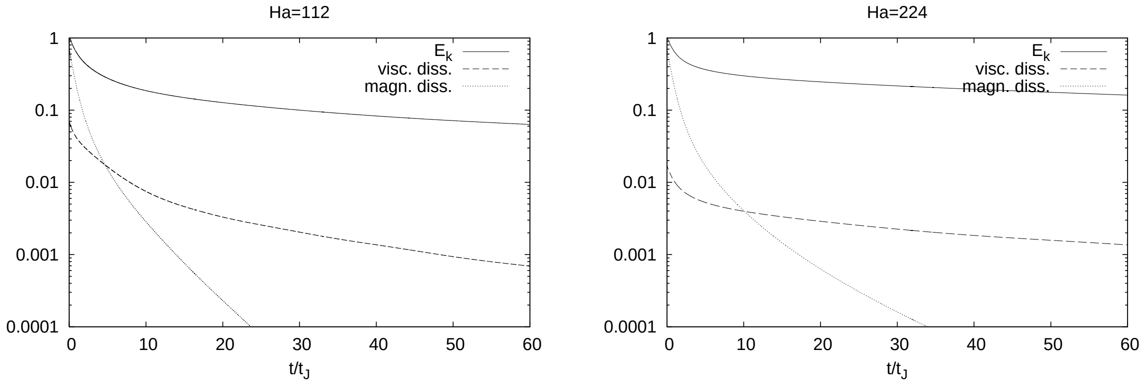

Figure 3: Total kinetic energy (normalized by its initial value) and viscous and magnetic dissipation rates (normalized by initial kinetic energy divided by t_J) in case with fully periodic domain for $Ha = 112$ (left panel) and $Ha = 224$ (right panel) in the function of Joule times.

5 Conclusions

We presented a new spectral method to calculate MHD flows in channel configuration. It is based on using the sequence of least dissipative eigenmodes from the dissipation operator instead of the traditional Fourier or Tchebychev basis. We used this method to calculate the evolution of freely decaying MHD turbulence between walls for $Ha = 112$ and $Ha = 224$. We compared the result with the cases calculated in a 3D periodic domain, which allowed us to quantify the influence of the channel walls on the temporal evolution of viscous and Joule dissipations.

Acknowledgments: The authors gratefully aknowledge financial support of the Leverhulme Trust (Grant F00/732J). The authors are also grateful to Professor Mahendra Verma, for making the TARANG code available to them. Finally the authors would like to express their gratitude to Antoine Huber for his work in the test numerical simulations carried out with OpenFOAM.

References

[1] V. Dousset and A. Pothérat. Characterisation of the flow around a truncated cylinder in a duct in a spanwise magnetic field. *J. Fluid Mech.*, 691:341–367, 2012.

[2] V. Dymkou and A. Pothérat. Spectral methods based on the least dissipative modes for wall-bounded MHD turbulence. *J. Theor. Comp. Fluid Mech.*, 23(6):535–555, November 2009.

[3] N. Okamoto, P. A. Davidson, and Y. Y. Kaneda. On the decay of low-magnetic-reynolds-number turbulence in an imposed magnetic field. *J. Fluid Mech.*, 651:295–318, 2010.

[4] A. Pothérat and T. Alboussière. Bounds on the attractor dimension for low-Rm wall-bound MHD turbulence. *Phys. Fluids*, page 25102 (12 pages), 2006.

[5] A. Pothérat and V. Dymkou. Dns of low-rm mhd turbulence based on the least dissipative modes. *J. Fluid Mech.*, 655:174–197, 2010.

[6] P. H. Roberts. *Introduction to Magnetohydrodynamics*. Longmans, 1967.

[7] M. K. Verma, A. Chatterjee, S. Reddy, R. Yadav, S. Paul, M. Chandra, and R. Samtaney. Benchmarking and scaling stuides of pseudo-spectral code tarang for turbulence simulations. *PRAMANA J. Phys.*, 81(4):617–629, 2013.

LES-STUDY OF MELT FLOW DRIVEN BY COMBINED INDUCTIVE AND CONDUCTIVE POWER SUPPLY IN METALLURGICAL MHD DEVICES

PAVLOVS[1] S., JAKOVICS[1] A., BAAKE[2] E., NACKE[2] B.
[1] Laboratory for Mathematical Modelling of Environmental and Technological Processes, University of Latvia, Zellu str. 8, LV-1002 Riga
[2] Institute of Electrotechnology, Leibniz University of Hannover, Wilhelm-Busch-Str. 4, D-30167 Hannover, Germany
E-mail: sergejs.pavlovs@lu.lv

Abstract: The computations of electromagnetic (EM) and hydrodynamic (HD) fields based on developed 3D model are performed for: i) almost axis-symmetrical MHD-device with bottom and submerged top electrodes with single phase alternating current (AC) and cylindrical coil around the melt; ii) MHD-device with three-phases current supplied over three submerged top electrodes as well as with EM stirrer in form of side non-symmetrical inductor, which produces “travelling” magnetic field. Obtained flow patterns are the results of competition of electro-vortex convection (EVC) and electromagnetic convection (EMC), which appear due to conductive and inductive current supply accordingly. For axis-symmetrical MHD-device the melt rotation appears as the effect of intercoupling of inductive or conductive current with magnetic fields, produced by other type of power supply.

1. Introduction

One of the popular types of industrial metallurgical equipment for melting and holding of ferrous and non-ferrous alloys (steel, ferrochrome, nichrome, etc.) uses power supply by conductive current – alternating or direct – over graphite electrodes (unsubmerged or submerged into the melt and/or slag), which have electrical contact with the melt and/or slag by arc. The heating of melt top surface may also be performed with plasma burner, thus conductive current due to jet of ionized gas is closed through the melt. The examples of such devices are electrical arc furnaces (EAF), ladle furnaces (LF), ore-melting furnaces, plasma furnaces, etc. With the purpose to intensify the circulation of melt the electromagnetic stirring (EMS) is used (for example, in LF, where EMS is the alternative to stirring with argon jet). EMS may be produced with side inductor (in LF) [1] or with bottom inductor (in EAF) [2].

Up to now the 3D numerical modelling of such MHD devices is performed for several particular cases: interaction of EMC and termogravitational convection (TGC) [2], EM field and energy aspects [3], EVC and mixture concentration field obtained with LES (Large Eddy Simulation) approach [4], heat transfer and gas flow over slag [5]. Brief overview of recent 2D and 3D modelling may be found in [6].

The authors resume their research, performed for originally developed 2D models with application of own code [7]: the aim is 3D modelling of melt flow in MHD devices with combined inductive and conductive power supply, taking into account the intercoupling effect of interaction of electrical current with magnetic field, produced by another type of power supply. In order to eliminate TGC influence on flow structure – the result of competition of EVC, EMC and MHD-rotation – melt is considered as isothermal conductive fluid.

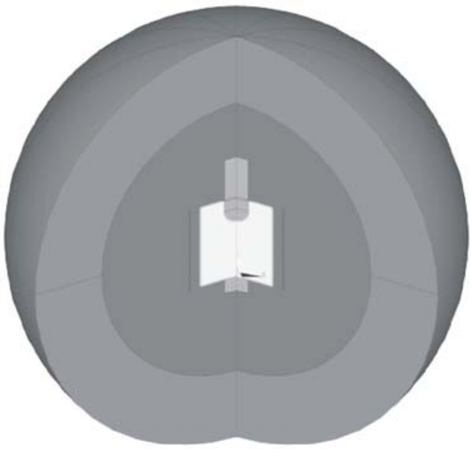

Figure 1: 3D geometry and zones of structured mesh for axis-symmetrical MHD device with submerged top and bottom AC electrodes and cylindrical single phase inductor.

Resultant *Lorentz* force in the melt [8] takes into account:

i) interaction of inductive or conductive currents with their generic magnetic fields;

ii) intercoupling of current and magnetic field produced by deferent types of power supply;

iii) phase displacement $\beta = \alpha^{el} - \alpha^{ind}$ between inductive and conductive current.

Intercoupling effects may be found in the case of equal frequency of inductive and conductive current – $\omega_{ind} = \omega_{el}$. For different frequencies $\omega_{ind} \neq \omega_{el}$ and for direct current (DC) in electrodes, time-averaged *Lorentz* force is equal zero.

1. Parameters of developed models and peculiarities of numerical computations

The geometries of developed 3D models of MHD devices with combined power supply are shown in Figures 1, 6. The geometrical, physical and operation parameters are estimated using published for advertising purposes fragmentary data [1] for industry-size LF (capacity approximately 70 *t*): radius and height of the melt – r_{melt} = 1.35 m and h_{melt} = 3 m; height of inductor – h_{ind} = 3 m; height of submerged part of electrodes – $h_{el}^{submerge}$ = 0.85 m. For melt nichrome (conductivity $\sigma_{melt} = 6.7 \cdot 10^5$ S/m) and equal values of current frequency in inductor and electrodes ($f_{ind} = f_{el}$ = 50 Hz) non-dimensional frequency of melt is $\hat{\omega}_{melt}^{ind} = \hat{\omega}_{melt}^{el} = 8 \cdot 10^2$.

EM field is computed with *ANSYS 14.0* in the melt, inductor and electrodes with geometries shown in Figures 1, 6. The melt turbulent flow is obtained using *ANSYS CFX 14.0* with 3D transient LES approach. As the initial distributions the results obtained with steady-state and transient Shear Stress Transport (SST) *k-ω* model of turbulence are used.

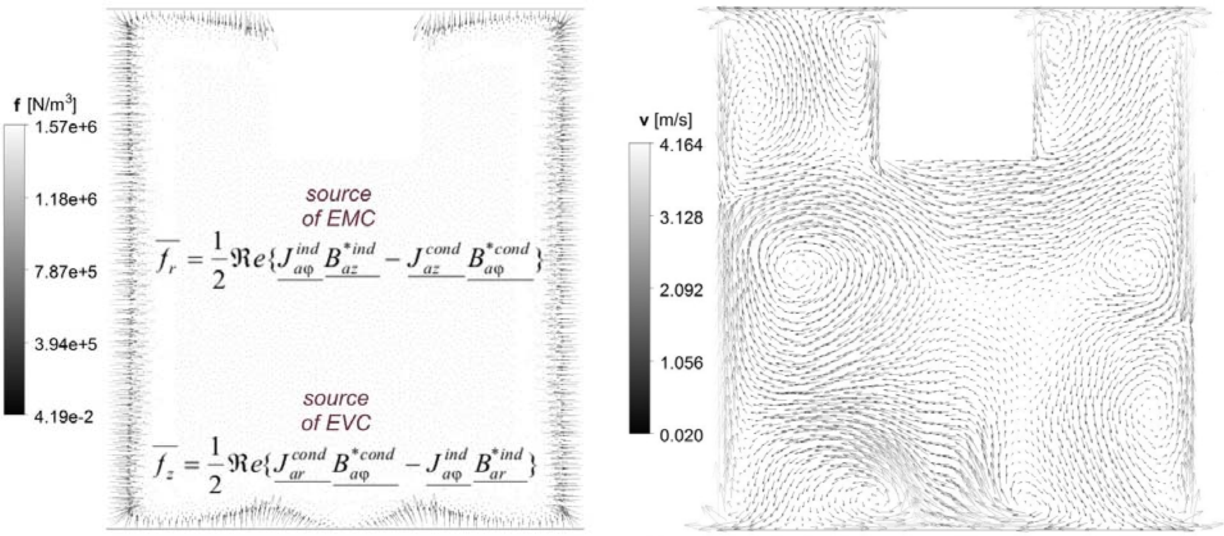

Figure 2: EM force vectors (left) and time-averaged velocity vectors (right) in vertical cross-section y = 0 (model in Figure 1).

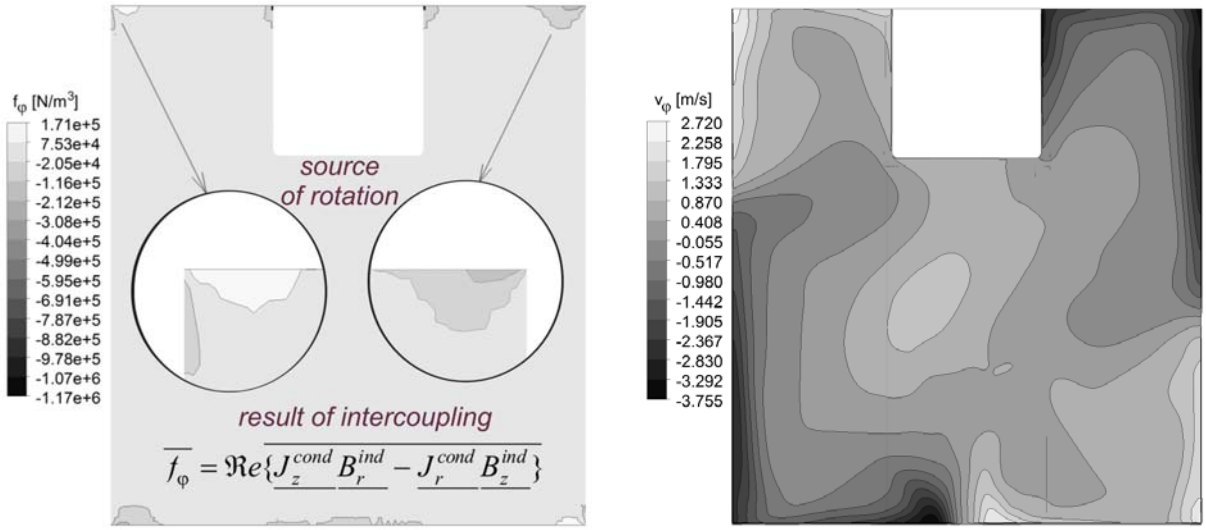

Figure 3: Isolines of azumithal components of EM force (left) and time-averaged velocity (right) in vertical cross-section y = 0 (model in Figure 1).

Structured mesh (Figures 6) is built with hexahedral elements. For EM field skin layers and for HD boundary layers at solid walls the mesh with inflation is generated.

During EM modelling ~ 2.5 millions of equations for complex variables are solved. Dimension of HD mesh is ~ 2.8 millions of elements. The time step is 0.005 sec.

2. 3D model of system with top and bottom electrodes and cylindrical inductor

The main features of 3D model are the following (Figure 1):

i) *Top electrode* has submerged part; *bottom electrode* contacts the bottom of the melt. The electrodes' axes coincide with symmetrical axis of melt vessel. Phases of current in top and bottom electrodes are equal $\alpha_{top}^{el} = \alpha_{bottom}^{el} = \alpha^{el}$.

ii) *Cylindrical inductor* has azimuthal dimension $\varphi_{cylindr}^{ind}$ = 359°; to ensure the applying voltage drop in boundary conditions the every inductor turn has thin (1°) vertical gap. The phases of current in inductor turns are equal $\alpha_1^{ind} = \alpha_2^{ind} = \ldots = \alpha_{12}^{ind} = \alpha^{ind}$.

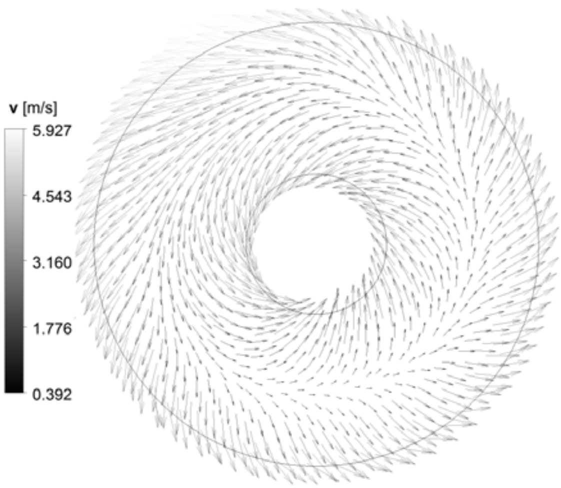

Figure 4: Time-averaged velocity vectors at melt top surface z = 3 m (model in Figure 1)

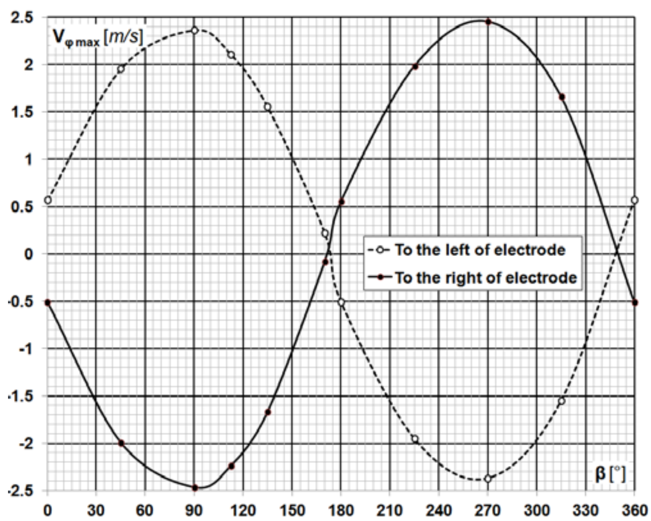

Figure 5: Maximum of azimuthal component of velocity $v_{\varphi\,max}$ at melt top (model in Figure 1) as the function of phase displacement β between currents in inductor and electrodes.

Characteristic distribution of resultant EM force in vertical cross-section y=0 is shown in Figure 2 (left). Because of noticeable skin-effect the EM force is concentrated in thin layer, which thickness is estimated with EM field penetration depth into the melt $\delta_{melt}^{ind} = \delta_{melt}^{el} << r_{melt}$.

EM force along cylindrical surface of melt has almost only radial component (except corner regions). The prevailing contribution to radial component $\overline{f_r}$, which is the main driver of EMC, gives the 1st term in upper expression, shown in Figure 2 (left). Flow patterns for system with "pure" inductor (t.i. without current over the electrodes) are typical for induction furnaces. There is not melt rotation around z-axis.

EM force along top and bottom horizontal surfaces of melt has almost only axial component (except corner regions). The prevailing contribution to axial component $\overline{f_z}$, which is the main driver of EVC, gives the 1st term in lower expression, shown in Figure 2 (left). Flow circulation for system with "pure" electrodes (t.i. without current in inductor) has opposite directions in comparison to EMC. There is not rotation of the melt around z-axis.

The circulation of the melt for system with combined power supply (Figure 2 (right)), is the result of competition of EMC, EVC and melt MHD-rotation around z-axis (Figure 4); phase displacement between inductive and conductive current is $\beta = 112.5^\circ$.

The melt rotation velocity $v_\varphi \sim 2.7–3.8$ m/s (Figure 3 (right)) is comparable with melt circulation velocity in meridional cross-section $v_{y=0} \sim 4.2$ m/s (Figure 2 (right)), which, in its turn, is less than total velocity at melt top $v_{top} \sim 5.9$ m/s (Figure 4). The high velocity values correspond to extreme current values in inductor and electrodes: I_{ind} =100 kA; I_{el} =1000 kA.

The directions of rotation in top and bottom zones of the melt are opposite (Figure 3 (right)), which coincide with directions of azimuthal component of EM force (Figure 3 (left)). The variation of phase displacement β in range from 0° to 180° makes it possible to control direction and velocity of melt rotation (Figure 5).

3. 3D model of system with three electrodes and side inductor

The main features of 3D model of system are the following (Fig. 2):

i) *Three electrodes* have submerged part with height $h_{el}^{submerge}$. Radial positions of electrodes' axes are $r_1^{el} = r_3^{el} = r_3^{el}$ =0.675 m; azimuthal positions $-\varphi_1^{el}$ =0°; φ_2^{el} =120°; φ_3^{el} =240°. Phases of current in electrode are α_1^{el} =0°, α_2^{el} =120°, α_3^{el} =240°.

ii) *Side inductor* with height h_{ind} has azimuthal dimension φ_{side}^{ind} = 60°. Inductor produces "travelling" magnetic field. The phases of current in inductor turns are: $\alpha_1^{ind} = ... = \alpha_4^{ind} = 0^\circ$; $\alpha_5^{ind} = ... = \alpha_8^{ind} = 120^\circ$; $\alpha_9^{ind} = ... = \alpha_{12}^{ind} = 240^\circ$ (numbering from bottom to top).

The 3D vectors of melt time-averaged velocity are presented in Figure 7. Inductor is turned to observer; vertical symmetry plane of model (Figure 6) is perpendicular to the page.

The EM force, which appears due to conductive current supply, is noticeable in zone around the electrodes near top of the melt. The EM force, which appears due to inductive current supply, is noticeable along cylindrical surface of the melt strait opposite to inductor, magnetic field of inductor "travels" up.

In the case of combine power supply the flow patterns, shown in Figure 7, are the result of competition of EMC and EVF and appears due to superposition of EM forces, produced by both conductive and induced current supply. Asymmetry (with respect to above mentioned vertical plane of model geometrical symmetry) of two-vortex flow in horizontal cross-section is most noticeable near top surface of the melt, where symmetrical flow of EMC competes with rotational symmetrical electro-vortex flow. Maximum value of velocity is ~1.2 m/s.

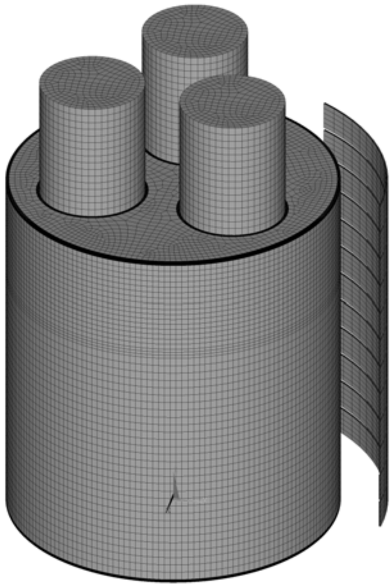

Figure 6: 3D geometry and structured mesh for MHD device with submerged three phase AC electrodes and side inductor, the source of “travelling” magnetic field.

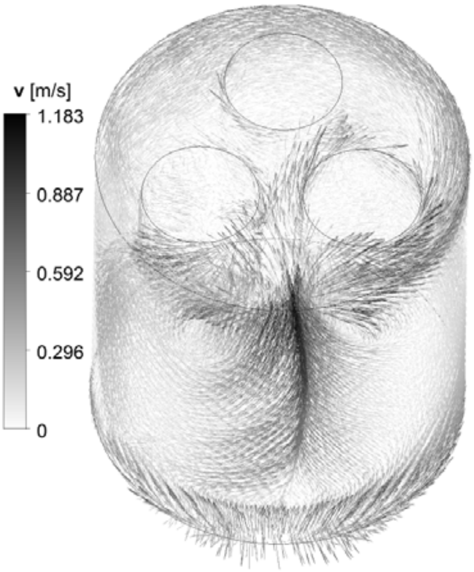

Figure 7: Time-averaged velocity 3D-vectors with “travelling” up magnetic field of inductor and phases $\alpha_1^{el} = 0^\circ$; $\alpha_2^{el} = 120^\circ$; $\alpha_3^{el} = 240^\circ$ (counter-clockwise) of current in electrodes (model in Figure 6).

4. Conclusions

The developed 3D models are universal enough for analysis of industry-size metallurgical MHD devices with conductive and inductive combined power supply in wide range of geometrical, physical and operational parameters.

The intercoupling effect (interaction of conductive current with induced magnetic field as well as interaction of induced current with magnetic field of conductive current) is illustrated with melt rotation around symmetry axis in MHD device with top and bottom single phase electrodes and cylindrical inductor.

The variation of phase displacement between inductive and conductive current makes it possible to control direction and velocity of melt rotation.

5. References

[1] Electromagnetic stirring for ladle furnaces. Västerås (Sweden): ABB (2008).

[2] Widlund, O.; Sand, U.; Hjortstam, O.; Zhang, X.: Modelling of electric arc furnaces (EAF) with electromagnetic stirring. Västerås (Sweden): ABB (2012).

[3] McDougall, I.: Finite element modelling of electric currents in AC submerged arc furnaces. Proceedings of conference INFACON XI on Innovations in Ferra Alloy Industry (2007), 1–8.

[4] Smirnov, S.A.; Kalaev, V.V.; Hekhamin, S.M.; Krutyanskii, M.M.; Kolgatin, S.N.; Nekhamin, I.S.: Mathematical simulation of electromagnetic stirring of liquid steel in a DC arc furnace. High Temperature, 48 (2010), 68–76.

[5] Yang, Y.; Xiao, Y.; Reuter, M.A.: Analysis of transport phenomena in submerged arc furnace for ferrochrome production. Proceedings of the 10th International Ferroalloys Congress (2004), 15–25.

[6] Jakovics, A.; Pavlovs, S.: Numerical modelling of EAF: electro-magnetic, hydrodynamic, thermal fields. In: Theory and practice of application of arc furnaces. Intensive Course Speccourse II. Edited by Nacke, B. St.Petersburg: Publishing House of ETU (2013).

[7] Pavlov, S.I.: Numerical modelling of closed flows of conductive fluid in electromagnetic field. Summary of Ph.D. Thesis. Leningrad: Polytechnic Institute (1984) (in Russ.).

[8] Pavlovs, S.; Jakovics, A.; Baake, E.; Nacke, B.: Melt flow patterns in metallurgical MHD devices with combined inductive and conductive power supply. Magnetohydrodynamic, (50) 2014 (in press).

PECULARITIES OF MHD FLOW SPIN-DOWN IN AN ANNULAR GAP

MIKHAILOVICH[1] B., SHAPIRO[2] A., STEPANOV[3,4] R.
[1]Department of Mechanical Engineering, Ben-Gurion University of the Negev
P.O.B. 653, Beer-Sheva 8410501, Israel
[2]Physics Department, Shamoon College of Engineering, Beer-Sheva 84100, Israel
[3] Laboratory of Hydrodynamics, Institute of Continuous Media Mechanics, 1 Korolev, Perm 614013, Russia
[4] Department of Applied Mathematics and Mechanics, Perm National Research Polytechnic University, Komsomolskii av. 29, 614990 Perm, Russia
E-mail: borismic@bgu.ac.il

Abstract: The behavior of azimuthal and radial velocity components of free decaying MHD flow in an annular gap with rectangular cross-section in an axial magnetic field has been studied. Experimental values of the velocity components of the flow were measured using a conductive anemometric system. Analysis of mean and oscillating characteristics has been carried out using a continuous wavelet transformation based on Morlet function. Signal scalograms were plotted and analyzed.

1. Introduction

Rotating magnetohydrodynamic (MHD) flows have been studied by various research teams for a number of years. Among them are flows in homopolar type facilities shown in Figure 1. These facilities have coaxial cylindrical electroconducting lateral walls and insulating end-faces with liquid metal in between [1-3].

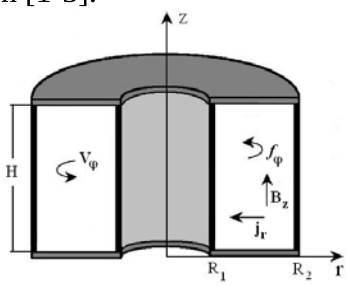

Figure1: Schematic view of experimental setup.

The device is located in a uniform axial magnetic field, and a rotating flow is generated by electromagnetic forces arising within the liquid metal volume at the passage of electric current between the cylindrical inner and outer walls-electrodes. The density of azimuthal electromagnetic body force $f_\varphi = j_r B_z$ is inversely proportional to the radius ($j_r = j_0 R_1 / r$, which leads to $f_\varphi = j_0 B_z R_1 / r$), and the flow becomes different from rotating flows generated by RMF [4,5], a rotating cylindrical container [6], cylindrical lateral walls (Couette-Taylor flow) or rotating end-faces [7].

The interest in said problem is connected with the study of the existence time for structures of various scales in a rotating flow after the electromagnetic body forcing is switched off and of the peculiarities of their decay. Such estimates are extremely useful for the analysis of characteristics of rotating liquid metal flows under the action of amplitude- and frequency-modulated rotating fields [8]. Their usage makes it possible to optimize the regime of electromagnetic stirring of melts and to improve the quality of the obtained products [5].

In the examined spin-down flow regime in an axial magnetic field, it is possible to measure the azimuthal and radial velocity components by the conductive method [8]. As known, his method is delayless (without any response time), does not require calibration and allows analyzing temporal evolution of mean and pulsational velocity values, their spectral properties and correlation characteristics.

2. Experimental setup

The experiments were performed on a facility described in [9]. A ternary eutectic Indium-Gallium-Tin alloy was used as the electroconducting liquid. The properties of the alloy are: $\rho = 6360\,kg/m^3$, $\sigma = 3.4\,S/m$, $\nu = 3.4\cdot10^{-7}m^2/s$ (density, electric conductivity and viscosity, respectively). Copper cylindrical vessel with the external radius R_2 = 35.25 mm and an internal copper electrode with the radius R_1 = 4 mm positioned along the vessel central axis form an annular cavity filled with the liquid metal. The end-faces of the vessel are electrically insulated and the volume is filled up to the level $H = 2(R_2 - R_1) = 2R_0$. The vessel is placed inside a solenoidal water-cooled electromagnet inducing an axial magnetic field. The interaction of the radial electric current j_r with the axial magnetic field B_z generates azimuthal electromagnetic Lorentz force f_φ which drives the liquid metal into rotation at the mean azimuthal velocity V_φ (Fig. 1). The electric current between coaxial electrodes, as well as the current in the electromagnet coil, are controlled by two autonomous Genesys programmable DC power supplies. The magnetic field is measured by FW Bell teslameter, model 6010; the magnetic field inhomogeneity in the volume occupied by the liquid metal does not exceed 8%. Three-electrode potential probe with the 1.5 mm distance between electrodes was used for measuring the azimuthal and radial components. The probe was connected to the Stanford Research Systems low-noise preamplifiers, model SR560, and programmable low-noise filters, model SR640. Analog signals were transformed into digital ones by the National Instruments DAQ card-6052E, and the data was processed and recorded with a 16-bit resolution at the rate of 1000 scans/s using the National Instruments LabVIEW-2012 software.

3. Main results

In the case under study, external boundaries of the flow region are motionless, and the flow structure is established under the action of azimuthal electromagnetic force. Here the radial distribution of the azimuthal velocity component $V_\varphi(r)$ points to the flow instability according to Rayleigh and to the possibility of the existence of the Taylor vortices in the stationary mode.

In this flow mode, the azimuthal component of the mean velocity exceeds the radial one. At that, turbulence level grows along the gap radius and is maximal near the external wall [9], [10]. The initial phase of spin-down mode is accompanied, side by side with a decrease in the velocity components, by a temporal change in the ratio between their amplitudes [9], which can be explained as follows. In a steady mode, the azimuthal velocity component is maximal, since the azimuthal electromagnetic force imposed a rotating motion on the liquid metal. An equilibrium between energy pumping (the work of azimuthal force) and losses for viscous and turbulent friction and Joule dissipation is established (lateral and end-face walls drag the flow whose kinetic energy is dissipated in boundary layers). After switching off the radial electric current (i.e. switching off the electromagnetic force generating the flow), the flow is rearranged – viscous boundary layers diffuse into the flow core and smear it after some time. At that, the ratio between the velocity components values of the decaying flow is also changed.

Such processes are observed in various rotating flows. For example, at the drag of a rotating cylinder with electroconducting liquid [6], the flow passes several stages including the generation of "solitary waves" propagating from the cylinder end-faces with a subsequent formation of a sequence of "internal waves", and then the stage of generation and development of the Taylor vortices near the lateral wall at the Reynolds number values exceeding the critical one. The determining role of azimuthal electromagnetic force in rotating flows is also observed at a combined impact of azimuthal and axial electromagnetic forces (RMF and TMF) [4, 11]. The flow structure is specified by the azimuthal component and is independent of the ratio between the electromagnetic force components. However, the problems of the existence of some regularity in the energy redistribution between the velocity components of a flow decaying in the magnetic field, their correlation, characteristic times of the process, etc., remain unsolved.

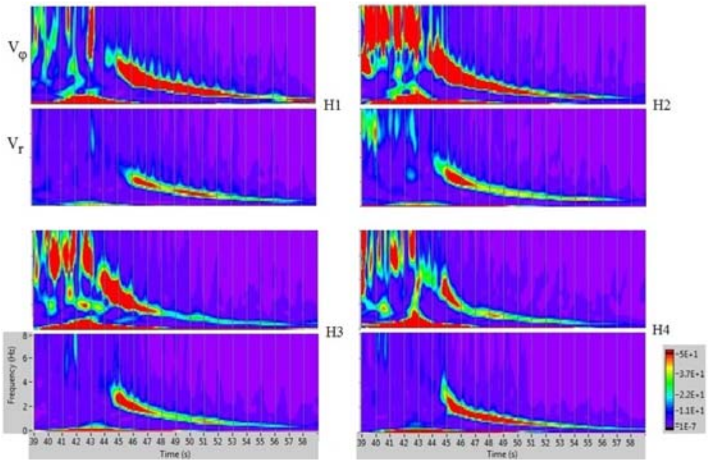

Figure 2: Scalograms of azimuthal and radial velocity components decay on different levels from a bottom (H_i = 38.5, 30, 20, 10 mm); R = 26 mm; B_z = 125 mT.

Switching-off the azimuthal electromagnetic force controlling the flow structure and the removal of energy "feeding" of the flow should lead to a rearrangement of its structure, including the smearing of the region with the Taylor vortices (if they are present) towards the internal wall of the annular channel. Besides, such rearrangement can be accompanied by the liquid circulation in the meridional plane [4] and, hence, by a respective additional decrease in the kinetic energy of both (radial and azimuthal) velocity components. Change in the ratio between the amplitudes of mean velocity components at the initial phase of spin-down regime is accompanied by a respective change in turbulence level. However, we should note that velocity components of transient spin-down flow were approximated by analytical functions, and velocity fluctuations were considered as deviations from them. At the same time, non stationary regime seems complex, and therefore, we consider the decay of low-frequency oscillations. Non-stationary nature of the spin-down regime is complicated to do the quantitative analysis using, e.g., fast Fourier transformation. We have examined several methods of data processing and used the wavelet analysis as the principal one [12, 13]. In our analysis, we have used signals of a conductive velocimeter normalized to the magnetic field value.

The presented scalograms of various spin-down modes are based on continuous wavelet transformation (CWT) using complex-valued Morlet wavelet. The respective program is a part of the Advanced Signal Processing Toolkit of LabVIEW 2012. They allow obtaining information on the frequencies pumped over from the azimuthal to the radial velocity component with a time shift. The wavelet analysis proves to be very efficient in the experimental data analysis of nonstationary turbulent flows [14]. The process is well illustrated in Figure 2, which shows the appearance of oscillations with the frequencies from 2 Hz to 4 Hz, which were previously absent, after switching-off the electromagnetic force in the radial velocity component. The results of flow characteristics analysis (continuous wavelet transformation based on Morlet function) are shown in Figures 3-5.

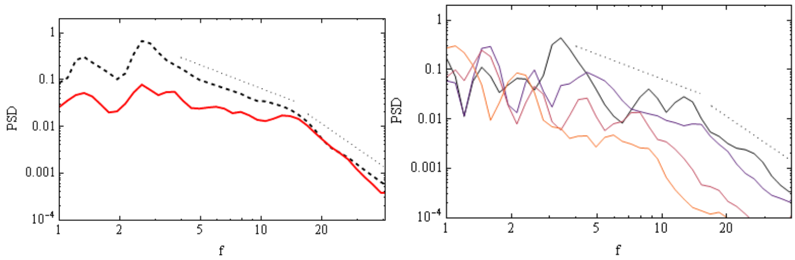

Figure 3: Wavelet power spectral density: left panel - azimuthal (black) and radial (red) velocity components in the stationary regime; right panel - total fluctuations energy in the decay regime for the different average intervals: 0-1 sec, 2-3 sec, 4-5 sec and 7-8 sec, downwards. Dotted lines show “-5/3” and “-3” power laws; B_z = 63 and 94 mT, R = 26 mm, H = 20 mm.

There are two energy spectrum intervals in the stationary regime corresponding to “-5/3” and “-3” power laws (fig.3). The second interval is characterized by energy equipartition for the fluctuations of azimuthal and radial velocity components. These two intervals remain likewise in decay regime, but amplitudes rapidly decrease and the frequency separation region changes from 15 Hz to approximately 6 Hz. Unlike this, lower frequency fluctuations are evaluated differently. The magnetic field impact on the decay process is illustrated in Figure 4 with temporal decreasing of dominant frequency fluctuations. As might be expected, the rate of fluctuations synchronization is determined by magnetic field value. It takes shorter time to get the same frequency of two velocity components with magnetic field increasing. It is also related to evolution of fluctuations amplitudes where the azimuthal energy is transferred to radial one.

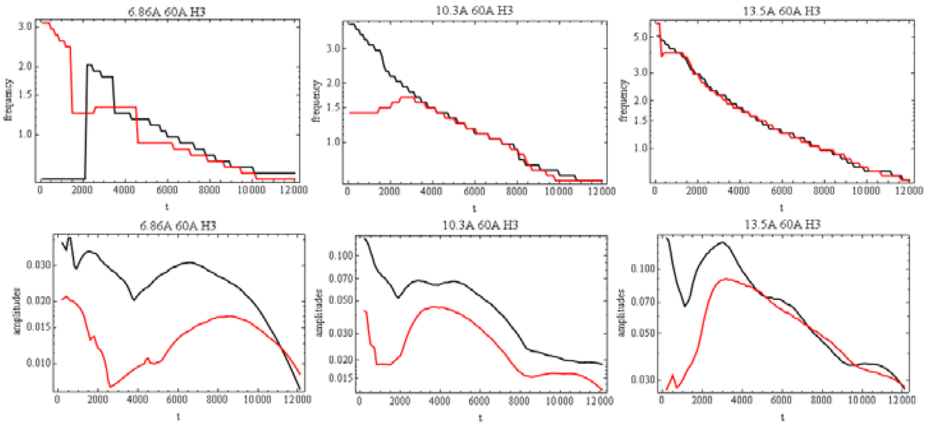

Figure 4: frequency (top panels) and amplitude (bottom panels) of dominating oscillations of azimuthal (black) and radial (red) velocity components in the decay regime for different magnetic field values (B_z = 63, 94, 125 mT from left to right, accordingly); R = 26 mm, H = 20 mm.

Components correlation is represented by the evolution of the phase shift between azimuthal and radial velocity components (fig.5). For stronger magnetic field, phase shift remains about 45 degrees while for the weaker magnetic field it vanishes with time (full correlation state).

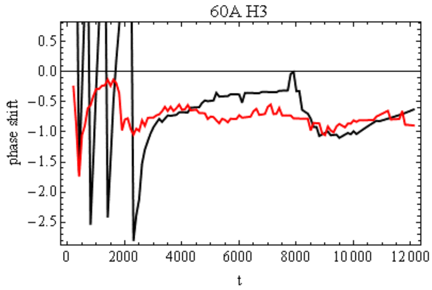

Figure 5: Phase shift between azimuthal and radial velocity components for different magnetic fields: B_z = 63 mT (black), B_z = 125 mT (red).

4. Conclusion

The obtained results allow to get an additional information on the peculiarities of the decay of a rotating MHD flows in an annular gap in the presence of axial magnetic field. It was established that in examined conditions the flow transformation is accompanied by energy exchange between velocity components. At that temporal evolution of fluctuations, the degree of their synchronization and correlations are determined by magnetic field value. We find that the energy of fluctuations at higher frequencies is similar to the energy at the steady regime. Lower frequency fluctuations become synchronized at the decay regime only. We demonstrated these peculiarities using the continuous wavelet transform because the standard cross correlation does not distinguish any particular relations for such phase and frequency modulated signals.

Acknowledgments. This collaborative study was partially supported by Perm region Government under the International Research Group Program. RS acknowledges support from the grant YD-520.2013.2 of the Council of the President of the Russian Federation. Numerical simulations were partially performed on the supercomputer "URAN" of Institute of Mathematics and Mechanics.

References

[1] Baylis J. A. & Hunt J. C. R. MHD flow in an annular channel; theory and experiment, Journal of Fluid Mechanics. (1971). vol. 48, part 3, pp. 423-428.

[2] Kapusta A., and Mikhailovich B. Mean characteristics of turbulent melt flow in a homopolar device of finite height. In: Proc. the VI International Conference on Electromagnetic Processing of Materials, Dresden, Germany (2009), pp. 656–659.

[3] Knaepen B. and Moreau R. MHD turbulence at low magnetic Reynolds number. Annu. Rev. Fluid Mech. (2008). 40:25–45.

[4] Davidson, P. A. The interaction between swirling and recirculating velocity components in unsteady, inviscid flow. Journal of Fluid Mechanics (1989), vol. 209, pp. 35-55.

[5] Kapusta A., Khavkin M., Lesin Sh., Mikhailovich B., Tilman B. Turbulent melt flow excited by amplitude-and-frequency modulated RMF. Journal of Iron and Steel Research, International, 2012. Vol.19, Supplement 1, pp. 483-486.

[6] Valentine D.T. and Miller K. D. Generation of ring vortices in axisymmetric spindown: A numerical investigation. Physics of Fluids, 6, 1535 (1994).

[7] Escudier M.P. Observations of the flow produced in a cylindrical container by a rotating endwall. Experiments in Fluids (1984), 2, pp. 189-196.

[8] Messadek K. and Moreau R. An experimental investigation of MHD quasi-two-dimensional turbulent shear flows. Journal of Fluid Mechanics (2002), vol. 456, pp. 137-159.

[9] Mikhailovich B., Shapiro A., Sukoriansky S., Zilberman I. Experiments with turbulent rotating MHD flows in an annular gap. Magnetohydrodynamics, Vol. 48 (2012), No. 1, pp. 43–50.

[10] Vantieghem S., Knaepen B. Numerical simulation of magnetohydrodynamic flow in a toroidal duct of square cross-section. International Journal of Heat and Fluid Flow, 32 (2011) 1120–1128.

[11] Grants I., Zhang C., Eckert S., Gerbeth G. Experimental observation of swirl accumulation in a magnetically driven flow. Journal of Fluid Mechanics (2008), vol. 616, pp. 135-152.

[12] Noskov V., Stepanov R., Denisov S., Frick P., Verhille G., Plihon N., and Pinton J.-F. Dynamics of a turbulent spin-down flow inside a torus. Physics of Fluids, 21, 045108, 2009.

[13] Mallat S. A wavelet tour of signal processing. Academic Press, 2009, Academic Press (is an imprint of Elsevier), 795 p.

[14] Frick P., Noskov V., Denisov S., and Stepanov R. Direct Measurement of Effective Magnetic Diffusivity in Turbulent Flow of Liquid Sodium // Physical Review Letters, 2010, V.105, P.184502

THE FLOW AND CRYSTALLIZATION OF LIQUID METAL IN THE PROCESS OF MHD-STIRRING

PAVLINOV A., KOLESNICHENKO I., KHALILOV R.
Institute of Continuous Media Mechanics, Perm, Russia
e-mail pam@ icmm.ru

Abstract : The process of crystallization of gallium alloy under stirring conditions is studied. A stirring flow is induced by the external rotating magnetic field generated by the MHD-stirrer containing a cylindrical vessel with gallium alloy. The evolution of the liquid-solid interface is studied by the UDV technique. The position of the interface on the echo profile is found by the wavelet analysis using the real-valued Gauss wavelet. The evolution of the interface during crystallization has been investigated for stirring flows of various intensity.

1. Introduction

Many technological processes (continuous ingot casting, preparation of special alloys) are accompanied by crystallization of metal in a liquid phase. The efficiency of these processes can be essentially improved by stirring molten metals. The paper describes a method of studying the process of crystallization in a gallium alloy. The volume of liquid metal is under the action of the alternating magnetic filed which induces a vortex electric current. The interaction of the electric current with the magnetic field generates an electromagnetic force, which initiates a vortex stirring flow. The stirrer consists of a ferromagnetic core and a set of copper coils, which generate an alternating magnetic field inside a cylindrical volume of liquid metal. The coils generate the rotating magnetic field (RMF) and travelling magnetic field (TMF). A cylindrical vessel filled with gallium eutectic is placed inside the stirrer. The described experimental and numerical investigation has focussed on the process of crystallization in a gallium alloy filling a cylindrical vessel with rigid boundaries. The end faces of the cylinder have different temperatures. The evolution of the interphase boundary was investigated using the Ultrasonic Doppler Velocimeter (UDV) [1, 2].

2. Experimental study

The main unit of the experimental setup is MHD-stirrer 1 (fig. 1), connected to power supply source 2. In our experiment, we used a three-phase transformer for this purpose. A cylindrical cavity of diameter 0.197m and length 0.320m inside the stirrer is designed to place a vessel with liquid metal. The stirrer generates either a travelling or a rotating magnetic field in the liquid metal. The investigation of the crystallization process was carried out for a gallium alloy Ga-Zn-Sn (87.5%Ga; 10.5%Zn; 2%Sn). This eutectic alloy crystallizes at $T_c=17^oC$. The length of the transition zone from a solid to liquid state is rather small for this alloy, which makes it possible to determine the position of the solid-liquid (S/L) interface with sufficient accuracy. Liquid metal is poured in a vertical cylindrical vessel 3 (fig. 1). The walls of the vessel are made of stainless steel 0.006m thick. The bottom of the vessel is made of copper and serves as heat exchanger 4. The exchanger is connected with thermostat 5, which uses alcohol-containing fluid. In our experiment the bottom heat exchanger was cooled to a preset temperature T_1, which was lower than the temperature of alloy crystallization ($T_1<T_c$). The second cylindrical heat exchanger 6 is located above the vessel. It is connected to thermostat 7, which operates on water. During the experiment the upper heat exchanger was heated to a preset temperature T_2, which was higher than the temperature of alloy crystallization ($T_2>T_c$).

The liquids inside the heat exchangers flow through a complex system of channels, which provides a uniform distribution of temperature over the surface. The external surface of the channel is covered by a thermal insulation material. Measurements were made with 9 short-length UDV transducers, which were located in a horizontal plane 8 and connected to UDV 9 in a multiplex mode.

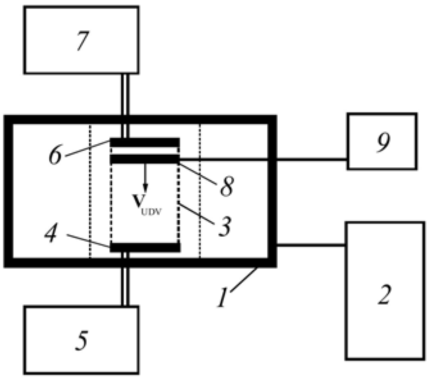

Figure 1: Scheme of experimental setup.

The evolution of the echo profile obtained without application of the wavelet analysis. The application of the wavelet analysis yields the relation for the interface position. It follows then that the wavelet-analysis can be used to define the interface position and to estimate the error of the method based on the wavelet width. The proposed technique was applied to processing of the experimental data obtained at different values of the stirring flow intensity. Note that in all cases the temperature of the lower heat exchanger was T_1=-25°C, and the temperature of the upper exchanger was T_2=21°C. The results of our experiment showed that with increasing intensity of the stirring flow the rate of crystallization decreases (fig. 2,3).

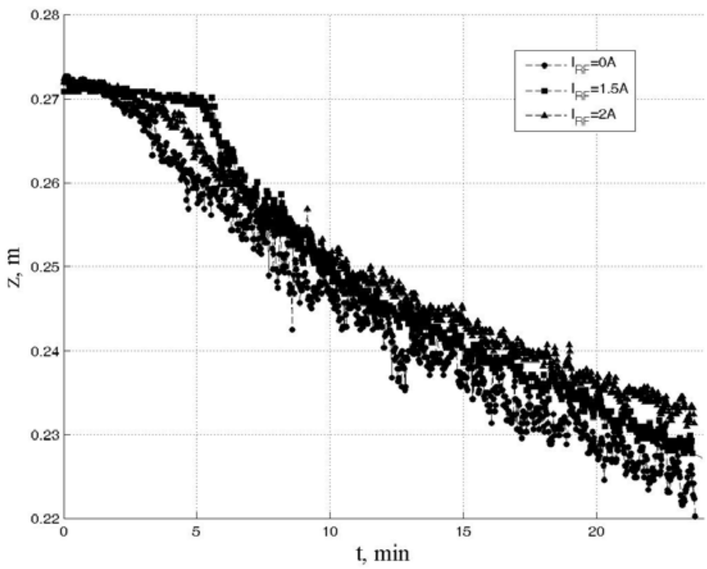

Figure 2: Evolution of the S/L interface in the process
of crystallization at different values of stirring flow intensity (RMF only).

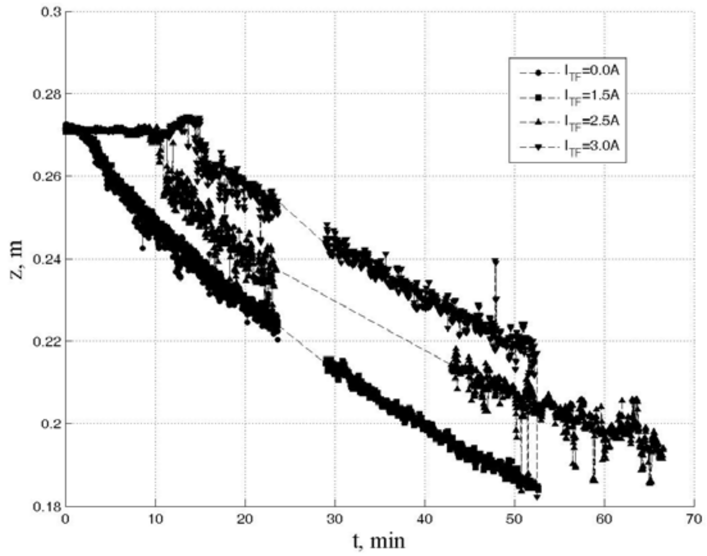

Figure 3: Evolution of the S/L interface in the process
of crystallization at different values of stirring flow intensity (TMF only).

3. Numerical study

In the numerical experiment we have studied the process of crystallization of gallium eutectic in a cylindrical crucible in the presence of MHD-stirring generated by traveling or rotating fields. The wall of the crucible were assumed to be thermally insulated, and the heat was taken away through the crucible lid. The heater is placed in the bottom. Electromagnetic forces in a liquid metal were determined as in [3], and hydrodynamics and the process of crystallization were analyzed in terms of the k-ε model and using the enthalpy - porosity method [4]. Boundary conditions used in the problem were prescribed similar to those of the physical experiment. The velocity component on solid boundaries was taken to be zero. The temperature on the upper and lower boundaries of the region was, respectively, higher and lower than the crystallization temperature of the metal. The heat flow through the side walls was absent. During calculations, the value of porosity varied, which made it possible to describe an increase in the solidified gallium eutectic (fig. 4,5).

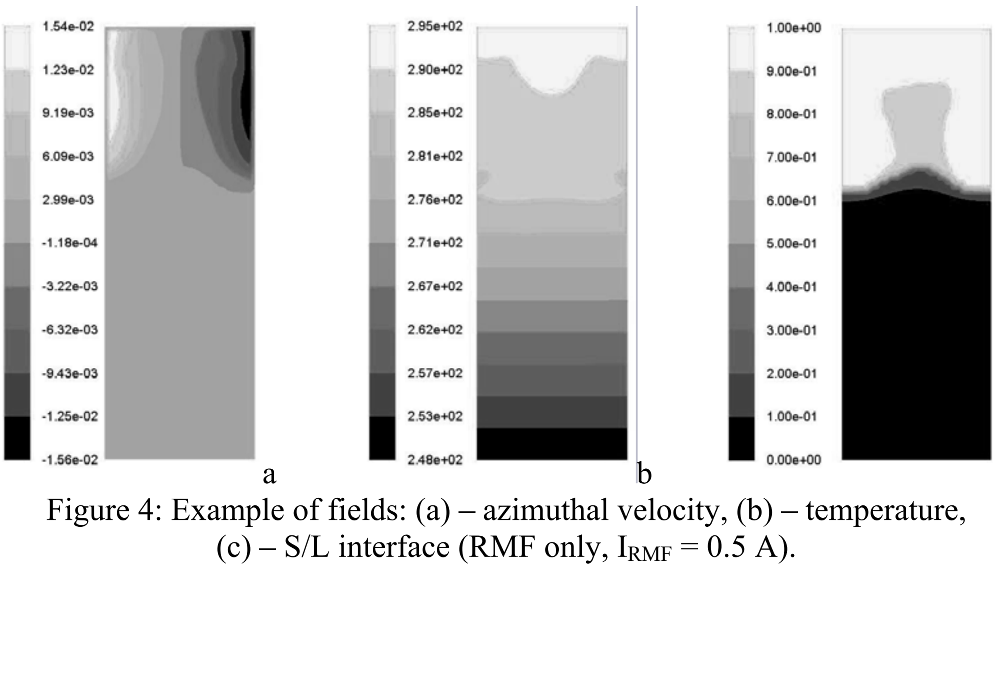

a b c

Figure 4: Example of fields: (a) – azimuthal velocity, (b) – temperature,
(c) – S/L interface (RMF only, I_{RMF} = 0.5 A).

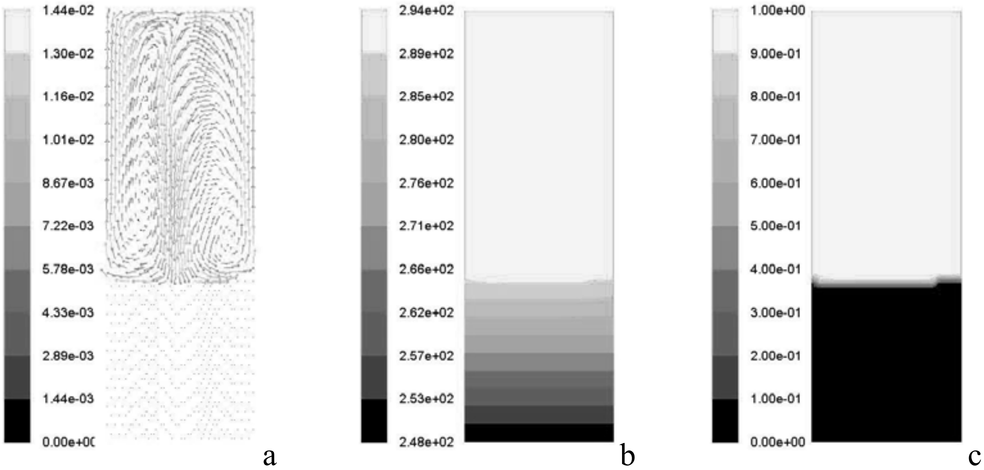

Figure 5: Example of fields: (a) – poloidal velocity, (b) – temperature, (c) – S/L interface (TMF only, I_{TMF} = 2 A).

3. Conclusion

Measurements taken in the process of crystallization met some difficulties. The S/L interphase becomes non perfect on the echo profile. We determined its position using the wavelet analysis. The PC application has been developed to allow implementation of this analysis in the automatic mode. We analyzed the wavelet-spectrum constructed for each echo profile with the help of the real-valued Gauss wavelet. After finding the maximum on the spectral plane we determined the position of the interface and the width of the diffused zone and thus estimated the accuracy of the proposed technique. We also explored the flows generated by the rotating and travelling magnetic fields. It has been found that the stirring flows affect the process of crystallization, namely, they reduce its rate.

Acknowledgements. Financial support from the International Research Group Program supported by Perm region Government and RFBR project 13-01-96042_r_ural_a is gratefully acknowledged.

4. References

[1] Oborin, P.; Kolesnichenko, I.: Application of the ultrasonic doppler velocimeter for study the flow and solidification processes in an electrically conducting fluid. Magnetohydrodynamics, 52 (2013), 231-236.
[2] Kolesnichenko, I.; Pavlinov, A.; Khalilov, R.: Movement of solid-liquid interface in gallium alloy under the action of rotating magnetic field. Magnetohydrodynamics, 49 (2013), 191-197.
[3] Kolesnichenko, I.; Khalilov, R.; Khripchenko, S.; Pavlinov, A.: MHD-stirrer for cylindrical moulds of continuous casting machines fabricated aluminum alloy ingots. Magnetohydrodynamics, 48 (2012), 221-233.
[4] Voller, V.R.; Prakash, C.: A Fixed-Grid Numerical Modeling Methodology for Convection-Diffusion Mushy Region Phase-Change Problems. Int. J. Heat Mass Transfer, 30 (1987), 1709–1720.

MAGNETOPLASMADYNAMIC THRUSTER (MPDT) IN AEROSPACE INDUSTRY: SOME NEW RESULT

ALI I AL MUSSA
King Abdulaziz City for Science and Technology,
Riyadh 11442, P. O. Box 6086, Saudi Arabia
E-mail: almussa@kacst.edu.sa

The trend of using Magnetoplasmadynamic thrusters (MPDT) in aerospace industry and spacecraft missions is widely believed to be very important and useful for its great efficiency as an electromagnetic propulsion and hence addressed here. Methods, techniques and approaches used in the study of MPDT are various. They include but not restricted to theories, experiments, observations, different numerical simulation methods, approaches and algorithms. One of the most outstanding problems in the MPDT is the challenge in the difficulty of sustain their efficiency increment. That is, generally, due to sinks losses, i.e. internal mode losses, plasma thermal loses radiations, etc.

In this work, we show results from our study and investigation in which we use specific approaches and certain theories (variational asymptotic methods and spectral finite element methods). Our main target, so, is to improve our understanding of MPDT problems in particular in aerospace field by, for, example, elucidate newsolution technique that provide the most efficient issues. We note that they give raise the simulation techniques or approaches compare to the expensive or (sometimes) unavailable experimental parametric studies.

ACCELERATION OF CONDUCTION LIQUID IN THE CYLINDER OF FINAL LENGTH UNDER THE INFLUENCE OF A ROTATING MAGNETIC FIELD

ZIBOLD A. F.
Artiom str., 127/54, Donetsk, Ukraine, 83001
E-mail: zibold@mail.donbass.com

Abstract: The non-stationary three-dimensional flow of a conducting liquid driven by a rotating magnetic field in the cylindrical vessel of the limited length is investigated

This work is considering non-stationary axisymmetric three-dimensional flow of a viscous incompressible electro-conducting liquid in the cylinder of final length. This flow arises under the influence of coaxially rotating magnetic field of any rotary symmetry. The problem is described by the system of two dimensionless equations with respect to azimuthal velocity v_φ and φ-component of vector potential of velocity ψ_φ:

$$\frac{\partial v_\varphi}{\partial t} - L v_\varphi + \frac{\mathrm{Re}_\omega}{h}\left[\frac{1}{r}\frac{\partial}{\partial r}\left(r\psi_\varphi\right)\frac{\partial v_\varphi}{\partial z} - \frac{\partial \psi_\varphi}{\partial z}\frac{1}{r}\frac{\partial}{\partial r}\left(r v_\varphi\right)\right] = Ha_{ac}^2 r^{2p-1}\left(1 - v_\varphi/r\right),$$

$$\frac{\mathrm{Re}_\omega}{h}\left[\frac{\partial\left(L\psi_\varphi\right)}{\partial z}\frac{1}{r}\frac{\partial\left(r\psi_\varphi\right)}{\partial r} - r\frac{\partial}{\partial r}\left(\frac{L\psi_\varphi}{r}\right)\frac{\partial \psi_\varphi}{\partial z} + 2\frac{v_\varphi}{r}\frac{\partial v_\varphi}{\partial z}\right] = \tag{1}$$

$$= L^2\psi_\varphi - Ha_{ac}^2 r^{2p-2}\left[2\Delta\psi_\varphi + \frac{\partial^2\psi_\varphi}{\partial z^2} + 4\left(p-1\right)\frac{1}{r^2}\frac{\partial\left(r\psi_\varphi\right)}{\partial r}\right]$$

with boundary conditions

$$v_\varphi\left(0,z,t\right) < \infty,\ v_\varphi\left(r,z,t\right)\big|_\Gamma = 0,\ \frac{\partial v_\varphi\left(r,0,t\right)}{\partial z} = 0,\ v_\varphi\left(r,z,0\right) = 0,$$

$$\psi_\varphi\left(0,z\right) < \infty,\ \psi_\varphi\left(r,z\right)\big|_\Gamma = \left.\frac{\partial \psi_\varphi\left(r,z\right)}{\partial n}\right|_\Gamma = 0, \tag{2}$$

where $T_0 = 1/\omega$ is the time scale, $v_0 = \omega R_0/p$ is the characteristic value of velocity, $Ha_{ac} = Ha/\sqrt{2}$ is the Hartmann number based on the active value of induction, $\mathrm{Re}_\omega = \omega R_0^2/p\nu$ is the Reynolds number defined by the relative velocity of the area boundary in the magnetic field, ψ_φ is the φ-component of the velocity vector potential **v** = rot **ψ**, $h = Z_0/R_0$, p is the number of pole pairs (the order of rotary symmetry of a rotating magnetic field), Γ is the internal surface of the cylinder,

$$\Delta = \frac{\partial^2}{\partial r^2} + \frac{1}{r}\frac{\partial}{\partial r} + \frac{1}{h^2}\frac{\partial^2}{\partial z^2},\ L = \Delta - \frac{1}{r^2}.$$

The analysis of the second equation of system (1) shows, that the reason of occurrence of a three-dimensional flow is the spatial change of the azimuthal velocity. In this connection change at time of the azimuthal velocity is defined from the first equation of system (1), and evolution in time arising meridional vortices structures is defined through change of the azimuthal velocity.

The solution of the system of the equations (1) with boundary conditions (2) is obtained by an iterative method with applying the Galerkin's method at each step of iteration. On the i-step of iteration from the first equation of the system (1) on known value ψ_{i-1} is defined a value of azimuthal velocity v_i. Then known values ψ_{i-1} and v_i are substituted in the second equation of the system from which a value ψ_i is find. Iteration begins with a value $\psi_0 = 0$. Used computing scheme of the method looks like:

$$\frac{\partial v_i}{\partial t} - Lv_i + Ha_{ac}^2 r^{2p-2} v_i + \frac{\mathrm{Re}_\omega}{h}\left[\frac{1}{r}\frac{\partial}{\partial r}\left(r\psi_{i-1}\right)\frac{\partial v_i}{\partial z} - \frac{\partial \psi_{i-1}}{\partial z}\frac{1}{r}\frac{\partial}{\partial r}\left(rv_i\right)\right] = Ha_{ac}^2 r^{2p-1},$$

$$L^2\psi_i - Ha_{ac}^2 r^{2p-2}\left[2\Delta\psi_i + \frac{\partial^2\psi_i}{\partial z^2} + 4(p-1)\frac{1}{r^2}\frac{\partial(r\psi_i)}{\partial r}\right] - \tag{3}$$

$$-\frac{\mathrm{Re}_\omega}{h}\left[\frac{\partial(L\psi_{i-1})}{\partial z}\frac{1}{r}\frac{\partial(r\psi_i)}{\partial r} - r\frac{\partial}{\partial r}\left(\frac{L\psi_i}{r}\right)\frac{\partial\psi_{i-1}}{\partial z}\right] = 2\frac{v_i}{r}\frac{\partial v_i}{\partial z}.$$

Other schemes of iterations are possible, however direct numerical experiment also has shown, that the scheme of iteration used above possesses the best convergence on parameters. Using procedure of the Fourier method, values v_φ and ψ_φ we define by decomposition in the series, satisfying boundary conditions (2):

$$v_\varphi(r,z) = \sum_{m,n} C_{mn} J_1(\beta_m r)\cos\gamma_n z \cdot e^{-\left(\beta_m^2+\gamma_n^2\right)t}, \tag{4}$$

$$\psi_\varphi(r,z) = \sum_{m,n} D_{mn}\left[J_1(\lambda_m r) + A_m I_1(\lambda_m r)\right]\cdot\left(\sin\alpha_n z + B_n sh\alpha_n z\right), \tag{5}$$

where β_m is the roots of equation $J_1(\beta_m) = 0$, γ_n is the roots of equation $\cos\gamma_n = 0$, i.e. $\gamma_n = (n-1/2)\pi$, λ_m is the roots of equation $J_1(\lambda_m)I_1'(\lambda_m) - J_1'(\lambda_m)I_1(\lambda_m) = 0$, α_m is the roots of equation $\sin\alpha_n ch\alpha_n - -\cos\alpha_n sh\alpha_n = 0$, $A_m = -J_1(\lambda_m)/I_1(\lambda_m)$, $B_n = -\sin\alpha_n / sh\alpha_n$.

Numerical experiment made it possible to study the driven spatial flow patterns and to track their evolution in time. The solution is obtained both for small and for big Hartmann numbers at which iterative process still converges. In asymptotics by time the form of hydrodynamic structures comes close to the hydrodynamic structures obtained by solving corresponding stationary problem [1-3].

The completed research promotes the best understanding of the hydrodynamic processes occurring in a cylindrical vessel under the influence of the rotating magnetic field, operating limited time (for example, at metal processing in installations of continuous action).

References

[1] Zibold, A. F.: (2008) Evolution of the hydrodynamical structure arising in the cylinder of the limited length under action of the rotating magnetic field. In: Proc. the 7th International PAMIR Conference on Fundamental and Applied MHD Presqu´île de Giens, France. **1** 467-472.

[2] Zibold, A. F.: (2011) Hydrodynamic structures generated by the rotating magnetic field in the cylinder of finite length. Applied Hydromechanics **13** (2) 17-27 (in Russian).

[3] Zibold. A. F.: (2014) Hydrodynamic structures generated by the rotating magnetic field in the cylindrical vessel. Fluid Dynamics Research *(*in press*)*.

MAGNETIC FIELD ADVECTION IN LIQUID SODIUM FLOW IN TOROIDAL CHANNEL

KHALILOV R., KOLESNICHENKO I., STEPANOV R.
Institute of Continuous Media Mechanics, UB RAS, Perm, Russia
E-mail: khalilov@icmm.ru

The interaction of a liquid sodium flow in a bronze toroidal channel with an alternating magnetic field is considered. The magnetic field traveling along the channel is generated by the external system of coils. The process of magnetic field transfer by the flow of liquid metal is investigated experimentally by measuring the induced phase shifts with respect to the external field. The phase shift obtained from the analysis of the experimental signals is evaluated based on the wavelet analysis.

The results of calculations have indicated that with increasing frequency of the magnetic field the skin-effect becomes more pronounced even near the resulting inhomogeneous magnetic field. Therefore, at high frequencies only the near-wall part of the sodium flow will predominantly participate in the field transport. The higher is the frequency of the alternating field, the thinner is the near-wall sodium layer that participates in field transport. Hence, by changing the magnetic field frequency, one can determine the intensity of field transport by various sodium layers, namely, the transport of the field from the thin near-wall layer (at high frequency) to the layer almost coinciding with the channel cross-section (at low frequency). This has led us to conclude that the proposed method can be used to recover the velocity profile of liquid metal in the channel. Numerical calculations show that magnetic field distribution throughout the cross-section of the channel filled with liquid metal is essentially inhomogeneous. One-dimensional approximation yields only preliminary estimates of profile recovery. For more accurate recovery of velocity data, the 3D magnetic field distribution should be used.

Experimental studies provided evidence that the velocity profile reconstruction is possible. The magnetic field excited in liquid sodium was significantly weakened because of the external bronze shell, nevertheless the sensitivity of the 24-charge system for voltage measurements was sufficient for determining the phase shift due to advection by sodium. The phase shift calculation based on the wavelet analysis is less sensitive to a noise and can be easily adopted for analysis of signal with a time dependent frequency. Three braking regimes produced three different values of the phase shift which means sensitivity to the flow intensity. In addition, different frequencies of the external magnetic field were considered. It helps to estimate the flow intensity at different depth. The obtained results will be used in the next stage of our investigation devoted to the development of the procedure required for recovering information about the velocity profile.

Numerical computation of liquid metal MHD duct flows at finite magnetic Reynolds number

Vinodh Bandaru, Thomas Boeck, Dmitry Krasnov, Jörg Schumacher
Institute of Thermodynamics and Fluid Mechanics,
Technische Universität Ilmenau,
P.O.Box 100565, 98684 Ilmenau, Germany
Corresponding author : vinodh-kumar.bandaru@tu-ilmenau.de

Abstract. A coupled finite difference-boundary element computational procedure for the simulation of turbulent liquid metal flow in a straight rectangular duct in the presence of an externally imposed magnetic field at finite magnetic Reynolds number (R_m) is presented. Periodicity is assumed in the streamwise direction and the duct walls are considered to be perfectly insulating. Details of the algorithm for the coupled electromagnetic solution of the interior and exterior will be discussed along with laminar flow results using idealized pseudo-vaccum magnetic boundary conditions.

Introduction. Turbulent conducting flows at finite magnetic Reynolds numbers occur in magnetohydrodynamic turbulence in plasmas, and in the generation of magnetic fields by the dynamo effect. In simulations the former case is typically studied as box turbulence without walls, and the latter in a closed spherical fluid domain. We are interested in turbulent liquid-metal duct flows in the presence of an externally generated magnetic field, which is of interest for metallurgical applications such as in the continuous casting of steel and aluminum. It can be expected to show complex interactions between the magnetic field and the flow. Studies of these interactions also guide the quantification of the reaction time in the measurement of transient liqud metal flows through Lorentz force velocimetry.

The magnetic Reynolds number R_m is a measure of the relative magnitude of the induced secondary magnetic field to the imposed magnetic field. We focus on the computation of velocity and magnetic fields in the interior of the duct, in the regime of $R_m \sim 1$. Since the secondary magnetic field (which is significant) also pervades the space outside the duct, proper modelling of the magnetic field in the interior requires a consistent treatment of the magnetic field across the duct boundaries. This is typically done through either of the following two approaches. The first approach is to extend the computational domain to model the magnetic field also outside the fluid domain. The second approach is to model the magnetic field only inside the duct but with magnetic boundary conditions that arise from the boundary integral formulation of the exterior field. Extending the domain to the exterior is computationally costly and also inconvenient for the parallelization of an existing DNS code [1]. Furthermore, since the exterior secondary magnetic field in itself is not in our interest, we prefer the boundary integral approach.

Characterizing the exterior magnetic field by the boundary integral procedure gives rise to non-local boundary conditions [2]. Such boundary conditions typically arise in the non-spectral simulation of dynamo and astrophysical processes. A hybrid finite volume-boundary element computational procedure has been first proposed by Iskakov et al.[2, 3] and since then has been applied by various researchers to simulate kinematic problems wherein the velocity field is given and the evolution of the magnetic field is sought (see, e.g., [4, 5]). In this work, we attempt to perform a full dynamic simulation of the flow and magnetic fields evolving together in the case of an MHD duct flow. A numerical procedure for the full MHD solution along with laminar flow solutions with idealized magnetic boundary conditions will be presented.

Governing equations and numerical procedure We consider the incompressible flow of an electrically conducting fluid driven by a mean pressure gradient in a straight square duct with an imposed magnetic field $\boldsymbol{B}_0$. Flow crossing the magnetic field contributes to a current density $\boldsymbol{J}$ which forms the source of a secondary magnetic field $\boldsymbol{B}$ that acts as a perturbation to the primary imposed magnetic field. The total magnetic field $\boldsymbol{B}_T = \boldsymbol{B}_0 + \boldsymbol{B}$ interacts with the current density $\boldsymbol{J}$ to produce a Lorentz force $\boldsymbol{F} = \boldsymbol{J} \times \boldsymbol{B}_T$ which acts as a body force on the flow field. This body force affects the flow field which in turn affects the magnetic field. The physics of this coupled evolution of the velocity and magnetic fields is governed by the Navier-Stokes and the magnetic field transport equations respectively with the constraints of solenoidality of both the fields. Using U, L, L/U, ρU^2, B_0 and $\sigma U B_0$ as the scales for the velocity, length, time, pressure, magnetic field and current density respectively, the governing equations in the interior of the duct in non-dimensional form are

$$\frac{\partial \boldsymbol{v}}{\partial t} + (\boldsymbol{v} \cdot \nabla)\boldsymbol{v} = -\nabla p + \frac{1}{Re}\nabla^2 \boldsymbol{v} + \frac{N}{R_m}\left((\nabla \times \boldsymbol{b}_T) \times \boldsymbol{b}_T\right), \tag{1}$$

$$\nabla \cdot \boldsymbol{v} = 0, \tag{2}$$

$$\frac{\partial \boldsymbol{b}}{\partial t} + (\boldsymbol{v} \cdot \nabla)\boldsymbol{b}_T = (\boldsymbol{b}_T \cdot \nabla)\boldsymbol{v} + \frac{1}{R_m}\nabla^2 \boldsymbol{b}, \tag{3}$$

$$\nabla \cdot \boldsymbol{b} = 0, \tag{4}$$

$$u = v = w = 0 \quad \text{at } y, z = \pm 1, \quad \text{periodicity in } x \text{ direction} \tag{5}$$

where x, y and z denotes the streamwise, spanwise and wall normal directions respectively and all the lower case variables correspond to non-dimensional quantities. The mean cross-sectional velocity U, the half width of the channel L, and a characteristic value of the imposed magnetic field strength B_0 have been taken for non-dimensionlization. Parameters in the equations are the Reynolds number $Re \equiv UL/\nu$, the magnetic interation parameter $N \equiv Ha^2/Re$, where $Ha \equiv B_0 L \left(\sigma/\rho\nu\right)^{1/2}$ is the Hartmann number and the magnetic Reynolds number $R_m \equiv UL/\lambda$. The secondary magnetic field in the exterior of the duct is curl free and hence represented as the gradient of a scalar potential, $\boldsymbol{b} = -\nabla\psi$. The solenoidal condition leads to the governing equation in the exterior as

$$\nabla^2 \psi = 0 \tag{6}$$

The numerical solution is carried out on a non-uniform rectangular grid, with clustering of grid points near the walls to resolve the Hartmann layers and side layers that are characteristic of duct MHD flows. A collocated grid arrangement is used with the variables $\boldsymbol{v}$, p and $\boldsymbol{b}$ stored at the same grid points. A finite difference scheme with semi-implicit time stepping is used for the discretization of the momentum and the magnetic field transport equations, wherein the diffusive terms are treated in an implicit manner. For the momentum equation, a fractional time step procedure is adopted to first compute an intermediate velocity field that is in turn projected onto a solenoidal velocity field through a pressure correction step. Poisson equations for the intermediate velocities and pressure are transformed into the Fourier space with respect to x and are solved using the software package FISHPACK [6]. The mean pressure gradient is adjusted in order to obtain a constant volume flux in the duct. Details of the numerical scheme for the solution of the velocity field can be found in Krasnov et al. [1].

Semi-implicit discretization of Eq.(3) with further simplification yields

$$-f\boldsymbol{b}^{n+1} + \nabla^2 \boldsymbol{b}^{n+1} = -f\boldsymbol{q} \tag{7}$$

for the magnetic field perturbation at the current time step $n+1$, where f is a discretization parameter and $\boldsymbol{q}$ contains the convective and field stretching terms at the previous time steps n and $n-1$. Since the domain is periodic in the streamwise direction, introducing the Fourier transform along the x-direction leads to

$$\boldsymbol{b}(x,y,z) = \sum_{k=-\frac{N_x}{2}}^{k=\frac{N_x}{2}-1} \hat{\boldsymbol{b}}(y,z) e^{i\alpha_k x} \tag{8}$$

where $\alpha_k = 2\pi k/L_x$ is the streamwise wavenumber, L_x being the length of the duct and N_x the number of grid points along the length of the duct. Substituting this in Eq.(7) and dropping the superscript yields

$$-(f+\alpha_k^2)\hat{\boldsymbol{b}} + \nabla_{yz}^2 \hat{\boldsymbol{b}} = -f\hat{\boldsymbol{q}} \tag{9}$$

which is to be solved for the Fourier coefficients $\hat{b}_x$, $\hat{b}_y$ and $\hat{b}_z$ in the interior of the duct. However, since Eq.(4) acts as an additional constraint on the magnetic field and overdetermines the sytem along with Eq.(3), we solve Eq.(9) only for the components $\hat{b}_y$ and $\hat{b}_z$ and reconstruct the component $\hat{b}_x$ from the condition

$$\hat{b}_x = \frac{-1}{i\alpha_k}\left(\frac{\partial \hat{b}_y}{\partial y} + \frac{\partial \hat{b}_z}{\partial z}\right),\ k \neq 0 \tag{10}$$

In this way the solenoidal property of the resulting magnetic field is preserved. For the mode with $k=0$, the component $\hat{b}_x$ is decoupled from the other two components and hence Eq.(9) is used to compute $\hat{b}_x$ with Dirichlet boundary conditions. The magnetic field in the real space is recovered from the Fourier components $\hat{b}_x$, $\hat{b}_y$ and $\hat{b}_z$ through the inverse Fourier transform.

Evaluation of the components $\hat{b}_y$ and $\hat{b}_z$ at each wavenumber requires boundary conditions that are consistent with the exterior field, the formulation of which is described here. The Fourier representation of Eq.(6) leads to the Helmholtz equation $(\nabla_{yz}^2 - \alpha_k^2)\hat{\psi} = 0$, which using the Green's second identity can be represented in the boundary integral form as

$$c\hat{\psi}(\boldsymbol{r'}) = \text{P.V.} \oint [G(\boldsymbol{r'},\boldsymbol{r})\hat{b_n}(\boldsymbol{r}) + \hat{\psi}(\boldsymbol{r})\frac{\partial G}{\partial n}(\boldsymbol{r'},\boldsymbol{r})] dl(\boldsymbol{r}) \tag{11}$$

for the values of $\hat{\psi}$ on the rectangular boundary, where n represents the boundary normal direction, $G(\boldsymbol{r'},\boldsymbol{r})$ is the Green's function of the Helmholtz operator [7] about the pole $\boldsymbol{r'} = y\boldsymbol{e}_y + z\boldsymbol{e}_z$ and the integration along the rectangular contour is in the sense of a Cauchy principal value. Eq.(10) is non-local in nature and is discretized using the boundary element method [8]. This involves dividing the rectangular contour into a number of small line elements called boundary elements (see Figure 1) and approximating the integral equation as the sum of integrals along each of these boundary elements. The grid points that store the variables lie at the ends of each of the elements and the variables $\hat{\psi}$ and $\hat{b_n}$ are assumed to be piecewise linear within each element. The integrals are evaluated numerically along all elements except at the pole using a four-point Gaussian quadrature in order to accurately account for the steep gradients in the Green's function. At the pole, the Green's function has a logarithmic singularity and

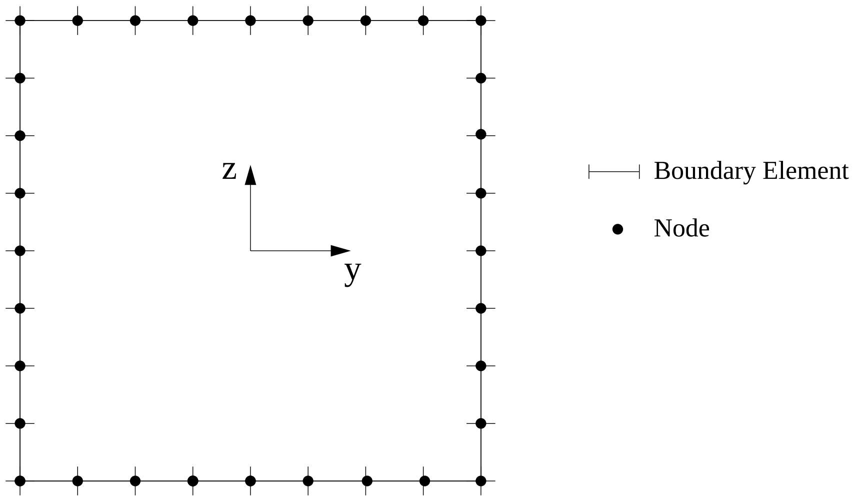

Figure 1: Grid with boundary elements and nodes used for the solution of the integral equation for $\hat{\psi}$.

is dealt with analytical integration over the element containing the pole. The boundary element discretization yields the discrete form of Eq.(11) which is a fully occupied linear system of equations $\boldsymbol{A}\hat{\boldsymbol{\psi}} = \boldsymbol{d}$ where $\boldsymbol{A}$ is a matrix and $\boldsymbol{d}$ a vector.

Eq.(12) along with $\hat{b}_\tau = -\frac{\partial\hat{\psi}}{\partial\tau}$ and the divergence free condition provides the boundary conditions for computing $\hat{b}_y$ and $\hat{b}_z$ from Eq.(9), which is solved by a coupled iterative procedure. The procedure is computationally intensive due to the fact that non-local boundary conditions translate into fully occupied linear systems unlike the sparse sytems that arise from local boundary conditions. The current density $\boldsymbol{j}$ is subsequently computed from the magnetic field $\boldsymbol{b}$ using the Ampère's law $\boldsymbol{j} = (\nabla \times \boldsymbol{b}_T)/R_m$.

Results and discussion. Simulations with pseudo vaccum magnetic boundary conditions were first performed in order to validate the solution of the magnetic field in the duct interior. For this purpose, it is assumed that for perfectly insulating walls, $j_n = 0$ is realized with vanishing tangential components of the magnetic field as

$$b_{\tau 1}, b_{\tau 2} = 0,\ \frac{\partial b_n}{\partial n} = 0 \quad \text{at } y, z = \pm 1 \tag{12}$$

the Neumann condition on b_n being obtained from Eq.(4). Starting with an initial laminar duct velocity profile and an imposed uniform magnetic field along the z-direction, the evolution of the velocity and magnetic fields is simulated at $R_m = 100$, until a steady state is reached. The contour of the streamwise velocity profile along with the corresponding magnetic field lines (in the x-z plane) are displayed in Figure 2.

It is observed that the velocity reaches the steady Hartmann-like profile through a series of oscillations that are damped eventually by diffusion, unlike the quasistatic regime which is diffusion dominated. These oscillatory states are reminiscent of Alfvén waves that are typical of high R_m MHD flows. The corresponding stretching of the magnetic field lines is also observed.

Simulation of turbulent MHD duct flow with full treatment of the magnetic boundary conditions as described in the previous section along with detailed validation of the procedure using a quasistationary approach in the limiting case of low magnetic Reynolds number is in progress. Benchmarking of the procedure's numerical efficiency will be made with subsequent studies of MHD turbulence at finite magnetic Reynolds number.

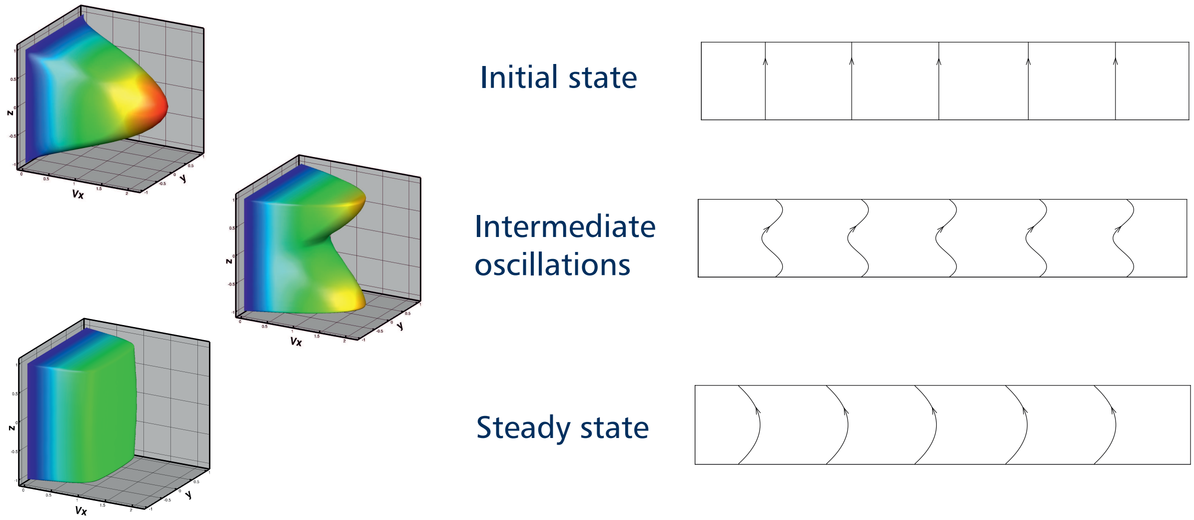

Figure 2: Contours of streamwise velocity profile at $Re = 2000$, $R_m = 100$, $Ha = 100$ in a cross-section (left). The corresponding magnetic field lines in the x-z plane, $y = 0$ (right). Grid size : $16 \times 128 \times 128$.

Acknowledgments. We acknowledge financial support from the Deutsche Forschungsgemeinschaft within the Research Training Group 1567.

References

[1] Krasnov, D., Zikanov, O. and Boeck, T.: Comparitive study of finite difference approaches in simulation of magnetohydrodynamic turbulence at low magnetic Reynolds number. Comp. Fluids 50 (2011) 46-59.

[2] Iskakov, A.B., Descombes, S. and Dormy, E.: An integro-differential formulation for magnetic induction in bounded domains: Boundary element finite volume method. J. Comp. Phy. 197 (2004) 540554.

[3] Iskakov, A., Dormy, E.: On magnetic boundary conditions for non-spectral dynamo simulations. Geophy. Astrophy. Fluid Dyn. 99-6 (2005) 481-492.

[4] Giesecke A., Stefani, F., Gerbeth, G. : Kinematic simulation of dynamo action by a hybrid boundary-element/finite-volume method. Magnetohydrodynamics 44 (2008) 237-252

[5] Gissinger C., Iskakov A., Fauve S., Dormy, E.: Effect of magnetic boundary conditions on the dynamo threshold of von Kármán swirling flows EPL 82 (2008) 29001.

[6] Adams J.C., Swarztrauber P., Sweet R. : Efficient fortran subprograms for the solution of separable elliptic partial differential equations. https://www2.cisl.ucar.edu/resources/legacy/fishpack.

[7] Stakgold, I. : *Boundary Value Problems of Mathematical Physics, Vol.2*, Macmillan (1968).

[8] Brebbia, C. and Walker, S.: *The Boundary Element Method for Engineers*, Pentech Press (1978).

ELECTROMAGNETIC INTERACTION OF A SMALL MAGNET AND A WALL-BOUNDED FLOW WITH CONDUCTING WALLS

KAZAK[1] O., HEINICKE[1,2] CH., WONDRAK[3] T., BOECK[1] T.
[1] Institute of Thermodynamics and Fluid Mechanics, Ilmenau University of Technology, P.O. Box 100565, 98684 Ilmenau, Germany
[2] Department of Applied Mechanics, Aalto University, PO Box 14300, 00076 Aalto, Finland
[3] Helmholtz-Zentrum Dresden-Rossendorf, Bautzner Landstraße 400, 01328 Dresden, Germany
E-mail address of corresponding author: oleg.kazak@tu-ilmenau.de

Abstract: We study the effects of electrically conducting walls on the interaction between a small cubic permanent magnet and liquid-metal flow in a cylindrical pipe using experiments and electromagnetic simulation. The problem is motivated by Lorentz force velocimetry, where the drag force on the magnet due to the induced eddy currents in the flow is used for flow measurement. Compared with insulating walls, the conducting walls lead to an increased drag force on the magnet. Except for low distances, the experimental results are satisfactorily reproduced in simulations using a point dipole approximation of the magnetic field.

1. Introduction

In recent years several novel methods for flow measurement based on electromagnetic induction have been developed. They work without direct contact with the molten metal, whereby the problems due to high temperature and chemical aggressiveness of these materials can be circumvented. One of them is the so-called Lorentz force velocimetry (LFV) [1]. In this method, a magnet next to the moving conducting fluid causes induction of eddy currents, which give rise to a braking Lorentz force on the flow. An equal but opposite force acts on the magnet, which can be measured. It depends on the magnitude and distribution of velocity and magnetic field in the flow domain. Several studies of LFV have examined the influence of the distance between magnet and fluid as well as effects of field distribution [2, 3]. We extend these previous studies by examining the influence of finite conducting walls between the magnet and conducting liquid.

2. Presentation of the problem

Local flow measurement with LFV can be realized when the magnetic field is only significant in a limited flow volume. For such purposes one can use small permanent magnets. First investigations in this direction were performed on duct flows with insulating walls [2]. The same equipment, i.e. magnet and force sensor, were also used in the present study. Lorentz force measurements were taken for flows of the alloy InGaSn in cylindrical pipes with insulating and conducting walls. The setup was the same as in previous studies of other flow sensors for conducting flows [4]. The walls of the three pipes are made from copper, brass and PVC. The flows are driven by an electromagnetic pump and the mean flow velocity is controlled by an inductive flow meter (ABB Copa-XL DN25). In the experimental study, the position of the cubic permanent magnet relative to the pipe was changed systematically in the radial and transverse directions, and the flow velocity was varied. For one measurement the drag component of the Lorentz force was recorded with a temporal resolution of 6.4 Hz and averaged over 40 s.

Differences between insulating and conducting pipe walls originate from different eddy current distributions. Although there is no induction in the stationary walls, the eddy currents generated in the liquid will pass through the conducting walls, and can thereby change the resulting Lorentz force.

For the numerical simulation of the problem we use the geometry and coordinate system shown in Fig. 1. The central axis of the pipe coincides with the x-axis. We only consider a finite section of the pipe in the axial direction whose length is adjusted depending on the distance of the magnet to the pipe.

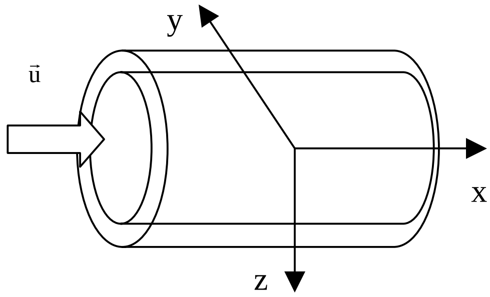

Figure 1: Pipe with conducting walls and coordinate system.

The geometrical and material properties are as follows: inner pipe diameter $d_1 = 27 \cdot 10^{-3}$ m, thickness of the wall $d_2 = 2.7 \cdot 10^{-3}$ m, wall conductivity for copper $\sigma_1 = 58 \cdot 10^6$ S/m, conductivity of InGaSn $\sigma_2 = 3.3 \cdot 10^6$ S/m, kinematic viscosity of InGaSn $\upsilon = 3.4 \cdot 10^{-7}$ m^2/s, density of InGaSn $\rho = 6492$ kg/m^3.

With these parameters one can estimate the Reynolds and magnetic Reynolds numbers for an average velocity $u = 1$ m/s that we consider in the simulations. The Reynolds number is $\mathrm{Re} = ud_1/\upsilon = 8 \cdot 10^4$, i.e. the flow is fully turbulent. The magnetic Reynolds number $\mathrm{Re}_m = \mu_0 \sigma_2 u d_1 \approx 10^{-2} << 1$ is low in this problem. We therefore use the quasistatic limit of the induction equation. We also assume the velocity field to be unaffected by the Lorentz force because the values are fairly small. The mean turbulent velocity distribution in the pipe is represented by [6]

$$u_x(r) = \frac{u_\tau}{\kappa} \ln\left(1 + \kappa \frac{u_\tau R}{\upsilon} \frac{1}{2}\left(1 - \frac{r^2}{R^2}\right)\right); \tag{1}$$

where u_τ is the friction velocity, $\kappa = 0.42$ is the von Karman constant, and $R = d_1/2$ is the inner pipe radius. The friction velocity is obtained by the constraint that (1) has to provide the correct value of the known mean velocity u. For u=1 m/s we obtain u_τ =0.074 m/s.

In the quasistatic formulation of the induction equation the induced currents are given by Ohm's law with the induced electric field represented by the negative electric potential gradient. Charge conservation then provides [5]

$$\nabla^2 \phi = \nabla \cdot \left(\vec{u} \times \vec{B}\right) \tag{2}$$

in the liquid. In the solid wall the velocity is absent, therefore

$$\nabla^2 \phi = 0\,. \tag{3}$$

The magnetic field is represented as a magnetic point dipole with magnetic moment $\vec{m}$. When the dipole is at the origin of the coordinate system, the field distribution is [1]

$$\vec{B}(\vec{r}) = \frac{\mu_0}{4\pi}\left(3\frac{\vec{m} \cdot \vec{r}}{r^5}\vec{r} - \frac{\vec{m}}{r^3}\right). \tag{4}$$

The eddy current density in the conducting walls is represented by

$$\vec{j}_1 = -\sigma_1 \nabla \phi_1 \tag{5}$$

and the eddy currents in the liquid by

$$\vec{j}_2 = \sigma_2 \left(-\nabla \phi_2 + \vec{u} \times \vec{B} \right). \tag{6}$$

The Lorentz force density is given by

$$\vec{F}_L = \vec{j} \times \vec{B} \, . \tag{7}$$

The boundary conditions (cf. fig. 1) are as follows:

- at the distance $R = 13.5 \cdot 10^{-3}$ m (inner pipe radius) from the x-axis the continuity boundary condition is

$$\vec{n} \cdot \left(\nabla \phi_1 - \nabla \phi_2 \right) = 0 \, ; \tag{8}$$

- at the distance $R + d_2 = 16.2 \cdot 10^{-3}$ m from the x-axis the insulating boundary condition is

$$\vec{n} \cdot \nabla \phi = 0 \, , \tag{9}$$

where $\vec{n}$ denotes the normal vector.

The magnetic fields in the experimental setup are generated by a cubic permanent magnet with a side length of l=10 mm, which is approximated by a magnetic point dipole located at the centre of the permanent magnet in the numerical simulations. The magnetic moment $\vec{m}$ in this case can be calculated from the measured distribution [2] of the magnetic field $\vec{B}$ at larger distances according to Eq. (4). The numerical value is $m = 1.1$ A·m^2.

For the numerical solution of the Poisson equations (2, 3) for the electric potential the PDE module in the Comsol 4.4 software package was taken. Different non-uniform meshes were tested. The domain area was split into elements unevenly: in the area near the permanent magnet, where large gradients of the magnetic field are situated, the elements were of small size. Mesh convergence tests were also carried out to ensure valid results. Typical numbers of elements were about10^6 .

3. Results

Figs. 2 and 3 show a comparison of experimental data and computational results for the total Lorentz force (obtained by integrating Eq. (7) over the whole conducting volume) at different positions of the permanent magnet for a copper pipe and an insulating PVC pipe. The magnetic moment of the cubic permanent magnet is perpendicular to the top and bottom sides of the magnet. In Figs. 2 and 3 the magnetic moment is always aligned with the z-axis. In Fig. 2 the center of the magnet is located on the z-axis (for a=0) and the bottom side of the magnet touches the wall of the pipe. From this reference configuration the magnet is then shifted by a distance a in the transverse direction, i.e. a is the y-position of the center of the magnet. In Fig. 3 the reference configuration (b=0) is the same, i.e. the center of the magnet is located on the z-axis and the bottom side of the magnet touches the pipe wall. The magnet is then shifted radially along the z-axis, and b denotes the displacement (in z) of the magnet from the reference configuration.

In both Fig. 2 and Fig. 3 the conducting walls consistently provide a higher Lorentz force, which decreases rapidly with the distance. The theoretical values from the computations overestimate the measured values. The disagreement between theory and experiment is significant at small distances and decreases with increase of a and b. This is not surprising since the dipole representation significantly overestimates the magnetic field at distances of the order of the side length of the magnet.

The relative error between experiment and theory is further illustrated in Fig. 4, which shows the ratio between theoretical and experimental Lorentz force values as function of distance. For both displacements (a and b) the error is as large as 80% at close distances and drops to about 2% or less at the largest distances. For the insulating pipe good agreement is found at smaller distances than for the copper pipe. This observation can be attributed to the effectively larger distance between eddy currents and field source for insulating walls, which implies that the dipole approximation of the field is more accurate. The same argument also suggests that – irrespective of the distance – forces are larger for conducing walls. We also remark that the non-monotonous behaviour with respect to *b* in Fig. 4 is not visible in Fig. 3. It could be due to measurement errors but we cannot completely rule out mesh effects.

Fig. 5 shows distributions of eddy current and Lorentz force densities on the inner surface of the pipe. The current density and Lorentz force are given in non-dimensional form as $j_0 = j / j_{scale}$, where $j_{scale} = \frac{\sigma_2 u \mu_0 m}{4\pi r^3}$ and $F_{L0} = F_L / F_{Lscale}$, $F_{scale} = \sigma_2 u \left(\frac{\mu_0 m}{4\pi r^3}\right)^2$. The distance is taken as $r = 7.7 \cdot 10^{-3}$m from centre of the permanent magnet to the liquid metal. The coordinate s is the circumferential distance on the pipe surface measured from the line y=0. The Lorentz force distribution is clearly correlated with eddy current density distribution and the orientation of the Lorentz force density is mostly opposite to the x-direction.

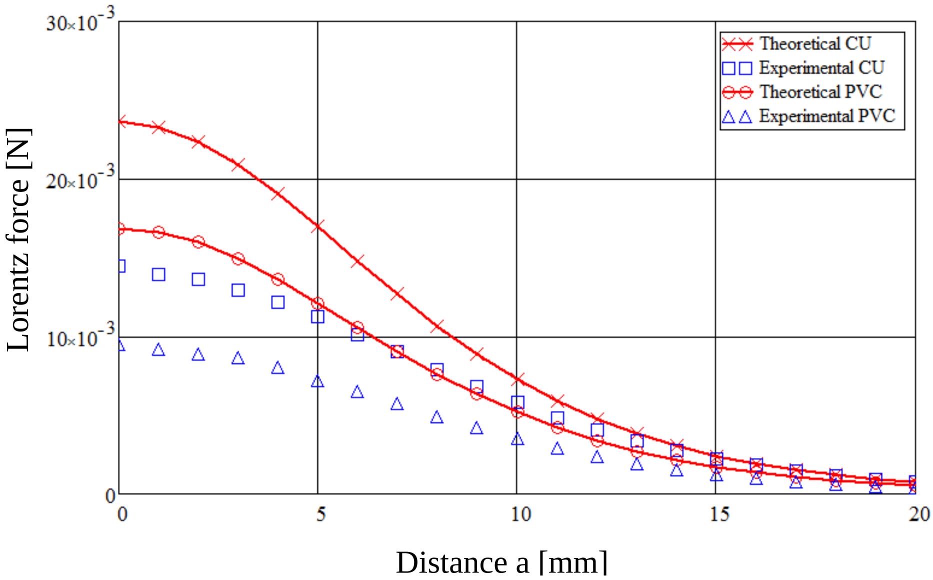

Figure 2: Lorentz force dependence on transverse distance.

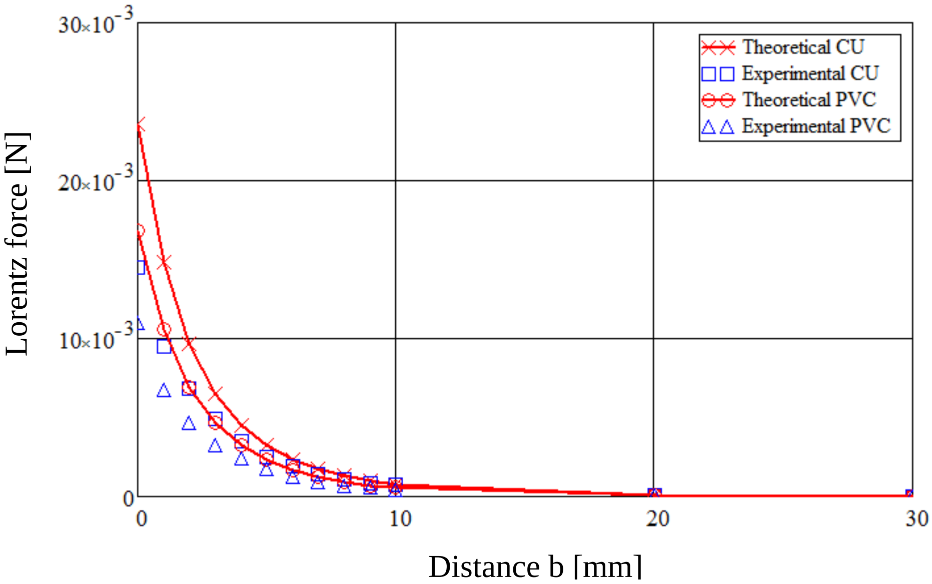

Figure 3: Lorentz force dependence on radial distance.

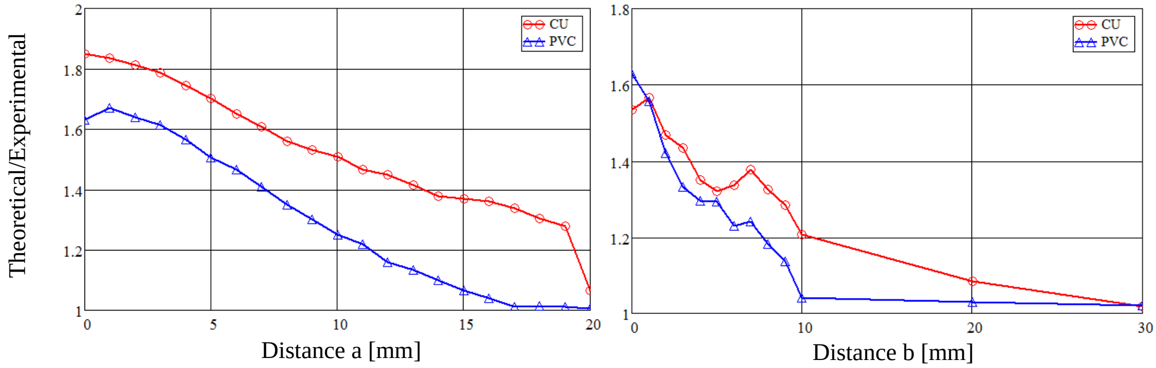

Figure 4: Ratio between theoretical and experimental Lorentz forces.

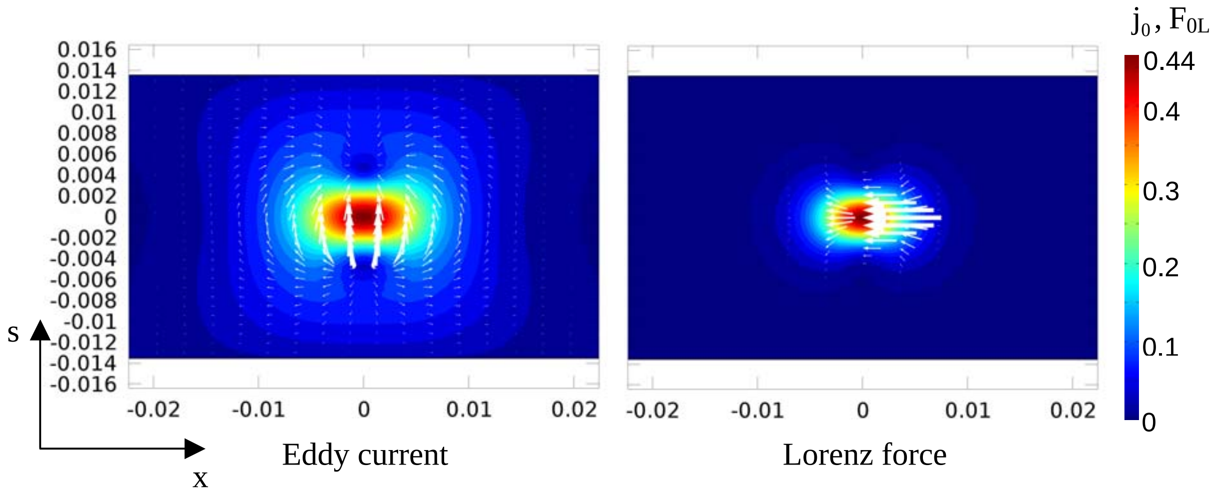

Figure 5: Eddy current and Lorentz force distribution on the inner pipe surface for insulating walls, velocity $u = 1$ m/s, a=10 mm and b=10 mm.

4. Conclusion We have performed experiments and simulations of a LFV test setup using liquid metal flows in pipes with insulating and conducting walls. The conducting walls are beneficial because they increase the measured force. Further work will focus on velocity variation and a more realistic approximation of the magnetic field.

5. Acknowledgments: The authors acknowledge the financial support by the Deutsche Forschungsgemeinschaft (research training group GRK 1567) and by the Helmholtz Alliance “Liquid Metal Technologies”. The authors also thank M. Zec for sharing his Comsol models for the insulating pipe geometry.

6. References

[1] Thess A., Votyakov E., Knaepen B., Zikanov O.: Theory of the Lorentz force flowmeter. New Journal of Physics, 9 (2007) 299.
[2] Heinicke C., Tympel S., Pulugundla G., Rahneberg I., Boeck T. and Thess A.: Interaction of a small permanent magnet with a liquid metal duct flow. Journal of Applied Physics 112, 124914 (2012).
[3] Kirpo M., Tympel S., Boeck T., Krasnov D. and Thess A.: Electromagnetic drag on a magnetic dipole near a translating conducting bar Journal of Applied Physics 109, 113921 (2011).
[4] Priede J., Buchenau D., Gerbeth G.: Contactless electromagnetic phase-shift flowmeter for liquid metals. Meas. Sci. Technol. 22, 055402 (2011).
[5] Davidson P.A.: An introduction to Magnetohydrodynamics, Cambridge University Press (2001) 432.
[6] Schade H., Kunz E.: Strömungslehre. Walter de Gruyter (2007) 558.

NUMERICAL CALCULATIONS OF 3D PbLi MHD FLOW IN A SQUARE DUCT WITH DIFFERENT WALL ELECTRICAL CONDUCTIVITIES

KRASTINS[1] I., SHISHKO[1] A., BULIGINS[2] L.
[1]Institute of Physics of University of Latvia, Miera st. 32, Salaspils, LV-2169, Latvia,
[2]Department of Physics, Faculty of Physics and Mathematics, University of Latvia
Zellu 8, Riga, LV-1002, Latvia
E-mail: leonids.buligins@lu.lv

Abstract: Numerical results of 3D steady MHD flow in a meter-long square duct with applied strong magnetic field are presented. They could be of use in developing liquid-metal (LM) blanket, in which PbLi is assumed as a breeding material, also for estimation of influence of MHD effects on liquid-metal corrosion processes of structural materials. Results show that change of wall conductance ratio from zero to a finite value in streamwise direction leads to creation of flow transition region, which is basically proportional to the Reynolds number and inversely proportional to some power of Hartmann number as shown in results.

1. Introduction

This study is more of academic interest, because of its simplicity and physical certainty. The problem is similar to that described by Sterl [1]. In the first half of the channel all walls are electrically insulating, but in the second half Hartmann walls are electrically conducting. In this kind of configuration in the vicinity of cross section at x = 0 there is a region where the flow changes from bulk type flow in the insulating part of the channel to strongly irregular flow in the conducting part of the channel with characteristic M-shaped 2D velocity profile.

Numerical results are based on velocity field obtainment and interpretation, varying inlet velocity (mass inflow) and also external magnetic field in high Hartmann number region, where turbulence can be neglected, and laminar flow assumption is used. Typical flow velocities in this kind of reactor blankets are few centimeters per second in order of magnitude, so flows with small velocities are considered. The transition region length dependence on Re number as well as Ha parameter is also determined.

ANSYS FLUENT 12.0 code [2] benchmarking is done by comparing velocity distribution in channel's outlet with Hunt's analytical solution [3].

In general, material properties are chosen from real-life experimental setup: applied external magnetic field B = 1..10 T, LM density ρ = 9400 kg/m^3, electrical conductivity σ = 0.77 MS/m, dynamic viscosity ρν = 0.00187 Pa·s; channel width a = 25 mm, wall thickness (thin-wall boundary condition is used) h = 3 mm.

2. Governing equations

The following Navier-Stokes equation of steady, incompressible MHD flow with continuity equation are solved numerically

$$\rho(\mathbf{v}\,\nabla)\mathbf{v} = -\nabla p + \rho\nu\nabla^2\mathbf{v} + (\mathbf{j}\times\mathbf{B}),$$
$$\nabla\,\mathbf{v} = 0.$$

Here $\mathbf{v}, p, \rho, \nu, \mathbf{j}$ **and** $\mathbf{B}$ are flow velocity, pressure, LM density, kinematic viscosity, induced currents and magnetic field respectively. From the following system of equations

$$\begin{cases} \nabla\times\mathbf{b} = \mu_0\mathbf{j} \\ \mathbf{j} = \sigma(\mathbf{E} + (\mathbf{v}\times\mathbf{B})) \\ \nabla\,\mathbf{b} = 0 \end{cases}$$

steady magnetic induction equation is derived and solved

$$\nabla^2 \mathbf{b} = \mu_0 \sigma[(\mathbf{v}\cdot\nabla)\mathbf{B} - (\mathbf{B}\cdot\nabla)\mathbf{v}],$$
where $\mathbf{B} = \mathbf{B}_0 + \mathbf{b}$ – the total magnetic field consisting of external and induced fields.

3. Boundary conditions

Mass flow inlet is chosen to reduce the entrance length, and Dirichlet boundary condition for pressure is used at the outlet. For an electrically insulating walls normal component of current density $j_n = 0$, which is equivalent to induced magnetic field tangential components $b_{\tau 1} = b_{\tau 2} = 0$ from Ampere's relation. For Hartmann walls in conducting part of the channel thin-wall condition is applied to better match used Hunt's analytical model.

4. Solution methodology

Numerical calculations are carried out in ANSYS FLUENT 12.0. By default, steady, incompressible laminar flow is solved using finite volume method and pressure-based method. In advance MHD module is activated, and solution is obtained using magnetic induction method, which solves induction equation [4]. Pressure-velocity coupling is achieved by using SIMPLE algorithm. Least Square Cell Based, Standard and First Oder Upwind methods are used in spatial discretization for gradient, pressure and momentum, as well as magnetic field, respectively.

Gradually increasing applied external magnetic field, solution is obtained for 1..10 T field after checking whether there is no more significant change in monitored residuals.

5. Mesh

3D structured mesh with dimensions of 1000 mm × 25 mm × 25 mm is used (fig 1). It consists of 1.4 million cells with special refinement at the walls. First cell size at the Hartmann wall is 4 µm, and every successive cell is 1.5 times larger, first cell size at the sidewall is 15µm, with size ratio of 1.3 for every successive cell in the direction of the center.

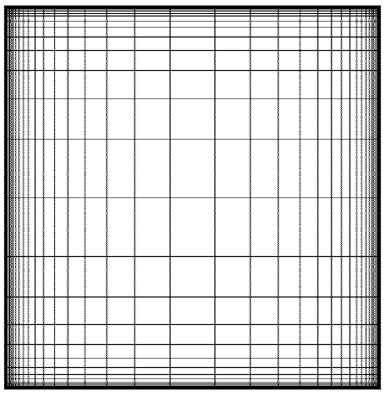

Figure 1: Mesh structure in flow cross section.

6. Results

MHD flow transition region. To show the transition region length dependence on the Reynolds number, mass flow rate at the inlet was varied, while other quantities were left unchanged. This was done for Re values ranging from 0.1 up to 7000 (fig 2).

Two regions can be distinguishable – the constant one with no dependence on Re, and the other one, which shows linear correlation between transition region length and Re number. Thus, there is some critical velocity value beyond which transition region length is independent of the flow velocity.

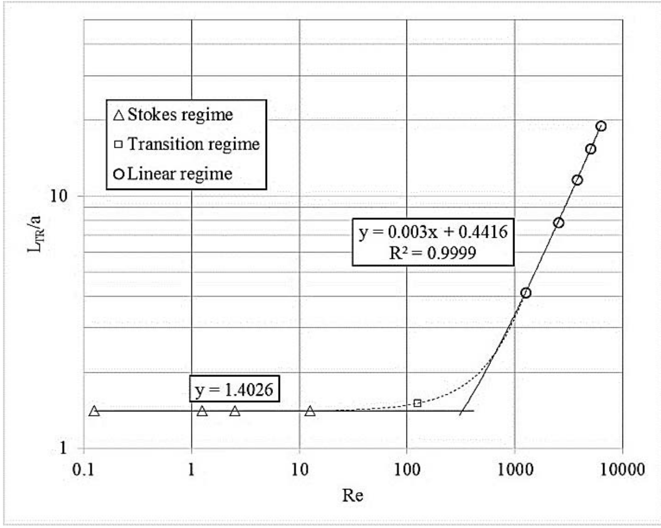

Figure 2: Non-dimensional transition region length dependence on Reynolds number at fixed magnetic field (Ha = 1015).

At fixed flow velocities external magnetic field value was varied. Data points were obtained at various magnetic field values ranging from 1 to 10 T. Taking the logarithm from non-dimensional transition region length and Ha number, plotted data points can be approximated with a linear function $Y = kX + C$ (fig 3).

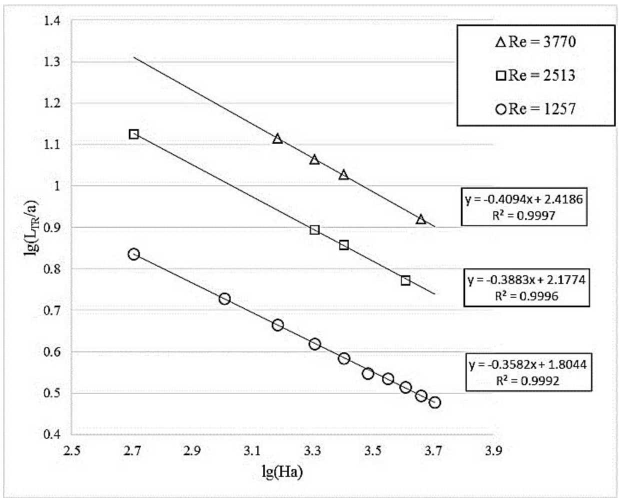

Figure 3: Non-dimensional transition region length dependence on Hartmann number at fixed inflow velocities.

Expression can be rewritten in form $\lg(y) = k \cdot \lg(x) + \lg(c)$. Taking the exponent from the latter expression, the true relation can be derived: $y = cx^k$. Displayed correlation coefficient squares confirm this dependence. From the slope values of the plotted lines can be concluded that the transition region length is inversely proportional to Ha number to the power of ≈0.4.

Invention of flow parameter. Combining the both previous relations, transition region length can be expressed as a function of Re and Ha numbers. Expression takes form $L_{TR} \sim \mathrm{Re} \cdot \mathrm{Ha}^{-0.4}$. One can guess that coefficient, which would make an equation from the expression, could consist of wall conductance ratio c or its power, because it is one of the main parameters of the MHD flow.

Transition region of quasi-static flow. If flow velocity tends to zero, then interaction parameter tends to infinity, and nonlinear elements of Navier-Stokes equation can be neglected, achieving the so-called Stokes regime, when viscous forces are dominant in fluid. From the plotted MHD flow core velocity (fig 4) can be seen that decreasing flow velocity by two orders no changes are visible. To confirm this observation flow direction in the channel was changed to opposite. Results showed perfect agreement. Thus, decreasing integral velocity v_0, at some critical value v_{cr} the transition to so called Stokes flow occurs, where the flow transition region and velocity distribution in this region no more depends on the magnitude of v_0 (Reynolds number), but depends only on Hartmann number and the magnitude of wall parameter. At flow velocities larger than the critical value ($v_0>v_{cr}$), the increase of the velocity v_0 leads to the increase of inertial forces, and, consequently, to the increase in length of flow transition region in the channel.

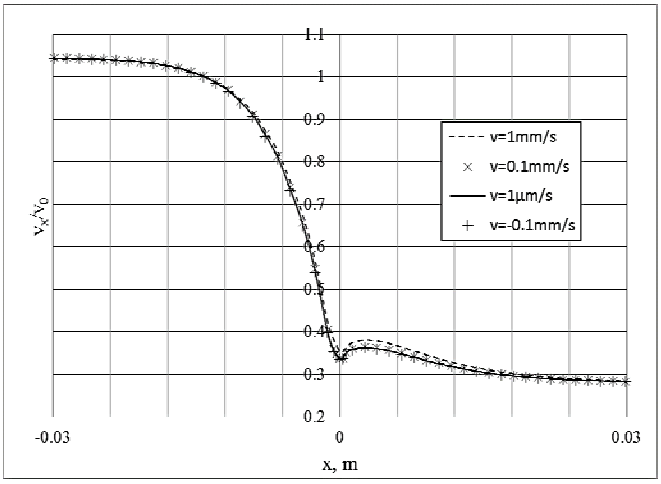

Figure 4: Non-dimensional flow velocity in transition region (Stokes regime)

7. Conclusions

When flow velocity is larger than critical velocity ($v>v_{cr}$), transition region length is proportional to Reynolds number. It is inversely proportional to the Hartmann number to a power of ≈ 0.4.

When flow velocity is smaller than critical velocity ($v<v_{cr}$) and tends to zero, transition region length tends to constant. No matter how small was the flow velocity, transition region length stays the same ≈ 1.4 a.

References

[1] Sterl, A.: Numerical simulation of liquid-metal MHD flows in rectangular ducts, J. Fluid Mech., vol. 216 (1990), pp. 175-189.

[2] FLUENT 12.0 produced by FLUENT Inc.

[3] Hunt, J.: Magnetohydrodynamicl flow in rectangular ducts, J.Fluid Mech., pp. 577-590, 1965.

[4] ANSYS, Inc., April 2009. [Online]. Available: http://www1.ansys.com/customer/content/documentation/120/fluent/flmhd.pdf [Accessed April 2014].

Upwind Finite Difference Solution of MHD Pipe Flow in an Exterior Conducting Region using Shishkin and Bakhvalov Typed Layer Adapted Grids

AYDIN S. Han
Department of Mathematics, Karadeniz Technical University, Trabzon, Turkey
shaydin@ktu.edu.tr

Abstract

We consider the magnetohydrodynamic (MHD) flow through a square pipe under the influence of a transverse magnetic field when the outside medium is also electrically conducting. MHD partial differential equations are of convection-diffusion type and it is well known that convection dominated problems have numerical instabilities on a uniform mesh with standard FDM. Therefore, an upwind FDM on Shishkin and Bakhvalov typed layer adapted grids are considered in order to obtain stable solutions for high values of the parameters. Results are visualized in terms of contour lines of the velocity and induced current.

1 Introduction

It is already known that there are many applications of MHD pipe flow such as the design of the cooling systems with liquid metals for nuclear reactors, electromagnetic pumps, MHD generators, and flowmeters measuring blood pressure, etc. The exact solution of the problem can be obtained only for some special cases [1, 2]. Therefore, there are many numerical methods applied to the solution of the MHD pipe flow (see [3, 4, 5] and references there in)

In this paper we consider MHD pipe flow of square cross-section under the influence of a transverse magnetic field when the outside medium is also electrically conducting. Governing coupled partial differential equations with coupled boundary conditions are obtained from the Navier-Stokes equations for conducting fluids, and Maxwells equations for electromagnetic field through Ohms law. The equations are written in non-dimensional form as [5];

$$\begin{aligned} \nabla^2 V(x,y) + ReRh\frac{\partial B}{\partial y}(x,y) &= -1 \\ \nabla^2 B(x,y) + Rm_1\frac{\partial V}{\partial y}(x,y) &= 0 \end{aligned} \qquad \text{in } \Omega_{in} \tag{1}$$

$$\nabla^2 B_{ext}(x,y) = 0 \qquad \text{in } \Omega_{ext} \tag{2}$$

with the no-slip condition on the pipe wall

$$V = 0 \qquad \text{on } \partial\Omega_{in} = \Gamma \tag{3}$$

and continuity conditions for the induced magnetic fields

$$B(x,y) = B_{ext}(x,y)\,, \qquad \text{on } \Gamma \tag{4}$$

$$\frac{1}{Rm_1}\frac{\partial B(x,y)}{\partial n} = \frac{1}{Rm_2}\frac{\partial B_{ext}(x,y)}{\partial n'}\,, \qquad \text{on } \Gamma \tag{5}$$

where n and n' are unit outward normals on Γ for the regions Ω_{in} and Ω_{ext}, respectively. Rm_1 and Rm_2 are the magnetic Reynolds numbers inside the pipe and in external medium.

We assume that cross section of the pipe is square and has sufficient length. The fluid is flowing through the pipe due to an applied constant pressure gradient $\frac{\partial p}{\partial z}$, and is viscous, incompressible, electrically conducting. The electrical permitivity and magnetic permeability of the fluid are assumed to be close to those of the external space. The axis of the pipe is coincident with the z-axis, and the y-axis is parallel with the magnetic induction at infinity. Thus, externally applied magnetic field with a constant intensity B_0 is assumed to be in y-direction. We also assume that the wall of the pipe and the outside medium are having the same electrical conductivity and magnetic permeability since the thickness of pipe wall is assumed to be very small (Fig 1). Although the external region is unbounded, an artificial boundary is considered far away from the pipe in order to perform numerical calculations. It is known that external induced magnetic field is almost zero at sufficiently far away distance from the pipe boundary. Therefore, on the artificial boundary Γ_∞, the external induced current (B_{ext}) is taken as either zero (homogenous Drichlet type) or free (homogenous Neumann type).

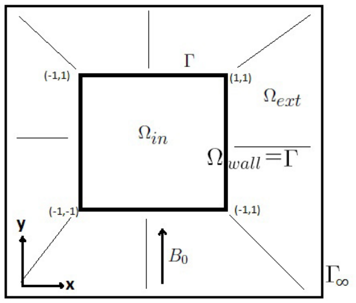

Figure 1: Problem definition

2 Mathematical Modelling

We have compared two different layer adapted meshes called Shishkin mesh and Bakhvalov mesh. However, in order to determine the structure of these meshes, we should transform the coupled equations to decoupled convection-diffusion typed equations as follows; Rewriting the equations by denoting $V_1 = V$ and $B_1 = \frac{ReRh}{M}B$, where $M = \sqrt{ReRhRm_1}$ is the Hartmann number of the fluid, the system (1) becomes [1]

$$\text{(6)} \qquad \begin{aligned} \nabla^2 V_1 + M\frac{\partial B_1}{\partial y} &= -1 \\ \nabla^2 B_1 + M\frac{\partial V_1}{\partial y} &= 0. \end{aligned} \qquad \text{in } \Omega_{in}$$

In order to decouple the equations, define new variables $U_1(x, y)$ and $U_2(x, y)$ as $U_1 = V_1 + B_1$ and $U_2 = V_1 - B_1$ which gives

$$\text{(7)} \qquad \begin{aligned} \nabla^2 U_1 + M\frac{\partial U_1}{\partial y} &= -1 \\ \nabla^2 U_2 - M\frac{\partial U_2}{\partial y} &= -1. \end{aligned}$$

From this form of the equations, it is said that, the problem has a boundary layer in y-direction depending on the value of the Hartmann number M. Also it is well known that standard numerical methods for these type of equations are unstable for the large values of the convection coefficient and fail to give accurate results. Therefore, we should consider a modified mesh along y-direction. In this study, we will consider two different type of layer meshes.

a) Shishkin mesh

Shishkin mesh is a piecewise uniform mesh. Depending on the location of the boundary layer, the domain is divided into two section. The location of the transition point is chosen in a way that half of the discretization points are placed near the boundary which develops boundary layer .

If we assume that the domain is $[0,1]$ and the boundary layer occurs at right hand side boundary (at the point $y=1$), than the location of the transition point λ is calculated as follows [6];

$$\lambda = min(\frac{1}{2}, \frac{1}{M}\ln N) \tag{8}$$

where N is the total number of the division of the interval $[0,1]$. Therefore, $\frac{N}{2}$ equally spaced points are on the interval $[0,1-\lambda]$ and the $\frac{N}{2}$ of them are again equally spaced on the interval $[1-\lambda,1]$. Explicitly,

$$y_i = \begin{cases} (1-\lambda)\,\frac{2i}{N} & i=0,...,N/2 \\ (1-2\lambda)+\frac{2\lambda i}{N} & i=N/2+1,...,N. \end{cases} \tag{9}$$

b) Bakhvalov mesh

Bakhvalov mesh is defined as the modified version of Shishkin mesh. Similar to Shishkin mesh, the transition point is calculated as

$$\lambda = min(\frac{1}{2}, \frac{2}{M}\ln N). \tag{10}$$

Again $\frac{N}{2}$ equally spaced points lie on the interval $[0,1-\lambda]$. However, boundary layer part of the points are not equally spaced, they are distributed exponentially. Explicit formulation for the location of the points is given as [6];

$$y_i = \begin{cases} (1-\lambda)\,\frac{2i}{N} & i=0,...,N/2 \\ 1+\frac{2}{M}\ln\left(\frac{N^2-2(N-i)(N-1)}{N^2}\right) & i=N/2+1,...,N. \end{cases} \tag{11}$$

Since, our problem is symmetric with respect to x-axis, the boundary layers exist at both upper and lower walls of the pipe. Therefore, location of the adaptive mesh points are symmetric also with respect to x-axis.

The difference operators for the first and second order derives are defined as usually for non-uniform mesh. The continuity of the induced magnetic field and the relationship between the solution inside the pipe and the solution on the external region is satisfied with the coupled boundary conditions. An upwind discretized form is as;

$$\textbf{Top}: B_{i,j} = B^{ext}_{i,j} = \frac{m_{ty}B^{ext}_{i,j+1} + B_{i,j-1}}{1+m_{ty}} \qquad \textbf{Bottom}: B_{i,j} = B^{ext}_{i,j} = \frac{B_{i,j+1} + m_{by}B^{ext}_{i,j-1}}{1+m_{by}}$$

$$\textbf{Left}: B_{i,j} = B^{ext}_{i,j} = \frac{B_{i,j+1} + m_{lx}B^{ext}_{i,j-1}}{1+m_{lx}} \qquad \textbf{Right}: B_{i,j} = B^{ext}_{i,j} = \frac{m_{rx}B^{ext}_{i+1,j} + B_{i-1,j}}{1+m_{rx}}$$

where $m_{ty} = \frac{Rm_1(y_i-y_{i-1})}{Rm_2(y_{i+1}-y_i)}, m_{by} = \frac{Rm_1(y_{i+1}-y_i)}{Rm_2(y_i-y_{i-1})}, m_{lx} = \frac{Rm_1(x_{i+1}-x_i)}{Rm_2(x_i-x_{i-1})}, m_{rx} = \frac{Rm_1(x_i-x_{i-1})}{Rm_2(x_{i+1}-x_i)}$.

The induced magnetic field values at the corner points are assumed to be the average of the neighbouring points.

3 Numerical Results and Discussion

We consider a long pipe of square cross-section defined by $\{(x,y) : -1 \leq x,y \leq 1\}$. The artificial boundary Γ_∞ is assumed as $\{|x| = 3, -3 \leq y \leq 3 \bigcup |y| = 3, -3 \leq x \leq 3\}$. The pipe region is discretized by 21×21 mesh points both in x and y-directions. The behaviors of the velocity of the fluid and inside and outside induced currents (induced magnetic fields) are visualized in terms of contour plots for very high values of magnetic Reynolds numbers Rm_1, Reynolds number Re and magnetic pressure number Rh of the fluid.

For moderate values of the Hartmann number ($Rm1 = 100, Rm2 = 1, Re = 1$ and $Rh = 10$), there is only slight disturbance on the velocity values obtained from uniform mesh. However, as Rm_1 getting large ($Rm_1 = 1000$), the need and effect of the stabilization are seen more clearly especially from velocity values. Unfortunately, stabilization with Shishkin typed mesh is not sufficient for stable solutions and Bakhvalov typed mesh is very effective compared to others. The numerical instabilities also start to appear in the induced magnetic field values obtained from uniform mesh (Figure 2).

Figure (3) shows equal velocity and induced current lines, respectively, for a very large value of Reynolds number $Re = 100$ when $Rm_1 = 100, Rm_2 = 1$ and $Rh = 10$. It seen from that, the effect of the stabilization in Bakhvalov types meshes is also seen from the induced current contours additional to the velocity contours. The similar behaviour is also seen from Figure (4) that displays the induced magnetic field contours for the case of Neumann type boundary condition on the artificial boundary.

Acknowledgements This work is supported by Karadeniz Technical University by Scientific Research Project (BAP) under Grant Number #10464.

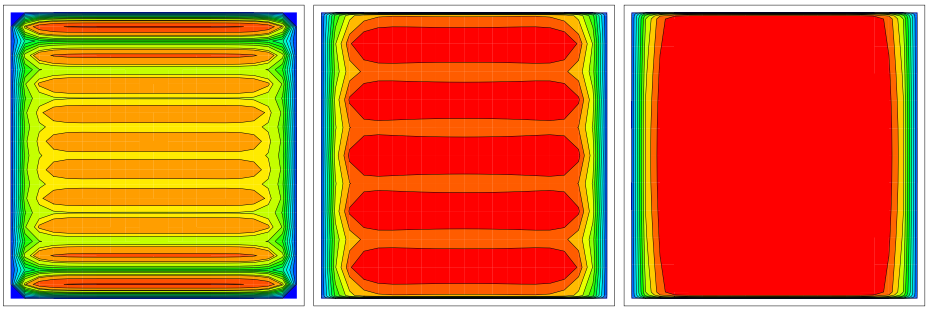

(a) Velocity

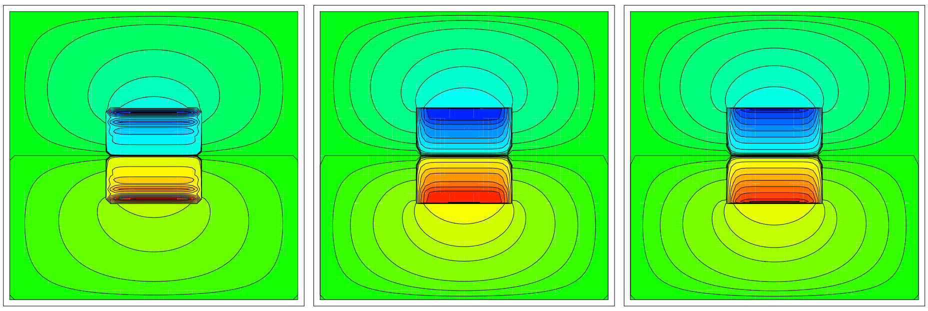

(b) Induced currents

Figure 2: Uniform (left), Shishkin(center) and Bakhvalov(right) typed solution contours for $Rm_1 = 1000, Rm_2 = 1, Re = 1, Rh = 10$

References

[1] Dragoş, L.: Magnetofluid Dynamics: Abacus Pres 1975

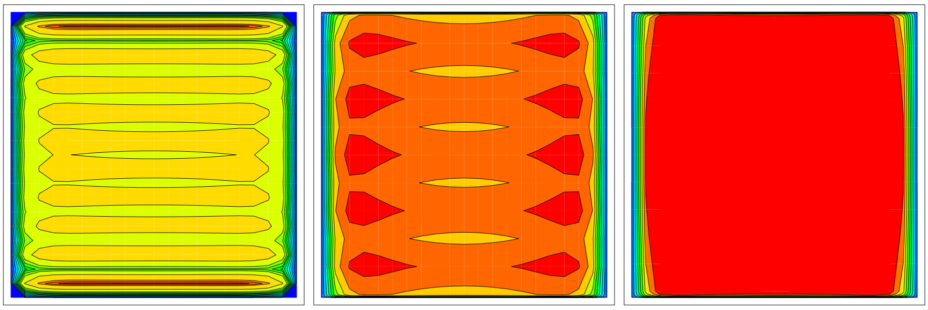

(a) Velocity

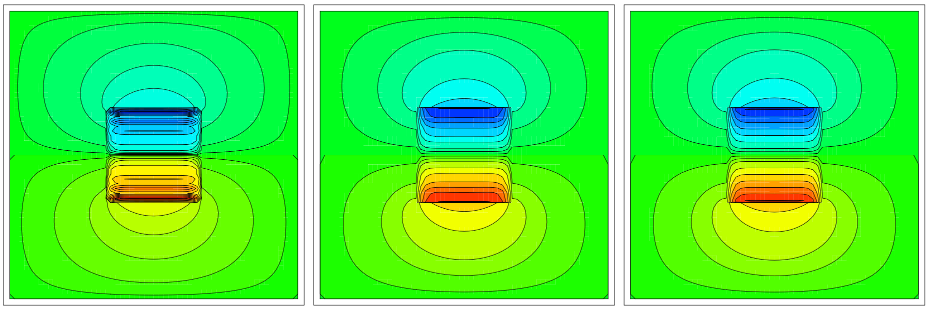

(b) Induced currents

Figure 3: Uniform (left), Shishkin(center) and Bakhvalov(right) typed solution contours for $Rm_1 = 100, Rm_2 = 1, Re = 100, Rh = 1$

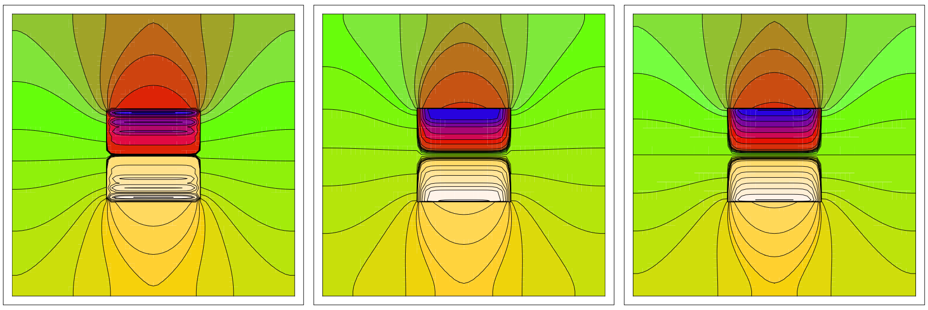

Figure 4: Uniform (left), Shishkin(center) and Bakhvalov(right) typed solution contours for $Rm_1 = 1000, Rm_2 = 1, Re = 1, Rh = 10$ and Neumann type boundary condition on the artificial boundary

[2] Shercliff, J.A.: . Steady motion of conducting fluid in a pipe under transverse magnetic fields. J. Fluid Mech. 1(6)(1956) 644-666

[3] Tezer-Sezgin, M.: Boundary element method solution of MHD flow in rectangular duct. Int. J. Numer. Methods Fluids. 18(1994) 937–952

[4] Tezer-Sezgin, M.; Han Aydın, S.: Dual Reciprocity Boundary Element Method for Magnetohydrodynamic Flow Using Radial Basis Functions. Int. J. Comput. Fluid D. 16(1)(2002) 49-63

[5] Tezer-Sezgin, M.; Han Aydın, S.: BEM solution of MHD flow in a pipe coupled with magnetic induction of exterior region. Computing. 95(1)(2013) 751–770

[6] Linβ, T.: An upwind difference scheme on a novel Shishkin-type mesh for a linear convection-diffusion problem. J. Comput. Appl. Math. 110(1999) 93–104

FEM Solution of MHD Flow Equations Coupled on a Pipe Wall in a Conducting Medium

TEZER-SEZGİN[1] Münevver, AYDIN[2] S. Han
[1]Department of Mathematics, Middle East Technical University, Ankara, Turkey
[2]Department of Mathematics, Karadeniz Technical University, Trabzon, Turkey
[1]munt@metu.edu.tr, [2] shaydin@ktu.edu.tr

Abstract

The Galerkin FEM with triangular linear elements is applied for solving MHD pipe flow equations coupled through boundary conditions on the pipe wall to the induced current Laplace equation of the exterior electrically conducting medium. The well known MHD characteristics as flattening velocity and boundary layer formation are observed inside the pipe for increasing values of Reynolds and magnetic Reynolds numbers. The continuation of induced currents of the fluid and external medium are maintained on the pipe wall accordingly with the corresponding magnetic Reynolds numbers values.

1 Introduction

The electrically conducting, viscous and incompressible fluid is driven down a straight pipe of sufficient length and of circular cross-section by a constant pressure gradient under an external magnetic field applied perpendicular to the axis of the pipe. MHD pipe flow finds some engineering and biomedical applications as MHD generators, pumps and instruments for measuring blood pressure.

Then, the MHD equations inside the pipe Ω_f located in an electrically conducting medium Ω_{ex} are given in nondimensional form as [1]

$$(1)\qquad \left.\begin{aligned} \nabla^2 V + Re \cdot Rh \cdot \frac{\partial B^f}{\partial y} &= -1 \\ \nabla^2 B^f + R_{m_f} \cdot \frac{\partial V}{\partial y} &= 0 \end{aligned}\right\} \quad \text{in } \Omega_f$$

$$\nabla^2 B^{ex} = 0 \qquad \text{in } \Omega_{ex}$$

with the boundary conditions on the pipe wall Γ

$$(2)\qquad \left.\begin{aligned} V(x,y) &= 0 \\ B^f(x,y) &= B^{ex}(x,y) \\ \frac{1}{R_{m_f}}\frac{\partial B^f}{\partial n} &= \frac{1}{R_{m_{ex}}}\frac{\partial B^{ex}}{\partial n'} \end{aligned}\right\} \quad \text{on } \Gamma$$

and on the far away fictitious external boundary Γ_{ex} either $B^{ex}(x,y)=0$ (insulated) or $\dfrac{\partial B^{ex}(x,y)}{\partial n}=0$ (conducting) conditions are taken (see Figure 1 for the domain of the problem). n and n' are unit outward normals on Γ for Ω_f and Ω_{ex} regions, respectively. Equations (1) are derived from the interaction of Navier-Stokes equations for conducting fluids with the Maxwell equations for electromagnetic field through Ohm's law.

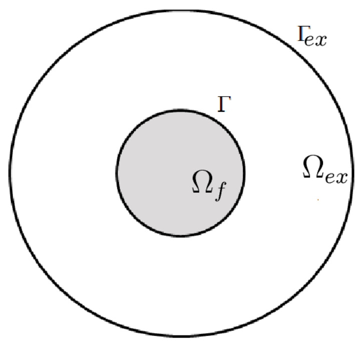

Figure 1: Domain of the problem

V, B^f and B^{ex} are the fluid velocity, induced magnetic fields of the fluid and external medium, respectively. Re and Rh are the Reynolds number and magnetic pressure of the fluid. Rm_f and Rm_{ex} are the magnetic Reynolds numbers of the fluid and external medium, respectively.

This coupled MHD problem (1)-(2) is solved by using BEM [2] for square and circular pipes and DRBEM [3] for circular pipe with the assumption that $B^{ex}\to 0$ as $x^2+y^2\to\infty$.

The Galerkin FEM application to the equations (1) with coupled boundary conditions (2), and one of the fictitious external boundary conditions is carried with linear approximations for V, B^f and B^{ex} as

$$V=\sum_{j=1}^{3}N_jV_j,\qquad B^f=\sum_{j=1}^{3}N_jB_j^f,\qquad B^{ex}=\sum_{j=1}^{3}N_jB_j^{ex} \tag{3}$$

where N_j's are linear triangular shape functions, V_j, B_j^f and B_j^{ex} are nodal values of V, B^f and B^{ex}.

The system of equations for one 3-nodal element 'e' is given as

$$\begin{bmatrix} K & -ReRhC & 0 \\ -Rm_fC & K & -\dfrac{Rm_f}{Rm_{ex}}D \\ 0 & 0 & K-D \end{bmatrix}\begin{Bmatrix} V_i \\ B_i^f \\ B_i^{ex}\end{Bmatrix}=\begin{Bmatrix} T \\ 0 \\ 0\end{Bmatrix} \tag{4}$$

where

$$\begin{aligned} K_{ij}&=\int_{\Omega^e}\left(\frac{\partial N_i}{\partial x}\frac{\partial N_j}{\partial x}+\frac{\partial N_i}{\partial y}\frac{\partial N_j}{\partial y}\right)d\Omega\quad,\quad C_{ij}=\int_{\Omega^e}\frac{\partial N_i}{\partial y}N_jd\Omega\ ,\\ D_{ij}&=\int_{\Gamma^e}\frac{\partial N_i}{\partial n'}N_jd\Gamma\quad,\quad T_i=\int_{\Omega^e}N_id\Omega \end{aligned}\qquad i,j=1,2,3 \tag{5}$$

and K and D matrices refering to B^{ex} are evaluted in the region Ω_{ex}.

2 Numerical Results

Numerical results are obtained from the solution of final assembled global system of equations for V^f, B^f and B^{ex} nodal values in Ω_f and Ω_{ex}, respectively.

For the insulating external boundary case fluid velocity, and fluid and external medium induced current contours are presented in Fig 2 and Fig 3 for increasing values of Rm_f and for increasing values of Rh, respectively.

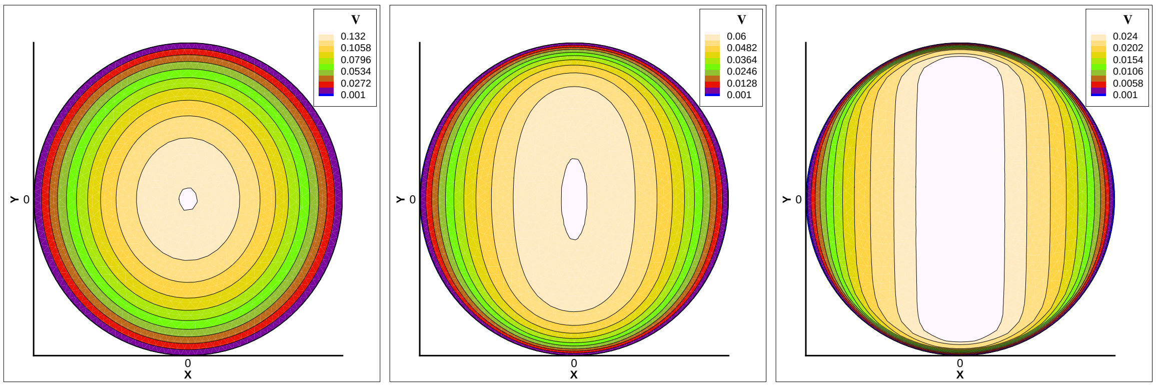

(a) Velocity

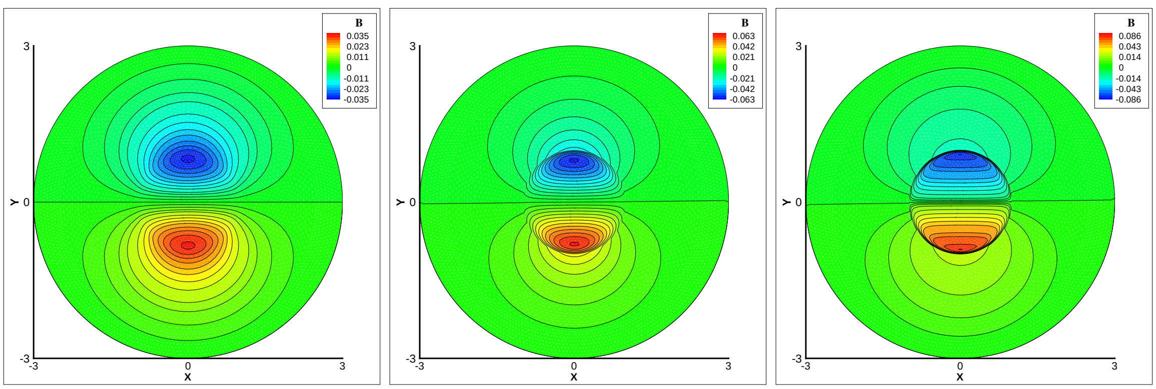

(b) Induced currents

Figure 2: Solution contours for $Rm_f = 1$ (left), $Rm_f = 10$(center) and $Rm_f = 100$(right) for $Re = 1, Rh = 10, Rm_{ex} = 1$

As fluid Rm_f increases flattening velocity is observed. Fluid becomes stagnant at the pipe center. Boundary layers are developed. Increase in Rm_f causes increase in B^f magnitude and fluid induced current tries to close itself inside the pipe. For equal Rm_f and Rm_{ex}, B^f and B^{ex} continue smoothly through the pipe wall.

As magnetic pressure Rh of the fluid increases both V and B^f, B^{ex} magnitudes drop but the continuation of B^f and B^{ex} through the pipe wall Γ is very well observed in Fig 3.

When the fluid $Rm_f = 10, 50, 100$ is much grater than external medium $Rm_{ex} = 0.01$ magnitude of B^f and correspondingly interaction through the conducting pipe wall is separated. Fluid induced current B^f behaves as if the induced current in a conducting wall pipe. Magnitude of B^{ex} is decreased and small compared to B^f (Fig 4).

In Fig 5, induced magnetic field lines are presented for the case of conducting external fictitious boundary Γ_{ex}. Fluid induced current B^f again closes itself inside the pipe as Rm_f increases, external induced current B^{ex} obeys the exit condition $\dfrac{\partial B^{ex}}{\partial n} = 0$ far away the pipe, they both continue on the pipe wall Γ.

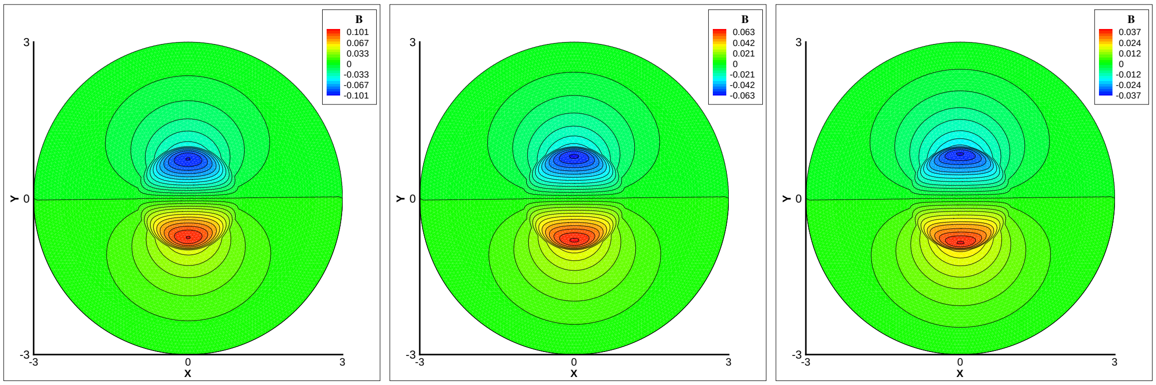

Figure 3: Induced current solution contours for $Rh = 5$ (left), $Rh = 10$(center) and $Rh = 20$(right) for $Re = 1, Rm_f = 10, Rm_{ex} = 1$

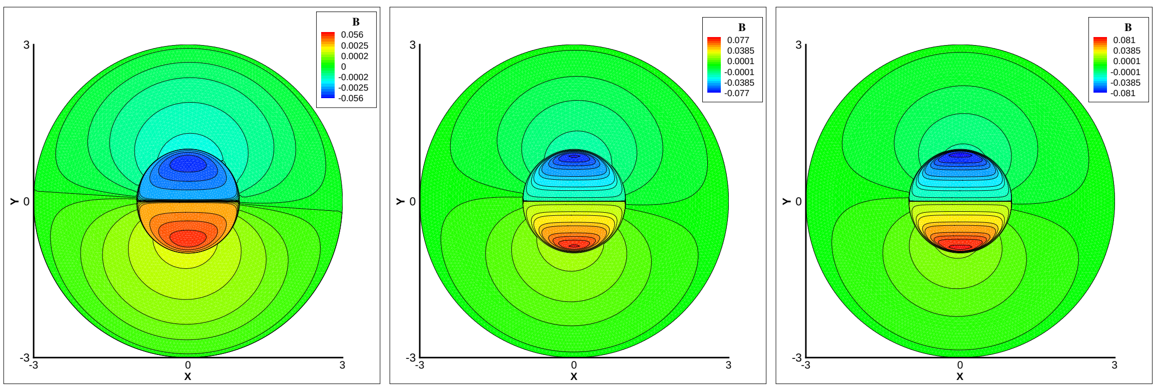

Figure 4: Induced current solution contours for $Rm_f = 10$ (left), $Rm_f = 50$(center) and $Rm_f = 100$(right) for $Rm_{ex} = 0.01, Re = 1, Rh = 10$

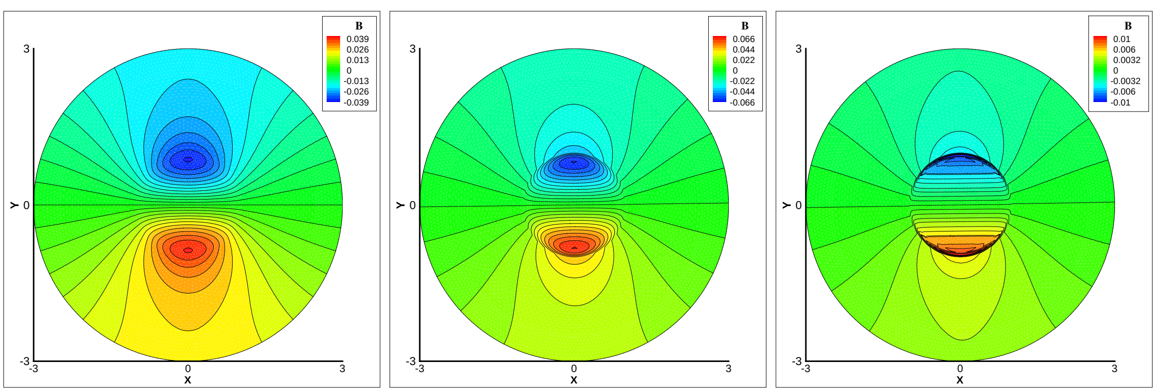

Figure 5: Induced current solution contours for $Rm_f = 1$ (left), $Rm_f = 10$(center) and $Rm_f = 100$(right) for $Re = 10, Rh = 10, Rm_{ex} = 1$

References

[1] Dragoş, L.: Magnetofluid Dynamics: Abacus Pres 1975

[2] Tezer-Sezgin, M.; Han Aydın, S.: BEM solution of MHD flow in a pipe coupled with magnetic induction of exterior region. Computing. 95(1)(2013) 751–770

[3] Han Aydın, S.; Tezer-Sezgin, M. : A DRBEM solution for MHD pipe flow in a conducting medium. Han Aydın, S.. 259(B)(2014) 720–729

EXPERIMENTAL RESEARCH OF THE HEAT TRANSFER LIQUID METAL DOWNWARD FLOW IN RECTANGULAR DUCT IN MAGNETIC FIELD

PODDUBNYI[1] I., RAZUVANOV[2] N., SVIRIDOV[1] V., IVOCHKIN[2] YU.
[1] National Research University "Moscow Power Engineering Institute", 14 Krasnokazarmennaya str., Moscow, Russia
[2] Joint Institute of High Temperatures of the Russian Academy of Science, 13/19 Igorskaya str., Moscow, Russia
E-mail: poddubnyyii@gmail.com

Abstract This work contains the results of experimental research and numerical simulation of heat transfer of the liquid metal (LM) downward flow in rectangular duct (with a side's ration 3/1) under coplanar magnetic field (MF). A temperature fields have been measured in condition of a one-sided and double-sided heating. The averaged fields of temperature, distributions of the wall temperatures and statistical characteristics of fluctuating part of the temperature have been obtained. A numerical simulation of hydrodynamic and heat transfer of LM flow in the conditions of the experiment has been performed.

1. Introduction

Liquid metals are used as a coolant for several projects of ITER Test Blanket Module [1, 2], essentially this is LiPb eutectic. This eutectic can be the coolant agent and neutron multiplier. In addition there are a lot of projects when LMs are used for cooling different parts of heat exchanger. For designing of new projects engineers who work in fission or fusion spheres should well know the laws of heat transfer of LM in magnetic field in a channel with different cross section. By the way rectangular ducts are widely used in applications. So that is why the task of investigation of the heat transfer laws of liquid metal (LM) in rectangular duct is very claim.

2. Governing equations

Test configuration of LM flow in a field of mass forces is shown in figure 1. Steady –state flow and heat transfer of mercury in vertical rectangular duct in a coplanar (a vector magnetic field **B** is directed along long side of duct cross section $B_x \neq 0$) MF. A ration a sides in duct cross section: a/b=56/17. The walls of duct are made from Russian stainless steel 12X18H10T with wall thickness dw/b=2.5/17. Liquid metal flows along a gravity vector with creation of adverse heat - gravitational convection.

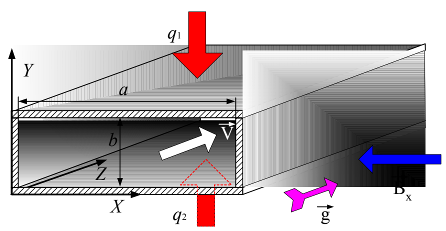

Figure 1. Investigated flow scheme

A double width of duct $d=2b$ took in as a characteristic size. There is a zone of hydrodynamic stabilization on a duct input Z_0=20 d, after that there is a heating zone with a heat - flux density on a both sides of duct q_1 and q_2. A zone of magnetic field is coincidences with heating zone, with length 25 d. The duct walls are electrically conducting. A ratio of steel's electrical conductivity to mercury electrical conductivity is 9.8/75.

The system of dimensionless equations consists from the conservation of the mass, momentum, energy and charge equations [3]. The equations in non-inductive approach (magnetic Reynolds number R_m <<1) are presented below.

$$\nabla \cdot \mathbf{V} = 0 \tag{1}$$

$$(\mathbf{V} \cdot \nabla)\,\mathbf{V} = -\nabla p^* + \frac{1}{\mathrm{Re}}(\nabla \cdot (1 + \frac{\varepsilon_t}{\upsilon})\nabla\ )\,\mathbf{V} + \mathbf{F} \tag{2}$$

$$(\mathbf{V}\cdot\nabla)\,\Theta = -\frac{1}{\mathrm{Re\,Pr}}\nabla\cdot(1+\frac{\mathrm{Pr}}{\mathrm{Pr}_t}\varepsilon_t)\nabla\,\Theta \quad (3)$$

$$\Delta\psi^* = \nabla(\mathbf{V}\times\mathbf{B}^*) \quad (4)$$

and by the Ohm's law for the moving media

$$\mathbf{j}^* = \mathbf{E}^* + \mathbf{V}\times\mathbf{B}^* \quad (5)$$

In these equations $\mathbf{V}(u_x,u_y,u_z)$, $\mathbf{j^*}(j_x,j_y,j_z)$, $\mathbf{B^*}(B_x,B_y,B_z)$, $\mathbf{E^*}(E_x,E_y,E_z)$, ψ^*, p^*, $\mathbf{F}(F_x,F_y,F_z)$ and ε_t denote the dimensionless velocity, current density, magnetic field, and electrical field, electric potential, pressure, vector of source of volumetric force and turbulent viscosity. In presented system of equations coordinates have been related to *d=2b (b* – width of duct*),* velocity V has been related to average velocity, pressure p^* to ρV_0^2; temperature $\Theta=(T-T_0)$ to $q_c d/\lambda$, ^{0}C (where T_0- intake temperature and $q_c=0.5(q_1+q_2)$.); $\mathbf{B}^*$ to magnetic field of external field B_0; current density $\mathbf{j}^*$ to a value $\sigma\ V_0B_0$; electric field поля $\mathbf{E}^*=-\nabla\psi$ to V_0B_0; $\mathbf{g}^*$ to intensity of gravity g_0. In momentum equation the volumetric force is equal

$$\mathbf{F} = \frac{\mathrm{Gr}_q}{\mathrm{Re}^2}\Theta\mathbf{g}^* + \frac{\mathrm{Ha}^2}{\mathrm{Re}}\left(\mathbf{j}^*\times\mathbf{B}^*\right) \quad (6)$$

The non-dimensional boundary conditions are presented below:

- on the duct input applied uniform velocity and input temperature $Z=0$: $V_z = 1, \Theta = 0$;
- on bottom duct wall: $V_i=0$, $\frac{\partial\Theta}{\partial n} = 1$;
- on upper duct wall: $V_i=0$, $\frac{\partial\Theta}{\partial n} = -1$;
- on all duct walls: $\frac{\partial\psi^*}{\partial n} = 0$

This equation system is solved in a packet for numerical simulation of processes of hydrodynamic and heat transfer ANES20XE [4].

3. Experimental facility

The experimental facility is mercury close – loop system (figure 2). Parameters of test facility are presented in table 1. The geometry of duct and test facility parameters allows performing the experiments by follow dimensionless numbers which determine of flow characteristics: Reynolds number 5000÷55000; Hartmann number up to 800; Grashof number up to 8e+8.

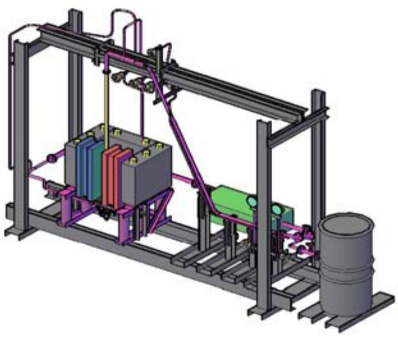

Figure 2: Model of the test facility.

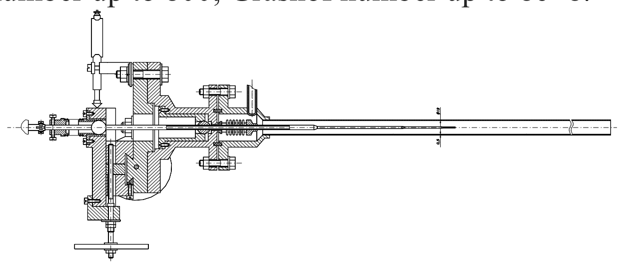

Figure 3: A microthermocouple lever-type probe.

The measurement of temperature field in a section which located on distance 20*d* from input of duct made using a microthermocouple lever-tipe probe for 2-dimensional measurement in LM flow (figure 3), which install on butt end of working section. A copper – constantan micro thermocouple with junction size 0.25 mm locates on end-on of probe. This thermocouple has an inaccuracy 0.2 ^{0}C. The probe coordinates determine based on detection device displacement with accuracy 0.03 mm. The duct wall temperature has been measured by probe in a moment of touch wall and further the field of flow temperature is interpolated on wall. The test facility is automated with using of measuring and computing complex, which has been created basically on modern hardware and software envelopes.

Table 1 – Test facility parameters

Length of gage section, m	2.0
Heat flux density, кW/m^2	0 - 45
Length of heated section, m	0.8
Magnetic field, T	0 – 1.0
Length of electromagnet, m	0.7
Length of uniform magnetic field, m	0.6

4. Results

The results for two character flowing scenarios are presented in this chapter: a scenario with slight impact of heat – gravitational convection (Re= 50000) and strong impact (Re=30 000) ones. All results are presented for case of one side wall heating, q_2=0.

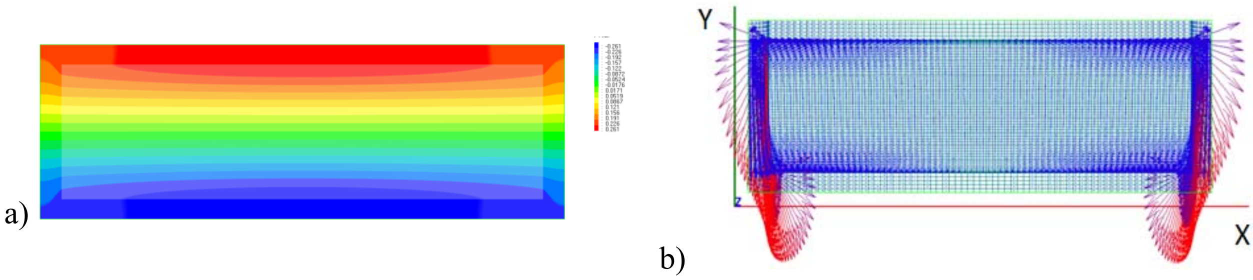

Figure 4. Voltage drop (a) and current density distribution (b) in duct section. Re = 50000, Ha = 800.

A representative distribution of electrical potential in duct section and vector plot of current density which is generated into flow of electrical conductive liquid in coplanar MF are shown in Figure 4. The duct walls are electro conductive in experiment. In this case a bridging of current happens both in short duct walls and in thin near-wall (Hartman) layer. Such distribution of current density on duct cross section explains a presence of decelerating forces near duct walls. This effect brings to deplanation of velocity profile along line of magnetic field, along axis X (figure 4). Also velocity profile in a plane perpendicular to the field is shown in figure 5. The velocity profile in case of low value of Reynolds number is non symmetry. This effect can be explained of influence of heat-gravitational convection – flow is decelerated near hot walls. Velocity profiles along axis *Y* are come to M – shaped form as Magnetic field increases.

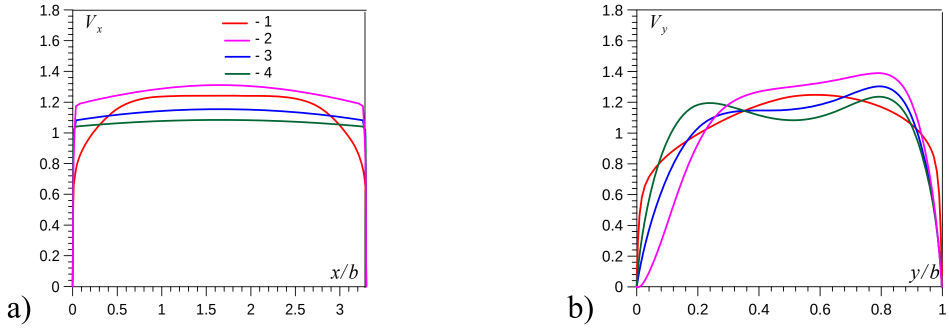

Figure 5: Longitudinal velocity's profiles in along *X* (a) и *Y* (b) axis in a section with coordinate Z = 20, $Gr_q = 4.0 \cdot 10^8$:1) Ha = 0; 2) 300; 3) 500; 4) 800.

The average nondimensional temperature's profiles in two perpendicular planes, along axis X and Y are shown in figure 6. Axis with coordinates *X=x/b* is directed in the line of long duct side and parallel magnetic field. Temperature profile along axis Y (in the line of short duct side) is significant nonuniform with maximal gradient on heated wall.

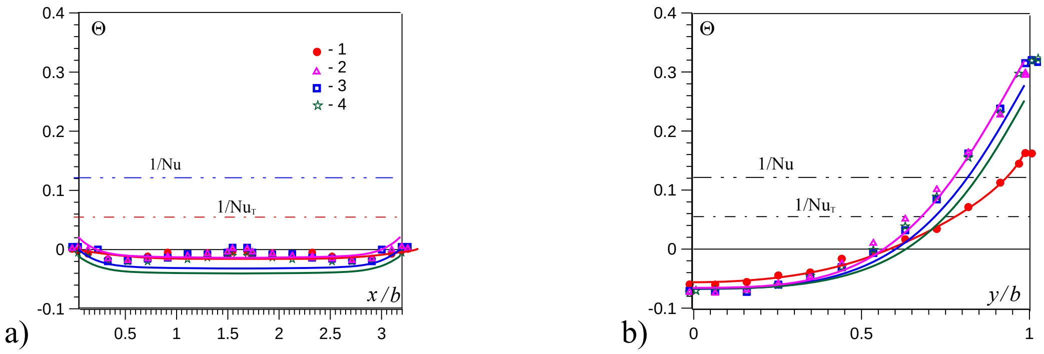

Figure 6: Average nondimentional temperature profiles along axis *X* (a) and *Y* (b) in section Z=20d, q_1/q_2= 35/0 kW/m^2, Re = 50000: 1) Ha=0; 2) 300; 3) 500; 4) 800.

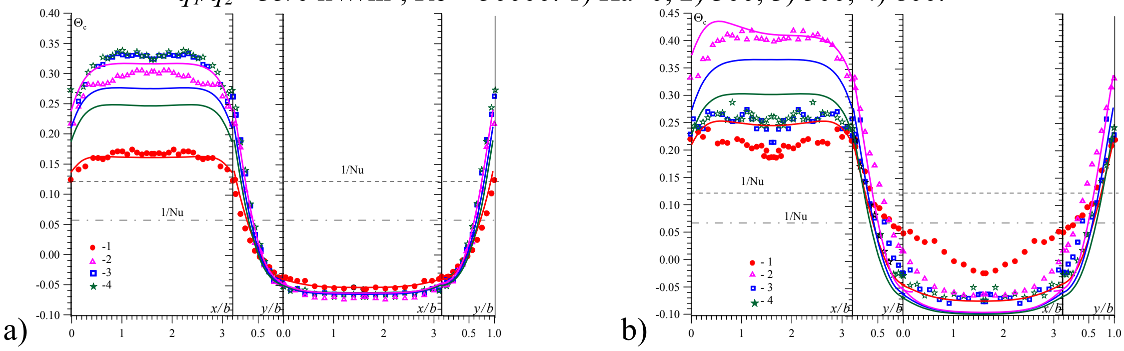

Figure 7: Distribution of nondimentional wall temperature Θ_c on duct perimeter in section Z=20*d*, q_1/q_2= 35/0 kW/m^2, a)Re = 50000 and b) Re = 30000: 1) Ha = 0; 2) 300; 3) 500; 4) 800.

A plot of variance nondimensional wall temperature of duct on perimeter is presented in figure 7a. For the comparison reciprocal variable of Nusselt numbers (1/Nu) for flat conduit are shown in figure 6: for developed turbulent flow which calculated using Lyon's integral equation $Nu_T=10+0.025Pe^{0.8}$ and stabilized laminar flow $Nu_{Л}=8.24$ in case of single side heating. There is a significant nonuniform in distribution of duct wall temperature in case of single side heating. The results of numerical simulation are also presented in this plot. There is a good coincidence analysis and experimental results.

Analogical measurements have been performed for different values of Reynolds number. For the scenarios with Re<30000 a strong effect of heat – gravitational convection is observed. The experimental results for these scenario show qualitative coincidence of the average temperature of flow with have been described higher. But phenomena is discovered – at the beginning wall temperature goes up with increasing Hartmann number up to Ha=300, as might have been expected. But with a further increase the Hartmann number, wall temperature goes down. It's seen that experimental dates and analysis results are different. This difference in results can be explain effect of developing heat – gravitational convection, which will be describe below and weren't included in analysis model. The plot of variance nondimensional wall temperature of duct on perimeter is presented in figure 7b.

The profiles of intensity temperature fluctuation in dust section in two perpendicular planes are shown in figure 8. Magnetic field drives out the turbulence. Generally, intensity of temperature fluctuation goes down up to zero with increasing Hartmann flow. This effect was observed in experiment with Reynolds number Re=50000. In case of scenario with Re=35000 intensity of temperature fluctuations grow up with increasing Hartmann number and is higher in several times that level of turbulence fluctuation.

The oscillograph traces of intensity temperature fluctuations which have been measured in center of duct section for different Hartmann numbers are shown in figure 9. The low-frequency signals are registered. On traces for higher Hartmann values signal is periodical with pronounced peaks. A fluctuation character isn't turbulence. This phenomenon is explained by the generation of large-scale secondary vortices induced by heat – gravitational convection, with axes of rotation parallel to the magnetic field flow, which are carried by the flow and thus causing the temperature fluctuation. The temperature fluctuations can be growing up to 15 ^{0}C in scenario with Hartmann number Ha=800. The value of fluctuation is compatible with temperature drop in duct section.

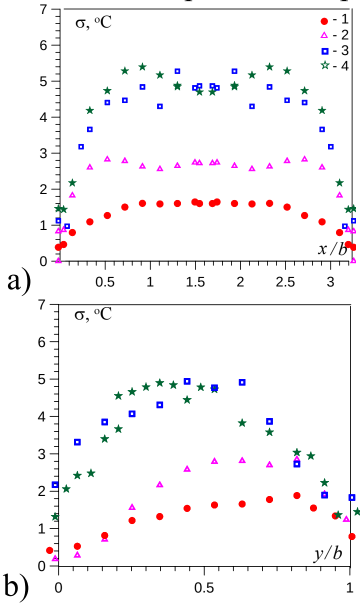

Figure 8: Intensity of temperature fluctuation's profiles along axis *X* (a) and *Y* (b) in section *Z*=20*d*, Re = 30000: 1) Ha=0; 2) 300; 3) 500; 4) 800.

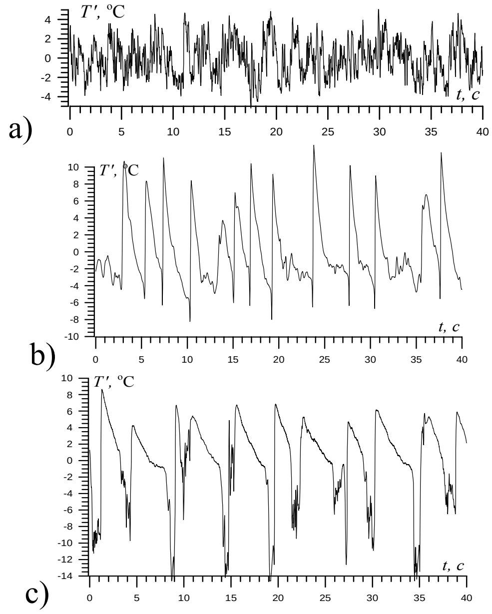

Figure 9: The oscillograph traces of intensity temperature fluctuations in low core: a) Ha = 0; b) 500; c) 800.

5. Conclusions

The significant nonuniform of the temperature distribution in the duct wall section was found in investigated configuration of flow and heating, which increases in the magnetic field. Observed MHD effect associated with the occurrence of the temperature with anomalous amplitude. These fluctuations are the result of development of the secondary flow in large-scale structures, which are the result of joint action for mass, electromagnetic and gravitational forces.

Data on values of temperature fluctuations are practical importance for the calculation of heat exchange's channels of fusion reactor. As walls temperature can change with such intensity. It leads to additional fatigue stresses, which can be causing of premature failure of the structural.

The work is supported by the Russian Fund for Basic Research, RF Ministry of Education and JSC "NIIEFA".

References

[1] Wong C.P.C., Salavy J.-F., Kim Y., Kirillov I., Kumar E.R., Morley N.B., et. al. Overview of liquid metal TBM concepts and programs. Fusion Engineering and Design. 83 (2008) 850-857.

[2] Giancarli L.M., Abdou M., Campbell D.J., Chuyanov V.A., M.Y. Ahn, Enoeda M. et. al. Overview of the ITER TBM Program. Fusion Engineering and Design. 87 (2012) 395-402.

[3] Genin L.G., Sviridov V.G. Hydrodynamic and heat transfer of MHD-flow in channels of reactors. Moscow. Publishing house MPEI 2001.

[4] Artemov V.I., Yankov G.G., Karpov V.E., Makarov M.V. Numerical simulation of heat-and mass transfer processes in parts of thermal and energetic environments. Heat Power Engineering. 7 (2000) 52-59.

LIQUID METAL FLOW AND HEAT TRANSFER IN RECTANGULAR DUCT UNDER THE INFLUENCE OF AXIAL MAGNETIC FIELDS

TIGRINE[1,2] Zahia, MOKHTARI[1,3] Faiza, BOUABDALLAH[1] Ahcène
[1] *USTHB* / Faculty of Physics, BP32 El Alia- 16111 Bab Ezzouar, Algiers-Algeria
[2]*UDES-CDER* / Development Unit of Solar Equipments, BP386, Bou-Ismail-42415 Tipaza-Algeria
[3]*MOULOUD MAMMERI UNIVERSITY* / Tizi Ouzou-Algeria
phyzahia@yahoo.fr

Abstract: The present work deals with the numerical analysis of the liquid metal 83Pb–17Li MHD flow which moves in a parallelepiped duct. Numerical method based on the finite volume is employed in simulations. The effect of different values of the magnetic field on the eutectic 83Pb–17Li alloy flow, heat and momentum transfer is studied for small and moderate values of the magnetic field strength. The estimates of the MHD flow, pressure and temperature have been analyzed for all duct surfaces and planes. We need to have more knowledge and interesting information in order to determine and control the MHD pressure drop encountered in the blanket fusion operating system. The distribution of pressure is very important in all duct walls and planes. It changes radically when axial magnetic field is applied. In the direction parallel to the magnetic field, the pressure gradient decreases near the walls and perpendicularly to the magnetic field, the pressure gradient increases**.**

1. Introduction

The controlled thermonuclear fusion is one of the main technological challenges to produce of the energy that will be very requested and needed for the near future. Liquid metal alloy such as lead lithium 83Pb-17Li is used as breeder material and coolant in advanced nuclear systems. It is being used to operate the blankets in fusion reactors at high temperature due to their higher thermal efficiency. Therefore, the lead lithium eutectic is considered to be very promising for the design of fusion blankets. Magnetohydrodynamic (MHD) metal liquid flows have been already studied by J. Hartmann [1]. Magnetic fields have several applications in liquid metal flows and can relaminarize the turbulent regimes in these flows. Different problems in liquid metal systems lie in the corrosion of their stainless steels EUROFER, instabilities flow, MHD pressure drop, Tritium permeation, MHD insulators, buoyancy effects and Heat transfer. Extensively, the properties of duct flows in the magnetic field present one of the basic problem in Magnetohydrodynamic because the study of MHD flows under real blanket conditions is still limited due to the complexity of the blanket geometry and the structural materials that consist mainly of martensitic and austenitic steel. Different studies proved that Magnetic field applied to a flowing liquid metal produces a force which alters the velocity field [2-5]. Numerical analyses have been conducted in previous papers [6,7] for a fully developed flow and unsteady vortical flows in a rectangular duct of cross section with a transverse magnetic field. Analytical researches of MHD flow in the magnetic field have been carried out [2,8]. Phenomena of MHD thermofluid of liquid-metal that are present in different concept blankets have been showed by N. Morley [9] and S.Smolentsev [10, 11]. The MHD pressure gradient for the fully developed flow in a rectangular duct is given by [12, 13]. Direct numerical simulations of transverse and spanwise magnetic field effects on turbulent flow were analyzed [14-15]. In this paper we present preliminary results on magnetohydrodynamic effect in a rectangular duct under vertical magnetic field at low Prandtl number. Numerical simulations in rectangular duct have been carried out. The main goal of this work is to determine the magnetic field effect on the eutectic alloy Pb–17Li flow in laminar regime.

2. Formulation of flow problem

The present work analyzes the influence of the magnetic field on the hydrodynamic liquid metal flow in a rectangular duct. We consider the steady flow of an incompressible liquid metal in a rectangular duct with insulating walls and with an externally applied magnetic field perpendicular to flow direction. The schematic of the physical and computational domain is shown in figure 1. The dimensions of the duct are L= 31.5mm (length), E=12mm (Width) and D=3mm (Height).

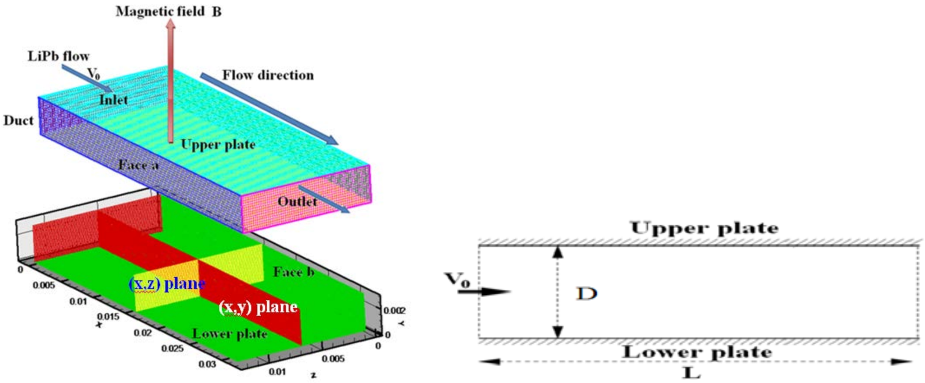

(a) (b)

Figure 1: Physical domain of computational duct: (a) Three-dimension mesh model used for numerical simulations and (b) Sketch of the cross-sectional area of the channel

The working fluid is 17Li-83Pb alloy with constant density ρ, kinetimatic viscosity ν and electric conductivity σ. Flow moves in the x-direction with mean velocity V_0= 5 cm/s at the inlet. Fixed temperatures are imposed on the walls of the melt duct and the inlet interface; viscous dissipation and Joule heating are negligibly small. The magnetic Reynolds number is so small that the flow field does not affect the magnetic field.17Li-83Pb eutectic was chosen as a good liquid because of its lowest melting temperature and its adequate stability. The physical properties of lead lithium used in our simulations are calculated at melting temperature. The magnetic permeability η is the same everywhere and equal to the vacuum magnetic permeability ($\eta=\eta_0$).

In general, the equation set of MHD for liquid-metal flows consists of Navier–Stokes and Maxwell equations, which are coupled with the equations for heat and mass transport. For an incompressible MHD flow in a duct they consist of equations for conservation of mass, conservation of momentum in three directions and the equation governing the electric potential. The magnetic field induces an electric current, which is calculated from the electric potential field. This MHD system can be expressed as follow:

$$\rho\left[\frac{\partial V}{\partial t}+(V.\nabla)\mathrm{V}\right]=-\nabla\mathrm{P}+\rho\nu\nabla^2\mathrm{V}+\mathrm{J}\times\mathrm{B} \qquad (1)$$

$$\nabla.\mathrm{V}=0 \quad , \quad \nabla.\mathrm{J}=0 \qquad (2)$$

$$\mathrm{J}/\sigma=-\nabla\varphi+\mathrm{V}\times\mathrm{B} \qquad (3)$$

$$\nabla.(\nabla\varphi)=\nabla.(\mathrm{V}\times\mathrm{B}) \qquad (4)$$

$$\frac{\partial T}{\partial t}+V.\nabla T=\nabla\left(\frac{k}{\rho C_p}\nabla^2 T\right) \qquad (5)$$

Where V, p, J, B,φ and t are velocity, pressure, current density, applied magnetic field, electrical potential and time, respectively. The term f on the right-hand side of the momentum equation denotes the gravitational force. In order to characterize inertial effects in MHD flows, such as the onset of MHD instabilities, transition regime, and the MHD effects, there are three important dimensionless parameters in MHD flows. Hartmann number $\mathrm{Ha} = \mathrm{BD}\sqrt{\sigma/\rho\nu}$ represents the ratio of electromagnetic to viscous forces, the hydrodynamic Reynolds number $\mathrm{Re} = \mathrm{V_0 D}/\nu$ gives a measure of the ratio of inertial forces to viscous forces and the interaction parameter number is given by $\mathrm{N} = \mathrm{Ha}^2/\mathrm{Re}$. The duct aspect ratio $\Gamma = \mathrm{E/D} = 4$. Prandtl number $\mathrm{Pr} = \nu/\alpha$ characterizes the importance of thermal diffusivity compared to molecular diffusivity where α is the thermal diffusivity.

In this work, the cases of MHD flow in insulating rectangular duct at Re=1363, 0≤Ha≤90 corresponding to the range of interaction parameter number 0≤N≤5 are studied. The boundary conditions for the present computation are given as follows:

(1) Velocity inlet, which corresponds to the inlet surface of LiPb eutectic, V_0=5cm/s.

(2) Outflow, which is corresponding to the outlet surface of LiPb fluid.

(3) Wall condition with fixed temperature, faces a and b at T_a=T_b=508K, lower and upper plate (T_c=623K, T_h =823K).

(4) All wall conditions are insulting σ_w=0, where the thickness of wall is neglected.

The problem is solved using the finite volume package Fluent with three-dimensional double precision, the first order upwind discretization for convection, the SIMPLE algorithm for pressure-velocity coupling and the STANDARD scheme for pressure interpolation. For the magnetic field equations the first order upwind is used. The convergence is handled by monitoring residuals of continuity, momentum and energy equations. Reynolds numbers is fixed to Re = 1363 (based upon total duct height D). The three-dimension mesh model of the rectangular duct is done by Gambit software. The computational domain is discretized with 1990656 cells, 6046272 Faces and 2065525 Nodes.

The most substantial parameters to predict MHD flows are pressure, velocity and temperature under the magnetic field effect .To simplify the analysis of eutectic flow behavior, the computations were performed for laminar flow in the duct. The magnetic field is applied in the vertical direction (oy), it is changed in the range of B =0, 0.5Tesla and 1Tesla ,which corresponds to Hartmann number values of Ha=0, 40 and 90, Reynolds number characterized by a velocity V_0=5cm/s is Re=1363. The magnetic interaction parameter N which mesures the ratio of electromagnetic forces to inertial forces, is deduced from the Hartmann and Reynolds numbers, it is equal to N=0, 1.2 and 5.

In order to study the effect of magnetic field in different areas of the considered geometry, we present our results in all externe duct surfaces, namely, upper and lower plate, inlet and outlet surfaces and faces a and b. In addition, we show the obtained results in three middle planes parallel to each side, (x,y) plane, (x,z) plane and (y,z) plane. Figure 2 displays the temperature distribution in different sections in the cases with and without magnetic field. In the studied system the upper plate is hot at T_h=823K whereas the lower one is relatively cold T_c=623K then heat is transferred from the upper to the lower plate and the whole fluid primarly by conduction. This heat transfer is obviousely shown in isotherms distribution. It can be seen that the temperature has a parabolic profile near the inlet surface in (x,y) plane, then it becomes asymmetric when one moves away from the inlet. High thermal gradients are present near the outlet surface and between the upper and the lower plate from the duct mid-length until the output. Although there are no important modifications when magnetic field intensity increases, thermal gradient decreases near the outlet surface and the parabolic profile disappears before as for the case without magnetic field. In (y,z) plane, isothermes are concentrated near the upper plate, however in the outlet surface the temperature gradient is better distributed from the upper to the lower plate. The temperature profile is not significantly affected by the imposed vertical magnetic fields for B=1T. Figure. 3 depicts the evolution of isotherms in (x,z) plane for the vertical magnetic fields strength B=0T and B=1T.

The distribution of temperature is important in this plane, it increases gradually along (x, z) plane from the inlet to the outlet surface. This temperature profile is due to the inhomogeneous heat transfer in the melt.

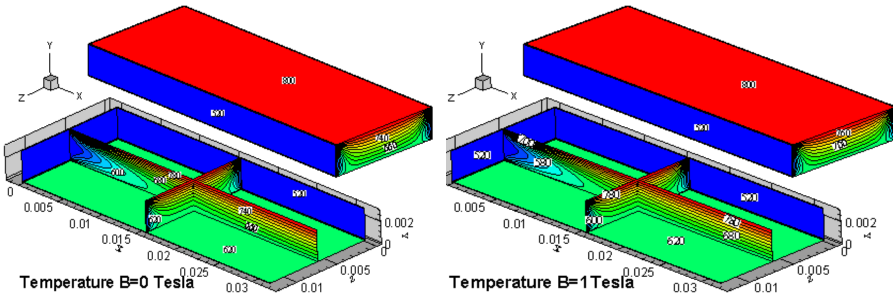

Figure 2: Temperature distribution in different planes without and with magnetic field B=1Tesla

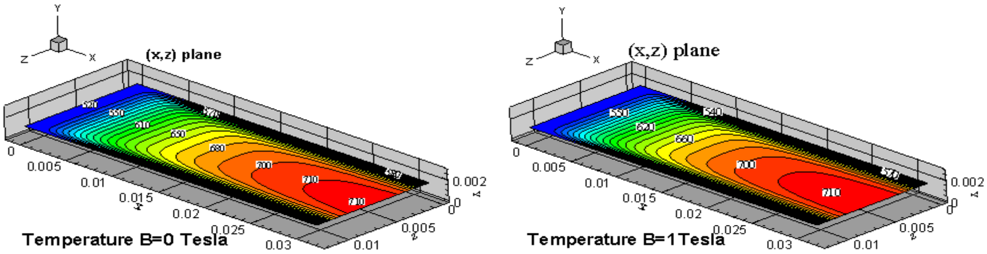

Figure 3: Temperature distribution in (x,z) plane without and with a vertical magnetic field B=0 and B=1Tesla

Now let us analyze the pressure field in this MHD problem (fig 4). Without magnetic field, the pressure is almost constant in the core of the flow and isobars are concentrated near the upper and lower walls, a strong pressure gradient therefore exists. The overall analysis shows that the pressure field is high at the inlet and decreases gradually as we approach the outlet when magnetic field is applied. When magnetic field of intensity B = 0.5T is imposed, isobars become flattened in a parallel direction to the magnetic field in (x,y) plane.

Vertical pressure gradients (dp/dy) decreases strongly in the fluid and near the upper and the lower plates. In the case without the magnetic field, the pressure gradient along the X axis is too weak , under magnetic field effect this gradient becomes considerably important for B = 1Tesla, this gradient increasing is evidently shown in figure 5.

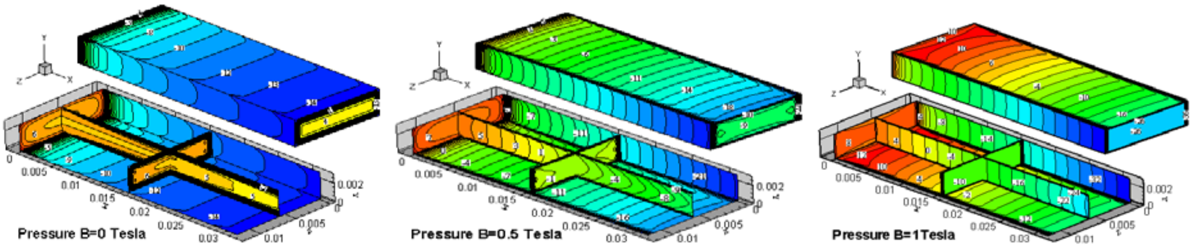

Figure 4: Presure distribution in the cases without and with magnetic field (B=0.5Tesla and B=1Tesla)

The magnetic field has reduced the pressure in the entire channel except at the entrance. In the direction parallel to the magnetic field, the pressure gradient decreases near the walls and perpendicularly to the magnetic field, the pressure gradient increases. As the magnetic field increases, the isobars become flat and straight across the channel in almost 40% of the duct for B = 0.5 T and in 100% of the channel for B = 1T. In (x, z) plane we note the same modifications as for the (x, y) plane, namely, pressure drop, decreasing vertical pressure gradient and increasing pressure along the X axis. In faces a and b, the pressure gradient is increased along the X axis. The effect of magnetic field on pressure profiles are reported in fig 6 which the local pressure values decreases with increase the magnetic field intensity.

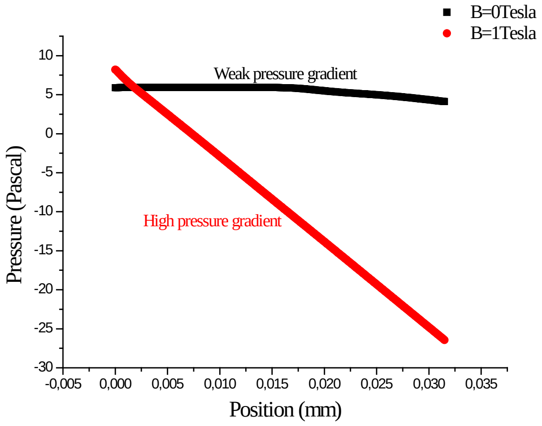

Figure 5: Evolution of pressure versus x-position at y= 1.5mm in (x,y) plane without and with magnetic field (B=1Tesla)

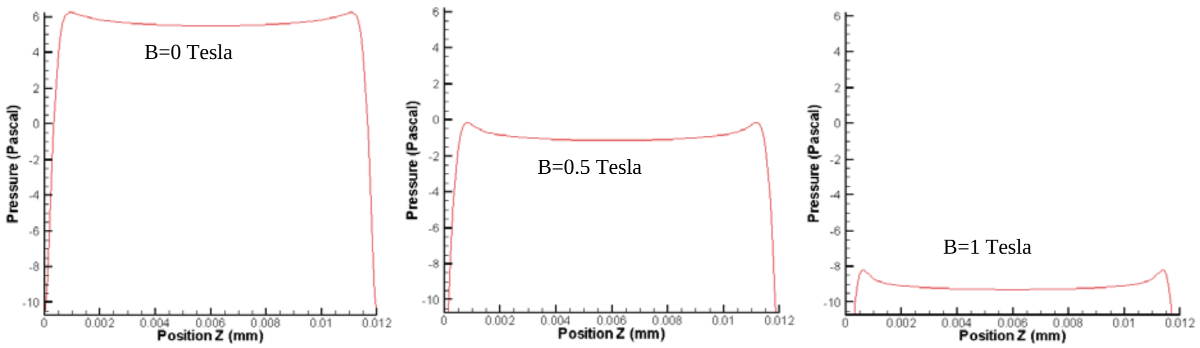

Figure 6: Pressure profiles without and with magnetic field

Figure 7 indicates velocity distribution in different sections with and without magnetic field. Parabolic velocity distribution is observed in (x,y) plane. In the case without magnetic field, the flow in the channel is induced by forced convection caused by the inlet velocity. The mean flow is maximum in the core of flow and minimal near the walls. A hydrodynamic boundary layer is clearly visual on the upper and lower plates and it is more concentrated in the upper plate. When a vertical magnetic field is imposed, the velocity profile in the channel crucially changes, or the velocity profiles become increasingly flat it favours the development "M-shaped" profile, see figure 7 for B=1T, as well as significantly changes the nature of metal flow. This M-shaped profile velocity observed even with insulating walls at plans which are parallel to B has been observed before by R.Moreau et al [2] and I. Bucenieks [3]. The velocity profiles under the effect of vertical magnetic field values as B = 0 Tesla, B = 0.5 Tesla and B = 1 Tesla were plotted (fig 8) and determined at 0.01575 m in the (y, z) plan of the duct heigh. The obtained results show that the velocity profiles decrease relatively in comparison with the case reference B=0 when the magnetic field is increased.

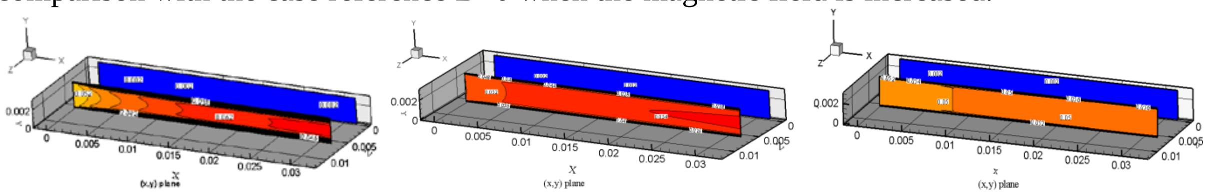

B=0Tesla B=0.5Tesla B=1Tesla

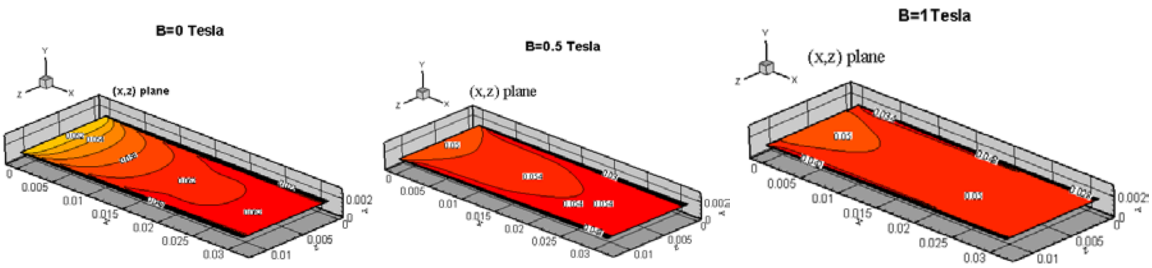

Figure 7: Velocity magnitude distribution in (x,y) plane without and with a magnetic field (B=0.5Tesla and B=1Tesla)

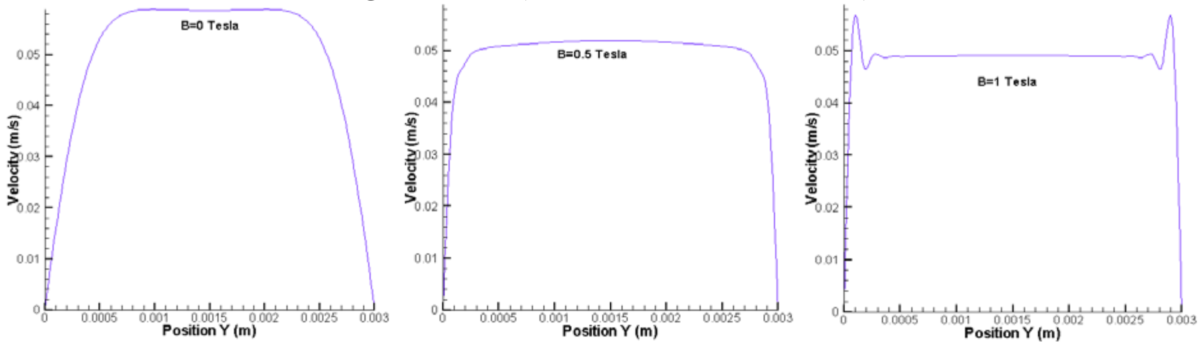

Figure 8: Velocity profiles for various values of magnetic field and with a magnetic field (B=0.5Tesla and B=1Tesla)

4. Conclusion

In the present work, numerical simulations in rectangular duct have been carried out under vertical magnetic field in order to provide a theoretical basis for practical applications, such as liquid-metal blankets of a fusion reactor. The magnetic interaction parameter is varied in the range of 0 to 5. Interesting effects of vertical magnetic field on mean flow and pressure have been observed. Pressure drop is induced with horizontal pressure gradients increasing. The presence of the vertical magnetic field changes decisively the velocity profile in the channel while it favors the formation of the so-called M-shaped velocity profile. Due to lower Prendth number value of LiPb, temperature profile for different planes is not affected by the various magnetic field strengths B=0.5T and B=1T.

4. References

[1] Hartmann, J.; Lazarus, F.: K Den Vidensk Selsk Mat-Fys Meddl. 15 (1937) 1-27.

[2] Moreau, R.; Smolentsev, S.; Cuevas, S.; PMC Physics B. 3:3 (2010)

[3]Bucenieks,I.;Krishbergs,R.;Platacis,E.;Lipsbergs,G.;Shishko,A.;Zik,A.;Muktepāvela,F.:Magnetohydrodynamics. 42 (2006) 237-251.

[4] Kharicha,A.; Alemany, A.; Bornas, D.: 43(2005) 589–615.

[5] Kharicha,A.; Alemany, A.; Bornas, D.: International Journal of Heat and Mass Transfer. 47(2004) 1997–2014.

[6] Smolentsev, S.; Cuevas, S.; Beltran, A.:J Comp Phys. 229 (2010)1558-1572 .

[7] Cuevas, S.; Smolentsev, S.; Abdou,M.: J Fluid Mech. 553 (2006) 227-252.

[8] Cuevas, S.; Picologlou, B.F. : Int. J. Engng ScL. 35 (1997) 485-503.

[9] Morley, N ; Malang, S. ; Kirillov, I. : Fusion Sci. Technol. 47(2005) 488–501.

[10] Smolentsev, S.; Moreau,R. ; Buhler, L.; Mistrangelo,C.: Fusion Engineering and Design. 85 (2010) 1196–1205.

[11] Smolentsev, S.; Moreau,R. ; Abdou, M. : Fusion Eng. Des. 83 (2008) 771–783.

[12] Norajitra, P.; Buhler, L.; Buenaventura,A.; Diegele,E.; Fischer,U.; Gordeev,S.; et al.:Technical Report FZKA 6780, Forschungszentrum, Karlsruhe (2003).

[13] Wang, H.; Tang, C.: Fusion Engineering and Design. (2012).

[14] Chaudhary, R.; Shinn, A.F.; Vanka, S.P.; Thomas, B.G.; Computers & Fluids.51 (2011)100-114.

[15] Wang Wei-huaa, Li Jin-ling , Liu Song-linga, Pei Xia, Huang Qun-yinga, FDS Team , Fusion Engineering and Design (2012).

INTERFACE EVOLUTION BETWEEN BINARY IMMISCIBLE FLUIDS UNDER WEAK MAGNETIC FIELD

JUN MAO[1], WENJUN LIU[2], QIANG WANG[1,*], LIJIA ZHAO[1], TIE LIU[1], JICHENG HE[1]

[1]Key Laboratory of Electromagnetic Processing of Materials (Ministry of Education), Northeastern University, Shenyang 110819, China

[2]Institute of Thermodynamics and Fluid Mechanics, Ilmenau University of Technology, 98684 Ilmenau, Germany

*E-mail address of corresponding author: wangq@mail.neu.edu.cn

Abstract: In order to investigate the interface evolution between liquid metal and magnetic fluid under weak magnetic field, the distributions of magnetic flux and magnetic force were simulated by using the ANSYS software, and the experiments of interface evolution were also conducted. Both the simulation and experimental results suggested that interface evolution under weak magnetic field was controlled by the distributions of magnetic flux and magnetic force. Finally, a circuit breaker which based on the principle of interface evolution between liquid metal and magnetic fluid is presented.

Keywords: Weak magnetic field, Magnetic fluid, Liquid metal, Binary immiscible fluids, Interface evolution.

1. Introduction

Binary immiscible fluids system is ubiquitously existed in nature. For this system, the interface evolution has already been utilized in many technologies due to its practical significance. For example, the interface evolution plays a significant role in the processes of electro-spraying[1], ink-jet printing[2] and surface-relief patterning[3]. Thus, how to effectively control the interface evolution becomes an important issue. Sugawara et al reported that the interface between water (diamagnetic) and air descends obviously in the presence of high magnetic field, and this is the so-called "Moses effect"[4, 5]. Similarly, the interface between air and saturated $CuSO_4$ aqueous solution (paramagnetic) rises under high magnetic field, and this is the "Reversed Moses effect"[4]. Correspondingly, for the binary fluids system which consists of weak magnetic fluids, once the difference of densities of fluids is negligible, the interface evolution is significant under high magnetic field, and this is the "Enhanced Moses effect"[6-8]. Thus, by adjusting the parameters of high magnetic field, the interface evolution between binary fluids can be effectively controlled. However, although the interface evolution can be controlled by high magnetic field, the high magnetic field itself is not industrial applicable. Since weak magnetic fields are widely available, therefore controlling the interface evolution by weak magnetic field is much more practical. Nevertheless, as the magnetic force of weak magnetic fluid is always negligible under weak magnetic field, it is unlikely to control the motion of this fluid by weak magnetic field. On the contrary, magnetic fluid (a kind of colloid which is uniformly distributed with nanoscale ferromagnetic particles)[9] is super-paramagnetic and has extremely high saturate magnetization[10]. Thus, for the magnetic fluid, quite significant magnetic force can be produced by weak magnetic field. Therefore, when considering the binary fluids system which consists of magnetic fluid and other fluid, it is expected that the interface evolution can be effectively controlled by weak magnetic field.

In this work, the interface evolution between liquid metal and magnetic fluid under weak magnetic field was investigated. The distributions of magnetic flux and magnetic force were simulated by the ANSYS software, and the experiments of interface evolution were also conducted. Finally, a circuit breaker which based on the principle of interface evolution between liquid metal and magnetic fluid is presented

2. Numerical simulations and experiments

Numerical simulations were conducted by the ANSYS software. Since the magnetic field can be imposed either under the side of bottom of container or under the middle of bottom of container, therefore two simulation models are named as Side type model and Middle type model, respectively. The free meshing method is used for both models, and the length of mesh is 2 mm. After the boundary conditions are given, the distributions of magnetic flux and magnetic force are simulated.

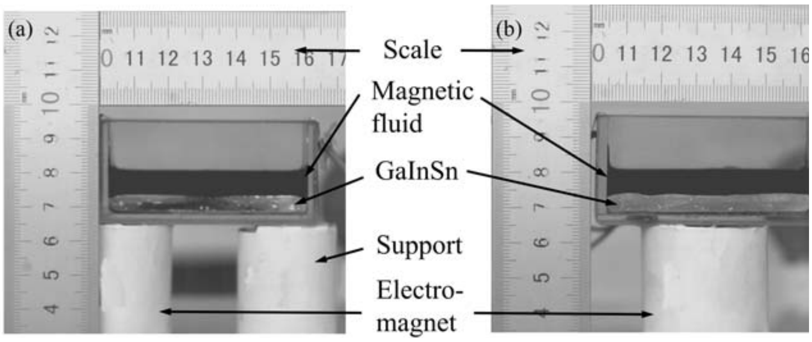

Figure 1: The experimental setups, (a) Side type setup, (b) Middle type setup.

The interface evolution processes were recorded by the high-speed camera. Figure 1 shows the experimental setups. The high-speed camera is Photron FASTCAM-APX 120K, and the speed is 500 frames per second. The weak magnetic field is produced by a DC electromagnet. The core of electromagnet is electrical pure iron, the total turns of electromagnet is 5654. Besides, the resistance is 408 Ω and the current is 0.52 A (dc). Similarly, the two setups are named as Side type setup and Middle type setup, respectively. The solution of magnetic fluid is engine oil, the density and saturate magnetization of magnetic fluid is 1320 kg/m^3 and 450±50 GS, respectively. Liquid metal is GaInSn, its melting point is 283.5K, and the density is 6620 kg/m^3. In all the experiments, both volume of the magnetic fluid and liquid metal are 3.6 ml.

3. Results and discussion

Figure 2 (a) shows the distributions of magnetic flux along the interface. For the Side type model, there are two peaks in the distribution of magnetic flux. The strongest peak is around the side wall, it corresponds to the very place where the fastest fall of the interface is. And the second peak lies at the right side of the strongest peak. For the Middle type model, there are two symmetrical peaks in the distribution of magnetic flux. Figure 2 (b) and 2 (c) shows the distributions of magnetic force. It is clear that magnetic force mainly concentrates on the position which corresponds to that of the DC electromagnet. Moreover, magnetic fluids are subjected to significant magnetic forces under weak magnetic field. Since magnetic force can drive the interface evolution, therefore, the simulation results show that it is possible to induce interface evolution by weak magnetic field.

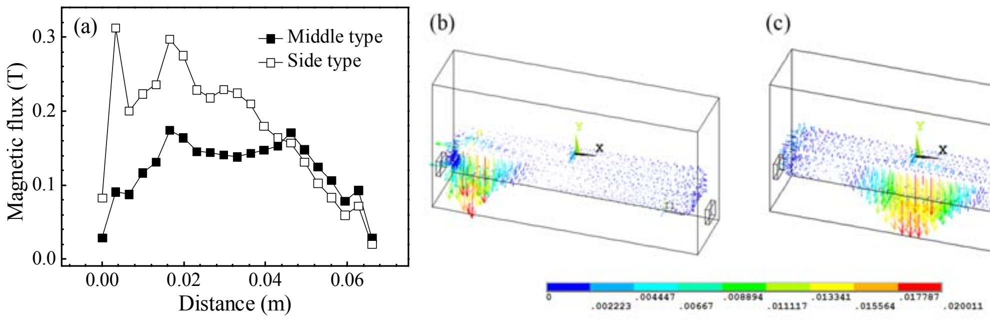

Figure 2: (a) Distributions of magnetic flux along the interface. Distributions of magnetic force, (b) Side type model, (c) Middle type model.

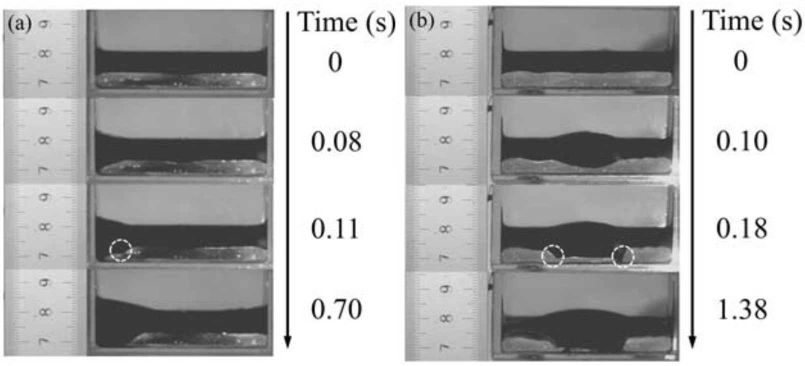

Figure 3: Interface evolution processes under weak magnetic field, (a) Side type setup, (b) Middle type setup.

Figure 3 shows the interface evolution processes under weak magnetic field. For the Side type setup, when t = 0 s, the interface is horizontal. When t = 0.08 s, the interface at the left side descends significantly, and the magnetic fluid rises. When t = 0.11 s, a sharp point occurs in the interface, and magnetic fluid is converged at the side wall of container. Finally, when t = 0.7 s, the interface descends to the lowest position. Similarly, for the Middle type setup, when t = 0 s, the interface is also horizontal. When t = 0.10 s, the interface descends, and the maximum fall occurs in the middle of interface. Besides, the magnetic fluid is also converged. When t = 0.18 s, there are two symmetrical sharp points occur in the interface. Then the interface descends gradually. Finally, when t = 1.38 s, the magnetic fluid was attracted to the bottom of the container, and the liquid metal is driven away to both sides of the container.

For the side type setup, when t = 0.08 s, the magnetic fluid rises. This is because that magnetic force is exerted on the magnetic fluid. When t = 0.11 s, a sharp point occurs in the interface. And the position of the sharp points is identical to that of the peak of simulated magnetic flux. Then the interface descends gradually. Finally, when t = 0.7 s, the interface descends to lowest position, and the liquid metal is entirely detached from the side wall of the container. Besides, by comparing the distribution of magnetic force and the interface evolution process, it also shows that the trend of interface evolution is in a good agreement with the distribution of magnetic force.

Similarly, for the Middle type setup, when t = 0.10 s, magnetic fluid is converged in the middle of the container. When $t = 0.18$ s, there are two symmetrical sharp points occur in the interface. The positions of the sharp points are also identical to that of the peaks of simulated magnetic flux. Then the interface descends gradually. Finally, when $t = 1.38$ s, the magnetic fluid is attracted to the bottom of the container, and the liquid metal is driven away to both sides of the container. Again, by comparing the distribution of magnetic force and the interface evolution process, it also shows that the trend of interface evolution is in a good agreement with the distribution of magnetic force.

By analyzing the simulation and experimental results, it is clear that significant interface evolution can be induced under weak magnetic field. And the distributions of magnetic flux and magnetic force play critical roles in deciding the interface evolution. Therefore, by adjusting the parameters of weak magnetic field, it is possible to effectively control the interface evolution between liquid metal and magnetic fluid.

4. Design of binary fluids circuit breaker

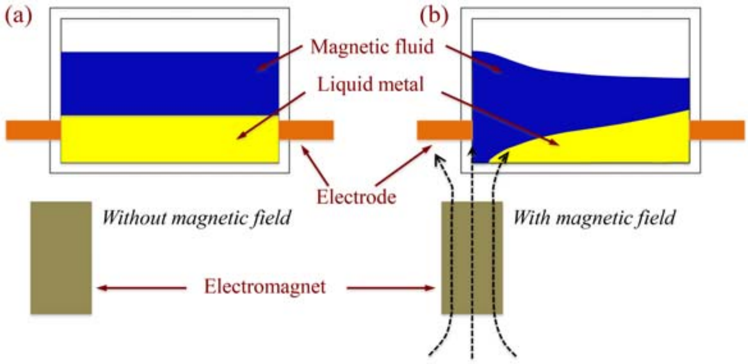

Figure 4. Principle of the binary fluids circuit breaker, (a) The state of interface when the circuit is normal, (b) The state of interface when fault current occurs.

Based upon the above results, a circuit breaker which consists of liquid metal and magnetic fluid is presented [11]. Figure 4 shows the principle of this circuit breaker. When the circuit is normal, the liquid metal is connected with electrodes. When fault current occurs, the magnetic field generator will be activated and produce magnetic field immediately. Therefore, it can attract magnetic fluid and driven away the liquid metal. Finally, the liquid metal is totally detached from the electrode, thus cut off the fault current. It should be noted that since the parameters of magnetic fluid can be adjusted, therefore, various binary fluid systems can be form by magnetic fluid and other fluid. In principle, all the interface evolution of these fluid systems can be effectively controlled by weak magnetic field.

5. Conclusions

The interface evolution between magnetic fluid and liquid metal under weak magnetic field was investigated. Simulation results show that magnetic flux has peak values, and magnetic fluid is subjected to significant magnetic force under weak magnetic field. Experimental results show that interface descends significantly under weak magnetic field. Moreover, sharp points occur during the interface evolution, and the positions of sharp point corresponded to that of the peak magnetic flux. Furthermore, the trends of interface evolution are in good agreement with the distribution of magnetic force. These results suggest that the interface evolution under weak magnetic field is decided by the distributions of magnetic flux and magnetic force. Thus, the interface evolution between magnetic fluid and liquid metal can be effectively controlled by adjusting the parameters of magnetic field. Finally, a circuit breaker which based on the principle of interface evolution between liquid metal and magnetic fluid is presented.

Acknowledgements. This work is supported by National Science Foundation of China under Grant No. 51174056 and also supported by the Fundamental Research Funds for the Central Universities under Grant No. N120509001.

References

[1] Ganan-Calvo, A. M.; Davila, J.; Barrero, A.: Current and droplet size in the electrospraying of liquids. Scaling laws. J. Aerosol Sci. 28 (1997) 249-275.

[2] Badie, R.; de Lange, D. F.: Mechanism of drop constriction in a drop-on-demand inkjet system. Proc. R. Soc. Lond. A. 28 (1997) 2573-2581.

[3] Schaffer, E.; Thurn-Albrecht, T.; Russell, T. P.; Steiner, U.: Electrically induced structure formation and pattern transfer. Nature. 403 (2000) 874-877.

[4] Hirota, N.; Homma, T.; Sugawara, H.; Kitazawa, K.; Iwasaka, M.; Ueno, S.; Yokoi, H.; Kakudate, Y.; Fujiwara, S.; Kawamura, M.: Rise and fall of surface level of water solutions under high magnetic field. Jpn. J. Appl. Phys., Part 2-Letts. 34 (1995) L991-L993.

[5] Ueno, S.; Iwasaka, M.: Properties of diamagnetic fluid in high gradient magnetic fields. J. Appl. Phys. 75 (1994) 7177-7179.

[6] Kitazawa, K.; Ikezoe, Y.; Uetake, H.; Hirota, N.: Magnetic field effects on water, air and powders. Phys B. 294 (2001) 709-714.

[7] Sugawara, H.; Hirota, N.; Homma, T.; Ohta, M.; Kitazawa, K.; Yokoi, H.; Kakudate, Y.; Fujiwara, S.; Kawamura, M.; Ueno, S.; Iwasaka, M.: Magnetic field effect on interface profile between immiscible nonmagnetic liquids - Enhanced Moses effect. J. Appl. Phys. 79 (1996) 4721-4723.

[8] Zhao, L. J.; You, Y.; Tian, Y. H.; Yang, H. K.; Wang, Q. A.; He, J. C. Interface profile evolution between binary immiscible fluids induced by high magnetic field gradients. Sci China Phys Mech & Astron. 53 (2010) 1319-1324.

[9] Rosensweig, R. E. 1985.: Ferrohydrodynamics. United Kingdom. Cambridge University Press.

[10] Chi, C. Q.; Wang, Z. S.; Zhao, P.Z. 1993.: Ferromagnetic hydrodynamics. Beijing. Publisher of Beihang University.

[11] Wang, Q.; Zhao, L. J.; You, Y.; Yang, H. K.; He, J. C. 2009: Method and device for self-recovery current limiting and circuit breaking by using conductive fluid and magnetic fluid. CRC Patent, CN101651323A.

MHD CHARACTERISTICS OF TEST BLANKET MODULE ELEMENTS

KIRILLOV I.R., OBUKHOV D.M., PERTSEV D.A.
D.V. Efremov Institute of Electrophysical Apparatus, St.Petersburg, Russia, 196641
E-mail address of corresponding author: obukhov@sintez.niiefa.spb.su

Abstract: MHD characteristics of TBM elements in magnetic field up to 1T were studied experimentally in NaK loop at temperature around 60°C: round pipe in transverse non-uniform magnetic field and a mock-up of TBM inlet manifold including inlet pipe, inlet collector and two rows of parallel poloidal (vertical) ducts with electrical heater between them to simulate ceramic element. MHD pressure drop and flow rate distribution were compared with engineering correlations.

1. Experiment description

MHD characteristics of Test Blanket Module (TBM) elements in high magnetic field (up to 1T) were studied experimentally as part of R&D program in support of Indian TBM concept to be tested in International Thermonuclear Experimental Reactor (ITER) [1, 2]. The TBM uses ceramic breeder and eutectic lead-lithium (LL) alloy as tritium breeders and helium and LL as coolants. Helium removes heat from the TBM first wall and structure elements, while LL flowing in a number of poloidal rectangular ducts removes heat generated in ceramic elements placed between these ducts.

MHD tests were performed in NaK loop at temperature around 60°C in magnetic field up to 1T on two mock-ups: round pipe in transverse non-uniform magnetic field and a mock-up of TBM inlet manifold.

A round pipe 1700 mm long with the outer radius $r_0 = 15.1$ mm, inner radius $r_i = L = 9.75$ mm, wall thickness 5.35 mm (SS) was placed in non-uniform magnetic field with characteristic lengths $x_0/r_i = 18$ and 32, where x_0 is non-uniform magnetic field region half length. To get $x_0/r_i = 32$ at one end of the magnet specially profiled pole pieces were used. For TBM tests in ITER this characteristic dimension x_0/r_i will be around 60.

TBM inlet manifold included inlet pipe, inlet collector and two rows of parallel poloidal (vertical) ducts with electrical heater between them to simulate ceramic element (Fig. 1). Its outer dimension along the magnetic field lines was 105 mm with 3 mm wall thickness. Region of uniform magnetic field had 470 mm height including 48 mm of inlet collector (with 3 mm bottom plate). The first poloidal duct (close to the inlet pipe) had two sub ducts of rectangular cross section 12×48 mm, the second one – three sub ducts 12×31 mm, inlet pipe inner diameter is 28 mm (wall thickness 3 mm).

Test parameters based on the corresponding characteristic length and B=1 T were: for round pipe – $Ha \le 385$, $N = Ha^2/Re \le 46$; for inlet manifold – $Ha \le 860$, $N \le 325$ as compared to those of TBM: $Ha = 2100$, $N \le 115$. Automatic data measuring system was used with pressure (pressure difference) sensors and wall potential sensors.

There was no electrical insulation on the duct and round pipe walls to simulate the possible first stage of TBM tests in ITER without electrical barriers.

2. Results and discussion

Experiments for the round pipe in a fringing magnetic field were conducted in 2011 and reported at the Russian Conference on Magnetohydrodynamics, Perm, 2012. Previous experimental results [3] for round and rectangular ducts were for $x_0/L \leq 15$. Later on, the results for round pipe with $x_0/L \approx 27$ were also published [4].

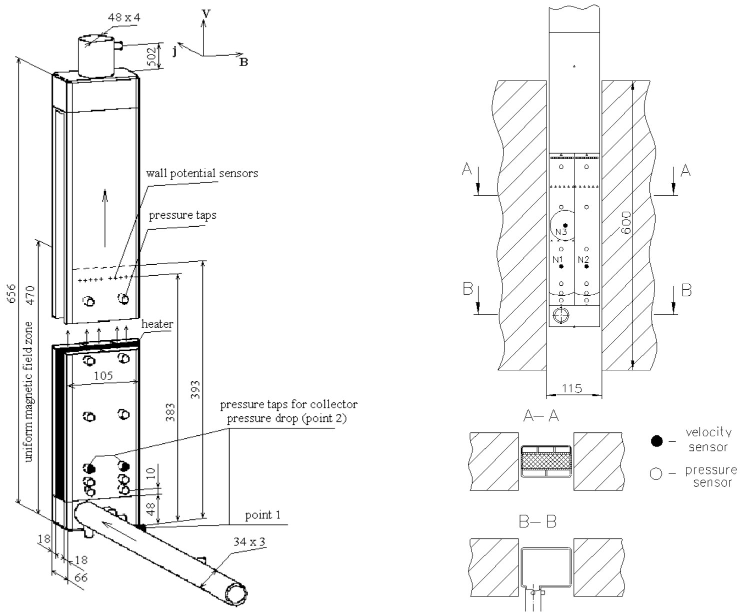

Figure 1: TBM manifold mock-up (a) and its placement in a magnetic field (b).

The measured magnetic field and pressure distribution are shown in Fig. 2 (magnet was moved in vertical direction while round mock-up was fixed to get more measuring points).

Pressure was measured with strain gage transducers (maximum pressure 0.6 MPa, main error 0.5% from measured pressure). Comparison of experimental data for non-dimensional pressure drop with theoretical ones (solid lines) is presented in Fig. 3 as a function of interaction parameter N= Ha^2/Re for three zones of magnetic field distribution (Fig. 2): 1 – region of non-uniform magnetic field with $x_0/r_i = 32$; 2 – region of close to uniform magnetic field; 3 - region of non-uniform magnetic field with $x_0/r_i = 18$. Well known correlations (see [3] for example) were used:

$$\Delta\overline{p} = \frac{\Delta p}{\sigma V_0 B_0^2 r_i} = \frac{k_p}{r_i}\int_{x_1}^{x_2} \overline{B}^2(x)dx\,, \qquad (1)$$

where $k_p = \dfrac{1}{1+c}$, $c = \dfrac{\sigma_w\left(r_o^2 - r_i^2\right)}{\sigma\left(r_o^2 + r_i^2\right)}$, σ, σ_w – liquid metal and duct wall electrical conductivities, V_0 – mean flow rate velocity, B_0 = 0.91 T – mean value in uniform field region, $\overline{B} = B/B_0$ – dimensionless magnetic field.

Having in mind the error of experimental data shown in Fig. 3, it may be concluded that under experimental conditions they are close and slightly higher than theoretical ones. 3-D effects in non-uniform field zones (1 and 3) are not large, so correlation (1) may be used for engineering estimation of MHD pressure drop in non-uniform magnetic field with $x_0/r_i \geq 18$. The same conclusion for $x_0/r_i \approx 27$ is made also in [4].

For the mock-up of TBM inlet manifold pressure distribution along the flow path obtained with pressure sensors is shown in Fig. 4 for flow rate 8 m^3/h, B=1 T, Ha=860 (for inlet pipe). More or less linear pressure distribution along the sub ducts may be seen. Inlet pipe is completely in magnetic field fringing zone just from the collector.

Non-dimensional MHD pressure drop in inlet manifold obtained with differential pressure sensors (between points 1 and 2 in Fig. 1) versus inlet pipe interaction parameter is shown in Fig. 5 for all sub ducts. Pressure drop is normalized with $\rho \cdot V_0^2 / 2$, where V_0 is inlet pipe mean flow velocity. Experimental error is not more than 6% as a rule.

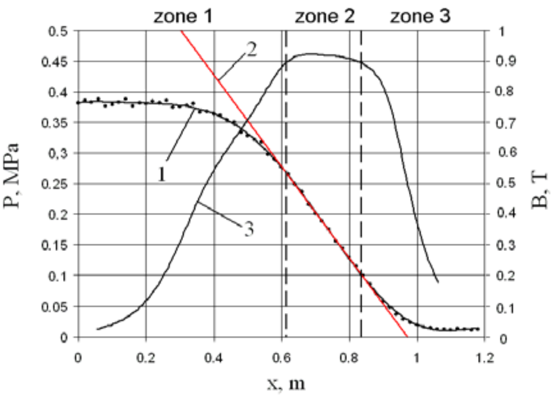

Figure 2: Magnetic field and pressure distribution over the pipe. 1 – pressure distribution along the duct (experimental points and approximation curve); 2 – linear dependence of pressure in close to uniform magnetic field zone (zone 2); 3 – magnetic field distribution

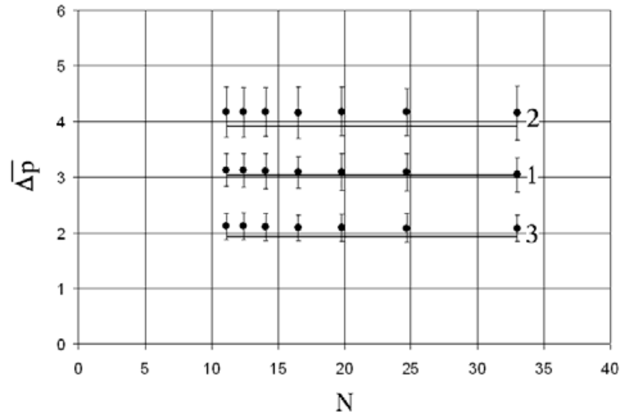

Figure 3: Non-dimensional pressure drop in zones 1-3 as a function of the interaction parameter (Ha_{max} = 385).

Pressure drop in part of the inlet pipe from point 1 to collector outer wall accounts for around 37.5% of pressure drop in manifold. Two curves corresponding to approximate theoretical predictions [5, 6] are shown for comparison:

- for transition from circular pipe to collector plus from collector to ducts

$$\Delta p_{3-D}^{MHD} = \sqrt{N} \cdot \frac{\rho \cdot V_0^2}{2} + \sigma \cdot V_{col.} \cdot L_{col.} \cdot B^2 \cdot Ha^{-1}, \tag{2}$$

- for flow in complex geometries

$$\Delta p_{3-D}^{MHD} = k \cdot N \cdot \frac{\rho \cdot V_0^2}{2}, \tag{3}$$

where L_{col} – collector half width in magnetic field direction (52.5 mm), V_{col} – collector mean flow velocity $V_{col} = \frac{Q}{2 \cdot L_{col} \cdot H_{col}}$, Q – flow rate, H_{col} – collector height (45 mm), k – parameter of geometry complexity (for TBM design optimization we used k=1.5). Experimental data correspond to the following empirical correlation:

$$\Delta p_{3-D}^{MHD} = 0.881 \cdot N \cdot \frac{\rho \cdot V_0^2}{2}.$$

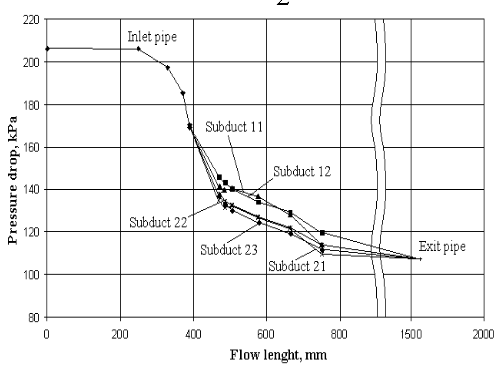

Figure 4: Pressure distribution along the flow path.

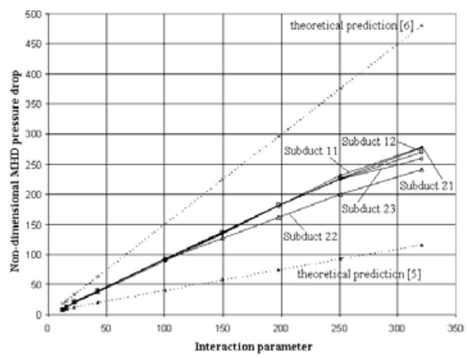

Figure 5: Non-dimensional MHD pressure drop in inlet manifold versus interaction parameter for different sub ducts.

Distribution of potential difference between side walls over ducts width (magnetic field direction) is shown in Fig. 6. Averaged over duct height liquid metal velocity obtained from circuit theory with known potential distribution and calculated electrical resistances of liquid metal and outer walls is also presented in Fig. 6. Integration of velocity distribution over sub ducts cross section gives flow rate in sub ducts (Table 1), sum of these flow rates differs from total flow rate measured with electromagnetic flow meter (EFM) less than 3%.

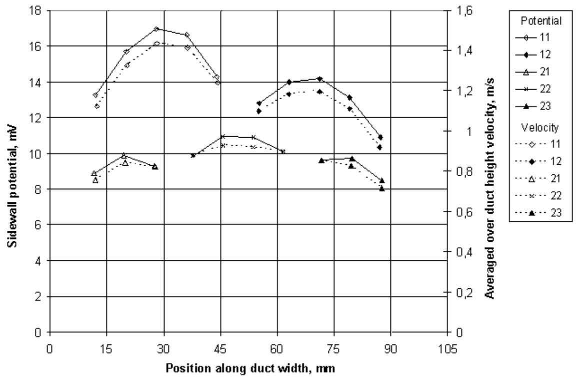

Figure 6: Potential and average over duct height velocity distribution in two sub ducts (sub ducts numeration from left to right – 11, 12) and three sub ducts (21, 22, 23)

As may be seen from Table 1 flow rate in sub duct 11 is larger than in sub duct 12 and that in sub duct 22 is larger than in sub ducts 21 and 23 for all total flow rates. There are two reasons for this phenomenon: different effective thickness of inner Hartman walls (all outer walls and sub ducts partitions were 3 mm) and influence of inlet pipe. Sub ducts 11 and 12 are symmetrical with respect to inner Hartmann wall, and flow rate increase in sub duct 11 may be explained exclusively by inlet pipe asymmetry with regard to channel 1 center line (inlet pipe is just opposite sub duct 11). This flow rates asymmetry is decreasing with interaction parameter increasing from 17.3% at N≈12 up to 15.2 % at N≈310.

Practically equal flow rates in sub ducts 21 and 23 reveal small influence of inlet pipe asymmetry on these ducts. At the same time sub ducts 21 and 23 are symmetrical with respect to Hartmann wall effective thickness and differ in that to sub duct 22. For sub duct 21 thickness of left Hartman wall is 3 mm, while effective thickness of right Hartman wall may be estimated as 1.5 mm, while for sub duct 22 effective thickness of both Hartman walls is 1.5 mm. Let's compare MHD pressure drop in sub ducts 21 and 22 using the following correlation [3]:

$$\Delta p^{MHD} = k_p \cdot \sigma \cdot V \cdot B^2 \cdot L,$$

where $k_p = \left[1 + \frac{\sigma \cdot a}{\sigma_{hw} \cdot t_{hw}} + \frac{1}{3 \cdot \beta} \cdot \frac{\sigma \cdot a}{\sigma_{sw} \cdot t_{sw}}\right]^{-1}$, σ_{hw}, σ_{sw} – electrical conductivity of Hartman and side walls; t_{hw}, t_{sw} – thickness of Hartman and side walls; a –sub ducts half width; β – ratio of sub duct half thickness to half width; L – sub duct length.

The ratio of MHD pressure drop in sub ducts 21 and 22 is the ratio of k_p: $\Delta p_{21}/\Delta p_{22}$ = k_{p21}/ k_{p22} = =1.3, and one may expect mean flow velocity (volume flow rate) in sub duct 22 higher by the same value in comparison to sub duct 21.

According to experiment (Table 1) Q_{22}/Q_{21}=1.1-1.12, i.e. slightly less, and this is explained by multichannel effect between sub ducts 22 and 21.

Table 1 .Flow rate in mock-up and sub ducts, m^3/h

Total flow rate (EMF)	CHANNEL-1		CHANNEL-2			Total flow rate in sub ducts and deviation from EMF
	Sub duct 11	Sub duct 12	Sub duct 21	Sub duct 22	Sub duct 23	
8.0	2.70	2.27	1.03	1.15	1.02	8.16 (2%)
6.29	2.12	1.79	0.80	0.89	0.79	6.39 (1.6%)
4.3	1.45	1.23	0.54	0.61	0.54	4.37 (1.6%)
2.3	0.77	0.66	0.29	0.33	0.29	2.33 (1.3%)
0.31	0.092	0.079	0.042	0.046	0.043	0.30 (3%)

3. Conclusion

MHD pressure drop for the round electro-conducting pipe in a fringing magnetic field with normalized decay length larger, at least $x_0/r_i=18$ may be estimated with the use of engineering correlations for fully developed flow and local magnetic field values.

For the mock-up of TBM inlet manifold with electro-conducting walls engineering correlations for pressure drop were derived. It was shown that influence of manifold on flow rate distribution between poloidal subducts is decreasing with parameter N increasing and for TBM conditions will be less than 5-7%. Different thickness of Hartmann walls in subducts will cause some nonuniformity in flow rate distribution between parallel sub ducts.

4. References

[1] E. Rajendra Kumar et al., Preliminary design of Indian Test Blanket Module for ITER, Fusion Engineering and Design 83 (2008) 1169-1172.

[2] I.R. Kirillov and D.A. Pertsev, Investigation of alternative configurations of the LLCB TBM to increase neutronic and thermo-hydraulics performances, Fusion Engineering and Design 85 (2010) 1054-1058.

[3] I.R. Kirillov, C.B. Reed, L. Barleon and K. Miyasaki, Present understanding of MHD and heat transfer phenomena for liquid metal blankets, Fusion Engineering and Design 27 (1995) 553-569.

[4] F.-C. Li, D. Sutevski, S. Smolentsev, M. Abdou, Experimental and numerical studies of pressure drop in PbLi flows in a circular duct under non-uniform transverse magnetic field, Fusion Engineering and Design 88 (2013) 3060-3071.

[5] T. Q. Hua, Y. Gohar, MHD pressure drops and thermal hydraulic analysis for the ITER breeding blanket design, Fusion Engineering and Design, 27 (1995) 696-702.

[6] S. Smolentsev et. al., MHD considerations for the DCLL inboard blanket and access ducts, Fusion Engineering and Design, 85 (2010) 1007-1011.

MODELLING OF THE HARTMANN LAYERS BY EFFECTIVE CORE BOUNDARY CONDITIONS

PRIEDE J.
Applied Mathematics Research Centre, Coventry University, UK
E-mail: j.priede@coventry.ac.uk

Resolution of thin Hartmann layers, which form in the liquid metal flows at the walls crossed by high magnetic field, is a serious challenge for numerical simulation of such flows. Since the structure of Hartmann layer is very simple, there have been numerous attempts to eliminate Hartmann layers by either some kind of averaging procedure or using near-wall-type boundary conditions as in turbulent flows. The first approach works well only for the flows which are nearly uniform along the magnetic field. On the other hand, the derivation and application of near-wall-type boundary conditions is rather questionable. I will present an alternative approach to the modelling of the Hartmann layer based on the singular asymptotic expansion techniques in combination with numerical solution for the core flow including the parallel layers. This approach results in a certain reduction of the governing equations which then needs to be compensated by the so-called core boundary conditions. First, such conditions are obtained for a rectangular duct flow in terms of the induced magnetic field. These conditions are then applied to various combinations of electrical conductivities of the walls that are either parallel or perpendicular to the field. As the field strength increases, the model results are shown to approach the exact solutions including the side layer for all combinations of wall conductivities. Second, alternative conditions are obtained in terms of the electric potential and also tested on the duct flow. The latter model is not only more general but also produces more accurate results at lower magnetic fields.

THE FRENCH FACILITY FOR HIGH MAGNETIC FIELDS

DEBRAY F., BEAUGNON E.
LNCMI CNRS Grenoble University, France
Email: francois.debray@lncmi.cnrs.fr

Abstract: The LNCMI (Laboratoire National des Champs Magnétiques Intenses) is part of the EMFL (European Magnetic Field Laboratory), together with the Nijmegen and the Dresden high magnetic field laboratories.The LNCMI provides to researchers magnetic fields up to 35 T in a 34 mm room temperature bore in a continuous mode at the Grenoble site and up to 80 T in a pulsed mode at the Toulouse site. Magnetic fields as well as related instrumentation are available in different bore sizes.

These last years, high field magnets have been used for diamagnetic levitation experiments (water in a 50 mm bore) and Hydrogen in a 170 mm warm bore diameter within a collaboration with the CNES and the CEA.

A new activity concerning metallurgy under high magnetic fields is rising including the development of dedicated high temperature furnaces.

For the design of the high field magnets, the LNCMI uses the polyhelix technology that is particulary suitable for high gradient magnets. The possibilities offer by such a technology will be presented to open discussion with potential users.

Figure: Top view of a 35 T high field magnet at LNCMI – Grenoble.

MOTION OF AN INSULATING SOLID PARTICLE NEAR A PLANE BOUNDARY UNDER THE ACTION OF UNIFORM AMBIENT ELECTRIC AND MAGNETIC FIELDS

SELLIER A.
LadHyX. Ecole polytechnique, 91128 Palaiseau Cedex, FRANCE
e-mail: sellier@ladhyx.polytechnique.fr

Abstract: This work presents a boundary approach to accurately compute at a reasonable cpu time cost the rigid-body motion of a solid and insulating particle immersed above a plane wall in a conducting liquid subject to ambient uniform electric and magnetic fields. Both insulating or perfectly conducting walls are addressed and the advocated formulation holds for arbitrary-shaped and arbitrary-located particles. It reduces to the determination of a few surface quantities on the particle boundary by numerically inverting seven boundary-integral equations.

1. Introduction

It is known, both theoretically [1] and experimentally [2], that an insulating solid particle suspended in a Newtonian and conducting liquid with uniform viscosity μ and conductivity $\sigma > 0$ migrates when subject to uniform ambient electric and magnetic fields $\mathbf{E}$ and $\mathbf{B}$. The particle rigid-body motion has translational velocity $\mathbf{U}$ (the velocity of one point attached to the particle) and angular velocity $\mathbf{\Omega}$ depending upon (σ, μ), the particle's geometry and the fields $\mathbf{E}$ and $\mathbf{B}$. For example, an insulating sphere with radius a translates without rotating at the velocity $\mathbf{U} = -a^2\sigma[\mathbf{E} \wedge \mathbf{B}]/(6\mu)$ (see [1]) whereas non-spherical insulating particles in general both rotate and translate [3,4].

In applications the liquid is however bounded and the particle's motion prevailing in an unbounded liquid domain might be strongly affected by the particle-boundary interactions. Such interactions have been investigated in the literature [5-7] by addressing the case of a particle located near a plane, solid and motionless wall Σ and distinguishing two different cases: the Case 1 of an insulating plane wall Σ in which the applied uniform electric field $\mathbf{E}$ is parallel to the wall and the Case 2 of an perfectly conducting plane wall Σ in which the uniform electric field $\mathbf{E}$ is normal to the wall. Case 1 has been handled in [7] but solely for a *distant and spherical* insulating particle while [5] copes only with Case 2 for a conducting or insulating and arbitrarily-located sphere. Finally, [6] deals with a non-spherical conducting particle in Case 2 by appealing to a boundary approach which has in practice been implemented solely when both vectors $\mathbf{E}$ are $\mathbf{B}$ are normal to the wall Σ. The present work proposes to solve the problem for an insulating particle with arbitrary shape and location in both Case 1 and Case 2 by exploiting a new and efficient flow decomposition.

2. Assumptions and governing electric and hydrodynamic problems

As sketched in fig 1, we consider a solid conducting particle $\mathcal{P}$ freely suspended in a Newtonian liquid metal, of uniform viscosity μ and conductivity $\sigma > 0$, above the $x_3 = 0$

plane and solid wall Σ. The particle has center of volume O' and smooth boundary S with unit normal $\mathbf{n}$ directed into the liquid domain Ω.

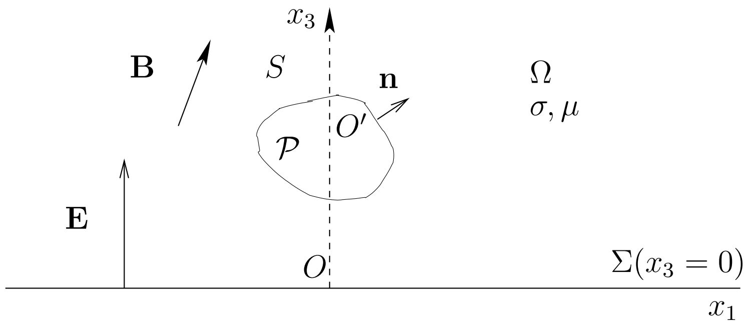

Figure 1: A solid and insulating particle freely suspended in a Newtonian liquid metal in the vicinity of the $x_3 = 0$ solid plane and motionless wall Σ. Here, the wall is perfectly conducting (Case 2) with the applied electric field $\mathbf{E}$ parallel with $\mathbf{e}_3$.

Under uniform ambient electric and magnetic fields $\mathbf{E}$ and $\mathbf{B}$ a liquid flow driven by the Lorentz body-force takes place and induces, by viscosity, a rigid-body migration of the particle $\mathcal{P}$. With respect to a Cartesian system (O, x_1, x_2, x_3) attached to the wall, such a so-called electro-magneto-phoretic motion is described by the particle translational velocity $\mathbf{U}$ (here the velocity of its point O') and angular velocity $\mathbf{\Omega}$. This works presents a boundary approach to determine the particle motion $(\mathbf{U}, \mathbf{\Omega})$ whatever the particle shape and location for two quite different types of walls:

(i) Case 1: an insulating wall with a uniform applied electric field $\mathbf{E}$ parallel with the wall Σ.

(ii) Case 2: a perfectly conductting wall with, as illustrated in fig 1, a uniform applied electric field $\mathbf{E}$ normal to the wall Σ.

Note that [7] solely deals with Case 1 for a *distant and spherical* particle whereas [6] solely considers the Case 2 for a particle with arbitrary shape and location.

The insulating particle affects the ambient electric field and the disturbed electric field reads $\mathbf{E} - \nabla\phi$ in the liquid domain Ω. The function ϕ satisfies the well-posed problem

$$\nabla^2\phi = 0 \text{ in } \Omega, \;\; \nabla\phi \to \mathbf{0} \text{ as } r = |\mathbf{OM}| \to \infty, \tag{1}$$

$$\nabla\phi.\mathbf{n} = \mathbf{E}.\mathbf{n} \text{ on } S, \; \nabla\phi.\mathbf{e}_3 = 0 \text{ on } \Sigma \text{ in Case 1}, \phi = 0 \text{ on } \Sigma \text{ in Case 2}. \tag{2}$$

Here, (1)-(2) is efficiently solved by using for each Case i the following integral representation

$$\phi(\mathbf{x}) = \frac{1}{4\pi}\int_S q(\mathbf{y})\{\frac{1}{|\mathbf{x}-\mathbf{y}|} - (-1)^i\frac{1}{|\mathbf{x}-\mathbf{y}'|}\}dS(\mathbf{y}) \;\; \text{for } \mathbf{x} \text{ in } \Omega \tag{3}$$

where $\mathbf{y}'$ designates the symmetric of the point $\mathbf{y}$ with respect to the wall Σ and the unknown surface charge density q on the particle surface S is obtained by enforcing the condition $\nabla\phi.\mathbf{n} = \mathbf{E}.\mathbf{n}$ on S (which results in a boundary-integral equation given in §3).

As previously mentioned, the liquid flows with pressure Q and velocity $\mathbf{u}$ with magnitude $V > 0$. The particle length scale a is such that the flow Reynolds number $\text{Re} = \rho V a/\mu$ vanishes. Assuming also vanishing Hartmann and magnetic Reynolds numbers, the magnetic field $\mathbf{B}$ is not disturbed and $(\mathbf{u}, Q)$ becomes a quasi-steady Stokes flow driven by the non-uniform Lorentz body force $\mathbf{f} = \sigma(\mathbf{E} - \nabla\phi) \wedge \mathbf{B}$. Setting $Q = P + \sigma(\mathbf{E} \wedge \mathbf{B}).\mathbf{x}$, one arrives at the following key problem for the flow $(\mathbf{u}, P)$

$$\nabla.\mathbf{u} = 0 \text{ and } \mu\nabla^2\mathbf{u} = \nabla P + \sigma\nabla\phi\wedge\mathbf{B} \text{ in } \Omega, \tag{4}$$
$$\mathbf{u} = \mathbf{U} + \mathbf{\Omega}\wedge\mathbf{O'M} \text{ on } S,\ \mathbf{u} = \mathbf{0} \text{ on } \Sigma,\ (\mathbf{u}, P)\to(\mathbf{0}, 0) \text{ as } |\mathbf{x}|\to\infty. \tag{5}$$

The particle rigid-body motion $(\mathbf{U}, \mathbf{\Omega})$ occurring in (5) has to be determined by enforcing additional relations. For a particle with negligible inertia those conditions are obtained by requiring the particle to be force-free and torque-free. If the flow $(\mathbf{u}, P)$ has stress tensor $\boldsymbol{\sigma}$ one then arrives at, recalling that O' is the particle center of volume and setting $\mathbf{x}' = \mathbf{O'M}$,

$$\mathbf{F} := \int_S \boldsymbol{\sigma}.\mathbf{n}dS = \sigma\mathcal{V}_{\mathcal{P}}(\mathbf{E}\wedge\mathbf{B}),\ \ \mathbf{C} := \int_S \mathbf{x}'\wedge\boldsymbol{\sigma}.\mathbf{n}dS = \mathbf{0} \tag{6}$$

where $\mathcal{V}_{\mathcal{P}}$ designates the particle volume. At a very first glance, one has to solve (4)-(6) in order to gain the desired particle migration $(\mathbf{U}, \mathbf{\Omega})$. The next sections show how one can actually circumvent the determination of the flow $(\mathbf{u}, P)$ by resorting to a suitable boundary formulation which finally reduces to the determination of a few surface quantities on the particle surface S!

3. Flow decomposition and key boundary-integral equations

By linearity, it is useful to adopt the following decompositions $\mathbf{u} = \mathbf{u}_h + \mathbf{w} + \mathbf{v}$ and $P = p_h + p$ such that the flow $(\mathbf{u}_h, p_h)$ obeys (4)-(5) for $\sigma = 0$ while the other flows satisfy

$$\nabla.\mathbf{w} = 0 \text{ and } \mu\nabla^2\mathbf{w} = \sigma\nabla\phi\wedge\mathbf{B} \text{ in } \Omega, \mathbf{w}\to\mathbf{0} \text{ as } |\mathbf{x}|\to\infty, \tag{7}$$
$$\nabla.\mathbf{v} = 0 \text{ and } \mu\nabla^2\mathbf{v} = \nabla p \text{ in } \Omega, \tag{8}$$
$$\mathbf{v} = -\mathbf{w} \text{ on } S,\ \mathbf{v} = -\mathbf{w} \text{ on } \Sigma,\ (\mathbf{v}, p)\to(\mathbf{0}, 0) \text{ as } |\mathbf{x}|\to\infty. \tag{9}$$

The flow $(\mathbf{u}_h, p_h)$ exerts on the moving particle a force $\mathbf{F}_h$ and a torque $\mathbf{C}_h$ (with respect to O') which are obtained by introducing six auxiliary Stokes flows $(\mathbf{u}_L^{(i)}, p_L^{(i)})$ (for $i = 1, 2, 3$ and $L = t, r$) free from body force, quiescent far from $\mathcal{P}$ and obeying the specific boundary conditions

$$\mathbf{u}_L^{(i)} = \mathbf{0} \text{ on } \Sigma,\ \mathbf{u}_t^{(i)} = \mathbf{e}_i \text{ on } S,\ \mathbf{u}_r^{(i)} = \mathbf{e}_i\wedge\mathbf{x}' \text{ on } S. \tag{10}$$

Upon introducing the surface tractions $\mathbf{f}_L^{(i)}$ exerted on S by the flows $(\mathbf{u}_L^{(i)}, p_L^{(i)})$ and the second-rank tensors $\mathbf{K}, \mathbf{W}, \mathbf{V}$ and $\mathbf{D}$ with Cartesian components

$$K_{ij} = -[\int_S \mathbf{e}_j.\mathbf{f}_t^{(i)}dS]/\mu, \quad W_{ij} = -[\int_S (\mathbf{e}_j\wedge\mathbf{x}').\mathbf{f}_r^{(i)}dS]/\mu, \tag{11}$$
$$V_{ij} = -[\int_S (\mathbf{e}_j\wedge\mathbf{x}').\mathbf{f}_t^{(i)}dS]/\mu, \quad D_{ij} = -[\int_S \mathbf{e}_j.\mathbf{f}_r^{(i)}dS]/\mu \tag{12}$$

one immediately gets the relations

$$\mathbf{F}_h = -\mu\{\mathbf{K}.\mathbf{U} + \mathbf{V}.\mathbf{\Omega}\},\ \ \mathbf{C}_h = -\mu\{\mathbf{D}.\mathbf{U} + \mathbf{W}.\mathbf{\Omega}\}. \tag{13}$$

The flow $\mathbf{w}$ has zero pressure and stress tensor $\boldsymbol{\sigma}_{\mathbf{w}}$ whereas the flow $(\mathbf{v}, p)$ has stress tensor $\boldsymbol{\sigma}_{\mathbf{v}}$. Such flows exert on the particle forces and torques (with respect to O') given by

$$\mathbf{F}_{\mathbf{w}} = \int_S \boldsymbol{\sigma}_{\mathbf{w}}.\mathbf{n}dS,\ \mathbf{C}_{\mathbf{w}} = \int_S \mathbf{x}'\wedge\boldsymbol{\sigma}_{\mathbf{w}}.\mathbf{n}dS,\ \mathbf{F}_{\mathbf{v}} = \int_S \boldsymbol{\sigma}_{\mathbf{v}}.\mathbf{n}dS,\ \mathbf{C}_{\mathbf{v}} = \int_S \mathbf{x}'\wedge\boldsymbol{\sigma}_{\mathbf{v}}.\mathbf{n}dS. \tag{14}$$

Accordingly, the relations (6) become the well-posed linear system

$$\mathbf{K}.\mathbf{U}+\mathbf{V}.\boldsymbol{\Omega}=\{\mathbf{F_w}+\mathbf{F_v}-\sigma\mathcal{V}_{\mathcal{P}}(\mathbf{E}\wedge\mathbf{B})\}/\mu,\ \mathbf{D}.\mathbf{U}+\mathbf{W}.\boldsymbol{\Omega}=\{\mathbf{C_w}+\mathbf{C_v}\}/\mu \tag{15}$$

for the unknown particle rigid-body motion $(\mathbf{U},\boldsymbol{\Omega})$. This system is shown in this paper to be entirely determined from the knowledge of a very few surface quantities on the particle boundary S : the previously-introduced (see §2) surface charge density q and the tractions $\mathbf{f}_L^{(i)}$. Such quantities are found to obey the following boundary-integral equations

$$\frac{q(\mathbf{x})}{2}+\frac{1}{4\pi}\int_S\{\frac{\mathbf{x}-\mathbf{y}}{|\mathbf{x}-\mathbf{y}|^3}-(-1)^i\frac{\mathbf{x}-\mathbf{y}'}{|\mathbf{x}-\mathbf{y}'|^3}\}.\mathbf{n}(\mathbf{x})q(\mathbf{y})dS(\mathbf{y})=-[\mathbf{E}.\mathbf{n}](\mathbf{x})\text{ for }\mathbf{x}\text{ on }S, \tag{16}$$

$$-\frac{1}{8\pi\mu}\int_S G_{jk}(\mathbf{x},\mathbf{y})[\mathbf{f}_L^{(i)}.\mathbf{e}_k](\mathbf{y})dS(\mathbf{y})=[\mathbf{u}_L^{(i)}.\mathbf{e}_j](\mathbf{x})\ \text{ for }\mathbf{x}\text{ on }S \tag{17}$$

where in (17) summation over indices k holds and $G_{jk}(\mathbf{x},\mathbf{y})$ denotes the Cartesian component of the so-called Green tensor analytically obtained in [8].

4. Relevant analytical solution for w and use of the reciprocal identity

As the reader may check using the representation (3), *one* solution to (7) is

$$\mathbf{w}(\mathbf{x})=\frac{\sigma}{8\pi\mu}\Big[\int_S q(\mathbf{y})\{\frac{\mathbf{x}-\mathbf{y}}{|\mathbf{x}-\mathbf{y}|}-(-1)^i\frac{\mathbf{x}-\mathbf{y}'}{|\mathbf{x}-\mathbf{y}'|}\}dS(\mathbf{y})\Big]\wedge\mathbf{B}\text{ for }\mathbf{x}\text{ in }\Omega\cup S\cup\Sigma. \tag{18}$$

The associated surface traction $\boldsymbol{\sigma}_\mathbf{w}.\mathbf{n}$ on the particle surface S then reads

$$[\boldsymbol{\sigma}_\mathbf{w}.\mathbf{n}](\mathbf{x})=-\frac{\sigma}{8\pi}\int_S q(\mathbf{y})\Big[\frac{(\mathbf{x}-\mathbf{y}).\mathbf{n}(\mathbf{x})(\mathbf{x}-\mathbf{y})\wedge\mathbf{B}+\mathbf{n}(\mathbf{x}).[(\mathbf{x}-\mathbf{y})\wedge\mathbf{B}](\mathbf{x}-\mathbf{y})}{|\mathbf{x}-\mathbf{y}|^3}$$
$$-(-1)^i\frac{(\mathbf{x}-\mathbf{y}').\mathbf{n}(\mathbf{x})(\mathbf{x}-\mathbf{y}')\wedge\mathbf{B}+\mathbf{n}(\mathbf{x}).[(\mathbf{x}-\mathbf{y}')\wedge\mathbf{B}](\mathbf{x}-\mathbf{y}')}{|\mathbf{x}-\mathbf{y}'|^3}\Big]dS(\mathbf{y}). \tag{19}$$

Thus, one can evaluate the required force $\mathbf{F_w}$ and torque $\mathbf{C_w}$ from the knowledge of q. Furthermore, $(\mathbf{v},p)$ and the flow $(\mathbf{u}_L^{(i)},p_L^{(i)})$ with stress tensor $\boldsymbol{\sigma}_L^{(i)}$ are Stokes flows free from body force and quiescent far from the particle. Therefore, the usual reciprocal identity [9] applies and yields

$$\int_{S\cup\Sigma}\mathbf{v}.\boldsymbol{\sigma}_L^{(i)}.\mathbf{n}dS=\int_{S\cup\Sigma}\mathbf{u}_L^{(i)}.\boldsymbol{\sigma}_\mathbf{v}.\mathbf{n}dS. \tag{20}$$

From the definition (14), the property (20) and the boundary conditions (9)-(10) one then gets the key relations

$$\mathbf{F_v}.\mathbf{e}_i=-\int_S\mathbf{w}.\mathbf{f}_t^{(i)}dS-\int_\Sigma\mathbf{w}.\boldsymbol{\sigma}_t^{(i)}.\mathbf{e}_3dS,\ \mathbf{C_v}.\mathbf{e}_i=-\int_S\mathbf{w}.\mathbf{f}_r^{(i)}dS-\int_\Sigma\mathbf{w}.\boldsymbol{\sigma}_r^{(i)}.\mathbf{e}_3dS. \tag{21}$$

By virtue of (18), the velocity $\mathbf{w}$ required on the boundaries S and Σ when applying the above links (14) is gained from the charge density q on the particle surface S. Finally, inspecting (21) shows that one also needs to compute each stress tensors $\boldsymbol{\sigma}_L^{(i)}$ on the plane wall Σ. Again, this is achieved from the knowledge of the traction $\mathbf{f}_L^{(i)}$ on the surface S, using this time the key integral representation

$$\mathbf{e}_l.\boldsymbol{\sigma}_L^{(i)}(\mathbf{x}).\mathbf{e}_k=\frac{1}{8\pi}\int_S T_{lkj}(\mathbf{x},\mathbf{y})[\mathbf{f}_L^{(i)}.\mathbf{e}_k](\mathbf{y})dS(\mathbf{y})\ \text{ for }\mathbf{x}\text{ in }\Omega\cup\Sigma \tag{22}$$

where the components T_{lkj} are available in closed analytical form in [10]. Those results are too long to be reproduced here. In exploiting (21) one then makes use of (22) on the wall Σ.

5. Concluding remarks

Owing to a suitable flow decomposition, it has been possible to reduce the determination of the particle rigid-body motion by solely appealing to a few surface quantities on the particle boundary: the charge density and the tractions exerted there when the particle either translates or rotates in absence of ambient electric and magnetic fields. The resulting boundary approach, valid whatever the particle shape and location, ends up with seven boundary-integral equations governing those key quantities. Such integral equations must be numerically solved in general or asymptotically inverted for a distant particle. Both circumstances will be addressed at the oral presentation which will report numerical results for spherical and non-spherical insulating particles and differents types (Case 1 and Case 2) of walls.

6. References

[1] Leenov, D.; Kolin, A.: Theory of electromagnetophoresis. I. Magnetohydrodynamic forces experienced by spherical and symmetrically oriented cylindrical particles. J. Chem. Phys. 22 (1954) 683-688.

[2] Marty, P.; Alemany, A.: Theoretical and experimental aspects of electromagnetic separation. In Metallurgical Applications of Magnetohydrodynalics (ed. H. K. Moffatt & M. R. E. Proctor). Metals Society. (1984) 245-259.

[3] Moffatt, H. K.; Sellier, A.: Migration of an insulating particle under the action of uniform ambient electric and magnetic fields. Part 1. General theory. J. Fluid Mech. 464 (2002) 279-286.

[4] Sellier, A.: Migration of an insulating particle under the action of uniform ambient electric and magnetic fields. Part 2. Boundary formulation and ellipsoidal particles. J. Fluid Mech. 488 (2003) 335-353.

[5] Sellier, A.: Migration of a solid conducting sphere immersed in a liquid metal near a plane conducting solid wall under the action of uniform ambient electric and magnetic fields. MagnetohydroDynamics. 42 Issue 2-3 (2006) 317-3262.

[6] Sellier, A.: Electromagnetic motion of a conducting particle immersed in a liquid metal near a solid wall. Proceedings of EPM2006, Sendai, 23-27 October 2006.

[7] Yariv, E & Miloh, T. Boundary effets on electro-magneto-phoresis. J. Fluid Mech. 622 (2009) 195-207.

[8] Blake, J. R.: A note on the image system for a Stokeslet in a no-slip boundary, Proc. Camb. Phil. Soc. 70 (1971) 303-310.

[9] Happel J.; Brenner H.: Low Reynolds number hydrodynamics, Martinus Nijhoff 1973.

[10] Pozrikidis C.: Boundary integral and singularity methods for linearized viscous flow, Cambridge University Press 1992.

MAGNETIC LEVITATION OF WEAKLY CONDUCTING LIQUID DROPLETS

BOJAREVICS[1] V., BEAUGNON[2] E.
[1]University of Greenwich, Park Row, London, SE10 9LS, UK
[2]CNRS-LNCMI, 25 rue des Martyrs, BP 166, 38042 GRENOBLE Cedex 9, France
E-mail: v.bojarevics@gre.ac.uk

Abstract: High DC magnetic field levitation for a noncontact liquid material properties measurements are investigated in detail using the numerical modeling techniques and comparing to the experimental observations of levitated water droplets, NaCl solution and ethanol. The shapes of droplets are compared using high frequency video recording and the corresponding numerically generated free surface images following the time evolution. By adding even a weak electrical conductivity to the liquid properties, the surface waves are damped considerably in the presence of the high magnetic field.

1. Introduction

High DC magnetic field levitation, using para- and dia-magnetic properties of the materials, can be used for advanced material research without the drawbacks related to the intense recirculating turbulent flow vortices appearing when the AC magnetic field is used for levitation. In practice a small vibration of the droplet center of mass position remains even in carefully conducted experiments [1]. Frequency measurements using the oscillating drop technique have been conducted for small size water droplets by Beaugnon et al. [2], and more recently by Hill & Eaves [1], in which a derivation of the frequency modifications due to the magnetic field are made and compared with the experimental results. The experimental results are replicated with the numerical simulations [3] accounting for the dynamic free surface change, internal flow and the centre of mass motion within the magnetic field from a magnet model. By adding an electrical conductivity to the liquid properties in the presence of the high magnetic field, the surface waves are either damped or their oscillation frequencies are shifted relative to the Rayleigh self-oscillation modes [4]. The numerical predictions for larger size liquid droplets show that the droplet centre of mass continues the oscillating motion without a significant damping [3]. This means that the magneto-gravitational potential, which for a static levitation would be constant along the droplet surface, experiences a similar oscillation as the free surface is moving across the potential isolines. The effect is more important for large size liquid droplets due to interaction of the surface wave modes and the magnetic force modulation.

These two effects are investigated in detail using the numerical modeling techniques and comparing to the experimental observations of levitated water droplets, NaCl solution and ethanol. The shapes of droplets are compared using high frequency video recording and the corresponding numerically generated images following the time evolution of the free surface.

2. Experimental procedures

The experiments were conducted at the Grenoble 'Laboratoire National des Champs Magnétiques Intenses' (LNCMI) on the vertical large bore magnet capable to reach 24 T in the centre position. The diamagnetic levitation is possible at the upper part of the magnet where the negative gradient of the magnetic field counteracts the gravitational force on the diamagnetic material droplet. The schematic view of the magnet, as generated from the numerical model used in this paper, is shown in the Figure 1. The magnet consists of several coil blocks carrying specially adjusted currents to ensure the required distribution of the magnetic field along the axis (the measured values are shown in the Figure 1). The computed

result, using the finite current element discretization and the Biot-Savart law, is shown for comparison in the same Figure 1.
A syringe connected via a plastic tube to a needle is used to inject a measured amount of diamagnetic liquid in the levitating zone of the magnet after the careful adjustment of the magnetic field intensity in order to obtain the magnetic 'trap' conditions. These adjustments need to be corrected for different material liquids and sizes of the levitated droplets. The experimental observations of levitated desalinated water, sodium chloride (NaCl) 20% water solution and pure ethanol droplets. The shapes of droplets are compared using high frequency video recordings from two cameras: at the side and top position of the droplet.

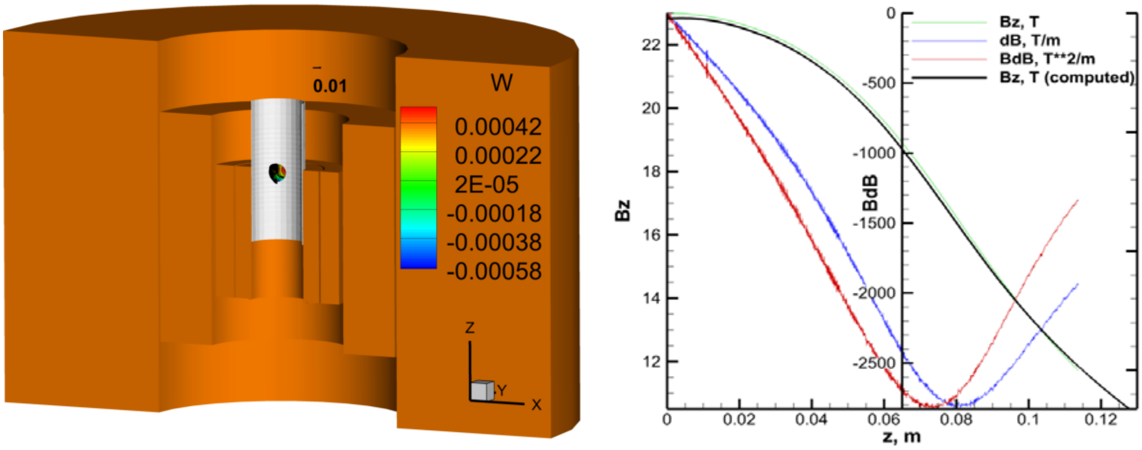

Figure 1: LNCMI (Grenoble) magnet numerical model representation used for DC magnetic levitation and the magnetic field measured and computed properties along the central axis.

3. The mathematical model and results

The mathematical basis of the present model is the time-dependent Navier-Stokes and continuity equations for an incompressible fluid [3]. The numerical solution of the problem is obtained using the pseudo-spectral collocation method, employing the continuous co-ordinate transformation for the shape tracking. The time-dependent fluid flow problem is set with appropriate boundary conditions: at the free surface of the liquid the normal hydrodynamic stress is compensated by the surface tension. The free surface position moves as determined by the force balance and the kinematic conditions.
The EM effects are computed at each new time step using the finite current element discretization and the Biot-Savart law. This means that the magneto-gravitational potential on the surface $U(R_s)$, defined by

$$\nabla(\rho g z - \chi_v |B|^2 / (2\mu_0)) = \nabla U \,, \tag{1}$$

experiences similar oscillation as the free surface is moving across the potential isolines. The effect is more important for large size liquid droplets leading to interaction of the surface wave modes and the magnetic force modulation. The position of the potential minimum determines the location of the magnetic 'trap' as seen in the Figure 2 for the stable and unstable levitation.

The numerical simulation was initiated by positioning the droplet in the stable magnetic potential minimum and perturbing the surface using the first 7 normal mode superposition of a small amplitude $0.01R_0$, where R_0 is the unperturbed spherical radius. The total perturbation is adjusted by the mode n=0 to preserve the volume of the initial sphere and to comply with the analytical Rayleigh normal mode frequencies (as will be shown in the Figure 6). The animated views of the computed droplet oscillations closely resemble those observed in the experiment, as can be seen from the instantaneous views in the Figures 3 and 4. The levitated ethanol droplet of 2 cm in diameter gives the most stable oscillations. The water droplet often is subject to relatively wild response to small perturbations, particularly when increasing the size to 3 cm.

When the salt solution was levitated, it was quite evident that the overall stability of the weakly electrically conducting droplet is improved, giving more smooth response to perturbations and a faster damping. This was particularly evident for the larger 3 cm size droplets. Figure 5 shows the computed oscillations of the free surface R_t at the top position of the droplet. The red dotted line shows the 7 normal mode only oscillation in the absence of the magnetic field. The solid line represents the water droplet oscillation in the 16.5 T field (in the magnet centre), which at the levitation position is about 11 -13 T variable field intensity. The dash-dotted line represents the 20% salt solution droplet oscillation. The damping effct of the electrical conductivity is particularly well seen from the graph on the right of the Figure 5, where the centre of mass $Z_c(t)$ position is deducted from the surface position $R_t(t)$ giving the surface wave only presentation.

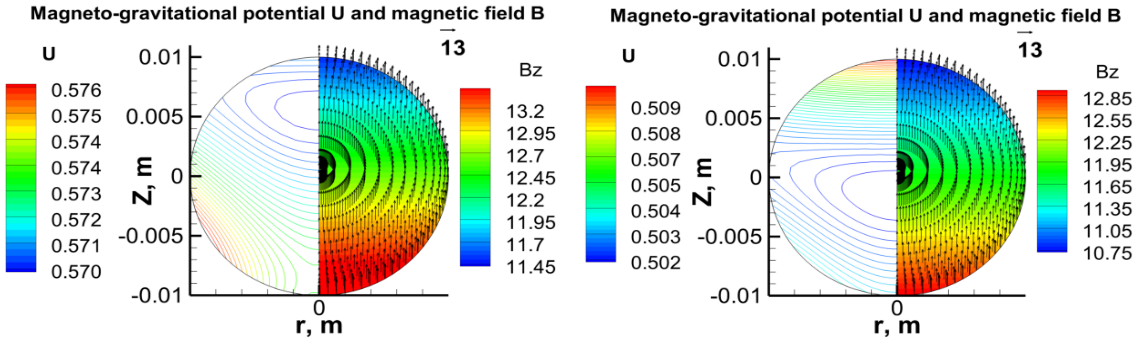

Figure 2: Computed magneto-gravitational potential and the magnetic field in the 2 cm diameter water droplet at t = 0: (left) unstable position at z = 0.072 m above the magnet centre, (right) stable position at z = 0.079 m.

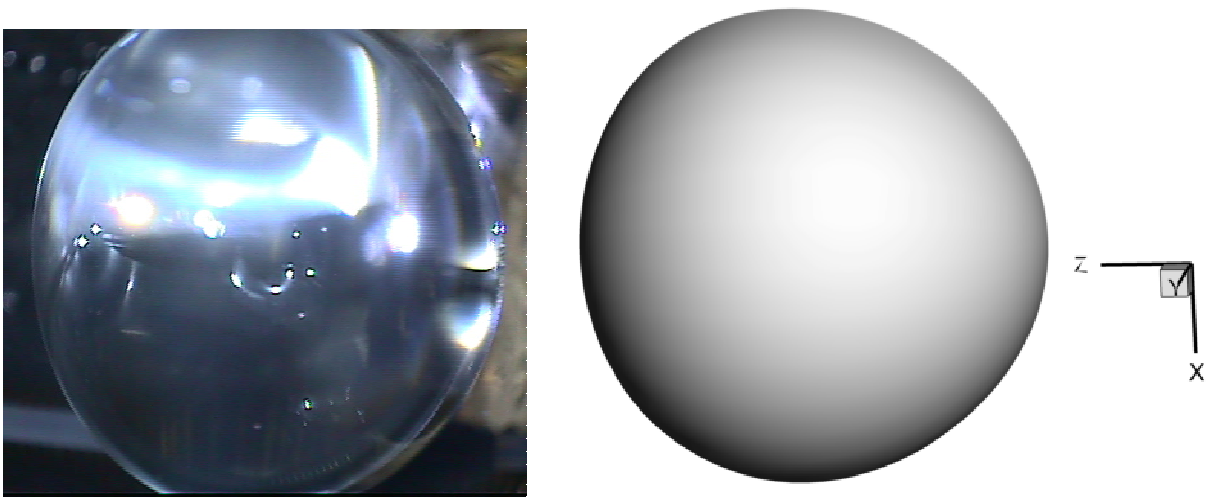

Figure 3: Images of the ethanol droplet D = 2 cm in the bore of experimental magnet and the numerically simulated (note that the vertical direction is horizontal in order to match the view from the side camera).

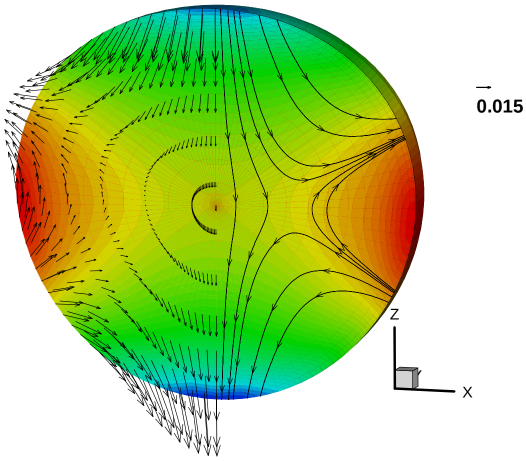

Figure 4: Images of 2 cm salt water droplet in the bore of experimental magnet at 16.1 T in the magnet centre and the numerically simulated at 16.5 T (accounting for 0.3 T air magnetic buoyancy correction).

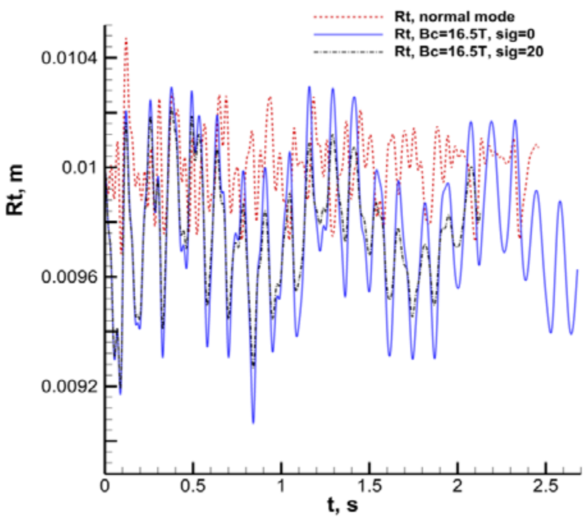

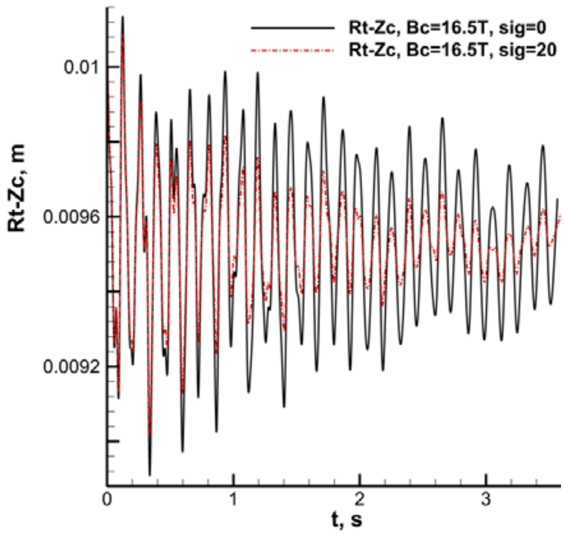

Figure 5: Computed oscillations of 2 cm water and salt water droplets in the bore of magnet at 16.5 T: a combination of 7 initial Rayleigh modes (dotted line), water with electrical conductivity 0, and the salt water conductivity 20 (1/Ωm).

The computed power spectra (Figure 6) provide the quantitative evidence for the frequency shift to slightly larger values as observed in the previous experiments [1,2]. It is encouraging to see that the additional property of the electrical conductivity of the salt water does not shift the frequency for the smaller droplets (2 cm). However the frequency shift is increased for the larger 3 cm droplet (see the Figure 6, right) because of the increased nonlinearity of the surface wave interaction, which is a well known phenomena even for the pure normal mode oscillations.

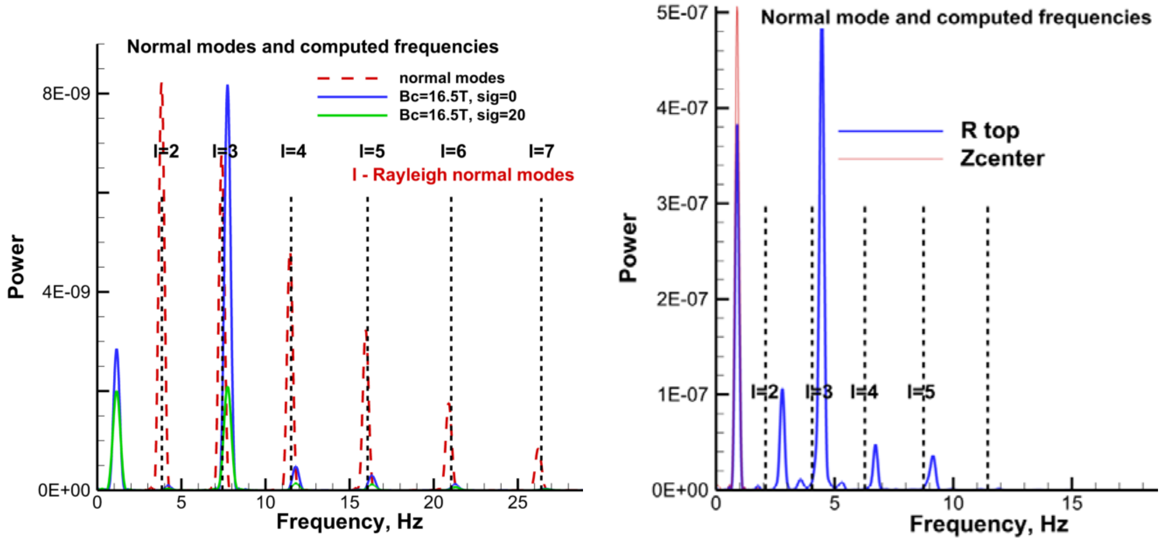

Figure 6: (Left) computed oscillation frequencies (power spectra) for the 2 cm water and salt water droplets in the bore of magnet at 16.5 T, and (right) - the 3 cm salt water droplet spectra at 16.7 T.

5. Conclusions

It is experimentally and numerically demonstrated that even a weak electrical conductivity has a significant effect to stabilize the magnetically levitated droplets using their diamagnetic properties. The damping effect is due to the low density induced electrical currents and does not affect the oscillation frequencies required to determine the surface tension material property. The presence of a weak electrical conductivity permits to levitate larger volumes of liquid in relatively more stable conditions.

6. References

[1] Hill R J A and Eaves L 2010, Phys. Rev E 81 (5) 056312
[2] Beaugnon E, Fabregue D, Billy D, Nappa J and Tournier R 2001, Physica B 294-295, 715-720
[3] S. Easter, V. Bojarevics, K. Pericleous. Journal of Physics: Conference Series (2011), **327,** 012027
[4] Priede J J. Fluid Mech. (2010), 671**,** 399.

Impact of surface viscosity upon an annular magnetohydrodynamic flow

Jules Delacroix[1] and Laurent Davoust[1, a)]

[1)] *Electromagnetic Processing of Materials (EPM) Group, Materials & Processes Science & Engineering Laboratory (SIMaP), Grenoble Institute of Technology (Grenoble-INP), 38402 St-Martin d'Hères, France*

Using the matched asymptotic expansion method based on the small parameter $1/Ha$, this paper addresses an original analytical coupling between surface rheology of *e.g.* a gradually oxidizing liquid metal surface, and a supporting annular MHD flow. It is shown that the level of surface viscosity drives the electrical activation of the Hartmann layers, heavily modifying the MHD flow topology and leading to the emergence of a Lorentz force, for which interaction with the flow is not classical.

I. INTRODUCTION

In many industrial applications, there is rising concern over how to model the interactions between an electro-conductive fluid and a second phase, when both of them are subjected to an external magnetic field. Typically, the issue of how a magnetohydrodynamic (MHD) flow with a liquid/gas interface is affected when oxidation occurs is of prime interest. It potentially affects many fields, such as metallurgy (stirring by bubble plumes in reactors), microelectronics (MHD-driven metal cooling processes [1]), or nuclear fusion technology (two-phase MHD issues with the breeder blanket based cooling loop [2]).

To our knowledge, little is actually known about surface rheology of MHD flows, *e.g.* when a liquid metal is progressively contaminated through oxidation processes. On the one hand, the viscoelastic properties of liquid metals have been experimentally investigated [3], highlighting radically different mechanical behavior characteristics that depend on the level of oxidation, but these works are not related with MHD. On the other hand, the MHD of single-phase laminar flows exposed to strong uniform magnetic fields has been studied extensively for many years, for numerous layouts [4–6], but the oxidation occurring at the liquid surface of a free-surface MHD flow is most of the time not taken into account. Consequently, the two-phase MHD of a more or less oxidized interface coupled with a pure liquid metal bulk is worthy of investigation, which is, to our knowledge, an original approach coupling both MHD and surface rheology.

II. OUTLINES

The system under consideration is displayed in Fig. 1. The interest in this configuration, which is inspired by the deep channel viscometer [7], is that it is likely to generate strong velocity gradients along the $\vec{e}_z$ axis, whereas these gradients develop preferentially along the $\vec{e}_r$ axis in the more conventional case of the Taylor-Couette layout. As shown later in equation (8), the coupling term between the interface and the sub-phase flow brings a $\partial v_\theta/\partial z$ term into play,

a)Electronic mail: laurent.davoust@simap.grenoble-inp.fr.

where v_θ is the azimuthal sub-phase velocity; the resulting shearing is expected to be more significant than in the Taylor-Couette layout, and the effects of varying boundary conditions at the liquid surface may be more easily highlighted. By considering the vertically applied magnetic field $\vec{B}_0$, it is shown in equation (1) that the generating term for the azimuthal magnetic induction B_θ is $\partial v_\theta/\partial z$ as well, which explains the interest in favoring gradients along $\vec{e}_z$.

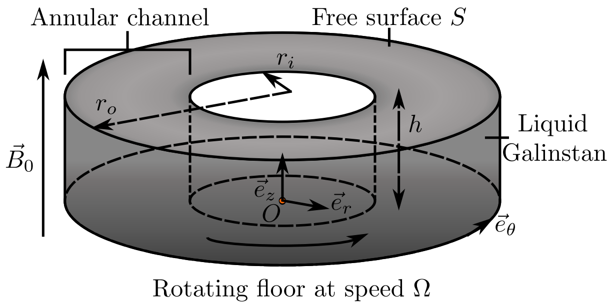

FIG. 1. Geometry under consideration.

The aim of this paper is to highlight the competitive effects between surface shearing and a strong transverse uniform magnetic field, especially with the emergence of an electrically active Hartmann layer along a gradually denser liquid surface, *e.g.* under oxidation processes.

III. MATHEMATICAL MODEL

A. Bulk flow

Using the Maxwell and Navier-Stokes equations, and assuming that the Reynolds number is low enough so that the inertial effects can be neglected, we can derive the following set of equations that govern the MHD problem and traduce the balance between electromagnetic and viscous effects (see *e.g.* [5,6]), where the superscript * refers to non-dimensional quantities:

$$\frac{\partial^2 B_\theta^*}{\partial r^{*2}} + \frac{1}{r^*}\frac{\partial B_\theta^*}{\partial r^*} - \frac{B_\theta^*}{r^{*2}} + \frac{\partial^2 B_\theta^*}{\partial z^{*2}} + Ha\frac{\partial v_\theta^*}{\partial z^*} = 0, \tag{1}$$

$$\frac{\partial^2 v_\theta^*}{\partial r^{*2}} + \frac{1}{r^*}\frac{\partial v_\theta^*}{\partial r^*} - \frac{v_\theta^*}{r^{*2}} + \frac{\partial^2 v_\theta^*}{\partial z^{*2}} + Ha\frac{\partial B_\theta^*}{\partial z^*} = 0, \tag{2}$$

with $r^* = r/h$, $z^* = z/h$, $v_\theta^* = v_\theta/\hat{V}$, $B_\theta^* = B_\theta/\hat{B}$, $Ha = B_0 h\sqrt{\sigma/\eta}$, and with $\hat{B} = \mu\hat{V}\sqrt{\sigma\eta}$, μ being the magnetic permeability of the fluid, and $\hat{V} = h\Omega$, so that $v_\theta^*(r^*, z^* = 0) = r^*$ for the rotating floor. The associated boundary conditions are written as follows (see *e.g.* [4] for the condition $B_\theta^* = 0$ all around the bulk flow):

$$v_\theta^*\,(r^* = \frac{r_i}{h}, z^*) = 0\,, \qquad B_\theta^*(r^* = \frac{r_i}{h}, z^*) = 0, \tag{3}$$

$$v_\theta^*\,(r^* = \frac{r_o}{h}, z^*) = 0\,, \qquad B_\theta^*(r^* = \frac{r_o}{h}, z^*) = 0, \tag{4}$$

$$v_\theta^*\,(r^*, z^* = 0) = r^*\,, \qquad B_\theta^*(r^*, z^* = 0) = 0, \tag{5}$$

$$B_\theta^*\,(r^*, z^* = 1) = 0\,, \tag{6}$$

$$v_\theta^*\,(r^*, z^* = 1) = v_{\theta S}^*(r^*). \tag{7}$$

B. Surface flow

The boundary condition (7) brings a new unknown into play, which is the surface velocity $v_{\theta S}$. This stands as the first term of the two-way coupling between the surface and MHD bulk flow equations and the liquid surface conditions. The latter can be derived from a momentum balance written on an elementary heterogeneous volume that straddles a liquid surface of zero thickness, and by introducing the relevant surface "excess" viscous shear viscosity, modelled with a Boussinesq-Scriven constitutive law (see *e.g.* [8] for further details):

$$Bo\left(\frac{\mathrm{d}^2 v^*_{\theta S}}{\mathrm{d}r^{*2}} + \frac{1}{r^*}\frac{\mathrm{d}v^*_{\theta S}}{\mathrm{d}r^*} - \frac{v^*_{\theta S}}{r^{*2}}\right) = \left.\frac{\partial v^*_\theta}{\partial z^*}\right|_{z^*=1}. \tag{8}$$

The Boussinesq number $Bo = \eta_S/\eta h$ describes the balance between bulk (η is the Newtonian bulk shear viscosity) and surface (η_S is the surface excess shear viscosity along the liquid surface) viscous shearing. To solve for this jump of momentum balance (JMB), the following two Dirichlet end-point boundary conditions are required:

$$v^*_{\theta S}\left(r^* = \frac{r_i}{h}\right) = 0, \quad v^*_{\theta S}\left(r^* = \frac{r_o}{h}\right) = 0. \tag{9}$$

C. Two-way coupling

The overall coupling process between the sub-phase flow v^*_θ and the surface flow $v^*_{\theta S}$ stems from a somewhat tedious calculation process, which consists of a matched asymptotic expansion for the bulk solution and the determination of a Green function for the surface velocity. Details of calculations are not detailed here, but they are fully available in [9].

IV. ASYMPTOTIC RESULTS AND INTERPRETATION

After relevant additional post-processing scaling [9] traduced by the * superscript, the choice is made to discuss only the asymptotic cases $Bo \gg Ha$ and $Bo \ll Ha$, as shown in Fig. 2. The reader may refer to [9] for further physical insight. The aim here is to indicate two radically different MHD regimes, and to see how the overall flow topology can be strongly modified.

When considering the velocity, the topology evolves from an exclusively radial dependence, with velocity gradients that are perfectly aligned with $\vec{e}_r$ (apart from those near the walls) for $Ha \gg Bo$ in figure 2a), to a motionless configuration for $Ha \ll Bo$ in figure 2b), where the velocity is mainly concentrated near the bottom right corner. This behavior is linked to significant physical phenomena. For figure 2a), the electromagnetic blocking is responsible for the dissipation of the secondary vortices, and for the fluid alignment with the rotating floor (rigid body motion). For figure 2b), the motionless topology is partly because of an inert interface for $Bo \gg Ha$, which imposes matching with a vanishing velocity at the interface, but other mechanisms are also brought into play, and are highlighted through analysis of the electromagnetic quantities.

The latter are obviously confined in the Shercliff layers when $Bo \ll Ha$, with two electrical loops near the side-walls, as shown in figures 2c) and 2e), with the core and the Hartmann layers

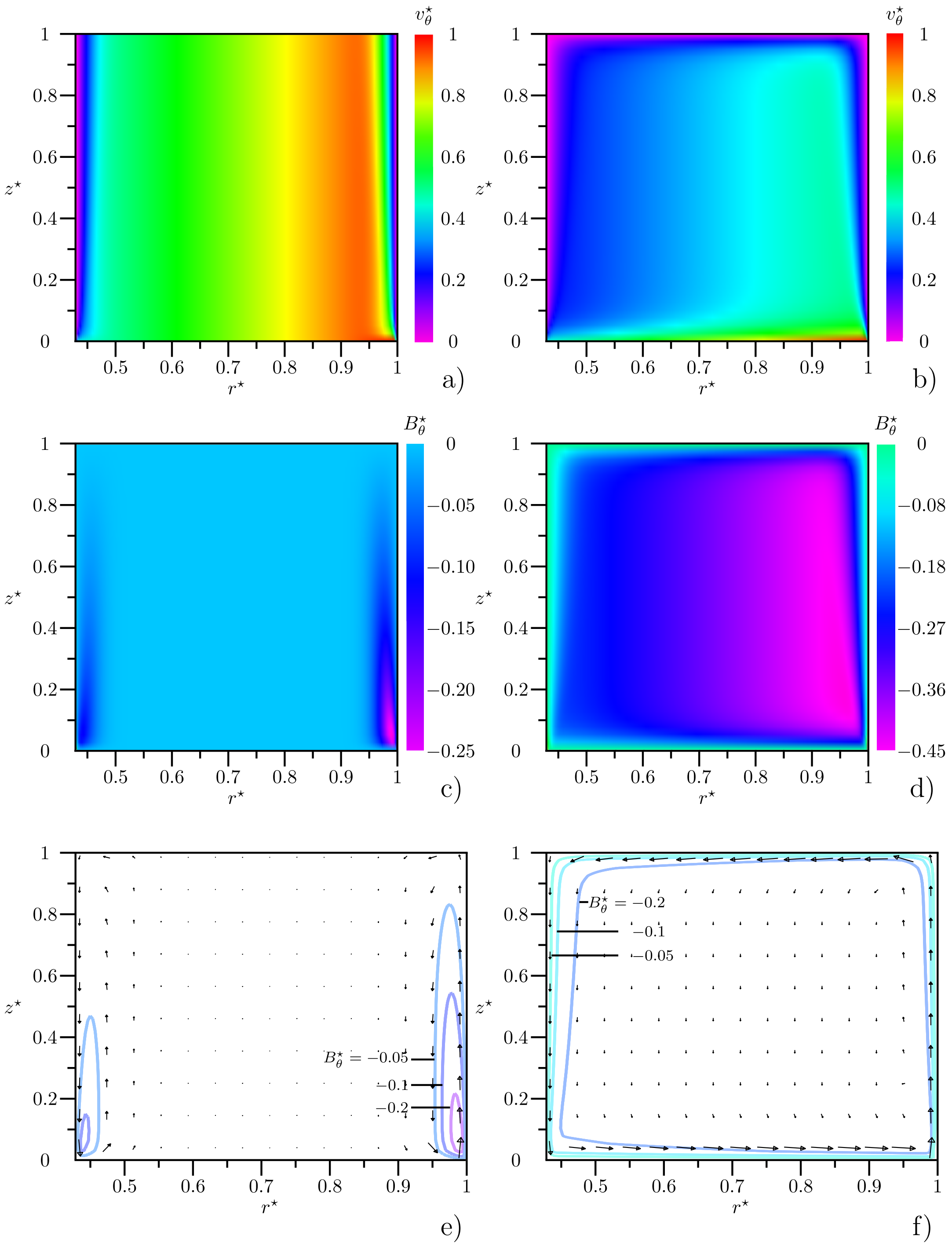

FIG. 2. Bulk MHD quantities for the two extreme cases $Bo \ll Ha$ (left-hand column) and $Bo \gg Ha$ (right-hand column). a) and b) represent $v_\theta^\star$, c) and d) represent $B_\theta^\star$, and e) and f) represent the vector current density $\vec{j}^\star$ with $B_\theta^\star$ streamlines. For a given velocity $\Omega = 0.25\,\mathrm{rpm}$, with $r_o = 7\,\mathrm{cm}$, $h = 1\,\mathrm{cm}$, $\sigma = 2.3\times10^6\,\mathrm{S{\cdot}m^{-1}}$ and $\eta = 2.4\times10^{-3}\,\mathrm{N{\cdot}m^{-1}}$, $\bar{J} = 4.1\times10^2\,\mathrm{A{\cdot}m^{-2}}$ for $Ha = 30$ (right-hand side) and $6.8\times10^2\,\mathrm{A{\cdot}m^{-2}}$ for $Ha = 50$ (left-hand side). $\vec{j}^\star$ is log-scaled by the magnitude $\exp\left(\left(\ln\left(\|\vec{j}^\star\|/\bar{J}\right)\right)/(1+p)\right)$, $p = 3$ for e) and $p = 1$ for f).

making a negligible contribution. The topology is dramatically different for $Bo \gg Ha$, where the core seems to be more involved, but the Hartmann layers in particular are now electrically active, with the setting of an "electric bridge" between the two side layers that is established through the Hartmann layers, as shown in figures 2d) and 2f). This is linked to the velocity topology mentioned earlier, with no particular gradients of $v_\theta^\star$ along the $\vec{e}_z$ axis in the case where $Ha \gg Bo$, other than near the side walls, whereas these gradients arise elsewhere and especially arise near the interface in the case where $Ha \ll Bo$. Depending on the regime, this means that the generation term of $B_\theta^\star$ in equation (1) either exists or does not, which could explain the Hartmann layers are electrically active or not.

Note also that the bottom Hartmann layer is only activated when the top layer is activated, whereas the "dynamic" configuration remains the same near the rotating floor. This is because of the current continuity equation $\nabla \cdot \vec{j} = 0$, which causes the electric current to close up inside the fluid. When the Hartmann layer at the top is activated, the current then flows across the boundary layers.

V. CONCLUSION

The competitive effects of surface rheology and supporting annular MHD flow have been highlighted: surface rheology is indeed found to monitor the generation of the Hartmann layers, and therefore a change in the topology of the electrical circuit, which dramatically affects overall MHD core flow.

[1] Liu, T.; Sen, P. and Kim, C-J: Characterization of nontoxic liquid-metal alloy galinstan for applications in microdevices. *Journal of microelectromechanical systems*, 21:443–450, (2012).

[2] Morley, N.B.; Smolentsev, S.; Barleon, L.; Kirillov, I.R. and Takahashi, M.: Liquid magnetohydrodynamics: recent progress and future directions for fusion. *Fusion Engineering and Design*, 51-52:701–713, (2000).

[3] Kolevzon, V. and Gerbeth, G.: Light-scattering spectroscopy of a liquid gallium surface. *J. Phys. D: Appl. Phys.*, 29:2071–2082, (1996).

[4] Shercliff, J.A.: Steady motion of conducting fluids in pipes under transverse magnetic field. In *Proc. Camb. Phil. Soc.*, volume 49, pages 136–144. Cambridge University Press, Cambridge, (1953).

[5] Hunt, J.C.R. and Stewartson, K.: Magnetohydrodynamic flows in rectangular ducts. ii. *J. Fluid Mech.*, 23:563–581, (1965).

[6] Molokov, S.Y. and Allen, J.E.: On the theory of the heiser and shercliff experiment. i: Mhd flow in an open channel in a strong uniform magnetic field. *J. Phys. D: Appl. Phys*, 25:393–400, (1992).

[7] Mannheimer, R.J. and Schechter, R.S.: An improved apparatus and analysis for surface rheological measurements. *Journal of Colloid and Interface Science*, 32:195–211, (1970).

[8] Slattery, J.C.; Sagis, L. and Oh, E.: *Interfacial transport phenomena*, chapter 4, B, pages 360, 712. New York: Springer-Verlag, 2007.

[9] Delacroix, J. and Davoust, L.: Electrical activity of the Hartmann layers relative to surface viscous shearing in an annular magnetohydrodynamic flow. *Physics of Fluids*, 26:037102-1–037102-21, (2014).

A SIMULINK MODELIZATION OF AN INDUCTIVE MHD GENERATOR

CARCANGIU S., FORCINETTI R., MONTISCI A.
Electrical and Electronic Eng. Dept., Piazza d'Armi – 09123 Cagliari (Italy)
E-mail: amontisci@diee.unica.it

Abstract: In this paper an inductive MHD generator is proposed, which aims to overcome the typical drawbacks of the conventional MHD generators, such as the need to operate at high temperatures and to have superconducting coils for the generation of the external magnetic field. The conceptual idea is described and the energy conversion process is illustrated by means of a finite element method model, which describes the fluid dynamic aspects, joined to a Simulink® model, which describes the electromagnetic phenomena involved in the process. Some results of analysis are reported, putting in evidence the influence of design parameters of the machine.

Index Terms: inductive MHD generator, static energy conversion, numerical modeling

1. Introduction

Interest in magneto hydrodynamic (MHD) power generation was originally stimulated by the observation that the interaction of a plasma with a magnetic field could occur at much higher temperatures than were possible in a rotating mechanical turbine [1]. In spite of this, a number of drawbacks have limited a wide use of this technology that, after have been deeply studied for at least three decades, at the end of the past century it has been quite completely abandoned. Such technological limits concern essentially the difficulty to maintain a high level of ionization of the gas at low temperature, the needed of an intense magnetic field (> 5 T) which has to be generated by means of superconducting coils, the deterioration of electrodes by means of which the generated electrical current is extracted by the plasma. Even, thanks to the development in different research topics, great improvement have been obtained in the recent years on superconductors [3] and ionised gases [2], the complexity of the apparatus pushes to prefer other competitors, such as turbogas. Furthermore, until now no efficient solution has been found concerning the duration of electrodes [4]. In [5], an inductive gas fed generator has been proposed that allows one to overcome the above mentioned drawbacks of the conventional MHD generators, but at the same time it holds all their advantages, such as the static conversion of the energy and the capability to work with very high temperatures. This is obtained by substituting the external magnetic field with an electrostatic field, and by using eddy currents rather than electrodes to retrieve the generated electrical current. A key aspect of the proposed generator is the fact that the charge carriers are separated in order to obtain two separated flows of unbalanced charge carriers. Due to the fact that the ionization of the gas is time varying, also the flows of charge carriers vary during the time, so that they can give rise to an induced electromotive force in a magnetically coupled coil. The paper is organized as follows. In Section 2 the physics involved in the process is described. In Section 3 the energy conversion is qualitatively described and is treated more in details in Sections 4, 5 and 6 by means of its mathematical model. In Section 7 the Simulink® model and some results are reported. The last section provides some conclusions.

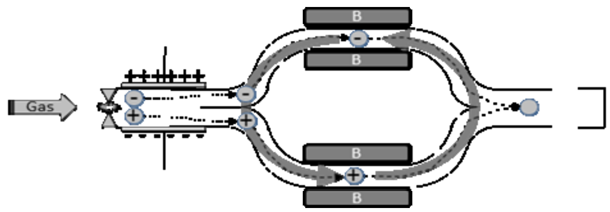

Figure 1: Inductive MHD generator functional scheme.

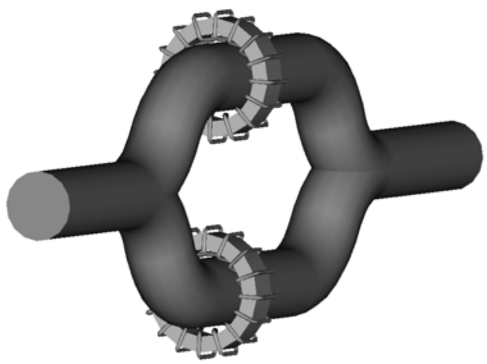

Figure 2: Inductive MHD generator layout.

2. System description

The working principle of the generator studied is quite simple (see Fig. 1). A high speed gas enters in the duct where in the first part it is ionized by a pulsating electric discharge. The charges of different sign are separate by an external electric field. Downstream of this process the flow is divided in two currents, one having an excess of positive charge, the other one of negative charge. In this way a time variant circulating electric current is generated, which involves the two branches of the duct. The current generated induces an electromotive force in two toroidal coils wrapped around the duct. The ionization of the fluid is obtained by means of electrodes powered by a high voltage generator to generate an electric pulsating discharge. After that the charges have been generated they have to be separated by means of an external electrical field. To this end, a capacitor externally powered by a DC high voltage generator is placed around the duct. In correspondence of the toroidal coils (Figs. 1 and 2) the energy conversion process is carried out, by inducing an electromotive force.

3. Energy conversion process

The energy conversion occurs in correspondence of the toroidal coils. Here the generator works as a conventional transformer, where the primary is represented by the plasma in the duct, while the secondary winding is the toroidal coil (Fig. 2). The electric current flowing in the electric load gives rise to an armature reaction, which in turn slows down the charge carriers into the plasma and then causing a gas expansion. The enthalpy jump one can obtain in the conversion depends on a great number of design parameters: the velocity of the gas, the geometry of the core, the number of coils of the windings and the section of the wire, and so on. In this work, the variation effect of some of these parameters has been investigated.

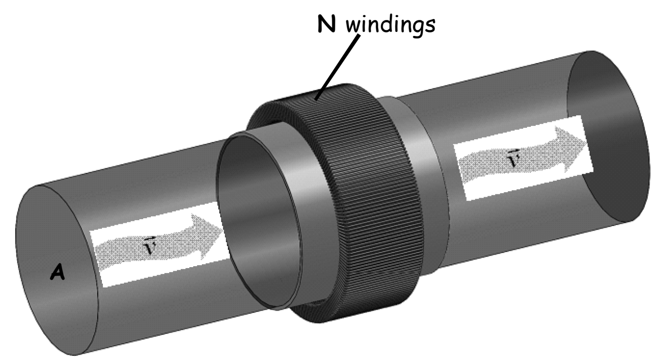

Figure 3: Detail of the generator corresponding to the section where the energy conversion takes place.

4. System modeling

First of all, the MHD problem has been split into a fluid dynamic part and the electromagnetic part. The former part is solved by means of the finite element analysis [5], while the latter one is solved by assigning to the charge carriers the same motion of the neutral particles. Such assumption can be justified because the charge carriers relative concentration is very low, therefore they cannot affect the average motion of the fluid. Furthermore in analyzing the electromagnetic aspects, we consider a mono-dimensional model of the flow. This means to neglect the unavoidable variations of the flow across the section of the duct.

In Fig. 3 a particular of one branch of the duct is shown. The charges participate to the motion of the neutrals. In addition, other two components of the velocity have to be considered: one due to the repulsive force between charges of the same sign, and one due to the reaction of the armature. The repulsive force among charges of the same sign strongly affects the efficacy of the transfer of energy, because the more the charges are distributed along the axis of the duct, the less will be the induction produced in the coil. To reduce the effect of the reciprocal repulsive force of the charges, a supplementary electrical field is applied to the flow by means of a metallic sleeve around the duct (Fig. 3). Therefore, four components of the velocity have to be taken into account in calculating the distribution of the charges during the time:

$$v(x,t) = v_T + \mu_E\left[E_\rho(x,t) + E_C(x) + E_R(x,t)\right] \tag{1}$$

where v is the velocity of the particle of charge in the position x at the time t, v_T is the dragging component which is constant, μ_E is the electrical mobility of the charge carriers, E_ρ is the electrical field due to the charges distribution, E_C is the electrostatic field provided by the sleeve, E_R is the electrical field due to the armature reaction. At the beginning of the branch, the charge has a Gaussian distribution, but in evolving in the duct such distribution changes, because of the electrical fields E_C and E_R, becoming asymmetric. In order to take into account such asymmetry, the combination of two Maxwellian distributions has been used to model the charge density distribution:

$$\rho = \left(1 - \frac{x}{D}\right) \cdot \frac{4Q_{tot}}{\sqrt{\pi}} \cdot \frac{x^2}{x_m^3} \cdot e^{-\frac{x^2}{x_m^2}} + \frac{x}{D} \cdot \frac{4Q_{tot}}{\sqrt{\pi}} \cdot \frac{(D-x)^2}{(D-x_m)^3} \cdot e^{-\frac{(D-x)^2}{(D-x_m)^2}} \tag{2}$$

where $\rho(x)$ is the charge density, Q_{tot} is the total charge of the cloud, x_m is the position along the axis of the duct of the maximum of charge density.

5. Electrical fields acting on the charge distribution

Given the charge distribution, it is possible to calculate the electric field $E_\rho(x,t)$ in the generic point x on the axis of the duct and then the component of velocity due to such field in (1). The $E_C(x)$ can be determined by solving an electrostatic problem. The $E_R(x,t)$ is the armature reaction. In the ideal case the magnetic field generated by the current circulating in the coil is completely contained within the core, but it gives rise to a vector potential in the duct, which derivative is proportional to an electric field opposite to the motion of the charges. In order to calculate said vector potential, we can use the same mathematical steps which allow to define the Biot-Savart law, obtaining the following relation:

$$d\vec{A} = \Phi \cdot \frac{d\vec{l} \times \vec{r}}{r^3} \tag{3}$$

Eq. (3) is formally identical to the Biot-Savart equation, as a consequence we will obtain that the force lines of electrical field generated by the flux Φ have the same shape of the magnetic field generated by a turn of electrical current, and it allows one to calculate the electric field along the axis of the duct, which represents the armature reaction. For symmetry the resultant potential vector $\vec{A}(x)$ is directed as the axis of the duct, so that in integrating the contributions $d\vec{A}$ due to the flux Φ along the torus, we have to consider their projection along the axis x:

$$\vec{A}(x)=\int_0^{2\pi}\Phi\cdot\frac{d\vec{l}\times\vec{r}}{r^3}=\left(\int_0^{2\pi}\frac{\Phi\cdot\sqrt{R^2+x^2}}{\left(\sqrt{R^2+x^2}\right)^3}\cdot\cos\varphi\cdot Rd\theta\right)\cdot\vec{i}=\frac{\Phi\cdot\sqrt{R^2+x^2}}{\left(\sqrt{R^2+x^2}\right)^3}\cdot\frac{R}{\sqrt{R^2+x^2}}\cdot R\int_0^{2\pi}d\theta=\frac{2\pi\cdot\Phi\cdot R^2}{\left(\sqrt{R^2+x^2}\right)^3}\cdot\vec{i} \tag{4}$$

Finally, it is possible to calculate the armature reaction as the time derivative of the vector potential:

$$\vec{E}_R=-\frac{\partial\vec{A}}{\partial t}=-\frac{2\pi\cdot R^2}{\left(\sqrt{R^2+x^2}\right)^3}\cdot\frac{d\Phi}{dt}\cdot\vec{i} \tag{5}$$

The (5) can be substituted in (1) to calculate the velocity of each charge of the distribution during the time, and then to determine the evolution of the charge distribution.

6. Power transfer to the electric load

The energy conversion process can be described by resorting to the Ampère equation, written for the plane which is orthogonal to the axis of the duct and which is symmetry plane for the torus:

$$\oint_L \vec{H}\cdot d\vec{l}=I-N\cdot i+\varepsilon\frac{d}{dt}\iint_S\left(E_\rho+E_R\right)dS \tag{6}$$

where H is the magnetic field evaluated along the torus of length L, I is the plasma electric current flowing in the duct, N is the number of turns of the secondary winding, i is the electric current circulating in such winding, ε is the permittivity. As it can be seen, field E_C does not appear in the displacement current term, because it is null in the origin for symmetry reasons. On the other hand, it implicitly affects the current I by influencing the charge distribution $\rho(x,t)$. Let us now to separately consider the terms of the (6). The circulation integral at the left-hand side can be so re-written:

$$\oint_L \vec{H}\cdot d\vec{l}=\oint_L\frac{\Phi}{\mu\cdot\Sigma}dl=\frac{\Phi L}{\mu\cdot\Sigma} \tag{7}$$

Table 1 - Design parameters of the MHD generator

Physical quantity	Symbol	Value [units]
Radius of duct	R	0.20 [m]
Permittivity	ε	$10^{-9}/36\pi$ [$F\cdot m^{-1}$]
Charge in the duct		10^{-5} [C]
Permeability	μ	0.0628 [$H\cdot m^{-1}$]
Gas velocity	v_T	150-200 [$m\cdot s^{-1}$]
Length of the sleeve		0.20 [m]
Charge on the sleeve		10^{-5} [C]
Ions mobility	μ_E^+	$2\cdot10^{-4}$ [$m^2\cdot V^{-1}\cdot s^{-1}$]
Electrons mobility	μ_E^-	$3\cdot10^{-2}$ [$m^2\cdot V^{-1}\cdot s^{-1}$]
Length of the torus	L	1.4 [m]
Cross area torus	Σ	0.02 [m^2]
Number of coil turns	N	2 000
Electric load	R_{el}	100-2 000 [Ω]

The current I in the right-hand side, is given by the concentration of charge ρ given by the (2), evaluated in the origin and then multiplied by the velocity, given by the (1):

$$I=\rho(t)\big|_{x=0}\cdot\left\{v_T+\mu_E\left[E_\rho(t)+E_R(t)\right]_{x=0}\right\} \tag{8}$$

The current i circulating in the winding is related to both voltage v_2 and electric load R_{el}. Let us assume, for sake of simplicity, the electric load to be resistive. Then the current i can be so expressed:

$$i=\frac{v_2}{R_{el}}=\frac{1}{R_{el}}\cdot\frac{d(N\cdot\Phi)}{dt}=\frac{N}{R_{el}}\cdot\frac{d\Phi}{dt}$$

and then the second term of the right-hand side of (6) becomes:

$$-N \cdot i = -\frac{N^2}{R_{el}} \cdot \frac{d\Phi}{dt} \tag{9}$$

Finally, for the third term, corresponding to the displacement current is:

$$\varepsilon \frac{d}{dt} \iint_S \left(E_\rho + E_R\right) dS = \varepsilon \frac{d\left(E_\rho + E_R\right)\big|_{x=0}}{dt} \iint_S dS = \varepsilon \cdot S \cdot \frac{d\left(E_\rho + E_R\right)\big|_{x=0}}{dt} \tag{10}$$

By substituting (7-9) in (6) we obtain an equation of the second order in the unique variable Φ.

7. Results

The equations of the model have been solved by using the Simulink® environment. In Table 1 the design parameters of the generator are reported. Among that, two parameters, namely velocity of the working gas and electrical load has been swept in order to evaluate the corresponding sensitivity of voltage and transferred power. The results show the high velocities and high loads allow to obtain higher power. As a feature to evaluate the suitability of the gas velocity, we can check if the whole cloud of charges crosses the toroidal winding in spite of the mutual repulsive force among the charges. The simulations show that a gas velocity of 150 $m \cdot s^{-1}$ is sufficient to drag the charges beyond the torus. This time depends on both gas velocity and total charge, therefore it has to be stated on the basis of design parameters. The duration of the pulse of the induced voltage indicates the minimum time interval between two consecutive discharges.

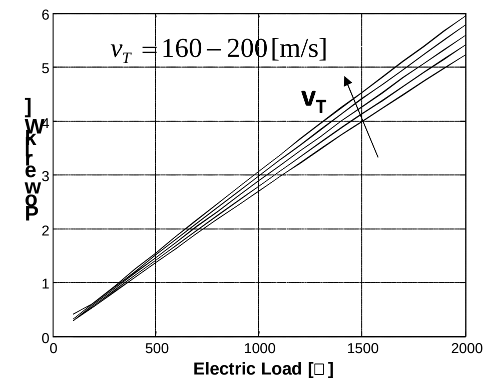

Figure 6: Trend of power with respect to load and velocity.

8. Conclusion

A conceptual study of an inductive MHD generator has been presented, which aims to overcome the typical drawbacks of the conventional MHD generators, such as the need to operate at high temperatures and to have superconducting coils for the generation of the external magnetic field. The process is described and analyzed by means of a mathematical model that has been solved by using the Simulink® environment. A parametric evaluation of the velocity of the working gas and electrical load has been done in order to evaluate the corresponding sensitivity of voltage and transferred power.

9. References

[1] R. J. Rosa, & Al., Plasmas in mhd power generation, *IEEE Trans. Plasma Sc.*, 19(6), pp. 1180-1190, 1991.
[2] E. W. McDaniel, *Collision phenomena in ionized gases*, Wiley, N.Y., 1964.
[3] R. J. Rosa, *Magnetohydrodynamic energy conversion*, Hemisphere Pub. Corp, Washington, 1987.
[4] J. Koester, R. Perkins, Discharge and corrosion characteristics of slagging metal electrodes for MHD power generator, *En. J. of Materials for Energy Systems*, 1(2), pp. 41–54, 1979.
[5] S. Carcangiu & Al., Performance analysis of an inductive MHD generator, *Magnetohydrodynamics*, 48(1), pp.3–11, 2012.

MHD ISSUES RELATED TO THE USE OF LITHIUM LEAD EUTECTIC AS BREEDER MATERIAL FOR BLANKETS OF FUSION POWER PLANTS

AIELLO[1] G., MISTRANGELO[2] C., BÜHLER[2] L., MAS DE LES VALLS[3] E., AUBERT[1] J., LI-PUMA[1] A., RAPISARDA[4] D., DEL NEVO[5] A.
[1]CEA-Saclay, DEN/DANS/DM2S, 91191 Gif Sur Yvette Cedex, France
[2]Karlsruhe Institute of Technology, Postfach 3640, 76021 Karlsruhe, Germany
[3]UPC-BarcelonaTech, C. Jordi Girona, 31. 08034 Barcelona, Spain
[4]Laboratorio Nacional de Fusión, CIEMAT, Avda. Complutense 40, 28040 Madrid, Spain
[5]ENEA UTIS-TCI, C.R. Brasimone, 40032 Camugnano, Italy

Abstract: The European Community is committed to the development of a DEMOnstration fusion power plant whose operation could start as soon as 2050. The blanket is one of the most critical components in a fusion reactor; three of the four blanket concepts currently under development are based on the use of the liquid eutectic alloy Pb-15.7Li. Since the blanket will operate under the strong magnetic field used to confine the plasma, electromagnetic forces will occur in the PbLi flow giving rise to magnetohydrodynamic (MHD) phenomena.

1. Introduction

In the constant search for new power sources, thermonuclear fusion could be the ideal solution to satisfy world's energetic needs for the next centuries. The European Community is committed to the construction and operation of the International Thermonuclear Experimental Reactor ITER that is being built in Cadarache (France). ITER will be the first fusion experiment to produce net power although this power will not be used to generate electricity. This is the objective of the next generation device, the DEMOnstration power plant that will demonstrate the production of electrical power and tritium fuel self-sufficiency [1]. One of the most critical components in a fusion reactor is the breeding blanket, the first structure directly exposed to the plasma and submitted to extremely severe operating conditions in terms of heat load and neutron damage. Its characteristics have a major impact on the overall plant design, performance, availability, safety and environmental aspects. After recalling the basic principle of fusion power, this paper will present the blanket concepts studied in the EU based on the use of the liquid metal eutectic Pb-15.7Li (PbLi afterwards). The general MHD issues to be solved in fusion blankets and their specific impact on each blanket concept will then be discussed.

2. The Tokamak configuration and the breeding blanket

In a Tokamak [2] fusion reactor the plasma is contained in a torus-shaped vacuum vessel and confined by an helical magnetic field, which is a combination of a magnetic field maintained in the direction of the magnetic axis by toroidal field (TF) coils and a poloidal magnetic field produced by high toroidal electric currents induced in the plasma ring by an external transformer (the central solenoid). Horizontal poloidal coils are needed to finally succeed in closing the magnetic field lines and to achieve plasma stability (Figure 1). The toroidal magnetic field and the poloidal field must be generated by superconducting magnets with a magnetic field up to 13T.

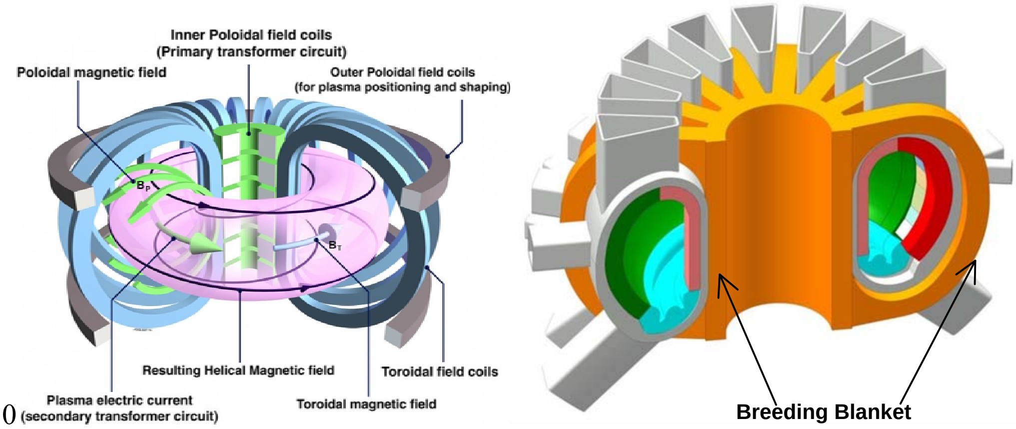

Figure 1: The tokamak concept and the breeding blanket.

The most suitable reaction for practical exploitation of nuclear fusion is the one between deuterium and tritium: $^2D + ^3T \rightarrow ^4He + n$. The amount of natural tritium is however not sufficient to sustain a reactor, but neutrons produced in the D-T fusion can lead to tritium generation when captured by lithium isotopes: lithium compounds must therefore be present in the structure surrounding the plasma (the blanket) in order to regenerate (breed) the tritium, hence the term ‘breeding blanket’. The blanket is the first structure exposed to the plasma (Figure 1). It has also the functions of converting the energy of fusion neutrons into heat suitable for electricity generation and protecting the reactor components and in particular the superconducting coils from excessive radiation damage. The blanket is the key ‘nuclear’ component in a fusion reactor.

Among liquid breeders, the eutectic alloy PbLi is now considered as the reference choice. Compared to solid breeders the liquid ones have a number of inherent advantages, such as high thermal conductivity, practical immunity to irradiation damage, the possibility to transport the breeder material outside the blanket for tritium extraction, and, in general, they allow relatively simple blanket designs. The main problems of liquid metal breeder blankets are safety concerns due to the chemical reactivity of the liquid metal, activation products, tritium control and the influence of a strong magnetic field on liquid metal flows. The latter point is further discussed in this paper.

3. Critical MHD issues in fusion blankets

Critical issues related to MHD interactions of the moving PbLi with the magnetic field are due to occurrence of increased pressure drops and special flow distributions. A review of MHD issues can be found for instance in [3]. Non-dimensional groups relevant to MHD flows are the Hartmann number Ha and the interaction parameter N. The former one gives a dimensionless measure for the strength of the magnetic field B. N describes the relative importance of Lorentz forces compared to inertia. MHD flows for fusion applications are characterized by intense magnetic fields B ($Ha \geq 10^4$) and small or moderate liquid metal velocities ($N = 10^4$-10^5). The described MHD phenomena are present in all liquid metal blankets but their impact on system performance is concept-specific. Of the four blanket concepts presently studied in the EU [4], 3 are based on the use of the PbLi eutectic (Figure 2): the Helium Cooled Lithium Lead (HCLL), the Dual Coolant Lithium Lead (DCLL) and the Water Cooled Lithium Lead (WCLL).

Blanket concept	*Critical MHD issues*
ALL	• 3D MHD pressure drop (bend, manifolds, non-uniform *B*,…) • (Mixed) Magneto-convection • MHD enhanced corrosion
HCLL	• Electric and thermal flow coupling • Uniform flow distribution in BUs (manifold design)

DCLL	• Pressured drop reduction by insulation
	• Turbulence and instabilities in long ducts
	• Flow imbalance in parallel channels
	• Specific FCI-related flow features:
	    • Flow in gap between wall and FCI
	    • Need and influence of pressure equalization slot/holes
	    • Effects of FCI junctions/gaps/cracks

WCLL	• Complex flow path around cooling tubes • Electrical coupling of parallel ducts • Uniform flow partitioning

Table 1 Main MHD issues for proposed blanket concepts

Pressure drops that balance electromagnetic forces in MHD flows are proportional to the electric current density j induced in the fluid. The magnitude of j depends on the resistance of the current path, which is determined by the wall conductivity in electrically conducting ducts and by the conductivity of thin viscous layers in insulating channels. Therefore, in the latter case minimum current density is achieved. This explains why MHD pressure drop reduction is obtained by electrically decoupling walls and fluid by means of suitable insulation.

For $Ha >> 1$ and $N >> 1$ the flow is most likely laminar and the velocity is uniform in the core, where electromagnetic and pressure forces balance each other, and viscous effects are confined to very thin boundary layers. In electrically conducting channels high-velocity jets are present in layers parallel to B. In turns, this may affect corrosion of the structural materials [5]. A slug flow is instead expected in insulated ducts.

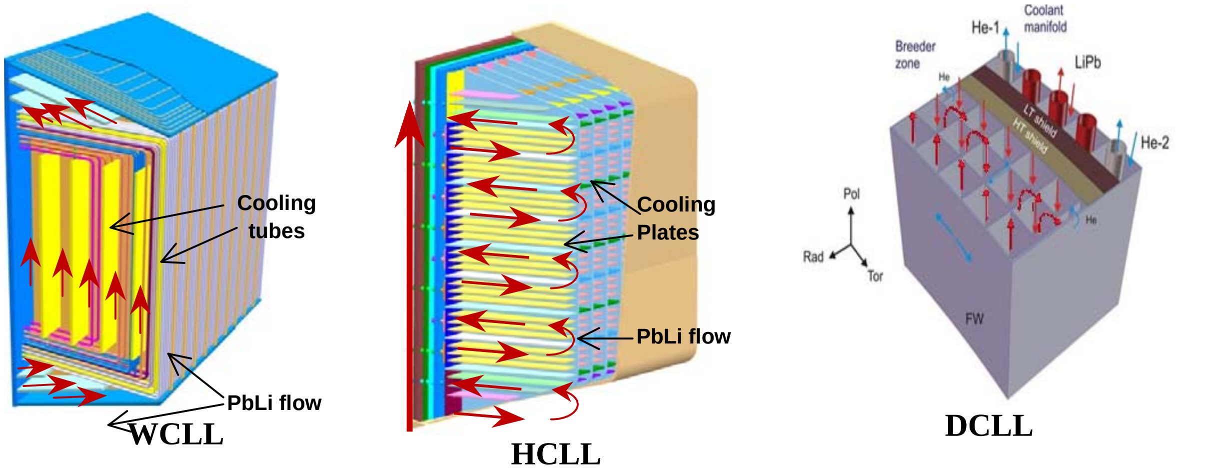

Figure 2: Blanket concepts based on the use of Pb15.7Li

4. Concept specific MHD issues in EU blankets

The 3 EU blanket concepts presently under consideration share the same configuration. The blanket is divided in several modules arranged to follow as close as possible the plasma shape. Each module is constituted by a Eurofer steel box reinforced by an internal grid of stiffening plates to withstand the pressurization of the box in case of accident. In the volume inside the box (the ‘breeding zone’ – BZ), the grid defines a system of channels for the flow of the PbLi whose characteristics are specific to each blanket concept. The 3 designs can be classified by the increasing difficulties and advantages they present. The WCLL uses water in pressurized water reactor (PWR) conditions (285-325°C, 15.5 MPa) for cooling, which would allow re-using part of the technology known from fission power plants. The HCLL uses instead Helium (300°C-500°C, 8 MPa), which allows higher coolant temperatures and enhanced efficiencies of the power conversion cycle. The DCLL concept uses He but also PbLi as coolant which permits achieving even higher temperatures (≥ 700°C).

<u>4.1 Water Cooled Lithium Lead (WCLL) blanket.</u> In the WCLL blanket [6] the PbLi enters from the rear of the module in the bottom part, it flows toward the FW, goes upward in the square channels formed by the stiffening grid, then backward in the top part of the module. The BZ is cooled by tubes bathing in the PbLi flow to collect the thermal power deposited by neutrons. Some plates have been foreseen at the module bottom and top to orientate the flow. Velocities are of the order of 5-10 mm/s. In this blanket concept, from the MHD point of view one should consider magneto-convection in long vertical channels, flows in ducts with internal obstacles, represented here by cooling tubes, and pressure drop in distributing and collecting manifolds. Another important issue is the uniform distribution of Pb-Li in parallel ducts. Flow imbalance should be avoided to guarantee uniform distribution of tritium concentration. Moreover, it has to be ensured that enough liquid metal reaches the FW and no recirculation or stagnant zones form. Numerical simulations are therefore required to predict MHD pressure drop and velocity distribution.

<u>4.2. Helium cooled Lithium Lead (HCLL) blanket.</u> In the HCLL blanket concept [7] the stiffening plates define a grid of elementary cells, called Breeding Units (BU), that are cooled by means of parallel Cooling Plates. All BUs in a column are fed in parallel through a vertical manifold on the back of the module. The inlet chamber feeds one out of two BUs then the Pb-Li flows towards the FW, goes to the BU immediately above and then horizontally flows to the outlet chamber at the back. MHD phenomena typical of HCLL blankets are related to electric and thermal flow coupling of neighboring channels. The so-called "multi-channel effect" depends on wall electric conductivity, flow direction and orientation of B. Electric flow coupling can be exploited for supporting uniform flow partitioning in BUs [8]. It has been shown experimentally that pressure drop in BUs is not an issue due to the small velocities. Results have been extrapolated to ITER TBM and a total pressure drop lower than 0.3MPa has been estimated [9]. However, in a blanket module many BUs are fed by a single manifold where velocities may reach large values. Here significant 3D MHD effects and pressure losses can occur. Simulations for MHD flows in HCLL model geometries showed also that natural convection can be intense resulting in large fluid recirculation and convective instabilities [10,11,12].

<u>4.3. Dual coolant Lithium Lead (DCLL) blanket</u>. In the DCLL blanket [13] the PbLi flows poloidally in the channels defined by the stiffening grid without any additional cooling. In order to reduce pressure drop caused by MHD interactions, poloidal Pb-Li channels are insulated by flow channel inserts (FCIs) made of sandwiched ceramic materials or SiC_f/SiC that ensure the electrical decoupling of the liquid metal from the channel walls. However, the impact of 3D MHD effects on pressure and velocity distribution has to be still thoroughly studied. 3D MHD flows that play a fundamental role in determining additional pressure drops are those in manifolds [14], in non-uniform magnetic fields, at junctions between FCIs [15],

near gaps or holes for pressure equalization [16], close to possible cracks [17]. In [14] MHD pressure drop in a DEMO DCLL blanket were estimated. It was highlighted that available empirical formulations used for 3D MHD pressure drops Δp_{3D} were not derived for geometries comparable to the manifold design. Therefore the contribution of the 3D flow to Δp_{3D} in this component remained the main uncertainty. Further studies are needed [18]. Due to imperfect insulation provided by FCI higher velocities are present in parallel boundary layers which can be destabilized leading to occurrence of turbulence. Recent calculations show the importance of mixed magneto-convection in the DCLL blanket [19]. FCI thermal and electrical properties and thickness have strong influence on MHD pressure drop, velocity profile and thermal blanket efficiency. Thus, the correct design of such FCI is of crucial interest [16].

5. Conclusions

MHD phenomena in PbLi-based fusion blankets change heat-transfer characteristics, pressure drop and the required pumping power for circulating the liquid metal. They also influence mass transport characteristics, affecting in turns tritium permeation and corrosion kinetics. Considerable efforts, both in modeling and experiments, have been made in the past years to investigate MHD issues in liquid metal blankets. Further efforts should be directed to enlarging our knowledge of MHD and heat transfer phenomena in channels of complex geometry but also in straight channels with perfect and non-perfect electro-insulated walls. In parallel, the use of dedicated experimental facilities and the development of more sophisticated predictive capability tools to perform fully coupled 3D numerical simulations should be pursued.

References

[1] F. Romanelli et al., Fusion Electricity: A roadmap to the realisation of fusion energy, EFDA, 2012.

[2] John Wesson. Tokamaks. Oxford Science Publications, 2004 .

[3] S. Smolentsev, R. Moreau, L. Bühler and C. Mistrangelo, MHD thermofluid issues of liquid-metal blankets: Phenomena and advances, Fusion Engineering and Design, vol. 85, pp. 1196-1205, 2010.

[4] A. Li Puma et al., Design and Development of DEMO Blanket Concepts in Europe. To be published in Fus. Eng. & Des.

[5] R. Moreau, Y. Bréchet, L. Maniguet, Eurofer corrosion by the flow of the eutectic alloy Pb–Li in the presence of a strong magnetic field, Fus. Eng. Des., Volume 86, Issue 1, January 2011, Pages 106-120.

[6] J. Aubert, G. Aiello, N. Jonquères, A. Li Puma, A. Morin, G. Rampal, Development of the water cooled lithium lead blanket for DEMO, to be published on Fus. Eng. Des.

[7] G. Aiello, J. Aubert, N. Jonquères, A. Li Puma, A. Morin, G. Rampal, Development of the Helium Cooled Lithium Lead blanket for DEMO, to be published on Fus. Eng. Des.

[8] C. Mistrangelo and L. Bühler, Electric Flow Coupling in the HCLL Blanket Concept, Fus. Eng. Des., vol. 83, pp. 1232-1237, 2008.

[9] C. Mistrangelo and L. Bühler, MHD Mock-Up Experiments for Studying Pressure Distribution in a Helium Cooled Liquid-Metal Blanket, IEEE Transactions on Plasma Science, vol. 38, no. 3, pp. 254-258, March 2010.

[10] C. Mistrangelo and L. Bühler, Magneto-convective flows in electrically and thermally coupled channels, Fus. Eng. Des., Volume 88, Issues 9–10, pp. 2323–2327, 2013.

[11] E. Mas de les Valls, L. Batet, V. de Medina, J. Fradera and L.A. Sedano, Modelling of integrated effect of volumetric heating and magnetic field on tritium transport in a U-bend flow as applied to HCLL blanket concept, Fus. Eng. Des., vol 86, pp. 341-356, 2011.

[12] E. Mas de les Valls, L. Batet, V. de Medina and L.A. Sedano, MHD thermofluid flow simulation of channels with uniform thermal load as applied to HCLL breeding blankes for fusion technology, Magnetohydrodynamics, vol 48, no. 1, pp. 157-168, 2012.

[13] E. Mas de les Valls, L. Batet, V. de Medina, J. Fradera, M. Sanmartí and L.A. Sedano, Influence of thermal performance on design parameters of a He/LiPb dual coolant DEMO concept blanket design, Fus. Eng. Des., vol. 87, pp. 969-973, 2012.

[14] L. Bühler and P. Norajitra, Magnetohydrodynamic Flow in the Dual Coolant Blanket, Forschungszentrum Karlsruhe FZKA 6802, 2003.

[15] L. Bühler and C. Mistrangelo, Influence of non-insulated gaps between flow channel inserts in ducts of DCLL blankets, in Proceedings of 25th Symposium on Fusion Engineering, June 11-14, San Francisco, 2013.
[16] S. Smolentsev, N. B. Morley and M. Abdou, "Magnetohydrodynamic and Thermal Issues of the SiCf/SiC Flow Channel Insert," Fusion Science and Technology, vol. 50, no. 1, pp. 107-119, 2006.
[17] L. Bühler, The influence of small cracks in insulating coatings on the flow structure and pressure drop in MHD channel flow, Fus. Eng. Des., vol. 27, pp. 650-658, 1995.
[18] C. Mistrangelo and L. Bühler, Liquid metal magnetohydrodynamic flows in manifolds of dual coolant lead lithium blankets, in Proceedings of the 11th International Symposium on Fusion Nuclear Technology, 16-20 September, Barcelona, 2013.
[19] S. Smolentsev, N. Vetcha and R. Moreau, Study of Instabilities and Transitions for a Family of Quasi-Two-Dimensional Magnetohydrodynamic Flows Based on a Parametrical Model, Physics of Fluids, vol. 24, p. 024101, 2012.

EFFECTS OF BROKEN SYMMETRY IN TURBULENT OR CHAOTIC SYSTEMS

PROCTOR[1] M., RUCKLIDGE[2] A., HUGHES[2] D.
[1]DAMTP, University of Cambridge, UK
[2]Applied Mathematics, University of Leeds, UK
E-mail: mrep@cam.ac.uk

A number of authors (e.g Courvoisier et al. 2010, Zheligovsky 2011) have discussed the problem of long-wavelength instabilities of fully developed but homogeneous MHD states. This involves the construction of coupled mean-field momentum and induction equations whose coefficients depend on averaged properties of the undisturbed state. While in very simple cases there is a possiblility that the coefficients can be calculated, generally they have to be computed by applying a perturbation (for example a uniform magnetic field) to the basic state and measuring the response. Even though the dynamics is typically highly nonlinear and the response to even a very small perturbation typically finite in detail, one might hope that there are sensible mean responses, linear in the perturbation amplitude that can be captured by averaging. We have looked at a number of dynamical systems, both maps and ODEs as well as time dependent basic MHD states with an original average symmetry to see if this supposition is justified by adding small symmetry-breaking terms and investigating the average response. We find that it is not always possible to get a sensible answer and that what happens depends of the nature of the chaos in the basic state. This is compared with similar problems where the 'chaos' is not internal, but driven by random processes.

References

[1] Courvoisier, A, Hughes, D.W. and Proctor, M.R.E.: Self-consistent mean-field MHD. Proc. Roy. Soc. A466, 583-601, 2010.
[2] Zheligovsky, V.: Large-Scale Perturbations of Magnetohydrodynamic Regimes. Springer-Verlag, 2011

EXPERIMENTAL INVESTIGATION OF THE LORENTZ FORCE RESPONSE TO THE TIME-DEPENDENT VELOCITY INPUT WHILE CONSIDERING FINITE MAGNETIC REYNOLDS NUMBER

SOKOLOV I., THESS A., KOLESNIKOV Y.
TU Ilmenau, Max-Planck-Ring 7, 98693 Ilmenau, Germany
E-mail: igor.sokolov@tu-ilmenau.de

Abstract: The Lorentz force velocimetry is a set of well-known techniques which are used to investigate velocity profiles or mass flux in channels filled with a liquid metal [1]. The technique is based on a linear dependence between Lorentz force and a conductor velocity. Usually, magnetic Reynolds number has to be small enough to keep this dependence linear. An increase of magnetic Reynolds number gives rise to the magnetic field distortion that makes Lorentz force velocimetry complicated. The presentation explains the dynamics of the Lorentz force at finite magnetic Reynolds number and shows the results of the magnetic field sweeping measurements.

1. Introduction

When an electrically conducting material moves across magnetic field lines, eddy currents are induced in the conductor. These currents carry an additional magnetic field which leads to a deformation of the applied magnetic field lines [1], [2]. As a consequence, the conducting material experiences a braking Lorentz force. The key point is that the Lorentz force is proportional to the conductor velocity. It means that having measured this force the velocity can be calculated. Although the method is very promising because it is accurate and contactless, it can be applied only if a primary magnetic field is not affected by a conductor. If the velocity is high, a secondary magnetic field created by eddy currents becomes strong enough to change the initial magnetic field distribution that leads to a nonlinear Lorentz force - velocity dependence. This phenomenon can be characterized by the magnetic Reynolds number Re_m which is finite in that case. The goal of this work is to study experimentally an error in the Lorentz force velocimetry due to finite Re_m effects as well as to show that the Lorentz force can be a powerful instrument to study an MHD task.

2. Problem definition

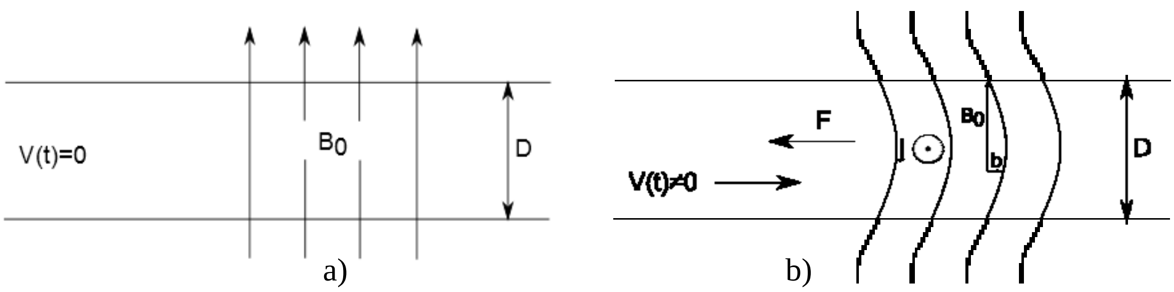

Figure 1: Sketch of the problem.

A problem studied here is sketched in fig. 1. A solid rod moves with a time-dependent velocity through a transverse magnetic field B_0, created by permanent magnets. If the rod experiences no motion, the applied magnetic field is not distorted (fig. 1a). In case of non-zero velocity, eddy currents j ensue that leads to a primary magnetic field disturbance by the induced magnetic field b (fig. 1b).

An interaction between the induced magnetic field and eddy currents gives rise to the Lorenz force F, which opposes the flow. The effects of magnetic field perturbation can be observed if magnetic Reynolds number Re_m is high enough. One possibility to obtain finite Re_m is to increase rapidly the velocity of the rod which moves through a transverse magnetic field, so that the acceleration (advection) time t_{adv} is several times smaller than the diffusion time, i.e.:

$$\mathrm{Re}_m = \frac{\mu\sigma D^2}{t_{adv}} \sim 1, \tag{1}$$

where μ is a magnetic permeability, σ is an electrical conductivity and D is a characteristic length (fig. 1b).

3. Experimental setup

The experimental setup (fig. 2) consists of two thick aluminium plates with a piezoelectric force sensor mounted between them. On the top plate there is a magnetic Halbach array which creates a constant transverse magnetic field in the range from 0 to 1 T depending on the distance between magnets. A hole 20 cm in diameter was made in the centre of the plates so that a thick massive solid rod could easily go through. Additionally, an array from 7 Hall sensors was installed in the area between the magnets and the rod for the induced magnetic field measurements. The velocity of the rod is controlled by a computer with 1 kHz frequency so that it can be changed from 0 to 1 cm/s within 60 ms (fig. 3a). By this setup we can measure simultaneously the Lorentz force acting on the rod and the magnetic field distortion by the induced magnetic field.

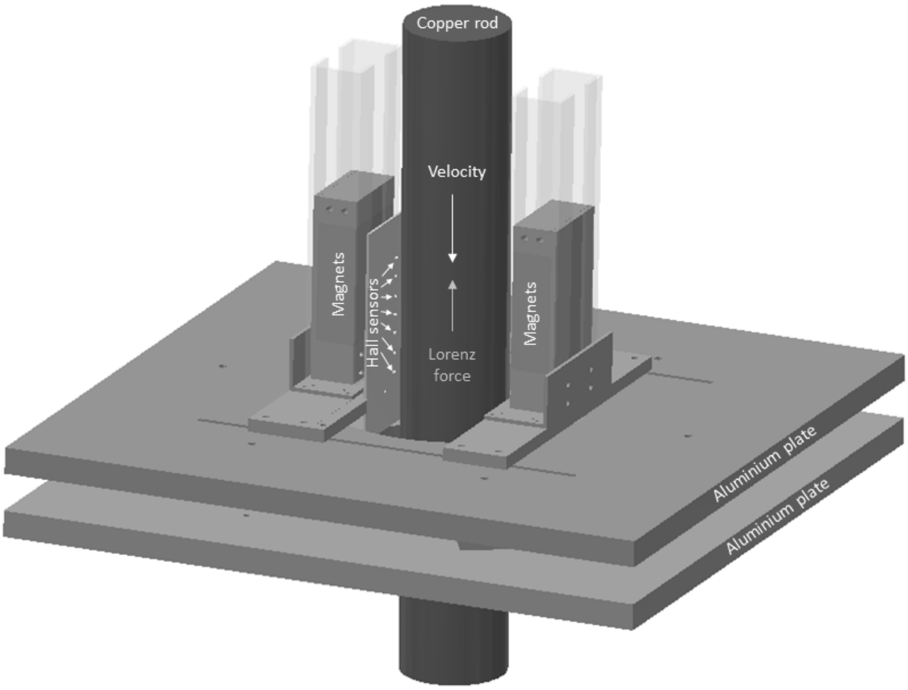

Figure 2: Experimental setup.

4. Measurement results

We measured Lorentz force as a function of the maximum rod velocity at different magnetic Reynolds numbers Re_m and different aspect ratios $D^* = D/L$ (L is the distance between magnets) for copper and aluminium rods (fig. 3b). The time response of Lorentz force is in good agreement with an analytical model developed in [3]. A decrease in Lorentz force at finite Re_m is explained by the magnetic field distortion due to the influence of the induced magnetic field b generated by eddy currents which circulate mainly in the area, where the magnetic field is non-uniform.

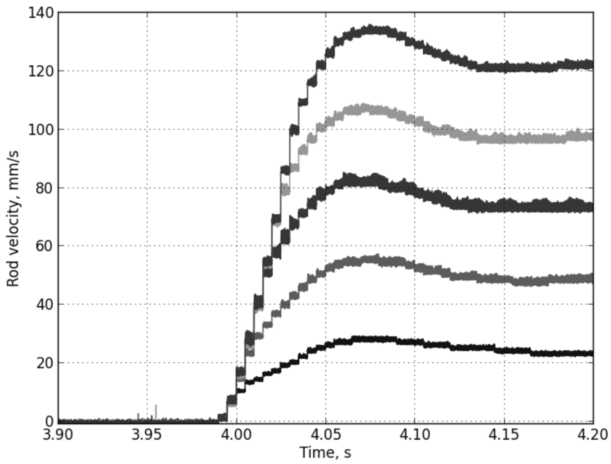

a)

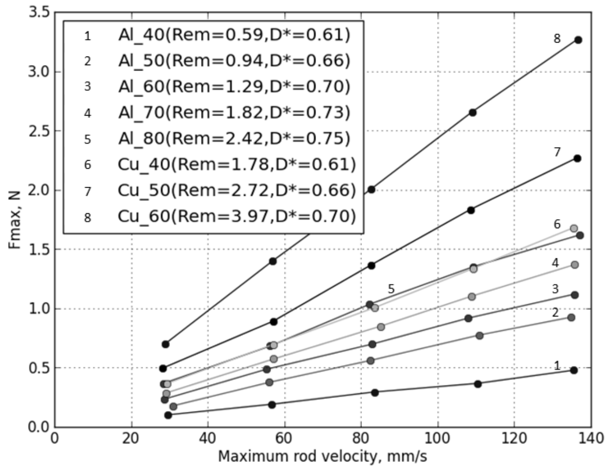

b)

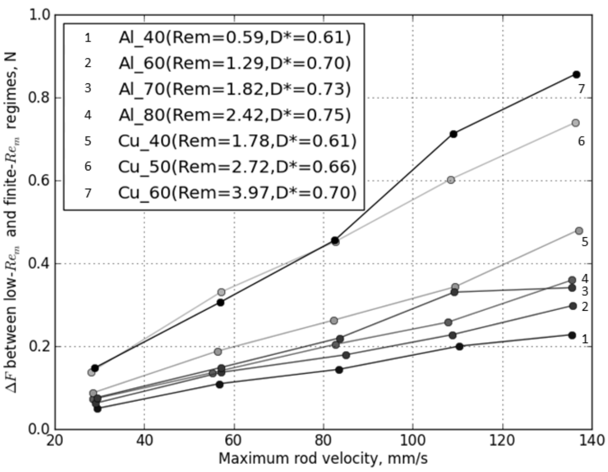

c)

Figure 3: 5 different signals of the rod velocity (a), the maximum Lorentz force acting on the rod as a function of velocity at different Re_m and D* (b), and the difference between low-Re_m and finite-Re_m cases (c).

The actual force was compared with the values obtained at low-Re_m regime (fig. 3c). As we expected, due to the magnetic field distortion, there is a drop of the Lorentz force in comparison with low-Re_m case. This difference increases if Re_m becomes higher.

Fig. 4a shows that by means of the Lorentz force it is possible to measure the energy which is dissipated inside the conductor:

$$\frac{d}{dt}\int \rho v^2 dV = -\frac{1}{\sigma}\int j^2 dV \sim F_L \cdot v \qquad (2)$$

We note that a higher Re_m leads to a smaller time response of the system. The response is measured by non-dimensional reaction time T98* which shows how fast the Lorentz force rises from 0 to 98% of its asymptotic value. It was shown that T98* strongly decays as a function of Re_m (fig. 4b). This stems from a general concept of a frozen state of magnetic field lines in a conductor when Re_m becomes finite or big.

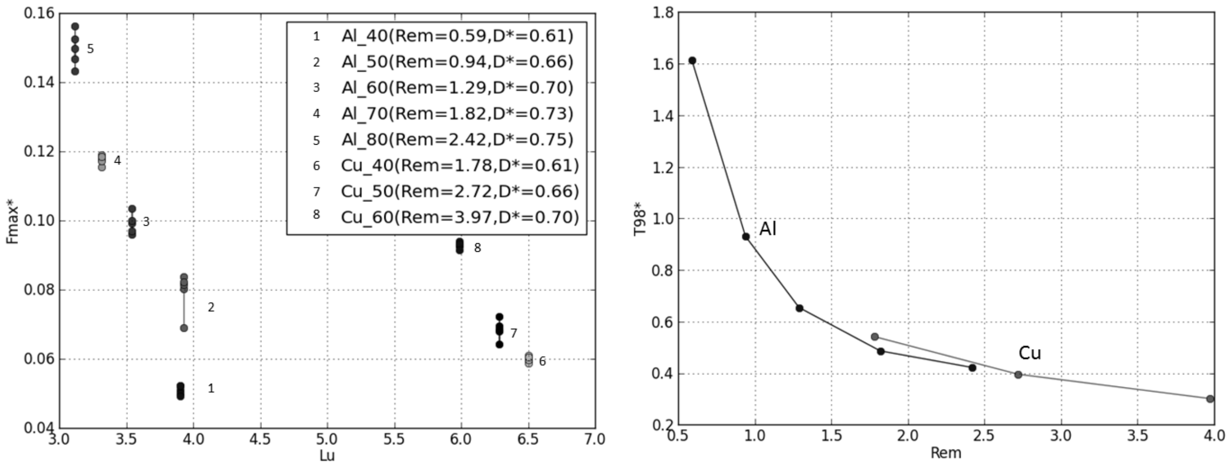

a) b)

Figure 4: The maximum of the nondimensional Lorentz force as a function of the Lundquist number at different Re_m and D* (a) and the nondimensional saturation time T_{98}* for different Re_m (b).

We have also measured $\partial B / \partial t$ (fig. 5a) which is linked with the eddy currents in the rod. Before the onset of the motion there is no induced magnetic field. But as soon as the rod starts to move, eddy currents ensue giving rise to the Lorentz force and to the induced magnetic field which deforms the applied one.

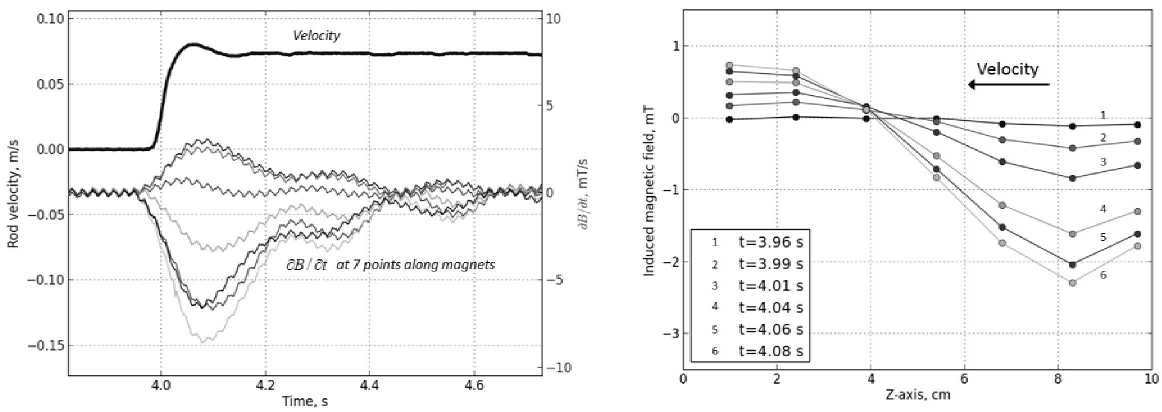

a) b)

Figure 5: Time-derivative of the induced magnetic field (a) and its evolution in time (b).

The evolution in time of the induced magnetic field is shown on figure 5b. It was observed that the rod drags magnetic field lines until the equilibrium between magnetic field advection and diffusion is achieved.

5. Conclusion

The Lorentz force response for a solid conductor to a time-dependent velocity input at finite magnetic Reynolds number has been studied. It was shown there is a difference between the values of the force in low-Re_m and finite-Re_m cases. The difference is explained by the fact that eddy currents create the induced magnetic field which distorts the primary one. This distortion has been measured by an array of Hall sensors and it was observed that the conductor drags the magnetic field lines along the travelling direction.

6. References

[1] Thess, A.; Votyakov, E.; Kolesnikov, Y.: Lorentz Force Velocimetry, Phys. Rev. Lett. 96 (2006) 164501.

[2] Weiss, N.: The expulsion of magnetic flux by eddies, P. Roy. Soc. A-Math. Phy. 293 (1966) 1434.

[3] Weidermann, Chr.; Sokolov, I.; Thess, A.: Lorentz force and Joule heat induced in an electrically conducting plate moving with time-dependent velocity under the influence of a homogeneous magnetic Field, IEEE Transactions on Magnetics, (2014) (in press).

INDUCTION-DRIVEN CONTACTLESS ACOUSTIC WAVE GENERATION IN A CRUCIBLE

PERICLEOUS K., LEBON B., DJAMBAZOV G., BOJAREVICS V.
University of Greenwich, UK
E-mail: K.Pericleous@gre.ac.uk

Ultrasound treatment is used in light alloys during solidification to refine microstructure, or disperse immersed particles. The process is driven by immersing a sonotrode probe into the melt and it is most effective when the probe vibrations lead to cavitation. The same method cannot be used in high temperature melts, or in the treatment of highly reactive alloys, where contact with the probe will lead to contamination. As an alternative, a contactless method of generating sound waves is investigated theoretically, using electromagnetic (EM) induction. An additional advantage of the EM method is the strong induced stirring of the melt due to Lorentz forces that distributes the effect and has the potential to treat large volumes of material. In a typical application, the induction coil surrounding the crucible - also used to melt the alloy - may be adopted for this purpose with suitable tuning. Under normal use, the vibrations induced by the induction coil are not sufficiently strong to induce cavitation in the liquid with any gas inclusions present. However, by tuning the induction coil frequency to the melt volume, sound resonance can be achieved leading to large amplitude sinusoidal pressure variation. As shown by Vives [1], large amplitudes leading to cavitation can also be effected by combining the AC induction field with a strong DC field.

Numerical simulations testing this sound generation mechanism have been performed for various cases, with and without resonance in the melt volume, with and without an auxiliary DC field. A computational hydrodynamic acoustics approach is coupled with Maxwell’s equations, and likely cavitation zones are identified using the Rayleigh-Plesset equation [2]. Near-resonance conditions are most likely to produce cavitation without mechanically endangering the crucible.

Acknowledgments. The authors acknowledge financial support from the ExoMet Project (co-funded by the European Commission (contract FP7-NMP3-LA-2012-280421), by the European Space Agency and by the individual partner organizations).

References

[1]. Vives, C.: J. Crystal Growth, vol. 158, 1–2, pp 118–127, 1996.
[2]. Plesset, M.S., Hsieh, D.Y.: Theory of gas bubble dynamics in oscillating pressure fields, Phys Fluids, 3, 882-892 (1960).

INVESTIGATION OF ACOUSTIC STREAMING JETS IN LIQUID

B. Moudjed[1], V. Botton[1], D. Henry[1], H. Ben Hadid[1] and A. Potherat[2]
[1] Laboratoire de Mécanique des Fluides et d'Acoustique, LMFA UMR5509 CNRS
Université de Lyon, École Centrale de Lyon, INSA de Lyon, Université Lyon I,
ECL 36 avenue Guy de Collongue, 69134 Ecully Cedex, France
brahim.moudjed@insa-lyon.fr
[2] AMRC, Applied Mathematics Research Center, Coventry University, Priory Street,
Coventry CV1 5FB, United-Kingdom

Abstract: The present paper performed a theoretical study of acoustic streaming. The approach is based on the time scale separation method where the streaming jet is considered varying very slowly in time compared to the acoustic period. An acoustical force is introduced in the Navier-Stokes equations and ensures the coupling between sound propagation and hydrodynamics. Dimensional analysis is used to give first clues for the theory of physical modeling. Through scaling analysis, two scaling laws featuring linear and square root variations of the streaming velocity level with the acoustic power have been found.

1. Introduction

"Not only motion can create sound but also sound can create motion" [1]. This sentence by Sir J. Lighthill explains in a few words what acoustic streaming is: the possibility of driving stationary and quasi-stationary flows using acoustic waves. This phenomenon can be present in many applications ranging from biomedical applications (low intensity ultrasounds based diagnostics and high intensity ultrasounds based treatment) to engineering applications (sonochemisty, velocimetry and potentially crystal growth).

Acoustic streaming is often presented as a second order flow with respect to acoustic as explained by Nyborg [2] on the basis of a small perturbation approach. However, this method seems to be limited because of two reasons. Firstly, assuming streaming velocity of second order leads to a motion equation featuring an acoustical force, pressure gradient and viscosity terms but negligible inertial terms since these are of fourth order. Secondly, in several experimental observations [3, 5], acoustic streaming velocities is not of second order with respect to the acoustic velocity wave propagation. Lighthill [1] suggested thus that this development is suitable for creeping motion which he characterizes with a Reynolds number less than one; for the other Reynolds number, he proposed to introduce inertial terms artificially.

Here, a new approach is proposed. First, we developed a scale separation method as an alternative to Nyborg's approach. Then, we focused to a dimensional analysis in order to consider an application to liquid metals. Finally, a scaling analysis of acoustic streaming jet provides flow velocity evolution as a function of the governing parameters of the problem.

2. Time scale separation method

Each variable (velocity, density and pressure) of the acoustic streaming problem is split into an acoustic part, varying rapidly, and a streaming motion part, varying very slowly compared to the acoustic part: it's the time scale separation method. Introducing these variables into the incompressible Navier-Stokes equation and averaging over an acoustic period, like RANS computation, we find:

$$\begin{cases} div\vec{u}_e = 0 \\ \rho \dfrac{d\vec{u}_e}{dt} = -gradp_e + \mu\Delta\vec{u}_e + \vec{f}_{ac} \,, \\ f_{ac,i} = -\rho div\left(\overline{u_{ac,\iota}\vec{u}_{ac}}\right) \end{cases} \tag{1}$$

where $\vec{u}_e$ represents the flow velocity, $\vec{u}_{ac}$, the acoustic wave velocity, p_e, the hydrodynamic pressure and ρ the fluid density. The additional volumetric force term $\vec{f}_{ac}$ in the incompressible Navier-Stokes equations ensures a coupling between the acoustic propagation and the hydrodynamic flow. This acoustic streaming force must be computed from the spatial variations in acoustic field, which are an output of the acoustic propagation problem. A commonly accepted expression, valid under the plane wave approximation, is:

$$\vec{f}_{ac} = \frac{2\alpha}{c} I_{ac}\vec{x}, \tag{2}$$

where I_{ac} is the acoustic intensity. Through this expression is not new [2], the time scale separation approach allows it to appear naturally in the full incompressible Navier-Stokes equations, which is consistent with experimental observations [3, 5]

3. Dimensional analysis

Since the pioneering work done by Eckart [6], a classical modeling approach is to consider acoustic streaming as the weak coupling between two sub-problems: acoustic propagation and the hydrodynamic flow. The first sub-problem, the acoustic propagation, consists in the description of the acoustic beam; in the framework of linear acoustics, the inputs for this problem are the ultrasounds source diameter d_s, frequency f, and power P_{ac}, and the liquid acoustic properties, *i.e.* sound celerity c, and acoustic attenuation coefficient α. The hydrodynamics sub-problem consists in the description of the quasi-steady flow driven by acoustic streaming; the inputs for this problem are the geometry of the fluid domain and the liquid mechanical properties, namely its kinematic viscosity ν, and density ρ. Ten dimensional variables are thus used; they are listed in table 1 with their corresponding usual units. The Vashy-Buckingham theorem implies that a set of seven dimensionless groups are necessary to describe the whole problem of acoustic streaming. We chose to define d_s, ν/d_s^2 and ρ/d_s^3 as characteristic distance, time and weight, respectively; this leads to the dimensionless groups listed in the last column of table 1.

Dimensional variable	Usual units	Fundamental units	Corresponding dimensionless groups
$N = \alpha/f^2$	$m^{-1}.Hz^{-2}$	$m^{-1}.s^2$	$\boldsymbol{N} = Nf^2L$
f	Hz	s^{-1}	$\boldsymbol{F} = fd_s^2/\nu$
$\lambda = c/f$	m	m	$\boldsymbol{S} = 1.22\lambda/d_s$
L, l et d_s	m	m	$\boldsymbol{L} = L/d_s$, $\boldsymbol{l} = l/d_s$
P_{ac}	W	$kg.m^2.s^{-3}$	$\boldsymbol{P} = P_{ac}d_s/(\rho\nu^3)$
U	$m.s^{-1}$	$m.s^{-1}$	$\boldsymbol{U} = Ud_s/\nu$
ν	$m^2.s^{-1}$	$m^2.s^{-1}$	-
ρ	$kg.m^{-3}$	$kg.m^{-3}$	-

Table 1: Variables of the acoustic streaming problem, their units and the corresponding dimensionless groups.

Each dimensionless parameter can be associated to a physical interpretation: $\boldsymbol{N}$ is a ratio between the length of the domain L and the typical attenuation distance $1/\alpha$, $\boldsymbol{F}$ is the dimensionless frequency and can be seen as a ratio of the period and the characteristic time for viscous diffusion of momentum at the scale d_s, $\boldsymbol{S}$ is typically the half angle of the diffraction cone of the sound beam, $\boldsymbol{L}$ and $\boldsymbol{l}$ are simply the ratios of the cavity length and width to the source diameter, $\boldsymbol{P}$ is the injected acoustic power normalized by a typical power dissipated by viscous effects and $\boldsymbol{U}$, the dimensionless velocity, is a local Reynolds number based on the observed velocity and the source diameter.

4. Toward the case of liquid metal

One of the difficulties when dealing with acoustic streaming in liquid metals is that the acoustic attenuation coefficient is not a very well-known property for this type of liquids. The acoustic attenuation coefficient in a liquid, α, is very often assumed to have three contributions. A first contribution is connected with the dynamical (or shear) viscosity μ, a second contribution is related to the bulk viscosity η, and a final contribution takes into account thermal effects. The expression proposed by Nash *et al.* [7] is:

$$N = \frac{\alpha}{f^2} = \frac{2\pi^2}{\rho c^3}\left(\frac{4}{3}\mu + \eta + \frac{c^2\beta^2\lambda T}{C_p^2}\right) \tag{3}$$

where f is the frequency, ρ is the density, c is the wave velocity, β is the thermal expansion coefficient, λ is the thermal conductivity, C_p is the specific heat, and T is the absolute temperature. The dynamical viscosity μ and the properties involved in the thermal contribution can generally be obtained for standard liquids with an acceptable accuracy, so that the main difficulty will come from the estimation of the bulk viscosity η.
We rely on this estimate of the attenuation coefficient, on the developed dimensional analysis and physical modeling techniques to assess the intensity of acoustic streaming expected in a liquid metal experiment. In particular, we consider the similarity of a hypothetic liquid metal set-up with our existing set-up [8]. We find that, under some assumptions, the similarity condition imposes the scale Σ, the ratio in frequency f, attenuation factor N and acoustic power P between the water-test and the liquid metal experiment. Under this condition the ratio in velocity observed in these apparatus is also given. Focusing on the case of liquid silicon and liquid sodium, featuring respectively a very high and a very low melting temperature, the similarity conditions is given in table 2.

	Scale Σ	f_{test}/f_{real}	$\boldsymbol{N}_{test}/\boldsymbol{N}_{real}$	$P_{ac,\ test}/P_{ac\ ,\ real}$	U_{test}/U_{real}
Silicon (1 750 K)	8.2	0.046	0.17	8.9	0.38
Sodium (393 K)	2.5	0.23	0.28	4.9	0.59

Table 2: Similarity conditions for a model experiment in water (subscript test) and a liquid metal experiment (subscript real). The case of silicon is considered in the first line, that of sodium in the second line.

Considering our set up as test experiment, the second line of table 2 shows that, in liquid sodium, a plane transducer of diameter 12 mm operating at 8.6 MHz would induce velocities on the order of 1.7 cm/s with an acoustic power of only 200 mW. Because of the scale Σ, we can also say that these velocities would be obtained after a smaller distance from the acoustic source. As mentioned earlier, this numerical application makes us think that it should be taken care of acoustic streaming side-effects when measuring small velocities by in ADV in liquid metals.

5. Scale analysis

We proposed in a recent paper [8] two scaling laws for acoustic streaming free jets, *i.e.* steady, laminar, acoustic streaming jets in a semi-infinite medium. As no confinement is considered and there is no reason for the jet to feature any significant curvature, the pressure gradient can safely be assumed not to play any significant role. The flow is thus governed by a balance between the combined effects of viscosity, inertia and the acoustic streaming force. We focus successively on the two asymptotic cases of negligible viscous effects and negligible inertia effects. Let us first consider the acceleration zone near the origin of the jet. We assume this region to be dominated by inertia effects, which balance the acoustic streaming force. the typical velocity u_e at a distance (x-x_0) from the origin of the jet is then expected to follow the following scaling law:

$$u_e \approx \kappa_1 \sqrt{\frac{2\alpha}{\rho c}\frac{P_{ac}}{\pi R_{ac}^2}(x - x_0)} \tag{4}$$

where κ_1 is a multiplicative factor of the order of 1.
Farther from the origin, we consider that the flow is nearly one-dimensional and ruled by the balance between the acoustic force and the viscous forces;

$$u_e \approx \kappa_2 \frac{\alpha P_{ac}}{\pi \mu c} \tag{5}$$

where κ_2 is a multiplicative factor of the order of 1. These two scaling are plotted in figure 1 with experimental data of Mitome [4], Frenkel *et al.* [5], Nowicki *et al.* [3] and Kamakura *et al.* [9] and for the present study. We see that the set of experimental data is in reasonable agreement with the proposed scaling laws and that both scaling laws are observed.

6. Conclusion

Acoustic streaming is a coupling between an acoustic propagation and an incompressible flow ensured by an acoustical force term (eq. (2)) in the Navier-Stokes equation. A time scale separation method was developed to derive this force expression. It consists in separating the short time scale of the acoustic propagation from the long time scale of the hydrodynamic flow. The same acoustical force expression than Nyborg was obtained, but our approach is more consistent with experimental observations: flow velocity is not of second order with respect to the acoustic velocity. Moreover, equations of motions thus naturally feature inertial terms. Ten dimensional variables are present in the acoustic streaming problem. Following this, seven dimensionless parameters are proposed to describe the whole acoustic streaming problem and make similarities with experimental set up with other liquid. In particular, it was found that flow velocity reached in Silicon and Sodium are respectively 2.5 and 1.5 times higher with an acoustic power 9 and 5 times lower. Finally, two velocity scaling laws are obtained for the streaming flow and plots of experimental measurements of the present work and former studies show the reliability of the scaling analysis in the range of parameters.

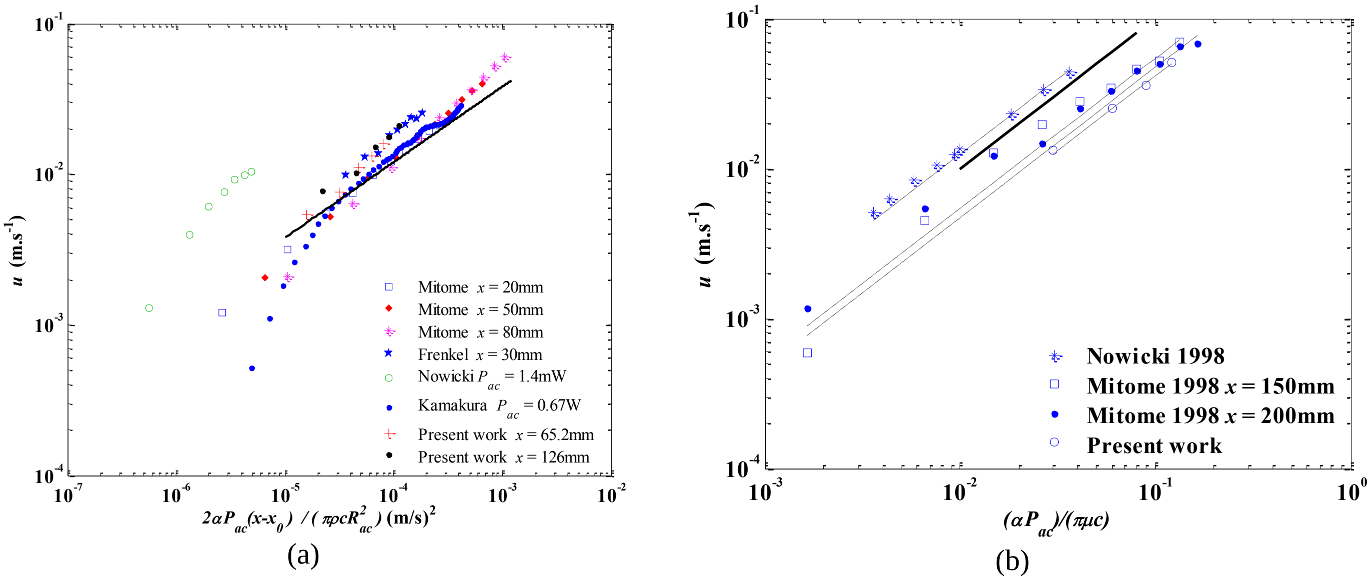

Figure 1: Comparison of the former and present experimental results with the scaling law given by (a) equation (4) and (b) equation (5).

7. References

[1] Lighthill S. J. (1978), Acoustic streaming, *J. Sound Vib.*, **61**, p. 391‑418.

[2] Nyborg W. L. (1998) *Acoustic streaming*. Academic Press.

[3] Nowicki A., Kowalewski T., Secomski W. and Wójcik J. (1998), Estimation of acoustical streaming: theoretical model, Doppler measurements and optical visualisation, *Eur. J. Ultrasound*, **7**, p. 73‑81.

[4] Mitome H. (1998), The mechanism of generation of acoustic streaming, *Electronics and communication in Japan*.

[5] Frenkel V., Gurka R., Liberzon A., Shavit U., and Kimmel E. (2001), Preliminary investigations of ultrasound induced acoustic streaming using particle image velocimetry, *Ultrasonics*, **39**, p. 153−156.

[6] Eckart C. (1948), Vortices and streams caused by sound waves, *Physical Review*, p. 68-76.

[7] Nasch P., Manghnani M. and R. Secco (1994), A modified ultrasonic interferometer for sound-velocity measurements in molten metals and alloys, *Rev. Sci. Instrum.*, **65**, p. 682‑688.

[8] Botton V., Moudjed B., Henry D., Ben Hadid H. and Garandet J. P. (2013), Acoustic Streaming Jet Scaling and Dimensional Analysis », *Submitt. Publ. Phys. Fluids*.

[9] T. Kamakura (1996), Time evolution of acoustic streaming from a planar ultrasound source, *J. Acoust. Soc. Am.*, **100**, p. 132-138.

COMPUTATIONAL FLUID DYNAMICS ANALYSIS OF THE OSCILLATORY FLOW IN A JET PUMP: THE INFLUENCE OF TAPER ANGLE

OOSTERHUIS*,[1] Joris P., BÜHLER[1] Simon, WILCOX[2] Douglas and VAN DER MEER[1] Theo H.

[1]Department of Thermal Engineering, University of Twente, The Netherlands
[2]Chart Inc., Troy, NY, United States
*j.p.oosterhuis@utwente.nl

Abstract: *A two-dimensional CFD model for predicting the oscillating flow through a jet pump is developed. Various taper angles are investigated and total minor loss coefficients are derived. A good correspondence is achieved with experimental results from the literature. However, at higher taper angles a dramatic decay in the jet pump pressure drop is observed, which serves as a starting point for the improvement of jet pump design criteria for compact thermoacoustic applications.*

1. Introduction

A jet pump is a crucial part of most closed-loop thermoacoustic devices. In such devices, a time-averaged mass flux known as Gedeon streaming can exist [1]. This time-averaged mass flux results in convective heat transport that can degrade the efficiency of thermoacoustic devices. To suppress Gedeon streaming, a jet pump can be used. Backhaus and Swift have shown that by correctly shaping a jet pump it is possible to take advantage of asymmetry in hydrodynamic end effects to impose a pressure drop across the jet pump [2]. A typical jet pump consists of a narrowed, tapered tube section as shown schematically in Figure 1. By balancing the pressure drop across the jet pump with that which exists across the regenerator in a thermoacoustic device, it is possible to suppress Gedeon streaming.

Despite the proven effectiveness of jet pumps, there is a lack of understanding about the exact fluid dynamics that lead to the observed pressure drop. Current criteria for the design of a jet pump assume that the flow at any point in time has little "memory" of its past history – which is often referred to as the "Iguchi-hypothesis" – allowing the acoustic behavior to be based on a quasi-steady approximation and the use of minor loss coefficients reported for steady flow conditions [2, 3, 4, 5]. Qualitative evidence exists which supports the current analysis theory, but quantitative agreement between the theory and experiments remains poor.

Previous studies include mainly experimental work and only a few computational studies have been published. Petculescu and Wilen measured the pressure drop for a series of jet pump geometries and derived minor loss coefficients [6]. They reported a difference between the measured and theoretical minor loss coefficients. Nevertheless, for the investigated geometries – up to a taper angle of $10°$ – good agreement between steady flow and oscillating experiments was obtained. Computational studies related to jet pumps mainly include the work of Boluriaan and Morris [7, 8]. Although the flow field was calculated for a fixed geometry and wave amplitude, the relation between wave amplitude and pressure drop was not published.

In this paper, the oscillating flow in the vicinity of a jet pump is investigated using a computational fluid dynamics (CFD) model. Validation is provided with the experimental results of Petculescu and Wilen [6]. Furthermore, the influence of the jet pump taper angle is analyzed by changing the jet pump length. This study shows the effect on the achieved pressure drop when making a jet pump more compact.

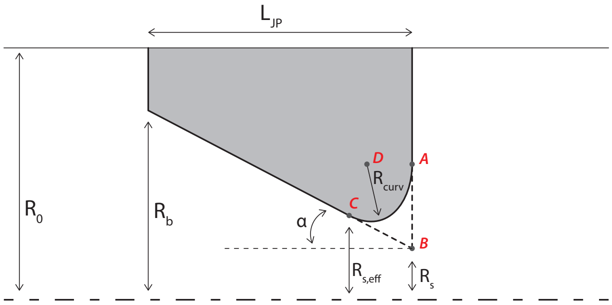

Figure 1: Jet pump with parameters that define the geometry (not to scale). Dashed line indicates centerline.

2. Modeling

A two-dimensional axisymmetric model of a jet pump is developed using the commercial CFD package COMSOL Multiphysics v4.4 [9]. To allow for the validation of the computational model, the jet pump dimensions and boundary conditions are based on data from the literature [6]. In all cases, air at a mean temperature of $T_0 = 20\,°\mathrm{C}$ and a mean pressure of $p_0 = 1$ atm is used as the working fluid. The driving frequency of the system is $f = 100\,\mathrm{Hz}$. Under these conditions, the viscous penetration depth is: $\delta_\nu = \sqrt{2\mu/\omega\rho} = 0.22\,\mathrm{mm}$.

Geometry The jet pump geometry is defined using a number of parameters: the big radius R_b, the effective small radius $R_{s,eff}$, the taper half-angle α and the radius of curvature at the small exit of the jet pump R_{curv}. All these parameters are shown in Figure 1, with R_s being the small radius of the jet pump without curvature ($R_{curv} = 0$), as defined in Equation 1:

$$R_s = R_{s,eff} - R_{curv}\left(\frac{\sin\alpha + 1}{\cos\alpha} - \cos\alpha\right) \tag{1}$$

The total length of the jet pump is calculated using Equation 2:

$$L_{JP} = \frac{R_b - R_s}{\tan\alpha} \tag{2}$$

Besides jet pump region, the computational domain comprises a region on both sides of the jet pump with length $L_{in} = 650\,\mathrm{mm}$ and radius R_0. The geometrical parameter values used for the validation case are listed in Table 1a.

For the simulations with variable taper angle, the exit radii R_b and $R_{s,eff}$ are kept constant and are identical to those in the validation case. By changing the jet pump length L_{JP}, the taper angle α will change and the effect of a more compact jet pump can be studied. The taper angles that are considered and resulting jet pump lengths are summarized in Table 1b.

Numerical model Within the described computational domain, the unsteady, incompressible Navier-Stokes equations are solved [9]. To solve these equations, the fully coupled direct MUMPS solver is used with a maximum time-step of $\Delta t = 1 \cdot 10^{-5}$ s. This yields $N_t = 1000$ time-steps per wave period. Additional isotropic diffusion of $\delta_{id} = 0.1$ is used to damp out initial transients and to obtain a stable solution. The assumption of incompressibility is justified by the ratio of the jet pump dimension to the acoustic wavelength: the jet pump length is much smaller than the acoustic wavelength ($L_{JP}/\lambda \ll 1$). Hence, the flow can be considered locally incompressible [10].

Parameter	Value
R_0	$7.9\,\mathrm{mm}$
R_b	$4.04\,\mathrm{mm}$
$R_{s,\mathit{eff}}$	$0.93\,\mathrm{mm}$
R_{curv}	$1.85\,\mathrm{mm}$
L_{JP}	$27.5\,\mathrm{mm}$

(a) Jet pump dimensions for validation case, based on [6].

α [°]	L_{JP} [mm]	α [°]	L_{JP} [mm]
3	64.3	15	12.6
5	38.5	20	9.3
7	27.5	30	5.8
10	19.1	45	3.4

(b) Resulting jet pump length L_{JP} for applied taper angles α.

Table 1: Dimensions of simulated jet pump geometries.

To simulate an acoustic wave inside the computational domain, an oscillating velocity boundary condition is used on the left side of the domain with $u(t) = u_1 \cdot \sin(2\pi f t)$. On the right side of the domain, a pressure boundary condition is used with a constant relative pressure of $p = 0\,\mathrm{Pa}$ to simulate an open end. No-slip wall boundary conditions are applied to both the tube wall and the jet pump wall. On the x-axis, an axisymmetric boundary condition is imposed.

Computational mesh The domain is discretized using a computational mesh consisting of 54,000 quadrilateral elements. An unstructured mesh is used near the jet pump, combined with a structured mesh in the far field. The elements are stretched in the direction of wave propagation, corresponding to the expected gradients [11]. Moreover, a mesh refinement is applied near all no-slip wall boundaries such that a total of $N_{bl} = 10$ elements exist within a distance of a viscous penetration depth δ_ν from the wall. A further refinement to $N_{bl} = 20$ elements showed a deviation in the mean pressure drop of less than $0.2\,\%$, which provides evidence for the mesh independence of the results.

Minor loss calculation Backhaus and Swift were the first to derive an equation for the mean pressure drop across a jet pump based on steady-flow minor loss coefficients [2]. The minor losses in steady flow can be calculated using: $\Delta p_{ml} = K\frac{1}{2}\rho u^2$, with K the minor loss coefficient dependent on the geometry and, in this case, $u(t) = u_1 \sin \omega t$ a pure sinusoidal flow velocity. By time-integration, a relation for the mean pressure drop across the jet pump can be derived:

$$\Delta p_{2,JP} = \frac{1}{8}\rho_0 |u_1|^2_{JP} \left[(K_{exp,s} - K_{con,s}) + \left(\frac{A_s}{A_b}\right)^2 (K_{con,b} - K_{exp,b}) \right] \tag{3}$$

where K_{con} and K_{exp} are the minor loss coefficients for the contraction and expansion phase, respectively, and $|u_1|_{JP}$ is the maximum velocity amplitude at the small exit of the jet pump. In the current paper, the mean pressure drop as a function of $|u_1|_{JP}$ is studied. Hence, it is possible to derive a "total" minor loss coefficient, incorporating the expansion and contraction effects at both exits:

$$K_{tot} = \frac{8\Delta p_{2,JP}}{|u_1|^2_{JP}\rho_0} \tag{4}$$

The total minor loss coefficient will be derived from the simulation results based on Equation 4. The use of more advanced models that correct for the non-harmonic velocity inside the jet pump is beyond the scope of this brief paper.

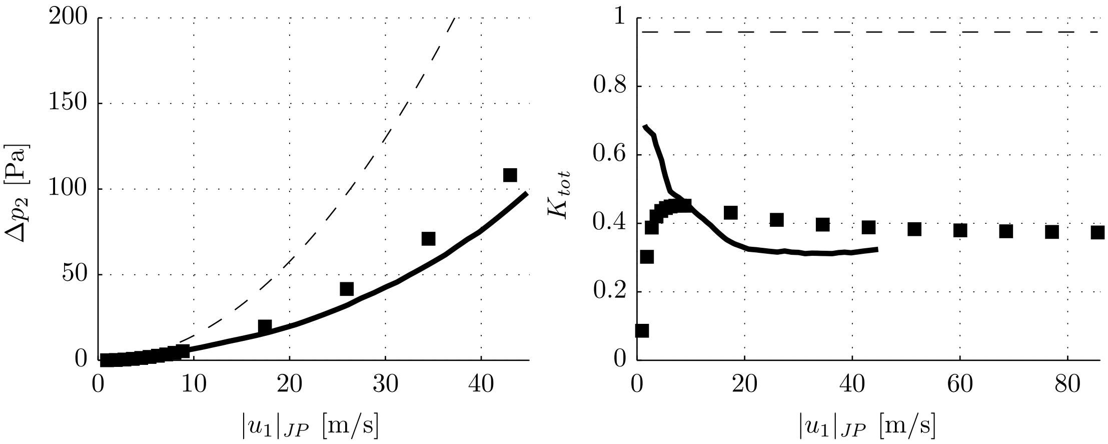

(a) Mean pressure drop Δp_2.

(b) Total minor loss coefficient K_{tot}.

Figure 2: Results of validation case, taper angle $\alpha = 7°$. Solid lines indicate results derived from [6], black squares (■) indicate simulation results and dashed lines are predictions using Eq. 3.

3. Results

The CFD model is validated by performing a range of simulations applying the reference geometry (see Table 1a). The velocity amplitude at the left boundary condition is varied from $|u_1| = 0.01$ m/s to 1.0 m/s. The resulting mean pressure drop is shown in Figure 2a. In Figure 2b, the behavior of K_{tot} as a function of the velocity amplitude is shown for both the reference data and the simulation results. It is clear that the regime where $\Delta p_2 \propto |u_1|^2_{JP}$ is only present at higher wave amplitudes, which is in accordance with earlier work [6]. A least-square fit based on Eq. 4 yields $K_{tot} = 0.32$ for the reference data and $K_{tot} = 0.38$ for the simulation results, while the theoretical total minor loss coefficient, calculated using Eq. 3, is $K_{tot} = 0.96$.

Influence of taper angle Starting from the previously used geometry, a set of simulations is carried out in which the jet pump taper angle – and consequently the jet pump length – is varied (see Table 1b). A fixed velocity amplitude of $|u_1| = 0.2$ m/s is used. A clear effect of the taper angle on the total minor loss coefficient K_{tot} is observed as shown in Figure 3: an increased taper angle leads to a decreased minor loss coefficient and thus to a decreased jet pump performance. Note that K_{tot} from simulation results is now based on a fixed velocity amplitude. These results are similar to those reported in the literature for the range of $\alpha = 3°$ to $10°$, but show a dramatic decay in K_{tot} for higher taper angles: from $\alpha = 20°$ on, no positive mean pressure drop was measured at all. This behavior is confirmed by studying the vorticity field: while for low taper angles the vortices propagate purely rightwards, at higher taper angles the vortex shedding becomes symmetric and vortices propagate in both directions. A detailed study of the vortex shedding and flow separation will be reported in a future publication.

4. Conclusion

A CFD model for the oscillating flow through a jet pump is developed and compared with earlier work. Total minor loss coefficients have been calculated, and in comparison to the theoretical values there is good agreement between simulation results and reference data. The effect of the taper angle has been studied, and for small taper angles the simulation results are equivalent to those reported in the literature. Moreover, for higher taper angles a dramatic decay in K_{tot} is

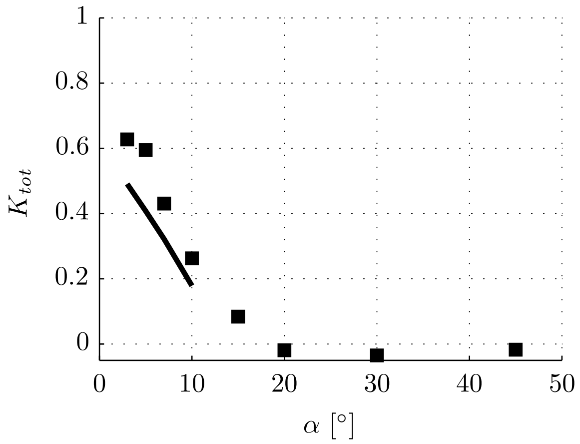

Figure 3: Effect of taper angle α on total minor loss coefficient K_{tot} for $|u_1|_{JP} = 0.2$ m/s. Solid line indicates results derived from [6], black squares (■) indicate simulation results.

observed which had not previously been reported. This certainly puts a price on the achievable pressure drop for compact jet pump designs.

The presented CFD model serves as a starting point for the numerical calculation of minor loss coefficients and a further validation of the used numerical methods will be carried out. Future research will focus both on a detailed explanation of the observed flow phenomena and on improved jet pump design criteria for compact thermoacoustic applications.

References

[1] Gedeon, D.: DC gas flows in Stirling and pulse-tube cryocoolers. *Cryocoolers* 9, 385–392 (1997)

[2] Backhaus, S. and Swift, G.: A thermoacoustic-Stirling heat engine: detailed study. *The Journal of the Acoustical Society of America* 107, 3148–3166 (2000)

[3] Iguchi, M., Ohmi, M., and Meagawa, K.: Analysis of free oscillating flow in a U-shaped tube. *Bulletin of the JSME* 25, 1398–1405 (1982)

[4] Swift, G., Gardner, D., and Backhaus, S.: Acoustic recovery of lost power in pulse tube refrigerators. *Journal of the Acoustical Society of America* 105, 711–724 (1999)

[5] Thurston, G.: Nonlinear acoustic properties of orifices of varied shapes and edge conditions. *The Journal of the Acoustical Society of America* 992, 2–5 (1958)

[6] Petculescu, A. and Wilen, L. A.: Oscillatory flow in jet pumps: Nonlinear effects and minor losses. *The Journal of the Acoustical Society of America* 113, 1282–1292 (2003)

[7] Boluriaan, S. and Morris, P. J.: Suppression of traveling wave streaming using a jet pump. In *41st AIAA Aerospace Sciences Meeting & Exhibit*. American Institute of Aeronautics and Astronautics, Reno, NY (2003)

[8] Morris, P., Boluriaan, S., and Shieh, C.: Numerical simulation of minor losses due to a sudden contraction and expansion in high amplitude acoustic resonators. *Acta Acustica united with Acustica* 90, 393–409 (2004)

[9] COMSOL: *COMSOL Multiphysics Reference Guide*. COMSOL (2012)

[10] Nakiboğlu, G.: *Aeroacoustics of corrugated pipes*. Phd thesis, Eindhoven University of Technology (2012)

[11] Bühler, S., Wilcox, D., Oosterhuis, J. P., and van der Meer, T. H.: Calculation of thermoacoustic functions with computational fluid dynamics. *Proceedings of Meetings on Acoustics* 19, (2013)

MARGINAL CONDITION FOR SPONTANEOUS OSCILLATIONS OF A THERMOACOUSTIC ENGINE COUPLED WITH A PIEZOELECTRIC ELEMENT. ANALYTICAL AND EXPERIMENTAL STUDY

BACCOLI[1*] R., MASTINO [1] C., BAZ[2] A.
Fisica Tecnica ed Energetica, Università degli Studi di Cagliari, Italy
E-mail address: rbaccoli@unica.it

Abstract: This paper deals with the problem to derive a marginal condition for the onset of spontaneous thermoacoustic oscillations of a gas in a circular tube, subject to a variable shape of the temperature gradient along the side wall, with one end rigidly closed and the other closed by a piezoelectric element converter. In this study the acoustic impedance of the piezo element is arbitrary in order to achieve marginal conditions between those exhibited with rigidly closed end, and those with end opened onto free atmosphere. Moreover, marginal condition is outlined adopting a variable shape of the temperature gradient with respect to the position of the stack along the tube. The solution includes all dissipative effects related to the compressive and shear viscosity and the heat transmission in the boundary layer at the side wall and end wall.

1. Introduction.

This study investigates one of the promising candidates in the field of energy conversion, namely a standing waves thermoacoustic engine. In thermoacoustic systems heat is converted into acoustic energy and vice versa.

Nomenclature

$p_e = p_0$ value of the uniform pressure related to the equilibrium state, [Pa];
T_e local gas temperature in equilibrium conditions, [°C];
ρ_e local gas density in equilibrium conditions, related to the local temperature T_e, [kg/m^3];
ν_e kinematic viscosity, related to the local temperature T_e, [m^2/s];
a_e local sound speed in equilibrium conditions, related to the local temperature T_e, [m/s];
c_v specific heat capacity at constant volume of working fluid, [kJ/kg°C];
c_p specific heat capacity at constant pressure of working fluid, [kJ/kg°C];
T_H temperature at the hot, closed end, [°C];
T_0 temperature at the cold, open or piezo system mounted end, [°C]; R radius of the tube [m];
γ c_p/c_v; Pr = Prandtl number; $C = 1 + \frac{\gamma - 1}{\sqrt{\mathrm{Pr}}}$; $C_T = 1/2 + \frac{1}{\sqrt{\mathrm{Pr}}}$+Pr;
ω = angular frequency, [1/s] $\sigma = \frac{\omega L_T}{a_0}$ dimensionless angular frequency;
u_x velocity in the axial direction, [m/s]; u_r = velocity in the radial direction, [m/s];
$\delta_e = \frac{1}{R}\sqrt{\frac{\nu_e}{i\omega}}$, represent a measure of how is deep the boundary layer respect to the radius R
δ_0 δ_e calculated for $T = T_0$ at the low end wall temperature and C is a gas constant.
$b = C\,\delta_0$ frequency equation is obtained in the zero and in the first order by expanding the wave perturbed pressure equation with respect to b ; i = imaginary part;
$x_p \in [-L_{-}, +L_p]$ ("p" region) domain were the temperature gradient is negative and characterized by a slow slope. Quantities are designated by attaching a subscript "p" (e.g. T_{ep}, T'_p, $\tilde{T}_p$);

L_p abscissa at the end wall where is placed the piezo-system converter. The temperature in this point is the lowest one and is indicated by T_0;

$x_n \in [-L_n, -L_*]$ ("n" region) domain were the temperature gradient is negative and characterized by an high slope. Quantities are designated by attaching a subscript "n" (e.g. T_{en}, T'_n, $\tilde{T}_n$);

$-L_n$ abscissa value that localize the position of the end wall resonator respect to the origin of the system reference. The temperature in this point is the highest one and is indicated by T_H;

$L_T = L_n + L_p$ length of the tube, [m];

$-L_*$ abscissa value that localize the point where the slope of the temperature gradient changes dramatically his value and $T_e(-L_*)$ is equal to T_*;

λ_p is a parameter that governs the magnitude and the sign of the slope of the temperature gradient in the "p" region so that $\frac{a_{ep}}{T_{ep}}\frac{dT_{ep}}{dx_p} = 2\frac{a_0\lambda_p}{L_p}$;

λ_n is a parameter that governs the magnitude and the sign of the slope of the temperature gradient in the "n" region so that $\frac{a_{en}}{T_{en}}\frac{dT_{en}}{dx_n} = 2\frac{a_0\lambda_n}{L_n}$;

$U_p = i\frac{2C_T}{C}be^{-\frac{\lambda_p \xi_p}{L_p}}\lambda_p\left(\frac{L_T}{L_p\sigma}\right)^2\psi_p$; $I_p = 1 + i\frac{2C_T}{C}be^{-\frac{\lambda_p \xi_p}{L_p}}\lambda_p\left(\frac{L_T}{L_p\sigma}\right)^2\frac{i\lambda_p}{2}$;

$g = (1-(1+\lambda_n)b)(1+\lambda_n)$; $d = \frac{2C_T}{C}\lambda_n(1+\lambda_n)b$; $J = \frac{kr\cdot\sigma^2}{L_n\cdot(1+\lambda_n)^2(1-2\cdot(1+\lambda_n))\cdot\frac{b}{C}}$ where

kr is a parameter that governs the volume size of the resonator cavity

A configuration of the system under study is shown in figure 1

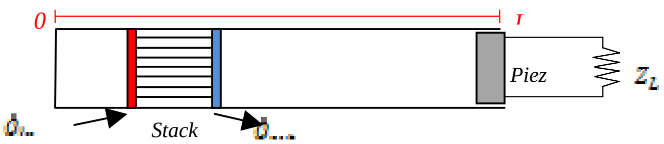

Figure 1: Schematic of standing-wave thermoacoustic engine integrated with a piezoelectric membrane (TAP).

The right theoretical frame in order to get the marginal condition was derived by Rott [1] [2] [3] and afterwards it was completed by Wheatley [4] and Swift [5]. Rott's works are about quarter wave length tube. The linearized problem requires to solve an eigenvalue problem for a second-order differential equation with variable coefficients in terms of the excess pressure wave. For smooth temperature distributions, this is a formidable task. Indeed Rott gave up the smooth profile of the temperature and adopted a discontinuous trend, thereby imposing a drastic discontinuity, though it is rather difficult to achieve experimentally. In 2001, the excellent work of Sugimoto et al [6,7], shed some light on what happens on the onset of thermoacoustic oscillations. Thanks to his work was discovered the mechanism whereby the boundary layer, under an appropriate temperature gradient, is able to supply a work to the wave pressure propagation up to exceed dissipative effects of the viscous boundary layer.

In what follows, this work adopts the Sugimoto's approach with only two minor extensions with the aim to offer two points of generalization. The first one is related to the boundary condition at one end, because the complex value of the piezoelectric impedance is taken into account, and the second effort is about the possibility to build a variable shape of temperature gradient by means of a sequence of piecewise parabolic distribution as shown in figure 2.

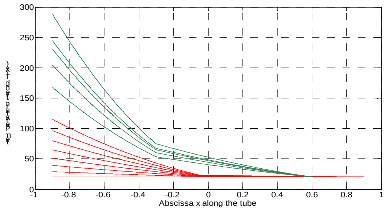

Figure 2: Some examples of the shape of the temperature imposed along the tube in stationary conditions.

2. A problem with a boundary layer structure: the main lossless flow and the viscous – thermal boundary layer

Here, we assume that the field of the acoustic flow has a boundary layer structure, which means that the influence of viscosity is confined to a thin layer near the wall. The flow is basically divided in a boundary layer region and the flow outside of it, namely the main flow.

By using the two system of equations regarding the main flow and the boundary layer on the side wall, it is possible to write down equation (1); that is a second order differential equation with variable coefficients of the axial coordinate "x" involving the Fourier transform "*P*" of the excess pressure p', in the main-flow region.

$$(1-2C\delta_e)a_e^2\frac{d^2P}{dx^2}+[1-2(C+C_T)\delta_e]\frac{a_e^2}{T_e}\frac{dT_e}{dx}\frac{dP}{dx}+\omega^2P=0 \qquad (1)$$

Equation (1) has been proposed by Sugimoto, (see eq. 23 in [7]) and it was used to get the stability analysis for the marginal conditions.

3. Boundary conditions at the ends wall of the tube.

When the tube is rigidly closed at one end and open on the other side, the boundary conditions for the main flow are well known, namely:

$\left(\frac{dp'}{dx}=-\frac{\frac{\gamma-1}{\sqrt{Pr\,\square\,\sqrt{\nu_L}}}}{a_L^2}\frac{d^{3/2}p'}{dt^{3/2}}\right)_{x=0}$ at the closed end; $(p'=0)_{x=L_p}$ at the opened end.

By using the idea of a renormalization of eq. (1) and in the framework of the first-order theory of the boundary layer, the frequency equation is then derived from the boundary conditions at the both ends of the tube when the temperature distribution is parabolic, from which the marginal condition, eq. (2), is obtained in closed form, in terms of the dimensionless angular frequency, $\sigma=\frac{\omega L}{a_0}$, as a function of the ratio, T_H/T_0;

$$i\psi\left(\frac{e^{iK^+\xi_L}+e^{iK^-\xi_L}}{e^{iK^+\xi_L}-e^{iK^-\xi_L}}\right)=\frac{\beta}{2}-\frac{2C_T}{C}\beta b+\left(1-\frac{1}{C}\right)\frac{R}{L}\sigma^2 b \qquad (2)$$

where β is a parameter that sets the slope of the parabola: $\frac{T_e(x)}{T_0}=\left(1+\beta\frac{x}{L}\right)^2$; K^+, K^- are the wave-numbers and they are given by: $K^{\pm}L=-\frac{i}{2}\beta\pm\psi$ with $\psi=\sqrt{\sigma^2-\frac{\beta^2}{4}}$. The solid curve in figure 3 shows the frequency of the neutral oscillations in the lossless case, as the magnitude of the thermoviscous effects increases, the value of sigma and temperature ratio decreases along the solid curve, but tends to deviate from the lossless trend

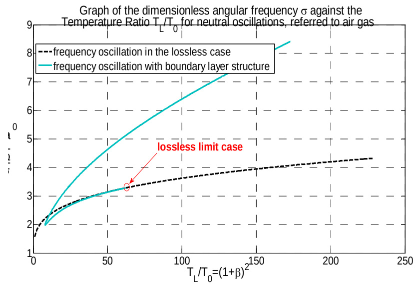

Figure 3: Sugimoto's case: marginal curve when a parabolic temperature gradient is imposed along the side wall tube. One end is opened and the other is rigidly closed. The curve represented in dashed lines is adopted for lossless case, whereas continuous is referred when loss are taken into account.

4. New boundary conditions

The effort of this work is to get new boundary conditions when the tube is rigidly closed at one end and at the other side is closed by means of a piezoelectric element with a variable impedance and the side wall is subject to a variable shape of the temperature. Eqs. (3) and (4), in the frequency domain, respectively represent the new boundary condition in $x = L_p$, where piezoelectric element is placed and the boundary condition in $x = 0$ where end wall is rigidly closed.

$$\left(\frac{dP}{dx} = -\frac{1 + G\left(Z_{piezo}\right)^{-1}}{G} i\omega Q_L P\right)_{x=L_p} \tag{3}$$

where $\frac{1}{G} = \frac{\frac{\gamma - 1}{\sqrt{Pr \,\square\, 1}}}{a_0{}^2}\sqrt{i\omega v_L 1\omega P}$ and $Z_{piezo} = \frac{\mathcal{F}\{p'\}}{\mathcal{F}\{u'_x\}}$ is the impedance of the piezoelectric system.

$$\left(\frac{dP}{dx} = -\frac{\frac{\gamma - 1}{\sqrt{Pr \,\square\, \sqrt{v_L}}}}{a_0{}^2}\sqrt[2]{i\omega^3}\, P\right)_{x=0} \tag{4}$$

When Z_{piezo} goes to ∞ (referred to the physical condition where end wall is rigidly closed), the new boundary condition converges just to the previous one, in accordance with Sugimoto et al. [7].

log □η↓(L↓n)/(η↓p↑ ∗)□ + b(η↓(L↓n) − η↓p↑ ∗) × "Λ" ↓"n" /("4" "ψ" ↓"n") "log" □{[("Λ" ↓"n" /("2" "L" ↓"n")
(5)

Quantities in equation (5) not defined yet, are explained in appendix A. A set of marginal curves in the loss case, as a function of the piezo-impedance, and the shape of the temperature trend (in terms of L_* and L_p) is depicted in figures 4, 5 and 6.

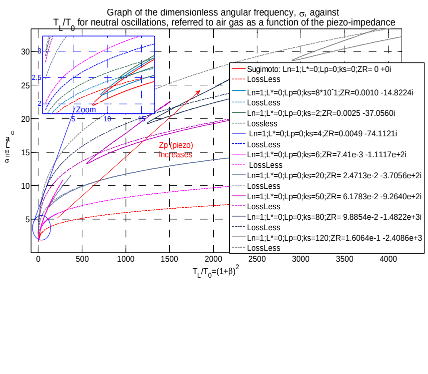

Figure 4. Marginal curve when a parabolic temperature gradient is imposed along the side wall tube. One end is opened and the other is closed by a piezo-electric element. The acoustic impedance of the piezo-element is arbitrary in order to achieve marginal conditions between those exhibited with rigidly closed end, and those with end opened to free atmosphere.

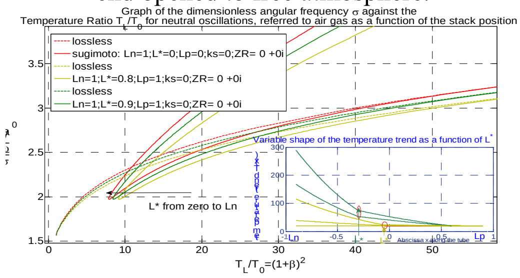

Figure 5. Marginal curve when the temperature trend is stretched due to different position of the stack, (L_* is different from zero). The curve represented in dashed lines is adopted for lossless case, whereas continuous is referred when loss are taken into account. One end is opened and the other is closed by a piezo-electric element with its impedance equal to zero.

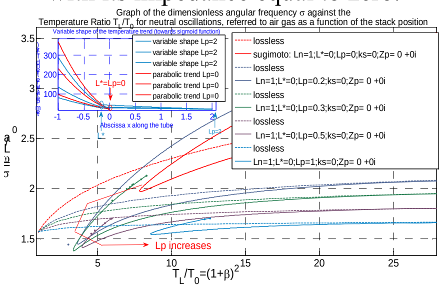

Figure 6 Marginal curve when the temperature trend is stretched due to different length of the tube respect to the position of the stack, (L_p is different from zero). The curve represented by dashed lines is for the lossless case, whereas the continuous line is referred when losses are taken into account. One end is opened and the other is closed by a piezo-electric element with its impedance equal to zero.

1. Conclusion

In this work, the main improvements to the best of our knowledge are summarized below. We found an analytical solution for the marginal conditions as a function of the value of the impedance of the piezoelectric element placed at the end wall of the tube. This solution is not only limited to the boundary conditions of opened and rigidly closed end.

The shape of the temperature gradient along the axial direction of the tube is variable and it is possible to realize changes where the slope is able to approximate at best the real temperature trends, as a function of the position of the stack along the tube and its length.

Based on the shape of the temperature gradient and the impedance of the piezoelectric element it is possible to determine the minimum threshold value for the temperature gradient required for the onset of oscillations.

Thanks to the flexibility of our model it is possible to get a theoretical prediction in order to match the resonant frequencies with the temperature ratio as a function of the electric load.

References

[1] Rott N. Damped and thermally driven acoustic oscillations in wide and narrow tubes, Z. Angew. Math. Phys. 20, 230–243 (1969).

[2] Rott N. Thermally Driven Acoustic Oscillations. Part II: Stability Limit for Helium. J. Applied Mathematics and Physics (ZAMP) Vol. 24, 1973.

[3] Rott N. Thermally Driven Acoustic Oscillations, Part V Gas-Liquid Oscillations. J. Applied Mathematics and Physics (ZAMP) Vol. 27, 1976.

[4] Wheatley J. C. Intrinsically irreversible or natural engines. In: Frontiers in Physical Acoustics, edited by D. Sette North Holland, Amsterdam, 1986, pp. 9395–475.

[5] Swift G. W. Thermoacoustic engines. J. Acoust. Soc. Am. 84, 1145 1988.

[6] Sugimoto N, Tsujimoto K. Amplification of energy flux of nonlinear acoustic waves in a gas-filled tube under an axial temperature gradient, J. Fluid Mech. vol. 456, pp. 377-409, (2002).

[7] Sugimoto N,Yoshida M. Marginal condition for the onset of thermoacoustic oscillations of a gas in a tube. Phys. Fluids 19, 074101 (2007); doi: 10.1063/1.2742422.

Appendix A

Hereafter are listed all quantities that appear explicitly in eq. (5).

$$\eta_p^* = \eta_p(-L_*) = 1 + \lambda_p = \sqrt{\frac{T_*}{T_0}}; \qquad \eta_{L_n} = \eta_n(-L_n) = \sqrt{\frac{T_*}{T_0}} - \frac{\lambda_n}{L_n}(-L_n + L_*) = \sqrt{\frac{T_H}{T_0}};$$

$$\xi_p^* = -\frac{L_p}{\lambda_p}(\log\eta_p - b\,\lambda_p);$$

$$h = i \cdot e^{-\frac{C}{\sigma R}\sqrt{\frac{\nu_0 L_T}{2a_0}}\lambda_p} \cdot e^{i\frac{C}{\sigma R}\sqrt{\frac{\nu_0 L_T}{2a_0}}\lambda_p} \cdot \frac{2C_T}{C} b\lambda_n \left(\frac{L_T}{L_n\sigma}\right)^2; \quad R_n = 1 + i\frac{2C_T}{C}\lambda_n \frac{e^{-\frac{\lambda_n \xi_n^*}{L_n}}}{L_n K_n};$$

$$\psi_p = \sqrt{\left(\frac{\lambda_p}{2}\right)^2 - \left(\frac{L_p\sigma}{L_T}\right)^2};$$

$$..0020K_p = \frac{1}{L_p}\left(-i\frac{\lambda_p}{2} + \psi_p\right);$$

$$\ell_p = \frac{1}{L_p}\left(-i\frac{\lambda_p}{2} - \psi_p\right); \quad G_n = 1 + i\frac{2C_T}{C}\lambda_n \frac{e^{-\frac{\lambda_n \xi_n^*}{L_n}}}{L_n \ell_n}\psi_p; \quad W = \frac{1 - g \cdot d \cdot J \cdot (L_T)^2}{L_n \cdot \sigma^2};$$

$$X_{n,p} = i\frac{\lambda_{n,p}}{L_{n,}\mathbf{p}}; \qquad Y_{n,p} = \frac{\psi_{n,p}}{L_{n,p}}; \quad S = \frac{\mathrm{L}_{\mathrm{p}0}\varrho_0\omega}{Z_{piezo}}$$

$$B = -\left(\frac{U_p}{R_n} + \frac{G_n L_n}{2\psi_n}\left(Y_p - \frac{U_p(X_n + Y_n)}{R_n}\right)\right);$$

$$P = \frac{U_p}{R_n} - L_n h\left(Y_p - \frac{U_p(X_n + Y_n)}{R_n}\right);$$

$$A = \frac{I_p}{R_n} - \frac{G_n L_n}{2\psi_n}\left(X_p - \frac{I_p(X_n + Y_n)}{R_n}\right); \quad D = \frac{I_p}{R_n} - L_n h\left(X_p - \frac{I_p(X_n + Y_n)}{R_n}\right);$$

$$V_s = \frac{\lambda_p}{2} + S - S \cdot b + \mathrm{L}_p \cdot T\frac{\sigma^2}{L_T}b; \qquad \psi_p = V_s - \frac{1}{2} \cdot S \cdot b \cdot (1 - b) \cdot \frac{2C_T}{C} \cdot \left(\frac{\lambda_p L_T}{\mathrm{L}_p\sigma}\right)^2$$

NUMERICAL SIMULATION OF FLOW DYNAMICS IN THE PERIODIC REGIME INSIDE AN IDEALIZED THERMOACOUSTIC ENGINE

MA[1,2] L., WEISMAN[1,2] C., BALTEAN-CARLES[1,2] D., DELBENDE[1,2] I., BAUWENS[3] L.
[1]UPMC, 4 Place de Jussieu–75005 Paris, France
[2]LIMSI-CNRS, BP133 – 91400 Orsay, France
[3]University of Calgary, T2N 1N4, Canada
E-mail: malin@ limsi.fr

Abstract: Flow dynamics in the stack and heat exchangers of a standing wave thermoacoustic engine are studied using 2D numerical simulations. The numerical approach is based on asymptotic coupling in the low Mach number limit, of a nonlinear dynamic model in the active cell with linear acoustics in the resonator. Computed results of the periodic regime are analyzed and exhibit two main features: instability and vortex dynamics.

1. Introduction

A simplified model of a loaded thermoacoustic engine consists of a long tube closed at one side and loaded at the other side, inside which the active cell is placed. The active cell comprises a stack of parallel plates placed between two heat exchangers. One heat exchanger is connected to a hot source and the other to a cold source. The combined effect of pressure fluctuations and oscillating heat exchange in the boundary layers on the stack plates provides a heat engine effect [1, 2, 3]. A multiple scale formulation allows for the global compressible flow problem to be reduced to a dynamically incompressible problem in the active cell, with boundary conditions obtained from linear acoustics in the resonator. The detail of this analysis can be found in [4, 5].

In the literature there are few studies dedicated to nonlinear hydrodynamics inside the active cell. The purpose of this paper is to show and analyse numerical results on flow dynamics in the periodic regime, such as instability and vortex dynamics. After a brief introduction of the model and the numerical method, the computed results of the periodic regime are presented and discussed in two steps: first, the influence of the load on the onset temperature and saturation is presented, validating the choice of the load value. Then, the flow patterns, temperature field and vorticity field are analysed and a possible mechanism of the observed instability is discussed qualitatively.

2. Numerical approach

2.1 Geometry and model

The geometry consist of a long resonator with length L_{res}, within which an active cell with characteristic stack length L_s is placed. The active cell consists of a stack of parallel plates and two heat exchangers (heater and cooler). The heater and the cooler are also made of parallel plates. We assume the vertical periodicity, so that the simulation can be reduced to a domain consisting of two half-plates and the space between them, and the corresponding fraction of the resonator cross-section. The active cell is small compared to resonator length, therefore two characteristic length scales are to be considered, L_{res} and L_s. The geometry of the entire resonator is shown in Fig. 1 (top). The resonator dead end is located at $\hat{x} = -l_L$, while the other end consist of a load modelled as a real impedance f at the fixed location

$\hat{x} = +l_R$, with $p(l_R, t) = fu(l_R, t)$. The active cell is considered as a discontinuity section positioned at $\hat{x} = 0$.
Turning to the stack scale, the geometry of the active cell is shown in Fig. 1 (bottom) and boundaries with the resonator are pushed to infinity. This represents the simulation domain. In our case, the length is $5L_s$ and the height is H .

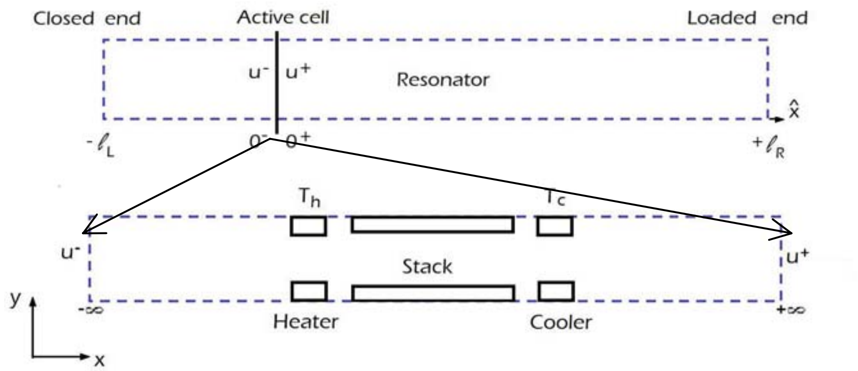

Figure 1: Geometry of linear acoustic system (top) and of active cell (bottom).

The multiple scale formulation is obtained with a perturbation asymptotic method, described in detail elsewhere [4, 5]. Key assumptions are that velocities are small compared with the speed of sound, and that the flow sweeps a length of the order of the length of the stack. These assumptions lead to a reference Mach number $\mathbf{M} = \frac{L_s}{L_{res}}$. Under these assumptions, the flow in the resonator is characterized by lossless linear acoustics with all dissipation concentrated on the loaded end, and the flow in the active cell is described by nonlinear dynamically incompressible model.
At solid boundaries, continuity of temperature and heat flux and no slip condition are imposed. Temperature $T = T_h$ is fixed on the heater plates, and $T = T_c$ is also fixed on the cooler plates. In the stack plates, the heat conduction equation is solved. The boundaries of the heat exchangers are considered adiabatic.
Matching these two solutions in the standard way provides appropriate boundary conditions to the flow inside the heat exchanger section, depending of the impedance value at the load end. From the standpoint of resonator acoustics, the heat exchanger section is transparent to pressure but provides a source of volume, as a result of the thermoacoustic effect.

2.2 Numerical method

The numerical solution is based upon a finite volume code solving the Navier-Stokes equations under low Mach number assumption [6]. Diffusion is solved implicitly and advection is explicit. Accuracy is second-order in both space and time. In the lossless resonator, acoustics in the two parts can be expressed as two plane waves that move respectively left and right at the speed of sound. At tube ends, using the boundary conditions, the relationship between the incident wave and the reflected wave are expressed as relations between the Riemann invariants, and written on characteristics at the left/right boundaries of the active cell as Riemann invariants considered at previous time. The acoustic pressure does not appear in the active cell, but it modifies these boundaries conditions at each time step.
A Cartesian regular two-dimensional mesh of the active cell is used in the current work (4096×64 grid points, i.e. 9 grid points across the stack half-plate width, and 37 grid points along the gap between heat exchanger and stack). The numerical calculation is performed

with the following initial condition: a random noise for the velocity field in the whole resonator and a steady state heat conduction condition for the temperature field inside the active cell and constant temperature in the resonator (T_h for the hot part and T_c for the cold part). In order to satisfy a stability criterion (CFL=0.025), the time step must be reduced with the increased horizontal velocity, so that from the initial state to the periodic regime, the whole simulation could be extremely long (about 400 reference acoustic periods), with 200 (initial amplification) to 10000 (periodic regime) time steps per reference acoustic period.

3. Results and discussions

3.1 Reference configuration

Results were obtained for an existing thermoacoustic engine described in [7]. The active cell is inserted in a long resonator tube, closed at both ends. Viscous dissipation inside the resonator plays the role of the load. The experiment uses helium under pressure (p_0), and the cold temperature is considered as the reference temperature, T_c = 293 K. The reference acoustic time (t_{ac}) is approximately equal to 1 ms.
All parameters of the experimental configuration are listed in Table 1. The gap between the stack and the heat exchangers (L_g) was arbitrarily chosen to be equal to twice the plate spacing.

L_{res} (m)	L_s (cm)	H (mm)	L_g (mm)	p_0 (bar)	T_h (K)	t_{ac} (ms)
1	3.5	1.06	1.54	4.4	351.6	1

Table 1: Geometry and condition of experimental device

Analysis of numerical results for initial amplification shows that the load plays an important role to the onset of a thermoacoustic engine. For a given value of a load f , there is a corresponding critical heater temperature, corresponding to each acoustic mode. The limit when f is infinite corresponds to a closed end and the limit when f is zero corresponds to an open end. In order to validate the load model, we identify the load value corresponding to a given experimental setup ($p_0 = 4.4$ bar, $T_h = 662$ K) from the experimental stability curve of the fundamental mode [7]. We obtain a load value of 171.36 $\mathrm{MPa}\cdot\frac{\mathrm{s}}{\mathrm{m}^3}$. Numerical simulation for this case indicates that the first mode (fundamental) is the most unstable, in agreement with the experiment.
When the heater temperature is further increased for the same mean pressure value, the numerical simulation with the same load value gives the next critical heater temperature $T_h = 820$ K, and both modes 1 and 2 are unstable, again in agreement with experimental results in [7].
In order to study the periodic regime, for a given value of f , we have to choose the heater temperature just above the critical value. By trial and error, we have found that high values of heater temperature (for example $T_h = 743$ K) require long numerical calculation for obtaining a saturated regime. Therefore, the previous load value is not suitable. Numerical experiments showed that, in order to obtain the periodic regime faster we have to choose a higher f . Here for a load of 1523.2 $\mathrm{MPa}\cdot\frac{\mathrm{s}}{\mathrm{m}^3}$, and the same mean pressure, we obtain the critical heater temperature T_h = 345.7 K. The periodic regime is obtained for $T_h = 351.6$ K. The entire simulation takes about 160 hours CPU time on an INTEL XEON.

3.2 Analysis of periodic regime

In this section, the periodic regime is discussed in detail. All results are presented below using dimensionless values.

Fig. 2 (left) shows the time evolution of the acceleration and the velocity at the left entrance of the simulation domain over one acoustic period. Fig. 2 (right) shows the temperature field over the entire active cell at selected times during the period. Due to the presence of the gap between the heat exchangers and the stack, the temperature gradient along the stack is only 50% of the maximum temperature gradient ($\frac{\Delta T}{L_s}$). The whole acoustic cycle is divided into 21 equal phases. There is interplay between acceleration of the flow and the longitudinal temperature gradient resulting in instability of the Rayleigh-Taylor type. Between the entrance and the exit, the flow has different densities, because of the longitudinal temperature imposed through the heat exchangers. If the hot light fluid is pushing the cool heavy flow, the instability occurs. When the acceleration switches its direction, the flow restabilizes. Here, flow acceleration is directly related to acoustics in the resonators.

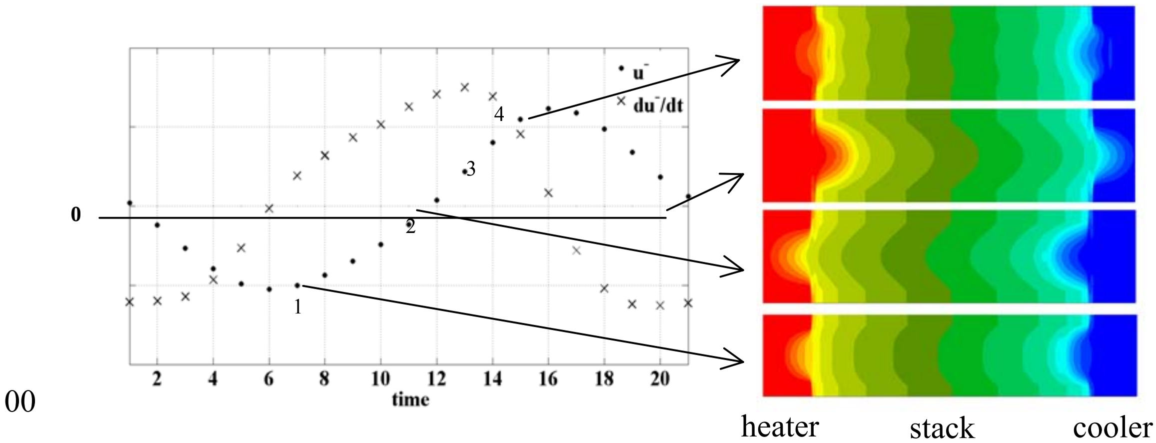

Figure 2: Left: Time evolution of acceleration and velocity at the left entrance of the simulation domain, evolution over one the acoustic period, times 1 to 21. The four points marked on the graph are used in Fig.3. Right: Temperature field over the entire simulation domain at selected times shown by the arrows.

Fig. 3 shows the instantaneous temperature field and the streamlines (left column), and the corresponding vorticity field (right column) between the stack and the heater at 4 different phases of the acoustic cycle (shown in Fig. 2). As expected, one can observe that vortices are generated between the heater and the stack where sudden changes of the cross section exist. Likewise, vortices can be also observed at inlet and outlet of heat exchangers, and between the stack and the cooler (not shown in Fig.3). All vortices are symmetrical in the active cell. From time 1 to time 4, vortices accumulate and roll into the gap between the heater and the stack as long as the flow velocity is significant. Time 1 corresponds to the beginning of flow reversal, and the two vortices grow and move out of the gap. At time 2, vortices move toward the center of the channel. From time 2 to time 3, vortices are sucked outside of the gap area and move toward the right, and recirculation vortices becomes visible in the boundary layer. This continues between time 3 and 4, and finally the plate spacing between two plates of stack can be divided into two boundary layers regions and the domain outside of it. The boundary layer regions absorb the two vortices close to the stack plates, and vortices disappear gradually. A quantitative study of these effects is currently in progress.

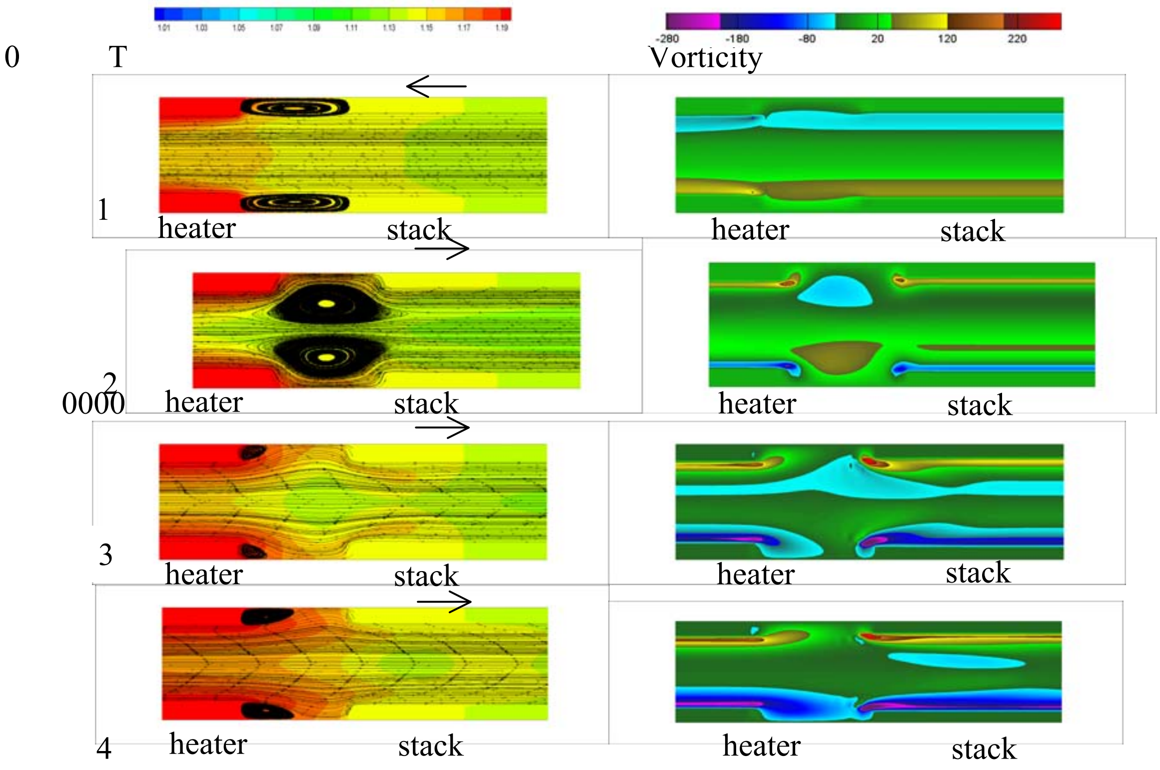

Figure 3: Temperature and streamlines (left) and vorticity fields (right) between the hot heat exchanger and the stack at 4 different time phases (marked on Fig. 2-left).

4. Conclusion

Using a direct simulation, an experimental device of a complete thermoacoustic engine was analysed. In order to obtain the saturation faster, we use a high load value leading to the lower onset temperature. Since due to the temperature difference between the hot and cold heat exchangers, a longitudinal temperature gradient exists, and since both oscillating flow and cross-section changes result in oscillating flow acceleration, the combined effect of the these two features results in a destabilizing/restabilizing mechanism of the Rayleigh-Taylor type. Likewise, the vortex dynamics associated with cavities and step like cross-section changes under oscillating flow show interesting features that are observed in the results, interplaying with temperature gradients and accelerations.

5. References

[1] Rott, N.; Damped and thermally driven acoustic oscillations in wide and narrow tubes. Z. Angew. Math. Phys. 20 (1969) 230-243.

[2] Swift, G.W.; Thermoacoustic engines. J. Acoust. Soc. Am., 84(1988) 1145-1180.

[3] Bauwens, L.; Oscillating flow of a heat-conducting fluid in a narrow tube. J. Fluid. Mech., 324 (1996) 135-161.

[4] Hireche, O.; Weisman, C.; Baltean Carlès, D.; Le Quéré, P.; François, M. X.; Bauwens, L.; Numerical Model of a Thermoacoustic Engine. Comptes rendus Mécanique. 338 (2010) 18-23.

[5] Hireche, O.; Weisman, C.; Baltean Carlès, D.; Le Quéré, P.; Bauwens, L.; Multiple Scale Analysis and Simulation of Thermoacoustic Engines. J. Acoust. Soc. Am.. 128 (2010) 3438-3448.

[6] Le Quéré, P.; Masson, R.; Perrot, P. ; Chebyshev collocation algorithm for 2D non-Boussinesq convection. J. Comp. Physics. 103 (1992) 320-335.

[7] Atchley, A.A; Kuo, F. M.; Stability curves for a thermoacoustic prime mover. J. Acoust. Soc. Am.. 95 (1994) 1401-1404.

MEAN TEMPERATURE PROFILE AT THE ENTRACE OF A THERMOACOUSTIC STACKED SCREEN HEAT EXCHANGER

BÜHLER[1] Simon, WILCOX[2] Douglas, OOSTERHUIS[1] Joris P.,VAN DER MEER[1] Theo H.
Affiliation: [1]Thermal Engineering, University of Twente, P.O. Box 217 - 7500AE Enschede - The Netherlands, [2]Chart Inc.-Qdrive, Troy, New York 12180 - USA
e-mail address of corresponding author: s.buhler@ utwente.nl

Abstract: The entrance effects at a stacked screen heat exchanger are investigated with two CFD test cases. The first CFD test case models an ideal heat exchanger adjacent to an open space. The influence of the heat conduction on the mean temperature is shown. The second test case models two screens of a stacked screen regenerator as two inline cylinders. The mean temperature profile is compared to the numerical solution of a reduced model equation. It is shown that viscous effects do not influence the mean temperature profile at low amplitude.

1. Introduction

Thermoacoustic refrigerators pump heat from a cold heat exchanger to an ambient heat exchanger while consuming acoustic power. The thermoacoustic heat pumping occurs in the regenerator, which is situated between two heat exchangers. On the other side of the cold heat exchanger a thermal buffer tube is placed in order to insulate the cold heat exchanger from the secondary ambient heat exchanger, while transferring the acoustic power [1]. Storch et al. [2] reported a distorted temperature profile within the thermal buffer tube, which does not follow the linear thermoacoustic theory derived by Rott [3] and reviewed by Swift [4]. This is due to the violation of the assumption that the displacement amplitude ξ_1 is much smaller than all other relevant dimensions in the wave propagation direction. In common thermoacoustic refrigerators the length of the heat exchanger is comparable with the displacement amplitude ξ_1 [4]. In this case the convective effects $(u \cdot \nabla)\, T$ at the entrance of the heat exchangers are not negligible as they lead to a change in mean temperature, which can be on the order of the adiabatic temperature oscillation. This nonlinear effect leads to an increase in thermal losses, as a steeper temperature gradient occurs in the thermal buffer tube [2].

The change in mean temperature was qualitatively explained by Swift [4] and Kittel et al. [5] by following gas parcels which start within two displacements amplitudes of the entrance of a heat exchanger in the Lagrangian point of view. Summing at one position in the Eulerian point of view the temperature of the gas parcels, the mean temperature profile close to the entrance of the heat exchanger can be obtained. This leads to a joining condition in the mean temperature which is widely accepted and implemented in one-dimensional codes like DeltaEC [6].
Analytical solutions were derived by Matveev et al. [7] and Gusev et al. [8] for the simplified case in which both the heat conduction in the wave propagation direction as well as the viscous effects are neglected.
Next to the analytical solution, also numerical models that include heat conduction in the wave propagation direction were presented by Matveev et al. [9] and Berson et al. [10]. These results were compared to experimental results and showed good agreement, but still left some questions open [9].

In this paper the results of a numerical model similar to the one presented in Matveev et al. [9] and Berson et al. [10] is compared to computational fluid dynamics (CFD) simulations. Two CFD models are presented and compared to the simplified models.

2. Method

In this paper two CFD models and two simplified models are applied in order to estimate the mean temperature profile close to the heat exchanger in a thermoacoustic heat pump. The CFD models are based on the commercial finite volume code ANSYS Fluent 14 [11]. The working fluid is helium at a mean pressure of $p_0 = 1\text{atm}$ and at a temprature of $T_0 = 300\text{K}$. In total five periods are simulated and the mean temperature is calculated by averaging the last period. In both models a traveling wave with a frequency of $f = 100\text{Hz}$ is modeled. The wave enters at the left side of the domain and leaves it at the right, through a non-reflecting boundary.

CFD models

The first test case consists of an ideal heat exchanger, with an open area. The model and the boundary conditions are presented in Figure 1. The ideal heat exchanger at the left of the domain is modeled with help of a dedicated acoustic boundary condition implemented via a Fluent User Defined Function (UDF), which is similar to the one described in Liao [12]. This boundary condition imposes the pressure at the boundary such that a traveling wave is introduced at the left of the domain with a pressure amplitude of $p_1 = 100\text{Pa}$. This wave travels through the computational domain and exits at the right, through another non-reflecting boundary condition. The two acoustic boundary conditions differ in the way the temperature of the incoming fluid is calculated. At the left boundary it is assumed that the incoming fluid is isothermal, in order to model the ideal heat exchanger. At the right boundary the temperature of the incoming fluid is calculated from the pressure assuming adiabatic wave propagation. The horizontal boundary conditions are set to be periodic. The total domain is five displacement amplitudes ξ_1 long and 0.04 displacement amplitudes ξ_1 high. The domain is discretized by 100 elements per displacement amplitude in both spatial directions.

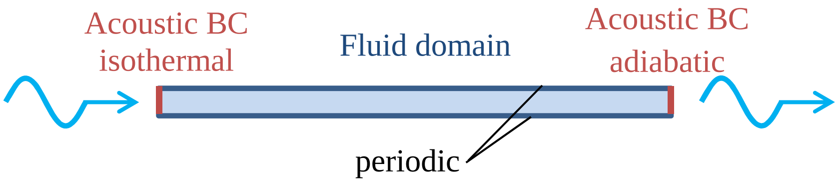

Figure 1: Boundary conditions of the thermal entrance effects model in case of an ideal heat exchanger.

The second case models the entrance effects for a simplified model of a stacked screen heat exchanger. As the main focus is on the entrance effects, only two screens are taken into account. The screens are modeled as an array of cylinders, reducing the problem to two space dimensions. Using periodic boundary conditions the domain can be simplified as shown in Figure 2. At the left and right of the domain the acoustic boundary conditions are applied such that an acoustic wave enters the domain at the left and exits at the right without reflection. The incoming wave has a pressure amplitude of $p_1 = 250\text{Pa}$. The temperature of the incoming fluid is calculated from the pressure assuming adiabatic wave propagation. The screens are assumed isothermal and a no-slip velocity boundary is imposed. The radius of the cylinders is $R = 0.046 \cdot \xi_1$ and the centre of the cylinders are separated by $6 \cdot R$. The total domain is $L_x = 14.5 \cdot \xi_1$ long and $L_y = 10 \cdot R$ high.

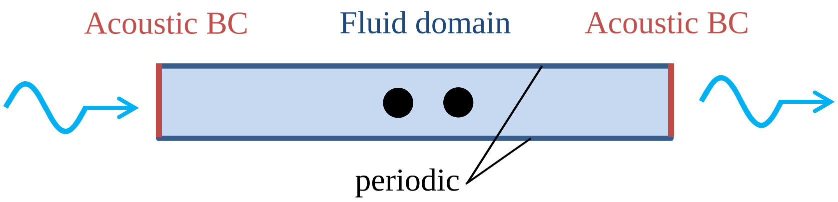

Figure 2: Boundary conditions of the stacked screen heat exchanger test case.

Simplified models

The aforementioned CFD models are compared against two simplified models. The first is the analytical solution derived by Matveev et al. [7] and the main assumptions for the derivation are:

- No viscous wall effects occur, one dimensional acoustics.
- No heat conduction besides the temperature gradient imposed by the heat exchangers.
- The pressure is spatially constant.

In the CFD models presented above a traveling wave is investigated with no temperature gradient. In this case the analytical solution for the mean temperature can be written as [7]:

$$T_m(x) = T_0 - \frac{2}{\pi}\left(1 - \left(\frac{x}{2\xi_1}\right)^{\frac{\pi}{2}}\right)\frac{\gamma - 1}{\gamma}\frac{p_1}{p_0}\,T_0 \tag{1}$$

The second simplified model solves the temperature equation numerically. While Matveev et al. [9] solved the temperature equation in the Lagrangian point of view, Berson et al. [10] solved the dimensionless temperature equation in the Eulerian coordinates. In this paper the second point of view is chosen and the following temperature equation is solved:

$$\frac{\partial T}{\partial t} = \frac{\gamma - 1}{\gamma}\frac{T}{p}\frac{\partial p}{\partial t} - u\frac{\partial T}{\partial x} + \frac{\gamma - 1}{\gamma}k\frac{T}{p}\left(\frac{\partial^2 T}{\partial x^2}\right) + K(T_{HX} - T) \tag{2}$$

where the factor K is the heat transfer coefficient between the heat exchanger and the fluid. Outside of the heat exchanger, K is set to zero. The pressure and the velocity are imposed assuming both a traveling wave and no spatial variations:

$$p(t) = p_0 + p_1\sin(\omega t) \tag{3}$$

$$u(t) = u_1\sin(\omega t) \tag{4}$$

The temperature equation is solved with the MATLAB function *pdepe()*, which solves initial-boundary problems for parabolic partial differential equations in one-dimension. The temperature is calculated for five periods and the temperature is averaged over the last period.

3. Results and discussion

The results for the two CFD models are discussed separately in the following subsections.

Ideal heat exchanger model

In this subsection the simulation results of the ideal heat exchanger CFD model are presented. The mean temperature profiles for two simulations are shown in Figure 3 over the dimensionless x-coordinate. The blue dotted line shows the mean temperature assuming a heat conductivity of $\kappa = 0.152\,\mathrm{W/mK}$ corresponding to helium. A clear minimum in the mean temperature can be seen within one displacement amplitude of the ideal heat exchanger. Furthermore, at the right of the domain heat is conducted towards the outside of the domain.

In Figure 3 the green line shows the mean temperature profile with zero heat conductivity. In this case the effect of the ideal heat exchanger only extends within two displacement amplitudes ξ_1. The black dashed line in Figure 3 shows the analytical solution given in Equation (1). The analytical solution overlays the green line as in both cases no heat conduction is assumed. It can be concluded that the applied boundary condition is correctly implemented and that the boundary can model an ideal heat exchanger. When heat conduction is taken into account in the simulation, the minimum temperature is smoothed out. Heat is conducted into the rest of the domain and the mean temperature profile is influenced beyond two displacements amplitudes ξ_1. The figure also indicates that additional losses are introduced due to the conduction over the right boundary [2].

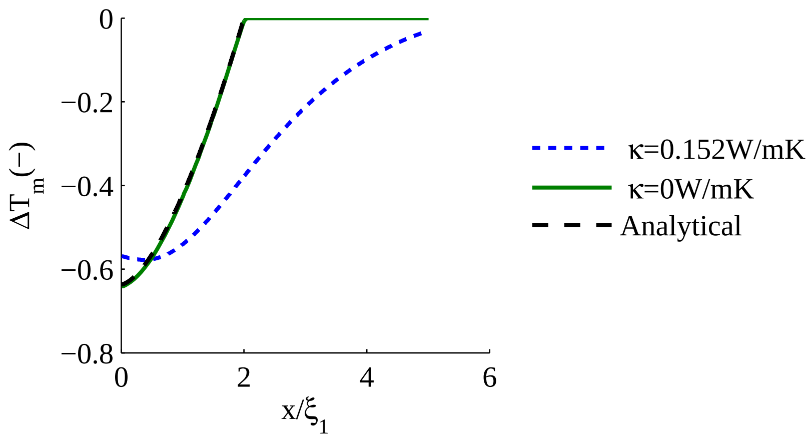

Figure 3: Deviation of the mean temperature normalized with the adiabatic temperature amplitude and plotted over the dimensionless x-coordinate.

Stacked screen model

In this subsection the results for the stacked screen CFD model are discussed. The temperature is averaged over the fifth period and plotted over the dimensionless x-coordinate in Figure 4. The two cylinders modeling the stacked screen heat exchanger are located at $x/\xi_1 = 0$. The profile is point symmetric around this point and the entrance effects on both sides of the heat exchanger are modeled. The black dash-dot line shows the numerical solution of the simplified model with a K-value chosen to fit the CFD simulation. The two mean temperature profiles are in good agreement with each other. This is also the case with the temperature profiles averaged over the first four periods. In other words, the viscous effects, which are neglected in the simplified model, do not have a large influence on the mean temperature profile at low pressure amplitudes.

4. Conclusion

A first step was taken with CFD to investigate the entrance effects near a stacked screen heat exchanger. Two CFD models were presented. From the first model it could be concluded that the dedicated boundary condition, modeling the ideal heat exchanger was correctly implemented and worked well. Furthermore, it is shown that heat conduction flattens the mean temperature profile compared to the case without heat conduction. With the second test case it is shown that solving only the one dimensional heat equation, Equation (2), for a given pressure and velocity gives similar results compared to CFD: i.e. viscous effects do not play an important role at low amplitudes.

In future work the regenerator model will be extended so that high pressure amplitude simulations can be carried out with various phasing between pressure and the velocity. This will allow the investigation of the influence of vortex generation on the heat transfer in the oscillating flow and provide a better understanding of the heat transfer in a stacked screen heat exchanger.

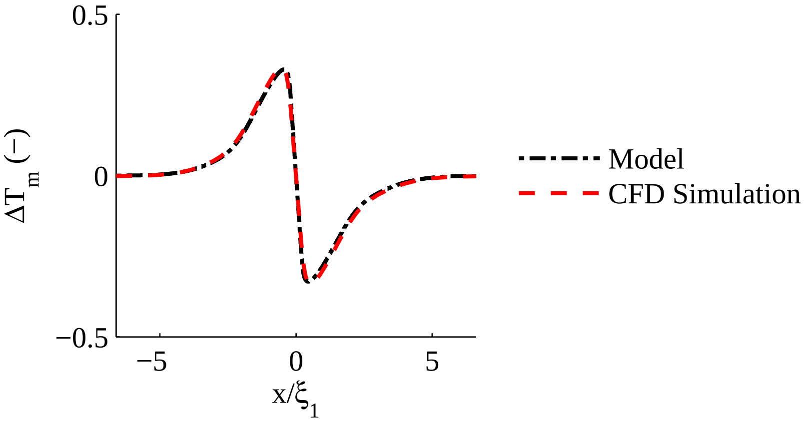

Figure 4: Temperature amplitude averaged over the fifth period normalized with the adiabatic temperature amplitude and plotted over the dimensionless x-coordinate.

5. References

[1] Backhaus, S. and Swift, G. W.: A thermoacoustic Stirling heat engine. *Nature* 399, 335-338 (1999)

[2] Berson, A., Poignand, G., Blanc-Benon, P., and Comte-Bellot, G.: Nonlinear temperature Field near the stack ends of a standing-wave thermoacoustic refrigerator. *International Journal of Heat and Mass Transfer* 54, 4730-4735 (2011)

[3] Gusev, V., Lotton, P., Bailliet, H., Job, S., and Bruneau, M.: Thermal wave harmonics generation in the hydrodynamical heat transport in thermoacoustics. *The Journal of the Acoustical Society of America* 109, 84-90 (2001)

[4] Kittel, P.: The Temperature Profile within Pulse Tubes. *Advances in Cryogenic Engineering* 43, 1927-1932 (1998)

[5] Liao, Z.-P.: Extrapolation non-reflecting boundary conditions. *Wave Motion* 24, 117-138 (1996)

[6] Matveev, K. I., Swift, G. W., and Backhaus, S.: Analytical solution for temperature profiles at the ends of thermal buffer tubes. *International Journal of Heat and Mass Transfer* 50, 897-901 (2007)

[7] Matveev, K. I., Swift, G. W., and Backhaus, S.: Temperatures near the interface between an ideal heat exchanger and a thermal buffer tube or pulse tube. *International Journal of Heat and Mass Transfer* 49, 868-878 (2006)

[8] Rott, N.: Thermoacoustics. *Advances in Applied Mechanics* 20, 135-175 (1980)

[9] Storch, P. J., Radebaugh, R., and Zimmerman, J. E.: *Analytical model for the refrigeration power of the orifice pulse tube refrigerator*. National Institute of Standards and Technology (U.S.) (1990)

[10] Swift, G. W.: *Thermoacoustics: a unifying perspective for some engines and refrigerators*. Acoustical Society of America through the American Institute of Physics (2002)

[11] Ward, B., Clark, J., and Swift, G.: *Design Environment for Low-Amplitude ThermoAcoustic Energy Conversion (DeltaEC) Users Guide (Version 6.2)*. Los Alamos National Laboratory (2008)

[12] ANSYS, Inc., *ANSYS FLUENT 14.0 User's Guide* (2013)

NUMERICAL SIMULATION OF THERMOACOUSTIC HEAT PUMPING

KHEIRA[1] N.B., ABIDAT[1] M., BALTEAN-CARLES[2] D., WEISMAN[2] K., HIRECHE[3] O.
[1]Université des Sciences et de la Technologie d'Oran Mohamed Boudiaf, BP 1505 El - M'naouar, Oran 31000, Algérie
[2]Laboratoire d'Informatique pour la Mechanique et les Sciences de l'Ingenieur (LIMSI – CNRS), BP 133, F – 91403, Orsay, FraNCE
[3]Ecole Nationale Polytechnique d'Oran, BP 1523 el – M'naouar 31000, Oran, Algérie
E-mail: anhare@live.fr

In this study thermoacoustic heat pumping is simulated numerically. The device consists of a straight wave guide closed at the left end whereas an acoustic wave is generated at the right end of the tube usinga loudspeaker. A stack of parallel plates is placed near the left end of the tube. As a result of proper coupling between the acoustic wave and the solid stack plates, heat is pumped from the right to the left of the stack.

It is assumed here that thermal and viscous effects are localized near the stack plates, a domain therefore called the "active cell", considered short with respect to resonator's length. The flow inside the active cell is nonlinear and modeled with a low Mach number approximation [1-2]. The flow is assumed to be inviscid, isentropic and unidirectional in the remainder of the resonator. Therefore, the effect of the loudspeaker is straightforwardly used as prescribed velocity and acoustic pressure conditions on the right part of the active cell. The part of resonator left of the active cell is short, and therefore the temperature is assumed to be homogeneous, and the related speed of sound will vary slowly in time as a result of heat pumping. Proper matching between both parts of the device results in specific velocities at the left end of the active cell which are calculated using linear acoustic equations in the resonator. The periodicity of the stack plate arrangement results in reducing the active cell to a slice between two half-plates of the stack, extending into the resonator on both sides, with a total domain length of twice the stack length. The compressible Navier-Stokes equations in the low Mach number approximation are solved in this computational active cell domain. The solution is obtained using a finite volume code, second order accurate in time and space [3].

The simulation gives time dependent temperature, velocity and density fields inside the active cell until the establishment of a mean temperature gradient along the stack as a result of heat pumping. The mean velocity flow in also analyzed and the results are compared with the literature.

References

[1] Paolucci, S.: On the filtering of sound from the Navier-Stokes equations. Sandia National Laboratories Report SAND82-8257(1982).
[2] Hireche, O., Weisman, C., Baltean-Carlès, D., Le Quéré, P., Bauwens, L.: Low Mach number analysis of idealized thermoacoustic engines with numerical solution. J. Acoust. Soc. Am. 128 (6), 3438-3448 (2010).
[3] Duthil, P., Weisman, C., Bretagne, E., François, M.X.: Experimental and numerical investigation of heat transfer and flow within a thermoacoustic cell. Int. J. Transport Phenomena, vol. 6 (4), 265-272 (2004).

EXPERIMENTAL AND NUMERICAL INVESTIGATION OF THE ACOUSTIC ABSORPTION COEFFICIENT AT VERY LOW FREQUENCY

DAVID W.Y.K., YOUSIF A.A.
Department of Mechanical, Manufacturing and Materials Engineering
The University of Nottingham Malaysia Campus, Jalan Broga, 43500 Semenyih, Selangor Darul Ehsan, Malaysia
Corresponding author e-mail: yousif.abakr@nottingham.edu.my

Abstract: Sound attenuation had always been an interesting topic of investigation. The low frequency range investigated by researchers is usually from few hundreds to few thousands of Hz, still far away from the interesting zone for a low frequency thermoacoustic engine which operates in only 30-150 Hz. An acrylic straight tube configuration is used to investigate the effectiveness of different absorbing materials by using multi-microphone impedance tube technique. Results show the elastic termination has better attenuation characteristics compared to other alternatives. The results were also compared with the DeltaEC simulation.

Keywords: Thermoacoustic, Low frequency, Impedance tube, Attenuation, DeltaEC

1. Introduction

The thermoacoustic engine is a device that converts heat to sound energy. Thermoacoustic engines work according to Rayleigh's criterion [1]. The SCORE^{TM} thermoacoustic engine is a waste-heat driven travelling-wave engine utilises the waste heat from a cooking stove to create travelling acoustic oscillations through a closed loop at an operating frequency of 30-150 Hz [2]. To simulate the engine a speaker is used to generate sound waves at one of the termination ends in a straight tube, passive attenuation can be used to experimentally obtain a travelling wave using suitable absorbing material in an open loop, simulating the conditions of the engine while being able to control the frequency and amplitude of the wave. The sound absorption coefficient is an important indicator to determine how much sound energy is dissipated and reflected. There are several methods to determine the acoustic properties of a material with the aid of a commercial impedance tube setup. The standing wave impedance tube method makes use of the measured standing wave ratio (SWR) for a specific frequency in the tube to determine the acoustic properties by means of a microphone. The advantage of this method is that it is not necessary to calibrate the microphone. The disadvantages to this method are the complex setup with a movable probe and the time needed to find the location of the maximum and minimum pressures [3].

Seybert and Ross [4] proposed a different method for impedance tube measurements of sound absorption using the pressure readings at two positions, called the two-microphone method, which was faster than the SWR method. The acoustic wave response is separated into its reflection and incident components using a transfer function between the microphones. Chu [5] improved this method by including the tube-attenuation effect, allowing the microphones to be placed far away from the sample. Boden and Abom [6] found that the two-microphone method has its lowest sensitivity when the two microphones are separated by a quarter wavelength. The influence of errors in the two-microphone method has been investigated [7]. Chu [8] has proven in order to obtain accurate results, one of the microphones has to be placed close to the minimum pressure. The drawbacks are that its accuracy significantly degrades at large wavelengths and at microphone separations near one-half wavelength [9]. Jones and Parrot [10] described the multiple-microphone method on the pressure measurements at more than three positions. The multi-microphone method has no restriction on microphones separation relative to wavelength and allows results to be plotted with a single line based on the transfer function of a few microphone combinations. Another improved method uses least squares curve fitting to optimize the response of all the microphone positions to produce results with minimum error [11]. This paper focuses on measuring the acoustic properties using the least squares technique with the aid of multi-microphone impedance tube system. The current study also includes the comparison with the numerical results produced by the DeltaEC predictions [12].

2. Least Squares Technique

The formulation of this method was developed based of an imaginary source equidistant from the specimen in an impedance tube but in the negative x-direction as depicted in fig 1.

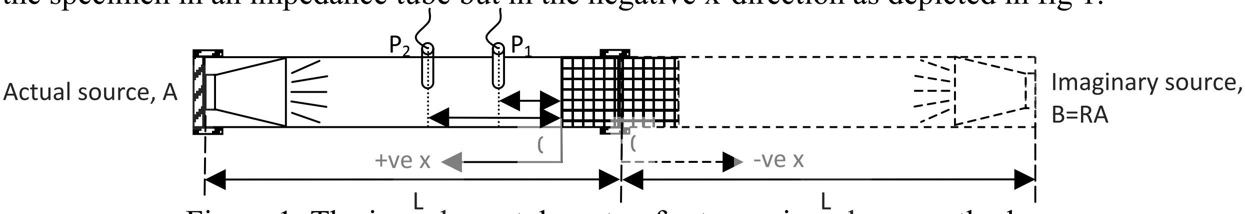

Figure 1: The impedance tube setup for two-microphone method.

The imaginary region is symmetrically mirrored at the end of the specimen from the actual source region. The amplitude of the imaginary source is given by

$$B = RA, \tag{1}$$

R is the complex reflection factor and A represents the amplitude of the actual source in Eq. (1). The relationship between the measured pressure from each microphone and both of the sources can be deduced with the aid of Green's function as shown in Eq. (2):

$$P_1 = Ag_{1A} + Bg_{1B} = A(g_{1A} + Rg_{1B}) \qquad P_2 = Ag_{2A} + Bg_{2B} = A(g_{2A} + Rg_{2B}) \tag{2}$$

where P_1 and P_2 are the pressure readings from the microphone 1 and 2 respectively. g_{1A} is the Green's function that relates the output of microphone 1 to the input of the actual source, A where g_{1B} is the Green function that relates the output of microphone 2 to the input of the imaginary source, B. Same relationship apply for Green functions, g_{2A} and g_{2B} with respect to microphone 2. Considering a plane wave is propagating in the tube, the Green functions can be expressed by Eq. (3):

$$g_{1A} = \frac{\rho_0 c}{2s} e^{-jk(L-dx1)} \qquad g_{1B} = \frac{\rho_0 c}{2s} e^{-jk(L+dx1)}$$

$$g_{2A} = \frac{\rho_0 c}{2s} e^{-jk(L-dx1)} \qquad g_{2B} = \frac{\rho_0 c}{2s} e^{-jk(L-dx2)} \tag{3}$$

where ρ_o is the air density, c is the speed of sound, s is the cross-sectional area of the tube, L is the total length of the system, dx1 and dx2 are the distances between the sample and the microphone 1 and 2 respectively. k represents the wave number which is defined as $2\pi f/c$. The transfer function, H_{12} is the pressure ratio between microphone 1 and 2 which can be rearranged to give the complex reflection coefficient, R as shown in Eq. (4) and (5). An optimised reflection coefficient, R_{opt} can be obtained by using a least squares solution with the aid of multi-microphone method. Eq. (6) can be used for any number of microphones M, where m indicates number of each microphone in the tube. The absorption coefficient, α of the sample can therefore be determined by Eq. (7):

$$H_{12} = \frac{P_2}{P_1} = \frac{s_{2A} + s_{2B} R}{s_{1A} + s_{1B} R} \tag{4}$$

$$R = \frac{s_{2A} - s_{1A} H_{12}}{s_{1B} H_{12} - s_{2B}} \tag{5}$$

$$R_{opt} = -\frac{\sum_{m=2}^{M} (s_{1A} H_{1m} - s_{mA})(s_{1B} H_{1m} - s_{mB})^{*}}{\sum_{m=2}^{M} |s_{1B} H_{1m} - s_{mB}|^{2}} \tag{6}$$

$$\alpha = 1 - |R_{opt}|^{2} \tag{7}$$

3. Experimental Setup

The experimental apparatus is composed of straight tubes and tapers which are made out of transparent acrylic plates. The total length of the system is 2.85 m and the wall thickness is 5mm. The straight tubes have internal square cross-sectional area of 0.0081 m^3 and the tapers have internal rectangular cross-sectional area of 0.0122 m^2 respectively. Tapers are used at two ends of the tube to smoothen the acoustic flow. The working fluid is air at atmospheric pressure. One extremity of the tube is attached to a loudspeaker while the tested sample is placed inside a wooden speaker box at the other end. Three different types of excitation signals were examined namely: Uniform white noise, Gaussian white noise, and Swept sine signal. A total of six microphones are used to measure the sound pressure along the length of the tube with the aid of a data acquisition system. There are basically three different types of absorbing materials, sponge, honeycomb and egg tray as shown in fig 2.

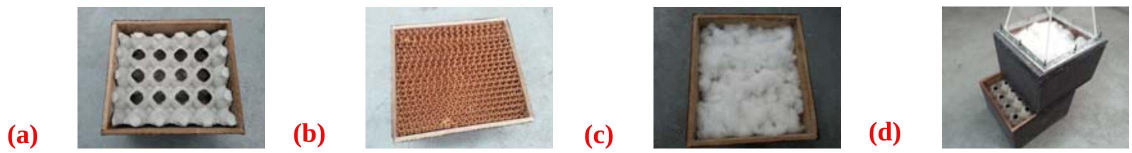

Figure 2: The four different types of materials that are under investigation: (a) Egg tray, (b) Honeycomb, (c) Sponge and (d) Egg tray and sponge combination.

4. DeltaEC^{TM} Modelling and Simulation

The Design Environment for Low-Amplitude ThermoAcoustic Energy Conversion (DeltaEC) model for the experimental setup is constructed by eighty three segments including the six Reverse Polish Notation (RPN) segments which are used to indicate the microphone locations and sixty three RPN segments after the HARDEND for the calculations of least squares technique. The impedance tube system is made out of six CONE segments and six DUCT segments. A total number of two GUESSes and two TARGETs are chosen. The first segment has always been a BEGIN segment and will be used as a loudspeaker that generates a sinusoidal wave in this case. Calculations have been done using a mean pressure P_m = 1 bar, a mean temperature T_m = 300 K and an acoustic pressure of 50 Pa. Air is used as working gas. Perspex is selected as the material for the components in the model with the aid of User Defined Function (UDF). The HARDEND acts as a rigid backing to reflect the acoustic wave. The GUESS vector, which has two components in this case, shows what variables

DeltaEC targets for a solution: the frequency and the volume flow rate. The initial guess of the frequency is 20 Hz and the initial value of the volume flow rate is 0.005 ms^{-1}.

5. Results and Discussion

In the range of the tested frequency, the type of input signal was found to be of small effect on the reflection and absorption coefficients, which is a good evidence of the validity of the experimental setup. Fig 3 presents the reflection and absorption coefficients of the rigid plate for different types of excitation signal from the source. The aluminium plate was found not to be a perfect rigid backing, but the reflection coefficient was close to unity in the tested frequency range. Moreover, the swept sine signal has shown deviation from all other signals and the numerical simulation in the low frequency range up to about 65 Hz, but the reflection coefficients for all types of signals behave in a similar manner elsewhere. The DeltaEC results were found to be in an good agreement with the experimental results. However the coefficients were slightly overestimated by the numerical simulation at the frequency above 120 Hz, this is due to nonlinear effects not taken into consideration by DeltaEC simulation.

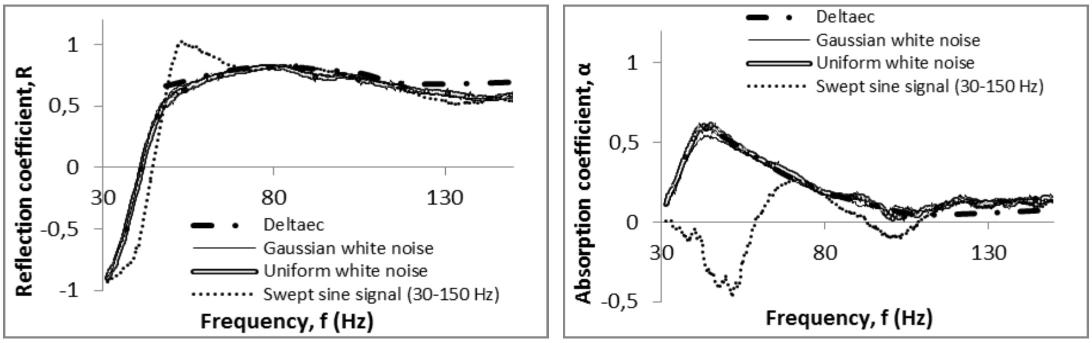

Figure 3: The results for reflection and absorption coefficients as a function of frequency when aluminium plate is used as the rigid backing.

The performance of the different material combinations was also under investigation. The elastic end shows the highest absorption coefficient relative to the other attenuation alternatives. The elastic end is essentially an acrylic plate with a thickness of 0.5 mm. Other attenuation arrangements work better at higher frequency range (few kHz) but for low frequency range, the elastic end was found to be better as shown in Fig 5. A general trend can be clearly observed that all the tested materials show a maximum absorption coefficient at the frequency of approximately 50 Hz. The absorption coefficient is gradually decreased after the peak value with increasing frequency. A compliance volume (empty box) gives a rather low absorption coefficient as compared to the rigid end (aluminium plate) at the frequency below 100 Hz. Whereas the absorption coefficient obtained for the rest of the absorbing material arrangements were higher than the rigid plate regardless of the frequency, which gives confidence in the validity of the results. Noting that the aluminium plate is approximately a rigid end and should reflect back most of the incident acoustic waves. Besides that, the sponge was found to have lower absorption coefficient compared to the elastic end, but it has a better absorption coefficient compared to all other materials or combinations of materials used in the frequency range above 50 Hz. All combinations of two materials performed better in the frequency range below 50Hz. With the inclusion of the sponge, all materials investigated exhibited a higher absorption coefficient when used in a combination of a pair of two materials together, compared with the case when each one is used separately. The sponge and honeycomb combination was found to have a better absorption coefficient than the egg tray and sponge combination.

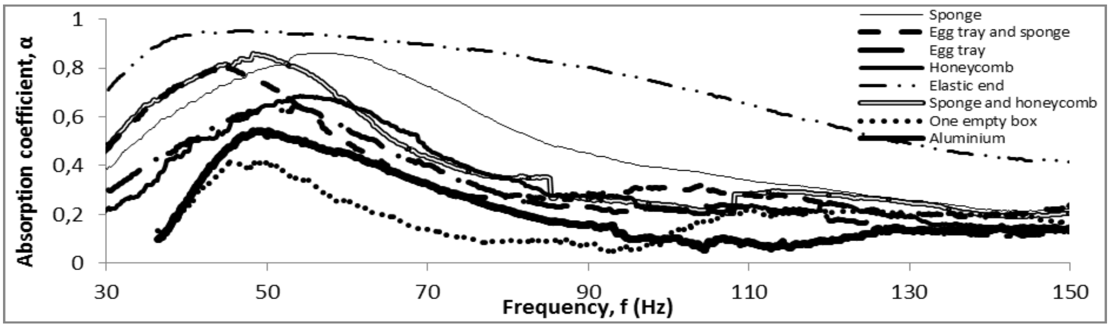

Figure 5: The responses of absorption coefficient as a function of frequency for all the tested materials when uniform white noise is used as the excitation signal.

6. Conclusions

The experimental setup for a low frequency travelling wave thermoacoustic engine was successfully modelled and simulated with DeltaEC and the comparison of the two results showed a very good agreement for a rigid end situation. Eight materials and combinations were investigated to realise that using an elastic end will work better for low frequency attenuation applications. The selection of the attenuation material or combination of material should be done very carefully and is strongly dependent on the target frequency. The outcomes of this work will be used for further ongoing investigations on loss assessments of the low frequency thermoacoustic engine. The validated DeltaEC model will be used to investigate a wider range of alternative for better optimisation.

References

[1] Swift, G., W.: A unifying perspective for some engines and refrigerators; USA; Acoustic Society of America; 2002.
[2] Chen, B., M.; Abakr, Y., A.; Goh, J., H.; Riley, P., H.; Hann, D., B.: Development and assessment of a SCORE Demo2.1 thermoacoustic engine; International Conference on Low-Cost, Electricity Generating Heat Engines For rural Areas; Nottingham; Uk; 2012.
[3] Fahy, F., J.: A simple method for measuring loudspeaker cabinet impedance; J. Audio Engineering Society; 41 (1993) 154-156.
[4] Seybert, A., F.; Ross, D., F.: Experimental determination of acoustic properties using a two-microphone technique; J. the Acoustical Society of America; 61 (1977) 1362-1370.
[5] Chu, W., T.: Extension of the two-microphone transfer-function method for impedance tube measurements; J. the Acoustical Society of America; 80 (1986) 347-348.
[6] Hans, B., Mats, A.: Influence of errors on the two-microphone method for measuring acoustic properties in ducts; J. the Acoustical Society of America; 79 (1986) 541-549.
[7] Mats, A.; Hans, B.: Error analysis of two-microphone measurements in ducts with flow; J. the Acoustical Society of America; 83 (1988) 2429-2438.
[8] Chu, W., T.: Further experimental studies on the transfer-function technique for impedance tube measurements; J. the Acoustical Society of America; 83 (1988) 2255-2260.
[9] Michael, G., J.; Patricia, E., S.: Comparison of methods for determining specific acoustic impedance; J. the Acoustical Society of America; 101 (1997) 2694-2704.
[10] Jones, M., G.; Parrott, T., L.: Evaluation of a multi-point method for determining acoustic impedance; Mechanical Systems and Signal Processing; 3 (1989) 15-35.
[11] Cho, Y., Nelson, P., A.: Least squares estimation of acoustic reflection coefficient" Institute of Acoustic Spring Conference; Salford; UK; 2002.
[12] Ward, B.; Clark, J.; Swift, G., W.: Design environmental for low amplitude thermoacoustic energy conversion; USA; Los Alamos National Laboratory; version 6.2; 2008.

THE POTENTIAL OF AN AIR-OPERATED THERMOACOUSTIC COOLER AT LOW PRESSURE

DAVID[1] W.Y.K., YOUSIF[1] A.A., NORMAH[2] M.G.
[1]Department of Mechanical, Manufacturing and Materials Engineering
The University of Nottingham Malaysia Campus, Jalan Broga, 43500 Semenyih, Selangor Darul Ehsan, Malaysia
[2]Faculty of Mechanical Engineering, University Technology Malaysia, 81310 UTM Skudai, Johor Bahru, Malaysia
Corresponding author e-mail: yousif.abakr@nottingham.edu.my

Abstract: Low cost thermoacoustic cooling system is still far beyond reach as it requires high-challenging pressurised gas which can only be obtained by using high cost fluids such as helium. This work investigates the potential enhancements of the thermoacoustic cooler using compressed air. The DeltaEC simulation is performed to study the coefficient of performance of the cooling system and the outcomes of this numerical simulation will be used to design a low cost thermoacoustic refrigeration system for developing countries. The study revealed the importance of the ambient duct length and the selection of the suitable frequency.

Keywords: Thermoacoustic, Compressed air, Refrigeration, Standing-wave, DeltaEC, COPR

1. Introduction

Standing-wave thermoacoustic refrigeration is a green technology which uses environmentally friendly working fluids to replace hazardous refrigerants. Besides that, another potential over the conventional cooling system is that it is simple in structure and has no moving parts. Moreover their miniaturisation is possible and would provide small-size refrigerators [1-2]. The standing-wave thermoacoustic cooler can potentially be applied in a wide range of cooling temperatures, from room temperatures to cryogenic temperatures. There are only limited research work done on room-temperature thermoacoustic coolers which use gases such as air to generate cooling [3]. Standing wave thermoacoustic refrigerator developed were mainly focused on the lowest achievable temperature for particular refrigeration applications including natural gas liquefiers or sensor cooling [4-5]. Most of the research work done up to date is making used of a relatively long stack compared with the resonator length and using helium as working gas and has a limited cooling load. As a result, some standing wave thermoacoustic refrigerators could reach cryogenic temperatures but with cooling capacities less than 10 W [6-9]. Presently thermoacoustic devices have low efficiency mainly due to the technical immaturity in designing the components of the devices. Hence, significant efforts are still needed to improve the thermoacoustic devices overall performance. The fundamental components of a thermoacoustic cooler include a stack, a resonance tube, two heat exchangers, and a loudspeaker which acts as a source to generate a standing acoustic wave. One of the noteworthy literatures, Wetzel and Herman showed a maximum value of 0.5 Carnot efficiency for the stack but the coefficient of performance for the commercial refrigerator can only reach up to 0.4 [10].

Efforts have been made to optimise the design of thermoacoustic coolers by improving the stack geometry. Several experimental works have shown that the linear thermoacoustic theory provides the optimum design of the thermoacoustic stack [11-12]. In order to generate an optimised temperature gradient, the stack is positioned between the pressure antinode and node. The stack materials should have low thermal conductivity, high heat capacity and an optimal value of the space between the stack layers. Tijani et al. investigated experimentally the optimisation of the stack spacing for maximum COP or for maximum cooling power [6-7]. It was observed that a stack spacing about three times larger than the thermal penetration depth is optimal for thermoacoustic cooling. Tasnim et al. conducted experiments on temperature fields at different locations on the stack plates and in the surrounding working fluid [13]. They found that axial heat transfer occurs in the stack extremities, as opposed to the hypothesis of a perfectly isolated stack used by Swift [14] in the linear thermoacoustic theory. The linear thermoacoustic theory prediction is based on the inviscid boundary-layer and short-stack approximation and neglecting the conduction of heat down the temperature gradient. Wetzel and Herman used a model based on the boundary layer approximation, and the short stack assumption to calculate the work flux and heat flux [10]. They optimised the system by adjusting nineteen design variables to achieve the best COP. Instead of using simplified work flux and heat flux equations, Minner et al. developed a design optimisation program that interacts with DeltaEC [15]. From a parametric study, they observed that the performance of the thermoacoustic refrigerator is sensitive to stack length, position, mean pressure and gas mixture, and less sensitive to the stack spacing.

The performance of the thermoacoustic cooler can also be affected by the design of the heat exchangers. Hence, two heat exchangers attached to both sides of the stack must also be optimised. Nsofor et al. studied the convection heat transfer coefficient on the outside surface of the heat exchanger in the thermoacoustic refrigeration system [16]. Results from the study showed that higher mean pressure will result in a greater heat transfer coefficient if the thermoacoustic cooler operates at the resonance frequency. Akhavanbazaz et al. conducted experiment on the impact of the heat exchange area in obstructing gas flow [17]. They found that heat exchanger with larger thermal contact area increase the heat exchange between the heat exchanger fluid and the stack, but it reduces the cooling power and increases the work input to the stack. Most of the literatures conceived to date only experimental work. In the present study, a numerical model of an air-operated thermoacoustic refrigerator for domestic cooling is designed with the aid of a linear one dimensional thermoacoustic software, DeltaEC developed by Ward et al. [18-19]. In order to predict the thermally induced acoustic waves accurately and also ensure the correct model used, the designed model was first validated against the work done by Tijani et al. [6-7]. The aim of this study is to perform parametric study on a household refrigeration system which operates in the temperature range between 273 and 305 K while having a high performance relative to Carnot value, COPR.

2. DeltaEC modelling

Design **E**nvironment for **L**ow-**A**mplitude thermoacoustic **E**nergy **C**onversion (DeltaEC) is used by researchers to evaluate the performance of the thermoacoustic devices [18-19]. The DeltaEC model of a thermoacoustic refrigerator is constructed by sixteen segments including the seven Reverse Polish Notations (RPN) segments which are used to perform the calculation of second law efficiency (COPR). A total number of four GUESSes and four TARGETs were chosen. The very first segment (zeroth segment) has been always a BEGIN segment. This segment contains global variables such as mean pressure, frequency, mean temperature and gas type. The calculations have been done using a constant temperature at the ambient heat exchanger T_h = 305 K and a regenerator length of 0.006 m. The BEGIN segment acts as a loudspeaker which generates sinusoidal standing wave in the refrigerator. A SURFACE segment comes next to account for oscillatory thermal losses at the first end of the resonator. The next segment is a lossy ambient temperature duct (DUCT) near the hot end of the stack. Heat exchangers (HX) are used to inject or remove heat. The first law of thermodynamics insists that this heat must equal to the difference between the upstream and the downstream total power ($\dot{H}_{tot}$). Copper is used as the material for both heat exchanges. The material selected for the parallel-plate stack which forms the heart of the refrigerator is Mylar. Both ambient and cold heat exchangers also possess parallel-plate geometry. Stainless steel was used for the rest of the components in the refrigerator. A taper section is connecting the large diameter tube to the small diameter tube. A spherical bulb or compliance was used to terminate the resonator. Air was used as the working gas.

The GUESS vector, which has four components, shows what Deltaec will regard as solution variables: the mean temperature, the volume flow rate, the heat rejected at the ambient heat exchanger, AHX and the length of the small diameter tube. The initial guess of the mean temperature is taken as 300 K and the initial value of the volume velocity is taken as $1\text{x}10^{-4}\text{ms}^{-1}$. A heat rate value of -10 W was chosen to be the initial guess for the AHX and the initial length of the small diameter tube is taken as 0.19 m. Basically, DeltaEC integrates the wave equation from BEGIN to END. Refine the GUESS vector to find a solution to the acoustics problem that arrives at the HARDEnd with zero complex volume flow rate. The phase difference between the pressure and volume flow rate was also targeted to be equal zero to enforce the resonance effect. The calculations of COP, COP Carnot and COPR were obtained with the aid of Reverse Polish Notation (RPN).

3. Results and Discussion

All the results are produced by incrementing the independent variable with an appropriate step value and running the calculations repeatedly. Meanwhile, amendments are made on the GUESS values so that iterations will still converge (providing reasonable estimates of TARGETs values). Fig. 1 depicts the relationship between the temperature difference at the stack extremities and the operating frequency at different cooling loads and different mean pressure values. All the plots show a maximum temperature difference at approximately 150 Hz. It can be seen that increasing the pressure will have a significant effect on increasing the temperature difference in the cooler, this behaviour is more obvious and can be noticed at higher cooling loads. At a cooling load of 4 W, the increase of pressure from 7 to 10 bars resulting in an increase of the maximum temperature difference by almost double.

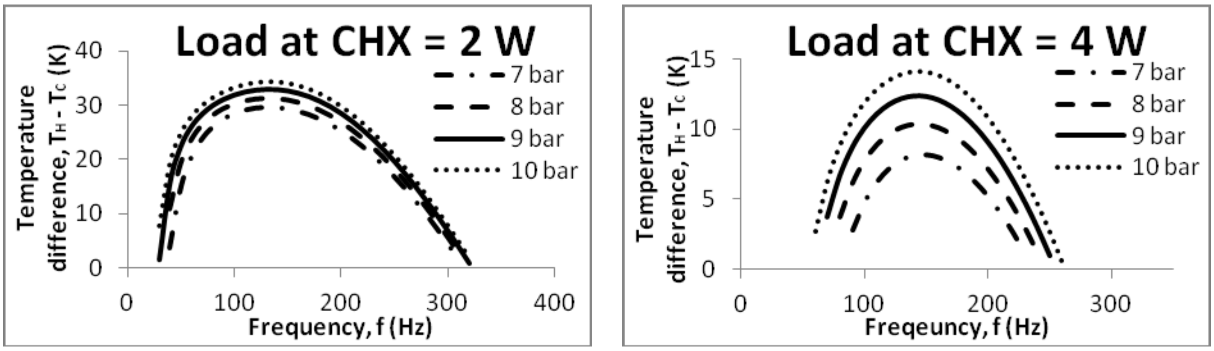

Figure 1: The results of temperature difference of the heat exchangers against the frequency of different heat load at the cold heat exchanger and different mean pressure when the drive ratio and the length of ambient duct are 2.5 % and 7.1 cm, respectively.

Furthermore, the coefficient of performance relative to Carnot's coefficient of performance is an important performance characterisation criterion for the thermoacoustic refrigerator. The response of COPR versus frequency for the different cooling loads and different mean pressure values is presented in fig 2. A nearly 30% of Carnot efficiency is achieved for a heat load at the cold heat exchanger of 0.5 to 1 W at the frequency around 45 Hz when mean pressure is between 7 to 10 bars. The mean pressure of 10 bar yields a higher COPR for all tested cooling loads compared to the other mean pressure values. For more reasonable load conditions between 3 to 4W the maximum COPR ranges between 7.5 to 15%. In general, the COPR decreases gradually from its peak value as both the frequency and the cooling load increase for all the examined mean pressure values.

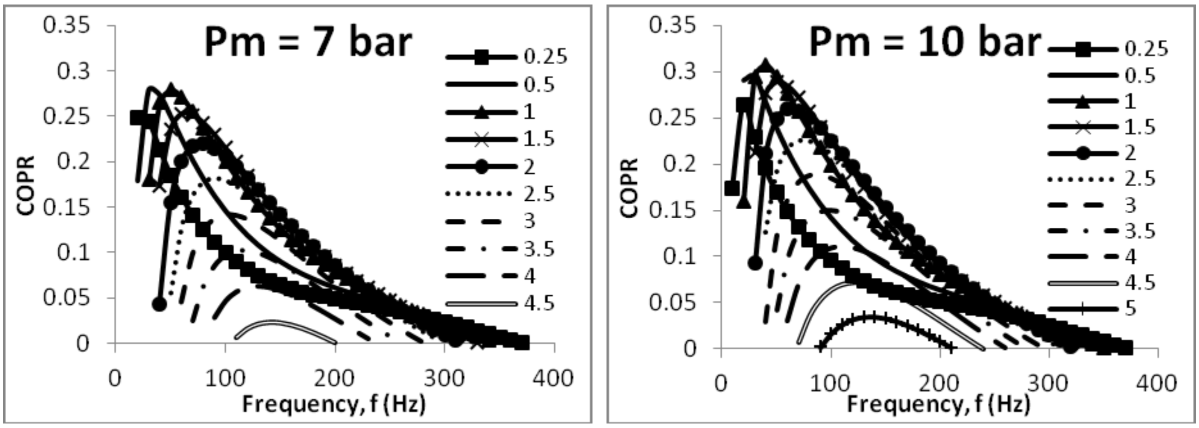

Figure 2: The graphs of COPR as a function of frequency for different mean pressure and different heat load at the cold heat exchanger when the drive ratio and the length of ambient duct are 2.5 % and 7.1 cm respectively.

In order to improve the thermoacoustic cooler footprint, thereby increase its potential application to be competed with the conventional refrigerator, the ambient duct is made smaller in size. Nevertheless, this will affect the performance of the overall system as the stack position from the loudspeaker also changes when the length of ambient duct is shortened. Fig. 3 shows the results of COPR against heat load at the cold heat exchanger for a constant frequency of 240 Hz. When a mean pressure of 10 bar is used, the best COPR is obtained when the ambient duct length is 2.1 cm. With the length of ambient duct increases, the COPR evolves in the same manner but with relatively low efficiency for each drive ratio value. It can be generally observed that the decreasing length of the ambient duct resulted in increasing the maximum COPR achieved at the same mean pressure. The drive ratio has no significant effect on the COPR or the location of its maxima at the same mean pressure.

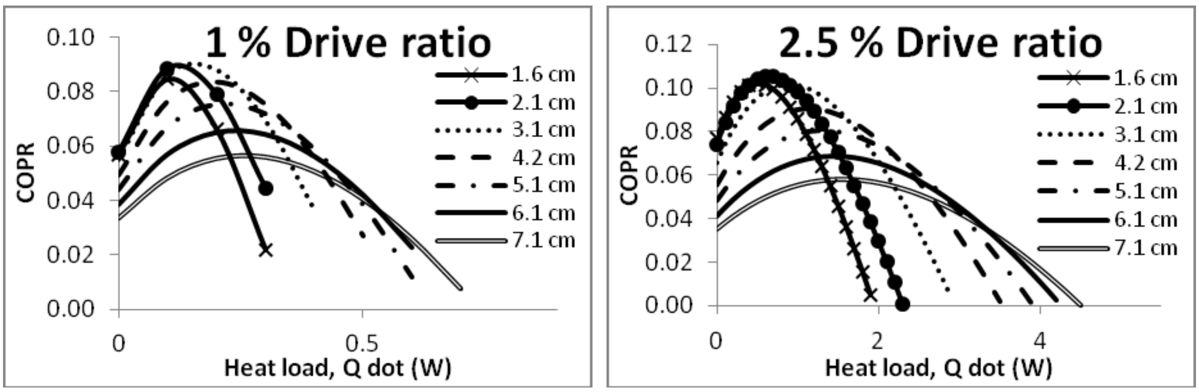

Figure 3: The results of COPR against heat load at the cold heat exchanger for different drive ratio and different the length of ambient duct when the mean pressure and operating frequency are 10 bar and 240 Hz respectively.

4. Conclusion

This work has successfully investigated the use of air as potential candidate for a low cost thermoacoustic cooler. In the proposed cooler, the pressure is not expected to be operating at more than 10 bars and the temperature difference is targeted to be ranging from 10-15 K below ambient conditions. The study revealed the importance of the ambient duct length as well as the selection of the suitable mean pressure and frequency. Air can be considered as an alternative fluid for a cooler at relatively low temperature difference requirements using renewable energy sources for the conditions of unavailability of conventional power sources.

References

[1] Swift, G., W.: A Unifying Perspective for some Engines and Refrigerators; USA; Acoustic Society of America; 2002.

[2] Symko, O., G.; Abdel-Rahman, E.; Kwon, Y., S.; Emmi, M.; Behunin, R.: Design and development of high frequency thermoacoustic engines for thermal management in microelectronics; Journal of Microelectronics; 35 (2004) 185-191.

[3] Channarong, W.; Kriengkrai, A.: The impact of the resonance tube on performance of a thermoacoustic stack; Frontiers in Heat and Mass Transfer; 2 (2011) 1-8.

[4] Luo, E.; Huang, Y.; Dai, W.; Zhang, Y.; Wu, Z.: A high-performance thermoacoustic refrigerator operating in room-temperature range; Chinese Science Bulletin; 50 (2005) 2662-2664.

[5] Dai, W.; Yu, G.; Zhu, S.; Luo, E.: 300 Hz thermoacoustically driven pulse tube cooler for temperature below 100 K; Applied Physics Letters; 90 (2011) 024104.

[6] Tijani, M., E., H.; Zeegers, J., C., H.; De Waele, A., T., A., M.: Design of thermoacoustic refrigerators Cryogenics; 42 (2002) 49-57.

[7] Tijani, M., E., H.; Zeegers, J., C., H.; De Waele, A., T., A., M.: Construction and performance of a thermoacoustic refrigerator; Cryogenics; 42 (2002) 59-66.

[8] Garrett, S., L.; Adeff, J., A.; Hofler, T., J.: Thermoacoustic refrigerator for space applications; Journal of Thermophysics and Heat Transfer; 7 (1993) 595-599.

[9] Berhow, T., J.: Construction and Performance Measurement of a Portable Thermoacoustic Refrigerator Demonstration Apparatus; USA; M. S. thesis; 1994.

[10] Wetzel, M.; Herman, C: Design optimisation of thermoacoustic refrigerators; International Journal of Refrigerator; 20 (1997) 3-21.

[11] Ke, H., B.; Liu, Y., W.; He, Y., L.; Wang, Y.; Huang, J.: Numerical simulation and parameter optimisation of thermoacoustic refrigerator; Cryogenics; 50 (2010) 28-35.

[12] Swift, G., W.: Thermoacoustic engines; Journal of the Acoustical Society of America; 84 (1988) 1145-1180.

[13] Tasnim, S., H.; Mahmud, S.; Fraser, R., A.; Measurement of thermal field at the stack extremities of a standing wave thermoacoustic heat pump; Frontiers in Heat and Mass Transfer; 2 (2011) 1-10.

[14] Swift, G., W.: Analysis and performance of a large thermoacoustic engine; Journal of the Acoustical Society of America; 92 (1992) 1515-1563.

[15] Minner, B., L.; Braun, J., E.; Mongeau, L., G.: Theoretical evaluation of the optimal performance of a thermoacoustic refrigerator; Ashrae; 103 (1997) 873-887.

[16] Nsofor, E., C.; Celik, S.; Xudong, W.: Experimental study on the heat transfer at the heat exchanger of the thermoacoustic refrigerating system; Applied Thermal Engineering; 27 (2007) 2435-2442.

[17] Akhavanbazaz, M.; Siddiqui, M., H., K.; Bhat, R., B.: The impact of gas blockage on the performance of a thermaocustic refrigerator; Experimental Thermal and Fluid Science; 32 (2007) 231-239.

[18] Clark, J., P.; Ward, W., C.; Swift, G., W.: Design environmental low amplitude thermoacoustic energy conversion; Journal of the Acoustical Society of America; 122 (2007) 3004-3014.

[19] Ward, B.; Clark, J.; Swift, G., W.: Design environmental for low amplitude thermoacoustic energy conversion; USA; Los Alamos National Laboratory; version 6.2; 2008.

INFLUENCE OF FEEDBACK LOOP CHARATERISTICS ON THE PERFORMANCE OF A TRAVELLING WAVE THERMOACOUSTIC ENGINE

JENN HSEN[1] (J. H. GOH), YOUSIF[2*] (Y. A. ABAKR), DAVID[3] (D.B. HANN)
[12] Department of Mechanical, Manufacturing and Materials Engineering/The University of Nottingham Malaysia Campus, Jalan Broga, 43500 Semenyih, Selangor Darul Ehsan, Malaysia.
[3] Department of Mechanical, Manufacturing and Materials Engineering/The University of Nottingham, University Park, Nottingham, NG7 2RD, UK
yousif.abakr@nottingham.edu.my

Abstract: A method to find experimentally the equivalent effective length of the Thermoacoustic (TA) Core of a TA Engine (TAE) was proposed. The TAE is first operated with various Feedback Loop (FL) length configurations. For every configuration, the frequencies of the sound waves were recorded to determine the wavelengths. These wavelengths are compared with the measured FL lengths and a constant deviation was observed, which gives the effective length of the TA Core as 55cm. This effective length is used in the calculation of a FL Ratio and the optimum FL Ratio was found to be 3.4.

1. Introduction

In 1979, Ceperley explained the fundamental principles of a Travelling Wave TAE and its potential of achieving higher efficiency compared to Standing Wave TAE [1]. However, it is until 20 years later only did this potential was significantly demonstrated by Backhaus and Swift [2]. By placing the regenerator in a toroid tube connected to a resonance tube, the Travelling Wave TAE designed by Backhaus et al. operated at 41% of Carnot efficiency, which was at least 50% higher than the best Standing Wave TAE at that time. Despite demonstrating that high efficiency is achievable, the design and operating conditions of this TAE is not feasible for many real world applications. Biwa et al. has shown that increasing the number of regenerators in the toroid is able to reduce the onset temperature of the TAE, thus increasing the possibility of different heat sources to the TAE [3]. Also, De Blok suggested that the regenerator in the toroid shape has to overcome large acoustic losses when connected to the resonance tube [4]. To overcome this, the resonance tube is removed entirely and the regenerators are connected in a complete loop, which is denoted as the FL. De Blok's design involves 4 regenerators positioned at quarter wavelengths apart so that the impedance of the TA core matches the impedance of the FL in a similar manner as a quarter wave impedance transformer, thus eliminating reflection in the FL [5]. The minimum onset temperature difference achieved by this engine is 30K [5]. These works have encouraged developments of multi-stage travelling wave TAEs.

In the University of Nottingham (UoN) and University of Nottingham Malaysia Campus (UNMC), together with the collaboration of the SCORE project [6], a two stage travelling wave TAE was designed and manufactured by Baiman et al. [7]. This TAE has two identical TA cores connected by the FL. Thus, the FL is separated into two sections. The lengths of these two FL sections are intended to be a quarter wavelength and three quarter wavelength to match the impedance of the TA core and the FL. However, the dimensions of the parts in the TA core also contribute to the length of the FL. Together with the complicated design in the TA core, it was found to be very challenging to obtain the optimum length configuration of the FL to achieve the quarter and three quarter wavelengths configuration.

This paper describes an experimental investigation conducted to obtain an equivalent length contributed by the TA core and subsequently obtain the optimum length configuration of the FL. An offset between the theoretical and measured length of the FL indicates the equivalent length of the TA core. If is found that the TA core of the TAE has an equivalent length of 55cm. This 55cm is included in the calculations of the FL Ratio and the optimum FL Ratio is 3.4. Modifications were made to the experimental set up as part of the future work.

2. Experiment

The Two Stage Travelling Wave TAE mentioned above was used in this experiment. The schematic diagram of the TAE is shown in Fig 1 and a detailed description of the TAE is presented in this paper. [7]. Referring to Fig 1, the FL connects both TA cores to form a closed loop. There are two U-Bends present in the loop. The straight sections of the FL are made by connecting PVC pipes of various lengths until the desired length is achieved. This allows the FL length to be varied and so does the operating frequency. During the experiment, the following data were measured and recorded:

- The frequency, f of the oscillation.
- The Peak Pressures at TA Core 1 and 2.
- The temperatures at the Hot Heat Exchangers (HHX) and Ambient Heat Exchangers (AHX). The difference between both heat exchangers' temperatures will be denoted as Temperature Difference (TD) for the rest of this paper.
- The length of section AB and section CD in Fig 1.

The HHX is heated from room temperature until 400°C, allowing the onset TD of the engine to be recorded. The AHX is kept at room temperature through water cooling. K-Type Thermocouples are attached to both sides of the Regenerator in both TA cores. The Pressure Transducers used are Kulite HKL-375 (M) Series. A self-written Labview Program is used to display the experimental data.

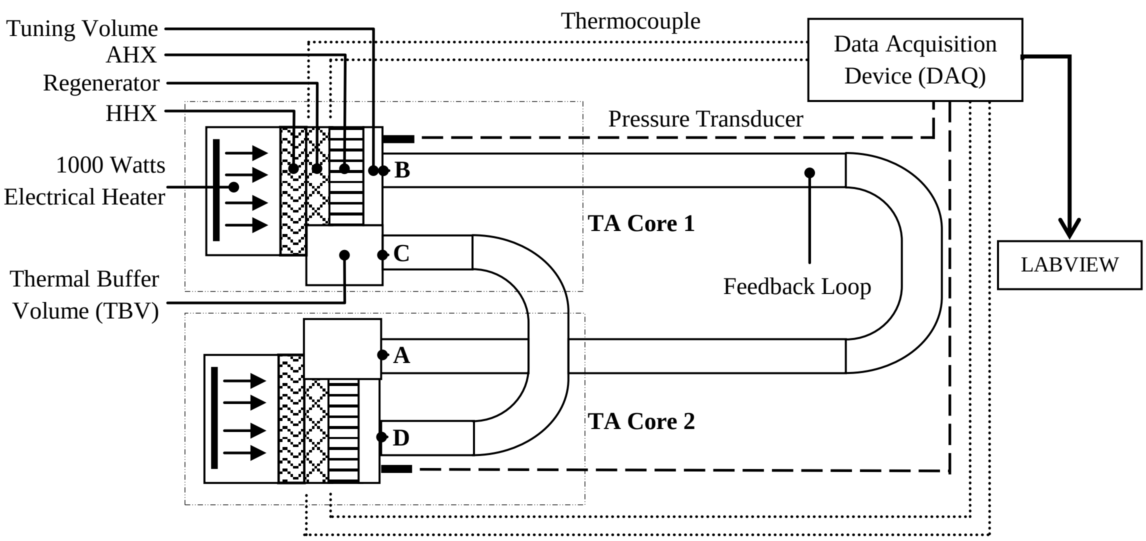

Figure 1: Schematic diagram of the Two Stage Travelling Wave TAE. Both TA cores are identical. Illustration is not to scale.

3. Results and Discussion

The lack of moving parts in a TAE allows the TA core to be designed to facilitate the performance of the heat exchangers. However, this would cause the TA core to be designed with complex geometries, as evident in the TAE used in this work. Due to this, it is very challenging to measure the effective length of the components in the TA core, which contributes to the overall length of the FL. Thus, an experimental investigation was carried out to estimate the effective length of the TA Core. The TAE was first tested at various FL configurations to obtain a range of operating frequencies. Then, by using the following relation,

$$v = f\,\lambda \qquad (1)$$

where v is the speed of sound (343 m/s) and *f* is the frequency of the wave in the engine, the wavelength, λ can be obtained. This wavelength is the Theoretical length of the FL. Fig 2 shows the measured and theoretical FL length at various frequencies. From equation (1), it is apparent that the wavelength and 1/*f* has a linear relationship, thus the FL lengths are plotted against 1/*f*. The Measured Length refers to the physically measured length. The lengths of both U-Bend centrelines are measured physically as 57cm. From Fig 2, it is observed that there is an offset of 1.1m between the Measured and Theoretical lengths for every frequency which reveals the length contributed by both TA cores. Thus, ignoring manufacturing tolerances, a single TA core contributes 0.55m.

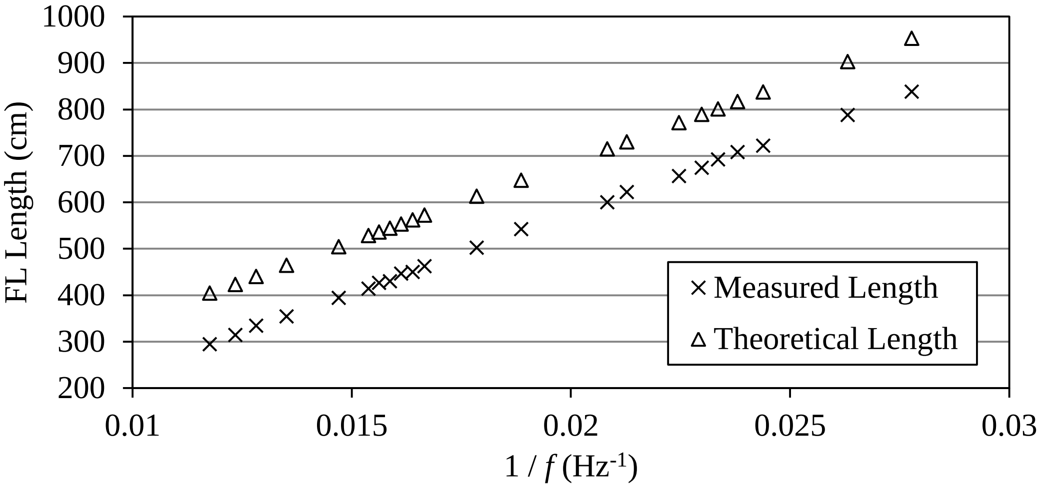

Figure 2: Measured (X) and Theoretical (Δ) FL length at various frequencies, *f*.

By adding 0.55m to the length of section AB and CD, the FL Ratio of every FL configuration was computed by

$$FL\ Ratio = \frac{0.55m + Length\ AB}{0.55m + Length\ CD} \qquad (2)$$

The TAE performance at various FL Ratios was compared in Fig 3. The Average Onset TD between both TA cores (left vertical axis) and Peak Pressures at TD of 300 ºC (right vertical axis) are plotted against the FL Ratio. When the TD reaches 300°C, the corresponding Peak Pressures in both TA cores are recorded to give a common point for comparison. The desired performance is for a low Onset TD and high Peak Pressure, which was observed at the FL Ratio of 3.4. Also, notice that at smaller FL Ratios, the Peak Pressure in TA Core 1 is lower than that in TA Core 2, but at larger FL Ratios the Peak Pressure in TA Core 1 is higher. The

FL Ratio that gives the highest Peak Pressures at TD 300 °C occurs when the Peak Pressure at both TA cores are similar, indicating that both TA cores are performing at its optimum at this FL Ratio. At FL Ratio of 3.4, the Length AB and CD are 5.51m and 1.23m respectively. The Onset TD recorded for TA Core 1 and 2 are 167.61 °C and 136.66 °C respectively. However, to achieve the quarter wavelength and three quarter wavelength configuration, a FL Ratio of 3.0 is desired. The TAE performs at its optimum at FL Ratio of 3.4 indicates that a slight impedance mismatch between the FL and the TA core is desired. A slight impedance mismatch will introduce a minor Standing Wave component to the sound wave which has shown to improve the performance of the TAE [8].

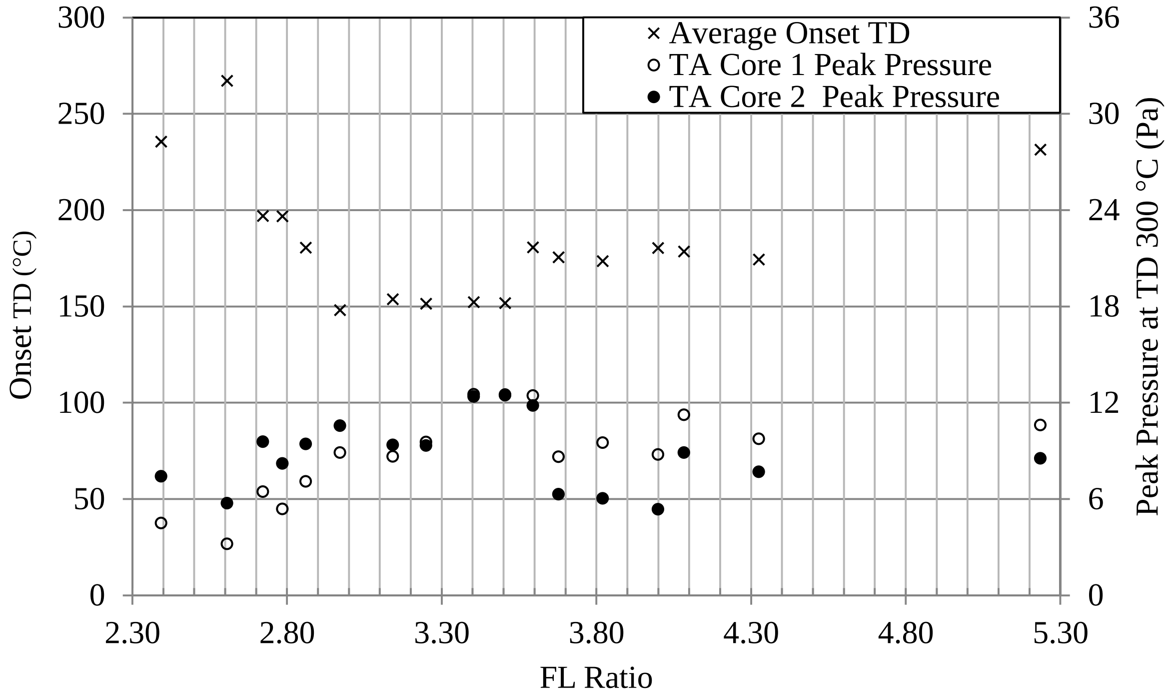

Figure 3: Comparison of the TAE performances at various FL Ratios.

Subsequently, 8 pairs of pressure transducers are added to the FL to investigate the sound wave produced by the TAE. The pressure transducers are 15cm apart in every pairings. The position and Peak Pressure recorded by the pressure transducers are shown by the markers (Δ) in Fig 4. Point A (from Fig 1) is set as the starting position and the position of all the components in the FL are referenced to Point A. The FL Ratio of the FL configuration shown in Fig 4 is 3.95, where the lengths of section AB and section CD are 625 cm and 117cm respectively. From Fig 4, it is observed that the sound wave produced by the TAE is amplitude modulated, indicating a Standing Wave component is present in the sound wave.

Unfortunately, at the time of writing of this paper (March 2014), the Peak Pressure along the FL of other FL Ratio has not been tested. It is intended to obtain the Standing Wave Ratio (SWR) of the sound wave produced by the TAE at various FL Ratios. The intensity of the sound wave along the FL could also be estimated [9]. These will be the subject of future work. The TAE used is still in its development stages and other features in the TA core are still not optimized. The work presented is useful in predicting the optimum length configuration of the FL of the TAE, especially when modifications are made to the TA core. It is also important to note that this experiment was conducted at the TAE's operating conditions.

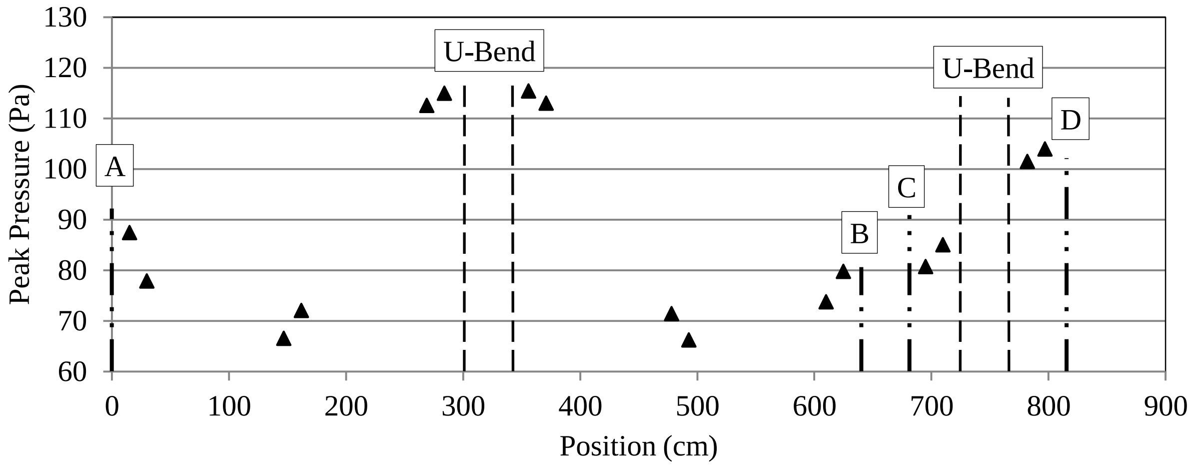

Figure 4: Peak Pressures along the FL.

4. Conclusion

In a Two Stage Travelling Wave TAE developed by the SCORE project, the FL was designed such that the two TA cores are a quarter wavelength apart and three quarter wavelength apart for the remainder of the FL. However, due to the complexity of the TA core, the length of the FL is hard to estimate as the effective length of TA core has to be accounted for as well. An experimental investigation to obtain the effective length of the TA core was explained. The effective length was found to be 55cm and this is then used in the calculations of a FL Ratio. A figure of Onset Temperature Difference and Peak Pressure versus FL Ratio was plotted to compare the TAE performance at various length configuration. It is found that the TAE performs best at a FL Ratio of 3.4.

Subsequently, pressure transducer pairs are added to the FL to measure the Peak Pressure along the FL. The Peak Pressure along FL of other configurations will be analyzed and compared to confirm that the FL Ratio of 3.4 is the optimum for the TAE. This will be included in future work.

5. References

[1] Ceperley, P. H.: A pistonless Stirling engine—the traveling wave heat engine. J. Acoust. Soc. Am. 66 (1979) 1508–1513.
[2] Backhaus, S.; Swift, G.: A Thermoacoustic-Stirling Heat Engine. Nature (London). 399 (1999) 335-338. doi:10.1038/20624 .
[3] Biwa, T.; Hasegawa, D.; Yazaki, T.: Low temperature differential thermoacoustic Stirling engine. Appl. Phys. Lett. 97 (2010). doi: 10.1063/1.3464554
[4] De Blok, K.: Low operating temperature integral thermo acoustic devices for solar cooling and waste heat recovery. Acoustics'08, Paris. PA15.
[5] De Blok, K.: Novel 4-stage traveling wave thermoacoustic power generator, Proceedings of ASME 2010 3rd Joint US-European FEDSM2010-ICNMM2010. http://www.thatea.eu/publications/
[6] Riley, P.H.; Saha, C.; Johnson, C.M.; Designing a Low-Cost, Electricity Generating Cooking Stove, Technology and Society Magazine IEEE, summer 2010. Digital Object Identifier 10.1109/MTS.2010.937029, 1932-4529/10/$26.00©2010IEEE.
[7] Chen, B. M.; Abakr, Y. A.; Goh, J. H.; Riley, P. H.; Hann, D.B.; Development and Assessment of a SCORE Demo2.1 Thermo-Acoustic Engine, International conference on Low-cost, electricity generating heat engines for rural areas. 2 3 April 2012 Nottingham UK.
[8] Petculescu, G.; Wilen, L. A.: Traveling-wave amplification in a variable standing wave ratio device. Acoust. Res. Lett. Onl. (2002) doi: 10.1121/1.1466675
[9] Fahy, H. J.; Sound Intensity. United States of America: Elsevier Applied science Publishers 1989.

COMPACT THERMOACOUSTIC COOLERS

LOTTON P., POIGNAND G., PENELET G., BRUNEAU M.
Laboratoire d'Acoustique de l'Université du Maine (LAUM), UMR CNRS 6613, Avenue Olivier Messiaen, 72085 Le Mans Cedex 09, France
E-mail: pierrick.lotton@univ-lemans.fr

Abstract : The paper focuses on works carried out on compact coolers at LAUM, including recent developments. System architectures are described and the main experimental results are presented. Finally, performance of such small scale thermoacoustic devices are compared with the one obtained with standing wave device having similar stack. Slightly higher efficiency than in the standing wave system is found, yet at much smaller size.

1. Introduction

The compactness of thermoacoustic devices is a topic of continuing importance in fundamental thermoacoustics and in its practical applications. It is still a challenging topic to scale down the devices without compromising their performance. Several attempts to reduce the size of thermoacoustic refrigerators have been carried out since the early 2000's. Initially, some authors proposed to reduce the dimensions of the systems, while maintaining a classical design by raising the acoustic frequency. Thus, miniaturized standing-wave refrigerators were developed using both a piezoelectric actuator as sound source and a micro machined stack whose dimensions are matched with the high working frequency [1-3]. However, the performance of these systems is limited in terms of both heat extracted from the cold source and coefficient of performance (COP).

Thus, other more efficient architectures have been developed. Research on such architectures has been conducted in recent years at Laboratoire d'Acoustique de l'Universite du Maine (LAUM). The compact coolers developed in this framework involve non resonant small cavity fitting the stack dimensions, instead of a half- (or quarter-) wavelength acoustic resonator. The small cavity is driven by a set of loudspeakers coupled through the stack. Tuning all speakers allows controlling both the acoustic pressure field and the particle velocity field inside the stack. The acoustic pressure and the particle velocity are not linked anymore by standing wave or travelling wave conditions, and can then be managed independently. Moreover, the working frequency is not related to resonance conditions, therefore either a quasi-isothermal stack (regenerator) or a quasi-adiabatic stack can be used in the same cavity. Then, optimal acoustic field for thermoacoustic process can be reached in terms of frequency, pressure amplitude, velocity amplitude and phase difference between pressure and velocity.

The aim of this paper is to focus on work carried out on this subject at LAUM, including recent developments. System architectures are firstly described. Analytical model of their behavior are then briefly given and some experimental results are presented. Finally, performance of such small scale thermoacoustic devices are compared with the one obtained with standing wave device having similar stack.

2. Compact cooler description

A first kind of compact thermoacoustic device has been designed at LAUM in accordance with patent requirements [4]. A schematic view of this device is given in Figure 1. It is a non resonant thermoacoustic device in which the resonator is replaced by a cavity fitting the dimensions of the stack. The acoustic pressure and the particle velocity are generated in the stack by a set of loudspeakers: a couple of face-to-face loudspeakers (supplied with electrical voltages in phase) generates the pressure field in the cavity, while another couple (supplied with electrical voltages $\pi/2$ out of phase) generates the particle velocity field along the z axis. The acoustic pressure and the particle velocity are not linked anymore by standing wave or travelling wave conditions, and can then be managed independently. Particularly, their amplitude ratio and relative phase can take any value. The working frequency is not imposed by resonance conditions anymore, so a diminution of the dimensions of such a system does not come necessarily with an augmentation of this working frequency. Consequently, acoustic pressure, particle velocity and frequency can be easily and independently controlled in order to create an optimal acoustic field and to monitor it during the thermoacoustic process.

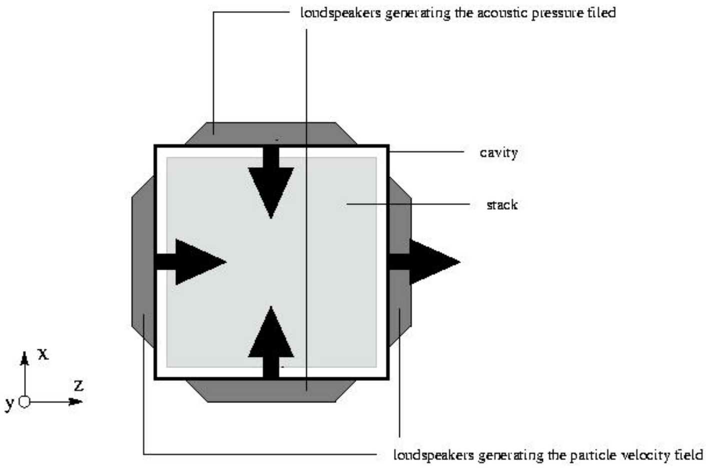

Figure 1: Compact thermoacoustic cooler using four acoustic sources.

Experiments on this prototype have showed that the particle velocity along the x axis close to the loudspeakers generating the pressure has the same order of magnitude as the optimal particle velocity generated along the z axis. Thus, the parcels motion between two plates of the stack is not a rectilinear motion anymore, but an ellipsoidal one. Then, the associated thermoacoustic heat transfer becomes a two-dimensional one and, consequently, the temperature difference is not necessarily established along the z-axis, as in a classical resonant thermoacoustic refrigerator. Moreover, this additional particle velocity along the x-axis leads to a significant additional global heating of the stack due to viscous dissipation.

These effects have then been taken into account in the design of a second generation of compact refrigerator prototype. A sketch of this second device is presented in Fig. 2. Similarly to the previous prototype, the thermoacoustic core almost fills the cavity, but it is surrounded by a peripheral channel. Only two loudspeakers are used in this prototype. The ends of the stack can then be considered set on either side of an acoustic inner source (labeled 1) which then creates the monochromatic displacement field needed in the acoustic process, in a frequency range such than the wavelength remains much greater than the dimensions of the cavity. A quasi-uniform pressure field is driven at the same frequency by another source (called outer source, labeled 2) set on a wall of the cavity. Similarly to the previous prototype, the working frequency, the amplitude and the phase difference between the pressure and the velocity fields can be tuned for optimizing the performance of the device. With this co-axial design, the particle velocity is uni-directional, as well as the main temperature gradient generated along the stack. This facilitates the implantation of heat exchangers.

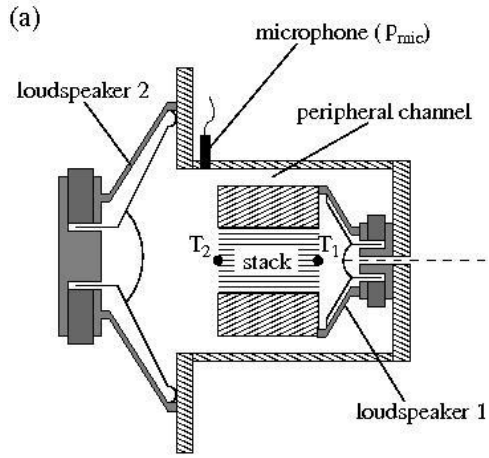

Figure 2: Co-axial compact thermoacoustic cooler.

3. Optimal acoustic field

An electrical network equivalent to the compact cooler is given on Figure 3, showing that the pressure and the velocity in the stack are easily controlled from the electrical tensions provided to both loudspeakers [6]. In 2006, Poignand et al. [4] have shown analytically that the thermoacoustic process in a stack can be optimized when tuning the acoustic field to optimal values of the acoustic pressure amplitude, the particle velocity amplitude, and their relative phase. The optimal values of particle velocity amplitude and relative phase depend on the frequency, on the shape and the dimensions of the stack, and on the thermo-physical properties of the fluid and the stack, while the optimal value of the acoustic pressure is the maximum pressure level which can be generated within the stack. This optimal field can easily be tuned within the stack of the non resonant compact coolers considered herein.

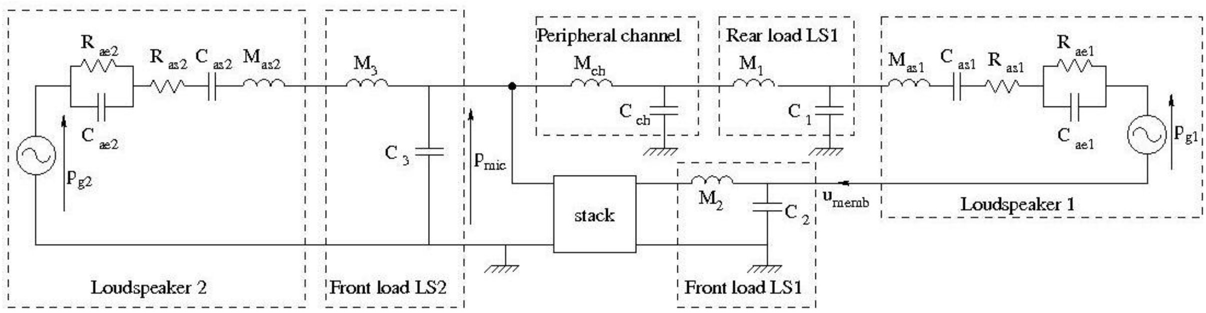

Figure 3: Electrical network equivalent to the co-axial compact cooler.

Experiments have been conducted on a prototype [7]. Experimental temperature difference between the stack ends are given in Figure 4. It shows the influence of the three acoustic parameters (the acoustic pressure amplitude p, the particle velocity amplitude u and the relative phase $\varphi = \varphi_u - \varphi_p$) on the compact system performance. The effect of each of the three acoustic parameters is investigated independently by fixing the two others parameters at their theoretical optimal value. Note that in this setup, the pressure peak amplitude is set to p = 1000 Pa which is close to the maximum pressure that can be generated by the loudspeaker 2 without harmonic distortion.

Figure 4.a shows the evolution of the temperature difference ΔT normalized by its maximum value ΔT_{max} as a function of the acoustic pressure p when $u = u_{opt}$ and $\varphi = \varphi_{opt}$. As predicted by the linear steady state theory [5] (solid line), the experimental results obtained

(crosses) show that the temperature difference ΔT increases with acoustic pressure. Figure 4.b shows the evolution of the temperature difference ΔT normalized by its maximum value ΔT_{max} as a function of the velocity amplitude u (when $p = p_{max}$ and $\varphi = \varphi_{opt}$). A good agreement is obtained between the theoretical predictions (solid line) and the experimental results (crosses). Especially, the experimental optimal velocity amplitude is found close to the theoretical one (u_{opt} = 1.4 m.s^{-1} for the experimental device under test). The normalized temperature difference $\Delta T/\Delta T_{max}$ versus the relative phase φ (when $p = p_{max}$ and $u = u_{opt}$) is shown in Fig. 4.c. When the phase shift φ varies between ($-3\pi/4$) and ($\pi/4$), the temperature difference $\Delta T/\Delta T_{max}$ is positive and the cold-side of the stack is near the loudspeaker 1 controlling the velocity, whereas for a phase φ comprised between $\pi/4$ and $5\pi/4$, the temperature difference is negative and the cold-side stack end is located near the loudspeaker 2 controlling the pressure. Thus, it is worth noting that the cold-side stack end location can be fixed by the phase φ. From the experimental results presented in Fig. 4.c, it can be noticed that there is an optimal phase $\varphi_{opt,exp} = 3\pi/4$ rad which corresponds to the theoretical optimal phase. However, the evolution of the experimental normalized temperature difference does not fit completely the theoretical one. This difference is due to the heating of the loudspeaker voice-coil controlling the velocity. This heating is added to the thermoacoustic heat flux and leads to an increase of the stack end temperature near the loudspeaker 1.

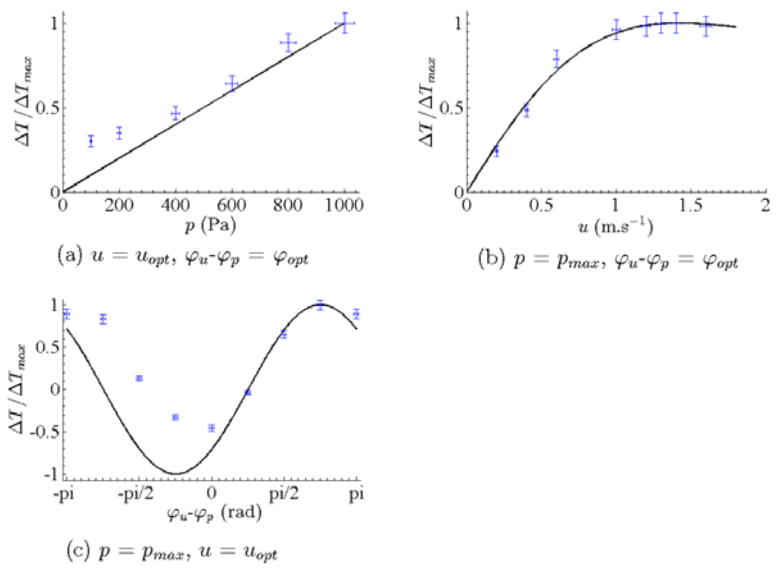

Figure 4: Normalized temperature difference $\Delta T/\Delta T_{max}$ between the stack ends measured ($\times$) and calculated (straight line) as a function of (a) the acoustic pressure p, (b) the particle velocity amplitude u and (c) their relative phase φ .

4. Comparison with resonant thermoacoustic coolers

Using the electrical network given in Figure 3 and the classical thermoacoustic theory allows the prediction of the theoretical temperature difference and COP obtained in a co-axial compact cooler tuned at its optimal operating point. This theoretical performance can then been compared with the one of a conventional standing wave acoustic refrigerator when using similar stack in both devices.

The standing wave cooler considered for the comparison consists of a half wavelength straight resonator driven by an acoustic source. The source is chosen to be the same loudspeaker as the one which controls the acoustic pressure field in the small cavity cooler.

The resonator length is adjusted in such a way that the resonance frequency of the system is the working frequency of the compact device (i.e. f = 200 Hz for the device under test). The same stack is used for both the compact device and the standing wave cooler. In the standing wave cooler, the stack is set at its better location along the resonator for which the temperature difference is maximal [4]. The small cavity cooler is set at its optimal working point. To fulfill the comparison of the two devices, their achieved temperature difference ΔT, thermoacoustic heat flux Q and global efficiency η, are compared when the same electric power is provided to the sources (here, P_{el} = 7.7 W). Actually, in the case of the compact device, P_{el} represents the total electric power provided to the two loudspeakers. The theoretical acoustic field in the stack as well as theoretical performance is given in Tab. 1 for both systems.

Small cavity cooler	Standing wave cooler
Acoustic field in the stack	
p = 1000 pa	p = 1335 pa
u_{opt} = 1.43 m.s^{-1}	u_s = 1.27 m.s^{-1}
φ_{opt} = 3π/4 rad	φ_s = π/2 rad
Theoretical performance	
ΔT_{max} = 15.8 K	ΔT_s = 13.8 K
Q_{max} = 0.17 W	Q_s = 0.15 W
P_{el} = 7.7 W	$P_{el,s}$ = 7.7 W
η = 2.14%	η_s = 1.88%

Table 1: Theoretical comparison between the behaviour of a small cavity cooler and the behaviour of a standing wave cooler.

3. Conclusion

The experimental results presented here illustrate the thermal behaviour of compact thermoacoustic devices as a function of the acoustic field inside the stack. They validate theoretical results, namely the existence of an optimal acoustic field leading to better performance in terms of temperature difference, heat flux or COP. Then, a theoretical comparison with performance reached with classical device having equivalent stack (standing wave device) show the potentiality of this compact thermoacoustic cooler. In particular, beyond its compactness and flexibility, the global efficiency of the proposed device is greater than, or at least of the same order of magnitude as, that of classical devices having equivalent stack although it is much smaller.

5. References

[1] T.J. Hofler, J.A. Adeff, "A miniature thermoacoustic refrigerator for integrated circuits", Proc. the 17th International Congress on Acoustics, Rome September 2-7, 2001, P. 119.

[2] B. Lihoreau, P. Lotton, M. Bruneau, V. Gusev, "Piezoelectric Source Exciting Thermoacoustic Resonator: Analytical Modelling and Experiment", Acta Acustica United With Acustica, Vol. 88 (2002) 986 – 997

[3] O.G. Symko, E. Abdel-Rahman, Y.S. Kwon, M. Emmi, R. Behunin "Design and development of high-frequency thermoacoustic engines for thermal management in microelectronics", Microelectronics Journal 35 (2004) 185–191

[4] G. Poignand, B. Lihoreau, P. Lotton, E. Gaviot, M. Bruneau, V. Gusev, Optimal Acoustic field in compact thermoacoustic refrigerators, Appl. Acoust., 68, p. 642-659, 2007

[5] G. Swift, "Thermoacoustic engines", *J. Acoust. Soc. Am.* 84 (4), 1145–1180 (1988).

[6] G. Poignand, P. Lotton, G. Penelet, M. Bruneau, Thermoacoustic, Small Cavity Excitation to achieve Optimal Performance, Acta Acustica united with Acustica, 97, p. 926-932, 2011.

[7] G. Poignand, A. Podkovskiy, G. Penelet, P. Lotton, M. Bruneau, "Analysis of a coaxial, compact thermoacoustic heat-pump", Acta Acustica united with Acustica, 99, pp. 898 – 904, ISSN 1610-1928, 2013

Bi-directional turbines for converting acoustic wave power into electricity

Kees de BLOK[1], Pawel OWCZAREK[2], Maurice-Xavier FRANCOIS[3]

[1] Aster Thermoacoustics, Smeestraat 11, 8194LG Veessen, The Netherlands
[2] Future Energy Management, Weegschaalstr.45, 7521cc Enschede, The Netherlands
[3] Hekyom, 3, rue de la Croix Martre, 91120 Palaiseau, France

e-mail address of corresponding author: c.m.deblok@aster-thermoacoustics.com

Abstract
Converting acoustic power from thermoacoustic engines into electricity using resonant linear alternators is a common approach but has severe limitations in terms of cost and scalability. The paper will describe in detail the experiments and measurement results on various bi-directional turbines in high frequent acoustic flow fields and at elevated mean pressures. The conclusion from the experiments so far is that this type of turbine could be a cost effective, scalable and efficient device for converting acoustic wave energy into rotation and from there into electricity.

1. Introduction

Thermoacoustics is a key enabling technology for the conversion of heat into acoustic power. Nowadays thermoacoustics in itself is well understood and has proven to be a generic applicable and efficient conversion technology. For practical and economic viable applications however, two issues have to be solved in a practical and cost effective way. (1) heat to be converted need to be supplied at high or medium temperature and rejected at a lower temperature from the process with minimal temperature loss and (2) high acoustic (wave) power generated has to be converted into electricity. Focus of this paper is on the conversion of the generated acoustic power into electricity.

Converting acoustic power from thermoacoustic engines into electricity using resonant linear alternators is a common approach but has severe limitations in terms of cost and scalability. The increase of moving mass with increasing power finally sets a practical limit to the output power caused by the extreme periodic forces in the construction and the difficulty to maintain clearance seals ($\approx$ 70 μm) stable over large stroke amplitudes.

Linear alternators make use of the pressure variation of the acoustic wave. There is however no physical reason why not using the periodic velocity component of the acoustic wave. A way to convert such a bi-directional flow into rotation is known from shore and off-shore electricity production plants based on an oscillating water column (OWC) [1,2,3]. In this type of power stations, waves force a water column in a chamber to go up and down. This chamber is connected to the open atmosphere and the periodic in- and outflow of air drives a bi-directional turbine of which the rotation direction is independent of the flow direction. In a thermoacoustic system similar periodic flow conditions exist, so in principle, bi-directional turbines can be deployed for conversion of acoustic wave motion as well.

In OWC plants, using air at atmospheric pressure, the reported conversion efficiency is in the range of 25 to 40%. This modest efficiency is because of the performance of (bi-directional) turbines depends on de density of the working fluid. Thermoacoustic engines, fortunately operate at elevated mean pressures up to 40 bar and the increased gas density will raise turbine efficiency up to 85%.
This makes bi-directional turbines a low cost and scalable candidate for converting the generated acoustic power into electricity. For testing and validating of this option a few bi-directional impulse turbines were are designed and build using 3-D rapid prototyping. In parallel, a numerical model was developed. From the results we could estimate the performance based on the pressure distribution on the blade and the measured performance.
The paper will describe in detail the experiments and measurement results on various bi-directional turbines in high frequent acoustic flow fields and at elevated mean pressures.
Results so far are encouraging. The conclusion from the experiments is that this type of turbine could be a cost effective, scalable and efficient device for converting acoustic wave energy into rotation and from there into electricity.

2. Description of the turbine under test

A bi-directional turbine consists of rotor with symmetric blade shape enclosed by two guide vane sets. The rotor is connected to a brushless electromotor used as generator. The dimensions and assembly is shown in Figure 1and Table 1.

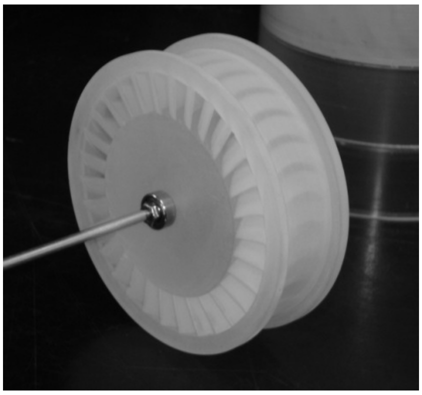
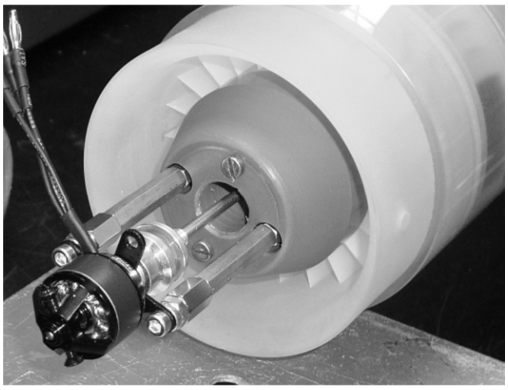

Figure 1 Rotor of the bi-directional turbine and the assemble with guide vanes and generator

Table 1 Dimensions of the turbine

Rotor diameter	84	mm
Blade height	6	mm
Blade chord	25	mm
Blade thickness	5.5	mm
Mutual space between blades	2.1	mm
Number of blades	31	

The generator is a brushless outer runner type A10-9L made by Hacker [4]. The output of the generator is connected to a set of 10W resistors which can be set to 1 to 5 Ω. Efficiency of this motor as generator is measured separately in order to be able to estimate the actual shaft power of the rotor

The acoustic source, generating the periodic flow, consist of a 12” 500W bass speaker with a maximum cone stroke of about 50mm p-p driven by a function generator and power amplifier. The 300 long coupling tube between speaker and turbine is equipped with a dpdx probe for measuring the acoustic power towards the turbine. Output power is measured by the electric power dissipated in the load resistor of the generator corrected for the known generator efficiency to yield the shaft power.

The mechanical turbine output power (P_m) at the rotor shaft is given by

$$P_m = To.\omega \qquad (1)$$

In which To is the torque and ω the rotational speed. Torque and rotational speed are both functions of gas velocity so output power is proportional with gas velocity squared. For thermoacoustic applications the gas velocity and pressure amplitude are related by the acoustic impedance. Velocity amplitude of a traveling in an acoustic wave guide (tube) is given by,

$$v_a = \frac{p_a}{\rho.c} \qquad (2)$$

In which p_a is the pressure amplitude, ρ the gas density and c the speed of sound.

Torque (To), pressure drop (Δp), flow coefficient (ϕ) and rotor efficiency (η_r) can be calculated using the expressions given in [3] which are summarized below.

$$To = C_T.0.5.\rho.(v_a^2 + U_R^2).b.l_t.z.r_R \qquad (3)$$

$$\Delta p = C_A.0.5.\rho.(v_a^2 + U_R^2).b.l_t.z.v_a \qquad (4)$$

In which ρ is the gas density, v_a the gas velocity in the blade section, U_r the circumferential velocity at mean radius of the rotor (r_R), b the blade height, l_t the blade chord and z the number of blades. These gas and geometric parameters can be used to dimension the turbine. The flow coefficient (ϕ) is defined as the mean axial flow velocity over the circumferential velocity $\phi = \frac{v_a}{U_R}$. Rotor efficiency is given by [ ] $\eta_r = \frac{C_T}{C_a.\phi}$

The torque coefficient (C_T), the input coefficient (C_A) represent the effect of blade shape, blade angle, aerodynamic losses, tip clearance etc. Both are a function of the Reynolds number and flow coefficient (ϕ).

Because of the nature of impulse turbines optimum performance is obtained when the circumferential speed equals the gas velocity ($\phi \Rightarrow 1$). In that case for an ideal turbine $C_T = C_A$. The performance of various impulse turbines therefore can be evaluated by measuring (or calculating) the C_T and C_A values as a function of ϕ.

Bi-directional turbines operating in acoustic flow conditions largely differ from those in OWC plants. In OWC plants the time between a change of flow direction is relatively long (10-30s) and is not constant in amplitude and interval time. This means that gas displacement through the turbine is large as compared to the blade chord leaving sufficient time for flow to develop during each half period even if the flow is irregular.

In acoustic wave motion the period time is short (e.g. 0.02s at 50Hz) but perfect regularly. As a consequence of the short period time the gas displacement in the turbine could be shorter than the blade chord. Consequently the short gas displacement prevents the flow to reach a steady state which will affect the C_T and C_A values in a positive way and from that the turbine performance.

On this turbines a series of measurements is performed of which the most remarkable results presented here is that bi-directional turbines operate well under high frequent acoustic flow conditions. From the measured data and the expressions given the rotor efficiency is measured and the result is plotted in Figure 2 for increasing acoustic input power at various frequencies.

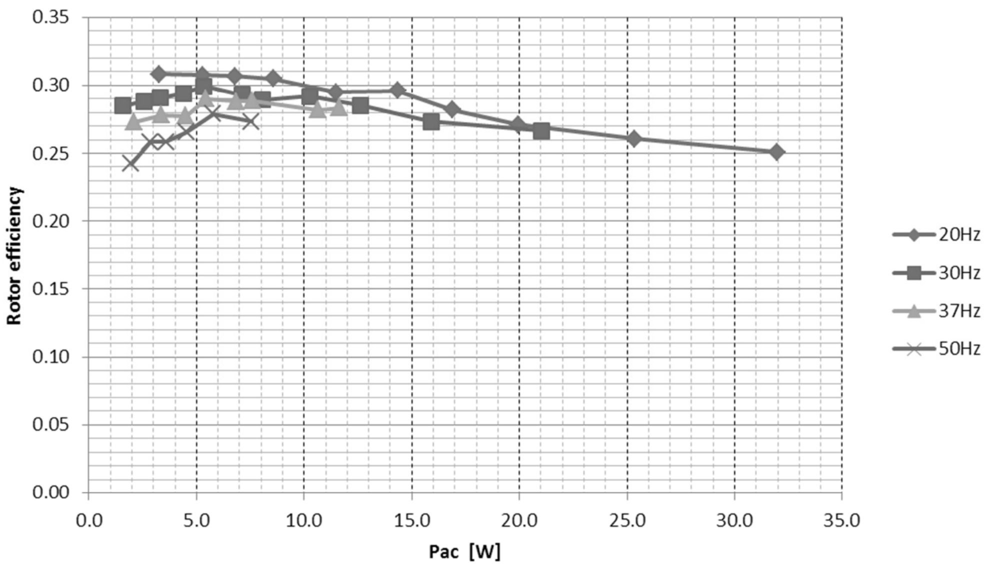

Figure 2 Measured rotor efficiency for the small bi-directional turbine

Initially, rotor efficiency for continuous flow is measured to be 23%. **Fout! Verwijzingsbron niet gevonden.** Figure 2 shows that rotor efficiency under AC flow conditions has clearly improves. It should be noted that the relatively strong fall-off with frequency at low power caused by the fact that displacement amplitude becomes in the range of the open space between rotor and guide vanes. For example, at low frequencies and 7W acoustic power the peak to peak gas displacement could be as large as 100mm. At 50 Hz and 2W the gas displacement is reduced down to only two times the gap width between rotor and guide vanes. Assuming that flow in the gap does not contribute to the torque this could explain the declining efficiency at low power.

3. Operation at elevated pressure

The measured efficiency for the small bi-directional turbine is in line with efficiencies reported in literature for OWC turbines operated with air at atmospheric pressure. Typical values are in the range of 30-40% and this efficiency is limited by the relative low density of the air.

Turbine operated with high density fluids like water could reach efficiencies up to 95%. Fortunately thermoacoustic engines are operated at high mean pressures proportionally increasing the density and with that the turbine efficiency. The relation between rotor efficiency and fluid density is given in Figure 3.

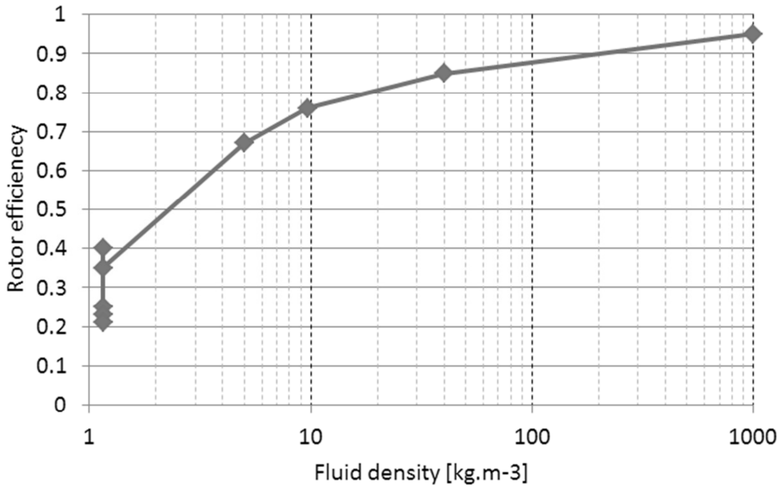

Figure 3 Turbine efficiency as a function of fluid density

Figure 3 shows that efficiency values found for bi-directional turbines operated at atmospheric pressure (≈ 1 $kg.m^{-3}$) are typical in the range of 20-40%. At increasing density, and finally for water (1000$kg.m^{-3}$), efficiency could be as high as 95%.

To confirm this trend an experiment (not describes here) is performed using a larger bi-directional turbine (300mm∅). This turbine is installed in a prototype of a multi-stage 100 kW_T thermoacoustic power generator (TAP) build at a paper manufacturing plant in the Netherlands [5]. The test with the turbine is performed at with air at 1 MPa mean pressure. The measured efficiency defined as the mechanical shaft power over the acoustic power in that case is measured to be 76%. This result confirms that efficiency of bi-directional turbines improves with increasing mean pressure or fluid density.

High end thermoacoustic engines typically run at elevated mean pressures up to 4MPa. So in the end, for acoustic wave energy conversion, this type of turbines could reach an efficiency up to 85%. Combined with a commercial high power 3 phase asynchronous electromotor as generator (η≈95%) an overall conversion efficiency from acoustic power to electricity of 80% seems feasible. This efficiency is comparable or even better than the performance reached for small scale linear alternators. Even more important, however is that bi-directional turbines for acoustic wave energy conversion eliminate the limitations in power and cost of linear alternators paving the way for up scaling thermoacoustic system to power levels in the MW range.

4. Conclusion

The feasibility of bi-directional turbines for the conversion of acoustic power into rotation and from there into electricity is experimentally investigated.

For a small axial bi-directional turbines a series of measurements is performed which confirms that bi-directional turbines operate well under high frequent acoustic flow conditions.

At elevated mean pressure as is common in thermoacoustic engines a rotor efficiency of 85% seems feasible

The bi- directional turbine as acoustic to electricity converter can be scaled up in power unlimited so eliminating the limitation in power and cost of linear alternators and paving the way for up scaling thermoacoustic system to power levels in the MW range.

5. References

[1] Bruno Pereias at all. “An improved radial impulse turbine for OWC”. Renewable Energy 36 (2011) 1477-1484.

[2] A Thakker , J Jarvis, A Sahed. “Quasi-steady state analytical model benchmark of an impulse turbine for wave energy extraction” International journal of rotary machinery Volume 2008, Article ID 536079, 12 pages

[3] Toshiaki Setoguchi at all. “Current status of self- rectifying air turbines for wave energy conversion” Energy Conversion and Management 47 (2006) 2382-2396.

[4] www.hacker-motor-shop.com

[5] Kees de Blok, “multi-stage traveling wave thermoacoustics in practice”, 19th International Congress on Sound and Vibration, Vilnius, Lithuania, July 8-12, 2012

FEASIBILITY ANALYSIS OF AN MHD INDUCTIVE GENERATOR COUPLED WITH A THERMO ACOUSTIC ENERGY CONVERSION SYSTEM

ALEMANY[2] A., CARCANGIU[1] S., FORCINETTI[1] R., MONTISCI[1] A., ROUX[3] J.P.
[1]*DIEE*, University of Cagliari, piazza d'Armi, 09123 Cagliari, Italy.
[2]*SIMAP/*Domaine Universitaire, BP 75 – 38402 Saint Martin d'Hères, France.
[3]*AREVA TA*, CS50497, 13593 Aix-en-Provence Cedex 3, Toulouse, France.
renato.forcinetti@diee.unica.it

Abstract : This paper fits in the feasibility analysis of a Magneto-Hydrodynamic (MHD) inductive generator, coupled with a Thermo-Acoustic (TA) energy conversion system. The MHD and TA processes have the great advantage to convert energy without mechanical moving components. In this work, first the design criteria are given, then the order of magnitude of the obtained parameters is used to model the system by using the finite element method (FEM) to confirm the theoretical results. The conceptual idea and the FEM model are described.

1. Introduction

MHD power generation systems were originally investigated starting from the fact that the interaction of a plasma with a magnetic field must take place at much higher temperatures than were possible in a mechanical turbine. This kind of machines can only be efficient if the charges concentration in the gas is at an adequate level. This is usually obtained by heating the gas to a high temperature and seeding it with ionizing elements. In conventional MHD generators a plasma passes through an intense magnetic field, so, by closing the circuit on a load, the induced electromotive force determines in the fluid an electric current [1]. The main problems of the known MHD generators are the high temperatures needed to ionize the gas and the high magnetic field (about 5T) required to have significant outlet energy. The proposed device does not require an external magnetic field to work, but it performs the energy conversion through the induction principle. The charge carriers are first created by means of an electrical discharge and then separated by an external, high voltage, electrostatic field. Once the equilibrium is reached, if the gas inside the duct gets to vibrate by the TA phenomena, the charge carriers give rise to an alternating electric current; this induces an electromotive force in a toroidal coil wrapped around the duct and connected to the load. Thermo acoustic engines can convert high temperature heat into acoustic power with high efficiencies and without moving parts. They are low mass and promise to be highly reliable. Coupling this system with an MHD generator will create a heat driven electric generator suitable for space applications [2] [3] [4].
The paper is organized as follows. In Section 2 the energy conversion process is qualitatively described. In Section 3 a first study has been done in order to propose a simplified theory about the performances of the generator and, therefore, to give the design criteria. Then a FEM analysis is performed to justify the assumptions of the design phase. In Section 4 is described the thermo-acoustic model; in Section 5 is described the electromagnetic model; some results are reported. The last section provides some conclusions.

2. Energy conversion process

The TA phenomena occur when a great gradient of temperature is present in the longitudinal direction of a duct containing a gas. In order to obtain said gradient we need a heat source and a stack inside the duct with a large surface. The TA effect allows transforming the thermal energy into vibration energy, where the gradient of temperature affects the flow rate of energy while the frequency is determined by the length of the duct. The most important features of TA are that there aren't mechanical moving parts, and the working fluid is quasi-static [5]. It represents a better solution with respect to the conventional MHD generators, which convert the energy of a flowing working fluid. The device proposed in this study (Fig. 1) allows one to perform the transformation from heat to electricity without moving parts and with a quasi-static working fluid. The thermo acoustic engine converts thermal energy into mechanical energy, then the MHD generator converts the mechanical energy into electricity. The working fluid is forced to become plasma by means of periodical electrical discharges supplied by two electrodes immersed in the gas and linked to a pulsed high voltage generator. In order to have enough charge density, the pressure of the gas plays a fundamental role. The fact that the electric charge is generated by means of an electric discharge, provided that the pulsing voltage is enough high, means that the gas can be ionized also at low temperatures and no seeding is necessary. The charge carriers of opposite sign are separated by means of two electrodes connected to a DC high voltage supply. Here, the voltage needed to maintain in equilibrium the two clouds of charges of different sign, linearly depends on the surface of the electrode, so that the shape of said electrodes have to be chosen carefully. Once the equilibrium is reached, if the gas inside the duct gets to vibrate, due to the TA effect, the unbalanced charge carriers participate to the motion of the surrounding neutrals, giving rise to an alternating current. Such current induces an electromotive force in a toroidal coil, wrapped around the duct in correspondence of the vibrating charges, which supplies the electrical load.

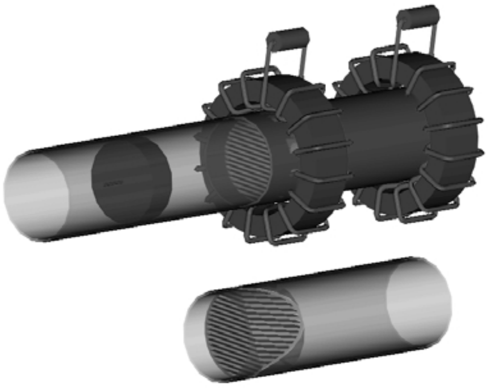

Figure 1: Schematic view of the MHD generator

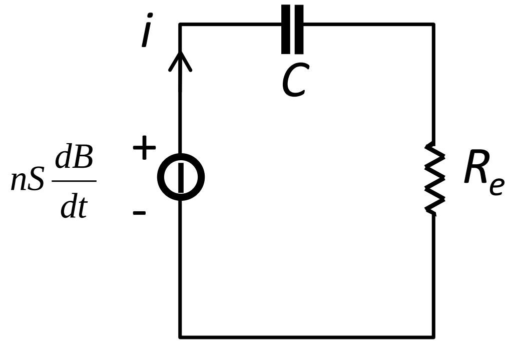

Figure 2: Electric circuit scheme

3. Theoretical development and demonstrative facility sizing

A first study has been done in order to propose a simplified theory about the performances of the MHD induction ionized gas generator coupled with the TA engine. The order of magnitude of the design parameters obtained has been used to modeling and simulate the system. This study starts from the equation of Ampère and the equation of the circuit (Fig. 2):

$$2\pi R \cdot B = \mu_f (I - n i) \tag{1}$$

In this expression $I = \bar{I} e^{j\omega t}$ is the total electric current in a cross section due to the charge oscillation, $i = \bar{i} \cdot e^{j\omega t}$, is the induced electric current in the toroidal coil, μ_f is the magnetic permeability of the core of toroidal coils, $B = \overline{B} e^{j\omega t}$, and R is the mean radius the core. This expression does not take into account the displacement current. Let be S the cross section of the core and n the number of turn coils. The electrical circuit comprises also the load resistance R_e and a capacity C to compensate the self of the coil, in such configuration the equation controlling the electrical circuit writes:

$$j\omega nS \cdot \overline{B} = \left(R_e + 1/j\omega C\right) \cdot \bar{i} \Rightarrow B^2 = 1/\omega^2 n^2 S^2 \left(R_e^2 + 1/\omega^2 C^2\right) \cdot i^2$$

Taking into account that $R_e = P_0/i^2$:

$$B^2 = \left(1/\omega^2 n^2 S^2\right)\left[\left(P_0^2/i^2\right) + \left(i^2/\omega^2 C^2\right)\right] \Rightarrow dB^2/di^2 = \left(1/\omega^2 n^2 S^2\right)\left[\left(-P_0^2/i^4\right) + \left(1/\omega^2 C^2\right)\right] = 0$$

Therefore, we can learn the value of the current which corresponds to the minimum of the magnetic induction: $i^2 = \omega C P_0$ and reminding again that $R_e = P_0/i^2 \Rightarrow R_e = 1/\omega C$

The previous position allows us to strongly reduce the complexity of the formulation of the problem and it tells us that the minimum value of the magnetic induction occurs when the impedance of both capacitor and resistor have the same modulus.

$$-\omega nS \cdot \overline{B} = \left(1/\omega C\right)\left(1 + j\right) \cdot \bar{i} \Rightarrow \bar{i} = -\left(\omega^2 nSC/2\right)\left(1 + j\right) \cdot \overline{B}$$

By considering the expression of the power: $P_0 = R_e i^2 = i^2/\omega C \Rightarrow C = 2P_0/\omega^3 n^2 S^2 B^2$

Such value of capacitance can be substituted in the Ampère equation:

$$\left[2\pi R/\mu_f - P_0/\omega SB^2\left(1 + j\right)\right] \cdot \overline{B} = \left[2\pi R \cdot B/\mu_f - \left(P_0/\omega SB\right)\left(1 + j\right)\right]e^{j\varphi} = I = \pi R_D^2 \rho v_0 \qquad (2)$$

where φ is the phase of $\overline{B}$. This equation allows us to calculate the electric current in the gas which allows to obtain the desired power and magnetic induction. First of all, taking into account that the I is the reference for the phases, we can calculate the phase φ. In fact, the phase of the term within brackets must be opposite to φ. We obtain:

$$\tan\varphi = \left[2\pi R\omega SB^2/\mu_f P_0 - 1\right]^{-1} \qquad (3)$$

Secondly, we can calculate the modulus of $\overline{B}$ which corresponds to the minimum value of the gas current I. To do that we have to minimize the modulus of the term within brackets, obtaining:

$$B^2 = \mu_f P/2\pi R\omega S \qquad (4)$$

This result has an important consequence. In fact, by (2) and (3) derives that we have the minimum of both B and I when the magnetic induction is in quadrature with respect to the gas current. By substituting (4) in the (2) we obtain:

$$\pi R_D^2 \rho v_0 = \sqrt{2\pi RP/\mu_f \omega S} \qquad (5)$$

The equations (4) and (5) allow us to perform the device sizing. The (4) establishes a direct relationship, for a given material of the torus core, between the required power, the size of the core and the frequency of the current. On the other hand, the (5) gives indications on the size and the operative conditions of the duct. As in the case of the magnetic induction, frequency and cross section of the core contribute to limit this parameter, while the permeability and the radius of the torus have an opposite effect. Therefore, if we have heavy constraints on both magnetic induction and electric current in the gas, it is preferable to act on frequency and cross section of the torus. Finally, in order to obtain the desired current I in the gas, we can observe that the radius of the duct has a stronger effect with respect to both density of charge and velocity amplitude. Taking into account that charge density and velocity amplitude have in general strict limits, we can foresee that the size of the device will be the key parameter in order to fulfill the requirements.

By means of a few substitutions we can obtain the current circulating in the coil:

$$\bar{i} = -\sqrt{\left(2\pi RP_0/\mu_f n^2 \omega S\right)}\left(1 + j\right) \qquad (6)$$

and the voltage drops in the gas:

$$\overline{U} = -\omega S\sqrt{\mu_f P_0/2\pi R\omega S} \qquad (7)$$

Finally, we can calculate the voltage to apply to the electrode in order to maintain the charges in equilibrium into the gas.

$$C_D = \varepsilon\left(2\pi R_D L\beta/\delta\right) = \pi R_D^2 L\rho/\Delta\varphi \Rightarrow \Delta\varphi = \delta R_D\rho/2\varepsilon\beta = \delta I/2\varepsilon\beta\pi R_D v_0 \quad (8)$$

where C_D is the capacitance of the electrode-gas system, ε is the vacuum dielectric constant, A_D is the gas-electrode interface surface, L is the length of the electrode, β is the ratio between the surface A_D and the surface of the internal wall of the duct corresponding to the electrode. The design parameters and the results for a demonstrative facility are reported in Table 1.

Table 1 Design Parameters and Results

Design Parameters			**Results**	
P_0 = 200 W R = 12 cm R_D = 7 cm ρ = 15 C/m^3	V_0 = 30 m/s n = 10 tr S = 3 10^{-3} m^2 $\omega = 2\pi \cdot 10^3$ rad/s	$\mu_f = \mu_0 \cdot 5 \cdot 10^4$ H/m δ = 0.5 mm β = 1000	i_0 = 1.6 A V_{coil} = 177 V I_0 = 11.28 A U_0 = 17.72 V	R_e = 200 Ω C = 0.8 μF $\Delta\varphi$ = 37.9 kV $\lvert B\rvert$ = 0.94 T

4. Thermo-acoustic analysis

The thermo-acoustic analysis has been done in order to study the velocity profiles. The device to be modeled is a glass tube containing Helium (He) in which the propagation of the vibration occurs at a temperature equal to 273°K and a pressure of 50 [bar]. As can be noted from the previous study (Section 3), in order to optimize the performance of the device, the dimensionless parameter β has to be maximized. This can be obtained using both a thicker cross section and materials with high surface roughness. Different than in normal (isentropic/lossless) acoustics, the thermo-acoustic formulation takes the dissipative effects of viscous shear and heat conduction into account. These effects cannot be neglected in acoustic wave propagation through narrow geometries. In fact, near walls viscosity and thermal conduction become important because it create a viscous and a thermal boundary layer where losses are significant [6]. The model is able to solve the equations simultaneously for the acoustic pressure, p, the particle velocity vector, $\mathbf{u}$, and the acoustic temperature T. The length scale at which the thermo-acoustic description is necessary is given by the thickness of the viscous boundary layer, and the thickness of the thermal boundary layer. The thickness of both boundary layers depends on the frequency. The properties of the gas are taken from [7]. In order to simulate the thermo-acoustic effect, a vibration with known amplitude and frequency was applied to the gas. In literature, several numerical studies have highlighted the phenomenon of "Dark space" [8]. The charge density starts to decrease rapidly near the boundary and becomes almost zero at the sleeve. These considerations appear to be very useful in the analysis of the device under study. In fact the charges will not adhere exactly to the wall, but will thicken in a cloud that will remain at a certain distance from the electrode; this allow one to avoid that the thickening of charging it occurs in correspondence

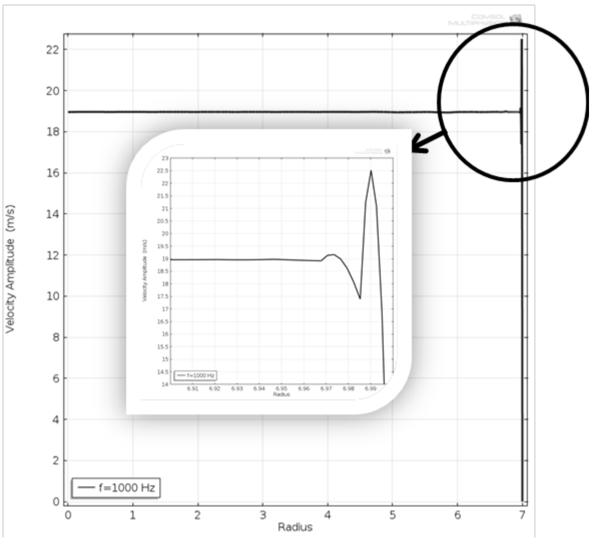

Figure 3: Velocity distribution in axial direction

of the boundary layers. The thermo-acoustic simulation solves a linearized, small parameter expansion of the Navier-Stokes equation, the continuity equation, and the energy equation. Between the results of the thermo-acoustic analysis, particularly it obtained the velocity distribution as function of the frequency and of the duct radius. As for a given gas the density and the fluid viscosity are known, the frequency, the radius of the duct, and the pressure are the main parameters that affect the velocity distribution. As the pressure is fixed, the only parameters that can be modified are the dimension of the tube and the working frequency. Finally, the velocity distribution at working frequency (1kHz) is reported in Fig. 3, with the detail near duct wall. The velocity profile has a flat shape in the center, with small peaks close to the wall.

5. Electromagnetic analysis

The 2D axisymmetric geometry model consists in a glass tube closed at the ends containing ionized helium gas. Two copper sleeve electrodes have been positioned at an equal distance from the duct extremities, and have been connected to a HVDC power supply. The electric potential V represents the dependent variable of the problem. A space charge density ρ (see Table 1) has been inserted near the sleeves. Between a parametric analysis, by varying the external source HVDC, an optimal value of voltage has been found. Applying this value to the electrodes, as can be noted from Fig. 4, the electrical potential profile is null and flat in the central zone between the two electrodes where the electrical field is thus equal to zero. This allows to achieve an equilibrium condition for the charge distributions that the electric field will cannot alter.

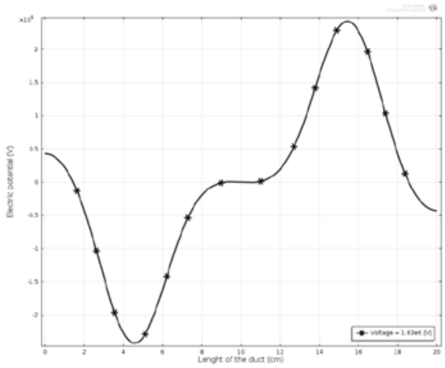

Figure 4: Optimal distribution of the electrical potential along the duct

6. Conclusions

The charge distribution thickened near to the electrode can be obtained by applying a suitable external potential difference. As can be noted from the electrostatic study the electrical potential profile is null and flat in the central zone between the electrodes where the electrical field is thus equal to zero. This allows to achieve an equilibrium condition for the charge distributions that the electric field will not be able to alter. Considering the "Dark space" phenomenon (see Section 4), from the previous thermo acoustic study is apparent that by acting properly on frequency and radius, one can get the best velocity profile for ensure an enough intense vibration of the particles thickened near the electrodes.

7. References

[1] Rosa, R. J.: Magnetohydrodynamic energy conversion. Hemisphere Pub. (1987).
[2] Alemany, A.; et al.: Thermoacoustic - MHD electrical Generator. Energy Procedia. 6 (2011) 92-100.
[3] Backhaus, S.; et al.: Thermoacoustic power systems for space applications. AIP Conf. 608 (2002) 939-944.
[4] Backhaus, S.; et al.: Traveling-wave thermoacoustic electric generator. Appl. Phys. L. 85 (2004) 1085-1087.
[5] Swift G., V.: Thermo acoustic energy conversion. Handbook of Acoustics. Springer. (2007) 239-254.
[6] Tijdeman, H.: On the propagation of sound waves in cylindrical tubes. J. Sound & Vibr. 39(1) (1975) 1-33.
[7] Petersen, H.: The Properties of Helium. Danish Atomic Energy Commission. Report n°224 (1970).
[8] Roy, S.; Gaitonde, D. V.: Ionized Collisional Flow Model for Atmospheric RF Application. 35th AIAA Plasmadynamics and Lasers Conference, Portland, OR. June 28-July 1 (2004).

The MHD generator - Thermoacoustic engine interface

Kees de BLOK[1], Maurice-Xavier FRANCOIS[2], Armands KRAUZE[3]

[1] Aster Thermoacoustics, Smeestraat 11, 8194LG Veessen, The Netherlands
[2] Hekyom, 3, rue de la Croix Martre, 91120 Palaiseau, France
[3] Institute of Physics, University of LATVIA, Miera str.32, Salaspils, LV-2169, Latvia

e-mail address of corresponding author: c.m.deblok@aster-thermoacoustics.com

Abstract :
Driving a MHD generator by a thermoacoustic engine is a promising concept concept without any moving mechanical parts. Because of the density of the conducting fluid in the MHD generator exceed largely the density of the thermoacoustic working gas transferring energy from the acoustic wave towards the moving fluid columns is a real challenge. Transferring a certain amount of acoustic power to such a high impedance requires a high acoustic pressure amplitude. This is not the preferred working condition for thermoacoustic engines which by default operate at less than half the pressure amplitude needed to power the MHD generator. This paper address the design of the acoustic interface between a thermoacoustic engine and a MHD generator.

1. Introduction

Thermoacoustics is a key enabling technology for the conversion of heat into acoustic (= mechanical) power. Nowadays, thermoacoustics in itself well understood and has proven to be an generic applicable and efficient conversion technology. This however, is only part of the story. For practical and economic viable applications the interface with the outside world is found to be even more important. Two major issues has to be solved, in a practical and cost effective way, to bring thermoacoustics to successful applications. (1) Heat to be converted need to be supplied at high or medium temperature and rejected at a lower temperature from the process with minimal temperature loss and (2) The generated acoustic (wave) power, which is proportional with input- heat and temperature, has to be converted into electricity in a scalable and efficient way.

Focus of this paper is on the conversion of the acoustic power generated by a thermoacoustic engine into electricity by an MHD generator in which the acoustic driven, periodic movement of a conducting fluid in a magnetic field convert the acoustic wave energy into electricity.
Main issue for this design is that the density of the (moving) conducting fluid in the MHD generator largely exceed the density of the thermoacoustic working gas. In acoustic terms, the high acoustic impedance of the MHD generator need to be matched to the lower impedance of the thermoacoustic engine. Transferring a certain amount of acoustic power to such a high impedance requires a high acoustic pressure amplitude while at the same time the actual fluid displacement and velocity is relatively low.

2. Acoustic impedance MHD generator

For this work we will consider the data available for a small scale MHD generator designed for having an electric output power of about 270W. This data is given in Table 1.

Table 1 Typical data of a 270W high amplitude MHD generator.

Mass	kg	0.395		Melt velocity vz	m/s	8.88
Frequency	Hz	50		Pressure drop re (Δp)	kPa	42
Efficiency MHD	-	0.75		Pressure drop im (Δp)	kPa	598
Volume flow rate U	m^3/s	0.016		Pressure drop $\|\Delta p\|$	kPa	600

According to Table 1, the acoustic impedance at the MHD generator input is

$$Z_{MHD} = \frac{\Delta P}{U} \qquad \text{N.s.m}^{-5} \quad (1)$$

This highly complex impedance (inertance) is independent of the gas type and mean pressure. Using the data in Table 1 gives for the absolute value of the acoustic impedance of the MHD generator $Z_{MHD} = 6e^5 / 0.016 = 37.5e^6$ N.s.m^{-5}.

3. Acoustic impedance thermoacoustic engine

The acoustic impedance of a thermoacoustic system is given by

$$Z_a = \frac{\rho . c_0}{A_0} \qquad \text{N.s.m}^{-5} \quad (2)$$

In which ρ is the density of the gas, c_0 the propagation velocity and A_0 the reference cross-sectional area of the acoustic resonance and feedback circuit of the thermoacoustic engine.

Default working gas for TA systems is helium at 4 MP mean pressure. Regenerator (or reference) diameter for a single stage standing wave resonator thermoacoustic engine able to deliver 330 W acoustic power is about 90 mm. Using these numbers, a typical value for the real acoustic (source) impedance of the TA engine Z_a = 6.47 kg.m-3 *1012 $m.s^{-1}$ / 0.064 m^2 = $1.02e^6$ N.s.m^{-5} which is significant lower than the acoustic (load) impedance of the MHD generator. In an acoustic system a step in impedance introduce a partial reflection of the forward propagating wave which means that only part of the wave is absorbed by the load. This reflection coefficient (r) defined as the ratio between reflected and forward wave is given by

$$r = \frac{Z_{MHD} - Z_a}{Z_{MHD} + Z_a} \qquad (3)$$

Which gives for the reflection coefficient a value of r = 0.95. Consumed power by the load is given by

$$P_{ac\_load} = P_{ac\_source} . (1 - |r|^2 \quad (4)$$

Which implies that only 0.1 of the acoustic source power is or can be consumed by the MHD generator for conversion into electricity.

4. Working gas

In general, for thermoacoustic systems, helium as chosen as working gas by default. For some applications however it is worth to consider another gas type. Because of the thermodynamic cycle in the traveling wave driven thermoacoustic process is nearly reversible, the efficiency in theory is independent of the working medium. In practice however some irreversibility remains and these irreversible loss terms are dominated by the γ value of the gas. In order to minimize this loss terms the γ value therefore should be high as possible which limit the choice to (inert) gasses or argon having a γ value around 1.6.Due to the higher density of argon the acoustic propagation speed is lower than for helium which means that for the same frequency (50Hz as required by the MHD generator), the length of the acoustic tubing could be made proportional shorter. As compared to helium, for argon the acoustic power density is less, which implies that at the same pressure amplitude or drive ratio the cross-sectional area of feedback loop and regenerator-hex unit need to be increased to get the same acoustic output power. In other words, length will reduce and diameters increase for the same acoustic power, cycle efficiency and oscillation frequency.

5. Dual TA engine driven MHD generator

From the data given in Table 1 the required pressure amplitude to drive the MHD generator is about 600 kPa. Driving the MHD generator from one side, assuming no back pressure at the other side, means that at 4 MPa mean pressure the TA engine drive ratio has to be 15%. Such a high drive ratio is hard to reach efficiently with a single stage TA engine because of the high associated acoustic losses [1,2].

Because of the MHD generator is symmetric in nature, an option to solve this limitation, is to drive the MHD generator from each side, both with half the pressure amplitude and opposite phase. Such a configuration could consist of two identical TA engines mutually coupled by the (impedance of) the MHD generator. Problem with this configuration however is that both (independent) TA engines tend to oscillate in phase [3], consequently eliminating the pressure difference across the MHD generator.

In order to force both engines to run in opposite phase they need to be coupled acoustically by sharing (part) the same resonance or feedback circuit. This can be done as follows. *Figure 1* shows a basic traveling wave TA engine consisting of a regenerator clamped between the high and low temperature heat exchanger. In this type of traveling wave engine reduction of gas velocity is obtained by increasing the regenerator-heat exchanger diameter with respect to the acoustic circuit diameter instead of impedance enhancement by interfering waves [4]. Losses of these diameter transitions are more than counterbalanced by the small feedback tube diameters and lower amplitude in traveling waves [5,6]

Input reflection of the section is minimized at 50 Hz by adding an impedance matching network (L_2, L_3). This is shown in *Figure 1*

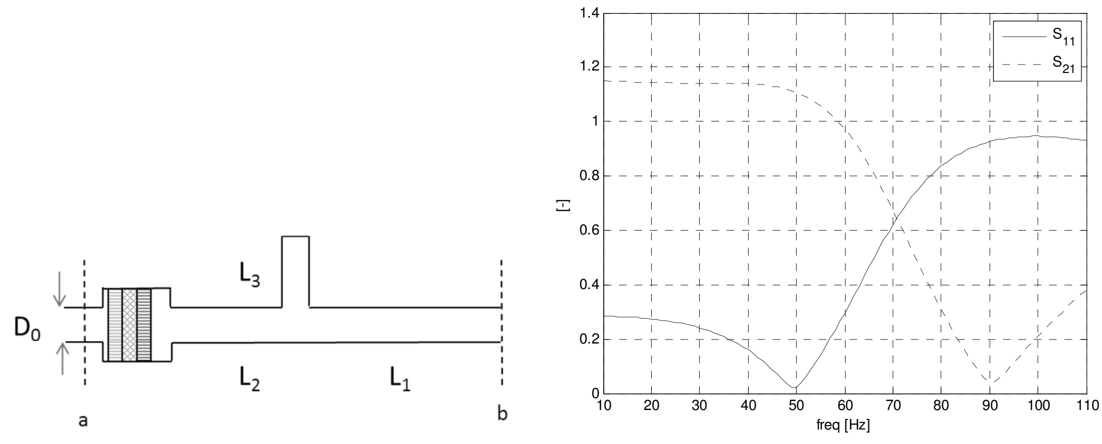

Figure 1 Traveling wave TA engine with input reflection (s11) at reference plane a, minimized by position (L_2) and length (L_3) of the acoustic matching stub (compliance)

Figure 1 shows that at the operating frequency of 50Hz the reflection (s_{11}) at the input (a) is minimized and that forward gain (s_{21}) exceeds one, which is an essential condition for oscillation. The length of L_1 is chosen such to make the acoustic length between reference planes a and b equal to ½ λ. So when connect b to a by a ½ λ long feedback tube we get a total of 2π radians phase shift and if the temperature is above onset, a (near) traveling wave will be generated and maintained in this loop.

Replace the ½ λ feedback tube by and identical TA section with an equivalent acoustic length of ½ λ then the circuit has the same acoustic feedback lengths but with double thermoacoustic gain. This is depicted schematically in **Fout! Verwijzingsbron niet gevonden.**.

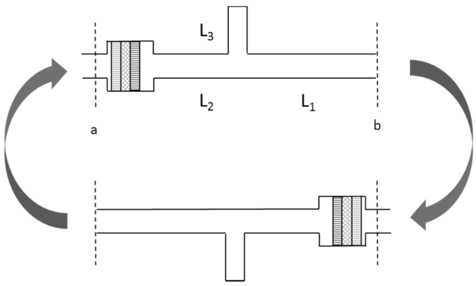

Figure 2 Two coupled TA engines

Because of the input reflection of both engines is minimized they acoustically terminate each other with an impedance close to ρ.c, yielding a traveling wave in the feedback loop. Traveling wave feedback has the advantage of transferring maximum acoustic power ate the smallest possible tube diameter and lowest pressure amplitude yielding the lowest acoustic losses [2,6]. Further the phase develops proportional with position along the loop, which means that at "mirrored" positions the pressure amplitude has opposite phase.

Therefore both terminals of the MHD generator will connected to opposite positions along the (traveling wave) acoustic feedback circuit. Because of the pressure amplitude at opposite positions has a mutual 180° phase shift, the pressure amplitude difference across the MHD generator will be twice the pressure amplitude or drive ratio at each individual engine stage.

In principle the high impedance MHD generator can be coupled everywhere in the circuit but an option to eliminate additional T-junctions is to connecting them between the end of the compliant stubs (L_3). The final configuration then looks as depicted in *Figure 3*

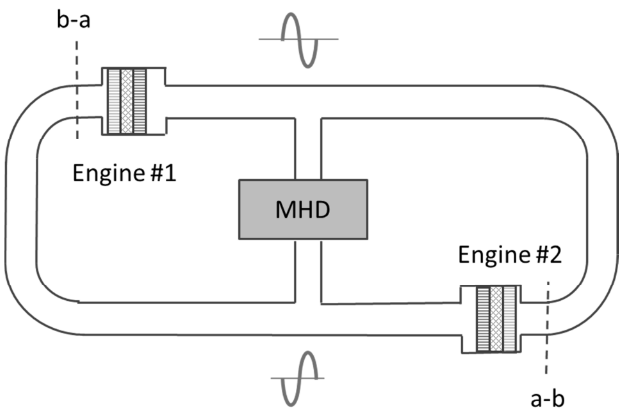

Figure 3 Dual TA engine driving the MHD generator in "push-pull" mode

Simulations for the configuration of Figure 3 shows that due to the "transformation function" of the acoustic circuit ≈ 620 kPa is generated across the across the MHD while the cold hex pressure amplitude of the TA engine is ≈ 110 kPa (drive ratio 3.3%). For an input temperature of 995K and a heat rejection temperature of 400K the thermal efficiency (without static heat losses) is calculated to be 35% which corresponds to an exegetic efficiency of 58%. From the simulations it is also observed that efficiency with argon as working gas could be as good as for helium.

6. Conclusions

Driving a MHD generator by a thermoacoustic engine yield an attractive concept without any moving mechanical parts. Initially the difference in acoustic impedance between MHD generator and thermoacoustic engine cause that only 10% of the engine output power can be consumed by the MHD generator

In this paper a geometry is proposed which match both impedances both by and alternative geometry using a dual stage thermoacoustic engine and by using a more heavy working gas

In this configuration the MHD generator is driven in "push-pull mode" by two traveling wave thermoacoustic engine stages. This way a high pressure amplitude is generated across the MHD generator while at the same time the thermoacoustic engine operates at a much lower pressure amplitude.

For this application argon instead of helium is considered as working gas and is found to strongly reduce acoustic tube length yielding a more compact device for the same power and efficiency

7. References

[1] Backhaus, S. & Swift, G. W. (2000): A thermoacoustic-Stirling heat engine: Detailed study. Journal of the Acoustical Society of America, 107[6], pp. 3148-3166, 2000.

[2] Kees de Blok, Hassan Tijani, Thierry Le Pollès. "Report on minimizing acoustic losses". THATEA project deliverable D1.2, 2009.

[3] P. S. Spoor and G. W. Swift "The Huygens entrainment phenomenon and thermoacoustic engines,", Journal of the Acoustical Society of America 108, 588-599 (2000).

[4] Blok, C.M. de & Rijt, N.A.H. van: Thermo-acoustic system, 1997, WO 99/20957, US 6,314,740 B1

[5] B.L Smith, G.W. Swift. "Power dissipation and time-averaged pressure in oscillating flow through a sudden area change" J. Acoust. Soc. Am. 113 (5), May 2003. p2455-2463.

[6] C.M. de Blok, "Low operating temperature integral thermo acoustic devices for solar cooling and waste heat recovery", Acoustics'08, Paris. PA15

AN ELECTRIC GENERATOR USING ONE HEAT DRIVEN THERMOACOUSTIC AMPLIFIER

BETRANCOURT[1] A., GENESTE[2] J.-F., JOUBERT[2] E., RECHAIN[2] B., FRANCOIS[1] M.-X.
[1]HEKYOM, 3 rue de la Croix Martre – 91120 Palaiseau, France
[2]EADS, France
E-mail: adrien.betrancourt@hekyom.com

Electric generator using thermoacoustic conversion could be a very good candidate for space applications. Indeed thermoacoustic systems are efficient and reliable. The only moving parts appear in the electroacoustic system and works at ambient temperature, contrary to the Stirling systems. A first prototype has been built to test the feasibility of matching one thermoacoustic amplification cell between two linear alternators from Chart Industries. The first one (1s132d) provides acoustic power which is amplified by thermoacoustic before being converted into electricity by the second linear alternator (1s175d). On this first prototype, an electric resistance provides the heat power to the thermoacoustic amplification cell. As the feedback electric loop between the two linear alternators to get a self-sufficient system is not set up, the electric power is dissipated into a RC load.

The system is working with 30 bars helium and with a frequency of 60 Hz. The system is built with two enclosures: one corresponding to the thermoacoustic wave guide and the second surrounded insulation placed around the wave guide. This insulation is supposed to be filled with argon or nitrogen gas in order to improve the insulation efficiency.

Some results concerning the sizing and the experimental analysis of the prototype will be presented at the conference. The system was design being able to accept heat source at temperature up to 950°C. Runs were performed varying acoustic input energy up to 200W for various hot source temperature scaling from 500°C to 900°C. They show that the system is very stable without nonlinear effects even for high temperature gradient in the buffer tube. As an example, the thermoacoustic cell (Heat exchangers, regenerator and buffer tube) reaches about 55% of Carnot with a hot temperature of 700°C taken into account the heat losses. By reducing them, the system can achieve near 70% of Carnot.

By improving the thermal insulation of our setup, it could be shown that the global efficiency could be greater than 25% with one thermoacoustic amplifier and 40% with 2 amplifiers using heat sources at 950°C.

Thermo-Acoustic Generators for space missions

Didier Alary[1], Cyrille Tourneur[1], Jaime Reed[2], Bruno Rechain[3], Maurice François[4]

[1]: Airbus Defence & Space – Space Systems – Toulouse – France
[2]: Airbus Defence & Space – Space Systems – Stevenage – United Kingdom
[3]: Airbus Group Innovations – Suresnes - France
[4]: Hekyom – Orsay - France

Abstract

Airbus Defence & Space - Space Systems, Airbus Group Innovations and Hekyom have analyzed in a self-funded joint study the possible use of Thermo-Acoustic generators for space applications. To make the analysis more pragmatic, two different cases have been considered:

1) A telecommunications satellite, in geostationary orbit, with an electrical power demand of 40kW
2) A deep space exploration mission, with an electrical power demand of 100W.

1 Thermo Acoustic Power Generation – the principles

A ThermoAcoustic engine is a heat engine which converts heat into acoustic power and ultimately into electricity if appropriate conversion devices (e.g. alternator) are used. The working fluid is a gas, usually helium, maintained at high pressure (generally around 25 bars) inside a pressure vessel. The acoustic conditions are provided to get a resonant system.

1.1 The TAG unit

The ThermoAcoustic engine architecture proposed here and patented by Hekyom allows a Stirling-type TA engine without the usual drawbacks of a conventional Travelling-wave TA engine which are usually bulky and heavy loop-type machines.
In this concept, a linear motor generates an acoustic wave which is amplified through a TA amplification cell composed of a cold and a hot heat exchanger with a regenerator in between. The acoustic wave is then delivered to the resonator and converted into electricity via a second linear alternator at the end of the pressure vessel. Some of the energy produced is sent back to the linear motor. The resulting power is the net power.
Figure below describes a 2-stage TAG architecture and shows the efficiency against hot and cold heat exchanger temperature. At 1000°C, this concept should achieve about 40% efficiency. *Note that using a 3-stage TAG architecture will improve the global efficiency and reduce the weight and power of the wave generator*

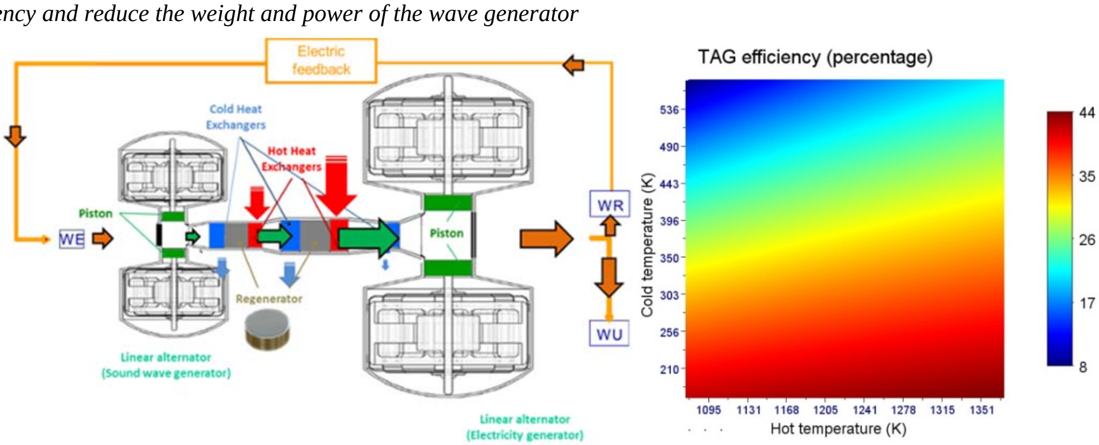

Figure 1 - TAG architecture and TAG efficiency as a function of hot and cold heat exchanger temperatures

1.2 TAG demonstrator

Airbus Group Innovations and Hekyom have jointly developed a Thermoacoustic engine aiming at demonstrating the high efficiency of the above TA engine architecture for high temperature applications. For the purpose of the demonstration, a single stage architecture has been designed and tested as the amplification of a 2-stage thermoacoustic engine is well known and easily predicted. A complex measurement set-up on the prototype has allowed correlating measured engine efficiency against predicted efficiency derived from in-house software (called "Crista"), as shown in Figure 2 below.

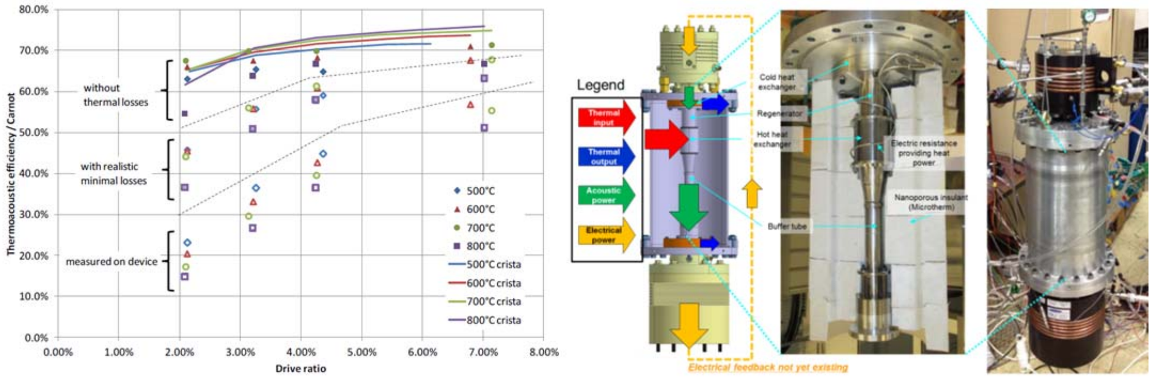

Figure 2 - Measured non-ideal efficiency (fraction of Carnot) and demonstrator set-up

This prototype has demonstrated the potential of the TAG to achieve a thermal efficiency of 40% at 1000°C for the hot temperature. Improvement on the design shall reduce the thermal losses that were measured during testing.

1.3 TAG in space – 2 test cases

Following the work performed between Airbus Group Innovations and Hekyom, a self-funded joint study on the possible use of Thermo-Acoustic generators for space applications have been engaged late 2012. In order to make the analysis more pragmatic, two different cases have been considered :
1) A telecommunications satellite, in geostationary orbit, with an electrical power demand of 40kW.
2) A deep space exploration mission, far from our sun, with an electrical power demand of 100W.

2 The telecom satellite case

Amongst all the spacecraft manufactured in the last 50 years, telecommunication satellites and space station are the two items that exhibit the biggest power demand. In this group, telecommunication satellites are setting the bench mark in terms of mass and power efficiency.
The market of the space solar array generators is completely driven by these missions which are good candidates to test the TAG technology.

2.1 Schematic of a solar based TAG power system

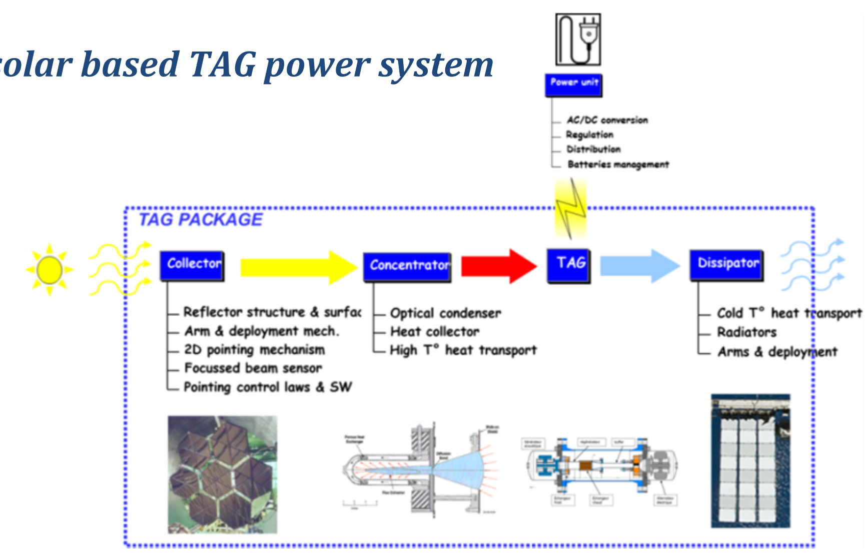

Figure 3 - Typical functional breakdown of a solar based TAG power subsystem

2.2 The study case requirements

We chose to direct the case on 2x20kWe maximum in order to focus the study on next generation satellites, but two other points of load have been selected at 2x5kWe and 2x10kWe, analyzed as de-scopings from the 40kW point.
The TAG implementation has to be compared to a standard solar array based system, with a mass of 2 x 210kg (including the drive mechanism) for a 2x20kWe end of life power capability.

2.3 Drivers first analysis

So as to minimize the overall surfaces of the light collector and the rejected heat dissipator to accommodable dimensions, high temperatures have to be selected for the hot point (1000 to 1200°C) and the cold point (150 to 200°C).

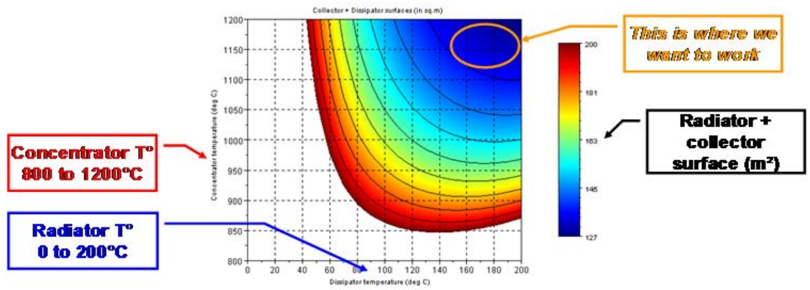

Figure 4 - Collector & dissipator surfaces as a function of hot & cold temperatures

As a consequence of this necessity, a high flux concentration (500 to 1000) is needed to achieve the required hot temperature, to minimize the infra red losses wrt the concentrated spot surface and to minimize the concentrator mass and complexity. This brings in turn the following constraints

- Stringent collector shape requirements (typ. 0.03° slope error for a 10m parabola) to achieve the concentration ratio
- Accurate 2 axis sun pointing of the collector (better than 0,05°) to keep the spot inside the concentrator. *Note that single axis pointing is used for PV solar arrays wrt the cosine law degradation - which does not apply for TAG case*
- Very high efficiency coatings (better than 95% to 90% after 15yrs) and cooling for secondary collecting surfaces
- Efficient & long life time hot temperature materials: for light to heat conversion (refractory metals or Ceramics – e.g. SiC), for hot heat transport (e.g. Li/Nb heat pipes), for insulation and adjacent units protection (very high temperature nanoporous foams and MLI)
- Efficient light transport technologies: Low weight optical fibers or light wave guides, with low absorption, high numerical aperture and able to sustain high temperatures on the light to heat conversion end

At system level, the first level criticalities are the following

- Large collector & dissipator accommodation wrt masking or contamination constraints regarding the large RF antennas collimated beams, the RF repeater heat radiator walls field of views and the large plume of the electrical thrusters
- Power up after launch vehicle separation and transients handling during eclipse and/or power demand shedding. *Note that 2x200kg of Be for heat storage could provide the capability to sustain the longest eclipse duration but power up constraints impose to keep the standard electrochemical batteries*
- Early operations, including perigee raising and orbital inclination reduction, drive the required angular domain
- Safety & testability issues for on ground integration, and also for failure and safe mode concepts

2.4 Families of assessed concepts

Family 1: Off axis collector – based on:

- Concentrator and TAG unit accommodated inside the satellite to minimize the rotating mass
- A large off axis collector (~70% surface efficiency), motorized with a gimbaled 2 axis annular mechanism. *Note that an additional protection device is needed vs non perfect pointing cases*
- Dedicated radiators, potentially behind the parabola (but non continuous rotation in that case for disentangling)

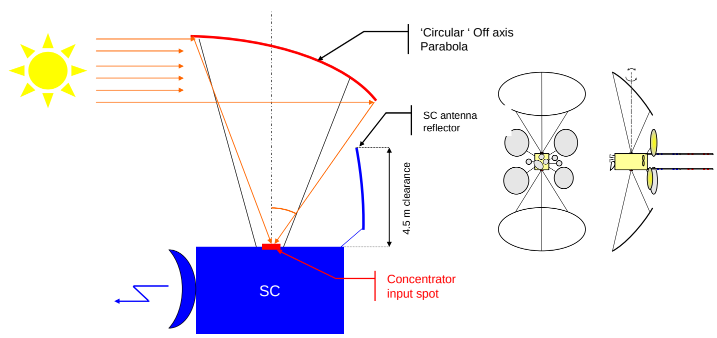

Family 2: Array collector – based on arrays of small collectors on deployable and rotating panels

- Small collectors: square parabolas or square Fresnel lenses
- Optical fiber + light waveguide light transport from the collectors to the concentrator
- Concentrator and TAG unit accommodated in the TAG supporting mast, involving a rotating electrical power transmission device. Dissipator is located on each panel rear face

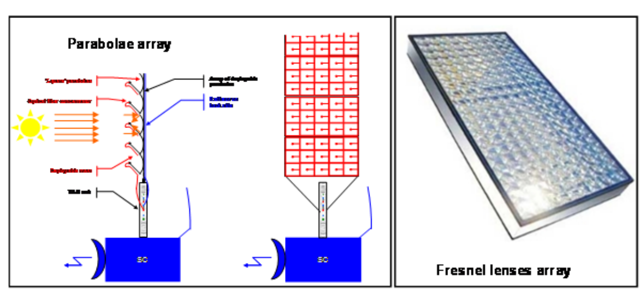

Family 3: Large collector fully external package – based on arrays of small collectors on deployable and rotating panels

- Preferably a Cassegrain collector amongst all the traded options (single Fresnel lens, single parabola, Gregorian, ..)
- Concentrator and TAG implemented between M1 and M2 reflectors – involves also a rotating electrical power transmission device
- Dissipator accommodated on the rear face of the M1 mirror

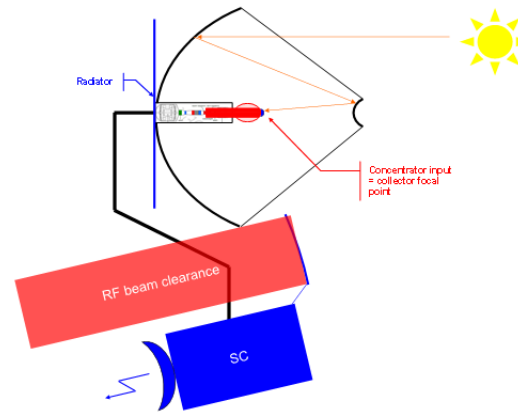

Several technological and conceptual trade-off have also been conducted at lower levels regarding:

- Collector concept (technology, deployment, focusing and pointing sensors)
- Mast concept (deployment, technology, mechanism)
- Concentrators & hot heat transport technologies
- Optical fiber + light waveguide candidate technologies
- Cold heat transport and dissipation

2.5 *Synthetic results*

The preferred concept is the Cassegrain solution (from family 3) which provides the highest overall efficiency (19%) and lowest mass (2 x 660 kg) of all the traded concepts, calling for a 10m M1 diameter per side.
Unfortunately, the TAG option is currently not competitive vs the current photo voltaic paradigm wrt the following issues:

- The mass issue: The specific power with TAG is ~30 We/kg whereas up to 85 We/kg can be considered with photovoltaic solutions over the same timeframe. Hence, with this mass penalty, the delta cost due to the TAG delta mass to launch in GEO is similar to the cost of the photovoltaic array itself
- The TRL issue, especially regarding low mass/high efficiency collectors, supporting mast and 2 axis accurate pointing mechanism, high temperature collectors, heat transport and nano porous insulation materials
- The system issues regarding accommodation, transients management, electrical propulsion compatibility, impacts on attitude control stability, failure modes and on ground testing.

3 The deep space exploration mission

All space missions require a source of power which can be derived either from the sun, nuclear sources, or chemical reactions. Historically the processes include:

- Solar power, based on photovoltaic cells (η=28%, rising to ~35%) – used on the majority of Earth orbiting satellites
- Chemical conversion, based on fuel cell technology (η~50%)
- Radioisotope Thermal Generators (RTGs) based on Thermoelectric conversion (η~7%)
- Nuclear fission reactors using thermionic conversion, e.g. SNAP/TOPAZ (η~5%)

Many alternative energy conversion processes have also been investigated with the aim of increasing the efficiency, including:

- Thermo-mechanical conversion from Radioisotope Heather Unit (RHU), Stirling/Brayton/TAG (η~30%)
- Thermo-photovoltaic or TI conversion of RHU (η~30%)
- Thermal collectors (e.g. solar or geothermal)
- Electro-dynamic in planetary magnetic fields (i.e. conversion of s/c fuel)
- Bringing a source of fuel to consume in a (semi-) conventional engine (e.g. H2)
- Local fuel production/scavenging (e.g. H2)
- Conversion of local radiation flux (e.g. around Jupiter)

Away from Earth Orbit, there are two specific challenges which need to be addressed:

1. At orbits further away than Mars the solar flux is so weak that a huge solar PV array is required
2. At orbits closer than Venus the solar flux is so strong that heat rejection from a PV solar array becomes extremely difficult

For these reasons Nuclear Power Sources (NPS) are extremely attractive as mission enablers.

3.1 *Existing Radio-isotopic Power Sources*

Nuclear Power Systems has enormous heritage since the 1960's, including the most famous example "Voyager" which was launched in 1977 and continues to operate to this day beyond our solar system. Developed by NASA these units consist of pellets of Pu-238 which slowly decays releasing heat which is converted to DC electricity by a Thermo-Electric Generator (TEG). The most recent development of this technology is currently providing all the power needed for the Curiosity rover to explore the surface of Mars. This "Multi-Mission Radioisotope Thermal Generator" (MMRTG) was developed by Boeing and generates 290W of electricity at beginning of life with an overall system efficiency of 6.8% (the ratio of electrical output to thermal input,

including controller system). 8.1kg of Pu-238 is carried on-board and the total MMRTG mass is 57 kg, leading to a specific power of 5.1We/kg.
An alternative concept based on a Stirling convertor (the ASRG, Advanced Stirling Radioisotope Generator) has also been developed in the US, most recently by Lockheed. The major advantage of the ASRG is the higher conversion efficiency of the Stirling convertor leads to a system efficiency of 28% and therefore need for much less Pu-238 (0.88kg for 123We at BOL); critically important since the US recently had a shortage of Pu-238. However with the recent re-start of US Pu-238 production the ASRG programme has been scaled back. Nonetheless the performance is impressive, with a specific efficiency of 6.9We/kg.

3.2 State of the art in Europe

In Europe there is growing interest in the development of an RTG capability to enhance the capability of future European deep-space missions. ESA have initiated the development of RTG technology with 3streams:

- Thermo-electric generator (TEG) converters for low power (5 to 50We)
  - Leicester University & Airbus DS (supported by Fraunhofer IPM) have developed a TEG-RTG breadboard
- Stirling for higher powers (250We)
  - SEA & RAL (supported by University of Oxford) are leading this activity with a breadboard under development
- Radioisotope activities are on-going with a focus on Am-241 (Am_2O_3) instead of Pu-238 due to availability and cost
  - National Nuclear Laboratory (NNL) in UK will lead extraction of Am-241
  - SEA, Leicester and Lockheed Martin developing containment and encapsulation

A key aspect is the fuel production and the plan is that Am-241 fuel pellets will be produced at Sellafield by chemically separating Am-241 from aged Magnox-derived plutonium dioxide. Although Am-241 has better availability and lower cost than Pu-238, it still requires a full suite of handling & safety protection and has a lower thermal output per kg (105Wth/kg compared to 411Wth/kg for Pu-238).

3.3 The study case requirements

The purpose of the Radioisotope TAG (RTAG) study was to determine if the TAG technology could offer any advantages compared to the other on-going developments in Europe. The first step was to define the requirements and four types of mission classes for exploration and planetary missions were defined:

- 10kW : human exploration
- 1 kW : multi-mission orbiters such as Cassini, JIMO-Light
- 100W : 'manoeuvrable' field science such as Mars Rovers, Aerobots, sub-surface Europa probe
- 10W : complement to solar cells, miniature geophysical packages

All require :

- a technology which is scalable since total number of missions will always be small
- to minimize amount of radioactive material by high efficiency (cost & safety)
- >5 years operation highly desirable to account for spectrum of possible life-times
- ability to self-start
- management of thermal power during cruise phase
- possibility for redundancy
- low radiation flux + compatible with RHU with impact protection
- output voltage ~ 28V DC and compatible with power demand profile of mission (e.g. peak or continuous power)
- and low vibrations

An **exploration mission of 100W** electric was selected as the baseline, which enabled a direct comparison with other developments. In this case this meant that the total mass (including $^{241}Am_2O_3$ fuel) should be <60kg (including radiators) to be competitive, with the other required identified as (based on outputs from Airbus Defense and Space/Leicester/SEA NSTP study for UKSA & ESA studies)

- Voltage 28V DC
- Exported vibrations <0.1N
- Reliability >90% for 15 years
- SPF free (*note that the ASRG is not SPF free*)
- Volume <= $0.5m^3$
- Capable of being mounted on a rover or boom
- Stackable/modular for multi-mission approach

3.4 Assessed concepts

The RTAG principle is based on a Radioisotope Heather Unit (RHU) consisting of a 200Wth (end-of-life) Am-241 encapsulated in a graphite impact shell and outer aeroshell. This system prevents the scattering of nuclear material in the event of a launcher failure on the pad or in Earth's atmosphere. Each module weighs 5kg and contains 1.9kg of Am-241. This does not represent an module in current production but instead is expected to be similar to the final design.

In the basic RTAG the RHU is insulated from the environment (both radiatively and conductively since the unit could be operated in both vacuum and air). The RHU is then connected to a TAG which is mounted in a thermo-mechanical structure including radiators to carry away the waste heat from the unit. Integral to the unit are conditioning and control electronics which ensure correct phaing and safe operation of the TAG, whilst also converting the AC output of the TAG in to DC current for the spacecraft bus.

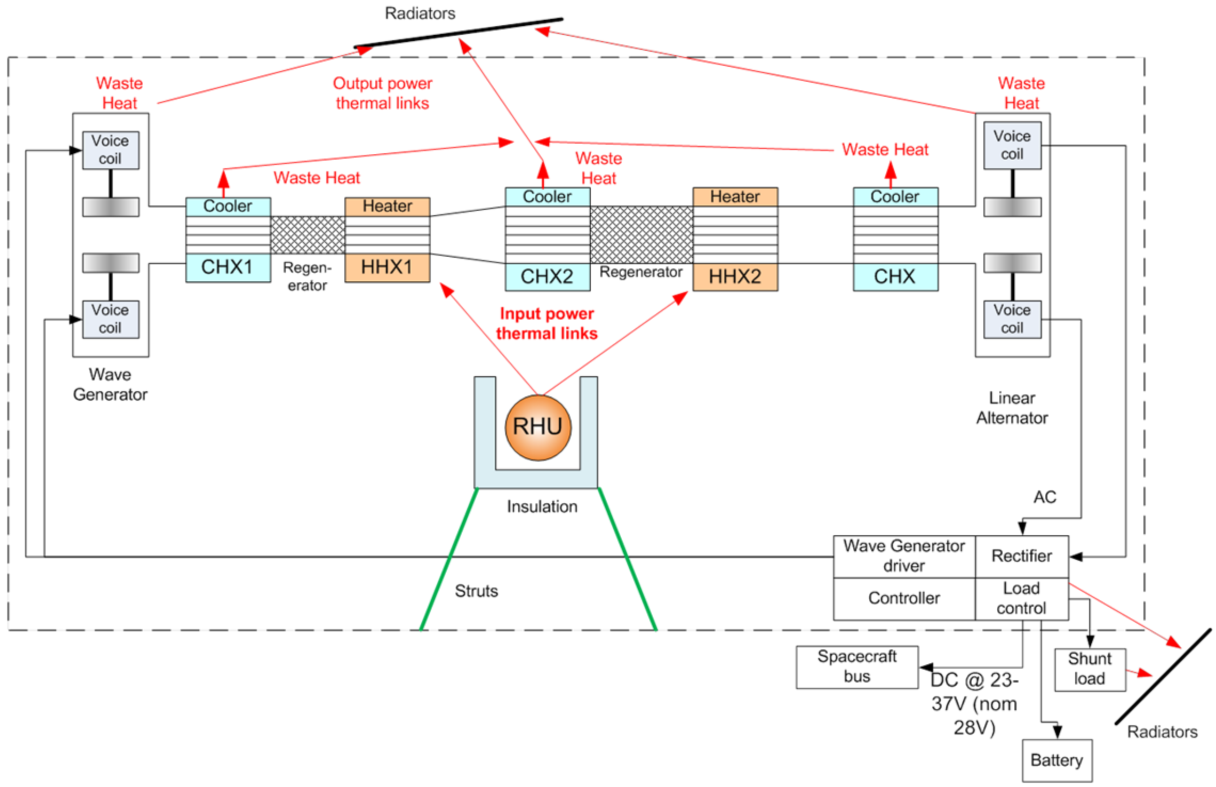

Figure 5 - The basic RTAG architecture

The first trade-off was on an overall concept for redundancy and modularity, with the aim to make the RTAG applicable to as wide a variety of exploration missions as possible (including both deep space and Mars surface). Because the rate of missions is likely to be very low (maybe one per 10 years) it was decided that the core architecture would remain the same but the external architecture would likely to be optimized for each mission. Hence the basic design was a single 100We output unit which, if necessary, could be used multiple times on the same spacecraft to provide more power.

Different trade-offs were carried out on the TAG mounting scheme, insulation system, heat exchanger and transport design (including direct conduction and heat pipes). A key trade-off was the external radiator design since a key aspect of a TAG is that the overall efficiency is strongly related to the cold-end temperature. Since the radiators are strongly impacted by the presence of convection and the first application was likely to be a Mars rover, the radiators were designed to take advantage of convection and also to fit into the fairing a descent module compatible with an Ariane 5 launcher. The possible advantages of deployable radiators was not used because of the additional complexity and need to limit the moments-of-inertia for the rover dynamics.

3.5 Synthetic results

The final RTAG concept consists of the RHU, TAG, thermo-mechanical enclosure, radiators, loop heat pipes, and various internal mounting systems. The design was supported by TAG analysis, preliminary mechanical and thermal models, and electrical simulation. With 2 x 400Wth RHU assemblies the best performance in the Mars atmosphere was 126W electrical output, i.e. a total system efficiency of 32%. It may be possible that this could be increased to 34% if recently observed improvements to TAG efficiency are also realized. The overall mass was estimated at 50.0kg which leads to a specific power of 2.5We/kg. It should be noted that the cause of the difference to the alternative US concepts is the lower thermal output per kg of the European Am-241 fuel, compared to Pu-238 which is used by NASA. The TAG efficiency is seen to be comparable to that of a Stirling convertor although the TAG has no moving parts at the hot end and is therefore expected to be more reliable.

A possible development program was defined for the RTAG with the main focus on the RHU (including the fuel production). A period of 6 years was deemed adequate for the entire project, although this is highly dependent on the fuel production success and also the funding available.

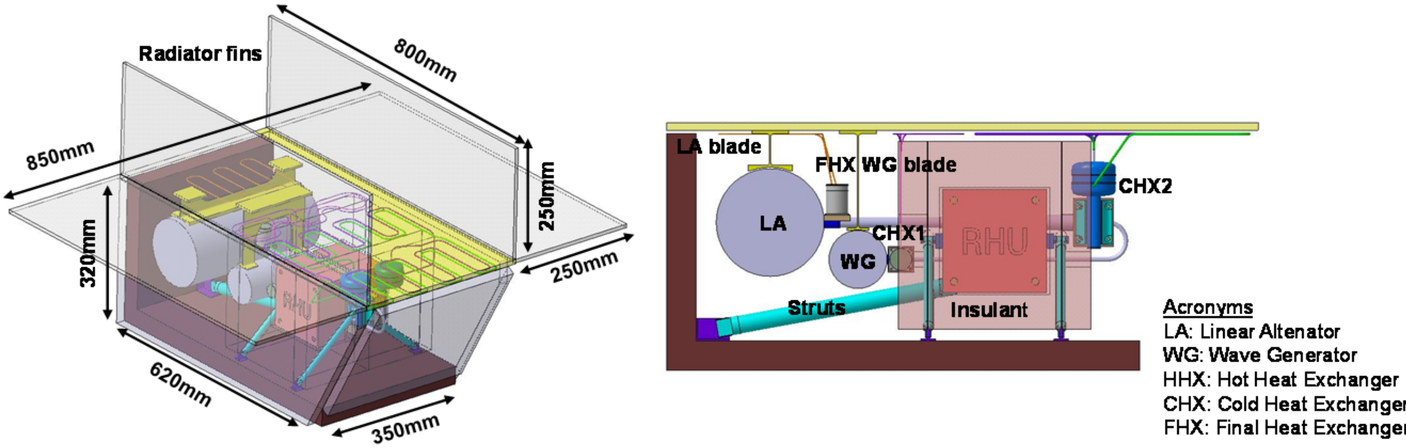

Figure 6 – The RTAG concept

Losses	Power [W]	% of input
TAG	176	44%
WG	3	1%
LA	27	7%
Controller	11	3%
Insulation	17	4%
RHU struts	8	2%
TAG conductive	30	8%
Sub-total	272	68%
Output DC	126	32%
Input Power	400	100%

Mass budget		
RHUs	10.0	20%
TAG core	1.1	2%
Controller	4.0	8%
Alternator	4.1	8%
Wave generator	0.5	1%
Insulant	6.1	12%
Box	14.1	28%
Top fins	3.4	7%
Side fins	3.4	7%
RHU supports	1.5	3%
Thermal HW	1.8	4%
Total mass	50.0	

Table 7 – RTAG power losses and mass budget

4 Conclusion

Thermo Acoustic Generator technology, while being not adequate compared to the photovoltaic conversion concepts for solar powered missions, is an attractive alternative for Radioisotope power based missions for which this technology can bring similar or slightly better specific power and efficiency figures (respectively 2.5 We/kg and 30%) than Stirling based conversion systems while augmenting the system reliability thanks to the reduction in moving parts.
So far, the thermo-acoustic generator is not yet part of the European roadmap for deep space electrical generator, but we have demonstrated it is a valid candidate. The ESA technological directorate ESTEC has been made aware of this new technology that should be considered in the panorama.

A NEW ARCHITECTURE FOR ELECTRICITY GENERATION ONBOARD TELECOMMUNICATIONS SATELLITES

GENESTE J.-F.
Airbus Group Innovations, D42 – B.P. 90112, 31703 Blagnac cedex France
E-mail: Jean-francois.geneste@airbus.com

Abstract: Replacing traditional PV solar arrays on telecommunications satellites by thermoacoustic engines brings to unacceptable over mass and therefore over cost of the satellites. In this paper we show that redesigning a complete satellite around thermoacoustic engines paves the way for such energy onboard together with lower global mass and much lower costs.

1. Introduction

The onboard energy of telecommunications satellites has increased over years, culminating around 20kW DC power today. However, costs also have increased for GaAs multi-junctions high efficiency cells, so that, on recurring satellites, the solar generator price can reach up to 20% of the satellite one. Finding a path to decreasing such a cost therefore is quite an interesting subject. However, the race today more seems to be in ever more efficient with ever more junctions photovoltaic cells, so that the competitiveness equation for the prime contractors which make satellites and sell them at world level always remains the same with no player able to make any real breakthrough compared to the others. It clearly is the objective of this paper to show the way we could create such havoc in the field and which would oblige most players to radically change their way of thinking their satellites architectures.

Indeed, like we experienced it in aeronautics, changing the onboard energy paradigm cannot consist only in changing the ad hoc devices on a standard product and then cross the fingers waiting for its working. Such type of trials were made with electric planes and showed to be no-ways. On the contrary, those who built new concepts of planes around a new type of energy generation (e.g. fuel cells) succeeded. This is what we intend to show in this paper: there is a potential for rupture through a radical change in the energy generation onboard spacecrafts. For this, we propose converting sun energy into heat and heat into electricity with the help of a thermoacoustic engine. We shall describe the potential problems we shall encounter and shall propose some "to be completed" solutions. But this is how incremental R&T works: we solve the problems pace to pace, knowing in advance that the realization is globally possible. Of course, current spacecrafts are optimized for the technologies they use, so there is no surprise that changing as an important subsystem as the energy generation will imply a brand new architecture which will need to be also optimized.

2. Possible alternatives to photovoltaic cells

Our purpose is to generate electricity from the sun. There are not so many ways to do so. The most straightforward possibility against photovoltaic generation is the one of thermal machines. In such a case, thermal energy is given by the sun and therefore the thermal machine must not be a one with internal combustion. In such a case, the best suited machine could or should be the Stirling engine which theoretical efficiency is given by the celebrated Carnot formula

$$\eta = 1 - \frac{T_c}{T_h}$$

where T_c is the cold temperature of the engine and T_h the hot one. However, traditional Stirling engines, that they be of α, β or γ type, all have mechanical moving parts and satellite makers do not like mechanical moving parts onboard. This is the reason why our choice has gone to thermoacoustic engines which are kind of Stirling engines. Roughly speaking, such engines are Stirling like but this is a sound wave which plays the role of the piston, so that there almost are no moving parts in them as we shall see.
There also is another reason why we choose thermal engines as a potential replacement to photovoltaic cells. Indeed, the latter use only a part of the spectrum of sun. Multi-junctions cells only deal with superposing different photosensitive layers which are transparent to the other wave lengths they are sensitive to. Theoretically, there seems to be no limitation to stacking such layers, but we know by experience, that the cost dramatically increases with the number of layers. On the other hand, increasing the efficiency of a thermoacoustic engine, whereas it already has an excellent one as we shall see, does not seem so costly.

3. Choice of the thermoacoustic engine

In its tradeoffs, Airbus Group Innovations has paid particular attention to the Hekyom solution which is shown in the figure hereunder.

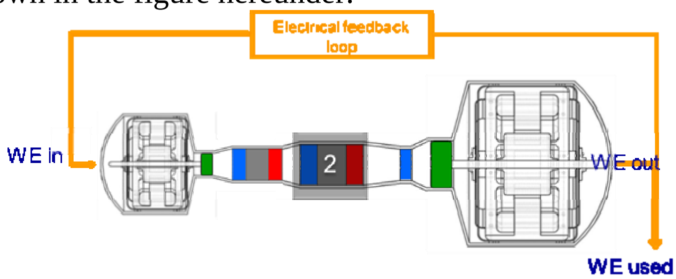

Figure 1: Hekyom thermoacoustic principle.

Let us quickly explain the working principle. The linear alternator on the left generates a primary sound which is thermally amplified and feeds the linear alternator on the right which creates electricity. A portion of the electricity is injected again in the system for further functioning.
Hekyom and Airbus Group Innovations have cooperated on the making of a 1-stage 250We demonstrator which allows expecting, in the end, a global efficiency sun to electricity of 40% as shown on the figure hereunder.

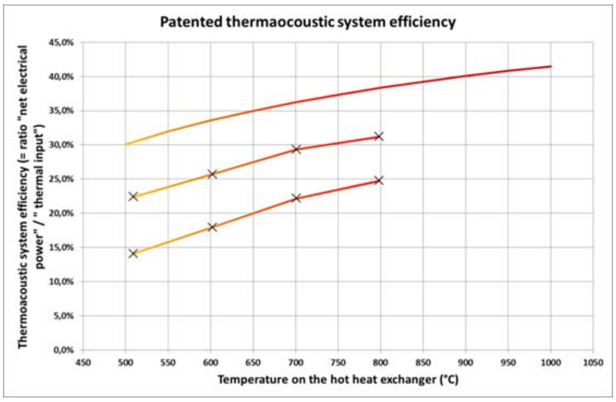

Figure 2 : Expected efficiency of the Hekyom engine.

Please notice that the expected global efficiency is as good as the one of today’s best available GaAs cells.

4. The problem

Several traditional satellites architectures have been studied. They basically consist in replacing the PV arrays by parabolic concentrators.
The results however were disappointing: the global mass was such that the cost reduction got from the use of a thermoacoustic engine was not worth, the over cost being due to the global over mass of the system. More precisely, given the price per kilogram in orbit, that is 20k$/kg, the launch cost increase overshot the savings due to the thermoacoustic engine, for reaching about the same cost in total as a standard solution.
But, let us comment some side questions. For a 20k$/kg, the cost of a TAG in a traditional architecture is about the same as the one of a traditional solar generator. However, space launchers are on the brink to enter a revolution. Such launchers as Falcon of Space X, for example, already propose a 10k$/kg for launches. With such figures, TAGs become competitive. Moreover, competition for launch costs is far from being over and we can expect dramatic upcoming decrease, so that TAGs will become even more interesting. In addition, the range of use of TAGs is much larger than the one of traditional solar arrays. We could even imagine some standard TAGs which would be used as off-the-shelf oversized low cost devices for plenty of space applications. In clear, this means that even if the savings on a given spacecraft in development is not there, it implies great savings for the whole ESA-led community of space. What will not be spent on solar arrays in the future thanks to TAGs can be used for some other new programs, as, for example, more near sun research satellites, leading Europe being the leader in sun physics.

5. The mass problem

Let us turn to the mass problem. For the sake of simplicity, we shall speak of a telecommunications satellite, but it remains valid for all applications. The problem splits into two parts: the weight of the thermoacoustic engine itself and the one of its environment (concentrators and their deployment).

6. The engine

Let us begin with the engine. The figure hereunder shows the demonstrator developed by Hekyom under Airbus Group Innovations order.

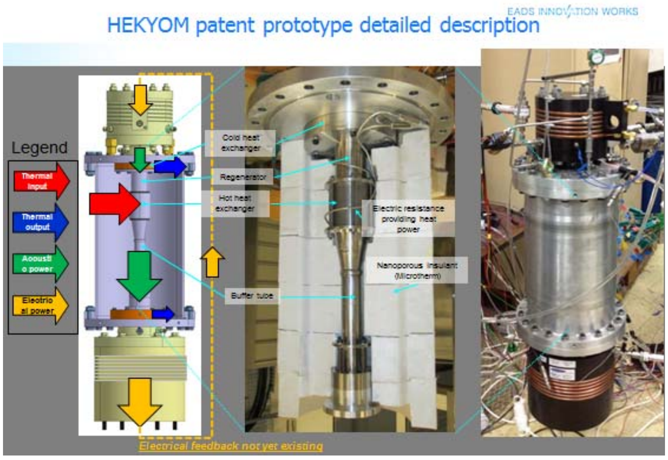

Figure 3: Hekyom demonstrator.

A first way to decrease the mass is to add a third stage, so that the input alternator will inject weaker power and therefore will be much lighter. A second way consists in designing a new type, much lighter of a linear output alternator. We are on track!
With such a potential solution, we expect to divide the mass of the engine by a factor of 2. Please be aware that this applies for all ranges of powers.

7. The sun capture structure

Now, we have to deal with the sun capture and concentration so that the engine can work. Traditional struts Mecano is not adapted because it is too heavy. In order to avoid such mass penalty, we think inflatable structures will better fit our needs. Moreover, the reader should be aware that on a traditional telecommunications satellite, the solar arrays need to follow the sun and then need to rotate a full turn per day, involving the use of an engine. Finally, since the energy source turns, there must be a rotating transmission of the current into the satellite. This therefore implies the use of a device called 'Solar Array Drive Mechanism" (SADM) which can pose problems of reliability and which costs a lot.
Before commenting on, let us first give a picture of our concept.

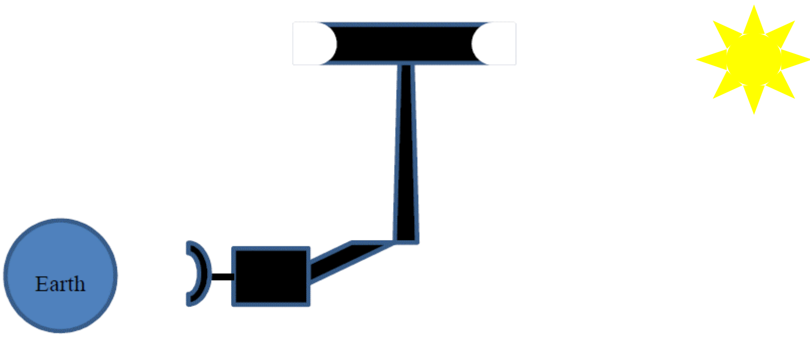

Figure 4: Possible architecture.

As can be seen on the figure, the mirror is a toroid. An alternative view of it is given hereunder.

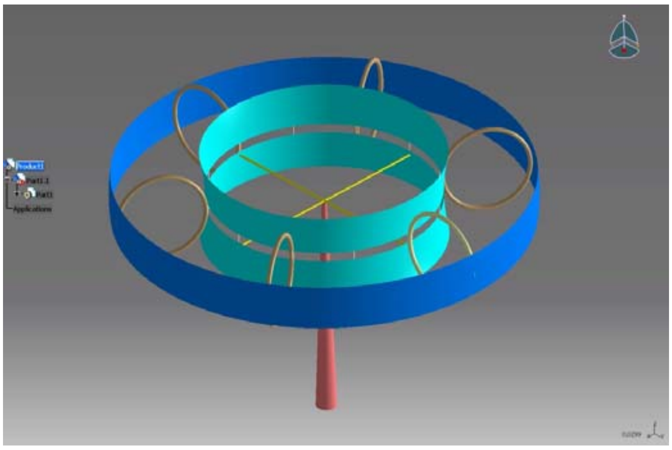

Figure 5 : Detailed view of the tororid.

The main problem is displayed on the figure hereunder.

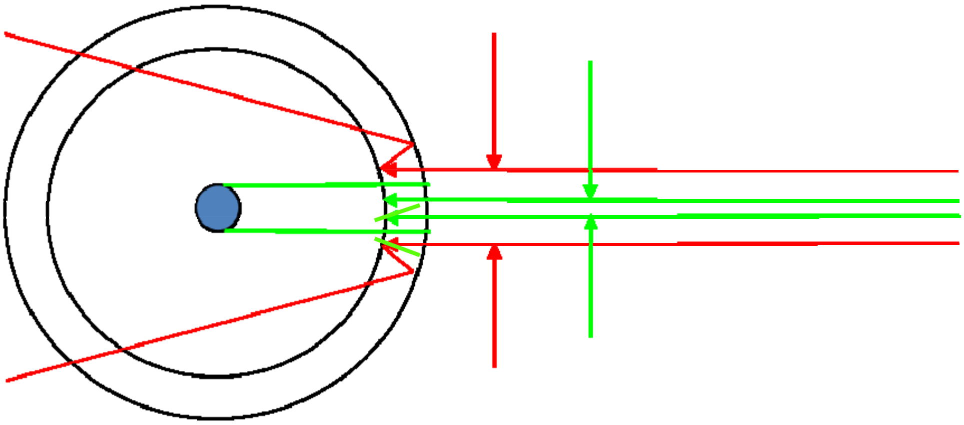

Figure 6: Light collector.

The question is: how much light are we going to be able to concentrate, since the entire diameter is not efficient? Roughly speaking, for a given efficient surface of the concentrator, we have the choice of the diameter of the torus. Since an infinite diameter torus would give 100% efficiency, we shall choose the greatest possible diameter and the efficiency will of course depend on that diameter. Moreover, we can imagine alternative solutions like the one displayed on the following figure.

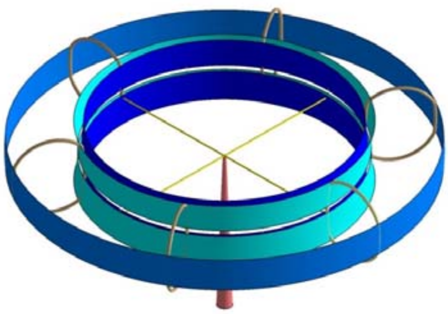

Figure 7: System with a tertiary mirror.

Since everything will be made of thin fabric, it is expected to be very light. Dealing with sunlight for heat creation only, allows not to be too binding for the geometry. Just please also remark that such a solution allows functioning without any rotating engine to follow the sun daily and no SADM! Of course, alternative architectures still are under study.

8. Making of the device

The making of the device is through inflation and polymerization of fabric under UV's. Typically, the mast is inflatable and could be, say, unfolded through inflation the same way as a fishing rod is. The typical mass for such a mast is about 1kg/m. Then the torus is inflated with tricks allowing having parts of it with a parabolic surface with the right characteristics and other parts which will disappear under UV's once the parabolic shapes will have hardened.

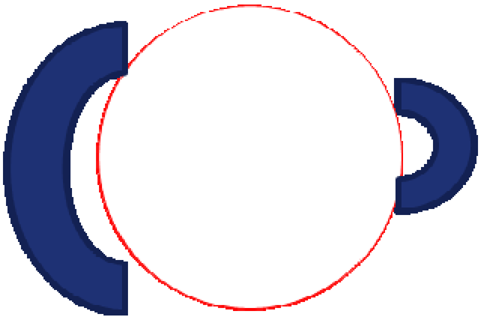

Figure 8 : device inflation

9. Remaining problems

We have no room to describe in detail in this paper all the remaining problems. They are in fact not numerous, but there is a major one which is the interface between light and heat in the neighborhood of the thermoacoustic engine. The targeted heat is about 1000°C so that we have to deal with what we call the solarization of the engine which is a difficult problem. But we think we are able to deal with it.

10. Synergy with the system

Finally, the mast is best suited for being the support of the radiator for the cold source. There, we propose to take the opportunity to use it in the same time as a radiator, as a tank for fluids and replacing the traditional battery on board by an H2/O2 fuel cell. It looks like on the figure below.

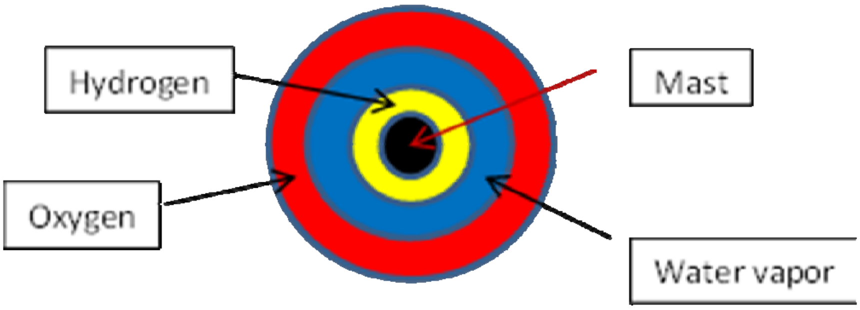

Figure 9: Gas storage for the fuel cell.

We suggest using pretty big tanks, with small pressure inside so that even water will remain under gas form and that the radiating surface is big enough to ensure an interesting cold temperature (less than 50°C).

Then we suggest coupling this radiator which we need whatever happens, with the telecommunications payload since what mainly limits the integration density of communications payloads is the Joule effect.

In the end, since fuel cells ultimately will have a global energy density about 10 times the one of batteries (Airbus internal study), the global mass will be much lighter than the one of a traditional satellite.

THERMOACOUSTIC PROCESS FOR ELECTRICITY GENERATION IN SPACE

FRANCOIS M.-X.
HEKYOM, 3 rue de la Croix Martre – 91120 Palaiseau – France
E-mail of corresponding author: maurice-xavier.francois@hekyom.com

Abstract: To produce electricity dedicated for space applications, the heat source accessibility, the weight, the dimensions and the global efficiency of the proposed solution are of a great importance. One of the conventional solutions is to use the Stirling engine, which have been experimented for many years. However this technology seems to have a limited reliability related in particular to the moving parts. A breakthrough in the conversion processes could be the thermoacoustic (TA) technology where the thermal to acoustic power switch is occurring. In this paper, a brief explanation of the TA process and recent technology development are presented in order to underline the TA competitiveness, its advantages and its weaknesses. Moreover, a conducted experimental investigation on a new acoustic design prototype is presented: the results have shown a relatively high efficiency, however more efforts are needed to enhance the performance of this system. Thus finally, some improvement-keys are proposed to boost the electricity production for space applications.

1. Introduction

For more than 30 years, arousing interests have been dedicated to TA technology. Since no moving parts, no exotic materials and no close tolerance are required, the TA system is a simple, highly reliable and low cost promising solution to generate electricity. Moreover, TA engines can be designed in a way to operate with high heat temperature sources (up to 1000 K). However as any nascent technology, it has been always quite difficult to fund the required research program allowing quick progress in the understanding and the breakdown of technical and theoretical barriers. This may explain the relatively low development of TA process applications.

Stirling process, invented two centuries ago is still considered as one of the best, or the best, thermodynamic cycle and engine for heat driven energy production. But recently, some lack of reliability has appeared for long space mission. On the other hand, for the last twenty years many improvements have been accomplished in the design and construction of TA engine.

Even if most of the barriers are the same for the two technologies as heat supply or acoustic to electrical energy conversion, it is known that TA process may strongly improve the reliability by suppressing nearly all or even all the moving parts.

In this paper, the physical process of TA is described. In the second part, the new acoustic topology proposed by HEKYOM is presented; the results of the experimental investigation conducted on the prototype are given. Finally, key-improvements currently developed in HEKYOM are proposed.

2. Thermoacoustic technology

To perform a thermodynamic cycle supposes a proper phasing of the successive occurring transformations. In the Stirling engine, this phasing is provided by the mechanical component of the systems (e.g. reciprocating pistons, displacers etc...) each intervening at a proper time to build up a thermodynamic cycle. As for the TA systems, this phasing is ensured by the propagation of a wave, who takes in charge the role of the mechanical components in any conventional Stirling engine. Amplitude of the created wave in the resonant cavity of the system must be high enough to replace the piston, the displacer and the expander in the Stirling engines.

As any engine, the performance of the TA technology is firstly revisited based on Carnot's criteria.

2.1. Heat engine and Carnot criteria. A source at high temperature T_h delivers heat Q_h to the engine which will convert part of this heat into energy W (mechanical or acoustic, Fig.1a). The unconverted heat Q_c is withdrawn to the sink at lower temperature T_c. The Carnot factor ($\eta_c = 1 - \frac{T_c}{T_h}$) which limits the real efficiency $\left(\eta_r = \frac{W}{Q_h}\right)$ is presented in (Fig.1b) according to the high heat temperature. The relative real efficiency to Carnot is defined by: $\eta_{rc} = \eta_r / \eta_c$.

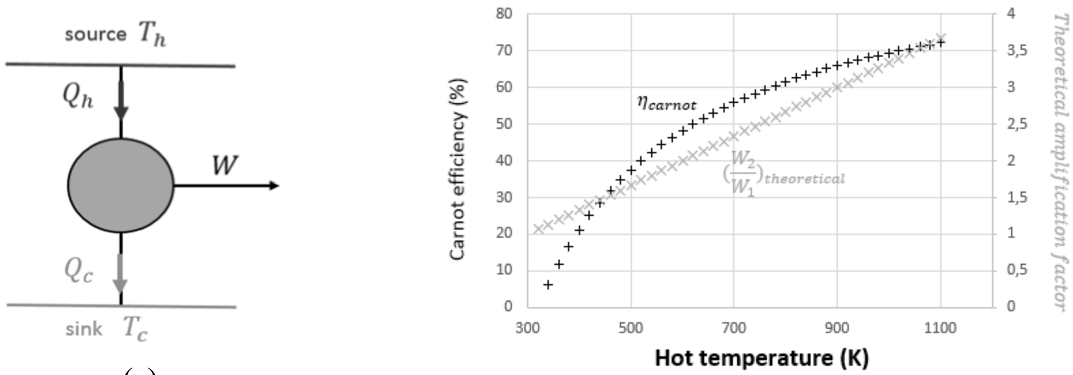

(a) (b)

Figure 1: (a) Ideal presentation of an engine (b) Graph showing the variation of the Carnot efficiency and the theoretical amplification factor of a thermoacoustic cell related to the variation of the hot temperature (T_c=300 K)

Then, for a diesel engine, η_{rc} is of the order of 45%, as for many engines except probably gas turbine. Note that it is important to talk about global efficiency including all losses occurring in the process.

2.2. Thermodynamic cycle occurring in a thermoacoustic process (physics at meso scale). In general, TA is the coupling phenomenon of the sound wave propagation described by the motion, pressure and temperature oscillations and the oscillating heat transfer between the compressible fluid (gas in the most of cases) travelling within a small channel and the neighboring solid boundaries. The channel diameter d must be of the order of the interaction scale between an oscillating fluid wetting a solid wall. This scale is known as the thermal boundary layer (δ_κ) which is in practice of the order of 1/10 mm. to get a significative energy interaction, it is thus necessary to associate a maximum of couple boundary layer + wall in the available volume.

In a TA process, the conversion of thermal to acoustic energy takes place in a porous medium (of length L) called regenerator or stack. This device is sandwiched between two heat exchangers (HEXs) to form the heart of the engine called the wave amplifier (Fig.2). Connected to thermal reservoirs, the cold HEX connected to the sink at T_c and the hot HEX connecting to the source at T_h are able to maintain a temperature gradient (ΔT), along the regenerator or stack. Due to this temperature gradient a sound wave is able to be amplified by extracting the heat (Q_h) from the hot source and evacuate the unconverted residual heat (Q_c) to the cold sink. Actually the motion wave of amplitude (2ξ) displaces the parcel of the working fluid in a way that the parcel of gas experiences compression and expansion depending on the oscillation in pressure while it is exchanging heat with the solid boundaries in the porous media. As such, the gas parcel will undertake a thermodynamic cycle and acoustic power is pumped by the wave generator. To be efficient, L must be 5 to 10 times the amplitude of the motion wave (2ξ). It is known that such a device can be used to onset and amplify the wave generation in a resonant cavity as well as to amplify a propagating wave passing through.

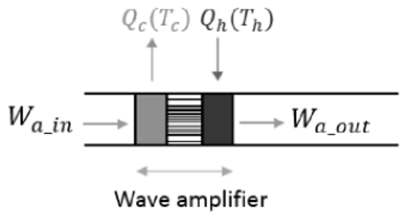

Figure 2: Scheme of a thermoacoustic wave amplifier. Acoustic characteristics are imposed by the resonant or not cavity boundary limits.

In a standing wave heat engine with a stack of plate, the oscillation pressure is about 90° out of phase with the oscillating velocity. In the stack the gas parcel experiences compression or expansion while it is displaced within a peak-to-peak distance (2ξ). Heat transfer occurs when the gas parcel is only tracing the limit of the boundary layer: the distance from the solid surface is approximately equal to (δ_κ). The fluid parcel undergoes a Brayton Cycle which is known to be irreversible in theory.

In a travelling wave heat engine, the oscillating pressure is in phase with the oscillating velocity. In the regenerator an enhanced thermal contact between the gas parcel and the solid surfaces is ensured by the small hydraulic ratios: y<< δ_κ; inevitable viscous losses in the solid matrix of the regenerator make the theoretical perfect thermal heat exchange impossible. The gas parcel travels along the channel within a peak-to-peak distance (2ξ) inside the thermal penetration depth, exchanging heat isothermally in each location of the regenerator. The fluid parcel undergoes a Stirling cycle which is known to be reversible in theory.

2.3. Acoustic topologies for thermoacoustic engine making. For space application, a great importance is accorded to the compactness which is defined as the ratio of the net output power to the internal system volume. Both, the increase of efficiency of conversion process and the decrease of the machine's dimensions, enhance the compactness of the TA system. On the other hand, it is important to pay attention to the acoustic losses associated with the type of resonator and also to the coupling efficiency to the load which is specific for each configuration. The TA systems developed in the past can be classified in four categories as proposed by K.de Blok in a very clear paper relative to acoustic losses and coupling aspects corresponding to these geometries: a standing-wave resonator, a standing wave resonator with Helmholtz resonator, an acousto-mechanical resonator and a multi-stage travelling wave system [1, 2, 3, 4].

2.4. Thermoacoustic wave amplifier. The following scheme (Fig.3) gives a representation of a TA amplifier, where 'in' and 'out' refer as the input and output electric (W_e) or acoustic (W_a) power.

If ρ_{1s132d} and ρ_{1s175d} are respectively the 1s132d and 1s175d Qdrive efficiencies, it is easily to obtain $W_{e\_in} = W_{a\_in}/\rho_{1s132d}$ and $W_{a\_out} = W_{e\_out}/\rho_{1s175d}$. In Fig.3, α and η_{rc} refer respectively to the imperfect amplification and Carnot efficiency of the amplification.

As seen above the acoustic gain is limited to the ratio of hot T_h and cold T_c heat sources temperature. For a nuclear energy source at T_h =1100 K, this ratio can be of the order of 3 (Fig.1b).

The net maximum acoustic benefit $W_{a\_out} – W_{a\_in}$ is then 2xW_{a_in}. It appears clearly that with two amplifiers supplied by an identical T_h heat source, the net acoustic gain would be 8xW_{a_in} and so on.

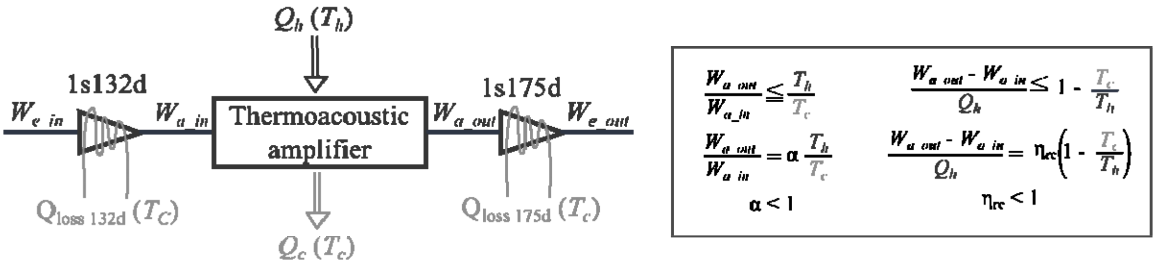

Figure 3: Scheme of the thermoacoustic wave amplifier developed at HEKYOM [5], where 1s132d and 1s175d are electroacoustic transducers from the manufacturer Qdrive

3. One way to take benefit of thermoacoustic process: the HEKYOM acoustic topology

An acoustic power of the order of 10 kW produced by a standing wave engine requires a low frequency, thus a greater length of the machine and therefore make the standing wave out of scope for space applications. The resonant travelling wave developed by K. de Blok can be considered for space application however compactness must be revisited [4].

A new acoustic topology has been developed in HEKYOM. The prototype funded by AIRBUS has shown a very satisfying result. The one stage TA amplifier shown in Fig. has a relatively high efficiency. Experimental data will be discussed in the subsection 3.2. The final aim is to obtain a compact machine with a higher efficiency compared to photovoltaic power. To prove it, one stage amplifier was considered as a sufficient positive proof.

3.1. Description of the prototype. A wave, generated by an electroacoustic generator Qdrive 1s132d (top of Fig.4a) is propagating through a TA cell which acts as a sound amplifier converting heat into acoustic energy. The amplified wave drives another electroacoustic converter 1s175d (bottom of Fig.4a) working in inverse mode.

The prototype was designed to receive heat at temperature up to 950°C. The TA cell is shown in Fig.4b, with its cold heat exchanger+ regenerator+ hot heat exchanger followed by the buffer tube and the ambient heat exchanger protecting the second Qdrive 1s175d (not shown). The white material is a nanoporous material from PROMAT industry which insulates the system and avoids the heat leaks. In order to insulate correctly the heater (simulated by joule effect), a double tubing was designed, the outer one being filled by nitrogen gas at the same pressure than the inner one where is the TA system. Unfortunately, the heater made in Molybdenum was not perfectly soldered by the manufacturer and the 2 vessels were obliged to be filled with helium gas carrying nearly 20% of heat losses.

3.2. Experimental results. Extensive experimentations were performed using a RC load, the capacitance compensating the Qdrive inertance. One varies as well the input acoustic energy, the frequency, the heat power corresponding to a given hot temperature. Comparisons with our calculation made with our software CRISTA [6] give a pretty good agreement (Fig.5). As an example, data for a run near 700°C are reported in Fig.4c. It can be noticed that for that run:

- ρ_{1s132d} = 74.2% and ρ_{1s175d} = 78.9% which are much lower than the expected values (85% for both) promised by Qdrive. 77.1 W and 122.3 W of heat losses are evacuated by water circuit respectively from the 1s132d and 1s175d;
- α = 80.7% which is a correct value in agreement with our calculation ;
- the heat losses due to the impossibility to surround the helium tube at 30 bars by a nitrogen gas filled tube are important and nearly 200W;
- the real efficiency relative to Carnot is no more than 55.1% because the heat losses;
- as these losses may be considered as easily avoided, the expected efficiency could have been 69.8%;
- the thermal efficiency is given by $(W_{e\_out} - W_{e\_in})/Q_h$ which corresponds to 17.6 % for this hot temperature of 700°C;

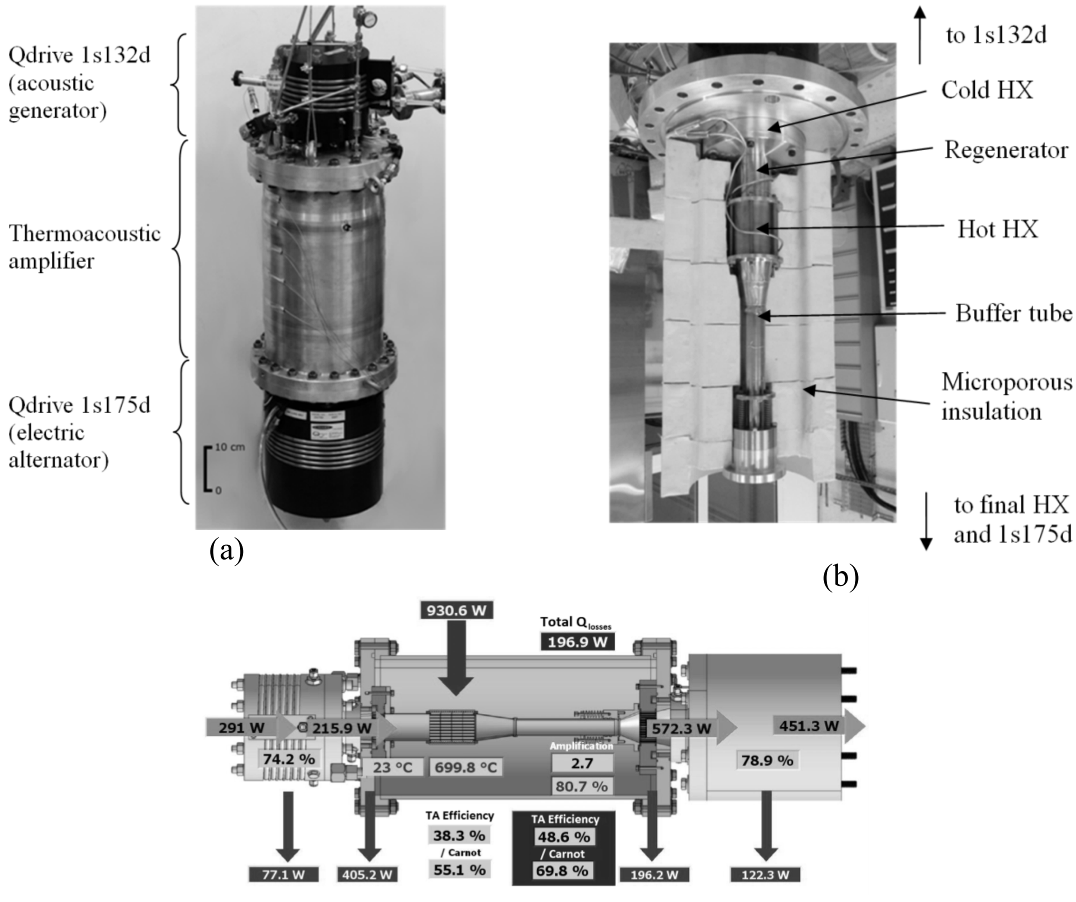

Figure 4: (a) Picture of the thermoacoustic system developed by HEKYOM (b) Internal picture of the thermoacoustic system (c) Scheme of the energetic balance of the system at 700°C.

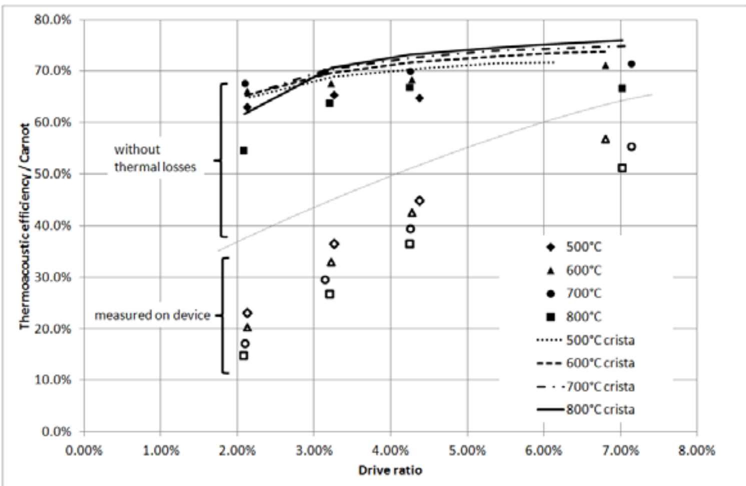

Figure 5: Efficiency of the thermoacoustic amplifier. To compare with the simulation software CRISTA, thermal losses are deduced to the experimental values

- taken in account the expected value of Qdrive efficiency (85%) and suppressing heat losses (not acoustic losses), the thermal efficiency would have been 36%;
- The figure shows the efficiency of the TA part relative to Carnot efficiency versus the drive ratio. Increasing the input acoustic power increases the drive ratio. Due to the limitation in current and stroke for the 1s132d Qdrive, it was not possible to exceed 7%.

In conclusion, the system works very well. It would be possible to improve the Qdrive efficiency, Qdrive manager said. It is reasonable to consider the heat losses as circumstantial. The very good agreement between data and calculation confirms that there is no streaming in such an acoustic configuration.

4. How to improve the thermoacoustic generator

We may propose several available modifications:

1. First of all, it is evident that the efficiency will increase if we used 2 or 3 amplifiers in series. In that case the input acoustic energy could be diminished quite much.
2. The computation has been already done and a prototype is under construction
3. The thermal insulation could be very much improved
4. The buffer length was chosen too large and a 2 stages system will be nearly of the same total length

We may indicate some new technique to be looked at. Some of them will be presented at the conference.

1. The output Qdrive is limited in capacity to 2x15kWe. Another technique converting acoustic energy into electrical energy consists using a bi-directional turbine associated to a rotating alternator. This has been already successfully tested at small acoustic energy of the order of one $kW_{acoustic}$ by K. de Blok [7].
2. The Qdrive technic must be improved and lighter material must be used in the manufacturing. Other approach could be thought for the electrical conversion concept. A system study has been performed by AIRBUS Group with the participation of HEKYOM. Results will be presented at the conference [8].
3. TA system can be used for moving a conductive liquid as Na. Space TRIPS European FP7 project is in progress.

For Space application it is clear that the problem of heat source is not yet solved except using nuclear heating source. Improvements still need to be done in order to be able to catch and transfer solar energy with a light and reliable way. Some interesting new idea will be presented at the conference also by AIRBUS Group.

5. Conclusion

In conclusion, TA process seems likely to be a good partner for electricity generator in space. Even if many improvements have to be done, the concept used by HEKYOM has proved to be efficient.

6. Acknowledgements

One wants to thank very much AIRBUS I.W. for their financial support and good cooperation during the contract and a special acknowledgment to Arnaud Guillou and Cynthia Haddad for helpful discussions.

7. References

[1] Swift G., Thermoacoustics: A Unifying Perspective for some Engines and Refrigerators, Fifth Draft. LANL. LA-UR 99-895 (2001).

[2] Backhaus S., Swift G.W., A thermoacoustic Stirling heat engine. Nature, 399, pp 335-338 (1999).

[3] Gardner D. L., Swift G.W., A cascade thermoacoustic engine. J. Acoust. Soc. Am., 114(4), pp 1905–1919 (2003).

[4] de Blok K., Multi-stage travelling wave thermoacoustics in practice, 19th International Congress of Sound and Vibration, Vilnius (Lituania), July 8 – 12, 2012.

[5] Bétrancourt A., Le Pollès T., Chabut E., François M.X., Thermoacoustic and energy conversion: future steps. 19th International Congress of Sound and Vibration, Vilnius (Lithuania), July 8 – 12, 2012.

[6] Bétrancourt A., Simulations numériques et validations expérimentales de machines de réfrigération thermoacoustiques, PhD thesis (in french), Paris : Université Pierre et Marie Curie (2008).

[7] de Blok K., Owczarek P., François M.-X., Bi-directional turbines for converting acoustic wave power into electricity, 9th PAMIR International Conference Fundamental and Applied MHD, Riga (Latvia), June 16-20, 2014.

[8] AIRBUS Group, TAG in Space, 9th PAMIR International Conference Fundamental and Applied MHD, Riga (Latvia), June 16-20, 2014.

REALIZATION OF MHD-ACTION AT MANUFACTURING OF ALLOYS WITH THE SPECIAL PROPERTIES ABOARD THE ORBITAL SPACE STATION

DUBODELOV V.I., SEREDENKO V.A., KYRYEVKYY B.A., SEREDENKO E.V.
Physico-Technological Institute of Metals and Alloys, NAS of Ukraine
Vernadsky Ave. 34/1, Kyiv-142, 03680, Ukraine
E-mail: mgd@ptima.kiev.ua ; mgd@i.kiev.ua

Abstract: It is set the parameters of the crossed electromagnetic fields (constant magnetic field & alternative electric field), which used for manufacturing of ingots with emulsified structure from alloys of monotectic systems in conditions of microgravity at space orbital station. It is defined, that Earth magnetic field at orbital conditions increases stability of interphase surface in melts consisting of two unmixed volumes. It is promoted the braking of wave disturbances at wave-lengths of 0.01-1.0 m.

1. Introduction

Presently, there are not enough the statistically synonymous experimental data for development of theoretical notions about technological processes in space terms. The authors of report over a long period of time research the processes of manufacturing of alloys with emulsified structure at electromagnetic actions, including in terms simulated the microgravity by electromagnetic balancing of phases [1-3]. Therefore, there are made the scientific experiments for studying the features of determinative physical and chemical processes, in particular, in alloys with immiscibility area of liquid phases at orbital terms, which are different sharply from earthly ones. These researches are directed for development of technological modes, designing and working-off of equipment & its main systems. At that, it is deciding the important task, namely organization in space the manufacturing of unique materials, including metallic alloys with improved properties or with principle new ones. Researches of alloys with immiscibility area at microgravity on near-earth orbit exposed the some features of behavior of liquid and solidifying alloys different from processes on Earth: 1) both monotectic alloys (Bi – Zn) and alloys without immiscibility area (Al – Si, Al – Cu, Al – Zn, Sn – Pb, Zn – Sn, Bi – Sb) were delaminated on two liquids. At that, homogeneous state in castings was not attained because intensifying of segregation of components and additives at acceleration of gravity ca. $1\cdot10^{-3}$-$1\cdot10^{-4}$ m/sec^2, different temperatures and holding time in molten state. This fact is connected with specific of heating (by radiation) and absence of thermal convection [4]; 2) the experiments on mutual diffusion of liquid phases with wide difference in density did not give statistically synonymous results because of remanent accelerations on space orbital objects [5]; 3) more intensive increasing fluctuations of concentration and suppression of formation of nucleus embryos of the dividing phases at melt cooling [6]; 4) at directed crystallization, it is accelerated the influence on the structure of different factors (composition of alloy, thermal gradient, solidification rate, convection instability, size of immiscibility area of phases [7]; 5) increasing role of non-equilibrium processes in the conditions of concrete distinctions of microgravity aboard spacecrafts, that results in different effects at structure formation [8].
At the same time, importance of electromagnetic actions at manufacturing of metallic alloys of monotectic systems with emulsified structure remains unstudied.

2. Presentation of the problem

Data about intensity of magnetic field on orbits for most of spacecrafts are ambiguous in the range 10^{-4}-10^{-6} T. Base of geomagnetic field is constant component. At orbit, it can be accepted ca. $1\cdot10^{-5}$ T. Action of magnetic fields (both constant and alternating ones) on liquid and solidifying alloys appears most strongly at phase transformations. At Earth conditions, influences on crystallization of metallic alloys appears already at magnetic field induction ca. $1\cdot10^{-3}$ T. Action of constant magnetic field at orbital microgravity on stability of interphase surface of monotectic melts is analyzed on the basis of equation [9]. According to it, there are indignations with the wavenumber *of* $k_w=2\pi/\lambda$ (λ – length of wave, m) on interphase surface which are repressed by constant homogeneous both vertical and horizontal magnetic field in the range $k_{w1}<k_w<k_{w2}$. For immiscible liquid-metal volumes, it is accepted:

$$k_{w1,2} = \frac{H^2}{8\pi\sigma_{1-2}} \pm \sqrt{\left(\frac{H^2}{8\pi\sigma_{1-2}}\right)^2 - \frac{\Delta\rho\ g}{\sigma_{1-2}}}\ , \tag{1}$$

where H – magnetic field intensity, A/m; σ_{1-2} – interphase tension of immiscible liquid-metal volumes, N/m; g – acceleration of gravity, m/sec^2; $\Delta\rho$ – difference of density of liquid-metal phases, kg/m^3.

As objects for study were selected the alloys covering practically complete range of differences of phases' density: а) copper – cast iron ($\Delta\rho\approx800$ kg/m^3, σ_{1-2}=0.025 N/m); б) Bi – Ga ($\Delta\rho\approx3400$ kg/m^3, σ_{1-2}=0.01 N/m); в) Al – Pb ($\Delta\rho\approx7700$ kg/m^3, σ_{1-2}=0.1 N/m). As main research object, it was selected Bi – Ga alloy (fig. 1 [10]).

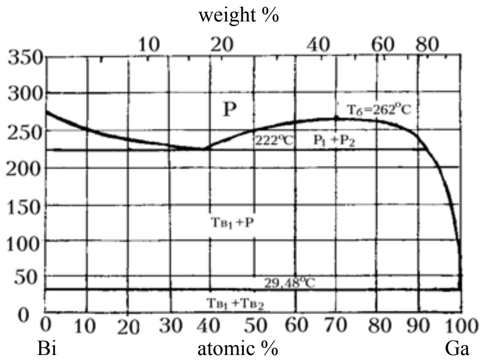

Figure 1: Bi – Ga monotectic alloy structural diagram:
P – area of homogenous liquid condition;
P_1 – Bi base saturated liquid solution;
P_2 – Ga base saturated liquid solution;
T_{B1} – Bi base saturated solid solution;
T_{B2} – Ga base saturated solid solution;
$T_б$ – temperature of binodal (critical temperature).

The alloy was studied at microgravity [6]. It has prospects for experiments aboard space station, because such alloy needs low energy consumption for melting in comparison with other alloys. Chemical composition of experimental alloy corresponds to immiscibility area of phases in melt (Bi – 75 weight % and Ga – 25 weight %). Base of alloy is Bi, as Ga has low melting temperature 29.5 °C (it exceeds insignificantly the usual room temperature). Moreover, at cooling of melt, it is necessary to utilize a little heat (Table 1, where ρ^e – specific resistance; c – specific heat capacity; q_m – melting heat).

Table 1. Main parameters of monotectic Bi – Ga alloy

Components of alloy	ρ, kg/m^3		ρ^e, Ohm·m		c, J/(kg·°C)		q_m, J/kg
	20 °C	300 °C	20 °C	300 °C	20 °C	300 °C	
Bi	9800	10300	$117\cdot10^{-8}$	$132\cdot10^{-8}$	1200	3800	$5.2\cdot10^4$
Ga	5900	5905	$54\cdot10^{-8}$	$30\cdot10^{-8}$	377	398	$8.2\cdot10^4$

As distinct from earlier orbital experiments, in the presented works it is foreseen heat generation directly in alloy due to heating by alternating electric current. Also, it is provided the creation of optimum thermal & forced processing of liquid alloy by crossed electric and magnetic fields. For providing of accelerated cooling at melt crystallization, it is used the metallic cooler. At Bi – Ga alloy, there is researched the possibility of magnetic field influence on the change of phase transitions in monotectic melt and change of crystallization type, first of all for increasing number of nucleus and crystallization rate in orbital terms. For providing of necessary effects of MHD-actions on the liquid monotectic alloy at microgravity, it is needed to select the proper parameters of magnetic and electric current systems. At development of space equipment, it becomes additionally complicated because of power, gravimetric, overall, and other limitations.

Evolution of wave disturbances on interphase surface of liquid volumes Bi and Ga at microgravity in thermodynamically equilibrium state (clean components A and B) is rated on equation by Birkhoff [11] at $\sigma_{1\text{-}2}$=0.01 N/m. At that, the minimum speed U, corresponding to transition boundary of system from $A(\tau)=A_0$ to $A(\tau)>A_0$ (A_0 – initial amplitude (or amplitude of harmonic disturbance at time $\tau = 0$), m;) connected with wave-length λ for an alloy Bi – Ga:

$$U = \sqrt{\frac{0{,}61\cdot 10^{-4}}{\lambda} + 2{,}8\cdot 10^{-3}\lambda} \tag{2}$$

According to (2), at short waves' range ($\lambda<5\cdot10^{-5}$ m) for evolution of instability on interphase surface of liquid Bi and Ga at microgravity, relative moving speed of volumes must exceed 1 m/sec, and for $\lambda=5\cdot10^{-6}$ m – 3.5 m/sec. Therefore for receipt of fine-dispersed emulsion in Bi – Ga melt at microgravity, it is appropriate to use condensation method (not dispersion).

At the contact holding of sample of alloy and using of most rational heating method by transmission of electric current through alloy, it is necessary to imposition of electric field (fig. 2).

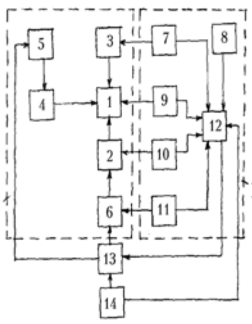

Figure 2: Block-scheme of the apparatus:
1 – technological capsule with alloy; 2 – system creating electric current of heavy density; 3 – magnetic system; 4 – solid cooler; 5 – manipulator; 6 – power supply block of the electric system; 7 – flux density sensor in the electromagnet gap; 8 – geomagnetic field flux density sensor; 9, 10 – alloy temperature and electrode loop sensors; 11 – electric current value sensor; 12 – information apparatus; 13 – control block; 14 – board electric power supply system; I – technological apparatus; II – information block.

Time for transition of alloy into liquid state with finite temperature is determined by active power consumption. The P_Σ power is used for heating of metal from t_0=20 °C to finite temperature t depends on general efficiency of heater η and efficiency of thermoinsulation (total thermal losses of the heated objects). At contact power supply to heated sample of alloy η will make no less than 0.95, and thermal losses P_h at chosen finite temperature t= 300 °C $>t_6$ (t_6 – temperature of binodal of alloy) it is possible to limit at the level of 0.1 W. At useful power consumption P in two orders less than power provided the power system aboard orbital station (namely ca. 5 W), the specific volume thermal power makes $(P+P_h)/V$=5.1 W/cm^3. The specific volume active power consumption makes $P_a=P/\eta$=5.3 W/cm^3. So, specific energy consumption makes $q=[c(t-t_0)+q_m]$=1158 W·sec/cm^3. Time τ_t for transition of alloy into liquid state with temperature 300 °C will make τ_t=218 sec. For determination of necessary electric current density in melt for providing the required volume thermal power, it is calculated (by additivity rule) average specific electric resistance of alloy ρ^e_a in temperature interval 20-300 °C calculated. It makes $\rho^e_a=1.1\cdot10^{-7}$ Ohm·m. The required electric current density in sample of Bi – Ga alloy makes $j=\sqrt{P_v/\rho^e_a}=215$ A/cm^2. At that, volume of alloy with passing large electric current is the short circuit area. It is expedient to use transformer chart working on AC. In this case, energy to alloy is passed through DC/AC-converter and transformer which has the one-turn secondary winding circuited on volume of alloy (fig. 3, 4).

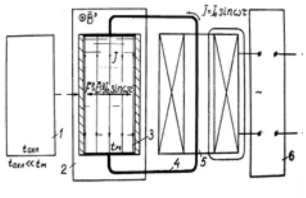

Figure 3: Scheme for creation of the electromagnetic actions on the monotectic alloy with emulsified structure aboard the orbital space station:
1 – cooler; 2 – constant magnet; 3 – alloy; 4 – loop with conductor; 5 – voltage transformer; 6 – electric current converter

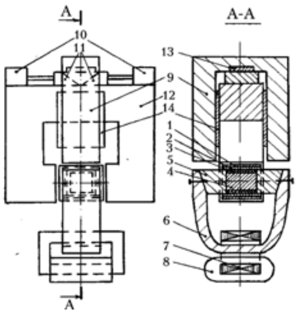

Figure 4: Construction of the technological apparatus:
1 – copper capsule; 2 – ceramic cartridge; 3 – elastic heat-electric insulator; 4 – alloy; 5 – copper electrodes; 6 – electrode bus; 7 – transformer limb; 8 – transformer winding; 9 – solid aluminum cooler; 10 – manipulator of the magnetic type; 11 – electro-mechanical cotter pin; 12 – constant magnet; 13 – ferromagnetic lamina; 14 – slides of the cooler.

However, at orbital experiments, there are appeared considerable kinetic difficulties during homogenization of monotectic melt over the bimodal temperature. Performed analysis had shown that homogeneity of single-phase fluid can be provided by MHD-actions, in particular, by imposition external magnetic field on alternating current in melt. At that, it is created electromagnetic vibration in liquid alloy. For generation of variable electromagnetic forces at affecting on melt phases at heating, rationally to place the alloy sample in the gap of constant magnet (this one is not required the energy for working (see fig. 3). Interaction of imposed on melt constant magnetic field with induction B with transverse alternating electric current with frequency ω will cause the origin of electromagnetic force in melt. This force acts differentially on the phases in melt with different ρ^e. Thus, according to (2) for the Bi – Ga melt from clean components, the acceleration of Ga volume is in 7.3 times more than Bi volume. After temperature-temporal processing of melt, it is under action of constant magnetic field. Degree and character of influence of constant magnetic field, including geomagnetic one, on stability of interphase surface in monotectic melts is estimated using equation (1). The analysis showed (fig. 5) that geomagnetic field on orbit promotes braking of wave disturbances on interphase surface in monotectic melts in the range of wave lengths $1{\cdot}10^{-2}$-1.0 m.

At imposition on cooling melt of the homogeneous constant magnetic field with intensity exceeding intensity of geomagnetic field, in liquid monotectic alloy on the space station, there are suppressed the flows, related to micro-accelerations due to inertial random motion.

At successive solidifying of monotectic melt in castings and ingots, there are areas which contain the different by sizes inclusions of second metallic phase. In this connection, for providing of homogeneity of inclusions by sizes and their uniform distribution, it is necessary to realize cooling of melt with optimum speed even in the zero-gravity state (weightlessness).

On base of results of computations and experiments on action of magnetic field on emulsified melts, for the first series of experiments in space terms it is recommended using of constant magnets with induction of magnetic field in the gap ca. 0.1 T. For acceleration of melt cooling after its overheating to 300 °C and homogenization, it can be used the metallic cooler entered into the contact with melt (see fig. 3).

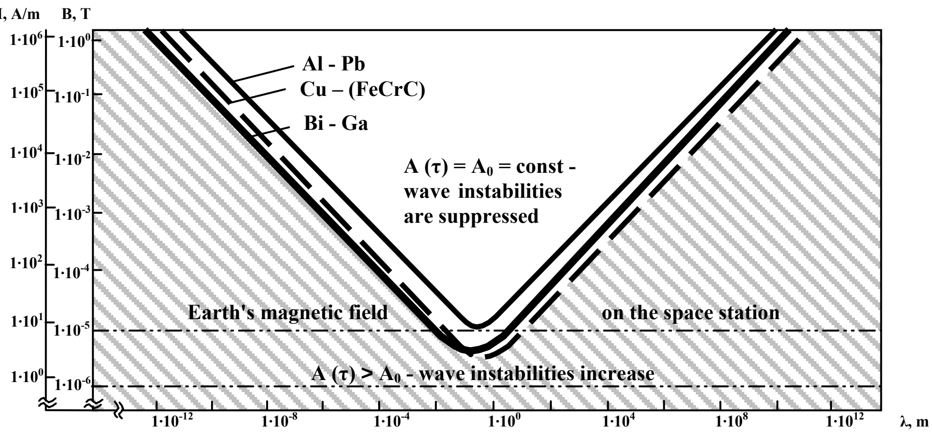

Figure 5: Constant magnetic field action on melts interphase stability at space station.

At the small volume of melt (1 cm^3) and low overheating above ambient temperature, the aluminium cooler by volume of 20 sm^3 will provide cooling rate of 27 °C/sec (according to calculation, heat of overheating relieving ca. 1000 J; heat conductivity coefficient of melt 20 $W/(m^3{\cdot}sec)$; heat capacity of the cooler $2{,}4{\cdot}10^6$ J/m^3; temperature of cooler 20 °C; areas of contact surface of cooler with melt $2{\cdot}10^{-4}$ m^2). At cooling, melt fusion will be found in immiscibility area of liquid phases during ca. 1 sec, and sedimentation in melt will not appear.

3. Conclusion

There are defined the terms for using of constant magnetic field (B=0.1 T) crossed with alternating electric one (q=1160 W·sec/cm^3; j=215 A/cm^2) at manufacturing of ingots from monotectic alloys (Bi – Ga) with emulsified structure at microgravity aboard space orbital station. It is set that geomagnetic field promotes stability of interphase surface in double-phase monotectic melts on orbit. It promotes braking of wave disturbances in the range of wave lengths $1{\cdot}10^{-2}$-1.0 m.

4. References

[1] Dubodelov, V. I.; et al. Some aspects of electromagnetic balancing a metallic drop in liquid matrix in monotectic system melt cooling. Proc.the 4th International Pamir Conference on Magnetohydrodynamic at Dawn of Third Millennium, Presqu'île de Giens, France, September 2000, vol. 2, p. 699-703.

[2] Seredenko, V. A. et al:. Production of composite alloy with an immiscibility gap in an alternating electromagnetic field . Joint 15th Riga and 6th PAMIR International Conference on Fundamental and Applied MHD, Riga, Jurmala, Latvia, June 27–July 1, 2005, vol. 2, p. 63-68.

[3] Seredenko, V. A. et al.: Action of constant magnetic field on refractory phase inclusions during solidification of the monotectic system alloy with composition of the lower liquidus zone. E-Book of Proc. the 7th International Conference on Electromagnetic Processing of Materials, October 22-26, 2012, Beijing, China.

[4] Presnyakov, A. A.; et al.: Behaviour of metallic melts at microgravity on orbital station “Mir”. Proc. Academy of Sciences of Kazakhstan. 1 (1996) 15-20 (in Russ.).

[5] Mathiak, G.; Willnecker, R.: Damping of convection in liquid diffusion experiments. Z. Metallk. 11, 91 (2000) 928 – 932.

[6] Itami, T.; Masaki, T.: The critical behavior under microgravity of liquid alloys with mutual immiscibility. Meas. Sci. And Technol. 2, 16 (2005) 343-345.

[7] Andrews, J. B.; et al.: The effect of processing conditions on solidified structures in immiscible systems. Mater. Sci. Forum. 77 (1991) 269-282.

[8] Milvidsky, M. G.; at al.: Growth of crystals of semi-conductors in space: results, problems, prospects. Crystallography. 5, 42 (1997) 913-923 (in Russ.).

[9] Levich, V. G.; Gurevich, Yu. Ya.: Influence of magnetic field on surface waves in conductive liquid. Proc. Academy of Sciences of USSR. 1, 143 (1962) 64-67 (in Russ.).

[10] Hansen, M.; Underco, K.: Structures of binary alloys. Moscow: Metallurgizdat 1962 (in Russ.).

[11] G. Birkhoff. Hydrodynamics. Princeton University Press, Princeton, New Jersey, 1960.

MHD Simulation of Plasma Rocket Exhaust

EBERSOHN[1] Frans H., LONGMIER[1] Benjamin W., and SHEBALIN[2], John V.
[1]*Dept. of Aerospace Engineering*/University of Michigan, Ann Arbor, MI 48109, USA
ebersohn@umich.edu
[2]*Astromaterials Research Office*/NASA Johnson Space Center, Houston, TX 77058, USA

Abstract:

The magnetohydrodynamic description of magnetic nozzle physics is presented and discussed. A parametric analysis was performed of the generalized Ohm's law for relevant plasma propulsion devices. Results suggest that all terms of the generalized Ohm's law should be retained in MHD simulations to capture the relevant physics.

1. Introduction

Plasmas have a long history of use in space propulsion primarily through ion and Hall thrusters. However, a need exists for thrusters which limit the interaction of plasma with walls of the thruster which enables scaling to higher temperature, higher energy plasmas and increases the overall lifetime of the thruster.[1,2] Among the key components in the development of these thrusters is the magnetic nozzle which guides the flow of plasma through the thruster. Magnetic nozzles are strong converging-diverging magnetic fields which direct the flow of the plasma and limit interaction with the walls. These nozzles are also integral to the thrust generation process by converting non-directed magnetoplasma energy of the plasma into directed kinetic energy. Understanding the physics of magnetic nozzles is crucial to the current design of electric propulsion thrusters and also has broader applications to astrophysical jets. [3]

Magnetohydrodynamics (MHD) has been previously used to study the flow of plasma through a magnetic nozzle. A number of theoretical and computational studies have been performed with a focus primarily on ideal and resistive MHD descriptions. Herein we summarize the results of these studies and argue that more complex MHD descriptions are required to accurately capture all of the relevant physics in a magnetic nozzle. Section II of this paper further introduces the physics of magnetic nozzles and summarizes previous studies with MHD. Section III presents a parametric study of relevant magnetic nozzle devices and Section IV concludes this paper.

2. Summary of Studies and Simulations of Magnetic Nozzle with MHD

The primary function of magnetic nozzles is to control the flow of plasma and generate thrust by accelerating the plasma in the axial direction. A simple schematic of a magnetic nozzle is shown in fig. 1. The plasma is generated in the plasma source and then guided by the magnetic field which is generated by either a current coil, as shown, or by permanent magnets. A converging-diverging magnetic field is typically employed to create a nozzle contour similar to de Laval nozzles used in chemical rockets. The thrust generation process can be divided into three essential components: 1.) Energy conversion to directed kinetic energy; 2.) Transfer of momentum from the plasma to the thruster; 3.) Detachment of the plasma from the initially confining magnetic field lines. These steps of the thrust generation process are coupled with one another.[4]

In this paper we consider magnetic nozzles primarily from the MHD perspective and will limit the discussion of the relevant physics to those in the fluid, MHD regime. The physics of the magnetic nozzle can also be considered from particle and kinetic perspectives, leading to additional physical mechanisms which generate thrust.

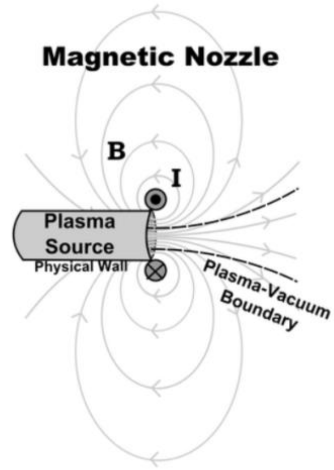

Figure 1: Schematic of magnetic nozzle.

Energy conversion mechanisms considered from an MHD perspective include generalized Hall effect and thermoelectric acceleration[5,6], directing the flow of fluid thermal energy[7], and Joule heating. Generalized Hall acceleration occurs due to the interaction of currents generated by the Hall effect with the applied field. Thermoelectric effects generate additional electric fields due to gradients in the electron density which can contribute to the Hall effect currents.[5] Hall effects can also result in a force which causes rotation of the plasma jet. [6] Fluid thermal energy is converted to axial kinetic energy due to the formation of a converging-diverging "magnetic wall". A current layer forms at the edge of the plasma which shields the inner plasma from the applied magnetic field and generates the confining force that guides the plasma flow. Simulations with resistive MHD codes (MACH2 and MACH3) have confirmed thrust generation by this process and show that the integrity of the current layer is crucial to efficient magnetic nozzle operation [8,9]. Joule heating describes the conversion of electromagnetic field energy into thermal energy in the plasma due to resistive heating.

Momentum transfer occurs due to the pressure of the plasma on the source walls and the Lorentz force resulting from the interaction of the induced currents and applied magnetic field. Diamagnetic induced currents are necessary to generate thrust in the plasma while paramagnetic currents can cause a drag force which reduces efficiency. [10]

MHD detachment scenarios considered include induced self-magnetic field effects[10], super-Alfvénic plasma flows[11], resistive diffusion[7,12], and magnetic reconnection. Self-field detachment can be achieved if strong diamagnetic currents are present which effectively cancel out the applied magnetic field.[10] Super-Alfvénic detachment can occur when the plasma flow velocity exceeds the Alfvén velocity. In this scenario the plasma drags the magnetic field lines along with it and significant field line stretching should occur.[11] Detachment through resistive diffusion occurs due to the plasma diffusing across the magnetic field lines due to collisions. This mechanism can result in drag losses on the plasma and significant anomalous diffusive transport can occur. [7,12] Finally, magnetic reconnection can facilitate detachment due to field line tearing and the formation of magnetic islands.

3. MHD Description and Parametric Analysis

The primary assumptions made in the derivation of the MHD governing equations are that the fluid behaves as a continuum, the ion mass is much greater than the electron mass ($m_{ion} \gg m_e$), and that the characteristic electron time scales are much faster than the bulk fluid time scales

($\omega_e \gg \omega_{fluid}$). The latter assumption implies that the electrons respond instantaneously to changes in the flow which leads to a simplification of the electron momentum equation into a force balance. This force balance can then be used to derive the generalized Ohm's law which provides closure to the MHD equations and allows for calculation of self-consistent magnetic fields.[13] The generalized Ohm's law is

$$\boldsymbol{E} = -\mathbf{U} \times \mathbf{B} + \frac{1}{n_e e}\boldsymbol{J} \times \boldsymbol{B} - \frac{1}{n_e e}\nabla(n_e k T_e) + \eta \boldsymbol{J} \tag{1}$$

In this equation the terms on the right hand side are referred to as the convective, Hall, electron pressure, and resistive terms respectively. The type of MHD model (ideal, resistive, Hall, etc.) and the physics captured by this model is defined by the terms which are kept in the Ohm's law. The relative importance of the terms in Ohm's law is found by an analysis comparing the terms.

The first relation of Ohm's law terms is shown in (2) and is found by comparing the convective to the resistive effects. The resulting non-dimensional number is known as the magnetic Reynolds number which gives a ratio of the convective to the resistive effects. High Re_m implies that the resistive effects are small which implies that the resistive term in Ohm's law can be ignored. For high Re_m the induced magnetic field can be large, which is important for the physical mechanisms such as formation of the current layer, induced field detachment, super-Alfvénic detachment, and magnetic reconnection.

$$Re_m = UL\sigma\mu_0 \tag{2}$$

The non-dimensional number comparing the Hall to the convective term and is shown in (3). The resulting non-dimensional number relates to the magnetization of the ions and compares a characteristic fluid frequency to the ion cyclotron frequency. Large values of this ratio imply that Hall effects are important compared to the convective contributions. Physically this relation implies that the ions are effectively demagnetized and a non-linear description is needed to describe their motion. Ion demagnetization is an important consideration in the detachment process as well as in the formation of Hall currents.

$$\Omega_{m,i} = \frac{\omega_{fluid}}{\omega_{c,i}} = \frac{U/L}{\omega_{c,i}} \tag{3}$$

Relation (4) compares the Hall term to the resistive term in Ohm's law. This ratio, known as the electron Hall parameter, compares the electron cyclotron frequency to the electron-ion collision frequency. The Hall parameter gives insight into the effective magnetization of the particles. Large Hall parameters suggest that the particles can complete cyclotron orbits many times before experiencing a collision, suggesting that the magnetic field significantly affects that species. This parameter is important in the thrust generation process because it can result in the formation of Hall currents which can contribute to the energy conversion process. For Hall currents to exist the ions must be effectively demagnetized so that a net current is produced.

$$\Omega_{H,e} = \frac{\omega_{ce}}{\nu_{ei}} \tag{4}$$

The final ratio is found by comparing the Hall to the electron pressure term and is shown in (5). The resulting non-dimensional number is known as the thermal β which gives a ratio of the plasma to the magnetic pressure. When this ratio is small the magnetic pressure is greater than the electron pressure and the electron pressure can be ignored in comparison to the Hall effects.

$$\beta = \frac{nkT_e}{B^2/2\mu_0} \tag{5}$$

These non-dimensional parameters are used to compare the terms in the generalized Ohm's law and identify the type of MHD model necessary to capture the important physical mechanisms in magnetic nozzles. We calculate these non-dimensional parameters for theoretical and experimental designs which incorporate magnetic nozzles shown in Table 1. The devices considered include the VAriable Specific Impulse Magnetoplasma Rocket (VASIMR) [14,15], fusion-based propulsion systems [8], the magnetoplasmadynamic arc jet (MPDA) [16], and the Helicon Double Layer Thruster (HDLT) [2,17]. The electron magnetization, $\Omega_{m,e}$, is also included as a measure of the validity of the MHD assumption that electron time scales are much faster than the bulk fluid timescales. Conditions change significantly as the plasma flows through the nozzle and the values selected represent only a single point.

		VASIMR [15]	Fusion [8]	MPDA [16]	HDLT [17]
Inputs	**Gas**	Argon	He	He	Argon
	n (#/m^3)	$1.00\cdot10^{19}$	$7.53\cdot10^{21}$	$5.00\cdot10^{20}$	$5.00\cdot10^{16}$
	T_{ion} (eV)	$1.00\cdot10^{2}$	$1.00\cdot10^{2}$	$1.50\cdot10^{1}$	$1.00\cdot10^{-1}$
	T_e (eV)	$6.00\cdot10^{0}$	$1.00\cdot10^{2}$	$5.00\cdot10^{0}$	$5.50\cdot10^{0}$
	U (m/s)	$4.00\cdot10^{4}$	$1.70\cdot10^{5}$	$2.00\cdot10^{4}$	$8.70\cdot10^{3}$
	L (m)	$5.00\cdot10^{-1}$	$1.80\cdot10^{-1}$	$3.00\cdot10^{-2}$	$1.50\cdot10^{-1}$
	B (Gauss)	$5.50\cdot10^{2}$	$9.44\cdot10^{3}$	$1.00\cdot10^{3}$	$1.38\cdot10^{2}$
Non-Dimensional Parameters	$\boldsymbol{\Omega_{m,e}}$	$8.27\cdot10^{-6}$	$5.69\cdot10^{-6}$	$3.79\cdot10^{-5}$	$3.03\cdot10^{-5}$
	$\boldsymbol{Re_m}$	$6.54\cdot10^{2}$	$2.83\cdot10^{5}$	$1.88\cdot10^{1}$	$3.03\cdot10^{1}$
	$\boldsymbol{\Omega_{m,i}}$	$6.04\cdot10^{-1}$	$4.16\cdot10^{-2}$	$2.77\cdot10^{-1}$	$1.75\cdot10^{0}$
	$\boldsymbol{\Omega_{H,e}}$	$4.56\cdot10^{2}$	$7.34\cdot10^{2}$	$1.59\cdot10^{1}$	$1.63\cdot10^{4}$
	$\boldsymbol{\beta}$	$7.98\cdot10^{-2}$	$3.41\cdot10^{-1}$	$1.01\cdot10^{-1}$	$5.81\cdot10^{-4}$

Table 1: Parametric Analysis of Magnetic Nozzle Systems

Small values of $\Omega_{m,e}$ found for all devices suggest that the basic MHD assumption of fast electron time scales is satisfied. The Re_m suggests that the resistive effects can not be ignored in most cases, with the exception being the fusion propulsion system. These calculations only consider classical diffusion, which has been shown to underestimate the resistive effects in plasmas. Bohm diffusion and anomalous diffusion processes may decrease the magnetic Reynolds number, increasing the importance of resistive effects. [12] The values of $\Omega_{m,i}$ are generally found to be near one, suggesting that the ions are nearly demagnetized and Hall effects may be on the order of the convective effects. Furthermore, as the plasma expands to weaker magnetic fields this term will become larger, increasing the effects of the Hall term. The ratios found for the electron Hall parameter also suggest that the Hall effects should be included when compared with the resistive effects. The electron pressure is found to be marginally important in all cases with the magnetic field pressure being stronger than the electron pressure as expected. Although this term is small in most, it is shown to be non-negligible in some.

Preliminary simulations have been performed using the Magneto Gas Kinetic Method (MGKM) which is generalized Ohm's law MHD code. The major result of these simulations shows rotation of the plasma jet and the formation of helical structure both in the velocity and currents within the jet. Challenges to future simulation are identified, with incorporation of the Hall term imposing restrictive time steps due to the unbounded Whistler wave characteristic.[18]

5. Conclusions

The physics of magnetic nozzles from an MHD perspective is discussed and previous studies are summarized and discussed. A parametric study of the generalized Ohm's law is performed. It is found from the parametric analysis and from a physics perspective that all terms of the generalized Ohm's law should be retained to capture all aspects of the thrust generation process. Future simulations and studies should thus include all terms in the generalized Ohm's law. Further considerations need to be taken concerning the continuum assumptions made in the MHD fluid model which are not considered here. [4]

6. References

[1] Jahn, R.G., (1968), "Physics of Electric Propulsion", McGraw-Hill.
[2] Charles, C., (2009),"Plasmas for Spacecraft Propulsion," J. of Physics: Applied Physics, Vol. 42, No. 16.
[3] Opher et. Al, (2004), "Magnetic effects at the edge of the solar system: MHD instabilities, the De Laval nozzle effect, and an extended jet", The Astrophys. Journal, 611, pp. 575.
[4] Ebersohn, F., Sharath, S., Staack, D., Shebalin, J., Longmier, B., and Olsen, C., (2012) "Magnetic Nozzle Plasma Plume: Review of Crucial Physical Phenomena," AIAA-2012-4274.
[5] Sasoh, A., (1994), "Generalized Hall Acceleration," J. of Prop. And Pow., 10, pp. 251.
[6] Longmier, B.W., et al., (2011), "Ambipolar ion acceleration in an expanding magnetic nozzle," Plasma Sources Science and Tech., 20.
[7] Gerwin, R., (2009), "Integrity of the Plasma Magnetic Nozzle", NASA/TP—2009-213439.
[8] Mikellides, I.G., et al, (2002), "Design of a fusion propulsion system-Part 2: Numerical simulation of magnetic-nozzle flows," J. of Prop. And Pow., 18, pp. 152.
[9] Lorzel, H. and Mikellides, P.,(2010), "Three-Dimensional Modeling of Magnetic Nozzle Processes," AIAA Journal, Vol. 48, No. 7, pp. 1494-1503.
[10] Ahedo, E. et al, (2010), "Two-dimensional supersonic plasma acceleration in a magnetic nozzle," Phys. of Plasmas, 17.
[11] Arefiev, A. and Breizman, B., "Magnetohydrodynamic scenario of plasma detachment in a magnetic nozzle," Physics of Plasmas, Vol. 12, 2005.
[12] Moses, et al, (1992), "Resistive plasma detachment in nozzle based coaxial based thrusters," AIP Conf. Proc., 246, pp 1293.
[13] Spitzer, L., (1965), "Physics of Fully Ionized Gases," McGraw-Hill.
[14] Chang-Diaz, F. "The VASIMR Rocket," Scientific American, Vol. 283, No. 5, 200 pp. 90-97.
[15] Araya, D.B. et al,(2011), "Parameterization of magnetic nozzle flow physics for an in-space propulsion application," AIAA-2011-4010.
[16] West, M.D. et al, (2008), "Testing a helicon double layer thruster immersed in a space-simulation chamber," J. of Prop. And Power, 24, pp 134.
[17] Inutake, M., et al., (2002) "Characteristics of a Supersonic Plasma Flow in a Magnetic Nozzle," J. Plasma Fusion Res., Vol. 78, pp. 1352.
[18] Ebersohn, F.,(2012), "Gas Kinetic Study of Magnetic Field Effects on Plasma Plumes", MS Thesis, TAMU.

ANALYTICAL CALCULATION OF THERMOACOUSTIC MAGNETOHYDRODYNAMIC GENERATOR

MIRHOSEINI[1] T., ALEMANY[2] A.
[1] KU Leuven, Department of Electrical Engineering ELECTA/ESAT, Belgium
[2]SIMAP/EPM, CNRS UMR 5266, 1340 rue de la piscine, 38402 ST Martin d'Hères, France
E-mail address of corresponding author: seyed.mirhoseini@esat.kuleuven.be

Abstract: This paper is devoted to the analytical investigation of a pulsating MHD flow in a cylindrical channel, submitted to an applied DC magnetic field and an imposed harmonically oscillating thermo-acoustically generated pressure gradient. Produced electrical current is extracted by induction coil in connection with compensation capacitor placed around the MHD channel. The effect of conducting wall is also taken into account. The generator is analytically modeled by solving the system of induction and Navier-Stokes equations simultaneously. Sensitivity analysis of efficiency, output power and different power losses versus MHD non-dimensional numbers are presented.

1. Introduction

Most of the magnetohydrodynamic devices make use of the fact that orthogonal electric and magnetic fields in a conducting medium will produce a Lorentz force and thus a particle velocity in the third orthogonal direction. This principle is based on the concept of devices such as electromagnetic pumps and propulsion systems [1]. The pumps transform electromagnetic energy into mechanical energy the reverse transfer occurs in acoustic MHD generators [2]. On the other hand, in the acoustic MHD devices the electromagnetic force and consequently the fluid flow are oscillatory [1, 3]. The schematic of the Thermoacoustic-MHD system is demonstrated in figure 1, where the MHD generator is submitted to thermo acoustic oscillatory pressure forces. Based on how to extract the produced electrical power from the generator, two types of machines can be considered:

- conduction machines, which produce strong electric currents at low voltage and require electrodes to collect the produced current, which may be a handicap for questions of water tightness, and,
- induction machines, that produce electric current with adjustable strength and voltage and do not require any electrodes [2], [4], [5].

This paper presents the results of the investigation of the MHD generator coupled with thermo acoustic engine. The liquid metal oscillates horizontally in the cylindrical MHD channel, under the effect of the oscillatory pressure difference due to the thermo acoustic engine. The magnet placed around the channel, produces a radial constant magnetic field. The interaction between this magnetic field and the liquid motion induce an AC current in the fluid, and AC induced magnetic field which producing AC current in the coil connected with the load. The system is depicted in figure 2.

2. Description of the model.

The main elements of the model are given in figure 2. The active part of the generator with the length l supposed to be larger than the MHD channel depth g , so that it could be considered as infinitely long. MHD channel contains a liquid metal with the density ρ , dynamic viscosity μ , relative magnetic permeability μ_f and electrical conductivity σ_f . The oscillatory pressure gradient applied by the thermo acoustic engine with the amplitude $\frac{\nabla p}{l}$ causes a velocity field with the value $u_0\hat{x}$ and a pulsation ω in the liquid metal. This velocity field is radially submitted to a constant magnetic field $B = -B_0\hat{r}$. The interaction will be resulted in an AC induced current $j\hat{\varphi}$ and an AC induced magnetic field $b\hat{x}$ producing an AC current i in the coil windings. Magnetic flux closes its path through the core and the yoke with relative permeability μ_i and μ_e, respectively. The coil has N turns and is connected in series with the load circuit, including a correction capacitor C_{Load} and a resistive load R_{Load}. The effect of the conducting wall on the power loss of the generator is also taken into account by placing a very thin metal layer with electrical conductivity σ_w in contact with the liquid metal. The main notations of the generator are listed in Table 1.

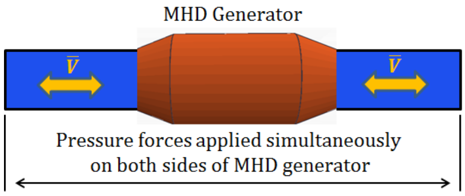

Figure 1. Schematic of the thermoacoustic MHD generator.

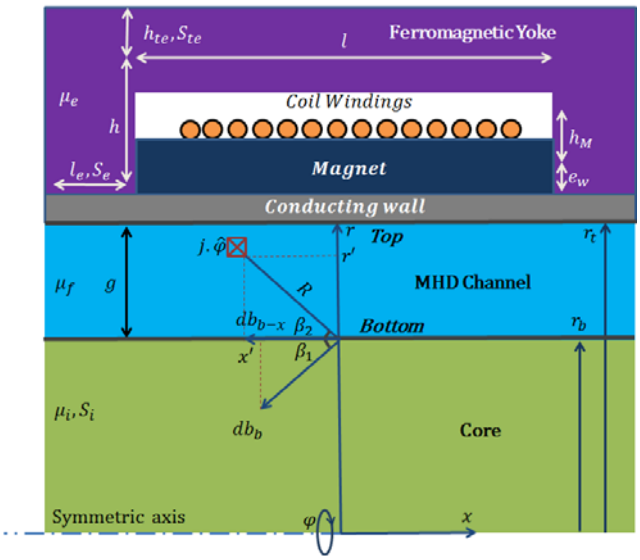

Figure 2. Schematic of the analytical model of the MHD generator, containing the core, MHD channel, ferromagnetic yoke, magnet and the induction coil.

3. Formulation of the problem

Governing equations are based on the following two sets:

a) Navier-Stokes equation which relates the velocity and the pressure with the Lorentz force
b) induction equation, which is a combination of Maxwell equations and Ohm’s law.

Two main approximations are considered in the calculations. Due to the long channel aspect of the system ($l \gg g$) and the symmetry in the φ direction, we have:

Table 1. Scales of the MHD generator

Scales	Explanation
r_b	inner radius of the MHD channel
r_t	outer radius of the MHD channel
g	channel gap
e_w	wall thickness
h_M	magnet thickness
h	inner height of the yoke
h_{te}	thickness of the yoke
L_B	length of the active part
l_e	length of the yoke pole
S_i	cross section of the core
S_{te}	cross section of the yoke
S_e	cross section of the yoke leg

$$\frac{\partial}{\partial \psi}, \frac{\partial}{\partial x} \approx 0 \tag{1}$$

Moreover, since the depth of the channel is assumed to be several times smaller than the radius of the channel ($g \ll r_t, r_b$), the variations of the channel radius in the differential equation are approximated with the average radius of the channel:

$$r = r_{ch} = \frac{r_b + r_t}{2} \tag{2}$$

The non-dimensional system of differential equations to be solved is achieved as follows:

$$\begin{cases} iu^* = -K_p + \frac{1}{R_\omega}\left(\frac{\partial u^*}{r_{ch}\partial r^*}\right) + \frac{N}{R_m}\frac{\partial b^*}{\partial r^*} \\ ib^* = \frac{u^*}{r_{ch}} + \frac{u\partial^*}{\partial r^*} + \frac{1}{R_m}\frac{\partial b^*}{r_{ch}\partial r^*} + \frac{1}{R_m}\frac{\partial^2 b^*}{\partial r^{*2}} \end{cases} \tag{3}$$

where u^* , b^* and r^* are the non-dimensional values for fluid velocity, induced magnetic field density in the fluid and the depth of the channel, respectively. Also K_p , *N*, R_ω and R_m are the pressure factor, interaction parameter, Reynolds number and magnetic Reynolds number respectively.

The order 4 of the differential system in (3) shows that 4 boundary condition are needed to be determined to solve the system. Two of the boundary conditions are defined simply by the non-slip wall constrain:

$$u^*(r^* = r_b) = 0 \ , \ u^*(r^* = r_t) = 0 \tag{4}$$

Magnetic boundary condition includes the induced magnetic flux density at the bottom b_{bx} and at the top b_{bt} of the MHD channel. The magnetic flux density at the bottom of the channel in the *x* direction is a summation of the following three induced flux densities:

- b_{xf} = Magnetic flux density because of induced current inside the fluid
- b_{xw} = Magnetic flux density because of induced current inside the wall
- b_{xL} = Magnetic flux density because of current in the load

The load circuit configuration consists of a resistive load R_{Load} , correction capacitor C_{Load} and the induction coil with N_c number of turns. The current in the load circuit is proportional to the induced magnetic field at the bottom of the MHD channel via (5).

$$i^* = \frac{C_{Load}\mu_0 N_c S_i \omega^2}{g(1 + iR_{Load}C_{Load}\omega)} b_{bx}^* \tag{5}$$

The last boundary condition is the induced magnetic flux density at the top of the MHD channel which item could be achieved by applying the Ampere law once at the bottom and once at the top of the channel:

$$b_{tx}^{*} = \frac{1}{2}\left[\left(\frac{\mu_f}{\mu_t}\right)^2\left(2\frac{g}{L_B}\frac{\mu_i}{\mu_f}\frac{S_i}{S_e}+1\right)+1\right]b_{bx}^{*} \tag{6}$$

4. Results and Discussion

The system of differential equations (3) could be solved with the four boundary conditions mentioned in the previous section. The analytical expression for the u^* and b^* are very long, and are not presented in this paper for the sake of abbreviation. The results are presented in this section for the non-dimensional values of $R_m = 0.051$, $R_\omega = 32512$, $K_p = 6.22$, $N = 0.57$ and the load factor of $5.68 \times 10^{-4} - i3.51 \times 10^{-3}$. Figure 3(a) represents the velocity profile in the channel. The core of the channel has constant velocity amplitude, while in the boundary layer, a reverse flow is observed that is caused by the viscosity. This effect is also visible in Fig. 3(b), representing the current density evolution near the wall at the same time. The phase shift of the velocity profile changes the induced magnetic flux density pattern in the boundary layer. Since the fluid induced current density is proportional to the *r*-derivation of the induced magnetic flux density, j also is deformed in the boundary layer.

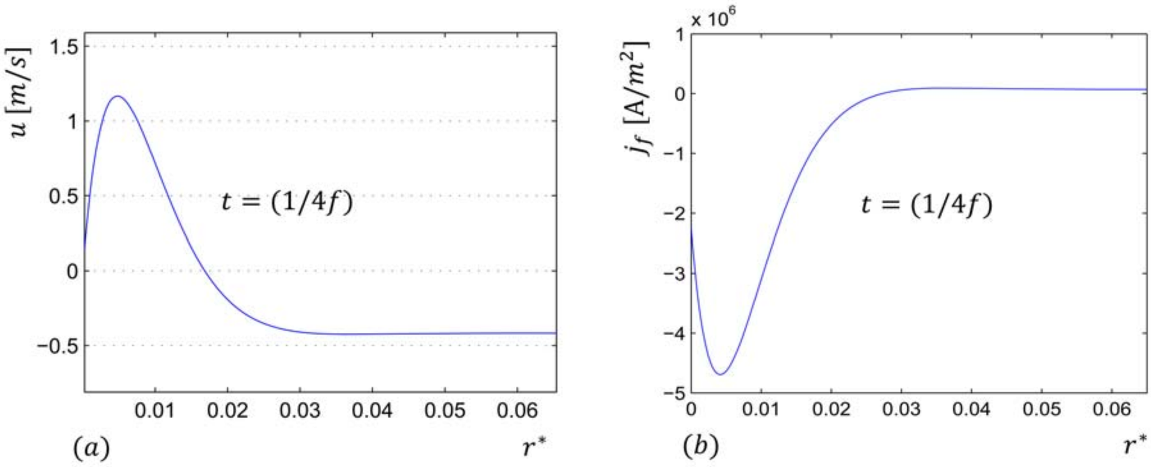

Figure 3. a) Velocity profile versus the channel depth at the time $t = 1/4f$, where a phase shif of velocity in the boundary layer is visible b) Induced current density profile versus the channel depth at the time $t = 1/4f$.

Efficiency behaviour as a function of magnetic Reynolds number and Reynolds number for fixed interaction parameter and different non-dimensional load resistances are demonstrated in figure 4 (a) and (b). It can be seen in Fig. 4(a) that for higher magnetic Reynolds number, the efficiency increases. That can be explained by the fact that by increasing the magnetic Reynolds number, the magnetic advection will dominate the magnetic diffusion in the fluid. This increases the effectiveness of the induction phenomenon and increases the induced current in the fluid and in the load. But by increasing the load resistance limits the current in the load circuit and will decrease the total output power. This enhances the efficiency of the system by making the fluid with better MHD qualities. The increase reaches saturation at higher values of R_m.

Figures 4(b) depicts the variations of the efficiency versus Reynolds number for four different non-dimensional load resistances and the constant interaction parameter and magnetic Reynolds number. This is a result of the fact that when increasing the frequency (R increases) the induced magnetic field does not penetrates in the conducting liquid and so the extracted power tends to zero as well as the efficiency.

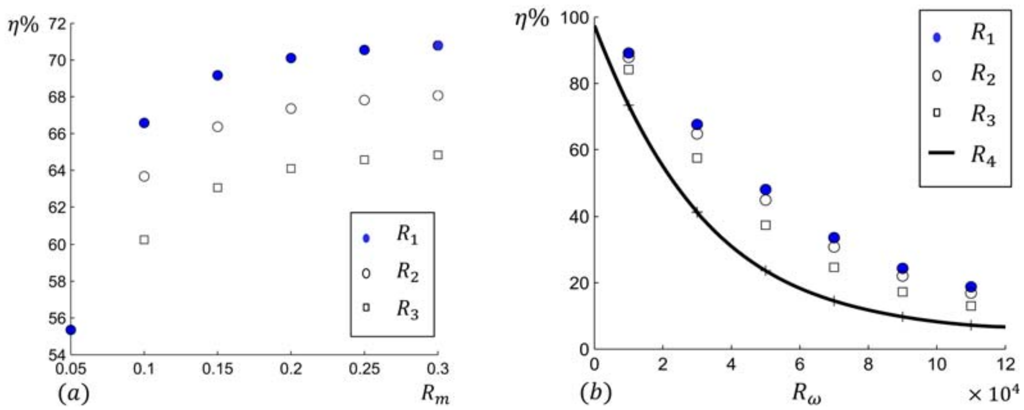

Figure 4. The efficiency versus a) magnetic Reynolds number and b) Reynolds number for different values of non-dimensional load resistances:
$R_1 = 4.57 \times 10^6$, $R_2 = 5.78 \times 10^6$, $R_3 = 9 \times 10^6$ and $R_4 = 1.98 \times 10^7$, with $N = 0.57$ and $R_m = 0.03$

5. Conclusion

This paper is about an analytical approach to study MHD generator which is in connection with a thermo acoustic engine that applies a fluid oscillation in the MHD channel. The analytical model is based on a system of differential equations, containing Navier-Stokes equation and the induction equation. The dimensionless differential equations are given exhibiting non-dimensional parameters. The solution of the system is achieved by applying the velocity and the induced magnetic field boundary conditions. The results of the different parameters and the sensitivity analysis of the system are presented for a specific situation.

6. References

[1] Castrejn-Pita, A. A.; Huelsz, G.: Heat-to-electricity thermoacoustic-magnetohydrodynamic conversion. Applied Physics Letters. 90, 174110 (2007).

[2] Alemany, A.; Krauze, A.: Al Radi, M.: Thermo acoustic - MHD electrical Generator. Energy Procedia, Vol. 6, 2011, 92100.

[3] Schreppl, S. C..; Busch-Vishni, I. J.: A magnetohydrodynamic underwater acoustic transducer. J. Acoust. Soc. Am., 89 (2), February 1991.

[4] Satyamurthy, P..; Venkatramani, N.: Quraishi, A. M.: Mushtaq, A.: A magnetohydrodynamic underwater acoustic transducer. Basic design of a prototype liquid metal magnetohydrodynamic power generator for solar and waste heat. Energy Conversion and Management, Vol. 40, 1999, 913-935

[5] Dixit, N. S.; Thyiagarajan, T. K.: Venkartramani, N.: Experimental study on the effect of insulating van and interaction parameter on current and voltage in a liquid metal MHD generator, J. Energy Conversion, Vol. 35, 1994, 643-649.

MEGAHIT: Update on the advanced propulsion roadmap for HORIZON2020

Mr. Jean-Marc Ruault, Mr Frédéric Masson
Centre National d'Etudes Spatiales (CNES) France,
jean-marc.ruault@cnes.fr, frederic.masson@cnes.fr
Dr. Jean-Claude Worms, Dr. Emmanouil Detsis
European Science Foundation, France, jcworms@esf.org, edetsis@esf.org
Mr. Enrico Gaia
Thales Alenia Space Italia, Italy, enrico.gaia@thalesaleniaspace.com
Dr. Frank Jansen
DLR Institute of Space Systems, Germany, frank.jansen@dlr.de
Dr. Alexander Semenkin
Keldysh Research Center, Russia, semenkin@kerc.msk.ru
Mr. Tim Tinsley
National Nuclear Laboratory, tim.tinsley@nnl.co.uk

1. Abstract:

A significant number of exploration missions, which require long duration and highly efficient power sources, require nuclear propulsion. The MEGAHIT project, funded by the European Commission under the 7th Framework Programme for Research and Technological Development, is a Supporting Action aiming at building a European roadmap for Megawatt level nuclear electric propulsion, in preparation of the Horizon 2020 programme. MEGAHIT sought to involve all interested European and Russian stakeholders (research, industry and agencies) in order to build a consolidated roadmap and to build a scientific and technical community on the topic in Europe and Russia. Mission analysis was conducted by KerC, and most promising missions were identified as Earth protection against NEOs, outer solar system exploration missions, and cargo missions to Moon or Mars. Large trade-off was conducted between possible technologies leading to down select 1 to 3 options for each main subsystem. A workshop was hold in Brussels on December 2013 and was attended by about a hundred specialists. It enabled the MEGAHIT consortium to consolidate the list of possible candidate technologies, to identify main technological gaps , and to establish the first drafts for the final roadmap.

2. Introduction:

Nuclear propulsion is an essential and enabling key asset for a significant number of exploration missions. Associated technological developments however require important financial efforts that can probably only take place in the frame of an international collaboration, sharing the efforts as this has been the case for the International Space Station.

MEGAHIT is a supporting action aiming at building a European roadmap for Megawatt level nuclear electric propulsion. It is funded by the European Commission under the 7^{th} Framework Programme for Research and Technological Development, in preparation of the Horizon 2020 programme, starting in 2014.

MEGAHIT is driven by a consortium that is coordinated by the European Science Foundation and that includes CNES, DLR, Keldysh Research Center, the National Nuclear Laboratory from

U.K. and Thales Alenia Space Italia. The consortium favors an open and participative approach in order that all interested stakeholders - research centers, agencies and industry- within consortium or not, can establish common research objectives and iniate research alliances. This approach will allow building a scientific and technical community on the topic in Europe and Russia. Potential collaboration opportunities at international level with other space fairing nations will be included.

3. Approach:

Megahit adopted an approach in 4 phases.

- **Phase 1: High level requirements**

Phase 1 collected inputs from space agencies and research centers on mission-related high level requirements.

- **Phase 2: Reference vision**

Phase 2 built a reference vision of what system we aim at, and what would be the best technological options.

- **Phase 3: Technological plans**

The rationale was that the best people for establishing technological plans are the stakeholders identified as being able to carry out the development. These stakeholders were associated through discussions and workshops on technologies they have expertise in.

Main workshop was held in Brussels on December 2013 and was attended by about a hundred specialists. The workshop had two goals: a) formalize the technological plans. and b) create a community, giving the opportunity to each stakeholder of having a complete view of the project, technologies and system.

- **Phase 4: Road-maps**

This is the current phase of the project. It aims at a synthesis of the three previous phases, translating into consistent road-maps what has been established in terms of key technologies and technological plans.

4. Missions and requirements

Mission analysis was conducted by KerC based on the following hypothesis/requirements:
Departure will be from a a sufficiently high orbit (800km or more). The spacecraft will be composed of at least 2 modules assembled in orbit: the transport power module with Nuclear Power Propulsion System (NPPS) (20tons) and the module with payload (20 tons). Radiators can be foldable. System can function 5 years in full power on a total lifetime of 10 years.

A strong requirement would be safety: the reactor shall remain subcritical at all times during launch, even in case of a launch failure.

Three family of missions emerged as the most promising:

- NEO deflection: deflection would be done acting as a gravity tractor. System could deflect a NEO of Apophis size.

- Outer solar system missions: several tons of payload could be sent in Europe or Titan within 3 years. A chemical stage, without gravity assist manoeuver, would put only 300kg of payload in this orbit.
- Cargo missions: Lunar orbit tug or manned Mars mission cargo support mission.

5. Reference Vision

Large trade-off was conducted between possible technologies (Cf. figure 1) leading to down select 1 to 3 options for each main subsystem. A very preliminary « high level » concept was established, to give rough order of magnitude of mass and thermodynamic maps

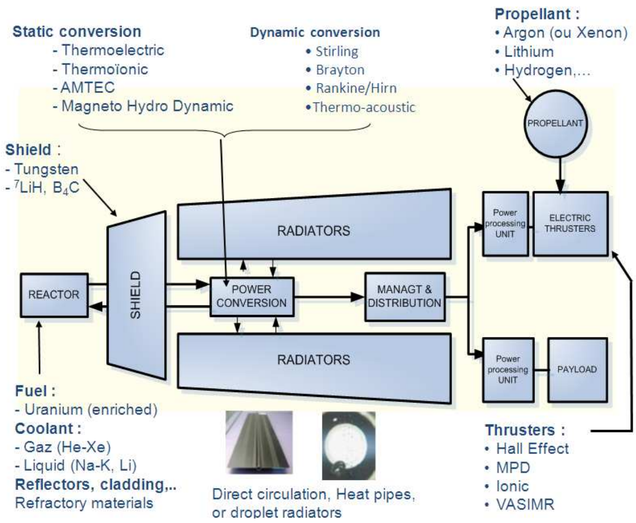

Figure 1 : general achitecture and list of candidates for subsystems.

Regarding the nuclear core, 3 fuel candidates UO2, UC and UN were retained for reference. High enrichment and fast spectrum were retained to optimize the mass, but also to follow UN recommendation to avoid Pu239 formation linked to thermal spectrum [1]. For shield, tungsten seems the best protection against gamma rays. Protection against neutron can be done with ^{6}Li, ^{6}LiH, and $^{10}B_4C$.

The reference for the thermo-electric conversion was taken to be the Brayton cycle. Heating is performed by the nuclear core at constant pressure, expansion is done in a rotating turbine coupled with an alternator. For power distribution, a hybrid architecture is preferred wrt centralized or channelized architectures. A direct-drive concept was chosen. Conversion based on thermo-acoustics coupled with Magnetohydrodynamic is a promising alternative to Brayton. This alternative may become the reference if current maturations going on in europe brings positive results.

The Radiator provides the cold source for the Brayton cycle. For radiator technology, a heat pipe system was selected due to its simplicity and good performance [2]. Droplet radiator is a promising technology under maturation, and was kept as a back-up. For other heat exchangers, plate heat exchanger was selected.

For electric thrusters, solutions with higher TRL levels were down-selected: hall-effect thrusters, ion engines and magnetoplasmadynamic (MPD) thrusters. MPD thrusters currently offer the highest thrust level [3].

On system level, it is proposed to consider a 1300K hot temperature as a reference because this level is mandatory to reach the specific mass objective for the system (<20kg/kWe). Two variants are then considered: a direct Brayton cycle with He-Xe an in-direct He-Xe Brayton cycle with a Lithium cooled core. In order to give an ambitious longer term perspective a third option was assessed: 1600K indirect Brayton cycle.

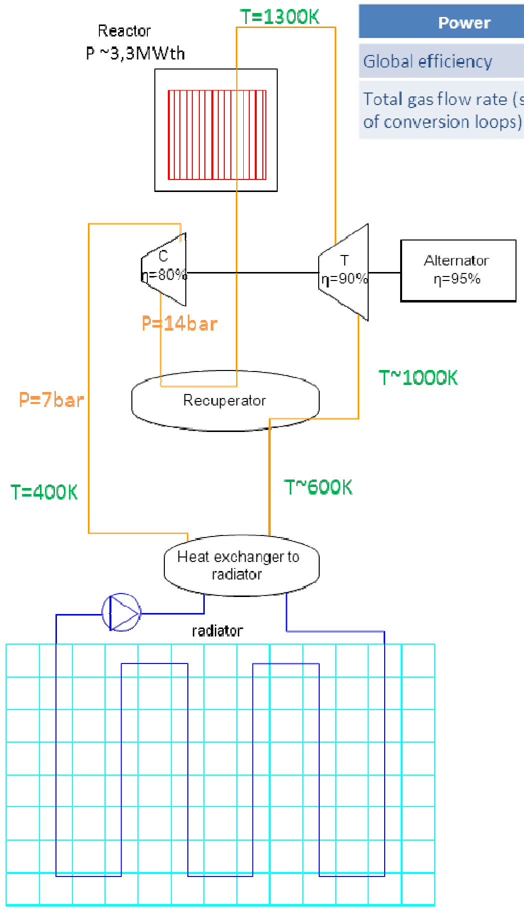

Power	1MWe
Global efficiency	~ 30%
Total gas flow rate (sum of conversion loops)	~45kg/s

Figure 2 : thermodynamic map for reference cycle n°1

Based on the technology trade-offs and on thermodynamic cycle, a preliminary architecture has been proposed:

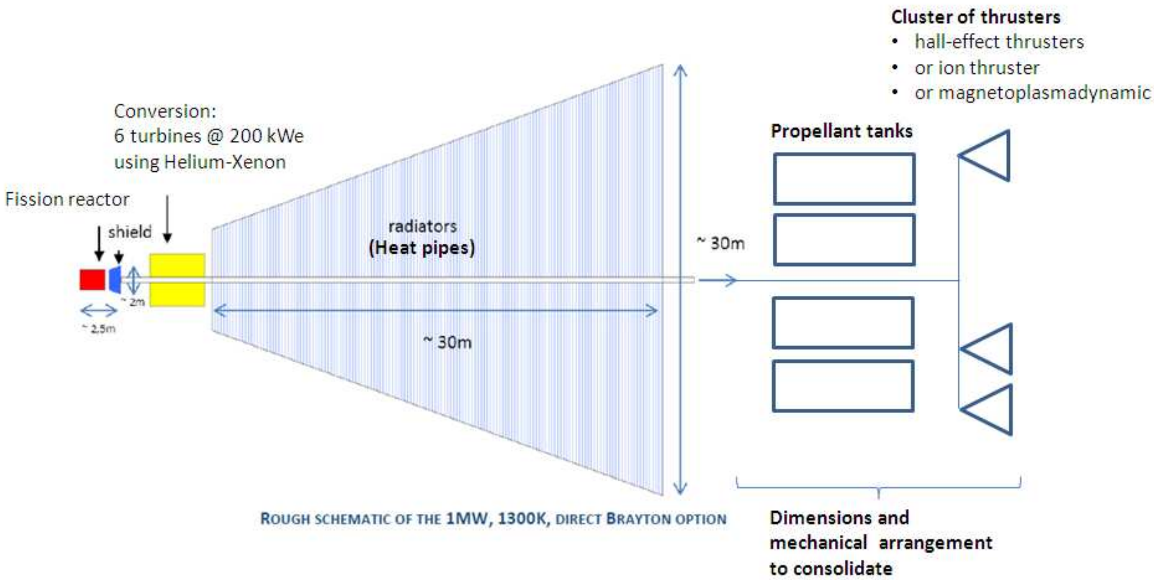

Figure 3 : preliminary architecture for nuclear electric propulsion system

6. First feedback from the workshop

The workshop enabled the MEGAHIT consortium to consolidate the list of possible alternatives, to identify the contested issues, and to establish the first drafts for the final roadmap.

Among the contested issues, the high working temperature and/or long life duration requirement will be a big challenge for the nuclear reactor, the turbine blade and disk, the bearings, and the heat exchanger between primary and secondary circuit (if a heat exchanger is required). New developments will be needed for these parts. A strategy for transient phases should also be defined, allowing coherent functionning between core, turbine, radiator and thrusters. The need to assemble many parts in orbit may require advances in robotics.

7. References

[1] 47-68 UN-COPUOS Resolution « Principles relevant to the use of nuclear power sources in outer space »
[2] “Intermediate Temperature Heat Pipe Life Tests” by W.G. Anderson of Advanced Cooling Technologies, Inc. and D.L. Ellis, NASA Glenn Research Center
[3] Gorshkov, O., Development of High Power Magnetoplasmadynamic Thrusters in the USSR, IEPC-2007-136
[4] Cliquet, E., Roux, J-P, et al., Study of space reactors for exploration missions, EUCASS 2011, Saint Petersburg, July 2-8th 2011

AUTHOR INDEX TO VOLUME 1